SET 2024

SHANGHAI

21st International Conference on Sustainable Energy Technologies
12 to 14th August 2024, Shanghai, China

Sustainable Energy Technologies 2024
Conference Proceedings: Volume 2

WSSET

World Society of Sustainable Energy Technologies

Proceedings of the 21st International Conference on Sustainable Energy Technologies

SET2024

12 – 14th August 2024, Shanghai, China

Edited by
Professor Saffa Riffat

Foreword

The 21st International Conference on Sustainable Energy Technologies (SET2024) held in Shanghai, China, from August 12–14, 2024, represented a significant milestone in the field of sustainable energy, uniting experts, researchers, and industry leaders from around the world. Organised through a collaborative effort between the World Society of Sustainable Energy Technologies (WSSET) and the Shanghai University of Electric Power, SET2024 served as a premier platform for the exchange of the latest technical innovations, presentation of cutting-edge research, and discussion of critical issues poised to shape the global energy landscape. This year's focus encompassed not only the research and development of sustainable energy technologies but also their applications, emphasizing the urgent need for energy security and the role of AI in achieving these goals.

The conference drew distinguished experts, scholars, and industry representatives who shared insights and recent advancements, fostering robust discussions and facilitating the practical application of scientific discoveries. This event also catalysed collaboration among universities, industries, and governments, reinforcing the essential link between research, policy, and industry practice.

The proceedings address core themes reflecting the multifaceted nature of sustainable energy development in Renewable Energy Technologies, Energy Storage and Conversion, Low Carbon Buildings and Sustainable Architecture, Sustainable Urban Development and Cities and Policies and Management. These topics highlight the interdisciplinary approaches and systemic shifts needed to support sustainable growth in energy sectors worldwide.

With participation from over 320 delegates and nearly 550 abstracts received, SET2024 provided an invaluable forum for exchanging both academic research and practical applications. We extend our sincere gratitude to all contributing authors for their commitment and invaluable contributions to both the conference and this publication. Special recognition goes to our international scientific committee for their guidance and thorough review of submissions, as well as to the organising committee, volunteers, and other contributors who made SET2024 a success. Our deep appreciation also goes to our sponsors PCM Products Ltd., Terry Payne, and UK EDU Ltd. for their generous support.

Thank you all for your commitment to advancing sustainable energy technologies and contributing to a shared future of innovation, sustainability, and collaboration.

Professor Saffa Riffat
Chair in Sustainable Energy Technologies
President of the World Society of Sustainable Energy Technologies
SET2024 Chair

Contents

#142: Transitioning building control and energy surveillance from Web 2.0 to Web 3.0 – A thematic review

Chaoju WANG[1], Tongyu ZHOU[2], Yinxue LYU[3], Isaac Yu Fat LUN[4], Jo DARKWA[5], Yuyan ZHOU[6], Yaru HE[7]

[1] University of Nottingham Ningbo China, 199 Taikang East Road Ningbo China, chaoju.wang@nottingham.edu.cn
[2] University of Nottingham Ningbo China, 199 Taikang East Road Ningbo China, Tongyu.Zhou@nottingham.edu.cn
[3] Sino-British College USST, 1195 Middle Fuxing Road Shanghai China, Shirley.Lyu@sbc.usst.edu.cn
[4] University of Nottingham Ningbo China, 199 Taikang East Road Ningbo China, Isaac.Lun@nottingham.edu.cn
[5] University of Nottingham, University Park Nottingham UK, Jo.Darkwa@nottingham.ac.uk
[6] University of Nottingham Ningbo China, 199 Taikang East Road Ningbo China, scyyz13@nottingham.edu.cn
[7] University of Nottingham Ningbo China, 199 Taikang East Road Ningbo China, scyyh13@nottingham.edu.cn

Abstract: In the Web 3.0 era, the integration of advanced sensing and actuation systems into buildings signifies a transformative step towards intelligent infrastructure. This evolution is marked by an increased focus on occupancy and space usage. With the deployment of numerous sensors, sophisticated data-driven frameworks emerge, enabling precise regulation and analysis of space utilisation and energy consumption. This advancement aids in energy conservation and emission reduction but also confronts the challenges of data management, necessitating substantial investments in software and hardware to ensure data accessibility and reliability. This thematic review synthesizes findings from 676 journal articles, examining the transformation to Web 3.0 in the building sector across three main areas: sensing networks, occupant-centric control, and performance evaluation. It investigates how occupant-centric paradigms are reshaping the mechanisms of data generation, control, and process in the Web 3.0 era. The discussion expands to the potential of leveraging smart buildings and large-scale sensor networks, underpinned by blockchain and Internet of Things technology, to enhance data interchange and consolidation across varied spaces and locations. This exploration uncovers novel avenues for innovation and emphasises the technological breakthroughs in the advancement of smart building ecosystems. However, the review also identifies a critical gap: the absence of standardized frameworks for decentralised network technologies in buildings, posing a substantial challenge for their efficient implementation. Future research should focus on algorithmic models under Web 3.0 to refine occupant-related theories across different spatial contexts, thereby enhancing the overall efficiency of building control and energy surveillance in the Web 3.0 era.

Keywords: Web 3.0, Smart Buildings, Occupant-Centric Control, Sensor Network, Blockchain

1. INTRODUCTION
1.1. Evolution of the Web and Smart Building Technologies

The internet has evolved from Web 1.0's static, read-only pages (Nath et al., 2014), which mirrored the early unidirectional intelligent building control systems (Yamada et al., 1999), to the highly interactive and user-engaged environment of Web 2.0 (Guo, 2022). This era introduced dynamic user-generated content and sophisticated building automation systems (Nagy et al., 2023), integrating advanced sensors and control systems that transformed buildings into smarter, more efficient, and more responsive entities (Peng et al., 2017). As the demand for energy efficiency and interactive systems grew, so did the need for standardisation and security in data handling, which were often lacking (JinCheng and Chuen, 2024).

Transitioning into Web 3.0, the focus has shifted to decentralised data exchange and ownership, employing technologies like blockchain and distributed computing to enhance data privacy and system efficiency (Chohan, 2022). This era supports a more integrated approach to smart building management, where data from diverse sources can be securely and efficiently managed, paving the way for buildings that are not only energy-efficient but also occupant-centric (Wu et al., 2022).

1.2. Research Gap

Despite the wealth of technologies (Nawari and Ravindran, 2019) discussed, literature reviews often focus narrowly on specific methodological tools or digital challenges within the smart building domain. Comprehensive literature reviews linking these technological advances to the infrastructural transitions in building environment control and energy usage from Web 2.0 to Web 3.0 are scarce.

1.3. Research Aim

This paper aims to review the evolution of monitoring and control systems within building environments across these web eras, particularly focusing on the implications of blockchain, decentralisation and thrustless interactions for occupant comfort, health, and preferences. It not only assesses past and current methodologies for controlling and monitoring indoor environments but also compares these efforts with emerging Web 3.0 strategies. This work deliberately excludes studies focused solely on energy policy and simulation research. Our analysis structured around three core components, i.e., sensing network, occupant-centric control, and performance evaluation, seeks to identify transformational roles and suggest further development of digital control systems in the Web 3.0 era.

2. METHODOLOGY
2.1. Literature Collection and Analysis

The collection and screening of literature are conducted in two stages. Initially, extensive searches through Web of Science and Google Scholar are carried out to index existing reviews on Web 3.0's impact on building environment control and energy monitoring. Key search terms included building control systems, environmental sensing, and occupant-centric control, with the search timeframe extending up to May 2024. In the second stage, the initially identified 7,574 papers were further screened for relevance, focusing on their application to building environment control within the Web 3.0 framework. Papers unrelated to the core focus, such as those from medical or materials science fields, were excluded, resulting in 676 pertinent reviews. Figure 1 presents the chronological distribution of these reviews, showing a notable increase in relevant publications from 2009 onwards, driven by advancements in digital environmental detection and IoT applications.

Figure 1: Chronological distribution of screened publications

2.2. Keywords mining result

Figure 2: Keywords mining result for filtered studies

Using VOS viewer, 3,879 initial keywords were narrowed down using a frequency threshold of eight mentions, resulting in 166 keywords that form the core thematic elements of this study. Figure 2 visualizes these keywords, grouped into three main research components:

- **Sensing network (red)**: The component is cantered around advanced technology and data management, highlighting the role of machine learning, IoT, and big data in optimizing building performance.
- **Occupant-centric Control (blue):** This component reflects the increasing emphasis on occupant needs in building environments and how control systems and measurements are becoming more intelligent to adapt to changing behaviour patterns and occupant demands.
- **Performance evaluation (green)**: This component focuses on evaluation metrics such as building performance, thermal comfort satisfaction, and sustainability. Data-driven evaluations employing techniques like reinforcement learning and neural networks are increasingly prevalent, promoting a consensus on sustainability efforts, including carbon emissions and life cycle assessments.

These components and their underlying keywords are analysed in detail in the following sections, exploring the efforts, current status, and trends in the transition process, highlighting how each component contributes to optimising the building environment in the Web 3.0 era.

3. SENSING NETWORK
3.1. Significance of sensing network in the building environment

Historically, automated control systems in large commercial buildings and institutions have restricted occupant interaction by providing only basic control over HVAC and lighting systems buildings (Park et al., 2019). However, the last decade has seen a significant shift towards occupant-centric controls, a change driven by enhanced spatial awareness and detailed data on indoor environmental conditions and occupant behaviours. This shift represents a move from environment-centric to occupant-centric systems, marking a significant evolution toward more personalized and adaptive building management.

In early research, the main focus of building environment control was predominantly on energy consumption and centralized control theories, which emphasized efficiency but often at the cost of occupant comfort and interaction quality (Dounis and Caraiscos, 2009). These limitations were partly due to the centralized characteristics of Web 2.0 systems, which focused on centralized data processing and lacked the flexibility to accommodate individual needs (Gholamzadehmir et al., 2020). Thus, this control mode had limitations in providing customized solutions and real-time responses. Traditionally, environment-centric control focused on maintaining optimal conditions based on preset parameters, often disregarding individual occupant preferences and behaviours. While effective in ensuring general comfort and energy efficiency, this approach lacks the flexibility to adapt to the dynamic needs of occupants. In contrast, occupant-centric control (OCC), facilitated by IoT, AI, and machine learning advancements, offers a more personalized approach (Stopps et al., 2021). This approach not only considers individual preferences but also adapts dynamically to changing occupant needs, enhancing both energy efficiency and comfort (Naylor et al., 2018).

Since the concept of Web 3.0 was introduced in 2013, interdisciplinary studies and the computer science field have increasingly focused on personalized control and distributed building control networks. This trend has shown a year-over-year increase. Web 3.0 emphasizes user data autonomy and privacy protection, and the structural design of massive data processing provides infrastructure

architecture support for the intelligent control of occupant-cantered building space (Nath et al., 2014). This evolution in building management enables economic and highly accurate optimization and management by real-time collection and analysis of extensive occupant behaviour and environmental data. Consequently, building control systems no longer merely respond to fixed environmental settings but can learn and adapt to occupants' preferences and behavioural patterns dynamically, thus optimizing energy efficiency and enhancing occupant comfort.

In the route of transition, advancements in computer science and network engineering have significantly improved the capabilities of architectural sensing networks. These networks now go beyond basic monitoring of model-related parameters to include integrated energy simulations, enhancing data collection and accuracy. A variety of devices such as sensors, cameras, and meters are utilized according to the specific goals and methodologies of the research. Once data is collected, control strategies and prediction models play a crucial role in identifying opportunities for energy savings, making these systems integral to intelligent building energy management strategies (Jurjevic and Zakula, 2023).

3.2. Technological advancements and improvements in the sensing network

In the transformation of sensing networks within the building environment, the infrastructures of the Web 2.0 and Web 3.0 eras differ notably in their utilization of internet backbone networks and embedded electronics. In Web 3.0, one of the key network features is the connection of datasets created in various coding languages across different locations (Pattal et al., 2009). This integration and analysis of data from diverse sources aim to reduce interoperability barriers. Nevertheless, Web 3.0 and 2.0 are not entirely disjointed; they share overlapping network technologies, such as in the development of embedded web services and sensing network protocols (Dobrojevic and Bacanin, 2022; Ozadowicz, 2024). Although still under development, Web 3.0 introduces unified, efficient, and feature-rich IoT infrastructure and building control systems across different brands, offering additional advantages like new functional interconnectivity. Table 1 shows the aspects differences in sensing network with requirements in data collection between Web 2.0 and 3.0.

Table 1: Comparison of sensing network specifications

Aspect	Web 2.0 Style	Transmitted to Web 3.0
Data Protocols	Transfer between local environment and web server	Peer-to-Peer (P2P) Network and distribution structure
Network Architecture	Centralized storage and organize	Decentralised, Distributed (Blockchain nodes, mesh networks)
IoT Network	Centralized Zigbee/ Wi-Fi systems	Decentralised Zigbee/ mesh Wi-Fi networks
Data Processing position	Central server processing	Edge and local processing
Data Privacy	Managed by central authority, higher risk	Enhanced through decentralization and encryption
Lag of data processing	Higher due to central processing	Lower due to local or near-source processing
Sensing Data Scalability	Limited by server capacity	Improved by adding more decentralised nodes
Cost	Higher infrastructure and maintenance costs	Potentially lower due to peer-to-peer systems and fewer middlemen

The shift towards IoT applications within the building environment reflects a transformative approach to infrastructure management. With decentralised architectures like mesh networks and blockchain nodes becoming more prevalent, IoT devices are now integrated to enhance operational efficiency and data security. For example, decentralised Bluetooth mesh networks allow for robust inter-device communication, enabling smart buildings to adjust systems like lighting and temperature dynamically based on real-time occupancy data (Ahmad et al., 2016; Niebla-Montero et al., 2022). This integration facilitates not only a significant reduction in energy consumption but also improves the scalability of sensing networks. By processing data at the edge, these IoT setups minimize latency and enhance privacy, with data encryption and localised decision-making reducing dependency on central servers (Fürst et al., 2016; Moudgil et al., 2023).

4. OCCUPANT-CENTRIC CONTROL
4.1. Significance of occupant-centric control in the building environment

The significance of models and algorithms in building control within the building environment cannot be overstated. These models are crucial for effectively utilizing data collected from sensing networks to control end devices through various energy management strategies. The parameters captured by sensing networks require translation through various energy management strategies and control models to effectively manage endpoint devices.

There are two primary types of environmental control strategies: passive and active.

- Passive control (indirect control): Passive control strategy influences occupant behaviour through energy awareness andpredicting future energy consumption to reduce utilization indirectly. This might include educating occupants about energycosts to motivate reduced energy use without directly interacting with HVAC or lighting systems. A lot of studies (Lo et al., 2014) in this field have shown that passive methods can effectively change the occupants' behaviour in energy consumption. These methods often utilize established evaluation techniques such as questionnaires and interviews to observe model performance (Torabi et al., 2022; Zhou et al., 2020).

- Active control (direct control): Active control strategy involves directly manipulating the building's actuators and sensor infrastructure to optimize physical system operations like power states and switching, thereby achieving immediate energy savings (Weinberg et al., 2023). Active control focuses on occupant-centric transformations, employing models that are either occupancy-centric or occupant behaviour-centric (Park et al., 2019). These models use data such as occupancy rates and counts to enhance system thermal comfort and energy consumption performance through various predictive and analytical models. Typically employed models include logistic regression and Support Vector Machines (SVM) for predicting occupancy scenarios(Gao et al., 2023); Random Forests and neural networks for analysing and predicting occupancy patterns based on historical data (Ngarambe et al., 2022); and statistical models such as empirical probability distributions (Buyle et al., 2013), and clustering techniques like k-means, along with k-nearest neighbour algorithms for more detailed analyses (Moradzadeh et al., 2022).

Both control strategies can be improved performance and reduce uncertainty through integrating occupant behaviour, with the core control logic illustrated as follows. By understanding and managing how occupants interact with building environments, systems optimize both comfort and energy efficiency. These methods include monitoring systems that dynamically adjust heating, lighting, and cooling based on occupancy and usage patterns, utilizing IoT devices (Wang et al., 2023), big data analytics (Tian et al., 2021), and machine learning (Zhang et al., 2023) to enhance real-time responsiveness (Jain and Garg, 2018). These monitoring systems typically gather occupant behaviour data through computer vision and environmental sensors for behaviour pattern recognition. Occupant preferences often show subtle variations in behaviour patterns, such as different adaptive actions within a space under varying lighting conditions. Consequently, behaviour-based models demand complex capabilities for real-time and dynamic responses. Typically employed models for analysing occupant behaviour include reinforcement learning (Nagy et al., 2023b), Markov chains (Gunay et al., 2013), Long Short-Term Memory (LSTM) networks (Markovic et al., 2021), and logistic regression (Dai et al., 2020). These tools are crucial for understanding and adapting to the specific actions of residents in real-time.
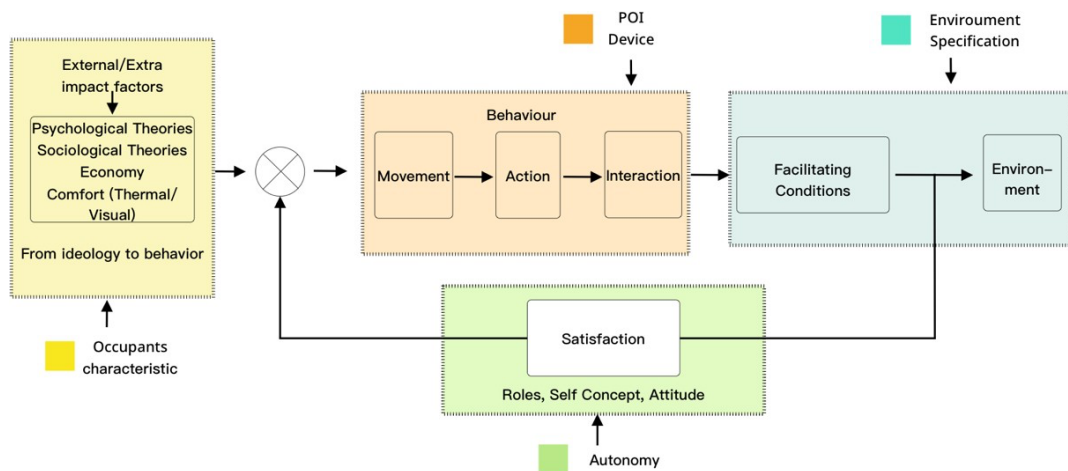
Figure 3: Control model for occupant behaviour centric

In the transformation of building environment systems towards Web 3.0, the processing and execution of control models play a crucial role. The integration of the IoT marks a shift towards decentralised, intelligent systems. While Web 2.0 relied heavily on centralized systems comprising sensors, actuators, and controllers for reactive building management, the transition to Web 3.0 introduces a more connected and collaborative framework. This shift enables decentralised, real-time control and monitoring, leveraging advanced sensing networks and wireless communication to enhance operational efficiency and adaptability.

4.2. Technological advancements and improvements in occupant-centric control

During the Web 2.0 era, the focus was on faster response times to local demands and matching space utilization changes. Systems were designed to be reactive, adjusting to real-time data from sensors to manage HVAC, lighting, and other environmental parameters. This reactive approach allowed buildings to adapt to immediate occupancy changes, providing a basic level of comfort and efficiency (Rhee and Kim, 2015). However, these systems often lacked the ability to predict future conditions or learn from historical data, limiting their effectiveness and efficiency (Hong et al., 2017).

In contrast, the transition to Web 3.0 emphasizes shared mechanisms and intelligent prediction across multiple buildings. Web 3.0 leverages decentralised technologies like blockchain and advanced AI algorithms to facilitate data sharing and collective learning among buildings. This approach enables systems to make more informed decisions based on a broader dataset, improving the accuracy and reliability of predictions (Wei et al., 2018). For example, by sharing anonymized data across a network of buildings, the system can learn from diverse occupancy patterns and environmental conditions, leading to more robust and adaptive control strategies (Mohandes et al., 2019). Web 3.0's shared mechanisms allow for the integration of data from multiple sources, creating a more comprehensive understanding of occupant behaviour and preferences (Tabadkani et al., 2021). This collective intelligence enhances the predictive capabilities of building management systems, enabling them to anticipate and respond to changes more effectively. The use of reinforcement learning, and neural networks further refines these predictions, allowing for continuous improvement and adaptation to evolving patterns (Weinberg et al., 2023). Additionally, the decentralization inherent in Web 3.0

provides enhanced data security and privacy, addressing the concerns associated with sharing occupant data (Woo et al., 2021). Table 2 summarises the differences between Web 2.0 and 3.0 in building management systems.

Table 2: Contrasts between Web 2.0 and Web 3.0 in building management systems

Aspect	Web 2.0 Style	Transmitted to Web 3.0
Occupant education	Relies on uniform documents or promotions	Environmental proactive behavioural interventions
Control transparency	Limited visibility into control logic	Increased transparency with blockchain integration
Interfaces	Standard, depend on manufacturer/supplier	Customizable, user-friendly interfaces
Human-related	Minimal focus on individual user needs	High customization based on user behaviour
System-related	Centralized control systems	Decentralised, autonomous systems
Reliability	Relies on central system stability	Enhanced by distributed nodes
Load flexibility	Rigid, inflexible load handling	Dynamic load adjustment capabilities
Cost	High due to centralized infrastructure	Potentially lower due to peer-to-peer systems

The primary objective of transitioning models and algorithms towards occupant-centric control is to achieve proactive control. Proactive control entails systems that not only respond to current conditions but also predict and pre-emptively adjust settings to optimize comfort and efficiency based on anticipated occupant behaviour and preferences. This shift aims to enhance the user experience by providing seamless and anticipatory adjustments, ensuring that the environment is always aligned with occupant needs without requiring manual intervention.

5. PERFORMANCE EVALUATION
5.1. Significance of performance evaluation in the building environment

For advancing both the efficacy and sustainability of architectural functionalities, the holistic approach to performance evaluation transcends mere operational checks, encompassing a broader spectrum of strategic assessments tailored to enhance energy conservation, ensure occupant comfort, and extend infrastructure longevity. Meticulously monitoring energy usage and system efficiencies not only leads to significant cost reductions but also aids in the rigorous adherence to environmental sustainability goals. With the advent of sophisticated analytics, building operations can identify specific inefficiencies, thus enabling targeted interventions that markedly improve energy management and reduce carbon footprints.

Evaluating occupants' needs and satisfaction has become increasingly paramount, reflecting a shift towards human-centric design principles in building management. This entails the optimization of environmental variables such as air quality, temperature, and lighting, which directly influence occupant productivity and well-being. Enhanced performance evaluation methods allow for the proactive adjustment of these parameters, ensuring that they meet the dynamic needs of building users while maintaining optimal energy usage.

The assessment of energy consumption performance and occupant-related factors can be divided into two categories: intrusive and non-invasive. Intrusive methods usually disrupt occupants' behaviour and the well-established evaluation techniques in information visualization (for example, questionnaires and interviews) are widely conducted in intrusive observation. Non-intrusive evaluations rely on the labelling of data sets and the tracking of performance metrics such as energy consumption within the control system. In non-intrusive methods occupants' behaviour is not affected by the experiment and measurements devices. It is different from the intrusive method that it can be used in long-term experiments and observations. Therefore, non-intrusive occupant observation is more widely used. From a technical point of view, the existing non-intrusive monitoring methods are mainly conducted through Wi-Fi, Internet of things (IoT) devices and sound sensors (Kim et al., 2020).

Incorporating predictive maintenance through performance evaluation marks a significant leap from traditional reactive maintenance strategies. By leveraging predictive analytics, potential system failures can be anticipated and addressed before they manifest, thereby avoiding costly downtime and extending the lifespan of critical building systems (Peruzzi et al., 2014). This proactive approach not only ensures continuous operational efficiency but also fosters a more sustainable management practice by optimizing resource use and minimizing waste.

The trajectory of performance evaluation in building environments is increasingly intertwining with Web 3.0 technologies. This synergy allows for a decentralised network of data sources and control mechanisms that enhance the granularity and responsiveness of building systems. In the vast field of building energy conservation research, the scale of performance evaluation is also expanding. As research cases transition from single building spaces to multiple spaces and even cross-regional assessments, a more open and scalable performance evaluation mechanism remains worthy of discussion and implementation (Li et al., 2024).

5.2. Technological advancements and improvements in performance evaluation

Web 2.0 systems often rely on questionnaires and surveys to assess occupant comfort and satisfaction within indoor environments. For example, participants' well-being might be surveyed using various methods, from less invasive questionnaires and sick leave reports to more invasive techniques like biological sampling. Many studies reported using questionnaires and scales to assess alertness/sleepiness, mental effort, workload, mental health, stress, subjective well-being, and quality of life, as well as symptoms like muscular ache, headache, eyestrain, and fatigue (Wu et al., 2023). Additionally, emotional states have been assessed through affective tests, self-reported mood assessments, and mood rating inventories (Boubekri and Boyer, 2017).

Web 3.0 focuses on more detailed metrics, especially with the integration of BIM (Building Information Modelling) and digital ledgers to track larger scale energy performance and more granular sustainability indicators. Additionally, it makes evaluating occupants' needs and satisfaction more dynamic and responsive. By incorporating occupant behaviour and more granular usage data, the accuracy and reliability of the data sources used in building performance assessment programs are enhanced. For instance, existing Standard Assessment Procedure (SAP) for new dwellings and Reduced SAP (RdSAP) for existing dwellings focus more on the cost-effectiveness performance of buildings rather than direct energy efficiency (Kelly et al., 2012). Integrating residential data on actual energy consumption to establish a standardized statistical database can strengthen the effective linkage between performance measurement, policy tools, and policy objectives (Carratt et al., 2020).

Table 3: Contrasts between Web 2.0 and Web 3.0 performance evaluation

Aspect	Web 2.0 Style	Transmitted to Web 3.0
Data Collection	Centralized systems gather limited, often manually reported data.	Decentralised systems automatically collect data from diverse sources.
Data Analysis	Data analysis often occurs in batch processes in centralized locations.	Real-time, continuous data analysis enabled by distributed computing.
Privacy & Security	Limited control over data privacy due to centralized data handling.	Enhanced privacy and security through encryption and decentralised storage.
Scalability	Scalability is limited by central server capacity.	Highly scalable through decentralised nodes reducing bottlenecks.
User Engagement	Minimal user interaction with systems, passive data usage.	Active user engagement with real-time feedback and interactive interfaces.
System Integration	Often siloed systems with limited integration capabilities.	Seamless integration across platforms and systems via interoperable protocols.
Cost Efficiency	Higher costs due to centralized infrastructure maintenance.	Lowered costs due to peer-to-peer operations and reduced middleman involvement.
Data Collection	Centralized systems gather limited, often manually reported data.	Decentralised systems automatically collect data from diverse sources.

6. CHALLENGES DURING THE TRANSITION
6.1. Implementation of Web 3.0

In reviewing 678 papers related to the digitalization of the built environment, it was found that only 32 examined network structures explicitly, and discussions around the structural development of Web 3.0 remain varied. A primary challenge identified is the integration of diverse IoT devices and sensors into a unified framework, which requires significant software innovation and addresses issues of data privacy through anonymization and secure protocols. As private data exchanges increase within robust data networks, enhancing protection against vulnerabilities and ensuring compliance with regulations like GDPR are critical.

The lack of universal standards for Web 3.0 technologies leads to potential fragmentation, necessitating a concerted effort to establish global standards that accommodate multiple stakeholders. Furthermore, these core concepts require extensive real-world testing and refinement to achieve a consensus on their practical application.

6.2. Role change in Web 3.0

In the Web 3.0 framework, traditional auxiliary controls offered to occupants—such as feedback interfaces—may lead to delays in implementing changes, affecting occupant satisfaction. Improving the speed and effectiveness of these controls is crucial. Additionally, balancing the personalized environmental needs of different occupants presents a challenge. While previous research in the Web 2.0 era highlighted a preference for retaining direct control over personal spaces, Web 3.0's decentralised solutions introduce complexities in adapting control systems to real-time changes in occupant behaviour and environmental conditions. Ensuring that occupants can maintain simple and effective control over their surroundings, without undue complexity or additional educational costs, is essential for a successful transition.

7. CONCLUSION

This paper has reviewed the literature on the transition of building environment control and energy usage surveillance infrastructure towards integrating Web 3.0 features. The rising concept of smart buildings and their large-scale applications announce a significant transformation, marked by the adoption of advanced sensing and actuation systems. Our review not only analyses specific case studies but also identifies the broader potential and challenges associated with the transition to Web 3.0:

- Technologies with Web 3.0 features, such as distributed networks and OCC, have received the attention and application of researchers in the built environment.
- The transition to Web 3.0 enhances the security of data transmission, protecting occupant privacy and enabling the expansion of sensing networks on a larger scale.
- In the transition to occupant-centric, control strategies are more reliant on online computing, using blockchain and smart contracts to update and secure control models.
- The focus of performance evaluation in smart buildings is shifting from generalised system control to more detailed terminal control, with performance indicators that are directly related to occupants' experiences.
- There remains a critical need to establish standards for decentralised network technologies and building control systems to ensure consistent and efficient implementation across the smart building industry.

The publication collection for this review was rigorously filtered to focus on relevant studies, but it may not cover all transitions to

Web 3.0 within building environments and control systems. Future research should continue to explore specific case studies and algorithmic models under Web 3.0. This will provide a comprehensive perspective on the reuse and evaluation of occupant-related theories and models across different spatial contexts, further enhancing the efficiency and functionality of smart buildings in the Web 3.0 era.

8. REFERENCES

Ahmad, M.W., Mourshed, M., Mundow, D., Sisinni, M., Rezgui, Y., 2016. Building energy metering and environmental monitoring - A state-of-the-art review and directions for future research. ENERGY Build. https://doi.org/10.1016/j.enbuild.2016.03.059

Boubekri, M., Boyer, L.L., 2017. A Comparative Study of Building Occupant Response to Luminous Displays in Real and Simulated Indoor Environments. Indoor Environ. 4, 113–120. https://doi.org/10.1159/000463617

Buyle, M., Braet, J., Audenaert, A., 2013. Life cycle assessment in the construction sector: A review. Renew. Sustain. ENERGY Rev. https://doi.org/10.1016/j.rser.2013.05.001

Carratt, A., Kokogiannakis, G., Daly, D., 2020. A critical review of methods for the performance evaluation of passive thermal retrofits in residential buildings. J. Clean. Prod. https://doi.org/10.1016/j.jclepro.2020.121408

Chohan, U.W., 2022. Web 3.0: The Future Architecture of the Internet? (SSRN Scholarly Paper No. 4037693). Social Science Research Network, Rochester, NY. https://doi.org/10.2139/ssrn.4037693

Dai, X., Liu, J., Zhang, X., 2020. A review of studies applying machine learning models to predict occupancy and window-opening behaviours in smart buildings. ENERGY Build. https://doi.org/10.1016/j.enbuild.2020.110159

Dobrojevic, M., Bacanin, N., 2022. IoT as a Backbone of Intelligent Homestead Automation. ELECTRONICS. https://doi.org/10.3390/electronics11071004

Dounis, A.I., Caraiscos, C., 2009. Advanced control systems engineering for energy and comfort management in a building environment-A review. Renew. Sustain. ENERGY Rev. https://doi.org/10.1016/j.rser.2008.09.015

Fürst, J., Chen, K., Aljarrah, M., Bonnet, P., 2016. Leveraging Physical Locality to Integrate Smart Appliances in Non-Residential Buildings with Ultrasound and Bluetooth Low Energy, in: 2016 IEEE First International Conference on Internet-of-Things Design and Implementation (IoTDI). Presented at the 2016 IEEE First International Conference on Internet-of-Things Design and Implementation (IoTDI), pp. 199–210. https://doi.org/10.1109/IoTDI.2015.35

Gao, H., Wang, X., Wu, K., Zheng, Y., Wang, Q., Shi, W., He, M., 2023. A Review of Building Carbon Emission Accounting and Prediction Models. BUILDINGS. https://doi.org/10.3390/buildings13071617

Gholamzadehmir, M., Del Pero, C., Buffa, S., Fedrizzi, R., Aste, N., 2020. Adaptive-predictive control strategy for HVAC systems in smart buildings - A review. Sustain. CITIES Soc. https://doi.org/10.1016/j.scs.2020.102480

Gunay, H.B., O'Brien, W., Beausoleil-Morrison, I., 2013. A critical review of observation studies, modeling, and simulation of adaptive occupant behaviors in offices. Build. Environ. https://doi.org/10.1016/j.buildenv.2013.07.020

Guo, Y.-Y., 2022. Revisiting the building energy consumption in China: Insights from a large-scale national survey. Energy Sustain. Dev. 68, 76–93. https://doi.org/10.1016/j.esd.2022.03.005

Hong, T., Yan, D., D'Oca, S., Chen, C., 2017. Ten questions concerning occupant behavior in buildings: The big picture. Build. Environ. 114, 518–530. https://doi.org/10.1016/j.buildenv.2016.12.006

Jain, S., Garg, V., 2018. A review of open loop control strategies for shades, blinds and integrated lighting by use of real-time daylight prediction methods. Build. Environ. https://doi.org/10.1016/j.buildenv.2018.03.018

JinCheng, Z., Chuen, D.L.K., 2024. Understanding the Evolution of the Internet: Web 1.0 to Web3.0, Web3, and Web 3+∗, in: Lee Kuo Chuen, D. (Ed.), Handbook of Digital Currency (Second Edition). Academic Press, San Diego, pp. 553–581. https://doi.org/10.1016/B978-0-323-98973-2.00052-6

Jurjevic, R., Zakula, T., 2023. Demand Response in Buildings: A Comprehensive Overview of Current Trends, Approaches, and Strategies. BUILDINGS. https://doi.org/10.3390/buildings13102663

Kelly, S., Crawford-Brown, D., Pollitt, M.G., 2012. Building performance evaluation and certification in the UK: Is SAP fit for purpose? Renew. Sustain. ENERGY Rev. https://doi.org/10.1016/j.rser.2012.07.018

Kim, J., Min, K., Jung, M., Chi, S., 2020. Occupant behavior monitoring and emergency event detection in single-person households

using deep learning-based sound recognition. Build. Environ. 181, 107092. https://doi.org/10.1016/j.buildenv.2020.107092

Li, T., Shapiro, M.A., Heidarinejad, M., Stephens, B., 2024. Ten questions concerning building electrification. Build. Environ. 261, 111653. https://doi.org/10.1016/j.buildenv.2024.111653

Lo, S.H., Peters, G.-J.Y., van Breukelen, G.J.P., Kok, G., 2014. Only reasoned action? An interorganizational study of energy-saving behaviors in office buildings. Energy Effic. 7, 761–775. https://doi.org/10.1007/s12053-014-9254-x

Markovic, R., Azar, E., Annaqeeb, M.K., Frisch, J., Treeck, C.V., 2021. Day-ahead prediction of plug-in loads using a long short-term memory neural network. Energy Build. 234. https://doi.org/10.1016/j.enbuild.2020.110667

Mohandes, S.R., Zhang, X., Mahdiyar, A., 2019. A comprehensive review on the application of artificial neural networks in building energy analysis. NEUROCOMPUTING. https://doi.org/10.1016/j.neucom.2019.02.040

Moradzadeh, A., Mohammadi-Ivatloo, B., Abapour, M., Anvari-Moghaddam, A., Roy, S.S., 2022. Heating and Cooling Loads Forecasting for Residential Buildings Based on Hybrid Machine Learning Applications: A Comprehensive Review and Comparative Analysis. IEEE ACCESS. https://doi.org/10.1109/ACCESS.2021.3136091

Moudgil, V., Hewage, K., Hussain, S.A., Sadiq, R., 2023. Integration of IoT in building energy infrastructure: A critical review on challenges and solutions. Renew. Sustain. ENERGY Rev. https://doi.org/10.1016/j.rser.2022.113121

Nagy, Z., Gunay, B., Miller, C., Hahn, J., Ouf, M.M., Lee, S., Hobson, B.W., Abuimara, T., Bandurski, K., André, M., Lorenz, C.-L., Crosby, S., Dong, B., Jiang, Z., Peng, Y., Favero, M., Park, J.Y., Nweye, K., Nojedehi, P., Stopps, H., Sarran, L., Brackley, C., Bassett, K., Govertsen, K., Koczorek, N., Abele, O., Casavant, E., Kane, M., O'Neill, Z., Yang, T., Day, J., Huchuk, B., Hellwig, R.T., Vellei, M., 2023a. Ten questions concerning occupant-centric control and operations. Build. Environ. 242, 110518. https://doi.org/10.1016/j.buildenv.2023.110518

Nagy, Z., Henze, G., Dey, S., Arroyo, J., Helsen, L., Zhang, X., Chen, B., Amasyali, K., Kurte, K., Zamzam, A., Zandi, H., Drgoňa, J., Quintana, M., McCullogh, S., Park, J.Y., Li, H., Hong, T., Brandi, S., Pinto, G., Capozzoli, A., Vrabie, D., Bergés, M., Nweye, K., Marzullo, T., Bernstein, A., 2023b. Ten questions concerning reinforcement learning for building energy management. Build. Environ. 241, 110435. https://doi.org/10.1016/j.buildenv.2023.110435

Nath, K., Dhar, S., Basishtha, S., 2014. Web 1.0 to Web 3.0 - Evolution of the Web and its various challenges, in: 2014 International Conference on Reliability Optimization and Information Technology (ICROIT). Presented at the 2014 International Conference on Reliability Optimization and Information Technology (ICROIT), pp. 86–89. https://doi.org/10.1109/ICROIT.2014.6798297

Nawari, N.O., Ravindran, S., 2019. Blockchain and the built environment: Potentials and limitations. J. Build. Eng. 25, 100832. https://doi.org/10.1016/j.jobe.2019.100832

Naylor, S., Gillott, M., Lau, T., 2018. A review of occupant-centric building control strategies to reduce building energy use. Renew. Sustain. ENERGY Rev. https://doi.org/10.1016/j.rser.2018.07.019

Ngarambe, J., Adilkhanova, I., Uwiragiye, B., Yun, G.Y., 2022. A review on the current usage of machine learning tools for daylighting design and control. Build. Environ. https://doi.org/10.1016/j.buildenv.2022.109507

Niebla-Montero, Á., Froiz-Míguez, I., Fraga-Lamas, P., Fernández-Caramés, T.M., 2022. Practical Latency Analysis of a Bluetooth 5 Decentralized IoT Opportunistic Edge Computing System for Low-Cost SBCs. Sensors 22,   8360. https://doi.org/10.3390/s22218360

Ozadowicz, A., 2024. Generic IoT for Smart Buildings and Field-Level Automation-Challenges, Threats, Approaches, and Solutions. COMPUTERS. https://doi.org/10.3390/computers13020045

Park, J.Y., Ouf, M.M., Gunay, B., Peng, Y., O'Brien, W., Kjaergaard, M.B., Nagy, Z., 2019. A critical review of field implementations of occupant-centric building controls. Build. Environ. https://doi.org/10.1016/j.buildenv.2019.106351

Pattal, M.M.I., Li, Y., Zeng, J., 2009. Web 3.0: A Real Personal Web! More Opportunities and More Threats, in: 2009 Third International Conference on Next Generation Mobile Applications, Services and Technologies. Presented at the 2009 Third International Conference on Next Generation Mobile Applications, Services and Technologies (NGMAST), IEEE, Cardiff, Wales, UK, pp. 125–128. https://doi.org/10.1109/NGMAST.2009.82

Peng, Y., Rysanek, A., Nagy, Z., Schlüter, A., 2017. Occupancy learning-based demand-driven cooling control for office spaces. Build. Environ. 122, 145–160. https://doi.org/10.1016/j.buildenv.2017.06.010

Peruzzi, L., Salata, F., Vollaro, A. de L., Vollaro, R. de L., 2014. The reliability of technological systems with high energy efficiency in residential buildings. ENERGY Build. https://doi.org/10.1016/j.enbuild.2013.09.027

Rhee, K.-N., Kim, K.W., 2015. A 50 year review of basic and applied research in radiant heating and cooling systems for the built environment. Build. Environ. https://doi.org/10.1016/j.buildenv.2015.03.040

Stopps, H., Huchuk, B., Touchie, M.F., O `Brien, W., 2021. Is anyone home? A critical review of occupant-centric smart HVAC controls implementations in residential buildings. Build. Environ. https://doi.org/10.1016/j.buildenv.2020.107369

Tabadkani, A., Roetzel, A., Li, H.X., Tsangrassoulis, A., 2021. A review of occupant-centric control strategies for adaptive facades. Autom. Constr. https://doi.org/10.1016/j.autcon.2020.103464

Tian, Z., Zhang, X., Wei, S., Du, S., Shi, X., 2021. A review of data-driven building performance analysis and design on big on-site building performance data. J. Build. Eng. https://doi.org/10.1016/j.jobe.2021.102706

Torabi, N., Gunay, H.B., O'Brien, W., Barton, T., 2022. Common human errors in design, installation, and operation of VAV AHU control systems-A review and a practitioner interview. Build. Environ. https://doi.org/10.1016/j.buildenv.2022.109333

Wang, H., Yu, D., Zeng, Y., Zhou, T., Wang, W., Liu, X., Pei, Z., Yu, Y., Wang, C., Deng, Y., Cheshmehzangi, A., 2023. Quantifying the impacts of posture changes on office worker productivity: an exploratory study using effective computer interactions asa real-time indicator. BMC Public Health 23, 2198. https://doi.org/10.1186/s12889-023-17100-w

Wei, Y., Zhang, X., Shi, Y., Xia, L., Pan, S., Wu, J., Han, M., Zhao, X., 2018. A review of data-driven approaches for prediction and classification of building energy consumption. Renew. Sustain. ENERGY Rev. https://doi.org/10.1016/j.rser.2017.09.108

Weinberg, D., Wang, Q., Timoudas, T.O., Fischione, C., 2023. A Review of Reinforcement Learning for Controlling Building Energy Systems From a Computer Science Perspective. Sustain. CITIES Soc. https://doi.org/10.1016/j.scs.2022.104351

Woo, J., Fatima, R., Kibert, C.J., Newman, R.E., Tian, Y., Srinivasan, R.S., 2021. Applying blockchain technology for building energy performance measurement, reporting, and verification (MRV) and the carbon credit market: A review of the literature. Build. Environ. 205, 108199. https://doi.org/10.1016/j.buildenv.2021.108199

Wu, S.R., Shirkey, G., Celik, I., Shao, C., Chen, J., 2022. A Review on the Adoption of AI, BC, and IoT in Sustainability Research. SUSTAINABILITY. https://doi.org/10.3390/su14137851

Wu, Y., Zhao, J., Cao, B., 2023. A systematic review of research on personal thermal comfort using infrared technology. ENERGY Build. https://doi.org/10.1016/j.enbuild.2023.113666

Yamada, F., Yonezawa, K., Sugawara, S., Nishimura, N., 1999. Development of air-conditioning control algorithm for building energy saving, in: Proceedings of the 1999 IEEE International Conference on Control Applications (Cat. No.99CH36328). Presented at the Proceedings of the 1999 IEEE International Conference on Control Applications (Cat. No.99CH36328), pp. 1579–1584 vol. 2. https://doi.org/10.1109/CCA.1999.801207

Zhang, X., Zhou, T., Kokogiannakis, G., Xia, L., Wang, C., 2023. Estimating the number of occupants and activity intensity in large spaces with environmental sensors. Build. Environ. 243, 110714. https://doi.org/10.1016/j.buildenv.2023.110714

Zhou, G., Gu, Y., Wu, Y., Gong, Y., Mu, X., Han, H., Chang, T., 2020. A systematic review of the deposit-refund system for beverage packaging: Operating mode, key parameter and development trend. J. Clean. Prod. https://doi.org/10.1016/j.jclepro.2019.119660

#144: Localized heating for visitor corridor within site museum using radiant floor heating and air curtain system

Jiaxuan Lɪ[1], Hanyu Lɪ[1], Runnan Sᴜɴ[2], Zhaolin Gᴜ[1], Xilian Lᴜᴏ[1,*]

[1] School of Human Settlements and Civil Engineering, Xi'an Jiaotong University, Xi'an，710049, China.
ljx18811517269@163.com
[2] School of Human Settlements and Civil Engineering, Xi'an Jiaotong University, Xi'an，710049, China.
767177096@qq.com
* School of Human Settlements and Civil Engineering, Xi'an Jiaotong University, Xi'an，710049, China.
xlluo@mail.xjtu.edu.cn

Abstract: A site museum is a special public building for preserving and exhibiting immovable historical sites. It typically features a large-space layout and requires high energy consumption for HVAC system. Its interior space can be categorized into three sections: visitor corridor, relics preservation area and a non-occupied space. Of these, the visitors corridor accounts for only about 20% of the total indoor space. Conventional air conditioning (AC) systems typically heat the entire exhibition hall, resulting in excessive energy consumption and inadequate thermal comfort for visitors. In this research, by using an air curtain to separate the visitor corridor from the large space exhibition hall, an underfloor heating system is proposed to provide local heating for the visitor corridor. An experimental exhibition hall and local heating system for the visitor corridor were constructed based on the spatial characteristics of Emperor Qin's Mausoleum Site Museum. A series of tests were conducted to evaluate the performance of the local heating system and consequently the system parameters were optimised. The results showed that the environmental parameters within the visitor corridor were regulated to temperatures of 18-22°C, relative humidity>30%, air velocity <0.3m/s, and a temperature difference of <2°C within the human-occupied space, providing a stable environment that meets the thermal comfort needs of visitors for short-term stays, and significantly reducing energy consumption compared to traditional HVAC systems and advancing energy conservation and emission reduction efforts. The proposed system provides an efficient and energy-saving strategy for local environmental control of visitor areas in large on-site exhibition halls.

Keywords: Local Heating, Underfloor Heating System, Air Curtain, Energy-Efficient Buildings, Indoor Thermal Comfort

1. INTRODUCTION

Site museums, specifically designated for the preservation and exhibition of immovable relics, constitute a distinct category of public buildings (Hu T. F. et al., 2015). These museums typically feature open-plan exhibition halls designed to facilitate intimate visitor interactions with the heritage relics. The internal layout is compartmentalized into visitors area, relics preservation area, and non-occupied space. Among them, the visitor areas, which generally constitute no more than 20% of the total expansive space, are strategically positioned as visitor corridors around the periphery of the relics areas (see Figure 1). There is a clear dichotomy in environmental requirements between visitors and relics (Huang X. Y. et al., 2023); however, the prevailing environmental control systems in large-space heritage exhibition halls fail to segregate the relics areas from the visitor areas. This lack of isolation adversely impacts on the environmental conditions within the relics areas due to the presence of visitors (Liu Z. J. et al., 2022). Furthermore, the spatial proportion of zones occupied by visitors and relics with specific environmental parameter requirements within the exhibition hall is comparatively minimal, as shown in Figure 1(b). Thereby, the substantial volume of non-occupied space within the exhibition hall markedly enhances the heating and cooling load when traditional full air-conditioning systems are employed for environmental control. This approach not only fails to achieve the thermal comfort standards required by visitors, especially during the heating season, but also leads to a predominant increase in the operational energy consumption of the air-conditioning system, which significantly contributes to the museum's exceptionally high building energy usage (Li H. X. et al., 2012). Therefore, the adoption of localized environmental control strategies within visitor corridors can substantially enhance thermal comfort for visitors, decrease the operational energy consumption of the HVAC system, and minimize disturbances to the relics areas environment induced by visitor presence.
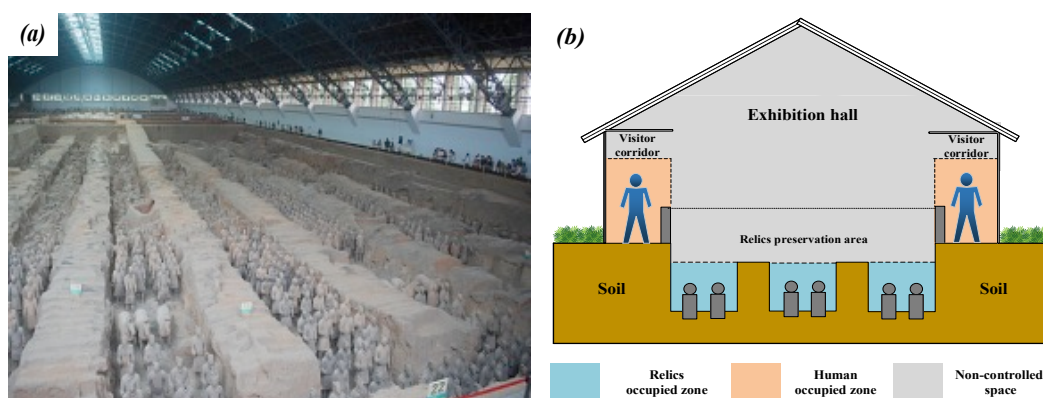

Figure 1: (a) The No.1 exhibition hall of Emperor Qin's Mausoleum Site Museum.(b) Schematic layout of environmental control zones in large space buildings.

Stratified air conditioning systems, employed in expansive structures such as sports arenas, shopping malls, and airport terminals, capitalize on the density variations of air across different temperatures to facilitate vertical stratification of environmental parameters. Common methodologies include displacement ventilation, jet ventilation, and radiant heat transfer. This strategic utilization effectively aligns with the localized thermal comfort requirements of occupants, ensuring occupied zones environmental control within these large spaces (Lin W. Y. et al., 2022). Notably, radiant heat transfer emerges as particularly advantageous due to its superior uniformity in maintaining consistent environmental conditions (Zhao K. et al., 2020). However, by comparing the layout of the occupied zones in Figure 1(a) and Figure 1(b), it is evident that the environmental control requirements within the exhibition halls of site museums manifest greater complexity compared to those in large spaces such as airport terminals. A distinct separation exists between the environmental needs of relics and visitors within exhibition halls, with these groups occupying specific and separate spatial zones. Customizing local environmental controls to address the distinct needs of various areas within the exhibition hall of site museums is imperative for minimizing the operational energy consumption of air conditioning systems and ensures that the environmental requirements of both visitors and relics are simultaneously met, optimizing both relics preservation and visitors thermal comfort. Considering the specialized preservation requirements of artifacts interred within the pits at the Terracotta Army Museum of Emperor Qin Shi Huang, Luo et al. (Luo X. L. et al., 2021) and Dang et al. (Dang Y. X. et al., 2022) have systematically conducted reconstructions of the localized environmental equilibrium between soil and air surrounding artifacts within experimental burial pits. This was achieved by employing attachment ventilation and displacement ventilation systems, facilitated through the establishment of simulated exhibition halls and burial sites. Additionally, they utilized the characteristics of inversion layer distribution of thermal demands across different areas, in conjunction with a nocturnal air curtain system, to facilitate localized heating for the relics areas (Luo X. L. et al., 2016). These advancements in research have substantially addressed the challenge of local independent environmental control tailored to the specific needs of relics areas.

Local environmental control in site exhibition halls still faces challenges, primarily due to the lack of isolation between visitor corridors, relics areas, and non-occupied space. Airflow between these regions induces fluctuations of environmental parameters in the relics areas (Huang Y. Y. et al., 2011) and inadequate insulation in the visitor areas (Luo X. L. et al., 2020), while additionally increased energy losses in the HVAC system (Li H. X. et al., 2012). Although glass walls can facilitate partitioning, the high humidity environment in relics areas often causes condensation on glass surfaces, resulting in water accumulation (Luo X. L. et al., 2021). Air curtains are extensively used because they can isolate different HVAC zones without obstructing visibility or impeding pedestrian traffic, finding applications in building entrance isolation, indoor pollutant separation, and fire prevention (Dang Y. X. et al., 2022; Yu L. X et al., 2018). Furthermore, air curtains are utilized for environmental segregation between visitor and relics areas within museums. To mitigate the adverse effects of air pollutants and fluctuations in temperature and humidity on the artifacts, Luo et al. (Luo X. L. et al.,

2020) devised and implemented an air curtain isolation and control demonstration system at the Terracotta Warriors' armor pit. This system has proven effective, achieving localized environmental control within the burial pit with an isolation efficiency exceeding 90%.

However, current research on archaeological sites exhibition halls predominantly addressed the problems of local environmental control within the relics preservation area. Studies focusing on the local environmental control of visitor corridors are scarce, especially during the challenging winter heating period. This is due to thermal buoyancy, which hinders the effective distribution of heated air from air conditioning systems to the lower human-occupied area of the building. Previously, Huang et al (Huang x.y et al ., 2023) employed jet ventilation within visitor corridors, utilizing high air velocities to ensure the circulation of warm air in human-occupied areas. Strategically, vertical air curtains were installed between the corridors and non-occupied spaces to facilitate precise, independent environmental control within the visitor corridors. However, operational outcomes had demonstrated that this high-velocity jet ventilation system induced a pronounced sensation of airflow discomfort among visitors (Ye X. et al., 2019). Consequently, to address the challenges of winter heating in visitor corridors of site exhibition halls, in this paper, a novel approachwas proposed, which integrated air curtain isolation with intermittent radiant underfloor heating for the visitor corridors, acknowledging the spatial zoning peculiarities of the Terracotta Warriors' large-space exhibition hall. By constructing a experimental exhibition hall and an experimental system, in this study, the environmental variations in visitor corridors under the operation of underfloor radiant heating and air curtain systems were independently investigated, both as the independent system and the coupled system to analyze the heating principles of the local heating system. And the influence of the coupled system on the effects of the local environment control in the visitor corridors was studied to evaluate the performance of the local heating system and to affirm the system's viability.

2. MATERIALS AND METHODS
2.1. Materials and Methods

In order to assess the operational performance of the experimental system, a corresponding simulation exhibition hall station was constructed in this study, referring to the architectural characteristics of the exhibition hall at the Emperor Qin's Mausoleum Site Museum, depicted in Figure 2(a). This exhibition hall was situated within the campus of Xi'an Jiaotong University, approximately 37 km from the Terracotta Warriors Museum, ensuring identical climatic and soil conditions. The experimental exhibition hall is divided into a relics area and a visitor corridor. The relics area comprises a rectangular pit measuring 4.0 m × 2.8 m × 2.0 m, with several soil columns approximately 0.5 m high at the pit bottom to simulate semi-exposed relics. Surrounding the relic preservation area, the visitor corridor encompassed it, and a segment of this corridor had been selected to establish a local environmental control experimental zone in this study. The dimensions of this zone in length, width, and height are 2.2 m × 2.3 m × 2.6 m, respectively. In the center of the visitor corridor, two thermal mannequins standing 1.75 m tall were symmetrically positioned to simulate visitors, each with a heat output of 95W.
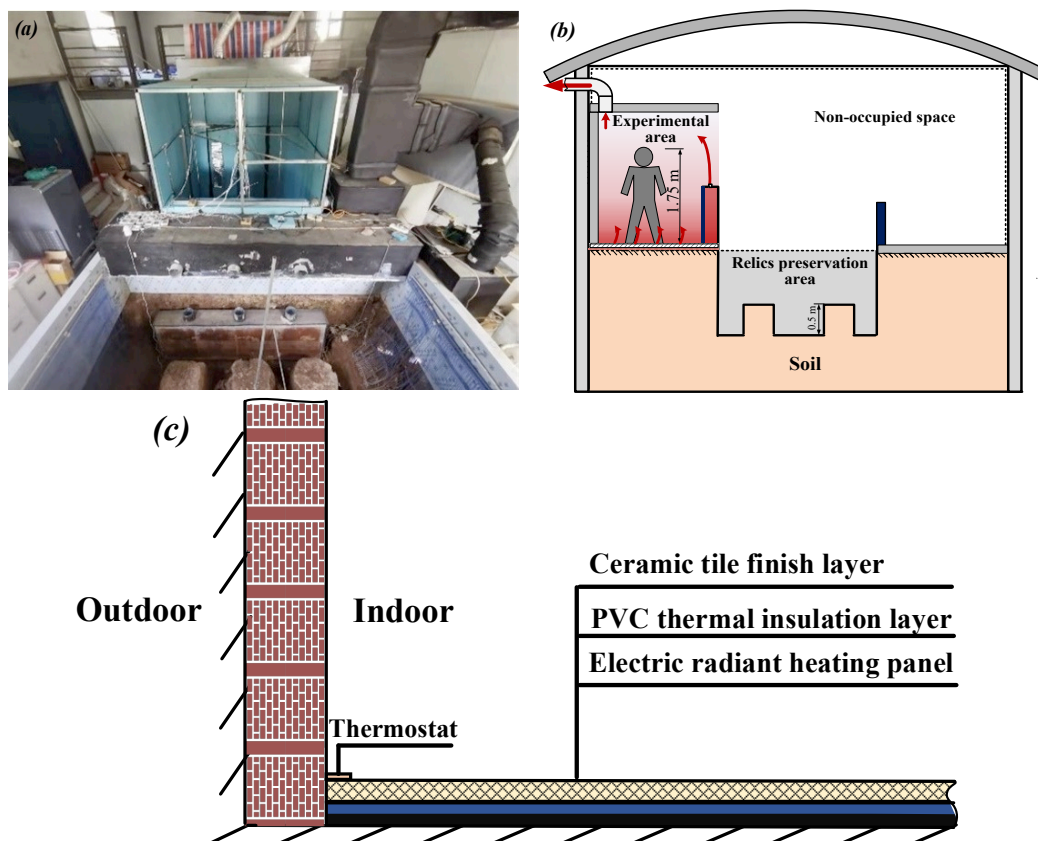

Figure 2: Structure of the experimental exhibition hall. (a) Interior layout of the exhibition hall. (c) Schematic diagram of the local heating system of the exhibition hall

The local environmental control system in the visitor corridor consists of a radiant floor and a thermal air curtain, as illustrated in Figure

2(b). The heating source for the radiant floor system consists of electric radiant panels, which cover an area equivalent to the visitors' corridor. These panels have a thickness of 0.25 cm. To prevent electrical leakage and surface overheating, an insulating layer is applied over the electric radiant panels, followed by a 1 cm thick layer of ceramic tiles. A thermostat is integrated into the radiant floor system to prevent continuous heating. The thermostat's sensor monitors the ambient temperature, automatically disconnecting the floor heating system when the temperature reaches 20°C and reactivating it when the temperature drops to 18°C. The system 's response time is within 5 min. The heating output of each simulated mannequin is 95 W.

2.2. Experimental methodology

To evaluate the independent control capabilities of this system on the local environment of the visitor corridor within the exhibition hall, this experiment measured the distribution and fluctuation of temperature and relative humidity (RH), as well as the distribution of wind speed in the visitor corridor experimental area. Additionally, temperature fluctuations were monitored in the relic preservation area, non-occupied areas, and outdoors. The layout of the relevant measurement points is depicted in Figure 4. Due to the positioning of the air curtain's inlets and outlets on both sides of the experimental area and their uniform distribution along the length of the area, coupled with the radiant floor covering the entire ground of the experimental area uniformly, the airflow organization within the visitor corridor of the experimental area exhibits two-dimensional flow characteristics. Consequently, the central plane of the experimental area was selected to represent the thermal environment of the visitor corridor. On this plane, three vertical lines at distances of 0.2 m, 1.0 m, and 1.9 m from the air supply outlet—designated as W (West), C (Centre), and E (East) were chosen. Along these vertical lines W, C, and E, measurement points for temperature and relative humidity (RH) were selected at heights of 0.1 m, 0.3 m, 1.1 m, 1.7 m, and 2.3 m from the ground. To assess the uniformity of temperature along the horizontal direction of the visitor corridor, as illustrated in Figure 3(a). In the center of the relic preservation area, a temperature measurement point T1 was selected at a height of 0.1 m above the pit bottom to represent the temperature within the relic preservation area, as illustrated in Figure 3(b).
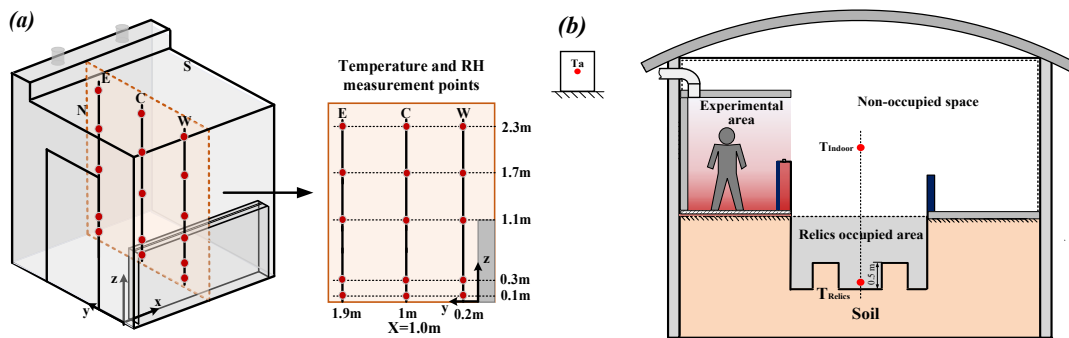

Figure 3: Arrangement of sensors. (a) Measuring position of the visitors corridor. (b) Measuring position of the relics preservation area, unoccupied space and outdoor environment

The parameters of the measuring instrument utilized in the experiment are listed in Table 1. Throughout the experimental process, temperature and relative humidity (RH) were recorded by sensors at fixed measurement points, with a sampling frequency of every 5 minutes.

The experiment was conducted from the end of December in 2023 to the beginning of January in 2024, which corresponds to the coldest period of the year in Xi'an, with an average outdoor temperature of 3.4°C. The operational hours of the experimental system coincided with the typical opening hours of most archaeological site museums in China, from 9:00 a.m. to 18:00 p.m. The system was activated one hour prior to preheating, and sampling was conducted from 9:00 a.m. to 18:00 p.m.

Table 1: Parameters of measuring instrument

Instrument	Model	Measurement accuracy	Measurement range
Temperature/RH sensor	TH11TO-EX	± 0.3 °C ± 2%rh	-40–85 °C 0–100%rh

2.3. Test cases

The challenge in winter heating is to address the issue of rising heat currents due to density differences, which leads to insufficient heating in the lower occupied zones and significant vertical temperature gradients. Radiant heating floors can provide uniform heating for occupied areas, ensuring a more consistent air temperature within these zones. However, on one hand, radiant floors require a relatively long preheating period; on the other hand, due to the openness of the visitor corridors, there is a significant exchange of cold and warm air between the inside and outside. The warm air curtain plays a crucial role in blocking the infiltration of cold air from outside the visitor corridor and the escape of warm air from within. It is a key factor in achieving independent environmental control of local areas within the visitor corridor. Additionally, the jet from the air curtain also assists in heating and humidity control. Therefore, to rigorously assess the efficacy of an integrated system combining underfloor heating with a hot air curtain, it is imperative to evaluate

14

the performance differences between systems operating independently versus those employing coupled control strategies. The jet velocity of the air curtain plays a pivotal role in its functionality. Insufficient jet velocity fails to establish a coherent air barrier, thereby diminishing the environmental isolation within visitor corridors. On the other hand, excessively high jet velocities can adversely affect the airflow dynamics within these spaces, leading to discomfort due to noticeable drafts, which ultimately compromises visitor thermal comfort. Thus, identifying the optimal jet velocity for the air curtain is crucial for maximizing its effectiveness while maintaining comfort levels. To achieve these objectives, the research findings for the following two scenarios were discussed in Chapter 3 of this study:

Scenario 1: The environmental control effectiveness in the visitor corridor was investigated under three different conditions: natural ventilation, operation of underfloor heating alone, and operation of the air curtain alone. The experimental cases were set as follows: all systems in the visitor corridor were shut off for the baseline measurement; the radiant floor was activated with the thermostat set to 20°C and the air curtain was turned off; the radiant floor was deactivated, and the air curtain was turned on with both supply and return airflow, and the average air curtain velocity was set to 2.5 m/s.

Scenario 2: The impact of air curtain jet velocity on the local environmental control within the visitor corridor was investigated. Both the underfloor heating and the air curtain systems were operated simultaneously, with the thermostat setting for the radiant floor set at 20°C. The average jet velocities of the air curtain were adjusted to 1.0 m/s, 1.5 m/s, and 2.5 m/s, respectively.

3. RESULT AND DISCUSSION
3.1. The performance of independent control systems for visitor corridors

In In the initial investigation, three different strategies for local environmental control in visitor corridors were assessed: natural ventilation (Case 1), underfloor heating (Case 2), and air curtain heating (Case 3). The operational param for each experimental configuration is delineated in Table 2. Herein, $\overline{V_C}$ and $\overline{T_C}$ correspond to the velocity and outlet temperature of the air curtain, respectively, $\overline{T_f}$ indicated the temperature of the heated floor, and $\overline{T_a}$ indicated the average external temperature during the periods when the exhibition hall was open to the public.

Table 2: Summary of system parameters in Cases 1-3

Case	Description	$\overline{V_C}$	$\overline{T_C}$	$\overline{T_f}$	$\overline{T_a}$	Date
		m/s	°C	°C	°C	
1	Natural ventilation	0	/	3.9	5.2	2023/12/31
2	Underfloor heating	0	/	29.8	8.0	2024/01/05
3	Air curtain	2.5	33.5	13.1	5.1	2024/01/07

Figure 4 showed the diurnal temperature variations along the visitor corridor from the inner wall (position E) to the center (position C) to the outer railing (position W) for Cases 1 to 3. Table 3 displayed the temperature fluctuations at various measurement points within the visitor corridor during the operational period of the exhibition hall for Cases 1 to 3. Figure 5a and Table 3 demonstrated that in Case 1, absent any heating sources within the visitor corridor and with the exhibition hall subjected to natural ventilation, the temperature readings across the corridor maintained remarkable uniformity, showing minimal variations both vertically and horizontally. The daily temperature distribution curves at various measurement points within the visitor corridor were consistent and exhibited diurnal trends similar to the outdoor temperature. During the opening periods of the exhibition hall, the average temperature fluctuations at positions E, C, and W within the human occupied zone (below 1.7 m) all equaled 4.6°C, with an average temperature 5.3°C closely mirroring the external temperature 5.2°C. This temperature significantly undershot the winter thermal comfort temperature recommendation for short-term visitor stays set forth in GB 50736-2012 (Dong Z. W. et al., 2021) at 17°C, which indicated that under natural ventilation, the temperature of visitor corridor was predominantly governed by external temperature fluctuations. Although the temperature distribution within the visitor corridor was uniform, the absence of heat sources failed to meet the thermal comfort needs of visitors.

Compared to Case 1, when the underfloor heating system was activated in Case 2, the visitor corridor experienced significant heating. However, due to the lack of isolation measures between the visitor corridor and the non-occupied space, the environmental parameters were noticeably disturbed by air circulation between these areas. The cold air from the non-occupied space intrudes into the visitor corridor over the railing, leading to substantial diurnal temperature fluctuations in the visitor corridor, which were strongly influenced by outdoor temperature variations. During the operational period of the exhibition hall, the average temperature fluctuated in the human occupied zone E, C, and W reached 7.7°C. These substantial temperature fluctuations can result in local thermal discomfort. The average temperatures in the human occupied zone E, C, and W were recorded at 13.7°C、13.5°C and 12.7°C, respectively, all remaining below 17°C. The persistent influx of cold air continued to inhibit the temperature within the visitor corridor from achieving the required standards.

When the air curtain heating was activated independently in Case 3, it can be observed that during the operational period, the warm air flow released by the air curtain primarily heated areas above 1.1 m in height. This resulted in insufficient heating near the floor, causing significant vertical temperature stratification at positions E, C, and W that the average temperature difference between 0.1 m and 0.7 m of the human occupied zone was exceed 6°C. The average temperatures at positions E, C, and W above 1.1 m were heated to 18.5°C、18.1°C and 18.6°C, while the average temperatures near the floor were only 12.8°C、12.7°C and 13.1°C, failing

to meet the required temperatures for short-term visitor comfort. Additionally, the air curtain heating system had a relatively long preheating time, leading to temperature fluctuations within the visitor corridor ranging 7-9°C.
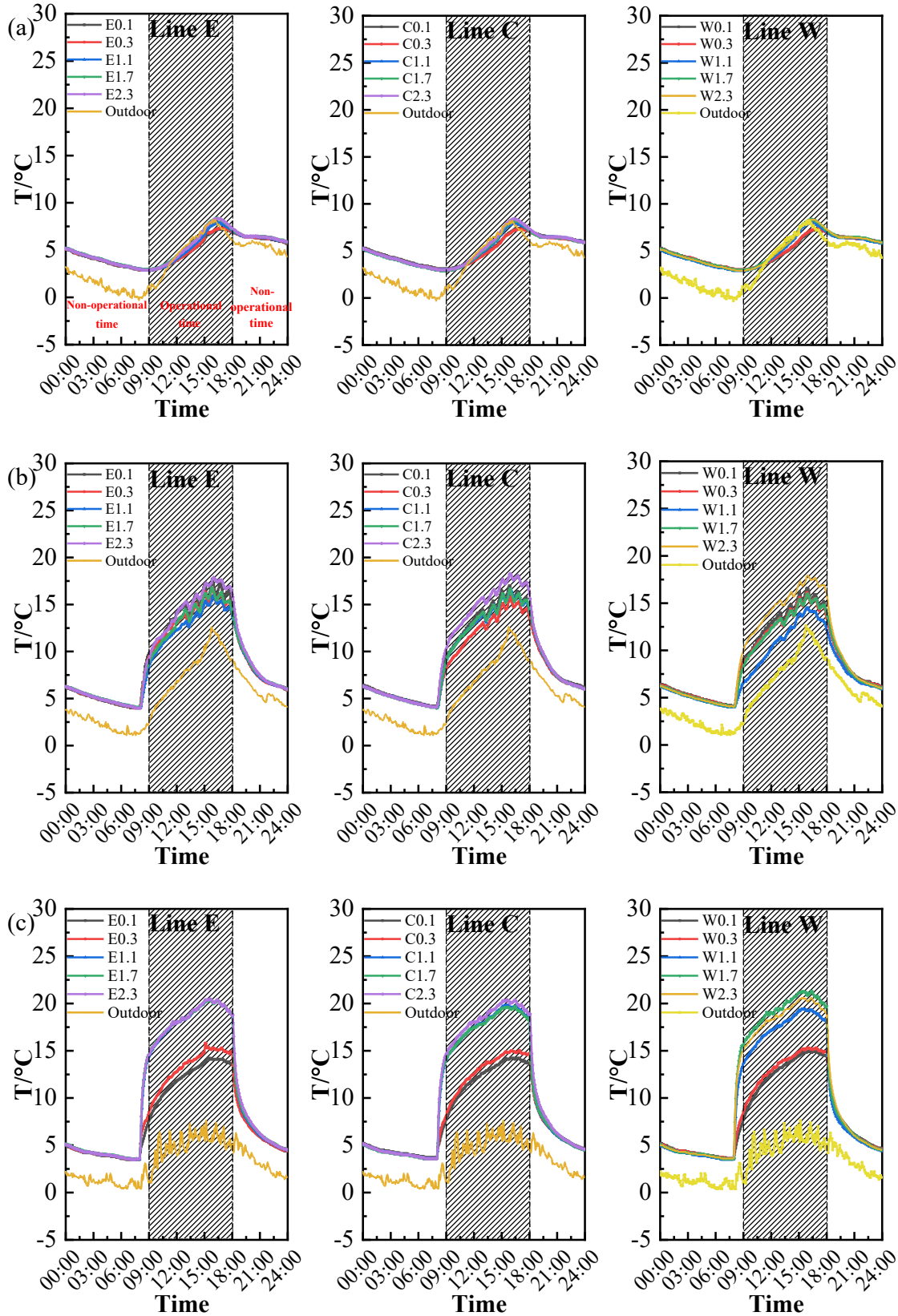

Figure 4: *Daily temperature variations for the lines E, C,W at different heights of the visitors corridor and outdoor.(a)Case 1.(b) Case 2 (c) Case 3*

16

Table 3: Summary of system parameters in Cases 1-3

Case	$\overline{\Delta T_{C0.1m}}$, °C	$\overline{\Delta T_{C0.3m}}$, °C	$\overline{\Delta T_{C1.1m}}$, °C	$\overline{\Delta T_{C1.7m}}$, °C	$\overline{\Delta T_{C2.3m}}$, °C
1	4.3	4.3	5	5.3	5.4
2	7.5	7.7	7.7	7.7	8
3	8.2	8.3	7.7	7.5	7.6
	$\overline{\Delta T_{E0.1m}}$, °C	$\overline{\Delta T_{E0.3m}}$, °C	$\overline{\Delta T_{E1.1m}}$, °C	$\overline{\Delta T_{E1.7m}}$, °C	$\overline{\Delta T_{E2.3m}}$, °C
1	4.3	4.5	5	5.4	5.4
2	7.9	7.3	7.5	7.9	8.7
3	8.2	8.9	7.9	7.7	7.8
	$\overline{\Delta T_{W0.1m}}$, °C	$\overline{\Delta T_{W0.3m}}$, °C	$\overline{\Delta T_{W1.1m}}$, °C	$\overline{\Delta T_{W1.7m}}$, °C	$\overline{\Delta T_{W2.3m}}$, °C
1	4.3	4.3	4.5	5.4	5.4
2	7.6	7.4	7.9	7.7	8.0
3	8.7	8.3	7.7	7.6	7.5

Table 4 presented the average RH in the human occupied zone during the operational period $\overline{RH_{occupy,9h}}$, the daily average outdoor RH $\overline{RH_{a,24h}}$, the daily average RH in the relics preservation area $\overline{RH_{relics}}$ and the daily average RH in the indoor non-occupied space $\overline{RH_{indoor}}$. The results indicated that under natural ventilation conditions, the RH levels in the visitor corridor, non-occupied space, and outdoor environment were very similar, with average RH values of 64.1%, 65.8%, and 68.0%, respectively. This further demonstrated that the exhibition hall environment under natural ventilation was controlled by the outdoor environment. The average RH in the human occupied zone of the visitor corridor for Case 2 with underfloor heating and Case 3 with the air curtain system were 51.3% and 39.1%, respectively, both of which meeting the first-level thermal comfort standards of greater than 30% for heating conditions as outlined in GB 50736-2012 错误!未找到引用源。. Compared to Case 1 and Case 2, the RH in the visitor corridor for Case 3 was lower, attributed to the lower outdoor RH on the day of Case 3, which resulted in a decrease in RH across all areas of the exhibition hall.

Table 4: Summary data of RH for visitor corridor, relics preservation area, non-occupied space and outside in Cases 1-3

Case	$\overline{RH_{occupy,9h}}$, %	$\overline{RH_{a,24h}}$, %	$\overline{RH_{relics}}$, %	$\overline{RH_{indoor}}$, %
1	64.1	65.8	88.5	68.0
2	51.3	64.1	89.0	53.6
3	39.1	57.9	81.5	56.7

3.2. Influence of air curtain airflow velocity on visitor corridor

According to the findings in Section 3.1, neither natural ventilation nor standalone underfloor heating or air curtain systems were able to meet the short-term thermal comfort needs of the visitor corridor in the exhibition hall during winter. However, coupling the underfloor heating with the air curtain system could be considered for independently regulating the environment of the visitor corridor. The air curtain airflow velocity is a crucial parameter in determining the feasibility of achieving local environmental control in the visitor corridor. Therefore, three different air curtain airflow velocity cases were set for testing. The operational parameters of the experimental system for each case were shown in Table 5.

Table 5: Summary of system parameters in Cases 4-6

Case	Description	$\overline{V_C}$ m/s	$\overline{T_C}$ °C	$\overline{T_f}$ °C	$\overline{T_a}$ °C	Date
4		1.0	30.7	36.2	2.4	2024/01/15
5	Floor heating and air curtain switched on	1.5	30.6	34.9	3.5	2024/01/16
6		2.5	29.9	31.5	4.8	2024/01/17

Figure 5 showed the diurnal temperature variation curves at the E, C, and W positions within the visitor corridor for Cases 4 to 6. The data indicated that during the non-operational hours (6:00 p.m. to 8:00 a.m.), the overall temperature within the visitor corridor, without the activation of environmental control systems, was predominantly influenced by the outdoor temperature, closely mirroring its fluctuations. Conversely, during the operational period (9:00 a.m. to 6:00 p.m.), it was observed that between 9:00 a.m. and 10:00 a.m., the temperatures within the visitor corridor for Cases 4 and 5 experienced a continuous rise of 1 to 2°C. Post 10:00 a.m., the temperatures stabilized, with fluctuations at the measurement points for Cases 4 and 5 remaining within 1°C from 10:00 a.m. to 6:00 p.m. However, in Cases 4 and 5, the temperature within the human occupied zone of the visitor corridor remained relatively low between 9:00 a.m. and 10:00 a.m., with average temperatures of 15.7°C and 15.6°C, respectively. These temperatures fell below the recommended value of 17°C, causing thermal discomfort for visitors during the morning hours. Furthermore, with air curtain velocities of 1 m/s and 1.5 m/s in Cases 4 and 5, significant vertical temperature stratification was observed at positions E and W.

Notably, the vertical temperature difference at position W exceeded 4 ° C, with some measurement points recording lower temperatures. This stratification was attributed to the insufficient isolation effect of the air curtain at lower velocities, which allowed noticeable cold air intrusion from the railing side. Consequently, the average temperature at 1.7m at position W in Cases 4 and 5 was only 14.7°C and 14.8°C, respectively, which fell below the recommended value of 17°C. The intruding cold air descended with increasing distance from the railing, resulting in the average temperature near the floor at position E, close to the inner wall, being only 15.0°C and 15.4°C, which also did not meet the standard. Therefore, air curtain velocities of 1.5 m/s and below were insufficient to achieve effective environmental control in the visitor corridor during winter. Furthermore, as shown in Table 4, due to the low temperatures within the visitor corridor at air curtain velocities of 1 m/s and 1.5 m/s, the temperatures did not reach the set values on the electric heating floor thermostats, causing the floor to continue heating. Consequently, the floor temperatures reached 36.2°C and 34.9°C, significantly exceeding the upper limit of the recommended 31°C for heated floors, potentially causing thermal discomfort for visitors.

Figure 5c showed that when the air curtain velocity in Case 6 increased to 2.5 m/s, the average temperatures at positions E, C, and W during the operation period were 18.7°C, 18.5°C, and 18.6°C, respectively. The overall temperature range was between 18°C and 20°C, with diurnal temperature fluctuations generally less than 1°C, meeting the thermal comfort requirements for visitors in winter. Compared to Cases 4 and 5, Case 6 exhibited minimal temperature stratification, with vertical temperature differences at different heights being less than 2°C. The temperatures at various measurement points across different positions were essentially consistent, which indicated that the air curtain effectively isolated the cold air outside the visitor corridor, resulting in a stable and uniform local environment within the visitor corridor. Additionally, small periodic temperature fluctuations were observed at various measurement points. This was due to the continuous heating of the floor to warm the air within the visitor corridor after the system was activated. Once the air temperature reached the set point of 20°C on the floor thermostat, the underfloor heating ceased and naturally cooled down. When the air temperature dropped to 18°C, the underfloor heating automatically resumed until the air temperature reached 20°C again. This design not only conserved electric heating energy but also effectively controlled the floor temperature, preventing thermal discomfort for visitors caused by continuous floor heating. As shown in Table 5, the average underfloor heating temperature decreased with the increase in air curtain velocity and the rise in room temperature. Case 6 exhibited the lowest average floor temperature at 31.5°C, which was close to the recommended value specified in ISO 7730.
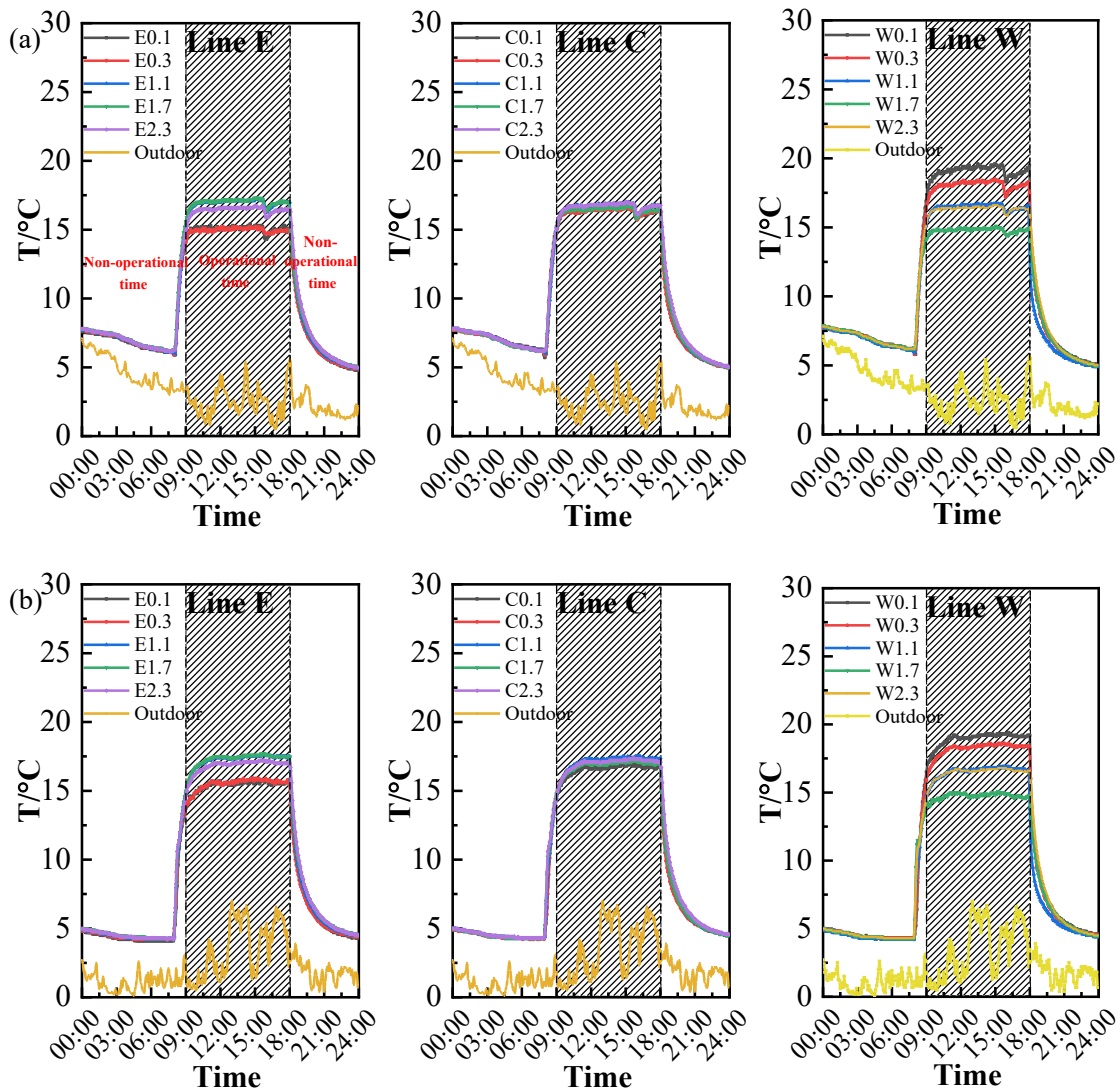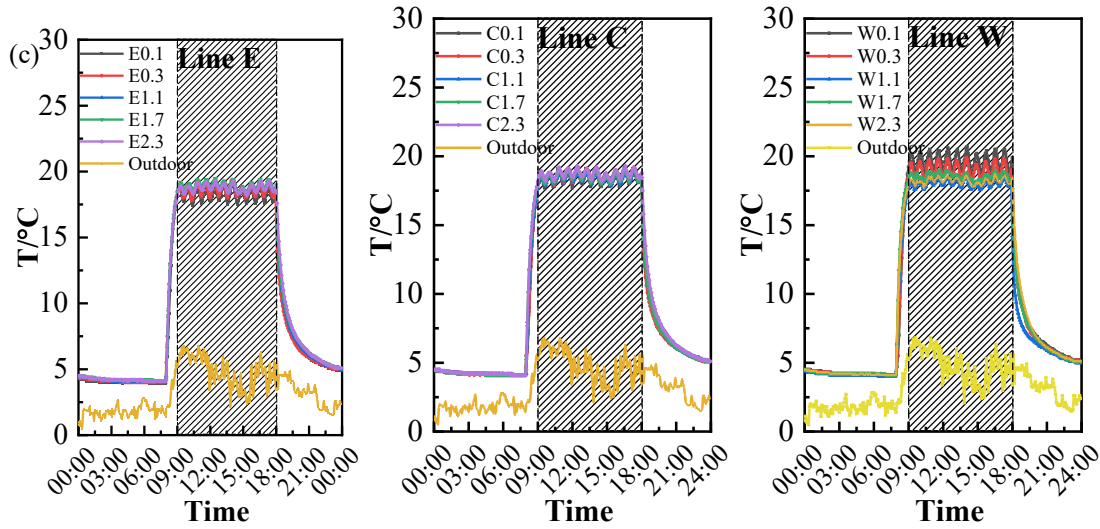
Figure 5: Daily temperature variations for the lines E,C,W at different heights of the visitors corridor and outdoor. (a) Case 4. (b) Case 5. (c) Case 6

Table 6 showed data for $\overline{RH_{occupy,9h}}$、 $\overline{RH_{a,24h}}$、 $\overline{RH_{relics}}$ and $\overline{RH_{indoor}}$. The results indicated that the average RH in the human occupied zone for Cases 4 to 6 were 48.5%, 49.1%, and 46.2%, respectively, meeting the first-level thermal comfort standard of more than 30% RH for heating conditions. Notably, Table 6 showed that in Cases 2 and 3, the average RH in non-occupied space exceeded 80%, surpassing the humidity comfort range for human. However, the RH within the visitor corridor remained stable and suitable, indicating that the underfloor heating and air curtain system could ensure that the local environment within the visitor corridor met the humidity requirements for visitors in winter.

Table 6: Summary data of RH for visitor corridor, relics preservation area, non-occupied space and outside in Cases 1-3

Case	$\overline{RH_{occupy,9h}}$, %	$\overline{RH_{a,24h}}$, %	$\overline{RH_{relics}}$, %	$\overline{RH_{indoor}}$, %
4	48.5	73.6	80.2	69.2
5	49.1	84.6	84.9	80.5
6	46.2	83.7	80.0	80.9

4. CONCLUSION

To achieve the objectives of reducing winter heating energy consumption in large-scale site museums, enhancing visitor thermal comfort, and minimizing visitor interference with environment of the relics area, a local heating system specifically for visitor corridors was designed in this study. An experimental setup was established, incorporating underfloor heating and air curtain systems within the visitor corridor of the experimental exhibition hall. A series of rigorous tests were conducted to assess the system's performance and optimize its parameters. The results indicated that:

The independent application of electric radiant floor heating and air curtain systems fails to meet the thermal comfort requirements for short-term visitor stays in winter within the visitor corridors. Underfloor heating provided uniform air heating, maintaining an average vertical temperature difference of only 1.25°C within the human occupied zone (up to 1.7m). However, the lack of isolation between the corridors and non-occupied space resulted in an average temperature of only 13.3°C and a daily fluctuation of 7.7°C. Conversely, the warm air curtain system effectively prevented cold air infiltration from non-occupied space and supplied upward warm airflow. Nonetheless, it inadequately heated the area below 1.1 m, leading to an average vertical temperature difference of approximately 6.3°C and a daily fluctuation of about 8.1°C within the human occupied zone.

The integrated system of floor heating and air curtain synergistically leverages the benefits of both modes while mitigating their individual limitations, thereby creating a comfortable thermal environment in the visitor corridors. The air flow velocity of air curtain is a pivotal factor influencing system efficacy. To establish an effective air curtain that prevents air exchange between the interior and exterior of the visitor corridor, an optimal air supply velocity is necessary. At an airflow velocity of 2.5 m/s, the average temperature within the human occupied zone was maintained at 18.6°C, with vertical temperature differentials of less than 2°C and daily temperature fluctuations under 1°C. Relative humidity (RH) was maintained between 45% and 50%, adhering to the level one thermal comfort standards for heating conditions. Additionally, the airflow velocity during the operation of the integrated system remained below the upper limit of 0.3 m/s for heating conditions, ensuring minimal airflow sensation and high thermal comfort for visitors.

5. REFERENCES

Dang Y. X., Luo X. L., Chang B., Huang X. Y., Feng Z. B., & Gu Z. L., 2022, Local attachment ventilation system for the unearthed relic preservation area within site museum, Sustainable Cities and Society, 77, 103537.

Dong Z. W., Zhang L. T., Yang Y. W., Li Q. F., Huang H., 2021, Numerical study on coupled operation of stratified air distribution system and natural ventilation under multi-variable factors in large space buildings, Energies, 14 (23), 8130-8130.

Hu T. F., Jia W. T., Cao J. J., Huang R. J., Li H., Liu S. X., Ma T., & Zhu Y. Q., 2015, Indoor air quality at five site museums of Yangtze River civilization, Atmospheric Environment, 123, 449-454.

Huang X. Y., Luo X. L., Shen C., Chang B., & Gu Z. L., 2023, Local heating of a visitor corridor within a large site museum exhibition hall via an integrated jet ventilation and air curtain system, Journal of Building Engineering, 69, 106206.

Huang Y. Y., Zhang L., & Han X. H., 2011, Application on the Stratified Air Conditioning System with Low Velocity in the Main Hall of the Temple, Advanced Materials Research, 1329 (280-280), 141-146.

Li H. X., Xiao W., Geng G., Li B. N., & Wang W., 2012, Field Test for Heat and Humidity Environment and Analysis of Air-Conditioning System Consumption, Advanced Materials Research, 610-613, 2875-2878.

Lin W. Y., Liu X. H., Zhang T., & Zhou Z. Q., 2022, Investigation of displacement and jet ventilation systems applied in an ice rink. Journal of Building Engineering, 50, 104179.

Liu Z. J., Wu M. N., Cao H. W., Liu H. Y., Wang H. N., Lv J. B., Rong R., & He J. Z., 2022, Impact of the visitor walking speed and glass barriers on airflow and Bioaerosol particles distribution in the typical open tomb, Building and Environment, 225, 109649.

Luo X. L., Gu Z. L., Yu C. W., Li K., & Xiao B., 2016, Preservation of in situ artefacts by local heating in earthen pit in archaeology museum in cold winter, Building and Environment, 99, 29-43.

Luo X. L., Huang X. Y., Feng Z. B., Li J., & Gu Z. L., 2021, Influence of air inlet/outlet arrangement of displacement ventilation on local environment control for unearthed relics within site museum, Energy & Buildings. 246, 111116.

Luo X. L., Lei S. L., Tian W., & Gu Z. L., 2020, Evaluation of air curtain system orientated to local environmental control of archaeological museum: A case study for the stone armor pit of Emperor Qin's Mausoleum Museum, Sustainable Cities and Society, 57, 102121.

Ye X., Kang Y. M., Yang F., & Zhong K. 2019, Comparison study of contaminant distribution and indoor air quality in large-height spaces between impinging jet and mixing ventilation systems in heating mode. Building and Environment, 160, 106159.

Yu L. X., Liu F., Beji T., Weng M.C., & Merci B., 2018, Experimental study of the effectiveness of air curtains of variable width and injection angle to block fire-induced smoke in a tunnel configuration. International Journal of Thermal Sciences, 134, 12-36.

Zhao K., Weng J. T. & Ge J., 2020, On-site measured indoor thermal environment in large spaces of airports during winter, Building and Environment, 167, 106463.

#145: Experimental study on cooling performance of underground pipe gallery ventilation enhanced by borehole heat exchanger

Cong SHEN[1,2], Tong WEI [1,2], Haonan JIANG [1], Zijun XU[2,3], Xilian LUO[1,*]

[1] School of Human Settlements and Civil Engineering, Xi'an Jiaotong University, Xi'an, 710049, China
[2] Key Laboratory of Shallow Geothermal Energy, Ministry of Natural Resources, Beijing, 100195, China
[3] Beijing Institute of Geothermal Investigation, Beijing 102218, China

Abstract: The building's underground pipe gallery can efficiently accommodate and consolidate various types of pipes, thereby enhancing land use efficiency. However, the abundant geothermal resources around the gallery remain underutilized. Shallow geothermal energy offers effective temperature regulation, providing warmth in winter and coolness in summer, thereby facilitating climate control in built environments. Research on the ventilation and heat exchange properties of these galleries remains limited. In this paper, a coupling system of cooling and ventilation in summer, which combines an underground pipe gallery with 6 U-shaped borehole heat exchangers, is studied. The performance of the system was evaluated by a full-scale experimental platform, and the cooling efficiency and the influence on the thermal environment of the room were explored under extreme weather conditions by directly using the underground pipe gallery and borehole heat exchanger to enhance cooling. The results showed that a significant temperature reduction of over 9.9 °C was achieved within the gallery. The cooling capacity is affected by ventilation volume, with lower volumes improving air-gallery heat exchange efficiency but reducing overall cooling capacity. Maximum cooling at a ventilation rate of 1918.8 m^3/h was 10.2 kW. The operation of the borehole heat exchanger significantly improved efficiency, with an average temperature reduction of over 16 °C and a peak cooling capacity of 13.3 kW, resulting in the test room being 1–2 °C cooler than a control room. Maximizing thermal comfort can significantly reduce air conditioning energy requirements. This research contributes to sustainable building design by quantitatively validating an underground pipe gallery coupled borehole heat exchanger system's cooling performance, offering a viable alternative to traditional energy sources for building air conditioning. It provides a sustainable and efficient climate control solution for the built environment.

Keywords: Passive Ventilation; Underground Pipe Gallery; Borehole Heat Exchanger; Full-Scale Experiment; Shallow Geothermal Energy

1. INTRODUCTION

Urban development has led to extensive underground space, totaling 2.962 billion m², comprising railway systems and utility galleries (Strategic Consulting Center et al., 2024). Abundant shallow geothermal energy (SGE) in the surrounding soil ensures stable internal air temperatures, offering natural heating and cooling (Dong et al., 2021).

Shallow Geothermal Ventilation (SGV) is a widely used passive technology of SGE for buildings in recent years (Liu et al., 2023), particularly suitable for underground spaces without heat source disturbance. It relies on the principle of drawing outdoor air into the ground, utilizing the high thermal inertia of the soil to preheat/precool the air in winter/summer, thus achieving indoor thermal comfort and reducing carbon emissions (Agrawal et al., 2019). With space cooling being the fastest-growing segment of energy consumption in the building sector, especially in hot regions, there has been a notable surge in electricity usage (IEA, 2018). Consequently, research efforts are focused on utilizing SGE as an alternative to conventional air conditioning for space cooling. Research on SGV currently focuses on earth-to-air heat exchanger (EAHE) because of its simple structure and easy operation. Outdoor environmental parameters predominantly influence their performance. D'Agostino et al (2020) investigated EAHE in different climatic zones in Italy. They found that the temperature difference between the inlet and outlet was less than 10 K in Lampedusa, while the maximum temperature difference was more than 17 K in Milan. Qi et al (2024) evaluated the EAHE system by multivariate analysis. They found that the inlet temperature had the greatest influence, followed by the inlet air velocity and the duct diameter.

Furthermore, in extreme weather conditions, the cooling capacity of EAHE may be insufficient, leading to outlet temperatures higher than the required supply air. Therefore, borehole heat exchanger (BHE) has been proposed, which uses vertical boreholes to transfer thermal energy with deeper soil layers to improve cooling efficiency without requiring additional land space, its number can vary from one to thousands depending on the demand (Lyu et al., 2020). Yuan et al (2017) proposed integrating a ground source heat pump with boreholes in an office building as an illustrative example. Simulation results indicated that this system enhances annual cooling efficiency and mitigates soil heat imbalance issues. However, various studies have focused on long pipe galleries, which often require special excavation or processing, resulting in complicated construction and hindering widespread adoption. Additionally, the cooling capacity of these galleries is restricted, and the combined use of heat pumps requires significant investment.

In this study, a full-scale experimental platform was constructed to investigate the building's existing underground pipe gallery (UPG) as an alternative to traditional EAHE, forming the Underground Pipe Gallery Ventilation system (UPGV) for primary air cooling. Additionally, six U-shaped boreholes, comprising the UPG coupled Borehole Heat Exchanger Ventilation system (UPG-BHEV), were installed to provide secondary air cooling and meet the building's air temperature requirements. The impact of UPGV and UPG-BHEV on indoor thermal environments under varying air volumes in hot summer was investigated. The system's cooling performance and potential for indoor cooling under different modes were assessed, offering practical solutions for utilizing existing building structures in high-density urban areas with limited land availability for EAHE installation. Furthermore, valuable insights for low-carbon building design and renovation strategies are provided.

2. METHOD
2.1. Case study

The full-scale test apparatus is situated in Xi'an, Shaanxi Province, China (34 °N, 108 °E). Specifically, the experimental site is housed in the Yuanju Building (No. 7 Building) on the iHarbor Campus of Xi'an Jiaotong University, which is a prime example of a "low-carbon building for synergistic conversion and use of natural energy sources" designed together with teachers and students to meet the dual-carbon goal. The building comprises of four floors above ground and one basement, with a total area of 10,010 m², as shown in Figure 1a. The test area is located on the first floor as a meeting room, and the building contains UPG connected to the room and vertical BHE, which forms a building ventilation system to provide fresh air to the room.

Due to the thermal inertia of the soil, the temperature tends to be lower than the air temperature in summer and vice versa in winter. In summer, UPG utilizes a fan to draw in warm outdoor air, which undergoes cooling through an air-gallery wall heat exchange system before being distributed throughout the room. When achieving the desired air supply temperature proves challenging, a BHE is employed for secondary air-water cooling following heat exchange with the soil via circulating water, thus ensuring the room's cooling needs are met.

The ventilation system mainly consists of UPG, BHE, and a test room with a control room to validate the cooling performance. The inlet of UPG is 1.3 m above the ground with dimensions of 1.5 m × 2 m. The UPG is buried at 1.5 m depth, 23.0 m length and a cross-section of 2.0 m × 2.0 m. The gallery contains a Φ = 0.3 m air condition supply and return pipes with thermal insulation to minimize the impact of the pipe on the air in the gallery. The gallery is ventilated with outside air by a 1.1 kW fan driven by a frequency converter. The inlet area of the fan is 0.2 m × 0.5 m. The test room measures 16.2 m × 9.0 m × 3.6 m and employs underfloor air distribution measuring 0.6 m × 0.2 m, while the control room measures 8.0 m × 9.0 m × 3.6 m. The BHE comprises 6 U-shaped boreholes, spaced 5.0 m apart and extending to a depth of 120 m. The secondary cooling system incorporates these boreholes, connections to the ground heat exchanger, a 0.73 kW water pump, and an expansion tank. The experimental system configuration is illustrated in Figure 1b.
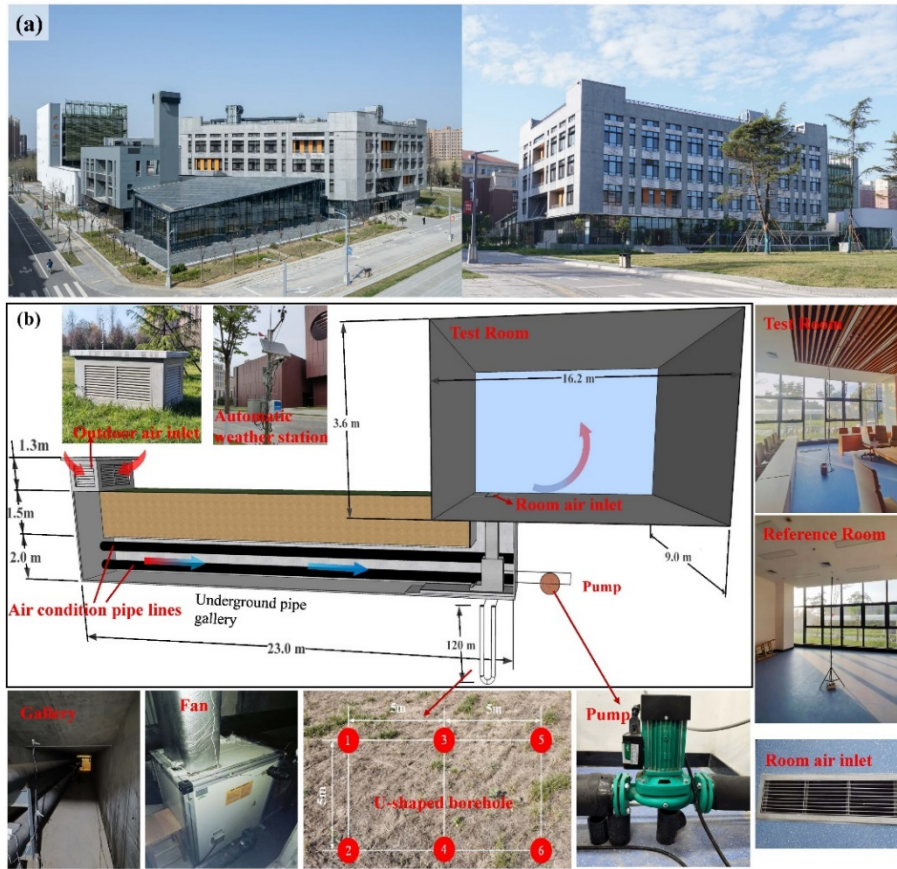
Figure 1: UPG-BHEV system. (a) Building layout; (b) Ventilation experiment schematic

2.2. Sensor layout

Various instruments were utilized to record and measure thermal parameters, as shown in Figure 2. An automatic weather station was established to record the outdoor temperature (T_a) and relative humidity (RH_a). Sensors G-A, G-B, and G-C were positioned in the middle of the cross-section at distances of 0.5 m, 10.5 m, and 17 m from the gallery inlet, respectively. Each measurement point was equipped with three temperature and humidity sensors at different vertical heights from the ground: 1.9 m, 1.2 m, and 0.1 m. The fan's air outlet is positioned at measurement points T_1. In the test room, sensors R1-4 are placed at vertical heights of 0.1 m, 0.7 m, 1.1 m, and 1.7 m to calculate the room's average temperature, denoted as T_{R1}. The same sensors in the reference room calculate the average temperature, T_{R2}.
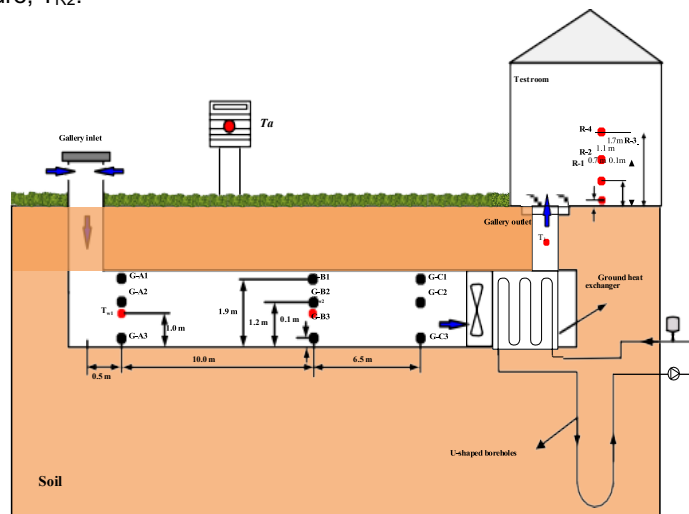

Figure 2: Detailed arrangement of sensors

Table 1: Specifications for various measuring instruments

Measurement Point	Parameter	Instrument	Measuring range	Accuracy
G-A–G-C; T_1; T_{R1}, T_{R2}	Air temperature and RH	TH20R-EX	-40–85 °C; 0–100%	± 0.2 °C; ± 2%rh
v	Wind speed	Testo 425	0–20m/s	± 0.03 m/s

2.3. Experimental scenarios

In this study, two experimental scenarios are considered to comparatively evaluate the cooling performance and impact on the indoor thermal environment of the experimental system, which is operated from 9:00 to 21:00. In Scenario 1, the outdoor air is directly cooled by UPG and then delivered to the room via a fan in cases 1-4 with UPGV operating mode; In Scenario 2, the outdoor air is cooled once by UPG, then undergoes secondary cooling through BHE before being delivered to the room by the fan in cases 5-8 with UPG-BHEV operating mode. The details are shown in Table 2.

Table 2: Test cases and outdoor air parameters

Case	Operating mode	Volumetric flow rate (m³/h)	Date	T_a /°C	RH_a /%
1	UPGV	502.2	2023/08/12	28.7	61.6
2	UPGV	1053.0	2023/08/04	33.6	60.0
3	UPGV	1488.38	2023/08/05	32.5	65.7
4	UPGV	1981.8	2023/08/13	31.0	55.5
5	UPG+BHEV	494.1	2023/08/03	30.2	49.9
6	UPG+BHEV	1064.9	2023/07/16	30.4	52.6
7	UPG+BHEV	1501.7	2023/07/17	31.8	52.1
8	UPG+BHEV	1982.9	2023/07/25	33.8	60.1

2.4. Calculations

Equation 1: The air mass flow rate in the system.
$$\dot{m} = \rho_a \bar{v} A$$

Where:

- $\dot{m}$ = the mass flow rate (kg/s)
- ρ_a = the air density (kg/m³)
- A= the cross-sectional area of the air inlet (m²)
- $\bar{v}$ = the air velocity (m/s)

Equation 2: The cooling capacity of the gallery.
$$Q_G = \dot{m} \, c(\dot{t_2} - t_1)$$

Where:

- c_p= the specific heat at constant pressure (1005 J/ (kg K))
- t_1 = inlet temperature (°C)
- t_2= outlet temperature (°C)

Equation 3: The indoor cooling efficiency.
$$\eta_T = \frac{T_a \dot{-} T_{R2}}{T_a - T_{R1}}$$

Where:

- T_a= the outdoor temperature (°C)
- T_{R1} = the test room temperature (°C)
- T_{R2}= the control room temperature (°C)

Equation 4: The indoor humidity change.
$$\eta_{RH} = \frac{RH_a \dot{-} RH_{R2}}{RH_a - RH_{R1}}$$

Where:

- RH_a= the outdoor relative humidity (%)
- RH_{R1} = the relative humidity in the test room (%)
- RH_{R2}= the relative humidity in the reference room (%)

3. RESULTS AND DISCUSSION
3.1. Analysis of the system cooling potential

As shown in Figure 3, the temperature change is observed at the inlet and outlet of the gallery. The outdoor temperature T_a exhibits a pronounced fluctuation. Figure 3a illustrates the temperature fluctuations of the UPGV, Case 1 exhibits a lower average outdoor temperature of 32.5 °C, while the average outdoor temperatures in other scenarios exceed 36 °C, with the peak temperature surpassing 41 °C. Following heat exchange with the gallery wall, the outlet temperature markedly declines, with average temperatures of 22.6, 24.5, 26.1, and 25.3 °C, respectively. This represents a reduction of 9.9, 12.8, 11.2, and 10.7 °C. As indicated in Table 3, a comparison of the temperature reduction per unit volume of airflow (ΔT_{V1}) reveals that Case 1 exhibits a superior performance, with a reduction of 0.020 °C·(m³/h)$^{-1}$. As the ventilation volume continues to increase, the cooling capacity of the gallery is reduced. Consequently, a lower wind speed is advantageous for comprehensive heat exchange between the wall and the air.

When the outdoor temperature is elevated and the cooling air temperature of the UPGV is insufficient to meet the cooling requirements of the room, the BHE is initiated at a flow rate of 1.3 m³/h. Figure 3b illustrates the temperature change curve of the inlet and outlet of UPG-BHEV. In comparison to UPGV, the outlet air temperatures of Case 5-8 are lower, at 19.3 °C, 18.9 °C, 19.6 °C, and 20.5 °C respectively. This results in a reduction in the average by 19.3 °C, 16.7 °C, 16.3 °C, and 16.5 °C respectively. The addition of the secondary cooling system resulted in a further increase in the temperature drop per unit volume of airflow.
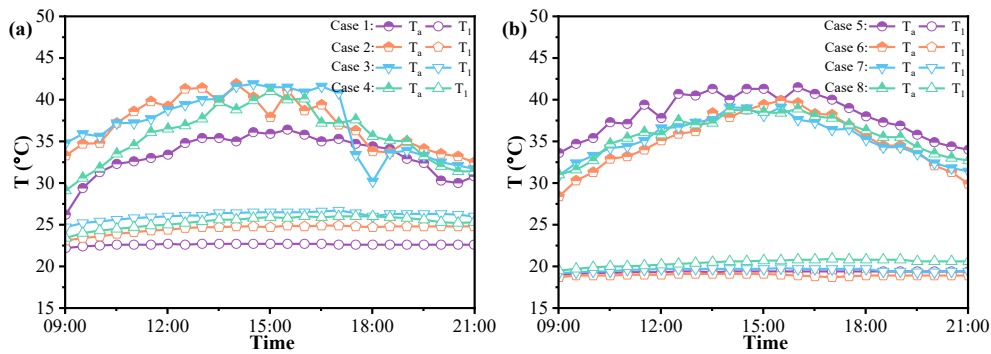

Figure 3: Inlet and outlet temperature of the system. (a)UPGV: Case 1-4; (b)UPG-BHEV: Case 5-8

Table 3: Inlet and outlet temperature of the ventilation system

Case	T_a /°C	T_{amax} /°C	T_{amin} /°C	T_1 /°C	T_{1max} /°C	T_{1min} /°C	ΔT /°C $=T_a-T_1$	ΔT_{V1} /°C·(m³/h)$^{-1}$
1	32.5	37.0	25.9	22.6	23.3	21.9	9.9	0.020
2	37.3	42.6	32.5	24.5	24.9	21.9	12.8	0.012
3	37.3	42.7	30.1	26.1	26.7	23.2	11.2	0.008
4	36.0	41.5	29.0	25.3	26.0	22.9	10.7	0.005
5	38.3	42.5	33.6	19.3	19.4	19.0	19.3	0.039
6	35.4	39.9	28.4	18.9	19.2	18.7	16.7	0.016
7	35.5	39.3	30.9	19.6	19.8	19.2	16.3	0.011
8	36.0	40.2	30.9	20.5	20.9	19.5	16.5	0.008

Figures 4a and 4b illustrate the cooling capacity of UPGV and UPG-BHEV across different airflow volumes. In Figure 4a for cases 1-4, the cooling capacity varies with outdoor temperature fluctuations, achieving maximum capacities of 2.4, 6.2, 8.1, and 10.2 kW, respectively. In Figure 4b for cases 5-8, the maximum cooling capacity reaches 3.9, 7.5, 9.8, and 13.3 kW, respectively, surpassing that of the UPGV by over 1.2 times. Therefore, selecting the appropriate cooling method based on the cooling demand can reduce the building's energy consumption at a lower cost.
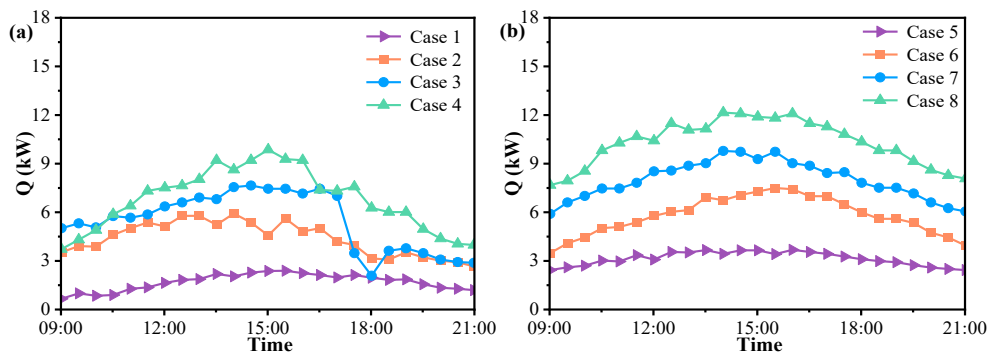

Figure 4: Variation in the thermal capacity. (a)UPGV: Case 1–4; (b) UPGV-BHEV: Case 5–8

3.2. Thermal behavior of underground pipe gallery

Figure 5acd illustrates the temperature changes along the gallery in Case 6. GA-1 records an average temperature decrease of 8.9 °C compared to the outdoors, due to the thermal inertia of the gallery stabilizing temperature fluctuations. At GB-GC, increasing the length above the gallery further reduces the air temperature, with a decrease of 1.8 °C. Conversely, Temperatures rise at positions GC-2-3 in closer proximity to building rooms, exceeding those at corresponding GB positions. Figure. 5bdf illustrates the relative humidity changes along the gallery. It is notable that the relative humidity increases along the gallery's length, averaging 4.2% higher than the outdoor levels, peaking above 90%. Therefore, density disparities cause warmer air to accumulate above the gallery, resulting in uneven mixing and reduced cooling efficiency at the duct outlets.
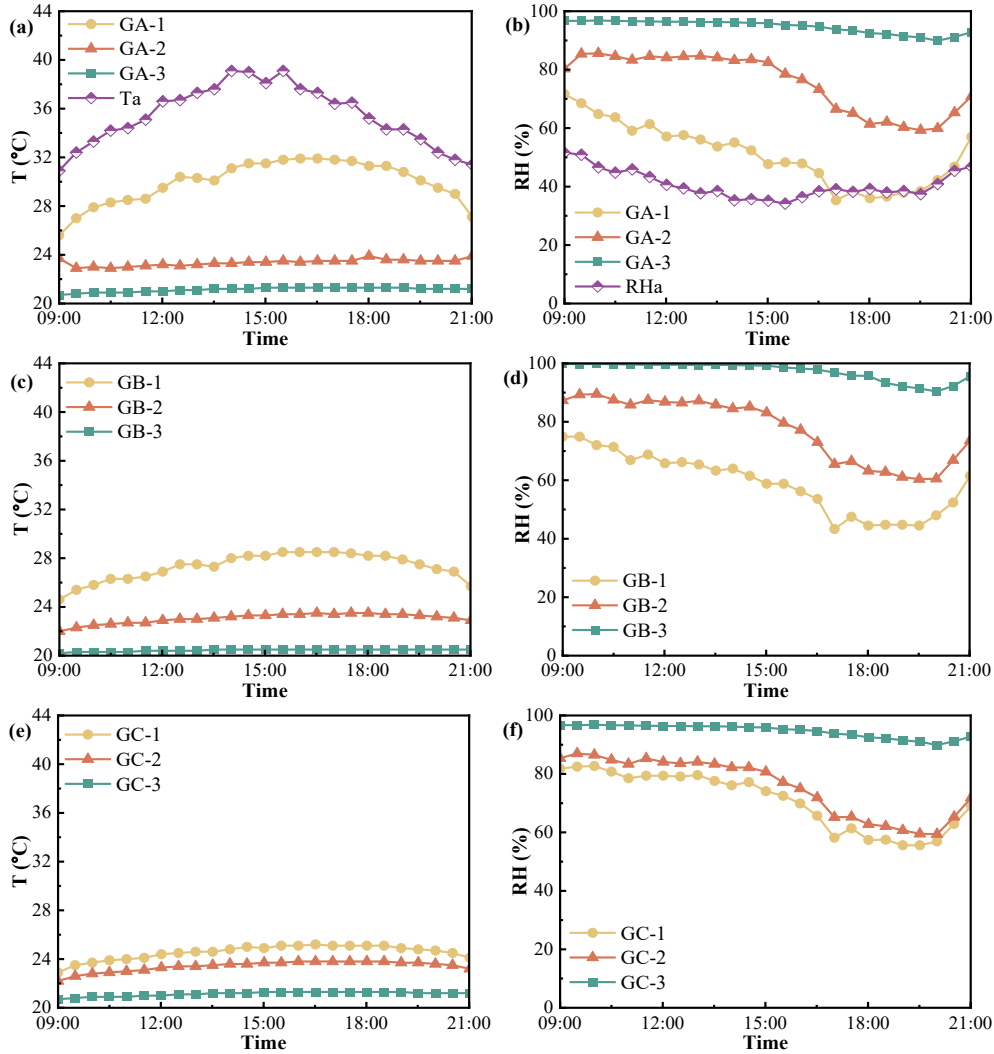

Figure 5: Temperature and relative humidity changes along the gallery in Case 6. (a, c, e) GA-GC Temperature variation; (b, d, f) GA-GC relative humidity variation

Table 4: Air temperature and relative humidity along the gallery

Position	G-A		G-B		G-C	
	T /°C	RH /%	T /°C	RH /%	T /°C	RH /%
1	26.6	64.0	25.1	68.9	23.3	76.3
2	22.5	81.8	22.2	83.0	22.4	81.1
3	20.9	94.5	20.3	97.7	20.9	95.4
Ave	23.3	80.1	22.5	83.2	22.2	84.3

3.3. Comparison of cooling preformance

The primary objective of the HVAC system is to create an indoor environment that is comfortable for the occupants. Consequently, the impact of ventilation on indoor thermal conditions is of crucial importance. In the test room, the maximum activity zone height of 2 m and is devoid of internal heat sources. Both test rooms and control rooms face north and are surrounded by glass. Figure 6 illustrates the changes in temperature and humidity distribution within the rooms. supply temperature, low airflow results in an insufficient cooling capacity. Significant temperature drops are observed only between 17:00 and 19:00, with a reduction in peak room temperature of 1.3 °C. Increased airflow resulted in notable improvements, with the maximum temperature difference between the test and contol rooms reaching 1.6 °C, and average temperature reductions of 0.8, 0.8, and 0.5 °C in Cases 2–4. Figure 6b illustrates the increasing humidity differences between the two rooms over the system runtime. This indicates that the supplied air is

humidifying, with increases of 4.3, 7.0, 10.7, and 9.1% respectively.

As shown in Figure 6c is the indoor temperature variations in the UPG-BHEV. In cases 5-8, the control room's indoor air temperatures are 27.5, 26.6, 26.7, and 27.4 °C, while the average temperatures in the test rooms are 27.0, 25.1, 25.2, and 25.7 °C respectively. This results in temperature reductions of 0.5, 1.5, 1.5, and 1.7 °C compared to the control room, with an increased temperature difference of up to 3.9 °C compared to UPGV. Figure 13d illustrates a comparison of relative humidity between the two rooms, showing that the cooling system raises the relative humidity in the rooms. In cases 5-8, the relative humidity levels are 69.2%, 65.6%, 70.7%, and 72.3%, respectively, indicating increases of 0.8%, 7.9%, 7.4%, and 9.2% compared to the control room.

To mitigate the impact of outdoor weather on experimental results, η_R, and η_{RH} have been introduced to gauge the system cooling effects. Table 5 illustrates that the UPGV's cooling performance is suboptimal when there is low airflow in Case 1, with Case 3 exhibiting the best cooling performance. This indicates a necessity for a comprehensive consideration of room cooling requirements and outdoor temperatures when selecting appropriate airflow rates for UPGV. It can be observed that the process of pre-cooling has a humidifying effect on the rooms in question, with the humidity levels occasionally exceeding the range of 40-70%. Consequently, it is recommended that dehumidification equipment be installed at the outlet when the outdoor relative humidity is high.
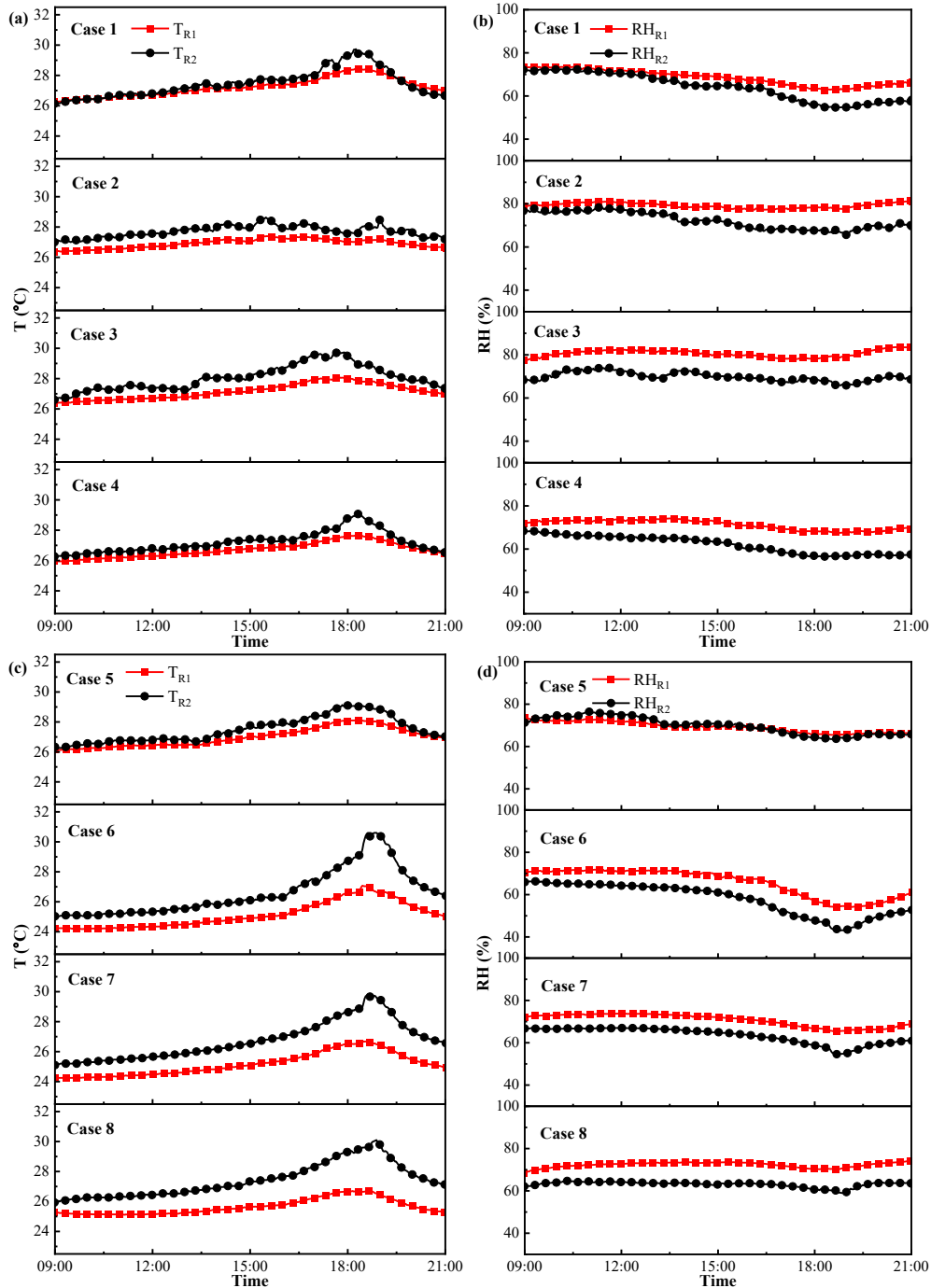

Figure 6: Variation of indoor temperature and humidity

Table 5: Comparison of indoor temperature and humidity

Case	T /°C				RH /%			
	T_{R1}	T_{R2}	ΔT	η_R	RH_{R1}	RH_{R2}	ΔRH	η_{RH}
1	27.2	27.5	0.3	0.97	68.4	64.1	4.3	0.77
2	26.9	27.7	0.8	0.92	79.2	72.2	7.0	0.76
3	27.2	28.0	0.8	0.85	80.6	69.9	10.7	0.62
4	26.7	27.2	0.5	0.95	71.2	62.1	9.1	0.70
5	27.0	27.5	0.5	0.94	69.2	69.7	0.8	1.01
6	25.1	26.6	1.5	0.86	65.6	57.7	7.9	0.69
7	25.2	26.7	1.5	0.86	70.7	63.3	7.4	0.73
8	25.7	27.4	1.7	0.87	72.3	63.1	9.2	0.66

The reduction in building cooling load typically depends on building physical parameters, engineering parameters of the underground pipe gallery and boreholes, and outdoor environmental parameters. Figure 11 illustrates the reduction in the cooling load of UGPV and UGP-BHEV. In cases 1–4, compared to the control room, the average reduction in cooling load is 0.04, 0.28, 0.43, and 0.33 kW, respectively. With the addition of secondary cooling, rooms in cases 5–8 show an average reduction in cooling load of 0.08, 0.52, 0.78, and 1.16 kW, indicating the effective cooling load reduction capability of the ventilation system. The system achieves maximum energy savings of 3.92 kWh and 13.87 kWh over continuous 12-hour operation periods.
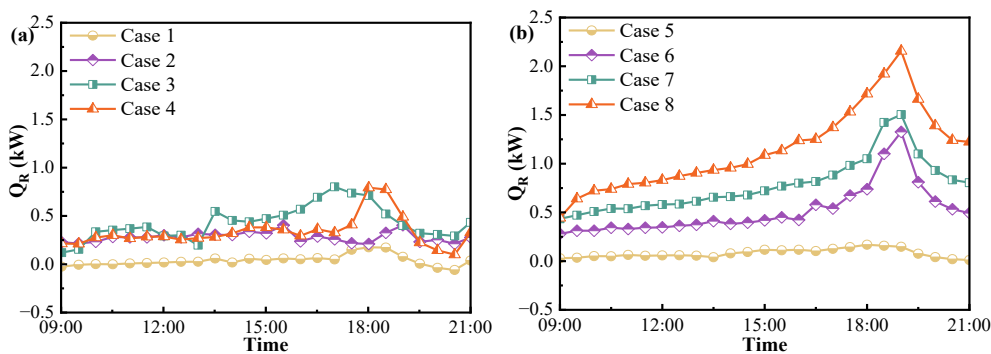

Figure 11: The reduction in building cooling load

4. CONCLUSION

This study evaluates the performance of UPGV and UPG-BHEV under varying ventilation volumes. The experiments, conducted on typical summer days, quantitatively assessed the thermal comfort provided by the system to the building. The main conclusions of this study are as follows:

The system pre-cools incoming hot air in the underground pipe gallery. The UPGV and UPG-BHEV lower the outlet air temperature by over 9.9 °C and 16 °C respectively, offering maximum cooling capacities of 10.2 kW and 13.3 kW. Temperature and humidity stratification were observed in the gallery. The ventilation system effectively lowers room temperature, decreasing the average temperature by 0.3–0.8 °C and further by 0.5–1.7 °C after the second cooling. Under continuous operation, the system saves up to 3.92 kWh and 13.87 kWh of energy.

At certain times, the room's humidity does not satisfy thermal comfort requirements, requiring extra dehumidification equipment. Future studies will concentrate on air supply techniques that don't depend on other energy sources to maintain appropriate building temperature and humidity. The experimental findings indicate that UPGV and UPG-BHEV have significant potential to reduce building cooling energy consumption during hot summers, demonstrating improved economy. The study's findings can offer technical guidance for the design and operation of other zero-energy buildings.

5. REFERENCES

Agrawal, K.K., Misra, R., Agrawal, G.D., Bhardwaj, M., Jamuwa, D.K., 2019. The state of art on the applications, technology integration, and latest research trends of earth-air-heat exchanger system. Geothermics 82, 34-50.

D'Agostino, D., Greco, A., Masselli, C., Minichiello, F., 2020. The employment of an earth-to-air heat exchanger as pre-treating unit of an air conditioning system for energy saving: A comparison among different worldwide climatic zones. Energy Build. 229.

Dong, X., Wu, Y., Chen, X., Li, H., Cao, B., Zhang, X., Yan, X., Li, Z., Long, Y., Li, X., 2021. Effect of thermal, acoustic, and lighting environment in underground space on human comfort and work efficiency: A review. Sci. Total Environ. 786, 147537.

IEA, 2018. The Future of Cooling, IEA, Paris https://www.iea.org/reports/the-future-of-cooling, Licence: CC BY 4.0.

Liu, Z., Xie, M., Zhou, Y., He, Y., Zhang, L., Zhang, G., Chen, D., 2023. A state-of-the-art review on shallow geothermal ventilation systems with thermal performance enhancement system classifications, advanced technologies and applications. Energy Built Environ. 4, 148-168.

Lyu, W., Li, X., Yan, S., Jiang, S., 2020. Utilizing shallow geothermal energy to develop an energy efficient HVAC system. Renew. Energ. 147, 672-682.

Qi, D., Liu, Q., Zhao, C., Li, S., Song, B., Li, A., 2024. Optimizing the thermal environment of greenhouse with multi-pipe earth-to-air heat exchanger system using the Taguchi method. Appl. Therm. Eng. 242, 122469.

Strategic Consulting Center of Chinese Academy of Engineering, Underground Space Branch of Chinese Society of Rock Mechanics and Engineering, Chinese Society of Urban Planning, 2024. 2023 China Urban underground space development blue book.

Yuan, T., Ding, Y., Zhang, Q., Zhu, N., Yang, K., He, Q., 2017. Thermodynamic and economic analysis for ground-source heat pump system coupled with borehole free cooling. Energy Build. 155, 185-197.

#149: Cu-doped TiO2 by induced oxygen vacancy for enhanced oxidative removal of arsenic from desulphurization wastewater

Experiments, density functional theory calculations and catalytic mechanisms

Mao Lin[1], Jiang Wu[2,*]

[1] Shanghai University of Electric Power, shanghai 200090, lm18642549077@163.com
[2] Shanghai University of Electric Power, shanghai 200090, wjcfd2002@163.com

Abstract: The heavy metal arsenic and its compounds cause serious damage to human health because of their carcinogenicity and accumulation in natural environments such as groundwater. Cu-doped TiO_2 catalyst was synthesized by impregnation-thermal decomposition method. The copper dopant induced the number of oxygen vacancies in titanium dioxide and increased the activity of oxygen molecules, which optimized the arsenic reaction pathway and improved the arsenic removal from desulfurization wastewater. The experimental results show that the Cu concentration was important factor affecting the arsenic removal of the composite material at atmospheric temperature (25 ℃) and pH=7, and the arsenic removal efficiency of CT10 reached 83.17%, which was 1.33 times higher than that of the original sample. Subsequently, the arsenic adsorption at different pH with optimal doping ratio was carried out to study the role of pH on modified catalysts, and it was found that the adsorption of arsenic by Cu/TiO_2 was the best when pH=5. Characterization analysis further showed that Cu doping effectively increased the oxygen vacancies concentration for promote the activation of oxygen molecules, enhanced the chemisorption of As on Cu/TiO_2 with high adsorption capacity for arsenic in wastewater. Combining the characterization and experimental results, the migration mechanism of arsenic from wastewater in Cu/TiO_2 composite catalysts is proposed, and the mode of action of Cu doping in the substrate adsorbent is investigated. The density-functional theory (DFT) was employed to calculate the modified catalyst band gap, combined with simulations to analyze the mechanism of oxygen vacancies caused by ion doping. The outcome of this work provided reference for future coupling of transition metal ions with catalysts and a realistic technological pathway for the catalytic remediation of heavy metal pollution in wastewater.

Keywords: Ion Doping Engineering; Oxygen Vacancy; Electron Transport; Cu/Tio_2 Composites; As Removal

1. INTRODUCTION

Due to its bioaccumulation, the rare but widespread element arsenic (As), which is highly biotoxic and carcinogenic, can irreparably harm ecosystems and human health. Coal contains a trace amount of arsenic, but the high consumption of coal makes Coal-fired power generation an essential cause of As emissions to nature. Air pollution control devices (APCDs) are present in the flue to catch more than 70% of the arsenic in fly ash. However, some of the captured As enters the desulfurization wastewater and ash flushing wastewater as liquid-phase arsenic with high mobility. Due to the mobility and difficulty of removal of As in solution, it has received increasing attention from society in recent years (Bunt et al., 2008).

Currently, adsorption, chemisorption filtration, biological treatment and ion dopant have become the very popular technologies to treat arsenic in solution. Adsorption technology has the advantages of being efficient, convenient, environmentally friendly, and sustainable, and has been widely investigated as an effective contamination removal technique in the aqueous phase. Nevertheless, the composition of desulfurization wastewater is far more complex than that of drinking water, in which elemental As is mainly present in various forms, such as As(V) and As(III). The latter is not only highly toxic, but also characterized by high mobility and has a lower affinity for various adsorbent surfaces (Zhang et al., 2021). Therefore, pre-treatment to reduce the As(III) concentration before the adsorption process begins is also essential. This method dramatically increases the steps and costs of water treatment. Therefore, it is crucial to select suitable adsorbents from modified activated carbon, alumina, iron-based materials and titanium dioxide for the removal of As from desulfurization wastewater (Chang et al., 2019).

Among inorganic arsenic adsorbents, titanium dioxide (anatase titanium dioxide), especially nano titanium dioxide (less than 100 nm), exhibits a good arsenic removal capacity (Bang et al., 2011). Dutta studied the As adsorption performance of P25 and found that the adsorption of As (V) by P25 was 0.7 mg/g higher than that of As (III). The application of nano TiO_2 as an arsenic adsorbent in water has made some progress and has been widely used in photocatalytic and adsorption studies. It seems to be a promising catalyst in order to transform As(III) into As(V), as well as an effective catalyst for the removal of As from water. Additionally, due to its high adsorption efficiency, it is very effective in the adsorption of As (V), copper oxide is progressively becoming a focus of attention (Wang et al., 2015). CuO accumulates an abundance of ·OH groups on the surface during adsorption, which is favourable for As removal. However, the adsorbent doped with CuO is easily agglomerated, which is not favourable for adsorption (Goswami etal., 2012).

Catalysts with oxygen vacancies on the surface have become a research priority because of their important applications in catalytic oxidation, photocells, photocatalysis, sensors, and other fields. Many researchers have proposed several mechanisms to induce oxygen vacancy generation and thus improve catalyst performance, such as ion doping engineering, construction of heterojunctions, and preparation of catalysts in reducing atmospheres. Among them, ion doping is favored for its good operability, ease of preparation, and outstanding results. In the study of ion doping induced oxygen vacancies to enhance the catalytic performance of catalysts, tang et al. prepared Cu-doped $BiOIO_3$ photocatalysts using a hydrothermal method, which effectively enhanced the adsorption activity of the catalysts (Wang et al., 2017). The doping of transition metal ions could effectively induce the oxygen vacancies on the catalyst surface, promote the migration and catalyst electron vacancies separation, thus improving the catalytic performance of the catalyst (Xia et al., 2012). In conclusion, Cu^{2+} ion doping induced oxygen vacancies in TiO_2 catalyst to enhance the performance of arsenic removal in desulfurization wastewater is not a feasible means, and it can provide further theoretical support for the performance of ion doping engineered modified catalyst.

In this work, Cu/TiO_2 nanocomposites were prepared by the impregnation-thermal decomposition method to adsorb As in the solution. To determine the ideal conditions for As removal and the highest adsorption efficiency, the Cu doped ratio and solution initial pH were adjusted during adsorption studies. DFT calculations further confirmed that Cu^{2+} doping optimized the arsenic removal pathway by narrowing the catalyst bandgap and gave a mechanism for the enhanced arsenic removal efficiency of the adsorbent. This work revealed that Cu/TiO_2 nanocomposite catalysts effectively optimize the reaction path of As in wastewater, which provides a new idea to develop heavy metal adsorbents and lays a foundation for the development of modified and efficient catalysts based on ionic doping engineering.

2. EXPERIMENT
2.1. Chemicals and materials

Sodium hydroxide (NaOH), Copper nitrate hydrate ($Cu(NO_3)_2 \cdot 3H_2O$), Hydrochloric (HCl) and Anatase titanium dioxide (TiO_2) were purchased by Titan Technology Co. The standard arsenic solution (1000mg/L) was purchased by Tongliao Technology Co. The initial solution was obtained by diluting the standard arsenic solution to 25 mg/L with deionized water. Throughout the experiment, HCl and NaOH were utilized to adjust the initial solution pH. The preparation is performed with analytical-grade chemical reagents and deionized water, so no foreign impurities contaminate the experiment.

2.2. Preparation of Cu/TiO2 composites

Cu/TiO_2 adsorbent was prepared by the impregnation-thermal decomposition method, as shown in Fig. 1. At first, $Cu(NO_3)_2 \cdot 3H_2O$ was dissolved in 20 ml of deionized water in a beaker by different masses after molar ratio calculation. The resulting mixture was mixed for 0.5 hours and then 4.0 g of anatase TiO_2 was added and fully dissolved in a heated environment until a homogeneous mixture was obtained. The mixture was then transferred to a desiccator at 80 ℃ for 12 h to obtain a blue-white solid. After the precursor was ground into powder, it was calcined in a muffle furnace for 4 h at a calcination temperature of 500 ℃ and a temperature increase rate of 5 ℃/min. Finally, the calcined solid was ground and pulverized to obtain Cu-doped TiO_2 catalysts with Cu to Ti molar ratios of 0.20:1, 0.10:1 and 0.01:1, labeled as CT20, CT10 and CT1, respectively. To ensure experimental accuracy, a pure sample of TiO_2 and copper oxide was prepared as a control group through the above process.
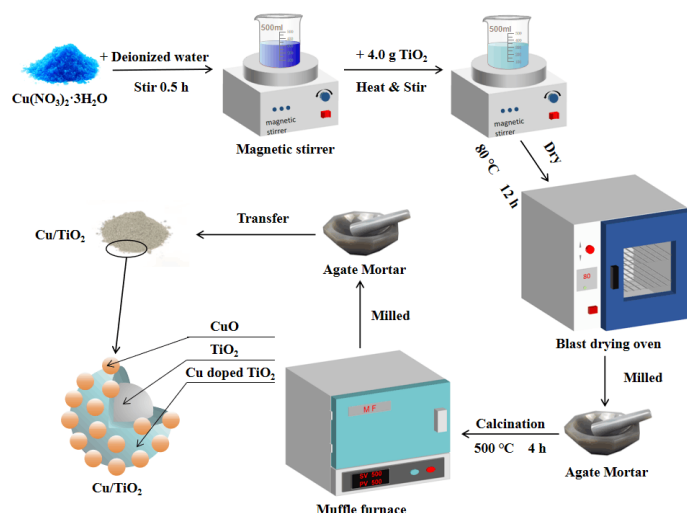
Figure 1: Preparation process diagram of Cu/TiO$_2$

2.3. Evaluation of adsorption performance for arsenic

As shown in Fig. 2, the catalyst adsorption of As was performed on a self-built experimental setup for arsenic removal, mainly including adsorption reactors (CEL-GPCR100, Ceaulight), thermostatic baths, magnetic stirrers, etc. The experiments were conducted under light-free conditions. The effects of different copper doping ratios and pH on the adsorption efficiency of As by Cu/TiO$_2$ adsorbent were researched by a series of experiments, respectively. 100 ml of initial solution (25 mg/L) was poured into the adsorption reactor, and 0.1 g (TiO$_2$, CT1, CT10, CT20) was added to the solution and dynamically adsorbed at 300 r/min at a temperature of 25℃over a period of 4h. Finally, 4.0 mL of the post-reaction suspension was taken, and the clear liquid was obtained after filtration using a 0.22 μm microporous membrane filter. The arsenic concentration in the filtered liquid was detected and the effect of different Cu doping rates on the arsenic adsorption capacity of the catalyst was found.

Equation 1: The arsenic adsorption efficiency of the as-prepared adsorbents

$$\eta = \frac{C_0 - C_e}{C_0} \times 100\%$$

where C_e (mg/L) and C_0 (mg/L) respect the concentration of arsenic after solution adsorption and the initial concentration before adsorption, respectively, and η(%) is the adsorption rate when the reaction reaches equilibrium.
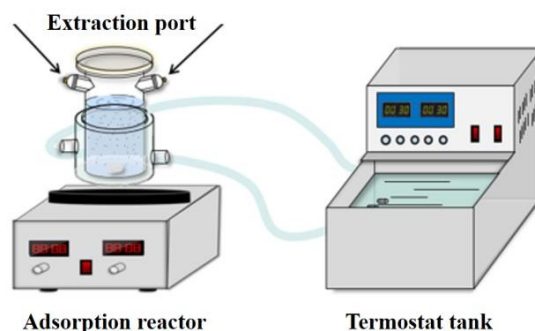

Figure 2: Experimental setup for liquid phase arsenic removal

The effect of initial pH of solution for arsenic removal by Cu/TiO2 adsorbent was studied. Firstly, 100 ml from the initial solution (25 mg/L) was added to the adsorption reactor and HCL and sodium hydroxide (concentration 0.1 mol/L) were added dropwise to adjust the pH=1, 3, 5, 7,9 respectively. Subsequently, the adjusted solution was placed in a magnetic stirrer, and an appropriate amount of Cu/TiO2 adsorbent was added to adsorb arsenic dynamically at room temperature (25 ℃) with 300 r/min for 4 h. Finally, inductively coupled plasma optical emission spectrometry (ICP-OES) was used to identify the amount of arsenic in solution after the adsorption reaction, and the relationship between the initial pH of the solution and the adsorption capacity was investigated.

2.4. Characterization

The structural information of the catalysts before and after modification was analyzed by x-ray diffraction analysis (XRD, Bruker D8 advance). The specific surface area of the catalyst was derived from the mass of adsorbed N_2 by the Brunauer-Emmett-Teller (BET) method. The pore capacity and microporous diameter of the catalysts were derived from the adsorption isotherms of the catalysts via the Barrett-Joyner-Halenda (BJH) method. The surface morphology of the catalysts before and after modification was observed via transmission electron microscope (TEM) and scanning electron microscopy (SEM, Oberkochen, Germany). The elements present in the adsorbent were quantified using energy dispersive spectroscopy (EDS). Finally, after experimentally determining the best doped samples, X-ray photoelectron spectroscopy (XPS) was performed on the best samples with the use of Al Kα X-ray radiation (1486.6 eV, Thermo Fisher Scientific, USA) in order to obtain information on their valence transitions and surfaces, and the electron paramagnetic resonance (EPR) of the catalyst was investigated in Brook A300.

2.5. First-principles calculation

The band gap structure of Cu-doped catalysts was investigated by CASTEP module based on density functional theory (Zhao et al., 2017) and the effect of copper doping on the catalysts was comparatively analyzed. The simulation optimization process utilized the Monkonhorst-Pack method. In addition, the K-space grid points have been chosen using a plane-wave truncation energy (400 eV) and an accuracy (2.0 × 10-6 eV/atom). The K-network option for the Brillouin zone is 3 × 3 × 2. The anatase TiO_2 space group is I41/amd and the lattice constants a, b, and c corresponding to 3.822 nm, 3.822 nm, and c = 9.846 nm, respectively.

3. RESULTS AND DISCUSSION
3.1. Characterization

The elemental composition and crystalline phase structure of the prepared pure and modified catalysts were investigated by X-ray diffraction (XRD). As shown in Fig. 3, the derivatization peaks of the prepared samples coincide with the standard XRD spectra of anatase TiO_2 (PDF#71-1166), which directly proves the successful preparation of titanium dioxide catalyst. By observing the characteristic peaks of the doped samples in the plots, no peak corresponding to rutile titanium dioxide was found, indicating that the anatase TiO_2 crystal phase morphology was wellmaintained during the material preparation (Wu et al., 2015). In addition, XRD patterns showed no characteristic peaks corresponding to copper oxide in the CT1 sample, indicating that the low doped amount of Cu had no significant effecton the crystalline phase composition and crystallinity of TiO_2(Yan et al., 2014). However, the intensity of the diffraction peaks was enhanced with the increase of the doping amount, which laterally indicated the successful doping of Cu ions. The peak position of the doped modified catalyst was slightly shifted to the right, which proved that the Cu dopant successfully entered the lattice of TiO_2. This is probably due to the substitution of Ti^{4+} by Cu^{2+}, which provides a theoretical basis for the subsequent modeling of Cu-doped TiO_2 structure optimization based on density-functional theory.
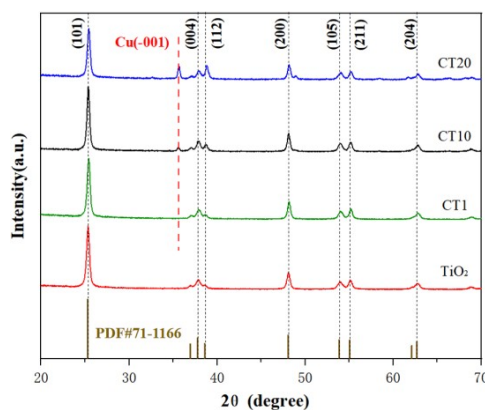

Figure 3: XRD patterns of TiO_2 (anatase), CT1, CT10, CT20 and CuO

The possible reason for this is that the doped copper oxide particles blocked part of the mesopores on the titanium dioxide surface, causing a reduction in the specific surface area of CT10. In addition, according to the XRD results, theentry of Cu^{2+} into the TiO_2 cell may also reduce the surface area of the catalyst. Apparently, the peak intensity of CT10is stronger than that of pure TiO_2 in Fig. 4. This indicates that the Cu-doped titanium dioxide catalyst has more oxygenvacancies than pure TiO_2. In addition, more oxygen vacancies on CT10 can enhance the activation of molecular oxygenand electron transfer of the catalyst, thus promoting the arsenic removal efficiency of the catalyst (Jiang et al., 2016).
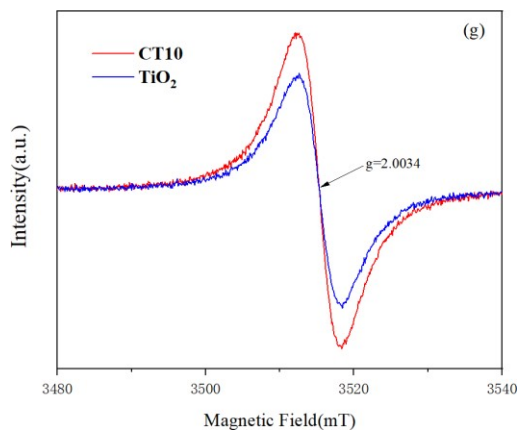
Figure 4: The EPR oxygen vacancy spectra of CT10 and TiO₂

3.2. Effect of different CuO-doping ratios

The Cu^{2+} doping ratio had a significant effect to adsorption properties of Cu/TiO_2 adsorbent. The adsorption efficiency of arsenic by the Cu/TiO_2 adsorbent with different Cu-doping ratios was first studied. Each experiment was conducted for 4 h at room temperature (25 ℃). The arsenic adsorption efficiencies of the prepared dopants and pure samples are illustrated in Fig. 5. And the doping ratio of Cu^{2+} is a crucial factor in determining the As removal efficiency. From Fig. 5, the adsorption ratio of arsenic gradually rises and then decreases as the copper oxide content increases, with the highest adsorption efficiency of 83.17% for CT10, which is 1.33 times higher than the adsorption rate of 62.76% of the original sample. The extremely low adsorption efficiency of arsenic in the copper oxide control group was 3.61%, which proved the poor adsorption capacity of pure copper oxide for As. This basically ruled out the influence of arsenic adsorption by copper oxide on the experimental results and verified the accuracy of the experiments. Cu doping into the TiO_2 lattice changed the chemical properties inside the catalyst [43], and in order to investigate the mechanism of enhanced As adsorption performance, we chose the best sample CT10 adsorbent for the subsequent study. Combined with the experimental results of different ratios of CuO doped, the arsenic removal efficiency was not linearly related to the specific surface area of catalysts. Based on this, it is necessary to focus on the chemisorption of arsenic by modified adsorbents.
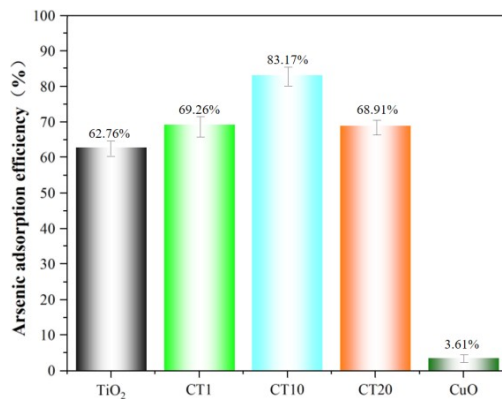

Figure 5: Comparison of As adsorption capacity at different CuO doped ratios. (Experimental conditions: 0.1 g of adsorbent, 25 mg/L initial arsenic concentration, pH=7, 25 ℃ and reaction for 4 h)

3.3. Effect of the initial pH in the solution for As adsorption capacity

The solution initial pH is also an essential factor for the As adsorption. Fig. 6 demonstrates the arsenic removal efficiency of arsenic removal by CT10 adsorbent at different pH (1,3,5,7,9). The adsorption efficiency of arsenic increased rapidly with increasing pH of the solution and then decreased slowly. The best adsorption performance is reached at pH=5, and the adsorption efficiency of CT10 on As reached 86.62%. When in the range of pH 5-7, the adsorbent had a better removal effect. This is because the morphology of the arsenic in the solution is closely related to pH. Due to different pH values, the existence of As ions is different, and the interaction of As ions with the adsorbent surface is also different. At low pH, H3AsO4 and H2AsO4 are the predominant forms of As present and Cu/TiO_2 is positively charged because protons are adsorbed on the adsorbed layer and lack electrostatic attraction to arsenate, which is not an anion. As the pH increases, arsenate ions gradually become more abundant, and the electrostatic attraction of Cu/TiO_2 adsorbent to arsenate ions increases subsequently, prompting both adsorption capacity and removal efficiency. However, when the solution pH is above the zero-point charge of Cu/TiO_2, protons within Cu/TiO_2 are released from the ·OH group, the adsorbent surface is thus negatively charged, which repels each other with the arsenate ions that are also anions, increasing the difficulty of contacting the arsenate ions with the surface active sites, making both the adsorption capacity and the removal efficiency start to decrease gradually. In addition, at higher pH, the ·OH group in the form of hydroxide(OH^-) also competes with arsenate ions for adsorption, leading to the adsorption capacity and adsorption efficiency decreased.
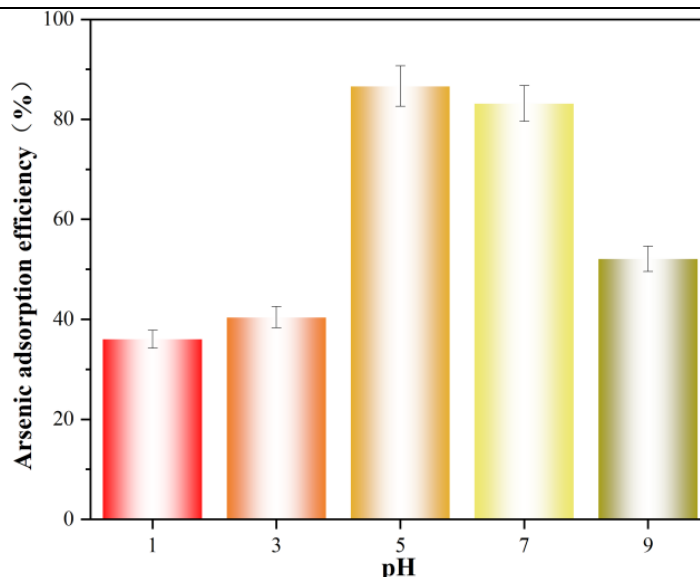
Figure 6: The adsorption efficiency of CT10 on As at different pH

3.4. CuO/TiO2 regeneration cycle experiment

Fig. 7 shows the experimental data of As removal efficiency by CT10 adsorbent in four consecutive adsorption- desorption regeneration cycles. From Fig. 7, it is evident that after each cycle of arsenic adsorption removing decreased. The CT10 adsorption efficiency for the first time for liquid phase arsenic reached 83.17%. After desorption, the second adsorption of CT10 was carried out, and its removal efficiency was 80.67%, which decreased by 3.57 percentage points. The third adsorption showed a sharp decrease, possibly related to the depletion of Cu(I) in CT10. According to Yin's study, the recycling procedure cannot fully eliminate the arsenic adsorbed on the surface of Cu/TiO2, and the remaining arsenic on TiO2 can occupy the active sites on its surface, resulting in the inability of the arsenic element to bind to it in subsequent experiments (Wu et al., 2015). And the arsenic elements that are not entirely desorbed will inhibit the production of hydroxyl radicals ($\cdot$OH) and superoxide anions ($\cdot O^{2-}$), resulting in less and less As(III) to As(V) oxidation, thus limiting the arsenic readsorption by the regenerated Cu/TiO2 adsorbent. However, remarkably, the regenerated Cu/TiO2 adsorbent material can still reach a removal efficiency of more than 60% after four cycles. Therefore, it is clear that the Cu/TiO2 composite has a good regeneration cycle and is a promising adsorbent.
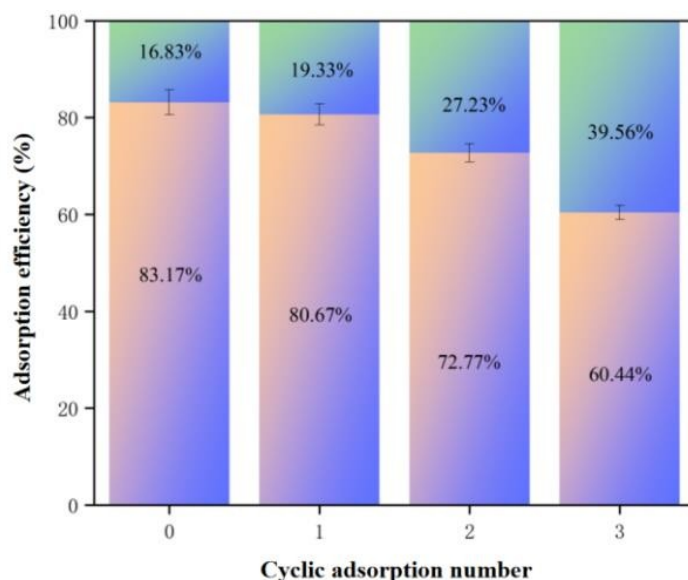
Figure 7: Adsorption-desorption regeneration cycle experiment of CT10

3.5. Computational results for Cu-doped TiO2

Previous XRD patterns, HRTEM and XPS patterns, it is shown that there is a Cu-doped TiO2 crystalline phase presentin the sample. This crystalline phase of Cu^{2+} entering inside the TiO2 cell in the sample has been proved by some experiments as a source of inducing room temperature ferromagnetism (Wei et al., 2018). Numerous studies have demonstrated that the presence of oxygen vacancies in anatase titanium dioxide induces lattice oxygen activation andenhanced carrier separation, which is an important factor affecting the catalyst activity. And Cu^{2+} doping instead of Ti^{4+} leads to the imbalance of internal potential as the main reason for

promoting oxygen vacancies (Torres et al., 2007).

For further investigating the mechanics of TiO2 catalysts to improve the arsenic removal efficiency, DFT simulations were conducted to calculate the changes in TiO2 band gap of before and after doping. As shown in Fig. 8c-d, the TiO2 band gap was 2.077 eV, while the value changes to 0.560 eV after Cu replaces Ti atoms in the model. The replacementof Ti by Cu^{2+} caused changes in the potential distribution as well as the chemical environment inside the catalyst, whichled to changes in the location of the oxygen anion, which in turn led to the movement of the oxygen vacancies to a morestable position, which further facilitated the oxygen vacancy generation effect (Nowotny et al., 2008). The above DFT calculations are in accordance with experimental and characterization results, and the reduction of band gap further proves the promotion of oxygen vacancies on the arsenic removal ability of the catalyst, which provides theoretical support for the transition metal ions doping modification of the catalyst to induce oxygen vacancies to enhance its catalytic performance.
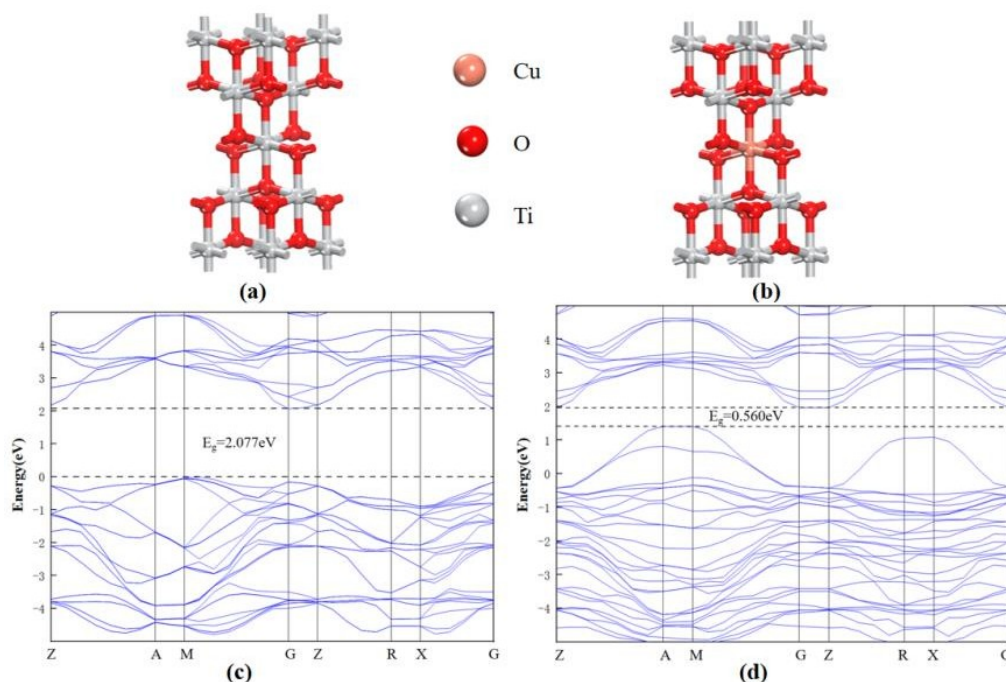

Figure 8: The geometry optimized structure of the (a) TiO₂ and (b) Cu/ TiO₂. The calculated band structure of (c) TiO₂ and (d) Cu/ TiO₂

Cu doping creates an impurity energy level between the valence band and conduction band of TiO_2. DFT calculations show that the modified TiO_2 catalyst has a CB potential value of -1.517 eV, compared to that with O_2 / $\cdot O^{2-}$ (-0. 28 eV). O_2 can gain electrons in the modified catalyst to form $\cdot O^{2-}$. The main substances that oxidize As(III) to As(V) are the hydroxyl radical ($\cdot OH$) and superoxide anion ($\cdot O_2^-$) in the reactive oxygen species (ROS) group, previously reported that $-O_2^-$ is the main active species at a pH of 7. The catalytic mechanism was inferred as shown in the following equation. In the oxidation, As(IV) is the intermediate product between As(III) and As(V), which is oxygenated by As(IV) dismutation (Eq. 6) or further oxidized by dissolved O_2, finally being transformed into As(V)(Roy et al., 2017).The migration path of arsenic adsorption on the Cu-doped TiO_2 catalysts surface is demonstrated as in Fig. 9.

Equation 2: Mechanism of catalytic As on modified TiO₂
$$Cu^{2+} + hv \rightarrow Cu^{2+} + \left(h^+ + e^- \right)$$

Equation 3: Mechanism of catalytic As on modified TiO₂
$$Cu^{1+} \xrightarrow{h^+} Cu^{2+} \xrightarrow{e^-} Cu^{1+}$$

Equation 4: Mechanism of catalytic As on modified TiO₂
$$H_2O \rightarrow H^+ + OH^-$$

Equation 5: Mechanism of catalytic As on modified TiO₂
$$O_2 + e^- \rightarrow \cdot O_2^-$$

Equation 6: Mechanism of catalytic As on modified TiO₂
$$H_2O + h^+ \rightarrow \cdot OH + H^+$$

Equation 7: Mechanism of catalytic As on modified TiO₂
$$OH^- + h^+ \rightarrow \cdot OH$$

Equation 8: Mechanism of catalytic As on modified TiO₂
$$2 \cdot O_2^- + As^{3+} + 4H^+ \rightarrow As^{5+} + 2H_2O$$

Equation 9: Mechanism of catalytic As on modified TiO₂
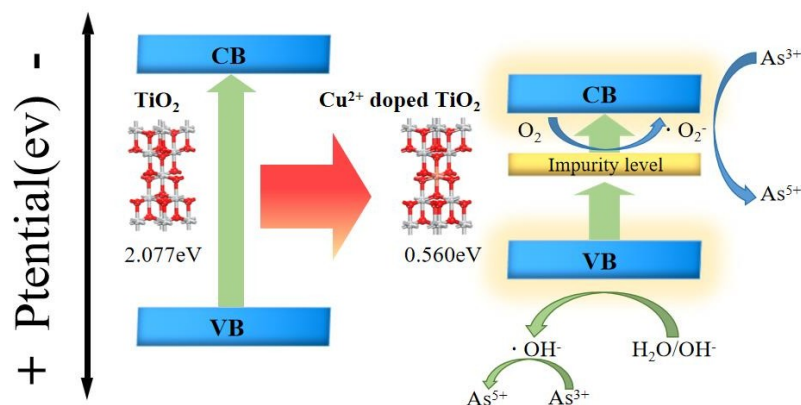$$2 \cdot OH + As^{3+} \rightarrow As^{5+} + O^{2-} + H_2O$$
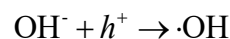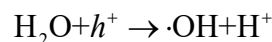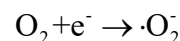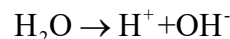
Figure 9: Mechanism diagram of the energy band changes of TiO_2 and Cu^{2+}-doped TiO_2 photocatalysts for arsenic removal

4. CONCLUSION

In this work, using efficiently synthesized Cu/TiO2 adsorbents by simply employing impregnation-thermal decompositionmethod, which effectively promotes the oxygen vacancies activity of the catalyst and thus enhances the adsorption efficiency of arsenic from catalytic wastewater. The As adsorption experiments illustrated that the adsorption efficienciesof CT10 on arsenic in simulated wastewater reached 86.62% at pH=5. It is worth mentioning that this pH is almost consistent with that in desulfurization wastewater. It was found that the doping of Cu^{2+} in the TiO2 lattice displaces Ti^{4+} and that the oxygen vacancies effect in CT10 on As adsorption is not a single process accompanied by the oxidation of As (III) to As (V), which provides support for subsequent simulations of ion-doped catalysts. The density functional theory (DFT) reveals that copper doping effectively narrows the bandgap of titanium dioxide by nearly 73% from 2.077eV to 0.56 eV. This not only analyzes the ·OH and ·O2 in the modified catalysts to optimize the arsenic catalyticoxidation pathway in wastewater and enhance the arsenic removal performance, but also provides support for the subsequent simulation of the doped ionic catalysts. It presents the proposed pathway for the conversion of arsenic in wastewater. This study offers a theoretical foundation for the enhancement of catalyst performance by doping modifiedinduced oxygen vacancy concentration in the catalyst, and a novel way for the removal of arsenic from arsenic- containing desulfurization wastewater and the recovery of adsorbents.

5. REFERENCES

Bang S, Pena M E, Patel M, et al. (2011) 'Removal of arsenate from water by adsorbents: a comparative case study', Environmental geochemistry and health, 33(1): 133-141.

Bunt J R, Waanders F B. (2008) 'Trace element behaviour in the Sasol-Lurgi MK IV FBDB gasifier Part 1-the volatile elements: Hg, As, Se, Cd and Pb', Fuel, 87(12): 2374-2387.

Chang L, Yang J, Zhao Y, et al. (2019) 'Behavior and fate of As, Se, and Cd in an ultra-low emission coal-fired power plant', Journal of Cleaner Production, 209: 722-730.

Goswami A, Raul P K, Purkait M K. (2012) 'Arsenic adsorption using copper (II) oxide nanoparticles[J]', Chemical engineering research and design, 90(9): 1387-1396.

H. Jang, R. Agarwal, P. Nukala, et al. (2016) 'Observing Oxygen Vacancy Driven Electroforming in Pt-TiO2-Pt Device via Strong Metal Support Interaction', Nano Lett 16(4) 2139-44. Available at: https://doi.org/10.1021/acs.nanolett.5b02951.

L. Zhao, B. Magyari-Köpe, Y. Nishi, (2017) 'Polaronic interactions between oxygen vacancies in rutile TiO2', Physical Review B 95(5) . Available at: https://doi.org/10.1103/PhysRevB.95.054104.

Nowotny M K, Sheppard L R, Bak T, et al. (2008) 'Defect chemistry of titanium dioxide. Application of defect engineering in processing of TiO2-based photocatalysts', The Journal of Physical Chemistry C, 112(14): 5275-5300.

Roy S, Luitel H, Sanyal D. (2017) 'Origin of ferromagnetism in Cu doped rutile TiO2-An ab-initio approach', Computational Condensed Matter, 13: 127-130.

Torres C E R, Golmar F, Cabrera A F, et al. (2007) 'Magnetic and structural study of Cu-doped TiO2 thin films', Applied surface science, 254(1): 365-367.

Wang T, Yang W, Song T, et al. (2015) 'Cu doped Fe3O4 magnetic adsorbent for arsenic: synthesis, property, and sorption application', RSC Advances, 5(62): 50011-50018.

Wei Y, Liu C, Luo S, et al. (2018) 'Deep oxidation and removal of arsenite in groundwater by rationally positioning oxidation and adsorption sites in binary Fe-Cu oxide/TiO2', Chemical Engineering Journal, 354: 825-834.

Wu J, Li C, Zhao X, et al. (2015) 'Photocatalytic oxidation of gas-phase Hg0 by CuO/TiO2', Applied Catalysis B: Environmental, 176: 559-569.

X. Wang, Z. Rui, Y. Zeng, H. Ji, Z. Du, Q. Rao, (2017) 'Synergetic effect of oxygen vacancy and Pd site on the interaction between Pd/Anatase TiO2 (101) and formaldehyde: A density functional theory study', Catalysis Today 297 151-158. Available at: https://doi.org/10.1016/j.cattod.2017.06.037.

Y. Xia, B. Zhang, J. Ye, Q. Ge, Z. Zhang, (2012) 'Acetone-Assisted Oxygen Vacancy Diffusion on TiO2(110)', J Phys Chem Lett 3(20)2970-4. Available at: https://doi.org/10.1021/jz301293y.

Yang R, Yang L, Tao T, et al. (2014) 'Contrastive study of structure and photocatalytic performance with three- dimensionally ordered macroporous CuO-TiO2 and CuO/TiO2', Applied surface science, 288: 363-368.

Zhang L, Song Q, Xu Z. (2021) 'Arsenic removal and recovery of germanium and tungsten in toxic coal fly ash from lignite by vacuum distillation with a sulfurizing reagent', Environmental Science & Technology, 55(6): 4027-4036.

#151: Performance evaluation and coke formation analysis of nickel-based catalysts for the diesel surrogate steam reforming to produce hydrogen for SOFCs

Haokun Liu[1], Guangtao Fan[1], Weiqi Wu[1], Xinhai Xu[1,*]

[1] School of Mechanical Engineering and Automation, Harbin Institute of Technology, Shenzhen 518055, China
*Corresponding author. E-mail: xuxinhai@hit.edu.cn

Abstract: Diesel steam reforming presents a promising and cost-effective method for supplying H_2 and CO for solid oxide fuel cells avoiding the problem of hydrogen storage. However, the requirement of costly noble metal catalyst and carbon deposition remain challenges. In this study, three Ni-based catalysts, namely $Ni-Al_2O_3$, $Ni-Al_2O_3-La_2O_3$ and $Ni-Al_2O_3-CeO_2$, are separately prepared to investigate the effects of promoters on Ni catalyst structure, performance, stability, and carbon deposition in a diesel surrogate steam reforming. Fresh and spent catalysts are characterized by H_2-temperature programmed reduction, X-ray diffraction, transmission electron microscopy and thermogravimetric analysis. The results show that the addition of La and Ce increases the dispersion of Ni, which is favorable for promoting the interaction of the catalyst with the reactants. Thermogravimetric analysis confirms that the modified catalysts exhibit lower levels of carbon deposition. However, the addition of La leads to the formation of $La_2O_2CO_3$, which may block the reaction sites of the catalyst surfaces and thereby affect the fuel conversion rate. On the other hand, the addition of Ce does not result in performance loss and can even improve the performance of the surrogate fuel reforming. Density functional theory calculations demonstrate that both La and Ce doping increase the activation energy of the carbon deposition reaction, which is pivotal in improving the catalyst resistance against coke formation. Moreover, the CO/CO_2 ratio is proposed as an in-time indicator to monitor the catalyst carbon deposition.

Keywords: Diesel Steam Reforming; Hydrogen; Ni-based Catalyst; Coke; Density Functional Theory

1. INTRODUCTION

The power supply for remote areas is typically relied on diesel generators because of the challenge of limited access to power grids. However, the diesel generators face issues such as noise, environmental pollution and low energy conversion efficiency. Solid oxide fuel cells (SOFCs) operating by consuming hydrogen-rich syngas offer an alternative for power supply in remote areas with the advantages of quite low noise, environmental friendliness and fuel flexibility (He, et al., 2023). The hydrogen-rich syngas can be on-site derived from reforming readily available diesel in remote areas, which makes the utilization of SOFCs a feasible approach and avoids the problems of hydrogen storage (Potemkin, et al., 2020). However, the lengthy hydrocarbon chain presented in diesel predisposes it to carbon deposition during the reforming process, thereby hampering both the efficiency of the reforming reaction and the lifetime of the catalyst. Consequently, the pursuit of methods enhancing the efficiency of diesel reforming and stability of catalyst attract lots of attention (Geng, et al., 2023). Current methodologies often employ noble metal catalysts such as rhodium (Rh), ruthenium (Ru), and platinum (Pt) in diesel reforming (Carrasco-Ruiz, et al., 2023). However, the extremely high cost of thesecatalysts limits the commercialization (Charisiou, et al., 2019). As a result, researchers paid lots of attention to the development of non-noble metal nickel (Ni) based catalysts. Ni catalysts are particularly attractive due to their widespread use in hydrocarbon cracking, owing to their high dispersion on support and cost-effectiveness (Younis, et al., 2018). Nevertheless, the direct application of nickel-based catalysts in diesel steam reforming tends to result in carbon deposition, leading to catalyst deactivation and diminished stability. To address this issue, the incorporation of additives into Ni-based catalysts has proven effective in enhancing their resistance to carbon deposition, thereby mitigating catalyst deactivation and improving overall stability (Chen, et al., 2023; Lu, et al., 2020). Thus, the exploration of non-noble metal Ni-based catalyst additives assumes paramount importance in the quest to enhance the efficiency and coking resistance of diesel fuel reforming catalysts.

It is well known that the nature of the catalyst carrier has a large influence on the catalyst activity (Vita, et al., 2018). Alumina support has advantages of high pore volume, large specific surface area, excellent thermal stability and good mechanical strength, and is widely used in industrial catalyst supports (Wan, et al., 2017). However, the acidic sites on the surface of alumina often promote the formation of carbon deposition and lead to catalyst deactivation (Zarei Senseni, et al., 2016). By adding a promoter to the Ni- based catalyst to form a bimetallic catalyst structure, it can reduce the activation energy of the reaction (Li, et al., 2020), promote the dispersion and reduction of non-precious metals (Daorattanachai, et al., 2018) and inhibit the carbon accumulation of active metals (Nataj, et al., 2018). In order to improve the carbon deposition resistance of Ni-based catalysts, researchers have tested a variety of different transition metals, lanthanide metals or alkaline metals as modifiers in the supports, in an effort to induce support mediated promotional efforts on the catalytic system (Charisiou, et al., 2018). For example, oxides such as CeO_2 and La_2O_3 can be used to change the chemical properties of alumina and reduce the acidic sites on the surface, thus inhibiting the formation of carbon and improving the stability and lifetime of the catalyst (Charisiou, et al., 2020; Xue, et al., 2021).

An approach which appears promising is adding La_2O_3 into the Ni-based catalyst. CO_2 is activated by La_2O_3 through the formation of $La_2O_2CO_3$, which can eliminate the carbon formation at the Ni-La_2O_3 interface by coke oxidation (Slagtern, et al., 1997; Verykios, 2003). Wang et al. investigated the influence of various additives on the catalytic activity and stability of Ni-based catalyst for steam reforming of biomass. The experiment test showed that the doping of the La on Ni/Al_2O_3 improved the dispersion of the surface-active particles and reduced the particle size, increasing its catalytic activity during H_2 production (Wang, et al., 2020). Xu et al. employed rare-earth (La, Ce, Yb)-promoted Ni/γ-Al_2O_3 catalysts in the process of diesel steam reforming. The experimental findings revealed that the Yb-Ni, Ce-Ni, and La-Ni catalysts demonstrated superior diesel conversion activity and enhanced resistance to carbon formation compared to the non-promoted catalyst (Xu, et al., 2011). Ahmed et al. studied the effect of using La_2O_3 as promoter for Ni/Al_2O_3 catalysts in dry reforming of methane. The study applied various techniques for characterization of both fresh and used catalysts. The study proved that the addition of La_2O_3 to the catalyst improved the dispersion of Ni and adsorption of CO_2, thus its activity and stability enhanced (Al-Fatesh, et al., 2014). Another approach which appears promising is the utilization of metal oxides that possess high oxygen storage capacity, as it has been reported that CeO_2 acts as an oxygen buffer, storing/releasing oxygen viaCe^{3+}/Ce^{4+} redox couple (Montini, et al., 2016).

The experimental test method allows us to investigate the effect of different catalysts against carbon deposition in diesel reforming reaction experiments. However, experimental studies also have some limitations. Traditional experimental studies are difficult to explain the kinetic and thermodynamic reaction mechanisms of chemical reactions. Density functional theory (DFT) calculation is an effective method to study the mechanism of catalytic reactions. The researchers used DFT calculations to assist in explaining the mechanism of the chemical reactions occurring over the catalyst in diesel reforming experiments. Xue et al. used DFT to verify the superior activity of the Ni-Rh surface compared to that of the Ni surface because of its weak interactions with oxygen-containing species (CH_2O^*, CHO^*, and O^*) (Xue, et al., 2021). Yan et al. studied the diesel steam reforming on Pt-Ni/CeO_2 bimetallic catalyst by DFT. The results show that the Pt-dominant bimetallic surface would not only weaken the surface O binding strength to improve the activity but also reduce the stability of deposited carbon atom to potentially improve the stability (Yan, et al., 2016). The DFT calculations of the adsorption and dissociation reactions of carbon oxides on the surface of bimetallic catalysts are important to elucidate the mechanism of carbon deposition mechanism in diesel steam reforming (Xue, et al., 2022).

Despite the extensive research efforts dedicated to non-noble metal Ni-based catalysts for hydrocarbons steam reforming, certain limitations still exist. Previous studies have demonstrated that the incorporation of La and Ce into nickel-based catalysts effectively suppresses carbon deposition from low carbon chain hydrocarbons. However, it remains unclear whether the same effect can be achieved with long-chain hydrocarbons such as diesel. Moreover, the mechanism related to carbon deposition inhibition remains insufficiently understood due to the presence of promoters. The characterization of catalyst samples after experimentation allows for a more direct analysis of carbon deposition. However, this type of sample characterization is destructive and cannot be performed in real-time during the experimental process. To address these challenges, it is necessary to identify a parameter that can represent the accumulation of carbon in the reaction and provide real-time characterization of catalyst carbon deposition. Considering the aforementioned objectives, further experimental investigations are required to determine the carbon resistance effects of La and Ce modified Ni-based catalysts in diesel steam reforming and explore potential reaction mechanisms. Such research endeavours will contribute to the optimization of catalyst design and enhance the efficiency and stability of the diesel hydrogen production process.

In this study, we prepared La_2O_3/CeO_2 modified γ-Al_2O_3 coated on a honeycomb ceramic as the support for the Ni catalyst. The effects of La_2O_3 and CeO_2 modified γ-Al_2O_3 on the dispersion and reduction of Ni were investigated by H_2-temperature programmed reduction (TPR), X-ray diffraction (XRD) and transmission electron microscopy (TEM). The impact of modified catalyst support on the activity and inhibition of carbon deposition of the Ni-based metal catalyst was analyzed using thermogravimetric analysis (TGA). To investigate the hydrogen production effect and carbon deposition resistance of Ni-based catalysts doped with La and Ce for diesel steam reforming, n-hexadecane is used as a surrogate to diesel, three sets of catalysts ($Ni-Al_2O_3$, $Ni-Al_2O_3-La_2O_3$, and $Ni-Al_2O_3$-CeO_2) were used for 10 hours experiments at temperature of 800 ℃, weight hourly space velocity (WHSV) of 5.9 h^{-1}, and steam to carbon (S/C) of 3.5. DFT was employed to study the adsorption and limiting step of carbonaceous species on the surface of Ni-based catalysts to elucidate the inhibitory effect of the modified catalyst support on carbon deposition. The present study further introduces an approach for assessing carbon deposition based on the ratio of CO to CO_2. This method offers an in-time monitoring of catalyst carbon deposition during the operation of diesel steam reforming.

2. EXPERIMENT
2.1. Catalyst preparation

In the experimental setup, cordierite honeycomb ceramic is employed as the catalyst support. The 400-mesh cordierite honeycomb ceramic has dimensions of 70 mm in length and 40 mm in diameter. To enhance the surface area of the support, a firmly adhered Al_2O_3 layer was first deposited on the inner walls of the honeycomb ceramic prior to the wet impregnation of the active component and promoters. Dry powdered aluminium sol is gradually added into deionized water while being stirred by a magnetic stirrer, yielding an aluminium sol solution with a colloidal solid content of approximately 15%. The honeycomb ceramic is immersed in this solution for 2 minutes, followed by drying at a controlled temperature of 120 ℃ in an oven for 6 h, then is heated in a muffle furnace at 600 ℃ for 2 h. After calcination, the honeycomb ceramic is weighed using an analytical balance, and the mass of the coated alumina is computed. These steps are reiterated until the desired quantity of alumina is coated on the inner walls of the cordierite monolith.

Subsequently, the active Ni component and promoters are loaded on the alumina support of the honeycomb ceramic via the wet impregnation method. Following the study of Yang (Yang, et al., 2010), it is mentioned that the catalyst exhibited excellent resistance to carbon accumulation when the mass ratio of NiO to La_2O_3 and CeO_2 are maintained at 10:3:3. Consequently, Nickel acetate tetrahydrate ($Ni(CH_3COO)_2·4H_2O$, 98%), lanthanum nitrate hexahydrate ($La(NO_3)_3·6H_2O$, 99%) and cerium nitrate hexahydrate ($Ce(NO_3)_3·6H_2O$, 99%) are blended with deionized water at a weight ratio of 33.3:7.97:7.57 (which can be converted to $NiO:La_2O_3:CeO_2=10:3:3$). Following wet impregnation, the honeycomb ceramic is subjected to drying at 120 ℃ for 3 h, followed by calcination at a heating rate of 2 ℃/min, reaching temperature of 700 ℃ for 4 h. The substances loaded on the alumina layer include NiO, La_2O_3, and CeO_2. Table 1 provides a summary of the compositions of the fresh catalysts, namely $Ni-Al_2O_3$, $Ni-Al_2O_3-La_2O_3$, and $Ni-Al_2O_3-CeO_2$. After heating, composition of the catalysts are as follows: γ-Al_2O_3 (15%), NiO (20%), La_2O_3 (6%), and CeO_2 (6%). The prepared unreduced fresh catalyst is further reduced in a muffle furnace with a 10% H_2-90% N_2 gas flow at 800 ℃ for 4 h (Xue, et al., 2022).

Table 1: Composition of the catalysts

	Composition of the catalysts
#1	15% γ-Al_2O_3 20% NiO
#2	15% γ-Al_2O_3 20% NiO 6% La_2O_3
#3	15% γ-Al_2O_3 20% NiO 6% CeO_2

2.2. Test setup

The $Ni-Al_2O_3$, $Ni-Al_2O_3-La_2O_3$, and $Ni-Al_2O_3-CeO_2$ catalysts were tested at 800 ℃. The n-hexadecane used for the experiment was set at the flow rate of 1 ml/min and the deionized water was set at 3.5 ml/min. The weight hourly space velocity (WHSV) of n-hexadecane was maintained at 5.9 h^{-1}, and the steam-to-carbon ratio (S/C) was set at 3.5. The experimental setup is shown in Figure 1. Water and fuel are supplied by constant flow pumps and heated by heaters to 150 ℃ and 300 ℃, respectively. The gasified reactants are premixed by a nozzle at the reformer inlet. Prior to the steam reforming experiment, 200 NmL/min of 10% H_2 + 90% N_2 was passed into the reformer at 800 ℃ for reduction for 4 h. During the experiment, the product gas is sequentially filtered and dried through the condenser tube, gas-liquid separator, and oil mist filter. The components of the exhaust gas (H_2, CO, CO_2, and CH_4) were detected by TCD through Agilent 7820A gas chromatography with PQ column and 5A molecular column. The flow rate of the gas was detected by a soap film flow meter. The catalytic performance evaluation of n-hexadecane conversion is expressed by Equation 1.

Equation 1:
$$X_{C_{16}H_{34}} = \frac{\dot{n}_{gen} \times (COmol\% + CO_2mol\% + CH_4mo\%)}{16 \times \dot{n}_{C_{16}H_{34}}} \times 100\%$$

Where:

- $\dot{n}_{gen}$ represents the normal flow rate of the dry reformate (at standard 273.15 K and 101.325 kPa) in the outlet of the reformer
- $\dot{n}_{C_{16}H_{34}}$ represents the normal flow rate of $C_{16}H_{34}$
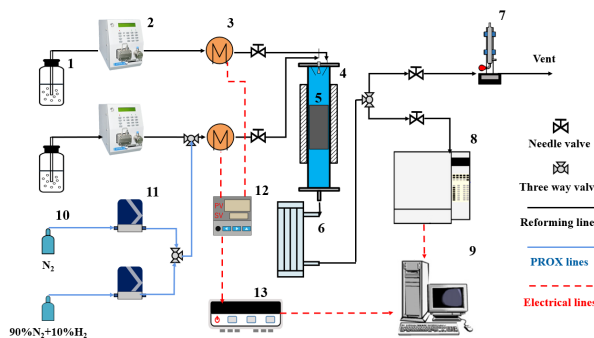
1 reactant n-hexadecane/water; 2 pump; 3 heater; 4 reformer; 5 cellular ceramic catalyst; 6 heat exchanger;
7 soap film flow meter; 8 gas chromatography; 9 computer;10 gas cylinder; 11 flow meter; 12 PID; 13 data acquisition

Figure 2: Diesel surrogate steam reforming experiment setup

2.3. Density functional theory calculation

The adsorption energy of C-containing substances on the catalyst surface was calculated by the Vienna ab initio simulation package (VASP). The PAW method was used to deal with the interactions between valence electrons and ions. And the PBE function was used as the exchange correlation function. The wave function for each k-point was expanded using plane waves, and the kinetic energy cutoff was set to 400 eV. The Brillouin zone was sampled using a 3 × 3 × 1 Monkhorst–Pack k-point grid. The structural optimization was conducted until the energy converged to 10-6 and forces converged to 0.01 eV/Å (Xue, et al., 2021; Xue, et al., 2022). Spin polarization was considered for all calculations due to the presence of magnetic atoms. The doped La/Ce models also included U calculations. The CI-NEB method was used to locate the transition state structure and reaction pathway, and the conjugate gradient method was used to optimize the minimum energy path based on forces until the maximum force was less than 0.05 eV/Å. The pure nickel catalyst surface had only two adsorption positions, the hcp and fcc sites. The surface with Ni doped La/Ce atoms had four adsorption positions. The adsorption energies for C and O atoms on the surface were calculated.

The adsorption energy (E_{ads}) was defined as Equation 2:

Equation 2:
$$E_{ads} = E_{adsorbates/catalyst} - E_{catalyst} - E_{adsorbates}$$

Where:

- $E_{adsorbates/catalyst}$ represents the total energy of the adsorbates on the catalyst surface
- $E_{catalyst}$ represents the energy of the exposed catalyst surface
- $E_{adsorbates}$ represents the energy of the free adsorbates

The activation energy of the reaction $E_{activation}$ is defined as Equation 3:

Equation 3:
$$E_{activation} = E_{TS} - E_{IS}$$

Where:

- E_{TS} refer to the transition state energy
- E_{IS} refer to the initial state energy

3.   RESULTS AND DISCUSSION
3.1. Physicochemical properties of fresh catalysts

Figure 2 illustrates the XRD characterization of the fresh catalysts, including Ni-Al_2O_3, Ni- Al_2O_3-La_2O_3, and Ni-Al_2O_3-CeO_2. It can be observed that apart from the distinguishing peaks of La and Ce elements, the other peaks are mostly unaffected, and no new diffraction peak or crystal phase emerges. The XRD pattern indicates the presence of both metallic Ni and NiO. All characterized samples were subjected to 10%H_2+90%N_2 reduction at 800℃. However, during the transfer of samples for characterization, a potential re-oxidation event may have occurred, as evidenced by the presence of NiO in the XRD analysis. It is noteworthy that in the actual experimental process, the reduction takes place within the reactor without the need to extract the catalyst, thereby mitigating the risk of catalyst oxidation upon exposure to air.
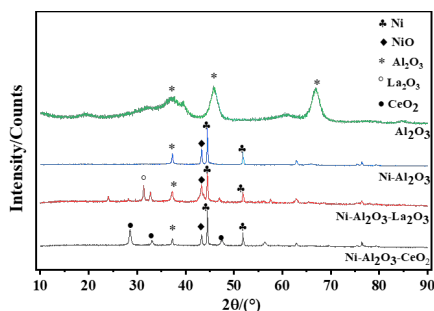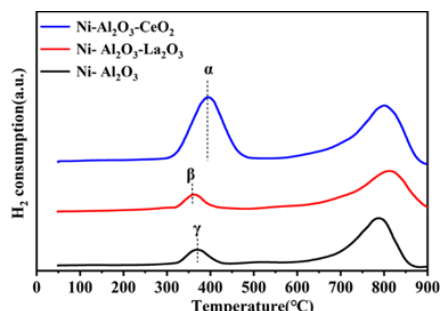
Figure 3: XRD of fresh catalysts

Figure 3: H$_2$-TPR of fresh catalysts

The reduction characteristics of the active metal are the key factors affecting the applicability of catalysts, which are detected using H$_2$-TPR measurements (Figure 3). The hydrogen consumption peaks of the three catalysts at different temperatures (300−500 ℃, 700-800 ℃) are due to the reduction of NiO species. It is worth noting that there are certain differences in the peak of the three catalysts in the low temperature section. As Figure 3 shows, peak α is stronger than peak β and γ, which is due to the reduction of surface CeO$_2$ (Xue, et al., 2020).

As shown in Figure 4, TEM images and the particle size distribution of the active metal were analyzed. The active metals and support of the various catalysts were found to be highly dispersed. The average particle sizes of the active metals in the Ni-Al$_2$O$_3$, Ni-Al$_2$O$_3$-La$_2$O$_3$, and Ni-Al$_2$O$_3$-CeO$_2$ catalysts were determined to be 30.4 nm, 23.17 nm, and 25.56 nm, respectively. The size of the metallic particles followed the trend Ni-Al$_2$O$_3$> Ni-Al$_2$O$_3$-CeO2> Ni-Al$_2$O$_3$-La$_2$O$_3$. The incorporation of doping additives facilitates the increased dispersion of Ni and reduces the agglomeration of Ni particles. It can be concluded that the doping of La and Ce atoms reduces theparticle size of Ni agglomerates and enhances the dispersion of Ni, thereby promoting the contact between the catalyst and reactants.
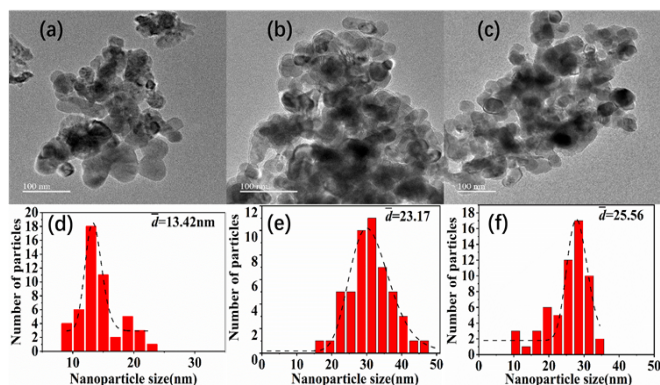

Figure 4: The TEM images of the fresh catalyst: (a) Ni-Al$_2$O$_3$; (b) Ni-Al$_2$O$_3$-La$_2$O$_3$; (c) Ni-Al$_2$O$_3$-CeO$_2$; The particle size distribution analysis of the fresh catalyst: (d) Ni-Al$_2$O$_3$; (e) Ni-Al$_2$O$_3$-La$_2$O$_3$; (f) Ni-Al$_2$O$_3$-CeO$_2$
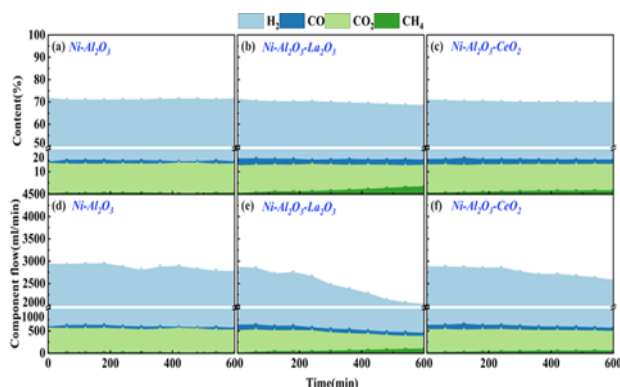
Figure 5: Content of produced gas in each experimental group: (a) Ni-Al$_2$O$_3$; (b) Ni-Al$_2$O$_3$-La$_2$O$_3$; (c) Ni-Al$_2$O$_3$-CeO$_2$; Component flow of produced gas in each experimental group: (d) Ni-Al$_2$O$_3$; (e)Ni-Al$_2$O$_3$-La$_2$O$_3$; (f) Ni-Al$_2$O$_3$-CeO$_2$

3.2. Reforming characteristics of different catalysts

Figure 5 illustrates the performance of n-hexadecane steam reforming with different catalysts under the conditions of reforming temperature of 800 ℃, WHSV of 5.9 h-1, an S/C of 3.5, and preheating temperatures of deionized water and n-hexadecane at 330 ℃. Figure 5 (a)-(c) depict the variation in the percentage of various product gas components over time for different catalysts. Figure 5(b) reveals that, with the progression of reaction, there is a notable increase in the CH$_4$ content. This phenomenon may be attributed to catalyst deactivation occurring in the later stages of the reaction, resulting in a diminished conversion rate of n-hexadecane. It can be observed from Figure 5 (a) and (c) that there is minimal change in the composition of the different gas components over time, indicating relatively stable catalytic performance among the catalyst Ni-Al$_2$O$_3$ and Ni-Al$_2$O$_3$-CeO$_2$. Figure 5 (d)-(f) presents the actual flux of various product gases over time under different catalyst conditions. From Figure 5 (e), it can be observed that in the La$_2$O$_3$- doped experimental group, there is a significant decrease in the actual flux of product gases such as H$_2$, CO, and CO$_2$ as the reaction progresses. In Figure 5 (b), the composition of product gases remains largely unchanged, indicating no significant alteration in the catalyst performance. It can be inferred that the catalyst has not deactivated, but the C$_{16}$H$_{34}$ that can be catalytically converted is decreasing, possibly due to a reduction in reaction sites on the catalyst. As a result, the products are not completely converted. From Figure 5 (f), it can be observed that there is a difference in the amounts of CO and CO$_2$ produced after CeO$_2$ doping. There is a higher conversion of CO$_2$ to CO. This further validates the hypothesis that the addition of CeO$_2$ has an impact on the relevant conversion reactions of CO and CO$_2$.

Figure 6 illustrates the conversion rates of n-hexadecane steam reforming. It can be observed that both Ni-Al$_2$O$_3$-CeO$_2$ and Ni-Al$_2$O$_3$ catalysts exhibit relatively stable catalytic performance towards n-hexadecane. Compared to the pure nickel catalyst, the addition of Ce element slightly enhances catalytic activity, but the improvement is not significant. The catalytic activity of the Ni-Al$_2$O$_3$-La$_2$O$_3$

decreases by approximately 20% within 10 hours. The addition of La element results in a noticeable decline in conversion rate. Combining the above-mentioned analysis with the negligible changes in the composition of product gases upon La doping, it can be concluded that the catalyst's properties remain relatively stable. However, there is a sharp decrease in the flow rate of product gases. The rapid decline in La conversion rate might be attributed to the formation of certain substances that occupy a significant number of surface reaction sites, consequently causing a rapid decrease in activity.
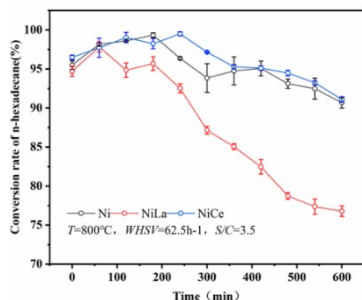

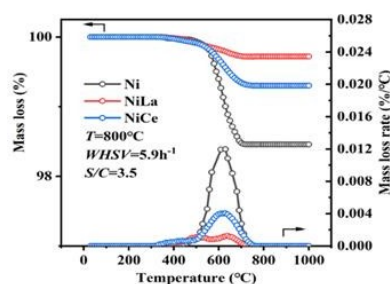Figure 6: Conversion rate of n-hexadecane steam reforming

Figure 7: Thermogravimetric analysis (TGA) of catalysts after 10h of n-hexadecane steam reforming

3.3. Physicochemical properties of used catalysts

Figure 7 presents the TGA characterization results of the spent catalysts, analyzing the changes in relative mass and the rate of relative mass change with increasing temperature. As shown in Figure 7, as the temperature rises, carbon deposition is evaporated, leading to a continuous decrease in the relative mass of the catalyst sample. The greater the mass loss, the higher thecarbon deposition on the catalyst. From Figure 7, it can be observed that the extent of carbon deposition follows the order of Ni-Al_2O_3> Ni-Al_2O_3-CeO_2> Ni-Al_2O_3-La_2O_3. Ni-Al_2O_3-La_2O_3 exhibits the least amount of carbon deposition, indicating its superior resistance to coking. The incorporation of La and Ce into the catalyst formulation significantly reduces the carbon content in the spent catalyst, thereby alleviating coking on the Ni-based catalyst. This provides preliminary evidence supporting the effectiveness of La and Ce doping in suppressing coking.

The stability of catalysts relies not only on the rate of carbon deposition but also on the type of carbonaceous species formed (Ma, et al., 2016; Son, et al., 2014). Previous research has indicated the formation of various types of carbonaceous deposits on catalyst surfaces. As is widely accepted, amorphous carbon combusts at temperatures between 200 ℃and 500 ℃, disordered carbon such as carbon nanotubes are between 500 ℃and 600 ℃ (Lehman, et al., 2011; Velasquez, et al., 2014). The mass loss occurring above 600 ℃ can be attributed to the oxidation of graphitic carbon species (Kumar, et al., 2019; Nogueira, et al., 2014). Graphite carbon and filamentous carbon have a more stable structure than disordered carbon. As is well known, the more ordered the carbon structure, the higher the temperature required for gasification (Liu, et al., 2011). Characterization results from Figure 7 of the TGA analysis indicate the onset of mass loss at 400 ℃, with the majority of the peak mass loss rates occurring in the temperature rangeabove 500 ℃. Hence, the carbonaceous deposits detected in this study primarily consist of graphitic carbon and carbon nanotubes.

Figure 8 presents the XRD characterization of the used Ni-Al_2O_3-La_2O_3 catalyst. As observed in Figure 8, the presence of a new component, $La_2O_2CO_3$ is analyzed in the used catalyst. According to Verykios' research, the Ni-La_2O_3 catalyst facilitates a reaction occurring at the interface between Ni- and La_2O_3. As CH_4 undergoes decomposition on Ni grains to produce H_2 and carbonaceous substances, CO_2 tends to adsorb onto La_2O_3, resulting in the formation of $La_2O_2CO_3$. The oxygen species within $La_2O_2CO_3$ subsequently react with carbonaceous deposits near the Ni surface, leading to the generation of CO(Verykios, 2003). Some of the carbon accumulation on Ni is attributed to the decomposition of hydrocarbons, such as CH_4. The elimination of carbonaceous deposits from Ni takes place at the interface between Ni and La_2O_3. As depicted in Figure 5(b) and (e), there is a noticeable increase in the CH_4 content. This observation suggests a decreasing number of active Ni sites available for the continued reaction of CH_4. When certain Ni sites on the catalyst surface deactivate, the $La_2O_2CO_3$ in contact with them becomes unable to sustain subsequent reactions. This phenomenon may lead to the progressive accumulation of carbonaceous deposits, potentially clogging adjacent pores, and consequently triggering a rapid catalyst deactivation. This finding is consistent with the previous speculation and confirms the earlier hypothesis that the addition of La affects the conversion of n-hexadecane. Although the incorporation of La can improves the resistance of the catalyst to carbon accumulation to some extent, it also generates $La_2O_2CO_3$, which may block the pores of the reactive sites on the catalyst, thereby impacting the conversion process.
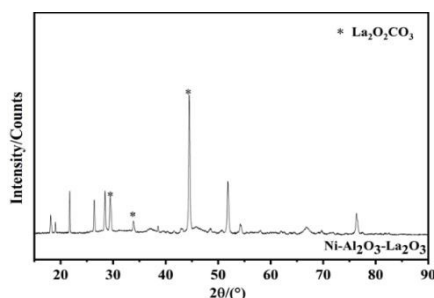

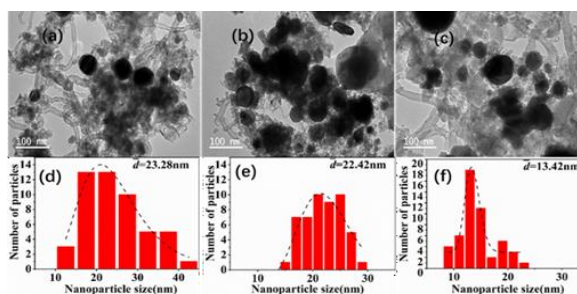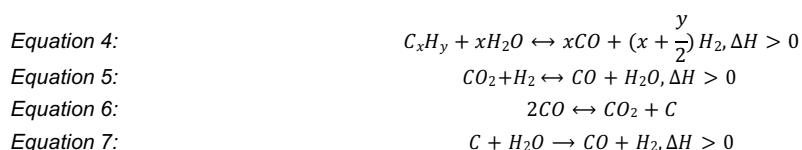Figure 8: XRD of the used Ni-Al_2O_3-La_2O_3 catalyst

Figure 9: The TEM images of the used catalyst: (a) Ni-Al_2O_3; (b) Ni-Al_2O_3-La_2O_3; (c) Ni-Al_2O_3-CeO_2;

The particle size distribution analysis of the used catalyst: (d) Ni-Al_2O_3; (e) Ni-Al_2O_3-La_2O_3; (f) Ni-Al_2O_3-CeO_2

To further investigate the structure and morphology of used catalysts, TEM micrographs were carried out as shown in Figure 9. The average particle sizes of the active metals in the Ni-Al$_2$O$_3$, Ni-Al$_2$O$_3$-La$_2$O$_3$, and Ni-Al$_2$O$_3$-CeO$_2$ catalysts were determined to be 23.28 nm, 22.42 nm, and 13.42 nm, respectively. In addition, a structure similar to carbon nanotubes was photographed in TEM electron microscopy, as shown in Figure 9 (a). The carbon nanotube's structure was present not only in the used pure Ni catalyst but also inthe La-doped and Ce doped catalysts. This agrees with the TGA characterization of the used catalysts. It is also moderate with the type of carbon deposition captured in other literature (Charisiou, et al., 2019). The generated carbon nanotubes destroy the structure of the catalyst and block the reaction site pores of the catalyst, which is not conducive to the occurrence of the diesel reforming reaction.

3.4. Energies of Carbon Species on catalyst surface

The diesel steam reforming reaction (Equation 4) is highly endothermic, which is influenced by the simultaneous occurrence of the reverse water gas shift reaction (RWGS) (Equation 5). It is known from the literature that the Boudouard reaction (Equation 6) is one ofthe most important carbon accumulation reactions in the reforming (Charisiou, et al., 2019). Moreover, part of the formed carbon canbe consumed by carbon gasification (Equation 7). It is important to carefully consider the kinetics and thermodynamics of these reactions when analyzing catalysts carbon deposition for diesel steam reforming.

$$\text{Equation 4:} \quad C_xH_y + xH_2O \leftrightarrow xCO + (x + \frac{y}{2})H_2, \Delta H > 0$$

$$\text{Equation 5:} \quad CO_2 + H_2 \leftrightarrow CO + H_2O, \Delta H > 0$$

$$\text{Equation 6:} \quad 2CO \leftrightarrow CO_2 + C$$

$$\text{Equation 7:} \quad C + H_2O \rightarrow CO + H_2, \Delta H > 0$$

In this study, Boudouard reaction is considered as the main carbon deposition reaction affected by the anti-coking of doped catalyst. To investigate the mechanism of the effect of doped catalyst on the Boudouard reaction, a molecular dynamics model was constructed to simulate the adsorption and dissociation processes of CO and CO$_2$ on the surface of the doped catalyst. During the study, as shown in Figure 10 the Boudouard reaction can be decomposed into two reaction processes (Equation 8, Equation 9):

$$\text{Equation 8:} \quad CO_2 \rightarrow CO + O$$

$$\text{Equation 9:} \quad C + O \rightarrow CO$$

As shown in Figure 10, the adsorption energies of the atoms of the Boudouard-related reactions on the catalyst surface were calculated using the DFT method. By calculating the difference in the steady state energies, we can obtain the activation energy of the relevant reaction, and the calculated activation energies are shown in Table 2. The activation energies of Ni-Al$_2$O$_3$, Ni-Al$_2$O$_3$-La$_2$O$_3$, and Ni-Al$_2$O$_3$-CeO$_2$ were 4.929, 2.759, and 2.919 eV, respectively. The activation energies value Ni-Al$_2$O$_3$> Ni-Al$_2$O$_3$-CeO$_2$> Ni-Al$_2$O$_3$-La$_2$O$_3$. The activation energy of the Boudouard reaction is smaller and the reaction is more favorable toward the consumption of carbon buildup and the production of CO. Therefore, for several catalysts, the catalyst resistance to carbon accumulation Ni-Al$_2$O$_3$-La$_2$O$_3$> Ni-Al$_2$O$_3$-CeO$_2$> Ni-Al$_2$O$_3$.
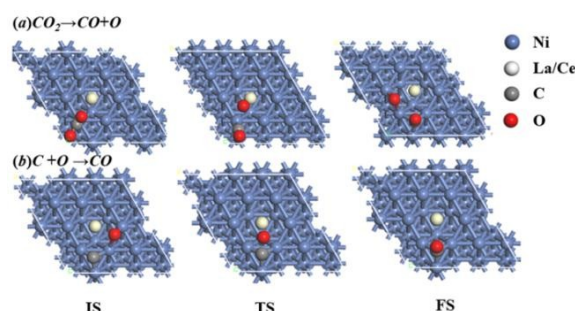
Figure 10: Transition state calculation of catalyst coke. Initial state (IS), transition state (TS) and, final state (FS)

configurations for the (a) CO$_2$→CO+O and (b) C+O→CO over the Ni, Ni-La and Ni-Ce surfaces

Table 2: Reaction activation energy of (a) CO$_2$→CO+O and (b) C+O→CO over the Ni, Ni-La and Ni-Ce surfaces

	（a）	（b）	Sum
Ni	3.199eV	1.730 eV	4.929 eV
NiLa	1.553 eV	1.206 eV	2.759 eV
NiCe	1.286 eV	1.633 eV	2.919 eV

The calculated reaction activation energies obtained from Figure 11 reveal significant insights. Based on the energy calculations of intermediate product transition states, the activation energy of reaction (Equation 8) can be significantly reduced by introducing La and Ce atoms. This reduction facilitates the generation of free oxygen, which can further react with the formed coke, thereby consuming the coke and achieving the anti-coking effect of the catalyst. Regarding reaction (Equation 9), the introduction of Ce does not result in significant changes, while the introduction of La lowers the reaction energy barrier for coke consumption, making it more favorable for coke elimination. This finding is consistent with the TGA results.

Figure 11: Energy profiles of the (a) $CO_2 \rightarrow CO+O$ and (b) $C+O \rightarrow CO$ over the Ni, Ni-La and Ni-Ce surfaces
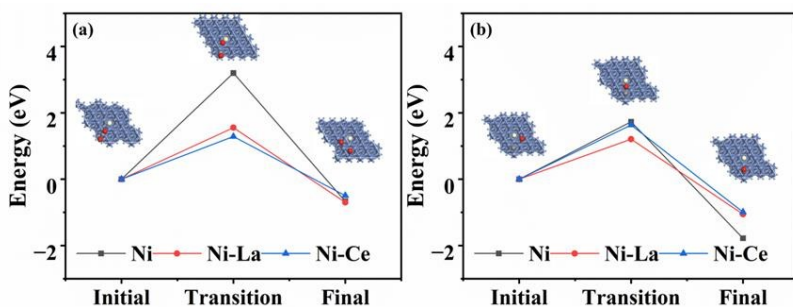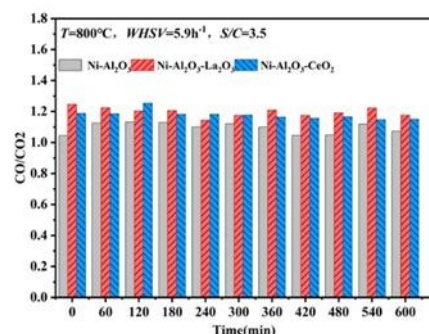

Figure 12: Ratio of CO/CO_2

TGA testing allows for the detection of catalyst coking. The Boudouard reaction is the main coking reaction in diesel steam reforming, and the CO and CO_2 content can partially reflect the degree of catalyst coking. A higher CO/CO_2 ratio indicates more CO produced and less CO_2, implying a stronger ability of the catalyst to eliminate carbon. As shown in Figure 12, the addition of La and Ce leads to an increase in CO concentration and a decrease in CO_2 concentration in the product gas, altering the equilibrium of the Boudouard reaction and driving it towards carbon consumption. Therefore, the CO/CO_2 ratio can indirectly represent the catalyst's ability to resist carbon deposition, with a higher CO/CO_2 ratio indicating a stronger carbon elimination capacity and a higher resistance to carbon deposition. From Figure 12, it can be observed that at different reaction times, the CO/CO_2 ratio follows the order: $Ni-Al_2O_3-La_2O_3 >$ $Ni-Al_2O_3-CeO_2 > Ni-Al_2O_3$, indicating that the catalyst with $Ni-Al_2O_3-La_2O_3$ composition exhibits the highest carbon elimination capacity, followed by $Ni-Al_2O_3-CeO_2$ and $Ni-Al_2O_3$. This observation is consistent with the TGA characterization results of the spent catalyst and the computational results from the DFT model.

4. CONCLUSION

In this study, three different catalysts, $Ni-Al_2O_3$, $Ni-Al_2O_3-La_2O_3$ and $Ni-Al_2O_3-CeO_2$ were examined for n-hexadecane steam reforming. The carbon deposition on used catalysts was characterized using thermogravimetric analysis. Additionally, the mechanism of surface carbon accumulation on the catalysts was elucidated by employing density functional theory modeling to calculate the activation energy of the Boudouard reaction. The computational results support the findings from the thermogravimetric analysis. The following conclusions can be drawn:

(1) The addition of La and Ce reduces the particle size of Ni clusters, enhances the dispersion of Ni, and facilitates the interaction between the catalyst and reactants, which is beneficial for improving resistance to carbon deposition. Thermogravimetric analysis characterization revealed the resistance is in the order of $Ni-Al_2O_3-La_2O_3 > Ni-Al_2O_3-CeO_2 > Ni-Al_2O_3$.

(2) Characterization of the used catalysts detected the formation of a novel compound, $La_2O_2CO_3$, which may contribute to decrease in the conversion rate of the $Ni-Al_2O_3-La_2O_3$ catalyst by obstructing the active sites. On the other hand, the addition of Ce was found to effectively suppress coke deposition without affecting the conversion rate in the steam reforming of n-hexadecane.

(3) Density functional theory calculations revealed the mechanism by which the addition of La and Ce enhances the catalyst's resistance to carbon deposition. The incorporation of La and Ce lowers the activation energy of the Boudouard reaction, facilitating carbon elimination. Consequently, the carbon resistance of the doped catalysts is improved.

(4) In practical operations, the CO/CO_2 ratio can be used as an in-time indicator to monitor catalyst carbon deposition. A higher CO/CO_2 ratio corresponds to a higher CO concentration and lower CO_2 concentration in the product gas, indicating a greater carbon consumption and stronger carbon resistance of the catalyst.

5. ACKNOWLEDGEMENT

6. REFERENCES

Al-Fatesh, A.S., Naeem, M.A., Fakeeha, A.H. and Abasaeed, A.E., (2014). 'Role of La2O3 as Promoter and Support in Ni/γ-Al2O3

Catalysts for Dry Reforming of Methane'. Chinese Journal of Chemical Engineering, 22 (1), pp. 28-37.

Carrasco-Ruiz, S., Zhang, Q., Gándara-Loe, J., Pastor-Pérez, L., Odriozola, J.A., Reina, T.R. and Bobadilla, L.F., (2023). 'H2-rich syngas production from biogas reforming: Overcoming coking and sintering using bimetallic Ni-based catalysts'. International Journal of Hydrogen Energy, 48 (72), pp. 27907-27917.

Charisiou, N.D., Italiano, C., Pino, L., Sebastian, V., Vita, A. and Goula, M.A., (2020). 'Hydrogen production via steam reforming of glycerol over Rh/γ-Al2O3 catalysts modified with CeO2, MgO or La2O3'. Renewable Energy, 162, pp. 908-925.

Charisiou, N.D., Siakavelas, G., Tzounis, L., Sebastian, V., Monzon, A., Baker, M.A., Hinder, S.J., Polychronopoulou, K., Yentekakis, I.V. and Goula, M.A., (2018). 'An in depth investigation of deactivation through carbon formation during the biogas dry reforming reaction for Ni supported on modified with CeO_2 and La_2O_3 zirconia catalysts'. International Journal of Hydrogen Energy, 43 (41), pp. 18955-18976.

Charisiou, N.D., Tzounis, L., Sebastian, V., Hinder, S.J., Baker, M.A., Polychronopoulou, K. and Goula, M.A., (2019). 'Investigating the correlation between deactivation and the carbon deposited on the surface of Ni/Al_2O_3 and $Ni/La_2O_3-Al_2O_3$ catalysts during the biogas reforming reaction'. Applied Surface Science, 474, pp. 42-56.

Chen, H., Sun, W., Hu, X., Wang, Q., Wu, T., An, S., Ding, C., Chen, C., Huang, L. and Wang, N., (2023). 'Additive WO_2 promotes Ni-based catalyst for hydrogen production from auto-thermal reforming of acetic acid'. Fuel, 339, pp. 126914.

Daorattanachai, P., Laosiripojana, W., Laobuthee, A. and Laosiripojana, N., (2018). 'Type of contribution: Research article catalytic activity of sewage sludge char supported Re-Ni bimetallic catalyst toward cracking/reforming of biomass tar'. Renewable Energy, 121, pp. 644-651.

Geng, J., Guo, Q., Pan, J., Chi, B. and Pu, J., (2023). 'Enhanced stability of co-reforming diesel and methanol into hydrogen-enriched gases for solid oxide fuel cell application'. Journal of Power Sources, 564, pp. 232830.

He, V., Gaffuri, M., Van Herle, J. and Schiffmann, J., (2023). 'Readiness evaluation of SOFC-MGT hybrid systems with carbon capture for distributed combined heat and power'. Energy Conversion and Management, 278, pp. 116728.

Kumar, A., Singh, R. and Sinha, A.S.K., (2019). 'Catalyst modification strategies to enhance the catalyst activity and stability during steam reforming of acetic acid for hydrogen production'. International Journal of Hydrogen Energy, 44 (26), pp. 12983-13010.

Lehman, J.H., Terrones, M., Mansfield, E., Hurst, K.E. and Meunier, V., (2011). 'Evaluating the characteristics of multiwall carbon nanotubes'. Carbon, 49 (8), pp. 2581-2602.

Li, L., Zuo, S., An, P., Wu, H., Hou, F., Li, G. and Liu, G., (2020). 'Hydrogen production via steam reforming of n-dodecane over Ni-Pt alloy catalysts'. Fuel, 262, pp. 116469.

Liu, L.P., Ma, X.J., Zhang, P. and Liu, Y.N., (2011). 'Hydrogen Production from Ethanol Steam Reforming over Ni-Cu/ZnO Catalyst'. Advanced Materials Research, 236-238, pp. 1067-1072.

Lu, G., Bai, Y., Ren, L., Wang, J., Song, X. and Yu, G., (2020). 'Role of phosphorus (P) additive in the performance of char-supported nickel (Ni) catalyst on tar reforming'. Energy Conversion and Management, 225, pp. 113471.

Ma, H., Zeng, L., Tian, H., Li, D., Wang, X., Li, X. and Gong, J., (2016). 'Efficient hydrogen production from ethanol steam reforming over La-modified ordered mesoporous Ni-based catalysts'. Applied Catalysis B: Environmental, 181, pp. 321-331.

Montini, T., Melchionna, M., Monai, M. and Fornasiero, P., (2016). 'Fundamentals and Catalytic Applications of CeO_2-Based Materials'. Chemical Reviews, 116 (10), pp. 5987-6041.

Nataj, S.M.M., Alavi, S.M. and Mazloom, G., (2018). 'Modeling and optimization of methane dry reforming over $Ni-Cu/Al_2O_3$ catalyst using Box–Behnken design'. Journal of Energy Chemistry, 27 (5), pp. 1475-1488.

Nogueira, F.G.E., Assaf, P.G.M., Carvalho, H.W.P. and Assaf, E.M., (2014). 'Catalytic steam reforming of acetic acid as a model compound of bio-oil'. Applied Catalysis B: Environmental, 160-161, pp. 188-199.

Potemkin, D.I., Rogozhnikov, V.N., Ruban, N.V., Shilov, V.A., Simonov, P.A., Shashkov, M.V., Sobyanin, V.A. and Snytnikov, P.V., (2020). 'Comparative study of gasoline, diesel and biodiesel autothermal reforming over Rh-based Fe/Cr/Al-supported composite catalyst'. International Journal of Hydrogen Energy, 45 (49), pp. 26197-26205.

Slagtern, A., Schuurman, Y., Leclercq, C., Verykios, X. and Mirodatos, C., (1997). 'Specific features concerning the mechanism of methane reforming by carbon dioxide over Ni/La_2O_3 catalyst'. Journal of Catalysis, 172 (1), pp. 118-126.

Son, I.H., Lee, S.J., Song, I.Y., Jeon, W.S., Jung, I., Yun, D.J., Jeong, D., Shim, J., Jang, W. and Roh, H., (2014). 'Study on coke formation over $Ni/γ-Al_2O_3$, $Co-Ni/γ-Al_2O_3$, and $Mg-Co-Ni/γ-Al_2O_3$ catalysts for carbon dioxide reforming of methane'. Fuel, 136, pp. 194-200.

Velasquez, M., Batiot-Dupeyrat, C., Gallego, J. and Santamaria, A., (2014). 'Chemical and morphological characterization of multi-walled-carbon nanotubes synthesized by carbon deposition from an ethanol–glycerol blend'. Diamond and Related Materials, 50, pp. 38-48.

Verykios, X.E., (2003). 'Catalytic dry reforming of natural gas for the production of chemicals and hydrogen'. International Journal of Hydrogen Energy, 28 (10), pp. 1045-1063.

Vita, A., Italiano, C., Ashraf, M.A., Pino, L. and Specchia, S., (2018). 'Syngas production by steam and oxy-steam reforming of biogas on monolith-supported CeO_2-based catalysts'. International Journal of Hydrogen Energy, 43 (26), pp 11731-11744.

Wan, Y., Liu, Y., Wang, Y. and Luo, G., (2017). 'Preparation of Large-Pore-Volume γ-Alumina Nanofibers with a Narrow Pore Size Distribution in a Membrane Dispersion Microreactor'. Industrial & Engineering Chemistry Research, 56 (31), pp. 8888-8894.

Wang, X., Su, X., Zhang, Q. and Hu, H., (2020). 'Effect of Additives on Ni-Based Catalysts for Hydrogen-Enriched Production from Steam Reforming of Biomass'. Energy Technology, 8 (9), pp. 2000136.

Xu, L., Mi, W. and Su, Q., (2011). 'Hydrogen production through diesel steam reforming over rare-earth promoted $Ni/\gamma-Al_2O_3$ catalysts'. Journal of Natural Gas Chemistry, 20 (3), pp. 287-293.

Xue, Q., Li, Z., Jiang, Z., Chen, M., Wang, Y., Yan, B. and Luo, G., (2021). 'Diesel reforming to hydrogen over the mesoporous Ni-MgO catalyst synthesized in microfluidic platform'. International Journal of Hydrogen Energy, 46 (74), pp. 36709-36720.

Xue, Q., Li, Z., Jiang, Z., Chen, M., Yan, B., Wang, Y. and Luo, G., (2021). 'Effect of characteristic component on diesel steam reforming to hydrogen over highly dispersed Ni-Rh- and Ni-based catalysts: Experiment and DFT calculation study'. Fuel, 303, pp. 121306.

Xue, Q., Yan, B., Chen, M., Wang, Y. and Luo, G., (2020). 'Hydrogen Production via Model Diesel Steam Reforming over a High-Performance $Ni/Ce_{0.75}La_{0.25}O_{2-\delta}-\gamma-Al_2O_3$ Catalyst with Oxygen Vacancies'. Industrial & Engineering Chemistry Research, 59 (34), pp. 15188-15201.

Xue, Q., Yi, H., Li, Z., Jiang, Z., Chen, M., Wang, Y., Yan, B. and Luo, G., (2022). 'Experimental and DFT studies on diesel-steam-reforming to hydrogen over a bimetallic Rh- Ni-based $MgO-Al_2O_3$ microsphere catalyst'. Fuel, 318, pp. 123632.

Yan, B., Yang, X., Yao, S., Wan, J., Myint, M., Gomez, E., Xie, Z., Kattel, S., Xu, W. and Chen, J.G., (2016). 'Dry Reforming of Ethane and Butane with CO_2 over $Pt/Ni/CeO_2$ Bimetallic Catalysts'. ACS Catalysis, 6 (11), pp. 7283-7292.

Yang, R., Xing, C., Lv, C., Shi, L. and Tsubaki, N., (2010). 'Promotional effect of La_2O_3 and CeO_2 on $Ni/\gamma-Al_2O_3$ catalysts for CO_2 reforming of CH_4'. Applied Catalysis A: General, 385 (1-2), pp. 92-100.

Younis, M.N., Malaibari, Z.O., Ahmad, W. and Ahmed, S., (2018). 'Hydrogen Production through Steam Reforming of Diesel over Highly Efficient Promoted $Ni/\gamma-Al_2O_3$ Catalysts Containing Lanthanide Series (La, Ce, Eu, Pr, and Gd) Promoters'. Energy & Fuels, 32 (6), pp. 7054-7065.

Zarei Senseni, A., Meshkani, F. and Rezaei, M., (2016). 'Steam reforming of glycerol on mesoporous nanocrystalline Ni/Al_2O_3 catalysts for H_2 production'. International Journal of Hydrogen Energy, 41 (44), pp. 20137-20146.

#152: Long-term performance analysis of a hybrid indirect evaporative cooling-mechanical vapor compression system in Saudi Arabia

Qian CHEN[1], Kim Choon NG[2]

[1] Institute for Ocean Engineering, Tsinghua Shenzhen International Graduate School, Tsinghua University, Shenzhen 518055, China, email: qian.chen@sz.tsinghua.edu.cn
[2] Water Desalination and Reuse Center, King Abdullah University of Science and Technology, Saudi Arabia, email: kimchoon.ng@kaust.edu.sa

Abstract: Air-conditioning is the major source of energy consumption in the Middle East region, accounting for more than 50% of the peak load. Indirect evaporative cooling (IEC) is a promising technology that can significantly reduce the energy consumption of air conditioning, but its performance degrades severely when air humidity is high. To overcome this limitation, the hybridization of indirect evaporative cooling and mechanical vapor compression (MVC) has been proposed, which uses IEC to pre-cool the outdoor air and then further processes the air to desired temperature and humidity. The hybrid IEC-MVC process possesses the merits of the two, i.e., low energy consumption and capability of humidity control. Herein, we evaluate the energy-saving potential of the hybrid system under the climatic conditions of Saudi Arabia. Based on a validated mathematical model, the annual cooling performance and energy consumption of hybrid IEC-MVC configuration is predicted under the climatic conditions of 14 major cities in Saudi Arabia, and results are compared with that of standalone MVC. Moreover, the water consumption of the IEC and potential amount of recoverable water are estimated. Results reveal that IEC handles more than 50% of the annual cooling load and reduces energy consumption by up to 40%. Moreover, in humid areas, the condensate recovered from MVC is able to replenish more than 70% of the water consumed by IEC.

Keywords: Indirect Evaporative Cooling; Long-Term Analysis; Energy Saving; Water Consumption

1. INTRODUCTION

In tropical areas like Saudi Arabia, buildings consume about 80% of the electricity (Krarti et al., 2017), and a significant portion of building air consumption is contributed by air conditioning (Eveloy and Ayou, 2019). Therefore, it is of great importance to improve the energy efficiency of air conditioning systems.

Currently, the air conditioning market in Saudi Arabia is dominated by mechanical vapor compression (MVC) systems due to high technology maturity. However, the energy consumption of MVC is bottlenecked by the high ambient temperature and poor air quality of Saudi Arabia (Shahzad et al., 2021, Chen et al., 2022a). The indirect evaporative cooling is a promising alternative to MVC. It employs the evaporation of water as the driving force of cooling, and the energy efficienc y is several times higher than that of MVC (Jradi and Riffat, 2014). Considering its working principle, IEC performs particularly well in hot and arid areas, where the water has more evaporation potential.

One limitation of IEC is its inability to control the air temperature, and the supply air temperature is higher when the ambient is hot. Moreover, IEC only provides sensible cooling and has no dehumidification capacity. Therefore, the supply air does not always meet the demand of thermal comfort in tropical areas like Saudi Arabia. Another limitation of IEC is the need for water supply, which is unavailable in arid areas.

To address the limitations of the IEC, the hybridization of IEC and MVC has been proposed. By connecting IEC and MVC in tandem, IEC can be used as a pre-cooler, and MVC further regulates air temperature and humidity to achieve thermal comfort *(Chen et al., 2021)*. Moreover, the condensate can be collected from MVC evaporator to replenish IEC. The merits of such a hybrid system have been demonstrated in many areas, including Beijing (Duan et al., 2019), Xi'an (Cui et al., 2019b)), Iran (Delfani et al., 2010), Italy (Zanchini and Naldi, 2019) and Singapore (Cui et al., 2019a, Cui et al., 2015).

This study evaluates the potential of the hybrid IEC-MVC system in Saudi Arabia. The climatic and geographical conditions of the country is firstly analyzed. Then, annual performance of hybrid IEC-MVC is predicted using the climatic data as the input, and results are compared with that of standalone MVC. Finally, the amount of water consumption by IEC and recoverable water from the hybrid system are predicted and compared.

2. QUANTIFICATION OF ANNUAL COOLING AND DEHUMIDIFICATION NEEDS

We firstly evaluate the annual need for cooling and dehumidification in different cities of Saudi Arabia. Cooling degree-days (CDD) is a commonly used index to quantify the need for sensible cooling, and it is obtained by summing up the difference between the daily-average temperature and a reference temperature of 18 ℃. To be more accurate, we conduct the same calculation but with a time interval of 1 hour, and the result is defined as cooling degree-hours (CDH):

$$CDH = \sum(T_{hourly} - 18\,°C)\ when\ T_{hourly} > 18\,°C \tag{1}$$

Similarly, we define the dehumidifying gram hours (DGH) to access the need for latent cooling. DGH is calculated by adding up the difference between the hourly-average humidity ratio and a reference humidity ratio of 9 g/kg:

$$DGH = \sum(\omega_{hourly} - 9\ g/kg)\ when\ \omega_{hourly} > 9\ g/kg \tag{2}$$

where ω_{hourly} is the humidity ratio.

3. QUANTIFICATION OF ANNUAL COOLING AND DEHUMIDIFICATION NEEDS

Figure 1 depicts the working principle of the hybrid IEC-MVC system proposed in our previous study (Chen et al., 2021). The IEC is made up of alternating dry and wet channels. Water is supplied to the wet channels, where it evaporates and cools the secondary air (which is room return air, RA, in the current study). The RA then cools down the outdoor air (OA) in the dry channels. Afterward,the OA is further cooled and dehumidified (if necessary) by the MVC evaporator, while the humid RA is mixed with another portion of outdoor air (OA2) and delivered to the condenser.

In our previous study, an experimental setup has been commissioned to validate the energy-saving potential of the hybrid IEC-MVC system (Chen et al., 2021). Based on the experimental data, a mathematical model was developed to predict the performance of the hybrid system (Chen et al., 2022b). The developed model is employed to predict the long-term performance of IEC-MVC in Saudi Arabia. We evaluate four key performance parameters that are evaluated, i.e., the cooling load undertaken by IEC, energy saving ofhybrid system over standalone OVC, water consumption of IEC and recoverable water from condensation.
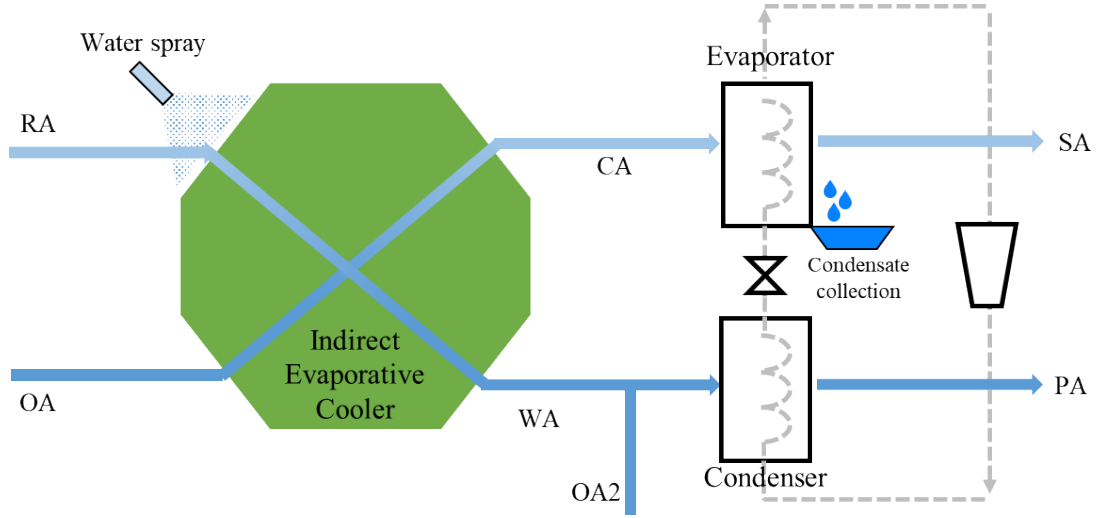
Figure 1: Schematic diagram of the hybrid IEC-MVC system (Chen et al., 2022a)

The cooling load undertaken by IEC is calculated as the ratio of cooling capacity between IEC and the hybrid system:

$$\emptyset_{IEC} = \frac{h_{OA} - h_{CA}}{h_{OA} - h_{SA}} \times 100\% \qquad (3)$$

where *h* represents the enthalpy of air.

The energy saving is calculated from the COP of the hybrid system and standalone MVC:

$$Energy\ saving = \frac{COP_{IEC-MVC} - COP_{MVC}}{COP_{IEC-MVC}} \times 100\% \qquad (1)$$

Water consumption of IEC is the water needed for evaporation in the wet channels:

$$\dot{m}_{consumption} = \dot{m}_R(\omega_{WA} - \omega_{RA}) \qquad (5)$$

And recoverable water equals the amount of condensate:

$$\dot{m}_{collection} = \dot{m}_O(\omega_{CA} - \omega_{SA}) \qquad (6)$$

4. PERFORMANCE ANALYSIS

This section analyzes the annual performance of the hybrid IEC-MVC system in 14 cities of Saudi Arabia. Simulations were conducted on an hourly basis using the annual weather data (temperature and humidity) and the results are summed up. Without loss of generality, we consider the flowrate of the air to be processed is 1 kg/s, and the results can be easily extended to any desired flowrate.

The 2nd and 3rd columns of Table 1 summarizes the annual weather data of different cities. As can be seen, most cities are hot and have very high demand for sensible cooling, with 8 of the 14 cities having CHD of close to or higher than 9000 ℃-hr/year. For example, the capital city Riyadh has a high CDH of 92248.4 ℃-hr/year, which means the air temperature needs to be reduced by 10.4 ℃ on average. On the other hand, the DGH is low for most cities, indicating low ambient humidity. However, the costal cities of the Red Sea or Persian Gulf are humid, and DGH for these cities are higher. The climatic conditions of each city have a great impact on the performance of IEC-MVC, which will be discussed below.

The 4th column of Table 1 shows the percentage of cooling contributed by IEC. In most cities, IEC contributes almost 50% of the annual cooling. Exceptions are observed in cities that are either humid (e.g., Jeddah, DGH=61307.65 g-hr; Jazan, DGH=58262.23 g-hr,) or cold (Abha, DGH= 17674.90 g-hr; Al-Bahah, DGH= 20167.7 g-hr). The annual energy saving of IEC-MVC over standalone MVC is directly correlated to the contribution of IEC, as shown in the 5th column. Electricity saving is up to 40% in hot and dry cities like Riyadh and Qassim. For humid cities like Dhahran, Mecca, Jeddah and Jazan, the benefit of the hybrid system is less obvious but still save 20-30% of electricity compared to MVC.

As Saudi Arabia faces severe water scarcity, the water consumption deserves special attention. The 6th of Table 1 shows the water consumption of IEC during operation, which ranges between 4 to 14 L/hr. The water consumption is proportional to the cooling load

of IEC and is high in cities with high CDH. However, for cities with high humidity, substantial amount of condensate can be recovered. For example, in Dhahran and Mecca, water collection rates are 8.25 and 7.9 L/hr, respectively, accounting for > 80% of IEC consumption. In Jeddah and Jazan, collected water even exceeds water consumption in IEC.

Table 1: Long-term performance summary of hybrid IEC-MVC in Saudi Arabia

City	CDH	DGH	IEC contribution	Energy saving	Water consumption	Recoverable water
	ºC-hr	g-hr	%	%	L/hr	L/hr
Riyadh	92248.40	432.57	54.35	40.52	8.57	0.18
Hail	71265.40	6.84	53.65	37.57	6.33	0.00
Qassim	88722.40	124.65	54.96	40.98	8.21	0.04
Dhahran	89967.10	22225.80	31.27	26.04	9.15	8.25
Al-Jouf	65980.40	9.24	53.71	37.83	5.87	0.00
Turaif	48481.60	86.82	50.14	33.44	3.94	0.01
Tabuk	62562.60	155.29	51.94	36.12	5.36	0.03
Mecca	107079.70	21044.16	32.77	24.78	10.86	7.90
Jeddah	97338.00	61307.65	19.25	14.64	10.15	24.02
Madinah	101092.60	995.84	53.49	40.15	9.53	0.25
Abha	17674.90	815.62	15.32	7.55	0.38	0.01
Jazan	111837.00	58262.63	22.39	17.20	12.22	23.56
Najran	58329.40	409.75	45.09	28.13	4.29	0.11
Al-Bahah	20167.70	1113.43	15.46	7.87	0.51	0.04

5. CONCLUSION

This study evaluates the long-term energy-saving potential and water consumption of the hybrid IEC-MVC cycle in Saudi Arabia. The main takeaways from the study include:

(1) Most cities in Saudi Arabia are hot and have high demands for sensible cooling, favoring the employment of indirect evaporative cooling;
(2) Over the whole year, IEC can handle >50% of cooling load in the arid cities and the energy consumption is reduced by 40% as compared to standalone MVC;
(3) Water consumption of IEC is proportional to the cooling load of IEC and can be replenished by recovered condensate from the MVC evaporator.

6. REFERENCES

CHEN, Q., BURHAN, M., SHAHZAD, M. W., YBYRAIYMKUL, D., OH, S., CUI, X. & NG, K. C. 2022a. Long-term performance of a hybrid indirect evaporative cooling-mechanical vapor compression cycle: A case study in Saudi Arabia. *Frontiers in Built Environment,* 8**,** 1032961.

CHEN, Q., JA, M. K., BURHAN, M., AKHTAR, F. H., SHAHZAD, M. W., YBYRAIYMKUL, D. & NG, K. C. 2021. A hybrid indirect evaporative cooling-mechanical vapor compression process for energy-efficient air conditioning. *Energy Conversion and Management,* 248**,** 114798.

CHEN, Q., JA, M. K., BURHAN, M., SHAHZAD, M. W., YBYRAIYMKUL, D., ZHENG, H. & NG, K. C. 2022b. Experimental study of a sustainable cooling process hybridizing indirect evaporative cooling and mechanical vapor compression. *Energy Reports,* 8**,** 7945-7956.

CUI, X., CHUA, K., ISLAM, M. & NG, K. C. 2015. Performance evaluation of an indirect pre-cooling evaporative heat exchanger operating in hot and humid climate. *Energy Conversion and Management,* 102**,** 140-150.

CUI, X., ISLAM, M. & CHUA, K. 2019a. An experimental and analytical study of a hybrid air-conditioning system in buildings residing in tropics. *Energy and Buildings,* 201**,** 216-226.

CUI, X., SUN, L., ZHANG, S. & JIN, L. 2019b. On the study of a hybrid indirect evaporative pre-cooling system for various climates. *Energies,* 12**,** 4419.

DELFANI, S., ESMAEELIAN, J., PASDARSHAHRI, H. & KARAMI, M. 2010. Energy saving potential of an indirect evaporative cooler as a pre-cooling unit for mechanical cooling systems in Iran. *Energy and Buildings,* 42**,** 2169-2176.

DUAN, Z., ZHAO, X., LIU, J. & ZHANG, Q. 2019. Dynamic simulation of a hybrid dew point evaporative cooler and vapour compression refrigerated system for a building using EnergyPlus. *Journal of Building Engineering,* 21**,** 287-301.

EVELOY, V. & AYOU, D. S. 2019. Sustainable district cooling systems: Status, challenges, and future opportunities, with emphasis on cooling-dominated regions. *Energies,* 12**,** 235.

JRADI, M. & RIFFAT, S. 2014. Experimental and numerical investigation of a dew-point cooling system for thermal comfort in buildings. *Applied Energy,* 132**,** 524-535.

KRARTI, M., DUBEY, K. & HOWARTH, N. 2017. Evaluation of building energy efficiency investment options for the Kingdom of Saudi Arabia. *Energy,* 134**,** 595-610.

SHAHZAD, M. W., LIN, J., XU, B. B., DALA, L., CHEN, Q., BURHAN, M., SULTAN, M., WOREK, W. & NG, K. C. 2021. A spatiotemporal indirect evaporative cooler enabled by transiently interceding water mist. *Energy,* 217**,** 119352.

ZANCHINI, E. & NALDI, C. 2019. Energy saving obtainable by applying a commercially available M-cycle evaporative cooling system to the air conditioning of an office building in North Italy. *Energy,* 179**,** 975-988.

#155: Effects of quantity and placement of epipremnum aureum on work efficiency and physiological responses of occupants

Lijun Zuo[1], Dan Wu[2], Mengsi Deng[3], Yanping Yuan[4, *]

[1] School of mechanical engineering, Southwest Jiaotong University, 610031, Chengdu, China, 1490326572@qq.com
[2] School of architecture, Southwest Jiaotong University, 611756, Chengdu, China, dan.wu@swjtu.edu.cn
[3] School of mechanical engineering, Southwest Jiaotong University, 610031, Chengdu, China, mengseideng@swjtu.edu.cn
[4] School of mechanical engineering, Southwest Jiaotong University, 610031, Chengdu, China, ypyuan@home.swjtu.edu.cn

Abstract: In the context of accelerating urbanization, in addition to energy and environmental issues, the concept of sustainable development also puts forward higher requirements for people's quality of life. Studies have shown that indoor plants could relieve negative emotions such as depression of indoor occupants and improve their work efficiency. However, the effects of quantity and placement of plants on indoor occupants have not been specifically discussed in existing studies. In this study, a common indoor plant, Epipremnum aureum was selected, and various combinations of quantity and placement of it were set up. 20 subjects were recruited, and the effects of plants on the work efficiency of subjects were studied by completing cognitive ability tests under different plant settings. The effects of plants on the physiological response of subjects were studied by monitoring physiological indicators such as heart rate variability and electrodermal activity (Fukusaki, #417). The results showed that the impact of plants on work efficiency was related to the characteristics of work and number and placement of plants, increasing the number of plants reduced the time required for participants to complete the operating task testing attention by 41.04 ms. Plants increased values of the standard deviation of the normal-to-normal interval (SDNN) and the root mean square of the successive differences (RMSSD) of subjects by 82.08 and 107.65 micro siemens, respectively, which indicated that plants could reduce the stress level of the subjects. The research results can provide a theoretical basis for the construction of an indoor plant landscape considering the work efficiency and health of occupants.

Keywords: Indoor Plants; Human-Nature Relations; Work Efficiency; Physiological Response

1. INTRODUCTION

Since the outbreak of COVID-19, indoor workers have experienced more serious psychological problems such as stress, anxiety and depression, especially in indoor working environments (Yeom, Kim, & Hong, 2021). Previous studies have shown that plants can effectively improve indoor air quality (K. J. Kim et al., 2018), reduce the psychological pressure of indoor workers (Deng & Deng, 2018; Kim, Cha, Koo, & Tang, 2018; Korpela et al., 2017), improve their work efficiency (Ko et al., 2020), and promote the happiness of indoor workers.

In 1984, Ulrich et al. studied the influence of natural landscape outside the window on the rehabilitation effect and psychological benefits of patients during hospitalization in the hospital and found that viewing natural landscape was conducive to improving patients' psychological depression and shortening hospital stay (Ulrich, 1984). Since then, a large number of studies have emerged on the effect of plants on the physiological response of indoor personnel. In some studies, objective physiological indicators such as heart rate, blood oxygen saturation, EDA, electrocardiogram and electroencephalogram are also monitored (Gladwell et al., 2012; Jang, Kim, Kim, & Pak, 2014; Zhang, Lian, & Wu, 2017). In addition to the study on the physiological response of plants to indoor workers, some relevant studies in office space also focus on the effect of plants on work efficiency. Relevant studies have shown that, based on the attention recovery theory, plants have a positive effect on the attention, response speed, working memory, cognitive ability and creativity of indoor office workers (J. Kim et al., 2018; Ko et al., 2020; Zuo, Wu, Yuan, Li, & Yu, 2020).

Studies have shown that visual associations with plants have a positive effect on reducing stress, restoring focus and boosting productivity. However, the effect of the number and placement of plants on occupants has not been discussed in previous studies. In this study, different number and placement combinations of plants were designed. The effects of number and placement of plants on indoor occupants' physiological response and work efficiency were investigated through monitoring physiological indicators of subjects and completing operational tasks.

2. MATERIALS AND METHODS
2.1. Experimental environment

The experiment was conducted in an office of Building 8, Xipu Campus, Southwest Jiaotong University, Chengdu City, Sichuan Province, China. The office was 3.8 meters wide and 7.4 meters deep. There were three desks, two lockers, a sofa and an air conditioner in the office. The schematic diagram of the office is shown in Figure 1.
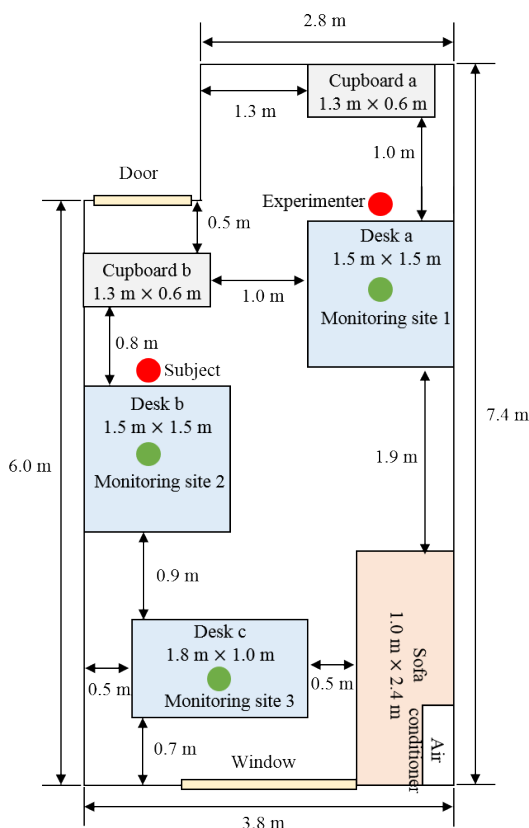

Figure 1: Schematic diagram of the office

2.2. Plants

E. aureum with strong formaldehyde purification capacity (Zuo, Wu, Yu, & Yuan, 2022), high aesthetic recognition (Berger, Essah, Blanusa, & Beaman, 2022), commonly used in related studies (Jang et al., 2014) was selected in this experiment. A preliminary

survey was conducted on all subjects before the start of the experiment, and it was found that among the alternative plants, all subjects were not allergic to, not partial to, not hate to *E. aureum*. In this study, plants were placed within or outside of the coincident view. When the plants were placed within the coincident view, the subjects could clearly form a three-dimensional image of the plants. When they were placed outside of the coincident view, the subjects could only vaguely perceive the existence of the plants. The number of plants was set to be one pot of plants on each side of the computer and two pots of plants on each side of the computer. The plant settings are shown in Table 1.

Table 1: Plant settings

Plant settings	Coincident view	Pot(s) at each side of computer
A	/	/
B	within	1
C	outside	1
D	within	2
E	outside	2

2.3. Participants

Within-subject design was adopted in this study. When selecting subjects, subjects with chronic medical conditions, uncorrected visual impairment, taking medication or stress treatment, and unskilled computer users were excluded (Emami, Amini, & Motalebi, 2018; Kjellgren & Buhrkall, 2010). 20 subjects were finally selected for the study, and the demographic information of subjects are shown in Table 2. During the experiment, the selected subjects were not allowed to smoke or drink alcohol for 24 hours before the experiment, were not allowed to exercise or consume caffeine for 12 hours before the experiment and were not allowed to eat or drink water for 1 hour before the experiment (Beil & Hanes, 2013; Gladwell et al., 2012).

Table 2: Demographic information of the subjects

Gender	Number	Age	Height(cm)	Weight (kg)	BMI (kg/m^2)
Male	9	25.00	174.89	65.94	21.56
Female	11	24.27	162.09	52.82	20.12

2.4. Measures

1. Operation task. The effects of *E. aureum* on work productivity were studied by analyzing subjects' performance of completing cognitive capacity tests at www.psytoolkit.org (J. Kim et al., 2018). PsyToolkit is a toolkit for demonstrating, programming, and running cognitive-psychological experiments and surveys ， and it is frequently used for academic studies and for teachingcognitive and personality psychology, and it is widely used in related research. An operational task measuring attention, Stimulus- Response Compatibility, an operational task measuring reaction speed, the Deary-Liewald Task, and the Cori Backward Block Test, an operational task measuring working memory, were selected in this study. When completing the Stimulus-Response Compatibility, subjects need to use the "A" and "L" keys on the keyboard to respond to the corresponding stimuli (words "left" and "right"). For example, when the subjects see the word "left", press the "A" key as quick as possible, even it appears on the right side of the screen. The Deary-Liewald Task consists of a simple task and a choice task. In the simple task, one white box will be shown on the screen, when a cross appears, subjects need to press the space bar as fast as possible. In the choice task, four white boxes will be shown on the screen, when a cross is presented in one of them, subjects need to press the corresponding key ("Z", "X", comma "," and full stop ".") as fast as possible. In the Corsi Backward Block Test, 9 blocks will be shown on the screen and some of them will light up in a sequence, subjects need to click the same blocks in the reverse sequence. For each trial, the sequences will increasingly get longer.

2. Physiological indicators. In this study, physiological indicators such as HRV and EDA were monitored (Gladwell et al., 2012; Zhao et al., 2019). HRV was measured by heart rate watch (PACER, polar, Finland) and heart rate band (H9, polar, Finland), EDA was measured using a multichannel physiograph (MP150, BIOPAC, USA). The SDNN and RMSSD were used as the analysis index of HRV, and the data were analyzed with Kubios HRV Standard software. The SDNN was related to the cardiovascular system, the higher the SDNN value, the lower the stress level of the subjects. The RMSSD was related to parasympathetic nervous system, the lower the RMSSD value, the higher the stress level of the subjects (Yeom et al., 2021). SCL was used as the analytical index of EDA, which was often used to reflect the human body's response to continuous environmental stimuli (J. Kim et al., 2018). The SCL data was analyzed by AcqKnowledge software which was used with multi-channel physiological recorder. To eliminate individual differences between subjects, the SCL value was converted to a Z-score.

2.5. Procedure

One day before the experiment, the subjects practiced the operation task and were informed of the experiment procedure. At the beginning of the experiment, the experimenters placed the plants according to the experimental design, the subjects entered the room and sat quietly for 15 minutes to adapt to the indoor environment. Then, the experimenter wore the HRV and EDA monitoring instrument for the subjects, and then the subjects sat still for 10 minutes to obtain the baseline data of HRV and EDA. Then, the subjects completed the task. After the completion of the operation task, the experimenter helped the subjects take off the monitoring instrument. Finally, the subjects left the room and ended the experiment. The experimental flow diagram is shown in Figure 2. The

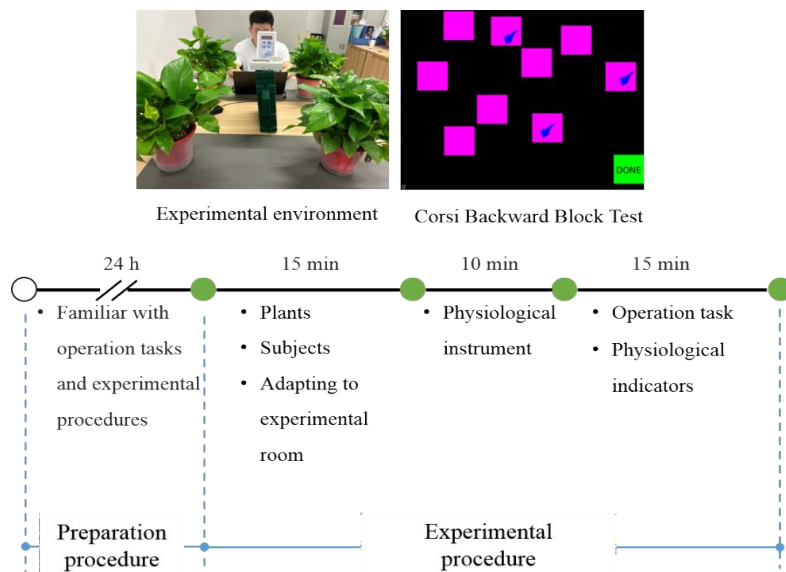study was approved by the Ethics Review Committee of Southwest Jiaotong University (SWJTU-2305-NSFC (084)).

Experimental environment   Corsi Backward Block Test

Figure 2: Schematic diagram of the office

2.6. Statistical analysis

Standard analysis comparing treatments was performed using a one-way analysis of variance (ANOVA) (SPSS v. 22.0, IBM, Inc., Armonk, NY, USA), and followed paired t-test, as the study was a cross-over study on repeated measures data. Results with a $p < 0.05$ were considered statistically significant. However, if the differences did not satisfy the normality assumption, a Friedman test was performed.

3.   RESULTS AND DISCUSSIONS
3.1. Effects of plants on work efficiency

The Stimulus-Response Compatibility was divided into compatible and incompatible, and Deary-Liewald Task was divided into simple task and choice task. Gender had a significant effect on the work efficiency of Stimulus-Response Compatibility-compatible (P=0.002), Stimulus-Response Compatibility-incompatible (P=0.002) and Deary-Liewald task-in simple task (P=0.002). Male subjects took 660.73 ms, 675.56 ms and 354.42 ms to complete these three tasks, while female subjects took 588.74 ms, 597.36 ms and 324.98 ms, respectively, and female subjects were more efficient in completing these three tasks.

The completion of the operation tasks under different plant settings is shown in Figure 3. Under different plant settings, the subjects completed Stimulus-Response Compatibility-compatible in 612.3, 654.9, 599.58, 637.2 and 580.6 ms, respectively [Figure. 3(a)]. The plant settings exhibited no significant effect on the subjects' efficiency in this task. Under different plant settings, the subjects completed Stimulus-Response Compatibility-incompatible in 656.85, 665.25, 624.84, 641.1 and 583.8 ms, respectively [Figure. 3(b)]. When natural *E. aureum* was placed outside of the coincident view, the number of plants had an effect on the work efficiency (P=0.021), and increasing the number of plants could increase the work efficiency of the subjects by 41.04 ms. Under different plant settings, the subjects took 330.4, 330.05, 334.63, 332.3 and 327.87 ms to complete the Deary Liewald task-in simple task, respectively [Figure. 3(c)]. The plant settings had no significant effect on the work efficiency of this task. Under different plant settings, the time required for the subjects to complete the Deary Liewald task-in choice task was 453.9, 471.8, 464.11, 462.7 and 455.47 ms, respectively [Figure. 3(d)]. The plant settings had no significant effect on the work efficiency of this task. In Cori Backward Block Test with different plant settings, subjects remembered the order of 5.75, 5.65, 5.42, 5.5 and 6.13 blocks, respectively [Figure. 3(e)]. Plant settings had no significant effect on working memory.

Similar to the study by Ko et al. (Ko et al., 2020) and Stone and Irvine (Stone & Irvine, 1993), in this study, no effect of plant settings was observed on the work efficiency under Stimulus-Response Compatibility-compatible, Deary Liewald Task, and Cori Backward Block Test. Similar to the experimental results of Kim et al. (J. Kim et al., 2018), the subjects in this study took less time to complete the Deary-Liewald task-in simple task than the Deary-Liewald task-in choice task. However, in contrast with the study by Kim et al. who reported that indoor plants increased work efficiency whereas artificial windows reduced work efficiency, this study did not find any effect of plants on the reaction speed of subjects. The inconsistency might be related to the fact that the study by Kim et al. was conducted in an underground space, whereas our study was conducted in an above-ground office. The analysis of Stimulus-Response Compatibility-incompatible in different plant settings revealed that both the number and placement of plants had an effect on subjects' attention. Similar to the results of Zuo et al. (Zuo et al., 2020), placing plants outside of the coincident view could reduce the impact of plants on directed attention, thereby improving work efficiency; moreover, increasing the number of plants was conducive to further improving work efficiency.
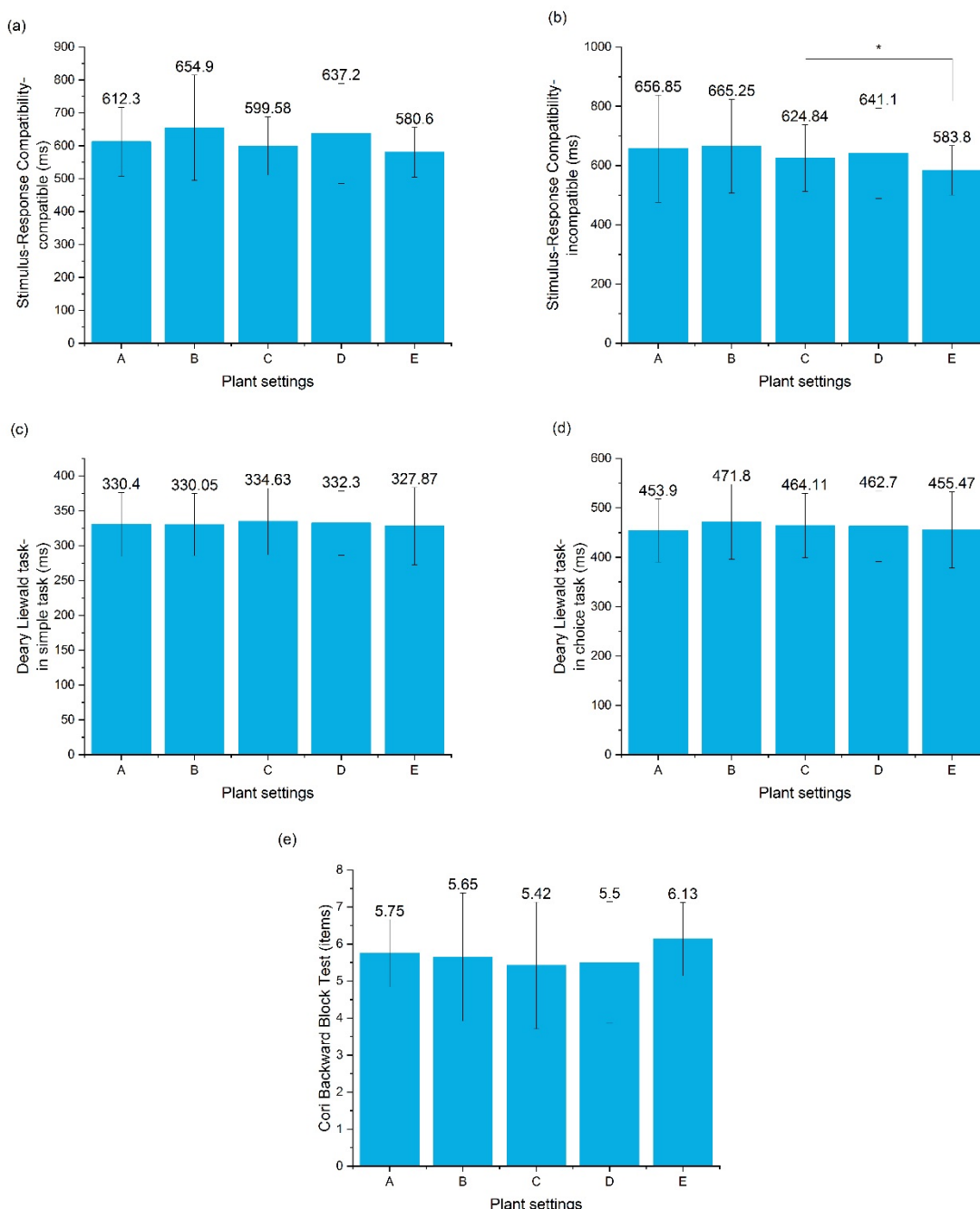
Figure 3: Work efficiency of the subjects

3.2. Effects of plants on physiology

Significant differences existed in SDNN (P = 0.003) and RMSSD (P = 0.008) among male and female subjects. SDNN of male and female subjects was 96.60 and 65.50 microsiemens, respectively, and RMSSD of male and female subjects was 106.04 and 72.88 microsiemens, respectively. This indicated that the stress level of male subjects was lower than that of female subjects during the experiment.

Physiological responses of subjects under different plant settings are shown in Figure 4. SDNN of subjects under different plant settings were 50.97, 75.42, 108.54, 109.29 and 133.05 microsiemens, respectively [Figure. 4(a)]. Compared with the control group, when the *E. aureum* was used, SDNN was increased by 24.45, 57.57, 58.32 and 82.08 microsiemens, respectively. RMSSD of subjects under different plant settings were 43.69, 85.03, 125.57, 131.89 and 151.34 microsiemens, respectively [Figure. 4 (b)]. Compared with the control group, RMSSD was increased by 41.34, 81.88, 88.20, and 107.65 microsiemens, respectively, when the *E. aureum* was used. The changes in SCL under different plant settings were −0.13, −0.14, −0.16, −0.16 and −0.18 μS, respectively [Figure. 4(c)]. Plant settings had no significant effect on the changes in SCL.

Monitoring physiological indicators is a common method to objectively analyze the influence of the environment on people. The heart rate referred to the number of heart beats per min. In a steady state, the heart rate slowed down when the parasympathetic nerve was activated, and it was accelerated when the sympathetic nerve was activated. Kahn et al. (Kahn et al., 2008), Beute et al. (Beute & de Kort, 2014), and Engell et al. (Engell, Loras, & Sigmundsson, 2020) reported that heart rate can be used to analyze the

physiological response of subjects under environmental stimuli. HRV is the change of heart rate over time rather than the raw data of heart rate. In this study and some recent studies, HRV was selected to evaluate the stress level of subjects. EDA was considered the most representative measure of arousal change, which varied according to changes in skin conductance caused bysweat gland activity (Valtchanov, Barton, & Ellard, 2010). Similar to this study, previous studies had used SCL as an analytical index of EDA and proved that natural plants had a significant impact on SCL (J. Kim et al., 2018; Yeom et al., 2021).
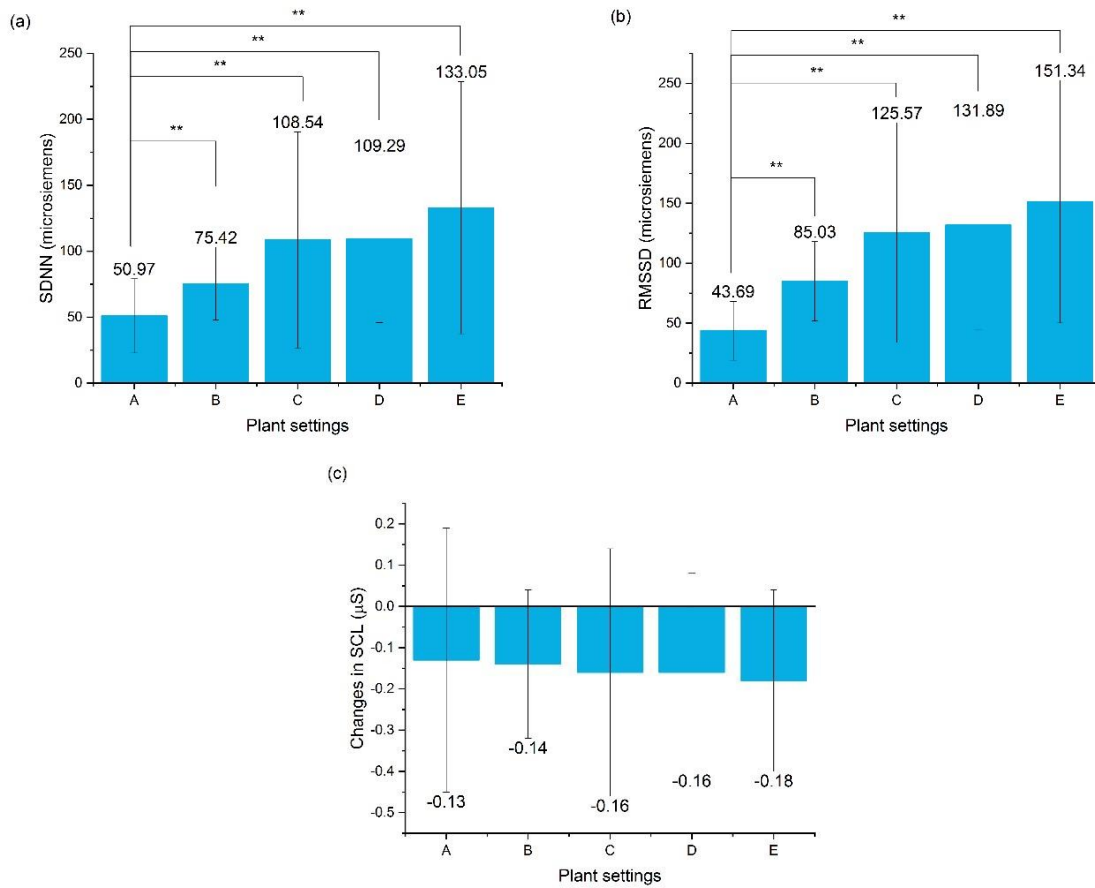

Figure 4: Physiological response of the subjects

4. CONCLUSION

Previous studies have not discussed whether the influence of indoor plants on indoor workers is related to the quantity and placement. In this study, plants *E. aureum* were used to create an office environment with various quantities and placement of plants, and the effects of plants on subjects' work efficiency and physiological response were investigated. The results of the study revealed that the plants had no significant effect on the reaction speed and working memory of the subjects, and the effect on their attention was related to the number and placement of the plants. Increasing the number of plants could reduce the time required to complete tasks by 41.04 ms. Plants increased the values of the standard deviation of the SDNN and the RMSSD of subjects by 82.08 and 107.65 micro siemens.

The subjects in the study were all students with similar age and living background, which might lead to certain limitations of the research results.

5. ACKNOWLEDGEMENT

6. REFERENCES

Beil, K., & Hanes, D. (2013) 'The Influence of Urban Natural and Built Environments on Physiological and Psychological Measures of Stress-A Pilot Study', International Journal of Environmental Research and Public Health, 10(4), pp. 1250-1267.

Berger, J., Essah, E., Blanusa, T., & Beaman, C. P. (2022) 'The appearance of indoor plants and their effect on people's perceptions of indoor air quality and subjective well-being', Building and Environment, 219, pp.

Beute, F., & de Kort, Y. A. W. (2014) 'Natural resistance: Exposure to nature and self-regulation, mood, and physiology after ego-depletion', Journal of Environmental Psychology, 40, pp. 167-178.

Deng, L., & Deng, Q. (2018) 'The basic roles of indoor plants in human health and comfort', Environmental Science and Pollution Research, 25(36), pp. 36087-36101.

Emami, E., Amini, R., & Motalebi, G. (2018) 'The effect of nature as positive distractibility on the Healing Process of Patients with cancer in therapeutic settings', Complementary Therapies in Clinical Practice, 32, pp. 70-73.

Engell, T., Loras, H. W., & Sigmundsson, H. (2020) 'Window view of nature after brief exercise improves choice reaction time and heart rate restoration', New Ideas in Psychology, 58, pp.

Gladwell, V. F., Brown, D. K., Barton, J. L., Tarvainen, M. P., Kuoppa, P., Pretty, J., . . . Sandercock, G. R. H. (2012) 'The effects of views of nature on autonomic control', European Journal of Applied Physiology, 112(9), pp. 3379-3386.

Jang, H. S., Kim, J., Kim, K. S., & Pak, C. H. (2014) 'Human Brain Activity and Emotional Responses to Plant Color Stimuli', Color Research and Application, 39(3), pp. 307-316.

Kahn, P. H., Jr., Friedman, B., Gill, B., Hagman, J., Severson, R. L., Freier, N. G., . . . Stolyar, A. (2008) 'A plasma display window? The shifting baseline problem in a technologically mediated natural world', Journal of Environmental Psychology, 28(2), pp. 192-199.

Kim, J., Cha, S. H., Koo, C., & Tang, S.-k. (2018) 'The effects of indoor plants and artificial windows in an underground environment', Building and Environment, 138, pp. 53-62.

Kim, K. J., Khalekuzzaman, M., Suh, J. N., Kim, H. J., Shagol, C., Kim, H.-H., & Kim, H. J. (2018) 'Phytoremediation of volatile organic compounds by indoor plants: a review', Horticulture Environment and Biotechnology, 59(2), pp. 143-157.

Kjellgren, A., & Buhrkall, H. (2010) 'A comparison of the restorative effect of a natural environment with that of a simulated natural environment', Journal of Environmental Psychology, 30(4), pp. 464-472.

Ko, W. H., Schiavon, S., Zhang, H., Graham, L. T., Brager, G., Mauss, I., & Lin, Y.-W. (2020) 'The impact of a view from a window on thermal comfort, emotion, and cognitive performance', Building and Environment, 175, pp.

Korpela, K., Nummi, T., Lipiainen, L., De Bloom, J., Sianoja, M., Pasanen, T., & Kinnunen, U. (2017) 'Nature exposure predicts well-being trajectory groups among employees across two years', Journal of Environmental Psychology, 52, pp. 81-91.

Stone, N. J., & Irvine, J. M. (1993) 'PERFORMANCE, MOOD, SATISFACTION, AND TASK TYPE IN VARIOUS WORK ENVIRONMENTS - A PRELIMINARY-STUDY', Journal of General Psychology, 120(4), pp. 489-497.

Ulrich, R. S. (1984) 'View through a window may influence recovery from surgery', Science (New York, N.Y.), 224(4647), pp. 420-421.

Valtchanov, D., Barton, K. R., & Ellard, C. (2010) 'Restorative Effects of Virtual Nature Settings', Cyberpsychology Behavior and Social Networking, 13(5), pp. 503-512.

Yeom, S., Kim, H., & Hong, T. (2021) 'Psychological and physiological effects of a green wall on occupants: A cross-over study in virtual reality', Building and Environment, 204, pp.

Zhang, X., Lian, Z., & Wu, Y. (2017) 'Human physiological responses to wooden indoor environment', Physiology & Behavior, 174, pp. 27-34.

Zhao, R.-L., Zhang, G., Wang, X., Zhang, B.-T., Guo, L.-N., Niu, L.-X., & Zhang, Y.-L. (2019) 'Psycho-Physiological Effects of a Peony-Viewing Program on Middle-Aged and Elderly Individuals at Different Phenological Stages', International Journal of Environmental Research and Public Health, 16(3), pp.

Zuo, L., Wu, D., Yu, L., & Yuan, Y. (2022) 'Phytoremediation of formaldehyde by the stems of Epipremnum aureum and Rohdea japonica', Environmental science and pollution research international, 29(8), pp. 11445-11454.

Zuo, L., Wu, D., Yuan, Y., Li, H., & Yu, L. (2020) 'Effect of arrangement and quantity of epipremnum aureum on work efficiency and subjective perceptions', Environmental Science and Pollution Research, 27(15), pp. 17804-17814.

#156: Coordinated and optimized control strategy for electric-hydrogen coupling taking into account the power distribution of multi-stack fuel cells

Jianlin Li[1], Zelin Shi[2], Zhonghao Liang[3]

[1] Jianlin Li, North China University of Technology (Beijing, China), dkyljl@163.com
[2] Zelin Shi, North China University of Technology (Beijing, China), 835597416@qq.com
[3] Zhonghao Liang, North China University of Technology (Beijing, China), yuwenniguang@163.com

Abstract: Aiming at the traditional multi-stack fuel cell system (MFCS) energy management strategy that cannot solve the problems of low efficiency and poor stability under complex operating conditions, an electro-hydrogen coupling coordinated and optimized control strategy taking into account the power allocation of the multi-stack fuel cell is proposed. In the state machine control layer, a fuel cell power allocation method is proposed to optimize the operating efficiency of the fuel cell, reduce the operating time of the fuel cell in the light load interval, and consider the residual power of the system, the state of charge (SOC) of the lithium battery, and the state of hydrogen (SOH) of the hydrogen storage tank to classify the operating states and reduce the operating time of each fuel cell in the system, so as to reduce the operating time of the fuel cell in the light load interval. The state is divided to reduce the number of switching times of the control modes of each device in the system and improve the service life and operational stability of the system; at the device control layer, the operation modes of each device are changed according to the control signals sent by the state machine to maintain the power balance of the system and smooth out the fluctuations of the DC bus voltage. Based on Simulink platform simulation, the results verify the rationality of the proposed control strategy.

Keywords: Electrohydrogen Coupled System; Multi-Stack Fuel Cell; Power Distribution; Coordinated Optimal Control

1. INTRODUCTION

The currently used single PEMFC has shortcomings of low output power and short service life, and the multi-stack fuel cell system (MFCS) composed of PEMFCs connected in parallel effectively compensates for the shortcomings of PEMFCs. The application of MFCS in the electric-hydrogen coupling system can effectively improve the efficiency of energy utilization, improve the problem of light abandonment, with the help of electric-hydrogen coupling system in the high dynamic response characteristics of the energy storage equipment to smooth the bus voltage fluctuations of the dc system, the optimization of the power distribution of the MFCS can effectively improve the overall operating efficiency of the system and reduce the consumption of hydrogen.

However, due to the stochasticity and instability of PV power generation, which seriously affects the stable operation of the system, the current research on the power allocation of multi-stack fuel cells and the coordinated control strategy of the electric-hydrogen coupling system is not comprehensive enough, which leads to the low operating efficiency of the fuel cell, poor dynamic regulation of the electric-hydrogen coupling system, and difficulty in realizing the smooth switching of the system's operating state under multiple operating conditions(Alam and Murad, 2020). For the study of multi-stack fuel cell power allocation is mainly through the equalization control and rotation control to change the number of fuel cell operation and does not take into account the operating efficiency of the fuel cell, resulting in a waste of photovoltaic energy (Wang *et al*., 2023). In the coordinated control of electric-hydrogen coupled system, the system operation state is mainly divided according to the power required to be leveled by the energy storage system, but the battery charging state and hydrogen storage state are not considered, resulting in frequent switching of the operation state of the electric-hydrogen coupled system, which reduces the service life of the energy storage equipment. Therefore, how to reasonably adjust the system operating state according to the parameters in the system as well as realize the rapid identification and smooth switching of operating modes through the coordinated control of the electric-hydrogen coupling system will contribute to the flexible operation of the electric-hydrogen coupling system, which has become an important challenge for the safe and efficient operation of the electric-hydrogen coupling system(Gao *et al*., 2023).

In order to solve the above problems, this paper proposes a hierarchical control strategy for the electric-hydrogen coupled system that takes into account the power distribution of the multi-stack fuel cell by considering the system residual power, the SOC of the energy storage system and the SOH of the hydrogen storage tank. First, the power allocation method of the multi-stack fuel cell is optimized according to the efficiency characteristic curve of the PEMFC to avoid the PEMFC operating in the light-load interval and to improve the service life and operating efficiency of the PEMFC. Secondly, the control system of the electric-hydrogen coupling system is designed as a two-layer control architecture, and the upper layer control collects the operation status and output power of each module in the system, and transmits the real-time signal flow to the bottom controller for switching between different operation statuses, so as to realize the energy complementarity between the multi-stack fuel cell and the lithium battery storage system, and to maintain the stability of the system power and bus voltage, and to enhance the stability of the operation of the electric-hydrogen coupling system in multiple operating conditions. Stability. Finally, the electric-hydrogen coupling system model is constructed, and the effectiveness of the layered control strategy proposed in this paper is verified based on Simulink simulation.

2. MODELING OF ELECTROHYDROGEN COUPLED SYSTEMS
2.1. System structure

The structure of the electric-hydrogen coupling system proposed in this paper is shown in Fig. 1. As can be seen from Fig. 1, the electric-hydrogen coupling system includes a photovoltaic power generation module, a lithium battery energy storage system (BESS), and a hydrogen energy storage system (HESS) (Smdani *et al*., 2023).
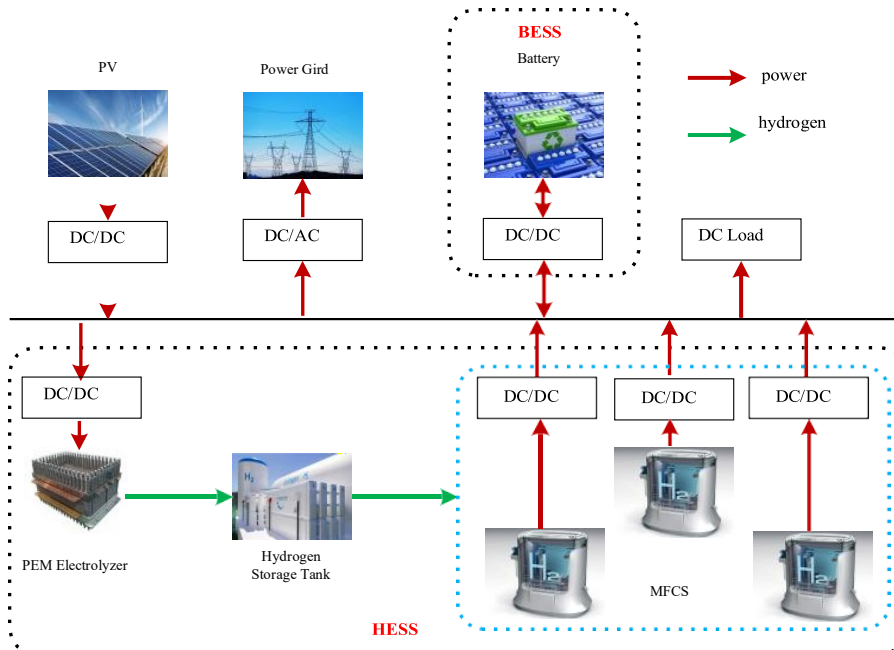

Figure 1: Structural diagram of electrohydrogen coupling system

2.2. Model building

Photovoltaic power generation module consists of multiple photovoltaic cells connected in series and parallel, utilizing the photovoltaic effect, absorbing solar energy and converting it into DC electrical energy (Pan et al., 2023). At the same time, in order to solve the instability problem of PV system usually add electrochemical energy storage in the system (Thuraisingham, 2021).

Equation 1: Photovoltaic power generation unit model.

$$
\begin{cases}
I = I_{sc}\left\{1 - C_1\left[\exp\left(\dfrac{U}{C_2 U_{oc}}\right) - 1\right]\right\} \\[2mm]
C_1 = \left(1 - \dfrac{I_{mp}}{I_{sc}}\right)\exp\left(\dfrac{-U_{mp}}{C_2 U_{oc}}\right) \\[2mm]
C_2 = \left(\dfrac{U_{mp}}{U_{oc}} - 1\right)\left[\ln\left(1 - \dfrac{I_{mp}}{I_{sc}}\right)\right]^{-1}
\end{cases}
$$

Where:

- I is the output current of the photovoltaic power generation module
- I_{sc} is the short-circuit current of the photovoltaic power generation module
- C_1 and C_2 are the specific parameters of the photovoltaic power generation module
- U is the output voltage of the photovoltaic power generation unit
- U_{oc} is the open-circuit voltage of the photovoltaic power generation module
- I_{mp} is the current at the point of the maximum power at the time of the photovoltaic power generation module work
- U_{mp} is the voltage at the point of the maximum power at the time of the photovoltaic power generation module work

Equation 2: Lithium battery storage mode I (Abdelghany et al., 2023).

$$
\begin{cases}
U_{bat} = U_{oc} - IR_0 - U_{c1} - U_{c2} \\[2mm]
I = \dfrac{U_{c1}}{R_1} + C_1\dfrac{dU_{c1}}{dt} \\[2mm]
SOC_t = SOC_{t-1} - \dfrac{1}{C_t U_{bat,t}}\int P_{bat,t}\,dt
\end{cases}
$$

Where:

- $U_{bat,t}$, C_t and $P_{bat,t}$ are the voltage of the lithium battery, the rated capacitance of the battery, and the rated power at the moment of t
- R_0 is the internal resistance of the dynamic circuit
- U_{c1} and U_{c2} are the voltages of the series-connected RC circuit
- SOC_t and SOC_{t-1} are the charging state of the lithium battery storage at the moment of t and $t-1$

Equation 3: Proton Exchange Membrane Electrolyzer Voltage Modeling (Jia, Ren and Xue, 2021).

$$
\begin{cases}
U_{el} = U_{ocv} + U_{act} + U_{ohm} \\[2mm]
U_{ocv} = U_{rev} + \dfrac{RT}{2F}\left[\ln\dfrac{P_{H_2}\sqrt{P_{O_2}}}{a_{H_2O}}\right] \\[2mm]
U_{rev} = 1.229 - 0.0009(T - 298) \\[2mm]
U_{act} = \dfrac{RT}{\alpha_{an}F}\operatorname{arcsin}h\left(\dfrac{i}{2i_{o.an}}\right) + \dfrac{RT}{\alpha_{cat}F}\operatorname{arcsin}h\left(\dfrac{i}{2i_{o.cat}}\right) \\[2mm]
U_{ohm} = \dfrac{\delta_{mem}}{\sigma_{mem}}i
\end{cases}
$$

Where:

- U_{el} is the output voltage of the PEM electrolyzer
- U_{ocv} is the open-circuit reversible voltage
- U_{act} is the electromotive force loss from electrolysis of water

- U_{ohm} is the ohmic polarization over electromotive force from the resistor
- U_{rev} is the reversible voltage of the PEM electrolyzer
- R is the gas constant
- T is the temperature of the electrolyzer
- F is Faraday's constant
- P_{H2}, P_{O2}, and a_{H2O} are the hydrogen pressure, the oxygen pressure, and the water activity
- α_{cat} and α_{an} are the charge transfer coefficients of the cathode and anode
- i is the current density
- $i_{o.cat}$ and $i_{o.an}$ are the exchange current densities of the cathode and anode
- R_{mem} is the equivalent resistance
- δ_{mem} is the thickness of the membrane
- σ_{mem} is the ionic conductivity

Equation 4: *Mathematical modeling of hydrogen storage tank pressure (Guo et al., 2020).*

$$\begin{cases} b = \dfrac{p_{H_2}}{p_{H_2 v}} \times 100\% \\[2ex] p_{H_2} = \dfrac{M R_c T_c}{V_c} \\[2ex] M = M_0 + \int \dfrac{\eta_{el} I_{el}}{2F}\,dt - \int \dfrac{\eta_{fc} I_{fc}}{2F}\,dt \end{cases}$$

Where:

- b is the percentage of gas storage state of the hydrogen storage tank
- p_{H2} is the value of internal pressure
- p_{H2v} is the value of internal rated pressure; M is the amount of internal hydrogen storage
- R_c is the gas constant
- T_c is the value of internal temperature
- V_c is the volume of the hydrogen storage tank
- M_0 is the amount of hydrogen storage in the moment of 0
- η_{el} is the efficiency of electrolyzer
- η_{fc} is the efficiency of the conversion of fuel cell
- I_{el} is the electrolyzer current
- I_{fc} is the fuel cell current

Equation 5: *Mathematical Modeling of Fuel Cells (Cheng and Zhang, 2021).*

$$\begin{cases} U = U_{nernst} - U_{act} - U_{ohm} - U_{conc} \\[1ex] U_{nernst} = 1.229 - 8.5 \times 10^{-4}(T - 298.15) + 4.308 \times 10^{-5} T\left(\ln P_{H_2} + 0.5 \ln P_{O_2}\right) \\[1ex] U_{ohm} = I\left(R_M + R_t\right) \\[1ex] U_{act} = 0.9514 - 3.12 \times 10^{-3} T + 1.87 \times 10^{-4} T \ln i - 7.4 \times 10^{-5} \ln C_{O_2} \\[1ex] U_{con} = n_1 \exp\left(-n_2 I / A\right) \end{cases}$$

Where:

- U_{nernst} is the theoretical electric potential of the fuel cell
- U_{act} is the activation overvoltage
- U_{ohm} is the ohmic overvoltage of the fuel cell
- U_{conc} is the concentration difference overvoltage of the fuel cell

3. HIERARCHICAL CONTROL STRATEGY FOR ELECTROHYDROGEN COUPLED SYSTEMS

The layered control strategy is the core of the smooth operation of the electro-hydrogen coupling system under complex working conditions, and the layered control strategy of the electro-hydrogen coupling system proposed in this paper adopts a two-layer control architecture (Barelli *et al.*, 2020), with the upper layer being the state machine control layer and the bottom layer being the equipment control layer, as shown in Fig. 2. The data is transmitted to the equipment control layer through the real-time signal flow, and the system operation state is switched after receiving the data from the upper layer (Somaiah and Agarwal, 2016).
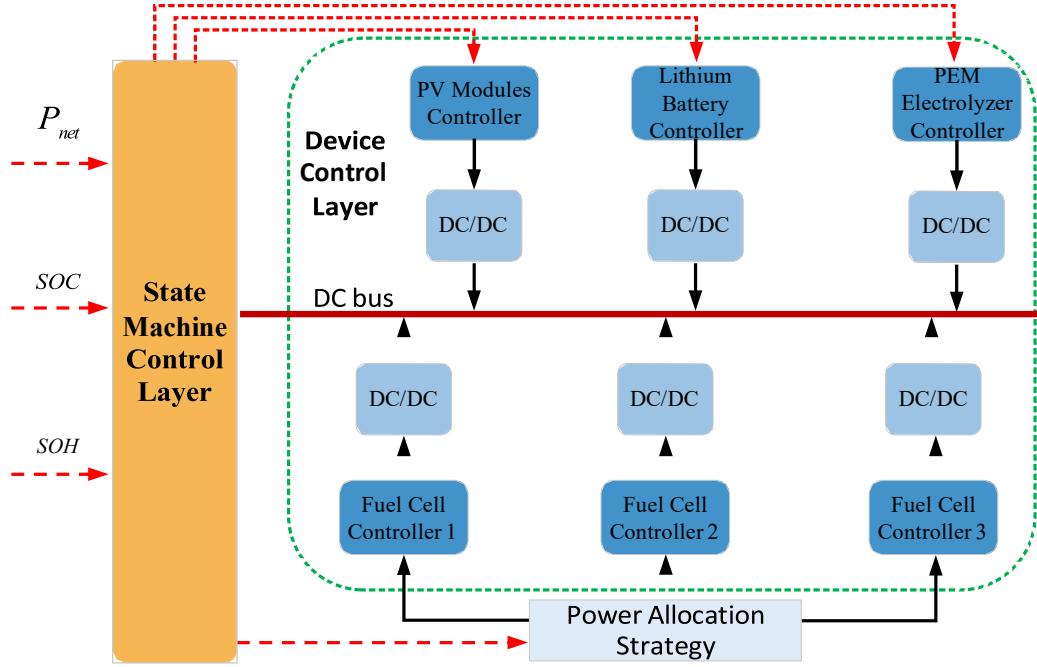
Figur 2: Block diagram of hierarchical control of electrohydrogen coupled system

3.1. Multi-stack fuel cell power allocation

The state machine control strategy proposed in this paper is divided into a total of eight states, which adjusts the system operating state in real time to avoid the PEMFC running in too low or too high a power state, to minimize the operating state of the electric-hydrogen coupling system under the premise of ensuring the power balance of the electric-hydrogen coupling system, and to improve the operating efficiency of the electric-hydrogen coupling system and the stability of the system under complex working conditions.

In order for the output power of the PEMFC to be at the optimal efficiency point, a state machine is used to control the MFCS for power allocation, and it is set that the PEMFCs are all operated at the optimal efficiency point.

Equation 6: Calculate the number of runs N.

$$\begin{cases} P_{net} = P_{pv} - P_{load} - P_{EL} + P_{BAT} \\ \max\{N \times P_{opt}\} < P_{net} \end{cases}$$

Where:

- P_{net} is the remaining power of the system
- P_{pv} is the power issued by the photovoltaic system
- P_{load} is the power consumed by the system load
- P_{EL} is the power of the electrolyzer
- P_{BAT} is the power of the lithium battery storage system
- N is the number of PEMFC operation
- P_{opt} is the power of the optimal efficiency point of PEMFC

3.2. State machine control layer

The state machine control strategy defines the upper and lower limit values of SOC of the energy storage system as SOC_H and SOC_L, respectively; the upper and lower limit values of SOH of the hydrogen storage tank are SOH_H and SOH_L, respectively; L_{BAT} is used to indicate that the lithium battery is in the too-low zone when $SOC<SOC_L$; M_{BAT} is used to indicate that the lithium battery is in the normal zone when $SOC_L<SOC<SOC_H$; and H_{BAT} is used to indicate that the lithium battery is in the too-high zone when $SOC>SOC_H$. Lithium batteries in the high range are denoted by H_{BAT}. Hydrogen storage tanks in the low range are denoted by L_{H2} for $SOH<SOH_L$; normal range are denoted by MH2 for $SOH_L<SOH<SOH_H$; and high range are denoted by H_{H2} for $SOH>SOH_H$.

65

The operating states of the electrohydrogen coupling system are as follows:

State 1: High SOH interval, system residual power is greater than 0, excessive pressure in the hydrogen storage tank should reduce the amount of hydrogen production, in order to avoid frequent start and stop of the electrolyzer to reduce the service life, the electrolyzer operates at the lowest power, and the excess power is absorbed by the energy storage system.

State 2: High SOH interval, the remaining power of the system is less than 0, the MFCS system starts to make up for the lack of power in the system, the SOC of the storage system is > SOC_L, the N PEMFCs operate at the optimal working condition, the storage system makes up for the remaining power, and the SOC is reduced.

State 3: High SOH interval, system residual power is less than 0, storage system $SOC<SOC_L$, N+1 PEMFCs operate at optimal operating conditions, residual power is absorbed by the storage system, and SOC increases.

State 4: Normal SOH interval, system residual power is greater than 0, the electrolyzer absorbs the system residual power, if the electrolyzer operates at maximum power there is still power left in the system, the energy storage system absorbs the residual power.

State 5: Normal SOH interval, the system residual power is less than 0, the MFCS system starts to make up for the lack of power in the system, the $SOC>SOC_L$ of the energy storage system, and the working state of the MFCS system is the same as that of State2.

State 6: Normal SOH interval, system residual power is less than 0, energy storage system $SOC<SOC_L$, MFCS system working state is the same as State3.

State 7: Low SOH interval, system residual power is greater than 0, the electrolyzer runs at rated power to produce hydrogen to keep the hydrogen content in the hydrogen storage tank in the normal range, and the residual power is consumed by the energy storage system.

State 8: Low SOH interval, the remaining power of the system is less than 0, the MFCS system cannot start normally because the hydrogen content in the hydrogen storage tank is too low, and the energy storage system makes up the remaining power.

3.3. Device control layer

The control modes of the PV system are categorized into three: maximum power tracking mode, standby mode and constant voltage mode (Falcão and Pinto, 2020). When the system SOC and SOH are in the reasonable interval, the PV system adopts the maximum power tracking mode based on the variable step-size perturbation observation, and the optimal control signal D_{pv} is obtained through the closed-loop control after collecting the voltage and current; when the SOC and SOH are in the over-limit interval, the PV system is switched to the constant-voltage mode using the voltage and current double closed-loop control to obtain the control signal D_{pv}; when the light is not enough to support the PV system, it is switched to the standby mode. When the light is not enough to support the PV system, it switches to standby mode (Abdin, Webb and Gray,2015).

The control modes of MFCS system and electrolyzer system are divided into constant power control and standby mode (Li *et al*., 2020). The power reference values P_{FC_ref} and P_{EL_ref} are obtained from the power management system, and the control signals D_{FC} and D_{EL} are obtained by using the power-current double closed-loop control (Zhang, 2022). The control modes of the energy storage system are divided into constant-voltage and standby modes, and the control modes are selected according to the real-time signals from the power management system (Fang and Liang, 2019).

4.   SIMULATION VERIFICATION
4.1. Power allocation strategy simulation verification

Currently, using more energy management methods for power equalization method, by the three fuel cells together for the system power supply, the remaining power of the system is divided equally. Set the initial value of SOH, SOC are 0.5, light intensity is 1250W/m^2, that is, the PV power is 20kW, the system load is 5kW, continue to increase the load of 10kW at 2s, the simulation results are shown in Figure 3.

As can be seen from Fig. 3: the system has residual power in 0-2s, the electrolyzer starts hydrogen production with 15kW rated power to make the system power balance. 2s increases the load after the system power deficit exists, and the residual power is shared equally by the fuel cells, at this time, the three fuel cells work in the light load interval, the working efficiency is low about 43% and it is easy to reduce the life of the fuel cells.
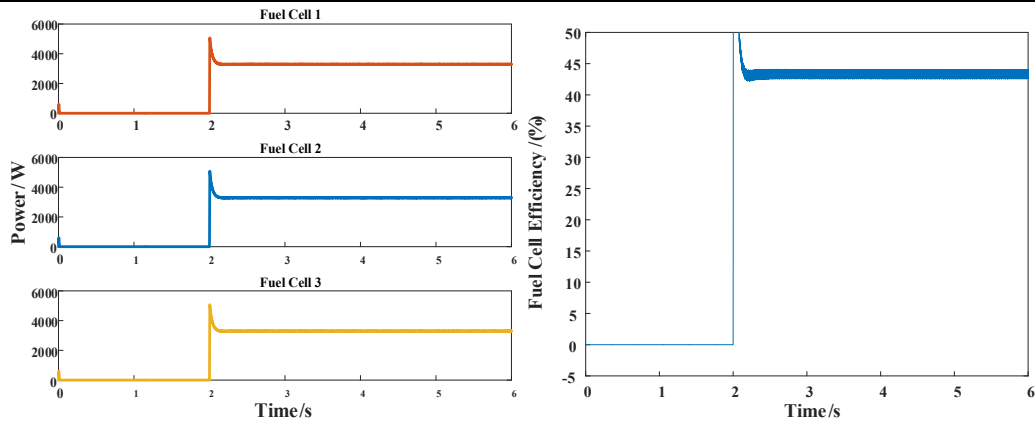
Figure 3: Simulation verification of conventional equalization strategy

In order to verify the effectiveness of the multi-stack fuel cell power allocation strategy proposed in the paper, the DC bus voltage is set to 480V, the DC side load is 10kW, the initial value of SOH is 0.2, the initial value of SOC is 0.5, and the light intensity is 635W/m^2, i.e., the photovoltaic power is 10kW, and the load consumes 15kW, and the load of 12kW is added to the system in 5s, and it continues to be increased in 9s with a 15kW load, the simulation results are shown in Fig. 4.
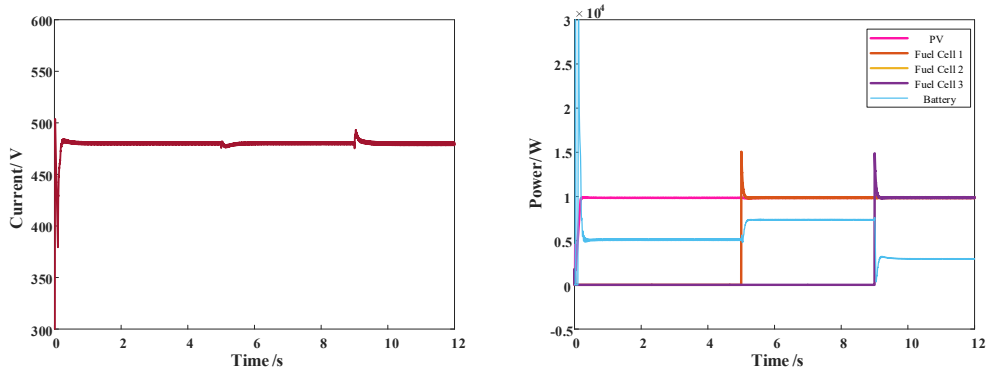

Figure 4: Simulation verification of MFCS power allocation strategy

From Fig. 4, it can be seen that: when the system starts to run, the hourly volt power is less than the load power, the SOH is in the normal interval, the system deficit of 5kW is less than P_{opt}, the MFCS is shut down, and the deficit is made up by the energy storage system. When the load is increased in 5s and 9s MFCS immediately adjusts the number of PEMFC operation to maintain the system energy balance, and the DC bus voltage is basically stabilized and maintained at 480V, which verifies the effectivenessof the MFCS power allocation strategy proposed in this paper.

4.2. Simulation validation of hierarchical control strategy for electrohydrogen coupled system

When the Li-ion battery SOC is in the normal interval, the initial value of SOH is set to 0.2, the initial value of SOC is 0.4, the light intensity is 1250W/m2, i.e., the PV power is 20kW, and the load consuming power is 10kW, and the light intensity is adjusted to 800W/m^2 at 4s, i.e., the PV power is 12kW, and the simulation results are shown in Fig. 5.
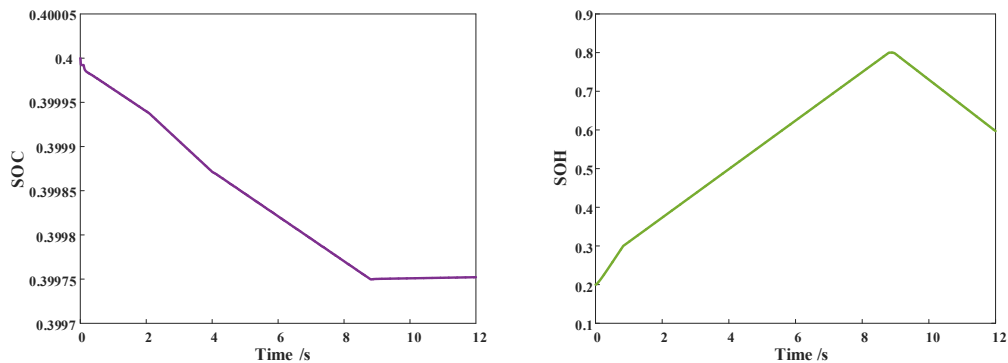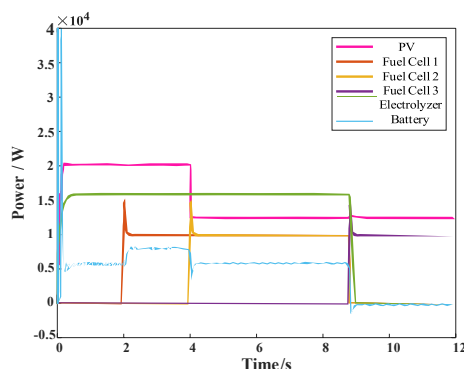
Figure 5: Simulation results of normal interval operation state

As can be seen from Fig. 5, the SOC and SOH are in the normal range when the system starts. At this time the electrolyzer starts hydrogen production resulting in a shortfall of 5kW, which is replenished by the energy storage system, the SOC decreases, and the state machine is adjusted to State4. 2s when the system load is increased by 13kW, the MFCS operates to make up for the shortfall and sets the number of PEMFCs operating at 1, and the operating state changes from State4 to State5. 4s when the number of PEMFCs operating to ensure normal hydrogen production in the electrolyzer is increased to maintain the system power balance. At 4s, in order to ensure normal hydrogen production in the electrolyzer, the number of PEMFC operations is increased to maintain the power balance of the system. At about 8.8s, the SOH reaches SOHH electrolyzer works with the lowest power, the state machine switches from State5 to State2 to maintain the system power balance and adjusts the number of PEMFC operation to 1. At this time, the remaining power of the system is 0, and the energy storage system stops working, which verifies the feasibility of the hierarchical control strategy in the case of the change of SOC>SOC_L and SOH. When the system changes the light intensity, increases the system load, and the electrolyzer starts and stops according to the SOH value, the system operation state is quickly switched, and the power of each module is quickly restored to a stable value after a short fluctuation to maintain the stable operation of the system, which improves the anti-disturbance ability and stability of the electrohydrogen coupling system.

5. CONCLUSION

In order to improve the full power range operation capability of the electric-hydrogen coupled system, this paper proposes a hierarchical control strategy of the electric-hydrogen coupled system that takes into account the power distribution of multi-stack fuel cells. The control system is divided into the state machine control layer and the device control layer, and the following conclusions are obtained through the simulation verification on the MATLAB/Simulink platform:

(1) The proposed MFCS power allocation strategy aims at maximizing the efficiency of PEMFC operation and improves the efficiency and service life of PEMFC operation by collecting the power of each module and dynamically adjusting the number of PEMFC operations.

(2) The working state of each device is controlled by state machine, which avoids as much as possible too many operating states of the electro-hydrogen coupling system, and plays a certain protective role for each device in the system, and the system smoothly switches the working state after a disturbance occurs, so that the dc bus voltage quickly recovers the stability, which contributes to the coordinated operation of the electro-hydrogen coupling system.

(3) The hierarchical control strategy proposed in this paper comprehensively considers the system residual power, SOC and SOH, optimizes the power allocation of the Li-ion battery storage system and hydrogen storage system under different system operating states, controls the SOH to be adjusted to the normal interval in the case of high efficiency of hydrogen production, reduces the changes in the control mode of the equipment, and improves the utilization rate of hydrogen energy.

6. REFERENCES

[1] Wang, H. and Sun, B., (2019). 'Dominant technology identification of wind power generation'. Current Science, 116(9), pp.1525-1532.

[2] Alam, M.M. and Murad, M.W., (2020). 'The impacts of economic growth, trade openness and technological progress on renewable energy use in organization for economic co-operation and development countries'. Renewable Energy, 145, pp.382-390.

[3] Wang, X., Zhou, J., Qin, B. and Guo, L., (2023). 'Coordinated control of wind turbine and hybrid energy storage system based on multi-agent deep reinforcement learning for wind power smoothing'. Journal of Energy Storage, 57, pp.106297.

[4] Gao, M., Han, Z., Zhao, B., Li, P. and Wu, D., (2023). 'Optimal planning method of multi-energy storage systems based on the power response analysis in the integrated energy system'. Journal of Energy Storage, 73, pp.109015.

[5] Smdani, G., Islam, M.R., Ahmad Yahaya, A.N. and Bin Safie, S.I., (2023). 'Performance evaluation of advanced energy storage systems: a review'. Energy & Environment, 34(4), pp.1094-1141.9

[6] Pan, C., Fan, H., Zhang, R., Sun, J., Wang, Y. and Sun, Y., (2023). 'An improved multi-timescale coordinated control strategy for an integrated energy system with a hybrid energy storage system'. Applied Energy, 343, pp.121137.

[7] Thuraisingham, R.A., (2021). 'Revisiting ICEEMDAN and EEG rhythms'. Biomedical Signal Processing and Control, 68, pp.102701.

[8] Abdelghany, M.B., Al-Durra, A., Zeineldin, H. and Gao, F., (2023). 'Integrating scenario-based stochastic-model predictive control and load forecasting for energy management of grid-connected hybrid energy storage systems'. International Journal of Hydrogen Energy, 48(91), pp.35624-35638.

[9] Jia, W., Ren, Y. and Xue, Y., (2021). 'Wavelet packet-fuzzy control of hybrid energy storage for power fluctuation smoothing of large wind farm'. Acta Energ. Sol. Sin, 42, pp.357-363.

[10] Guo, L., Wei, B., Han, X. and Li, W., (2020). 'Capacity optimal configuration of hybrid energy storage in hybrid AC/DC micro-grid based on ensemble empirical mode decomposition'. High Voltage Engineering, 46(02), pp.527-537.

[11] Cheng, L. and Zhang, F.H., (2021). 'Wavelet transform method for hybrid energy storage system smoothing power fluctuation'. Electric Power Automation Equipment, 41(3), pp.100-104.

[12] Barelli, L., Ciupageanu, D.A., Ottaviano, A., Pelosi, D. and Lazaroiu, G., (2020). 'Stochastic power management strategy for hybrid energy storage systems to enhance large scale wind energy integration'. Journal of energy storage, 31, pp.101650.

[13] Liu, J., Luo, W., Yang, X. and Wu, L., (2016). 'Robust model-based fault diagnosis for PEM fuel cell air-feed system'. IEEE Transactions on Industrial Electronics, 63(5), pp.3261-3270.

[14] Somaiah, B. and Agarwal, V., (2016). 'Distributed maximum power extraction from fuel cell stack arrays using dedicated power converters in series and parallel configuration'. IEEE Transactions on Energy Conversion, 31(4), pp.1442-1451.

[15] Falcão, D.S. and Pinto, A.M.F.R., (2020). 'A review on PEM electrolyzer modelling: Guidelines for beginners'. Journal of cleaner production, 261, pp.121184.

[16] Abdin, Z., Webb, C.J. and Gray, E.M., (2015). 'Modelling and simulation of a proton exchange membrane (PEM) electrolyser cell'. International journal of hydrogen energy, 40(39), pp.13243-13257.

[17] Li, X., Wen, H., Hu, Y., Du, Y. and Yang, Y., (2020). 'A comparative study on photovoltaic MPPT algorithms under EN50530 dynamic test procedure'. IEEE Transactions on Power Electronics, 36(4), pp.4153-4168.

[18] Zhang, S., (2022). 'Optimal control of hybrid energy storage system of new energy power generation system based on improved particle swarm algorithm'. Journal of Interconnection Networks, 22(03), pp.2145004.

[19] Fang, R. and Liang, Y., (2019). 'Control strategy of electrolyzer in a wind-hydrogen system considering the constraints of switching times'. International journal of hydrogen energy, 44(46), pp.25104-25111.

[20] Gordan, B., Jahed Armaghani, D., Hajihassani, M. and Monjezi, M., (2016). 'Prediction of seismic slope stability through combination of particle swarm optimization and neural network'. Engineering with computers, 32, pp.85-97.

[21] Mohammadi, A. and Mehrpooya, M., (2018). 'A comprehensive review on coupling different types of electrolyzer to renewable energy sources'. Energy, 158, pp.632-655.

#158: Research progress of sludge blending technology in coal-fired power plants

Wenlong HUANG[1], Fangqin LI[2]

[1] Shanghai university of electric power, China Shanghai, aiwen_1@outlook.com
[2] Shanghai university of electric power, China Shanghai, fq_l@163.com

Abstract: As urbanization accelerates, the volume of sewage sludge continues to rise. Co-firing sludge with coal presents an effective solution for the environmentally sound treatment of sludge. This study provides an overview of the fuel characteristics of sludge, examines advancements in sludge co-firing with coal research, and assesses the impact of sludge co-firing on heat transfer, heating surface integrity, heavy metal emissions, and NO_x emissions in coal-fired power plant boilers. The temperature distribution within the boiler is predominantly influenced by the moisture content of the sludge, the co-firing ratio, and the overall boiler load. Adjusting the sludge co-firing ratio or implementing alternative low NO_x control methods can partially mitigate NO_x emissions. However, an increase in the sludge blending ratio may lead to a slight reduction in coal combustion efficiency. With appropriate sludge moisture levels and a low co-firing ratio, minimal changes are observed in the wear of economizer heating surfaces.

Keywords: Sludge; Coal; Boiler Load; Heavy Metals; Co-Firing Ratio

1. INTRODUCTION

With the continual advancement of China's economy, the pace of urbanization has accelerated, resulting in an enhanced standard of living for its citizens. However, concomitant with this progress is the escalating volume of urban sewage. In tandem with sewage treatment, the production of sludge, a by-product of sewage treatment, is also on the rise. Sludge exhibits a complex composition, comprising high organic content, a plethora of bacteria, viruses, heavy metals, and other contaminants. It is typified by high moisture, elevated ash content, low fixed carbon, and a diminished calorific value (Su, 2015). Various methods are employed for the treatment of sludge, including ocean dumping, landfills, biodegradation, utilization in building materials, and incineration. However, the former methods entail drawbacks such as residual harmful substances, heavy metal contamination, squandering of land resources, and water pollution (Huang et al., 2021). Incineration can be facilitated through dedicated incineration equipment or by retrofitting existing equipment for co-incineration with mixed fuels. The latter approach not only mitigates investment and operational costs but also maximizes energy utilization from the sludge, potentially enabling power generation or heating. This holds significant implications for alleviating the energy supply-demand imbalance and curbing energy expenditures.

2. RESEARCH STATUS OF SLUDGE FUEL CHARACTERISTICS AND BLENDING
2.1. Fuel characteristic

A striking characteristic of sludge lies in its elevated water content. Following mechanical dewatering and hot drying, the water content of urban sewage treatment sludge can be reduced to approximately 40% (Huang and Xu, 2021). Investigations reveal that in over 80% of sludge samples from China, the mass fraction of organic matter falls within the range of 20.5% to 60% (Ma et al., 2011). The composition and concentration of heavy metals are contingent upon the specific type of sludge. While the ranking of heavy metal concentrations may vary slightly across studies, a wealth of literature consistently identifies zinc, copper, and chromium as the top three, predominantly stemming from electroplating, metallurgical, tanning, and textile dyeing wastewater (An et al., 2023). The volatile content varies among different types of sludge, with the combustion of volatiles constituting the primary source of calorific value in the sludge combustion process. Higher volatile substance content in sludge augments its combustibility. Additionally, sludge is characterized by its high ash content, which closely resembles that of biomass, exhibiting elevated levels of alkali metals, chlorine, sulfur, phosphorus, among others, and a low ash melting point. When co-firing with pulverized coal in furnaces, this can exacerbate issues such as boiler slagging, ash accumulation, corrosion tendencies, and heightened particulate matter emissions, thereby impacting boiler unit operations (Qi, 2022). In contrast to pulverized coal combustion, which predominantly involves fixed carbon combustion, sludge combustion primarily entails the combustion of precipitated materials with high volatile content (Wang et al., 2020).

2.2. Research status

Researchers both domestically and internationally have conducted extensive studies on the blending of sludge, including experimental investigations, blending experiments within coal-fired power plants, and associated numerical simulations. Given the high moisture content of sludge, drying is imperative when mixing it with pulverized coal. Presently, the primary drying methods for mixed sludge in coal-fired power plants encompass direct drying, indirect drying, and direct-indirect drying. In a study by Zhang et al. (2021), the combustion characteristics and reaction kinetics of blending sludge and coal with varying moisture content were explored. It was observed that the moisture content of the sludge exerted a notable influence on the combustion process of pulverized coal sludge. Specifically, the moisture content of the sludge in the blended samples had the most significant impact on parameters such as the pre-exponential factor and activation energy. Moreover, the comprehensive combustion index of sludge with high moisture content was found to be lower than that of dehydrated sludge. The interaction between sludge and coal combustion exhibited a positive synergistic effect. It was determined that when the moisture content of the sludge does not exceed 30% and the mass ratio of fired sludge remains below 20%, the fired sludge can enhance the ignition characteristics during the combustion process to a certain degree. When two different types of sludge were co-fired with coal in a tube furnace, Zhou et al. (2022) demonstrated that higher water content in the sludge led to a decreasing trend in SO_2 emissions. They also noted that optimizing the water content of the sludge could enhance SO_2 emissions during co-combustion. For NO discharge, there are different rules with the change of sludge moisture content. Li et al. (2019) discovered that as the proportion of sludge added to coal increased, the ash melting point of the mixed fuel decreased. In a study by Guo et al. (2022), who conducted co-combustion of sludge and Jundong coal in a horizontal tube furnace, it was found that sludge content exhibited a negative correlation with SO_2 emissions, while showing minimal impact on NO emissions. Moreover, higher sludge content facilitated the melting of ash particles, and the size of these particles showed a positive correlation with combustion temperature.

Zhu et al. (2016) employed the component transport vortex dissipation model and the mixed fraction PDF model to conduct numerical simulations of pulverized coal and sludge blending in a 100MW tangential circular boiler. Their findings revealed that the component transport vortex dissipation model provided superior accuracy in simulating the impact of water content on furnace combustion. In comparison to the mixed fraction PDF model, it offered a more rational approach for numerically simulating the blending of sludge with varying moisture content. Yin et al. (2015a) conducted numerical simulations to investigate the effects of dyeing sludge blending ratio and water content on pollutant emission characteristics in a coal-fired boiler. They observed a substantial initial increase followed by a steady rise in the volume fraction of NO_x emission from the furnace outlet with increasing dyeing sludge blending ratio, which further escalated with higher water content. Xu et al. (2023) delved into the synergistic effects on co-combustion characteristics by simulating the co-firing of sludge and coal under diverse conditions. Their results showcased positive synergies between sludge and coal combustion, enhancing combustion rate, oxygen consumption, and carbon dioxide production. During co-combustion, sludge combustion was restrained while coal combustion was promoted.

Li et al. (2022) conducted a sludge blending test on power plant boilers. As the mixing ratio increased, the heavy metal content of fly ash, slag and desulphurized gypsum increased, which increased the risk of secondary pollution. The existing flue gas purification process can ensure that the ultra-low emission requirements of coal burning flue gas can be met. The concentration of pollutants

such as heavy metals and their compounds generally increased after mixing sludge, but it still met the relevant discharge requirements.

3. EFFECT OF SLUDGE BLENDING ON COAL-FIRED BOILERS
3.1. Effect of sludge blending on heat transfer

Due to the high ash content, moisture content, and low calorific value of the sludge, its combustion can alter flame intensity and smoke volume, consequently impacting the distribution of radiation and convection heat within the boiler. He et al. (2023) conducted a numerical simulation study on sludge blending in a 630MW supercritical direct current boiler. They observed that at a sludge moisture content of 40%, the outlet temperature of each heating surface initially increased and then decreased as the sludge blending ratio rose. Beyond a mixing ratio of 10%, the outlet temperature of each heating surface began to decline, attributable to the sludge's low calorific value and high moisture content. The increased sludge mixing introduces more water into the furnace, yet water evaporation demands significant heat, thus leading to a decrease in furnace temperature. Additionally, the sludge's high ash content means that as it is continuously incorporated, ash levels rise, diminishing fuel combustion efficiency and further lowering furnace temperature. Ji et al. (2023) simulated the mixing of sludge in a 1000MW supercritical boiler, finding that at a 30% sludge moisture content, as the mixing ratio increased from 1.3% to 4.8%, the furnace center temperature exhibited a decreasing trend. Similarly, Li (2021) conducted a numerical simulation on sludge co-firing in a 600MW pulverized coal boiler. They noted that at a 10% sludge mixing ratio, as the mixed sludge's water content rose from 10% to 40%, the overall furnace temperature tended to decrease. Cao et al. (2023) conducted a numerical simulation study on a 630MW supercritical direct current boiler to assess the effects of different loads on mixed sludges. The results indicated that at a sludge water content of 40% and a mixing ratio of 10%, the outlet temperature of each heating surface decreases as the boiler load decreases. Similarly, He et al. (2023) performed a numerical simulation on the mixing of sludge in the same boiler model under various loads, confirming this finding (Figure 1). In addition, in their experiment with
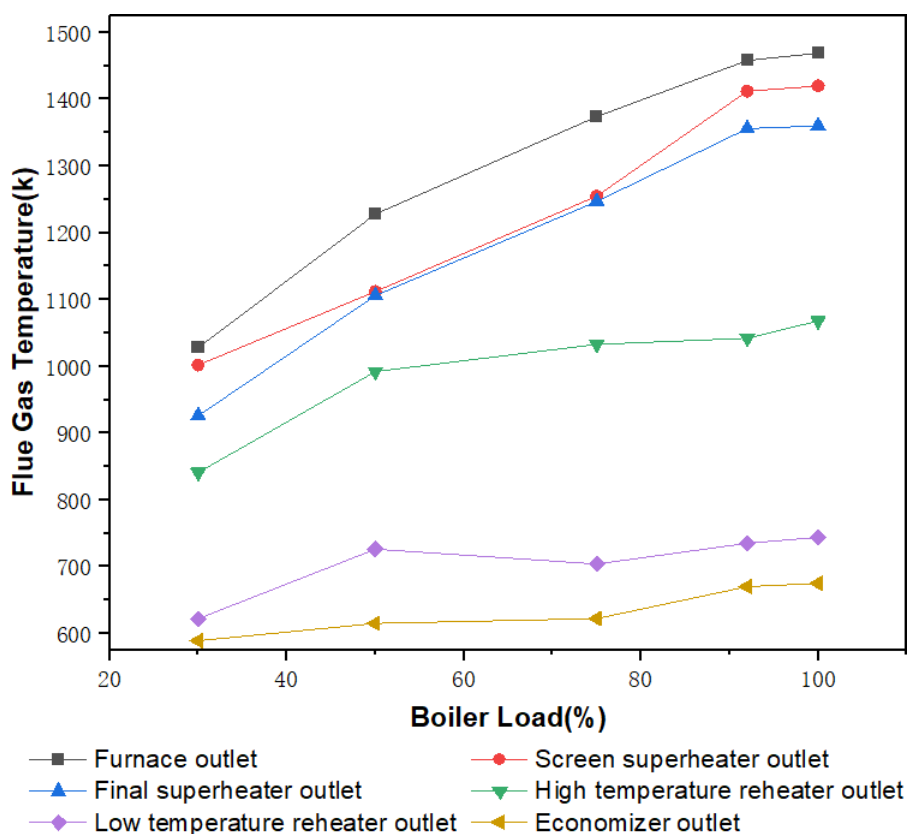

Figure 1: Effect of boiler load on flue gas temperature at the exit of each heating surface of boiler (He et al., 2023)

co-firing sludge in a 700MW tangentially fired pulverized coal boiler, Ye et al. (2023) observed a 1.03% decrease in boiler thermal efficiency at 50% rated load when 6% sludge was co-fired. They also found that the carbon content in the slag increased proportionally with higher sludge co-firing ratios. Wei et al. (2023) simulated the impact of sludge co-firing position on combustion in a 660MW tangentially fired ultra-supercritical boiler. They observed that when the sludge co-firing inlet shifted from a lower position (as in Figure 2, positions 2-7) to a higher position entering the furnace, temperatures near the sludge co-firing layer notably decreased, while other coal-fueled inlets maintained better temperatures. This phenomenon occurs because introducing a more low-calorific-value sludge into the furnace, while keeping the total heat value constant, leads to waste of heat in the flue gas due to moisture evaporation and the latent heat of ash. Consequently, when sludge and coal are mixed and fed into the furnace, the temperature in the main combustion zone of the boiler is lower compared to when no sludge is co-fired.

In summary, the temperature distribution in the boiler is primarily influenced by the sludge's moisture content, mixing ratio, location of co firing, and boiler load. With constant sludge mixing ratio and water content, the impact on heat transfer increases as the boiler load decreases. Conversely, with constant sludge blending ratio and boiler load, the impact on heat transfer increases as the water content rises.
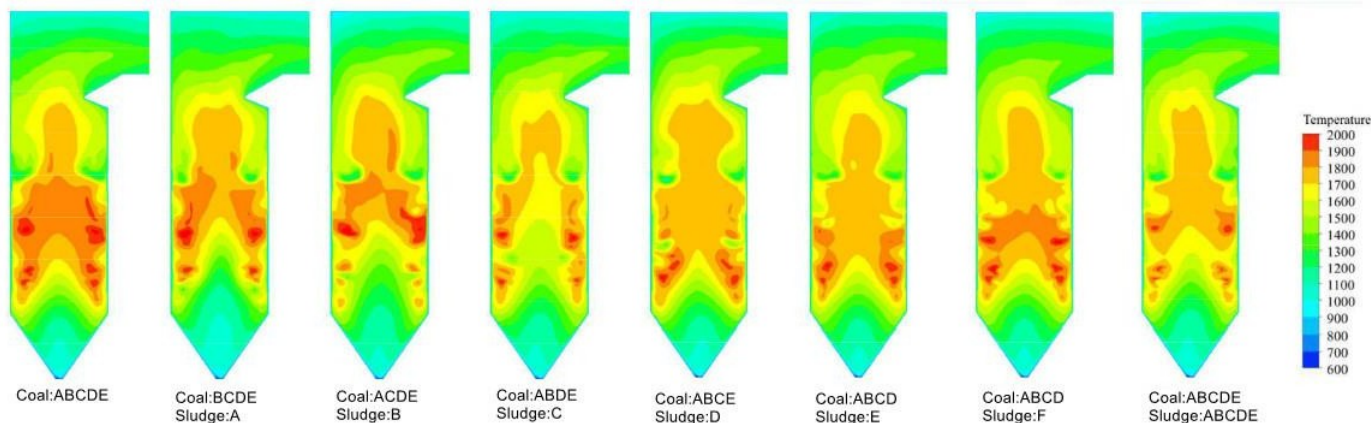
Figure 2: Combustion temperature distribution in the vertical section of the furnace (Wei et al., 2023)

3.2. Effect of sludge blending on combustion and NO$_x$

Sludge contains more proteins, leading to a higher nitrogen content compared to raw coal. If blending is not carefully controlled, there's a risk of increased NO$_x$ emissions. In their study, Yin et al. (2015b) conducted numerical simulations on a series of 420t/h corner-cut pulverized coal boilers. Their findings revealed that the NO emission concentration from pulverized coal mixed firing at full boiler load was lower than that from burning single coal. Additionally, they observed a slight decrease in pulverized coal burnout rate with an increasing sludge mixing ratio. Table 1 is a summary of the amount of NO$_x$ generated by sludge blending ratio and sludge moisture content. It can be seen from the table that the amount of NO$_x$ generated is not always negatively correlated with the blending ratio.

Table 1: Summary of sludge blending ratio, sludge moisture content and NO$_x$ generation

Boiler Load / (%)	Moisture Content / (%)	Co-firing Ratio / (%)	NO$_x$ Emissions / (mg·m^{-3})	Reference
100	0	0	266	Yin et al. (2015b)
100	10	10	244.7	Yin et al. (2015b)
100	10	20	222.2	Yin et al. (2015b)
100	0	0	348.5	Li (2021)
100	10	10	295.8	Li (2021)
100	20	10	297.9	Li (2021)
100	30	10	308.7	Li (2021)
100	40	3	339.3	Li (2021)
100	40	5	333.4	Li (2021)
100	40	7	329.6	Li (2021)
100	40	10	310.7	Li (2021)
75	40	0	475.64	He et al. (2023)
75	40	2	479.78	He et al. (2023)
75	40	4	481.74	He et al. (2023)
75	40	6	483.91	He et al. (2023)
75	40	8	488.35	He et al. (2023)
75	40	10	495.43	He et al. (2023)
75	40	15	557.88	He et al. (2023)
75	40	20	638.15	He et al. (2023)
75	25	10	519.46	He et al. (2023)
75	30	10	508.77	He et al. (2023)

Boiler Load / (%)	Moisture Content / (%)	Co-firing Ratio / (%)	N$_x$ Emissions / (mg · m^{-3})	Reference
75	35	10	496.95	He et al. (2023)
75	40	10	495.43	He et al. (2023)
75	45	10	494.16	He et al. (2023)
100	80	0	242.62	Meng et al. (2021)
94.88	80	5	224.74	Meng et al. (2021)
89.75	80	10	210.63	Meng et al. (2021)
84.63	80	15	180.70	Meng et al. (2021)
79.51	80	20	137.94	Meng et al. (2021)
74.38	80	25	113.63	Meng et al. (2021)
100	0	0	264.7	Zhu et al. (2016)
100	5	10	258.9	Zhu et al. (2016)
100	20	10	229.2	Zhu et al. (2016)
100	30	10	203.9	Zhu et al. (2016)
100	40	10	181.4	Zhu et al. (2016)

Similarly, Meng et al. (2021) performed a numerical simulation on the mixing of sludge in a 600MW tangential pulverized coal boiler to investigate the impact of excess air coefficient in the main combustion zone and air distribution mode on NO$_x$ emissions. Their results indicated that increasing the excess air coefficient in the main combustion zone led to a slight rise in furnace outlet temperature, coupled with a substantial increase in NO$_x$ concentration at the outlet. This was also confirmed in Wang et al. (2023)'s research. In Table 2, a NO$_x$ concentration of a waist drum air distribution method reached 214.51 mg m^{-3}, and the NO$_x$ concentration of shrunk middle was the smallest among these air distribution methods. Yang et al. (2022) conducted numerical simulations on a 660MW tangentially fired boiler to investigate the impact of sludge co-firing position on NO$_x$ emissions. They found that maintaining a constant overall co-firing ratio and reducing the sludge co-firing ratio per layer by increasing the number of co-firing layers effectively raised the furnace exit temperature. However, the mass concentration of NO$_x$ increased by 5.9%. Conversely, lowering the height of the sludge co-firing layer extended the residence time of sludge in the furnace, thereby increasing the furnace exit temperature without a significant change in NO$_x$ emissions. Similarly, Chen et al. (2023) and others simulated a 1000MW tower boiler and found that co-firing sludge in different layers of coal burners resulted in reduced average temperatures and NO$_x$ emission concentrations at corresponding heights of sludge co-firing burners. In contrast to Yang's findings, they observed that as the position of sludge co- firing rose, the temperature at the furnace exits increased while NO$_x$ emission concentrations decreased.
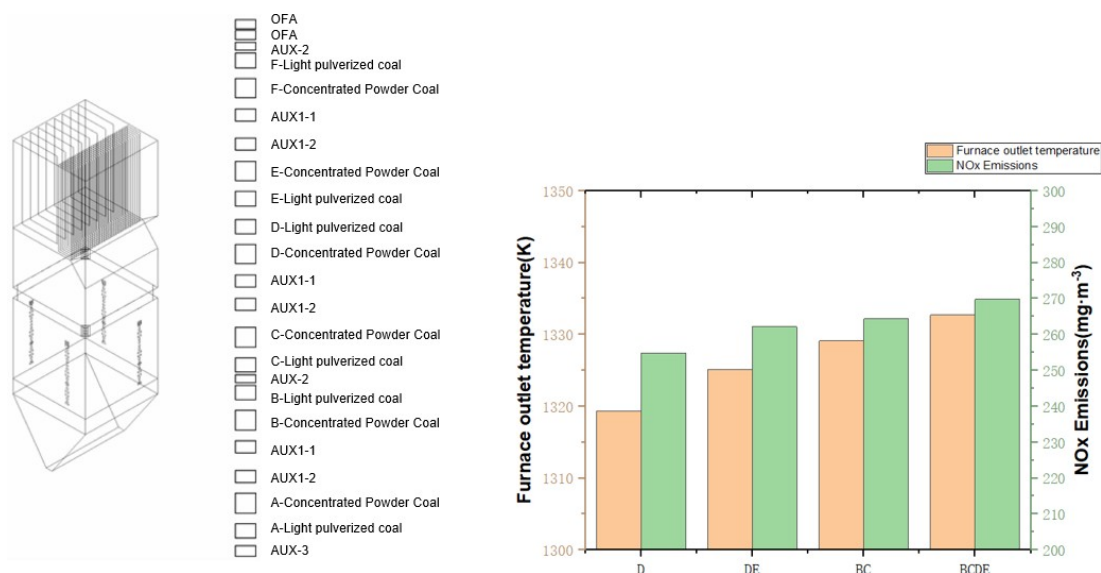

Figure 3: Influence of different burning methods on furnace outlet parameters (Yang et al., 2022)

Furthermore, Lv et al. (2023) conducted a sludge blending test using high-temperature preheating technology. They discovered that augmenting the proportion of sludge could mitigate NO$_x$ emissions and enhance carbon burning through preheating treatment. When the excess air ratio in the preheating zone reached 0.5, NO emissions were minimized. Under these conditions, 62% of the fuel nitrogen could be converted to gas, with 89.7% of it being N$_2$. Elevating the preheating temperature to 1200℃ resulted in a 48.3% reduction in NO emissions and a 43.2% decrease in unburned carbon in fly ash. In this regard, NO emission can be reduced to a certain extent by controlling the sludge blending ratio or adopting other control measures, but the burning-out rate of pulverized coal will decrease slightly with the increase of the sludge blending ratio.

Table 2: Characteristic parameter at the furnace outlet in different SA distribution conditions (Wang et al., 2023)

SA distribution typer	Flue gas temperature / (K)	NOx concentration /(mg·m^{-3})	H2O content / (%)
Equal	1374	182.49	9.46
Pagoda	1391	211.55	9.46
Pagoda down	1395	171.81	9.46
Shrunk-middle	1413	154.78	9.46
Waist drum	1380	214.51	9.46

3.3. Effect of sludge blending on heating surface

The ash content and composition of sludge influences its ash melting point during blending. A low content of iron oxide leads to the formation of low-temperature eutectics, while diopside and anorthite reduce the ash melting temperature post mixing with coal. Conversely, the presence of ferric oxide in forms like calcium and magnesium olivine, mullite, and monomer can elevate the ash melting temperature after coal and sludge mixing (Yin et al., 2014). To mitigate the risk of slagging resulting from sludge mixing and combustion, adjustments to the acid-based ratio parameter can be made. Another approach involves using chemicals to enhance the sludge drying and dewatering process, addressing furnace slagging issues that arise from municipal sludge incineration (Zou et al., 2023). The moisture in sludge increases the total flue gas and flow rate of the boiler, potentially heightening wear on the heating surface. Under low sludge blending ratios, the wear on the economizer heating surface increases with higher sludge moisture content, albeit to a minor degree (Zhang et al., 2019). Similarly, in a study by Zhang et al. (2020), testing the mixing of domestic sludge in a 1000MW power plant boiler revealed that controlling the sludge mixing ratio within 10% had minimal impact on the elemental composition of coal and fly ash concentration. Moreover, it did not escalate wear on the economizer or other heating surfaces. In Table 3, the fly ash mass fraction data of each heating surface of a 300MW unit boiler of a power plant for mixing domestic sludge are shown. It can be seen from Table 3 that the fly ash mass fraction of each heating surface increases with the increase of the sludge mixing ratio. When the mixing ratio is less than 10%, the fly ash quality changes little. Therefore, the power plant can control the sludge blending and burning ratio according to the actual operation.

Table3: Mass fraction of fly ash under different blending ratio (Feng et al., 2021)

Co-firing Ratio / (%)	Front screen to economizer	Hot section of air preheater	Cold section of air preheater
0	0.004	0.004	0.004
3	0.006	0.005	0.005
6	0.008	0.007	0.007
8	0.008	0.007	0.007
10	0.009	0.009	0.009
20	0.015	0.014	0.014

Hence, maintaining an appropriate sludge moisture content and low mixing ratio helps minimize wear on the economizer heating surface. Regular inspection and cleaning of the heating surface are also vital for removing ash and dust, thus preserving its cleanliness.

3.4. Effect of sludge blending on heavy metals

Sludge often contains various heavy metals such as lead, cadmium, and mercury, with their concentration depending on the heavy metal levels in the wastewater treatment process and the source of the sludge. If the heavy metal content in the sludge is high, adding coal dust may increase the release of heavy metals during the combustion process. The content and residual presence of heavy metals in ash after co-firing depend on the type of sludge, the mixing ratio, and the interaction with coal. When heavy metals form fewer volatile compounds, they are found in the ashes, while those forming more volatile compounds are present in fly ash or flue gas.

In studies conducted by Ge et al. (2017), bituminous coal was co-fired separately with industrial sludge and domestic sludge. It was found that the leaching rates of As, Zn, and Cr in the ash after co-firing domestic sludge with bituminous coal were generally higher than those after co-firing industrial sludge with bituminous coal. The concentrations and residual rates of Zn and Cr in the ash generally increased with higher sludge mixing ratios, while the concentrations and residual rates of As decreased. Zheng et al. (2023) conducted experiments using an electric heating tube furnace to investigate the combustion of sludge and coal mud under different conditions. The results indicated that the retention of heavy metals during co-firing was mainly influenced by the interaction between mineral components. Under single-component combustion conditions, SiO_2, Al_2O_3, and Fe_2O_3 easily reacted with heavy metals to form fewer volatile compounds and remained in the ash. However, co-firing promoted the decomposition of silicate and aluminate compounds, thereby increasing the residual rates of heavy metals on the basis of generating a large amount of SiO_4 and other compounds. Additionally, chlorine elements easily reacted with Pb, Cr, and Cd to form volatile chlorides, promoting the volatilization of heavy metals. Li et al. (2011) conducted co-firing experiments in a small tube furnace and found that co-firing sewage sludge significantly increased the heavy metal content in both fly ash and bottom ash, with Zn and Pb showing the largest increases while Ni, Mn, and Cu decreased. With the addition of organic chlorine, the heavy metal content in fly ash showed a clear increasing trend, with Zn being the most prominent. However, most experiments indicated that the concentrations of various heavy metals in ash and

flue gas after co-firing sludge with coal were lower than those specified in national standards (Li and Wang, 2016, Zhang et al., 2019, Liu et al., 2017). Therefore, regular monitoring and control of heavy metal emissions are necessary. By implementing strict emission standards and monitoring measures, the emission of heavy metals during the combustion of coal mixed with sludge can be effectively controlled, thus protecting the environment and human health.

4. CONCLUSION

By co-firing sludge, it's possible to substitute some coal usage, thereby reducing dependence on traditional energy sources. This has a positive significance in mitigating the energy supply-demand imbalance and lowering energy costs.

The technology of blending coal powder with sludge is relatively complex in operation, requiring consideration of factors such as the blending ratio of coal powder and sludge, sludge moisture content, adjustments to combustion equipment, and control of air distribution during combustion. Additionally, sludge composition is varied and complex, with sludge from different sources potentially having different effects during the co-firing process, necessitating targeted process improvements and optimization.

With the rapid development of new energy sources, thermal power plants will shoulder heavier peaking tasks in the future. However, research on co-firing sludges at low loads is currently limited.

5. REFERENCES

AN, D., GENG, R., ZHU, J. & CHEN, H. 2023. Review on The Characteristics of Urban Sludge And Its Impact on Carbon Emissions during Disposal. Environmental Science and Technology, 36, 21-25.

CAO, W., LI, X., HOU, B., CHANG, S. & HE, L. 2023. Influence of sludge co-combustion on the combustion stability in a 630 MW pulverized coal boiler. Clean Coal Technology, 29, 245-253.

CHEN, L., ZHU, L., LI, F. & ZHU, Q. 2023. Simulation Study of the Effect of Sludge Blending Method on the Combustion of Coal-fired Boilers. JOURNAL OF ENGINEERING FOR THERMAL ENERGY AND POWER, 38, 122-129.

FENG, B., LI, D., SUN, C., FENG, Y., LIANG, H., SU, Z. & ZHANG, W. 2021. Key Technology Research and Engineering Application of the Co-combustion of Sludge and Coal in a 300 MW Coal-fired Boiler. Power Equipment, 35, 131-136.

GE, J., GUO, Y., WU, L., SU, H., YANG, J., ZHANG, C. & CHEN, G. 2017. Transferring Law of Heavy Metals As, Zn and Cr and Leaching Characteristic of Ash During the Process of Co-combustion of Bituminous Coal and Sludge. Guangdong ElectricPower, 30, 37-42+54.

GUO, S., GAO, J., ZHAO, D., ZHAO, C., LI, X. & LI, G. 2022. Co-combustion of sewage sludge and Zhundong coal: Effects of combustion conditions on gaseous pollutant emission and ash properties. Sustainable Energy Technologies and Assessments, 54.

HE, L., PAN, X., ZHONG, Z., YANG, Y., ZHANG, S., ZHANG, Q., WANG, Y. & SUN, L. 2023. Numerical simulation of pulverized coal and sludge mixed combustion in a 630 MW supercritical direct current boiler. Clean Coal Technology, 29, 188-195.

HUANG, C. & XU, Q. 2021. Analysis of Sewage Sludge Treatment and Disposal in Guangzhou in 2019. Shandong Chemical Industry, 50, 247-248+251.

HUANG, W., LIN, Y., LUO, Z., WU, J., ZUANG, G., QIAN, X. & ZHU, L. 2021. Progress on Research and Technology of Sludge Blending Combustion in Coal-fired Power Plants. Journal of Shanghai University of Electric Power, 37, 1-4+22.

JI, Z., LI, J., SHI, M., WU, J., FAN, Z., ZHU, J. & HUANG, Y. 2023. Numerical Simulation of Sludge Mixing Temperature Field in 1000 MW Boiler. Journal of Shanghai University of Electric Power, 39, 1-4.

LI, D., CUI, C., JIANG, Y., SHI, W., ZHANG, P., MO, F., LIAO, Y. & MA, X. 2019. Investigation of Fusion Characteristics in Co-combustion of Coal With Municipal Sludge. Power Generation Technology, 40, 347-354.

LI, D., QUQ, Z., MIAO, J., CHEN, T., CHEN, Z., CHEN, Z. & FENG, Y. 2022. Field experiment on mixed combustion of municipaldomestic sludge in coal-fired units. Clean Coal Technology, 28, 39-46.

LI, F. 2021. Numerical Simulation on Co-Combustion ofPulverized Coal with Sludge in a 600MW Coal-FiredBoiler. Master's thesis.

LI, G., HU, Y., CHEN, G., ZHONG, Y. & ZHANG, X. 2011. Transferring characteristics of heavy metals during co-incineration of municipal sewage sludge and solid waste. Journal of Fuel Chemistry and Technology, 39, 155-160.

LI, M. & WANG, D. 2016. Transform of Pollutants in process of co-combustion of papremaking sludgewith coal. Coal Conversion, 39, 86-91.

LIU, Z., ZHENG, X. & ZHANG, Y. 2017. Analysis and Research on Air Pollution of Municipal Sludge and Coal Co-firing Power Plants. Environmental Impact Assessment, 39, 34-38.

LV, Z., XIONG, X., RUAN, R., WANG, Y. & TAN, H. 2023. NO emission and burnout characteristics in co-combustion of coal and sewage sludge following high-temperature preheating. Fuel, 331.

MA, X., WENG, H. & ZHANG, J. 2011. Regional characteristics and trend of heavy metals and nutrients of sewage sludge in China. China Environmental Science, 31**,** 1306-1313.

MENG, T., XING, X., ZHANG, J., ZHOU, L., ZHANG, T. & WANG, C. 2021. Numerical simulation study on the effect of air distribution on combustion of coal-fired boiler blended with sludge. Clean Coal Technology, 27**,** 263-271.

QI, Z. 2022. BEHAVIOR OF ASH FORMATION ANDCHARACTERISTICS OF PARTICULATE MATTER GENERATION DURING THE COMBUSTION OF COAL SLIME AND SEWAGE SLUDGE. Master's thesis.

SU, H. 2015. Experimental Study on the Transferring Characteristics and Leaching Behavior of Heavy Metals during the Cocombustion of Coal and Different Sludges. Master's thesis.

WANG, C., CHEN, M., ZHAO, P., ZHOU, L., HOU, Y., ZHANG, J., LYU, Q. & CHE, D. 2023. Investigation on Co-combustion characteristics and NOx emissions of coal and municipal sludge in a tangentially fired boiler. Fuel, 340.

WANG, H., LI, D., ZENG, X. & LIAO, Y. 2020. Adaptability of Numerical Simulation Model for the Combustion Process of Sludge Mixed with Coal. JOURNAL OF ENGINEERING FOR THERMAL ENERGY AND POWER, 35**,** 179-186.

WEI, D., AN, D., WANG, T., ZHANG, H., GUO, Y. & SUN, B. 2023. Influence of fuel distribution on co-combustion of sludge and coalin a 660 MW tangentially fired boiler. Applied Thermal Engineering, 227.

XU, T., WANG, C., HONG, D., LI, S. & YUE, S. 2023. The synergistic effect during co-combustion of municipal sludge and coal: Experimental and ReaxFF molecular dynamic study. Energy, 262.

YANG, K., DING, S. & ZHANG, T. 2022. Analysis of Sludge Blending Combustion on Wall Type Tangentially-fired Boiler. Journal of Chinese Society of Power Engineering, 42**,** 800-805+820.

YE, J., CHEN, C., ZOU, X., RAO, M., WEI, S., MAO, T., QIN, S., KUANG, C., CHEN, G., HU, Z., CHEN, T., JANG, Y. & WANG, Q. 2023. Engineering application of coal & sludge co-fired power generation on a 700 MW coal-fired boiler. Clean CoalTechnology, 29**,** 61-68.

YIN, L., DENG, C., ZHANG, C., FANG, Q., XU, Q. & CHEN, G. 2014. Fusion characteristics in co-combustion of coal with industrial and municipal sludge. Journal of Fuel Chemistry and Technology, 42**,** 1068-1076.

YIN, L., XU, Q., HU, Z., MA, X., CHEN, Y. & YU, Z. 2015a. Combustion and NO Emission Characteristics of Coal-Textile Dyeing Sludge Mixture in a Tangentially-fired Boiler. Journal of Chinese Society of Power Engineering, 35**,** 178-184+196.

YIN, L., ZHU, T., ZHANG, C., FANG, Q., XU, Q. & CHEB, G. 2015b. Co-combustion of sludge in a 100 MW unit coal-fired boiler: numerical simulation. THERMAL POWER GENERATION, 44**,** 28-33+41.

ZHANG, J., LIU, H., ZHOU, K., WEN, C. & HUANG, W. 2021. The Rmogravimetric Analysis on the Co-Combustion Characteristics and Kinetic of Sewage Sludge with Different Moisture Contents and Power Coal. BOILER TECHNOLOGY, 52**,** 30-37.

ZHANG, Q., ZHOU, Q. & LIANG, J. 2019. Co-combustion of coal and sludge technology and its engineering practice in coal-fired power plant. Industrial Water Treatment, 39**,** 7-11.

ZHANG, Z., LI, D., FENG, Y. & SU, Z. 2020. Investigation and Applications of Co-combustion of Sludge in a 1000 MW Coal Fired Boiler. JOURNAL OF ENGINEERING FOR THERMAL ENERGY AND POWER, 35**,** 210-216.

ZHENG, X., JIA, L., WANG, Y., ZHANG, J., CHEN, S., QIAO, X. & FAN, B. 2023. Effect of sewage sludge mixed with coal slime on heavy metal retention characteristics. Chemical Industry and Engineering Progress, 42**,** 3233-3241.

ZHOU, K., LIU, H., ZHANG, J., YAN, K., WANG, D., SHI, X. & WEN, C. 2022. NO and SO2 Emission Behaviors of Co-Combustion of Power Coal and High Water or De-Water Sewage Sludge. BOILER TECHNOLOGY, 53**,** 8-15.

ZHU, T., YIN, L., ZHAN, Z., XU, Q., FANG, Q., ZHANG, C. & CHEN, G. 2016. Adaptability of PDF transport model and eddy-dissipation model in simulation of coal combustion and co-combustion with sludge in coal-fired boiler. Journal of Central South University (Science and Technology), 47**,** 2864-2872.

ZOU, X., WANG, L. & ZHOU, S. 2023. The solution of slagging problem in municipal sludge incineration furnace. Kohai Story Expo**,** 52-54.

#159: Combustion characteristics of ammonia-hydrogen blended fuels in a microcombustion engine

Yu ZHOU[1], Jianquan LIU[2], Jie WEI[3], Wenlong ZHOU[4]

[1] Shanghai University of Electric Power, Shanghai, China, 1976680737@qq.com
[2] Shanghai University of Electric Power, Shanghai, China, liujianquan@shiep.edu.cn
[3] Shanghai University of Electric Power, Shanghai, China, 2630114751@qq.com
[4] Shanghai University of Electric Power, Shanghai, China, 763456159@qq.com

Abstract: As carbon-free and clean energy sources, the application of ammonia and hydrogen in fuel combustion is of great significance for the realisation of the strategic goal of "carbon neutrality". In this paper, the combustion characteristics of hydrogen- ammonia blended fuel in a micro gas turbine are investigated by numerical simulation, and the flow distribution characteristics, pressure loss, NOx emission and fuel combustion velocity in the combustion chamber are analysed under different ammonia blending ratios. The results show that: the central reflux zone in the combustion chamber has a tendency of hysteresis   and expansion due to the increase of the ammonia ratio; the pressure loss, NOx emission and the exit exhaust temperature increase with the increase of the doping ratio; and the exit temperature distribution coefficient has a tendency of increasing and then decreasing with the increase of the doping ratio.

Keywords: Gas Turbine; Numerical Simulation; Hydrogen/Ammonia Blended Fuel; Combustion Characteristics

1. INTRODUCTION

Faced with the growing problem of global climate change, countries are responding proactively by adopting carbon-neutral programmes. In the energy and power sectors, scientists have proposed a number of strategies to reduce carbon emissions, including the introduction of low-carbon, zero-carbon and carbon-neutral fuels (Wei Sheng-li, 2024).
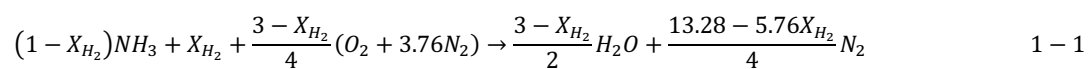
Ammonia is gaining interest as a carbon-free fuel for power generation with a relatively high energy density, as it can be stored as aliquid at 1.1 MPa and 300 K and has a low calorific value of 18.8 MJ/kg, making it a viable alternative to hydrogen as it has already reached safe storage and transport conditions for industrial use. Grinberg-Dana et al. demonstrated that ammonia has the highest energy production ratio as a fuel compared to methane, methanol and dimethyl ether (Charles Lhuillier, 2020).

In gas turbine combustion applications, many scholars around the world have carried out research on ammonia-hydrogen hybrid combustion. R.C. Orbay (2013) numerically and experimentally characterised the main flow structure within a gas turbine cyclonic combustion chamber as consisting of large-scale recirculation zones, mainly exhibiting geometric expansion and classical bubble-type vortex breakdown; the heat released by combustion enhances axial turbulence generation within the chamber, and also enhances the tangential velocity of the central rotating flow, resulting in a combination of axial velocities and central turbulent zones with a higher. Song Quan-bin (2023) investigated the combustion in the combustion chamber under different hydrogen doping ratios by numerical simulation, and the results showed that hydrogen mixing of ammonia helps to improve the instability of ammonia combustion, and the combustion efficiency is greatly improved when the volume ratio of hydrogen doping is higher than 35%.In experiments on mixed ammonia/hydrogen combustion on a spark ignition engine, Charles Lhuillier (2020) showed that combustion under conditions of low hydrogen slightly rich and medium hydrogen slightly poor fuels had the highest efficiency, while high hydrogen poor fuels were also expected to have high combustion efficiency performance. Bo Liang (2023) studied the flame of mixed ammonia-hydrogen combustion in a limited confined space, and the relevant experimental data showed that the change of the flame burning rate first increased and then decreased, and then fluctuated up and down, and this phenomenon was most obvious in the case of low fuel equivalence ratios and low ammonia mixing ratios, and the ammonia mixing ratios affected by the equivalence ratios were around 0~20%.In a study related to ammonia-hydrogen lean premixed combustion in the combustion chamber of a cyclone gas turbine by A. Valera-Medina (2017), a 50:50 (vol/vol) ammonia-hydrogen mixture was used to theoretically calculate the fuel ratio for a theoretical low-NOx combustion suitable for power generation. In the lean premixed mode, the NOx produced by combustion at a fuel equivalence ratio of 0.5 is about half of that at 0.8, which provides an identifiable method for reducing the NOx production. Zhou Yong-hao (2021) in the ammonia-hydrogen cyclone flame combustion experiments found that the mixing ratio of ammonia and hydrogen has a significant effect on the flame structure, that is, the instability of ammonia combustion will be improved with the reduction of the proportion of hydrogen resulting in the flame from the stable "M" type to the "V" type change.

2. COMPUTATIONAL MODELLING AND MESHING

2.1. Modelling

The model design is derived from the computational model of Liu Hong (2022). The turbulence is set to realizable k-ε..The fuel is a gaseous fuel mixture of hydrogen and ammonia. Turbulence-Chemical Volume Reaction Selection Eddy-Dissipation Model. The NOx generation model consists of thermal and fuel types. The combustion chamber inlet is the mass inflow port, and the outlet is the pressure outlet. The pressure-velocity coupling is based on the Coupled scheme, and the spatial discretisation is in the second-order windward mode. The chemical reaction equations are shown in equation 1-1 (Charles Lhuillier，2020) .

$$\left(1 - X_{H_2}\right)NH_3 + X_{H_2} + \frac{3 - X_{H_2}}{4}(O_2 + 3.76N_2) \rightarrow \frac{3 - X_{H_2}}{2}H_2O + \frac{13.28 - 5.76X_{H_2}}{4}N_2 \qquad 1 - 1$$

$$X_{H_2} = \frac{n_{H_2}}{n_{H_2} + n_{NH_3}} \qquad 1 - 2$$

Where:

-X_{H_2}=Molar fraction of hydrogen in an ammonia-hydrogen mixture
-n_{H_2}= Amount of hydrogen (mol)
-n_{NH_3}=Amount of ammonia (mol)

2.2. Grid-independent verification

In order to take into account, the calculation accuracy and reduce the calculation load, the structural grids of 450,000, 1,000,000 and 1,200,000 were designed for the calculation. Comparing the results of radial velocity at a certain position in the axial direction in the three sets of grids, it was found that the calculation accuracy of the 450,000 grid was slightly lower than that of the 1,000,000 grids, while the calculation accuracy of the 1,000,000 grid was similar to the 1,200,000 grids, and the 1,000,000 grid was finally adopted for the calculation. Finally, the 1 million grid is used for the calculation.

2.3 Combustion modelling feasibility validation

The ammonia hydrogen was set to simulate with the same parameters as the experimental settings in the reference 7 (A. Valera-Medina, 2017), and the temperatures at the relative positions were measured in equal proportions, and finally the simulation results were compared with the experimental results, which proved the feasibility of ammonia-hydrogen mixed combustion under this simulation condition by Figure 1.
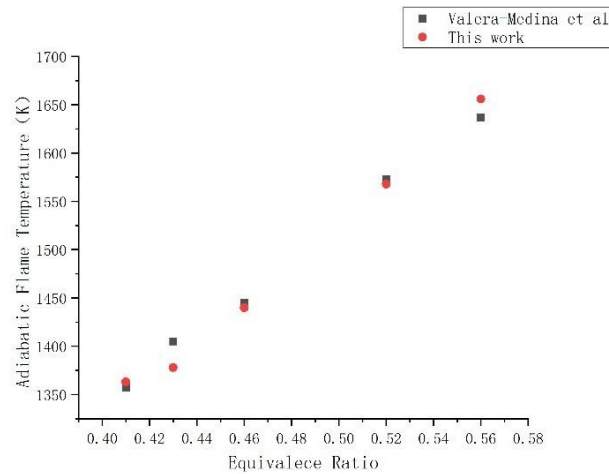

Figure 1: Validation of the arithmetic example

3. RESULIS AND ANALYSES

Ammonia-hydrogen fuel mixture with 10% NH_3, 20% NH_3, 30% NH_3, 40% NH_3, 50% NH_3 molar volume ratios were set, and the angle of the fuel inlet diagonal flow was 45°, the temperature of the inlet was 300K, and the outlet of the combustion chamber was 101325Pa.

3.1. Flow field analysis

Figure 2-a, Figure 2-b, Figure 2-c, Figure 2-d, and Figure 2-e show the mixed ammonia-hydrogen combustion under different molar ratio doping conditions. From the figure, it can be seen that the outer reflux zone was generated at the outer wall side of the diffuser section of the combustion chamber, and the axial central reflux zone was generated axially at the centre of the combustion chamber. The distributions of the outer and central reflux zones are symmetrical, and the generation of the reflux zone is conducive to the full combustion of the fuel, and the low velocity zone in the reflux zone is also conducive to the stable combustion of the flame (R.C.Orbay, 2013). Comparing the reflux zones under different mixing ratios, it is found that the overall effect of different ammonia mixing ratios on the flow field is concentrated in the central reflux zone, and this change is reflected in the fact that with the increase of the ammonia mixing ratio, the shape of the central reflux zone is elongated under the original ellipse-like situation, and this change is most obvious in the interval of 10%~30%. Comparison of the central reflux zone in the 30%~50% interval shows that the axial elongation tends to slow down, and the radial stretching tendency is more obvious compared with the axial stretching. This is attributed to the fact that the flame propagation velocity of ammonia is much smaller than that of hydrogen (S. Mashruk, 2022), and that the flame propagation velocity of hydrogen is affected by a variety of conditions, in this case the hydrogen flame propagation velocity is affected by the hydrogen mixing ratio.
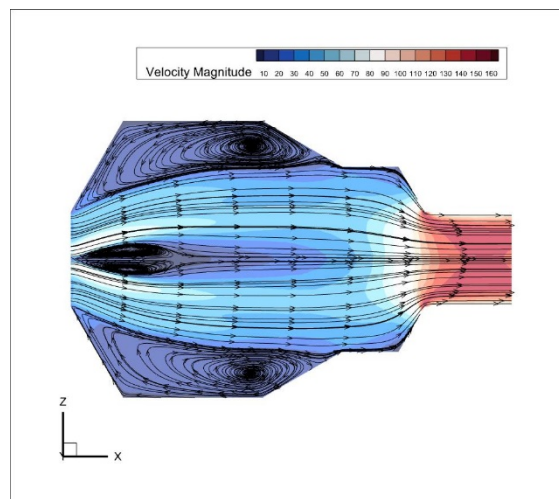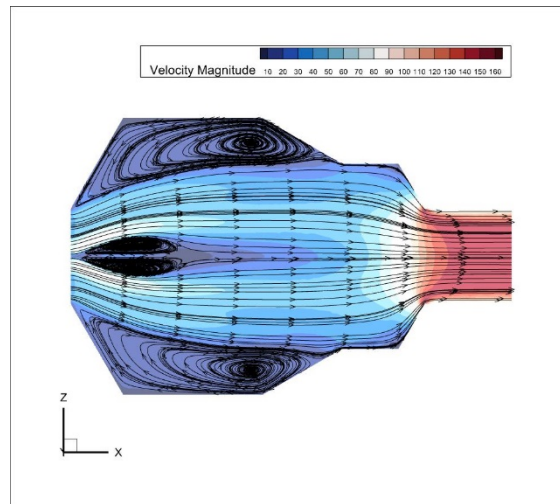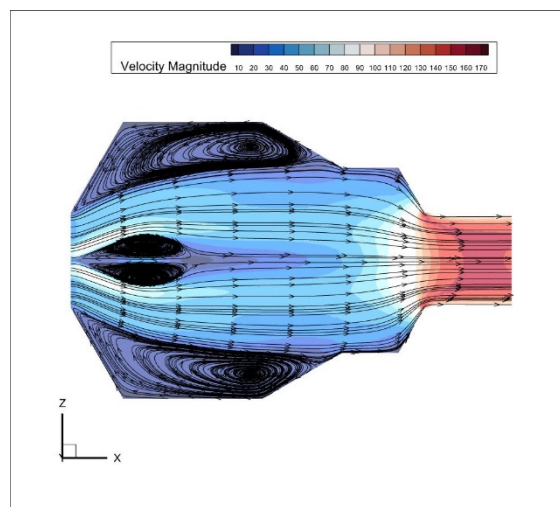

Figure 2-a: 10%molNH_3

Figure 2-b: 20%molNH$_3$
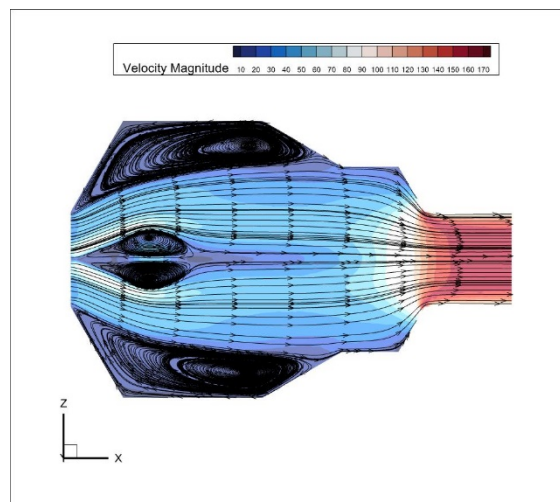

Figure2-c: 30%molNH$_3$
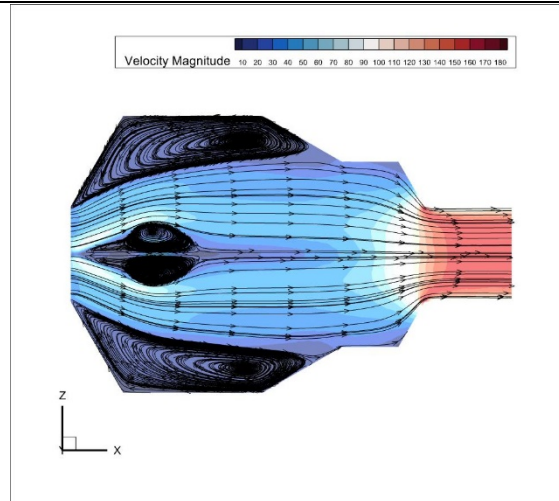

Figure2-d: 40%molNH$_3$

Figure2-e: 50%molNH$_3$

3.2. Combustion characterization

The combustion of a mixed gas fuel in a combustion chamber result in a reduction in the total pressure of the gas stream during the flow due to gas viscosity and temperature rise (Liu Jie-cai，2016), defined as the total pressure loss ε, which is calculated as shown in equation 2-1:

$$\varepsilon = \frac{P_1 - P_2}{P_1} \qquad 2-1$$

Where:

-P_1=Combustion chamber inlet pressure (Pa);

-P_2=Combustion chamber outlet pressure (Pa).

As can be seen from 0, the total pressure loss coefficient is increasing with the increase of ammonia blending ratio, but the increase in the magnitude of the slowing down trend. The reason for this is that the overall pressure loss increases due to the increase of gas flow resistance loss and thermal resistance loss, while the overall pressure loss slows down due to the increase of the mixing ratio of ammonia, the rise of mixed gas flow resistance loss and thermal resistance loss is smaller, so that the overall pressure loss change amplitude slows down.
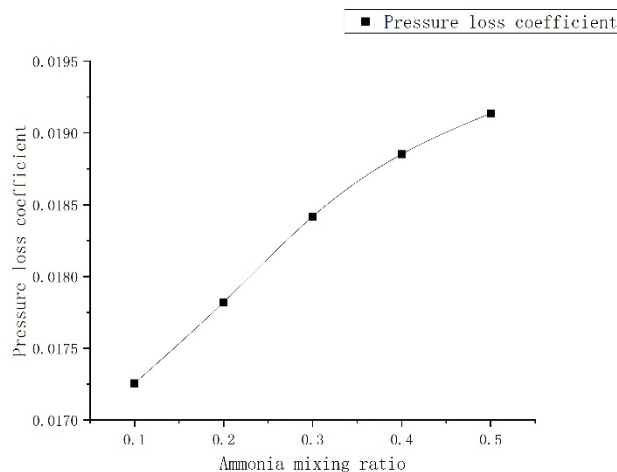

Figure 3: Effect of ammonia blending on pressure loss coefficient

0 shows the outlet temperature distribution inhomogeneity factor (OTDF) (Li Xiang-sheng, 2022) versus blended ammonia, defined as equation 2-2:

$$OTDF = \frac{T_{max} - T_2}{T_2 - T_1} \qquad 2-2$$

Where:

$-T_1$=Combustion chamber inlet temperature (K)
$-T_2$=Combustion chamber outlet temperature (K)
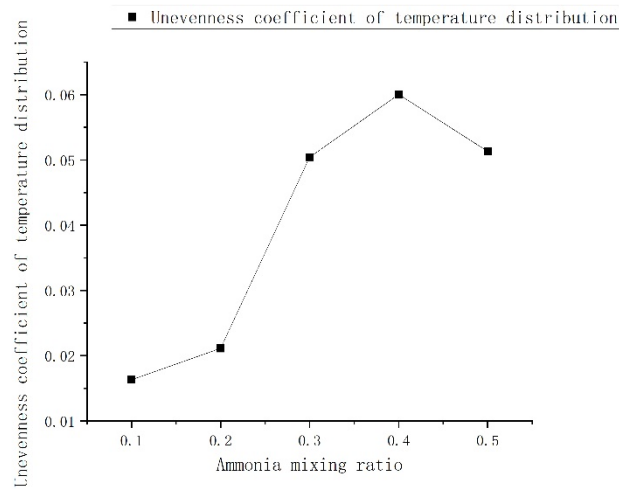$-T_{max}$=Maximum combustion chamber outlet temperature (K)

Figure 4: Effect of ammonia blending on the inhomogeneity coefficient of temperature distribution

As can be seen in 0, there is an increase and then a decrease in the temperature distribution inhomogeneity coefficient, and this transition occurs at the time of the 30 per cent increase to the 50 per cent blending ratio. Hydrogen-ammonia combustion due to the inertness of ammonia and the activity of hydrogen (Gao Zheng-ping，2022), with the increase in the proportion of ammonia and the decrease in the proportion of hydrogen, the chemical reaction of the fuel mixture to extend the time lag in the ignition of the mixture of gases, the gas mixture takes longer time to be ignited, and thus the reaction occurs in the location of a certain lag, the high temperature zone of the flame to the exit direction, which is the cause of fluctuations in the temperature distribution coefficient is also the reason for a small increase in the exit exhaust temperature (as shown in Fig. 5). This is the reason for the fluctuation of the temperature distribution coefficient and also the reason for the small increase of the outlet exhaust gas temperature (as shown in 0).
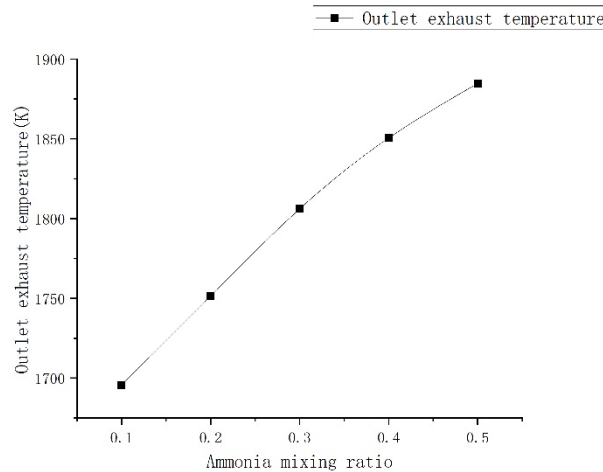
Figure 5: Effect of ammonia blending on outlet flue gas temperature

0 shows the variation of NO emission at the gas turbine outlet with the ammonia blending ratio. In hydrogen-ammonia blended fuel, NO mainly comes from fuel-type NOx produced by ammonia fuel combustion, followed by thermal-type NOx produced by high-temperature combustion. (Yang Wang, 2021) As the proportion of ammonia is increased, the concentration of NO dominated by fuel-type NOx increases significantly, which makes it difficult to meet the requirement of low NOx emission.

Figure 6: Effect of Ammonia Doping on NO Emissions at the Combustion Chamber Outlet

3.3. Effect of ammonia blending ratio on velocity distribution

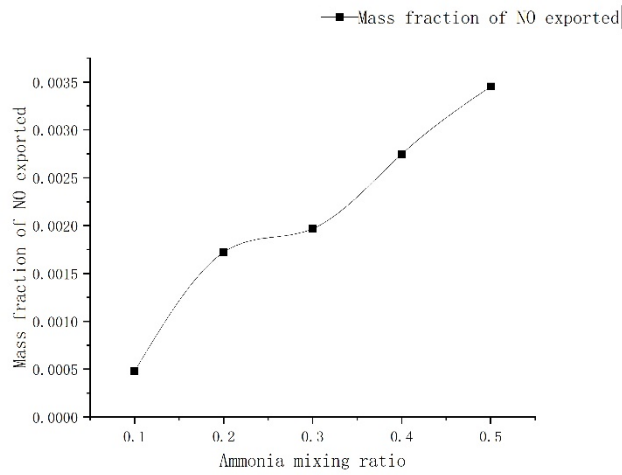0 and 0 show the radial velocity distribution at a certain position in the axial direction and the axial velocity distribution in the axial line under different ammonia doping ratios. It can be seen that the velocity distribution is good symmetry, the radial distance between the velocity peaks under different mixing ratios is elongated with the increase of the mixing ratio, and the velocity between the velocity peaks is obviously reduced and then increased, which is due to the heat released from the combustion enhanced axial turbulence, and at the same time enhanced the tangential velocity of the central rotating flow, which resulted in the increase of axial and radial velocities of the central reflux zone. From the gradient of velocity change between the two peak velocities on the radial velocity distribution graph, it can be seen that the gradient of velocity change shows a gradual slowing down trend with the increase of ammonia blending ratio. From the axial distance distribution of the front-end velocity peaks on the axial velocity distribution graph, it can be obtained that the position of the combustion reaction affected by chemical hysteresis shifted relatively backward with the increase of ammonia blending ratio.
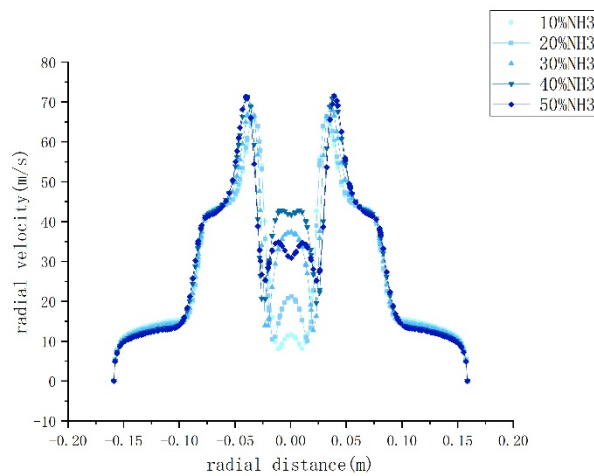

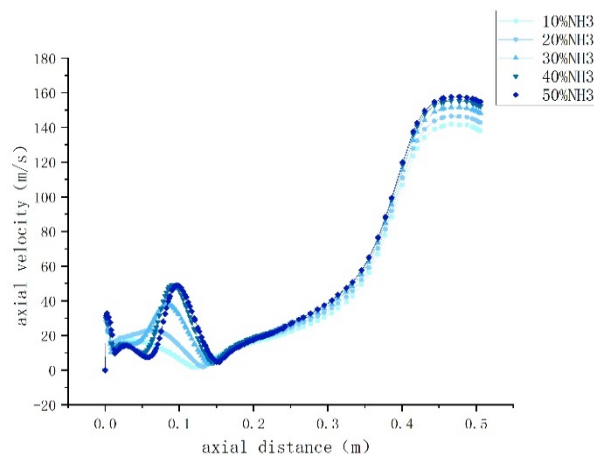Figure 7-a: Radial velocities at 80 mm in the axial direction for different ammonia mixing ratios

Figure 7-b: Axial velocity distribution on the central axis for different ammonia blending ratios

84

4. CONCLUSION

Numerical simulations related to ammonia-hydrogen mixed combustion in the combustion chamber of a micro gas turbine have been carried out and the following conclusions have been drawn:

As the proportion of ammonia blending increases, the total pressure loss coefficient is increasing, but there is a slowing down trend in the increase.

Due to the increase in the blending ratio of ammonia, the fuel-type NO_x inevitably increases, leading to an increase in NO emissions at the outlet.

Due to the characteristics of ammonia combustion hysteresis leads to the gas mixture needs a longer time to be ignited, thus the reaction occurs in the location of a certain lag, the high temperature region of the flame to the exit direction, leading to fluctuations in the exit temperature distribution coefficient and the centre of the reflux zone with the ammonia doping ratio of the increase in the stretching, expansion of the changes that have taken place.

5. REFERENCES

A. Valera-Medina, D.G. Pugh, P. Marsh, G. Bulat, P. Bowen, 2017.Preliminary study on lean premixed combustion of ammonia-hydrogen for swirling gas turbine combustors,International Journal of Hydrogen Energy,Volume 42, Pages 24495-24503.

Bo Liang, Mingrui Yang, Wei Gao, Yuting Jiang, Yanchao Li, 2023.Study on premixed hydrogen-ammonia-air flame evolution in a horizontal rectangular duct,Fuel,Volume 354, Pages 129427.

Charles Lhuillier, Pierre Brequigny, Nathalie Lamoureux, Francesco Contino, Christine Mounaïm-Rousselle, 2020.Experimental investigation on laminar burning velocities of ammonia/hydrogen/air mixtures at elevated temperatures,Fuel,Volume 263, Pages 116653.

Charles Lhuillier, Pierre Brequigny, Francesco Contino, Christine Mounaïm-Rousselle, 2020.Experimental study on ammonia/hydrogen/air combustion in spark ignition engine conditions,Fuel,Volume 269, Pages 117448.

Charles Lhuillier, Pierre Brequigny, Francesco Contino, Christine Mounaïm-Rousselle, 2020.Experimental study on ammonia/hydrogen/air combustion in spark ignition engine conditions,Fuel,Volume 269, Pages 117448.

Gao Zheng-ping，Tu An-qi，Li Tian-xin et al. 2022.Progress in Ammonia Combustion Technology for Zero-Carbon Electricity[J]. Clean Coal Technology, 28(03):173-184.

Li Xiang-sheng，Guo Yin，Yu Hong-fei et al. 2022.Study on the effect of hydrogen doping on combustion and emission performance of gas turbine combustion chamber[J]. JOURNAL OF XI'AN JIAOTONG UNIVERSITY, 56(06):9-16.

Liu Jie-cai，2016.Study on the influence law of two-stage cyclone structure on combustion performance of combustion chamber[D]. Nanjing University of Aeronautics and Astronautics

Liu Hong，Zeng Zhuo-xiong，Guo Kai-fang. 2022.Effect of Equivalent Ratio on H2/Air Combustion Characteristics of Micro Gas Turbines[J]. Journal of Engineering for Thermal Energy and Power, 37(05):72-78.

Liu Hong，Zeng Zhuo-xiong，Guo Kai-fang. 2022.Effect of Equivalent Ratio on H2/Air Combustion Characteristics of Micro Gas Turbines[J]. Journal of Engineering for Thermal Energy and Power, 37(05):72-78.

R.C. Orbay, K.J. Nogenmyr, J. Klingmann, X.S. Bai, 2013.Swirling turbulent flows in a combustion chamber with and without heat release,Fuel,Volume 104, Pages 133-146.

S. Mashruk, M.O. Vigueras-Zuniga, M.E. Tejeda-del-Cueto, H. Xiao, C. Yu, U. Maas, A. Valera-Medina, 2022.Combustion features of CH4/NH3/H2 ternary blends,International Journal of Hydrogen Energy,Volume 47, Pages 30315-30327.

Yang Wang, Xiaohu Zhou, Long Liu, 2021.Theoretical investigation of the combustion performance of ammonia/hydrogen mixtures on a marine diesel engine,International Journal of Hydrogen Energy,Volume 46, Pages 14805-14812.

Zhou Yong-hao，Zhang Zon-ling，Hu Si-Biao et al. 2021.Experimental Study on Flame Stability and Combustion Limit of NH3/H2 Premixed Cyclones[J]. Journal of Engineering Thermophysics, 42(01):246-253.

#160: Thermo-hydraulic study of the 19-pin sodium-cooled fast reactor fuel assembly clogging accident

Wenlong Zhou[1], Jianquan Liu[2], Yu Zhou[3], Jie Wei[4]

[1] Shanghai University of Electric Power, Shanghai, China, 763456159@qq.com
[2] Shanghai University of Electric Power, Shanghai, China, liujianquan@shiep.edu.cn
[3] Shanghai University of Electric Power, Shanghai, China, 1976680737@qq.com
[4] Shanghai University of Electric Power, Shanghai, China, 2630114751@qq.com

Abstract: Sodium-cooled fast reactors (SCRs) are one of the fourth-generation nuclear energy systems that can fully utilise nuclear resources and dispose of nuclear waste. Sodium-cooled fast reactors have hexagonal core fuel assemblies with tightly arranged rod bundles, which are prone to clogging accidents. In this paper, a CFD model is established for the fuel assembly of a sodium-cooled fast reactor, and computational fluid dynamics (CFD) is used to simulate the thermo-hydraulic characteristics of sodium flow in the prototype fuel assembly and the porous plugged prototype fuel assembly. From the simulation results, a CFD solution for an assembly model with 19 rod bundles was obtained. The CFD model has been validated against benchmark clogging experiments in the literature. In the study, the location of the clogging incident and the area of the clogging are considered, and comparative analyses of the flow velocity and temperature at the outlet and inside the assembly are carried out to draw conclusions. It can be seen that for the simulation of channel blockage accidents, the temperature field change at the outlet cross section is smaller and the flow velocity change at the component outlet is more sensitive. Inside the assembly, however, the return zone caused by the blocking block makes the maximum temperature change in the overall basin reach close to 100 k. This indicates that for the overall monitoring of the sodium temperature at the fuel assembly outlet is not able to detect the internal blocking in time, and that the change in the velocity field at the outlet face may be able to be used as a monitoring tool for the occurrence of the blocking flow accident.

Keywords: Sodium-Cooled; Fast Reactor; Clogging Accident; CFD Calculations

1. INTRODUCTION

Sodium-cooled fast reactors are one of the reactor types selected by the International Forum on Generation 4 Nuclear Energy Systems, and they are considered to be the most promising advanced nuclear energy system that is expected to realise the sustainable development of nuclear energy in China, due to the effective use of nuclear resources and the incineration and transmutation of high-level waste.One of the most promising advanced nuclear energy systems that are expected to achieve the sustainable development of nuclear energy in China[1-2]. In contrast to most currently operating pressurised water reactors, the fuel assemblies of sodium-cooled fast reactors make extensive use of ortho-hexagonal cassette assemblies with a dense rod bundle structure arranged in a hexagonal shape inside the assembly. The assemblies are secured to the fuel elements by spiral-wound metal wires, which partially facilitate hot and cold mixing of the coolant between the subchannels and improves the heat transfer capacity of the coolant [3].

A large number of experimental and numerical simulation studies have been carried out internationally to address this problem. YANGYun et al. carried out studies on plugging accidents in different media and analysed that the hazard of plugging accidents in solid media is higher than that of plugging accidents in porous media, and that the maximum temperature rise downstream of the plugging block decreases with the increase of porosity [4]. M. Naveen Raj et al. investigated the thermo-hydraulic characteristics of sodium flow in a prototype fuel assembly with porous internal plugging and proposed that sodium temperature inhomogeneity at the exit of the fuel rod bundle can be used as an effective plugging flow indicator [5]. N. Govindha Rasu et al. simulated the three-dimensional flow field of 19 bundles of sodium-cooled fast reactor fuel assemblies of seven helical pitch flow lengths and concluded that sodium boiling will likely occur within the fuel rod bundles at porous plugging with porosity less than 45% [6]. Ram Kumar Maity et al. conducted a thermo-hydrodynamic study of the core temperature monitoring system for sodium- cooled fast reactors and proposed that the core temperature monitoring system can effectively detect changes in fuel assembly flow and cladding assembly flow due to fuel assembly blockage [7]. Xiang Chai et al. used the RANS method to calculate the effect of blockage on the heat transfer process within the 61-needle filament-wound rod bundle of a sodium-cooled fast reactor, and the study showed a localised effect of the blockage flow, with variations in the envelope and coolant temperatures tending to disappear downstream of the blockage [8]. Junjie Lin et al. investigated the effect of filament winding on the heat transfer of fast reactor rod bundles and concluded that the increase in the number of filament winding increases the pressure difference, and the regular vortex phenomenon due to the non-uniformity of the pressure distribution is conducive to the mixing of the flow field [9].

In this paper, commercial computational fluid dynamics CFD software is used to model and numerically simulate a 19-bar bundle sodium-cooled fast reactor fuel assembly with filament winding to analyse the effects of different types of plugging accidents on the exit face of the fuel assembly.

2. FUEL ASSEMBLY PARAMETERS

The CEFR fuel assembly has 61 fuel rods in a single cassette, which are tightly arranged in a hexagonal dense rod bundle structure, with each rod being held in place by a metal wire wrap. Even if only a single cassette fuel assembly is simulated, the computational volume is still too large, so the modelling in this paper is for a partially heated section of 19 fuel rods, which can reduce the computational cost and still represent the flow and heat transfer characteristics of the complete CEFR fuel assembly to a certain extent. A schematic diagram of the filament winding assembly for 19 fuel rods is shown in Figure 1.1.
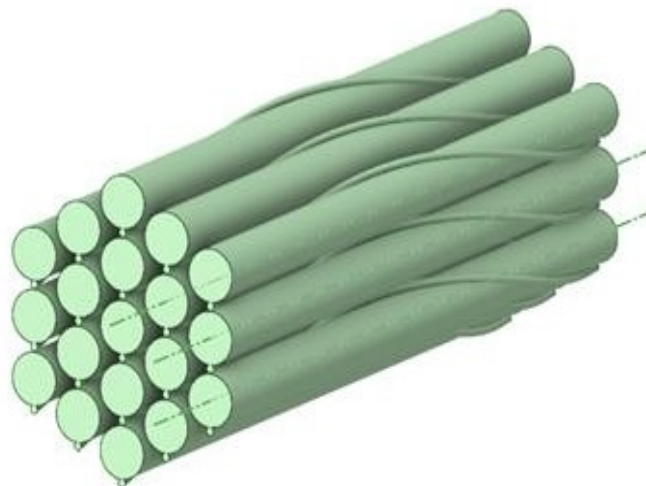

Figure 1.1: Schematic diagram of filament winding assembly for 19 fuel rods

The geometric parameters are shown in Table 1.1. Where to ensure accuracy during mesh generation, there is a 0.045 mm overlap region between the fuel rod and the winding filament, i.e., the winding filament is partially embedded in the fuel rod.

Table 1.1: Geometrical parameters

parametric	numerical value
Component length H	200mm
Fuel assembly side length L	18.67mm
Fuel rod diameter D	6mm
Winding Diameter d	0.95mm
Fuel rod spacing P	7mm
Fuel rod and winding spacing e	3.43mm
Number of winding pitches	1
Number of fuel rods	19

3. GEOMETRIC MODELLING AND MESHING

A schematic of the calculated fluid domain derived from the filament winding assembly is shown in Figure 2.1. Figure 2.2 shows the front view of the fluid domain.

Figure 2.1: Computational fluid domain   Figure 2.2: Front view of the fluid domain

For the meshing of this structurally complex filament winding assembly, Fluent-Meshing was used for structural meshing. The final grid number selected after grid-independence validation was about 10 million. Model validation Numerical model validation was selected from ORNL experimental data on high flow inlets plugging of a 19 bar bundle assembly with a winding filament using sodium as coolant.

Figure 2.3 Grid diagram

4. SIMULATION OF FLOW BLOCKING INCIDENTS

4.1. Numerical settings

The pressure inlet is chosen as the boundary condition for the inlet and the inlet temperature is 633.15 K. The walls of the fuel rods are uniform heat flow density and the rest of the solid walls are stationary with no slip. The parameters are shown in Fig. 3.1.

Table 3.1: Parametric conditions

frontiers	set up
Entrance boundary conditions	200000Pa
Export Boundary Conditions	0Pa
Fuel cartridge boundary	adiabatic
Filament winding boundary	adiabatic
Fuel rod surface heat flow density（q_w）	1872559W/m^2

The coolant is liquid sodium and the polynomials for the physical properties of liquid sodium are shown in equations (3.1-3.4).

$$\rho = 1016.82 - 0.239T \qquad (3.1)$$

$$C_P = 1629.1 - 0.83267T + 0.00046208T^2 \qquad (3.2)$$

$$\lambda = 105.1843 - 0.049T \qquad (3.3)$$

$$\mu = 0.00385 - 1.66448 \times 10^{-5}T + 3.00411 \times 10^{-8}T^2 - 2.48661 \times 10^{-11}T^3 + 7.8085 \times 10^{-15}T^4 \qquad (3.4)$$

Of which:

-ρ= densities, kg/m^3

-C_P= constant-pressure specific heat capacity, J/(kg·K)

-λ= thermal conductivity, W/(m·K)

-μ= dynamic viscosity, N·S/m^2

For the selection of the turbulence model, the k-epsilon Standard model is chosen, and the wall function is selected to be solved by the Enhanced Wall Function (EWF), which is able to accurately represent the wall behaviour and can well describe the flow heat transfer characteristics within the thermal boundary layer.

4.2. Simulation of flow blocking incidents

The flow plugging accident modelled in this paper occurs inside the assembly, and the axial position of the plug block inside the assembly is shown in Figure 3.1. The plugs are uniformly set in the internal and 95~105mm from the inlet area.

Figure 3.1: Plug block axial position
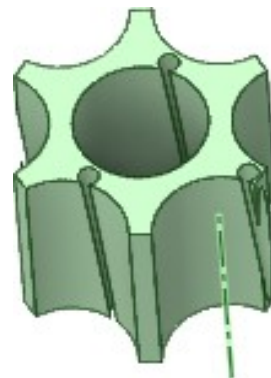
Figure 3.2: Plug block diagram for multi-channel flow blocking incidents

In this paper, transient calculations are carried out for the component plugging accident in the simulation, with 0.001s as the time step and 100 steps, in order to facilitate the study of the change of internal temperature and velocity field with time when the plugging accident occurs. For the simulation of the component for normal working conditions, multi-channel plugging accident conditions and

single-channel plugging accident conditions, the specific plugging area is shown in Fig. 3.3 and Fig. 3.4.
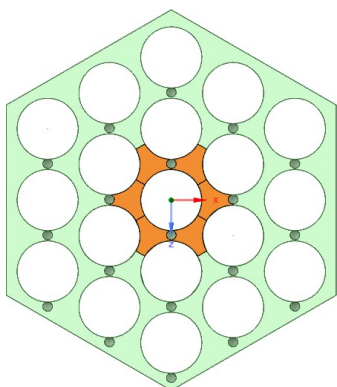
Figure 3.3: Schematic diagram of multi-channel flow blocking
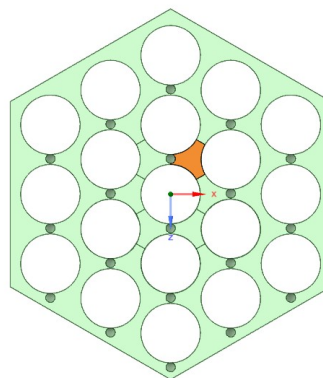
Figure 3.4: Schematic diagram of single-channel flow blocking

5. ANALYSIS OF SIMULATION RESULTS

5.1. Impact of flow blocking on maximum temperature in the watershed
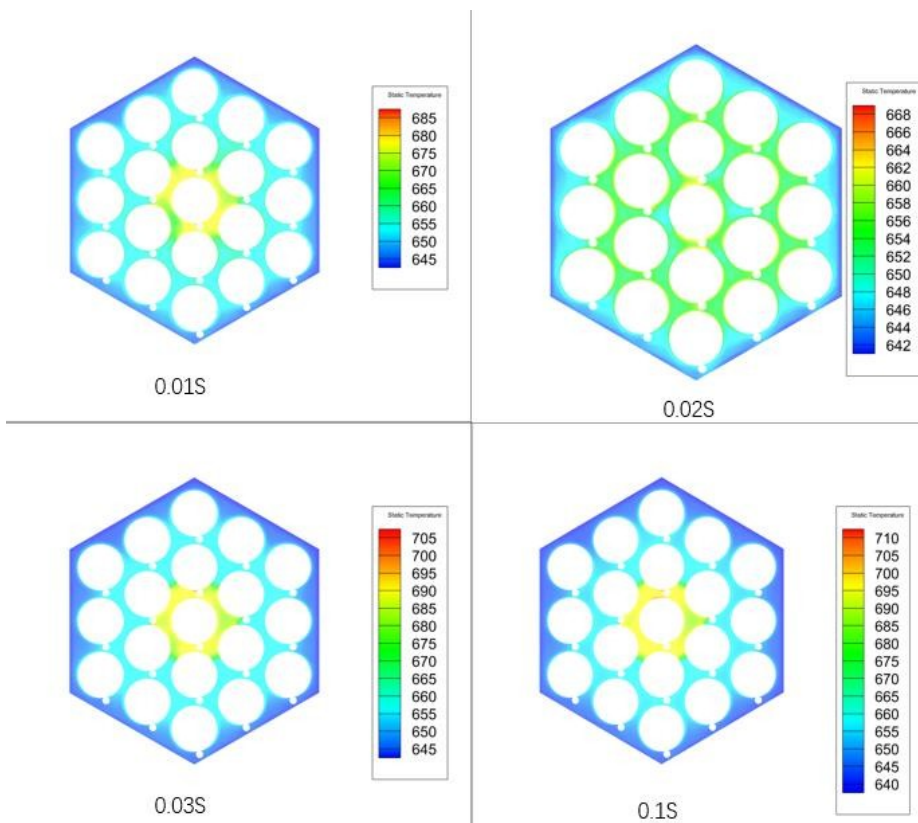
Figure 4.1: Temperature distribution at different moments of the cross-section where the highest temperature point is located aftera multi-channel
flow blocking incident

Through the analysis of the simulation results, it is concluded that the temperature field of the basin is close to a steady state at 0.01 seconds after the flow blocking accident. In this paper, the interface where the highest temperature of the whole basin is located when the steady state is reached is selected as the standard surface, and Fig. 4.1 shows the temperature distribution of this cross-section at different moments. From the figure, it can be seen that the temperature near the surface of the fuel rod increases first and then spreads outwards, and the temperature difference between the centre region and the edge region of the channel gradually increases with the change of time.

5.2. Effect of plugging on the outlet face
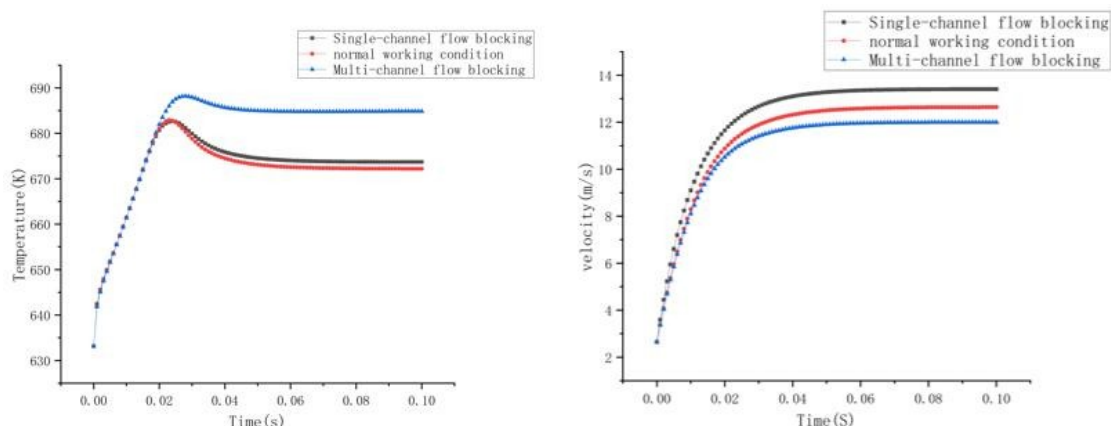
Figure 4.2: Maximum temperature and maximum flow rate at the outlet surface of the working condition as a function of time

The trend of the maximum temperature and flow velocity at the exit surface of the three conditions with time is shown in Fig. 4.2, which shows that the flow field of the three conditions gradually reaches a steady state after 0.06 seconds, and the difference in velocity and temperature between the three conditions basically no longer changes. The maximum flow velocity at the exit of the three conditions gradually differed after the beginning of the simulation, but the maximum temperature at the exit of the three conditions differed only after 0.02 s. This shows that for the flow velocity at the exit, the difference between the three conditions is very small. This suggests that it would be easier to detect anomalies in the detection of flow velocity at the outlet.

Figure 4.3: Comparison of outlet temperature distribution for normal common condition (a), single-channel plugging (b), and multi-channel plugging (c)

Figure 4.4: Comparison of outlet velocity distributions for normal working conditions (a), single-channel flow blocking (b) and multi-channel flow blocking (c)

After stabilisation, the outlet temperature distribution of each condition is shown in Figure 4.3. After stabilisation, there is not much difference in the outlet temperature distribution of each condition, of which the maximum temperature of the outlet under the multi-channel plugging condition is increased by 14k compared with the normal condition, and the change is only 2%. The single channel plugging condition has no change compare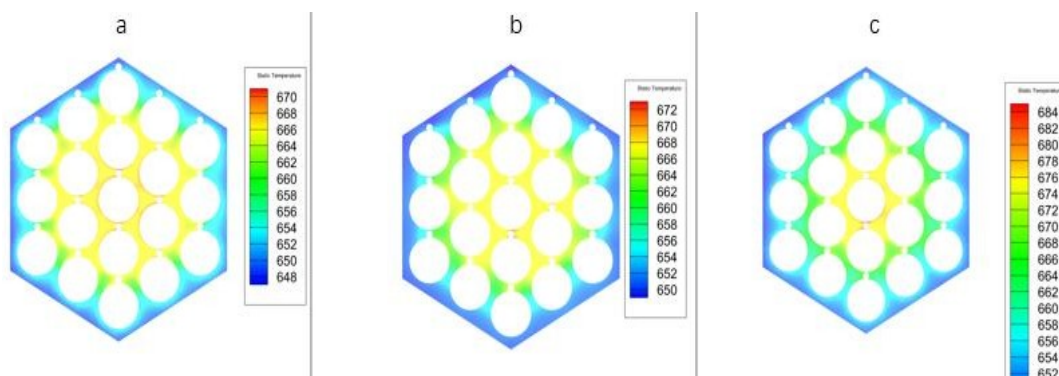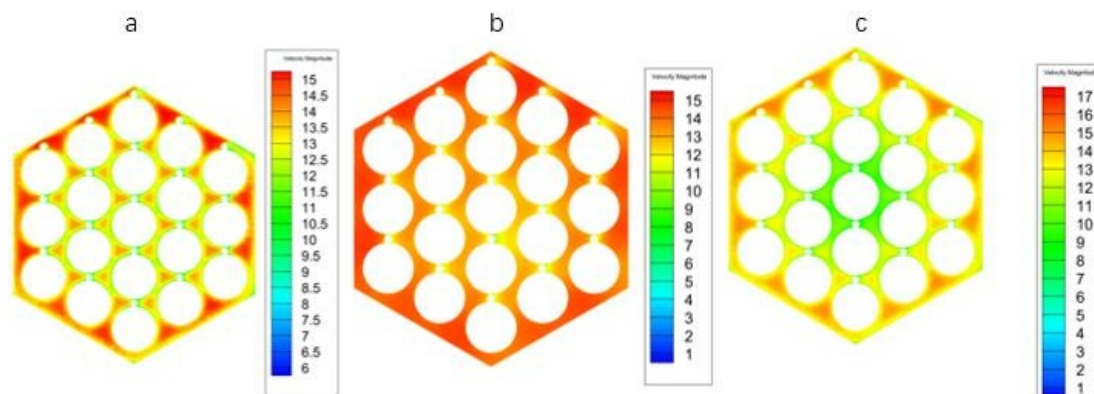d with the normal condition. After stabilisation, the outlet temperature distribution of each condition is shown in Fig. 5.4, and the maximum velocity of the outlet under the multi-channel flow blocking condition reaches 17m/s, which is about 13% higher than the normal condition. This indicates that when temperature changes are detected at the outlet, a serious plugging accident may have formed inside the component, compared with which the outlet velocity change will be more sensitive to the plugging accident.

6. CONCLUSION

In this paper, the numerical simulation of plugging accidents was carried out on a 19-needle sodium-cooled fast reactor core by Computational Fluid Dynamics CFD software to analyse the effects of different plugging accidents on the exit surface of the coolant flow field in different plugging accidents, and the main conclusions drawn are as follows:

1) After 0.01 seconds of blocking, the entire flow field has reached a near steady state, and the temperature of the channel where the block is located will be significantly higher than that of other regions.

2) In the event of a plugging accident, changes in velocity at the outlet face of the basin will be more sensitive than changes in temperature at the outlet face, thus it can be conjectured that changes in the velocity field at the outlet face may be able to be used as a means of monitoring the occurrence of a plugging accident.

7. REFERENCES

[1] ICHIMIYA M. The status of generation IV sodium-cooled fast reactor technology development and its future project[J]. Energy Procedia,2011,7(2)：79-87

[2] XU MI & YANG HONGYI.(2016). Sodium-cooled fast reactors and their safety characteristics. Physical (09),561-568.

[3] YANG YUN. Analysis of sodium-cooled fast reactor fuel assembly plugging accidents based on numerical simulation [D]. Shanghai Jiao Tong University,2019

[4] YANG YUN.(2019). CFD analysis of single-box sodium-cooled fast reactor fuel assembly plugging accidents. Atomic Energy Science and Technology (12),2398-2404.

[5] Raj, M.N.;Velusamy, K.;Maity, R.K..Thermal hydraulic investigations on porous blockage in a prototype sodiumcooled fast reactor fuel pin bundle[J].Nuclear Engineering and Design,2016,Vol.303(1): 88-108

[6] Govindha Rasu, N;Velusamy, K;Sundararajan, T;Chellapandi, P.Thermal hydraulic effect of porous blockage infuel subassembly of sodium cooled fast reactor[J].ANNALS OF NUCLEAR ENERGY,2014,Vol.70: 64-81

[7] Maity, R.K.;Velusamy, K.;Selvaraj, P.;Chellapandi, P..Computational fluid dynamic investigations of partial blockage detection by core-temperature monitoring system of a sodium cooled fast reactor.[J].Nuclear Engineering and Design,2011,Vol.241(12): 4994-5008

[8] Chai, Xiang (AUTHOR)(xiangchai@sjtu.edu.cn);Zhao, Lei (AUTHOR);Hu, Wenjun (AUTHOR);Yang, Yun (AUTHOR);Liu, Xiaojing (AUTHOR);Xiong, Jinbiao (AUTHOR);Cheng, Xu (AUTHOR).Numerical investigation offlow blockage accident in SFR fuel assembly.[J].Nuclear Engineering & Design,2020,Vol.359: 110437

[9] Lin, Junjie;Huang, Mei;Zhang, Shichun;Wang, Boxue;Huang, Jiyuan;Matsuda, Hiroshi;Morita, Chihiro.CFD investigation for a 7-pin wrapped-wire fuel assembly with different wires.[J].Annals of Nuclear Energy,2021,Vol.164: 108626

#163: A novel arrangement of metal fin heat recovery device in a dual channel wind scoop windcatcher system for reducing the building energy demand in temperate climates

Jiaxiang Li[1], John Calautit[2], Carlos Jimenez-Bescos[3]

[1] University of Nottingham, Nottingham, UK, jiaxiang.li@nottingham.ac.uk
[2] University of Nottingham, Nottingham, UK, ezzjkc@exmail.nottingham.ac.uk
[3] University of Westminster, London, UK, c.jimenezbescos@westminster.ac.uk

Abstract: The windcatcher, an innovative natural ventilation apparatus, facilitates the provision of fresh air and ensures indoor thermal comfort under suitable external conditions. This research introduces an advanced dual-channel windcatcher system that employs a rotary wind scoop, offering ventilation regardless of wind direction and incorporating passive and low-energy technologies. A cost-effective, low-pressure loss heat recovery design for the rotary scoop windcatcher was devised, featuring stationary fins between the supply and return channels. This design allows for heat recovery in the natural ventilation system, with heat being consistently transferred through the metallic fins. A Computational Fluid Dynamics (CFD) model, corroborated by experimental data, was adapted to assess ventilation performance and heat recovery efficiency. The findings revealed that the windcatcher system, equipped with a heat recovery (HR) unit, maintained over 95% of its initial ventilation rate. Furthermore, a heat recovery efficiency exceeding 15% was attained by utilizing a one-meter-long heat recovery unit in this study.

Keywords: Windcatcher, CFD, Heat Recovery, Natural Ventilation, Wind Tunnel

1. INTRODUCTION

As energy prices continue to rise and concerns over global warming intensify, researchers are exploring ways to increase energy efficiency across various sectors. One sector that could make a significant contribution to achieving asustainable energy economy is the built environment. The construction and built environment industries are responsiblefor over 40% of the direct and indirect global carbon emissions (He, Yang et al. 2014). Heating, Ventilation and Air Conditioning (HVAC) systems are responsible for over half of the energy consumption in buildings, with air conditioningbeing one of the fastest-growing energy users in the built environment (Pérez-Lombard, Ortiz et al. 2008, Liu, Justo Alonso et al. 2022). This places a significant burden on the electricity grid in many parts of the world. Therefore, researchers are seeking sustainable and cost-effective solutions that provide good indoor thermal comfort and air qualityto building occupants while minimizing the use of air-conditioning (Jomehzadeh, Hussen et al. 2020).

Natural ventilation is an attractive solution and has been the focus of many research studies. But natural ventilation is typically insufficient to provide the required indoor thermal comfort in unfavourable hot and cold climatic conditions. Thus, researchers are looking for sustainable and economical solutions to provide building occupants with good indoorthermal comfort and air quality while minimizing the use of air-conditioners, such as combining natural ventilation with other passive/low-energy strategies, including solar heating, heat recovery, cooling and dehumidification (Jomehzadeh,Hussen et al. 2020, Zhang, Yang et al. 2021, Bamdad, Matour et al. 2022).

Heat recovery systems were proposed in the ventilation system but mainly in mechanically ventilated buildings. In the natural ventilation system, the windcatcher is a suitable natural ventilation device for heat recovery integrations with both supply and return channels. Much research investigated the heat recovery system in windcatcher systems using heat pipes (Calautit, O'Connor et al. 2016, Chaudhry, Calautit et al. 2017, Calautit, Tien et al. 2020), solid tubes (Liu, Jimenez-Bescos et al. 2022) and thermal mass wheels (Calautit, O'Connor et al. 2019, Calautit, O'Connor et al. 2020).However, the high price of the heat pipes would result in high capital cost and maintenance cost. Moreover, the pressure loss through the system results in a low ventilation rate in natural wind conditions and additional fans are necessary for the system.

In addition, the traditional multidirectional ventilation device cannot provide a stable heat recovery, because the heat exchange between supply and return channels was not always stable (Mahon, Friedrich et al. 2022). The heat recoveryin a conventional four-sided windcatcher was investigated, but the frequent switching of inlet and outlet would decreasethe heat recovery efficiency (Liu, Jimenez-Bescos et al. 2022, Mahon, Friedrich et al. 2022).

The supply-to-return area ratio in the traditional four-sided windcatcher is not constant which might be switched between1 and 3. At the condition with a supply-to-return area ratio of 3, the heat recovery between the supply and return channels is not balanced and the recovery efficiency was not maximized. As shown in Figure 1, the varying wind direction would also cause reverse flow and the heat recovery performance will be decreased (Khan, Su et al. 2008). Moreover, the channels on the opposite sides were not adjacent, which further limited the efficiency of heat recovery. Thus, although effective heat recovery with so many limitations is something better than nothing, investigating a suitable design to overcome the limitation of traditional passive heat recovery is necessary for low-carbon natural ventilation inbuildings and industries.
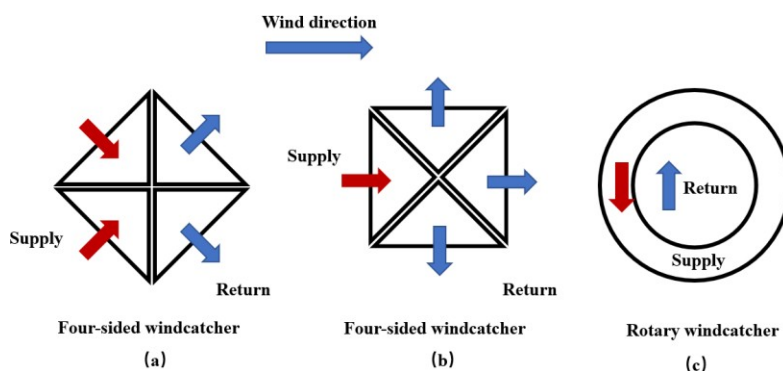
Figure 1: Comparison of the ventilation airflow direction in a typical multi-directional windcatcher and the proposed rotary windcatcher (a) wind direction from an edge in four-sided windcatcher (45°from the face) (b) wind direction from a face in four-sided windcatcher (c) in rotary scoop windcatcher

In prior research, the potential for heat recovery integration in building natural ventilation was explored through the proposal of a novel windcatcher design (Figure 2). This innovative design offers independent ventilation, irrespective ofthe prevailing wind direction (Li, Calautit et al. 2023). The windcatcher design incorporates a rotary wind scoop and a concentric tube arrangement that ensures fixed supply and return channels. Consequently, the impact of fluctuating wind directions is effectively eliminated.

The unique characteristics of this windcatcher design make it suitable for the application of a passive heat recovery device. This device, which utilizes metal fins to capture heat from the return duct, can be seamlessly integrated into thewindcatcher structure to provide efficient, low-cost heat recovery. The metal fins enable the transfer of heat from the outgoing air to the incoming air, thereby recovering heat that would otherwise be lost.
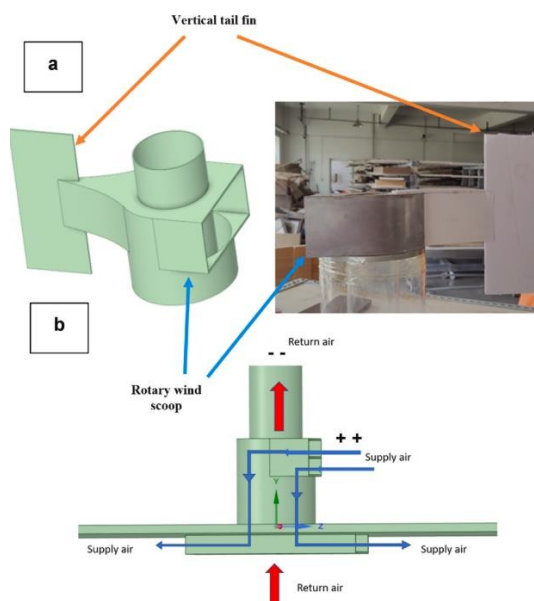
Figure 2: (a) Proposed rotary scoop windcatcher for passive heat recovery integration (Li, Calautit et al. 2023) and (b) operation

The aim of this study is to advance the development of a heat recovery unit within the rotary scoop windcatcher with low-pressure loss. This aim will be achieved through the utilization of Computational Fluid Dynamic (CFD) simulations.This research will encompass three distinct yet interconnected objectives: (1) experimental validation of the model; (2)evaluation of the ventilation performance of the windcatcher, with integrated heat recovery unit; and (3) assessment ofthe overall heat recovery performance of the unit.

To achieve the first objective, experimental validation will be conducted to ensure the accuracy and reliability of the model. Subsequently, the performance of the integrated windcatcher with a heat recovery unit will be evaluated. Lastly,the heat recovery unit's overall performance will be assessed, taking into account various factors such as the rate of heat recovery, temperature efficiency, and pressure loss. This research will advance the understanding of heat recoveryunits within rotary scoop windcatchers, providing insights into their performance and limitations.

2. METHOD

This section discussed the method which included numerical CFD modelling using ANSYS Fluent software and experimental wind tunnel testing to validate the model. The data obtained from the simulations and experiments were used to evaluate the ventilation performance and heat recovery efficiency of the device.

2.1. Proposed system model and prototype

In the initial windcatcher design, the supply and return channels were separated by the internal tube. However, the limited contact surface area posed a challenge to achieving efficient heat recovery. To address this issue, metal fins were inserted into the internal tube to increase the contact area, resulting in the creation of a heat recovery unit (Figure3).

The heat recovery unit was fabricated using aluminium fins with a thickness of 1 mm. The fins had a length of 95 mm, with 62mm on the supply side and 32mm on the return side. The fins were arranged at an angle of 12 degrees, and a total of 72 fins were used. To simulate the heat transfer process, aluminium panels with a thickness of 1mm were employed in the numerical simulations. The use of aluminium panels was favoured due to their superior strength, lowerthermal conductivity than steel, and lower cost than copper. After decreasing the thickness of the metal panels to approximately 1mm, the thermal resistance of the panels was negligible, and the heat transfer efficiency was primarily influenced by the convection heat transfer coefficient between the air and the metal panels. The height of the fins varied between 0.5m and 1m for evaluating the heat recovery efficiency.

The validated windcatcher tubes had external and internal diameters of 450mm and 300mm, respectively. The ventilation performance of the windcatcher was previously validated in research (Li, Calautit et al. 2023), and this studyfocused on evaluating the performance of the heat recovery unit.

The incorporation of the metal fins heat recovery unit in the windcatcher system offers a promising approach for reducingthe building energy demand. The results of this study could have significant implications for sustainable building design,particularly in temperate climates, where natural ventilation is commonly used, and efficient heat recovery systems arein high demand.
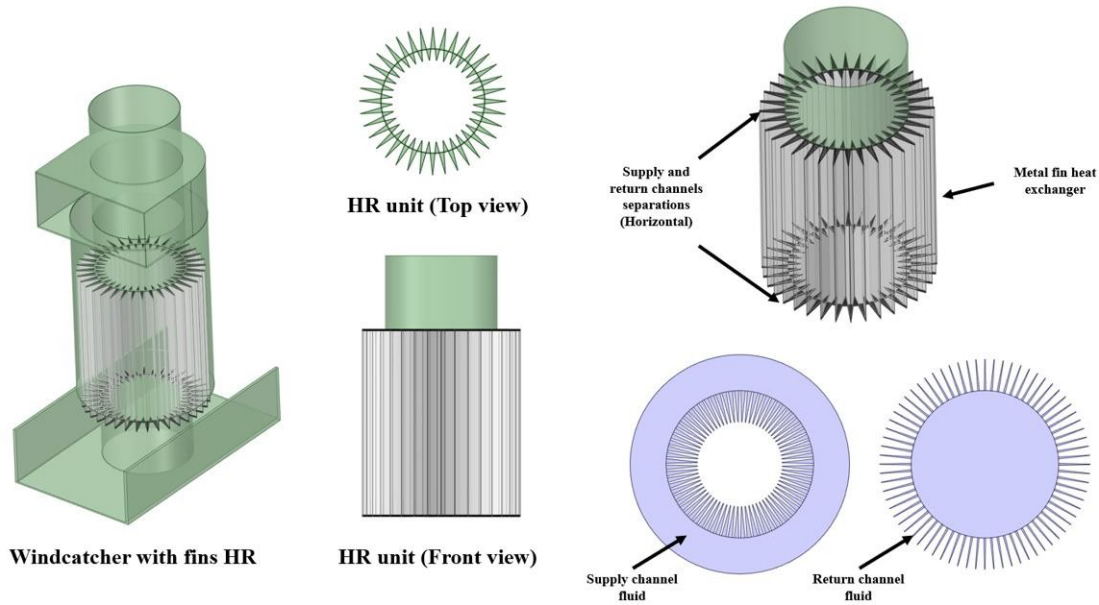
Figure 3: Windcatcher with metal fins heat recovery unit and the supply & return air channels

2.2. Experimental wind tunnel testing

To evaluate the performance of the windcatcher prototype, a test room cube with the dimensions 1.2m x 1.2m was constructed, using 50mm thick insulation board to ensure thermal insulation (Figure 4). To prevent airflow short- circuiting and ensure good air circulation inside the test room, two L-shape anti-short circuit devices (ASCD) were installed, as per previous research (Li, Calautit et al. 2023). The windcatcher prototype was placed in the centre of thetest room.

A 4m long open wind tunnel (Figure 4) was constructed for testing the windcatcher ventilation rate. The wind tunnel wasequipped with a contraction section, screen mesh, and honeycomb flow conditioners, as described in previous research(Li, Calautit et al. 2023). The screen mesh and flow conditioners were used to establish a turbulent flow from the industrial fans, creating a stable airflow suitable for evaluating the CFD model, as reported in previous research (Li, Calautit et al. 2023).

The wind speed profiles measured from the outlet of the wind tunnel were used as the inlet boundary conditions for theCFD simulations, providing a reliable representation of the actual airflow conditions. The resulting data were used to evaluate the ventilation performance of the windcatcher and to optimize its design for maximum efficiency.

The use of a dedicated test room and wind tunnel facility allowed for controlled experimental conditions and provided valuable insights into the performance of the windcatcher prototype. The results of this study have significant implications for sustainable building design, offering a promising approach to reducing energy consumption and associated with greenhouse gas emissions.

Figure 4: Wind tunnel and CFD model set-up and the dimension of the model

2.3. CFD modelling

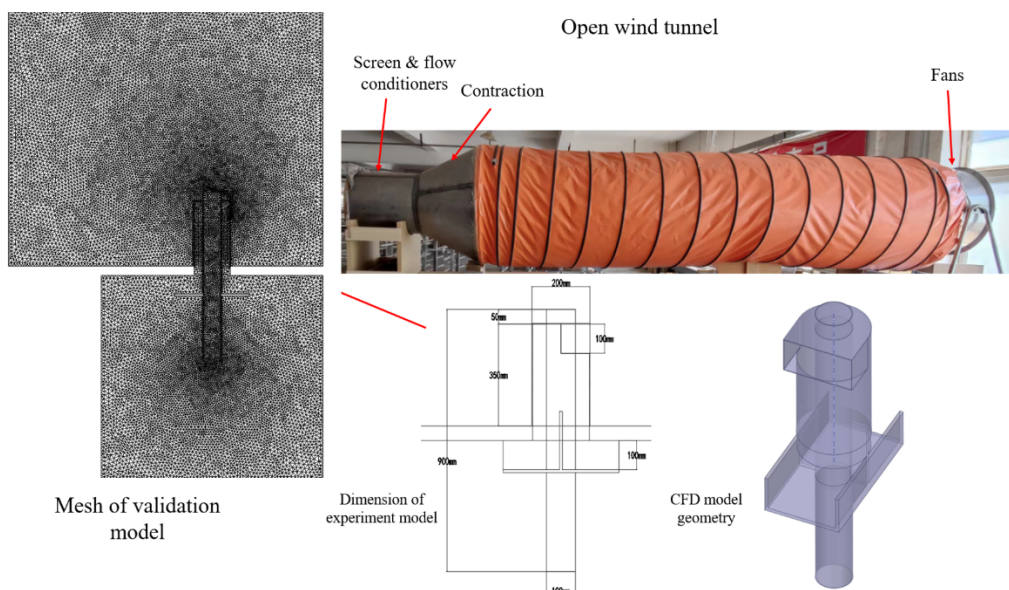In this research, the performance of the suggested system is assessed through the implementation of Computational Fluid Dynamics (CFD) simulations. The commercial software, FLUENT, is employed for conducting airflow simulations. Concurrently, the three-dimensional model is developed utilizing Spaceclaim, which is integrated into the Ansys Workbench software environment.

The mass, momentum and energy equations are solved for the airflow within this model. The Reynolds-averaged Navier-Stokes and k-epsilon equations are applied, in accordance with previous research (Li, Calautit et al. 2023). A second-order upwind scheme is utilized to discretize all transport equations. The widely adopted Semi-implicit Methodfor Pressure-Linked Equations (SIMPLE) segregated pressure-based algorithm solver is implemented for turbulent airflow simulations. The governing equations for mass (eqn.1), momentum (eqn.2), and k and epsilon (eqn.3 and 4) areincorporated within the model.

$$\frac{\partial \rho}{\partial t} + \nabla \cdot (\rho u) = 0 \tag{1}$$

$$\frac{\partial \rho}{\partial t} + \nabla \cdot (\rho u u) = -\nabla p + \rho g + \nabla \cdot (u \nabla u) - \nabla \cdot \tau_t \tag{2}$$

$$\frac{\partial (\rho k)}{\partial t} + \nabla \cdot (\rho u k) = \nabla \times \left[\left(\mu + \frac{\mu_t}{\sigma_k} \right) \nabla k \right] + P_k - \rho \varepsilon \tag{3}$$

$$\frac{\partial (\rho \varepsilon)}{\partial t} + \nabla \cdot (\rho u \varepsilon) = \nabla \cdot \left[\left(\mu + \frac{\mu_t}{\sigma_\varepsilon} \right) \nabla \varepsilon \right] + \frac{C_{1\varepsilon} P_k}{k} \varepsilon - C_{2\varepsilon} \rho \frac{\varepsilon^2}{k} \tag{4}$$

In order to test the heat recovery potential of the windcatcher, the governing energy equation (5) was added to the CFD simulation method.

$$\frac{\partial (\rho e)}{\partial t} + \nabla \cdot (\rho e u) = \nabla \cdot (k_{eff} \nabla T) - \nabla \cdot (\sum_i h_i j_i) \tag{5}$$

Where:

- u = velocity (m/s).
- t = time (s)
- ρ = density (kg/s)
- g = gravitational acceleration (m/s²)
- p = pressure (Pa)
- τt = stress tensor of the turbulence stresses (Pa)
- μ = dynamic molecular viscosity (Pa·s).
- μ_t =turbulent viscosity (Pa·s)
- P_k = turbulent production of kinetic energy (kg·m^{-1}·s^{-3})
- e = specific internal energy (J/kg)
- $C_{1\varepsilon}$ and $C_{2\varepsilon}$ = empirical constants (dimensionless).
- keff= effective heat conductivity (W/(m·K))
- hi = specific enthalpy of fluid (J/kg)
- T = air temperature (K)
- ji= mass flux (kg/(m²·s))

Table 1: CFD settings and boundary conditions in accordance with previous research (Li, Calautit et al. 2023)

Term	Value and settings
Inlet	
Velocity (m/s)	0-3 (profiled wind speed for validation)
	1-7 (constant wind speed for optimizations)
Initial Gauge Pressure (Pa)	0
Specification Method	k-epsilon RNG
Outlet	
Gauge Pressure (Pa)	0 (atmospheric)
Wall	
Shear Condition	No slip
Roughness Models	Standard
Roughness Height	0
Roughness Constant	0.5
Converged residuals	
Continuity / k / Epsilon	0.001
X/Y/Z velocity	0.0001

To simplify, the heat recovery efficiency of the windcatcher and the ventilation performance of the windcatcher were evaluated separately. The mesh element number of the heat recovery simulation of a 0.5m and 1m long heat recoveryunit were 2.16 million and 3.42 million, respectively. The mesh elements of the windcatcher with and without a heat recovery unit were 12.6 million and 4.22 million, respectively.

In the heat recovery evaluation, the external supply air temperature was 0 ℃ (273 K) and the internal return air temperature was 27℃ (300 K). The heat recovery efficiency was evaluated by the internal energy difference between the supply and return air and heat flux through the metal fins.

3. RESULTS AND DISCUSSION
3.1. Model validation

The experimental validation results, together with the velocity contour, are depicted in Figure 5. In the case of the scaled prototype, fresh air was supplied at rates ranging from 1.7 L/s/m² to 9.18 L/s/m², taking into account outdoor wind speeds varying between 0.5 m/s and 2.5 m/s. The mean discrepancy in the ventilation rate between the ComputationalFluid Dynamics (CFD) simulation and the experimental data was 0.156 L/s/m², with an average variance of 4.5%. An observed linear relationship emerged between the average wind speed and the ventilation rate. The investigation showed that the difference in ventilation rate between the CFD model, which integrated profiled wind from the open wind tunnel, and the homogeneous environment wind under comparable average wind speeds was insignificant.
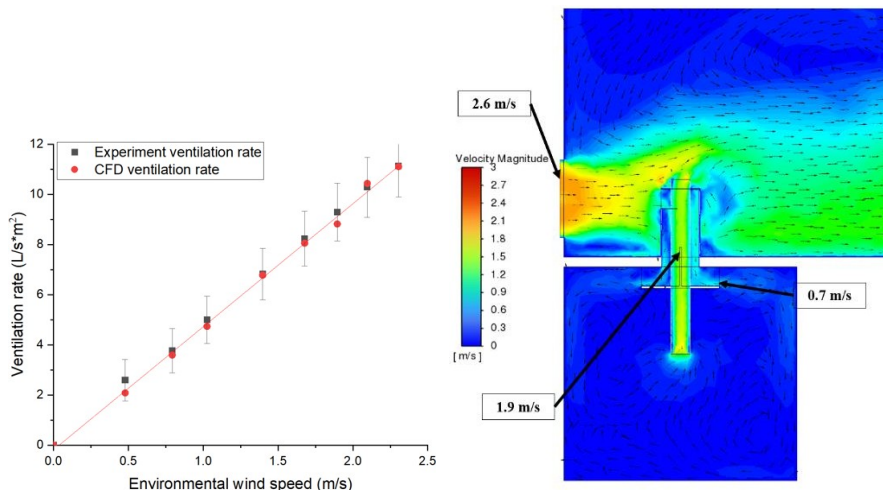
Figure 5: Experimental and CFD results comparison and the velocity contour of the validation model

3.2. Ventilation performance

The ventilation performance of the windcatcher model without the HR unit and the model with a 0.5m long HR unit areshown in Figure 6. Similar linear relationships between the ventilation rate and the environment were achieved, and theHR unit only decreased 4.5% of the total ventilation rate. As the fins only increased the contact surface area without affecting the section area in the long channel, the overall ventilation rate was not significantly affected (Figure 6). The high ventilation rate of the initial windcatcher remained for a sufficient fresh air supply, and a low-pressure loss increment in the 0.5m long HR unit provides the potential of installing a longer HR unit in the windcatcher system.
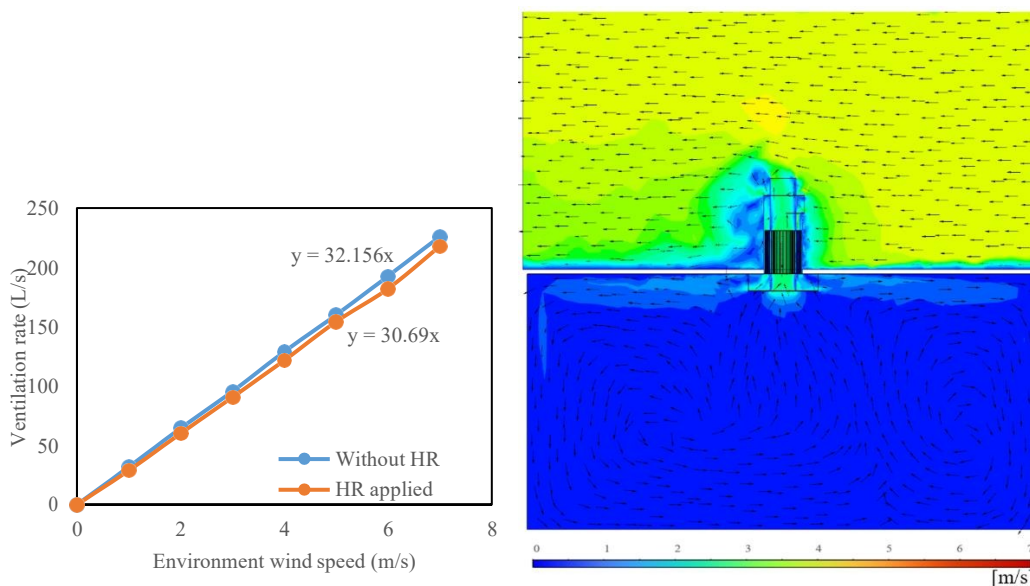
Figure 6: Ventilation performance and velocity contour of the windcatcher model with and without HR unit (0.5m long fins)

3.3. Heat transfer efficiency

The heat transfer rate and efficiency of the 0.5m HR unit are shown in Figure 7. and the HR efficiency of HR units withdifferent lengths is shown in Figure 9. With the increase of mass flow rate, the heat transfer rate increased steadily, butthe HR efficiency was

slightly decreased. A higher airflow velocity around the heat recovery surface increased the convectional heat transfer coefficient but the convectional heat transfer coefficient was not proportional to the airflow velocity and the increase of the convectional heat transfer coefficient was decreased with the increase of airflow velocity. Thus, the HR efficiency decreased from 10% to 6.5%. HR efficiency of about 15% was achieved in a windcatcher with a 1m long HR unit which would decrease to 14% at a higher ventilation rate condition. However, in most cases, the ventilation rate of the ventilation system would not be increased to over 300 L/s which requires an environment windspeed of over 10 m/s. Thus, the heat recovery efficiency would remain at a higher level.

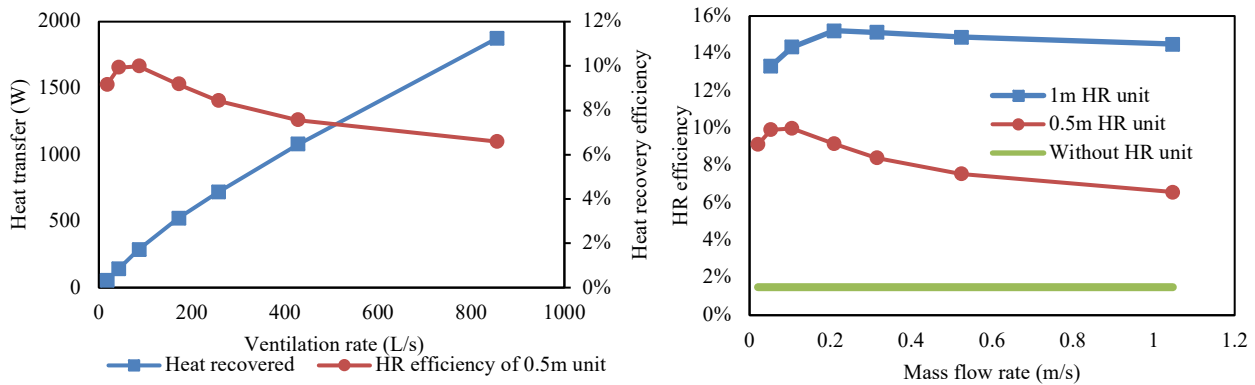*Figure 7: Heat transferred through metal fins and the heat recovery efficiency of a 0.5m heat recovery unit after increasing the ventilation rate, and heat recovery efficiency of 0.5m and 1m heat recovery units*

The temperature contour with a 27 ℃ temperature difference between supply and return air in the 1m heat recovery unit and the velocity contour under a high airflow rate are shown in Figure 8. A heat recovery unit with an efficiency of 15%, could increase the supply air temperature by 4 ℃ under a 27℃ temperature difference between supply and return air. The airflow velocity between the fins decreased, and the pressure loss of the system increased, which decreased the total ventilation rate of the windcatcher.
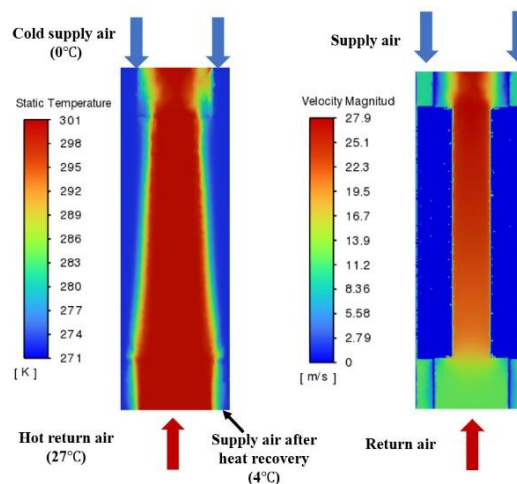
Figure 8: Temperature and velocity contour in the 1m heat recovery unit

4. CONCLUSION AND FUTURE WORKS

In this study, a passive heat recovery system utilizing low-pressure loss metal fins was proposed for integration into a rotary scoop windcatcher. The initial scaled windcatcher model was assessed through wind tunnel experiments and Computational Fluid Dynamics (CFD) simulations. Subsequently, a full-scale windcatcher model was optimized based on the scaled model, with the heat recovery unit applied to the full-scale configuration. Ventilation performance and heat recovery efficiency were evaluated using CFD simulations.

The full-scale windcatcher demonstrated a ventilation rate exceeding 160 L/s when subjected to an outdoor wind speed of 5 m/s. The ventilation rate loss incurred by a 0.5 m heat recovery unit amounted to a mere 4.5%, maintaining a high ventilation rate of over 150 L/s under the same outdoor wind speed. The heat recovery efficiency of 0.5 m and 1 m heat recovery units approximated 9% and 15%, respectively, with the potential for further enhancement by employing longer heat recovery units. A 4°C increase in supply air temperature was achieved by a windcatcher with a 1 m heat recovery unit under a 27°C temperature differential.

In this preliminary investigation, a simple design and operation principle were employed for the heat recovery system. Heat recovery efficiency was intentionally limited to preserve high ventilation efficiency. The contact surface-to-volume ratio in the channels can be further augmented by increasing the number of fins and obstructing the space beyond the fins. Given that ventilation efficiency was not significantly impacted by the heat recovery unit, the unit's length can be extended to attain higher heat recovery efficiency without compromising ventilation efficiency. Furthermore, the windcatcher's height is typically elevated to capture wind at higher speeds and minimize interference with the building's edge. Sufficient space for a heat recovery unit is available, allowing for an overall heat recovery

efficiency increase thatsatisfies both designers and occupants.

Future research should evaluate the metal fins heat recovery device using wind tunnel experiments. Additionally, optimizing the metal fins and windcatcher geometry will be essential for attaining higher ventilation rates and heat recovery efficiency.

5. NOMENCLATURE

e	Specific internal energy (J/kg K)
Gb	Generation of turbulence kinetic energy due to buoyancy
Gk	Generation of turbulence kinetic energy due to mean velocity gradients
h_i	Specific enthalpy of fluid (J/kg)
j_i	Mass flux (kg/s)
k_{eff}	Effective heat conductivity (W/m K)
m	Mass of fluid(kg)
p	Pressure (Pa)
P_k	Turbulent production of kinetic energy
ΔQ	Heat flux through the heat recovery unit (W)
σ_k	Turbulence model constant of k
σ_ε	Turbulence model constant of ε
t	Time (s)
T	Air temperature (K)
u	Velocity (m/s)
$\bar{V}$	Average airflow velocity in the return duct (m/s)
V_c	Airflow velocity in the centre of the return duct (m/s)
αk	Inverse effective Prandtl numbers for k
$\alpha\varepsilon$	Inverse effective Prandtl numbers for ε
μ	Dynamic molecular viscosity (Pa s)
μ_t	Turbulent viscosity（m2/s）
ρ	Density (kg/m^3)
τ_t	Divergence of the turbulence stress
ASCD	Anti-short circuit device
CFD	Computational Fluid Dynamic
HVAC	Heating, ventilation and air-conditioning
HR	Heat Recovery

6. REFERENCES

Bamdad, K., S. Matour, N. Izadyar and T. Law (2022). "SIntroducing extended natural ventilation index for buildings under the present and future changing climates." Building and Environment: 109688.

Calautit, J., D. O'Connor, S. Shahzad, K. Calautit and B. Hughes (2019). "Numerical and experimental analysis of a natural ventilation windcatcher with passive heat recovery for mild-cold climates." Energy Procedia 158: 3125-3130.

Calautit, J. K., D. O'Connor and B. R. Hughes (2016). "A natural ventilation wind tower with heat pipe heat recovery for cold climates." Renewable Energy 87: 1088-1104.

Calautit, J. K., D. O'Connor, P. W. Tien, S. Wei, C. A. J. Pantua and B. Hughes (2020). "Development of a natural ventilation windcatcher with passive heat recovery wheel for mild-cold climates: CFD and experimental analysis." Renewable Energy 160: 465-482.

Calautit, J. K., P. W. Tien, S. Wei, K. Calautit and B. Hughes (2020). "Numerical and experimental investigation of the indoor air quality and thermal comfort performance of a low energy cooling windcatcher with heat pipes and extended surfaces." Renewable Energy 145: 744-756.

Chaudhry, H. N., J. K. Calautit and B. R. Hughes (2017). "Optimisation and analysis of a heat pipe assisted low-energy passive cooling system." Energy and Buildings 143: 220-233.

He, B.-j., L. Yang, M. Ye, B. Mou and Y. Zhou (2014). "Overview of rural building energy efficiency in China." Energy Policy 69: 385-396.

Jomehzadeh, F., H. M. Hussen, J. K. Calautit, P. Nejat and M. S. Ferwati (2020). "Natural ventilation by windcatcher (Badgir): A review on the impacts of geometry, microclimate and macroclimate." Energy and Buildings 226: 110396.

Khan, N., Y. Su and S. B. Riffat (2008). "A review on wind driven ventilation techniques." Energy and Buildings 40(8): 1586-1604.

Li, J., J. Calautit, C. Jimenez-Bescos and S. Riffat (2023). "Experimental and numerical evaluation of a novel dual-channel windcatcher with a rotary scoop for energy-saving technology integration." Building and Environment: 110018.

Li, J., J. K. Calautit and C. Jimenez-Bescos (2023). "Experiment and numerical investigation of a novel flap fin louver windcatcher

for multi-directional natural ventilation and passive technology integration." Building and Environment 242: 110429.

Liu, M., C. Jimenez-Bescos and J. Calautit (2022). "CFD investigation of a natural ventilation wind tower system with solid tube banks heat recovery for mild-cold climate." Journal of Building Engineering 45: 103570.

Liu, P., M. Justo Alonso and H. M. Mathisen (2022). "Heat recovery ventilation design limitations due to LHC for different ventilation strategies in ZEB." Building and Environment 224: 109542.

Mahon, H., D. Friedrich and B. Hughes (2022). "Wind tunnel test and numerical study of a multi-sided wind tower with horizontal heat pipes." Energy 260: 125118.

Pérez-Lombard, L., J. Ortiz and C. Pout (2008). "A review on buildings energy consumption information." Energy and Buildings 40(3): 394-398.

Zhang, H., D. Yang, V. W. Y. Tam, Y. Tao, G. Zhang, S. Setunge and L. Shi (2021). "A critical review of combined natural ventilation techniques in sustainable buildings." Renewable and Sustainable Energy Reviews 141: 110795.

#166: Characterization of transmutation of transuranic elements in pressurized water reactors

Jie Wᴇɪ, Jaquan Lɪᴜ, Wenlong Zʜᴏᴜ, Yu Zʜᴏᴜ

School of Energy and Mechanical Engineering, Shanghai University of Electric Power，Shanghai，201306

Abstract: As of the end of June 2022, there are 660 nuclear power units in operation worldwide, with a total installed capacity of about 394 million kilowatts. The main combustion feedstock of these nuclear power plants contains elements such as U-235, U-238, Pu-239, etc. These fuel nuclei undergo radiation capture, fission, transmutation, and other reactions with neutrons in the reaction vessel, which leave many nuclides with strong radioactivity and long decay cycles in the spent fuel after combustion and bring many problems to the disposal of spent fuel. Although the subcritical accelerated starter system (ADS) has a hard neutron energy spectrum and has certain advantages for transmutation of transuranic elements, its commercialization level is low, and transmutation of transuranic elements using pressurized water reactors (PWRs), which are more widely commercialized nowadays, can quickly and effectively alleviate the problem of spent fuel treatment in nuclear power plants. In this paper, the transmutation characteristics of transuranic elements in spent fuel in pressurized water reactors are investigated. In this study, transuranic elements in spent fuel are introduced into pressurized water reactor (PWR) fuel, and the changes in the effective multiplication factor and the neutron flux density distribution of PWR core assemblies are analyzed under different arrangement modes of transuranic elements. The results show that the introduction of transuranic elements into the pressurized water reactor core causes a decrease in the Keff value; moreover, the core neutron energy spectrum is hardened due to the capture and depletion of a portion of thermal neutrons after I- 129 is added into the core.

1. INTRODUCTION

By the end of June 2022, there were 660 nuclear power units in operation worldwide, with a total installed capacity of about 394 million kilowatts. The rapid development of nuclear power has made an important contribution to the establishment of a safe and efficient modern energy system, but the increasing accumulation of large amounts of spent fuel has adversely affected the continuous cycle and development of nuclear power. For commonly used commercial light water reactors (LWRs), the general refuelling cycle is between 1 and 1.5 years, and with an average fuel consumption of 50 GW-d/tU, it is estimated that the spent fuel unloaded from a nuclear power unit with an installed capacity of 1,000 MWe is about 20 tU per year. Domestically, the storage of spent fuel in China is more than 80 million tonnes by January 2022, and the new spent fuel added is about 1,000 tHM per year [1]. And the existing spent fuel treatment capacity is far from being able to meet the demand for spent fuel treatment, especially some fission products with high radioactivity and long lifespan are the pressing issues of nuclear waste treatment. On 27 October 2017, the preliminary collation of the carcinogen list published by the International Agency for Research on Cancer of the World Health Organization references that radioactive iodine is in the list of group 1 carcinogens. Iodine-129 is one of the radioisotopes of iodine with a half-life of 15.7 million years, which undergoes beta decay and decays into xenon-129, an extinct natural radioisotope [2]. Currently, one of the most promising methods for treating high-level radioactive waste is separation transmutation [3]. Separation is the extraction of the usable U and Pu elements, minor actinides (MA) and long-lived fission products (LLFP) from the spent fuel, and transmutation refers to the treatment of MA and LLFP elements to obtain nuclides with a short lifetime or low radioactivity.

Accelerator-driven subcritical systems (ADS), fast reactors, and thermal neutron reactors are some of the major devices that can be transmuted in international research. The subcritical reactors of the ADS have higher neutron energy spectra, higher fluxes, and wider energy distributions for transmutation of MAs and LLFPs [4]. However, neither ADS nor fast reactors are yet in commercial operation. The move to investigate the transmutation of transuranic elements using widely commercialised thermal reactors is of general interest. In this paper, taking the pressurised water reactor fuel assembly as a model, transuranic elements are added to the original fuel elements in two ways, and the power distribution and effective multiplication factor changes of the fuel assembly under different transuranic element addition methods are investigated, and certain improvement measures are proposed to improve the slowing down situation and the initial excess reactivity.

Therefore, this paper explores the neutronics properties of the core after the introduction of the transuranic element iodine-129 in the modelling of pressurised water reactor components.

2. BASELINE MODELS AND CALCULATION METHODS

The widely commercialised pressurised water reactor (PWR) is chosen as the baseline model for this paper, which is the AP1000 nuclear reactor, which is a Generation 3 nuclear power reactor developed by Westinghouse on the basis of the AP600 pressurised water reactor. There are 157 fuel assemblies in the core, each of which contains 264 fuel rods, 24 control rod guide tubes and 1 core measurement conduit, with a rated thermal power of 3400 MW. In this paper, the fuel assemblies are simulated using the MCNP program. Monte Carlo (MC) method is a solution method born in the process of studying the Boltzmann neutron transport equation. Based on the MC method, many particles transport software have been developed at home and abroad, including MCNP, FLUKA, Geant4, MONK, Serpent, Open MC, McCARD, RMC, Super MC, JMCT and so on. Among them, the Monte Carlo program MCNP is a general-purpose particle transport calculation tool developed by LANL Laboratory in the United States. It can be used to simulate neutron, photon, electron and many other kinds of particle transport. The transport of particles in MCNP is realised by defining the material and constructing the actual three-dimensional geometric model, which is widely used due to the advantage of dealing with complex geometries. In the field of neutron transport, it can be used to calculate the effective multiplication factor, reaction rate, neutron flux and energy spectrum, power peak factor, core shielding, and so on.

This paper investigates the effect of the introduction of I-129 on the neutronics parameters of pressurised water reactor cores. The element iodine exists as two isotopes in the spent fuel of light water reactors (LWRs), the long-lived I-129, which accounts for 80%, and the more stable I-127, which accounts for 20%. I-129, with a half-life of 15.7 million years, undergoes β-decay, decays to Xe-129, and releases one electron and one neutrino.129I can be converted to a stable nuclide in the transmutation system by neutron capture and decay. Introducing a large amount of I-129 into the core can improve the transmutation performance of the core, but it will change the physicochemical properties of the core to some extent when the introduced I loading is too large. Therefore, in the study of the effect of the introduction of I-129 on the neutronics performance of pressurised water reactors, the maximum molar ratio of I in the core was set to 1 mol%.

3. EXPERIMENTAL RESULTS AND ANALYSES

Transient neutrons have a short lifetime and cause an increase in neutron density and power in a very short period of time, triggering a core accident that may lead to reactor uncontrollability. In contrast, the presence of slow-generation neutrons in the core has a longer slow-generation time, which extends the average time interval between the two generations of neutrons, thus slowing down the rate of change of neutron density. Therefore, slow-generation neutrons are a key reactor safety parameter for measuring reactor controllability and influencing the study of core reactivity feedback effects [5]. Since the effect of slow-generating neutrons on the neutron lifetime cannot be ignored, the effect of long-lived fission products on the effective neutron generation time is simultaneously assessed based on the transient neutron lifetime output from the software.

The effective slow-generating neutron fraction (β_{eff}) is calculated using the following equation,

$$\beta_{eff} = 1 - \left(K_p / K_{eff} \right)$$

Where Keff is the effective proliferation factor for the MCNP5 software cycle run and Kp is the transient neutron proliferation factor.

The effective neutron generation time (Λeff) is calculated as.

$$\Lambda_{eff} = l_p / K_{eff}$$

where Λeff is the effective neutron generation time and lp is the transient neutron lifetime calculated by the software.

The effects of introducing different loadings of I-129 into a pressurised water reactor core on the Keff and βeff of the core are investigated, respectively, and the results are shown in Table 1. Since LLFPs nuclides have a large neutron capture cross section, their introduction into the reactor may cause a decrease in the effective multiplication factor of the core. As shown in the data in Table 1, I-129 has a large thermal neutron capture cross section, and when I-129 is introduced into the core, a large number of thermal neutrons in the core will be absorbed by I-129, which will cause a decrease in the Keff value. From Table 1, it can be seen that the βeff value increases and then decreases with the increase of I-129 loading, and the βeff value is the largest at 0.7 mol% of I-129 loading at 0.35401%, and then decreases.

Table 1: Keff, Kp, βeff at different LiI device amounts

LiI loading /mol%	Keff	standard error	Kp	standard error	βeff
0	1.00774	0.00022	1.00502	0.00023	0.26991%
0.3	0.96805	0.00022	0.96478	0.00025	0.33779%
0.5	0.94369	0.00023	0.94047	0.00023	0.34121%
0.7	0.92087	0.00022	0.91761	0.00020	0.35401%
1	0.88837	0.00020	0.88612	0.00023	0.25327%
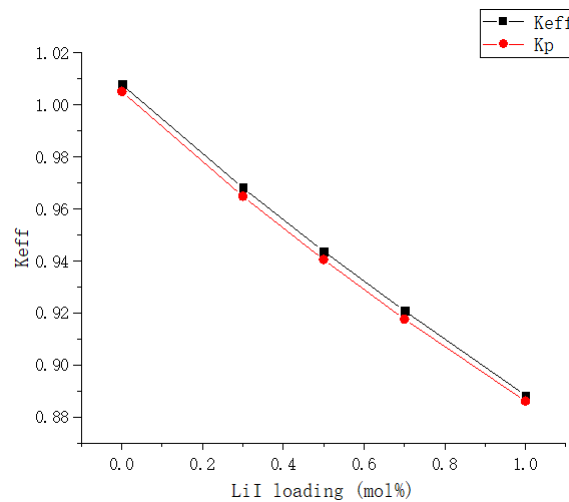
Figure 1: Keff, Kp for different LiI device amounts

The study calculates the effect of the introduction of I-129 into a pressurised water reactor (PWR) core on the neutron energy spectrum of the core, using the En energy card, which divides the neutron energies within 0Mev to 20Mev into different intervals of the tally energy intervals. At the same time, the F4 tally card was used to cycle through the calculations with the whole core as the counting unit. Tables 2 and 3 show the neutron energy spectra of the pressurised water reactor core after the introduction of I-129.

From Fig. 3, it can be seen that the neutron shares of different energy segments are different, with a lower share of high-energy neutrons and a higher share of low-energy neutrons. Under the initial loading conditions of the PWR core, the share of fast neutrons with a larger energy ratio of 0.1 Mev is 20.1884%, and the share of thermal neutrons with a smaller energy ratio of 0.1 Mev is 79.8116%. According to the calculated data in Table 3, it can be seen that the proportion of fast neutrons larger than 0.1 MeV increases gradually with the increase of the molar ratio of I-129 introduced into the core, which are 20.4430%, 20.6011%, 20.7615% and 20.9845%, respectively, which indicates a decrease of the number of thermal neutrons. This may be due to the fact that I-129 added into the core captures and consumes a part of thermal neutrons, which leads to the hardening of the core neutron energy spectrum.

Table 2: Table of neutron flux densities for pressurised water reactors with different molar I loading

neutron energy (MeV)	neutron flux density				
	Initial loading	0.3mol%I	0.5mol%I	0.7mol%I	1mol%I
1.0E-08	2.51852E+11	2.41524E+11	2.35632E+11	2.26820E+11	2.16942E+11

1.0E-07	1.41672E+13	1.35991E+13	1.32551E+13	1.28692E+13	1.23856E+13
1.0E-06	3.27509E+13	3.17478E+13	3.11510E+13	3.04616E+13	2.95930E+13
1.0E-05	1.68042E+13	1.64818E+13	1.62602E+13	1.60598E+13	1.57683E+13
1.0E-04	1.96634E+13	1.93607E+13	1.91404E+13	1.89547E+13	1.86660E+13
1.0E-03	2.45058E+13	2.44043E+13	2.42981E+13	2.42310E+13	2.40884E+13
1.0E-02	2.77916E+13	2.77746E+13	2.77221E+13	2.76916E+13	2.76375E+13
1.0E-01	2.90227E+13	2.90356E+13	2.90088E+13	2.90149E+13	2.89866E+13
1.0E+00	2.67363E+13	2.67872E+13	2.67850E+13	2.67928E+13	2.67950E+13
1.0E+01	1.49758E+13	1.49920E+13	1.49929E+13	1.49870E+13	1.49770E+13
2.0E+01	1.40480E+10	1.43508E+10	1.42063E+10	1.39945E+10	1.40366E+10
total	2.06684E+14	2.04439E+14	2.02863E+14	2.01304E+14	1.99128E+14
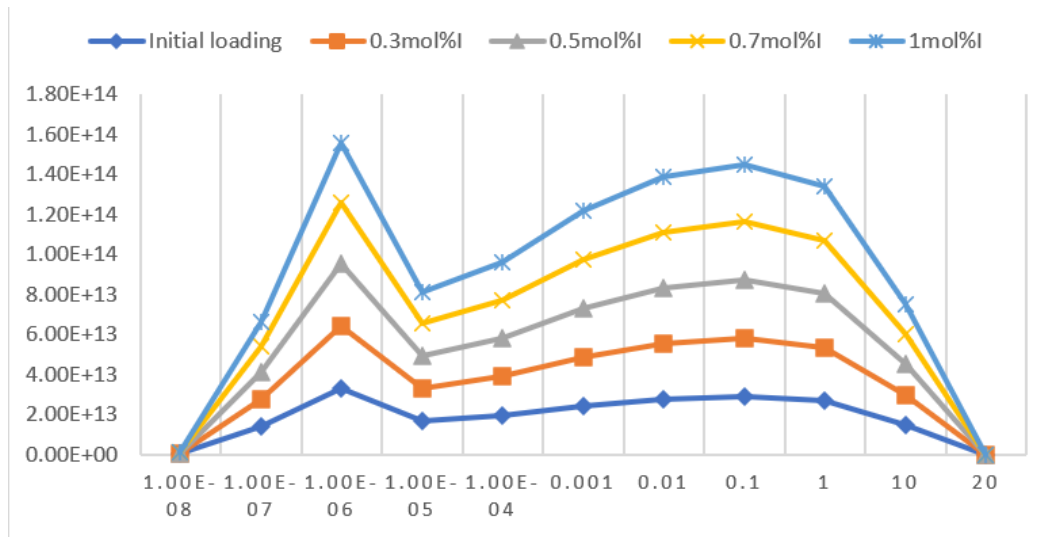
Figure 2: Neutron flux density distribution of pressurised water reactors with different molar I loading

Table 3: Table of neutron flux density shares

neutron energy (MeV)	Neutron flux density share				
	Initial loading	0.3mol%I	0.5mol%I	0.7mol%I	1mol%I
1.0E-08	0.12185%	0.11814%	0.11615%	0.11268%	0.10895%
1.0E-07	6.85452%	6.65191%	6.53402%	6.39292%	6.21992%
1.0E-06	15.84588%	15.52923%	15.35568%	15.13214%	14.86130%
1.0E-05	8.13038%	8.06196%	8.01536%	7.97788%	7.91868%
1.0E-04	9.51375%	9.47016%	9.43514%	9.41596%	9.37387%
1.0E-03	11.85665%	11.93720%	11.97759%	12.03702%	12.09694%
1.0E-02	13.44642%	13.58576%	13.66543%	13.75611%	13.87926%
1.0E-01	14.04206%	14.20257%	14.29970%	14.41347%	14.55677%
1.0E+00	12.93583%	13.10278%	13.20349%	13.30962%	13.45617%
1.0E+01	7.24575%	7.33324%	7.39065%	7.44496%	7.52129%
2.0E+01	0.00680%	0.00702%	0.00700%	0.00695%	0.00705%
total	1	1	1	1	1
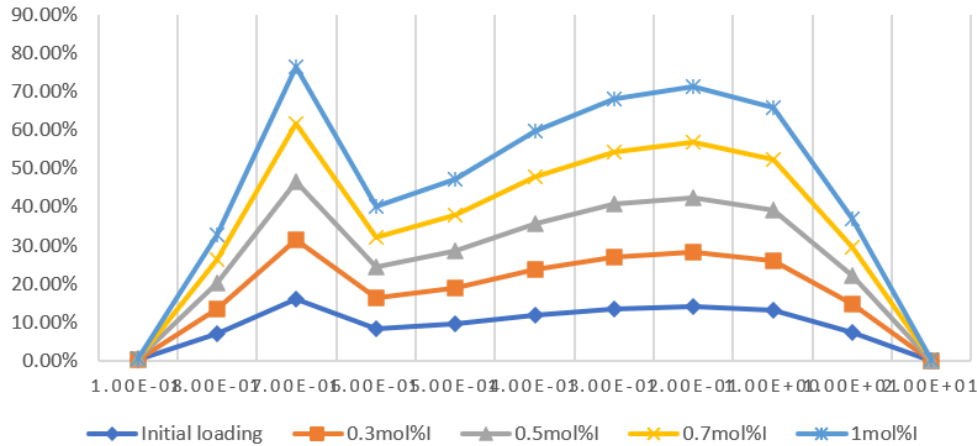
Figure 3: Distribution of neutron flux density shares

4. CONCLUSION

(1) I-129 has a large thermal neutron capture cross-section, and when I-129 is introduced into the core, a large number of thermal neutrons in the core will be absorbed by I-129, which causes a decrease in the Keff value.

(2) From the calculation results, it can be seen that the βeff value increases and then decreases with the increase of I-129 loading, and the βeff value is the largest at 0.35401% when the I loading is 0.7 mol, and then decreases.

(3) The proportion of fast neutrons larger than 0.1 MeV gradually increases with the increase of the molar proportion of I-129 Introduced into the core, which may be due to the fact that the I-129 added into the core captures and consumes a part of the thermal neutrons, which leads to the hardening of the neutron energy spectrum of the core.

5. REFERENCES

[1] Zhe HONG, Shangui ZHAO, Chunlong ZHANG, Fangfang CAO, Xinhua LIU, Guoan YE. Analysis of the demand for off-pump storage of spent fuel in China[J]. Nuclear Science and Engineering, 2016, 36 (03): 411-418.

[2] Snyder G, Fehn U. Global distribution of 129 I in rivers and lakes: implications for iodine cycling in surface reservoirs[J]. Nuclear Instruments & Methods in Physics Research, 2004, 223:579-586.

[3] D. Warin, Status of the French research program on partitioning and transmutation. J. Nucl. Sci. Technol. 44(3), 410-414 (2007). https://doi.org/10.1080/18811248.2007.9711302.

[4] A. Gulevich, A. Kalugin, L. Ponomarev et al., Comparative study of ADS for minor actinides transmutation. Prog. Nucl. Energy 50(2), 359-362 (2008).

[5] Winfried Z, Nadine B, Alexander A, et al. Sensitivities of delayed neutron fractions in the framework of SCALE 6.2 [J]. Annals of Nuclear Energy, 2021, 153.

#169: Experimental investigation of battery thermal management through immersion cooling utilizing electronic fluoride liquid

Ruixin MA[1]; Zekun JIANG[1]; Changtian XU[1]; Jiaxuan WANG[1]; Weicheng XUAN[1]; Yang XU[1]; Binbin YU[1,2*];Junye SHI[1,2*]; Jiangping CHEN[1,3]

[1] Institute of Refrigeration and Cryogenics, Shanghai Jiao Tong University, Shanghai 200240, China
[2] Shanghai Jiao Tong University ZhongGuanCun Research Institute, Liyang 213300, China
[3] Shanghai Engineering Research Center of High Efficient Cooling System, Shanghai, 200240, China
Corresponding Author E-mail addresses: ybbedc@sjtu.edu.cn; jyshi@sjtu.edu.cn

Abstract: Lithium-ion batteries face increased thermal dissipation challenges during fast charging. Battery thermal management system based on immersion cooling is a novel and promising solution with excellent thermal performance. In this study, an experimental investigation is performed to assess the battery thermal management performance of immersion cooling, utilizing electronic fluoride liquid as the immersion fluid. A battery simulator is designed to replicate the heat generation of a 40 Ah NCM prismatic lithium-ion battery, thereby mitigating technical risks. The results demonstrate that electronic fluoride liquid cooling, equipped with a refrigeration cycle, operates effectively and exhibits excellent thermal control performance. The battery heat is still well dispersed even with heating power as high as 183.75 W. At a charging/discharging rate of 5C/1C, the maximum average temperature is 36.28 ℃ at the end of charging, and the minimum is 21.94 ℃ at the end of discharging, well below the upper limit of 65 ℃. Correspondingly, the maximum and minimum temperature difference is 20.26 ℃ and 1.81 ℃, respectively. Furthermore, the effect of fluid temperature (15, 20, and 25 ℃) and flow rate (0.5, 1, and 1.5 L min^{-1}) is investigated. It is found that increasing the liquid flow rate reduces both the average temperature and temperature difference. In contrast, lower fluid temperature decreases the battery's average temperature but increases the temperature difference.

Keywords: Battery Thermal Management, Immersion Cooling, Electronic Fluoride Liquid

1. INTRODUCTION

To effectively address energy security concerns and mitigate environmental pollution, there has been a vigorous pursuit of reforms in the automotive industry, with electric vehicles emerging as a pivotal developmental direction [1]. In contrast to conventional fuel-powered automobiles, electric vehicles utilize electrical energy as their propulsion source, thereby significantly reducing dependence on fossil fuels, and mitigating pollutant and greenhouse gas emissions. Additionally, they possess advantages such as low noise, high efficiency, simple structure, and ease of maintenance [2].

The performance of the power battery, a crucial component of electric vehicles, directly influences the performance, reliability, and safety of electric vehicles [3]. The development of the electric vehicle industry imposes higher requirements on the fast-charging technology of lithium-ion batteries. However, as battery charging rates increase, the heat released from increased current density also significantly escalates, necessitating effective thermal management systems. Elevated temperatures will lead to battery damage, performance degradation, or even safety hazards. Managing and controlling heat generation is one of the crucial factors in ensuring the safe operation of lithium-ion batteries [4, 5]. The primary function of battery thermal management systems is to maintain the batteries within an optimal temperature range, particularly under high charge/discharge rates or extreme environmental conditions, while maintaining uniform temperature distribution to prevent thermal runaway [6].

Conventional battery thermal management systems typically include air cooling, liquid cooling, and phase change material cooling, depending on the medium used for heat dissipation [7, 8]. In recent years, immersion cooling has garnered considerable attention. In the realm of high-end electronic product heat dissipation, some studies have already leveraged immersion heat transfer to achieve effective thermal management, far surpassing traditional methods [9]. Immersion heat transfer can also achieve excellent temperature uniformity, prompting increasingly in-depth research in battery thermal management. This advanced method submerges the battery in a thermally conductive liquid, effectively transferring heat from the battery to the surrounding environment. It exhibits higher heat dissipation performance, enabling rapid and uniform reduction of battery heat generation, thereby enhancing battery efficiency and safety. With the proliferation of battery technology in various application scenarios, including low and high-temperature environments (such as low and high latitude regions) and the growing demand for battery power (such as ultra-fast charging), immersion cooling emerges as a crucial advanced battery thermal management technology [10].

To investigate the BTM performance of immersion cooling, contrasting studies were carried out in comparison with alternative cooling methods. Satyanarayana et al. [11] performed an experiment comparison of thermal management performance between immersion cooling and air cooling methods. The immersion cooling utilizing mineral oil and therminol oil exhibited better performance in thermal control and thermal uniformity compared to air cooling, especially under conditions during high-rate discharge. Lin et al. [12]. conducted a comprehensive comparative analysis encompassing air cooling, single-phase immersion, indirect cooling, and two-phase immersion. The results showed that the two-phase immersion achieves better thermal control performance. A series of studies in the past few years have indicated the superior performance of immersion cooling compared to other cooling methods [13]. On the other hand, the selection and comparison of different immersion fluids are also pivotal considerations. The typical immersion fluids can be grouped into several broad categories: electronic fluorinated liquids [14], hydrocarbons [15], esters, silicone oils [16], and water based [17]. The comparative study on the properties of different immersion liquid media is also being carried out gradually [18, 19].

Fluorinated liquid is a typical two-phase fluid, and documented BTM studies based on fluorinated liquid have been increasing gradually in recent years. In 2014, Gils et al. [14] conducted a BTM through boiling heat transfer, in which an 18650 battery is immersed in Novec7000 liquid. the boiling heat transfer thermally homogenises the battery and can be influenced by pressure variation. More recently, Li et al. [20] utilized SF33 fluorinated liquid as the immersion fluid for 18650 battery cells and compared the performance under 2C, 4C, and dynamic load conditions with static immersion and forced air cooling. The results indicated that static fluorinated liquid immersion exhibits favorable performance, especially under high-rate charge-discharge conditions. Considering the continuous operation of a battery system, Williams et al. established an experiment system to study the effectiveness of a hydrofluoroether dielectric liquid (Novec 7000) immersion cooling for a single 26650 battery [21] and a battery module consisting of four 26650 batteries [22]. In this experiment system, vapour produced during liquid's phase change is condensed by a copper coil located above the liquid pool. The results showed that this design is capable of the thermal control of fast charge of 4C. The more closely spaced battery arrangement slightly improves heat transfer performance.

Some previous works have carried out battery thermal management systems with electronic fluoride liquid, demonstrating good thermal performance. However, current thermal management systems are typically equipped with complete refrigeration cycles. For fluorinated fluid immersion cooling, there is a scarcity of experimental research based on current refrigeration cycle systems. The operational patterns and performance advantages of liquid immersion thermal management systems have not been fully revealed. Therefore, further experimental research is needed to explore their applications in battery thermal management based on immersion cooling. In this study, a battery immersion cooling experiment system is built to investigate the thermal management performance of immersion cooling utilizing electronic fluoride liquid. The average temperature and temperature difference between natural convection and immersion cooling is compared. Besides, for immersion fluid, the effect of flow rate and temperature is investigated.

2. EXPERIMENT SYSTEM
2.1. Immersion cooling battery unit design

To investigate the immersion effect of single battery, a typical immersion cooling battery unit was designed, with its geometric model and physical illustration depicted in Figure 1. The immersion cooling battery unit comprises an immersion tank, a top cover, and a battery. The immersion tank used in the experiment is a 3D-printed plastic enclosure capable of accommodating individual battery. The inlet and outlet of the immersion fluid adopt a "bottom-in, top-out" configuration, allowing the immersion fluid to flow out of the

immersion shell through the outlet at the top of the battery, thereby achieving complete immersion. Temperature sensors, power lines, and other conductors can be routed out through side holes in the shell without affecting the immersion range of individual battery. Protuberances are positioned on both sides of the shell, with a 4 mm gap between the shell's surface and the battery's main surface.
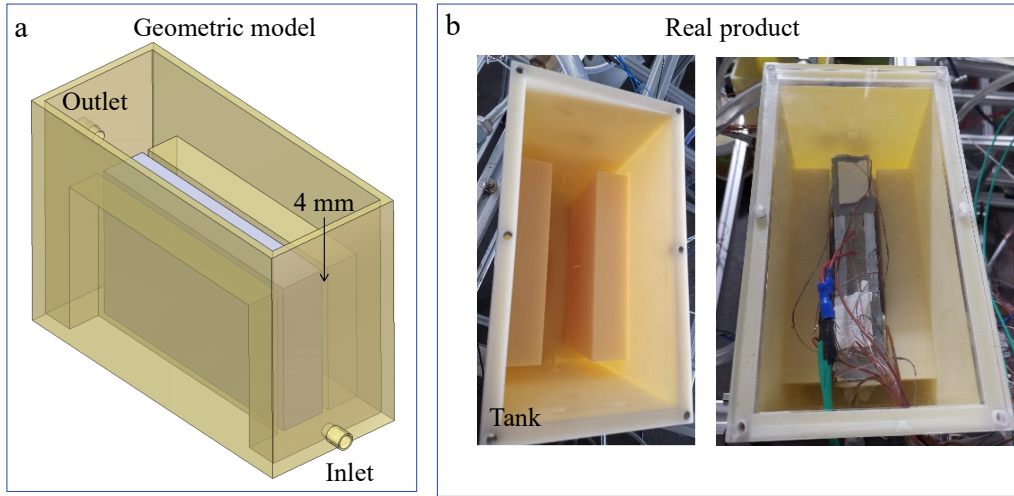

Figure 1: Diagram of immersion cooling battery unit. (a) Geometric model; (b) real product

2.2. Battery simulator and heat generation

In this study, a prismatic NCM lithium-ion battery is utilized. The capacity is 42 Ah and the dimensions are 148 × 27 × 91 mm. Particularly, a battery simulator with identical dimensions is fabricated based on the battery. As depicted in Figure 2, the battery simulator consists of an aluminum shell, thermal conductive potting compound and heating bar. The heating bar is positioned in the middle of the aluminum shell with adjustable heating power. Thermal conductive potting compound is used to fill the remaining spaces. The three-view drawing shows the physical dimensions and of battery simulator, and a total of 9 temperature points are measured. The battery simulator allows for the simulation of the heat generation and temperature changes of real batteries, while reducing the safety risks associated with high rate charging cycles. By using the battery simulator, the heat generation of the battery under different charging rates, including ultra-fast charging conditions, can be simulated in a controlled experimental environment. This allows for a better understanding of the battery's thermal response characteristics, providing reference data for safety assessments in practical battery applications.
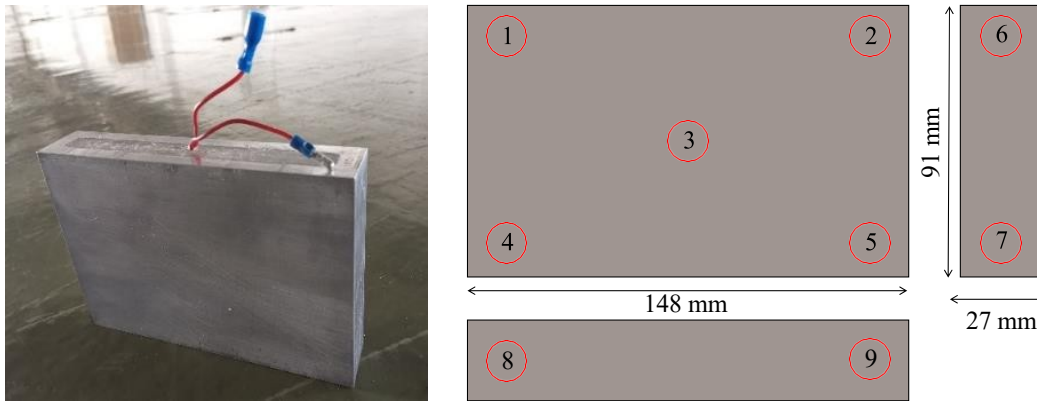
Figure 2: Geometric specifications of battery simulator

During the charge and discharge processes of lithium-ion batteries, heat generation primarily involves two mechanisms: Joule heating and entropy change heat. Joule heating arises from the heat generated when current passes through resistance, while entropy change heat involves the heat change resulting from entropy change in chemical reactions, calculated by the formula as shown in Eq. 1. For the battery addressed in this study, heat generation power under various operating conditions was computed based on the physical parameters of the battery, as presented in Table 1. Notably, the theoretical heat generation power during 5C charging reaches a remarkable 183.75 W, representing an extreme heat generation scenario.

$$q = I(V_{ocv} - V) - IT\frac{dV_{ocv}}{dT} = I^2R - IT\frac{dV_{ocv}}{dT} \qquad (1)$$

Table 1: Heat generation at various charging/discharging rate

Charging rate	Heat generation (W)	Discharging rate	Heat generation (W)
1C	7.35		
2C	18.75	1C	8.10
3C	66.15		
5C	183.75		

2.3. Properties of fluorinated liquid

Novec 7100 (3M company) electronic fluorinated liquid is employed. Fluorinated liquid typically refers to a liquid containing fluorine compounds. The primary components of Novec 7100 are fluorinated hydrocarbon compounds. It exhibits characteristics such as low surface tension, low viscosity, and low dielectric constant, making it widely applicable in electronic devices. As a thermal management immersion medium for batteries, this substance is non-flammable and compatible with plastics. Additionally, Novec 7100 boasts excellent insulation properties, making it suitable for battery thermal management systems and possessing the potential to interrupt thermal runaway processes. At atmospheric pressure, the boiling point of this substance is 61 ℃, higher than the normal operating temperature of batteries, thus meeting experimental requirements. The specific physical properties of this substance are detailed in Table 2.

Table 2: Property parameters of Novec 7100

Property	Value
Melting point (℃)	-135
Boiling point @ 1 atm (℃)	61
Density (kg/m3)	1510
Viscosity (mPa·s)	0.6
Latent heat of evaporation (kJ/kg)	125.4
Specific heat capacity (kJ kg^{-1}·K^{-1})	1.18
Heat conductivity (W m^{-1}-K^{-1})	0.075
Dielectric strength (0.1" gap, kV)	＞25

2.4. Circulation cooling system design

Figures. 3a and 3b illustrate the system schematic and physical drawings of circulation cooling system for immersion cooling, respectively. The system includes two circuits: the immersion fluid circuit and the cooling medium circuit. Heat exchange between the two circuits is facilitated by a plate heat exchanger. In the immersion working fluid circuit, the pump serves as the power component of the immersion fluid circuit, driving the liquid sequentially through the flow meter, heat exchanger, ball valves, immersion cooling battery unit and liquid accumulator. Within the immersion cooling battery unit, the immersion fluid absorbs heat released by the battery simulator, resulting in temperature elevation and even phase change processes. The immersion fluid exiting the immersion tank flows into the liquid accumulator, ensuring a single-phase immersion fluid at the pump inlet to guarantee pump reliability. The immersion liquid within the immersion fluid enters the pump inlet, completing the flow circulation of the immersion fluid. In the coolant circuit, the constant temperature water tank provides cooling to the circuit. The low-temperature coolant flowing out of the water chilling unit enters the heat exchanger after passing through ball valves, where it exchanges heat with the high-temperature immersion medium on the other side, simultaneously raising the coolant temperature while lowering the immersion medium temperature. Finally, the heated coolant returns to the water chilling unit for cooling, completing the coolant circulation process.
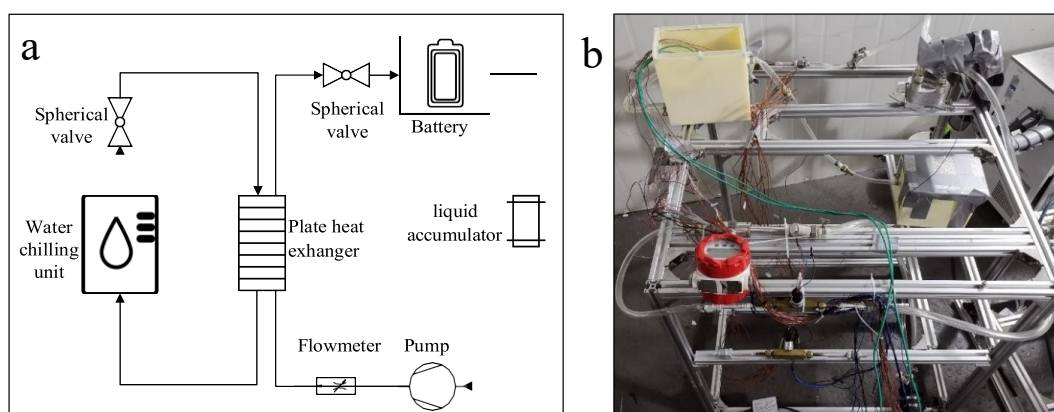
Figure 3: Schematic diagram of experimental setup. (a) System schematic; (b) physical drawings

The reliable operation of the system necessitates the appropriate selection of components. The pump utilized is a variable-speed centrifugal pump known for its compact size, long lifespan, low noise, and high efficiency. During the experiment, pump speed is adjusted through potentiometer control, thereby regulating the flow rate of the immersion liquid. The heat exchanger is an aluminum plate heat exchanger. Experimental verification demonstrates that when both sides of the heat exchanger are liquid, its heat transfer capacity exceeds 5 kW, far surpassing the battery heat generation, thus meeting experimental requirements. The water chilling unit equipped with cooling coils serves as the cooling source for the circulation cooling system. The experiments are conducted in an

environmental simulation chamber. The experimental conditions involve continuous cycling of charge and discharge processes in the single battery until the temperature characteristics of the adjacent two cycles are consistent or the battery temperature reaches 65 ℃.

2.5. Error analysis

The major errors during this experiment come from the directly measured parameters, including temperature, flow rate and power. The parameter measurement range and accuracy on the experimental platform designed in this study are presented in Table 3. In summary, the measurement errors in this experiment are relatively small, indicating high accuracy and reliability.

Table 3: Test range and accuracy of test parameters

Parameter	Measuring range	Uncertainty
Temperature (℃)	-50~150	±0.2℃
Flow rate ($m^3 h^{-1}$)	0.04-0.4	±1.0%
Heating power (W)	0-200	±0.01W
Pump power (W)	0-100	±0.1W

3. RESULTS AND DISCUSSION
3.1. Temperature characteristics under natural convection

In an environmental simulation chamber at 25 ℃, the battery simulator undergoes cycling heating, resulting in surface temperature characteristics at various charge and discharge rates. The average temperature and temperature difference of the battery are depicted in Figure 4. Overall, the average temperature of the battery exhibits a process of temperature rise during charging and temperature decrease during discharging. For the 1C-1C condition, after two complete charge/discharge cycles, the average temperature of the cell stabilizes at approximately 40.62 ℃. As the average temperature increases, the temperature difference gradually increases to around 4 ℃. Similarly, the 2C-1C condition reaches a steady state after three complete charge and discharge cycles. With an increase in the charge rate, both the average temperature and temperature difference of the battery gradually rise. When the charge rate reaches 4C, the battery temperature sharply increases. At t=680 s (11.3 min), the average temperature reaches 65 ℃, leading to experiment termination. At this point, the surface temperature difference of the cell is 9.42 ℃.
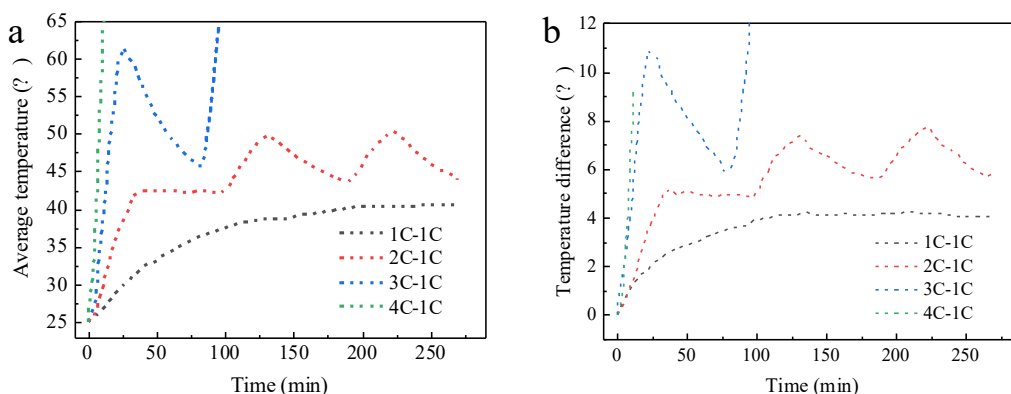
Figure 4: Evolution of battery temperature under natural convection. (a) Average temperature; (b) temperature difference

3.2. Temperature characteristics under immersion cooling

In the circulation cooling system, the flow rate of immersion fluid is adjusted to 1 L min^{-1} and the water chilling unit is set to maintain an inlet temperature of 20 ℃ for the immersion liquid. The heat generation of the battery simulator is adjusted to undergo a cycling heating process with different charge rates and 1C discharge. The average temperature and temperature difference are shown in Figure 5. In two cycles of charge-discharge process, the average temperature can be controlled at a very low value attributed to the superior performance of immersion cooling. Even at the charge rate of 5C, the maximum average temperature is 36.28 ℃ at the end of charging, and the minimum is 21.94 ℃ at the end of discharging. The temperature is well below the upper limit of 65 ℃. Correspondingly, the maximum and minimum temperature difference is 20.26 ℃ and 1.81 ℃, respectively.
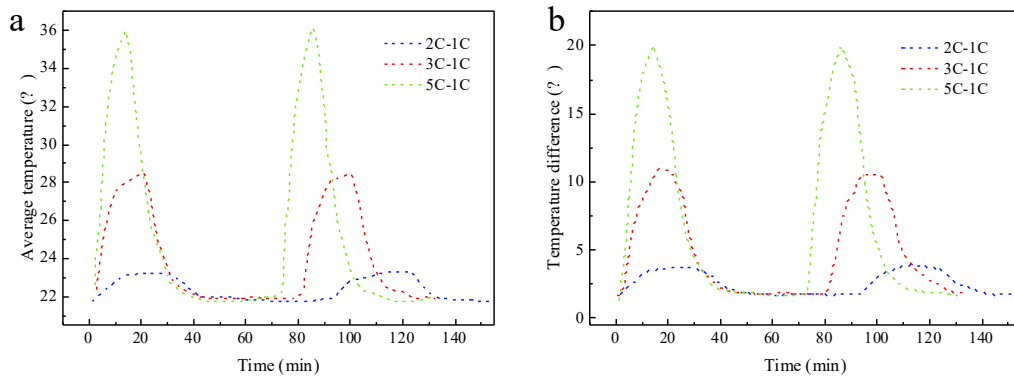
Figure 5: Evolution of battery temperature under immersion cooling. (a) Average temperature; (b) temperature difference.
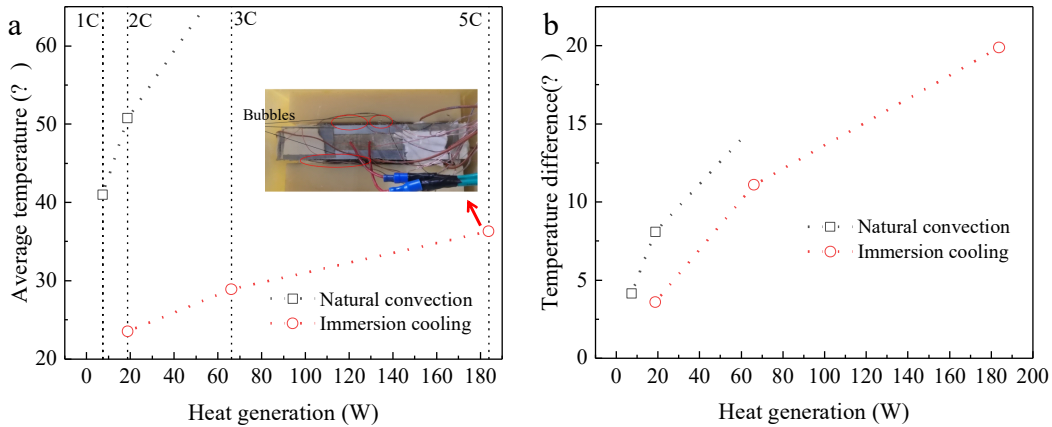

Figure 6: Temperature Comparison with and without Immersion Cooling. (a) Average temperature; (b) temperature difference

To visually observe the differences between immersion cooling and non-immersion cooling, a comparison of the average temperature and temperature difference of the battery under different charge and discharge conditions is presented in Figure 6. Under immersion cooling, the average temperature and temperature difference of the battery show significant decrease across different charge and discharge conditions. The immersion cooling can decrease the average temperature significantly. Under nature convection, the battery charging rate is limited to 2C. For immersion cooling, the battery heat is still well dispersed even if the heating power is as high as 183.75 W (5C). In this case, the bubbles are observed on the battery surface because the boiling point of electronic fluoride liquid is 61 ℃. Obviously, immersion cooling utilizing electronic fluoride liquid can meet the demand for a faster discharge rate for future technology. As shown in Figure 6b, the immersion cooling system markedly improves the temperature distribution. At a charge and discharge rate of 2C/1C, the temperature difference decreases by 4.50 ℃ compared to the case without immersion cooling.

3.3. The effect of cooling flow rate and temperature

Adjusting the heat generation of the battery simulator to undergo the process of 3C-1C charging and discharging, the effect of immersion cooling flow rate and temperature is investigated. The temperature of immersion fluid remains at 25 ℃, and the flow rate of the immersion fluid is set to 0.5 L min^{-1}, 1 L min^{-1} and 2 L min^{-1}, respectively. The battery temperature characteristics with different flow rates are shown in Figure 7. It can be found that the increase in flow rate provides a limited thermal management performance improvement. As shown in Figure 7a, during the process of 3C-1C charging and discharging, the maximum temperature is 29.98 ℃, 28.53 ℃ and 28.15 ℃ when the immersion fluid is 0.5 L min^{-1}, 1 L min^{-1} and 2 L min^{-1}, respectively. It is noteworthy that, at a flow rate of 0.5 L min^{-1}, the maximum temperature of the first and second charging processes is 28.79 ℃ and 29.98 ℃, respectively. A relatively low flow rate fails to remain at a steady temperature. On the other hand, a similar phenomenon can be found for temperature differences in Figure 7b. The increasing flow rate slightly improves the temperature uniformity. The maximum temperature difference is 11.78 ℃, 10.92 ℃ and 10.53 ℃ when the immersion fluid is 0.5 L min^{-1}, 1 L min^{-1} and 2 L min^{-1}, respectively.
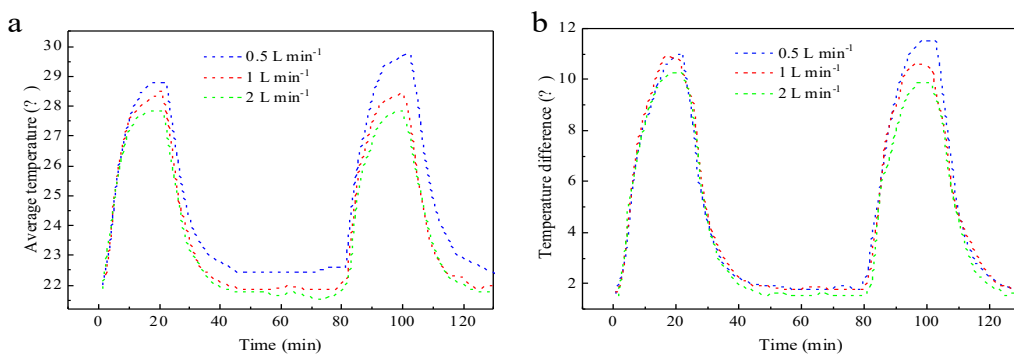

Figure 7: Effect of flow rate of immersion fluid. (a) Average temperature; (b) temperature difference

The flow rate of 1 L min⁻¹ is selected, and the temperature characteristics are compared when the temperature of immersion fluid is 15 ℃, 20 ℃and 25 ℃. As depicted in Figure 8a, the temperature of immersion fluid has a significant effect on the evolution of battery surface temperature. During the process of 3C-1C charging and discharging, the maximum temperature is 23.57 ℃, 28.53 ℃ and 31.94 ℃when the temperature immersion fluid is 15 ℃, 20 ℃and 25 ℃, respectively. The decrease in temperature of immersion fluid can lead to a significant decrease in average temperature. In contrast, the relatively low temperature of immersion fluid will lead to an increase in temperature difference. Compared to the case when the temperature of immersion liquid is 20 ℃, the maximum value of temperature difference increases by 0.90 ℃and decreases by 2.04 ℃when the temperature of immersion liquid is 15 ℃and 25 ℃, respectively.
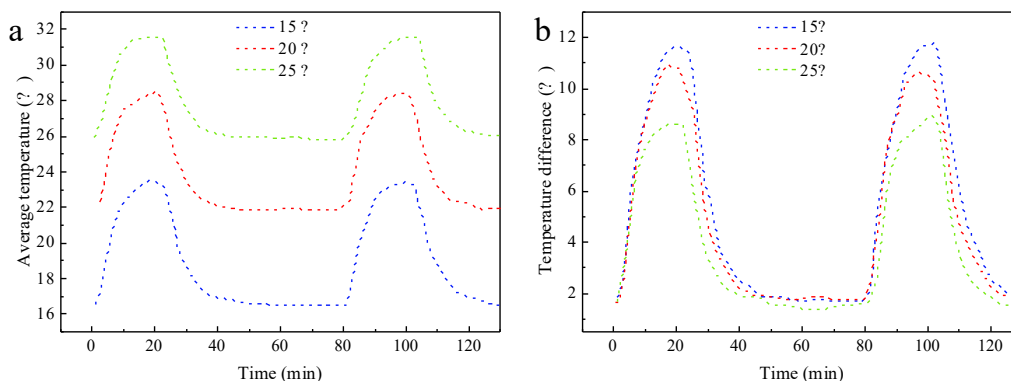

Figure 8: Effect of temperature of immersion fluid. (a) Average temperature; (b) temperature difference

4. CONCLUSION

Immersion cooling is a promising and high-performance battery thermal management technology. In this study, Novec 7100, an adelectronic fluoride liquid, serves as the immersion fluid. A battery immersion cooling system, incorporating a complete refrigeration cycle, is established to evaluate the thermal management capabilities. To study the conditions of ultra-fast charging for high-capacity batteries, a battery simulator is designed to replicate the heat generation of a 40 Ah NCM prismatic lithium-ion battery, thereby reducing technical risks. The average temperature and temperature difference between natural convection and immersion cooling is compared. Besides, the effect of immersion fluid flow rate and temperature is investigated.

Within the safe temperature limit of 65 ℃, the battery charging rate is limited to 2C under natural convection. For immersion cooling, the battery heat is still well dispersed even if the heating power is as high as 183.75 W (5C). The bubbles are observed because the boiling point of electronic fluoride liquid is 61 ℃. Furthermore, the effect of fluid temperature (15, 20, 25 ℃) and flow rate (0.5, 1, 1.5 L min⁻¹) is investigated. The increase in flow rate provides a limited thermal management performance improvement. During the process of 3C-1C charging and discharging, the maximum temperature is 29.98 ℃, 28.53 ℃ and 28.15 ℃ when the immersion fluid is 0.5 L min⁻¹, 1 L min⁻¹ and 2 L min⁻¹, respectively. On the other hand, the decrease in immersion liquid temperature will significantly lower the average temperature but will also increase the temperature differential. Evidently, using electronic fluorinated fluid for immersion cooling can meet the future technological demands for faster discharge rates. The research findings are expected to provide guidance for the design of immersion thermal management solutions.

5. REFERENCES

1.   Yu B, Long J, Zhang Y, Ouyang H, Wang D, Shi J, Chen J: Life cycle climate performance evaluation (LCCP) of electricvehicle heat pumps using low-GWP refrigerants towards China's carbon neutrality. Applied Energy 2024, 353:122061.

2.   Deng J, Bae C, Denlinger A, Miller T: Electric vehicles batteries: requirements and challenges. Joule 2020, 4:511-515.

3.   Ma R, Qi X, Feng X, Wu W: Rapid Optimization of Thermal Runaway Propagation Inhibition in Composite Phase Change Material-based Battery Module. IEEE Transactions on Transportation Electrification 2024:1-1.

4.   Ma R, Feng X, Zhao T, Zhang W, Liu M, Wu W: Composite phase change material for preventing battery thermal runaway propagation: Critical condition and inhibition strategy. Journal of Energy Storage 2023, 72:108237.

5.   Wang J, Feng X, Yu Y, Huang H, Zheng M, Xu Y, Wu J, Yang Y, Lu J: Rapid temperature-responsive thermal regulator forsafety management of battery modules. Nature Energy 2024:1-8.

6.   Wu W, Wang S, Wu W, Chen K, Hong S, Lai Y: A critical review of battery thermal performance and liquid based battery thermal management. Energy conversion and management 2019, 182:262-281.

7.   Ma R, Ren Y, Wu Z, Xie S, Chen K, Wu W: Optimization of an air-cooled battery module with novel cooling channels basedon silica cooling plates. Applied Thermal Engineering 2022, 213:118650.

8.   Xu J, Guo Z, Xu Z, Zhou X, Mei X: A systematic review and comparison of liquid-based cooling system for lithium-ion batteries. ETransportation 2023:100242.

9. Pambudi NA, Sarifudin A, Firdaus RA, Ulfa DK, Gandidi IM, Romadhon R: The immersion cooling technology: Current andfuture development in energy saving. Alexandria Engineering Journal 2022, 61:9509-9527.

10. Roe C, Feng X, White G, Li R, Wang H, Rui X, Li C, Zhang F, Null V, Parkes M, et al: Immersion cooling for lithium-ion batteries – A review. Journal of Power Sources 2022, 525:231094.

11. Satyanarayana G, Ruben Sudhakar D, Muthya Goud V, Ramesh J, Pathanjali GA: Experimental investigation and comparative analysis of immersion cooling of lithium-ion batteries using mineral and therminol oil. Applied Thermal Engineering 2023, 225:120187.

12. Lin X-W, Zhou Z-F, Yin J, Zhu X-G, Shi M-Y, Chen B: A comparative investigation of two-phase immersion thermal management system for lithium-ion battery pack. Journal of Cleaner Production 2024, 434:140472.

13. Dubey P, Pulugundla G, Srouji AK: Direct comparison of immersion and cold-plate based cooling for automotive Li-ion battery modules. Energies 2021, 14:1259.

14. Van Gils RW, Danilov D, Notten PHL, Speetjens MFM, Nijmeijer H: Battery thermal management by boiling heat-transfer. Energy Conversion and Management 2014, 79:9-17.

15. Sundin DW, Sponholtz S: Thermal Management of Li-Ion Batteries With Single-Phase Liquid Immersion Cooling. IEEEOpen Journal of Vehicular Technology 2020, 1:82-92.

16. Zhou Y, Wang Z, Xie Z, Wang Y: Parametric Investigation on the Performance of a Battery Thermal Management Systemwith Immersion Cooling. In Energies, vol. 15; 2022.

17. Suresh Patil M, Seo J-H, Lee M-Y: A novel dielectric fluid immersion cooling technology for Li-ion battery thermal management. Energy Conversion and Management 2021, 229:113715.

18. Jithin KV, Rajesh PK: Numerical analysis of single-phase liquid immersion cooling for lithium-ion battery thermal management using different dielectric fluids. International Journal of Heat and Mass Transfer 2022, 188:122608.

19. Li X, Zhou Z, Zhang M, Zhang F, Zhou X: A liquid cooling technology based on fluorocarbons for lithium-ion battery thermal safety. Journal of Loss Prevention in the Process Industries 2022, 78:104818.

20. Li Y, Zhou Z, Hu L, Bai M, Gao L, Li Y, Liu X, Li Y, Song Y: Experimental studies of liquid immersion cooling for 18650lithium-ion battery under different discharging conditions. Case Studies in Thermal Engineering 2022, 34:102034.

21. Williams NP, Trimble D, O'Shaughnessy SM: Liquid immersion thermal management of lithium-ion batteries for electric vehicles: An experimental study. Journal of Energy Storage 2023, 72:108636.

22. Williams NP, Trimble D, O'Shaughnessy SM: An experimental investigation of liquid immersion cooling of a four cell lithium- ion battery module. Journal of Energy Storage 2024, 86:111289.

#170: Studies on sulfur releasing and migration during thermal pyrolysis of anaerobic digestate

Yuqian GUO[1], Jian ZHANG[1*], Ruina ZHANG[2,3], Guoan YUAN[2,3]，Zhenglong ZHANG[1], Zilong ZHANG[1]

[1] University of Shanghai for Science and Technology, Shanghai, 200093
[2] Shanghai Institute for Design and Research on Environmental Engineering Co.，Ltd, Shanghai, 200232
[3] Shanghai Institute for Design & Research on Environmental Engineering CO., Ltd Shanghai 200232

Abstract: Municipal food waste undergoes anaerobic fermentation for decomposing into usable biogas, and then partly into solid waste, anaerobic digestate. The thermal pyrolysis applications of digestate could further utilize its organic chemical energy. In this article, the pyrolysis processes of digestate and straws were respectively investigated in a drop-tube furnace at different temperatures. And sulfur migration during pyrolysis was analyzed by using all-sulfur test and X-ray photoelectron spectroscopy (XPS). Furthermore, thermo-gravimetric mass spectrometry (TG-MS) was used for tracking the gas-phase releasing of organic and inorganic sulfur. The main results include: 1) Higher sulfur content of 0.56% in the digestate waste due to anaerobic digestion process, as different from sulfur About 0.2% exists in the straw. 2) The sulfur in the digestate is released by about 60% and 85% at 400°C and 600°C, respectively. However, most of the sulfur in the biomass straw remains in the char. 3) During pyrolysis, the sulfur migration possess three processes: ① Sulphate generation within digestate occurs mainly at 200-400°C, while biomass straw mainly at 400-600°C; ② Sulphate undergoes thermal decomposition under 600-1000°C; and ③ The macromolecular organic sulfur (incl. sulphone, sulphoxide, thiophene) is dominant at 1000°C. It provides a certain mechanistic understanding of the sulfur releasing and migration process of anaerobic digestate.

1. INTRODUCTION

The large amount of urban food waste is one of the most important environmental problems today [1]. It is predicted that in Asian countries, in the period of 2005-2025, urban food waste would increase from 2.78×108 to 4.16×108 ton. At present, the annual growth rate of China's food waste has been more than 10% and continues to increase at near future. According to incomplete statistics, the production of kitchen waste in first-tier cities, e.g. Beijing and Shanghai, has exceeded 1000 t/d.

Anaerobic fermentation of kitchen waste is a commonly used process today [2]. Biogas is produced in fermentation. And solid digestate is also a derived solid waste by-product [3]. There are various ways for subsequent treatment of digestate, including composting, soil amendment, biogas fermentation, incineration treatment and thermal pyrolysis [4].

Solid digestate is also rich in organic matter, which could result in more renewable fuels (bio-gas and bio-oil products [5]) obtained through the pyrolysis process. Pyrolysis is significant for both environmental protection and sustainable recycling of solid waste. Using high temperature or higher-pressure conditions, the organic materials in the waste are decomposed into combustible gases. Meanwhile some ash components could exist in solid residues yet to avoid some element (e.g. S and Cl) into the bio- product. Therefore, the control or decreasing about sulfur releasing process is useful to improve the quality of bio-products.

The authors' group has carried out some research about the pyrolysis characteristics of anaerobic digestate from kitchen waste [6]. And this article focuses on the experimental study of sulfur release patterns in digestate pyrolysis. In addition, two other biomasses e.g. rice and corn straws, were considered and conducted in experiments to compare with those of anaerobic digestate.

2. EXPERIMENTALS
2.1. Experimental material

The digestate was collected from a kitchen-waste anaerobic digestion plant in Shanghai. The kitchen waste includes some vegetable stalks and grease. And rice straw and corn stalks were collected in the field near Shanghai City. The samples were dried at 105°C in a drying oven for 3hrs to remove the moisture, and then crushed and sieved as ready for the experiments.

The proximate and elemental analyses were carried out on the above samples. The results are shown in Table 1. There is 77.53% of the moisture in the received base of digestate, as higher than ~16% of the moisture in the biomass. The content of element O in dry basis biomass straw is very high, with a percentage of ~48-57%. S was 0.56% in digestate and ~0.2% in biomass. Ash content was 37.52% in dry basis digestate and ~9% in straw. And they all contain less fixed carbon.

Table 1: Proximate and elemental analyses of samples

	digestate	rice straw	corn straw
1) Proximate analysis，wt%			
Moisture，ar	77.53	15.53	16.44
Volatile matter，db	62.04	88.06	89.35
Fixed carbon，db	0.45	2.12	1.02
Ash，db	37.52	9.82	9.63
Heating value, MJ/Kg，db	8.98	12.58	15.18
2) Elemental analytics (%，db.)			
C	25.76	26.85	35.25
H	4.05	5.18	5.3
O	28.15	56.93	48.56
N	3.73	0.68	1.14
S	0.56	0.21	0.17
3) Mole ratio of an element，db			
H/C	1.89	2.32	1.80
O/C	0.82	1.59	1.03

Table 2: Ash composition analyses of samples

	digestate	rice straw	corn straw
Na2O/%	3.48	2.43	0.9
K2O/%	2.64	23.03	20.5
CaO/%	54.21	9.19	13.13
MgO/%	2.38	3.69	5.26
SiO2/%	14.6	40.56	43.65
Al2O3/%	4.61	1.09	1.91
P2O5/%	10.2	1.81	6.03
SO3/%	2.17	9.3	2.77
Fe2O3/%	3.05	1.84	1.21
Cl/%	1.98	5.89	4.01

The samples were burnt at low temperature of 400°C in a muffle furnace. The mineral composition of the experimental ash samples was analysed using X-ray fluorescence spectrometry (XRF). The results of the ash composition test are shown in Table 2. The digestate ash contained abundant CaO (54.21%). The biomass contained more K_2O, which in rice and corn straws reaches 23.03% and 20.5%, respectively.

2.2. Experimental Methods

The vertical drop tube furnace is used, as shown in Fig. 1. The furnace height is 1.8m and diameter is 50mm. The reactor temperature is set to maintain a constant temperature, e.g. 400, 600, 800 and 1000°C, respectively. The carrier gas is nitrogen with a feeding rateof 10L/min. The digestate samples were fed into the chamber using a powder feeder with about 0.5g/min. The pyrolysis reaction occurs in the chamber, through which the samples conduct volatilization to form char particles. Then the residue chars were collected in the flask under the drop-tube furnace with the temperature controlled in an ice water tank.
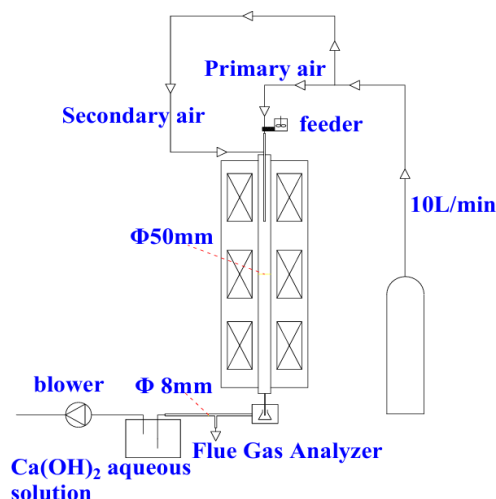

Figure1: Schematic diagram of the experimental setup of the settling furnace

The whole sulfur content (St) of the samples, including raw samples and pyrolysis char samples, were tested in *a* KZDL-3C rapid and intelligent sulfur detector. The Coulometric titration method was used and referred from *Determination of total sulfur in coal GB/T 214-2007* and *Determination of total sulfur in solid biomass fuels GB/T 28732-2012.*

The char samples obtained were examined by X-ray photoelectron spectroscopy (XPS). The Avantage software was used to assess the sulfur contents such as sulphide, thiophene, sulphoxide, sulphone and sulphate, for which the XPS test data were fitted.

In addition, thermal gravimetric-mass spectrometry (TG-MS) experiments were carried out towards the as-received samples. The temperature increased at the rate of 10°C/min. And the release process of H_2S, SO_2, COS, and CS_2 were tracked when runningthe mass spectrometry.

3. RESULTS AND DISCUSSION
3.1. Analysis of sulphur content in residual char after pyrolysis

From Fig. 2(a), it could be seen that the total S content decreases with the increase of pyrolysis temperature during the digestate pyrolysis process, and more S is released into the flue gas with gaseous state. The percentage ratio of sulfur release from the digestate samples in pyrolysis is shown in Fig. 2(b). It could be seen that a large amount of sulfur releases from 400 to 600°C. The sulfur release rate in digestate is increasing and a large amount of S is released. At above 600 °C, the efficiency of sulfur release from digestate starts to decrease slowly, and above 800°C, sulfur content is almost not changed, as witness the residual sulfur is stable in char with about 5-8% of the initial total sulfur still remaining in the digestate char sample at higher temperature.
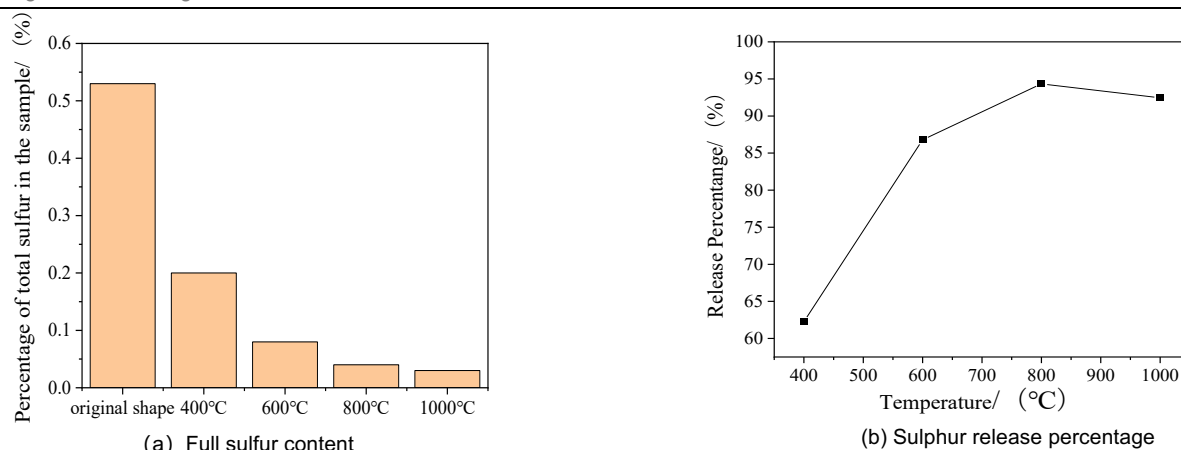
(a) Full sulfur content   (b) Sulphur release percentage

Figure 2: Analysis of total sulfur and percent sulfur release in digestate samples after pyrolysis at different temperatures

We also conducted straw samples under pyrolysis at different temperatures. Figure 3 shows the relationship between sulfur content maintained in straw char samples and pyrolysis temperatures, where (a) is rice straw and (b) is corn straw. The sulfur releasing from straw is significantly different from those of digestate. The proportion of S released from both biomass straws was very small and most of it remained in the residual char samples yet [9].

Comparison of the two samples in the experiment revealed that the digestate contains a significant amount of sulfur. The sulfur in digestate comes from various sources, e.g. food waste feedstock, sulfur compounds produced during microbial metabolism, chemical reagents involved in treatment works and waste effluents [10].
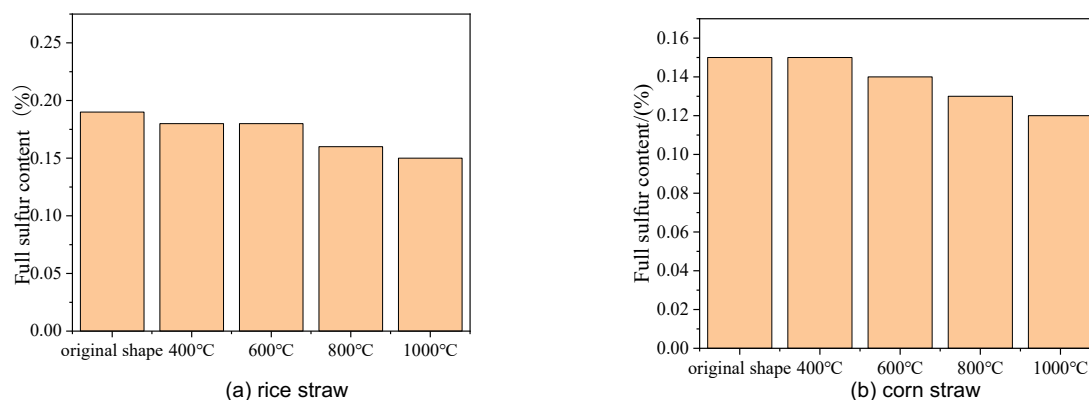

(a) rice straw   (b) corn straw

Figure 3: Analysis of all-sulfur data of straw char samples after pyrolysis at different temperatures

3.2. XPS study of sulphur composite in residual coke

The structure of sulfur contents in digestate is complex. The same type of sulfur atoms possibility exists with different peak positions in the XPS spectrum, as due to the different connecting patterns or bond position in the different molecular structure. The XPS peak fitting curve of digestate and the relative distribution of sulfur content are shown on Fig. 4. As can be seen from the figure, sulfide sulfur, thiophene sulfur, sulfoxide sulfur, sulfone sulfur and sulfate sulfur in digestate have their corresponding characteristic peaks, and the different peak positions characterize the elements and energy level orbitals, which are related to the chemical state [11], among which the 2p peak binding positions of sulfur are as follows: 161.2~163.6 eV for sulfide sulfur; 164.0~164.4 eV for thiophene sulfur; 165.0~166.0 eV for sulfoxide sulfur; 167.0~168.3eV for sulfone sulfur; >168.4eV for other inorganic sulfur such as sulfate sulfur. The characteristics of the XPS peaks of the sulfur in the digestate are also consistent with those in the studies [11,12].

The relevant fitting studies were also carried out on the straw, and the XPS peak fitting curves of the two biomass straws are shown in Figs. 5 and 6. Rice straw and corn straw also have five characteristic peaks each, which corresponds to the five different binding energies of each sulfur form.

Finally, Avantage software was used to determine the sulfur contents of the three samples fitted to the XPS test data. In XPS plots, the intensity of characteristic peaks is proportional to the concentration of surface elements [13]. In order to visualise the variation of sulfur content of each sample. In this study, the XPS test data were directly plotted to show the relative distribution of sulfur content under different pyrolysis temperatures, as shown in Figure 7, in which the components and quantities are presented in various forms such as sulphate, sulphide, thiophene, sulphoxide and sulphone.
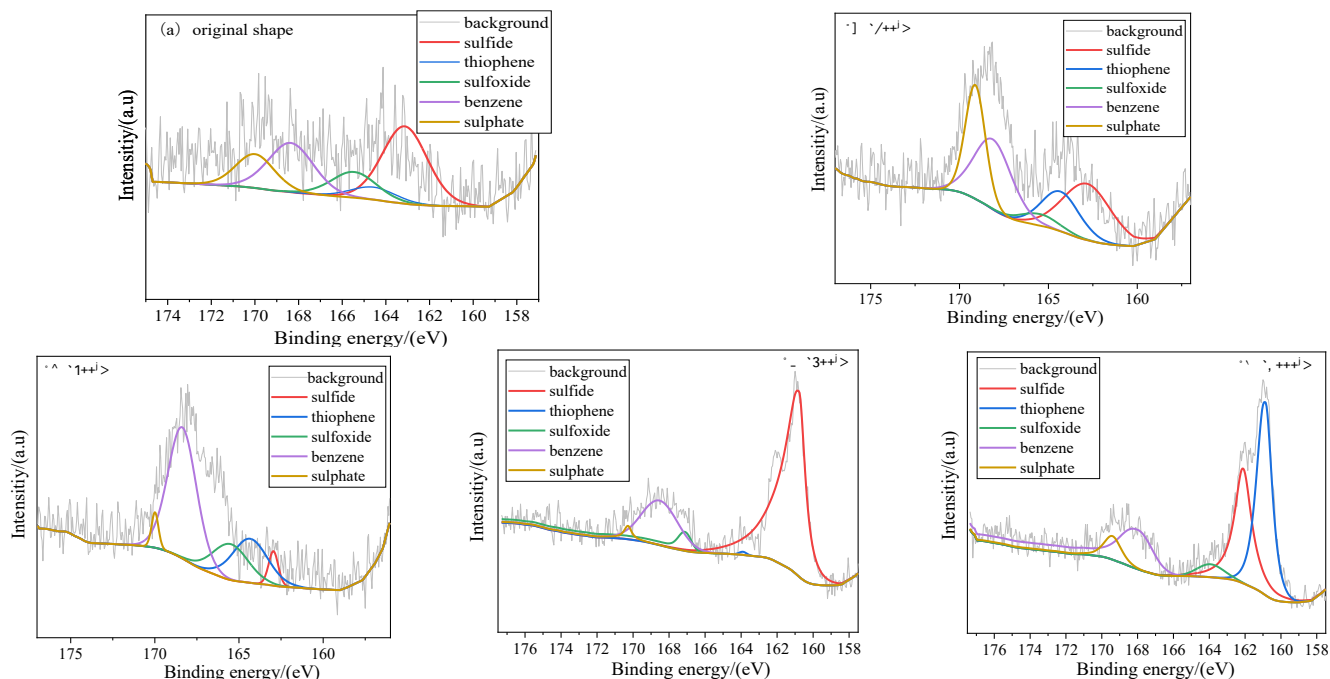
Figure 4: XPS peak fitting curves of sulfur content in anaerobic digestate char samples after pyrolysis
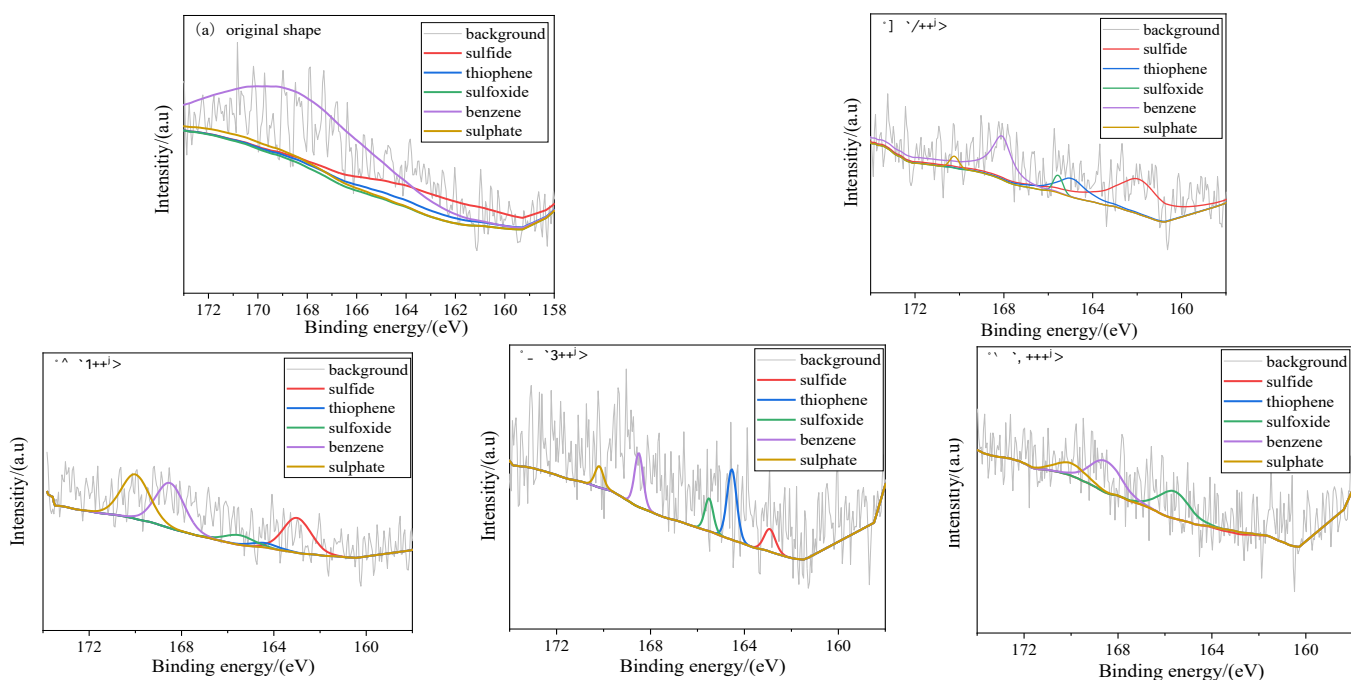
Figure 5: XPS peak fitting curves of sulfur content in char samples of rice straw after pyrolysis

Among them, the biogas samples were dominated by the form of sulphide, which accounted for about 72%, while the rice straw and corn straw samples were mainly dominated by the form of sulphoxide, which accounted for about 64.5% and 42%, respectively. The sulfur content of each type also corresponds to the intensity of different peaks in Figs. 4, 5 and 6.

Figure 7(a) shows the comparison of the content of sulfur forms in the digestate at different pyrolysis temperatures. The proportion of sulphide showed a trend of decreasing, then increasing and then decreasing with the increase of temperature, which was consistent with the pattern in the study of Tian L et al [14]. At below 400°C, the sulfide is mainly converted to the direction of sulfate; at 400°C-600°C, sulfide and sulfate are again mainly converted to the direction of sulfone, and the percentage content of sulfoxide and thiophene is also increased; at 600°C-800°C, the percentage of sulfide is again rapidly increased due to the conversion of thiophene, sulfoxide, and sulfone; and at 800°C-1000°C, the sulfide changes to the direction of organic sulfur. So, it leads to an increase of the proportion of macromolecule thiophene. The above pattern is consistent with the pattern of Figure 2.
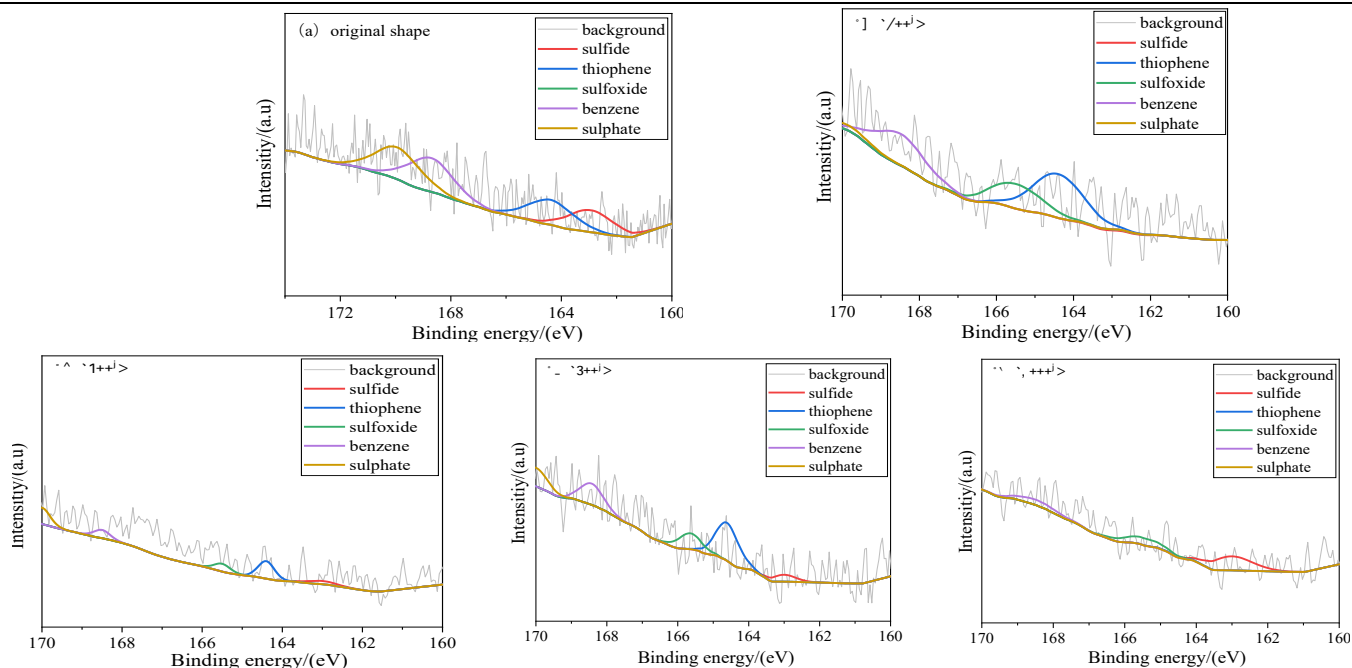
Figure 6: XPS peak fitting curves of sulfur content in char samples of corn stover after pyrolysis
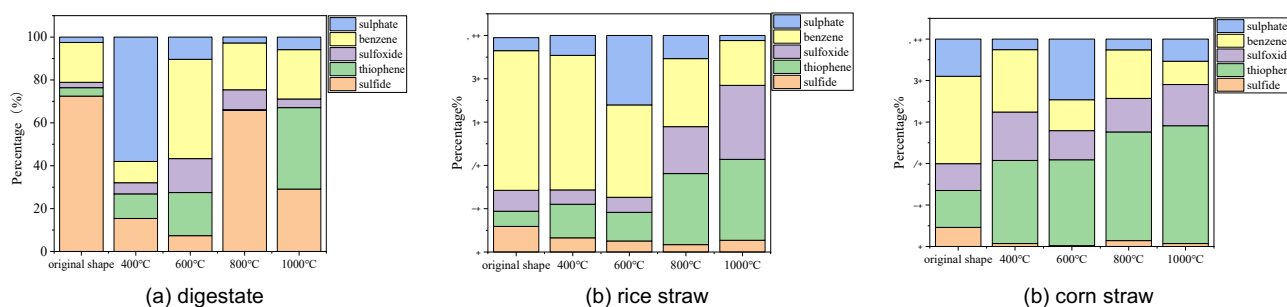
Figure 7: Quantity of Sulphur forms in the three samples after pyrolysis under different temperatures (XPS)

Figures 7(b) and 7(c) show the comparison of the content of sulfur forms in rice straw and corn stover at different pyrolysis temperatures. The percentage content pattern of each constituent is roughly the same. The main difference is that the percentage of sulfide in rice straw is higher than that in corn straw at different temperatures of pyrolysis. The highest sulfate content is found at 600°C, and higher temperatures are accompanied by sulfate decomposition and decrease in the content. The results of the XPS test show that there is a small amount of sulfide present at different temperatures. At high temperatures, organosulfur changes to macromolecular organosulfur, which is difficult to decompose. Macromolecular thiophene content increases and sulfone and sulfoxide content decreases at high temperatures.

The interconversion between the three different sulfur forms existed in digestate, rice straw and corn stover samples. S in digestate samples mainly existed in the form of inorganic sulfur, with sulfate predominating at low temperatures (400 °C) and sulfone predominating at mid-temperatures (600 °C), while S in rice straw and corn stover samples mainly existed in the form of organic sulfur, with macromolecular organic sulfur at low temperatures (400 °C) (sulfone, sulfoxide, thiophene) dominated at low temperature (400 °C), and a large amount of sulfate was precipitated only at medium temperature (600 °C). However, both the digestate samples and the rice straw and corn stover samples, at high temperatures (1000 °C), the main constituents were macromolecular organic sulfur (sulfone, sulfoxide, thiophene), which were difficult to decompose. The above pattern is consistent with the literature [14-16].

3.3. TG-MS analysis of sulphur gas-phase release

A TG-MS coupled analyser was used to investigate S migration and release characteristics in the samples, and the results of S release from digestate and biomass straw are shown in Figures 8 and 9.

Figure 8: Release processes of sulfur-containing compounds from pyrolysis of digestate: (a) inorganic sulfur, (b) organic sulfur

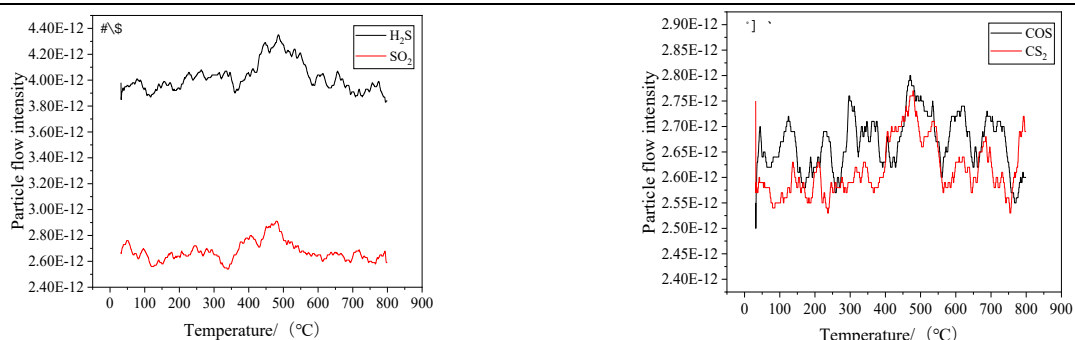As can be seen from Fig. 8, the interval of S-containing gases released from the pyrolysis of digestate was concentrated at 400~500°C, in which the concentration of H2S was significantly higher than that of other S-containing gases, and the release content of COS and CS2 was close to that of COS, so that the generation of H2S by digestate samples was the main pathway of S releaseunder the pyrolysis environment.

As can be seen from Fig. 9, the S-containing gases released from pyrolysis of both biomass straws, such as H2S, COS, CS2, SO2, etc., were concentrated at temperatures greater than 300 °C and above. All kinds of S-containing gases released from rice straw were more than those released from rice straw. Generation of H2S is the main pathway for S release in pyrolytic environments [17]. This is due to the fact that more O atoms within the solid samples are bound to the organic matter, but also produce more sulfur-containing free radicals as the temperature increases, and these radicals react with hydrogen to produce more H2S [18].

Therefore, sulfur release from digestate, rice straw and corn stover during pyrolysis are all mainly in the form of H2S.
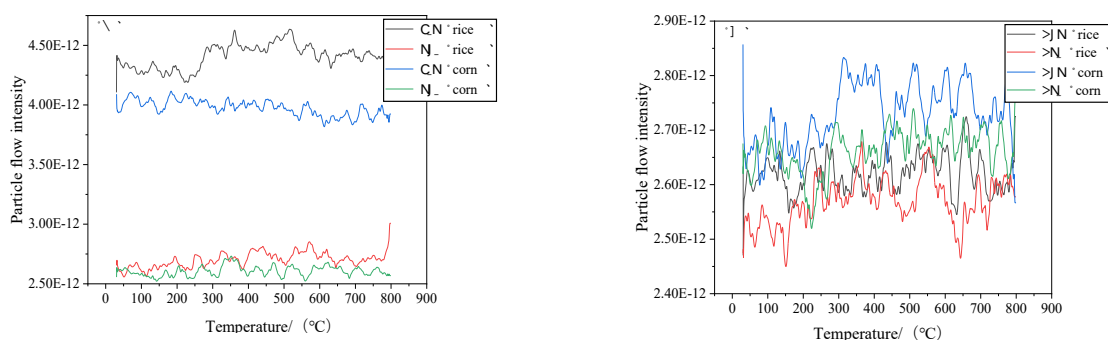
Figure 9: Release process of sulfur compounds from straw samples: (a) inorganic sulfur, (b) organic sulfur

3.4. Mechanistic discussion of sulphur migration in residual coke during pyrolysis

Analysing the migration and release of S from the above mentioned digestate and straw, this paper summarises the migration of S in the coke sample samples under pyrolysis at different temperatures and what may happen as follows:

1）More sulphate is generated in digestate coke samples at 200~400°C, and more sulphate is generated in straw coke samples at 400~600°C.

$$FeS_2 \rightarrow 2FeS+S \tag{1}$$

$$S+MO+O_2 \rightarrow MSO_3 \tag{2}$$

Reaction (1) Reaction started at 300~500°C;

In the description of reaction (2), M refers to the alkali metals Na, K, Ca, and Mg. Under pyrolytic conditions, the O required for S to be oxidised is from the solid waste itself, forming a salt present in the solid coke sample.

2）Thermal decomposition of sulphate in digestate and straw at 600-1000°C.

$$Fe_2(SO_4)_3 \rightarrow Fe_2O_3+3SO_3 \tag{3}$$

$$Na_2SO_4 \rightarrow Na_2O+SO_2+O_2 \tag{4}$$

$$K_2SO_4 \rightarrow K_2O+SO_2+O_2 \tag{5}$$
$$CaSO_4 \rightarrow CaO+SO_2 +0.5O_2 \tag{6}$$

Reaction (3) is fast reaction in the temperature range of 400/500~620°C; and faster above 710°C. Reaction (4) and reaction (5) are under 600-800°C. Reaction (6) occurs at 1000°C. The above pattern is consistent with the description in the literature [19].

3） Both digestate and straw charred samples form large molecules of organic S substances at high temperatures, the reaction is complex, typical reactions are：

$$FeS_2 +C \rightarrow Fe+CS_2 \tag{7}$$

$$FeS_2 +C_2H_2 \rightarrow C_4H_4S+CO_2 \tag{8}$$
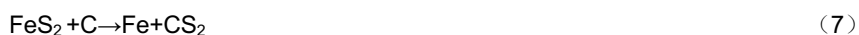
The high temperature conversion migration process of sulfur is reflected in reactions (7) & (8). Some FeS2 are also reduced to Fe at temperatures below 700°C. When the temperature is 800-900°C, inorganic S is converted to thiophene. Inorganic S in solids is converted to large molecules of S-containing compounds. The increase in the proportion of large molecule S-containing compounds also indicates that the small molecule S-containing compounds in the pyrolysis leave the particles in a gaseous state and are released into the ambient flue gas. These are the same laws as in the literature [19].

4. CONCLUSION

(1) Biogas has a higher content of sulfur, which can come from different sources, e.g. biodegradation processes, wastewater and waste, imported organic matter, soil and vegetation, process conditions and operations.

(2) Sulfur release process, the sulfur release process in digestate is not the same as in biomass. In digestate samples, most of the S (about 95%) leaves the surface of the sample particles in pyrolysis and enters into the pyrolysis gas, while S in biomass straw is not easy to be released in the pyrolysis process and is sequestered in the charred samples. Regarding both of them, sulfur release is mainly migrated in the form of H_2S.

(3) Sulfur exists in different forms, organic sulfur, iron sulphide sulfur and sulphate sulfur in digestate. During pyrolysis, there are three reaction pathways for the migration of S in the char samples of digestate and straw, such as: 1) at lower temperatures, it will be generated into sulphate first; 2) at 600~1000℃, sulphate undergoes thermal decomposition; and 3) at high temperatures (1000℃), both of them have their main constituents as macromolecular organosulfur (sulphone, sulphoxide, and thiophene), which are difficult to be decomposed.

(4) In addition, the most prominent difference between digestate pyrolysis and straw pyrolysis is that digestate generates sulphate at a low temperature of 200~400℃, which is different from straw generating sulphate at 400~600℃.

5. ACKNOWLEDGEMENT

6. REFERENCES

[1] Negri C，Ricci M，Zilio M，et al. Anaerobic digestion of food waste for bio-energy production in China and Southeast Asia: A review[J]. Renewable and Sustainable Energy Reviews，2020，133：110138.

[2] Moure Abelenda A，Ali A，Semple K T，et al. Aspen Plus® Process Simulation Model of the Biomass Ash-Based Treatment of Anaerobic Digestate for Production of Fertilizer and Upgradation of Biogas[J]. Energies，2023，16(7)：3039.

[3] Zhang J，Lv C，Tong J，et al. Optimization and microbial community analysis of anaerobic co-digestion of food waste and sewage sludge based on microwave pretreatment[J]. Bioresource Technology，2016，200(2)：253-261.

[4] Min Ye，Liu J，Ma C，et al. Improving the stability and efficiency of anaerobic digestion of food waste using additives: A critical review[J]. Journal of Cleaner Production，2018(192)：316-326.

[5] Czekała W，Nowak M，Piechota G. Sustainable management and recycling of anaerobic digestate solid fraction by composting: A review[J]. Bioresource Technology，2023，375：128813.

[6] Zhang J，Zhang T，Zhang R，et al. Pyrolysis characteristics of anaerobic biogas solid residue from kitchen waste[J]. Waste and Biomass Valorization，2024，15(2)：1141-1153.

[7] Vassilev S V，Baxter D，Andersen L K，et al. An overview of the organic and inorganic phase composition of biomass[J]. Fuel，2012，94：1-33.

[8] Han K，Gao J，Qi J. The study of sulfur retention characteristics of biomass briquettes during combustion[J]. Energy, 2019，186：115788.

[9] Yang T，Kai X，Sun Y，et al. The effect of coal sulfur on the behavior of alkali metals during co-firing biomass and coal[J]. Fuel，2011，90(7)：2454-2460.

[10] Wilfert P，Dugulan A I，Goubitz K，et al. Vivianite as the main phosphate mineral in digested sewage sludge and its role for

phosphate recovery[J]. Water research，2018，144：312-321.

[11] Kozowski M. XPS study of reductively and non-reductively modified coals[J]. Fuel，2004，83(3)：259-265.

[12] Marinov S P，Tyuliev G，Stefanova M，et al. Low rank coals sulfur functionality study by AP-TPR/TPO coupled with MS and potentiometric detection and by XPS[J]. Fuel Processing Technology，2004，85(4)：267-277.

[13] Verma H R. Atomic and Nuclear Analytical Methods[M]. New York：Springer Verlag，2007.

[14] Tian L，Yang W，Chen Z，et al. Sulfur behavior during coal combustion in oxy-fuel circulating fluidized bed condition by using TG-FTIR[J]. Journal of the Energy Institute，2016，89(2)：264-270.

[15] Yperman J，Franco D，Mullens J，et al. Determination of sulfur groups in pyrolysed low-rank coal by atmospheric-pressure tpr[J]. Fuel，1995，74(9)：1261-1266.

[16] Meng N，Jiang D，Liu Y，et al. Sulfur transformation in coal during supercritical water gasification[J]. Fuel，2016，186：394-404.

[17] A M L，A Y Q，B J C，et al. Sulfur release and migration characteristics in chemical looping combustion of high-sulfur coal[J]. Process Safety and Environmental Protection, 2021，151：1-9.

[18] Shen Y，Hu Y，Wang M，et al. Speciation and thermal transformation of sulfur forms in high-sulfur coal and its utilization in coal-blending coking process: A review[J]. Chinese Journal of Chemical Engineering，2021，35：70-82.

[19] Chung C，Pottimurthy Y，Xu M，et al. Fate of sulfur in coal-direct chemical looping systems[J]. Applied Energy，2017，208：678-690.

#172: Coupling mechanism between green power market and carbon market in China

Peng CHEN[1], Panpan LIU[1], Li LAN[1], Mingxing GUO[1], Hao MA[1], Hongbo REN[2]

[1] State Grid Shanghai Economic Research Institute, Shanghai 200233, China
[2] College of Energy and Mechanical Engineering, Shanghai University of Electric Power, Shanghai 201306, China, tjrhb@163.com

Abstract: To address climate change, China has gradually introduced market mechanisms including national carbon market and voluntary greenhouse gas emission reduction trading mechanism. On the other hand, under the background of the "dual carbon" goal, vigorously promoting the strategic path of deepening the energy revolution has brought new strategic opportunities to renewable energy and formed market mechanisms such as green power certificate trading and green power trading. The carbon market and green power market are closely related in terms of core product attributes, policies, technology, market positioning, etc. Effective coordination at the institutional level will be conducive to forming a joint force to promote the development of clean energy and carbon reduction in industry and society. However, currently, various environmental rights products are still in a relatively isolated development state and lack effective mechanisms for mutual recognition and connection. In this study, by combining the current development status of the green power market, carbon market and other market construction in China, the operating mechanism of each typical market is analyzed, and the correlation and interactive impact mechanisms among multiple markets is explored. Following which, the problems of inaccurate carbon emission accounting and duplicate certification of emission reductions in the process of connecting and recognizing different types of environmental rights products such as green power certificates, green power consumption, carbon emission rights, and CCER are discussed. Finally, a framework for the connection and mutual recognition between the green power market and carbon market is constructed, and relevant policy recommendations are proposed.

1. INTRODUCTION

To address climate change and achieve China's goals of peaking carbon dioxide emissions and reaching carbon neutrality, China has not only focused on traditional policies such as adjusting the energy mix and upgrading industrial structures but has also gradually introduced market mechanisms (Wu, et al., 2023). These efforts include the continuous development of the national carbon market and the establishment of the China Certified Emission Reduction (CCER) mechanism for voluntary greenhouse gas emission reductions (sun, et al., 2024). These measures leverage market force to enhance the nation's capacity to combat climate change. In 2011, the National Development and Reform Commission (NDRC) approved carbon emission trading pilot projects in seven regions: Beijing, Tianjin, Shanghai, Chongqing, Guangdong, Hubei, and Shenzhen (Xu, et al., 2023). These pilots began trading operations sequentially starting in 2013. On July 16, 2021, the national carbon market officially commenced trading. This market initially included 2,162 key emission entities from the power generation sector, covering approximately 4.5 billion tons of annual carbon dioxide emissions, making it the largest carbon market in the world by scale (Zhao, et al., 2022).

Building a new power system centered on renewable energy is a crucial strategy for achieving the goals of carbon peaking and carbon neutrality. To fully leverage market mechanisms and stimulate potential on both the supply and demand sides, China has introduced Green Power Certificate trading and Green Power Trading (Yu, et al., 2023). These initiatives are designed to promote the development of green energy. On September 7, 2021, China launched a pilot program for green power trading. In this initial phase, 259 market participants from 17 provinces conducted transactions totaling 7.935 billion kilowatt-hours of green electricity through both online and offline platforms (Lin, et al., 2022).

Currently, China has developed a framework where three distinct market mechanisms operate in parallel: Green Power Certificate (GPC) trading, Green Power Trading, and carbon trading, which includes carbon quotas and China Certified Emission Reduction (CCER). Although GPC, Green Power, and carbon trading each have their own independent sets of rules, they are intricately connected through their policy objectives, market mechanisms, and participants. The shared goal of these markets is to optimize resource allocation efficiency through market mechanisms and to facilitate low-cost, low-carbon development across industries. To ensure the efficient and smooth operation of these multiple market mechanisms, it is essential to deeply analyze the integration of the green power market and the carbon market. This includes examining how mechanisms like CCER can establish connections between the green power trading market and the carbon market, thereby preventing power users from incurring double environmental costs in both the power and carbon markets. Such research is crucial for effectively utilizing price signals, maximizing the role of market-based resource allocation, enhancing energy efficiency, and achieving the goals of carbon peaking and carbon neutrality in a scientific and efficient manner.

2. CURRENT STATUS OF THE SYNERGISTIC DEVELOPMENT OF CHINA'S ELECTRICITY, CERTIFICATE, AND CARBON MARKETS
2.1. Evolution of policies in the Electricity, Certificate, and Carbon markets

Electricity Market Reform Stage (Early 2000s to Early 2010s): During this period, China embarked on a journey to reform its electricity market, aiming to promote marketization and competition within the sector. In 2002, the National Power Trading Center was established to facilitate the creation of a power trading market. Subsequently, in 2005, the National Development and Reform Commission (NDRC) released the "Outline of Power Sector Reform and Development," outlining the goals and direction for market-oriented reforms in the electricity sector.

Establishment of the Green Certificate System Stage (Early 2010s to Mid-2010s): As the focus on renewable energy grew, China began to develop the Green Power Certificate (GPC) system. In 2010, the NDRC published the "Outline for Green Power Development," which set forth the goals and policy measures for the GPC system. In 2012, the NDRC issued the "Interim Measures for the Administration of Green Power Certificates," establishing a framework for the certification, issuance, and trading of green certificates.

Carbon Market Pilot Stage (Mid-2010s to Present): With increasing attention on climate change, China began piloting carbon markets. In 2013, the National Development and Reform Commission (NDRC) issued a notification titled "Notice on Carrying Out Pilot Projects for Carbon Emission Trading," which outlined the regions and sectors selected for carbon trading pilots. By 2017, China initiated the construction of a national carbon emission trading market, which has since become one of the largest carbon markets globally.

Integration Stage of the Electricity, Certificate, and Carbon Markets: China is currently advancing the integration of the electricity, green certificate, and carbon markets. The NDRC released the "Guiding Opinions on Promoting the Marketization of the Power Sector," which set forth goals and policy measures to integrate these markets. This initiative aims to harmonize electricity trading with the development of green energy by combining the power market, the green certificate market, and the carbon market. The objective is to enhance the consumption of renewable energy and to facilitate carbon emission reductions through seamless market integration.

The evolution of policies in China's electricity, certificate, and carbon markets is an ongoing process of development and refinement. As the national energy policies adapt and market demands evolve, these policies are likely to undergo further adjustments and optimization. Concurrently, the integration of these markets faces several challenges, such as ensuring policy stability, refining market mechanisms, and improving data oversight and trading regulations. Strengthening policy support and enhancing market mechanisms will be crucial for the healthy development of the integrated electricity, certificate, and carbon markets in China.

2.2. Current Status of the Development of the Electricity, Certificate, and Carbon Markets

China has established parallel systems for the electricity market and the carbon market. However, these markets still operate independently and have not yet achieved a cohesive synergy for energy saving and carbon reduction. The electricity market includes various trading categories, such as green electricity and green certificates (GPCs). When companies purchase green electricity through this market, they receive a green power consumption certificate issued by the Beijing or Guangzhou Power Trading Center. The carbon market allocates carbon emission rights to businesses in the form of allowances, which can then be traded as commodities. This mechanism allows companies to buy and sell carbon emission allowances to manage their carbon footprints effectively. At present, the demand for green electricity among businesses is increasing, and green power trading has become a crucial link between the electricity and carbon markets. However, there is still no substantive interaction between these two markets. On the one hand, the mutual recognition system between the electricity and carbon markets has not yet been established. The electricity market and the carbon market are managed by different regulatory bodies—the energy sector oversees the electricity market, while the environmental sector manages the carbon market. This separation leads to a lack of coordination in operational mechanisms and evaluation standards. Additionally, there are multiple methods and authorities for certifying green consumption, resulting in fragmented and overlapping management. On the other hand, the price transmission mechanism between the electricity and carbon markets is not yet smooth. Current policies primarily support the development of the green electricity industry, benefiting renewable energy producers. However, these policies have not sufficiently incentivized consumers to actively participate in the consumption of low-carbon energy.

2.3. The Issue of Double Counting Environmental Value

Double Counting Issues between CCER and Green Certificates

According to the "Administrative Measures for Carbon Emission Trading (Trial)" issued by the Ministry of Ecology and Environment on December 31, 2020, China Certified Emission Reductions (CCERs) are defined as verified and registered greenhouse gas emission reductions derived from projects involving "renewable energy, forestry carbon sinks, methane utilization, and other initiatives." The current status of CCERs, as outlined in the article "Brief Analysis of Policy Coordination after the Restart of CCER," shows that most of the registered and approved projects are focused on wind power and photovoltaic (solar) projects. Similarly, according to the "Notice on the Pilot Implementation of the Renewable Energy Green Power Certificate Issuance and Voluntary Subscription Trading System," all Green Certificates (GPCs) are derived from onshore wind and photovoltaic projects. This indicates a high overlap between the types of projects eligible for both CCERs and Green Certificates.

The issue of double counting between Green Certificates and CCERs involves two main aspects. On the supply-side, renewable energy projects such as wind and solar can apply for both Green Certificates and CCERs. The overlapping eligibility raises a crucial question in system design: how to prevent the same project from being submitted under both mechanisms? This is an urgent issue that needs to be addressed to ensure the integrity of the environmental value system. On the demand Side, currently, there is a low overlap between companies using CCERs and those using Green Certificates in China. CCERs are primarily purchased by companies to comply with carbon obligations, while Green Certificates are more often bought by firms voluntarily committing to carbon neutrality. This discrepancy makes it difficult for companies using Green Certificates to verify the uniqueness of the environmental rights they purchase. Additionally, there is ongoing debate on whether the Scope 2 emissions offset by Green Certificates can be considered zero when calculating the company's own carbon footprint.

CCERs were suspended in March 2017, while the issuance of Green Certificates began in January 2017. Due to the timing mismatch and the initial market resistance to subsidized Green Certificates, the issue of double counting was not prominent before the launch of the national carbon market. However, since President Xi Jinping announced the "dual carbon" strategy in September 2020, there has been a renewed interest in restarting CCERs. This has led to an increased demand for developing CCER projects. Simultaneously, both domestic and international companies have become more proactive in pursuing carbon neutrality. For many end-users, especially in the final step towards achieving carbon neutrality, Green Certificates—particularly unsubsidized ones—are preferred due to their simplicity, fast certification process, and lower costs compared to CCERs. Given that CCERs and Green Certificates essentially represent the same environmental value, avoiding double counting or double trading for the same project is fundamental to maintaining the integrity of these environmental assets. As the "dual carbon" strategy progresses, the issue of double counting between CCERs and Green Certificates is likely to become increasingly significant.

Double Counting Issues between CCERs and Allowances

According to the "Administrative Measures for Carbon Emission Trading (Trial)," major emitting entities within industries covered by the national carbon emission trading market, which emit more than 26,000 tons of CO_2 equivalent annually, must control their greenhouse gas emissions. These entities are required to report their carbon emissions data, settle their carbon emission allowances, disclose information related to trading and activities, and comply with the supervision and management of the ecological environment authorities.

Many registered CCER projects, such as natural gas combined cycle power generation, fuel substitution, waste heat utilization, and distributed photovoltaic and biomass power generation within industrial settings, are operated by entities that qualify as "major emitting entities" under the regulations. The regulations stipulate that these major emitting entities can use CCERs to offset their carbon emission allowance obligations, with the offset not exceeding 5% of their total carbon allowances. Importantly, the CCERs used for this purpose must not come from emission reduction projects that are already subject to the national carbon emission trading market's allowance management.

Since the national carbon market is still in its early stages, only the power sector is currently included in the allowance management system. However, according to the "Administrative Measures for Carbon Emission Trading (Trial)," other major emitting sectors will gradually be incorporated into the system in the future, and the scope of key emitting entities will be dynamically adjusted based on their actual production activities. At present, there is no clear guideline on whether the emission reductions generated by CCER projects from entities not yet included in the allowance management can be used for compliance purposes. Many companies not currently covered by the national carbon market's allowance management still undergo annual greenhouse gas emissions verification. According to the "Guide to Verification of Corporate Greenhouse Gas Emission Reports (Trial)" and relevant industry guidelines, the carbon reduction contributions from CCER projects are already included within the boundaries of these companies' carbon emission accounting. Although, strictly speaking, these companies do not yet participate in the allocation and settlement of carbon allowances, their overall carbon reduction contributions, as calculated through CCER projects, should be considered by regulatory authorities when formulating rules for allowance allocation and settlement. This consideration is crucial to addressing potential double counting issues that might arise from these CCER projects.

On the other hand, although the national carbon market began trading only in 2021, regional pilot carbon markets in cities like Beijing, Shanghai, and Guangdong have been in operation for several years. These pilot markets have clearly stipulated that CCERs from companies within their emission control scopes are not accepted. However, there are no explicit restrictions on CCER projects operated by emission control companies outside these pilot areas. For key emitting entities in the national carbon market, regulations clearly state that they can no longer participate in regional pilot carbon markets. Nevertheless, inconsistencies in carbon accounting rules across different markets and the lack of transparency in accounting reports make it challenging to verify and manage double counting. If a CCER project comes from an emission control company within a local pilot area, and its emission reductions have already been accounted for and reflected in the local pilot's allowance settlement, using these same CCERs again in the national carbon market or other pilot carbon markets would result in double counting.

Additionally, CCER projects typically have crediting periods lasting 10 to 20 years. The current rules do not strictly differentiate the issuance of emission reductions by year. Considering the varying control rules applicable in different years, the issue of double counting becomes even more complex.

3. THE INTERACTION MECHANISM OF THE POWER-CERTIFICATE-CARBON MARKETS AND THE CONSTRUCTION OF AN SD MODEL

The green certificate trading market, carbon emission rights trading market, and electricity market are interconnected by renewable energy producers and traditional energy power plants. They interact through green certificate prices, carbon emission rights prices, electricity prices, and numerous endogenous and exogenous variables, forming a complex system.

3.1. Interaction mechanism of the Electricity, Certificate, and Carbon markets

After implementing the green certificate trading system, renewable energy generators not only engage in electricity trading in the power market but also trade green certificates in the certificate market. This results in increased profits for green energy producers, leading to higher investments in renewable energy capacity and increased supply of green electricity. Conversely, after implementing the carbon emission trading system, traditional energy generators not only trade electricity in the power market but also need to purchase emission quotas for CO_2 emissions beyond the allocated free allowances from the government. This increases the operating costs for traditional energy generators, reducing their profits and subsequently decreasing investments in traditional energy capacity. As a result, the growth rate of traditional electricity supply decreases, contributing to the adjustment of energy source structure and carbon emission reduction goals. Additionally, CCERs participate in the carbon market as supplementary to carbon quotas, with renewable energy being a reporting entity, thus establishing a connection between the carbon market and the green electricity and certificate markets.

The prices in the three markets (green certificate price, CCER price, carbon price) are interlinked as follows: ①When the green certificate price increases, the CCER price decreases, and the carbon price decreases. ②When the carbon price increases, the CCER price decreases, and the green certificate price decreases. Therefore, through the interconnected pricing mechanism between green electricity and traditional electricity markets, green certificate trading and carbon trading influence electricity prices in the power market. These electricity prices, in turn, affect electricity demand, and the interaction between electricity demand and supply in the electricity market ultimately achieves market equilibrium through market mechanisms. This qualitative explanation illustrates the interactive mechanisms among the three markets, ultimately leading to the adjustment of the national energy structure and the achievement of carbon dioxide emission reduction goals.

3.2. SD model development of the Electricity, Certificate, and Carbon markets

The objective of the system dynamics model is to: study the interaction mechanisms between the green certificate market and the electricity market, and simulate the trends of endogenous factors (under the green certificate trading mechanism, such as green certificate price, installed renewable energy capacity, and renewable energy generation); study the interaction mechanisms between the carbon trading market and the electricity market, and simulate the trends of endogenous factors (under the carbon emission trading mechanism, such as carbon price, CCER price, installed traditional energy capacity, and traditional energy generation); study the interaction mechanisms among the three markets of the green certificate market, carbon trading market, and electricity market, and simulate the trends of endogenous factors (including green certificate price, installed renewable energy capacity, renewable energy generation, installed traditional energy capacity, traditional energy generation, electricity price, total electricity demand, and total electricity supply).

Establishing a system dynamics model requires setting certain boundaries to better understand the system, without getting overly caught up in irrelevant details. Therefore, this study encompasses four system dynamics (SD) models, including three single-market SD models and one comprehensive SD model. The single-market SD models comprise: the Green Certificate Trading Market SD model, the Carbon Trading Market SD model, and the Electricity Market SD model. The comprehensive SD model explores the interaction among the Green Certificate Market, Carbon Market, and Electricity Market. ①In the Green Certificate Trading Market SD model, the endogenous factors include: green certificate price, planned renewable energy installed capacity, actual renewable energy installed capacity, renewable energy generation, number of green certificates issued to renewable energy generators, green certificates held by generators, expected purchase and sale quantities of green certificates, and excess demand for green certificates. Exogenous factors include: electricity demand growth rate, electricity demand, quota growth rate, and quota proportion. ②In the Carbon Trading Market SD model, the endogenous factors include: carbon quota price, CCER price, planned traditional energy installed capacity, actual traditional energy installed capacity, traditional energy generation, carbon quota demand, CCER demand, carbon quotas held by buyer generators, CCERs held by buyer generators, carbon quotas held by seller generators, CCERs held by green energy generators, expected sales and purchases of carbon quotas, expected sales and purchases of CCERs, excess demand for CCERs, and excess demand for carbon quotas. Exogenous factors include: unit GDP carbon emission reduction rate, unit GDP carbon emissions, GDP growth rate, GDP, share of electricity industry, and electricity demand growth rate. ③In the Electricity Market SD model, the endogenous factors include: electricity price, profit margins for renewable and traditional energy, planned renewable energy installed capacity, planned traditional energy installed capacity, actual renewable energy installed capacity, actual traditional energy installed capacity, renewable energy generation, traditional energy generation, electricity supply, electricity demand, and excess electricity demand. Exogenous factors include: electricity demand growth rate. Ultimately, through the mechanism of market equilibrium (partial equilibrium), the three markets utilize the transmission of green certificate prices, carbon prices, and CCER prices to increase the proportion of renewable energy generation and decrease the proportion of traditional energy generation, thereby achieving the ultimate goals of adjusting the power source structure and reducing carbon dioxide emissions.

System dynamics modeling involves drawing corresponding stock-flow diagrams based on causal loop diagrams; establishing mathematical equations to describe the relationships between qualitative and semi-quantitative variables; constructing equations and procedures, followed by preliminary testing and evaluation of the model; once validated, inputting initial data and policy variables into the program to simulate experiments on a computer. In this study, system dynamics modeling is implemented using Vensim software, which includes a comprehensive set of coupled nonlinear differential equations and individual differential equations for each stock.

3.3. Simulation and scenario analysis

Through economic theory derivation and system dynamics modeling, it was found that many factors can influence the effective operation of the interaction markets involving green certificates, carbon emissions rights, and electricity. The initial simulation duration set for the system dynamics model in this paper is 10 years, with time units measured in months. Additionally, to ensure comprehensive and accurate research outcomes, all initial values of variables are based on data from the year 2020.

To verify the impact of different market couplings on the overall market and power structure, this study will analyze scenarios based on current national and regional pilot projects in China. Furthermore, an imaginary future scenario will be set as a supplement. Simulation and scenario analysis will be conducted for these three scenarios, as detailed in Table 1.

Table 1: Scenario setting

	CCER offsets carbon quotas	Green electricity offsets carbon quotas	Green certificates participate in carbon markets
Scenario 1	√	√	
Scenario 2	√		
Scenario 3	√	√	√

Green certificate trading market

On the basis of the aforementioned system dynamics models interacting across the three major markets, combined with the scenario settings in this chapter, simulations were conducted as shown in Figure 1. Scenario 1 depicts the trend of green certificate (GC) prices under the coupling mechanism of the carbon-electricity market, Scenario 2 under the carbon market mechanism, and Scenario 3 under the coupling mechanism of the carbon-electricity certificate market. From the graph, it is evident that the GC price fluctuates from a low initial price to the upper limit, maintaining this high level for a period before reverting to lower market prices. Specifically, in the first year, the GC price remains largely stable around the initial price of 40 yuan per certificate. Over the next two years, the GC price gradually increases at a steady, slow rate to the limit of 300 yuan per certificate, where it remains at this high level for about two years. Subsequently, the GC price decreases at different rates to approximately 150 yuan per certificate, fluctuating slightly around this price line, with predictions indicating stability over time.
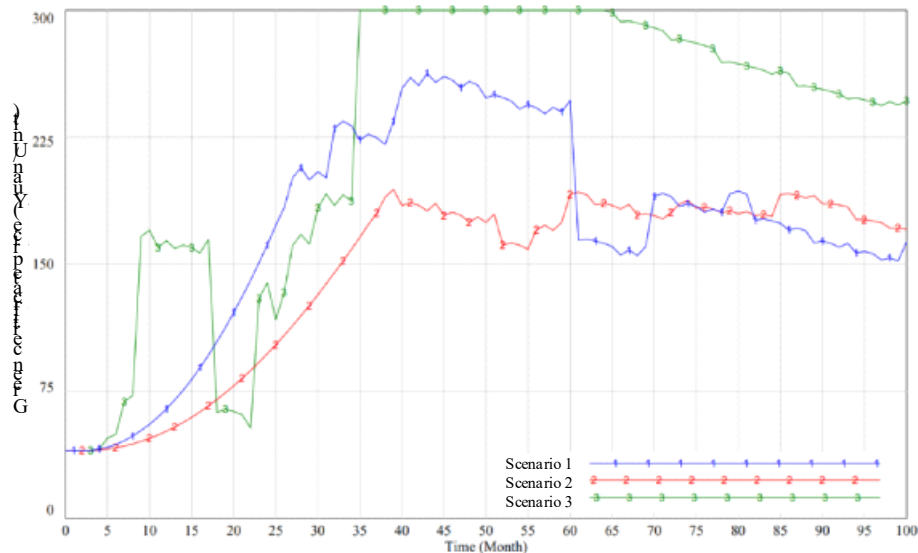
Figure 1: The trend of green certificate prices under different degrees of market coupling

2020, Baseline Price Phase: During this period, the price of green certificates remained stable at around 40 yuan per certificate because the initial batch of renewable energy installations had not been completed, and thus had no significant impact on the green certificate market. 2021-2023, Steady Increase Phase: Due to the continuous increase in demand for green certificates and delays in the construction of renewable energy projects, the market faced a supply shortage. As a result, the price of green certificates rose steadily to 300 yuan per certificate over three years. This rise was driven by growing demand for electricity and green certificates, along with green electricity producers holding onto certificates to mitigate risks. To maximize demand, green electricity producers would hold certificates for a month and sell them just before they expired, maintaining the price increase. 2023-2025, Sustained High Price Phase: As the demand for electricity and the proportion of required green certificates continued to grow, the market remained tight. Green electricity producers, holding onto a portion of certificates to hedge against price risks, kept the market in a state of constant tension and shortage. This persistent demand and limited supply kept the price of green certificates at the upper limit. 2017-2018, Rapid Decline Phase: The profitability of green electricity producers, calculated as the sum of electricity price and green certificate price, encouraged them to expand their renewable energy capacity and improve technology. With the completion and operation of new installations, the supply of green certificates in the market surged, leading to an oversupply. Since external buyers would only purchase enough certificates to meet the required quota, surplus certificates accumulated, causing the price to drop rapidly. 2018-2020, Stabilization Phase: During this period, the external demand for green certificates increased steadily, and green electricity producers had ample capacity to meet market needs. The market for green certificates reached equilibrium under market mechanisms, with the price stabilizing around 150 yuan per certificate after experiencing minor fluctuations. Regarding the difference in the trend of TGC (Tradable Green Certificates) prices under the coupling mechanism shown in Figure 3-9, it is because when the carbon trading mechanism was first implemented, the baseline carbon price was relatively low at 43 yuan per ton. The cost of purchasing carbon credit (i.e., compliance costs) was less than the cost of implementing energy-saving measures or investing in renewable energy. Therefore, traditional energy power plants preferred to continue or even increase their investment in coal power and accept penalties rather than invest in renewable energy. This lack of sufficient pressure to invest in renewable energy led to a prolonged period before the supply of green certificates could meet demand, thus extending the duration of high green certificate prices.

Therefore, both Scenario 1 (carbon-electricity coupling) and Scenario 3 (electricity-green certificate-carbon coupling) will invigorate the green certificate market to some extent, fostering its development. In the early stages, Scenarios 1 and 3 will enhance the profit margins for renewable energy generation, leading to short-term fluctuations in the price of green certificates.

Carbon Trading Market

By simulating the system dynamics models of both the standalone carbon emission trading mechanism and the coupled three-market mechanism, we can observe the trend of carbon prices, as shown in Figure 3-10. The fluctuation curves across the three scenarios are similar, with slight differences in the process of reaching a steady state in the later stages. The overall trend of carbon quota changes can be divided into the following four stages:

Baseline Price Phase: Traditional energy power plants already hold a portion of the carbon quotas, resulting in minimal excess demand. At this stage, most power plants are still observing the carbon quota market, leading to prices remaining stable at the baseline level. Steady Increase Phase: Initially, the penalty cost for carbon emissions is lower than the cost of implementing emission reduction measures. This situation encourages an increase in capacity installations, causing a stable rise in the demand for carbon quotas, thereby creating a supply shortage in the carbon quota market. Rapid Decline Phase: As carbon quota prices remain high, the profit margins of traditional energy power plants are significantly squeezed, leading to market conditions where supply exceeds demand. Stabilization Phase: The carbon quota market achieves stability through market mechanisms.

For the first five years, the coupling of the electricity-green certificate-carbon markets has no significant impact on carbon quota prices. However, after this period, market coupling causes a slight increase in carbon prices. Compared to electricity-green certificate-carbon coupling, the electricity-carbon coupling has a greater impact on the carbon market, leading to higher instability.
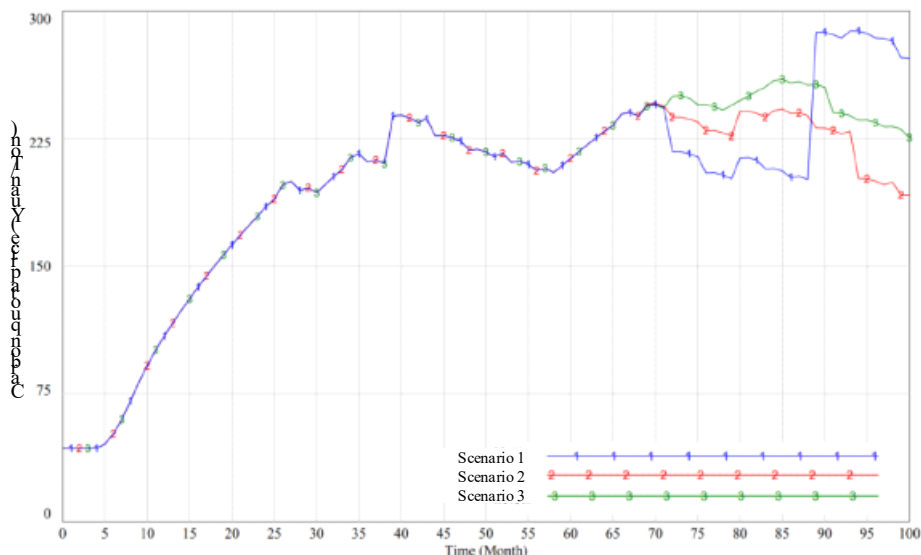
Figure 2: Carbon Quota Price Trends Under Different Degrees of Market Coupling

CCER Market

By conducting simulations using both the standalone system dynamics model for carbon trading and the coupled three-market system dynamics model, we can observe the CCER price trends as illustrated in Figure 3. The overall CCER price trajectory can be divided into the following four phases:

Baseline Price Phase: During this period, the initial batch of renewable energy installations has not yet been completed, and there is weak demand for carbon markets. As a result, CCER prices remain relatively unchanged. Steady Rise Phase: As the demand for carbon quotas increases, CCERs, being more cost-effective compared to carbon quotas, become more attractive. This leads to a sustained increase in CCER demand, causing a supply-demand imbalance where supply is insufficient to meet the growing demand. Stable Decline Phase: With the continuous rise in CCER prices and the stabilization of the carbon market, the CCER market experiences a shift to an oversupply situation. Equilibrium Phase: The carbon market eventually stabilizes under market mechanisms, achieving equilibrium. (This phase's full development might not be visible within the simulation time frame.)

The different scenarios can be explained as follows: Scenario 1 (Electricity-Carbon Coupling): The mechanism allowing green electricity to offset carbon quotas reduces the demand for CCERs, intensifying the market's oversupply condition. Scenario 3 (Electricity-Green Certificates-Carbon Coupling): By integrating CCERs with the green certificate market, the supply of CCERs increases, further reinforcing the market's oversupply condition.
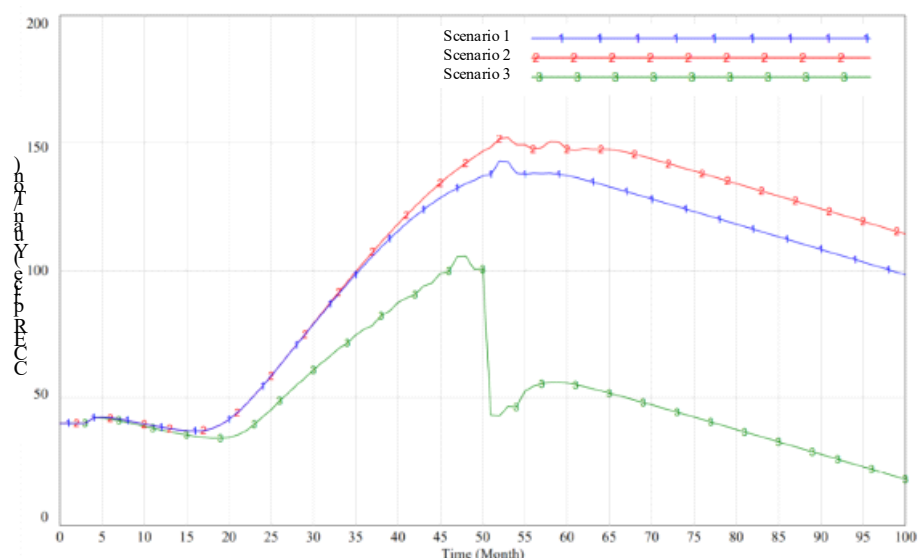

Figure 3: CCER price trends under different market coupling degrees

Power Structure

By calculating the generation capacity of renewable energy and traditional energy, the future trend of the power structure can be observed, as shown in Figure 4. The changes in the power structure can be divided into three phases:

Construction Phase: During this initial period, all markets are still in their early stages. Both the profit margins for renewable energy and traditional energy are quite small, resulting in the power structure remaining largely unchanged. Stable Growth Phase: As the prices of green certificates and CCERs rise, the profit margins for renewable energy continue to increase. Conversely, as the price of carbon allowances rises, the profit margins for traditional energy significantly shrink. This leads to a much faster rate of renewable energy construction compared to traditional energy. Stabilization Phase: As electricity, green certificates, and carbon markets gradually stabilize, the installed capacity of renewable energy continues to grow. However, the increasing capacity leads to a decrease in the profit margins for renewable energy, causing both renewable and traditional energy installations to stabilize.

From this, we can conclude that the implementation of the green certificate trading system and the carbon emissions trading system optimizes the power structure, significantly increasing the proportion of green energy. Both Scenario 1, where there is coupling between the carbon and electricity markets, and Scenario 3, where there is coupling between the electricity, green certificates, and carbon markets, will improve the power structure to some extent. The degree of market coupling does not affect the ultimate power structure but rather influences the process of its improvement.
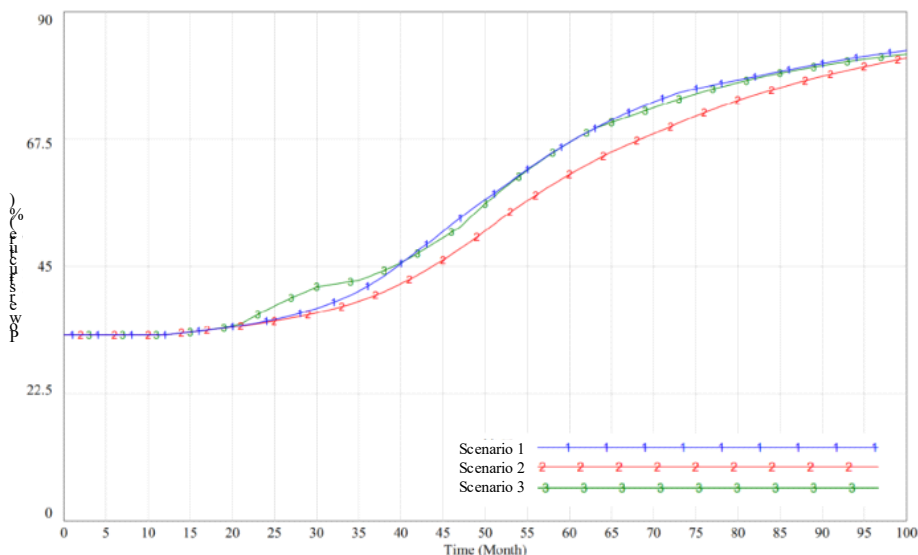

Figure 4: Changes in power structure under different degrees of market coupling

4. ISSUES AND RECOMMENDATIONS FOR INTEGRATION OF THE POWER, GREEN CERTIFICATE, AND CARBON MARKETS

As the dual carbon goals (carbon peaking and carbon neutrality) are advanced, the pace of electrification accelerates, power market reforms enter deeper phases, and the carbon market continues to evolve. The market-oriented processes for renewable energy on both the generation and consumption sides are further expedited, tightening the interconnections between the green power market and the carbon market. The main relationships between the power, green certificate, and carbon markets are characterized as follows: Policy Mechanisms: Complementary and mutually reinforcing, Price Linkages: Interactive and interdependent, Market Participants: Significant overlap, Environmental Rights: Intersecting and intertwined. Therefore, the simultaneous development of the green power market, green certificate market, and carbon market can fully leverage market mechanisms to optimize energy resource allocation and climate governance. This integrated approach drives the low-carbon energy transition and supports the achievement of carbon reduction targets.

Currently, in China, the green power market, green certificate market, and carbon market are interrelated and influence each other through various green power consumption mechanisms. However, they face challenges such as lack of coordination and poor integration. To address these issues, the links between these markets should be strengthened, particularly in terms of market scope, pricing systems, product frameworks, and governance structures.

Market Scope

There are differences in the spatial development trends of the electricity market, green certificate market, and carbon market. The market space of the electricity market continues to expand with economic and social development and GDP growth. The carbon market, with the potential restart of CCER and its overlap with the electricity market and green certificate market, is evolving.

On one hand, green electricity trading is in its initial stages, expected to exhibit a coexistence of "certificate-electricity integration" (green electricity trading) and "certificate-electricity separation" (green certificate trading) in the short term. Currently, the national carbon market only includes the electricity industry, with entities such as coal-fired power generation and gas-fired power generation. The CCER mechanism has not yet restarted, and the common entities between the national carbon market and the electricity market only cover major entities such as coal-fired power and gas-fired power.

On the other hand, as the carbon market continues to expand, it is gradually incorporating carbon emission entities from industries such as construction, industry, and cement. The CCER mechanism is set to restart, and the methodologies released so far include grid-connected solar thermal power generation and grid-connected offshore wind power generation, leading to certain overlaps with

the green certificate market and electricity market.

Therefore, from the perspective of market scope, it is necessary to design scientific methods for defining and managing market scope to achieve overlap without redundancy. In the process of defining market scope, the following points should be considered:

1) With the deepening of carbon peak and carbon neutrality initiatives, the total quota space of the national carbon market will gradually tighten. However, the electricity sector still faces a considerable expansion period to support sustained economic growth, and to undertake emission reduction responsibilities transferred from industries such as industry and transportation. Therefore, it is necessary to reasonably delineate the "electricity-carbon" market space to resonate and promote each other, avoiding mutual restraint and weakening.

2) The allocation space of carbon quotas and the setting of industry benchmarks should be moderately relaxed to provide sufficient transformation time for the electricity industry.

3) Fully meet the emission requirements for emergency backup power supply, and appropriately exempt carbon emission quotas when feasible.

Price System

China's electricity market is in a transitional phase from planning to marketization. In the short term, it is difficult for carbon prices and electricity prices to effectively transmit, and the construction of both markets needs to consider mutual influences and constraints. From theoretical and international practices, under conditions of electricity marketization, carbon prices can transmit to electricity prices, and electricity prices can also influence carbon prices in reverse.

On one hand, carbon prices are added to the pricing of thermal power enterprises in the electricity market, affecting transaction prices. On the other hand, supply-demand conditions and price changes in the electricity market affect the electricity generation of thermal power plants. Changes in electricity generation affect the demand for carbon quotas, thereby influencing the level of carbon prices.

Therefore, by establishing a smooth "electricity-carbon" market price transmission chain, carbon costs can be distributed across different industries in society, guiding energy conservation and:

1) Improving the carbon price transmission mechanism for non-grid-connected electricity and non-market participants, reflecting the principle of fair sharing.

2) Enriching diverse channels for carbon cost mitigation to avoid excessive levies and pushing up end-user electricity prices in the electricity sector.

3) Innovating the mechanism for sharing benefits among "electricity-carbon" market entities, coordinating carbon-related fund rebalancing, and creating a virtuous cycle and incentives.

Product System

Mutual recognition among product systems serves as a bridge to promote coordinated development among different market systems. It is necessary to construct a connection mechanism for various environmental rights products such as green electricity in multiple markets and strengthen information interconnection and interoperability. Establishing an environmental rights product framework for the electricity-carbon market system aims to incentivize renewable energy development, facilitate the orderly phase-out of coal-fired units, and enhance the enthusiasm of users for green electricity consumption.

When calculating indirect carbon emissions from electricity, consideration can be given to crediting enterprises for green electricity consumption based on green electricity certification. This approach aims to accurately reflect the true emission levels of enterprises and unify the environmental value of green electricity with the carbon reduction value.

5. CONCLUSION

This paper delves into the potential stakeholders of the green electricity market and the carbon market. It analyzes the interests, profit models, and responsibilities of various market participants, including power generation companies, power grids, and electricity users. The study identifies the roles and obligations of these stakeholders and their micro-level interactions. By investigating the complex coupling relationships of benefit flows and management flows among multiple trading entities in a coordinated market, the paper constructs a stakeholder matrix.

Using a SD model, the paper designs an integration model for the carbon market and the green electricity market and conducts simulation analyses to explore future market trends and analyze their causes. It examines the role of power grid companies in multiple markets, investigates their entry points, and proposes strategic recommendations for grid companies to participate in diverse markets. The paper also scrutinizes the intrinsic mechanisms of overlapping applications and double counting within the green certificate system, green electricity trading, and the CCER market. It provides strategies to effectively address these issues following the restart of CCER. From the perspectives of different policy stakeholders—government, enterprises, and users—it offers policy recommendations that support the development of multi-market coupling.

6. REFERENCES

Xinyu Wu, Zhengting Jiang, 2023, Time-varying asymmetric volatility spillovers among China's carbon markets, new energy market and stock market under the shocks of major events. Energy Economics, 126, 107004.

Luxi Sun, Zhili Wang, Shuning Kong, Xiaohua Xia, 2024, Correlation and spillover effects between the carbon market and China's stock market: Evidence from wavelet and quantile coherency network analysis. International Review of Economics & Finance, 93, 1175-1196.

Li Xu, Yasir Ahmed Solangi, Rong Wang, 2023, Evaluating and prioritizing the carbon credit financing risks and strategies for sustainable carbon markets in China. Journal of Cleaner Production, 414, 137677.

Lili Zhao, Fenghua Wen, 2022, Risk-return relationship and structural breaks: Evidence from China carbon market. International Review of Economics & Finance, 77, 481-492.

Anqi Yu, Shuyang Peng, Yizhi Jasmine Li, Kun Guo, 2023, Analysis of the Effectiveness of Carbon Emission Trading Market in China. Procedia Computer Science, 221, 1440-1447.

Boqiang Lin, Chongchong Zhang, 2022, The overall and time-varying efficiency test for the carbon market in China. Journal of Environmental Management, 322, 116072.

#176: Performance analysis and optimization of multiple compression brayton cycle for space nuclear system

Tong Lu[1], Haochun Zhang[2], Fangwei Ma[3], Ersheng You[4]

[1] School of Energy Science and Engineering, Harbin Institute of Technology, Harbin, 150001, China, lutong982013@163,com
[2] School of Energy Science and Engineering, Harbin Institute of Technology, Harbin, 150001, China, hczhang@hit.edu.cn
[3] School of Energy Science and Engineering, Harbin Institute of Technology, Harbin, 150001, China, 1037595442@qq.com
[4] Nuclear Power Institute of China, Chengdu, 610213, China, youersheng@126.com

Abstract: With the rapid development of deep space exploration and space technology, the demand for energy used in space has gradually increased. For space energy systems, in addition to system efficiency, the mass of the whole system is also an important indicator to determine the launch cost and the feasibility of the design scheme. By using the Brayton cycle, the system of space nuclear energy can obtain higher energy conversion efficiency and more compact structure. In this paper, under the background of space nuclear energy, the mixture of Helium and Xenon was multiple compressed and split after the radiant radiatorto reduce compressors consumption. Also, the cycle fluid was bled after the turbine directly entered the reactor for heating, so as to increase the inlet temperature of the reactor and reduce the total circulation heat absorption. After establishing the thermodynamic model and mass estimation model of the multiple compression system, the effects of bleeding ratio, number of compressors, pressure ratio, compressor inlet temperature and turbine inlet temperature on the thermal efficiency and mass of the Brayton system were studied. Then, taking thermal efficiency and total mass of the system as optimization objectives, the multiple compression Brayton system is optimized by genetic algorithm.

Keywords: Space Nuclear Technology, Brayton Cycle, He-Xe, Multiple Compression, NSGA-Ⅱ

1. INTRODUCTION

With the rapid development of deep space exploration and space technology, the demand for space energy has gradually increased. With long service life, high energy density and compact structure space nuclear energy technology is the ideal space energy for deep space exploration (Bennett et al, 1996. Bennett, 2008). The space nuclear energy conversion system can be divided into static and dynamic conversion methods (Fan et al, 2017). Compared with static conversion, dynamic energy conversion systems have higher system efficiency which is an ideal space nuclear energy conversion scheme (Guan et al, 2024). Dynamic conversion includesBrayton cycle, Rankine cycle and Stirling cycle (Liu et al, 2019). Using Brayton cycle in space nuclear energy technology can obtain higher system energy conversion efficiency. Therefore, many scholars have carried out research on the Brayton cycle system.

Xu et al. (Xu et al, 2021) proposed and established a helium-xenon (He-Xe) thermal physical property model based on virial coefficient and compared it with the ideal gas model to clarify that the addition of xenon gas makes the He-Xe mixed working medium show obvious non-ideal gas characteristics. Liu et al. (Liu et al, 2020) used Non-dominated Sorting Genetic Algorithm (NSGA-Ⅱ) tominimize the total system mass by optimizing key parameters of system components. The performance of the He-Xe Brayton cycleand each component design module are calculated. The optimum values of key parameters corresponding to the minimum mass ofthe system at a specific turbine inlet temperature are given. Romano et al. (Romano et al, 2020. Romano et al 2021) optimized heat pipe radiators for He-Xe Brayton cycles in space reactors. The cooling side thermal model and the Brayton cycle model are coupled to obtain the design scheme of the cooling system under different cycle parameters. At the same time, the minimum specific mass is taken as the optimization objective, and the inlet temperature of the optimized gas cooler is 513.2K. Miao et al. (Miao et al, 2022)used a mixture of nitrous oxide and helium (N2OeHe) as the working fluid of space nuclear recompression Brayton cycle to study the effects of splitting ratio, pressure ratio, maximum temperature, minimum temperature and minimum pressure on the performance of recompression Brayton cycle system and the mass of Brayton unit.

For space energy systems, in addition to system efficiency, the mass of the system is also an important indicator to determine the launch cost and the feasibility of the design scheme (Demuth, 2003). At the same time, for the Brayton cycle system, the working fluid still has high energy quality after heating by the reactor and doing work by turbine (Wang et al, 2017). Therefore, in this paper, part of the working fluid was bled after the turbine to directly enters the reactor for heating, so as to increase the inlet temperature of the reactor and reduce the total circulation heat absorption. The compressor is the main power consumption equipment in the Brayton cycle, so the inlet temperature of the compressor should be reduced as much as possible. This paper adopted the scheme of multiple compression, intercooling and splitting. After multiple compression and cooling, the working fluid can reach the highest pressure required by the cycle.

In this paper, under the background of space nuclear energy, the Brayton cycle system was bled and multiple compressed, and He-Xe mixture was used as the cycle working fluid. The thermodynamic model and mass estimation model of the system were established. The effects of bleeding ratio, number of compressors, pressure ratio, compressor inlet temperature and turbine inlet temperature on the thermal efficiency and mass of multiple compression Brayton system were studied. At the same time, taking the thermal efficiency and mass of the system as the optimization objectives, NSGA-Ⅱ was used to optimize the system.

2. MULTIPLE COMPRESSION BRAYTON SYSTEM MODEL
2.1. Description of the multiple compression Brayton system

The schematic diagram of the space nuclear multiple compression Brayton system (SNMCBS) is shown in Figure 1.
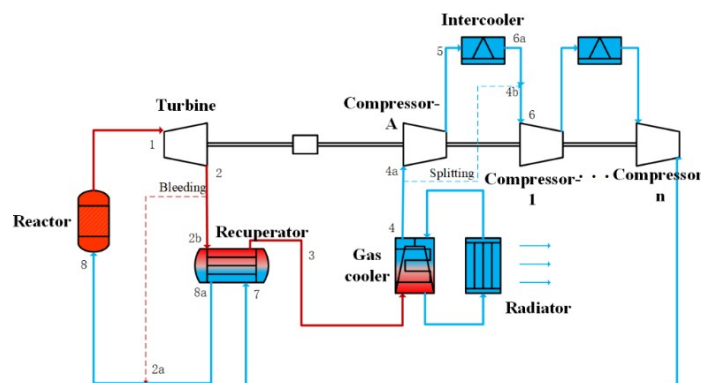
Figure 1: Schematic diagram of SNMCBS

The heat source of the system is the reactor, and the cold source is the space environment. He-Xe mixture with the molar mass of 40g/mol (El-Genk et al, 2006) is selected as the working fluid. He-Xe is heated by the reactor and enters the turbine to do work through expansion (process 1→2). At this time, the working fluid outlet the turbine still has a high energy quality. Thus, part of the working fluid is bled directly into the reactor for heating (process 2→2a), and the remaining working fluid enters the recuperator for heat exchange (process 2b→3). After the recuperator the large amount of heat still in the working fluid is discharged into space in the form of thermal radiation through the gas cooler and radiator, which cools the temperature of the working fluid to the compressor inlet temperature (process 3→4). In order to reduce the inlet temperature of the compressor as much as possible, part of the working fluid is split directly into the next compressor (process 4→4b), and the remaining working fluid is compressed into compressor-A (process 4a→5). The working fluid is cooled to the inlet temperature of compressor-A by an intercooler before entering the next compressor (process 5→6a). After mixing the working fluid, it will be compressed by n compressors. And an intercooler is arranged

between each compressor, so that the working fluid can reach the highest pressure required by the system (process 6→7). After that, the working fluid enters the recuperator for heat exchange and heating (process 7→8a). Finally, it will be mixed with the bleed part and heated into the reactor (process 8→1) to complete the whole thermal cycle process.

2.2. Thermodynamic model

It is defined that the bleeding ratio x is the ratio of the working fluid mass flow rate which directly enters the reactor and the total working fluid mass flow rate, and the splitting ratio y is the ratio of the working fluid maa flow rate which split in front of the compressor-A and the total working fluid mass flow rate which need compressed.

The compressor pressure ratio π can be expressed as:

Equation 1: Pressure ratio

$$\pi = \frac{p_5}{p_4} = (\frac{T_{5s}}{T_4})^{\frac{\gamma}{\gamma-1}} = \frac{p_7}{p_6} = (\frac{T_{7s}}{T_6})^{\frac{\gamma}{\gamma-1}}$$

Where:

- γ = specific heat ratio

The compressor efficiency η_{CP} can be expressed as:

Equation 2: Compressor efficiency

$$\eta_{CP} = \frac{c_{p,0}(T_{5s} - T_4)}{c_{p,4-5}(T_5 - T_4)}$$

The turbine pressure ratio π_T can be expressed as:

Equation 3: Turbine pressure ratio

$$\pi_T = \frac{p_1}{p_2} = (\frac{T_1}{T_{2s}})^{\frac{\gamma}{\gamma-1}}$$

The turbine efficiency η_T can be expressed as:

Equation 4: Turbine efficiency

$$\eta_T = \frac{\overline{c_{p,1-2}}(T_1 - T_2)}{c_{p,0}(T_1 - T_{2s})}$$

The recuperator effectiveness ε can be expressed as:

Equation 5: Recuperator effectiveness

$$\varepsilon = \frac{h_8 - h_7}{h_2 - h_7} = \frac{\overline{c_{p,7-8}}(T_8 - T_7)}{c_{p,2}T_2 - c_{p,7}T_7}$$

Power of turbine W_T can be expressed as:

Equation 6: Power of turbine

$$W_T = m\overline{c_{p,1-2}}(T_1 - T_2)$$

Where:

- m= total mass flow rate of working fluid (kg/s)

Power of compressor-A $W_{CP,A}$ can be expressed as:

Equation 7: Power of compressor-A

$$W_{CP,A} = (1 - x)(1 - y)m\overline{c_{p,4-5}}(T_5 - T_4)$$

Power of compressor-n W_{CP,n^*} can be expressed as:

Equation 8: Power of compressor-n

$$W_{CP,n^*} = (1 - x)m\overline{c_{p,6-7}}(T_7 - T_6)$$

Net power of SNMCBS W_{net} can be expressed as:

Equation 9: Net power of SNMCBS

$$W_{net} = W_T - \left(W_{CP,A} + \sum W_{CP,n^*}\right)$$

Input heat by the reactor Q_{in} can be expressed as:

Equation 10: Input heat by the reactor

$$Q_{in} = m\overline{c_{p,8-1}}(T_1 - T_8)$$

Thermal efficiency of SNMCBS η_{th} can be expressed as:

Equation 11: Thermal efficiency of SNMCBS

$$\eta_{th} = \frac{W_{net}}{Q_{in}}$$

2.3. Mass estimation model

The mass of Brayton units (including turbine, compressor and generator) is estimated as follows:Specific mass of Brayton unit α_{BRU} can be expressed as (Levine, 2006):

Equation 12: Specific mass of Brayton unit

$$\alpha_{BRU} = -5.893 \left(\frac{T_1}{1000}\right)^2 + 5.829 \frac{T_1}{1000} + 12.19$$

Mass of Brayton unit M_{BRU} can be expressed as (Barrett et al, 2005):

Equation 13: Mass of Brayton unit

$$M_{BRU} = C \cdot \alpha_{BRU} P_e^{0.7} N_{BRU}^{0.3} \frac{1 + 0.52 ln\pi_T}{1.93}$$

Where:

- C= empirical coefficient (1.8)
- P_e= electrical power of SNMCBS
- N_{BRU}= number of Brayton unit

The mass of heat exchanger (including recuperator, intercooler and gas cooler) is estimated as follows:

The total heat transfer area of the heat exchanger A_{HEX} is (Lee et al, 2013):

Equation 14: Total heat transfer area of heat exchanger

$$A_{HEX} = \frac{(1-x)mc_{p,c}}{U} \left(\frac{\varepsilon}{1-\varepsilon}\right)$$

Where:

- U= Heat transfer coefficient ($W/m^2 \cdot K$)

The heat exchanger volume V_{HEX} is (John et al, 2006):

Equation 15: Heat exchanger volume

$$V_{HEX} = \frac{A_{HEX}}{STF}$$

Where:

- STF= stacking factor (3280.8 m^2/m^3)

The dimensions of the heat exchanger are:

Equation 16: Heat exchanger dimensions

$$L_H = V_{HEX}^{\frac{1}{3}}$$
$$L_L = 2L_H$$
$$L_W = \frac{1}{2}L_H$$

Where：

- L_H= height of heat exchanger (m)
- L_L= length of heat exchanger (m)
- L_W= width of heat exchanger (m)

The mass of heat exchanger core M_{cor} is:

Equation 17: Heat exchanger core mass

$$M_{cor} = \rho_{cor} V_{HEX}$$

Where:

- ρ_{cor}= heat exchanger core density (1000 kg/m^3)

The mass of heat exchanger case M_{cas} is:

Equation 18: Heat exchanger case mass

$$M_{cas} = 2\delta\rho_{cas}(L_H L_W + L_H L_L + L_W L_L)$$

Where:

- δ= case thickness (5 mm)
- ρ_{cas}= heat exchanger case density (3900 kg/m^3)

The mass of heat exchanger duct M_{duct} is:

Equation 19: Heat exchanger duct mass

$$M_{duct} = 0.25 M_{cas}$$

Then, the heat exchanger mass M_{HEX} can be expressed as:

Equation 20: Heat exchanger mass

$$M_{HEX} = M_{cor} + M_{cas} + M_{duct}$$

The mass of radiator is estimated as follows:

The radiation area A_{rad} is (Juhasz, 2008):

Equation 21: Radiation area

$$A_{rad} = \frac{Q_{in}(1 - \eta_{th})}{\sigma \omega T_4^4}$$

Where:

- σ= Stephens-Boltzmann constant ($5.67 \times 10^{-11} kW/m^2 \cdot K^4$)
- ω= material emissivity (0.9)

The total radiation area A_{RAD} is:

Equation 22: Total radiation area

$$A_{RAD} = f \cdot A_{rad}$$

Where:

- f= form factor (1.5)

The mass of radiator M_{RAD} is (Juhasz, 2007):

Equation 23: Radiator mass

$$M_{RAD} = \alpha \cdot A_{RAD}$$

Where:

- α= mass to area ratio (3 kg/m^3)

Thus, SNMCBS total mass $Mass_{tot}$ can be expressed as:

Equation 24: SNMCBS mass

$$Mass_{tot} = M_{BRU} + M_{HEX} + M_{RAD}$$

3. RESULTS AND DISCUSSION

For SNMCBS, the bleeding ratio, the number of compressors, the pressure ratio, the compressor inlet temperature and the turbi ne

inlet temperature will affect the temperature and pressure of the circulating working fluid and the thermal work conversion of each component of the system, thus affecting the efficiency and mass of the system. Therefore, based on the thermodynamic model and mass estimation model of SNMCBS, the influences of key parameters of the system, such as bleeding ratio, compressor number, pressure ratio, compressor inlet temperature and turbine inlet temperature, on the thermal efficiency and mass of the system were analysed. At the same time, NSGA-Ⅱ was used to optimize the system.

The selection of working conditions of SNMCBS with fractional compression is shown in Table 1.

Table 1: The selection of SNMCBS working conditions

Parameters	Value
Environment temperature	$T_0 = 200K$
Turbine inlet temperature	$T_1 = 1200K$
Compressor-A inlet pressure	$p_4 = 0.7MPa$
Compressor-A inlet temperature	$T_4 = 400K$
Compressor-n number	n=2
Pressure ratio	$\pi_{CP1} = \pi_{CP2} = \cdots = \pi_{CPn} = 1.5$
Turbine efficiency	$\eta_T = 0.88$
Compressor efficiency	$\eta_{CP} = 0.86$
Generator efficiency	$\eta_G = 0.95$
Recuperator effectiveness	$\varepsilon = 0.9$
Bleeding ratio	x=0.2
Splitting ratio	y=0.4
Mass flow rate	m=1.8 kg/s

3.1. Influence of compressor inlet temperature, T_4

Figure 2 shows the variation of SNMCBS thermal efficiency with pressure ratio under different compressor inlet temperature conditions. It can be seen that under the same pressure ratio condition, the system thermal efficiency decreases gradually with the compressor inlet temperature increasing. Under the same compressor inlet temperature condition, the system thermal efficiency also decreases with the gradual increase of pressure ratio. And the higher the compressor inlet temperature, the more the system thermal efficiency decreases with the increase of pressure ratio. In the process of increasing the compressor inlet temperature from 350K to 400K, the pressure ratio changes between 1.5~2.5, and the reduction of the system thermal efficiency increases 7.39%~10.14%.

The total mass of SNMCBS under different compressor inlet temperatures varies with the pressure ratio that is shown in Figure 3. Under the same pressure ratio condition, with the compressor inlet temperature increasing, the system mass gradually decreases. Under the same compressor inlet temperature, the mass of the system increases gradually with the increase of pressure ratio. And the higher the compressor inlet temperature, the less the system mass increases with the increase of the pressure ratio. In the processof increasing the compressor inlet temperature from 350K to 400K, the pressure ratio changes between 1.5~2.5, and the increase in the system total mass is reduced from 2221.98kg to 1555.65kg.
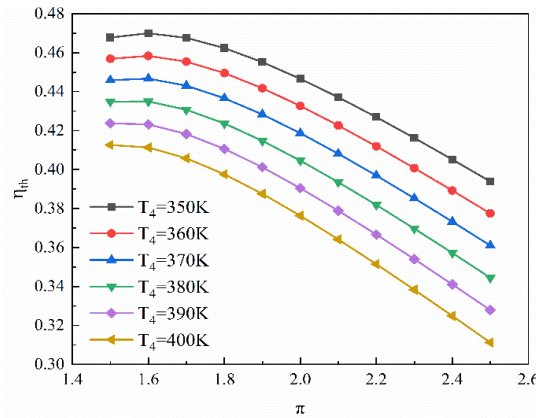

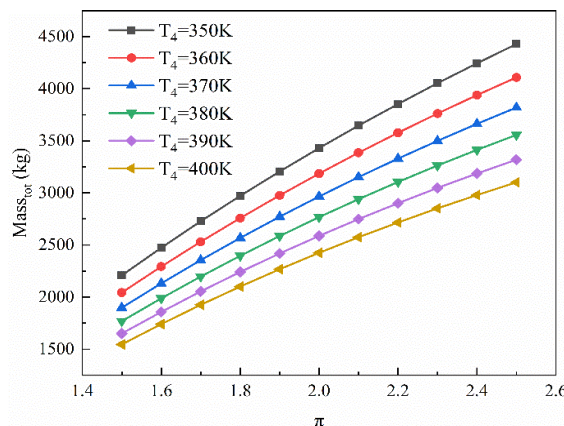*Figure 2: Influence of T_4 on the system thermal efficiency*

Figure 3: Influence of T_4 on the system mass

3.2. Influence of turbine inlet temperature, T_1
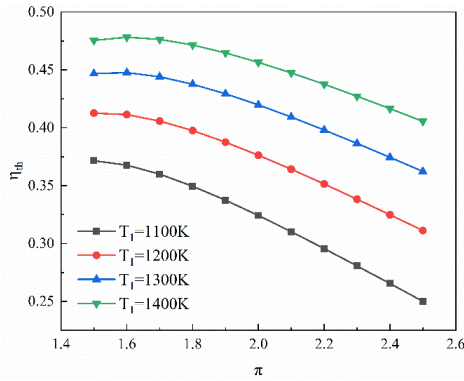
Figure 4: Influence of T_1 on the system thermal efficiency
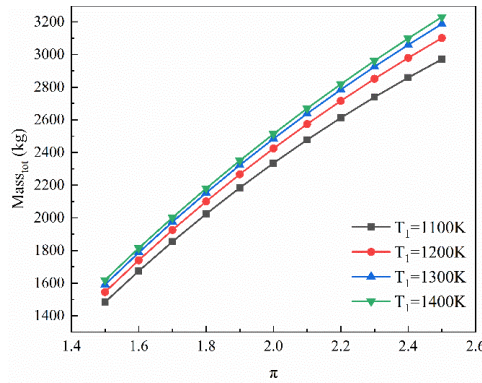
Figure 5: Influence of T_1 on the system mass

Figure 4 shows the influence of different turbine inlet temperatures on the system thermal efficiency as the pressure ratio changes. It can be seen that under the same pressure ratio condition, the system thermal efficiency is gradually improved with the increase of the turbine inlet temperature. Under the same turbine inlet temperature, the system thermal efficiency decreases gradually with the increase of pressure ratio. And the higher the turbine inlet temperature, with the increase of the pressure ratio, the lower the thermal efficiency of the system. In the process of increasing the turbine inlet temperature from 1100K to 1400K, the pressure ratio changes between 1.5~2.5, and the reduction of the system thermal efficiency is reduced from 12.14% to 6.99%.

As shown in Figure 5, the system total mass varies with the pressure ratio under different turbine inlet temperatures. Under the same pressure ratio condition, the system mass gradually increases with the increase of the turbine inlet temperature. Under the same turbine inlet temperature, the system mass increases gradually with the increase of pressure ratio. And the higher the turbine inlet temperature, the more the total mass increases with the increase of the pressure ratio. In the process of increasing the turbine inlet temperature from 1100K to 1400K, the pressure ratio changes between 1.5~2.5, and the system mass increases 1487.47kg~1611.22kg.

3.3. Influence of bleeding ratio, *x*

Figure 6: Influence of bleeding ratio on the system thermal efficiency

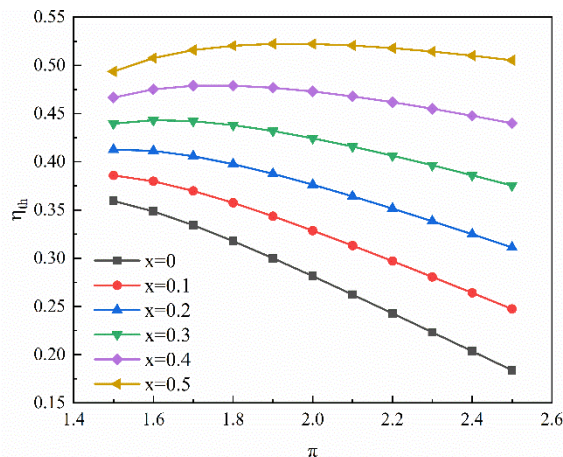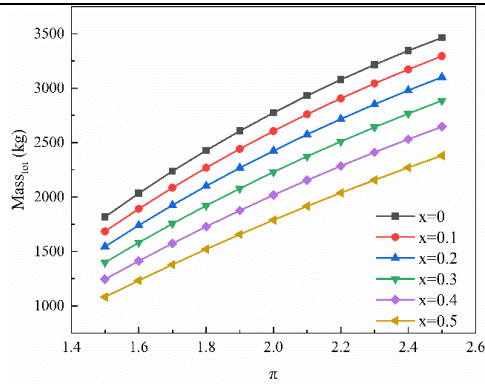*Figure 7: Influence of bleeding ratio on the system mass*

Figure 6 shows the impact of the system thermal efficiency with different bleeding ratio as the pressure ratio changes. Under the same pressure ratio, the system thermal efficiency is gradually improved with the increase of the bleeding ratio. Under the same bleeding ratio, the system thermal efficiency decreases gradually with the increase of pressure ratio. And with the increase of the bleeding ratio and the increase of the pressure ratio, the system thermal efficiency decreases less. In the process of increasing the bleeding ratio from 0 to 0.5, the pressure ratio changes between 1.5~2.5, and the reduction of the system thermal efficiency is reduced from 17.56% to 2.65%.

The total mass of the system varies with the pressure ratio under different bleeding ratio is shown in Figure 7. It can be seen that under the same pressure ratio condition, with the increase of the bleeding ratio, the system mass gradually decreases. Under the same bleeding ratio condition, the total mass gradually increases with the increase of the pressure ratio. The higher the bleeding ratio, the less the system mass increases with the increase of the pressure ratio. In the process of increasing the bleeding ratio from 0 to 0.5, the pressure ratio changes between 1.5~2.5, and the increase in the system mass is reduced from 1646.61kg to 1298.91kg.

3.4. Influence of compressor-n number, *n*

As shown in Figure 8, the system thermal efficiency varies with the pressure ratio under the condition of different compressor-n numbers. Under the same pressure ratio, the system thermal efficiency decreases gradually with the increase of the compressor-n number. Under the same compressor-n number, the system thermal efficiency decreases gradually with the increase of pressure ratio. And with the increase of the pressure ratio, the system thermal efficiency decreases more. In the process of increasing the number of compressor-n from 2 to 4, the pressure ratio changes between 1.5 and 2.5, and the reduction of system thermal efficiency increases from 10.14% to 28.83%.

Figure 9 shows the effect of different compressor-n numbers on the system total mass as the pressure ratio changes. Under the same pressure ratio condition, the system mass gradually increases with the increase of compressor-n number. Under the same number of compressor-n, with the increase of pressure ratio, the system total mass gradually increases. And the more compressors, as the pressure ratio increases, the more the system mass increases. In the process of increasing the number of compressor-n from 2 to 4, the pressure ratio changes between 1.5 and 2.5, and the system total mass increases from 1555.65kg to 2192.97kg.
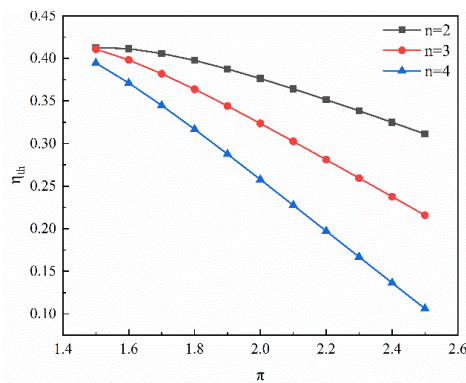
Figure 8: Influence of compressor-n number on the system thermal efficiency
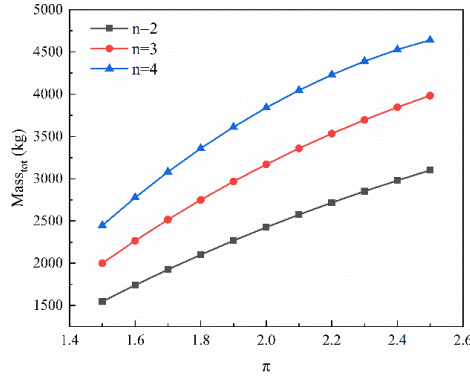
Figure 9: Influence of compressor-n number on the system mass

3.5. System optimization

In this paper, NSGA-Ⅱ which is the most widely and successfully applied in genetic algorithms (Besarati et al, 2009), was used for system optimization. The bleeding ratio x, the compressor-n number n, the pressure ratio π, the compressor inlet temperature T_4, and the turbine inlet temperature T_1 were taken as the optimization parameters. The system thermal efficiency and total mass were taken as objective functions.

The regression equation of objective functions obtained by response surface method are as follows:

Equation 25: Regression equation of system thermal efficiency

$$\eta_{th} = 0.1346 - 0.001384A + 0.000337B \\ + 0.2218C - 1.0161D \\ + 0.2006E - 0.09606CE \\ + 0.189DE - 0.01502E^2$$

Equation 26: Regression equation of system total mass

$$Mass_{tot} = 3058.5167 - 55.4767A \\ + 7411.5947C - 8450.5598D \\ + 2042.6771E - 13.7114AC \\ + 27.0882AD - 5.6041AE \\ + 0.09092A^2$$

Where:

- A= compressor inlet temperature, T_4
- B= turbine inlet temperature, T_1
- C= pressure ratio, π
- D= bleeding ratio, x
- E= number of compressor-n, n

The constraint conditions are:

Equation 27: Constraint conditions

$$\begin{cases} 350K \leq A \leq 400K \\ 1100K \leq B \leq 1400K \\ 1.5 \leq C \leq 2.5 \\ 0 \leq D \leq 0.5 \\ 2 \leq E \leq 4 \end{cases}$$

In this optimization, the initial population number was set to 300, the crossover factor in the breeding process is 0.7, and the variation factor is 0.3. After 200 generations of breeding, the Pareto optimal boundary curve of SNMCBS is obtained, as shown in Figure 10.
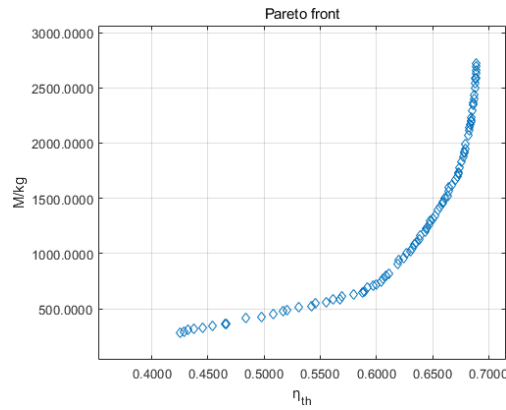
Figure 10: Pareto optimal boundary of SNMCBS

The Pareto optimal solution set of double objective optimization is shown in Table 2.

Table 2: Pareto optimal solution set

Parameter		T_4	T_1	π	x	n	η_{th}	$Mass_{tot}$
	1	367.82	1116.9	1.51	0.4	2	0.4335	1225.64
Optimal	2	363.36	1186.5	1.52	0.4	2	0.4613	1320.02
solution	3	361.28	1294	1.51	0.4	3	0.5358	1856.37
	4	361.88	1267.1	1.52	0.4	3	0.529	1862.65

Table 2 shows the parameter settings when the system thermal efficiency and total mass are both optimized. It can be seen that the compressor inlet temperature is between 361K~368K, the turbine inlet temperature is between 1116K~1294K, the pressure ratio can be determined to be about 1.5, the bleeding ratio is 0.4, the number of compressor-n is 2 or 3. And the optimal thermal efficiency of the system is between 0.43 and 0.54. The optimal total mass of the system is between 1225kg~1863kg.

4. CONCLUSION

In this paper, under the background of space nuclear energy, the working fluid in Brayton cycle was bled and multiple compressed. The thermodynamic model and mass estimation model of SNMCBS were established by using He-Xe mixture as the circulating working fluid. The effects of bleeding ratio, number of compressors, pressure ratio, compressor inlet temperature and turbine inlet temperature on the system thermal efficiency and total mass were studied. At the same time, taking the thermal efficiency and total mass as the optimization objectives, NSGA-Ⅱ was used to optimize the system. The conclusions are as follows:

- For SNMCBS, the system thermal efficiency gradually increases with the increase of the turbine inlet temperature and bleeding ratio. And with the increase of compressor inlet temperature, pressure ratio and compressor-n number, the system thermal efficiency gradually decreases.

- For SNMCBS, with the increase of the turbine inlet temperature, the pressure ratio and the compressor-n number, the system total mass gradually increases. And with the increase of compressor inlet temperature and bleeding ratio, the system total mass decreases.

- NSGA-Ⅱ was used to optimize SNMCBS with double objective, and the Pareto optimal boundary of the system was obtained. The compressor inlet temperature ranges from 361K to 368K, and the turbine inlet temperature ranges from 1116K to 1294K. The pressure ratio can be determined to be about 1.5, the bleeding ratio is 0.4, and the number of compressor-n is 2 or 3. The system optimal thermal efficiency is between 0.43 and 0.54, and the optimal total mass is between 1225kg and 1863kg.

5. REFERENCES

Bennett GL, Hemler RJ, Schock A, 1996. Space nuclear power-An overview. Journal of Propulsion and Power, 12 (5), 12-15.

Bennett GL, 2008. Mission interplanetary ： using radioisotope power to explore the solar system. Energy Conversion and Management, 2008 (49), 382-392.

Fan SQ, Li MH, Li SZ, et al, 2017. Thermodynamic analysis and optimization of a Stirling cycle for lunar surface nuclear power system. Applied thermal engineering, 111, 60-67.

Guan C, Chai X, Zhang T, et al, 2024. Mass and efficiency optimization of a He-Xe Brayton cycle for mobile, land-based nuclear microreactors. Energy Conversion and Management, 301, 118011.

Liu Y, Wang Y, Huang D, 2019. Supercritical CO2 Brayton cycle: A state-of-the-art review. Energy, 189, 115900.

Xu C, Kong F, Yu D, et al, 2021. Influence of non-ideal gas characteristics on working fluid properties and thermal cycle of space nuclear power generation system. Energy, 222, 119881.

Liu H, Chi Z, Zang S, 2020. Optimization of a closed Brayton cycle for space power systems. Applied Thermal Engineering, 179, 115611.

Romano LFR, Ribeiro GB, 2021. Optimization of a heat pipe-radiator assembly coupled to a recuperated closed Brayton cycle for compact space power plants. Applied Thermal Engineering, 196, 117355.

Romano LFR, Ribeiro GB, 2020. Cold-side temperature optimization of a recuperated closed Brayton cycle for space power generation. Thermal Science and Engineering Progress, 17, 100498.

Miao X, Zhang H, Sun W, et al, 2022. Optimization of a recompression supercritical nitrous oxide and helium Brayton cycle for space nuclear system. Energy, 242.

Demuth S.F, 2003. SP100 space reactor design. Progress in Nuclear Energy, 42(3), 323-359.

Wang C, Chen J, Qiu S, Tian W, 2017. Performance analysis of heat pipe radiator unit for space nuclear power reactor. Annals of Nuclear Energy, 103, 74–84.

El-Genk MS, Tournier JM, 2006. Selection of noble gas binary mixtures for Brayton space nuclear power systems. 4th International Energy Conversion Engineering Conference and Exhibit (IECEC). San Diego: AIAA.

Levine B, 2006. Space nuclear power plant pre-conceptual design report, for information. Knolls Atomic Power Lab. SPP-67210-0010.

Barrett MJ, Johnson PK, 2005. Performance and mass modeling subtleties in closed-Brayton-cycle space power systems. 3rd International Energy Conversion Engineering Conference. San Francisco, CA: American Institute of Aeronautics and Astronautics.

Lee SM, Kim KY, Kim SW, 2013. Multi-objective optimization of a double-faced type printed circuit heat exchanger. Applied Thermal Engineering, 60(1-2), 44-50.

John S, Lee M, 2006. A Comparison of Coolant Options for Brayton Power Conversion Heat Rejection Systems. AIP Conference Proceedings, 813 (1), 682–693.

Juhasz AJ, 2008. High conductivity carbon-carbon heat pipes for light weight space power system radiators. 6th International Energy Conversion Engineering Conference (IECEC), 5784.

Juhasz A, 2007. Heat Transfer Analysis of a Closed Brayton Cycle Space Radiator. 5th International Energy Conversion Engineering Conference and Exhibit (IECEC). St. Louis, Missouri.

Besarati S, Atashkari K, Jamali A, et al, 2009. Multi-objective thermodynamic optimization of combined Brayton and inverse Brayton cycles using genetic algorithms. Energy Conversion and Management, 51(1), 212-217.

#179: Optimization of carbon-based hydration salt composite for thermochemical adsorption heat storage and application

X.K. Xu [1], X.L. Chang [2], Ting Yan [3], W.G. Pan [4], L.W. Wang [5]

[1] College of Energy and Mechanical Engineering, Shanghai University of Electric Power, Shanghai 201306, China,
m178521082578@163.com

[2] College of Energy and Mechanical Engineering, Shanghai University of Electric Power, Shanghai 201306, China,
cxlyf1008@163.com

[3] College of Energy and Mechanical Engineering, Shanghai University of Electric Power, Shanghai 201306, China,
yt81725@126.com

[4] College of Energy and Mechanical Engineering, Shanghai University of Electric Power, Shanghai 201306, China,
pweiguo@163.com

[5] Institute of Refrigeration and cryogenic engineering, Shanghai Jiao Tong University, Shanghai 200240, China,
lwwang@sjtu.edu.cn

Abstract: Thermochemical adsorption heat storage (TAHS) based on hydrated salts can store large amounts of thermal energy at low losses and can be used effectively in industries such as building space heating and domestic hot water. However, pure hydrated salts suffer from low thermal conductivity, and hydrothermal stability such as deliquescence and decomposition under certain conditions. To overcome these drawbacks and increase the heat storage density of the material, its commercialization and widespread practical application was achieved. The impregnation of carbon-based materials with salts is the most used method to achieve efficient TAHS systems. This paper reviews the principles of TAHS for heat storage and the criteria for the selection of adsorption and storage materials. In addition, the common physical parameters for heat storage of pure salt and thermal chemisorption are introduced. Three optimization methods for pore size, composition and system design are presented to address the gaps in the current experiments and applications of thermal chemisorption.

1. INTRODUCTION

With industrialization and population growth, the extensive use of fossil fuels has exacerbated the greenhouse effect. In 2019, global energy-related carbon dioxide emissions reached a new high of 3.31 billion tons, The continuous increase in carbon dioxide emissions has attracted worldwide attention. To ensure stable global climate and ecological security, the Intergovernmental Panel on Climate Change (IPCC) has set the limit of temperature rise to 1.5 degrees Celsius and aims to reach peak greenhouse gas emissions by 2025 and achieve net zero carbon emissions by 2050 (Bastida et al., 2019). In order to solve the energy crisis and environmental problems and achieve zero emissions goals, the innovative use of renewable energy is also requisite except for improving the efficiency of existing energy infrastructure (Bastida et al., 2019). So far, more than 50% of the final energy consumption still heavily relies on the combustion of fossil fuels. There is still a lot of room for the development of renewable energy. However, although the renewable energy market has grown rapidly in terms of installed capacity and investment, its share in the final thermal energy demand is still low (Chen et al., 2021). One important reason for this underutilization is that renewable energy as an unstable energy source cannot directly meet users' needs for heating stability and adjustable flexibility. As a result, thermal energy storage (TES) as a critical strategy has been widely recognized and attracted people's attention (Al-Shetwi et al., 2020).

There are three main forms for the purpose of heat storage: sensible heat storage (SHS), latent heat storage (LHS), chemical heat storage (CHS) (Figure 1). SHS is a means of storing thermal energy through the temperature change of the material itself. The SHS materials mainly include water, rock, concrete, etc. Although SHS has the advantages of relatively simple principle and low cost, its application is limited by relatively low energy storage density, non-constant heat output temperature and high heat loss (Zhang and Wang, 2020, Gao et al., 2020). Phase change materials store/release thermal energy as the latent heat of melting/solidifying at a constant temperature that corresponds to the phase transition temperature. This process, known as latent heat storage (LHS), offers a greater energy storage capacity than sensible heat storage (SHS) (Aydin et al., 2015). Nevertheless, LHS has the disadvantages of supercooling, poor crystallization and nucleation phenomena, and ease of leakage of melting phase change materials during the phase transition, which restricts their further applications (Zhao and Wang, 2019). CHS has a very high theoretical energy density, which is about 3-30 times higher than SHS and 2-20 times higher than LHS. Moreover, CHS has negligible heat loss during thermal energy storage period and even has the potential for inter-seasonal thermal energy storage. Therefore, it can provide an feasible solution for long-term thermal energy storage in a more compact and efficient manner (Yan et al., 2015). CHS can be divided into chemical reaction heat storage, thermochemical absorption heat storage and thermochemical adsorption heat storage (TAHS). Thermochemical storage processes are characterized by the destruction and reorganization of the molecular structure of substances between reactants, and the reaction conditions are harsh. (Yan et al., 2015). Thermochemical adsorption refers to the reaction of solid adsorption thermal storage material to the gas adsorbent, while thermochemical absorption refers to the reaction of the liquid absorbent to the gas absorbent Thermochemical adsorption. In contrast, Thermochemical adsorption is more suitable for low-grade solar thermal energy and industrial waste heat temperature zones (Palomba and Frazzica, 2019, An et al., 2019). Among them, the hydrated salt system has the advantages of high heat storage density, low regeneration temperature (solar collectors or waste heat can be utilized), low cost, etc., and has a broad development space in building space heating and domestic hot water production (Scapino et al., 2017a).

Although TAHS based on hydrated salts has many advantages in its application, there are also some related problems, this type of problem is mainly due to poor heat and mass transfer and poor cycle stability (Zhang and Wang, 2020, N'Tsoukpoe et al., 2014). Specific manifestations include agglomeration, melting, deliquescence, reduced activity (Criado et al., 2014, Steiger et al., 2008). These characteristics make it challenging to use hydrated salts as monomers in CHS systems. In response to these questions. Carbon-based materials offer a solution (Kumar et al., 2021). On the one hand, with the introduction of carbon-based materials with high thermal conductivity, the thermal conductivity of the composites is improved, which in turn enhances the charging/discharging reaction rate of the TAHS, on the other hand, the carbon-based materials with different sizes and pore structures provide a stable support structure for the hydrated salt. It also prevents or reduces agglomeration and swelling However, with the addition of carbon-based materials, the thermal storage density of the composites will be reduced, Therefore, an optimal solution needs to be found to balance the advantages and problems associated with the introduction of carbon-based materials. (Tso and Chao, 2012, Zhang et al., 2007). In terms of the theoretical energy density of TAHS materials, there is still a gap between theoretical energy density and actual energy density, which leads to the gap between laboratory and commercial applications. Therefore, it is necessary to find stable materials with adsorption properties, suitable preparation methods and reactor structures to improve the efficiency of TCES systems for optimal application (Cot-Gores et al., 2012).

(a)   **(b)**   **(c)**
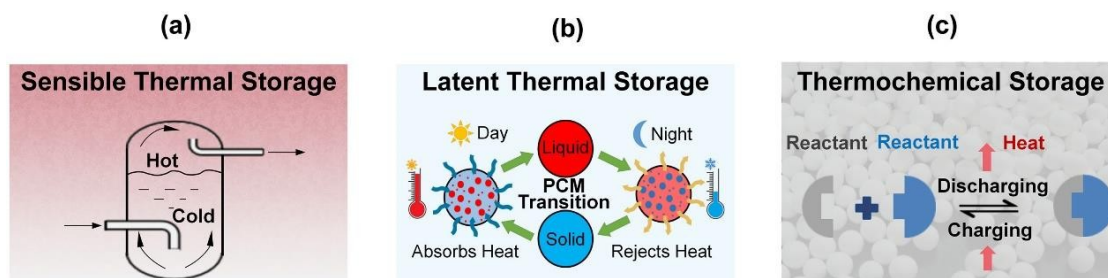
Figure 1: Illustration of three different TES technologies: (a) sensible heat storage (Belz et al., 2015). (b) latent heat storage (Faraj et al., 2020). (c) thermochemical heat storage. Bottom: temperature versus stored heat during charging/discharging processes (Zeng et al., 2023)

TAHS based hydrated salts have been well studied and developed. At the material level, Cabeza et al. (Cabeza et al., 2017) selected promising salt hydrates based on their feasibility and limitations. Lin et al. (Lin et al., 2021) categorized hydrated salts and analyzed and reviewed chlorides, sulphates, and several common hydrated salts. Marín et al. (Marín et al., 2021) made some progress on the use of lithium as a relevant compound for CHS. Some important advances have been made in adsorption systems for CHS. At the

reactor and system measurement level, Scapino et al. (Scapino et al., 2017b) reviewed the TES system mainly from the reactor perspective, discussed the heat and mass transfer in the reactor during the heat storage process, the corrosion resistance of the materials and other issues, and made recommendations for experimental metrics to implement common key performance indicators to assess the application performance and economic value of the reaction system. Zhang and Wang et al. (Zhang and Wang, 2020) provided a detailed classification of reactor types and evaluated open and closed reactors in terms of input problems, output performance and performance parameters. However, most of the above studies focused on the reaction characteristics and optimization of hydrated salts as well as the application of TCES systems and lacked the consideration of the characteristics and application of thermal energy storage systems from the point of view of adsorbent matrices. Herein, a systematic review of carbon-based materials for TAHS. A systematic review of the optimization strategies and application of carbon-based salt hydration composite for TAHS for thermal energy storage and energy conversion is provided. Therein, we mainly address CNT-based materials, graphene-based materials, and graphite-based materials for TAHS in detail. I hope this will point the way to future goal oriented Carbon-based materials for TAHS.

2. THERMAL STORAGE PROPERTIES OF CARBON-BASED COMPOSITE HYDRATED SALT MATERIALS
2.1. Concept of thermochemical adsorption heat storage

According to the different types of reactions, CHS can be divided into TAHS, thermochemical absorption, and thermochemical reaction storage. Thermochemical reaction storage involves the disruption and rearrangement of molecular structures between reactants, while the essence of thermochemical adsorption and absorption storage processes lies in the capture and subsequent release of reaction heat by energy storage materials (adsorbents/sorbate) with specific gases (adsorbates/sorbate) (Zhang and Wang, 2020). Silica gel/water, zeolite/water, inorganic salt/water, chloride/ammonia, NaOH/water, and others are commonly used thermochemical energy storage materials (Yu et al., 2013, Xu et al., 2018). Hydrated salts, on the one hand, exhibit desirable traits such as high heat storage capacity, environmental adaptability, and economy (Dake et al., 2021). Moreover, they are suitable for medium to low-temperature energy storage applications, offering effective utilization of low-grade energy sources like industrial waste heat and solar energy. Thus, they had extensive applications in the field of construction, including residential heating, domestic hot water supply, and seasonal thermal energy storage (Fumey et al., 2019).

The reversible gas-solid reaction of vapor-salt working pair can be described as follows:

$$MX \cdot nH_2O + yH_2O \rightleftharpoons MX \cdot (n + y) H2O + y\Delta H_r \qquad (1)$$
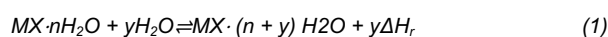
Where:

- $MX \cdot nH_2O$ = hydrated salts of the salt
- MX/ H_2O = working pairs
- ΔH_r = the heat released (stored) in the reaction

The thermochemical principle of TAHS based on hydrated heat storage is shown in Figure 2 shows that the working process can be divided into charging, storage and discharging (Yan and Zhang, 2022).

The heat storage reaction controls the storage and release of energy by the direction of the reversible reaction. The adsorbent and the sorbent, as a working pair, are the two dependent factors that determine the adsorption principle, and the reaction is controlled by the combination and separation of the two materials. TAHS based on hydrated heat storage is carried out in two stages. In the heat storage stage, the adsorbent undergoes desorption reaction. Under the action of external heat source, the bonding force between the adsorbent and water will break, and then the attached material will gradually desorb the adsorbent. At this stage, energy storage is realized by the conversion of thermal energy to chemical potential energy. During the discharge process, the adsorbent binds to the sorbate and releases energy. At relatively low temperatures, the temperature and pressure in the reaction vessel are lowered, resulting in an equilibrium drop, and the salt reacts with the work material to produce a large amount of heat to meet the external heat demands (Zhang and Wang, 2020).
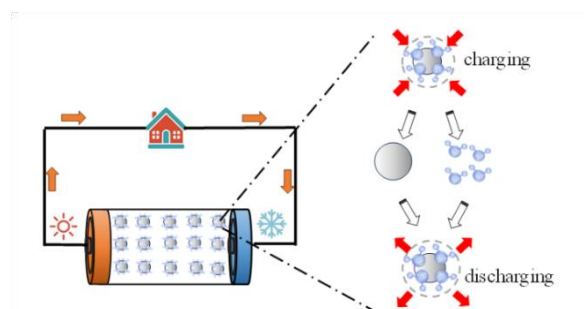
Figure 2: Thermochemical adsorption heat storage concept

The interaction between solid and gas phases is rather intricate and can be summarized as physical adsorption, capillary condensation, deliquescence, crystal hydrate formation, and vapor absorption at the surface of solid particles. Inorganic salts primarily undergo hydration reactions, deliquescence, and absorption when interacting with water vapor. In the realm of Relative Humidity (RH) < Deliquescence Relative Humidity (DRH), an interaction occurs between inorganic salts and water vapor, giving rise to the formation of hydrated salts. This phenomenon is known as the process of hydration. Due to variations in the water absorption

process of inorganic salts during this stage, the resulting products also differ. Taking $MgCl_2$ as an example, within this process, $MgCl_2·2H_2O$, $MgCl_2·4H_2O$, and $MgCl_2·6H_2O$ are formed. In the realm of RH > DRH, the phenomenon of continuous water absorption by the hydrated salts ensues. At this stage, the resulting reactants tend towards stability and uniformity. Soon thereafter, Subsequently, the occurrence of deliquescence in the hydrated salts surfaces, forming a saturated solution film atop their exterior. In due course, the hydrated salts gracefully dissolve, while the film persistently absorbs water vapor, until a state of saturated salt solution is gracefully achieved. In this state, solid hydrated salts, liquid saturated salt solution, and gaseous water vapor coexist, thus bequeathing this ethereal journey with the appellation of a trilateral adsorption process. In this state, solid hydrated salts, liquid saturated salt solution, and gaseous water vapor harmoniously, rendering this process as the trinity of adsorption. Should the ambient relative humidity persistently escalate, the saturated solution shall transform into a dilute solution, thus invoking the process known as liquid absorption. Conversely, the dehydration of inorganic salts represents the antithesis of water absorption, as the process of desorption/dehydration unfolds in the opposite direction (Yan and Zhang, 2022). However, when pure salt hydrates are employed solely for thermal energy storage, a decline in performance can be observed due to issues such as agglomeration and insufficient heat and mass transfer. To address this quandary, the salt hydrates are embedded within a porous matrix. This ingenious approach not only broadens the range of applicable salt hydrates but also enables the effective utilization of highly hygroscopic salts. With the introduction of a porous matrix, not only does it lend itself to the entire realm of thermochemical adsorption for heat storage, but it also incorporates the facet of physical adsorption. This augmentation enhances the heat storage performance of the entire process. Furthermore, the porous matrix adeptly alleviates the issue of deliquescence in salt hydrates. It provides an effective storage medium for salt solutions, and the cumulative pore volume of the composite adsorbent further elevates the maximum adsorption capacity of the entire process (Xu et al., 2019).

2.2. Thermochemical adsorption materials

Thermal energy cannot be efficiently converted to electrical energy for heating and storage due to its low quality and is generally used directly in the form of thermal energy for space heating and domestic hot water production, which requires the output temperature of this heat so their more stable nature, but their lower heat storage density and higher cost price hindered the further development of such physisorption materials. Meanwhile, hydrated salts have become the most widely used material of choice for medium- and low-temperature CHS due to their high heat storage density, more suitable exothermic temperature, and low cost (Scapino et al., 2017b).

Even though hydrated salts are the most promising materials for CHS, not all hydrated salts are suitable for energy storage applications. Currently, hydrated salts that are widely used include mainly sulfates ($MgSO_4$, $CuSO_4$, $Al_2(SO_4)_3$), bromides ($SrBr_2$ and LiBr), etc. (Zhao et al., 2021). Because diverse types of hydrated salts have different structures, leading to differences in their physicochemical properties, different types of saline compounds have certain choices for different external conditions. Therefore, the suitability of different types of hydrated salts for different application scenarios can be analyzed based on the following physical and chemical properties.

Thermal conductivity is an important characteristic of hydrated salts. The thermal conductivity of the material mainly has an impact on the heat transfer rate of the charging and discharging process, which in turn affects the efficiency of the overall heat storage system. To a certain extent, materials with higher thermal conductivity can enhance heat transfer. When the thermal conductivity of the material is high, the rate of adsorption and desorption increases. Currently, most of the hydrated salts have low thermal conductivity (Li et al., 2022). Fopah Lele et al. (Fopah Lele et al., 2015) measured the thermal conductivity of four chemical salts and guarded hot cartridge reactor (GHC), where numerical simulations were performed based on closed and open thermal storage systems and the thermal conductivity was fitted with a polynomial function using temperature as the independent variable. This led to the conclusion that the thermal conductivity of the four brine compounds $CaCl_2$, $CaCl_2·6H_2O$ $SrBr_2$, $SrBr_2·6H_2O$, $MgCl_2$, $MgCl_2·6H_2O$ varied between 0.2 ~ 0.7 W/ (m K) between 20 °C and 70 °C. This indicates that the thermal conductivity of the pure salt is low and does not meet the application requirements in isolation, therefore, it needs to be optimized.

Cycle stability is also an important measure. During the ongoing cycle, the volume of the brine compound is changed, and some materials can swell and agglomerate, leading to the closure of stomata and restricting the vapor flow channels, which lowers the rate of the reaction as well as the cyclability, causing a decrease in the cycling efficiency of the whole system (Clark et al., 2020). Donkers et al. (Donkers et al., 2016) studied $CuCl_2$, $CuSO_4$, $MgCl_2$ and $MgSO_4$ during ten reaction cycles and they concluded that during the first dehydration cycle, the hydrated salt crystals break into a pseudomorph in which the hydrated salt releases water molecules more readily. The fracturing effect is greater when the hydrate volume changes more. By comparing between these, witha limited number of runs, copper dichloride proved to be the most promising heat storage material. However, the lower ESD (1.3 GJ/m^3) is disadvantaged compared to the other three hydrated salts.

When using pure salt for TAHS, the conversion of brine compounds from low to high hydrates needs to take place at a high-water vapor pressure. But when the relative humidity/pressure is high, at the end of hydration a saturated salt solution is obtained instead of a salt solution, which is called deliquescence. The happening of the liquid solution causes a loss of reaction salt and worsens mass transfer. considered deliquescence as a first order phase change from solid form to liquid and the chemical and physical properties of the material change as the relative humidity changes. Whiting et al. (Whiting et al., 2014) found that when the relative humidity exceeds a threshold, $MgCl_2·6H_2O$ surface then generates a film that affects the efficiency of the system. In addition, when the hydration temperature is too high, $MgCl_2·6H_2O$ will undergo undesirable reactions affecting the hydrolysis process, for example, $MgCl_2·6H_2O$ will decompose into Mg (OH)Cl and HCl, and when the $MgSO_4·7H_2O$ particles are restricted in the diffusion process, the dehydration process produces an aqueous solution, and so on and so forth, the reaction will stall.

3. SALT IN CARBON-BASED MATRIX

Although hydrated salts have high energy density when used for TAHS, the performance is not ideal when used alone. For example,

the low thermal conductivity of hydrated salts, poor heat transfer performance, the formation of hard films during hydration of $MgSO_4$, excessive hydration and aggregation of $CaCl_2$ high hydrate, irreversible harmful side reactions of $MgCl_2$ low hydrate, and other defects affect the effectiveness of the entire system. Stability is weakened, energy density is reduced, corrosion is generated affecting the system lifetime (Yu et al., 2015). To improve the effectiveness of the overall system, researchers have used porous materials as matrices to improve the mass transfer performance and stability of hydrated salts. With the addition of a certain number of hydrated salts in a certain porous matrix compounded with a carbon-based porous matrix, the reaction kinetics and chemical stability of the whole system were improved. In addition to this, different carbon-based porous matrix properties, advantages and influencing factors vary and should be analyzed in relation to the carbon-based material of the hydrated salt to be combined (Li et al., 2022).

3.1. CNTs-hydrated salts

CNTs are typical carbon nanomaterials, which exhibit large surface area, high thermal conductivity, low bulk density and chemical stability. When CNTs are involved in the TAHS and heat storage of hydrated salts, it not only improves the thermal conductivity and specific heat of the material, but also helps to optimize the compact TCES system. Yang et al. (Yang et al., 2017) modified lithium hydroxide monohydrate with carbon nanotubes (WMCNTs), carbon nanorods (CNSs), and activated carbon (AC) for chemical heat storage. Pure $LiOH \cdot H_2O$ exhibits remarkably high energy density (1440 kJ/kg) and a mid-temperature reaction process. Despite these merits, in its pure salt state, its hydration rate and thermal conductivity remain relatively low level. In comparison, carbon-based nanomaterials like carbon nanotubes (CNTs) and carbon nanospheres (CNSs) showcase notable attributes, including a substantial surface area, heightened thermal conductivity, low volumetric density, and commendable chemical stability (Figure 3a) (Hou et al., 2020). Furthermore, the introduction of oxygen functionalities in the nanomaterials enhances nanomaterials hydrophilic properties significantly. When these carbon, nanomaterials are combined with $LiOH \cdot H_2O$, they accelerate the rate of hydration reactions. Additionally, the presence of CNSs and MWCNTs further enhances the heat storage density of the composite material, yielding values of 2020 kJ/kg and 1804 kJ/kg, respectively (Figure 3b). Theoretically, the thermal conductivity of MWCNTs can reach 3000 W/ (m K) in the longitudinal direction, but the thermal conductivity of $LiOH \cdot H_2O$/MWCNTs is still maintained at a low level (Figure 3c) (Balandin, 2011). This may be due to the low dimensionality of WMCNTs. Alexander et al. (Balandin, 2011) modified a CHS material based on lithium hydroxide monohydrate with in situ formed three-dimensional nickel carbon nanotubes (Ni-CNTs), The incorporation of Ni-CNTs into the composite material not only leads to a substantial increase in thermal conductivity, ranging from 3.13 to 3.78 W/ (m K), but also, owing to the presence of hydrophilic functional groups on the surface of Ni-CNTs that foster hydrogen bonding interactions with H_2O, establishes an effective hydrophilic reaction interface and surface effects (Figure 3d). These effects significantly reduce the activation energy of the thermochemical reaction, resulting in a remarkable decrease in the activation energy of Ni-CNTs-$LiOH \cdot H_2O$-1 to 23.3 kJ/mol. Furthermore, the use of Ni-CNTs as a substrate contributes to a substantial enhancement in the heat storage density of $LiOH \cdot H_2O$, with a remarkable increase to 3935 kJ/kg. This value surpasses that of pure lithium hydroxide by an impressive factor of 5.9 (Figure 3e).

Chan et al. (Chan et al., 2015) applied MWCNTs and 13X as an additive to improve the adsorption performance of the composite adsorbent. The incorporation of MWCNTs has engendered a notable augmentation in the total pore volume and specific surface area of the adsorbent, thereby elevating the adsorbent's water adsorption capacity from 0.09 kg/kg to a commendable 0.5 kg/kg. Additionally, it has conspicuously heightened the thermal conductivity of the composite adsorbent. Under conditions spanning the temperature spectrum of 30-70°C, the composite adsorbent's thermal conductivity has ascended from the modest range of 0.08-0.13 W/(m K) to a remarkable spectrum of 0.27-0.8 W/ (m K). Within the text, the significance of MWCNT incorporation is substantiated through the utilization of a finite element simulation model. The simulation results serve as a compelling testament, unequivocally establishing CNT-CA-1 (the MWCNT-embedded 13X/$CaCl_2$ adsorbent) as a paragon of superior heat storage performance when compared to the other two materials. In contrast to the utilization of zeolite 13X molecular sieve in isolation, CNT-CA-1 attains a remarkable 6.5-fold increase in specific cooling power (SCP), reaching an impressive 1113.4 W/kg. Furthermore, the addition of MWCNT adsorbent resulted in a substantial increase in the adsorbent's coefficient of performance (COP) and SCP performance, exceeding 20%, when used simultaneously with Zeolite 13X/$CaCl_2$.
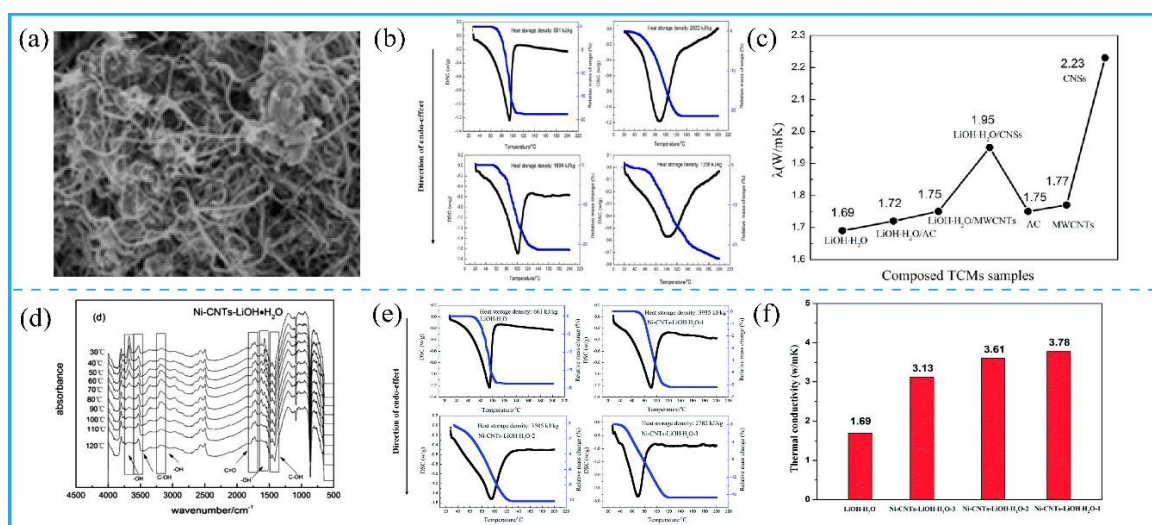
Figure 3: (a) SEM images of $LiOH \cdot H_2O$/MWCNTs (Yang et al., 2017). (b) TG-DSC curves of as-synthesized samples: LiOH-CNSs /MWCNTs/AC after 1 h hydration (Yang et al., 2017). (c) Thermal conductivity of CNSs, MWCNTs, AC, $LiOH \cdot H_2O$, LiOH-H2O-CNSs/MWCNTs/AC (Yang et al., 2017). (d) The in situ DRIFT spectroscopy of dehydration reaction of Ni-CNTs–$LiOH \cdot H_2O$ (Balandin, 2011). (e) TG-DSC curves of as-synthesized samples: Ni-CNTs–LiOH-1/LiOH-2/ LiOH-3after 1 h hydration (Balandin, 2011). (f) Thermal conductivity of $LiOH \cdot H_2O$, Ni-CNTs–$LiOH \cdot H_2O$-1/$LiOH \cdot H_2O$-2 /$LiOH \cdot H_2O$-3 (Balandin, 2011)

3.2. Graphite-hydrated salts

Graphite is a material composed of carbon atoms. Its crystal structure is made up of multiple planes arranged in a regular pattern, with each atom on each plane arranged in a regular pattern as well. Graphite has high thermal conductivity and stability. Its thermal conductivity is 1.5-3 times that of copper, and it can maintain stable thermal conductivity even at high temperatures. In addition, graphite also has a relatively high specific surface area and porosity, making it a promising carbon-based matrix. Cammarata et al. (Cammarata et al., 2018) prepared $SrBr_2$@natural graphite shape-stable composite adsorbent materials, and the results showed that the use of graphite greatly improved the thermal conductivity of TCS composite materials. Compared with pure salt, thermal conductivity increased by a factor of. The use of graphite not only improves the hydration/dehydration kinetics, but also reduces the hysteresis of the hydration/dehydration cycle of the pure $SrBr_2$ salt. Within the temperature range of 50-150 °C, the composite material has good heat storage performance, and the energy storage density can reach 500 kJ/kg. However, due to the limitations of heat transfer and mass transfer, not all stored energy can be released.

The natural graphite is processed by intercalation, washing, drying and high-temperature expansion to obtain a porous worm-like expanded graphite (EG). When EG is involved in a porous matrix to participate in the TAHS, it not only augments the thermal conductivity of pure salt by a factor of 5 to 10, but also serves as a porous matrix, averting the aggregation of pure salt particles. Li et al. (Li et al., 2020) developed a shape stable LiOH/EG composite material with EG as a porous matrix. The thermal conductivity of the sample with 8wt% EG doping was 6.52 W/ (m K), which was 6.5 times higher than that of pure salt, and the energy density was 1120 kJ/kg, and it had good stability. Zhao et al. (Zhao et al., 2016) has developed a 10 kWh short-term adsorption TES device using LiCl/EG composite adsorbent. Under experimental conditions, the heat storage capacity reached 10.25 kWh, and the heat storage density of the composite adsorbent was 3142 kJ/kg.

When natural graphite containing intercalated compounds is heated to an appropriate temperature, the compounds can rapidly decompose and produce a large amount of gas, causing the graphite to expand along the axial direction into worm-like expanded natural graphite (ENG). Lahmidi et al. (Lahmidi et al., 2006) illuminates that while hybridization with ENG can ameliorate the agglomeration predicaments inherent in pure $SrBr_2$, the specimens of highest density exhibit subpar mass transfer performance and diminished power output, thus necessitating a delicate equilibrium between volumetric density and mass transfer. Korhamer et al. (Korhammer et al., 2016) prepared composite materials incorporating ENG-$CaCl_2$ for thermal energy storage. The findings of this investigation revealed that, despite an increase in thermal conductivity, the materials exhibited a significant propensity for hygroscopic degradation. Under the conditions of KCl supplementation, it is possible to effectively alleviate this issue, results findings elucidate that, in terms of hygroscopicity, following dehydration at T = 200 °C, the ingress of H_2O molecules into the 2 KCl/$CaCl_2$- ENG composite material surges to 7.4. Concerning energy density, in contrast to untreated $CaCl_2$, the energy loss for the 2 KCl /$CaCl_2$-ENG composite material, post-dehydration at T = 200°C, is merely 5.5%.

Mix calcium nitrate and ethylenediamine with ENG, stir until uniform, then let it stand at room temperature to form a white precipitate. Filter, wash and dry to obtain ENG-TSA (Wang et al., 2011). The thermal conductivity of the solid composite material treated with sulfuric acid of ENG-TSA can reach 7 W/ (m K) (Wang et al., 2006). Xu et al. (Xu et al., 2018) developed a new type of 13X zeolite/$MgSO_4$/ENG-TSA composite material (Figure 4c, d). The theoretical energy storage capacity of magnesium sulfate is 3377.0 kJ/kg. Experimental results. Due to the existence of ENG-TSA, the composite material exhibits excellent heat transfer rate and shows a higher temperature rise rate in the adsorption heat recovery process.
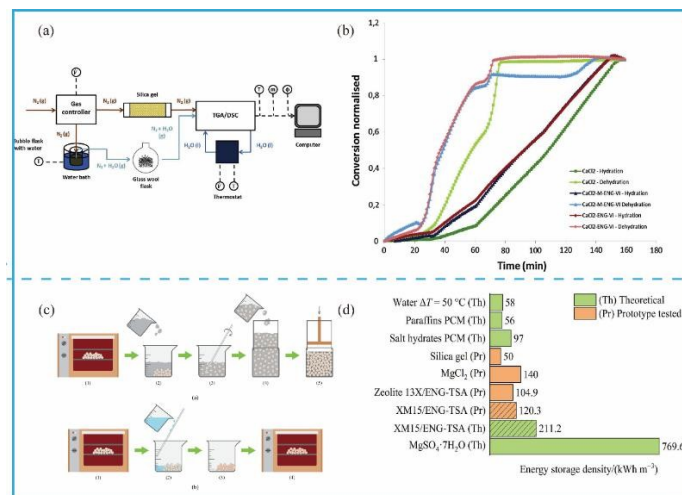
Figure 4: (a) Schematic illustration of composite materials based on chlorides for thermal energy storage experimental setup (Rammelberg et al., 2016). (b) Water sorption/desorption cycle of $CaCl_2$-MSH-ENG-VI, CaCl2-ENG-VI and untreated $CaCl_2$ (Rammelberg et al., 2016). (c) The preparation procedures of zeolite 13X/ENG-TSA and zeolite 13X/$MgSO_4$ (Balandin, 2011). (d) Comparison of energy storage densities of zeolite 13X/ENG-TSA, XM15/ENG-TSA, $MgSO_4·7H_2O$, and some typical TES media (Balandin, 2011)

3.3. Graphene-hydrated salts

2D graphene, a monolayer crystal of carbon atoms in the form of a hexagonal lattice, Graphene has better physical properties than other materials, such as high thermal conductivity, high electron mobility, high Young's modulus values, and large surface area.

Therefore, 2D graphene is a promising candidate for enhancing the thermal conductivity and photothermal and electrothermal conversion efficiency of composite materials. 2D graphene and its derivatives include graphene foams, graphene aerogels and so on (Chen et al., 2021).

$MgCl_2$ has high hydration enthalpy. But At temperature range from 20 °C to 100 °C and RH = 33%, $MgCl_2$ exhibits hygroscopic behavior, the phenomenon reduces the thermal density of the material, and during the hygroscopic process, moreover HCl and MgOHCl are produced, which can cause severe corrosion of the reactor. In addition, under the conditions of T = 30 ℃ with DRH ≈ 90%, although the hydrated salt of $MgSO_4$ has promising reaction enthalpy and good structural stability. Its low kinetics limit its application. To solve these problems, Ousaleh (Ait Ousaleh et al., 2020) combines $MgSO_4$, $MgCl_2$ and their mixtures into graphene matrix novel hybrid thermochemical materials that have been prepared for medium and low temperature heat storage applications. The Cyclic wetness impregnation protocol was used to improve the cyclic stability of the graphene substrate, so that the hydrated salts could be uniformly and well distributed in the graphene substrate, and control hydrated salt dispersion into graphene sheets and prevented the agglomeration issue by facilitating the water vapor diffusion during the hydration process (Figure 5a). $MgSO_4$ will decompose at 56.6 ℃ to produce an unstable phase, followed by decomposition to form $MgSO_4·H_2O$ (Figure 5b). This process will produce a mass loss of 40.9% and a reaction enthalpy of 1585.9 kJ/kg. The reaction temperature of $MgCl_2$ is 150 ℃, and the reaction enthalpy is 1280.2 kJ/kg. However, $MgCl_2$ exhibits severe corrosiveness in an environment above 165 ℃. The stability of the mixed material has been improved when the two salts are mixed. When graphene is further added, the composite material is further optimized. The storage density of Graphene-$MgSO_4$ and Graphene-$MgCl_2$ reached 1194.3 kJ/kg. Although it is lower than that of pure salt, its heat storage capacity is still higher than that of other composite materials. The use of graphene as an inert matrix provided the ability to control the dehydration temperature of the resulted composites and can be widely used in building technology. The composites also had relatively good cycling stability, with a slight decrease of 1.3% and 9.6% in the storage density of Graphene-$MgSO_4$ after 10 and 60 cycles, respectively (Figure 5c). with a much lower loss rate compared to the decrease in storage density involved in unimpregnated $MgSO_4$. The reaction enthalpy of Graphene-$MgSO_4$ decreased by 14.2% after 60 cycles and increased by 64.2% compared to $MgCl_2$. In addition, the compromised behavior was recorded for Graphene-$MgSO_4$-$MgCl_2$ with excellent cycling stability and switch temperature range for low-temperature applications.

Yang et al. (Yang et al., 2016) The GO-LiOH composites were prepared by hydrothermal method by oxidizing graphene. The $LiOH·H_2O$ content of GO as a matrix was about 27.9 wt.% Even though the brine compound could be relatively well distributed in the matrix material, the overall energy density decreased due to its low loading rate, the matrix did not improve the thermal storage density of the brine compound much. Yan et al. (Yan et al., 2021) exhibited GO as a raw material to synthesize graphene aerogel (GA). The GA was first synthesized by using chemical reduction of GO, followed by hydrothermal reaction, freeze-drying and wet impregnation methods (Figure 5d). Then, $CaCl_2$ was enclosed in the GA matrix. The GO unique three-dimensional network porous structure and high porosity of the matrix improved the adsorption properties of the composite adsorbent (Figure 5e). The salt loading of the composite adsorbent was as high as 96%, which greatly enhanced the energy density of the composite material. Moreover, there exist chemical interactions between functional groups of GO and divalent metal ions (Mg^{2+}, Ca^{2+}, Cu^{2+}, Co^{2+}), It can form a stable structure by chemical cross-linking and provide abundant sites, which is beneficial for the efficiency of hydrated salts and dehydration processes. The $CaCl_2$@GA composite sorbent exhibits multistep water sorption−desorption process, including solid−gas chemisorption from anhydrous $CaCl_2$@GA to $CaCl_2·4H_2O$@GA at low RH, solid−liquid deliquesce to strong $CaCl_2$ solution@ GA, and liquid−gas absorption from strong $CaCl_2$ solution@ GA to weak $CaCl_2$@GA at high RH. The long adsorption process enables the composite material to have a good water absorption of 2.89 g/g. Through experimental research on laboratory-scale $CaCl_2$@GA (Figure 5f). it was found that its energy density reached 1580 kWh/m^3 and power density reached 815W/kg, with excellent thermal stability and fast adsorption kinetics performance (Kong et al., 2012). This is beneficial to improve the efficiency of hydrated salts hydration and dehydration processes. Yan et al. (Zhou and Zhang, 2019) further prepared GOA-$MgCl_2·6H_2O$ thermochemical composites by hydrothermal and freeze-drying methods (Figure 5g). Because of the problem of low crystallinity of $MgCl_2$, the charging (dehydration) temperature of the composite adsorbent was reduced. With the increase of GOA content, the charging temperature gradually decreased. The heat absorption peak temperature of GOA-M50 (50%wt. $MgCl_2$) was 90 °C lower than that of pure $MgCl_2$. When the loading rate of $MgCl_2·6H_2O$ reached 90%, the energy density was 1598 kJ/kg (Figure 5i). This characteristic makes the dehydration (loading) temperature more flexible and can be controlled by adjusting the loading rate of GOA. This technology can be applied to solar heat storage temperature to optimize solar energy utilization cost and efficiency.
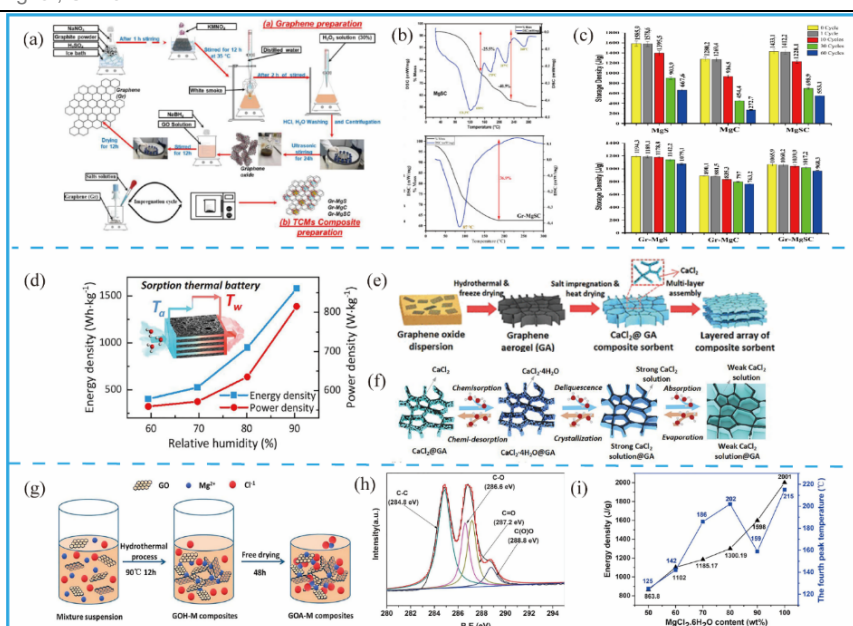
Figure 5: (a) Synthesis protocol of graphene and TCMs composites (Ait Ousaleh et al., 2020). (b) DSC-TG of MgSO₄, MgCO₃, MgSO₄/MgCO₃ and the composites (Ait Ousaleh et al., 2020). (c) Storage density measurements of MgSO₄, MgCO₃, MgSO₄/MgCO₃ and the composites during the cyclability test (Ait Ousaleh et al., 2020). (d) Synthesis and characterization of graphene aerogel-based composite sorbents (Yan et al., 2021). (e) Synthesis procedure of graphene aerogel (GA)-based composite sorbents (CaCl₂@GA) (Yan et al., 2021). (f) Energy density and power density of CaCl₂@GA sorbent at RH from 30% to 90% with thickness of 2.1 mm (Yan et al., 2021). (g) Schematic illustration of fabrication process and formation mechanism of GOA-M composites (Zhou and Zhang, 2019). (h) XPS pattern of C1s of GO (Zhou and Zhang, 2019). (i) Dependance of energy storage density and the fourth peak temperature of the GOA-M composites on MgCl2·6H₂O content (Zhou and Zhang, 2019)

4. CONCLUSION

Compared to sensible heat storage and latent heat storage, hydrated salt based CHS has a higher energy density and near zero heat loss, enabling long-term energy storage. However, the use of hydrated salts alone for heat storage still faces several challenges, such as low thermal conductivity, agglomeration, and deliquescence. This leads to a reduction in the energy storage density of the overall system. Therefore, hydrates can be combined with carbon-based materials to stabilize the properties of hydrates to meet the needs of different scenarios.

To address these issues, this article provides a systematic overview of carbon-based materials that participate in TAHS. Based on their structure, these materials are divided into 1D, 2D and 3D materials. For example, 1D (carbon nanotubes/fibers), 2D (graphene) and 3D (EG/hydrogel) materials are analyzed in detail with respect to their structure, preparation methods, energy conversion and advanced utilization.

A summary of hydrated salts that participate in TAHS is provided. For the application of hydrated salts in TAHS, there are many physical quantities as indicators of TAHS. It is necessary to introduce carbon-based materials into composite material analysis to measure the performance of composite materials in application scenarios. Subsequently, this article provides important examples of CNT-based, graphite-based, and graphene-based materials that are combined with hydrated salts and measures them with the above physical parameters.

The composite of carbon-based materials and hydrated salts does not superimpose the advantages or theoretical data of the two or there are significant differences between specific systems in operation. This article optimizes the composite adsorbent through pore structure, composition ratio and system structure to enhance its energy storage capacity.

Currently, TAHS technology is further developed to cover a wider range of applications such as heat redistribution, energy conservation and emission reduction. TAHS has excellent performance in passive solar buildings based on TAHS principles and atmospheric water harvesting. With the development of carbon-based materials and improvement strategies, it is believed that this technology will become a universal application of high-performance batteries, making effective use of renewable energy and suitable energy distribution a reality.

5. REFERENCES

AIT OUSALEH, H., SAIR, S., MANSOURI, S., ABBOUD, Y., FAIK, A. & EL BOUARI, A. 2020. New hybrid graphene/inorganic salt composites for thermochemical energy storage: Synthesis, cyclability investigation and heat exchanger metal corrosion protection performance. Solar Energy Materials and Solar Cells, 215, 110601.

AL-SHETWI, A. Q., HANNAN, M. A., JERN, K. P., MANSUR, M. & MAHLIA, T. M. I. 2020. Grid-connected renewable energy sources: Review of the recent integration requirements and control methods. Journal of Cleaner Production, 253.

AN, G. L., WANG, L. W. & GAO, J. 2019. Two-stage cascading desorption cycle for sorption thermal energy storage. Energy, 174, 1091-1099.

AYDIN, D., UTLU, Z. & KINCAY, O. 2015. Thermal performance analysis of a solar energy sourced latent heat storage. Renewable and Sustainable Energy Reviews, 50, 1213-1225.

BALANDIN, A. A. 2011. Thermal properties of graphene and nanostructured carbon materials. Nat Mater, 10, 569-81.

BASTIDA, L., COHEN, J. J., KOLLMANN, A., MOYA, A. & REICHL, J. 2019. Exploring the role of ICT on household behavioural energy efficiency to mitigate global warming. Renewable and Sustainable Energy Reviews, 103, 455-462.

BELZ, K., KUZNIK, F., WERNER, K. F., SCHMIDT, T. & RUCK, W. K. L. 2015. 17 - Thermal energy storage systems for heating and hot water in residential buildings. In: CABEZA, L. F. (ed.) Advances in Thermal Energy Storage Systems. Woodhead Publishing.

CABEZA, L. F., SOLé, A. & BARRENECHE, C. 2017. Review on sorption materials and technologies for heat pumps and thermal energy storage. Renewable Energy, 110, 3-39.

CAMMARATA, A., VERDA, V., SCIACOVELLI, A. & DING, Y. 2018. Hybrid strontium bromide-natural graphite composites for low to medium temperature thermochemical energy storage: Formulation, fabrication and performance investigation. Energy Conversion and Management, 166, 233-240.

CHAN, K. C., CHAO, C. Y. H. & WU, C. L. 2015. Measurement of properties and performance prediction of the new MWCNT-embedded zeolite 13X/CaCl$_2$ composite adsorbents. International Journal of Heat and Mass Transfer, 89, 308-319.

CHEN, X., CHENG, P., TANG, Z., XU, X., GAO, H. & WANG, G. 2021. Carbon-Based Composite Phase Change Materials for Thermal Energy Storage, Transfer, and Conversion. Adv Sci (Weinh), 8, 2001274.

CLARK, R.-J., MEHRABADI, A. & FARID, M. 2020. State of the art on salt hydrate thermochemical energy storage systems for use in building applications. Journal of Energy Storage, 27.

COT-GORES, J., CASTELL, A. & CABEZA, L. F. 2012. Thermochemical energy storage and conversion: A-state-of-the-art review of the experimental research under practical conditions. Renewable and Sustainable Energy Reviews, 16, 5207-5224.

CRIADO, Y. A., ALONSO, M. & ABANADES, J. C. 2014. Kinetics of the CaO/Ca(OH)$_2$ Hydration/Dehydration Reaction for Thermochemical Energy Storage Applications. Industrial & Engineering Chemistry Research, 53, 12594-12601.

DAKE, R. A., N'TSOUKPOE, K. E., KUZNIK, F., LèYE, B. & OUéDRAOGO, I. W. K. 2021. A review on the use of sorption materials in solar dryers. Renewable Energy, 175, 965-979.

DONKERS, P. A. J., PEL, L. & ADAN, O. C. G. 2016. Experimental studies for the cyclability of salt hydrates for thermochemical heat storage. Journal of Energy Storage, 5, 25-32.

FARAJ, K., KHALED, M., FARAJ, J., HACHEM, F. & CASTELAIN, C. 2020. Phase change material thermal energy storage systems for cooling applications in buildings: A review. Renewable and Sustainable Energy Reviews, 119, 109579.

FOPAH LELE, A., N'TSOUKPOE, K. E., OSTERLAND, T., KUZNIK, F. & RUCK, W. K. L. 2015. Thermal conductivity measurement of thermochemical storage materials. Applied Thermal Engineering, 89, 916-926.

FUMEY, B., WEBER, R. & BALDINI, L. 2019. Sorption based long-term thermal energy storage – Process classification and analysis of performance limitations: A review. Renewable and Sustainable Energy Reviews, 111, 57-74.

GAO, J. T., XU, Z. Y. & WANG, R. Z. 2020. Experimental study on a double-stage absorption solar thermal storage system with enhanced energy storage density. Applied Energy, 262.

HOU, J. H., TU, X. Y., WU, X. G., SHEN, M., WANG, X. Z., WANG, C. Y., CAO, C. B., PENG, H. & WANG, G. X. 2020. Remarkable cycling durability of lithium-sulfur batteries with interconnected mesoporous hollow carbon nanospheres as high sulfur content host. CHEMICAL ENGINEERING JOURNAL, 401.

KONG, J.-Y., CHOI, M.-C., KIM, G. Y., PARK, J. J., SELVARAJ, M., HAN, M. & HA, C.-S. 2012. Preparation and properties of polyimide/graphene oxide nanocomposite films with Mg ion crosslinker. European Polymer Journal, 48, 1394-1405.

KORHAMMER, K., DRUSKE, M.-M., FOPAH-LELE, A., RAMMELBERG, H. U., WEGSCHEIDER, N., OPEL, O., OSTERLAND, T. & RUCK, W. 2016. Sorption and thermal characterization of composite materials based on chlorides for thermal energy storage. Applied Energy, 162, 1462-1472.

KUMAR, S., SAEED, G., ZHU, L., HUI, K. N., KIM, N. H. & LEE, J. H. 2021. 0D to 3D carbon-based networks combined with pseudocapacitive electrode material for high energy density supercapacitor: A review. Chemical Engineering Journal, 403, 126352.

LAHMIDI, H., MAURAN, S. & GOETZ, V. 2006. Definition, test and simulation of a thermochemical storage process adapted to solar thermal systems. Solar Energy, 80, 883-893.

LI, W., KLEMEŠ, J. J., WANG, Q. & ZENG, M. 2020. Development and characteristics analysis of salt-hydrate based composite sorbent for low-grade thermochemical energy storage. Renewable Energy, 157, 920-940.

LI, W., KLEMEŠ, J. J., WANG, Q. & ZENG, M. 2022. Salt hydrate–based gas-solid thermochemical energy storage: Current progress, challenges, and perspectives. Renewable and Sustainable Energy Reviews, 154, 111846.

LIN, J., ZHAO, Q., HUANG, H., MAO, H., LIU, Y. & XIAO, Y. 2021. Applications of low-temperature thermochemical energy storage systems for salt hydrates based on material classification: A review. Solar Energy, 214, 149-178.

MARíN, P. E., MILIAN, Y., USHAK, S., CABEZA, L. F., GRáGEDA, M. & SHIRE, G. S. F. 2021. Lithium compounds for thermochemical energy storage: A state-of-the-art review and future trends. Renewable and Sustainable Energy Reviews, 149, 111381.

N'TSOUKPOE, K. E., RESTUCCIA, G., SCHMIDT, T. & PY, X. 2014. The size of sorbents in low pressure sorption or thermochemical energy storage processes. Energy, 77, 983-998.

PALOMBA, V. & FRAZZICA, A. 2019. Comparative analysis of thermal energy storage technologies through the definition of suitable key performance indicators. Energy and Buildings, 185, 88-102.

RAMMELBERG, H. U., OSTERLAND, T., PRIEHS, B., OPEL, O. & RUCK, W. K. L. 2016. Thermochemical heat storage materials – Performance of mixed salt hydrates. Solar Energy, 136, 571-589.

SCAPINO, L., ZONDAG, H. A., VAN BAEL, J., DIRIKEN, J. & RINDT, C. C. M. 2017a. Energy density and storage capacity cost comparison of conceptual solid and liquid sorption seasonal heat storage systems for low-temperature space heating. Renewable and Sustainable Energy Reviews, 76, 1314-1331.

SCAPINO, L., ZONDAG, H. A., VAN BAEL, J., DIRIKEN, J. & RINDT, C. C. M. 2017b. Sorption heat storage for long-term low-temperature applications: A review on the advancements at material and prototype scale. Applied Energy, 190, 920-948.

STEIGER, M., LINNOW, K., JULING, H., GüLKER, G., JARAD, A. E., BRüGGERHOFF, S. & KIRCHNER, D. 2008. Hydration of $MgSO_4 \cdot H_2O$ and Generation of Stress in Porous Materials. Crystal Growth & Design, 8, 336-343.

TSO, C. Y. & CHAO, C. Y. H. 2012. Activated carbon, silica-gel and calcium chloride composite adsorbents for energy efficient solar adsorption cooling and dehumidification systems. International Journal of Refrigeration, 35, 1626-1638.

WANG, K., WU, J. Y., WANG, R. Z. & WANG, L. W. 2006. Effective thermal conductivity of expanded graphite–$CaCl_2$ composite adsorbent for chemical adsorption chillers. Energy Conversion and Management, 47, 1902-1912.

WANG, L. W., METCALF, S. J., CRITOPH, R. E., THORPE, R. & TAMAINOT-TELTO, Z. 2011. Thermal conductivity and permeability of consolidated expanded natural graphite treated with sulphuric acid. Carbon, 49, 4812-4819.

WHITING, G. T., GRONDIN, D., STOSIC, D., BENNICI, S. & AUROUX, A. 2014. Zeolite–$MgCl_2$ composites as potential long-term heat storage materials: Influence of zeolite properties on heats of water sorption. Solar Energy Materials and Solar Cells, 128, 289-295.

XU, J. X., LI, T. X., CHAO, J. W., YAN, T. S. & WANG, R. Z. 2019. High energy-density multi-form thermochemical energy storage based on multi-step sorption processes. Energy, 185, 1131-1142.

XU, S. Z., LEMINGTON, WANG, R. Z., WANG, L. W. & ZHU, J. 2018. A zeolite 13X/magnesium sulfate–water sorption thermal energy storage device for domestic heating. Energy Conversion and Management, 171, 98-109.

YAN, T., LI, T., XU, J., CHAO, J., WANG, R., ARISTOV, Y. I., GORDEEVA, L. G., DUTTA, P. & MURTHY, S. S. 2021. Ultrahigh-Energy-Density Sorption Thermal Battery Enabled by Graphene Aerogel-Based Composite Sorbents for Thermal Energy Harvesting from Air. ACS Energy Letters, 6, 1795-1802.

YAN, T., WANG, R. Z., LI, T. X., WANG, L. W. & FRED, I. T. 2015. A review of promising candidate reactions for chemical heat storage. Renewable and Sustainable Energy Reviews, 43, 13-31.

YAN, T. & ZHANG, H. 2022. A critical review of salt hydrates as thermochemical sorption heat storage materials: Thermophysical properties and reaction kinetics. Solar Energy, 242, 157-183.

YANG, X., HUANG, H., WANG, Z., KUBOTA, M., HE, Z. & KOBAYASHI, N. 2016. Facile synthesis of graphene oxide-modified lithium hydroxide for low-temperature chemical heat storage. Chemical Physics Letters, 644, 31-34.

YANG, X., LI, S., HUANG, H., LI, J., KOBAYASHI, N. & KUBOTA, M. 2017. Effect of Carbon Nanoadditives on Lithium Hydroxide Monohydrate-Based Composite Materials for Low Temperature Chemical Heat Storage. Energies, 10.

YU, N., WANG, R. Z. & WANG, L. W. 2013. Sorption thermal storage for solar energy. Progress in Energy and Combustion Science, 39, 489-514.

YU, N., WANG, R. Z. & WANG, L. W. 2015. Theoretical and experimental investigation of a closed sorption thermal storage prototype using LiCl/water. Energy, 93, Part 2, 1523-1534.

ZENG, Z., ZHAO, B. & WANG, R. 2023. Water based adsorption thermal battery: Sorption mechanisms and applications. Energy Storage Materials, 54, 794-821.

ZHANG, P., WANG, C. & WANG, R. 2007. Composite Reactive Block for Heat Transformer System and Improvement of System Performance. Journal of Chemical Engineering of Japan, 40, 1275-1280.

ZHANG, Y. & WANG, R. 2020. Sorption thermal energy storage: Concept, process, applications and perspectives. Energy Storage Materials, 27, 352-369.

ZHAO, B. C. & WANG, R. Z. 2019. Perspectives for short-term thermal energy storage using salt hydrates for building heating. Energy, 189.

ZHAO, Q., LIN, J., HUANG, H., WU, Q., SHEN, Y. & XIAO, Y. 2021. Optimization of thermochemical energy storage systems based on hydrated salts: A review. Energy and Buildings, 244.

ZHAO, Y. J., WANG, R. Z., LI, T. X. & NOMURA, Y. 2016. Investigation of a 10 kWh sorption heat storage device for effective utilization of low-grade thermal energy. Energy, 113, 739-747.

ZHOU, H. & ZHANG, D. 2019. Effect of graphene oxide aerogel on dehydration temperature of graphene oxide aerogel stabilized $MgCl_2 \cdot 6H_2O$ composites. Solar Energy, 184, 202-208.

#183: Non-destructive evaluation of thermal conductivity in wood materials using dielectric property measurements with ground penetrating radar

Jinxia HU[1,2], Ryad BOUZOUIDJA[1,2], Tingting Vogt WU[1,2], Zoubir-Mehdi SBARTAÏ[1,2]

[1] Université de Bordeaux, CNRS, Bordeaux INP, I2M, UMR 5295, F-33400, Talence
[2] Arts et Metiers Institute of Technology, CNRS, Bordeaux INP, Ensam Université

Abstract: Accuracy and effectiveness of predicting the heat transfer in constructive materials are increasingly important for energy performance and provide crucial insights into building inspections. However, directly establishing thermal conductivity for architecture walls is challenging and time-consuming, and existing measurement methods are highly technical with restrictive boundary conditions. Therefore, we propose a data-driven method, predicting thermal conductivity from relative permittivity using ground-penetrating radar (GPR) non-destructive technique rather than direct measurement. The experiments were conducted on spruce, fir, beech and pine using GPR measurement at 2.6 GHz frequency and heat flow meter method. Our results indicate a strong linear correlation between thermal conductivity and dielectric properties, independent of wood species and type (hardwood or softwood). This correlation suggests that thermal conductivity can be accurately estimated through dielectric property measurements, demonstrating the potential for predicting thermal conductivity using GPR. This approach can be used on site, simplifies the measurement process, eliminating the need for direct thermal conductivity assessments and steady-state conditions.

1. INTRODUCTION

Global energy consumption is projected to increase by 27% by 2040, highlighting significant challenges in mitigating climate change (Gillingham *et al.*, 2021). Building materials contribute to approximately 40% of global energy consumption and nearly a quarter of global greenhouse gas emissions (Sun *et al.*, 2021). Hence, incorporating green renewable energy sources into building architecture is crucial for transforming them into energy-neutral or even energy-producing structures. Wood is widely used as a building material thanks to its notable sustainability and advantages originating from being a renewable and CO_2 storing resource (Li *et al.*, 2019; Goldhahn, Cabane and Chanana, 2021). The thermal conductivity of wood and insulation materials is an important parameter in building thermal engineering and energy conservation (Troppová *et al.*, 2015), precisely measuring thermal conductivity is key to optimizing building materials for energy efficiency, structural integrity, and comfort, as it determines a material's ability to conduct heat, essential for designing effective insulation, managing heat flow, and assessing material durability and performance under various environmental conditions, thereby influencing long-term maintenance and operational strategies (Filippidou, Nieboer and Visscher, 2019).

Currently, there are two ways by which thermal conductivity namely the steady-state method and transient method. On one hand, the use of steady state methods such as the heat-flow meter apparatus (Kawasaki and Kawai, 2006) and the guarded hot plate method, which is a standard method to measure the thermal conductivity of any specimen, especially for the materials which have low thermal conductivity (Sonderegger and Niemz, 2009; Nardi *et al.*, 2018). However, the more disadvantage of these method is that required steady-state conditions and can be invasive, time-consuming, and impractical for in-situ applications (Singh, Sharma and Narad, 2020). On the other hand, the principal merit of the transient methods is a relatively short duration of the experiments (Asako *et al.*, 2002) as well as measurements for samples of different shapes. For example, excitation pulse method based on the theory of response factors investigated and tested in three case studies by (Rasooli, Itard and Ferreira, 2016), although the results are compared to the ones obtained by ISO 9869 method (BSI, 2014) showing a good agreement, it still need validity for the walls strongly inhomogeneous in the direction of the heat flux. Moreover, (Balaras and Argiriou, 2002) illustrated some of the use and advantages of thermography in building diagnostics such as inspections of insulation problems. Regardless of the advantage of this method to the others in shortening the measurement time, it is limited to light constructions and steady climate conditions due to the required steady climate conditions such as indirect solar radiation, low wind speed, and complete evacuation of the building. Therefore, it is imperative to develop innovative strategies to overcome these challenges.

Experimental work carried out by several researchers on wood and certain wood-derivatives indicated that their thermal conductivity increases when the density grows (Vololonirina, Coutand and Perrin, 2014). Besides, it has been reported in the literature that the permittivity also increases with the density by GPR (Razafindratsima, Sbartaï and Demontoux, 2017). Therefore, the thermal conductivity of wood may be predicted by employing their dielectric properties. (Saeed *et al.*, 2022) conducted experiments to correlate thermal conductivity with dielectric properties by capacitance from an unshielded two-electrode system, exploring a method to enhance in-situ building energy efficiency evaluation. The authors reported that a coefficient of determination *r²* score of 0.88 was observed between thermal conductivity and relative dielectric of wood-frame construction with multilayers (Saeed, Malen and Krishnamurti, 2023) at 100 kHz frequency. However, the permittivity measurement only be conducted for 10 kHz and 100 kHz frequencies in this study, as (D'Alvia *et al.*, 2022) indicated that at higher frequencies, the measurement of dielectric constant of wood is more precise, while ensuring the integrity of the wood. Therefore, the use of low frequencies leads to limited accuracy, and a significant amount of research is still needed to confirm the relationship between dielectric constant and thermal conductivity. In addition, low frequency with capacitance is difficult to implement on site and cannot give the permittivity of hight thickness building walls.

For all these reasons, this study proposes a novel data-driven approach that leverages relative permittivity measurements obtained through a non-destructive ground-penetrating radar (GPR) technique to predict thermal conductivity. For that purpose, we conducted experiments on a certain material with different densities, including softwood and hardwood. Furthermore, the results of these experiments are presented and the correlation between thermal conductivity and relative dielectric constant with density is studied. With density as the linking factor, we explore the correlation between thermal conductivity and dielectric properties. By enhancing the understanding and assessment of material thermal performance, this work contributes to driving the architectural industry towards a more sustainable and eco-friendly direction, facilitating the practical application of green building and ecological construction.

2. PREPARING MATERIAL AND METHODS
2.1. Sample preparation

Four types of wood (beech, fir, pine and spruce) were used for experimental measurements. Beech and pine belong to the hardwood family, while fir and spruce belong to the softwood family. These species were chosen either because of their very common use or to cover a very wide range of densities. For example, fir and beech wood were widely used in eastern Europe for the construction of roofs and ceilings (Kolář *et al.*, 2021, pp. 1400–1900), pine and spruce occur in historical timber constructions (Klein and Grabner, 2015). Working with these species makes it possible to evaluate the effect of density on the dielectric and thermal properties of wood: Average size is 15×10×8 (cm × cm × cm) for wood. The samples densities calculated by Equation 1 are presented in Table 1.

$$\textit{Equation 1 } Density \ = \frac{m}{V}$$

Where:

- m = the wet mass of the sample in kg
- v = the volume of the sample in m³

All the measurements were made at room temperature (20 ± 2 °C).

2.2. Permittivity measurement using GPR technique

GPR technique is promising for moisture evaluation in timber structures and their early-stage diagnosis (Reci *et al.*, 2016). The electromagnetic signal received by GPR in the presence of a wood sample is subject to various influencing factors, including moisture content, wood density, temperature, and fiber orientation. These factors impact electromagnetic field attenuation, phase shift, and polarization. The methodology of defining the permittivity is explained in (Reci *et al.*, 2016). In this work, GPR equipment is composed of an electromagnetic waves pulse generator SIR 3000 from GSSI, and a pair of transmitting (Tx) and receiving (Rx) antennas in fixed-offset of 4.6 cm configuration. The ground-coupled bow-tie dipoles are employed and optimized with a frequency of 2.6 GHz. Direct and reflected signals were recorded with 2048 temporal sampling. All the measurements are carried out in a perpendicular direction (as in Figure 1), for which the electric field is perpendicular to the wood fiber. The velocity is then estimated and the dielectric constant calculated by following expression:

$$\text{Equation 2 } \varepsilon_\mathrm{r} = \left(\frac{c}{v}\right)^2$$

Where:

- ε_r = the relative permittivity of wood
- c = the speed of light in a vacuum in m s^{-1}
- v = the electromagnetic velocity in m s^{-1}

For each material type, three samples were tested.
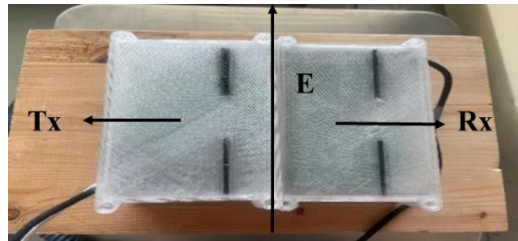

Figure 1: GPR measurements on the wood sample using ground coupled antennas. Electric field is perpendicular to fibers

2.3. Thermal conductivity using heat flow meter

Heat flow meter is traditionally recognized as the most commonly used apparatus for thermal conductivity measurement in steady-state of homogeneous materials according to the International Standard ISO 8301(Scarpa *et al.*, 2017). It is an essential instrument designed to measure and analyse the transfer of thermal energy, often referred to as heat flux, within various systems and materials. Its principle is to reproduce the uniform, unidirectional and constant thermal flux density existing through an infinite homogeneous slab-shaped specimen caught between two infinite isothermal planes. The thermal conductivity is obtained by the one-dimensional (1D) Fourier equation for a steady-state method (Dubois and Lebeau, 2015), as follows:

$$\text{Equation 3 } \lambda = q\,\frac{\Delta\mathrm{T}}{\mathrm{d}}$$

Where:

- q = heat flux in W m^{-2}
- ΔT = temperature difference across the sample in K
- d = thickness of specimen
- λ = thermal conductivity in W m^{-1} K^{-1}

In this study, only results with the heat flux perpendicular to fiber direction values are presented.

3. RESULTS
3.1. Thermal and dielectric properties

The values of density, the relative permittivity and thermal conductivity estimated for the materials used in this study are summarized in Table 1. For spruce, the results of the permittivity values are in line with the results found by (Razafindratsima, Sbartaï and Demontoux, 2017), who reported a permittivity range of 1.30 to 2.60 for perpendicular direction, respectively. The value of thermal conductivity obtained is in good agreement with the data of (Lagüela *et al.*, 2015) who reported thermal conductivity of 0.120 W m^{-1} K^{-1}. (Laboratory (U.S.), 1987) also reported values between 0.090 and 0.150 W m^{-1} K^{-1} for dry wood with density between 370 and 430 kg m^{-3}. For pine, the dielectric constant values are 1.73, which is consistent with the experimentally measured values of 1.83

(Kol, 2009), respectively. The thermal conductivity is 0.166 W m^{-1}K^{-1}, aligned with 0.167 W m^{-1} K^{-1} (Kol, 2009). For fir and beech, the results of the permittivity values are also close with the results found by (D'Alvia *et al.*, 2022), who reported a permittivity range of perpendicular direction is 2.0-2.25. In contrast, the values of thermal conductivity in this study are slightly higher than those reported by (Kol, 2009; Pásztory, Horváth and Börcsök, 2017; Flity *et al.*, 2024) since the density of the samples studied are higher than those reported in the latter study. In general, the values of permittivity and thermal conductivity obtained agree well with the literature.

Table 1: Comparison of measured permittivity and thermal conductivity with literature values

material	Density	ε	Ref. ε	λ	Ref. λ
	(kg m^{-3})	(-)	(-)	(W m^{-1}K^{-1})	(W m^{-1}K^{-1})
spruce	385.94	1.35	1.3-2.6[a]	0.135	0.12-0.15[d]
pine	508.33	1.73	1.83[b]	0.166	0.167 [d]
fir	567.21	1.97	2.0-2.25[c]	0.185	0.130-0.138[e]
beech	783.33	2.48	2.1-2.2[c]	0.217	0.179-0.191 [f,g]

[a] (Razafindratsima, Sbartaï and Demontoux, 2017) [b] (Kol, 2009) [c] (D'Alvia *et al.*, 2022) [d] (Lagüela *et al.*, 2015) [e] (Kol, 2009) [f](Pásztory, Horváth and Börcsök, 2017) [g] (Flity *et al.*, 2024)

3.2. Correlation of dielectric constant with density

Figure 2(a) shows the behaviour of the permittivity versus density at the electric field perpendicular to fiber direction. As can be observed, the permittivity increased linearly with the density, which is agree with those of the literature (Tanaka *et al.*, 2014). When an alternating voltage is applied to a dielectric, the molecules tend to align themselves with the field, and the movement depends on the internal binding forces in the material (Sahin and Ay, 2004). According to this, in less dense woods, there are fewer polar groups to accompany dielectric polarization, which means that the dielectric properties of high dense woods are higher than those of denser woods. In the figure, the regression lines derived from Equation 2 were fitted to the plots using the least-squares method. These regression lines fitted well to the plots for permittivity and had determination coefficients of r² = 0.99, indicating a very strong correlation. The nearly perfect linear fits and high r² values suggest that density is a major factor in determining the permittivity of material in the case of dry specimens.

Besides, our results for the measured dielectric properties compare favourably with those reported in the literature with perpendicular direction, as shown in Figure 2(a). The values obtained in this study fall between those predicted by (Torgovnikov, 1993), (Tanaka *et al.*, 2014), (Wang *et al.*, 2019) and (Saeed *et al.*, 2022). This variation is dependent on the different frequency ranges used in each study. As reported by (D'Alvia *et al.*, 2022), the dielectric constant decreases as the frequency increases. The slopes of the grey and orange lines are steeper than the slope observed in our study, as their results frequency were derived using frequencies of 10 kHz and 100 kHz, respectively, which are significantly lower than the 2.6 GHz frequency used in this work. In contrast, the slopes of the yellow and blue lines, measured over the frequency range of 0.1-0.2 THz, are considerably lower, aligning more closely with our findings.
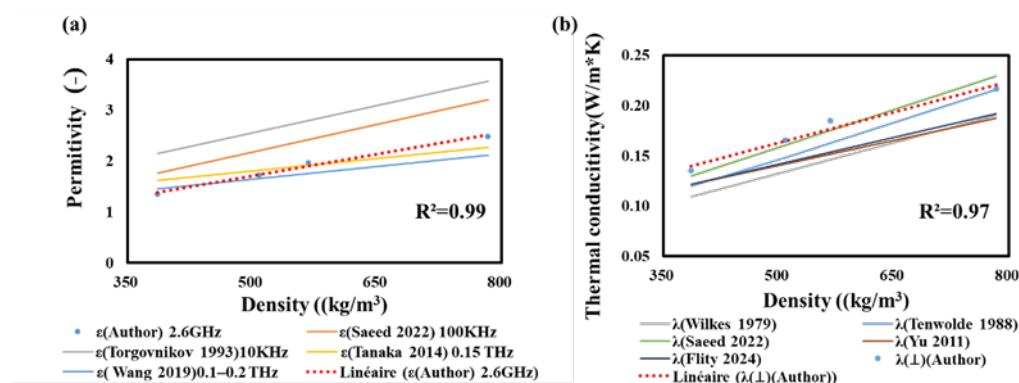
Figure 2: This figure shows the relationship between (a) permittivity and (b) thermal conductivity as a function of density in the perpendicular direction. It compares the measured data with the predicted data from equations based on past literature

.

3.3. Correlation of thermal properties with density

Figure 2(b) presents the results of thermal conductivity in perpendicular with increasing density. The strong positive linear relationship indicates that the less dense the wood is, the lower the conductivity is. This could be attributed to the fact that denser materials typically have more closely packed molecules or atoms, which can facilitate the transfer of heat more efficiently compared to less dense materials (Griffiths, Kaye and Petavel, 1997). For this reason, the thermal conductivity of beech attains its maximum value. The high r² value (0.97) underscores the robustness of this correlation, suggesting that density is a significant factor in determining the thermal conductivity of the material. This finding is crucial for material science and engineering applications, particularly in designing materials where efficient heat transfer is required, such as in thermal insulation, heat exchangers, and electronic packaging. Furthermore, Figure 2(b) also shows that the linear fit curves of perpendicular thermal conductivity are in close agreement with the

correlation obtained by (Saeed *et al.*, 2022) and (TenWolde, McNatt and Krahn, 1988). However, it shows some deviations from those reported by (Yu *et al.*, 2011), (Flity *et al.*, 2024) and (Wilkes, 1979), as most of the cited studies use dry density. Overall, the results we obtained align well with those reported in other studies.

3.4. Correlation of dielectric properties and thermal conductivity

Figure 3 presented thermal conductivity as a function of permittivity in perpendicular direction. It is observed that thermal conductivity increases linearly with permittivity as indicated by the red dotted regression lines, the coefficient of determination (R^2) values for the plots up to 0.99. The correlation in perpendicular direction at ambient temperature were compared with the literature (Saeed *et al.*, 2022), since it is almost the only parameter for which sufficient data are available in the literature, and the linear fit curve shows good agreement. Based on this strong correlation, we concluded that the relative dielectric constant could be used as a robust metric for predicting the thermal conductivity of wood, which could be pivotal for developing energy-efficient and thermally optimized building materials.
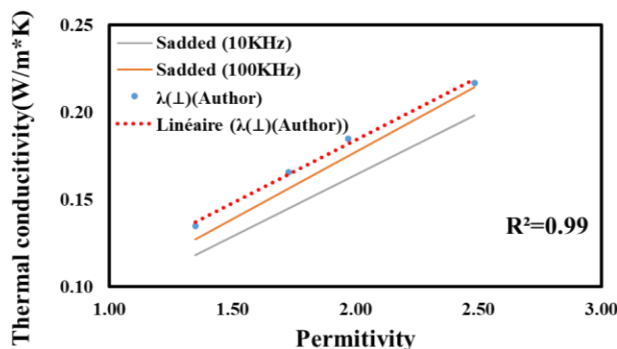

Figure 3: This figure reports the relation between thermal conductivity and permittivity

4. CONCLUSION

In this study, we measured the permittivity of various woods (spruce, fir, pine, and beech) using Ground Penetrating Radar (GPR) at a frequency of 2.6 GHz and heat-flow meter, respectively. The obtained values for thermal conductivity and permittivity are in good agreement with existing literature. The linear correlations between permittivity and thermal conductivity with the density are proposed. Furthermore, the results indicated that this correlation is independent of the type of wood (hardwood or softwood) and it increases linearly with density. Moreover, a strong correlation between thermal conductivity and the relative dielectric constant for wood materials is evident from the experimental data. Identifying this correlation marks a significant advancement in the field, indicating that thermal conductivity can be accurately estimated through dielectric property measurements.

This suggests that the potential for predicting thermal conductivity of these materials using GPR has been demonstrated. This approach simplifies the measurement process by eliminating the need for direct thermal conductivity assessments and the requirement for steady-state conditions. The ability to efficiently and non-destructively assess thermal properties using GPR technology has the potential to improve and optimize the evaluation of building materials, offering a practical and precise alternative to traditional methods. Future work will focus on the analysis of the effect of different influential parameters on this correlation between thermal conductivity and permittivity, paying special attention to the role played by humidity: as wood is a porous material with a high tendency to absorb water, its analysis with different humidity contents will be closer to its in-use reality.

5. REFERENCES

Asako, Y. et al. (2002) 'Effective thermal conductivity of compressed woods', International journal of heat and mass transfer, 45(11), pp. 2243–2253. Available at: https://doi.org/10.1016/S0017-9310(01)00330-1.

Balaras, C.A. and Argiriou, A.A. (2002) 'Infrared thermography for building diagnostics', Energy and Buildings, 34(2), pp. 171–183. Available at: https://doi.org/10.1016/S0378-7788(01)00105-0.

BSI (2014) 'ISO 9869-1: 2014-Thermal insulation—Building elements—Insitu measurement of thermal resistance and thermal transmittance; Part 1: Heat flow meter method'.

D'Alvia, L. et al. (2022) 'Permittivity-Based Water Content Calibration Measurement in Wood-Based Cultural Heritage: A Preliminary Study', Sensors, 22(6), p. 2148. Available at: https://doi.org/10.3390/s22062148.

Dubois, S. and Lebeau, F. (2015) 'Design, construction and validation of a guarded hot plate apparatus for thermal conductivity measurement of high thickness crop-based specimens', Materials and Structures, 48(1), pp. 407–421. Available at: https://doi.org/10.1617/s11527-013-0192-4.

Filippidou, F., Nieboer, N. and Visscher, H. (2019) 'Effectiveness of energy renovations: a reassessment based on actual consumption savings', Energy Efficiency, 12(1), pp. 19–35. Available at: https://doi.org/10.1007/s12053-018-9634-8.

Flity, H. et al. (2024) 'Thermal conductivity parallel and perpendicular to fibers direction and heat capacity measurements of eight wood species up to 160 °C', International Journal of Thermal Sciences, 195, p. 108661. Available at: https://doi.org/10.1016/j.ijthermalsci.2023.108661.

Gillingham, K.T. et al. (2021) 'The climate and health benefits from intensive building energy efficiency improvements', Science Advances, 7(34), p. eabg0947. Available at: https://doi.org/10.1126/sciadv.abg0947.

Goldhahn, C., Cabane, E. and Chanana, M. (2021) 'Sustainability in wood materials science: an opinion about current material development techniques and the end of lifetime perspectives', Philosophical Transactions of the Royal Society A: Mathematical, Physical and Engineering Sciences, 379(2206), p. 20200339. Available at: https://doi.org/10.1098/rsta.2020.0339.

Griffiths, E., Kaye, G.W.C. and Petavel, J.E. (1997) 'The measurement of thermal conductivity', Proceedings of the Royal Society of London. Series A, Containing Papers of a Mathematical and Physical Character, 104(724), pp. 71–98. Available at: https://doi.org/10.1098/rspa.1923.0095.

Kawasaki, T. and Kawai, S. (2006) 'Thermal insulation properties of wood-based sandwich panel for use as structural insulated walls and floors', Journal of Wood Science, 52(1), pp. 75–83. Available at: https://doi.org/10.1007/s10086-005-0720-0.

Klein, A. and Grabner, M. (2015) 'Analysis of Construction Timber in Rural Austria: Wooden Log Walls', International Journal of Architectural Heritage, 9(5), pp. 553–563. Available at: https://doi.org/10.1080/15583058.2013.804608.

Kol, H. (2009) 'Thermal and dielectric properties of pine wood in the transverse direction', BioResources, 4.

Kolář, T. et al. (2021) 'Wood species utilization for timber constructions in the Czech lands over the period 1400–1900', Dendrochronologia, 70, p. 125900. Available at: https://doi.org/10.1016/j.dendro.2021.125900.

Laboratory (U.S.), F.P. (1987) Wood Handbook: Wood as an Engineering Material. The Laboratory.

Lagüela, S. et al. (2015) 'Thermal conductivity measurements on wood materials with transient plane source technique', Thermochimica Acta, 600, pp. 45–51. Available at: https://doi.org/10.1016/j.tca.2014.11.021.

Li, T. et al. (2019) 'A radiative cooling structural material', Science, 364(6442), pp. 760–763. Available at: https://doi.org/10.1126/science.aau9101.

Nardi, I. et al. (2018) 'Quantification of heat energy losses through the building envelope: A state-of-the-art analysis with critical and comprehensive review on infrared thermography', Building and Environment, 146, pp. 190–205. Available at: https://doi.org/10.1016/j.buildenv.2018.09.050.

Pásztory, Z., Horváth, N. and Börcsök, Z. (2017) 'Effect of heat treatment duration on the thermal conductivity of spruce and poplar wood', European Journal of Wood and Wood Products, 75, pp. 843–845.

Rasooli, A., Itard, L. and Ferreira, C.I. (2016) 'A response factor-based method for the rapid in-situ determination of wall's thermal resistance in existing buildings', Energy and Buildings, 119, pp. 51–61. Available at: https://doi.org/10.1016/j.enbuild.2016.03.009.

Razafindratsima, S., Sbartaï, Z.M. and Demontoux, F. (2017) 'Permittivity measurement of wood material over a wide range of moisture content', Wood Science and Technology, 51(6), pp. 1421–1431. Available at: https://doi.org/10.1007/s00226-017-0935-4.

Reci, H. et al. (2016) 'Non-destructive evaluation of moisture content in wood using ground-penetrating radar', Geoscientific Instrumentation, Methods and Data Systems, 5(2), pp. 575–581. Available at: https://doi.org/10.5194/gi-5-575-2016.

Saeed, N. et al. (2022) 'Experimental correlation of thermal conductivity with dielectric properties of wood and wood-based materials: Possibilities for rapid in-situ building energy evaluation', Journal of Building Engineering, 50, p. 104178. Available at: https://doi.org/10.1016/j.jobe.2022.104178.

Saeed, N., Malen, J. and Krishnamurti, R. (2023) 'Predicting Effective Thermal Conductivity of Multilayered Assemblies Related to Wood-Frame Construction Based on Dielectric Properties: Data Exploration for Application to Rapid In-Situ Building Energy Evaluation'. Rochester, NY. Available at: https://doi.org/10.2139/ssrn.4387394.

Sahin, H. and Ay, N. (2004) 'Dielectric properties of hardwood species at microwave frequencies', Journal of Wood Science, 50(4), pp. 375–380. Available at: https://doi.org/10.1007/s10086-003-0575-1.

Scarpa, M. et al. (2017) 'New Measurement Procedure for U-value Assessment via Heat Flow Meter', Energy Procedia, 113, pp. 174–181. Available at: https://doi.org/10.1016/j.egypro.2017.04.050.

Singh, S., Sharma, V. and Narad, S. (2020) 'Instruments to Measure Thermal Conductivity of Engineering Materials-A Brief Review', J. Adv. Res. Mech. Eng. Technol, 7(1), pp. 16–25.

Sonderegger, W. and Niemz, P. (2009) 'Thermal conductivity and water vapour transmission properties of wood-based materials', European Journal of Wood and Wood Products, 67(3), pp. 313–321. Available at: https://doi.org/10.1007/s00107-008-0304-y.

Sun, J. et al. (2021) 'Enhanced mechanical energy conversion with selectively decayed wood', Science Advances, 7(11), p. eabd9138. Available at: https://doi.org/10.1126/sciadv.abd9138.

Tanaka, S. et al. (2014) 'Applicability of effective medium theory to wood density measurements using terahertz time-domain spectroscopy', Journal of Wood Science, 60(2), pp. 111–116. Available at: https://doi.org/10.1007/s10086-013-1386-7.

TenWolde, A., McNatt, J.D. and Krahn, L. (1988) Thermal properties of wood and wood panel products for use in buildings. DOE/OR/21697-1. Forest Service, Madison, WI (USA). Forest Products Lab. Available at: https://doi.org/10.2172/6059532.

Torgovnikov, G.I. (1993) Dielectric Properties of Wood and Wood-Based Materials. Berlin, Heidelberg: Springer (Springer Series in Wood Science). Available at: https://doi.org/10.1007/978-3-642-77453-9.

Troppová, E. et al. (2015) 'Influence of temperature and moisture content on the thermal conductivity of wood-based fibreboards', Materials and Structures, 48(12), pp. 4077–4083. Available at: https://doi.org/10.1617/s11527-014-0467-4.

Vololonirina, O., Coutand, M. and Perrin, B. (2014) 'Characterization of hygrothermal properties of wood-based products – Impact of moisture content and temperature', Construction and Building Materials, 63, pp. 223–233. Available at: https://doi.org/10.1016/j.conbuildmat.2014.04.014.

Wang, H. et al. (2019) 'Determination of Dielectric Function of Water in THz Region in Wood Cell Wall Result in an Accurate Prediction of Moisture Content', Journal of Infrared, Millimeter, and Terahertz Waves, 40(6), pp. 673–687. Available at: https://doi.org/10.1007/s10762-019-00594-0.

Wilkes, K.E. (1979) 'Thermophysical properties data base activities at Owens-Corning Fiberglas', in Proceedings of the ASHRAE/DOE-ORNL Conference, Thermal Performance of the Exterior Envelopes of Buildings, ASHRAE SP, pp. 662–77.

Yu, Z.-T. et al. (2011) 'Experimental Measurements of Thermal Conductivity of Wood Species in China: Effects of Density, Temperature, and Moisture Content', Forest Products Journal, 61(2), pp. 130–135. Available at: https://doi.org/10.13073/0015- 7473-61.2.130.

#190: Study on the performance of tube internally-cooled falling film dehumidifier based on CFD

Donggen PENG[1], Yuanlong LI[1]

[1] School of Infrastructure Engineering, Nanchang University, Nanchang, China, pengdonggen@ncu.edu.cn

Abstract: With the growing energy crisis, there is an increasing focus on renewable energy sources. Liquid desiccant dehumidification is a technology that requires less energy, and the desiccant can be regenerated using renewable energy sources. Compared to other numerical research methods, the CFD technique can provide information on the state of heat and mass transfer, as well as the flow of the solution inside the dehumidifier. Therefore, a two-dimensional internally-cooled tube falling film dehumidifier model was developed based on CFD technique in this study and validated by comparison with data from previous studies. During the transient analysis, it was observed that the solution maintained a constant speed when flowing along the tube wall. After flowing downward for approximately 16 s, it reached the bottom of the dehumidifier tube, resulting in a dehumidification rate of 96.1% compared to the stable dehumidification case. In the steady-state study, it was found that air inlet temperature and solution flow rate had little effect on the dehumidification effect of the dehumidifier under baseline conditions. An increase of 10°C in the air inlet temperature resulted in only a 6.5% decrease in absolute moisture removal (AMR), while a 33.3% increase in solution flow rate resulted in only a 3.2% increase in AMR. The dehumidification performance of solution isothermal dehumidification is 32 % higher than that of adiabatic dehumidification. The results of this study will provide a reference for the practical application of internally-cooled tube falling film dehumidifier.

Keywords: CFD; Internally-Cooled; Heat And Mass Transfer; Falling Film Dehumidification

1. INTRODUCTION

Indoor ambient air humidity is an important factor affecting human thermal comfort (Nicol F, 2004). For Nanchang area, in order to provide comfortable indoor ambient air in spring and summer, it is necessary to dehumidify the air prior to its supply into buildings. Traditional vapour compression air-conditioning system reduces humidity by processing the air to the dew point temperature, while the processed air often requires reheating before supplying it to the building. This process requires a considerable amount of energy (Li Z, et al., 2005), which contributes to the global energy crisis. Furthermore, the condensate produced tends to result in the growth of bacteria in the air conditioning system, which can affect human health (Rostamzadeh H, et al., 2018). Liquid desiccant dehumidification (Wang SQ, Tu R and Zhang QX, 2022; Cheng XS, et al., 2019;) is a method that can dehumidify air above its dew point temperature, using the difference in partial pressure of water vapour between the surface of the solution and the air as the driving force for mass transfer. Only low amounts of energy are required to provide the power to transport the solution, while the liquid desiccant can be regenerated with low-grade thermal energy such as solar energy (Peng DG, Zhang XS and Yin YG, 2008). Liquid desiccant dehumidification air conditioning systems are helping to alleviate the energy crisis (Potnis SV and Lenz TG, 1996).

The dehumidifier is the main component in the liquid desiccant dehumidification system, and many scholars have studied the dehumidifier by experiment in the past (Koronaki IP, et al., 2013; Ahmed HA, et al., 2017; Kiran Naik B and Muthukumar P, 2019). Early dehumidifiers were adiabatic, but the temperature of the solution inside such dehumidifiers would increase continuously during dehumidification (Fumo N and Goswami DY, 2002), which would have a negative effect on the dehumidification performance. To solve the problem of increasing solution temperature during the dehumidification process, some scholars have built an experimental device for an internally-cooled dehumidifier. (Yin YG, et al., 2008) compared the dehumidification performance of internally-cooled and adiabatic dehumidifier and found that internally cooled dehumidifier performed significantly better than adiabatic dehumidifier. Besides experimental studies, many scholars have studied dehumidifiers by simulation. The finite difference method has been widely used in the simulation study of internally cooled dehumidifiers due to high accuracy (Luo YM, et al., 2014). (Liu XH, et al., 2009) developed the model without considering the film thickness based on the finite difference method and compared the performance of internally cooled and adiabatic dehumidifiers. (Ali A, Vafai K and Khaled ARA, 2004) and (Dai YJ and Zhang HF, 2004) considered the effect of liquid film thickness on the results and developed a model for an internally cooled dehumidifier with uniform film thickness. The film thickness invariant model has high predictability under conditions of high solution flow rate, while the solution flow rate is low, the prediction results of this model are significantly lower than the actual situation (Mesquita LCS, Harrison SJ and Thomey D, 2006). (Hueffed AK, Chamra LM and Mago PJ, 2009) proposed a simplified model that took into account the relationship between the liquid film thickness and the heat and mass transfer coefficients, and the model had a high agreement with the experimental data. However, most of the mathematical models based on the finite difference method only focus on the inlet and outlet parameters after the dehumidifier has been operated at a steady state, it is hardly possible to study the heat and mass transfer process as well as the dynamics of gas and liquid inside the dehumidifier.

In recent years, the CFD technique has been used by many researchers for the study of dehumidifiers. CFD simulations can obtain the internal and inlet/outlet parameters of the dehumidifier at any time during operation. (Luo YM, Yang HX and Lu L, 2014) and (Peng DG and Cheng NY, 2022) modelled an adiabatic falling film dehumidifier, and investigated the transient/steady performance of the dehumidifier during operation. (Das A, Das RS and Das K, 2022) investigated the solution flow in the non-flat falling film channel and compared the heat and mass transfer in flat and non-flat falling film channels. (Lu H, Lu L and Gao XX, 2021) incorporated baffle plates on the falling film wall of a dehumidifier and performed CFD numerical simulations. The flow characteristics of the solution were investigated, and the dehumidification performance of different numbers of baffle plates in the falling film channel was compared as well. However, all the above studies were on adiabatic dehumidifiers and there were fewer studies on internally cooled dehumidifiers with better dehumidification performance. Therefore, a CFD model of an internally-cooled tubular falling film dehumidifier was established in this study and model was validated by comparison with literature (Peng DG, Li YL and Cheng NY, 2024) data. The flow characteristics of the gas-liquid fluid inside the tube and the heat and mass transfer between the gas and liquid were investigated, and the steady-state performance of the dehumidifier was parametrically studied.

2. MODEL ESTABLISHMENT
2.1. Geometric model

(a) Geometrical model of the dehumidifier and setting of boundary conditions.

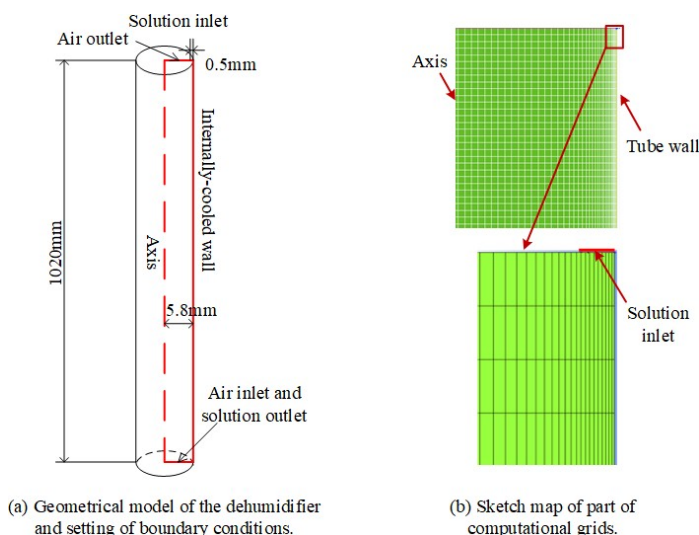(b) Sketch map of part of computational grids.

Figure 1: Dehumidifier physical and mesh model

For falling-film dehumidifiers, the counter flow type has a better dehumidification effect than the concurrent flow type (Liu XH, et al., 2009). Consequently, the counter flow type falling film dehumidifier tube was chosen as the research object in this study. There were many channels for air and liquid desiccant in the dehumidifier, but in the dehumidification process between the channels almost no affect each other. In this study, only a single dehumidification tube was created for the CFD model to save computational resources. As illustrated in Figure 1(a), the dehumidification tube was 1020 mm in length with an inner diameter of 5.8 mm, and the solution inlet width was set to 0.5 mm. The solution flowed downward along the wall from the top of the tube, and the air entered from the bottom of the tube in the opposite direction to the solution flow. In the dehumidification tube, the solution and air came into contact, as the water vapour partial pressure on the surface of the solution was lower than the partial pressure of water vapour in the air, causing the water vapour in the air to move to the solution side, thus achieving the effect of dehumidification the air. Figure 1(b) shows a schematic of the local mesh of the dehumidifier. The geometric model in this study was relatively simple, with the use of a structured grid. The solution flowed along the wall, and the thickness of the liquid film was minimal during the flow process. To obtain the characteristics of the liquid film descending process, a fine mesh size of less than 0.05 mm was used near the tube wall. The grid size gradually increased along the axial direction, and in the direction of solution flow, the grid size was consistent.

2.2. Governing equations

In CFD numerical calculations, the most crucial aspect was the solution of the equations of conservation of momentum, mass and energy. Furthermore, the dehumidification process entailed a two-phase flow of gas and liquid, with mass transfer occurring at the interface between the two phases. Therefore, it was essential to accurately capture the interface between the gas and liquid. The reconstructed gas-liquid interface in the PLIC scheme of the VOF model was highly analogous to the actual gas-liquid interface (Min JK and Park S, 2011), and it was employed in this study. Previous studies (Luo YM, Yang HX and Lu L, 2014; Das A, Das RS and Das K, 2022; Lu H, Lu L and Gao XX, 2021) calculated hg based on permeation theory, where hg is only related to contact time and diffusion coefficient. Nevertheless, in our study (Peng DG, Xu SH and Yang HX, 2020), the mass transfer coefficient was also found to be strongly related to the air flow rate. Therefore, in this study, the empirical formula proposed by (Antonio Rocha J, Bravo J and Fair J, 1996) was used to calculate hg. The mathematical equations of the various mathematical equations involved in the CFD simulation were as follows.

Equation 1: Momentum conservation equation.

$$\partial(\rho\vec{u})/\partial t + \nabla \cdot (\rho\vec{u}\vec{u}) = -\nabla P + \nabla \cdot (\mu(\nabla\vec{u} + \nabla\vec{u}^T)) + \rho\vec{g} + \vec{F}$$

Where:

ρ= density (kg/m^3); P= pressure (Pa); u= velocity vector (m/s); g= gravitational acceleration (m/s^2); t = time (s); F= source term (N/m^3); μ= dynamic viscosity (kg/(m·s)); u^T= turbulence velocity vector (m/s)

Equation 2: Mass conservation equation.

$$\partial\rho/\partial t + \nabla \cdot (\rho\vec{u}) = 0$$

Equation 3: Energy conservation equation.

$$\partial(\rho E)/\partial t + \nabla \cdot (\vec{u}(\rho E + P)) = \nabla \cdot (k_{eff}\Delta T - \Sigma h_k \cdot J_k + S_E)$$

Where:

E= energy (J/kg); h$_k$= sensible enthalpy of the kth species (J/kg); k$_{eff}$= effective thermal conductivity (W/(m·K)); J$_k$= mass flux of the kth species (kg/(m^2·s)); T= temperature (K); S$_E$= the energy source term (W/m^3)

Equation 4: Species transport equation.

$$\partial(\alpha_q\rho_q x_{k,q})/\partial t + \nabla \cdot (\alpha_q\rho_q\vec{u}x_{k,q} - \alpha_q D_{k,q}\nabla x_{k,q}) = S_{lg.k}$$

Where:

α= the volume fraction (%); k= the kth component; q= the qth phase; D= the diffusion coefficient (m^2/s); x= the mass fraction (%); S$_{lg,k}$= the mass source terms(kg/m^3)

Equation 5: VOF multiphase model equation.

$$\rho = \alpha_l\rho_l + \alpha_g\rho_g \; ; \; \mu = \alpha_l\mu_l + \alpha_g\mu_g \; ; \; \alpha_g + \alpha_l = 1$$

Where:

l= liquid phase; g= gas phase

Equation 6: Mass transfer equation.

$$S_{lg.k} = K(d_g - d_e)A$$

Where:

K= the total mass transfer coefficient (kg/m²·s); d_e= the equivalent humidity of the liquid desiccant surface (kg/kg); d_g= the humidity of the bulk air (kg/kg); A= specific surface area per unit volume (m⁻¹)

Equation 7: Total mass transfer coefficient K equation (Zhang L, et al,2010).

$$1/K = 1/h_g + 1/\psi h_l$$

Where:

ψ= the coefficient related to the concentration and temperature of lithium chloride solution; h_g = the gas phase mass transfer coefficient (kg/(m² · s)); h_l= the liquid phase mass transfer coefficient (kg/(m² · s))

Equation 8: Gas/ liquid phase mass transfer coefficient h_g/h_l equation

(Antonio Rocha J, Bravo J and Fair J, 1996).

$$h_g = 0.054(D_g\rho_g/d)\left((U_l + U_g)d\rho_g/\mu_g\right)^{0.8}(\mu_g/\rho_g D_g)^{0.333}$$

$$h_l = 2\rho_l\sqrt{D_l/(\pi t)}$$

Where:

D_g= the diffusion coefficient of water vapour in air (m²/s); d= the equivalent diameter (m); U= the effective velocity (m/s); t= the contact time (s)

Equation 9: Gas-liquid interface heat source

$$S_E = S_{lg.k}H_l$$

Where:

H_l= the latent heat of vaporisation of liquid water (J/kg)

2.3. Boundary condition setting and simulation strategy

The model was simulated using FLUENT 2022R1 software, and the gas-liquid phase mass transfer was realised by the user defined foundation (UDF). The boundary conditions of the model were set as shown in Figure 1. The top of the dehumidification tube was set as a solution velocity inlet with a width of 0.5 mm and an air velocity inlet with a width of 5.3 mm, where the velocity of the air inlet was set as a negative value to induce an upward air flow. The bottom of the dehumidification tube was set as a backflow pressure outlet. The dehumidification tube wall was set as a no-slip, adhesion force wall, the liquid phase contact angle was set to 0, and the value of the heat flux was set to a negative number. The centre of the tube was set as the axis, while the 2D plane was set as an axisymmetric model.

The pressure-velocity coupling was implemented by the SIMPLE algorithm built into FLUENT, and the spatial discretisation of the pressure was performed using the PRESTO! scheme. The turbulence equation and the component transport equation for water vapour in the gas phase were solved by the first-order windward difference method, while the momentum and energy equations were solved by the second-order windward difference method. This study was based on the transient solution, to ensure the stability of the solution process, the global Courant number was controlled to be around 0.05, the corresponding time step was 0.0002s. The simulation was initialised with the dehumidification tube full of air, the solution failed to enter the dehumidification tube, and the wall of the tube was set to correspond to the heat flux. The focus of this study was on the dehumidifier in the liquid desiccant dehumidification system, so lithium chloride solution with better dehumidification performance was chosen for the selection of liquid desiccant.

3. MODEL VALIDATION
3.1. Grid Independence Study

In CFD studies, the required computational resources are often proportional to the number of grids employed in the model. The mesh accuracy has a significant impact on the accuracy of the simulation results. Therefore, an appropriate set of mesh is very important to balance the computational resources and the accuracy of simulation results. In this study, four sets of meshes with different grid numbers of 850x42, 1020x50, 1224x60, and 1360x60 were established to study the grid independence solution. The same operating conditions were used for the four sets of meshes and the base values in Table 1 were the detailed simulation parameters for the grid independence study.

Table 1: Simulation of operating conditions

Parametric	Air inlet			Solution inlet			Cooling type	
	Temperature	Velocity	Humidity	Temperature	Velocity	Concentration	Uniform heat flux	Uniform temperature
Symbol	$T_{g,in}$(°C)	$U_{g,in}$(m/s)	$d_{g,in}$(g/kg)	$T_{l,in}$(°C)	$U_{l,in}$(m/s)	X(%)	H(W/m²)	T_c(°C)
Base value	35.5	0.83	22	32	0.03	30	-200	/
Range	25.5~35.5	/	18~28	26~36	0.03~0.04	28~32	-500~0	27~32

As shown in Figure 2, the first two grids have a large difference in the moisture content at the outlet air and the last three grids are closer to each other. The deviations of the second and third grids from the fourth grid are 0.16% and 0.10% respectively. Therefore, under the premise of ensuring the accuracy of the simulation results and in order to save computational resources, the 1224x60 grid model was used in the subsequent transient/steady state study of the dehumidifier.
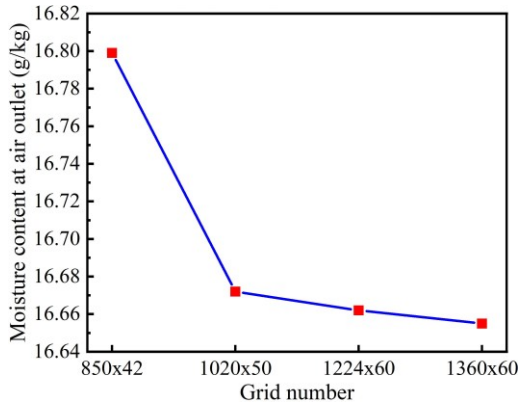

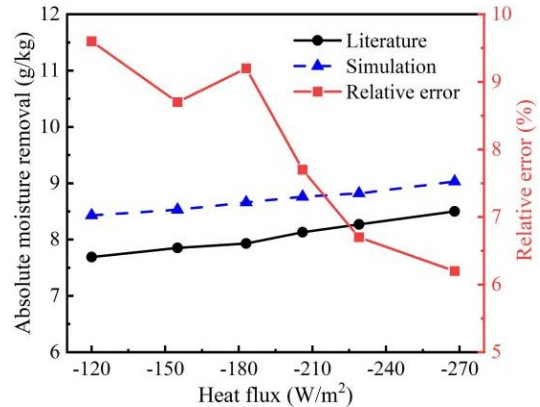Figure 2: Humidity at air outlet for different number of grids

Figure 3: AMR in literature and simulation for different heat flux

3.2. Validation of Literature Data

Table 2: Literature operating conditions

Parametric	Air inlet			Solution inlet			Uniform heat flux
	Temperature	Velocity	Humidity	Temperature	Velocity	Concentration	
Symbol	$T_{g,in}(℃)$	$U_{g,in}(m/s)$	$d_{g,in}(g/kg)$	$T_{l,in}(℃)$	$U_{l,in}(m/s)$	$X(\%)$	$H(W/m^2)$
Base value	35.5	2	22	30	0.03	35	/
Range	/	/	/	/	/	/	-120~-268

In our previous work (Peng DG, Li YL and Cheng NY, 2024), the performance of a 3D tube-out evaporative cooling falling film dehumidifier was investigated by CFD. The effect of different evaporative cooling parameters on the dehumidification performance was investigated and the heat fluxes corresponding to various evaporative cooling parameters were derived. In this study, a 2D model with consistent dimension was developed and the AMR under the same operating conditions was simulated to validate the 2D model of this study. The literature specific operating conditions are shown in Table 2. Figure 3 shows the comparison between the AMR of the dehumidifier in literature (Peng DG, Li YL and Cheng NY, 2024) and this study for different wall heat flux. From the figure it can be seen that as the heat flux increases, the AMR also increases, this is because the greater the wall heat flux indicates that the solution to the tube wall to transfer more heat, so that the solution temperature is reduced, which reduces the partial pressure of water vapour on the surface of the solution to enhance the mass transfer driving force. The simulation results of the model developed in this study are both in good agreement with the data from previous work at different heat fluxes. The maximum relative error is 9.6%, the minimum relative error is only 6.2%, and the average relative error is 8.0%.

4. TRANSIENT CHARACTERISATION OF DEHUMIDIFIER

Whether the falling film dehumidifier is studied by experimental or other numerical methods, it is difficult to obtain the flow state of the solution in the dehumidifier as well as the results of the mass and heat transfer between the air and the liquid, whereas the CFD study has a unique advantage in this regard and therefore a transient study of the flow state of the solution was performed. The calculated outdoor air-conditioning parameters in summer in Nanchang area (National Standard of the People's Republic of China, 2015) were used as the base values of air parameters in this study. According to the literature (Cheng XS, et al., 2019), the base value of air-liquid mass ratio was selected to be about 0.7, and the temperature of tap water in Nanchang area in summer is 32°C, so the base temperature of the solution was set to be 32°C. The selection of heat flux at the tube wall was referred to the literature (Luo YM, et al., 2017). The operating conditions for transient simulation were the base values in Table 1.
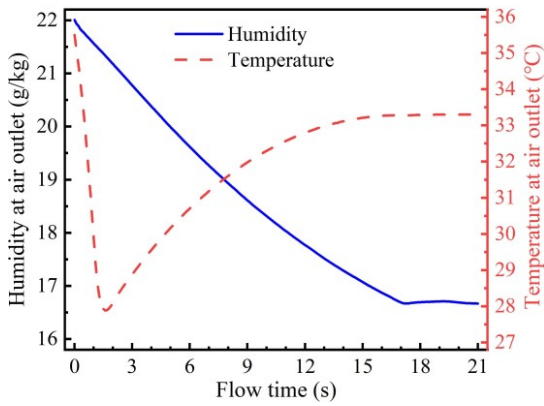
Figure 4: Variation of air outlet temperature and humidity with solution flow time
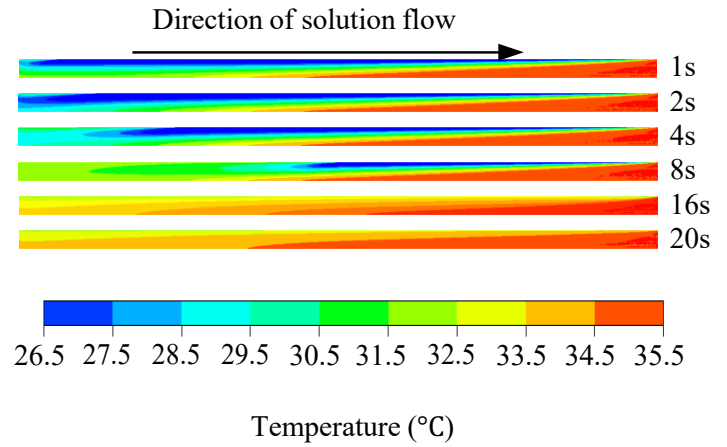

Figure 5: Temperature contours of the film-forming stage in the dehumidifier

Figure 4 shows the variation of air outlet temperature and moisture content as a function of solution flow time. From the figure, it can be seen that the outlet air temperature (OAT) decreased dramatically before 1.6s and then increased gradually. At 16.2s, the OAT tends to stabilise at 33.3°C, but the humidity content of the air outlet fails to stabilise and tends to decrease. At 17.2s, the humidity content of the air outlet decreases to the lowest point of 16.84g/kg, then fluctuates slightly, and finally tends to stabilise at 16.84g/kg. Figure 5 shows the temperature contours inside the tube at different times. At the initial time, a uniform heat flux was set up in the tube wall, which caused the air near the wall to transfer a corresponding amount of heat to the tube wall, whereas the air has a lower specific heat capacity, resulting in a sudden drop in the temperature of the air near the tube wall. In the early stages of solution flow, the liquid film area was small with less latent heat being released by dehumidification. Meanwhile, the amount of heat transferred from the air to the tube wall increased with time, resulting in a decrease in the air temperature inside the tube in the early stages of dehumidification. As the dehumidifier operated, the area of the liquid film inside the tube increased and the latent heat of dehumidification was increased. At the same time, the area of air in direct contact with the wall of the tube decreased, causing the temperature of the air in the upper part of the tube to rise gradually. As the solution flowed to the bottom of the dehumidifier tube, the temperature distribution inside the tube changed insignificantly.
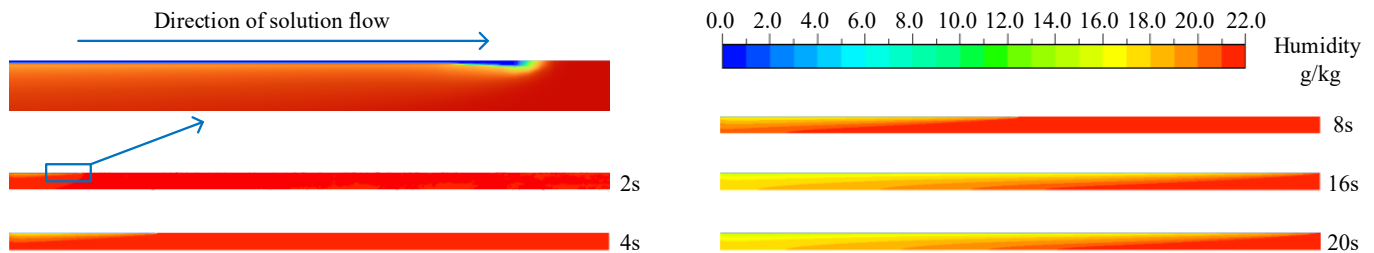

Figure 6: Contours of moisture content during the film-forming phase in the dehumidifier

Figure 6 shows the moisture content distribution in the tube at different times before the solution flows to the bottom of the tube. As shown in Figure 6, when the solution flowed 2s, the solution flow distance was 0.122m, at this time the dehumidification area in the tube was small, the dehumidification effect was not obvious; solution flowed 4s, the solution flow distance was 0.249m, at this time near the solution side of the air humidity was reduced. When the solution flowed 8s, the solution flow distance was 0.504m, the humidity content of the air outlet was 19.04g/kg, reaching the maximum dehumidification capacity of 57.2%. When the solution had flowed for 16s, the solution had flowed to the bottom of the tube, the moisture content of the outlet air was 17.04g/kg to achieve the maximum dehumidification capacity of 96.1%. The reason for AMR failing to reach maximum was that it needed time for the air to pass through the dehumidifier tube, causing a delay in the change in humidity at the air outlet. From the distance of solution flows at different time points, it can be inferred that the solution flows along the wall of the tube at a uniform speed. The combined effects of gravity, surface tension, viscosity and air resistance keep the solution velocity constant.

5. STEADY-STATE CHARACTERISATION OF DEHUMIDIFIER

The dehumidification process was considered to have reached steady state when the moisture content of the air at the outlet, the outlet temperature, and the temperature of the solution in the tube gradually stabilised. Subsequently, the effects of air temperature and humidity, solution flow rate, temperature and concentration, as well as different cooling methods on the performance of the dehumidifier when reaching the steady state were investigated. The baseline values and variation ranges of each parameter for the steady state simulation are shown in Table 1.

5.1. Effect of air inlet parameters

Effect of air inlet temperature

The AMR, OAT and liquid film average temperature (LFAT) for different air inlet temperatures are given in Figure 7. From the figure, it can be seen that both OAT and LFAT in the tube increase with the air inlet temperature. As the air inlet temperature rose from 25.5°C to 29.5°C, the LFAT rose from 31.49°C to 31.97°C, which was lower than the inlet temperature, indicating that the latent heat absorbed by the solution during the dehumidification process in the temperature section was lower than the heat transfer from the solution to the air and the tube wall, causing the solution in the tube to cool. As the air inlet temperature increased from 31.5°C to 35.5°C, the LFAT increased from 32.18°C to 32.58°C, and the solution was heated during the dehumidification process. When the air inlet temperature increased by 10℃, the LFAT only increased by 1.09℃, due to the thermal resistance between air and liquid and the large specific heat capacity of the solution, the effect of air temperature on LFAT was insignificant. When the air inlet temperature increased from 25.5°C to 35.5°C, the AMR decreased slightly from 5.52g/kg to 5.16g/kg, a decrease of only 6.5%. Due to the small increase in LFAT in the tube, this results in a very slight increase in the partial pressure of water vapour at the surface of the solution, resulting in a small decrease in AMR.

Effect of air inlet humidity

Figure 8 illustrates that as the moisture content of the air inlet increased, the OAT, the LFAT, and the AMR also increased. When the humidity content of the air inlet was 18 g/kg, the LFAT was 31.73 ℃, which was lower than the solution inlet temperature. This indicates that the heat transferred from the solution to the tube wall is higher than the sum of the latent heat of vapourisation absorbed by the solution and the heat transferred from air to the solution in the dehumidification process. As the humidity content of the air inlet increased from 18g/kg to 28g/kg, the AMR increased from 3.19g/kg to 8.01g/kg, representing a 151.1% increase. Concurrently, the LFAT rose from 31.73°C to 34.1°C, an increase of 2.73°C, while the temperature of the air outlet rose from 32.89°C to 34.03°C, a rise of 1.14°C. This is due to the fact that an increase in the humidity content of the inlet air will directly increase the gas-liquid water vapour partial pressure difference and enhance the mass transfer drive, thus significantly increasing the AMR and releasing the latent heat with the increase. By comparison, it can be found that even though the specific heat capacity of the solution is much larger than that of the air, the temperature rise of the solution is still 2.39 times higher than that of the air at the outlet. This indicates that the latent heat released by the water vapour in the dehumidification process is mainly absorbed by the solution.
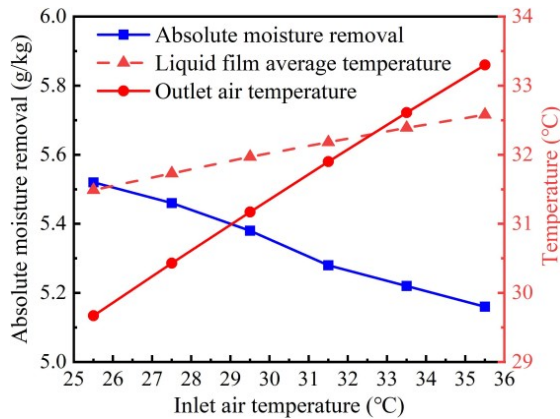
Figure 7: Effect of air inlet temperature on performance
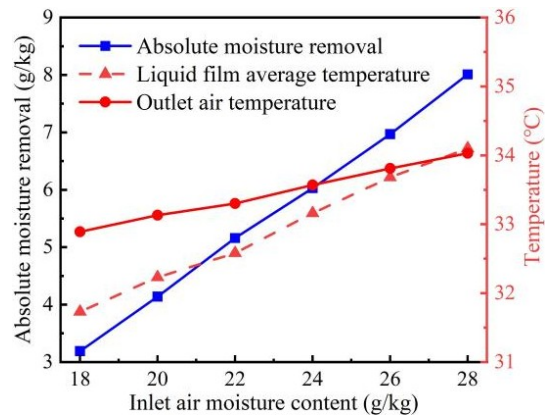
Figure 8: Effect of air inlet moisture content on performance

Figure 9 shows the temperature and humidity contours inside the dehumidification tube at different air inlet humidity contents. As shown in the Figure 9(a), the temperature of the air entered the dehumidification tube reduced in the direction of flow due to the tube wall was set uniform heat flux and the solution temperature was lower than the air inlet temperature. The rate of decline is slower with higher humidity content. This is due to the fact that a greater humidity content of the gas-liquid water vapour partial pressure difference results in a more effective mass transfer effect, which leads to a greater release of latent heat during the process of dehumidification. This results in a slower decline in air temperature. The Figure 9(b) shows that the dehumidification effect is significant for high humidity air but limited for low humidity air. In the direction of vertical solution flow, the humidity of the air increases with the distance from the liquid film, because the mass transfer of the dehumidification process mainly occurs at the gas-liquid interface, and the water vapour movement in the air is dominated by diffusion with a poor mass transfer effect.

(a)

(b)
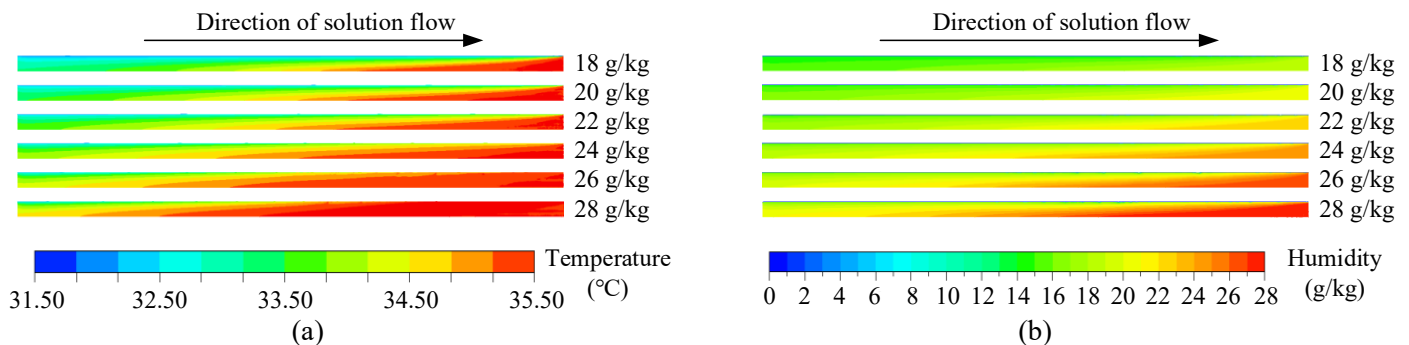
Figure 9: Temperature and humidity contours for different air inlet humidity contents

169

5.2. Effect of solution inlet parameters

Effect of solution inlet temperature

As illustrated in Figure 10, an increase in the inlet solution temperature from 26°C to 34°C is accompanied by a corresponding rise in LFAT, which increases from 28.9°C to 34.03°C. This temperature is higher than the inlet temperature. At a solution inlet temperature of 36°C, the LFAT is 35.36°C, which is lower than the inlet temperature. The dehumidification effect of high temperature solution is poorer, causing the release of latent heat to be smaller, while the solution temperature is higher than the air temperature, the solution to the air heat transfer. This results in the latent heat absorbed by the solution during the dehumidification process to be lower than the amount of heat transferred from the solution to the tube wall and the air. Consequently, causing the overall temperature of solution to decrease. As the solution, the inlet temperature rose from 26°C to 36°C, the AMR of the dehumidifier decreased from 7.76g/kg to 3.71g/kg, representing a 52.2% reduction. Concurrently, the OAT increased from 30.13°C to 35.49°C. The OAT increased from 30.13°C to 35.49°C. This is due to the fact that a 10°C increase in the solution inlet temperature results in LFAT increase of 6.46°C, which in turn causes a significant increase in the partial pressure of water vapour on the solution surface and a reduction in the mass transfer driving force. The increase in OAT is influenced by the combined effect of a reduction in the temperature difference between the gas and liquid phases and a decrease in the latent heat of water vapour release.

Effect of solution inlet concentration

As shown in Figure 11, the AMR from the dehumidifier increased as the solution concentration increased. The main reason for this is that the increase in solution concentration results in a reduction in the partial pressure of water vapour on the solution surface, thus increasing the mass transfer drive between air and solutions. With a solution inlet velocity of 0.03 m/s, the AMR increased from 4.36 g/kg to 6.11 g/kg when the solution concentration was increased from 28% to 32%, which is an increase of 40.1%. In addition, increasing the solution flow rate also increased the AMR. When the solution inlet velocity was increased from 0.03m/s to 0.04m/s, the AMR at each solution concentration increased by only 0.11-0.25g/kg. For the internally cooled falling-film dehumidifier, a 33.3% increase in solution flow rate resulted in an increase in AMR of 3.2% on average. This shows that increasing the solution concentration is more effective in improving the dehumidification performance than increasing the solution flow rate. The OAT and LFAT increased as the solution concentration increased, which is due to the fact that the high concentration solution has a stronger mass transfer drive during dehumidification, absorbing more water vapour and thus releasing more latent heat, causing the temperatures of the air and the solution to rise. When the solution flow rate increased, the OAT and the LFAT slightly decreased. This is because the base temperature of the solution is lower than the base temperature of the air, increasing the solution flow rate can enhance the cooling effect of the top end of the dehumidification tube on the air, but also inhibit the solution temperature rise inthe dehumidification process.
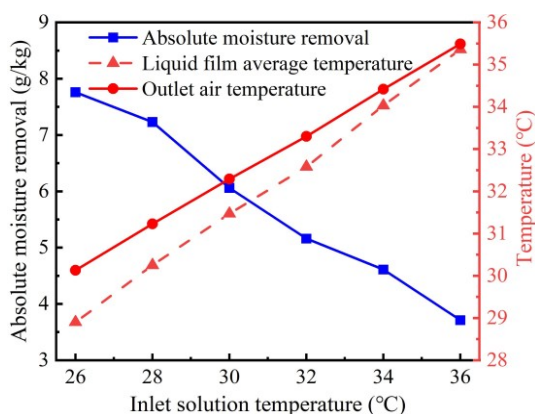
Figure 10: Effect of solution inlet temperature on performance
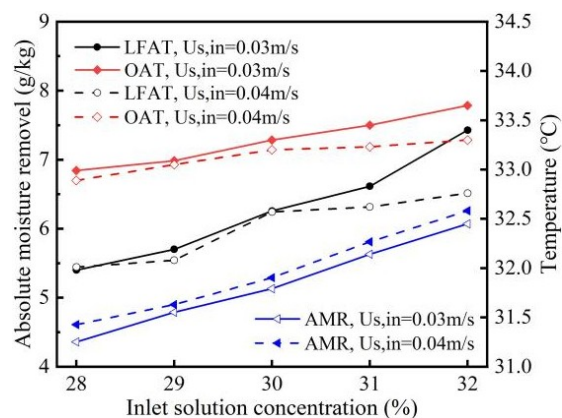
Figure 11: Effect of solution inlet parameters on performance

5.3. Effect of cooling method

Effect of uniform heat flux

Figure 12 shows the effect of different heat fluxes on LFAT. As can be seen from the figure, when the heat flux was less than 300 W/m^2, the temperature of the solution in the tube increased as the distance of the solution from the inlet increased, and the heat transferred from the liquid film to the wall of the tube at this time was small, less than the heat transferred from the air to the liquid film and the latent heat of evaporation absorbed by the liquid film. When the heat flux was greater than 300 W/m^2, the solution temperature gradually decreased as the flow distance increased. Due to the high humidity content when the air entered the dehumidifier tube, resulting in a large AMR and a large latent heat release, in addition, the air entered the dehumidifier tube at a high temperature, which caused a small increase in the solution temperature at the outlet section.

Figure 12: Along-track temperature variation of solution at different heat flux
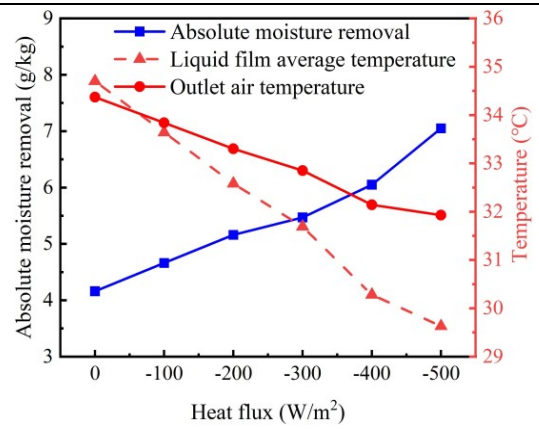
Figure 13: Effect of uniform heat flux on performance

As shown in Figure 13, as the heat flux increased, the LFAT and the OAT both decreased, and the LFAT decreased significantly faster than the OAT decreased. This is due to the direct heat transfer between the solution and the wall of the tube, while the air is heating transfer with the solution, and has a large effect on the temperature of the solution as the heat flux increases. When the heat flux was 0W/m², this was adiabatic dehumidification, the dehumidification amount was 4.16g/kg, the LFAT was 34.6℃, and the OAT was 34.27℃. In the base conditions, even with adiabatic dehumidification, the air is still cooled. The AMR gradually increased as the heat flux increased. When the heat flux was increased to 500W/m², the AMR increased to 7.05g/kg, the OAT decreasedto 31.93℃, which was lower than the solution inlet temperature, and the LFAT decreased to 29.63℃. For dehumidifier with long falling film channel, increasing the heat flow density can effectively reduce the LFAT, thus increasing the AMR.

Effect of uniform cooling temperature

The air and solution parameters at different cooling temperatures are given in Figure 14. From the figure, it can be seen that as the cooling temperature increased, the LFAT and OAT increased basically linearly. When the cooling temperature increased from 27°C to 32°C, the OAT increased from 29.67°C to 33.07°C, the LFAT increased from 27.05°C to 32.02°C, and the solution temperature was almost the same as the wall temperature. Due to the long falling film channel, it takes about 16s for the solution to flow from the top to the bottom of the dehumidifier tube, and the solution with limited flow rate can be sufficiently cooled in the dehumidifier tube, making the solution temperature consistent with the cooling temperature. Therefore, for the long falling film channel dehumidifier, to ensure that the internal cooling temperature and the solution inlet temperature can be consistent to achieve isothermal dehumidification. The AMR of the dehumidifier was 8.03 g/kg at a cooling temperature of 27°C. When the cooling temperature increased to 32°C to match the solution inlet temperature, the AMR decreased to 5.49 g/kg, a 32% improvement over adiabatic dehumidification. The low cooling temperature causes the dehumidifier to have excellent dehumidification performance, but the preparation of low temperature cooling water often requires additional equipment and energy, so the ideal dehumidification condition is to cause the solution to achieve isothermal dehumidification.

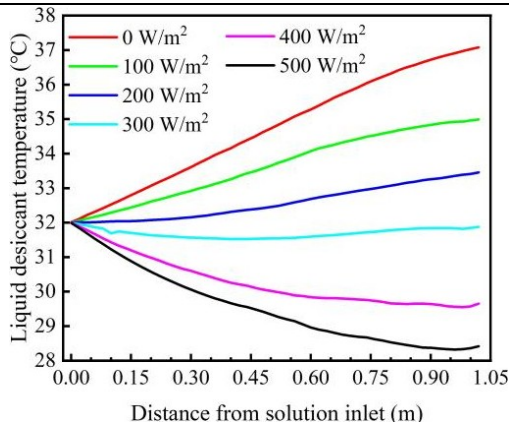Figure 14: Effect of uniform cooling temperature on performance

Figure 15: Sensitivity coefficients for each operating parameter

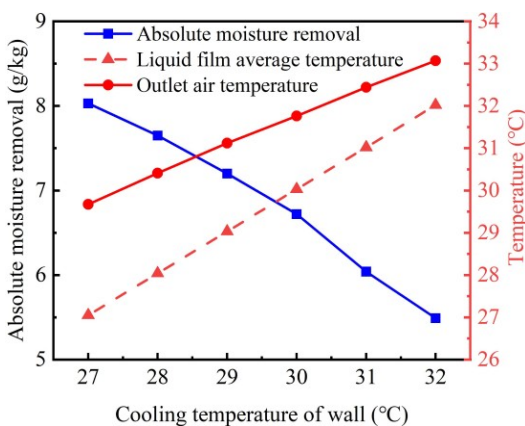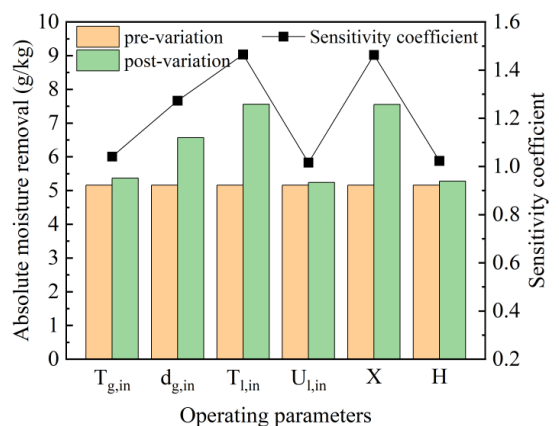## 5.4. Sensitivity coefficient analysis for each parameter

To compare the effect of different operating parameters on the dehumidification performance, the sensitivity coefficients of each operating parameter are studied. Take the absolute moisture removal corresponding to the base operating parameter as the initial value, each parameter is varied, ensuring that the rate of change is the same. When one parameter is changed, the other parameters are controlled to remain unchanged and the operating parameters before and after the change are shown in Table 3.The sensitivity coefficient is defined as the ratio of the absolute moisture removal before and after the change in this study. The sensitivity coefficients of each operating parameter are shown in Figure 15. The sensitivity coefficient of solution flow is the smallest, the sensitivity coefficients of air inlet temperature and heat flux are close to the solution flow, which are all less than 1.05; the sensitivity coefficients of solution inlet temperature and concentration are significantly larger than the other parameters which are all more than 1.45. It can be seen that the solution inlet temperature and concentration are the most important factors affecting the dehumidification performance, and the air inlet temperature, solution flow and heat flux have less influence on the dehumidification performance.

Table 3: Operating conditions before and after the change

Parameters	$T_{g,in}$(℃)	$d_{g,in}$(g/kg)	$T_{l,in}$(℃)	$U_{l,in}$(m/s)	X(%)	H(W/m²)
Pre-variation	35.5	22	32	0.03	30	-200
Post-variation	29.6	25.67	26.7	0.035	35	-233

5. CONCLUSION

In this paper, a two-dimensional CFD model of a tube internally-cooled falling film dehumidifier was established, and the transient/ steady state characteristics of the tube were investigated with the calculated parameters of the outdoor air conditioning in summer in Nanchang area as the reference parameters. The following results were obtained:

(1) The solution flows along the wall of the tube at constant speed, the change of liquid film area inside the tube will affect the air velocity distribution inside the tube. Dehumidifier operation 16s dehumidification area has reached the maximum, but this time the AMR for the dehumidifier running stable 96.1%.
(2) The internally-cooled falling film dehumidifier still has an excellent dehumidification effect on high temperature air. The AMR of the dehumidifier for air at 35.5℃ is 93.5% of that for air at 25.5℃.
(3) For different concentrations of solutions, the effect of flow rate on AMR is very small. Dehumidifier in the actual application of high concentration and low flow rate of the solution can be selected as the operating conditions.
(4) When the cooling wall temperature is uniform, the solution temperature in the tube for stable dehumidifier operation is almost equal to the wall temperature. The isothermal dehumidification condition of AMR is 1.32 times the adiabatic dehumidification condition.

The current study is based on the case where the inlet parameters of the dehumidifier are constant. However, in the actual operation of the dehumidifier, the inlet parameters may change as the environment changes. Therefore, the response characteristics of each inlet parameter of the dehumidifier when the inlet parameter varies and what control strategy can be adopted to ensure that the moisture content of the outlet air of the dehumidifier is stable can be investigated in the future.

6. REFERENCES

Ahmed HA, Ismail IM, Saleh WF, et al, 2017. Experimental investigation of humidification-dehumidification desalination system with corrugated packing in the humidifier. Desalination, 410, 19–29.

Ali A, Vafai K, Khaled ARA, 2004. Analysis of heat and mass transfer between air and falling film in a cross flow configuration. International Journal of Heat and Mass Transfer, 47, 743–755.

Antonio Rocha J, Bravo J, Fair J, 1996. Distillation Columns Containing Structured Packings: A Comprehensive Model for Their Performance. 2. Mass-Transfer Model. Industrial and Engineering Chemistry Research, 35, 1660–1667.

Cheng XS, Peng DG, Yin YG, et al, 2019. Experimental study and performance analysis on a new dehumidifier with outside evaporative cooling. Building and Environment, 148, 200–211.

Dai YJ, Zhang HF, 2004. Numerical simulation and theoretical analysis of heat and mass transfer in a cross flow liquid desiccant air dehumidifier packed with honeycomb paper. Energy Convers Manage, 45, 1343–1356.

Das A, Das RS, Das K, 2022. Performance enhancement of a liquid desiccant absorber with triangular corrugated structured packing. Journal of Building Engineering, 45, 103677.

Fumo N, Goswami DY, 2002. Study of an aqueous lithium chloride desiccant system: air dehumidification and desiccant regeneration. Solar Energy, 72(4), 351–361.

Hueffed AK, Chamra LM, Mago PJ, 2009. A simplified model of heat and mass transfer between air and falling-film desiccant in a parallel-plate dehumidifier. Journal of Heat Transfer, 131(5), 052001-1-7.

Kiran Naik B, Muthukumar P, 2019. Experimental investigation and parametric studies on structured packing chamber based liquid

desiccant dehumidification and regeneration systems. Building and Environment,149, 330–348.

Koronaki IP, Christodoulaki RI, Papaefthimiou VD, et al, 2013. Thermodynamic analysis of a counter flow adiabatic dehumidifier with different liquid desiccant materials. Applied Thermal Engineering, 50, 361–373.

Li Z, Liu XH, Zhang L, et al, 2005. Analysis on the ideal energy efficiency of dehumidification process from buildings. Energy and Buildings, 42, 2014-2020.

Liu XH, Chang XM, Xia JJ, et al, 2009. Performance analysis on the internally cooled dehumidifier using liquid desiccant. Building and Environment, 44, 299–308.

Lu H, Lu L, Gao XX, 2021. Mass transfer enhancement of falling film liquid desiccant dehumidification by micro-baffle plates. International Journal of Heat and Mass Transfer, 169 ,120945.

Luo YM, Chen Y, Yang HX, et al, 2017. Study on an internally-cooled liquid desiccant dehumidifier with CFD model. Applied Energy, 194, 399–409.

Luo YM, Yang HX, Lu L, 2014. Liquid desiccant dehumidifier: Development of a new performance predication model based on CFD. International Journal of Heat and Mass Transfer, 69, 408–416.

Luo YM, Yang HX, Lu L, et al, 2014. A review of the mathematical models for predicting the heat and mass transfer process in the liquid desiccant dehumidifier. Renewable and Sustainable Energy Reviews, 31, 587–599.

Mesquita LCS, Harrison SJ, Thomey D, 2006. Modeling of heat and mass transfer in parallel plate liquid-desiccant dehumidifiers. Solal Energy, 80, 1475–1482.

Min JK, Park S, 2011. Numerical study for laminar wavy motions of liquid film flow on vertical wall. International Journal of Heat and Mass Transfer, 54, 3256–3266.

National Standard of the People's Republic of China, 2015. Design Code for Heating, Ventilation and Air Conditioning of Civil Buildings. China Construction Industry, GB50736-20122015.

Nicol F, 2004. Adaptive thermal comfort standards in the hot-humid tropics. Energy Build, 36, 628–637.

Peng DG, Cheng NY, 2022. Experimental and CFD study on circular tube falling film dehumidification performance. Experimental Heat Transfer, 35(7), 1016-1037.

Peng DG, Li YL, Cheng NY, 2024. Study on the performance of tube evaporative cooling dehumidifier based on CFD. Applied Thermal Engineering, 241, 122419.

Peng DG, Xu SH, Yang HX, 2020. Heat and mass transfer characteristics and dehumidification performance improvement of an evaporatively-cooled liquid dehumidifier. Applied Thermal Engineering, 178, 11557.

Peng DG, Zhang XS, Yin YG, 2008. Theoretical storage capacity for solar air pretreatment liquid collector/regenerator. Applied Thermal engineering, 28, 1259-1266.

Potnis SV, Lenz TG, 1996. Dimensionless mass-transfer correlations for packed-bed liquid desiccant contactors. Industrial and Engineering Chemistry Research, 35(11), 4185–4193.

Rostamzadeh H, Rostamzadeh J, Matin PS, et al, 2018. Novel dual-loop bi-evaporator vapor compression refrigeration cycles for freezing and air-conditioning applications. Applied Thermal Engineering, 138, 563-582.

Wang SQ, Tu R, Zhang QX, 2022. Dynamic performance analyses and optimization studies on air dehumidifiers using multi-stage desiccant plates. Applied Thermal Engineering, 212, 188546.

Yin YG, Zhang XS, Wang G, et al, 2008. Experimental study on a new internally cooled/heated dehumidifier/regenerator of liquid desiccant systems. International journal of refrigeration, 31, 857–866.

Zhang L, Hihara E, Massuoka F, et al,2010. Experimental analysis of mass transfer in adiabatic structured packing dehumidifier/regenerator with liquid desiccant. International Journal of Heat and Mass Transfer, 53, 2856–2863.

#192: Study on solar tube technology for application in a novel light-driven air dehumidification system

Xiang Xu, Xiaoli Ma*, Xudong Zhao, Chang Zhou, Jing Li

School of Engineering and Computer Science
University of Hull, UK, HU6, 7RX, Emails: xiang.xu-2022@hull.ac.uk; x.ma@hull.ac.uk; xudong.zhao@hull.ac.uk;
c.zhou-2020@hull.ac.uk; jing.li@hull.ac.uk

Abstract: *Decarbonisation of the energy systems is critically required to meet the global obligations set out in the Paris Climate Change Agreement. An evaporative cooling system, by using the latent heat of water cycling in the atmosphere, can cool air without the use of significant electrical and thermal energy. However, its cooling capacity is limited by the moisture content of the intake air. To achieve near-zero-carbon air-conditioning operation at any climate condition, the combination between an evaporative air cooling (e.g. dew point air cooling) and a renewable-driven air dehumidification is clearly a promising solution. A novel light-driven air dehumidification system using a photo-thermal material which can absorb solar light energy to excite photo-induced drying process is under investigation by authors, in the meantime, a novel solar tube system which can collect, concentrate and transmit solar light for application in the light-driven air dehumidification system is studied. This paper introduces the novel light-driven air dehumidification system and its driven source, i.e., solar tube system, and presents computer simulation work for study on light transmission performance in the solar tube system. Computer model for light transmission performance simulation on both straight and bend solar tubes has been developed and validated. Simulation work has been carried out for various geometries and light incidence angles. The results are analysed and discussed.*

Keywords: *Solar Tube; Light Transmittance; Light Transmission Efficiency; Air Dehumidification*

1. INTRODUCTION

Decarbonisation of the energy systems is critically required to meet the global obligations set out in the Paris Climate Change Agreement. Air conditioning (AC) is one of the major energy systems applied globally with a market size of around £80 billion per annum [1]. Current AC technologies require large amounts of electrical or thermal energy, the annual electrical demand by AC globally has reached over 2,020 TWh, accounting for 20% of the world electricity use and resulting in 1,100 mega-tons of carbon emission [2]. In line with the carbon intensive nature of the AC industry, decarbonisation of AC systems is clearly a global interdisciplinary challenge. In line with the carbon intensive nature of the AC industry, decarbonisation of AC systems is clearly a global trend with interdisciplinary challenges.

An evaporative cooling system, by using the latent heat of water cycling in the atmosphere, can cool air without the use of significant electrical and thermal energy. However, its cooling capacity is limited by the moisture content of the intake air. To achieve a near-zero-carbon air-conditioning operation at any climate condition, the combination between an evaporative air cooling (e.g. dew point air cooling) and a renewable-driven air dehumidification is clearly a promising solution. A novel light-driven air dehumidification technology using a photo-thermal material which can absorb solar light energy to excite photo-induced drying process is under investigation by authors, in the meantime, a novel solar tube system which can collect, concentrate and transmit solar light for application in the light-driven air dehumidification system is studied. These are introduced as follows:

Novel light-driven dehumidification technology

Sorbents have been regarded as the promising dehumidification materials for developing next-generation air conditioning, such as metal-organic frameworks (MOFs), hydrogels and salt-embedded composites, due to present great potential for water vapor separation [3]. The novel light-driven dehumidification technologies, which characters controlling humidity through the sorbent's simultaneous moisture sorption and desorption. In dehumidification process, the sorbent materials could spontaneously capture and adsorb moisture from air without additional energy input, along with moisture internal transfer to desorption side. To maintain the capability of material on harvesting moisture, the low-grade energy input, such as solar energy, is required for moisture released from desorption surface. Different with conventional thermal-driven and solar-driven dehumidification, the solar light energy will be directly induced to and absorbed by the desorption surface of sorbent for exciting water cluster evaporating from the surface, thus facilitating high energy-efficient desorption process with the sorbent [4-6].

Commonly, due to the desorption the surface is designed directly exposed to outdoors to receive solar energy, which results in the sorbent susceptible to environmental contamination and erosion. In addition, the solar angle changes daily will influence the desorption surface absorbs solar light, in further impact the dehumidification performance. In this case, to achieve the sorbent desorption process indoors, authors investigated a novel solar tube system which enables nature solar light concentrated, redirected and induced to the desorption surface, enhance the dehumidification system performance.

Novel solar tube system for light driven dehumidification system operation

The novel solar tube system comprises a larger Fresnel Len that collects and concentrate the sun light and a smaller Fresnel Lens that collimates the concentrated sun light into parallel light, a super-silver mirror-finish aluminium solar tube system transmits the sun light to the desorption layer surface of the dehumidification bed to excite photo-induced drying process, and a few infrared bulbs work as a light supplement to provide artificial light at night or low light intensity at day time. A sunlight track/control system with light sensors will be coupled into the Fresnel Lens to enable the lens to track the sunlight and control the intake luminous flux. More details can be seen in section 2.

This paper presents a computer simulation work for study on light transmission performance in a novel solar tube system suitable for the novel light-driven dehumidification technology application. Computer model for light transmission performance simulation on both straight and bend solar tubes has been developed and validated. Simulation work has been carried out for various solar tube geometries and light incidence angles, light losses from Fresnel lens and dome is considered. The results are analysed and discussed.

2. CONFIGURATION OF THE NOVEL SOLAR TUBE SYSTEM

The configuration of the solar tube system to be simulated is shown in Figure 1.

As shown in Figure 1(a), the solar tube is comprised of a straight tube section and a 90° bend tube section with a solar tube dome, which is integrated on the upper end of the tube and located on the roof, to collect the sun light. Before entering the dome, the sunlight is concentrated and collimated by the larger Fresnel lens (Fresnel lens 1) and the smaller Fresnel lens (Fresnel lens 2) respectively. The two Fresnel lenses are integrated into a sun tracking shelf to track the sunlight to maximize the light collection.
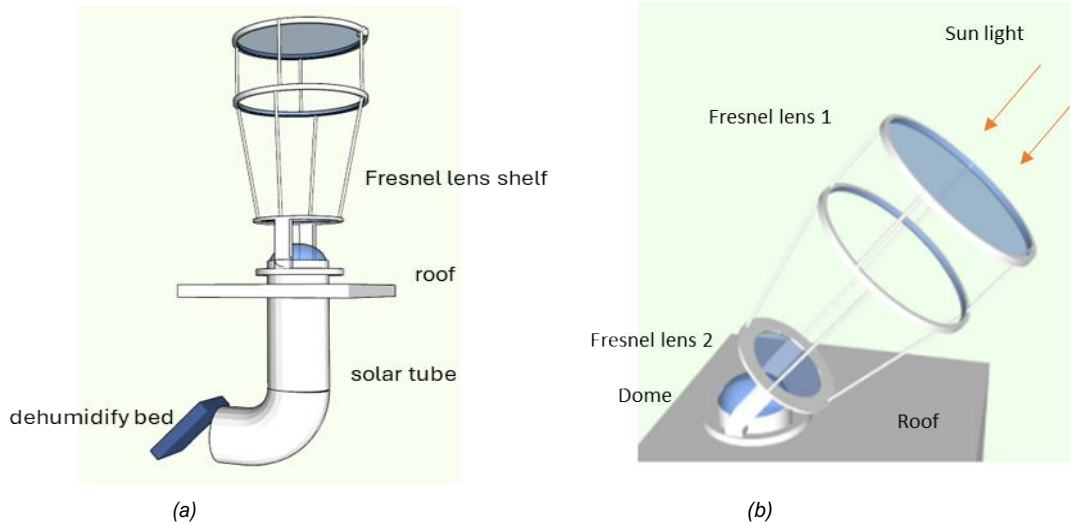
(a)   *(b)*

Figure 1: Solar tube system (a) Configuration of the entire solar tube system; (b) Fresnel lens solar tracking

The light dome collects both direct sunlight and sky scatter light, and the light transmits through the solar tube by reflection. The configuration of the solar tube system is designed specifically for solar driven air dehumidification application, while dehumidification bed is located indoors. The concentrated sunlight transmits to the lower end of the solar tube through the tube and is then projected onto the dehumidification bed to excite photo-induced drying process.

3. COMPUTER SIMULATION METHODOLGY

Numerical mathematical models have been established and computer program has been developed, which is divided into two main programme parts. The first part is the arithmetic logic of the main procedure of the light procedure, which is divided into two models of cloudy and sunny days, and in the sunny day model, it is divided into two procedures of light transmission, and a closer algorithm is chosen as the algorithm of the present study through verification. The second procedure is the simulation of the subroutine, which mainly calculates the efficiency of light concentration and the final size of the emitted light due to the length of the bend radius of the bender in the transmission of the concentrator.

3.1 Mathematical models

3.1.1 LIGHT TRANSMMISION EFFICIENCY

This section presents a model for performance evaluation of solar tube by measuring luminous flux entering and leaving the solar tube in lumens and subsequantly determining the efficiency of the device. Unlike the solar tube for lighting, we use all the solar power including invisible light in the simulation, so we use the "W" directly from the sun, not turn it in to "lm". The luminous flux" in the formulas should be changed into "solar power ".

3.1.1.1 Light transmission efficiency of straight section of the solar tube

The performance of the straight section of the solar tube is assessed by equation (1-1) and (1-2), as below [7]:

$$\psi_{so}(\Theta) = \psi_{si}(\Theta)\rho^{\frac{L\tan\Theta}{D}} \tag{1-1}$$

D is the diameter of the circular tube, or minimum cross-sectional width of rectangle tube [8].

$$\eta_s(\Theta) = \frac{\psi_{so}(\Theta)}{\psi_{si}(\Theta)} \tag{1-2}$$

Where:
- $\Psi so(\Theta)$---Total luminous flux leaving the straight section, lm;
- $\Psi si(\Theta)$---luminous flux entering the straight section, lm;
- $\eta s(\Theta)$---light transmission efficiency of the straight section;
- L---length of the straight solar the tube, m;
- D--- diameter of the circular tube, or minimum cross-sectional width of rectangle tube;
- Θ--- incidence angle between the light beam and the normal, degree;
- ρ ---reflectance of the solar tube internal surface;

3.1.1.2 Light transmission efficiency of bend section of the solar tube

The performance of the bend section is assessed by equations (1-3) and (1-4), as below:

The total luminous flux leaving the bend section of the solar tube expressed by:

$$\psi_{bo}(\Theta) = \psi_{bi}(\Theta)\rho^{n_b} \tag{1-3}$$

176

And the efficiency of the bend section of the solar tube is expressed by:

$$\eta_b(\Theta) = \frac{\psi_{bo}(\Theta)}{\psi_{bi}(\Theta)} = \rho^{n_b} \tag{1-4}$$

Where,

$\Psi bi(\Theta)$ is the total lumininous flux of the light entering the bend tube section, for our system, it is equal to that of the light leaving the straight tube, i.e.,

$$\psi_{bi}(\Theta) = \psi_{so}(\Theta) \tag{1-5}$$

n is the number of reflection through the bend tube, expressed by:

$$n_b = \frac{\beta}{2\phi} \tag{1-6}$$

Where, ϕ in equation (1-6) can be obtained by solving the established equation (1-7),

$$cos^2\phi + \frac{2r_1[cos^2(\Theta+90^o)-1]}{r_2}cos\phi + [r_1^2 - cos^2(\Theta + 90^o)(r_1^2 + r_2^2)] = 0 \tag{1-7}$$

To reduce the complex look of the equations, we can replace $cos^2(\Theta + 90^o)$ with "m" in equation (1-7), i.e,

$$\text{Assume: m} = cos^2(\Theta + 90^o) \tag{1-8}$$

And also, by reforming the equation (1-7), it can be expressed by:

$$r_2 cos^2\phi + 2r_1(m - 1)cos\phi + r_2[r_1^2 - m(r_1^2 + r_2^2)] = 0 \tag{1-9}$$

The equation (1-9) can be solved by the formula for finding the root of a quadratic equation of one variable (QEOV), i.e.,by equation (1-10):

$$x = \frac{-b \pm \sqrt{b^2 - 4ac}}{2a} \tag{1-10}$$

Where,

$$x = cos\phi \tag{1-11}$$

$$a = r_2 \tag{1-12}$$

$$b = 2r_1(m - 1) \tag{1-13}$$

$$c = r_2[r_1^2 - m(r_1^2 + r_2^2)] \tag{1-14}$$

There may be 2 roots (x1 and x2) in the solution, the right one for our application can be found by judging its value range, i.e, $0 \ll cos\phi \ll 1$

The angle ϕ can be founs by:

$$\phi = arccosx \tag{1-15}$$

Where:

$\Psi bo(\Theta)$---Total luminous flux leaving the bend section, lm;
$\Psi bi(\Theta)$---luminous flux entering the bend section, lm;
$\eta b(\Theta)$---light transmision efficiency of the bend section;
nb---number of reflection through the bend tube;
β---angle of bend, degree;
ϕ---angle between the light incidence surface of the solar tube and the line connecting circular section center to the first light reflection point in the tube, degree;
r1---inner radus of the circular section, m;
r2---outner radus of the circular section (r2=r1+D), m;
D---- diameter of the circular solar tube or minimum cross-sectional width of retangle solar tube, m;

3.1.1.3 Total light transmission efficiency of the solar tube system

The total efficiency of the solar tube system is determined by efficincy of straight tube section, efficeny of bend tube section as well as light loss coefficient from Fresnel lens, concave lens and dome, and is expressed by:

$$\eta_T(\Theta) = \tau_T \eta_s(\Theta) \eta_b(\Theta) \qquad (1\text{-}16)$$

$$\tau_T = \tau_d \tau_f \tau_c \qquad (1\text{-}17)$$

Where:

- $\eta_T(\Theta)$ -- total light transmission efficiency of the solar tube system;
- τ_T ------total light loss coefficient from dome, frensnel lens and concave lens;
- τ_f ---- light loss coefficient of Fresnel lens;
- τ_c ----- light loss coefficient of concave lens;
- τ_d ---- light loss coefficient of dome;

3.1.2 Light transmittence

Another method for solar tube performance evaluation is light transmittance.

3.1.2.1 Light transmittence of straight section of the solar tube

The light transmittence of straight section of solar tube is expressed by [9]:

$$Ts(\Theta) = \frac{4}{\pi} \int_{s=0}^{1} \frac{S^2}{\sqrt{1-S^2}} \rho^{int\left[\frac{ptan\theta}{S}\right]} \left(1 - (1-\rho)\left(\frac{ptan\theta}{S} - int\left[\frac{ptan\theta}{S}\right]\right)\right) ds \qquad (2\text{-}1)$$

Where, p is the aspect ratio of the light pipe, expressed by:

$$p = \frac{L}{D} \qquad (2\text{-}2)$$

Where:
- $Ts(\Theta)$---light transmittence of straight section of solar tube;
- p---ratio of the light pipe length to its diameter (Aspect ratio);

3.1.2.2 Light transmittence of bend section of the solar tube

The light transmittience of bend section of solar tube expressed by:

$$T_b(\Theta) = \frac{4}{\pi} \int_{s=0}^{1} \frac{S^2}{\sqrt{1-S^2}} \rho^{int\left[\frac{n_b}{S}\right]} \left(1 - (1-\rho)\left(\frac{n_b}{S} - int\left[\frac{n_b}{S}\right]\right)\right) ds \qquad (2\text{-}3)$$

Where:

- n_b is the number of the reflection in the internal surface of the bend section;
- n_b can be determined by equation (1-6), ϕ in equation (1-6) is calculated by equation (1-7) and equations (1-9)-(1-15).

3.1.2.3 Total light transmittence of solar tube system

The total transmittence of the system is calculted by:

$$T_T(\Theta) = \tau_T T_s(\Theta) T_b(\Theta) \qquad (2\text{-}4)$$

Where:

- T(Θ) --- the total transmittance of the solar tube system;

3.1.3 Light transmission model on cloudy days

In the absence of direct sunlight, the luminance (j (ϑ, ϕ, ϕ0, r0)) reaching the diffusing end of the solar tube is the product of three functions, it can be expressed by [10]:

$$j(\Theta, \phi_S, \phi_0, r_0) == L_a \rho^N t_C \qquad (3\text{-}1)$$

$$N = ns + nb \qquad (3\text{-}2)$$

n_s is the number of reflections inside the straight tube, expressed as:

$$n_s = \frac{L\tan\theta}{D}$$

(3-3)

n_b is the number of reflectioins in bend tube section, it can be dtermined by equation (1-6), ϕ in equation (1-6) iscalculated by equation (1-7) and equations (1-9)-(1-14).

Where:

- L_a---luminace of the arbitrary sky element (cd/m²)
- ρ --- reflectance of the interior surface of the solar tube;
- N ---total number of reflections through the entire tube;
- n_s---reflection number in straight tube section;
- Lz --- zenith luminance (cd/m²);
- t_C ---Total transmission coefficient of dome, fresnal lens and oncave lens;

In this case, ζ and α represent the entry direction of the scattered natural light into the roof dome of the solar tube. t_C relates to the transmission of the dome roof and depends on the transparency of materials used, the value usually sits between 0.8 and 0.92 (Kocifaj et al, 2008). This equation factors in transmission through the roof dome when calculating the levels of illuminance reaching the diffuser.

3.2 Model validation

The validation of the algorithmic model was carried out by comparing the simulation results from LightTools software and that from the established algorithm model. The simulation assumes the reflection coefficient of the reflective material in the light pipe to be 99.7%, the incident angle Θ is 10°, 20°, 30°, 40°, 50°, 60°, 70°, 80° respectively, the length of the straight section of light pipe is 1.5m, and the angle of bend section of the light pipe is 90°. The outputs of the simulation are the intensity of light radiation at the exit of the light pipe and the efficiency of the transmitted light. The output of light radiation intensity from LightTools is 93 W/m², 90 W/m² , 85 W/m² , 73 W/m² , 69 W/m² , 48 W/m² , 28 W/m² , and 8 W/m² respectively, while the outputs from the established model are 94.28 W/m² , 88.13 W/m² , 86.11 W/m² , 75.39 W/m² , 65.65 W/m² , 49.13 W/m² , 30.44 W/m² , and 6.77 W/m² respectively. Figure 13 shows the light concentrator model in LightTools. The reliability of the algorithm model is verified by analysing the correlation between the algorithm output results and the simulation results of LighTools.

Due to the differences between the logic of the algorithm's arithmetic equation and the simulation software, there is a certain error between the simulation results from the established algorithm model and that from the LightTools software. The Pearson's correlation coefficient between the two was calculated by Origin software to be 0.997, and Sig. = 0.01 is less than 0.05 (Figure 13). It indicates that the algorithmic model in this study has an obvious correlation with the light radiation transmission and output intensities obtained from the LightTools software, and the algorithmic model can be used for subsequent simulation.
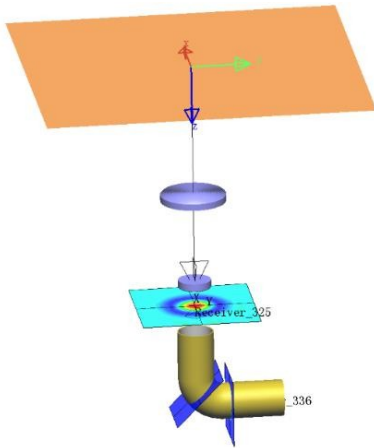
Figure12: Simulation with Lighttools software
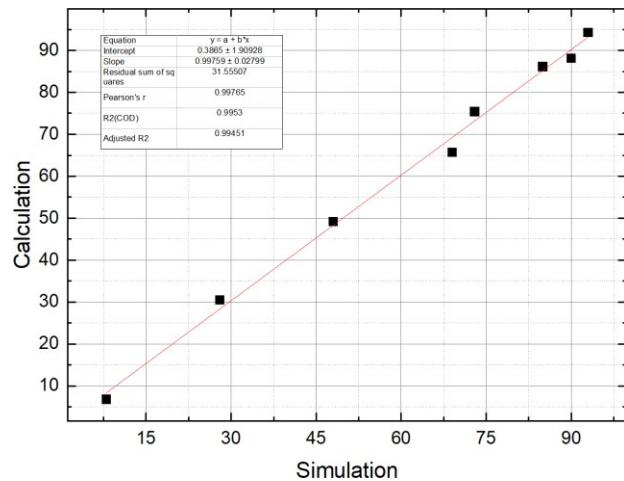
Figure 13: Correlation analysis of the simulation data of the light gathering algorithm model

3.3. Simulation methodology

The transmission performance was carried out for solar radiation through the solar tube system, which includes Fresnel lens, a light dome with a straight tube section plus a bent tube section. The simulation methodology is listed in Table 1 and Table 2. As shown in Table 2, each simulation has a variable parameter 1, for each variable parameter 1, simulation is carried out for a range of related variable parameter 2, the other parameters are assumed to be that in Table 1.

Table 1: Fixed parameters

Input light intensity	Straight tube length	Tube diameter	Bend angle of bend section
114 W	1.5m	0.04m	90ºC

Table 2: Variable parameters

	variable parameter 1	Related variable parameter 2	Simulation output
1	Ө (From o° to 80°，step is 1°)	ρ (99.7%/98%/95%/93%/90%/85%)	ηs,ns
2	D (From 0.15m to 0.6m，step is 0.05m)	Ө (From o° to 75°，step is 15°)	ηs, ns, Ψso, ηb
3	L (From 0.5m to 8 m，step is 0.05m)	Ө (From o° to 75°，step is 15°)	Ψso, ηs
4	β (From 15° to 90°，step is 15°)	Ө (From o° to 75°，step is 15°)	ηb,nb
5	Hourly data		ψbo
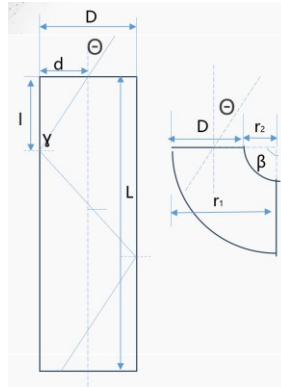
Figure14: The position of the parameter in tube

4. RESULTS AND DISCUSSION

4.1. Relations between transmission efficiency, number of reflections, reflectivity and incidence angle
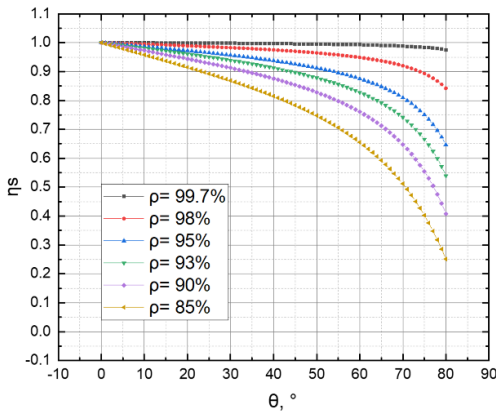
Figure15: Variation of light transmission efficiency in a straight tube with light incidence angle for different reflectivity
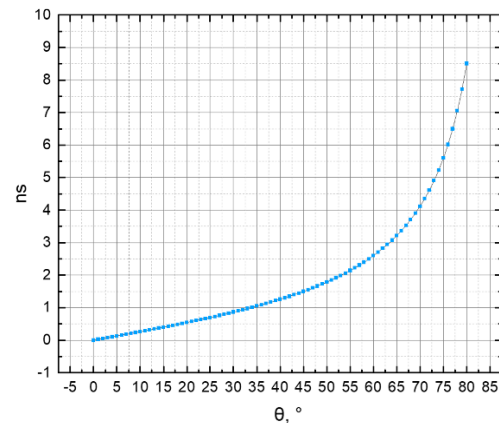
Figure16: Variation of number of light reflections in straight tubes with solar incidence angles for different reflectivity

Figure 15 shows the variation of light transmission efficiency of the straight tube section with angles of incidence for five different reflective material with different reflections. The results indicate that there is a significant increase in the conduit efficiency of the straight tube as the reflectivity increases. As the angle of incidence increases, the transmission efficiency of the light tube decreases. And when the reflectivity of the light pipe decreases, the transmission efficiency of the light pipe with low reflectivity decreases more as the incidence angle of solar radiation increases. The optical tube reflectivity of 99.7% of the optical transmission efficiency with the change of light incidence angle decreases the smallest. Angle of incidence increases from 0 ° to 80 ° results in only 0.025 reduction in transmission efficiency.

The transmission efficiency of the light tube with a reflectance efficiency of 85% varies most obviously with the angle of light incidence: the angle of incidence increases from 0 to 50 °, the light transmission efficiency decreases by 0.75; the angle of incidence increases from 50 to 80 °, the light transmission efficiency is reduced from 0.75 to 0.25, this indicates the reduction rate increases with the increase of the angle of the light incidence. When the angle of incidence increases from 60 ° to 80 °, light radiation transmission decreases from 40% -50%. The variation of the number of reflections in the straight tube can be seen from Figure 16, as the tube material reflectivity does not affect the reflection number, the curve is fitful for the case of any reflectivity. By Figure 16, it is seen that with the angle of incidence increases, the number of reflections increases more rapidly in the angle range of 60°- 80°.

4.2. Relation between transmission efficiency, tube diameter and light angle of incidence
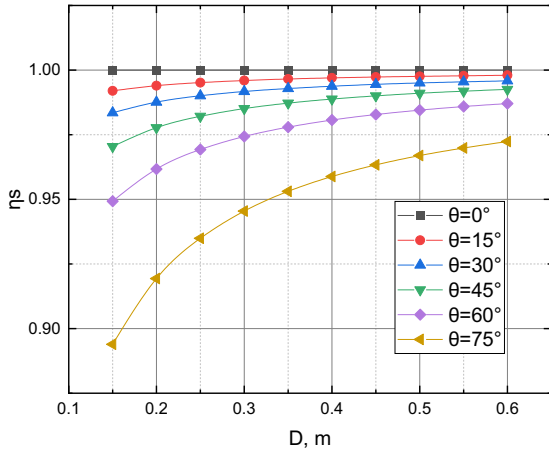
Figure 17: Variation of light transmission efficiency in straight tubes with tube diameters for different solar incidence angles
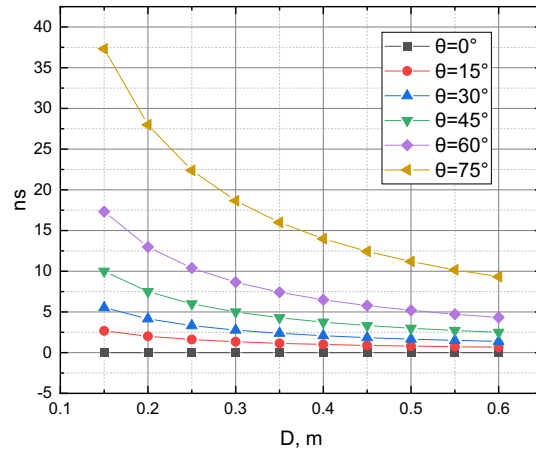
Figure18: Variation of number of light reflections in straight tubes with tube diameters for different solar incidence angles

Figure 17 shows variation of the light transmission efficiency in straight tubes with diameters of straight tube for different incidence angles. The results show that there is a significant increase in the light transmission efficiency of the straight tube with the increase of the diameter and with the increase of the incidence angle, the transmission efficiency of the light tube decreases. However, the efficiency increases with the diameter gets less obvious with the decrease of the incidence angle. In the case of incident angle of 0 degree, the light transmission efficiency keeps constant with the increase of tube diameter. This is because the light travels through the tube vertically and without reflection on the tube surface, as shown in Figure 18.

With the increase in the angle of incidence of light changes, the light tube material reflection efficiency of 75% of the transmission efficiency is the maximum: when the tube diameter increased from 0.15m to 0.33m, the light transmission efficiency increased from 0.9 to 0.95; tube diameter increased from 0.33m to 0.6m, the light transmission efficiency increased from 0.95 to 0.975. With the increase in the tube diameter, the increase in the efficiency of the light transmission is slower. Figure 18 shows that as the angle of incidence increases and the diameter of the tube decreasing, the number of reflections of light increases and the rate of increase grows
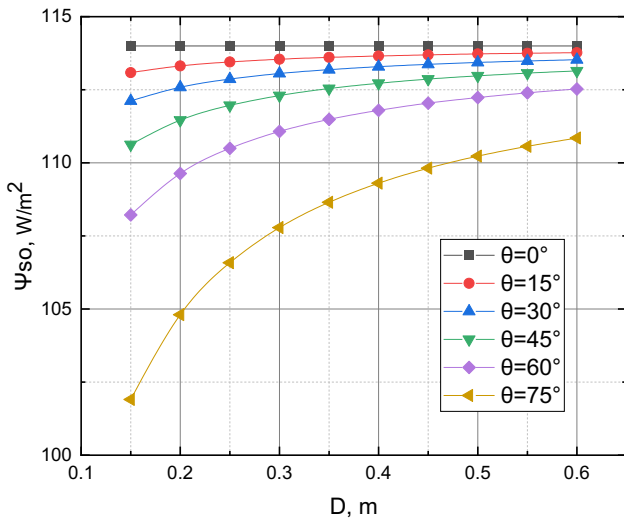
Figure 19: Variation of light intensity at the outlet in straight pipe with tube diameter for different solar incidence angles
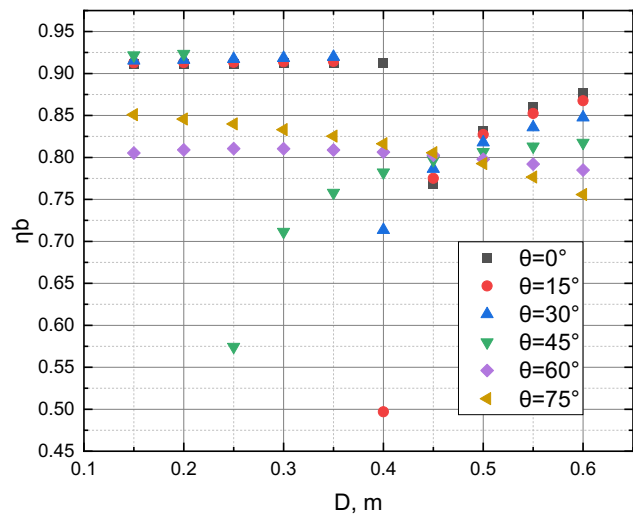
Figure 20: Variation of light transmission efficiency in bends with tube diameter for different solar incidence angles

Figure 19 shows that there is a significant increase in light intensity of the light output from the straight tube as the diameter of the tube increases. With the angle of incidence increases, the light intensity decreases. For example, for the angle of incidence of 45, when the diameter of the tube from increases from 0.15m to 0.6m, the light intensity at tube outlet increases from 110.3W/m² to 113 W/m², when the angle of incidence of 75, the diameter of the tube from 0.15m to 0.6m, the emitted light from 101.5W/m² to 110.8 W/m².

Figure 20 shows that with the increase in the angle of incidence, there are different trends in the transmission efficiency of light in different tube diameters. As the tube diameter increases, the transmission efficiency at incident angles of between 0° and 45° decreases firstly and then increases. When the angle of incidence between 60° and 75°, the transmission efficiency of light decreases with the increase of the tube diameter.

4.3 Relation between transmission efficiency, number of reflections, tube lengths and angle of incidence
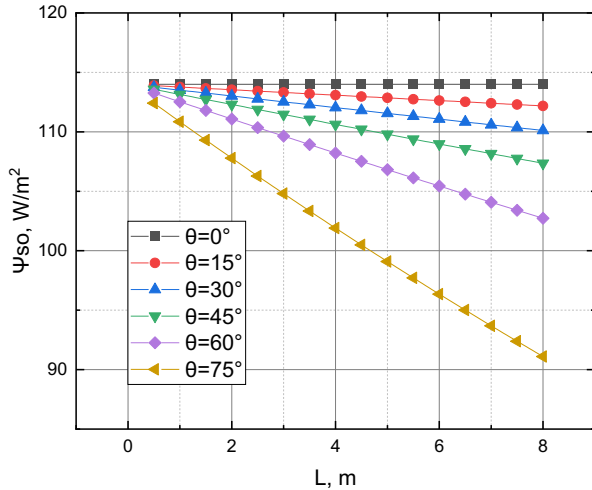
Figure 21: Variation of Intensity of light radiation at the outlet with straight tube length for different solar incidence angles
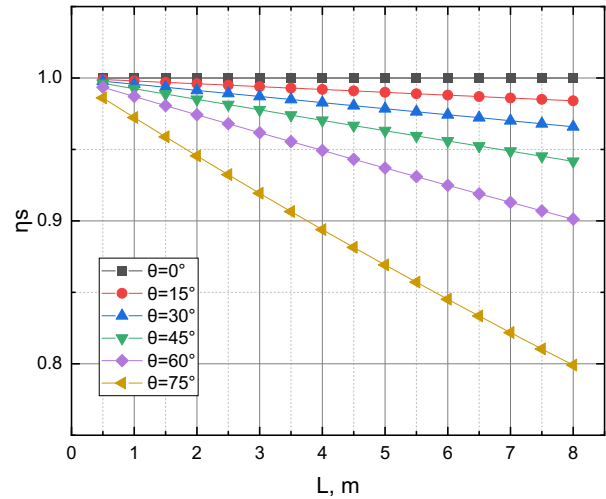
Figure 22: Variation of Light transmission efficiency in straight tubes based on different solar incidence angles and tube lengths

Figure 21 and Figure 22 show the variation of light intensity at the outlet of straight tube and efficiency of the light transmission through the straight tube for different angles of incidence. The results show that as the length of the tube decreases, the light transmission efficiency of the straight tube is significantly improved. As the angle of incidence decreases, the transmission efficiency of the light tube increases. When the incident angle is certain and the length of the light tube increases, the light transmission efficiency of the light tube with a low incident angle changes at basically the same rate. At an angle of incidence of 0°, the transmission efficiency of light with the change in tube diameter is almost unchanged. When the reflectivity of the light tube is 75%, its light transmission efficiency with the change in the angle of incidence of light is the largest. When the tube length increases from 0.5m to 8m, the light transmission efficiency decreases from 0.98 to 0.8. When the reflectivity of the light pipe is 45%, the light transmission efficiency decreases from 0.99 to 0.945 as the length of the pipe is increased from 0.5 m to 8 m.

4.4 Relation between transmission efficiency, number of reflections, angle of incidence and bend angle of the bend section
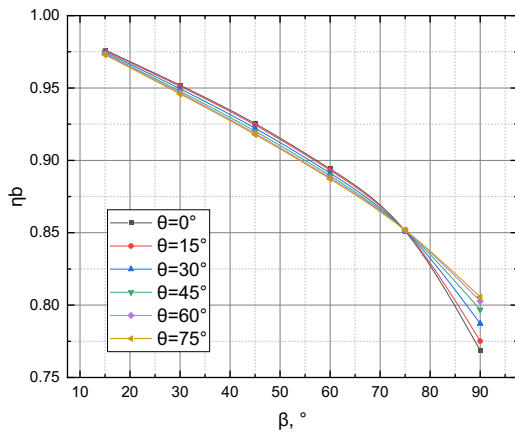
Figure23: Variation of Light transmission efficiency of bend section with bend angle for different solar incidence
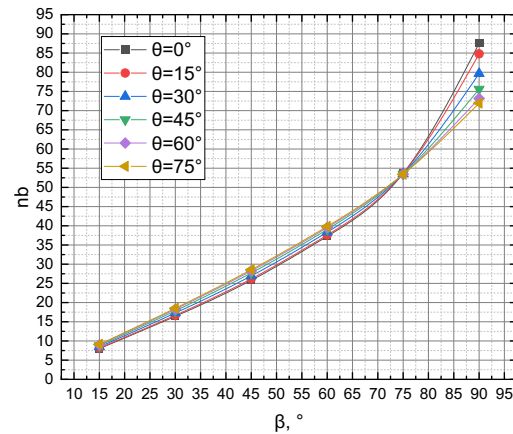
Figure 24: Variation of number of light reflections with bend angle for different solar incidence angles

Figure 23 and Figure 24 show the output light intensity and light transmission efficiency of in the bent tubes with different bend angles for six different solar incidence angles, the solar tube geometry used in this simulation can be seen in Table 1. The results show that as the angle of the bend decreases, the light transmission efficiency of the bend is significantly improved. When the angle of the bend is greater than 75°, the light transmission efficiency decreases faster: as the angle of the bend increases from 15° to 75°, the transmission efficiency decreases from 0.975 to 0.875; as the angle of the bend increases from 75° to 90°, the transmission efficiency decreases from 0.875 to 0.7625.

Changes in the angle of incidence relative to changes in the angle of the bend on the light transmission efficiency is not obvious. When the angle of incidence of sunlight is less than 75°, with the decrease in the angle of incidence of the sun, the light transmission efficiency increases. When the solar incidence angle is greater than 75°, the light transmission efficiency decreases as the solar incidence angle decreases.
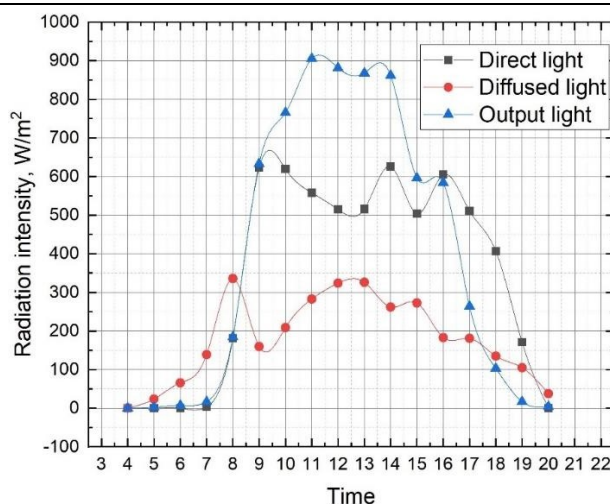
Figure25: Solar light intensity and output light intensity from the light tube system in a typical summer day in the UK

Figure 25 shows the relation between the intensity of solar radiation and direct and diffuse solar radiation for the full time of the day on a simulated summer day in the UK. The direct solar light starts to increase abruptly to about 650 W/m² at about 9 o'clock and keepsfluctuating at about 550 W/m² until 17 o'clock when it starts to decrease. And the diffuse light started to increase from 7 am to 17 pm, and the diffuse radiation intensity was in the range of 150 W/m²-325 W/m². The light radiation intensity output through the light tubesystem can be stabilised at 900 W/m² at 11:00-14:00 pm. It increases from 200 W/m² to 900 W/m² at 8:00-11:00 p.m., and decreases from 900 W/m² to 200 W/m² at 14:00-17:00 p.m.

5. CONCLUSION

This paper presents a numerical simulation work for a novel solar light tube system which include Fresnel lens, a solar tube consisting of a straight section and bend section. The established numerical model is verified by LightTools software. The results show that optimizing the novel solar tube system in terms of surface reflectance, light tube length, diameter and bend angle can improve the light transmission efficiency, the light transmission efficiency is also greatly influenced by incidence angles as variation of incidence angles affects the number of reflections. As a summary, the transmission efficiency of sun light can be improved by decreasing the incidence angle of sunlight, increasing the reflectivity of the reflective surface in the light pipe, increasing the diameter of the light pipe, decreasing the length of the light pipe, and decreasing the angle of the bend pipe.

6. REFERENCES

[1]   Grand View Research 2019-2025, 2019, https://www.grandviewresearchanalysis/air-conditioning-systems-indistry;

[2]   IEA, The Future of Cooling, 2018;

[3]   Poredoš, P., H. Shan, and R. Wang, Dehumidification with solid hygroscopic sorbents for low-carbon air conditioning. Joule, 2022. 6(7): p. 1390-1393.

[4]   Zhang, Y., et al., Super hygroscopic nanofibrous membrane-based moisture pump for solar-driven indoor dehumidification. Nat Commun, 2020. 11(1): p. 3302.

[5]   Shi, W., et al., Unidirectional Moisture Delivery via a Janus Photothermal Interface for Indoor Dehumidification: A Smart Roof. Adv Sci (Weinh), 2023. 10(20): p. e2301421.

[6]   Zhang, K., et al., A Zero-Energy, Zero-Emission Air Conditioning Fabric. Adv Sci (Weinh), 2023. 10(11): p. e2206925.

[7]   Mohelnikova, J. (2008) Daylighting and energy savings with tubular light guides. WSEAS Transactions on Environment and Development, 3(4), 200 - 209.

[8]   Whitehead, L. A. (1998) New simplified design procedures for prism light guide luminaires. Journal of the Illuminating Engineering Society, 27(2), 21 - 27.

[9]   Swift, P. D. & Smith, G. B. (1995) Cylindrical mirror light pipes. Solar Energy Materials and Solar Cells, 36(2), 159 - 168.

[10] Kocifaj, C., Darula, S., Kittler, R. (2008) HOLIGILM: Hollow light guide interior illumination method - An analytic calculation approach for cylindrical light-tubes. Solar Energy, 82(3), 247-259.

#195: Solar PV powered cooling for rural healthcare facilities in Malaysia

Amirudin ABDULLAH[1], Hasila JARIMI[2,3], Tianhong ZHENG[4], Ahmad FAZLIZAN[5], Ubaidah SYAFIQ[6], Saffa RIFFAT[7]

[1] Solar Energy Research Institute. The National University of Malaysia, 43600 Bangi Selangor
[2] Solar Energy Research Institute. The National University of Malaysia, 43600 Bangi Selangor
[3] Department of Architecture and Built Environment, The University of Nottingham, University Park, Nottingham, NG7 2RD
[4] Department of Architecture and Built Environment, The University of Nottingham, University Park, Nottingham, NG7 2RD
[5] Solar Energy Research Institute. The National University of Malaysia, 43600 Bangi Selangor
[6] Solar Energy Research Institute. The National University of Malaysia, 43600 Bangi Selangor
[7] Department of Architecture and Built Environment, The University of Nottingham, University Park, Nottingham, NG7 2RD

Abstract: This paper presents an analysis of an off-grid solar cooling system designed for rural healthcare facilities in Malaysia where electricity access is limited or unreliable. The system utilizes a DC-powered vapor compression cooling unit driven by photovoltaic (PV) solar panels with energy storage in both a thermal tank and a battery. The primary aim is to maintain indoor air temperatures within a comfortable range and improve air quality in this area. The performance of the system was monitored over various conditions, and the results show that indoor temperatures were kept between 22 °C to 26 °C, even when external temperatures reached 35 °C. Additionally, a cost-benefit analysis shows that the system achieves a return on investment (ROI) within 12 months. The study concludes that this solar-powered cooling solution is both economically viable and environmentally sustainable for rural healthcare applications.

Keywords: Off- Grid Cooling, Sustainable Rural Cooling, Levelized Cost of Cooling

1. INTRODUCTION

Building operations account for 30% of global final energy consumption and 26% of energy-related emissions. Of these emissions, 8% are direct emissions from buildings, while 18% are linked to the production of electricity and heat used within buildings. In 2022, energy consumption for space cooling increased by over 5% compared to 2021. This growing demand for cooling significantly impacts peak electricity loads, particularly on hot days, potentially leading to power outages [1]. Conventional air-conditioning systems typically rely on electrically driven AC vapor compression cycles powered by fossil fuels, which contribute substantially to CO2 emissions and exacerbate global warming.

Solar cooling technologies offer a sustainable alternative by converting solar energy into cooling through two main mechanisms: solar photoelectric conversion and solar thermal conversion [2]. In photoelectric conversion, photovoltaic (PV) cells transform solar energy into electricity to power conventional vapor-compression chillers, which may be DC- or AC-powered. In contrast, solar thermal conversion uses solar collectors to convert solar energy into thermal energy, which drives cooling systems such as absorption, adsorption, and desiccant cooling. Among these, solar absorption cooling is the most common, considered both cost-effective and widely available [2]. However, compared to solar absorption systems, solar PV refrigeration systems are simpler in design and easier to maintain [3]. Recent studies indicate that in some regions, the economic performance of PV cooling systems can surpass that of solar thermal systems due to declining PV panel costs [4]. Despite their potential, direct PV-powered compressors cannot operate during nighttime or low solar irradiance, highlighting the need for energy storage. In off-grid PV cooling systems, batteries are often used to store energy, but they increase both costs and risk of accidents. As a result, researchers are exploring ways to reduce battery usage in these systems [3]. For larger PV refrigeration systems, battery costs remain high, and frequent replacements due to degradation increase both investment and operational costs, while raising environmental concerns at the end of their lifecycle. Consequently, integrating thermal storage with PV-powered vapor compression systems has garnered significant attention in recent years. Several studies have explored the use of ice thermal storage in refrigeration and air-conditioning systems. A system using ice thermal storage and battery storage with an AC compressor demonstrated, through theoretical calculations and experimental testing, that it could stably serve users for 4 hours at night. However, the refrigerator's ice-making efficiency was only 50.19%, leading to low energy efficiency [5]. Another study on a refrigerated warehouse system using a DC variable frequency compressor with different PV capacities showed that increasing the PV capacity-to-compressor power ratio by 10% reduced solar intensity requirements and shortened the temperature reduction time by 32 minutes [6].

For a 3HP household air conditioning system with ice thermal storage and a single coil cold storage, experimental results revealed that a refrigerator powered by the grid had a coefficient of performance (COP) 6.31% higher than one powered by distributed PV energy. Additionally, the COP of a water chiller air conditioning system was 1.38 times higher than that of the ice storage mode [7]. Semi-dynamic modeling of a PCM ice storage system with battery and AC compressor for building retrofits suggested that a PCM-to-battery storage capacity ratio greater than 6 is required to achieve optimal renewable energy penetration [8]. Experimental and theoretical work on a photovoltaic direct-driven ice storage air-conditioning system (PDISAC) showed that it could maintain room temperatures below 298.15 K for two hours at night [9]. Finally, a photovoltaic vapor compression system for a 50-liter refrigerator, tested in a hot arid climate with and without PCM, proved suitable for post-harvest crop refrigeration in remote areas, achieving a COP of 1.22 and maintaining a storage temperature of 5°C by the third day and 0°C by the sixth day [10]. Despite these advancements, current solar-powered cooling systems still face significant limitations.

These include high startup current demands, performance fluctuations due to inconsistent solar radiation, and the high cost of battery storage. Additionally, many systems are either too complex or not sufficiently optimized for rural healthcare settings, where ease of use and reliability are critical. Therefore, there is a need for a simpler, more cost-effective off-grid solar cooling solution that can maintain indoor air quality and comfort while being affordable and easy to implement in rural areas. To address this gap, this research focuses on designing a DC-powered vapor compression cooling system that integrates both thermal and battery energy storage. The system is tailored specifically for rural healthcare facilities to ensure stable cooling performance under fluctuating solar conditions. The objectives of this study are: (1) to design an off-grid DC vapor compression system powered by solar energy, (2) to evaluate its performance in maintaining indoor air quality and thermal comfort, and (3) to conduct an economic analysis to determine its feasibility in rural clinic settings.

2. RESEARCH METHODOLOGY
2.1. Experimental setup

The off-grid solar cooling system designed for this study integrates photovoltaic (PV) solar panels with a DC-powered vapor compression cooling unit and energy storage. The system consists of three main components: (1) the solar PV panels, (2) a battery bank for energy storage, and (3) a thermal storage tank. The DC vapor compression cooling unit operates directly from the energy stored in the batteries, while the thermal storage tank acts as an additional reservoir of cooling energy to ensure stable temperatures during low solar radiation periods or at night. This setup adds an extra layer of energy storage, helping to regulate indoor air temperature during periods with limited sunlight. The schematic of the experimental setup is presented in Figure 1. Meanwhile, the system components are summarized in Table 1.

Table 1: The system components

Items	Specification	Quantity
Solar PV panels	350 Wp Rating power at STC =350 W Voc = 46.2 V Isc = 9.38 A	6 panels for DC compressor 2 panels for auxiliary components such as water pump and fan coil unit.
Balance of Systems	Electrical battery storage 12 V 200 Ah	2 units of battery

	MPPT solar charge controller 60 Amp 24V Inverter at 300-Watt capacity	1 unit of other components
Water pump	30 Watt, 24 VDC powered water pump	
Fan coil unit	50-Watt BLDC motor fan at maximum of 5 kW cooling capacity	1 unit
Compressor	DC 90 v-280V, Power: 410 Watt – 1920 Watt	1 unit
Refrigerant	R32	
Thermal battery	Water	300 l tank with Double coil for water and direct cooling for water

Figure 1: The schematics on the experimental setup

2.2. Experimental design

The system was installed in a test room as presented in Figure 2, designed to simulate the typical conditions of rural healthcare in a tropical climate. The room has a floor area of 15 square meters and was equipped with temperature and humidity sensors to monitor performance. External environmental conditions, such as solar radiation and ambient temperature, were also recorded throughout the experiment. The system was tested over a period of one month, with measurements taken daily from 8:00 AM to 5:00 PM. During the testing period, solar radiation levels were recorded using a pyranometer, and indoor air quality parameters were monitored using a multi-channel data logger. The data collected included room temperature, relative humidity, compressor power consumption, and solar radiation levels.

Figure 2: (a) The PV setup and the test house used for the case-study (b) The setup for the vapour compression unit and the thermal storage unit (c) The Balance of System (BOS) for auxiliary components and (d) The fan coil unit

186

2.3. Performance Metrics

The performance of the system was evaluated based on its ability to maintain indoor air temperatures between 22°C and 26°C, even during periods of peak external temperatures. Relative humidity was also closely monitored to ensure it remained within acceptable comfort levels, typically ranging from 30% to 70%, which is critical for maintaining a comfortable indoor environment. The energy consumption of the DC compressor was tracked throughout the day to assess its operational efficiency under varying solar radiation conditions. Additionally, the output of the solar panels was recorded to analyze the system's overall energy balance, with a focus on the efficiency of solar energy conversion and its ability to sustain the system's energy demands throughout the day.

2.4. Economic Analysis

An economic evaluation was conducted to assess the feasibility of implementing the system in rural areas. The analysis included the total cost of installation, operation, and maintenance, as well as the potential cost savings from reduced fuel consumption compared to diesel generators typically used in rural settings. The return on investment (ROI) was calculated by comparing the initial capital costs with the energy savings achieved over time.

3. RESULTS AND DISCUSSION
3.1. Performance analysis

Figure 3 (a) presents the temperature variation in the room, ambient temperature (Ta), and solar radiation (G) over the course of a week, with a specific focus on the system's operation during five active days. This system is specifically designed to provide reliable cooling for rural healthcare facilities that often operate during daytime hours. During these five operational days, the cooling system effectively maintains indoor temperatures within a comfortable range, despite significant fluctuations in both ambient temperature and solar radiation throughout the day. The room temperature remains relatively stable between 24 °C and 26 °C, even as the outdoor temperature peaks around midday. This indicates the system's ability to provide a consistent indoor climate, critical for maintaining comfort and operational efficiency in rural healthcare facilities that may have limited or not have consistent grid access. Meanwhile, Figure 3 (b) provides a more detailed daily analysis of the system's performance over three days. The close-up highlights how the system responds to fluctuating solar radiation and ambient temperature while operating during healthcare facilties hours (typically 8 AM to 5 PM). The graph shows that while the ambient temperature and solar radiation rise significantly during the middle of the day, the room temperature remains relatively stable. This is crucial for healthcare facilities in rural areas, as maintaining a cool and comfortable environment is essential for the well-being of patients and staff. The cooling system, powered by solar energy, performs optimally during peak sunlight hours, but a slight rise in room temperature towards the late afternoon suggests that improvements, such as enhanced energy storage, could further stabilize indoor conditions when solar input decreases.Overall, the system demonstrates its effectiveness in meeting the cooling needs of rural healthcare facilities over a 5-day operational period, offering a sustainable solution that minimizes reliance on electrical battery storage while maintaining thermal comfort.
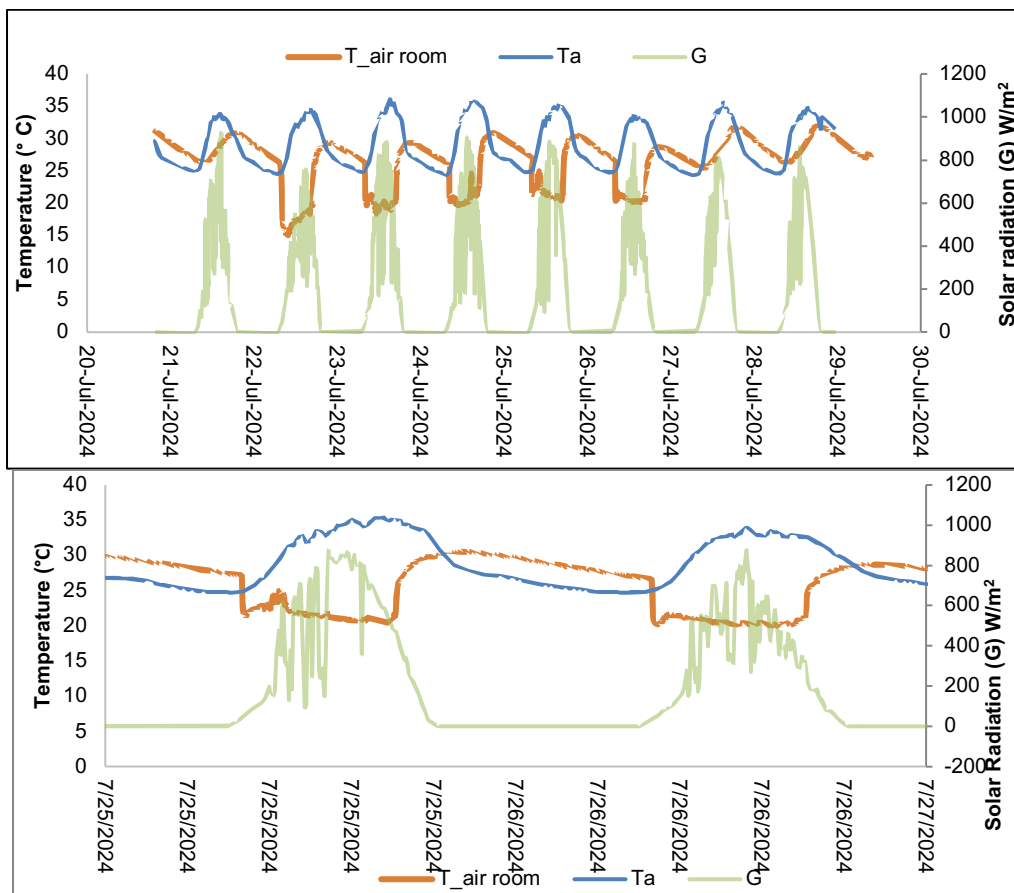
Figure 3: (a) The temperature variation in the room, ambient temperature and solar radiation with time of the day in 1 week. (b) The detail outlook on the variation the parameters with time of the day

Figure 4 illustrates the variation in relative humidity (RH) for both indoor and outdoor environments, alongside solar radiation over a week. The indoor RH levels remain relatively stable between 55% and 65%, ensuring a comfortable indoor environment for both patients and healthcare staff. Meanwhile, outdoor RH fluctuates more dramatically, particularly in the early morning and late evening, following a clear diurnal pattern with the rise and fall of solar radiation. The table complements this figure by providing detailed data on room temperature, comfort level, solar radiation (G), ambient temperature, mean radiant temperature, and relative humidity (RH) at different times of the day. Despite ambient temperatures reaching as high as 31.5 °C during the afternoon (15:00), the room temperature is maintained between 24.2 °C and 26.5 °C, ensuring a comfortable indoor environment. This consistency in temperature control is critical in rural healthcare facilities where reliable cooling is essential for patient care and medical equipment functionality. The relative humidity (RH) values from the table show that the system keeps indoor RH within the comfortable range (around 57-68%), even as outdoor RH varies significantly throughout the day. In this study we also have conducted a case study with real user perspective to receive feedback in terms of thermal comfort. As the day progresses, solar radiation peaks during midday, leading to higher ambient temperatures and outdoor RH. Despite these fluctuations, the indoor environment remains stable in both temperature and humidity, with only a slight increase in temperature and RH noted towards the late afternoon (16:30-17:00). The system continues to provide comfortable conditions, with only a slight shift to "slightly uncomfortable" around the end of the operational day, which is a minor concern that could be mitigated with extended operation or additional energy storage. This combination of data from Figure 4 and the table demonstrates the system's effectiveness in maintaining a stable and comfortable indoor environment in rural healthcare facilities, even during periods of high solar radiation and fluctuating outdoor conditions. The performance of the cooling system, in conjunction with the management of indoor relative humidity, emphasizes its suitability for rural healthcare facilities, where maintaining patient comfort and efficient system operation are both crucial.
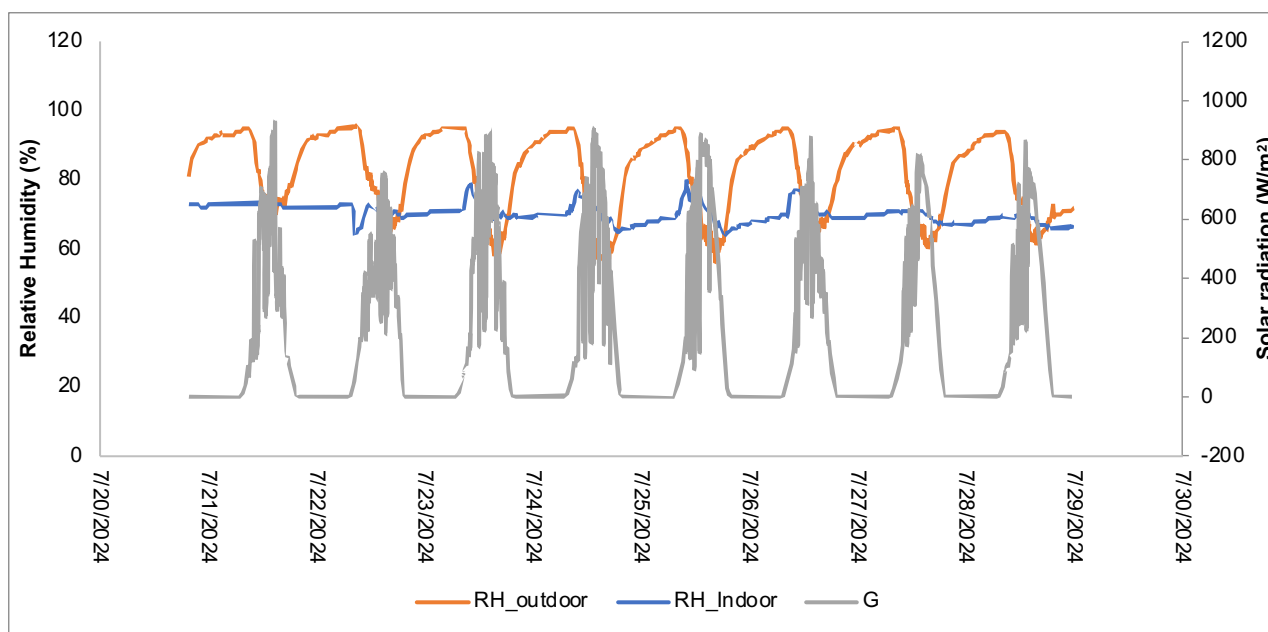
Figure 4: The variation in relative humidity in the test room

Table 2: Thermal comfort analysis of the test room

Time	Room temperature	Comfortable level	G (W/M2)	Ambient temperature (°C)	Mean radiant temperature (°C)	RH (%)
9:30	24.7	comfortable	176	26.9	22	68.9
10:00	24.3	comfortable	149	26.2	20.8	63
10:30	24.7	comfortable	225	27.3	21.1	66.7
11:00	24.2	comfortable	780	28.8	20.4	61.2
11:30	24.3	comfortable	709	28.5	20.5	60.7
12:00	24.4	comfortable	340	28.4	20.4	60.3
12:30	24.5	comfortable	793	29.5	20.5	60
13:00	24.9	comfortable	685	30	20.6	59.4
13:30	25.1	comfortable	604	29.7	20.8	59.7
14:00	25.6	comfortable	722	30.2	21.1	59.1
14:30	26	comfortable	313	30.8	21.1	58.3

15:00	26.4	comfortable	236	31.5	21.8	56.6
15:30	26.1	comfortable	313	30.8	21.6	57.2
16:00	26.2	comfortable	236	31.5	21.7	57.1
16:30	26.5	slightly uncomfortable	718	30.5	22.6	57.2
17:00	26.5	slightly uncomfortable	208	29.5	22.8	57.9

3.2. Economic analysis

As illustrated in Figure 5, the total installation cost of the solar-powered air conditioning system with very minimal battery storage and cold energy storage tank (thermal energy storage) is USD 7,749, with annual operating costs of USD 336, leading to a total Year 1 cost of USD 8,085. Since the application is focusing on rural areas, the system offers annual savings of USD 8,285 through fuel cost reduction, primarily by offsetting the diesel consumption required for a 5-kW air conditioning system. The calculated payback period is approximately 12 months (0.98 years), meaning the initial investment will be fully recovered within the first year of operation. After this period, the system will continue to generate substantial savings, particularly beneficial in rural settings where grid electricity is either unreliable or unavailable. This system not only reduces operational costs but also enhances sustainability by decreasing reliance on diesel and cutting down on carbon emissions, making it a viable long-term solution for off-grid cooling needs.
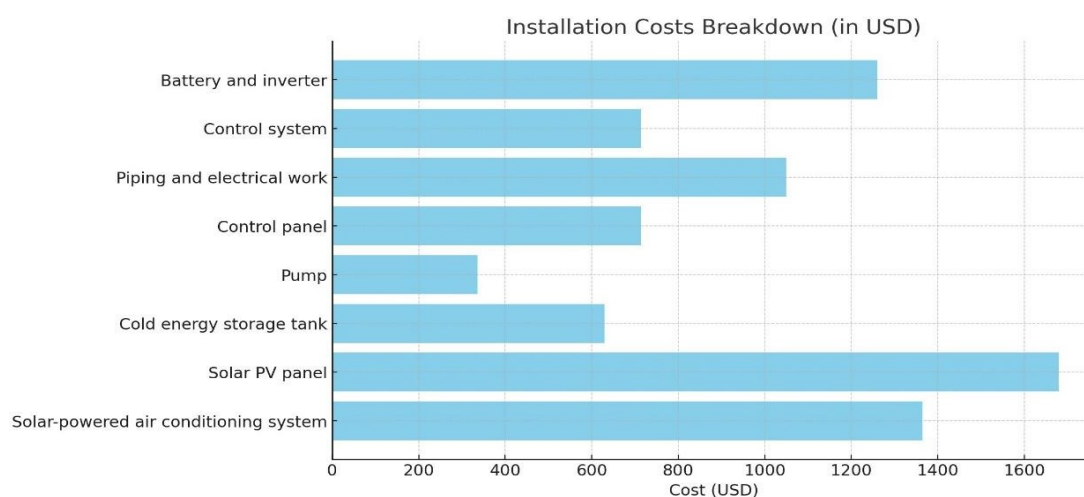
Figure 5: Installation breakdown cost

4. CONCLUSION

Installation costs of USD 7,749 and annual operating costs of USD 336, offers significant fuel savings of USD 8,285 per year. The calculated payback period of approximately 12 months (0.98 years) indicates a rapid return on investment, making the system financially viable within the first year of operation. Beyond this, the system will continue to deliver long-term economic benefits by eliminating diesel fuel consumption and reducing operational costs. Moreover, the use of renewable solar energy and battery storage enhances the system's reliability, ensuring consistent cooling throughout the day, even in periods of low solar radiation. This makes it particularly suitable for remote locations where access to grid electricity is limited or unavailable. In addition to the financial benefits, the system contributes to environmental sustainability by decreasing reliance on fossil fuels and reducing carbon emissions, aligning with global efforts to mitigate climate change. Overall, this solar-powered cooling system demonstrates the potential for a cost-effective, energy-efficient, and environmentally friendly alternative to traditional fuel-based cooling solutions, offering a sustainable path forward for rural healthcare and other off-grid applications. However, although promising, it is crucial to consider the logistics and practicality of the proposed system as it involves the installation of solar PV panels which is highly dependant on the availability of solar radiation. Hence, future research includes the development of design or framework for easy to install -plug and play system for practical feasibility of the technology.

5. ACKNOWLEDGEMENT

6. REFERENCES

[1]   IEA (2023), Tracking Clean Energy Progress 2023, IEA, Paris https://www.iea.org/reports/tracking-clean-energy-progress- 2023,

[2]   Y. Gao, J. Ji, Z. Guo, and P. Su, "Comparison of the solar PV cooling system and other cooling systems," International Journal of Low-Carbon Technologies, vol. 13, no. 4, pp. 353–363, Dec. 2018, doi: 10.1093/ijlct/cty035.

[3]   Y. Gao, J. Ji, K. Han, and F. Zhang, "Comparative analysis on performance of PV direct-driven refrigeration system under two control methods," International Journal of Refrigeration, vol. 127, pp. 21–33, Jul. 2021, doi: 10.1016/j.ijrefrig.2021.03.003.

[4]   O. Ayadi and S. Al-Dahidi, "Comparison of solar thermal and solar electric space heating and cooling systems for buildings in different climatic regions," Solar Energy, vol. 188, pp. 545–560, Aug. 2019, doi: 10.1016/j.solener.2019.06.033.

[5]   Y. Xu, X. Ma, R. H. E. Hassanien, X. Luo, G. Li, and M. Li, "Performance analysis of static ice refrigeration air conditioning system driven by household distributed photovoltaic energy system," Solar Energy, vol. 158, pp. 147–160, Dec. 2017, doi: 10.1016/J.SOLENER.2017.09.002.

[6]   J. Liang, W. Du, D. Wang, X. Yuan, M. Liu, and K. Niu, "Analysis of the Refrigeration Performance of the Refrigerated Warehouse with Ice Thermal Energy Storage Driven Directly by Variable Photovoltaic Capacity," International Journal of Photoenergy, vol. 2022, 2022, doi: 10.1155/2022/3441926.

[7]   Y. Xu and M. Li, "Impact of instantaneous solar irradiance on refrigeration characteristics of household PCM storage air conditioning directly driven by distributed photovoltaic energy," Energy Sci Eng, vol. 10, no. 3, pp. 752–771, Mar. 2022, doi: 10.1002/ese3.1050.

[8]   E. Varvagiannis, A. Charalampidis, G. Zsembinszki, S. Karellas, and L. F. Cabeza, "Energy assessment based on semi-dynamic modelling of a photovoltaic driven vapour compression chiller using phase change materials for cold energy storage," Renew Energy, vol. 163, pp. 198–212, Jan. 2021, doi: 10.1016/j.renene.2020.08.034.

[9]   K. Han et al., "Experimental and numerical investigation on a novel photovoltaic direct-driven ice storage air-conditioning system," Renew Energy, vol. 172, pp. 514–528, Jul. 2021, doi: 10.1016/j.renene.2021.03.053.

[10]   A. A. M. El-Bahloul, A. H. H. Ali, and S. Ookawara, "Performance and Sizing of Solar Driven dc Motor Vapor Compression Refrigerator with Thermal Storage in Hot Arid Remote Areas," in Energy Procedia, Elsevier Ltd, 2015, pp. 634–643. doi: 10.1016/j.egypro.2015.02.171.

#196: Bridging energy demands: hybrid floating solar photovoltaic-hydropower system for sustainable development in emerging economies"- A case of Nigeria

Louis GYOH[1,*], Tarelayefa INGO[2], and Hamid POURAN[3]

[1,2,3] *Faculty of Science & Engineering, University of Wolverhampton, United Kingdom.*

Abstract: Climate change is a global challenge, particularly affecting emerging economies. Projections indicate a surge in poverty and energy demands by 2030, making sustainable renewable energy systems crucial. This study uniquely addresses the potential of Hybrid Floating Solar Photovoltaic-Hydropower (FPV) systems as a cost-effective solution to mitigate the effects of climate change while meeting escalating energy demands. It focuses on its applicability in Nigeria, an emerging economy. Despite its promise, literature lacks comprehensive discussions on FPV systems. This study examines technical potential, economic viability, and barriers to FPV deployment in Nigerian hydropower reservoirs through a mixed-method approach. Leveraging NREL's System Advisory Model and expert surveys, findings reveal that even modest coverage of reservoirs with FPV could significantly augment electricity generation. A 10% coverage of ten selected hydropower reservoirs could generate an estimated 28.151 GW of solar power, translating to 49.33 TWh of energy annually. Economic assessments, which should instil confidence in the audience, particularly stakeholders and policymakers, demonstrate the profitability of FPV deployment, with Levelized Cost of Energy (LCOE) ranging from 4.26 to 5.45 cents/kWh, and an average Internal Rate of Return (IRR) of 13.04% over a 25-year project lifetime, suggesting its scalability. Moreover, non-technical barriers such as economic, environmental, and regulatory challenges, alongside technical complexities, emerge as obstacles. An implementation framework is proposed to guide policymakers in adopting this technology, emphasising its potential to address energy needs sustainably and foster socio-economic development in emerging economies.

1. INTRODUCTION

Climate change presents a significant global challenge, with the World Bank projecting that it will drive over 100 million more people into poverty by 2030. This impact will be particularly severe for emerging economies, which are experiencing rapid economic growth and urbanization, leading to a substantial increase in energy demands. Global energy consumption is expected to rise by 37% by 2030, with 96% of this growth occurring in developing countries, making sustainable energy solutions an urgent necessity. Consequently, researchers and policymakers must take prompt and effective action to address this pressing challenge.

Hybrid Floating Solar Photovoltaic-Hydropower (FPV) systems offer a cost-effective way to establish new solar plants without requiring additional land. They improve the efficiency of hydropower and could help to decouple energy demand from urbanisation and population growth in emerging economies.

A study focusing on Nigeria found that even a moderate coverage of the country's hydropower reservoirs with FPV systems could significantly increase electricity generation. However, addressing non-technical barriers such as economic, environmental, socio-cultural, and policy/regulatory challenges, along with technical hurdles like supply chain maturity and grid integration, is crucial to realising this potential. The study proposes an implementation framework to assist policymakers in making informed decisions regarding adoption of FPV and aims to encourage further research and interest in FPV systems as a viable solution to meet the increasing demand for green energy in emerging economies.

2. LITERATURE REVIEW: IMPACTS OF CLIMATE CHANGE ON EMERGING ECONOMIES

Climate change has emerged as a critical global challenge with profound socioeconomic implications, particularly for emerging economies (IPCC, 2022). According to the World Bank, climate change could push over 132 million additional people into poverty by 2030, primarily affecting low- and middle-income countries where vulnerabilities are highest (Jafino et al., 2020). These regions are often less equipped to cope with climate impacts due to limited financial resources, inadequate infrastructure, and a higher dependence on climate-sensitive sectors such as agriculture (Hallegatte et al., 2016). The increasing frequency and intensity of extreme weather events, sea-level rise, and shifting climate patterns threaten food security, health, and overall economic stability in emerging economies (IPCC, 2022). For instance, a study by Burke et al. (2015) suggests that climate change could reduce average global income by 23% by 2100, with disproportionate effects on poorer countries. In agriculture-dependent economies, climate variability and change are projected to exacerbate rural poverty, particularly in sub-Saharan Africa and South Asia (Hertel & Rosch, 2010).

Moreover, the urban poor in developing countries are especially vulnerable to climate-related risks due to their often-precarious living conditions and limited adaptive capacity (Satterthwaite et al., 2020). The combination of rapid urbanization and climate change poses significant challenges for emerging economies in terms of infrastructure development, resource management, and public health (Revi et al., 2014).

2.1. Rising Energy Demands and Economic Development

Emerging economies are rapidly industrializing and urbanizing, leading to a surge in energy demands (IEA, 2023). The World Energy Outlook projects a significant increase in global energy consumption by 2050, driven by population growth and expanding middle classes (UNDESA, 2022). However, meeting these needs sustainably is a challenge due to reliance on fossil fuels and their environmental impacts (IPCC, 2022). Transitioning to renewable energy sources is crucial for sustainable development and climate mitigation (IRENA, 2023). Developing countries should embrace renewable energy technologies to achieve sustainable economic growth while addressing climate change (Goldemberg, 2020).

2.2. Sustainable Renewable Energy Solutions

Renewable energy systems play a crucial role in addressing the interconnected challenges of energy security and climate change (IPCC, 2022). Technologies such as solar, wind, hydro, and biomass offer cleaner alternatives to fossil fuels, contributing to the reduction of greenhouse gas emissions (REN21, 2023). Among these, solar energy, particularly photovoltaic (PV) systems, has gained prominence due to its declining costs and scalability (Lazard, 2023). However, land availability for large-scale solar installations can be a constraint, especially in densely populated or ecologically sensitive areas (Hernandez et al., 2015). This limitation underscores the need for innovative solutions like Hybrid Floating Solar Photovoltaic-Hydropower (FPV) systems, which can maximize energy generation while minimizing land use (World Bank Group et al., 2019).

2.3. Hybrid Floating Solar Photovoltaic-Hydropower (FPV) Systems

The floating solar photovoltaic (FSPV) technology combines solar panels with hydropower infrastructure to generate renewable energy. FSPV systems offer advantages including efficient land use, increased panel efficiency due to the cooling effect of water, and reduced water evaporation from reservoirs. This technology helps to protect dams from insulation and enhances hydropower generation by reducing evaporation losses. Despite growing interest, the deployment of floating FSPV systems is still relatively new, and potential adopters are looking to understand the benefits of integrating floating FSPV with hydropower.

2.4. Technical Potential and Case Studies of FPV Systems

The technical potential of Floating Photovoltaic (FPV) systems depends on factors such as resource availability, system performance, and environmental constraints. Studies have explored the potential of integrating solar PV with hydropower, highlighting advantages such as dispatchable power output and reduced PV curtailment. Globally, it is estimated that the international potential of FPV ranges between 400 and 1,000 GW, with promising prospects for renewable energy.

In a study conducted in Brazil by Santos et al. (2019), it was found that utilizing 10% of the area of the country's four largest hydroelectric power plants for floating photovoltaic (FPV) systems could yield significant electricity generation. The Balbina hydroelectric plant, for instance, was estimated to have the potential to generate 47,910 GWh annually from FPVs, roughly four times its current electricity production.

In India, research by Acharya and Devraj (2019) estimated that the available surface area for FPVs is around 18,000 km², with a potential capacity of 280 GW. Moreover, the FPV potential of the Sobradinho and Tucuruí plants was found to be 112,632 GWh/year and 59,906 GWh/year, respectively, representing four and two times the plants' annual electricity generation. These findings highlight the promising potential of FPV systems in a rapidly developing country like India and underscore the role of renewable energy in meeting the nation's increasing energy demands.

A study on the High Dam and Aswan Reservoirs in Egypt found that integrating floating solar PV could generate up to 11.9 GWh/year and 11.3 GWh/year of additional energy, as well as save 0.1 million cubic meters of water. Africa installed 1 GW of new solar capacity in 2022, bringing the continent's total to 11.6 GW. Results from a simulation in Brazil show that 81% coverage of a reservoir by FPV generates 835,820 MWh of electricity and saves 2,595,000 m³ of water from evaporation. Singapore has a floating solar farm covering 45 football fields with 122,000 panels and aims to quadruple its solar energy production by 2025. Africa has over 100,000 square kilometres of freshwater reservoirs suitable for floating solar farms, with the potential to yield 100GW by utilizing just 1% of this area.

Assessing the technical potential of FPV systems involves evaluating factors such as solar irradiation, water surface availability, and integration with existing hydropower plants. Studies have shown that FPV systems can significantly enhance energy output compared to standalone PV or hydropower systems. Simulation tools like the National Renewable Energy Laboratory's (NREL) System Advisory Model (SAM) are often used to model and optimise the performance of these hybrid systems. Such assessments are critical for understanding the feasibility and scalability of FPV deployments.

3. METHODOLOGY

This study uses a mixed-method approach to explore Nigeria's potential for deploying Hybrid Floating Solar Photovoltaic-Hydropower (FPV) systems. The research is divided into three phases: data collection, technical and financial analysis, and assessment of barriers. The methodology involves gathering data from hydropower plants and reservoirs in Nigeria to estimate the FSPV installed capacity and energy production. It also considers spatial meteorological data and selects suitable locations for FSPV installation. Mathematical models and assumptions are applied to calculate the potential installed capacity and annual energy generation from FSPV for each selected reservoir.

3.1. Data Collection

Secondary Data Review

Literature Review: We conducted a comprehensive review of the existing literature on Nigeria's FPV systems, renewable energy technologies, and energy infrastructure. This review encompassed academic journals, industry reports, policy documents, and case studies.

Data Sources: For our secondary data, we used reputable databases such as the International Renewable Energy Agency (IRENA), World Bank, International Energy Agency (IEA), and Nigeria's national energy agencies.

Primary Data Collection

We conducted semi-structured interviews with key stakeholders, such as energy policymakers, industry experts, and academic researchers. The interviews aimed to gather insights on the practical challenges, policy landscape, and technical considerations for FPV deployment in Nigeria. In addition to the interviews, we distributed structured surveys to a larger group of stakeholders to quantify their perceptions of barriers and opportunities for FPV systems. The survey responses complemented the qualitative data gathered from the interviews.

3.2. Technical and Economic Analysis

Technical Potential Assessment

The study selected potential FPV deployment sites based on grid-connected hydropower plant availability, artificial water body presence, and high solar irradiation levels. Ten hydropower reservoir locations were chosen, including three large dams and seven small to medium-sized dams. The technical performance of FPV systems was simulated using the NREL System Advisory Model (SAM), which considered solar panel efficiency, water cooling effects, and seasonal variations in solar and hydropower generation.

The capacity estimation involved modelling different coverage scenarios and calculating the corresponding electricity output.

Fig.1A Kainji Dam Hydro-Electric Power Station

Fig.1B Jebba Dam Hydro-Electric Power Station

Fig.1C Shiroro Dam Hydro-Electric Power Station

Figures 1: A, B and C shows the three major (large) hydropower plants in Nigeria- Kainji, Shiroro, and Jebba Hydro-Electric Power Station.
(*Source: Google Maps*)

4.   RESULTS AND DISCUSSION

The section provides an overview of the FSPV resource potential for ten hydropower reservoirs/dams in Nigeria. The analysis results will assist investors, stakeholders, and policymakers in understanding the potential for generating electricity from FSPV systems and increasing renewable energy generation. The study presents results from a mathematical model and simulations using The System Advisor Model (SAM) software developed by The National Renewable Energy Laboratory (NREL) of the USA.

FSPV Potential in Nigeria- Mathematical Model

Equations (1) and (2) were applied to arrive at the total power and energy generated from the selected hydropower reservoirs, assuming the installation of FSPV panels. The results of these calculations are shown in Table 2.1. Two scenarios of FSPV reservoir area coverage of 1% and 10%, respectively, have been calculated for each of the reservoirs. Table 2.1 shows the FSPV resource potential, and the energy generated for the selected reservoirs. The total surface area of the hydropower dams with 10% FSPV installed generates an estimated 28.151 GW of solar power, which translates to 49.33 TWh of energy. We have also compared the installed capacities and the expected / potential when each hydropower reservoir is covered with 1% FSPV panels. Figure 1 shows a graph of FSPV potential in Nigeria for the selected reservoirs, with a 1% reservoir surface area coverage by FSPV. The results indicate that the total FSPV that can be installed in Nigeria, considering the selected reservoirs, is 2,815 MWp, about 133% of the installed capacity of these ten selected dams.

The comparison of FSPV installed capacity with Nigeria's electricity generation shows that FSPV power is about twice the country's installed capacity, seven times more than the current available generation, and almost 2.5 times more than its projected hydropower capacity. Kainji Dam has the highest FSPV potential of 11,891 MWp, while Oyan River Dam has the least potential of 380 MWp. Kainji Dam also has the highest energy generation at 20,830 GWh/year, while Oyan River Dam generates the least at 670 GWh/year.

Potential Installed Capacity of FSPV and Energy generated

The installed potential FSPV capacity (MWp) for each of the reservoirs is calculated using equation (1)

Equation 1: Potential Installed Capacity of FSPV   ICFSPV = Covered area (%) x $\left[\frac{Total\ Reservoir\ surface\ area\ (m2)}{CDFSPV} \right]$

Where:

- CDFSPV = capacity density of the FSPV, which is calculated for the Sungrow equipment by Lopez et al. as 10,512 m²/MWp.

Energy generated (GWh/year) by FSPV for the selected reservoirs is obtained applying the following equation,

Equation 2: Energy generated (GWh/year) by FSPV EP$_{FSPV}$ = A_{Tres} * $r_{A.\ FSPV}$ * I_{Opt} * y * PR * $\frac{rAC}{DC}$

Where:

- EPFSPV = annual electricity production (MWh/year),
- A_{Tres} = total area of the reservoir (m^2),
- A_{FPV} = total reservoir' area covered with FPV (m^2),
- r_A = ratio of reservoir area covered by FPV (A_{FSPV}/A_{Res}),
- y = PV area factor (kWp/m^2),
- PR = system performance ratio,
- $r_{AC/DC}$ = losses due to solar clipping,
- Iopt = annual sum of solar irradiation energy at optimal angle of inclination averaged for the reservoir area (kWh/m^2).

Energy generated by Hydropower reservoirs

The electrical energy generated by the hydropower plants is calculated using equation (3)

Equation 3: Electrical energy generated by the hydropower plants $P= Q* \rho *g*h* \eta$

Where:

- P = mechanical power in Watts (W),
- Q = volumetric flow rate in the pipe (m3/s),
- ρ = density of water (1000 kg/m3),
- g = acceleration due to gravity (9.81 m/s²),
- h = difference in height between inlet and outlet (hydraulic head), (m),
- η = efficiency of the turbine (0.9). Global efficiency ratio (usually between 0.7 and 0.9).

Table 2.1: Potential Capacity for installing 1% and 10% respectively of Floating Solar PV Systems and Energy Generated for selected Hydropower reservoirs/ water bodies in Nigeria

Reservoir/water body	A_{res} (km^2)	Hydropower		FSPV Coverage (1%)			FSPV Coverage (10%)		
		IC_{Hydro} (MWp)	EP_{Hydro} (GWh)	PIC_{FSPV} (MWp)	EP_{FSPV} (GWh)	EP_{FSPV}/EP_{Hydro} (%)	PIC_{FSPV} (MWp)	EP_{FSPV} (GWh)	EP_{FSPV}/EP_{Hydro} (%)
*Kainji Dam	1250	760	1,394	1,189	2,083	149	11,891	20,830	1494
*Shiroro Dam	312	600	1,135	297	520	46	2,970	5,200	458
*Jebba Dam	350	578.4	341	333	583	171	3,330	5,830	1710
**Dadin Kowa dam	300	39	146	285	500	342	2850	5000	3424
**Ikere Gorge	80	37.5	662	76	133	20	760	1330	201
**Gurara I	150	30	115	143	250	217	1430	2500	2174
**Tiga Dam	178	10	109	169	297	272	1690	2970	2725
**Bakolori Dam	80	11	47	76	133	283	760	1330	2830
**Oyan River Dam	40	3	69	38	67	97	380	670	971
**Kafin Zaki Dam	220	40	0.735	209	367	499	2090	3670	4993
Total	2,960	2,108.9	4,018.7	2,815	4,933	123	28,151	49,330	1,228

Source: Author
Where:
- $A_{Res.}$ = Total reservoirs' area.
- IC_{Hydro} = Installed capacity of hydropower plants.
- EP_{Hydro} = Electricity production of hydropower plants.
- PIC_{FSPV} = Potential installed capacity of FSPV plant.
- EP_{FSPV} = Electricity production of FSPV plants.
- * = Large hydropower plants/ reservoirs
- ** = Small to medium hydropower plants/ reservoirs
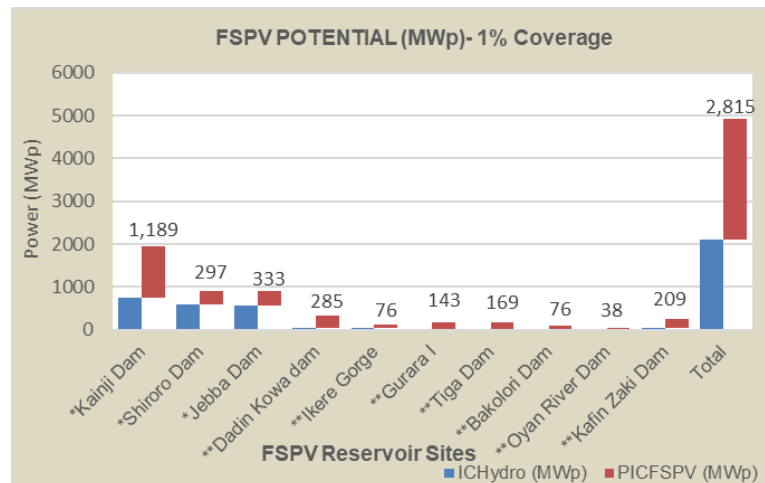
Figure 2: FSPV Potential in Nigeria (1% reservoir coverage)
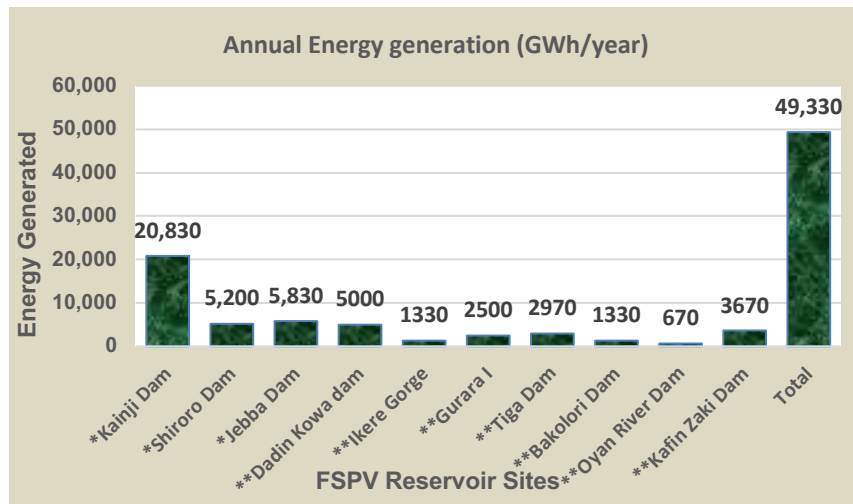
Figure 3: Energy Generated from FSPV (10% reservoir coverage)

4.1. FSPV Simulation Using SAM

The System Advisor Model (SAM) is a free software developed by The National Renewable Energy Laboratory (NREL) of the USA that enables detailed performance and financial analysis of renewable energy systems. The financial model inputs include energy costs, incentives, financial parameters, and revenue.

Table 2.2: Simulated Results of Floating Solar PV on 10 Hydropower reservoirs in Nigeria using the NREL System Adviser Model (SAM), with modules tilted at 10° angle

Parameter	Large Hydropower Reservoirs				Small to medium Hydropower Reservoirs					
	Kainji	Shiroro	Jebba	Dadin Kowa	Ikere Gorge	Gurara I	Tiga	Bakolori	Oyan River	Kafin Zaki
PVOUT-Average daily total (kWh/kWp)	4.82	4.82	5.25	6.18	4.88	5.09	6.14	6.02	4.73	5.97
PVOUT-Yearly Total (kWh/kWp)	1759	1759	1916	2256	1781	1858	2241	2197	1726	2179
Performance ratio in Year 1	0.81	0.81	0.81	0.75	0.77	0.76	0.76	0.76	0.76	0.76
Annual Energy in Year 1 (kWh)	14,596,948	14,551,893	14,840,599	17,240,624	13,922,118	14,345,545	17,197,082	17,034.628	13,446,586	16,894,864
Capacity Factor in Year 1	0.167	0.166	0.169	0.197	0.159	0.164	0.196	0.194	0.153	0.193
Levelized Cost of Energy (LCOE), c/kWh	5.02	4.48	4.93	4.64	5.26	5.11	4.26	4.30	5.45	4.33
NPV (Net Present Value-USD$)	793,569	630,708	793,569	793,569	793,569	793,569	793,569	793,569	793,569	793,569
IRR (Internal Rate of Return - %)	13.04	12.78	13.04	13.05	13.04	13.04	13.04	13.04	13.04	13.04

Source: Author
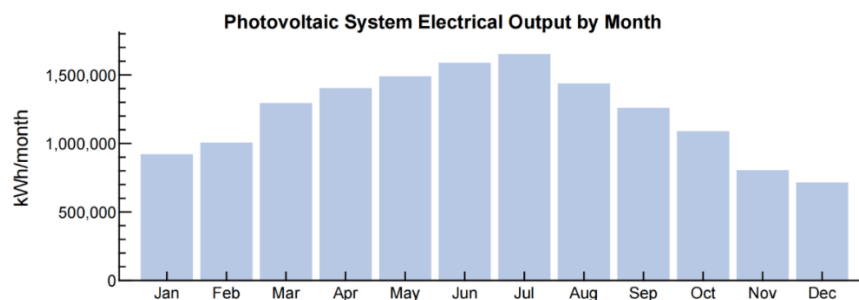
Figure 4: Simulated Monthly Energy Production from FSPV for Kainji hydropower Dam using NREL's System Advisor Model (SAM)

Photovoltaic System Electrical Output by Month
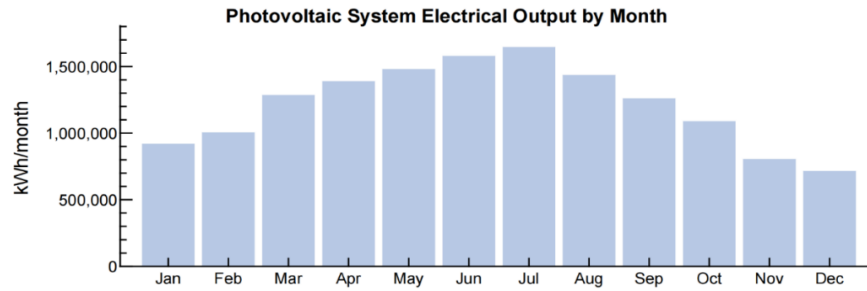
Figure 5: Simulated Monthly Energy Production from FSPV for Shiro hydropower Dam using NREL's System Advisor Model (SAM)

Photovoltaic System Electrical Output by Month
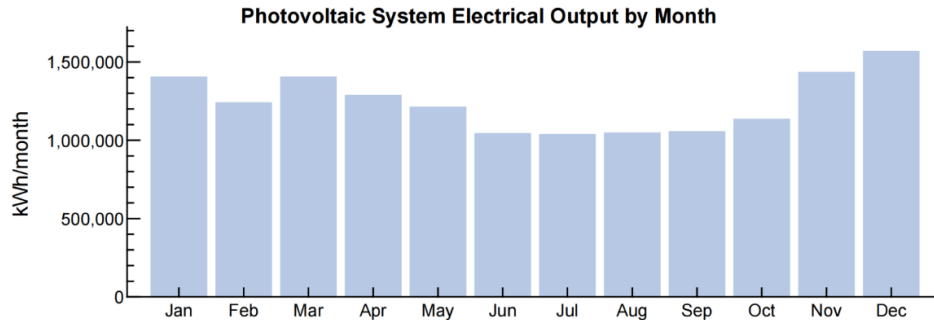
Figure 6: Simulated Monthly Energy Production from FSPV for Jebba hydropower Dam using NREL's System Advisor Model (SAM)

4.2. Economic Viability
Analysis ofFinancial Metrics:

Below is the shortened version of the text:

A comprehensive cost-benefit analysis was conducted for FPV systems, considering installation costs, operational and maintenance expenses, and projected revenue from electricity generation. Key financial metrics used included Net Present Value (NPV), Internal Rate of Return (IRR), and Levelized Cost of Energy (LCOE). The calculated LCOE ranges between 4.26 and 5.45 cents/kWh, with an average IRR of 13.04% over the project's 25-year lifetime, indicating the project's economic feasibility. See Table 2.2 for detailed results.

4.3. Barriers Assessment

Identification of Barriers

Barriers to deploying hybrid Floating Solar PV-Hydropower Technology in Nigeria were identified by engaging stakeholders from the public and private sectors, NGOs, academia, and energy professionals.

Potential Barriers to the deployment of Hybrid Floating Solar PV- Hydropower Technology in Nigeria

FSPV technology, despite its many advantages, encounters various challenges in its development as an emerging renewable energy source. These challenges include economic, environmental, technical, regulatory, and cultural barriers. According to MacGillivray et al. (2013), barriers refer to influential market factors and challenges that can have a negative impact on the adoption of renewable energy generation, including FSPV, thus hindering the achievement of power sector policy objectives. These barriers can be divided into technical and non-technical categories, which are discussed below:

Non-Technical Barriers: Through literature review, expert interviews, and surveys, economic, environmental, socio-cultural, and policy/regulatory barriers have been identified. These include financing challenges, regulatory hurdles, public acceptance, and environmental impacts.

Technical Barriers:

Barriers to the adoption and integration of technology can stem from operational and engineering system characteristics. Technical barriers in this context include issues with interconnection and transmission, concerns about the durability of photovoltaic (PV) panels and components, and insufficient transmission capacity that can strand PV assets. Poor planning of transmission infrastructure may hinder the integration of utility-scale PV systems into the electricity grid, impacting profitability. Additionally, uncertainties about extreme weather events and their impacts, as well as the lack of clear operation and maintenance (O&M) and equipment standards

for PV installation, can present barriers to PV deployment. The absence of universally accepted standards in the PV industry and a uniform methodology for quantifying the value and performance of PV systems further complicate the situation, hindering efforts for conducting a comprehensive cost-benefit analysis and deterring private sector interest in PV technology.

Non-technical Barriers to RE Deployment

MacGillivray et al. (2013) describe non-technical barriers as regulatory, institutional, economic, and socio-cultural factors that impede technology adoption. For example, lack of incentives for emerging RETs may stall the development of FPV systems, or lack of public interest and /or acceptance of FPV technology due to visible impacts and competing uses of water bodies are non-technical barriers to deploying FPV technology.

Environmental barriers

The deployment of Floating Photovoltaic (FPV) systems as a renewable energy technology faces challenges regarding its potential impact on the environment and ecology. Factors such as project size, site characteristics, and local environmental concerns play a role. Organisations stress the importance of assessing the environmental footprint of the system and associated facilities, as well as the ecological impacts on the aquatic ecosystem.

Regulatory Barriers

Regulatory barriers, such as uncertainties regarding water rights, can cause delays in the development of Floating Photovoltaic (FPV) systems and lead to increased costs. These barriers often impact different stages of FPV project development. Bureaucratic processes involving lengthy, unclear, and expensive environmental permit approval processes for FPV systems can make these projects more financially appealing to potential investors. Additionally, a lack of cooperation among regulatory agencies presents a significant challenge to the deployment of FPV technology. The World Bank, ESMAP, and SERIS note that FPV deployment can take between 3 months to several years for a project to move from initiation to "shovel-ready," and that permitting and financial closing are likely to take longer than for more familiar ground-mounted solar PV projects.

Cultural Barriers

Cultural barriers, such as the lack of public interest and acceptance of FPV technology due to its visible impacts and competing uses of water bodies, could pose significant obstacles to deployment. Negative past experiences with renewable energy projects may lead to unfavourable public opinion towards FPV systems (Urban et al., 2018), resulting in strong opposition to their deployment.

Economic Barriers

The deployment of Floating Photovoltaic (FPV) systems may face economic barriers due to uncertain, unfavourable, and inconsistent government policies. Subsidies on fossil fuel products can make it difficult for newer technologies like FPV systems to compete in the energy market. Stable, transparent, and reliable policies are necessary to attract private investment in long-term energy markets. Additionally, the shortage of trained personnel and training institutes in emerging economies can hinder the deployment of FPV systems, impacting installation and maintenance costs. The absence of government incentives for emerging renewable energy technologies may hinder the development of FPV systems.

Barrier Analysis and Implementation Framework

The study categorised the barriers into thematic areas to systematically analyse them, which helped us understand the relative importance and interdependencies of the different obstacles. Additionally, the research developed a barrier analysis framework to identify strategies for overcoming these challenges. This framework was informed by best practices from other regions and tailored to the Nigerian context.

4.4. Implementation Framework

Policy Recommendations

Based on the findings from the technical and economic assessments, policy recommendations have been developed. These recommendations are intended to offer practical guidance to Nigerian policymakers to advance the adoption of FPV systems. Implementing floating solar photovoltaic (FPV) systems in Nigeria and other emerging economies requires a clearly defined framework. The crucial steps for successful deployment are as follows:

Site Selection:

Identify suitable water bodies (reservoirs, lakes, or rivers) for FPV (floating photovoltaic) installation. Consider the proximity to existing hydropower infrastructure and solar irradiance levels.

Technical Feasibility Assessment:

Evaluate water depth, stability, and environmental impact. Assess electrical insulation, anchoring methods, and corrosion-resistant

materials.

Policy and Regulatory Framework:

–   Establish clear policies and regulations to encourage the integration of renewable energy. This should include providing incentives for specific hybrid systems like floating solar-hydropower projects.

–   Offer tax breaks, subsidies, and grants specifically for floating solar-hydropower projects.Hybrid Integration:
–   Explore hybrid systems combining FPV with existing hydropower stations.

–   Optimize energy production by leveraging complementary roles of photovoltaic and wind turbine systems.Grid Connection and Infrastructure:
–   Streamline grid integration procedures; Ensure reliable transmission and distribution infrastructure. Also ensure that net metering policies allow excess energy to be fed back into the grid.

–   Environmental and Social Impact Assessment:

–   Conduct comprehensive ecological impact assessments to address environmental concerns and community impacts.

–   Involve local communities in decision-making processes and ensure protection of biodiversity.Capacity Building:
–   Train local workforce, including engineers, technicians, and project managers, in FPV installation and maintenance. Promote knowledge exchange through workshops, conferences, and partnerships.

Research and Development (R&D) Support:

Invest in R&D for technology optimization initiatives aimed at improving technology efficiency, durability, and cost-effectiveness. Continuously support innovation and collaborate with universities and research institutions to explore innovative solutions and address emerging challenges and opportunities.

Public Awareness Campaigns:

–   Raise public awareness about the advantages of floating solar-hydropower systems.

–   Highlight their positive effects on energy security, water conservation, and climate resilience.

A comprehensive approach involving stakeholders, research institutions, and policymakers will drive successful implementation of FPV-HEPP renewable energy in emerging economies like Nigeria.

Stakeholder Engagement

A framework for implementation was proposed, highlighting the importance of collaboration among multiple stakeholders. This included roles for the government, private sector, financial institutions, and community organizations in the deployment process.

Future Research Directions

The study identified crucial areas for further research and development to bridge existing knowledge gaps and support the expansion of FPV systems in Nigeria and other emerging economies.

By integrating these methodologies, the study aims to provide a thorough analysis of FPV systems' potential and challenges, offering valuable insights for policymakers, industry stakeholders, and researchers.

5. CONCLUSION AND RECOMMENDATIONS

This study analyses the potential for Hybrid Floating Solar Photovoltaic-Hydropower (FPV) systems in Nigeria. The findings suggest significant opportunities and challenges for FPV deployment in the country. FPV systems could generate an estimated 28.151 GW of solar power, exceeding Nigeria's current installed electricity capacity. The study also identified barriers to FPV deployment and provided key recommendations to address them, including establishing clear policies and regulations, providing financial incentives, investing in workforce training, and conducting environmental impact assessments. If implemented effectively, these steps could accelerate the adoption of FPV technology in Nigeria and serve as a model for other emerging economies.

Future research should focus on:

1. Long-term environmental impacts of large-scale FPV deployments on aquatic ecosystems and water quality.

2. Optimal designs for hybrid FPV-hydropower systems that maximize synergies between the two technologies.

3. Detailed economic analyses that consider various financing mechanisms and policy scenarios.

4. Social acceptance studies to better understand and address community concerns about FPV projects.

5. Comparative analyses of FPV potential across different emerging economies to identify best practices and lessons learned.

In conclusion, Hybrid Floating Solar Photovoltaic-Hydropower systems represent a promising solution for addressing the two critical challenges of energy security and climate change mitigation in Nigeria and other emerging economies. While significant barriers

exist, the potential benefits of increased renewable energy generation, water conservation, and economic development make FPV systems worthy of serious consideration by policymakers and energy planners. As the global community endeavours to achieve the UN sustainable development goals and transition to clean energy, innovative technologies like FPV systems will play an increasingly significant role in shaping the future of energy production in the developing world.

6. REFERENCES

Acharya, M., & Devraj, S. (2019). Floating Solar Photovoltaic (FSPV): A Third Pillar to Solar PV Sector? The Energy and Resources Institute, Volume. https://doi.org/XXXX

Bridle, R., & Kitson, L. (2014). The impact of fossil-fuel subsidies on renewable electricity generation. International Institute for Sustainable Development.

Brown, M. A. (2008). Market failures and barriers as a basis for clean energy policies. Energy Policy, 36(1), 1-11. https://doi.org/10.1016/j.enpol.2007.09.014

Burke, M., Hsiang, S. M., & Miguel, E. (2015). Global non-linear effect of temperature on economic production. Nature, 527(7577), 235-239. https://doi.org/10.1038/nature15725

Choi, Y. K. (2014). A study on power generation analysis of floating PV system considering environmental impact. International Journal of Software Engineering and Its Applications, 8(1), 75-84.

DNV GL. (2021). [Report on floating solar PV projections]. DNV GL.

Ecofin Agency. (2023). [Report on Africa's floating solar potential]. [Publisher Name].

Energy Outlook. (n.d.). [Report on global energy consumption projections]. [Publisher Name].

Farfan, J., & Breyer, C. (2018). Combining floating solar photovoltaic power plants and hydropower reservoirs: A virtual battery of great global potential. Energy Procedia, 155, 403-411. https://doi.org/10.1016/j.egypro.2018.11.038

Feng, Y., Lin, H., Ho, S. L., Yan, J., Dong, J., Fang, S., & Huang, Y. (2016). [Title of the article on solar PV integration with hydropower]. [Journal Name], Volume, [Page range]. https://doi.org/XXXX

Ferrer-Gisbert, C., Ferrán-Gozálvez, J. J., Redón-Santafé, M., Ferrer-Gisbert, P., Sánchez-Romero, F. J., & Torregrosa-Soler, J. B. (2013). A new photovoltaic floating cover system for water reservoirs. Renewable Energy, 60, 63-70. https://doi.org/10.1016/j.renene.2013.04.007

Gokhale-Welch, C., & Watson, A. (2019). [Title of the work on policy environment and private investment]. National Renewable Energy Laboratory.

Goldemberg, J. (2020). [Title of the work on leapfrogging in energy development]. [Publisher Name].

Haas, J., Khalighi, J., de la Fuente, A., Gerbersdorf, S. U., Nowak, W., & Chen, P. J. (2020). Floating photovoltaic plants: Ecological impacts versus hydropower operation flexibility. Energy Conversion and Management, 206, 112414.

https://doi.org/10.1016/j.enconman.2019.112414

Hallegatte, S., Bangalore, M., Bonzanigo, L., Fay, M., Kane, T., Narloch, U., Rozenberg, J., Treguer, D., & Vogt-Schilb, A. (2016). Shock waves: Managing the impacts of climate change on poverty. World Bank. https://openknowledge.worldbank.org/handle/10986/22787

Hernandez, R. R., Easter, S. B., Murphy-Mariscal, M. L., Maestre, F. T., Tavassoli, M., Allen, E. B., Barrows, C. W., Belnap, J., Ochoa- Hueso, R., Ravi, S., & Allen, M. F. (2014). Environmental impacts of utility-scale solar energy. Renewable and Sustainable Energy Reviews, 29, 766-779. https://doi.org/10.1016/j.rser.2013.08.041

Hertel, T. W., & Rosch, S. D. (2010). Climate change, agriculture, and poverty. Applied Economic Perspectives and Policy, 32(3), 355-385. https://doi.org/10.1093/aepp/ppq016

International Energy Agency (IEA). (2021). Net Zero by 2050: A Roadmap for the Global Energy Sector. IEA. https://www.iea.org/reports/net- zero-by-2050

International Energy Agency (IEA). (2023). World Energy Outlook 2023. IEA. https://www.iea.org/reports/world-energy-outlook-2023

International Renewable Energy Agency (IRENA). (2023). World Energy Transitions Outlook 2023: 1.5°C Pathway. IRENA. https://www.irena.org/publications/2023/Mar/World-Energy-Transitions-Outlook-2023

Intergovernmental Panel on Climate Change (IPCC). (2022). Climate Change 2022: Impacts, Adaptation and Vulnerability. Contribution of Working Group II to the Sixth Assessment Report of the Intergovernmental Panel on Climate Change. Cambridge University Press.

Jafino, B. A., Walsh, B., Rozenberg, J., & Hallegatte, S. (2020). Revised estimates of the impact of climate change on extreme poverty by 2030. World Bank Policy Research Working Paper No. 9417. https://openknowledge.worldbank.org/handle/10986/34555

Lazard. (2023). Lazard's Levelized Cost of Energy Analysis—Version 16.0. Lazard. https://www.lazard.com/perspective/levelized-cost-of- energy-levelized-cost-of-storage-and-levelized-cost-of-hydrogen/

Lee, N., Grunwald, U., Rosenlieb, E., Mirletz, H., Aznar, A., Spencer, R., & Cox, S. (2020). Hybrid floating solar photovoltaics-hydropower systems: Benefits and global assessment of technical potential. Renewable Energy, 162, 1415-1427. https://doi.org/10.1016/j.renene.2020.08.080

Liu, L., Wang, Q., Lin, H., Li, H., Sun, Q., & wennersten, R. (2017). Power generation efficiency and prospects of floating photovoltaic systems. Energy Procedia, 105, 1136-1142. https://doi.org/10.1016/j.egypro.2017.03.483

Lopes, T. S., Alves, A. J., Valer, L. R., Fedrizzi, M. C., & Zilles, R. (2011). Performance analysis of photovoltaic systems on water surfaces. [Journal N ame], Volume, [Page range]. https://doi.org/XXXX

MacGillivray, A., Jeffrey, H., Winskel, M., & Bryden, I. (2013). Innovation and cost reduction for marine renewable energy: A learning investment sensitivity analysis. Technological Forecasting and Social Change, 87, 108-124. https://doi.org/10.1016/j.techfore.2013.11.005

REN21. (2023). Renewables 2023 Global Status Report. REN21 Secretariat. https://www.ren21.net/reports/global-status-report/

Revi, A., Satterthwaite, D. E., Aragón-Durand, F., Corfee-Morlot, J., Kiunsi, R. B. R., Pelling, M., Roberts, D. C., & Solecki, W. (2014). Urban areas. In C. B. Field et al. (Eds.), Climate Change 2014: Impacts, Adaptation, and Vulnerability. Part A: Global and Sectoral Aspects. Contribution of Working Group II to the Fifth Assessment Report of the Intergovernmental Panel on Climate Change (pp. 535-612). Cambridge University Press.

Sahu, A., Yadav, N., & Sudhakar, K. (2016). Floating photovoltaic power plant: A review. Renewable and Sustainable Energy Reviews, 66, 815-824. https://doi.org/10.1016/j.rser.2016.08.051

Santos, L., Soares, I., Mendes, C., & Ferreira, P. (2019). [Title of the study on FPV potential in Brazil's hydroelectric plants]. [Journal Name], Volume, [Page range]. https://doi.org/XXXX

Satterthwaite, D., Archer, D., Colenbrander, S., Dodman, D., Hardoy, J., Mitlin, D., & Patel, S. (2020). Building Resilience to Climate Change in Informal Settlements. One Earth, 2(2), 143-156. https://doi.org/10.1016/j.oneear.2020.02.002

Solar Energy Research Institute of Singapore (SERIS). (2021). [Report on global floating solar PV market]. SERIS.

Spencer, R. S., Macknick, J., Aznar, A., Warren, A., & Reese, M. O. (2019). Floating photovoltaic systems: Assessing the technical potential of photovoltaic systems on man-made water bodies in the continental United States. Environmental Science & Technology, 53(3), 1680- 1689. https://doi.org/10.1021/acs.est.8b04735

Taboada, M. E., Cáceres, L., Graber, T. A., Galleguillos, H. R., Cabeza, L. F., & Rojas, R. (2017). Solar water heating system and photovoltaic floating cover to reduce evaporation: Experimental results and modeling. Renewable Energy, 105, 601-615. https://doi.org/10.1016/j.renene.2016.12.094

United Nations Department of Economic and Social Affairs (UNDESA). (2022). World Population Prospects 2022. UN DESA. https://population.un.org/wpp/

Urban, F., Siciliano, G., Wallbott, L., Lederer, M., & Nguyen, A. D. (2018). Green transformations in Vietnam's energy sector. Asia & the Pacific Policy Studies, 5(3), 558-582. https://doi.org/10.1002/app5.251

World Bank. (n.d.). Climate change overview. Retrieved [Month Day, Year], from https://www.worldbank.org/en/topic/climatechange/overview

World Bank, ESMAP, & SERIS. (2019a). Where sun meets water: Floating solar market report. World Bank. https://openknowledge.worldbank.org/handle/10986/31880

World Bank, ESMAP, & SERIS. (2019b). Where sun meets water: Floating solar handbook for practitioners. World Bank. https://openknowledge.worldbank.org/handle/10986/32804

#197: Experimental study on stepwise scaled-up solar driven atmospheric water harvesters

Shiqiang Su[1, 2], Zhao Shao[1], Ruzhu Wang[1]

[1] School of Mechanical Engineering, Engineering Research Center of Solar Energy and Refrigeration, MOE, Shanghai Jiao Tong University, Shanghai,China
[2] Shandong Linuo-Paradigma Co., Ltd., Jinan, China

Abstract: To ease the global water crisis, different research on solar-driven sorption-based atmospheric water harvesting (SAWH) prototypes on small-scale were explored while practical designs for larger sizes need more effort. To bridge the gap between the laboratory and factory, based on the structure of a flat plate solar collector, devices with stepwise scaling-up dimensions of 500mm×400mm and 800mm×600mm were reported in this paper. Integrated compact and modular structure which combines the solar absorption plate, desorption chamber, and condenser were used in the devices, they were tested under practical outdoor conditions of daily solar radiation ranging from 20-22 MJ•m^{-2}, achieved water harvesting amounts of 170 g and 410 g, respectively. Combined with the current industrialization of solar thermal technology, personalized sizes of solar-driven SAWH products can be produced in the future, expecting to give new pathway for drinking water anytime and anywhere.

Keywords: Atmospheric Water Harvesting, Sorption, Solar, Stepwise Optimization

1. INTRODUCTION

Fast-growing areas in the world are facing dry climate challenges due to frequent extreme weather events caused by global climate change. It is estimated that more than half of the world's population will face water scarcity by around 2050 (Boretti, 2019). The global arid and water-shortage areas are mainly distributed in northwest China, the central and western United States, northern India, North Africa and the Middle East, etc., most of which are far from the coast featuring dry inland climate. It suggests that seawater desalination, rainwater collection, artificial rainfall and other conventional technologies are difficult to apply in these areas. Therefore, the development of novel, efficient and cheap water harvesting technology to meet water demand has shown research significance and application value (Abualhamayel, 1997).

In recent years, the capture of water vapor directly from the air to produce fresh water has become a hot spot for extensive research in the world (Xu, 2021). With up to 12.9 trillion tons of water in the atmosphere, and more than 10 grams of water per kilogram of air even in arid deserts, air extraction technology is one of the potential approaches to alleviate water scarcity in arid regions (French, 2018).Currently, the technical path of AWH includes mist water harvesting (Zheng, 2010), chiller-driven condensation water harvesting (Al-Farayedhi, 2014), membrane separation air water harvesting(Bergmair, 2014) and adsorption air water harvesting (Ji, 2002). Among them, adsorption AWH technology has gradually become a research hotspot due to its advantages of simple structure, high water harvesting efficiency, the use of solar energy, and low-grade thermal energy as driving energy. Adsorption AWH technology has received extensive attention in recent years (Tu, 2018).

Figure 1 is the schematic diagram of the solar thermally driven adsorption air harvesting system. The basic working process of the system can be divided into open adsorption process (Figure 1a) and closed desorption-condensation process (Figure 1b). The basic working principle of the system is: using the difference between the vapor pressure on the surface of the adsorbent and the vapor pressure of the ambient air as the moisture absorption power at night to complete the adsorption process; Then using solar energy during the daytime to increase the vapor pressure on the surface of the adsorbent to achieve the purpose of desorption of water vapor; Finally, the water vapor is converted into liquid water by condensation.
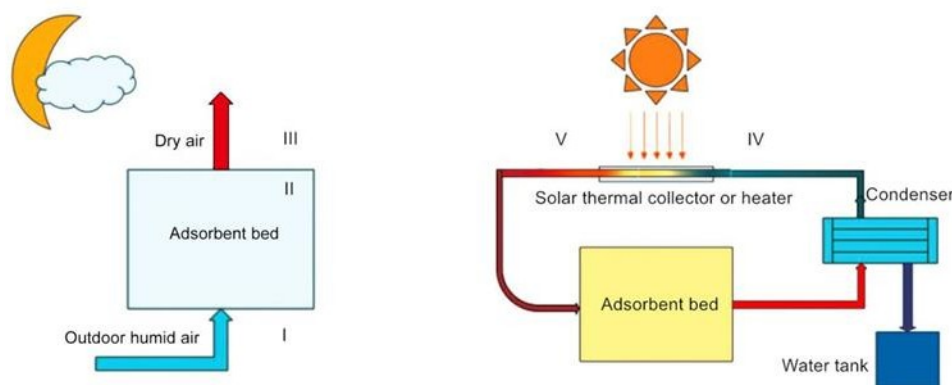
(a) Adsorption process at nighttime   (b) Desorption-condensation process in the daytime

Figure 1: Schematic diagram of solar thermal driven adsorption AWH system (Wang, 2020)

The hygroscopic and discharging characteristics of the hygroscopic agent play a key role in the water harvesting effect of the adsorption AWH system (Lapotin, 2019). Therefore, the development of efficient hygroscopic agents is crucial to the improvement of the system performance. Early adsorbents were mainly traditional materials, mainly including traditional physical adsorption materials such as silica, activated alumina and zeolite, as well as hygroscopic materials such as inorganic salts and salt solutions. Physical adsorption materials using the internal pore structure and the surrounding air between the water vapor pressure difference to achieve adsorption has the advantages of being easy to produce, low in price, non-toxic and tasteless, and chemical stability. However, it also has shortcomings such as low moisture absorption and high regeneration temperature. Hygroscopic materials are dried by combining water to form hydrates or solutions, which are corrosive and easy to liquefy under high humidity conditions, and in turn cause the loss of hygroscopic agents and the hidden dangers of corrosion adsorption beds. The above shortcomings limit the application of the two kinds of materials in AWH systems. Researchers have made great efforts in adsorbent modification and devised more economical approaches that use porous materials and hygroscopic salts combined with composite adsorbents (Aristov, 2002). So far, there are many types of hygroscopic salt composite adsorbents, including traditional porous materials as the matrix of composite adsorbents, such as silica-salt (Bu, 2012; Cheng, 2017), molecular sieve salt (Xu, 2016; Ji, 2004), activated carbon fiber-salt (Zheng, 2016; Ejeian, 2020), and vermiculite-salt (Zhang, 2018; Grekova, 2017).

Currently, the production of high-efficiency air water harvesting devices has gradually become an important research direction. AWH devices can classify heat-driven adsorption AWH devices from cold/heat source, active/passive working mode and intermittent/continuous cycle mode. SAWH devices can be divided into batch and continuous according to the working continuity of AWH devices (Qi, 2020). Figure 2 and Figure 3 classify and summarize the various device forms and principles in the previous literatures.
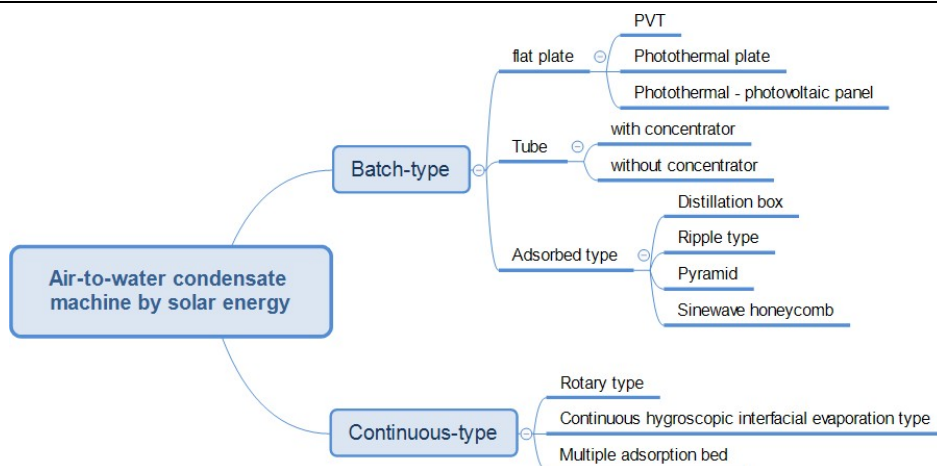
Figure 2: SAWH device under existing research

PVT(Renyuan, 2022)	Photothermal plate(Kim, 2017)	Photothermal - photovoltaic panel(Zero, 2019)	Without concentrator(Zhao, 2020)
With concentrator(Wang, 2021)	Distillation box(Kumar, 2015)	Ripple type(Gad, 2001)	Pyramid(Kabeel, 2007)
Sinewave honeycomb(Wang, 2017)	Rotary type(Li, 2020)	Continuous hygroscopic interfacial evaporation type(An, 2021)	Multiple adsorption bed(Fathieh, 2018)

Figure 3: Schematic diagram of a SAWH device

It can be seen from Figure 2 and Figure 3 that compared with other AWH devices, the SAWH device has the advantages of simple system, compact structure, strong adaptability, scalability, good economy, clean and renewable input energy, etc. Therefore, it has attracted a large number of scholars and achieved certain results so that a variety of system forms have emerged, with great development potential. However, up to now, the research of this technology is still conducted at the laboratory stage; there is still a long way to go before the application of the technology is promoted. To realize the leap from experimental research to factory production and application, this paper refers to the structure of solar flat plate collector, designs three sizes of air water harvesting device with flat plate solar adsorption from small to large, and conducts test and result analysis by gradually enlarging the size of the device, and finally explores the feasibility of the application and promotion of the structural product.

2. SELECTION AND PREPARATION OF ADSORBENTS

The selection and preparation of adsorbents has an important impact on the water harvesting effect. According to the material characteristics and related research, the physical adsorbent silica has the advantages of good adsorption performance, low regeneration temperature and cheap price, together with the shortcomings of low adsorption capacity. However, LiCl inorganic salts have high water absorption performance as adsorbent. Their water absorption performance is unstable, and liquelysis tends to occur at high relative humidity. The Silica-LiCl composite not only retains the high water absorption characteristics of hygroscopic salts but also retains the adsorption stability of porous materials. Meanwhile, the liquelyzed salt solution is stored in the pores of the porous materials, which effectively alleviates the problem of liqueous hydrolysis of salts. Therefore, Silica-LiCl composites were used as adsorbents.

To prepare the adsorbents, the first step it to dissolve lithium chloride in distilled water with a mass ratio of 30%, and then completely soak the dry silica material in lithium chloride solution; seal and soak for 24h. Filter it before putting it into an oven at 100 ℃ to dry to make Silica-LiCl composite adsorbent. The prepared Silica-LiCl composite adsorbent is shown in Figure 4.

a) Silica   b) Anhydrous LiCl   c) Silica-LiCl composite

Figure 4: Physical diagram of Silica-LiCl composite adsorbent

To verify the water absorption performance of the Silica-LiCl composite adsorbent, the completely dried adsorbent was placed in the condition with a constant temperature 25℃ and humidity 80% RH for adsorption. The adsorption time span was 16h, and the adsorbent adsorption capacity was 0.41 g•g^{-1}.

a) EDS layered image   b) Cl element distribution

c) Si element distribution   d) O element distribution
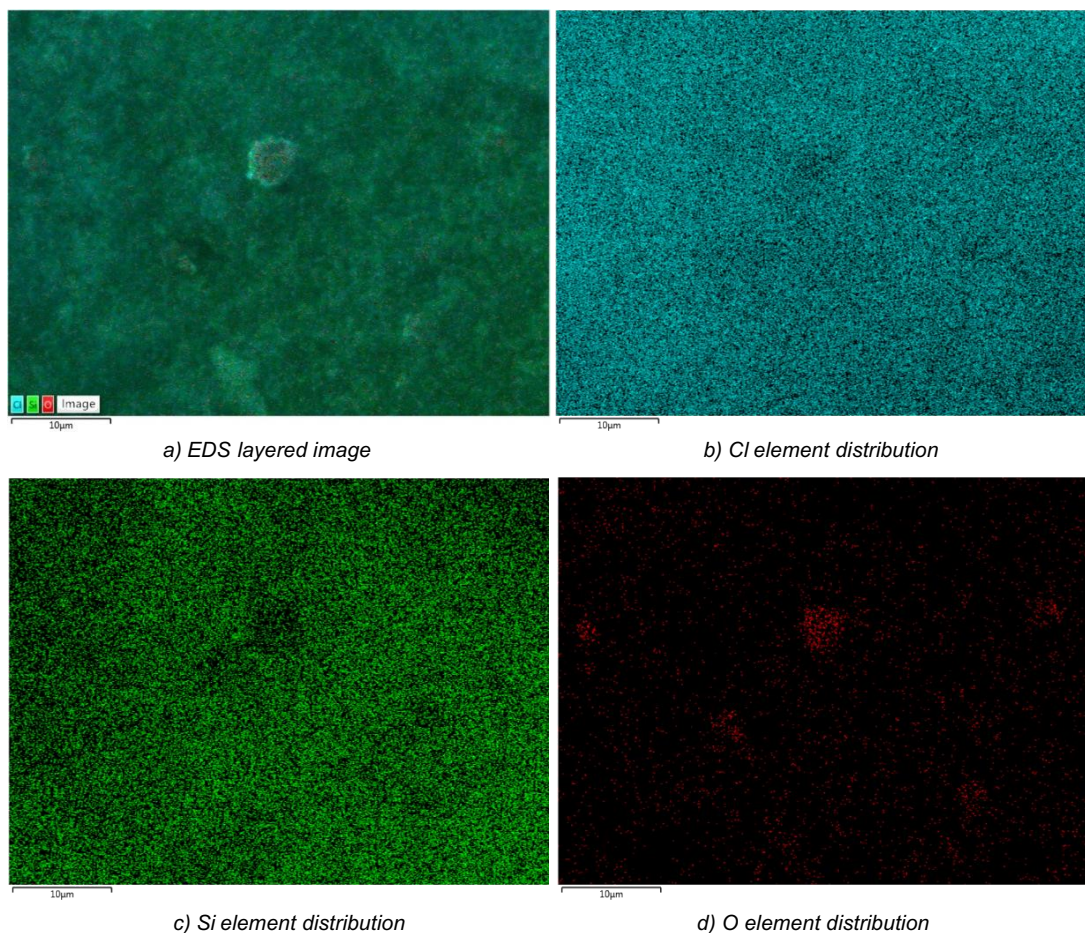
Figure 5: EDS layered image of Silica-LiCl

The EDS analysis on the prepared Silica-LiCl composite adsorbent is conducted, as shown in Figure 5. The distribution images of Si and O elements show that the two elements were evenly distributed on the surface of the silica gel (SG) particles, while the distribution image of Cl elements shows that the distribution of Cl elements was consistent with that of Si and O elements, with a uniform distribution. Meanwhile, from the EDS layered images, it can also be shown that Cl elements were densely and uniformly distributed between Si and O elements, which indicated that LiCl particles were well adsorbed on silica gel particles.

205

3. DESIGN OF SAWH DEVICES

Solar flat plate collector product technology is mature, simple structure, high heat exchange efficiency. SAWH device borrows the flat plate collector product structure, combined with AWH requirements for design. The basic structure and principle of the device are shown in Figure 6. The device structure encompasses glass cover plate, heat absorbing plate, adsorbent, evaporation chamber, heat insulation plate, condensation cavity, and air inlet and water outlet. The adsorbent is close to the heat absorbing plate to obtain a higher desorption temperature. The heat-absorbing plate is a magnetron sputtering selective coating, the absorptance is 0.92, the frame is made of aluminum alloy material. The air cavity between the glass and the heat-absorbing plate is designed to reduce the frontal heat conduction. The adsorbent performs water vapor adsorption at night. In this case, a pipeline fan is mounted at the upper air inlet, with the lower water harvesting remaining open. The external air is blown into the device via the fan, so that the adsorbent is in the same air environment as the outside space for water vapor adsorption. The device dehydrates water during the daytime. In this case, the upper air inlet is blocked, the lower water harvesting is connected with the water receiver, under the irradiation of sunlight, and the heat is transferred to the adsorbent on the back of the heat absorbing plate via the solar heat absorbing panel. To improve the heat conduction efficiency, the back of the solar heat absorbing panel is arranged with aluminum thermal conductive fins. Once the temperature of the adsorbent rises above the desorption temperature, the adsorbed water begins to evaporate and desorb into the evaporation chamber and enters the condensation cavity via the heat insulation plate. The water vapor condenses in the condensation chamber and the condensed droplets enters into the water receiver for collection. The heat insulation plate structure ensures the passage of water vapor while reducing the amount of heat transfer to the condensing cavity and increasing the temperature difference between the evaporation chamber and the condensing chamber. To improve condensation efficiency, aluminum thermal conductive fins are arranged outside the back plate of the device so that the heat exchange with the outside air increases.

(a) Adsorption process   *(b) Desorption process*
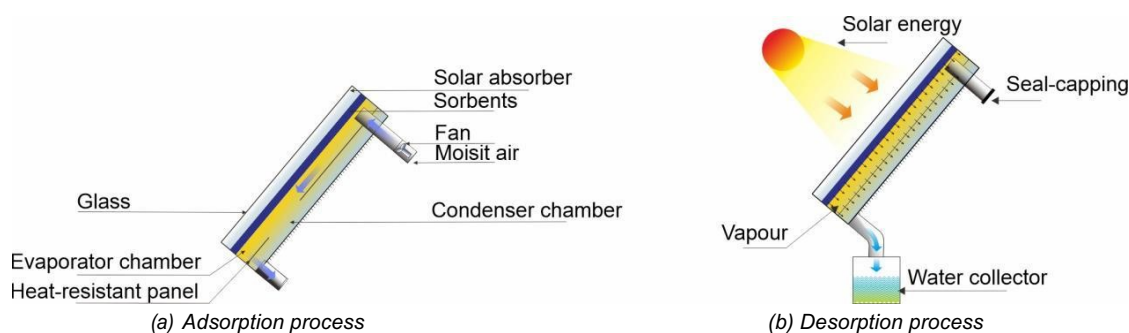
Figure 6: Structure and working principle of adsorption SAWH device

In this study, three samples sized in 200mm×200mm, 400mm×500mm, 600mm×800mm were designed and produced. Figure 7 shows the actual samples, and their parameters are shown in Table 1.
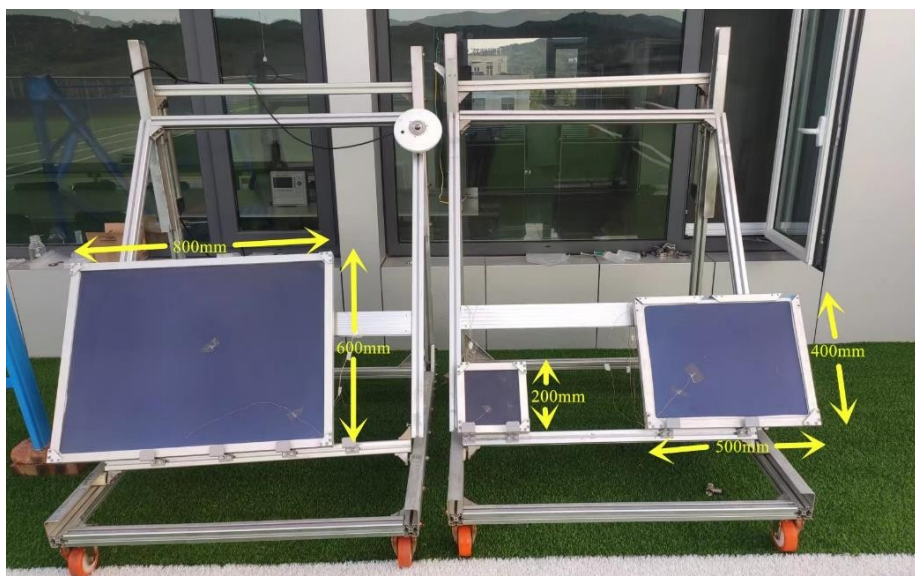
Figure 7: Sample diagram

Table 1: Sample parameters

Parameters	Sample 1	Sample 2	Sample 3
Size (mm)	200×200	400×500	600×800
Aperture area (m^2)	0.03	0.17	0.44
Adsorbent weight (kg)	0.22	1.2	3.09
Sample weight (kg)	3.74	13.82	32.03

The measuring instruments, equipment and their accuracy used in the experiment process are shown in Table 2.

Table 2: Measuring devices

Name	Model	Precision
Data acquisition instrument	TOPPRIE TP700	/
Temperature sensor	Thermocouple	0.01℃
Pyranometer	TBQ-2	/
Temperature and humidity data logger	Elitech GSP-8A	0.1℃ 0.1%RH
Measuring cylinder	/	1ml
Scale	/	10g

4. EXPERIMENTAL PROCESS AND RESULTS
4.1. Experimental results and analysis of sufficient adsorption/desorption capacity of different devices

To obtain the actual adsorption/hydrolysis absorption capacity of the product, the continuous and sufficient adsorption and water absorption test was conducted under the condition of full adsorption at night and continuous desorption during the daytime. The test sites were Jinan, Shandong, and the autumn season. First, the three samples were placed in the natural environment at night for ventilation adsorption, adsorption every night for 15h until the product adsorbed water saturation, with a cumulative adsorption for four nights. Figure 8 shows the temperature and humidity curve of the natural environment for the mentioned four nights. Table 3 is the adsorption data of three devices, where the sorbent achieved water uptake 0.41 g•g^{-1} after water vapor adsorption in a constant temperature 25℃ and humidity 80%RH. Can be compared to the adsorption data of 0.41 g•g^{-1} after water vapor adsorption, after four nights of adsorption under natural conditions, the three devices reached the saturated adsorption state. Make sure that all the devices meet the adsorption requirement. It can be found that the adsorption capacity of the structural device is related to the type of adsorbent, regardless of the size of the product.
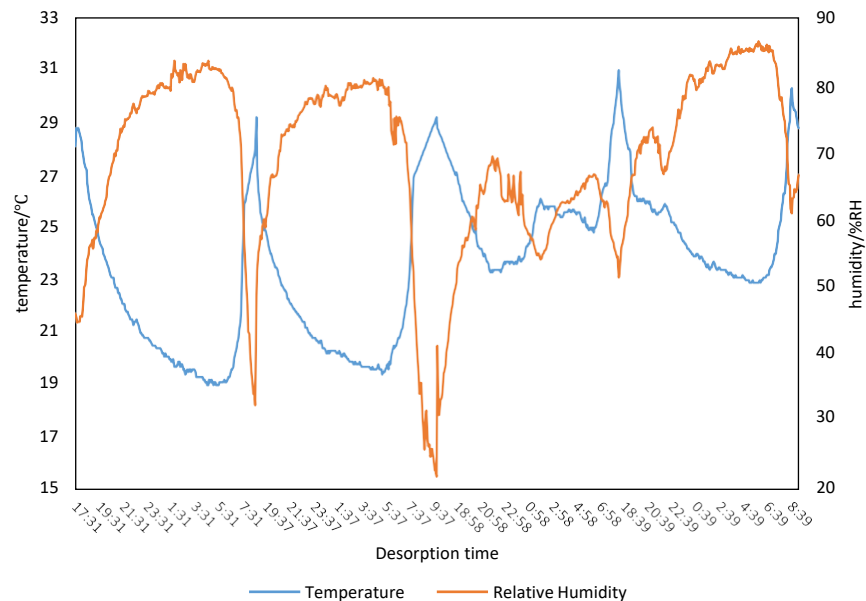
Figure 8: Full adsorption test under natural environment temperature and humidity

Table 3: Data of sample adsorption test

Sample #	Adsorbed water (g)	Water harvest per unit weight of sorbent (g·g^{-1})
Sample 1	90	0.41
Sample 2	470	0.39
Sample 3	1320	0.43

The three samples exposed to sufficient adsorption were placed under the natural sunlight irradiation during the daytime for full desorption and water absorption, and desorption was conducted for three consecutive days for 7 h per day. The desorption water data were given in Table 4. Figure 9 shows one of the temperature curves of different positions of each sample, the cumulative irradiance of sunlight is 18.98 MJ•m^{-2}. From the temperature curve and water harvesting data, it can be seen that the larger the sample size, the higher the corresponding temperature of each location, the faster the sample water withdrawal, the more water is withdrawn at the same time.

According to the irradiance of the day, it can be concluded that the heat absorptions of the three sample heat absorbing plates are 0.52 MJ, 3.04 MJ and 7.66 MJ, respectively. According to the product structure, the heat dissipation areas of the three samples were calculated to be 0.1 m^2, 0.44 m^2 and 1.03 m^2, and the heat dissipation areas corresponding to the heat gained by the three samples were 0.19 $m^2 \cdot MJ^{-1}$, 0.15 $m^2 \cdot MJ^{-1}$, and 0.13 $m^2 \cdot MJ^{-1}$, respectively. The larger the heat dissipation area, the greater the heat loss of the device and the lower the temperature. Therefore, the larger the size of the device, the smaller the heat loss and the higher the internal temperature. It can be seen from the temperature curve that the temperature of the evaporation chamber of sample 1 is slightly higher than 60 ℃ at noon, and the temperature is below 60 ℃ for the rest of the time. This is because the temperature is too low to cause poor water harvesting effects of the product. The maximum temperature of the evaporation chamber of sample 2 and sample 3 was 75 ℃ and 100 ℃, respectively. The water harvest of sample 3 was 691 g, the water harvest per unit mass of adsorption material reached 0.22 $g \cdot g^{-1}$, which was 1.57 times that of sample 2. The water harvest per unit lighting area was 1574 $g \cdot m^{-2}$, which was 1.65 times that of sample 2.

Sample 1
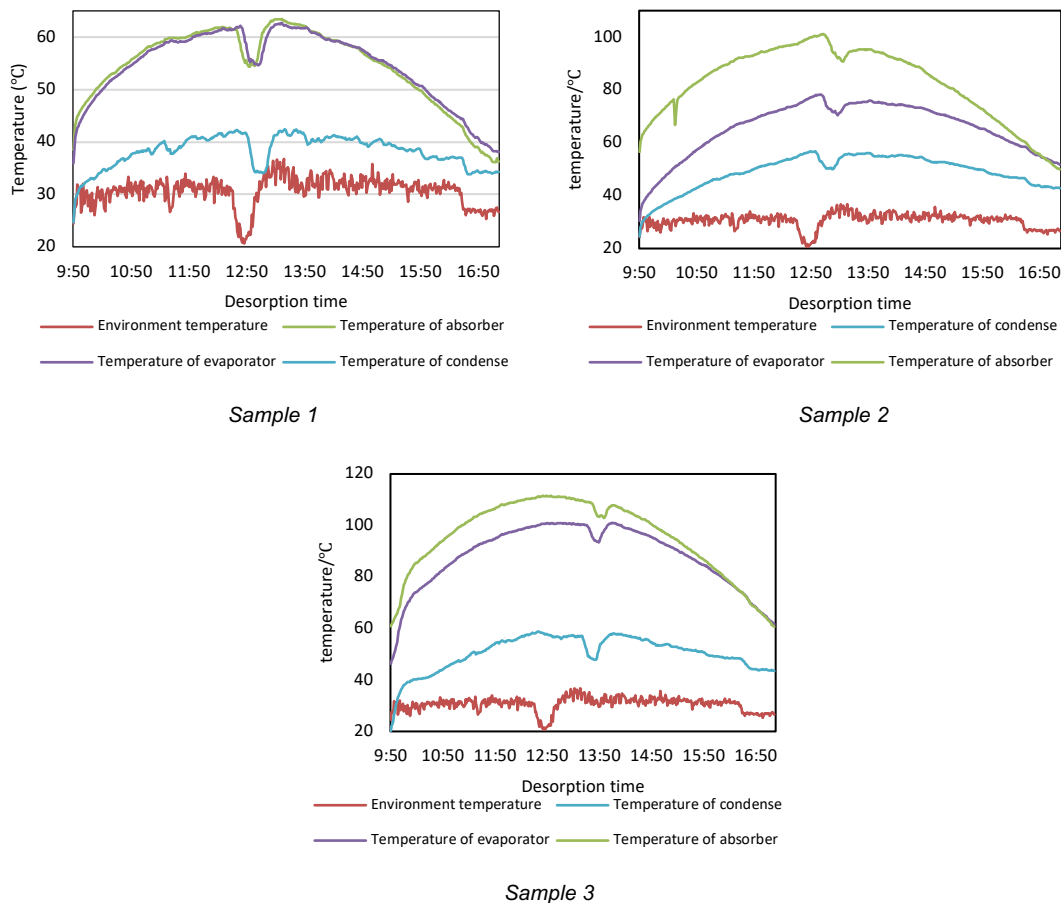
Sample 2

Sample 3

Figure 9: Temperature and humidity curve of natural environment under fully desorption experiment

Table 4: Water harvesting data of three samples under fully desorbed

Sample #	Desorpted water (g)	Water harvested (g)	water harvest per unit weight of sorbent ($g \cdot g^{-1}$)	water harvest per unit Aperture area ($g \cdot m^{-2}$)
Sample 1	10	3	0.01	100
Sample 2	240	166	0.14	954
Sample 3	870	691	0.22	1574

The results of this experimental process show that the water absorption capacity of the product is related to its size. Under the same structure, the larger the lighting area, the better the water absorption capacity of the product. When the size is so small that the adsorbent temperature is lower than its regeneration temperature, the product will lose the ability to draw water.

4.2. Continuous adsorption/desorption field tests and analysis

To obtain the effect of the sample in the actual use process, the test was conducted for three consecutive days according to the scheme of night adsorption and daytime desorption, that is, three adsorption/desorption cycles. Table 5 shows the adsorption capacity and desorption volume test data for three days. There was a difference in the adsorption capacity of the three nights. It was found that the adsorption capacity was greatly affected by the humidity of the adsorption environment. Figure 10 shows the humidity change curve of the three adsorption periods. It can be seen that the greater the humidity, the greater the amount of water vapor adsorbed by the sample. From the three-day water harvesting data, it can be seen that there is a certain difference in the water harvest of the two samples in three days, which is related to many factors such as sample adsorption state, environment, irradiance, etc. Table 6 is the irradiance data corresponding to the three days during the water harvesting test. It is obvious that the irradiance

data is consistent with the difference in water harvest in three days. The higher the irradiance, the greater the water withdrawal, and when the irradiation is better, the smaller increase in irradiance will cause a large increase in water withdrawal. In the three-day adsorption-desorption experiment, the daytime solar irradiation was 17.25 MJ•m^{-2}, 18.72 MJ•m^{-2}, and 21.24 MJ•m^{-2}, respectively, and the water harvest of sample 2 and sample 3 was 103g / 107g / 170g and 218g / 227g / 410g, respectively. Among them, the water harvest of sample 3 was better, up to 410 g, and the water harvesting capacity was 934 g•m^{-2}.

Table 5: Cyclic adsorption and desorption experiment data

Sample #	Night-1 Adsorbed water (g)	Day-1 Water harvested (g)	Night-2 Adsorbed water (g)	Day-2 Water harvested (g)	Night-3 Adsorbed water (g)	Day-3 Water harvested (g)
Sample 2	170	103	90	107	200	170
Sample 3	300	218	190	227	320	410

Table 6: The irradiance received daily during the desorption process

Date	Day-1	Day-2	Day-3
Solar irradiance/ MJ·m-2	17.25	18.72	21.24
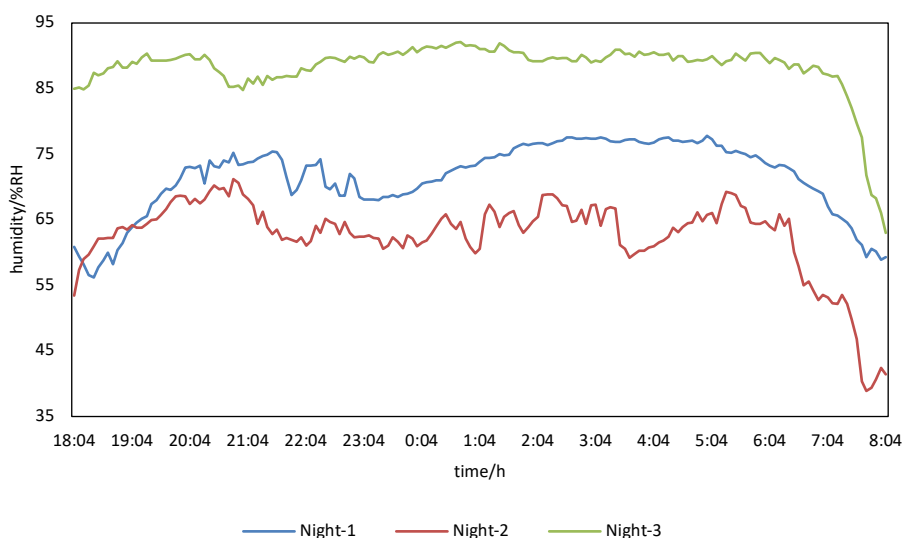
Figure 10: Humidity plots for the three adsorption stages

5. CONCLUSION

Based on the purpose of industrial application, this paper conducts experimental studies on the SAWH products. By analyzing relevantexperimental findings, we draw the following main conclusions:

Using Silica-LiCl composite material as adsorbent, a Silica-LiCl composite adsorbent suitable for industrial product applications was prepared, and the adsorption was carried out in a constant temperature 25℃ and humidity environment 80% RH, the adsorption time was 16h, and the adsorbent adsorption capacity was 0.41 g•g^{-1}.

Drawing on the structure of the most commonly used flat plate collector in solar thermal utilization, three SAWH devices of size 200mm×200mm, 500mm×400mm and 800mm×600mm were designed and manufactured, and the full adsorption/desorption test and continuous adsorption/desorption test were conducted. The results of the full adsorption/desorption experiment show that the structural device meets the requirements of air water withdrawal, and the full adsorption capacity can reach up to 0.43 g•g^{-1}. The adsorption capacity of the device is related to the type of adsorbent, independent of the size of the product; the water absorption capacity is related to the size of the product. Under the same structure, the larger the lighting area, and the better the water absorption capacity of the product. When the size is so small that the adsorbent temperature is lower than its regeneration temperature, the product will lose the ability to take water. The results of continuous adsorption/desorption experiment show that the adsorption capacity is affected by the adsorption environment. The greater the humidity, the greater the adsorption capacity of the sample, the greater the water harvesting capacity is affected by the irradiance; the better the irradiance, the larger the water harvesting capacity. The test was conducted under the actual conditions of outdoor solar radiation of 21.24 MJ•m^{-2}, and the water harvest of the sample of size 400mm×500mm and 600mm×800mm reached 170 g and 410 g, respectively.

This paper, based on research of passive solar air water harvesting devices, utilizes the efficient structural design of advanced solar flat plate collectors to optimize the device design. Three prototype devices of different sizes were fabricated. Through water collection experiments and data analysis on these three different-sized devices, the influence of size on water harvesting efficiency was determined. This study provides design guidance and a pathway for the productization of technology.

6. REFERENCES

Abualhamayel H I, Gandhidasan P, 1997. A method of obtaining fresh water from the humid atamosphere[J]. Desalination. 113(1): 51-63.

Al-Farayedhi A A, Ibrahim N I, Gandhidasan P,2014. Condensate as a water source from vapor compression systems in hot and humid regions [J]. Desalination, 349: 60-67.

An Meiyan, Wang Jiebing, Xu Zhenyuan, et al, 2021. Continuous atmospheric water harvester based on solar interfacial evaporation of LiCl solution[J]. CIESC Journal, 72(S1): 70-76.

Aristov Y, Restuccia G, Caccilla G, et al, 2002. A family of new working materials for solid sorption air conditioning systems [J]. Applied Thermal Engineering, 22(2): 191-204.

Bergmair D, Metz S J, De Lange H C, et al, 2014. System analysis of membrane facilitated water generation from air humidity [J]. Desalination, 339: 26-33.

Boretti A, Rosa L, 2019. Reassessing the projections of the world water development report[J]. npj Clean Water, 2(1): 15.

Bu Xianbiao, Wang Lingbao, Ma Weibin, 2012. Effect of pore size of silica gel on the water uptake and refrigeration of composite adsorbent[J]. Journal of Harbin Engineering University, 33(8): 989-995.

Cheng Junfeng, Zhao Huizhong, Liu Xueyan, et al, 2017. Research on the preparation and adsorption property of a new composite adsorbent for extracting water from air[J]. New chemical materials, 45(10): 162-164.

Ejeian M, Entezari A, Wang Ruzhu, 2020. Solar powered atmospheric water harvesting with enhanced LiCl/MgSO4/ACF composite[J]. Applied Thermal Engineering, 176: 115396.

Fathieh F, Kalmutzki J M, Kapustin A E, et al, 2018. Practical water production from desert air[J]. Science Advances,4(6).

French J R, Friedrich K, Tessendorf S A, et al, 2018. Precipitation formation from orographic cloud seeding [J]. Proceedings of the National Academy of Sciences of the United States of America, 115(6): 1168-1173.

Gad H E, Hamed A M, El-Sharkawy I, 2001. Application of a solar desiccant/collector system for water recovery from atmospheric air[J]. Renewable energy: an international journal, 22(4): 541-556.

Grekova A, Gordeeva L, Aristov Y, 2017. Composite "LiCl/vermiculite" as advanced water sorbent for thermal energy storage[J]. Applied Thermal Engineering, 124: 1401-1408.

Ji Jiangang, Li Lixin, Jiang Weigang, 2002. Research on a new method of water inter from air- condenses the water from air using adsorbents [J]. Energy conservation,10: 34-36.

Ji Jiangang, Li Lixin, Jiang Weigang, 2004. New adsorbent for solar driven technology of fresh water production from air[J]. Chemical engineering (CHINA), 32(3): 6-8.

Kabeel A E, 2007. Water production from air using multi-shelves solar glass pyramid system[J]. Renewable energy, 32(1): 157-172.

Kim H, Yang S, Rao R S, et al, 2017. Water harvesting from air with metal-organic frameworks powered by natural sunlight[J]. Science,356(6336).

Kumar M, Yadav A, 2015. Experimental investigation of design parameters of solar glass desiccant box type system for water production from atmospheric air[J]. Journal of renewable and sustainable energy, 7(3): 033122.

Lapotin Alina, Kim Hyunho, Rao Sameer R, et al, 2019. Adsorption-based atmospheric water harvesting: impact of material and component properties on system-level performance [J]. Accounts of Chemical Research, 52(6): 1588-1597.

Li R, Shi Y, Wu M, et al, 2020. Improving atmospheric water production yield: Enabling multiple water harvesting cycles with nano sorbent[J]. Nano Energy,67(C).

Qi Heshan, 2020. Design and Research on Interfacial Solar-thermal Atmospheric Water Harvesting [D]. Nanjing University.

Renyuan L, Mengchun W, Sara A, et al, 2022. An integrated solar-driven system produces electricity with fresh water and crops in arid regions[J]. Cell Reports Physical Science,3(3).

Tu Y, Wang R, Zhang Y, Wang J, 2018. Progress and expectation of atmospheric water harvesting [J]. Joule, 2(8): 1452-1475.

Wang Ge, Liu Fangzhou, Zheng Hongfei, et al, 2021. Experimental study on multi-surface concentrating and tracing-free solar air water intake device[J]. Acta energiae solaris sinica, 42(07): 257-261.

Wang J Y, Liu J Y, Wang R Z, et al, 2017. Experimental investigation on two solar-driven sorption based devices to extract fresh water from atmosphere[J]. Applied thermal engineering, 127: 1608-1616.

Wang Wenwen, Ge Tianshu, Dai Yanjun, et al, 2020. Status of solar-driven sorption-based atmosphere water harvesting [J]. Solar energy,01: 33-46.

Xu Jiaxing, 2021. Theoretical and experimental study of solar-driven atmospheric water harvesting based on multiform water sorption of hygroscopic salt [D]. Shanghai Jiao Tong University.

Xu Jiaxing, Li Tingxian, Wang Ruzhu, 2016. Sorption characteristics and heat storage performance of MgCl2/13x zeolite composite sorbent[J]. CIESC Journal, 67 (S2): 348-355.

Zhang Y N, Wang R Z, Li T X, 2018. Sorption characteristics and thermal storage performance of expanded vermiculite/CaCl2 composite sorbent[J]. CIESC Journal, 69(1): 363-370.

Zhao Huizhong, Lei Min, Huang Tianhou, et al, 2020. A review on the development of water extraction from atmospheric air[J]. Applied Chemical Industry, 49(02): 414-419+425.

Zero Mass Water, 2019. Perfecting your water [EB/OL]. https://www.zeromasswater.com/.

Zheng Xu, Wang Ruzhu, Ge Tianshu, 2016. Experimental study and performance predication of carbonbased composite desiccants for desiccant coated heat exchangers[J]. International Journal of Refrigeration, 72: 124-131.

Zheng Y, Bai H, Huang Z, et al, 2010. Directional water collection on wetted spider silk [J]. Nature, 463(7281): 640-643.

#200: Thermal- structural coupling characteristic analysis of shield energy tunnel under design condition

Shouheng SHEN[1], Hui ZHANG[1], Xinru WANG[1], Yongming JI[1], Songtao HU[1]

[1] School of Environmental and Municipal Engineering, Qingdao University of Technology, Qingdao Municipality, Shandong Province, China, shinshouheng@163.com

Abstract: With the development of society and the growth of population, the demand for energy continues to increase. Utilizing subway source heat pump technology to extract shallow geothermal energy for cooling or heating for users, making shield tunnel subways become energy tunnels, is one of the most effective technologies to solve the problem of energy demand. However, the thermal impact of heat exchanger operation on tunnel structures still needs further research. Based on COMSOL Multiphysics software, this paper analyzes the heat exchange performance of the Capillary Heat exchanger (CHE) in energy tunnels and the structural mechanical response of shield tunnel segments during CHE operation under typical heating season and cooling season conditions. The results indicate that the performance of precast CHE in energy tunnels is excellent. A single-ring energy tunnel can provide cooling and heating capacities of 601.62W and 466.28W, respectively, during the cooling and heating seasons, with heat transfer efficiency of 63.46W/m² and 49.19W/m² respectively. The operation of the CHE during the cooling season leads to elongation of the tunnel segments, while during the heating season, compression of the tunnel segments occurs. The maximum tensile stress and maximum compressive stress generated in heating season are 0.60 MPa and 0.73 MPa respectively, while in cooling season they are 0.56 MPa and 0.87 MPa respectively. The compressive stresses generated during the cooling and heating seasons due to CHEoperation are far below the compressive limit of C50 concrete, with tensile stresses representing 33% and 23% of the axial tensile strength, respectively. The calculation results indicate that under the design conditions of the heat pump unit, when the heat exchange between the CHE and the tunnel reaches steady state, the impact of CHE heat exchange on the structural integrity of the shield tunnel is relatively minor.

Keywords: Heat Pump, Capillary Heat Exchanger, Energy Tunnel, Thermal-Structural Coupling

1. INTRODUCTION

According to the data released in the "Annual Development Research Report on Building Energy Conservation in China 2022", in 2020, the energy consumption during the operational phase of buildings in China was 1.06 billion tec (National Bureau of Statistics, 2022), accounting for 21.3% of the total national energy consumption. The carbon emissions were 2.16 billion tons of CO_2, approximately 21.7% of the total national carbon emissions (Jiang et al., 2022).

Against this backdrop, the importance of promoting clean energy heating becomes increasingly prominent. Shallow geothermal energy, as a type of clean energy, mainly utilizes the heat energy from the Earth's interior through technologies like heat pumps to achieve centralized heating. Shallow geothermal energy has advantages such as renewability, high efficiency, energy conservation, and environmental friendliness. It not only reduces energy consumption and environmental pollution but also improves heating efficiency and comfort.

The waste heat within subway tunnels, as a form of shallow geothermal energy, has also received widespread attention. Academician Qihu QIAN, a member of the Chinese Academy of Sciences, recipient of the highest international science and technology award, and professor at the Army Engineering University, clearly stated at the "Geothermal Energy Development and Utilization with Earth Energy Storage Systems" seminar: "We should strengthen research and utilization efforts on 'tunnel energy' to turn waste heat in tunnels into sources for heating and cooling" (Geothermal energy information, 2023).

Laying the heat exchange pipeline in underground continuous walls, building foundation piles, and tunnel linings, and utilizing geothermal heat pump technology to extract shallow geothermal energy, allowing the building's foundation components to become part of an underground energy structure. Among these, the underground energy structure based on tunnels as foundation components is referred to as an energy tunnel.

Brandl (2006; 2016) conducted on-site experiments in the Lainz Tunnel in Austria, testing its heat exchange capacity. Through geothermal heat pump technology, they used energy piles buried in the tunnel as front-end heat exchangers to provide heating or cooling for a nearby school, further exploring the economic feasibility and viability of installing heat exchangers in tunnels. Adam and Markiewicz (2009) proposed an innovative construction method where they placed the ground heat exchanger pipes in geotextile fabric, referred to as "energy geotextile." This technique enables the prefabricated construction of tunnel linings and ground heat exchangers. By employing this construction method, not only can the waterproofing performance of tunnel linings be ensured, but also protection for the heat exchange pipeline can be provided, thus enhancing construction efficiency. To further reduce the difficulty of laying heat exchange pipes and their impact on tunnel structures, the team led by Songtao HU at Qingdao University of Science and Technology proposed laying capillary heat exchangers (CHEs) in the lining of subway tunnels, as front-end heat exchangers for ground heat pump systems (Wang et al, 2013). The capillary front-end heat exchanger extracts waste heat generated by various equipment in the subway tunnel to provide heating for users, thus this ground heat pump system is referred to as a subway source heat pump system (SSHPS). These capillary heat exchangers have advantages such as simple construction methods, small footprints, large heat exchange area, uniform heat exchange, high overall heat transfer coefficient, flexible layout, and easy integration with subway tunnel structures. The applicability, heat exchange performance, and design parameters of capillary heat exchangers in mining method tunnels have been validated through scaling experiments, numerical simulations, and demonstration projects.

Currently, shield tunnel, due to its relatively high technical and economic feasibility, is increasingly serving urban construction in China. Combining CHE with shield tunnel segments as front-end heat exchangers for subway source heat pumps is referred to as shield tunnel energy segments. This can make a significant contribution to urban energy conservation, emissions reduction, and sustainable development. However, the service life of urban tunnels is typically around 100 years, and the thermal stress generated by the operation of heat exchangers should not be ignored. Xia et al. (2014) established a thermal-structural coupling finite element model for energy tunnels and studied the mutual influence between heat exchangers installed in tunnels and tunnel structures in cold regions. Zhu (2020) analyzed the maintenance process, construction process, as well as stress and strain changes in tunnel segments during the heat exchange process based on the energy tunnel experimental section of the Qinghua Garden on the Beijing-Zhangjiakou Railway. Donna et al. (2016), based on the energy tunnel section of Line 1 of the Turin Metro in Italy, studied the stress and strain performance of shield tunnel segments during heat exchange through on-site experiments. The experimental results showed that the stress and strain generated in the lining during heat exchange are within an adjustable range.

The research results mentioned above demonstrate that the impact of heat exchangers on tunnel structures during heat exchange in energy tunnels is relatively small. However, different types of heat exchangers, due to their different installation forms, may have varying mechanical impacts on tunnel structures during heat exchange.

There are significant differences in structure, physical performance, and construction methods between capillary heat exchangers (CHEs) and traditional ground heat exchangers. Therefore, one cannot simply infer the heat transfer characteristics and the structural-mechanical impact on tunnel structures of one type of heat exchanger based on the other. This study analyzed the thermal- structural coupling characteristics of prefabricated CHEs in energy shield tunnel segments during heat exchange based on a specific engineering project in Qingdao city.

2.   PREPARING THE MANUSCRIPT

The principle of the SSHPS is based on shield tunnel, as shown in Figure 1. The system utilizes capillary tubes laid inside the shield tunnel segments as front-end heat exchangers, with each shield tunnel segment serving as a heat exchange unit. Utilizing the reverse Carnot cycle of the heat pump unit, in cooling season, heat is extracted from buildings and transferred and released into the subway tunnel to achieve cooling. In heating season, waste heat or residual heat is extracted from the subway tunnel and used for heating buildings to maintain comfortable temperatures.
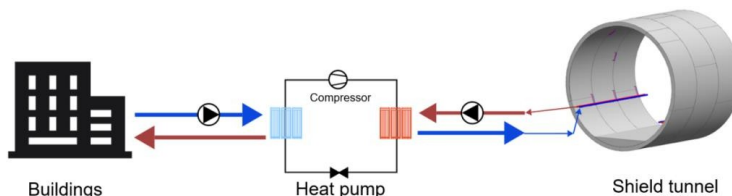
Figure 1: Principle of the SSHPS

2.1. Geometric model

The shield tunnel segments are arranged in a 1+2+3 combination, comprising the crown segment (F), adjacent segment (L1, L2), and standard segment (B1, B2, B3). CHE is prefabricated only in the two adjacent segments (L1, L2) and the two standard segments (B1, B3) adjacent to the adjacent segments. Therefore, each ring of the shield tunnel contains two capillary loops on the left and right sides. The main capillary pipes inside the segments are arranged along the circumferential direction of the tunnel, while the branch pipes are arranged using a non-uniform distribution method.

In this study, the spacing between individual capillary branch pipes inside the tunnel segment is 5mm, and the spacing between each group of capillary branch pipes is 44mm. The diameter of the CHE branch pipes is 4.3mm with a wall thickness of 0.85mm. The diameter of the main branch pipe is 18mm with a wall thickness of 2mm. The way of laying CHE in segments is shown in Figure 2.

Referring to the demonstration project, the inner diameter of the shield tunnel segment is 5.5 meters, the outer diameter is 6.2 meters, and the height is 1.5 meters. The depth of the tunnel top is approximately 15 meters. The shield tunnel segments in the actual engineering project are assembled in a staggered manner. To reduce computational complexity, this simulation only considers the case where the top block is located directly above the tunnel. Following the principle of symmetry, only half of the tunnel segment is considered for calculation, comprising half of the crown segment (F), half of the standard segment (B2), as well as the adjacent segment (L1) and the standard segment (B1). To minimize the influence of boundary conditions on the model calculation results, the length and width of the surrounding rock are both set to 75 meters. The geometric model is established as shown in Figure 2.
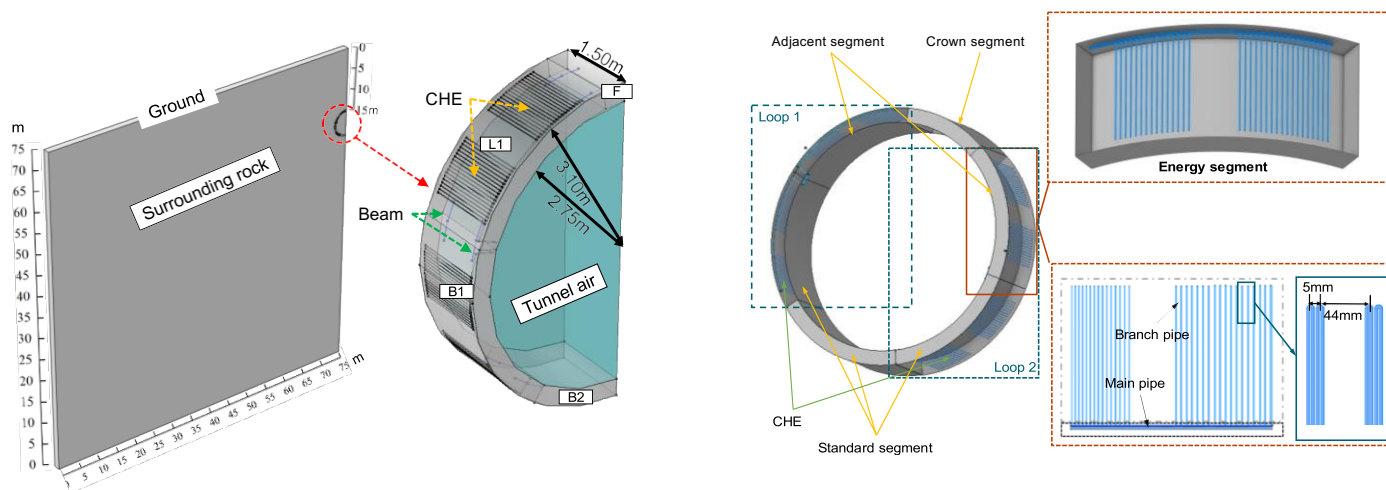
Figure 2: Geometric model and capillary laying method

2.2. Numerical model

This study utilized the COMSOL Multiphysics finite element software to simulate the heat exchange performance of the CHE and the structural-mechanical response of the shield tunnel segments under typical cooling season and heating season design conditions in energy tunnels. The simulations were conducted using the Turbulent Flow Module, Heat Transfer in Solids and Fluids Module, Non-Isothermal Pipe Flow Module, Solid Mechanics Module, and Beam Module, respectively, to model the airflow in the tunnel, heat transfer between tunnel air, tunnel segments, and surrounding rock, heat transfer between CHE and tunnel segments, and tunnel stress.

As described above, the following unidirectional fluid-thermal-structure coupling physical field is constructed.

In Figure 3, the diamond block represents the different geometric calculation domains in this study, the square represents the physical field used in this study, and the oval represents the coupling calculation method between two or more physical fields.
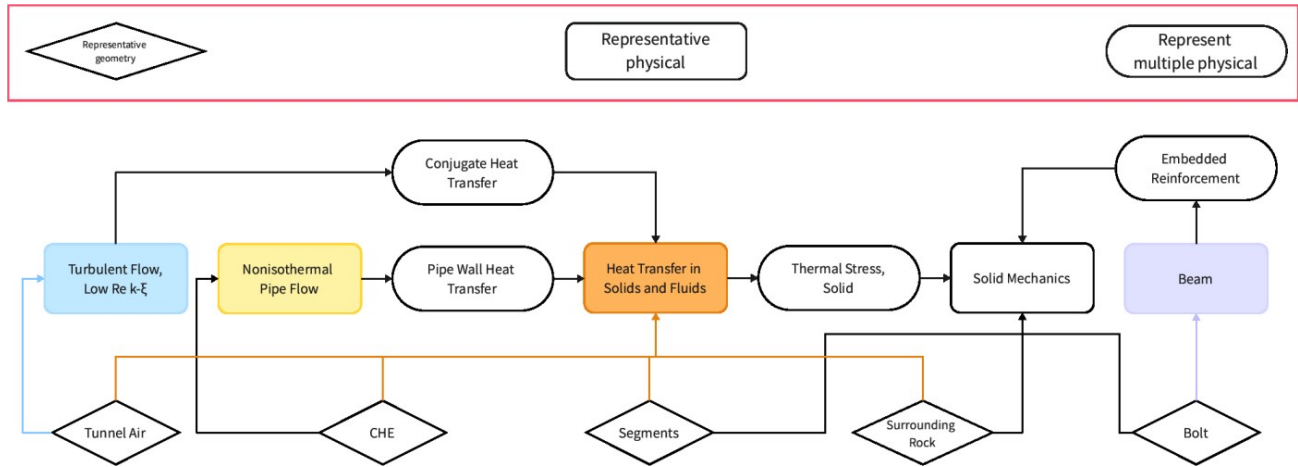
Figure 3: The multi-physics coupling method is used in this study

The research focus of this study is the analysis of the thermal-structural coupling characteristics of tunnel segments in energy shield tunnels. It explores the heat transfer characteristics of the prefabricated CHE and the structural-mechanical response of shield tunnel segments during CHE operation, involving several complexes coupled physical field problems. To simplify calculations, the following assumptions are made:

（1） Surrounding rock, lining, and CHE have constant material properties and are isotropic.
（2） Contact thermal resistance is neglected.
（3） The influence of groundwater flow on the heat transfer process is disregarded.
（4） During system operation, the fluid inside the CHE and the airflow in the tunnel remain constant.
（5） The surrounding rock is simplified as a linear elastic model.
（6） Gravity is ignored.

Based on the aforementioned simplifications, the numerical model obtained in this study is as follows:
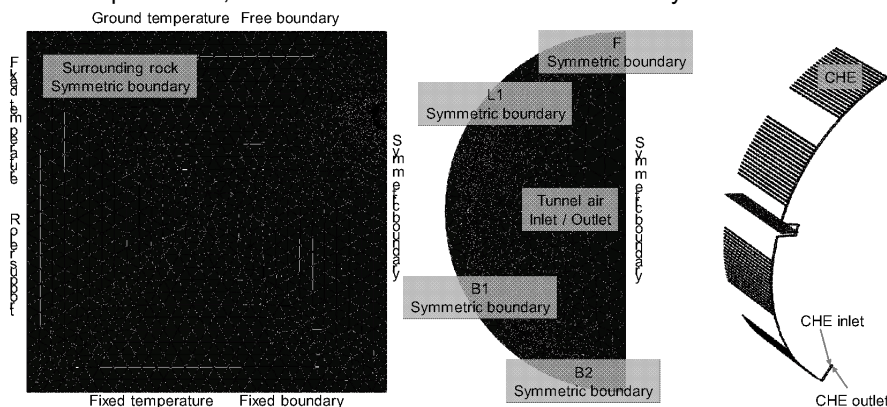
Figure 4: Geometric model of energy tunnel

As shown in Figure 4, the numerical model is configured as follows:

- The left boundary is set as roller support, allowing only vertical displacement and restricting horizontal displacement.
- The top boundary is set as the ground (free boundary).
- The bottom boundary is set as a fixed boundary, allowing for settlement of the surrounding rock.
- For shield tunnels with more than 4 segments, the "Code for Design of Metro" recommends using a beam-spring model for calculation (11.6 Code for design of metro. GB50157-2013). This method considers that the bolted joints of circular lining structures can bear certain forces, and the deformation of the joints is linearly related to internal forces, treating the joints as elastic hinges.

Hence, in the simulation process, linear elastic solid elements are used to simulate the segments and surrounding rock, while springs are used to simulate the joints. The axial spring constant and tangential spring constant of the joints are set to 3×107kN/m and 1×106kN/m (Zhu and Tao, 1998), respectively. Other physical property parameters of the model were set with reference to an actual

engineering project in Qingdao, as shown in Table 1.

Table 1: Physical property parameters of the model

	Density (kg/m³)	Thermal conductivity (W/m)	Specific heat capacity (J/(kg*K))	Young modulus (GPa)	Poisson's ratio (1)	Thermal expansivity (1/K)
Segment	2700	5.56	935	33.5	0.2	0.00001
Surrounding rock	2800	3.49	920	0.009	0.3	0.000007
CHE pipe	900	0.24	2000			
Water	998.2	0.60	4182			
Air	1.225	0.0242	1006.43			

2.3. Boundary conditions

The variation of wind speed inside the tunnel mainly consists of three different stages: when trains pass through, no trains pass, and during nighttime ventilation. When trains pass through, the maximum wind speed inside the tunnel is approximately 6.5 m/s. After the train passes through, the air inside the tunnel becomes relatively stable, with the wind speed is about 0.5 m/s (Zhanget al, 2020). Since the simulation method used in this study is steady-state calculation, the tunnel wind speed is set to the average speed during train operation, which is approximately 4.61 m/s (Ji, Wu and Hu, 2023). According to measurements from the demonstration project, the average tunnel temperatures during the cooling and heating seasons are approximately 28°C and 12°C,respectively.

Based on previous research findings, the recommended flow velocity for the CHE is 0.08 m/s (Gao, 2015). According to Section 29.3.3 of the "Practical Handbook of Heating, Ventilation, and Air Conditioning Design (Second Edition)" (Volume II), the design temperatures for the outlet of the ground source heat pump unit on the source side are 6°C and 35°C for the heating and cooling modes respectively (Lu, 2008). Therefore, the inlet water temperature of the CHE is set to 6°C and 35°C for the heating and cooling seasons respectively.

For the simulation of heating season and cooling season, the ground temperature is taken as the average outdoor temperature during the heating and cooling seasons in Qingdao, which are approximately 2.8°C and 25°C, respectively. The fixed temperature is taken as the annual average outdoor temperature in Qingdao, which is 14.6°C (Ji et al, 2022).

The values of boundary conditions are summarized in Table 2.

Table 2: Boundary conditions

	Cooling season	Heating season
Wind speed (m/s)	4.61	
Tunnel air inlet temperature (℃)	28	12
Tunnel air outlet relative pressure (Pa)	0	
CHE flow velocity (m/s)	0.08	
CHE inlet temperature (℃)	35	6
CHE outlet relative pressure (Pa)	0	
Ground temperature (℃)	25	2.8
Fixed temperature (℃)	14.6	

2.4. Model verification

Using numerical simulation software to evaluate thermal stress has become very common, and the accuracy of these results has been confirmed. Given the large scale of the energy tunnel structure in this study and the high likelihood of damage to measurement points during the experimental process, constructing a test bench to simulate different conditions would incur extremely high costs for excavating tunnels and manufacturing segments, and would be difficult to implement. However, to ensure the accuracy of the numerical simulation in this paper, experimental data from the Turin Metro Line 2 were used to verify the accuracy of the model setup method (Insana, 2020). The following verification model was constructed according to the model setup method in this study

By comparing the simulation results with the experimental measurements, as shown in Figure 5: Model authenticity verification: (a) Model used for verification; (b) Verification results, the simulation results indicate that the temperature and pressure at the measurement points have the same trend as the experimental results The maximum relative error between the simulated and experimental values for the temperature at the measurement points is 6%, with an average relative error of only 3%. For the pressure at the measurement points, the maximum relative error between the simulated and measured values is 7%, with an average relative error of only 5%. This indicates that the model set up and calculation methods used in this study are correct, and the simulation results are reliable. Therefore, using the model setup method from this study to simulate the thermal-mechanical coupling characteristics of energy tunnel segments is accurate and reliable.
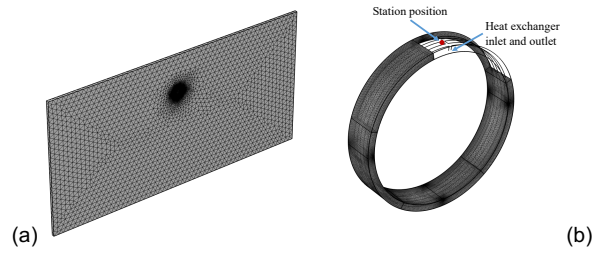
Figure 5: Model authenticity verification: (a) Model used for verification; (b) Verification results

3. RESULTS

Based on the simulation settings described above and using a steady-state calculation method, the thermal performance of the prefabricated CHE in the energy tunnel and the structural-mechanical response of the tunnel under design conditions were simulated in heating season and cooling season**.**

3.1. Heat-transfer characteristic

Figure 6 is the temperature field after the operation of the CHE.
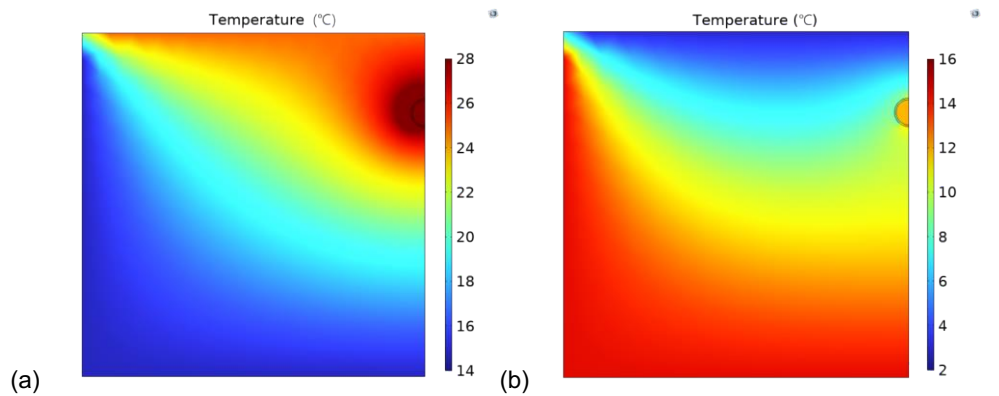
Figure 6: Temperature field of the model after the operation of CHE: (a) cooling season; (b) heating season

Compared to the initial temperature field, there are significant changes in the temperature field around the tunnel. In heating season, the temperature of the surrounding rock slightly decreases, while in cooling season, the temperature of the surrounding rock around the tunnel significantly increases. The reason for this phenomenon is that in heating season, the inlet temperature of the CHE is 6°C, while the initial temperature around the tunnel is approximately 11°C, resulting in a temperature difference of 5°C. In cooling season, the inlet temperature of the CHE is 35°C, while the initial temperature around the tunnel is approximately 27°C, resulting in a temperature difference of 8°C. The temperature difference in heating season is significantly smaller than in cooling season, leading to smaller changes in the temperature field.

And in heating season, with the inlet temperature of the CHE set to 6°C, the computed outlet temperature of CHE is approximately 8.22°C. The temperature difference between inlet and outlet under steady-state design conditions is about 2.22°C. The average temperature of the fluid inside the CHE pipe is 8.74°C. In cooling season, with the inlet temperature of CHE set to 35°C, the computed outlet temperature of CHE is approximately 32.12°C. The temperature difference between inlet and outlet under steady-state design conditions is about 2.88°C. The average temperature of the fluid inside the CHE pipe is 31.40°C.

Overall, in both heating season and cooling season, the temperature distribution of CHE exhibits higher variations at the sides and lower variations in the middle. This is because the CHE on the sides is less influenced by the heat exchange from other CHEs, resulting in higher heat transfer efficiency. The heat transfer rates of CHE are illustrated in Figure 7.

The distribution trend of heat transfer in the CHE in heating season and cooling season follows the same trend as the temperature distribution. The main pipe of the supply water pipe, where the CHE inlet is located, exhibits the highest heat transfer, but the main pipe and branch pipes of the return water pipe, where the CHE outlet is located, have opposite heat conduction directions (in heating season, the branch pipes absorb heat while the return water pipes release heat; in cooling season, the branch pipes release heat while the return water pipes absorb heat).

In heating season, the average heat transfer per unit pipe length is 0.60 W/m, and the total heat transfer of CHE in the entire numerical model is 233.14 W. Thus, it can be calculated that the heat transfer per loop of the prefabricated CHE in the shield energy tunnel is approximately 466.28 W. In cooling season, the average heat transfer per unit pipe length is 0.77 W/m, and the total heat transfer of

CHE in the entire numerical model is 300.81 W. Therefore, the heat transfer per loop of the prefabricated CHE in the shield energy tunnel is approximately 601.62 W.
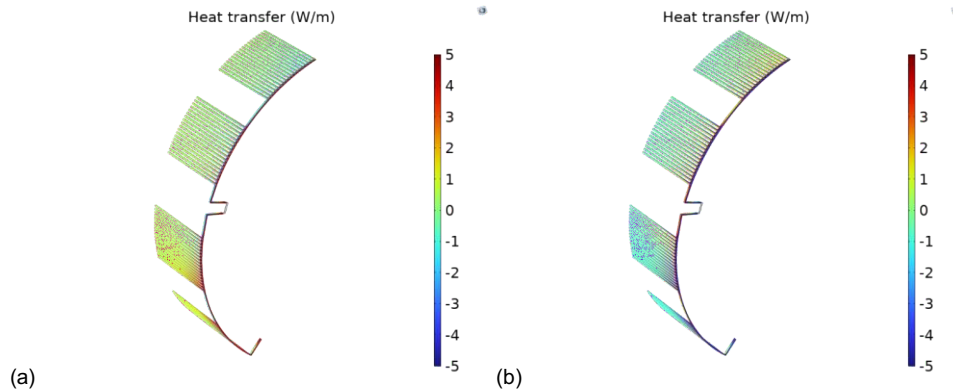

Figure 7: Heat transfer in CHE: (a) cooling season; (b) heating season

The projected area of CHE in the model is calculated to be approximately 4.74 m². Therefore, it can be inferred that the unit area heat transfer of the prefabricated CHE in the shield energy tunnel in heating season and cooling season is 49.19 W/m² and 63.46 W/m², respectively.

3.2. Structural characteristic

In this study, the steady-state calculation method was employed to simulate the structural mechanical response of the subway tunnel after the operation of the CHE, primarily focusing on the thermal stress of the shield tunnel segments.

The material of the energy tunnel segments is reinforced concrete, which meets the first and second strength theories of material mechanics. In numerical analysis software, the equivalent stress and principal stress can be used to determine the stress distribution and stress state of the object. If the principal stress is positive, the segment is in tension; if the principal stress is negative, the segment is in compression.

Equivalent stress (Von Mises stress) is a stress representation method proposed by Austrian engineer Von Mises. It predicts the deformation behavior of materials under complex stress states by considering the stress components in different directions. Although equivalent stress cannot directly assess the failure risk of materials, it provides an overview of stress distribution. Its calculation method is as follows:

Equation 2: Calculation method of equivalent stress.
$$\sigma_{eq} = \sqrt{1/2 \left((\sigma_1 - \sigma_2)^2 + (\sigma_2 - \sigma_3)^2 + (\sigma_3 - \sigma_1)^2\right)}$$

Where:

 - σ_{eq} = Equivalent stress (MPa)
 - σ_1 = Major principal stress (MPa)
 - σ_2 = Secondary principal stress (MPa)
 - σ_3 = Third principal stress (MPa)

Under the design conditions for the cooling season, with the heat exchanger inlet temperature at 35°C and an internal flow rate of 0.08m/s, the stress distribution and stress state of the segment are shown in Figure 8.

In the cooling season, *Figure 8* shows significant stress concentration on the side where the CHE main pipe is located. This is because temperature change or temperature difference alone does not directly produce stress. If the boundaries of the object are not constrained, allowing it to expand freely, no stress will be generated inside the object. Stress is only generated when the boundaries of the object are constrained, restricting its deformation, and causing internal stress due to resistance to the constraints. The main pipe of the heat exchanger is the area with the highest heat exchange rate in the entire exchanger, leading to stress concentration on the side of the segment where the main pipe is located. The maximum stress point of the segment appears at the CHE inlet andoutlet, reaching 0.88 MPa. This is because the temperature gradient is greatest at this location, resulting in the highest thermal stress. The secondary maximum values are located beneath the waist of the inner side of the tunnel segments. Therefore, during construction, it is important to avoid overlapping stresses at the CHE inlet with other stress concentrations.
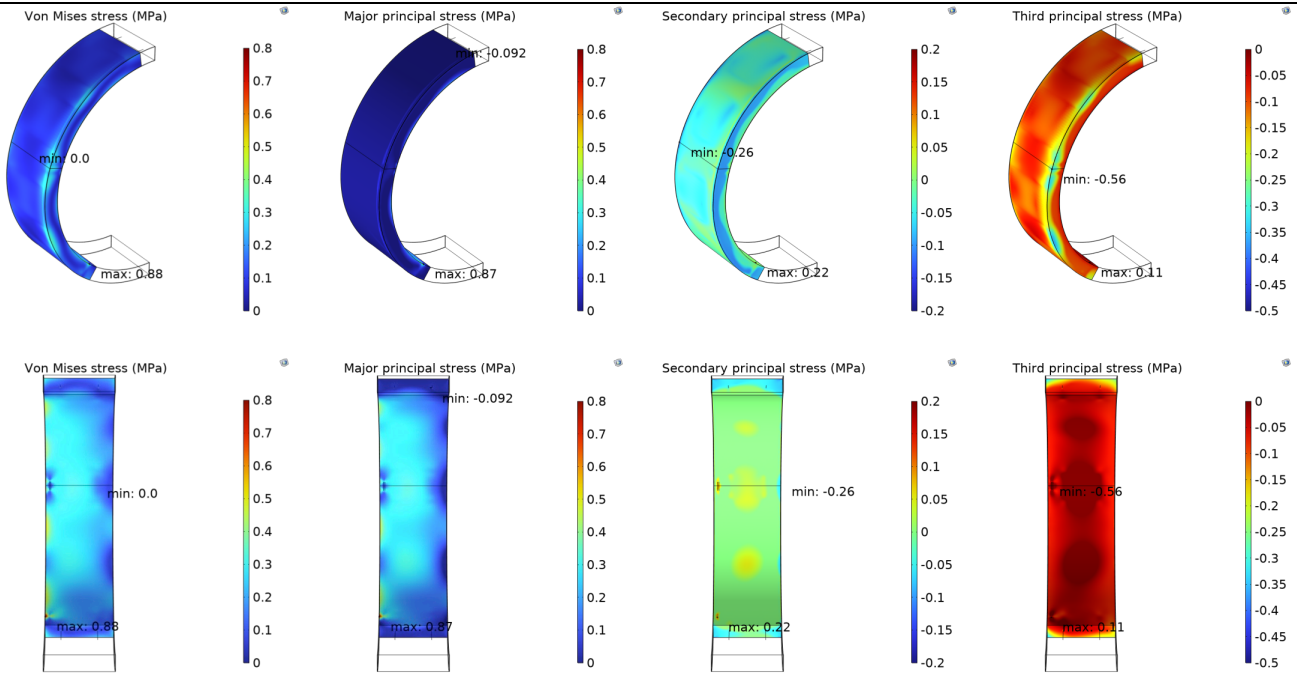
Figure 8: Stress distribution and stress state of segment in cooling season

In the cooling season, the heat pump system uses the CHE to release heat into the segment, thereby cooling the users. This process causes the temperature of the segment to gradually increase.

As shown in the principal stress results in Figure 8, the segment is generally under tensile stress, but the deformation of the segment is restricted by the surrounding rock, resulting in the outer arc surface being under compressive stress and the inner arc surface under tensile stress, which is the opposite of the winter condition. The maximum equivalent stress on the segment is 0.88 MPa, located at the CHE inlet. The maximum compressive stress point is on the outer arc surface waist, with a value of 0.56 MPa, and the maximum tensile stress point is at the CHE inlet, with a value of 0.87 MPa. The axial compressive strength limit of C50 concrete is 50 MPa, and the axial tensile strength limit is 2.64 MPa. Due to the operation of the CHE, the compressive stress on the segment is only 1.12% of the compressive strength limit, which is far below the tensile strength limit of concrete, and the tensile stress is 32.95% of the concrete's tensile strength limit.

Under the design conditions for the heating season, with the heat exchanger inlet temperature at 8°C and an internal flow rate of 0.08m/s, the stress distribution and stress state of the segment are shown in Figure 9.
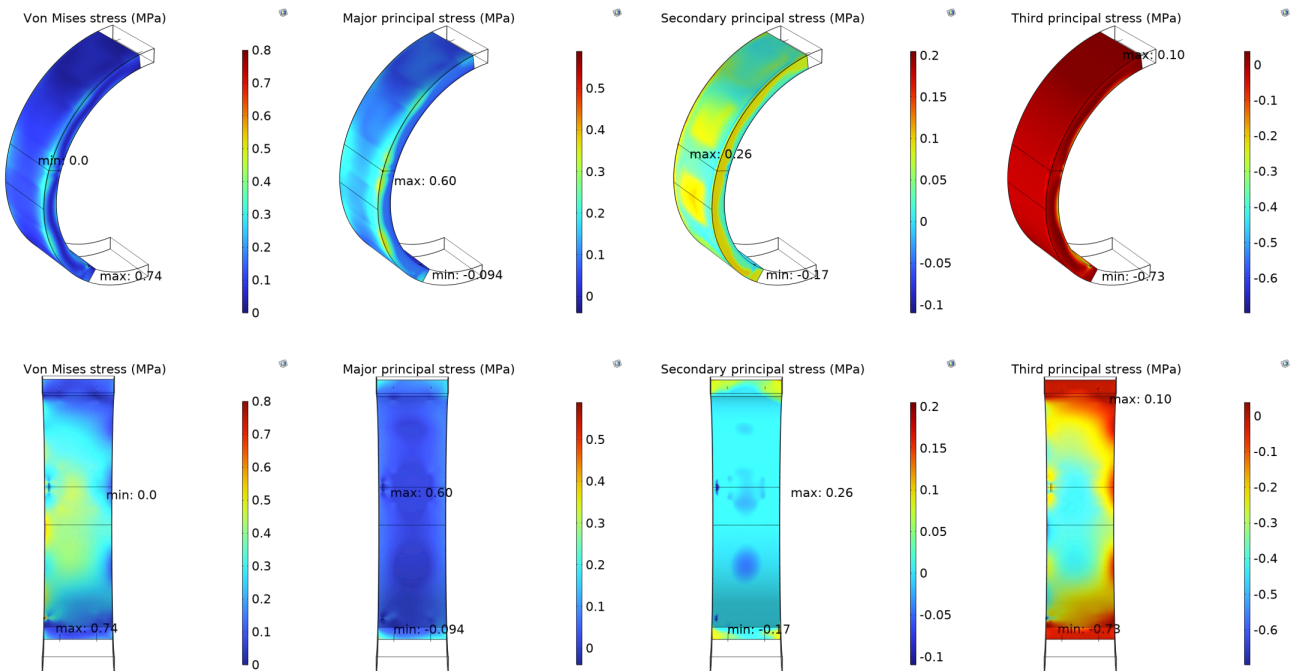

Figure 9: Stress distribution and stress state of segment in heating season

As shown in Figure 9, the side of the energy shield tunnel segment with the main pipe exhibits a stress concentration phenomenon similar to that in the cooling season. The reason for this phenomenon is also the same as in the cooling season. However, the maximum equivalent stress during the heating season is 0.74 MPa, slightly lower than the 0.88 MPa in the cooling season.

We speculate there are two main reasons for this difference. First, the temperature gradient near the maximum stress point in the cooling season is greater. The CHE inlet water temperature is 35℃ in the cooling season, while the tunnel air temperature is 28℃, a difference of 7℃. In the heating season, the CHE inlet water temperature is 8℃, and the tunnel air temperature is 12℃, a difference of 4℃. The temperature difference in the cooling season is approximately 1.75 times that of the heating season. The maximum stress point on the segment is located on the inner side, with the capillary pipe side being the tunnel air inlet, making the temperature at the maximum stress point similar to the tunnel air temperature. This leads to a higher temperature gradient near the maximum stress point in the cooling season compared to the heating season. Temperature gradients are the primary cause of thermal stress.

Second, the temperature change in the segment is greater in the cooling season compared to the heating season. Before the CHE operation, the average volume temperature of the segment is 27.73℃ in the cooling season and 11.68℃ in the heating season. After CHE operation, the average volume temperature is 30.26℃ and 10.45℃, respectively, with differences of 2.53℃ and 1.23℃. The temperature changes before and after operation in the cooling season is 2.06 times that in the heating season. Temperature change is the second cause of thermal stress. Combining these two factors, the thermal stress generated in the segment is greater during the cooling season when the heat exchanger is operating.

However, the stress states during the heating season and the cooling season are opposite. In the heating season, the tunnel segment is generally in a compressed state. Yet, the deformation of the segment is also constrained by the surrounding rock of the tunnel, causing the outer side of the segment to be in tension and the inner side to be in compression. The maximum tensile stress on the outer surface of the segment is 0.60 MPa, approximately 22.72% of the tensile strength limit of C50 concrete, and it is located at the junction between the two segments. The maximum compressive stress on the inner surface of the segment is 0.73 MPa, about 1.46% of the compressive strength limit of C50 concrete, and it is located at the inlet and outlet of the CHE.

4. DISCUSSION

If the heat exchanger is not considered, and only the gravitational load and the external support from the surrounding rock are taken into account, the maximum tensile stress point in the shield tunnel segment will appear at the junction of the tunnel segm ent crown, as per Zhu (2020), with a maximum tensile stress of approximately 1.75 MPa. When the segments are installed in the standard manner, with the crown segment directly above the tunnel, the maximum tensile stress point due to gravitational load will not coincide with the maximum stress point caused by the operation of the CHE.

During the construction of shield tunnels, segments are generally installed in a staggered pattern, and the position of the segments will rotate as the tunnel boring machine advances. If the segments rotate 140° or 220°, the inlets and outlets of the CHE will be located at the top of the tunnel, causing the two maximum stress points to coincide. This will result in a maximum tensile stress of 2.62 MPa, reaching 99.24% of the concrete's tensile strength limit, which could potentially cause cracking of the concrete and threaten the safety of the tunnel. Therefore, during construction, the segments with the inlets and outlets of the CHE should not be installed at the top of the tunnel. This will not only avoid the superposition of maximum stresses but also facilitate the connection of the CHE to the supply and return water pipes within the tunnel.

5. CONCLUSION

This study, based on COMSOL Multiphysics finite element analysis software, utilized steady-state numerical calculation methods to simulate the thermal-structure coupling characteristics of the prefabricated capillary heat exchanger (CHE) in the energy shield tunnel under design conditions, leading to the following conclusions:

- Under the design conditions of the heat pump unit, the system exhibits good heat transfer performance. When the inlet temperatures are 35°C in cooling season and 6°C in heating season, the outlet water temperatures of CHE are approximately 32.12°C and 8.22°C, respectively. Each ring of the energy shield tunnel can provide heat transfer rates of 601.62W and 466.28W in heating season and cooling season, respectively, with heat transfer efficiencies reaching 63.46W/m² and 49.19W/m².
- Due to CHE operation, the maximum tensile and compressive stresses generated in cooling season are 0.87MPa and 0.56MPa, respectively, while in heating season, they are 0.60MPa and 0.73MPa, respectively. The compressive stresses are far below the compression limit of C50 concrete, while the tensile stresses account for 33% and 23% of the axial tensile strength, respectively.
- If the maximum tensile stress point caused by the operation of the capillary heat exchanger coincides with the maximum tensile stress point due to gravitational load and soil support, the combined tensile stress will reach 99.24% of the concrete's tensile strength limit. This could potentially cause the segments to crack. Therefore, during construction, it is crucial to avoid installing the segments with the capillary heat exchanger inlets and outlets at the top of the tunnel. This will not only prevent the superposition of the two maximum tensile stresses but also facilitate the connection of the capillary tubes in the energy shield segments with the supply and return mains within the tunnel.

Therefore, the prefabricated CHE in the energy shield tunnel demonstrates good heat transfer performance, with minimal impact on the tunnel segment. However, caution should be exercised to avoid complete overlap between the inlet and outlet of CHE on the segments and the positions of maximum tensile stress occurring during the tunnel construction process.

6. ACKNOWLEDGEMENT

7. REFERENCES

National Bureau of Statistics, (2022) 'China Statistical Yearbook'. Beijing shu tong dian zi chu ban she. (In Chinese)

Jiang, Y. Hu, S. and Zhang Y., et al. (2022) 'China building energy efficiency annual development research report'. (In Chinese)

Geothermal energy information. (2023) Qian, Q.H: establish and improve the mechanism of shallow geothermal energy application. Available at: https://mp.weixin.qq.com/s/r9odhwxjE340mrIfddnxjA (Accessed: 15 August 2023).

Brandl, H. (2006). 'Energy foundations and other thermo-active ground structures'. Géotechnique, 56(2), pp.81-122.

Adam, D., and Markiewicz, R. (2009) 'Energy from earth-coupled structures, foundations, tunnels and sewers'. Géotechnique, 59(3), pp.229-236.

Wang, H.Y. Hu, S.T. and Chang Z. et al. (2014) The invention relates to a capillary soil source heat pump system applied to a subway tunnel. (2014-03-05). CN103615841A.

Xia, C.C. Yang, Y. Zhang, G.Z. and Zou, Y.C. (2014) 'The internal source heat pump heat exchange tube and tunnel structure interact'. Journal of Tongji University (Natural Science Edition), (1), pp.51-57. (In Chinese)

Yang, Y. Xia, C.C. and Zhu, J.L. (2014) 'Study on temperature stress induced by heat exchange tube of tunnel ground source heat pump'. Journal of Central South University: Natural Science Edition, 45(11), pp.3970-3976. (In Chinese)

Zhu, Z.N. (2020) 'Analysis of heat transfer, stress and construction problems of energy shield tunnel'. (Master's thesis, Tsinghua University).

Di Donna, A. and Barla, M. (2016) 'The role of ground conditions on energy tunnels' heat exchange'. Environmental geotechnics, 3(4), pp.214-224.

Ministry of Construction of the People's Republic of China. (2013) 'GB 50157-2013 Code for design of metro'. Beijing: China Building Industry Press.

Ministry of Construction of the People's Republic of China. (2005) 'GB 50366-2005 Technical code for ground-source heat pump system'. Beijing: China Building Industry Press.

Zhu, H.H. and Tao, L.B. (1998) A beam-spring system model for stress analysis of shield tunnel lining structures. Journal of Rock and Soil Mechanics, 19(2), pp.26-32. (In Chinese)

Zhang, Y. Zhang, Q. Bi, H.Q. and Wang, J.Y. (2020) 'Experimental study on wind speed and its variation in metro piston duct'. Refrigeration and air conditioning (Sichuan), 34(04), pp. 463-467. (In Chinese)

Ji, Y.M, Wu, W.Z. and Hu, S.T. (2023) 'Long-term performance of a front-end capillary heat exchanger for a metro source heat pump system'. Applied Energy, 335, p.120772.

Gao, H. (2015) Research on Heat Transfer Characteristics of Capillary Heat exchangers in Subway Tunnel (Doctoral dissertation, Qingdao: Qingdao University of Technology).

Lu Y.Q. (2008) 'Practical heating and air conditioning design manual. second ed'. Beijing: China Construction Industry Press. (In Chinese).

Ji, Y.M. Wu, W.Z. Qi, H.Y. Wang, W.Q and Hu, S.T. (2022) 'Heat transfer performance analysis of front-end capillary heat exchanger of a subway source heat pump system'. Energy, 246, p.123424.

Insana, A. (2020). Thermal and structural performance energy tunnels. Politecnico di Torino.

#202: High-performance mixed-matrix membranes based on COF/polymer for CO2 separation

Zixuan Yu [1], Boyu Li[2], Xiaohui Liu [3], Zhuo Li [4] , Wenquan Tao [5]

[1] Tongji University, 1239 Siping Road, Shanghai, China, kgrox@tongji.edu.cn
[2] Tongji University, 1239 Siping Road, Shanghai, China, lbyyyy@tongji.edu.cn
[3] Tongji University, 1239 Siping Road, Shanghai, China, liuxiaohui21@tongji.edu.cn
[4] Tongji University, 1239 Siping Road, Shanghai, China, zhuoli2013@tongji.edu.cn
[5] Tongji University, 1239 Siping Road, Shanghai, China, wqtao@mail.xjtu.edu.cn

Abstract: The gas separation performance of mixed-matrix membrane (MMM) highly depends on the properties of nano-fillers and polymer matrix and their interfacial compatibility. Herein, we report the fabrication of a COF-based MMM (COF-300-Amide/Pebax2533) for CO_2 separation, in which highly crystalline amide-linked COF-300-Amide particles used as nano-additives and incorporated into Pebax2533 polymer via solution casting method to obtain the membrane. The COF-300-Amide was obtainedby oxidizing imine-linked COFs (COF-300) for irreversible and high crystalline synthesis. The membrane of COF-300- Amide/Pebax2533 showed uniform and continuous morphology, which demonstrated that the nano-particles had good interfacial compatibility with the Pebax2533 matrix. GCMC simulation and dcTST method were used to calculate the CO_2 adsorption/diffusion properties in COFs. The interfacial interaction between the nano-fillers and substrate was thoroughly quantified by molecular dynamics (MD) simulations. The resultant membrane demonstrates a simultaneous enhancement of individual gas permeability (681.6 Barrer) and CO_2/N_2 ideal selectivity (41.3), surpassing Robenson upper bound (2008). Moreover, the synthesized COF with high crystallinity greatly enhanced the stability of COF-300-Amide/Pebax2533 with an anti-decomposition temperature of 397.1 °C and a lasting sustainability over 28 days. The study demonstrates the great potential of the developed COFs-based MMMs in promoting CO_2 separation applications.

Keywords: Mixed-Matrix Membranes, Amide-Linked Cofs, Pebax2533 Matrix, CO_2 Separation, Molecular Dynamics Simulations

1. INTRODUCTION

The excessive emission of CO_2 from industrial activities has seriously threatened the environment and human health (Qiao et al., 2019). To achieve environment-benign and energy-efficient CO_2 capture, membrane-based gas separation technology has been considered a promising strategy, compared to adsorption, low-temperature, and high-pressure technologies (Hepburn et al., 2019). However, the performance of current commercial membranes for CO_2 separation is still insufficient to meet the requirements for industrial applications (Liu et al., 2019a), which suffer from the trade-off limitation between permeability and selectivity, and the sustainability in long-term service. To overcome such limitations, the development of mixed-matrix membranes (MMMs) has shown the potential to improve CO_2 gas separation (Guo et al., 2022).

MMMs are normally fabricated by embedding inorganic or organic materials as fillers into the polymer matrix, and the membrane performance is determined by the properties of fillers, polymer matrix, and their interfacial compatibility (Chen et al., 2022b). In recent years, many kinds of fillers such as silica, zeolites, carbon molecular sieves, and metal-organic frameworks (MOFs) have been developed (Qian et al., 2020, Wang et al., 2023), however, a significant challenge of these fillers is the poor interfacial compatibility with polymer matrix which leads to the formation of non-selective permeation pathways, thereby significantly reducing the overall selectivity of the membranes (Guo et al., 2020). Covalent-organic frameworks (COFs), being organic polymers themselves, exhibit significantly excellent compatibility with the polymer matrix due to similarity and intermiscibility (Fu et al., 2016). Besides, COFs can form highly ordered and periodic network structures that offer structural diversity, functional pore walls, and distinctive pore sizes (Ying et al., 2021). These features thus make COFs suitable for preparing MMMs with outstanding selectivity performance for gas separation yet with excellent interfacial compatibility (Dai et al., 2023). COFs however have inferior sieving effects for gases, because their pore sizes (0.8-4.7 nm) are typically larger than the kinetic diameters of gas molecules like CO_2 (0.33 nm), N_2 (0.36 nm) and H2 (0.29 nm) (Wang et al., 2021). Tune COFs with appropriate pore sizes thus is essential to ensuring MMMs with outstanding performance.

The structure and properties of COFs vary significantly on the construction units and linkages (WallerGándara and Yaghi, 2015), which significantly affect COFs' crystallinity, stability, and processability. The amide bond is a chemical linkage that is irreversible under typical ambient conditions as well as normal solvents, acids, and bases. Li et al. (2023c) synthesized highly crystalline amide-linked COFs by the post-modification of imine-linked COFs, which remarkably increased the affinity to CO_2 and impeded the passage of N_2.

Inspired by the above research progress, we aim to investigate the utility of amide-linked COFs as fillers for developing MMMswith high performance for CO_2/N_2 separation. COF-300-Amide was synthesized to serve as the filler, and the Pebax2533 was used as the polymer matrix, to prepare COF-based MMMs (COF-300-Amide/Pebax2533) for CO_2/N_2 separation. COF-300- Amide/Pebax2533 shows a simultaneous increase in selectivity and permeability for CO_2/N_2 separation, alongside enhanced resistance to aging and decomposition at higher temperatures. The MMMs exhibit significant chemical and thermal stability improvements due to the synergistic effects of the COF-300-Amide and the Pebax2533 matrix, which is also quantitatively by molecular simulation methods.

2. MATERIAL AND METHOD
2.1. Material

All the reactants and solvents were purchased from commercial suppliers without further purification. TAM and PA were purchased from Jilin Chinese Academy of Sciences Yanshen Technology Co., Ltd. 1,4-Dioxane, $NaClO_2$, sodium thiosulfate pentahydrate ($Na_2S_2O_3 \cdot 5H_2O$) and 2-Methyl-2-butene were purchased from Shanghai Aladdin Biochemical Technology Co., Ltd. Aniline and glacial AcOH were purchased from Shanghai Macklin Biochemical Co., Ltd. Ethanol and tetrahydrofuran (THF) were purchased from Guangdong Guanghua Sci-Tech Co., Ltd. Pebax2533 was supplied by Arkema Co., Ltd.

2.2. Preparation of COF-300 and COF-300-Amide

The COF-300 and COF-300-Amide were synthesized according to the literature (WallerGándara and Yaghi, 2015). The imine-linked COFs (COF-300) were chosen as the pristine materials, and the amide-linked COF-300-Amide was then synthesized by oxidation of COF-300.

2.3. Preparation of COF-300-Amide/Pebax2533 membrane

Before fabricating the membrane, the Pebax2533 and COF-300-Amide were dried at 150 °C overnight to remove adsorbed moisture. 0.3 g Pebax2533 was added to 6.0 g ethanol and magnetically stirred at 90 °C for 4 h to form a homogeneous solution. 0.05 g COF-300-Amide powder was added to the above-mentioned solution and sonicated for 30 min to disperse COFs uniformly. Then, the mixed solution was poured into a 6 cm diameter Teflon dish and evaporated at room temperature for 24 h. Afterward, the Teflon dish was dried in a vacuum oven at 60 °C for 12 h to obtain MMMs of COF-300-Amide/Pebax2533, composed of COF-300-Amide as fillers and Pebax2533 as substrate. The membrane fabrication scheme is illustrated in Fig. 1
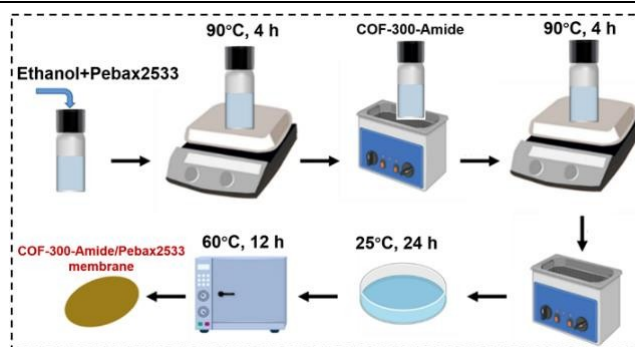
Figure 1: Scheme of fabricating COF-300-Amide/Pebax2533 membrane

2.4. Gas separation experiment

The single gas permeation measurements of CO_2 and N_2 were implemented to evaluate the membrane capabilities for gas separation (Li et al., 2023a). The test of the binary gas mixture CO_2/N_2 was conducted according to the literature (Liu et al., 2024). The feed gas flow of CO_2 and N_2 was each maintained at 50 mL min^{-1}. The residual gas was swept by using Ar gas after the membrane was installed in the permeation system. The gas composition was quantified by gas chromatography (GC). All the experiments were conducted under the temperature of 25 °C and repeated three times.

2.5. Simulation method

The MD models for COFs and Pebax2533 were constructed to study their interfacial interaction. The Pebax2533 super-units were built by the PA unit and PE unit. CO_2 and N_2 adsorption loadings for COF-300 and COF-300-Amide were calculated in GCMC simulation using RASPA codes (Dubbeldam et al., 2016). The diffusion coefficients (D_0) of CO_2 and N_2 were calculated by the mean-square displacement (MSD) of molecules. However, the adsorption loading of N_2 in the two COFs was very low, which resulted in the calculation of the average MSD inaccuracy. Thus, the dcTST method was used to calculate the diffusion coefficient of the gases (BeerdsenSmit and Dubbeldam, 2004). All the MD simulations were performed using the LAMMPS package (Plimpton, 1995).

First, the surface slab for COF-300 and Amide-300 was constructed by cutting off the (0 0 1) plane, because the 1D channel of the COFs is perpendicular to it. Unsaturated atoms at the COF surface were saturated by H atoms. For the COF structures, the Dreiding force field was applied to describe the atoms, and the partial charges were calculated by CP2K using REPEAT method. The size of the COF-300 and Amide-300 slab model was approximately to be 40 Å × 40 Å × 45 Å.

The Pebax-2533 copolymer is composed of PA12 as PA unit and PTMO as PE unit, and the weight ratio of PTMO is 80%. In this study, one PA unit and eleven PE units were combined to form a Pebax-2533 chain, and the weight ratio of PA to PE is 1:4.02, which is consistent with the composition of Pebax-2533. The Pebax-2533 model contained 40 chains. Dreiding force field was used for Pebax-2533. The atomic charges of Pebax were calculated by ORCA5 and Multiwfn software.

To construct the interface model of COF/Pebax, 21-steps methodology was applied. During the simulation process, the nonbonded van der Waals (vdW) interactions were considered using the 12-6 form of the Lennard-Jones (L-J) potential with the cutoff of 12.5 Å, with cross-interaction parameters computed according to the Lorentz-Berthelot mixing rules. The PPPM algorithm with a precision of 10-5 was used to calculate Coulombic interactions. After that, a 1 ns simulation run in NVT ensemble at 300 K was conducted, and the simulation data were collected for the analysis.

In the dcTST method, the diffusion is considered as a process that the gas molecules hop from one cage to another. A reaction coordinate q was defined, which indicated the progress of the diffusion event from one cage to another. The location of the energy barrier between the two cages is denoted by q*. The gas molecule is restrained at different reaction coordinate q along the hop path with the harmonic potential, and the gas molecule can move at small regions. Various simulations were performed to sample the regions, and the result can be generated as a free energy profile using the weighted histogram analysis method (WHAM).

3. RESULTS AND DISCUSSION
3.1. Characterization of COF-300 and COF-300-Amide

Fig. 2a shows the unique morphology of COF-300 particles, which were then oxidized as COF-300-Amide (Fig. 2b). The topology of some particles was destroyed, implying a slight degradation of the materials' crystallinity. The core of the oxidation process that converts COF-300 into COF-300-Amide is the oxidation of the imine bonds in COF-300 to amide bonds. From the FTIR spectroscopy (Fig. 2c), the peak at 1617 cm^{-1} is C=N imine stretch in COF-300 (Hao et al., 2023), whereas it disappears and is replaced by the C=O amide stretch (1530 cm^{-1} and 1640 cm^{-1}) (Kang et al., 2022) in COF-300-Amide, indicating the conversion of imine to amide bond. Fig. 2d shows the results of the XPS spectra. In the COF-300 spectrum, the characteristic peak at 397.98 eV corresponds to the –N= in the imine bonds (Chen et al., 2022a), and the other peak at 399.58 eV is likely due to the –NH$_2$ at the ends of the TAM monomers used in the synthesis of COF-300 (Liu et al., 2019b). For the COF-300-Amide, only a small amount of the imine signal remains, indicating that the oxidation is quite complete, and the characteristic peak at 399.50 eV could be assigned to the -NH- in the amid bonds (Fusalba and Bélanger, 1999). PXRD results (Fig. 2e) show that the peaks of COF-300-Amide are slightly broader and less intense than that of COF-300, demonstrating morphological observations in the SEM images. However, the persistence of

these multiple sharp peaks within the PXRD of COF-300-Amide is a strong testament to the material's maintained high degree of crystallinity. The results of the thermogravimetric analysis (Fig. 2f) show that the two materials have similar decomposition temperatures, indicating that the thermal stability of COF-300-Amide was not deteriorated by the reduced crystallinity.
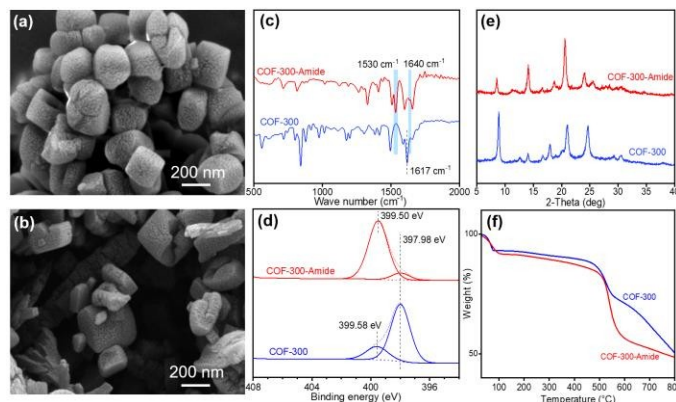

Figure 2: SEM of (a) COF-300 and (b) COF-300-Amide; (c) FTIR spectroscopy of COF-300 and COF-300-Amide; (d) XPS N1s spectra of COF-300and COF-300-Amide; (e) PXRD diffraction patterns of COF-300 and COF-300-Amide; (f) TG analysis of COF-300 and COF-300-Amide

3.2. Molecular simulation of COF-300 and COF-300-Amide

To quantify the adsorption and diffusion properties of CO_2 and N_2 in COF-300 and COF-300-Amide, molecular dynamics simulations were conducted. By replacing the C=N groups in the COF-300 crystal with the OC=NH group, the Amide-300 crystal was obtained. The cell sizes of COF-300 and Amide-300 are 19.64×19.64×8.95 Å. CP2K (Kühne et al., 2020) software was used to optimize the structure of the obtained cells for subsequent calculation and simulation. The pore limiting diameter (PLD) of COF-300 and Amide-300 were calculated by Zeo++ software (Willems et al., 2012) and are 3.83 Å and 3.34 Å respectively. The adsorption isothermal properties for COF-300 and COF-300-Amide are compared in Fig. 3a, respectively. For COF-300-Amide, the CO_2 adsorption loading is much higher than that of COF-300 at the same pressure, which also grows faster than that of COF-300 at low pressure and is gradually saturated as the pressure increases. This is because the adsorption site of CO_2 in COF-300-Amide is occupied, and the pore volume is filled at low pressure (FrostDüren and Snurr, 2006). In contrast, the adsorption of COF-300 continues to rise at high pressure which indicates that the COF-300 pores still have much volume for CO_2 to fill in, due to the fewer adsorption sites for CO_2 than COF-300-Amide. For N_2 adsorption, the linear adsorption isotherm shows that the adsorption sites for N_2 do not exist in COF-300. The N_2 adsorption loading in COF-300-Amide is rather low, showing a linear relationship with the pressure, which indicates that there is no N_2 adsorption site in COF-300-Amide.

To reveal the molecular mechanisms of CO_2 adsorption sites, the RDF calculation was performed to study the interaction between CO_2 molecules and two COFs, and the results are presented in Fig. 3b. The C=O and -N-H groups in COF-300-Amide and the C=N-C group in COF-300 were selected to calculate the RDF. For COF-300-Amide, the dark yellow curve has the highest peak at r = 3 Å, indicating the strong interaction of the C=O group in COF-300-Amide and CO_2, which contributes greatly to CO_2 adsorption. As for the -N-H group in COF-300-Amide, the peak of the blue curve is at r = 5.3 Å, but the distance is too long to have the interaction between the group and CO_2 molecules. The results suggest that CO_2 molecules are adsorbed on the C=O part of the amide group, and the strong interaction between CO_2 and the C=O group is the main reason for the improved adsorption of COF-300-Amide. ForCOF-300, the peak of the pink curve at r = 4.1 Å confirms the interaction between CO_2 and the COF-300 framework, but the long distance between CO_2 and the N atom also shows that the interaction is weak. The results are consistent with the adsorption performance of the two COFs in Fig. 3a. More importantly, the adsorption selectivity for CO_2/N_2 in COF-300-Amide is 186.9, much higher than that of COF-300. These results confirm that the adsorption performance of COF-300 after oxidation for CO_2 was greatlyenhanced.

The diffusion property of CO_2 and N_2 in the two COFs greatly influences the permeation performance. The umbrella sampling method was conducted to calculate the diffusion coefficient of gases in the two COFs. The free energy along the channels were calculated (Fig. 3c-3d). The peaks in the free energy profile represent the energy barrier for diffusion. For COF-300-Amide, the free energy for N_2 is dominated by the pore size, while the free energy for CO_2 is determined by the interaction between CO_2 molecules and the COF framework (Fig. 3c). For COF-300, the free energy profiles of CO_2 and N_2 show a very different variation tendency (Fig. 3d). This is primarily due to the presence of CO_2 adsorption sites within the structure of COF-300-Amide, the absence of N_2 adsorption sites, and the sieving effect caused by the pore sizes.
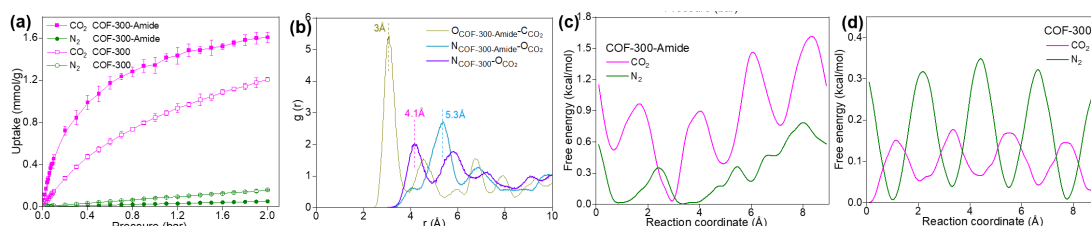

Figure 3: (a) Adsorption isotherm of COF-300 and COF-300-Amide; (b) RDF results; free energy of (c) COF-300-Amide and (d) COF-300

Because of the larger pore size of COF-300, the gases diffuse more quickly than COF-300-Amide. The diffusion coefficient for CO_2 is lower than N_2 for both COF-300 and COF-300-Amide, but still in the same order of magnitude. The separation selectivity for the two COFs thus is determined by the adsorption process. Furthermore, the lower diffusion coefficient for CO_2 than N_2 is due to the strong interaction between CO_2 molecules and the COF structures, which makes CO_2 molecules diffuse slowly. In COF-300, the CO_2 diffusion coefficient is 4.48 times higher than that of COF-300-Amide due to the weak interaction.

3.3. Characterization of COF-300-Amide/Pebax2533 membrane

The cross-section SEM of the pristine Pebax2533 membrane and COF-300-Amide/Pebax2533 membrane are shown in Fig. 4a and Fig. 4b-4d, respectively. They both exhibit dense structures without apparent voids due to the great chain flexibility of Pebax2533 (Clarizia et al., 2019). The COF-300-Amide/Pebax2533 membrane (Fig. 4b) has a thickness of 140 μm and shows a continuous morphology, indicating the excellent compatibility between COF-300-Amide (the black circle in Fig. 4d) and Pebax2533 (Tahir et al., 2019).

Fig. 2e shows the PXRD patterns of COF-300-Amide filler and COF-300-Amide/Pebax2533 membrane. No shifts are observed in any diffraction peaks of COF-300-Amide/Pebax2533, indicating that the membrane preparation didn't affect the crystallinity of the COF-300-Amide particles in the MMMs. Additionally, compared to the pristine Pebax2533 membrane, COF-300-Amide/Pebax2533 shows a much higher anti-degradation temperature of 397.1 °C than that of COF-300 of 360.7°C (Fig. 2g). The increased decomposition temperature is attributed to the strong interactions between fillers and polymer matrix (Li et al., 2023b). These results confirm that the highly crystalline COF-300-Amide was successfully synthesized through the oxidation of COF-300 and could be utilized as an ideal filler to fabricate MMMs further.
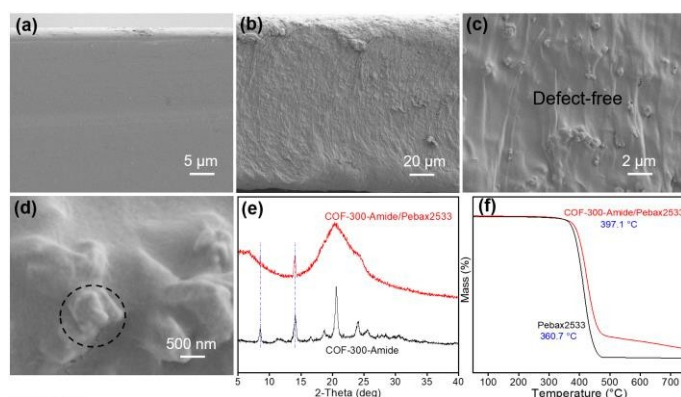

Figure 4: Cross-section SEM images of (a) pristine Pebax2533 membrane, and (b)-(d) COF-300-Amide/Pebax2533 membrane; (e) PXRD diffraction patterns of COF-300-Amide and COF-300-Amide/Pebax2533; (f) TG analysis of COF-300-Amide and COF-300-Amide/Pebax2533

3.4. Interfacial interaction between COF-300-Amide and Pebax2533

The interface compatibility between fillers and matrix is crucial for MMM performance. The interface model and the atomic density distribution of the COF-300/Pebax2533 membrane and COF-300-Amide/Pebax2533 membrane are presented in Fig. 5a-5b, respectively. For the two membranes, the overlap region between COFs and Pebax2533 along *z* direction demonstrates good interfacial adhesion. The low atomic density of Pebax2533 in the COFs region also confirms that the Pebax2533 chains are difficult to infiltrate into the 1D channel structure of COFs and thus avoid pore blockage.

In the RDF calculation, the N atom in the amino group of COF-300 and the N, O atoms in the amide group of COF-300-Amide were considered. For Pebax2533, 5 types of O atom and the N atom in the PA unit were considered as marked in Fig. 5c. The RDF results are correspondingly presented in Fig. 5d-5f, in which the peaks at the distance of r < 4 Å are considered as hydrogen bonds, because the hydrogen bonding force is weak when the distance between the N, O atoms is larger than 4 Å. Fig. 5d shows the RDF of COF-300 and Pebax2533, and the peaks of N-O3, N-O4, N-O5 indicate the existence of the hydrogen bonds between the amino group of COF-300 and the carboxyl, ester group of Pebax2533. For the -NH2 part of the COF -300-Amide, the yellow (N-O5) and purple (N-O4) curves show a rather high peak (Fig. 5e), indicating the strong hydrogen bonds -N-H--O=C-. The black curve of N-H…N interaction between the amino groups of the COF-300-Amide and Pebax2533 also shows a peak at r=3.8 Å. For the -C=O part of the COF-300-Amide, the O-N peak and the O-O3 peak in Fig. 5f show that the hydroxyl and the amino part of the Pebax2533 have a strong interaction with COF-300-Amide. These results confirm that both COF-300 and COF-300-Amide have a profound interfacial interaction with Pebax2533, due to the abundant functional groups at the surfaces of COFs and Pebax2533. Good compatibility at the interface consequently facilitates the gas separation of MMMs.

The fillers in the matrix may disturb the polymeric chain packing, thus increasing the free volumes between the polymer chains or creating nanovoids between the polymer/filler interface (Wolińska-Grabczyk et al., 2017). The voids and defects at the interface can be evaluated by calculating the pore size distribution (PSD) at the interface region. Poreblazer4.0 software (Sarkisov and Harrison, 2011) was used with the helium atom used as a probe. The PSD results at the interface region of COF-300/Pebax2533 and COF-300-Amide/Pebax2533 are shown in Fig. 5g. Most voids at the interface have a size of 2-3 Å, less than the kinetic diameter of N_2 (3.3 Å) and CO_2 (3.6 Å). Thus, it is unlikely for the gas molecules to transport at the interfacial voids. The small pore size at the interface also confirms the good compatibility between COFs and Pebax2533. In addition, the pore size of COF-300-Amide/Pebax2533 interface is slightly smaller than that of COF-300/Pebax2533, indicating that COF-300-Amide/Pebax2533 has a better compatibility between the fillers and the matrix.

The functional groups of fillers and matrix can enhance the affinity or reactivity between the MMMs and the targeted gases (Imtiaz et al., 2022) Pebax2533 matrix possesses high CO_2/nonpolar gas (N_2) selectivity coupled with intrinsically higher CO_2 permeability due to the presence of polar ether oxygen atoms in the soft segment which results in good CO_2 affinity (Ghasemi EstahbanatiOmidkhah and Ebadi Amooghin, 2017a). The functionalized surface and gas path of COF-300 and COF-300-Amide with imine and amide both have greater CO_2 affinity (Das et al., 2022), which could enhance CO_2 transport along the CO_2-philic micro-environment but N_2, resulting in an improved CO_2/N_2 selectivity.
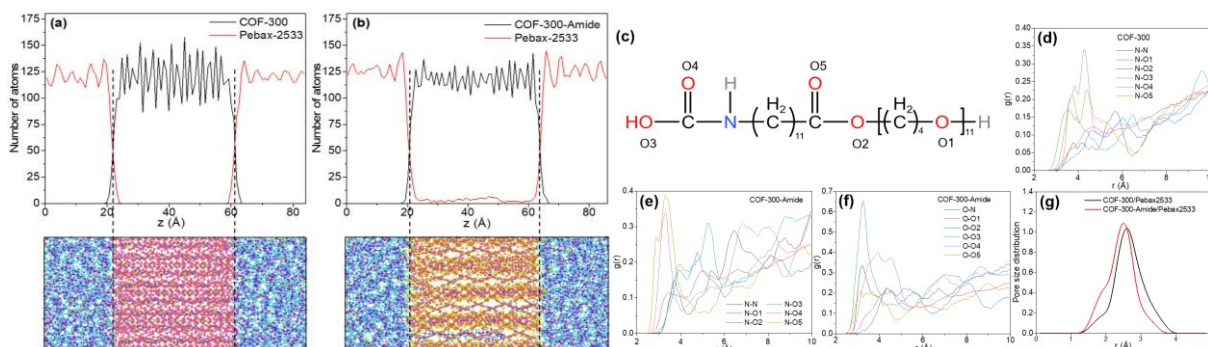

Figure 5: Interface model and atomic density distribution of (a) COF-300/Pebax2533 and (b) COF-300-Amide/Pebax2533; RDF calculation results of COF/Pebax2533 interface; (c) N, O types of Pebax2533 used in the calculation; (d) RDF results of N atom in COF-300 and Pebax2533; (e) RDF results of N atom in COF-300-Amide and Pebax2533; (f) RDF results of O atom in COF-300-Amide and Pebax2533; (g) pore size distribution at theinterface region of COF-300/Pebax2533 and COF-300-Amide/Pebax2533

3.5. Gas separation performances of COF-300-Amide/Pebax2533

The single gas transport properties of the developed MMMs were tested at 25 °C. Fig. 6a shows the CO_2 permeabilities of the Pebax2533, COF-300/Pebax2533 and COF-300-Amide/Pebax2533 membranes. Compared to Pebax2533 (permeability: 219 Barrer; selectivity: 23.1), both COF-300/Pebax2533 and COF-300-Amide/Pebax2533 membranes exhibit enhanced gas permeability and selectivity of 740.9 Barrer/33.2 and 681.6 Barrer/41.3, respectively. The inherent adsorption of both COF-300 and COF-300-Amide to CO_2 improved the permeability of CO_2 due to the dipole-quadrupole interaction between the COF fillers and CO_2 molecules (Zhu et al., 2023) and restricted the transport of nonpolar N_2 molecules with larger size than CO_2 molecules, resulting in enhanced CO_2/N_2 selectivity. It should be noted that COF-300-Amide/Pebax2533 shows a slight decrease in permeability and an increase in selectivity compared to COF-300/Pebax2533, which can be attributed to the smaller pore size of COF-300-Amide after oxidation that constrained the diffusion of CO_2 in the porous structure (Krishna, 2012).

Additionally, the long-term stabilities of the membranes were investigated, by testing the permeability/selectivity performance of the membrane every seven days. The selectivity performance of the COF-300/Pebax2533 and COF-300-Amide/Pebax2533 membranes dropped only 11.5% and 9.3% after 28 days (Fig. 6b-6c). So far, the performance of the two developed MMMs surpassed Robenson upper bound (Fig. 6d) and shows competitive performance compared with other reported Pebax-based and advanced MMMs (Ebadi Amooghin et al., 2019, Sanaeepur et al., 2016, SanaeepurNasernejad and Kargari, 2015, Seong et al., 2022, Nafisi and Hägg, 2014, Wang et al., 2014, Ghasemi EstahbanatiOmidkhah and Ebadi Amooghin, 2017b, Wu et al., 2021, Zhao et al., 2017, Fam et al., 2017, MeshkatKaliaguine and Rodrigue, 2019, Dai et al., 2019, Sanaeepur et al., 2019).

The permeability and selectivity both reduced by increasing the feeding pressure, which could be attributed to the saturation of the COF-300-Amide particle fillers at a higher pressure (Ju et al., 2023). The CO2 permeability and selectivity dropped from 650.7 Barrer/40.7 to 617.1 Barrer/38.3 as the feed gas pressure increased from 1 bar to 2 bar. N2 molecules primarily transport within the membrane through a solution-diffusion mechanism in the matrix (Wang et al., 2020). However, as the pressure increases, some N2 molecules can also permeate through the COF particle fillers under high pressure, affecting the permeation process of CO2 molecules and thereby reducing the separation performance. Although the separation performance for mixed gases decreased due to this competition between CO2 and N2 molecules, the COF-300-Amide/Pebax2533 also exhibited an excellent performance.
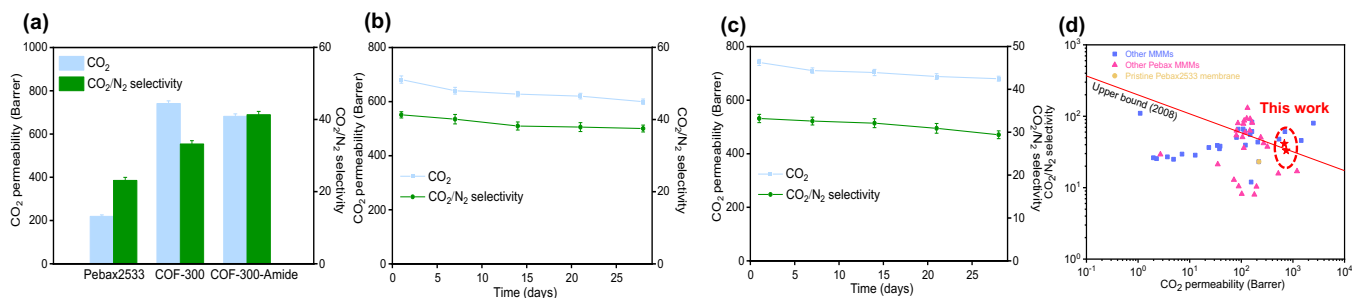

Figure 6: (a) Separation performances of Pebax2533, COF-300 /Pebax2533 and COF-300-Amide/Pebax2533: (b) the stability of COF-300-Amide/Pebax2533 in 28 days; (c) the stability of COF-300/Pebax2533 in 28 days; (d) comparison of the permeability performance between this work and other reported membranes

4. CONCLUSION

We have demonstrated highly crystalline amide-linked COFs as fillers combined with Pebax2533 as a polymer matrix to enhance the separation performance of MMMs for CO_2. The amide groups from COF-300-Amide contribute to a strong interaction with the polymer matrix via hydrogen bonds at the interface resulting in defect-free MMMs. In addition, the narrower pore size of COF-300-Amide crystallites in the membrane promoted the specific transport of gas molecules, thus leading to an increase of CO_2/N_2 selectivity through the adsorption-diffusion mechanism. Meanwhile, the ether oxygen bond and amide group, as CO_2-philic groups, promote CO_2 transport and strengthen the facilitated transport mechanism. As a result, we believe that the novel stable and irreversible COFs could offer a promising solution for enhancing the interfacial compatibility of MMMs, and the theoretical analysis based on molecular simulation shed light on the rational design of high-performance MMMs for gas separation.

5. REFERENCES

Beerdsen, E., Smit, B. & Dubbeldam, D. (2004) 'Molecular Simulation of Loading Dependent Slow Diffusion in Confined Systems',

Physical Review Letters, 93(24), pp.248301. Available at https://link.aps.org/doi/10.1103/PhysRevLett.93.248301.

Chen, Q.-Y., Yang, L., Liu, L., Li, X.-X., Li, H.-D., Zhang, Q. & Cao, D.-J. (2022a) 'XPS and NMR analyze the combined forms of Pb in Cladophora rupestris subcells and its detoxification', Environmental Science and Pollution Research, 29(38), pp.57490-57501. Available at https://doi.org/10.1007/s11356-022-19880-x.

Chen, S., Zhao, D., Feng, Y., Liu, H., Li, S., Qiu, Y. & Ren, J. (2022b) 'The preparation and characterization of gel-mixed matrix membranes (g-MMMs) with high CO2 permeability and stability performance', Journal of Membrane Science, 652, pp.120471. Available at https://www.sciencedirect.com/science/article/pii/S0376738822002186.

Clarizia, G., Tasselli, F., Simari, C., Nicotera, I. & Bernardo, P. (2019) 'Solution Casting Blending: An Effective Way for Tailoring Gas Transport and Mechanical Properties of Poly(vinyl butyral) and Pebax2533', The Journal of Physical Chemistry C, 123(17), pp.11264-11272. Available at https://doi.org/10.1021/acs.jpcc.9b01459.

Dai, G., Zhang, Q., Xiong, S., Deng, L., Gao, Z., Chen, A., Li, X., Pan, C., Tang, J. & Yu, G. (2023) 'Building interfacial compatible PIM-1-based mixed-matrix membranes with β-ketoenamine-linked COF fillers for effective CO2/N2 separation', Journal of Membrane Science, 676, pp.121561. Available at https://www.sciencedirect.com/science/article/pii/S037673882300217X.

Dai, Z., Deng, J., Peng, K.-J., Liu, Y.-L. & Deng, L. (2019) 'Pebax/PEG Grafted CNT Hybrid Membranes for Enhanced CO2/N2 Separation', Industrial & Engineering Chemistry Research, 58(27), pp.12226-12234. Available at https://doi.org/10.1021/acs.iecr.9b01466.

Das, A., Sarkar, P., Maji, S., Pati, S.K. & Mandal, S.K. (2022) 'Mesoionic N-Heterocyclic Imines as Super Nucleophiles in Catalytic Couplings of Amides with CO2', Angewandte Chemie International Edition, 61(51), pp.e202213614. Available at https://onlinelibrary.wiley.com/doi/abs/10.1002/anie.202213614.

Dubbeldam, D., Calero, S., Ellis, D.E. & Snurr, R.Q. (2016) 'RASPA: molecular simulation software for adsorption and diffusion in flexible nanoporous materials', Molecular Simulation, 42(2), pp.81-101. Available at https://doi.org/10.1080/08927022.2015.1010082.

Ebadi Amooghin, A., Mashhadikhan, S., Sanaeepur, H., Moghadassi, A., Matsuura, T. & Ramakrishna, S. (2019) 'Substantial breakthroughs on function-led design of advanced materials used in mixed matrix membranes (MMMs): A new horizon for efficient CO2 separation', Progress in Materials Science, 102, pp.222-295. Available at https://www.sciencedirect.com/science/article/pii/S0079642518301075.

Fam, W., Mansouri, J., Li, H. & Chen, V. (2017) 'Improving CO2 separation performance of thin film composite hollow fiber with Pebax®1657/ionic liquid gel membranes', Journal of Membrane Science, 537, pp.54-68. Available at https://www.sciencedirect.com/science/article/pii/S0376738817303824.

Frost, H., Düren, T. & Snurr, R.Q. (2006) 'Effects of Surface Area, Free Volume, and Heat of Adsorption on Hydrogen Uptake in Metal−Organic Frameworks', The Journal of Physical Chemistry B, 110(19), pp.9565-9570. Available at https://doi.org/10.1021/jp060433+.

Fu, J., Das, S., Xing, G., Ben, T., Valtchev, V. & Qiu, S. (2016) 'Fabrication of COF-MOF Composite Membranes and Their Highly Selective Separation of H2/CO2', Journal of the American Chemical Society, 138(24), pp.7673-7680. Available at https://doi.org/10.1021/jacs.6b03348.

Fusalba, F. & Bélanger, D. (1999) 'Electropolymerization of Polypyrrole and Polyaniline−Polypyrrole from Organic Acidic Medium',

The Journal of Physical Chemistry B, 103(42), pp.9044-9054. Available at https://doi.org/10.1021/jp9916790.

Ghasemi Estahbanati, E., Omidkhah, M. & Ebadi Amooghin, A. (2017a) 'Interfacial Design of Ternary Mixed Matrix Membranes

Containing Pebax 1657/Silver-Nanopowder/[BMIM][BF4] for Improved CO2 Separation Performance', ACS Applied Materials & Interfaces, 9(11), pp.10094-10105. Available at https://doi.org/10.1021/acsami.6b16539.

Ghasemi Estahbanati, E., Omidkhah, M. & Ebadi Amooghin, A. (2017b) 'Preparation and characterization of novel Ionic liquid/Pebax membranes for efficient CO2/light gases separation', Journal of Industrial and Engineering Chemistry, 51, pp.77-89. Available at https://www.sciencedirect.com/science/article/pii/S1226086X17300904.

Guo, A., Ban, Y., Yang, K., Zhou, Y., Cao, N., Zhao, M. & Yang, W. (2020) 'Molecular sieving mixed matrix membranes embodying nano-fillers with extremely narrow pore-openings', Journal of Membrane Science, 601, pp.117880. Available at https://www.sciencedirect.com/science/article/pii/S0376738820301265.

Guo, Z., Wu, H., Chen, Y., Zhu, S., Jiang, H., Song, S., Ren, Y., Wang, Y., Liang, X., He, G., Li, Y. & Jiang, Z. (2022) 'Missing-linker Defects in Covalent Organic Framework Membranes for Efficient CO2 Separation', Angewandte Chemie International Edition, 61(41), pp.e202210466. Available at https://onlinelibrary.wiley.com/doi/abs/10.1002/anie.202210466.

Hao, M., Xie, Y., Lei, M., Liu, X., Chen, Z., Yang, H., Waterhouse, G.I.N., Ma, S. & Wang, X. (2023) 'Pore Space Partition Synthetic Strategy in Imine-linked Multivariate Covalent Organic Frameworks', Journal of the American Chemical Society. Available at https://doi.org/10.1021/jacs.3c08160.

Hepburn, C., Adlen, E., Beddington, J., Carter, E.A., Fuss, S., Mac Dowell, N., Minx, J.C., Smith, P. & Williams, C.K. (2019) 'The technological and economic prospects for CO2 utilization and removal', Nature, 575(7781), pp.87-97. Available at https://doi.org/10.1038/s41586-019-1681-6.

Imtiaz, A., Othman, M.H.D., Jilani, A., Khan, I.U., Kamaludin, R. & Samuel, O. (2022) 'ZIF-filler incorporated mixed matrix membranes (MMMs) for efficient gas separation: A review', Journal of Environmental Chemical Engineering, 10(6), pp.108541. Available at https://www.sciencedirect.com/science/article/pii/S2213343722014142.

Ju, X., Yang, Z., Wang, J., Cui, B., Xin, Y., Zheng, Y. & Wang, D. (2023) 'Converting Nanoflower-like Layered Double Hydroxides into Solvent-Free Nanofluids for CO2 Capture', ACS Applied Materials & Interfaces, 15(48), pp.56181-56191. Available at https://doi.org/10.1021/acsami.3c13000.

Kang, C., Zhang, Z., Usadi, A.K., Calabro, D.C., Baugh, L.S., Chai, K., Wang, Y. & Zhao, D. (2022) 'Tunable Interlayer Shifting in Two-Dimensional Covalent Organic Frameworks Triggered by CO2 Sorption', Journal of the American Chemical Society, 144(44), pp.20363-20371. Available at https://doi.org/10.1021/jacs.2c08214.

Krishna, R. (2012) 'Diffusion in porous crystalline materials', Chemical Society Reviews, 41(8), pp.3099-3118. Available at http://dx.doi.org/10.1039/C2CS15284C.

Kühne, T.D., Iannuzzi, M., Ben, M.D., Rybkin, V.V., Seewald, P., Stein, F., Laino, T., Khaliullin, R.Z., Schütt, O., Schiffmann, F., Golze, D., Wilhelm, J., Chulkov, S., Bani-Hashemian, M.H., Weber, V., Borštnik, U., Taillefumier, M., Jakobovits, A.S., Lazzaro, A., Pabst, H., Müller, T., Schade, R., Guidon, M., Andermatt, S., Holmberg, N., Schenter, G.K., Hehn, A., Bussy, A., Belleflamme, F., Tabacchi, G., Glöß, A., Lass, M., Bethune, I., Mundy, C.J., Plessl, C., Watkins, M., Vandevondele, J., Krack, M. & Hutter, J. (2020) 'CP2K: An electronic structure and molecular dynamics software package - Quickstep: Efficient and accurate electronic structure calculations', The Journal of Chemical Physics, 152(19), pp.194103. Available at https://aip.scitation.org/doi/abs/10.1063/5.0007045.

Li, B.-Y., Liu, J.-X., He, X.-T., Mao, S., Tao, W.-Q., Li, Z. & Hong, Y.-X. (2023a) 'Polyaniline-grafted Cu-MOFs via coordination-driven strategy constructs facilitated transport hybrid membrane for CO2 separation', Separation and Purification Technology, 323, pp.124486. Available at https://www.sciencedirect.com/science/article/pii/S1383586623013941.

Li, B., Liu, J., He, X., Wang, R., Tao, W. & Li, Z. (2023b) 'Covalent "Bridge-crosslinking" strategy constructs facilitated transport mixed matrix membranes for highly-efficient CO2 separation', Journal of Membrane Science, 680, pp.121755. Available at https://www.sciencedirect.com/science/article/pii/S0376738823004118.

Li, Y., Zhou, Z., Hong, Y., Dong, X., Yang, Y., Liang, Z., Sun, J., Chen, X., Liu, W. & Zheng, Z. (2023c) 'Synthesis of a Highly Crystalline Amide-Linked Covalent Organic Framework', Chinese Journal of Chemistry, 41(4), pp.405-410. Available at https://onlinelibrary.wiley.com/doi/abs/10.1002/cjoc.202200563.

Liu, J., Zhang, S., Jiang, D.-E., Doherty, C.M., Hill, A.J., Cheng, C., Park, H.B. & Lin, H. (2019a) 'Highly Polar but Amorphous Polymers with Robust Membrane CO2/N2 Separation Performance', Joule, 3(8), pp.1881-1894. Available at https://www.sciencedirect.com/science/article/pii/S2542435119303198.

Liu, R., Meng, S., Ma, Y., Niu, L., He, S., Xu, X., Su, B., Lu, D., Yang, Z. & Lei, Z. (2019b) 'Atmospherical oxidative coupling of amines by UiO-66-NH2 photocatalysis under milder reaction conditions', Catalysis Communications, 124, pp.108-112. Available at https://www.sciencedirect.com/science/article/pii/S1566736719300809.

Liu, X., Li, B., Liu, J., He, X., Liu, H., Mao, S., Tao, W. & Li, Z. (2024) 'How polymer infiltration affects metal-organic frameworks-based facilitated hybrid membrane performances for CO2 separation', Journal of Membrane Science, 690, pp.122219. Available at https://www.sciencedirect.com/science/article/pii/S037673882300875X.

Meshkat, S., Kaliaguine, S. & Rodrigue, D. (2019) 'Enhancing CO2 separation performance of Pebax® MH-1657 with aromatic carboxylic acids', Separation and Purification Technology, 212, pp.901-912. Available at https://www.sciencedirect.com/science/article/pii/S1383586618329691.

Nafisi, V. & Hägg, M.-B. (2014) 'Development of dual layer of ZIF-8/PEBAX-253 3 mixed matrix membrane for CO2 capture', Journal of Membrane Science, 459, pp.244-255. Available at https://www.sciencedirect.com/science/article/pii/S0376738814000994.

Plimpton, S. (1995) 'Fast Parallel Algorithms for Short-Range Molecular Dynamics', Journal of Computational Physics, 117(1), pp.1-

19. Available at https://www.sciencedirect.com/science/article/pii/S002199918571039X.

Qian, Q., Asinger, P.A., Lee, M.J., Han, G., Mizrahi Rodriguez, K., Lin, S., Benedetti, F.M., Wu, A.X., Chi, W.S. & Smith, Z.P. (2020) 'MOF-Based Membranes for Gas Separations', Chem Rev, 120(16), pp.8161-8266. Available at https://www.ncbi.nlm.nih.gov/pubmed/32608973.

Qiao, Z., Zhao, S., Sheng, M., Wang, J., Wang, S., Wang, Z., Zhong, C. & Guiver, M.D. (2019) 'Metal-induced ordered microporous polymers for fabricating large-area gas separation membranes', Nature Materials, 18(2), pp.163-168. Available at https://doi.org/10.1038/s41563-018-0221-3.

Sanaeepur, H., Ahmadi, R., Sinaei, M. & Kargari, A. (2019) 'Pebax-Modified Cellulose Acetate Membrane for CO2/N2 Separation', Journal of Membrane Science and Research, 5(1), pp.25-32. Available at https://www.msrjournal.com/article_32062_79b8287570dcc5b8b69879938f33a15f.pdf.

Sanaeepur, H., Kargari, A., Nasernejad, B., Ebadi Amooghin, A. & Omidkhah, M. (2016) 'A novel Co2+ exchanged zeolite Y/cellulose acetate mixed matrix membrane for CO2/N2 separation', Journal of the Taiwan Institute of Chemical Engineers, 60, pp.403-413. Available at https://www.sciencedirect.com/science/article/pii/S1876107015004836.

Sanaeepur, H., Nasernejad, B. & Kargari, A. (2015) 'Cellulose acetate/nano-porous zeolite mixed matrix membrane for CO2 separation', Greenhouse Gases: Science and Technology, 5(3), pp.291-304. Available at https://onlinelibrary.wiley.com/doi/abs/10.1002/ghg.1478.

Sarkisov, L. & Harrison, A. (2011) 'Computational structure characterisation tools in application to ordered and disordered porous materials', Molecular Simulation, 37(15), pp.1248-1257. Available at https://doi.org/10.1080/08927022.2011.592832.

Seong, M.S., Yu, H.J., Ha, S.Y., Chang, W.S., Kim, H.-J. & Lee, J.S. (2022) 'Poly(poly(ethylene glycol) methyl ether acrylate) micelles for highly CO2 permeable membranes', Journal of Membrane Science, 662, pp.120917. Available at https://www.sciencedirect.com/science/article/pii/S0376738822006627.

Tahir, Z., Aslam, M., Gilani, M.A., Bilad, M.R., Anjum, M.W., Zhu, L.-P. & Khan, A.L. (2019) 'SO3H functionalized UiO-66 nanocrystals in Polysulfone based mixed matrix membranes: Synthesis and application for efficient CO2 capture', Separation and Purification Technology, 224, pp.524-533. Available at https://www.sciencedirect.com/science/article/pii/S1383586619311608.

Waller, P.J., Gándara, F. & Yaghi, O.M. (2015) 'Chemistry of Covalent Organic Frameworks', Accounts of Chemical Research,

48(12), pp.3053-3063. Available at https://doi.org/10.1021/acs.accounts.5b00369.

Wang, P., Peng, Y., Zhu, C., Yao, R., Song, H., Kun, L. & Yang, W. (2021) 'Single-Phase Covalent Organic Framework Staggered Stacking Nanosheet Membrane for CO2-Selective Separation', Angewandte Chemie International Edition, 60(35), pp.19047-19052. Available at https://onlinelibrary.wiley.com/doi/abs/10.1002/anie.202106346.

Wang, S., Liu, Y., Huang, S., Wu, H., Li, Y., Tian, Z. & Jiang, Z. (2014) 'Pebax–PEG–MWCNT hybrid membranes with enhanced CO2 capture properties', Journal of Membrane Science, 460, pp.62-70. Available at https://www.sciencedirect.com/science/article/pii/S0376738814001604.

Wang, S., Yang, Y., Liang, X., Ren, Y., Ma, H., Zhu, Z., Wang, J., Zeng, S., Song, S., Wang, X., Han, Y., He, G. & Jiang, Z. (2023) 'Ultrathin ionic COF Membrane via Polyelectrolyte-Mediated Assembly for Efficient CO2 Separation', Advanced Functional Materials, 33(24), pp.2300386. Available at https://onlinelibrary.wiley.com/doi/abs/10.1002/adfm.202300386.

Wang, Y., Li, L., Zhang, X., Li, J., Wang, J. & Li, N. (2020) 'Polyvinylamine/amorphous metakaolin mixed-matrix composite membranes with facilitated transport carriers for highly efficient CO2/N2 separation', Journal of Membrane Science, 599, pp.117828. Available at https://www.sciencedirect.com/science/article/pii/S0376738819333022.

Willems, T.F., Rycroft, C.H., Kazi, M., Meza, J.C. & Haranczyk, M. (2012) 'Algorithms and tools for high-throughput geometry-based analysis of crystalline porous materials', Microporous and Mesoporous Materials, 149(1), pp.134-141. Available at https://www.sciencedirect.com/science/article/pii/S1387181111003738.

Wolińska-Grabczyk, A., Kubica, P., Jankowski, A., Wójtowicz, M., Kansy, J. & Wojtyniak, M. (2017) 'Gas and water vapor transport properties of mixed matrix membranes containing 13X zeolite', Journal of Membrane Science, 526, pp.334-347. Available at https://www.sciencedirect.com/science/article/pii/S037673881631064X.

Wu, Y., Zhao, D., Chen, S., Ren, J., Hua, K., Li, H. & Deng, M. (2021) 'The effect of structure change from polymeric membrane to gel membrane on CO2 separation performance', Separation and Purification Technology, 261, pp.118243. Available at https://www.sciencedirect.com/science/article/pii/S1383586620327155.

Ying, Y., Yang, Z., Shi, D., Peh, S.B., Wang, Y., Yu, X., Yang, H., Chai, K. & Zhao, D. (2021) 'Ultrathin covalent organic framework film as membrane gutter layer for high-permeance CO2 capture', Journal of Membrane Science, 632, pp.119384. Available at https://www.sciencedirect.com/science/article/pii/S037673882100332X.

Zhao, D., Ren, J., Wang, Y., Qiu, Y., Li, H., Hua, K., Li, X., Ji, J. & Deng, M. (2017) 'High CO2 separation performance of Pebax®/CNTs/GTA mixed matrix membranes', Journal of Membrane Science, 521, pp.104-113. Available at https://www.sciencedirect.com/science/article/pii/S0376738816314478.

Zhu, B., He, S., Wu, Y., Li, S. & Shao, L. (2023) 'One-Step Synthesis of Structurally Stable CO2-Philic Membranes with Ultra-High PEO Loading for Enhanced Carbon Capture', Engineering, 26, pp.220-228. Available at https://www.sciencedirect.com/science/article/pii/S2095809922002892.

#203: Enhanced air-cooling battery module in combination with heat pipes embedded in heat spreader

Jiansheng Zhang[1], Jinghe Shi[2], Xiaobin Xu[3], Wenlin Yuan[4], Peng Shi[5], Hengyun Zhang[6*]

[1] Shanghai University of Engineering Science, Shanghai, China 201620, 1573391039@qq.com
[2] Shanghai University of Engineering Science, Shanghai, China 201620, 1433625514@qq.com
[3] Nanjing University of Aeronautics and Astronautics, Nanjing, China 210016, 1016149312@qq.com
[4] Shanghai University of Engineering Science, Shanghai, China 201620, 1874693225@qq.com
[5] Shanghai University of Engineering Science, Shanghai, China 201620, 2322583226 @qq.com
[6*] Shanghai University of Engineering Science, Shanghai, China 201620, zhanghengyun@sues.edu.cn

Abstract: In this paper, a battery module coupling heat pipes and air-cooling for cylindrical battery is proposed, with heat pipes embedded in a heat spreader plate to efficiently transfer the heat to the external environment. The thermal performance of the battery module was studied both numerically and experimentally. To evaluate the thermal behavior of the battery module under different discharge rates and air velocities, detailed temperature distributions were obtained through numerical simulations. The results indicate that the maximum temperature and temperature difference of the batteries increase with the discharge rates from 1C to 3C and decrease with the air velocity from 1m/s to 2m/s, all within 40 °C and 5 °C, respectively, meeting the design requirements. An experimental test setup for the battery module was established, and the test results were compared with the simulation results. Under discharge rates from 1C to 3C, the average relative errors between simulation and experiment were 0.60%, 1.10%, and 3. 39%, respectively, indicating high accuracy of the simulation model. Comparative studies were conducted on the temperature characteristics of battery modules with and without heat pipes. The results show that the maximum temperature and maximum temperature difference of the battery module with the presence of heat pipes decreased by 4.92% and 19.41%, respectively, demonstrating the significant role of heat pipes in the thermal management of the batteries. The present study could offer new insights into thermal enhancement with air-cooling for automotive battery packs.

Keywords: Cylindrical Lithium-Ion Battery, Battery Thermal Management System, Heat Pipe, Experimental Study

1. INTRODUCTION

Lithium-ion batteries (LIBs) have become the primary energy source for electric vehicles due to their high-power density, long lifespan, and low self-discharge rate. However, the heat generated during battery operation may cause temperatures to exceed 50 °C, leading to capacity degradation, shortened lifespan, and even thermal runaway incidents resulting in fires and explosions (Feng et al, 2020). A well-designed battery thermal management system (BTMS) can maintain the battery within the appropriate temperature range, enhancing safety and prolonging lifespan (Guo et al, 2023). The BTMS aims to keep the battery operating within the optimal temperature range, typically between 25 °C and 40 °C with a temperature difference of less than 5 °C (Zhang et al, 2024). Various cooling media are utilized in BTMS, including air, liquid, phase change material, heat pipe, and so on. While air cooling and liquid cooling are widely adopted, their combination with other cooling techniques such as heat pipes is one of the important research directions in thermal management systems.

As highly efficient two-phase heat transfer devices, heat pipes are capable of transferring heat from one system to another efficiently at small temperature gradients. In coupling with other cooling methods at the condensation section, heat pipes can transfer h eat from the battery to the ambient over long distances, thereby enhancing the flexibility and reliability of the cooling system l ayout (Bernagozzi et al, 2023; Wang et al. 2023) Wu et al. (2017) arranged the evaporation section of flat heat pipes with phase change materials inside prismatic battery modules and cooled the condensation section of the heat pipe through forced convection. Wang et al. (2024) proposed a heat pipe composite fin cooling structure for prismatic battery modules, which includes flat heat pipes, phase change materials, liquid cooling plates, and aluminum fins. At an ambient temperature of 30 °C and a discharge rate of 2C, th e maximum temperature and maximum temperature difference of the battery module are kept within 45.9 °C and 2 °C, respectively. Xie et al. (2022) flattened the evaporation section of tubular heat pipes in aluminum plates to study the cooling effect of embedded heat pipes on pouch battery modules. He et al. (2022) designed a thermal management system for 18650 cylindrical batteries coupling tubular heat pipes with liquid cooling, using aluminum plates as the heat transfer elements between the battery and the heat pipe. The results show that the contact angle between the aluminum plate and the battery is increased to 75°, the maximum temperature and maximum temperature difference of the battery module are decreased to 37.58 °C and 3.67 °C, respectively. Jianget al. (2024) cooled 18650 cylindrical battery modules using a composite structure of tubular heat pipes/spray, and embedded arc- shaped copper pieces in the evaporation section of the heat pipe to increase the contact area between the heat pipe and the battery. Behi et al. (2020) proposed a design using L-shaped flat heat pipes and fins to cool 18650 battery modules. In general, there remain challenges such as difficulty in integrating heat pipes with cylindrical batteries, low grouping efficiency, and low utilization of heat pipes.

To address the above issues, a battery module with heat pipes embedded in a heat spreader plate is proposed to evaluate the thermal performance. For the battery module with 5x4 18650 batteries, three heat pipes are embedded in the heat spreader to uniformize the temperature differences across different rows of batteries. The heat pipe coupled air-cooling battery module is simulated numerically under different C-rates and air velocities. Furthermore, an experimental test for the battery module is conducted in comparison with the numerical simulation. Based on the validated numerical model, the effectiveness of the embedded heat pipes was analyzed. The study shows that coupling air cooling with heat pipes can significantly enhance the thermal performance of the battery module.

2. GEOMETRICAL MODEL

A cylindrical battery module coupled with heat pipes and air cooling is proposed, as depicted in Figure 1. The BTMS consists of a battery module consisting of 5x4 LG18650 batteries, a heat spreader plate, heat pipes, and fins. The shaped heat pipes were embedded in the heat spreader plate through brazing to enhance the heat transfer between the heat pipes and the cylindrical surface of the battery, and fins were installed on the condensation section of the heat pipes to enhance the downstream heat dissip ation. The battery terminals were connected in 5P4S by nickel plates, with the spacing of 25 mm in Y direction and 22 mm in X direction. Among them, the length, width, and thickness of the embedded heat spreader plate are 122 mm, 109 mm, and 6 mm, respectively. The diameter of the heat pipe is 4mm, with a thickness of 0.5 mm for each fin, and the distance between the two fins is 7.5 mm.
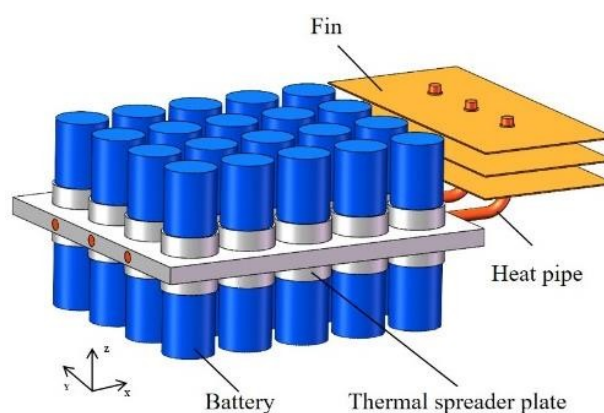

Figure 1: Cylindrical battery module using embedded heat pipe coupled with air-cooling

3. MATERIALS AND METHODS
3.1. Model description

Due to the symmetrical structure of the battery module, half of the model was established using Solidworks software to reduce the time of calculations. The STEP format file of the geometric model was imported into Fluent, and the mesh was generated using poly-hexcore. Since the fin thickness is only 0.5 mm, local refinement was applied to the fins, and boundary conditions were set for the velocity inlet, pressure outlet, adiabatic surface, and symmetry surface sequentially, as shown in Figure 2(a). The parameters of the material properties in the numerical model are listed in Table 1. It is worth noting that in this paper, the transient heat generation rate of 1-3C is programmed as a UDF (User-Defined Function) and imported into Fluent 19.0 software for calculation (Shi, 2024).

Table 1: Physical properties of materials used in BTMS numerical model

	Densities（kg/m3）	Specific heat capacity（J·kg^{-1}·°C^{-1}）	Thermal conductivity（W·m^{-1}·°C $^{-1}$）
Air	1.225	1006	0.0242
Battery	2787	1002	kz= 15.44, kr = 1.045 0
Heat pipe	8978	381	1.753×104 0
Heat spreader plate	2719	871	155
Fin	8978	381	387.6
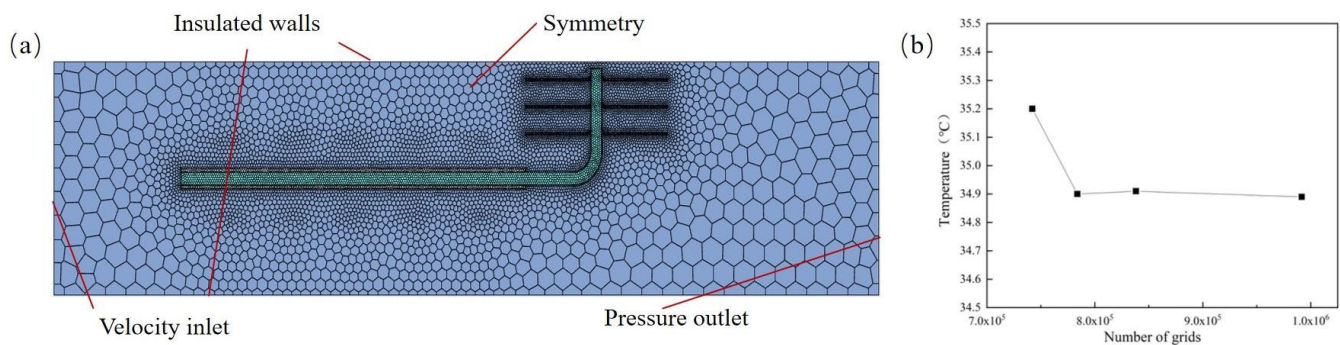
Figure 2: (a) Computational domain of number model; (b) grid independence analysis results

In the air-cooling battery thermal management system proposed in this paper, the Reynolds number of the inlet air is typically greater than 3000, and thus the air flow in the battery thermal management system is turbulent. Therefore, the Reynolds-averaged Navier-Stokes equations are used to calculate the airflow characteristics, and the k-ε turbulence model is applied to compute the turbulent flow field. Using an air velocity of 2 m/s and the maximum temperature during the battery discharge process at 3C as the measurement criteria, as shown in Figure 2(b), when the number of mesh increases from 783,795 to 991,648, the results only differ by 0.03%. To effectively reduce computational time and improve efficiency, the amount of mesh of 991.648 is selected for the simulation model.

3.2. Experimental test method

In this study, experimental validation is conducted on a 5×4 array of 18650 battery model under an ambient temperature of 25 °C. To ensure the workability of the battery module, parameters such as internal resistance, voltage, and capacity of individual batteries need to be consistent. The average internal resistance of 20 individual batteries is 13.98mΩ, with a standard deviation of 1.45%. The discharge capacity is 2500 mAh with standard deviation of 0.64%, and the average voltage at 100% state of charge is 4.176 V with the deviation of 0.02%. To record the actual temperature of the battery module during the experiment, Type K thermocouples (ETA-G-K-30) with an error less than 0.2 °C were used to monitor temperature changes. To avoid electrical connections to the battery module, the thermocouples were fixed on the surface 2 mm away from the positive electrode by soldering, as shown in Figure 3.

Figure 3 depicts the experimental test platform of the air-cooling battery module in combination with heat pipes, including fan (DELTA-PEC1212DE), DC power supply (GPD-2303S), battery charger (NEWRARE-60V100A-H), temperature data acquisition device (HIOKI-LR8410R), anemometer and so on. The battery module was connected to the battery charger for charge and discharge cycles, and the DC power supply was connected to the fan to control the air velocity.
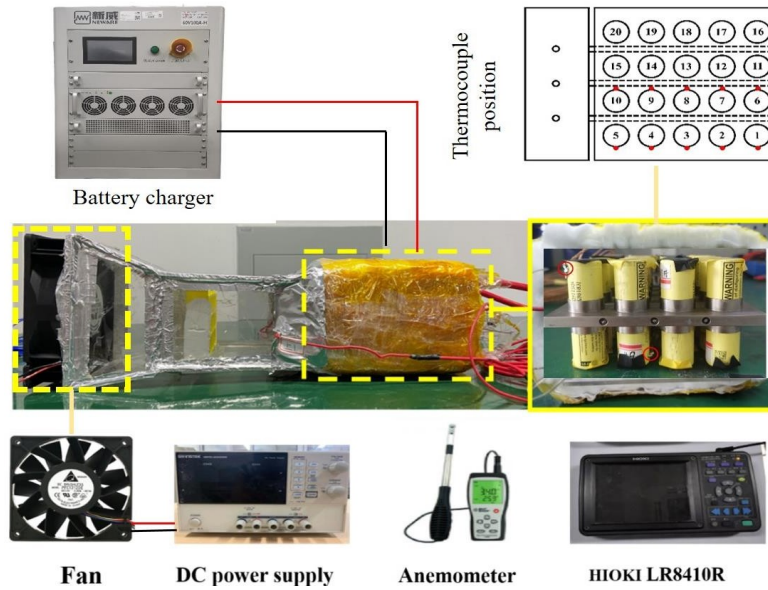
Figure 3: Experimental setup diagram of the air-cooling battery module in combination with heat pipes

To verify the accuracy of the simulation model, the discharge processes of 1C, 2C and 3 C rates were simulated at an ambient temperature of 25 °C and an air velocity of 2 m/s and compared with the maximum temperature of the battery module in the experimental test. The results are shown in Figure 4. The average relative errors between the simulation and experimental results during 1C, 2C, and 3C discharging processes are 0.60%, 1.10%, and 3.39%, respectively, which indicate that the simulation model has a high accuracy. The slight deviation between simulation and experiment is on the one hand caused by the contact thermal resistance of different contact surfaces in the system. On the other hand, neglecting the phase change heat transfer of the heat pipe may also contribute to the error.
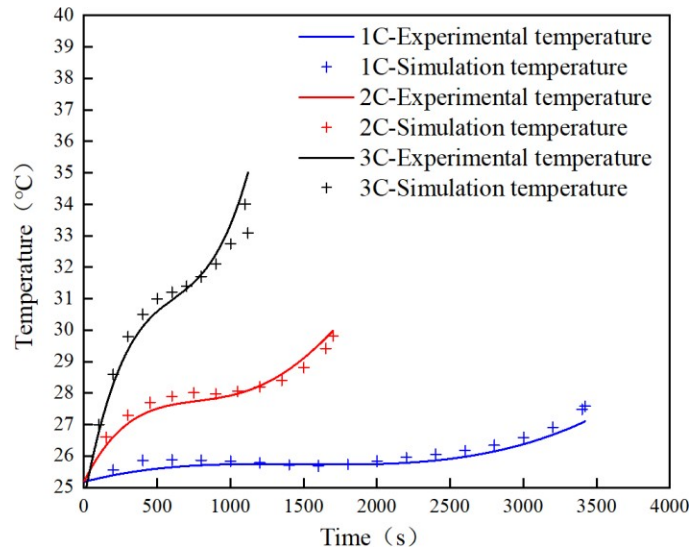
Figure 4: Comparison of experimental temperature and simulation results for No.10 battery

4. RESULTS AND DISCUSSION
4.1. Forced-air cooling performance

Figure 5 shows the temperature characteristics of Battery No. 10 varying with discharge rates and air velocities. Due to the heating effect of the air along the flow distance, the maximum temperature of the battery module occurs in battery No. 10 and the minimum temperature occurs in battery No. 1, and the maximum temperature difference of the module is the difference between battery No. 10 and battery No. 1. The variation of the maximum temperature of the battery module with time is investigated under different ai r velocity and discharge rates, as shown in Figure 5 (a-c). The battery temperature rises rapidly at the beginning of discharge, because the heat generated by the battery at the beginning of discharge is much greater than the heat taken away by the air cooling and the heat pipe, and at this time, the heat pipe has not been fully activated. After the heat pipe starts working, the battery temp erature remains stable, which indicates that the balance between the heat generated by the battery and the heat dissipated by the heat pipes has been reached. At the end of discharge, the temperature again increases rapidly while the voltage drops rapidly. At this stage, the resistance of lithium ions to intercalate the cathode electrode material rises rapidly, causing a significant increase in the internal polarization resistance of the battery, leading to a sharp increase in heat generation.
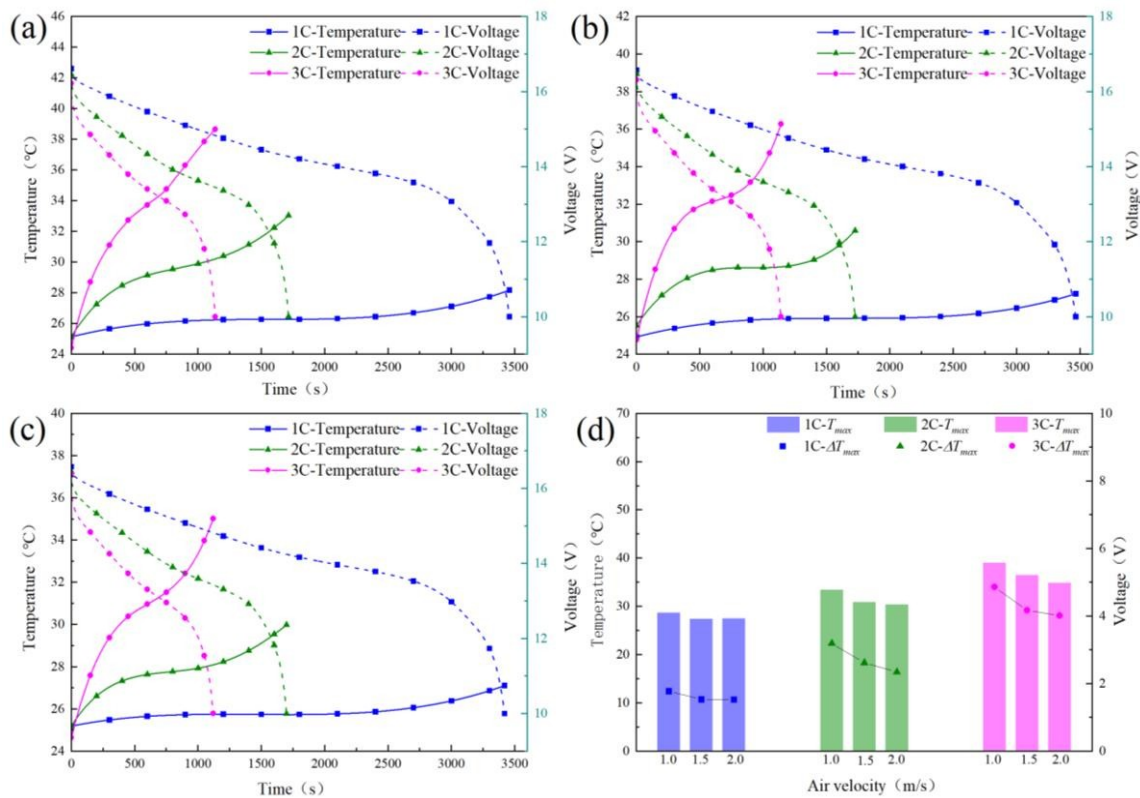
Figure 5: Measured Temperature characteristics of #10 cells under forced convection conditions:（a）1.0 m/s；（b）1.5 m/s；（c）2.0 m/s；(d) the maximum temperature and temperature difference of the battery module

The maximum temperature (Tmax) and the maximum temperature difference (ΔTmax) of the battery module under different air velocities are shown in Figure 5 (d). The maximum temperatures of the battery module under forced convection (air velocity: 1.5 m/s) are 27.4 °C, 30.83 °C, and 36.49 °C for discharge rates of 1-3C, and the maximum temperature of the battery module decreases with the increase of air velocity. However, under the condition of low discharge rate of 1C, the maximum temperature isalmost unchanged when the air velocity is increased from 1.5 m/s to 2.0 m/s. This is because the air is saturated with convec tive heat transfer.

The maximum temperature difference of the battery module also decreases with the increase of air velocity, and the decrease is more obvious at the high discharge rate of 3C. Under the discharge rate from 1C to 3C, the maximum temperature difference of the battery module under forced convection (air velocity: 1.5 m/s) are 1.53°C, 2.61°C, and 4.17°C, and the maximum temperature difference is all kept less than 5 °C.
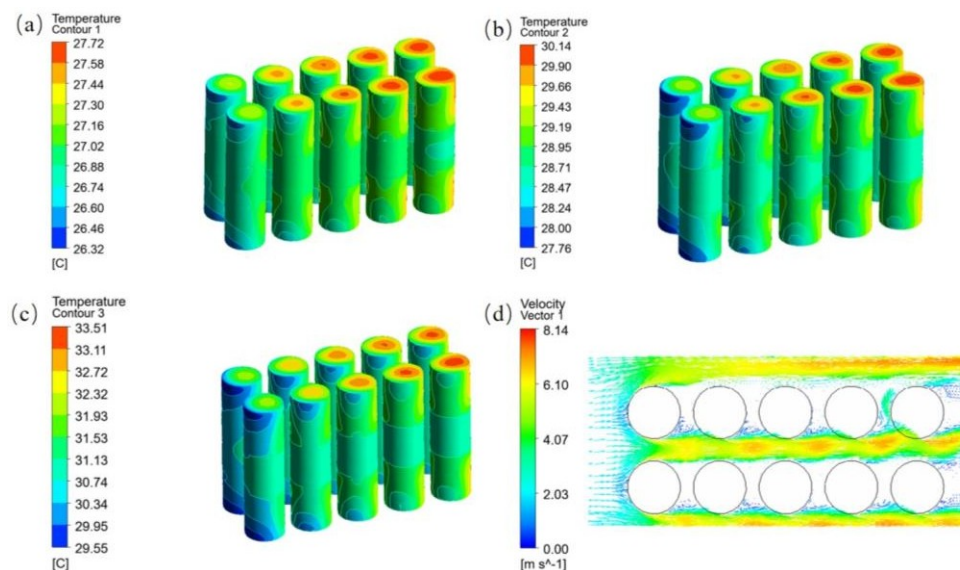
Figure 6: The body temperature nephogram of the battery module at an air velocity of 2 m/s:(a）1C；(b）2C；(c）3C；(d) the velocity field at the 3/4 battery height

Figure 6 shows the battery body temperature nephogram and velocity field at the 3/4 height of the battery module at an air velocity of 2 m/s and discharge rates of 1C to 3C. The maximum temperature and maximum temperature difference of the battery module at discharge rates of 1C to 3C are 27.72°C, 30.14°C, 33.51°C and 1.4°C, 2.38°C, 3.96°C, respectively. It is found that even at a high discharge rate of 3C, the BTMS proposed in this paper can keep the maximum temperature and maximum temperaturedifference of the battery module within 35°C and 4°C, respectively, at an air velocity of 2 m/s.

4.2. Effect of the heat pipe

To investigate the effect of heat pipes on the temperature distribution of the battery module, the case with embedded heat spreader plate and heat pipe and the case with embedded heat spreader plate but without heat pipe are compared. Under the condition of ambient temperature of 25 °C and air velocity of 2 m/s, the temperature nephogram of the battery module during 3C discharge are shown in Figure 7. In comparison, the maximum temperature and maximum temperature difference of the battery module with heat pipe are reduced by 4.92% and 19.41%, respectively. The comparative results show that heat pipes play an important role in the heat dissipation of the battery module, which helps to reduce the temperature inconsistency of the battery module and improve the cycle life of the battery.
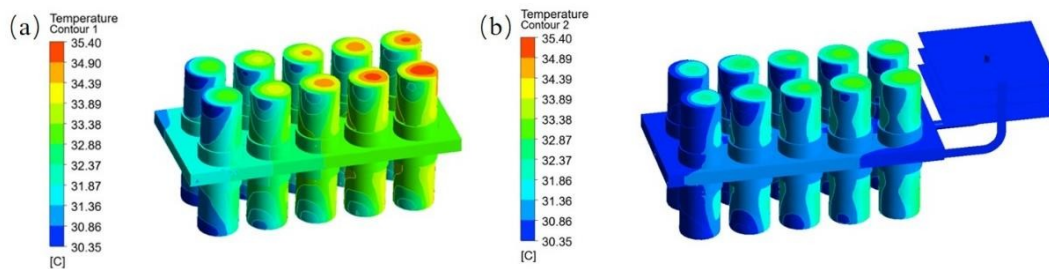
Figure 7: Battery module temperature nephogram at 3C: (a) embedded heat spreader without heat pipe; (b) embedded heat spreader with heat pipe

5. CONCLUSION

The present study proposes enhanced air-cooling battery modules in combination with heat pipes embedded in heat spreader to leverage both the high thermal conductivity of the heat pipe and the stable heat dissipation of air cooling, and a simulation model is developed to investigate the performance of the battery module. The major findings are summarized as follows.

(1) A novel battery module based on embedded heat pipe coupled with air cooling is proposed. Under discharge rates ranging from 1C to 3C, the maximum temperature and maximum temperature difference of the battery module are maintained within 40 °C and 5 °C, respectively, thereby significantly enhancing the cooling capabilities of air cooling.

(2) A numerical simulation model of the battery module with heat pipe embedded in a heat spreader plate is established. The simulation results are compared with experimental data, revealing average relative errors of 0.60%, 1.10%, and 3.39% in the maximum temperature for discharge rates of 1-3C, thus indicating the high fidelity of the simulation model.

(3) Compared with the battery module with heat spreader plate but without heat pipe, the maximum temperature and temperature difference of the battery module with heat pipe are reduced by 4.92% and 19.41% respectively, which proves that the heat pipe plays an important role in the battery thermal management process.

6. REFERENCES

Feng X. et al. (2020) 'Mitigating thermal runaway of lithium-ion batteries', Joule, 4(4), pp. 743-770.

Guo Z. et al. (2023) 'Investigation of battery thermal management system with considering effect of battery aging and nanofluids', International Journal of Heat and Mass Transfer, 202, pp. 123685.

Zhang S. et al. (2024) 'Optimizing the air flow pattern to improve the performance of the air-cooling lithium-ion battery pack. Applied Thermal Engineering, 236, pp. 121486.

Bernagozzi M. et al. (2023) 'Heat pipes in battery thermal management systems for electric vehicles: A critical review', Applied Thermal Engineering, 219, pp. 119495.

Wang Y. et al. (2023) 'A coupled model and thermo-electrical performance analysis for flat heat pipe-based battery thermal management system', Applied Thermal Engineering, 233, pp. 121116.

Wu W. et al. (2017) 'Experimental investigation on the thermal performance of heat pipe-assisted phase change material based battery thermal management system', Energy Conversion and Management, 138, pp. 486-492.

Wang J. et al. (2024) 'Thermal management performance and optimization of a novel system combining heat pipe and composite fin for prismatic lithium-ion batteries', Energy Conversion and Management, 302, pp. 118106.

Xie Y. et al. (2022) 'Improving thermal performance of battery at high current rate by using embedded heat pipe system', Journal of

Energy Storage, 46, pp. 103809.

He L. et al. (2022) 'Structure optimization of a heat pipe-cooling battery thermal management system based on fuzzy grey relational analysis', International Journal of Heat and Mass Transfer, 182, pp. 121924.

Jiang Z. et al. (2024) 'Experimental study on 18650 lithium-ion battery-pack cooling system composed of heat pipe and reciprocating air flow with water mist', International Journal of Heat and Mass Transfer, 222, pp. 125171.

Behi H. et al. (2020) 'A new concept of thermal management system in Li-ion battery using air cooling and heat pipe for electric vehicles', Applied Thermal Engineering, 174, pp. 115280.

Shi J. et al. (2024) 'Experimental determination of heat generation rates of lithium -ion batteries by thermal protection method', Science China Technological Sciences.

Yu H. (2023) 'Thermal parameters of cylindrical power batteries: Quasi-steady state heat guarding measurement and thermal management strategies', Applied Thermal Engineering,231, pp. 120959.

Worwood D. (2017) 'A new approach to the internal thermal management of cylindrical battery cells for automotive applications', Journal of Power Source.

#207: Integrated energy planning towards carbon neutrality for university campus in Northern China

Ying LI[1], Yanzhe DOU[2], Baoping XU[3], Jinshan WANG[4]

[1] North China Electric Power University, Beijing, liying@ncepu.edu.cn
[2] North China Electric Power University, Beijing, douyz1@outlook.com
[3] Corresponding author: North China Electric Power University, Beijing, Baoping.Xu@nottingham.ac.uk
[4] North China Electric Power University, Beijing, wjsncepu@163.com

Abstract: Nowadays, the energy consumptions in buildings constitute about one-third of the world's total energy utilization, and this is projected to rise to 40% by 2030. The university campus, with large number of buildings, plays an important role in energy consumption. Therefore, planning an intergrade energy system towards carbon neutrality for the campus has become an urgent issue to be settled. In this study, a general framework of intergrade energy planning for the university campus is proposed by systematically analyzing the dynamic characteristics of energy demand, resources and storage units. Firstly, the energy consumption models for typical classified buildings in the campus are built, and the dynamic energy demand of campus buildings is predicted. Secondly, the application condition of renewable energy in the campus is investigated and the potential of renewable energy is evaluated from the aspects of solar energy, shallow geothermal energy, deep geothermal energy, and sewage source. Finally, to achieve the balance between energy supply and demand sides, both short-term and long-term energy storage technologies for the campus integrated energy system are proposed. The results show that due to the different functions and usage habits of typical buildings, there are obvious complementary characteristics of the daily load distribution between typical buildings, while there is a large fluctuation in the seasonal load distribution. The application of renewable energy such as photovoltaics has an unbalanced problem between supply and demand sides. Therefore, the construction of a green, safe and economical energy storage system is the key approach for the campus to achieve carbon neutrality, which requires a dynamic balance analysis between supply and demand sides.

Keywords: Integrated Energy Planning; Carbon Neutrality; University Campus; Dynamic Supply and Demand Matching; Short-And Long-Term Energy Storage

1. INTRODUCTION

In recent years, the significant increase in global greenhouse gas emissions and environmental pollution has highlighted the importance of integrated energy systems as carriers for energy conservation and emission reduction (A.G. Olabi and Mohammad Ali Abdelkareem, 2022). In 2020, the total energy consumption of buildings in China accounted for 45.5% of the national total energy consumption (Haoju Song, 2018). University campuses with their large number of buildings and diverse building types, have become a significant component of building energy consumption.

Campus integrated energy systems, as a new energy production and consumption system, are characterized by being clean, efficient, and capable of coupling multiple energy sources and accommodating renewable energy (Yongbao Chen et al., 2022). These systems facilitate the integration of various energy sources and the enhancement of renewable energy (Yuwei Wang et al., 2022), which is of great significance for the low-carbon development of the energy industry. Therefore, universities should take the social responsibility of carbon reduction and energy saving by actively building integrated energy systems and creating low-carbon campuses.

This study takes a university campus in North China as an example and conducts analysis from three perspectives: load, source, and storage. The analysis includes modeling and dynamic load analysis of different types of campus buildings, estimation of the campus's renewable energy potential, and analysis of the campus's seasonal and daily energy storage. Furthermore, a low-carbon campus integrated energy system plan is proposed, and the campus's carbon emissions are evaluated, providing insights for the development of low-carbon campuses.

2. OVERVIEW OF CAMPUS BUILDINGS AND DYNAMIC LOAD ANALYSIS
2.1. Overview and modeling of campus buildings

The university currently has 73 existing buildings with a total floor area of 583,148.17m^2. In this study, the campus buildings are classified into teaching buildings, library buildings, dormitory buildings, gymnasium buildings, canteen buildings and laboratory buildings. Among them, teaching buildings account for the largest proportion of the total campus floor area at 64%, followed by dormitory buildings at 27%. Together, these two types of buildings make up 82% of the total campus floor area. Therefore, this study mainly focuses on these two types of buildings, along with library buildings as representatives of other campus buildings, for modeling and comparative analysis.

Based on the construction drawings, the DeST energy consumption simulation software is used to model the existing typical buildings among the three categories: teaching buildings, library buildings and dormitory buildings. The three types of buildings are modelled in turn as shown in Figure 1(a), (b), (c). After establishing the models, thermal parameters such as enclosure materials, thermal resistance, room lighting, equipment, and occupancy schedules are set according to the specific parameters of the buildings.

(a) Teaching building   (b) Library building   (c) Dormitory building
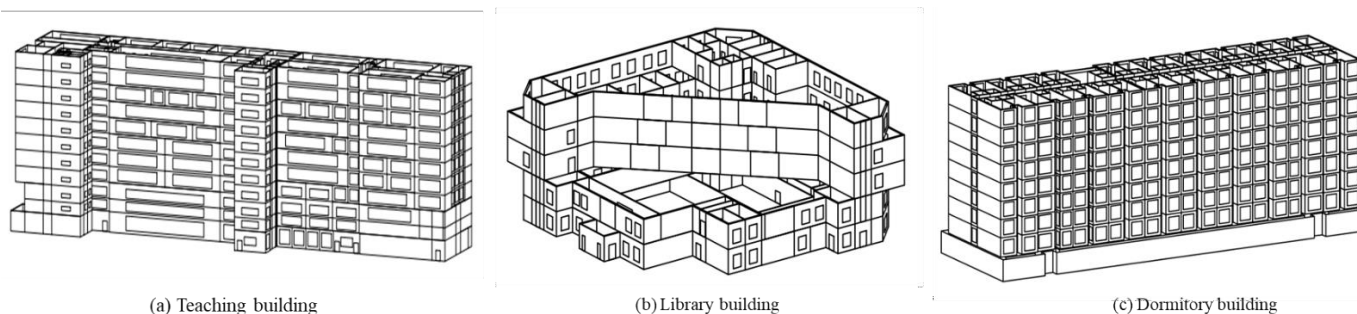
Figure 1: 3D models of typical buildings on campus

2.2. Hourly load of buildings on a typical day

The "hourly peak ratio" is the ratio of the hourly load to the peak load within a day, which effectively reflects the dynamic characteristics of a building's typical daily load. Based on meteorological parameters in Beijing and typical heating and cooling cycles, January 5th is chosen as a typical day for heating, July 4th for cooling, and April 15th for transitional seasons. The hourly peak ratios for heating load, cooling load, and electrical load on these typical days for the three types of buildings are illustrated in Figure 2.
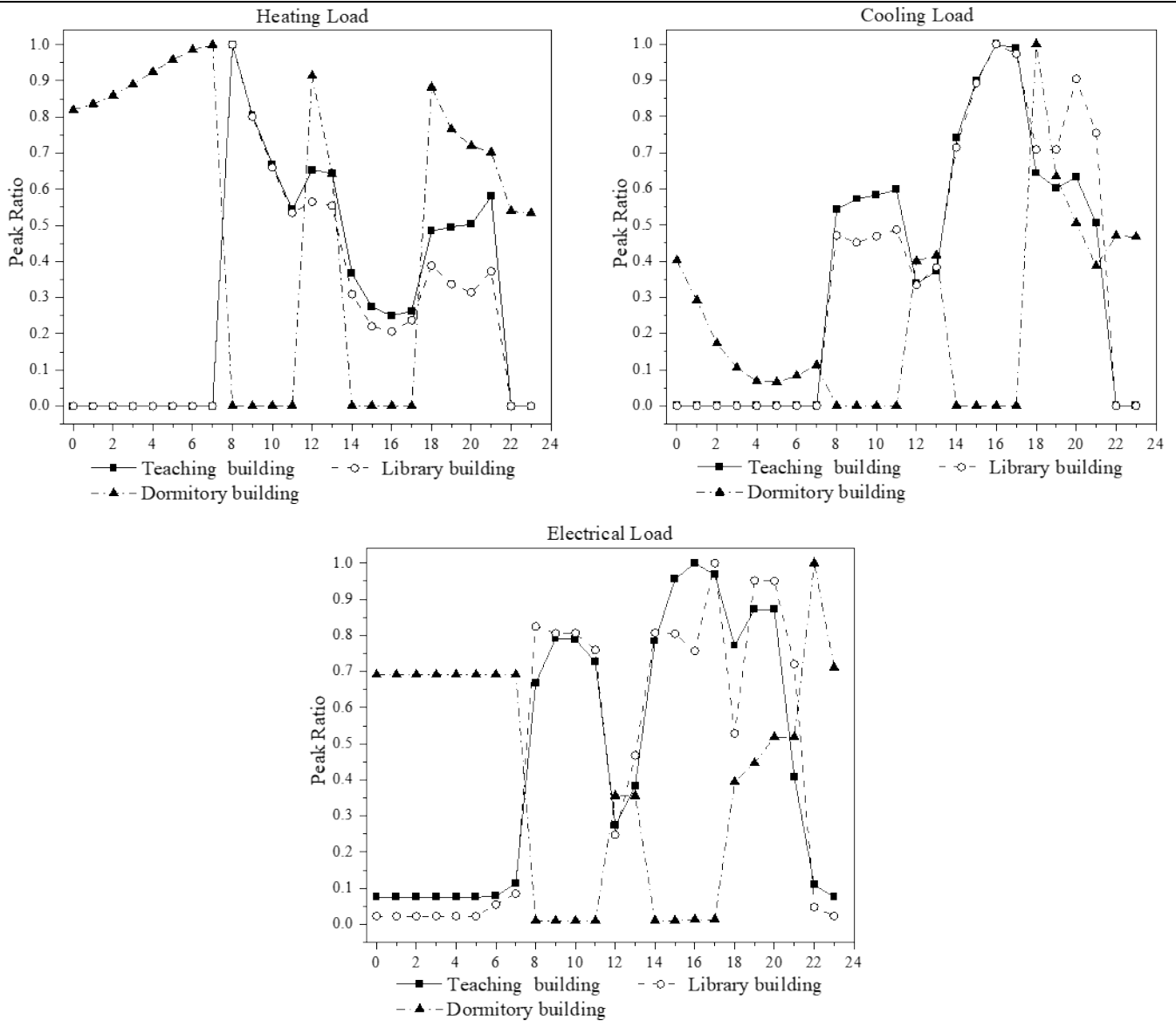
Figure 2: Hourly ratio of heating, cooling, and electrical load for different buildings

As shown in Figure 2, it can be observed that the load variation trends of teaching buildings and library buildings are generally similar, with main usage times from 8:00 to 21:00. On typical heating days, the peak heating load occurs at 8:00 and reaches its trough at 16:00. Initially, as outdoor temperatures rise and teachers and students enter the buildings, the heating load decreases from 8:00 to 11:00. From 11:00 to 13:00, due to the midday break, the number of occupants indoors decreases, resulting in a slight increase in heating load. Subsequently, with a further increase in outdoor temperatures and the start of classes and office work, the heating load decreases further from 13:00 to 16:00, reaching its minimum. Finally, from 16:00 to 21:00, as temperatures drop students finish classes, and the number of occupants in rooms decreases, the heating load increases again. On typical cooling days, the peak cooling load occurs at 16:00, with the trough appearing at 12:00. Similarly influenced by outdoor temperatures and usage patterns, the cooling load follows a pattern of initially increasing, then decreasing, increasing again, and then decreasing, which is similar to the variation in timing and reasons observed for the heating load. On typical days during the transitional seasons without considering heating or cooling, the electrical load primarily consists of lighting and equipment loads. During the main usage times of these two types of buildings, the peak electrical load is influenced by the start of lightning, occurring at 16:00 and 17:00. The trough electrical load is influenced by the midday break and occurs at 12:00.

The usage pattern of dormitory buildings differs from the previous two types of buildings, mainly occurring from 11:00 to 13:00 and from 18:00 to 7:00 the next day. Therefore, the load variation trends in dormitory buildings also differ from those in the previous two types. From 18:00 to 7:00 the next day, influenced by residents returning to their dormitories and using equipment, as well as the decreasing outdoor temperatures, the peak heating load in dormitory buildings occurs at 7:00, with a trough at 23:00. The peak cooling load occurs at 18:00, with a trough at 5:00. The electrical load in dormitory buildings, affected by lighting and residents returning to their dormitories and using equipment, peaks at 22:00, with a trough at 12:00.

In summary, teaching, library, and dormitory buildings exhibit distinct complementary characteristics in their load distribution. Integrating these buildings into a combined energy system can smooth out overall load fluctuations, enhancing the partial load regulation capabilities of the system's units.

2.3. Annual hourly load of buildings
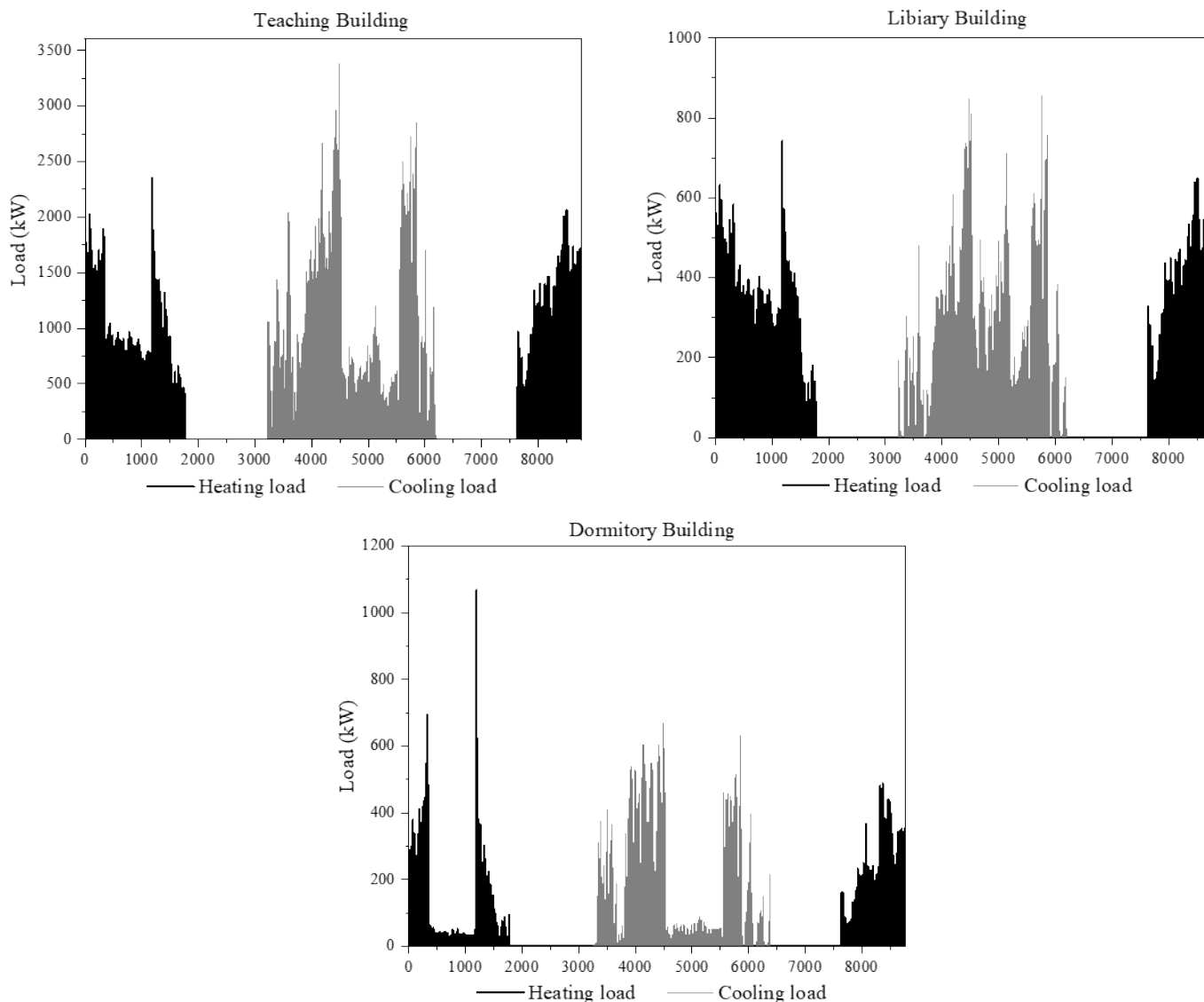
Figure 3: Annual hourly heating and cooling load for different buildings

As shown in Figure 3, the peak heating load for the three typical buildings occurs on 19 February and the peak cooling load occurs on 6 July. During the summer and winter holidays, the cooling and heating loads of the three typical buildings are reduced due to the fact that the students and teachers leave the school. However, the degree of load reduction varies with the holiday usage of the typical building, with the library reducing the least and the dormitory building reducing the most. Also affected by holidays, the electrical load of all three typical buildings decreases during the summer and winter holidays, with the difference in the degree of decrease being similar to the trend of the heating and cooling loads.

2.4. Total load forecasting for campus buildings

Combined with the campus load index, we can use the unit area index method to predict the overall building load in campus. The cooling, heating and electrical loads of the building are shown in Table 1.

Table 2: Indexes and loads of various types of buildings on campus

Type of buildings	Area (m²)	Electrical index (w/m²)	Electrical load (MW)	Heating index (w/m²)	Heating load (MW)	Cooling index (w/m²)	Cooling load (MW)
Teaching	375897	36	13.53	43	16.16	81	30.45
Dormitory	157870	28	4.42	34	5.37	43	6.79
Library	9741	36	0.35	43	0.42	81	0.79
Gymnasiums	44000	35	1.54	75	3.3	106	4.66
Canteens	19734	40	0.47	50	0.99	120	2.37
Labs	7065	42	0.75	34	0.75	60	1.37

250

Towards the goal of a low-carbon campus, this paper utilizes electric heat pumps to provide heat and cooling energy to campus buildings during the heating and cooling seasons. Based on the predicted heating and cooling loads, the electrical load required for the electric heat pumps can be calculated from Equation 1 and Equation 2.

Equation 1: Electrical load for heating. $$L_{he} = L_h/COP_h$$

Where:

- L_{he} = power (kw)
- L_h = building heating load (kw)
- COP_h = coefficient of performance of heat pump operation during the heating period ($\approx$3)

Equation 2: Electrical load for cooling. $$L_{ce} = L_c/COP_c$$

Where:

- L_{ce} = power (kw)
- L_c = building cooling load (kw)
- COP_c = coefficient of performance of heat pump operation during the cooling period ($\approx$5)

Table 2: Electrical load for heating and cooling of all types of buildings in campus

Type of buildings	Electrical load for heating	Electrical load for cooling.
Teaching	5.39	6.09
Dormitory	1.79	1.36
Library	0.14	0.16
Gymnasiums	1.10	0.93
Canteens	0.33	0.47
Labs	0.25	0.27

3. EVALUATION OF RENEWABLE ENERGY POTENTIAL IN CAMPUS
3.1. Solar energy
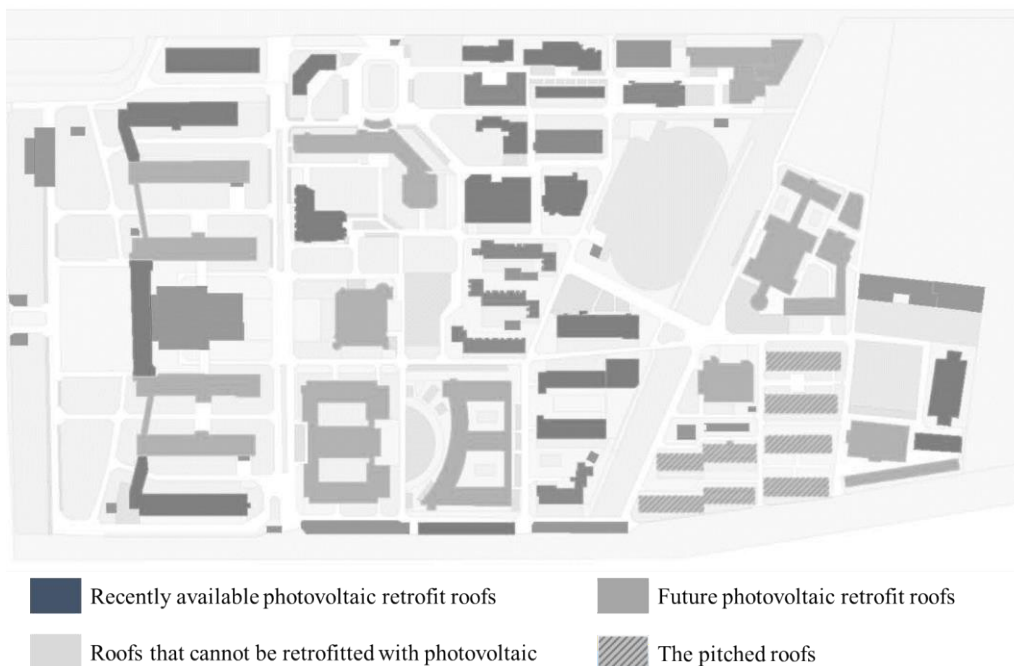
Figure 4: Building zoning for photovoltaic retrofits

From Figure 4, it can be seen that the existing buildings on the campus have a flat roof area of about 87, 633 m^2 and a pitched roof area of about 12,929 m^2. The installed photovoltaic capacity is calculated from Equation 3.

Equation 3: Installed solar photovoltaic capacity.
$$P_{solar} = HA \times (S_P + S_X) \times K \times K_g / t$$

Where:

- P_{solar} = kilo watt peak (kwp)
- HA = total annual solar radiation per unit area (≈1400kwh/m^2)
- S_P = total flat roof area (m^2)
- S_x = total pitched roof area (m^2)
- K = correction factor for roof area (≈0.52)
- K_g = photovoltaic efficiency (≈0.18)
- t = annual converted sunshine hours (≈1300h)

Installing photovoltaic panels on all existing flat and sloped roofs across campus would achieve the maximum solar PV potential. The total PV electricity generation on campus is approximately 13.29 million kWh, and the total installed capacity is approximately 9647.9 kWp.

3.2. Shallow geothermal energy

Location of available green space on campus
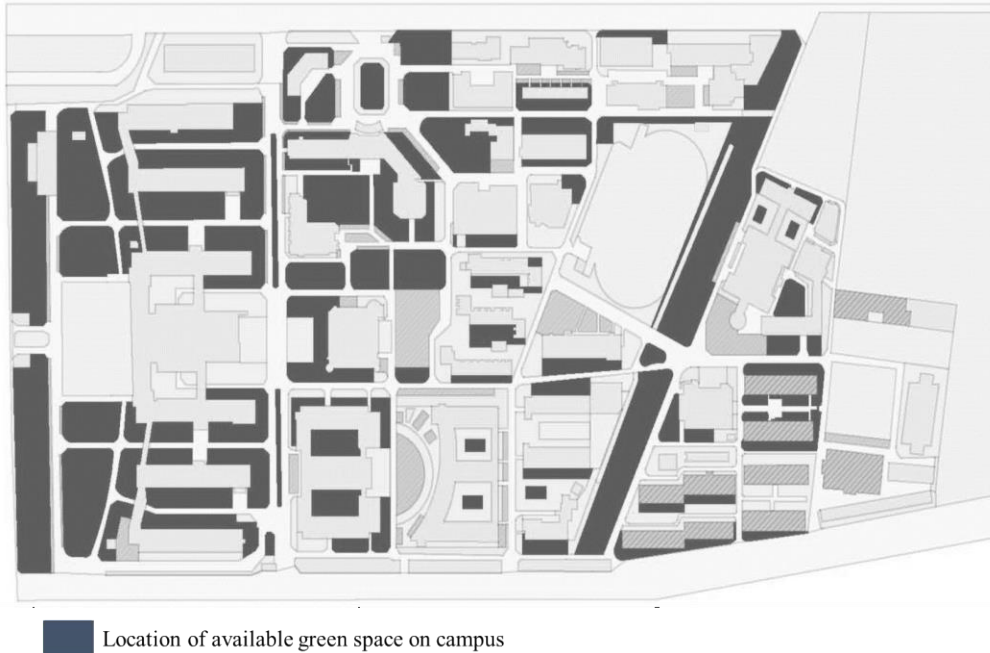
Figure 5: Map of available green space areas in campus

According to the zoning evaluation of suitable areas for ground source heat pump systems in the plain area of Beijing, the campus can utilize approximately 48,500 m^2 of green space as shown in Figure 5. Referring to operational parameters from existing ground source heat pump installations, one pipe can be buried per 25 m^2 at a depth of 150 meters. In summer, the heat exchange rate per unit length of buried pipe is 35W/m, while in winter, it is 70W/m.

Equation 4: Summer cooling capacity of soil source heat pumps.
$$Q_{soil,} = \frac{Q'_{soil,s}}{1 + 1/COP_s}$$

Where:

- $Q_{soil,}$ = power (kw)
- $Q'_{soil,s}$ = heat emissions to the soil in the summer (kw)
- COP_s = coefficient of performance of soil source heat pumps operation in summer (≈5)

Equation 5: Winter heating capacity of soil source heat pumps.
$$Q_{soil,} = \frac{Q'_{soil,w}}{1 + 1/COP_w}$$

Where:

- $Q_{soil,}$ = power (kw)
- $Q'_{soil,w}$ = heat absorbed from the soil in winter (kw)
- COP_w = coefficient of performance of soil source heat pumps operation in winter (≈4)

Based on the above, the campus soil source heat pump has a heating capacity of 13,552 kW in winter and a cooling capacity of 16,940 kW in summer, capable of providing heating and cooling for approximately 180,000 m² of office and research buildings. The total heat rejected by the soil source heat pump in summer is 30248,064 MJ, while the heat extracted in winter is 33058,207 MJ, representing a difference of approximately 8.5%. This indicates a balanced heat extraction and rejection of the soil source heat pump system.

3.3. Deep geothermal energy

Based on the requirement that the well density within the area must be less than 1/ 10 km², and considering the deep geothermal potential for this university as well, the geothermal heat pump capacity is calculated from Equation 6 based on the parameters of the geothermal wells located 15 kilometres away from the University.

Equation 6: Installed capacity of geothermal heat pumps.

$$P_{earth} = \frac{c \times m \times (t_g - t_h) \times 1000}{\left(1 - \frac{1}{COP_e}\right) \times 3600}$$

Where:

- P_{earth} = power (kw)
- c = specific heat of water (kJ/kg℃) (4.2 kJ/kg℃ for water)
- m = flow rate of water(m³/h)
- t_g = temperature of discharge water (℃)
- t_h = temperature of return water (℃)
- COP_e = coefficient of performance of geothermal heat pumps (≈4.5)

The calculated geothermal heat pump capacity is approximately 2200 kW, which can provide heat for approximately 30,000 m² of office and research buildings.

3.4. Sewage treatment plant

The school has two sewage treatment plants with daily actual sewage treatment capacities of 1000 t/d and 1500 t/d, respectively. Based on the operational parameters of the sewage source heat pump on campus, the summer cooling capacity and winter heating capacity of the sewage source heat pump can be calculated, as shown in Equation 7 and Equation 8.

Equation 7: Summer cooling capacity of sewage source heat pumps.

$$P_{water,s} = \frac{c \times G \times \Delta T_s \times 1000}{(1 + 1/COP'_S) \times 24 \times 3600}$$

Equation 8: Winter heating capacity of sewage source heat pumps

$$P_{water,w} = \frac{c \times G \times \Delta T_w \times 1000}{(1 - 1/COP'_w) \times 24 \times 3600}$$

Where:

- $P_{water,}$ = power (kW)
- $P_{water,}$ = power (kW)
- c = specific heat of water (kJ/kg℃) (4.2 kJ/kg℃ for water)
- G = sewage flow (t/d)
- o T_s = flow rate of water (8℃)
- o T_w = temperature of discharge water (6℃)
- COP'_S = coefficient of performance of geothermal heat pumps (≈5)
- COP'_w = coefficient of performance of geothermal heat pumps (≈4)

The campus sewage source heat pump has a summer cooling capacity of approximately 581 kW and a winter heating capacity of approximately 484 kW. It can provide heating and cooling for approximately 6000 m² of office and research buildings on campus.

4.   ANALYSIS OF LONG-TERM AND DAILY ENERGY STORAGE IN CAMPUS
4.1. Long-term energy storage
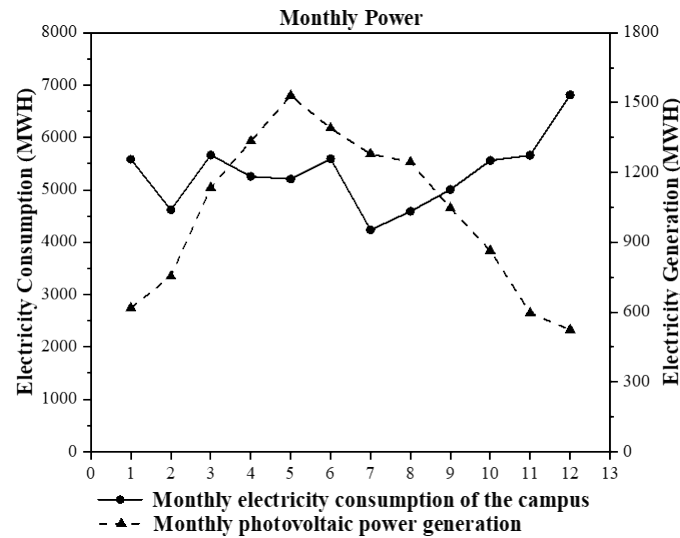
Figure 6: Seasonal matching of campus electricity consumption and solar PV generation

Figure 6 illustrates the monthly electricity consumption of campus buildings and the monthly electricity generation from PV panels. It shows a clear trend of surplus generation in summer and insufficient generation in winter. Therefore, it is necessary to consider methods such as seasonal thermal energy storage and seasonal electricity energy storage to match electricity consumption with generation across different seasons. Recover and store the heat dissipated by the air conditioner in summer and calculate the amount of heat that can be stored as shown in Equation 9.

Equation 9: Summer heat storage quantity. $$Q_{st,} = Q_c \times 0.5 \times (1 + 1/COP_{ts})$$

Where:

- $Q_{st,s}$ = summer heat storage quantity (MWh)
- Q_c = summer cooling consumption of buildings (MWh)
- COP_e = coefficient of performance of soil source heat pumps in summer (≈4)

For the above three types of buildings that have been calculated by DeST, the summer cooling consumption can be directly superimposed. For the other buildings on campus, the cooling load index method is used to estimate the cooling load by selecting the appropriate simultaneous use rate and the number of working hours. It can be obtained that the campus can store heat capacity of about 9,300 MWh in summer, and heat consumption of about 12,000 MWh in winter. The heat storage capacity in summer can meet about 75% of the heating capacity in winter.

Seasonal electricity storage can be achieved using photoelectrolysis of water for hydrogen storage with an efficiency of 50 percent. The green power load in winter is estimated at 70% of the green power load in summer and can be superimposed on the total power consumption of the three types of buildings that have already been calculated with DeST. For other campus buildings, the total power consumption in summer and winter is estimated according to the load indicator. It is calculated that the seasonal storage capacity of the university is about 9200MWh, accounting for about 35% of the winter electricity consumption capacity, and the required photovoltaic power generation capacity is about 18400MWh.

4.2. Daily energy storage

Figure 7 depicts the typical daily matching of hourly campus electricity consumption and photovoltaic (PV) generation during transitional seasons. From 11:00 to 14:00, PV generation significantly exceeds campus electricity consumption, while during other times, PV generation is lower than campus electricity consumption. It may be beneficial to consider short-term daytime cooling, thermal storage, and energy storage technologies to align hourly campus electricity consumption with PV generation.
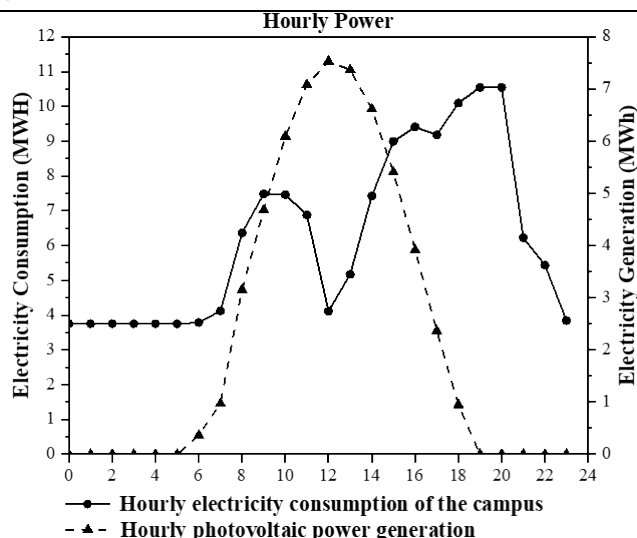
Figure 7: Matching of hourly campus electricity consumption and solar PV generation

For short-term daytime energy storage, V2G (Vehicle-to-Grid) smart charging technology can be utilized. Electric vehicle batteries can be used as buffers for campus electricity grids and renewable energy sources. When vehicles are low on charge, they can draw energy from the campus grid; when there is a short-term power deficit in the campus grid, surplus electric vehicles can actively supply energy back to the grid. The campus has a total of 827 parking spaces, each supporting a 13.3 kW storage capacity. Together, these can support up to 11,000 kWp of solar PV system storage capacity, which exceeds the planned PV installation capacity of 9,647.9 kWp. This setup can address short-term solar power instability, smoothing peak loads.

Techniques like ice storage can be employed effectively for daytime thermal energy storage. This involves ice production during nighttime hours and using the melting ice during the day to provide cooling, serving as a chilled water source for air conditioning during peak electricity demand periods. This approach helps avoid running high-power chillers during peak periods, with cooling system electricity peak shaving rates reaching approximately 60% (Luo et al., 2017). Alternatively, passive and active thermal energy storage tanks can be used for heat storage and release. This method allows for the transfer of heating load under thermal comfort constraints, accounting for approximately 5.6% to 8.4% of the total heat demand. During daytime demand response events, peak shaving rates can reach between 40% to 87% (Foteinaki et al., 2020).

5. INTEGRATED ENERGY SYSTEM PROGRAMME FOR LOW CARBON CAMPUS
5.1. Integrated energy system construction
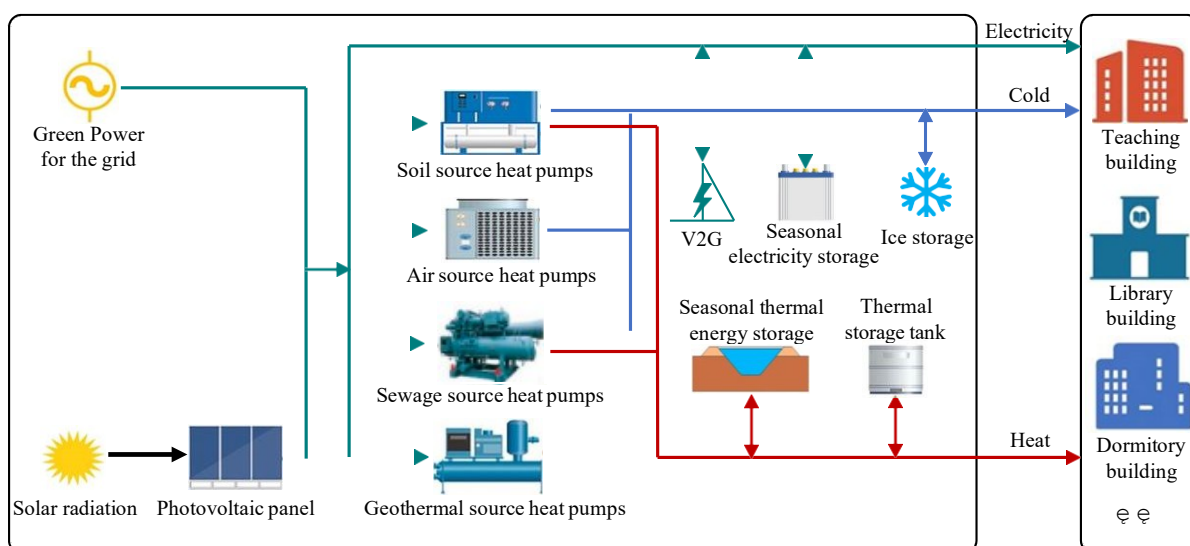
Figure 8: Conceptual diagram of an integrated energy system for the low-carbon campus

Based on the source-load-storage analysis, this paper constructs a low-carbon campus integrated energy system as shown in Figure 8. The heating load of the campus buildings is borne by soil source heat pumps, sewage source heat pumps, geothermal heat pumps, and seasonal thermal energy storage; the cooling load of the campus buildings is covered by soil source heat pumps and sewage source heat pumps, while the dormitory buildings use unitary air conditioners and the remaining cooling load is covered by air source (heat recovery); and the electrical load of the campus buildings is borne by campus solar photovoltaic and municipal power supply. The electrical load of the campus buildings is covered by campus solar photovoltaic and municipal power supply. The calculated energy structure ratio is shown in Figure 9 below.

(a) Heat Source

(b) Cold Source

(c) Power source
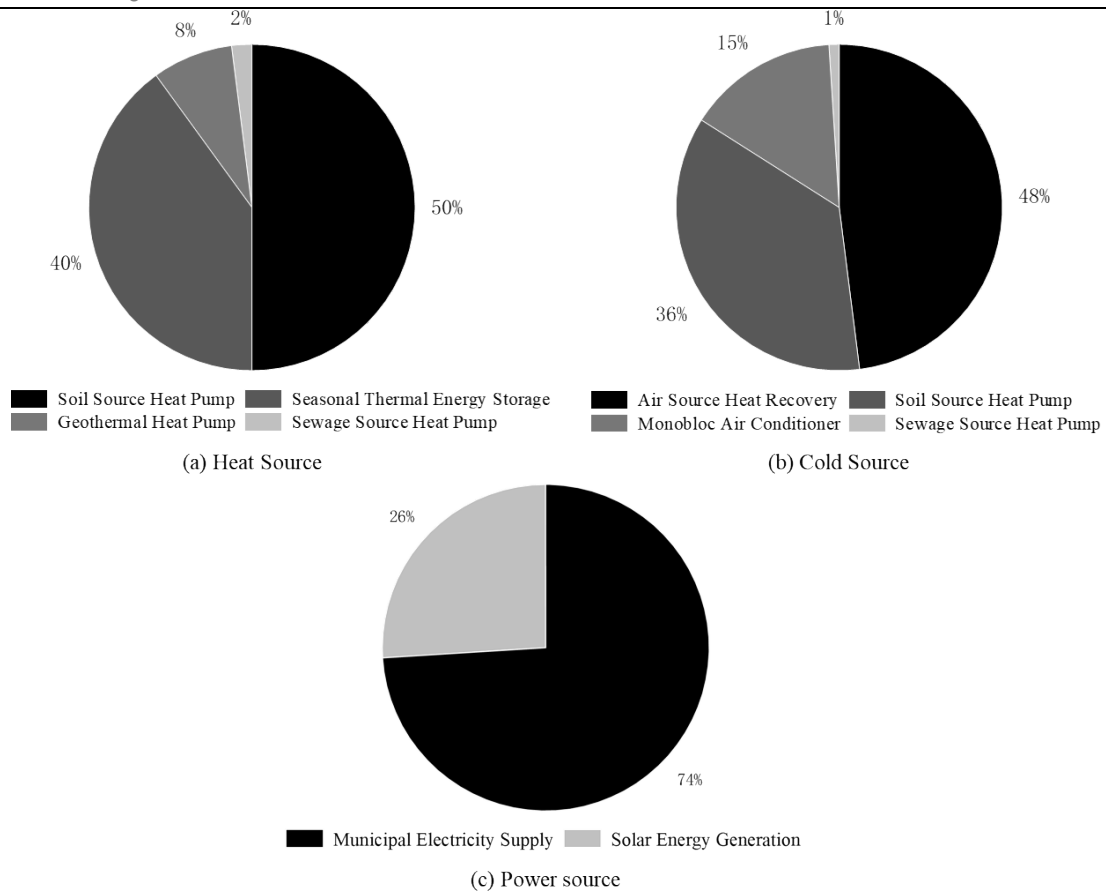
Figure 9: Energy structure diagram

5.2. Carbon neutrality assessment

Campus carbon neutrality is defined as the campus-generated green electricity replacing fossil fuel electricity in municipal supply. By 2050, the proportion of green electricity in the municipal supply can reach 0.6. Combining the campus's annual electricity consumption of 46.0525 million kWh and the proportion of municipal electricity supply to total campus electricity consumption at 74%, it is calculated that under the carbon neutrality scenario, campus-generated green electricity amounts to 13.16 million kWh. As calculated earlier, the total solar photovoltaic generation is approximately 13.29 million kWh, slightly exceeding the campus-generated green electricity under the carbon neutrality scenario. Therefore, it can be concluded that the campus will achieve carbon neutrality by 2050 with the current system in place.

6. REFERENCES

A.G, Olabi. and Mohammad, A. (2022) 'Renewable energy and climate change', Renewable and Sustainable Energy Reviews. Volume 158, April 2022, 112111. Available at: https://doi.org/10.1016/j.rser.2022.112111.

Foteinaki, K. and Li, R. (2020) 'Evaluation of energy flexibility of low energy residential buildings connected to district heating', Energy and Buildings. Volume 213, 15 April 2020, 109804. Available at: https://doi.org/10.1016/j.enbuild.2020.109804.

Hanju, S. (2018) 'National Energy Conservation in Colleges and Universities Energy consumption in colleges and universities accounts for 1/10 of the total social energy consumption', Financial sector, 2018(19), pp. 28-29.

Luo, N. and Hong, T. (2017) 'Data analytics and optimization of an ice-based energy storage system for commercial buildings', Applied Energy, Volume 204, pp. 459-475. Available at: https://doi.org/10.1016/j.apenergy.2017.07.048.

Yongbao, C. and Xiaolei, Y. (2022) 'Optimal Control Strategies for Demand Response in Buildings under Penetration of Renewable Energy', Buildings.2022, 12, 371. Available at: https://doi.org/10.3390/buildings12030371.

Yuwei, W. and Yuanjuan, Y. (2022) 'Wasserstein and multivariate linear affine based distributionally robust optimization for CCHP-P2G scheduling considering multiple uncertainties', Applied Energy, Volume 306, Part A, 15 January 2022, 118034. Available at: https://doi.org/10.1016/j.apenergy.2021.118034.

#209: Effect of Mo-doping or Nd-deficient on NdBaCo2O$_{5+\delta}$ as oxygen electrode material for IT-SOEC

Changling QUAN[1], Zaiguo FU[1*], Yan SHAO[2], Binxia YUAN[1], Yanhua LEI[3], Qunzhi ZHU[2]

[1] College of Energy and Mechanical Engineering, Shanghai University of Electric Power, Shanghai, China, quancl@mail.shiep.edu.cn
[2] College of Electric Power Engineering, Shanghai University of Electric Power, Shanghai, China, wjshaoyan@mail.shiep.edu.cn
[3] College of Ocean Science and Engineering, Shanghai Maritime University, Shanghai, China, yhlei@shmtu.edu.cn

Abstract: The Intermediate-Temperature Solid Oxide Electrolysis Cells (IT-SOECs) is an efficient energy conversion and storage device utilized in the process of water electrolysis for hydrogen production. NdBaCo2O5+δ (NBC) double perovskite has garnered significant interest for its potential application in IT-SOECs. However, NBC required improved electrochemical performance at intermediate temperatures and a reduced thermal expansion coefficient (TEC). In this study, high-performance NdBaCo2-yMoyO5+δ (NBCMoy, y=0-0.07) and Nd1-xBaCo2O5+δ (Nd1-xBC, x=0-0.06) were synthesized through Mo-doping or Nd-deficient on NBC. Mo-doping and Nd-deficient increased the adsorbed oxygen (Oabs) concentration of NBC from 71.76% to 78.21% in NBCMo0.05 and 74.20% in Nd0.98BC, separately. Consequently, their electrochemical performance was improved. At 800 ℃, the polarization resistances of NBCMo0.05 and Nd0.98BC were 0.035 Ω·cm2 and 0.071 Ω·cm2, respectively, which were only 33% and 67% of the NBC. Furthermore, both materials exhibited a lower coefficient thermal expansion. NBCMo0.05 is a promising candidate for the oxygen electrode in IT-SOECs.

Keywords: IT-SOEC, Mo-Doping, Nd-Deficient, Double Perovskite, Electrochemical Performance

1. INTRODUCTION

Solid Oxide Electrolysis Cells (SOECs) are recognized as one of the most promising energy conversion technologies due to their high energy conversion efficiency, low emissions, and flexible fuel choices (Li et al., 2023). The air electrode is a critical component of SOECs, requiring excellent oxygen evolution reaction (OER) activity and electrochemical stability (Zhang et al., 2023). Compared to traditional electronic conductor oxygen electrode materials, mixed ionic-electronic conductors (MIECs) enhance OER catalytic activity, expand the triple-phase boundary (TPB) active area, and effectively lower the operating temperature range of SOECs. These improvements extend the lifespan of cell components and reduce production costs (Zheng et al., 2017; Yi et al., 2016). Among MIECs, double perovskite oxides $LnBaCo_2O_{5+\delta}$ (Ln = rare earth) have been extensively studied as intermediate- temperature solid oxide cells (IT-SOCs) oxygen electrodes due to their high conductivity, rapid oxygen ion diffusion rates, surface exchange kinetics, and excellent electrochemical performance (Liu et al., 2017).

However, $LnBaCo_2O_{5+\delta}$ materials have high thermal expansion coefficients (TECs), leading to thermodynamic incompatibility with common electrolyte materials. Additionally, their OER catalytic activity and stability at intermediate temperatures need improvement. Cation doping, creating defects, and composite electrodes are common methods to reduce the TEC and enhance the electrochemical performance and stability of $LnBaCo_2O_{5+\delta}$ materials. For example, Xu et al. (Xu et al., 2020) studied Mo-doped $PrBaCo_2O_{5+\delta}$ (PrBCO), and found that while high-valence Mo doping decreases electrochemical performance, it effectively reduces TEC and improves electrochemical stability, benefiting practical applications. Introducing A-site cation vacancies in the double perovskite structure impacts the physicochemical properties of oxygen electrode materials (Liu et al., 2021). Yi et al. (Yi et al., 2016) demonstrated that Nd deficiencies in NBC promote oxygen vacancy formation, significantly enhancing the electrochemical performance of NBC as an intermediate-temperature solid oxide fuel cell (IT-SOFC) cathode material. Donazzi et al. (Donazzi et al., 2015) investigated the effects of Ba-deficiency on the crystal structure and electrochemical properties of NBC, noting that increased Ba-deficiency shifts thelattice structure from orthorhombic *Pmmm* to tetragonal *P4/mmm* and introduces more oxygen vacancies, thereby improving conductivity and electrochemical performance.

Previous studies have shown that incorporating medium-sized ions (such as Pr, Nd, and Gd) into the A-site of $LnBaCo_2O_{5+\delta}$ can significantly optimize the performance of solid oxide fuel cells (SOFCs) (Wang et al., 2023). NBC materials offer a superior balance between thermal expansion properties and conductivity, making them promising candidates for SOEC oxygen electrodes (Liu et al., 2017). Therefore, this study synthesized and characterized $NdBaCo_{2-y}Mo_yO_{5+\delta}$ (NBCMoy) and $Nd_{1-x}BaCo_2O_{5+\delta}$ (Nd1-xBC). The effects of Mo-doping and Nd-deficient on the crystal structure, thermal expansion properties, electrical conductivity, and electrochemical performance of NBC were investigated.

2. EXPERIMENTAL

2.1. Sample preparation and cell fabrication

$NdBaCo_{2-y}Mo_yO_{5+\delta}$ (NBCMoy, y=0-0.07) and $Nd_{1-x}BaCo_2O_{5+\delta}$ (Nd1-xBC, x=0-0.06) samples were synthesized via the sol-gel method. Stoichiometric amounts of $Nd(NO_3)_3 \cdot 6H_2O$, $Ba(NO_3)_2$, $Co(NO_3)_2 \cdot 6H_2O$, and $(NH_4)_6Mo_7O_{24} \cdot 4H_2O$ were dissolved in deionized water. EDTA and citric acid were added as complexing agents, and ammonia was used to adjust the pH to 7. The molar ratio of metal cations to citric acid to EDTA was maintained at 1:2:1. The solution was heated and stirred at 80 °C until a gel formed. The gel was then dried at 180 °C for 12 h, calcined at 1200 °C for 10 h, and ground to obtain the desired powder.

The powders were pressed into rectangular bars (20×5×3 mm) under a pressure of 50 MPa and sintered at 1000 °C for 2 h for electrical conductivity and TEC testing. The bars achieved a density greater than 95%, as verified by the Archimedes method, meeting the requirements for subsequent testing.

The electrochemical performance of the oxygen electrodes was tested using symmetric cells: NBCMoy | YSZ | NBCMoy and Nd1-xBC | YSZ | Nd1-xBC. Electrode slurries were prepared by mixing the electrode powders with a binder (5 wt% ethyl cellulose and 95 wt% terpineol) in a 1:1 mass ratio. The slurries were uniformly mixed and screen-printed onto both sides of YSZ electrolyte pellets. After sintering at 900 °C for 2 h, the symmetric cells were formed with an effective area of 0.5 cm². Platinum paste was applied to the electrode areas as a current collector, and a separate platinum ring was printed as a reference electrode on one side.

2.2. Characterization

The phase composition and crystal structure of the samples were characterized using powder X-ray diffraction (XRD) with Cu Kα radiation. The step size was 0.02° and the scanning range was 10°-80°. X-ray photoelectron spectroscopy (XPS) was employed to analyze the surface valence states of oxygen, cobalt, barium, and molybdenum in NBCMoy and Nd1-xBC. The electrical conductivity of the materials was measured by the 4-probe DC method in the temperature range of 200 °C to 850 °C at 50 °C intervals under an air atmosphere. The TEC was measured using a dilatometer within the 50 °C to 850 °C range at a heating rate of 5 °C·min⁻¹. The microstructure of the cross-sections of symmetric cells was examined using scanning electron microscopy (SEM). Electrochemical impedance spectroscopy (EIS) analysis was conducted using an electrochemical workstation within the frequency range of 100 kHz to 100 mHz, with a signal amplitude of 10 mV, and operating temperatures ranging from 600 °C to 800 °C.

3. RESULTS AND DISCUSSION

3.1. Phase structure

Figures 1(a) and 1(b) show the powder XRD patterns of the synthesized NBCMoy and Nd1-xBC materials, respectively. The XRD

patterns exhibit a double peak at 2θ=30°-35°, characteristic of the tetragonal crystal system with space group P4/mmm, typical of the double perovskite structure (Wang et al., 2022). The XRD data were refined using Jade software, and the lattice parameters were calculated. The structural parameters of the NBCMoy and Nd1-xBC samples are presented in Table 1.

As shown in Table 1, high-valence Mo^{6+} doping reduces the lattice volume of NBCMoy. This reduction is likely because the smaller ionic radius of Mo^{6+} partially replaces the larger Co ions, causing lattice contraction (Yang et al., 2022). In contrast, Nd-deficient in NBC leads to lattice expansion, resulting in an increased lattice volume (Liu et al., 2021).
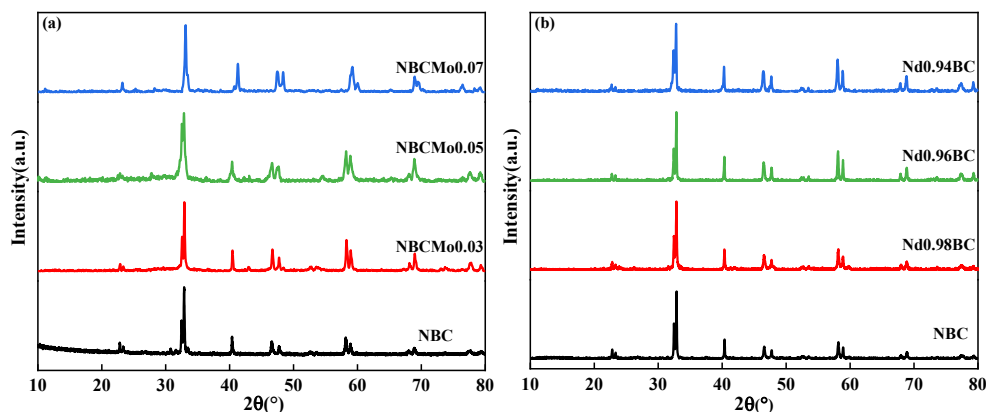
Figure 1: XRD patterns of NBCMoy powder (a) and Nd1-xBC powder (b)

Table 1: XRD refinement results of NBCMoy and Nd1-xBC powder

Samples	Lattice parameters			Volume $(Å^3)$	Space group
	$a(Å)$	$b(Å)$	$c(Å)$		
NBC	3.8971	3.8971	7.6172	115.67	P4/mmm
NBCMo$_{0.03}$	3.8877	3.8877	7.6162	115.11	P4/mmm
NBCMo$_{0.05}$	3.8901	3.8901	7.6266	115.41	P4/mmm
NBCMo$_{0.07}$	3.8891	3.8891	7.6375	115.52	P4/mmm
Nd$_{0.98}$BC	3.8969	3.8969	7.6189	115.70	P4/mmm
Nd$_{0.96}$BC	3.9000	3.9000	7.6136	115.80	P4/mmm
Nd$_{0.94}$BC	3.9041	3.9041	7.6192	116.13	P4/mmm

3.2. XPS analysis

To investigate the surface elemental chemical states of NBCMoy and Nd1-xBC, XPS spectra of the O1s, Co2p, Ba3d, and Mo3d (for NBCMoy) were analyzed. All spectra were calibrated to the C1s peak at 284.8 eV. Figure 2(a) and (b) present the XPS spectra of the O1s for NBCMoy and Nd1-xBC, respectively. The curves can be deconvoluted into lattice oxygen (O_{lat}), adsorbed oxygen (O_{ads}), and surface chemisorbed carbonate species (O_{CCS}) (Jin et al., 2021). The content of O_{ads} indicates changes in oxygen vacancies, thus the quantities of different oxygen species were quantitatively calculated, as shown in Table 2.

It is evident that Mo-doping and Nd-deficient effectively increase the proportion of O_{ads}. The O_{ads} in NBC increased from 71.76% to 78.21% in NBCMo0.05 and to 74.20% in Nd0.98BC. These results indicate that Mo doping and Nd-deficient generate more oxygen vacancies in the material, facilitating oxygen ion adsorption and dissociation on both the lattice and surface, thereby enhancing the OER catalytic activity of the material.
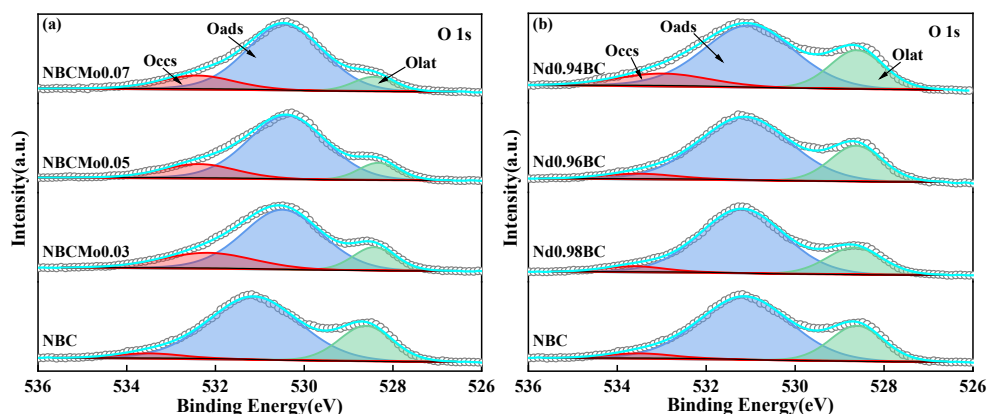
Figure 2: XPS spectra and curve-fitting of O1s in NBCMoy (a) and Nd1-xBC (b)

Table 2: Fitting results of O1s XPS spectra of different oxygen species and $O_{ads}/(O_{lat} + O_{ads})$ ratios

Samples	O_{lat} (%)	O_{abs} (%)	O_{ccs} (%)	$O_{ads}/(O_{lat}+O_{ads})$
NBC	528.60/24.03%	531.12/71.76%	533.49/4.21%	0.75
NBCMo$_{0.03}$	528.35/12.89%	530.53/77.16%	532.66/9.95%	0.86
NBCMo$_{0.05}$	528.32/10.66%	530.42/78.21%	532.55/11.13%	0.88
NBCMo$_{0.07}$	528.37/9.24%	530.39/76.73%	532.41/14.03%	0.89
Nd$_{0.98}$BC	528.65/20.92%	531.17/74.20%	533.59/4.88%	0.78
Nd$_{0.96}$BC	528.61/24.19%	531.11/71.22%	533.51/4.59%	0.75
Nd$_{0.94}$BC	528.68/25.48%	531.13/66.85%	533.43/7.67%	0.72

Figure 3(a) and (b) show the XPS spectra of the Co2p and Ba3d for NBCMoy and Nd1-xBC, respectively. Due to the overlap of the characteristic peaks of Co2p and Ba3d, it was necessary to separate the Ba3d peaks from the spectra. The characteristic peaks at 779.8 eV (3d5/2) and 795.0 eV (3d3/2) are attributed to Ba3d (Liu et al., 2021; Xia et al., 2020). Peaks detected at 780.8 eV and 795.5 eV indicates the presence of Co^{4+} in Co2p3/2 and Co2p1/2, respectively (Liu et al., 2021; Jin et al., 2024). Peaks observed at 778.2 eV and 793.4 eV correspond to Co^{3+} in Co2p3/2 and Co2p1/2. The absence of other satellite peaks in the binding energy range of 785.0-790.0 eV indicates the absence of lattice Co^{2+} in the crystal structure (Li et al., 2022).

The fitting results suggest that the concentrations of Co^{4+} in the NBCMoy and Nd1-xBC samples are higher than in the NBC sample. An increase in Co^{4+} concentration implies a rise in carrier concentration, enhances the charge transport properties related to the OER (Jin et al., 2024). Figure 3(c) presents the XPS spectrum of the Mo3d orbital for NBCMoy. As shown, there are two main peaks at 232.2 eV and 235.4 eV, corresponding to Mo^{6+} (3d5/2) and Mo^{6+} (3d3/2), respectively (Li et al., 2022; Cai et al., 2019). This indicates that only Mo^{6+} is present in NBCMoy, consistent with the findings of Xu et al. (Xu et al., 2020).
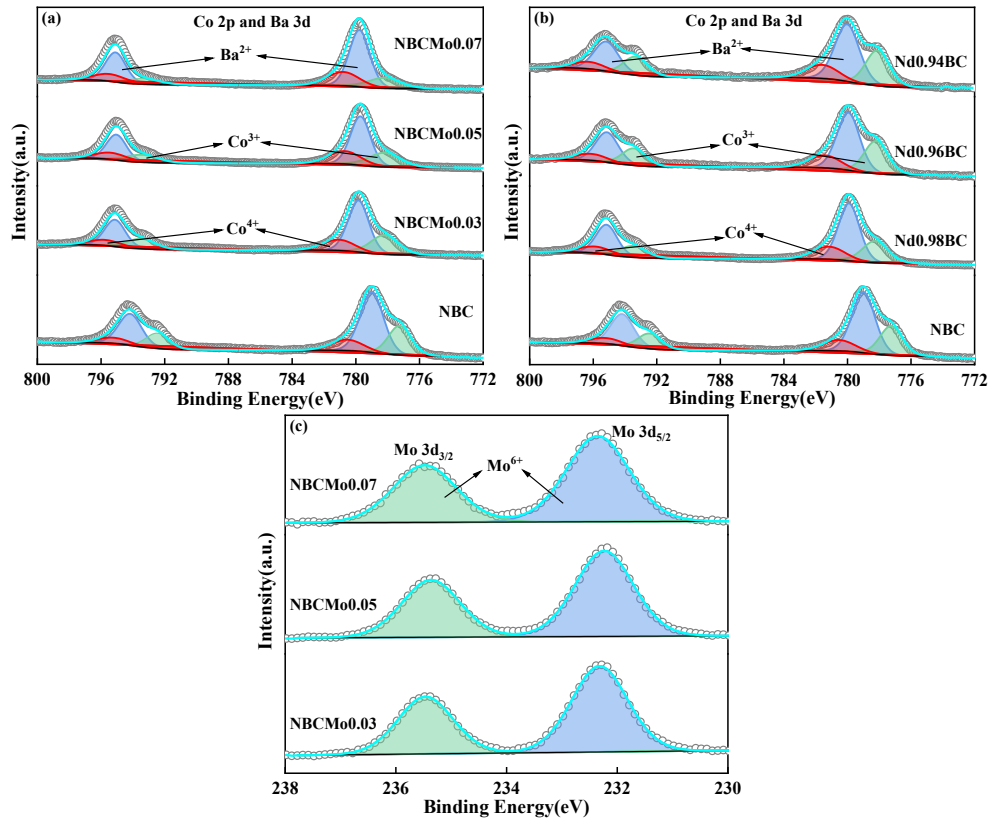
Figure 3: XPS spectra and curve-fitting of Co2p/Ba3d in NBCMoy (a) and Nd1-xBC (b) Mo3d in NBCMoy (c)

3.3. Thermal expansion behaviour and Electrical conductivity

The long-term stability of SOECs is linked to the thermodynamic compatibility of their components. Figure 4(a) displays the thermal expansion curves of NBC, Nd0.98BC, and NBCMo0.05 samples. Compared to NBC, the TEC values of Nd0.98BC and NBCMo0.05 are reduced by 9% and 30%, respectively. The thermal expansion curve of NBCMo0.05 is nearly linear, indicating excellent thermal stability. The introduction of Mo^{6+} can suppress the chemical expansion caused by the reduction of Co (Zhang et al., 2015). However, the thermal expansion curves of NBC and Nd0.98BC samples are nonlinear, primarily due to the instability of the high oxidation state of Co at elevated temperatures and the loss of lattice oxygen caused by charge compensation (Ullmann et al., 2000).

Electrical conductivity is an important parameter for the OER of oxygen electrode. Figure 4(b) illustrates the change in electrical conductivity of NBC, Nd0.98BC, and NBCMo0.05 samples with temperature. Electrical conductivity initially increases and subsequently decreases over the entire temperature range. The conduction mechanism of NdBaCo$_2$O$_{5+\delta}$-based materials is attributed to the p-type small polaron conduction mode, where electron conduction occurs via hopping along Co^{4+}-O^{2-}-Co^{3+} bonds

(Zhang et al., 2008). Below 300 °C, the increase in conductivity may be attributed to the thermal activation of charge-carrier mobilities. Above 300 °C, the conductivity decreases with rising temperature, exhibiting metallic-like behavior due to the increase in oxygen vacancies and the thermal reduction of Co^{4+}, which lowers the carrier concentration (Liu et al., 2021). Despite the slight reduction in conductivity due to Mo doping and Nd deficiency, the materials maintain conductivities above 100 S·cm^{-1} in the 600-800 °C range, which meets the requirements for IT-SOEC oxygen electrodes.
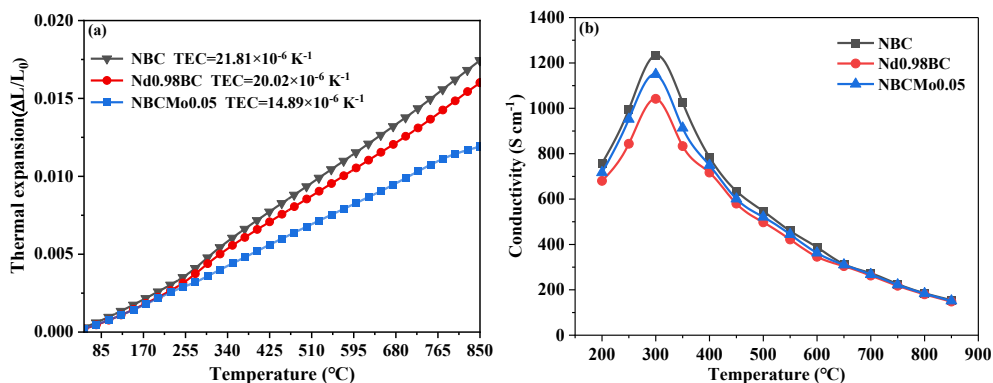
Figure 4: Thermal expansion of NBC, Nd0.98BC and NBCMo0.05 samples (a), and electrical conductivity of NBC, Nd0.98BC and NBCMo0.05 samples (b)

3.4. Electrochemical performance

The electrochemical performance of NBCMoy and Nd1-xBC oxygen electrodes was analysed using EIS testing on symmetric cells at 600-800 °C, as shown in Figure 5. The area-specific resistance (ASR) decreased with increasing temperature for all samples, indicating improved electrode activity (Donazzi et al., 2015). Both modification methods effectively reduced the ASR of NBC.
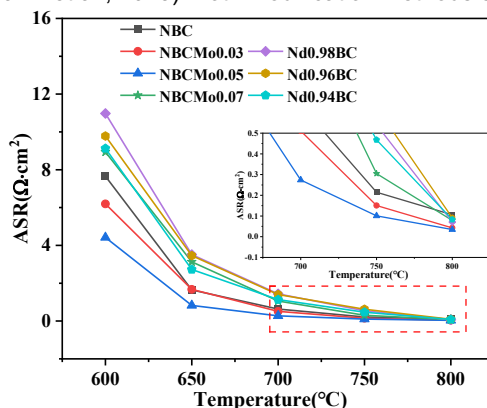
Figure 5: ASR values of each sample in the temperature range of 600-800 °C

Figure 6 presents the EIS results of NBCMoy and Nd1-xBC oxygen electrodes in the air at 800 °C. The ASR values were determined by the difference between the low-frequency and high-frequency intercepts on the real axis (Harzand et al., 2024). At 800 °C, NBCMo0.05 and Nd0.98BC electrodes exhibited the lowest ASR values, 0.035 Ω·cm² and 0.071 Ω·cm², respectively. These values represent reductions of 67% and 33% compared to NBC. High oxygen vacancy concentrations improve oxygen ion transport, thereby lowering ASR (Chen et al., 2023). This observation aligns with the previous XPS O1s results, which showed that Mo-doping and Nd-deficient increased oxygen vacancies in the lattice. NBCMo0.05's ASR value outperforms other NBC-based electrodes, such as $NdBa_{0.9}Ca_{0.1}CoFeO_{5+\delta}$ (0.0482 Ω·cm² at 800 °C) (Chen et al., 2023), $NdBa_{0.5}Ca_{0.5}Co_{1.5}Fe_{0.5}O_{5+\delta}$-GDC (0.079 Ω·cm² at 800 °C) (Tian et al., 2018), and $NdBa_{0.5}Sr_{0.25}Ca_{0.25}Co_2O_{5+\delta}$ (0.064 Ω·cm² at 800 °C) (Yao et al., 2018).
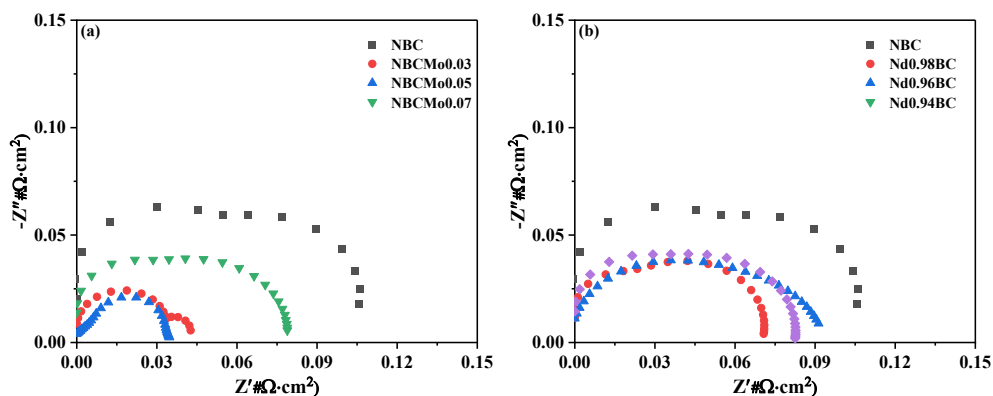
Figure 6: Electrochemical impedance spectra of the NBCMoy (a), and Nd1-xBC (b) oxygen electrodes in the air at 800 °C

The microstructure of the oxygen electrode is influenced by surface properties such as porosity and TPB area (Yi et al., 2016). The SEM image in Figure 7 shows the cross-section of the anode and electrolyte interface in the symmetric cell. The YSZ electrolyte layer exhibits high density, which ensures excellent contact between the oxygen electrode powder and the electrolyte layer without noticeable delamination. Additionally, the oxygen electrode has a distinct porous structure. This porous configuration, coupled with intimate contact with the electrolyte, facilitates oxygen diffusion and charge transfer, effectively enhancing the rate of the OER reaction.
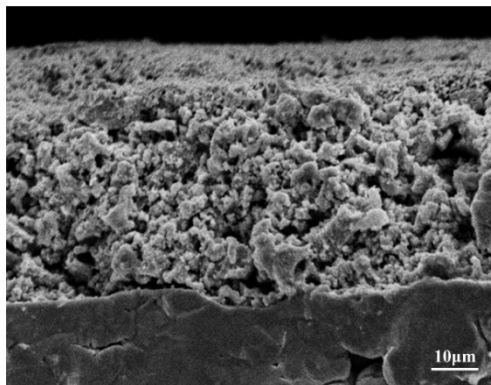
Figure 7: SEM image of symmetric cell cross-section

4. CONCLUSION

In this study, $NdBaCo_{2-y}Mo_yO_{5+\delta}$ (NBCMoy, y=0-0.07) and $Nd_{1-x}BaCo_2O_{5+\delta}$ (Nd1-xBC, x=0-0.06) materials were synthesized by the sol-gel method to evaluate their potential as IT-SOEC oxygen electrodes. Minor Mo doping and Nd-deficient did not alter the tetragonal *P4/mmm* crystal structure of the materials. XPS results revealed an increase in oxygen vacancies and Co^{4+} content in NBCMoy and Nd1-xBC, which contributed to the enhanced catalytic activity of OER. Meanwhile, the TEC of NBCM0.05 and Nd0.98BC samples were 14.89×10^{-6} K^{-1} and 20.02×10^{-6} K^{-1}, respectively, showing a decrease compared to NBC material. Finally, we performed electrochemical tests on the synthesized NBCMoy and Nd1-xBC oxygen electrodes using symmetric cells, and at 800 °C, the ASR of NBCM0.05 material was only 0.035 $\Omega\cdot cm^2$. These findings demonstrate that doping Mo ions in NBC materials is an effective strategy.

5. REFERENCES

Cai. H., Zhang. L., Xu. J., et al. (2019) Cobalt–free $La_{0.5}Sr_{0.5}Fe_{0.9}Mo_{0.1}O_{3-\delta}$ electrode for symmetrical SOFC running on H_2 and CO fuels[J]. Electrochimica Acta, 320: 134642.

Chen. M., Zhang. H., Yao. C., et al. (2023) Ca and Fe co-doped $NdBaCo_2O_{5+\delta}$ double perovskites as high-performance cathodes for solid oxide fuel cells[J]. Journal of Alloys and Compounds, 968: 172084.

Donazzi. A., Pelosato. R., Cordaro. G., et al. (2015) Evaluation of Ba deficient $NdBaCo_2O_{5+\delta}$ oxide as cathode material for IT-SOFC[J]. Electrochimica acta, 182: 573-587.

Harzand. A. G., Golmohammad. M., Zargar. S. A., et al. (2024) Study of structural, electrical, and electrochemical properties of $Sr_{3-x}Pr_xFe_{1.8}Co_{0.2}O_{7-\delta}$ cathode for IT-SOFCs[J]. Solid State Ionics,404: 116421.

Jin. F., Li. J., Gao. Y., et al. (2024) Boosting the electrocatalytic activity of $NdBaCo_2O_{5+\delta}$ via calcium co-doping as bifunctional oxygen electrodes for reversible solid oxide cells[J]. Fuel, 368: 131625.

Jin. F., Liu. X., Chu. X., et al. (2021) Effect of nonequivalent substitution of $Pr^{3+/4+}$ with Ca^{2+} in $PrBaCoFeO_{5+\delta}$ as cathodes for IT-SOFC[J]. Journal of Materials Science, 56: 1147-1161.

Li. H., Zhao. Y., Wang. Y., et al. (2016) $Sr_2Fe_{2-x}Mo_xO_{6-\delta}$ perovskite as an anode in a solid oxide fuel cell: Effect of the substitution ratio[J]. Catalysis Today, 259: 417-422.

Li. J., Sun. N., Liu. X., et al. (2022) Investigation on $Nd_{1-x}Ca_xBaCo_2O_{5+\delta}$ double perovskite as new oxygen electrode materials for reversible solid oxide cells[J]. Journal of Alloys and Compounds, 913: 165245.

Li. L., Dong. Z., Xia. T., et al. (2023) A series of bifunctional $ReBaCo_2O_{5+\delta}$ perovskite catalysts towards intermediate-temperature oxygen reduction reaction and oxygen evolution reaction[J]. Chemical Engineering Journal, 468: 143762.

Liu. S., Zhang. W., Li. Y., et al. (2017) $REBaCo_2O_{5+\delta}$ (RE= Pr, Nd, and Gd) as promising oxygen electrodes for intermediate-temperature solid oxide electrolysis cells[J]. RSC advances, 7(27): 16332-16340.

Liu. X., Jin. F., Sun. N., et al. (2021) Nd^{3+}-deficiency double perovskite $Nd_{1-x}BaCo_2O_{5+\delta}$ and performance optimization as cathode

materials for intermediate-temperature solid oxide fuel cells[J]. Ceramics International, 47(23): 33886-33896.

Tian. Y., Liu. Y., Wang. W., et al. (2020) High performance and stability of double perovskite-type oxide $NdBa_{0.5}Ca_{0.5}Co_{1.5}Fe_{0.5}O_{5+\delta}$ as an oxygen electrode for reversible solid oxide electrochemical cell[J]. Journal of Energy Chemistry, 43: 108-115.

Ullmann. H., Trofimenko. N., Tietz. F., et al. (2000) Correlation between thermal expansion and oxide ion transport in mixed conducting perovskite-type oxides for SOFC cathodes[J]. Solid state ionics, 138(1-2): 79-90.

Wang. H., Lei. Z., Wang. X., et al. (2023) Exploring the influence of rare earth ions at A-site on the properties of $LnBaCo_2O_{5+\delta}$ cathode for solid oxide fuel cells[J]. Ceramics International, 49(16): 27222-27229.

Xia. W., Liu. X., Jin. F., et al. (2020) Evaluation of calcium co-doping in double perovskite $PrBaCo_2O_{5+\delta}$ as cathode material for IT-SOFCs[J]. Electrochimica Acta, 364: 137274.

Xu. J., Cai. H., Hao. G., et al. (2020) Characterization of high–valence Mo–doped $PrBaCo_2O_{5+\delta}$ cathodes for IT–SOFCs[J]. Journal of Alloys and Compounds, 842: 155600.

Yang. Q., Chen. M., Teketel. B. S., et al. (2022) Influences of equal A-site rare-deficiency or B-site high-valent metal doping on $NdBaFe_2O_{5+\delta}$ employed as the symmetrical electrode for solid oxide fuel cells[J]. Journal of Alloys and Compounds, 918: 165368.

Yao. C., Zhang. H., Liu. X., et al. (2018) Investigation of layered perovskite $NdBa_{0.5}Sr_{0.25}Ca_{0.25}Co_2O_{5+\delta}$ as cathode for solid oxide fuel cells[J]. Ceramics International, 44(11): 12048-12054.

Yi. K., Sun. L., Li. Q., et al. (2016) Effect of Nd-deficiency on electrochemical properties of $NdBaCo_2O_{6-\delta}$ cathode for intermediate-temperature solid oxide fuel cells[J]. International Journal of Hydrogen Energy, 41(24): 10228-10238.

Zhang. K., Ge. L., Ran. R., et al. (2008) Synthesis, characterization and evaluation of cation-ordered $LnBaCo_2O_{5+\delta}$ as materials of oxygen permeation membranes and cathodes of SOFCs[J]. Acta Materialia, 56(17): 4876-4889.

Zhang. P., Guan. G., Khaerudini. D. S., et al. (2015) B-site Mo-doped perovskite $Pr_{0.4}Sr_{0.6}(Co_{0.2}Fe_{0.8})_{1-x}MoO_{3-\delta}$ (x= 0, 0.05, 0.1 and 0.2) as electrode for symmetrical solid oxide fuel cell[J]. Journal of Power Sources, 276: 347-356.

Zhang. X., Liu. B., Yang. Y., et al. (2023) Advances in component and operation optimization of solid oxide electrolysis cell[J]. Chinese Chemical Letters, 34(5): 108035.

Zheng. Y., Wang. J., Yu. B., and Zhang. W. (2017) A review of high temperature co-electrolysis of H_2O and CO_2 to produce sustainable fuels using solid oxide electrolysis cells (SOECs): advanced materials and technology. Chemical Society Reviews, 46.5: 1427-1463.

#217: Preparation and optimization of thermal conductivity of melamine urea-formaldehyde@n-hexadecane phase change microcapsules (MEPCMs)

Xuefei Zhang[1], Wei Zhang[2], Chengyao Wang[3*]

[1] College of Energy and Mechanical Engineering, Shanghai University of Electric power, 201306, fionaz_cn@outlook.com
[2] College of Energy and Mechanical Engineering, Shanghai University of Electric power, 201306, zhangweiwyyx2021@163.com
[3] College of Energy and Mechanical Engineering, Shanghai University of Electric power, 201306, wangchengyao@shiep.edu.cn
* Corresponding author: wangchengyao@shiep.edu.cn

Abstract: Encapsulating phase change materials in shells, phase change microcapsules (MEPCMs) effectively settle drawbacks of phase change materials, such as leakage, and are widely used in realms of intelligent temperature control and textiles, building energy conservation, and thermal energy storage systems. To improve the thermal conductivity, melamine urea-formaldehyde@n-hexadecane MEPCMs were modified by adding graphene oxide (GO) to the shell based on in-situ polymerization method. Factors influencing the outcome of modification, including proportion of GO, are explored. Characteristics of MEPCMs are demonstrated with field emission scanning electron microscopy (FE-SEM), Fourier transform infrared spectroscopy (FT-IR), differential scanning calorimetry (DSC), thermogravimetric analysis (TGA), and Hot Disk constant analyser. The results indicate that the GO/ MUF@n-hexadecane MEPCM possesses satisfactory thermal storage performance and thermal stability. As the GO proportion was 0.1wt%, the average latent heat value of MEPCMs was the highest, reaching 217.2 J/g, the encapsulation efficiency was also the highest, reaching 95%. As GO proportion is 0.3wt%, thermal conductivity coefficient of MEPCM is 0.1554W/(m·K), 89.05% higher than unmodified MEPCM, and the microstructure is integrated. This novel material provides a promising solution for the application of carbon material in the field of thermal energy storage microcapsule composite PCMs.

Keywords: Phase Change Microcapsules; Phase Change Materials; Modification; Thermal Conductivity; Thermal Storage

1. INTRODUCTION

Nowadays in order to achieve the "dual carbon" strategic goal as soon as possible and improve the heat energy efficiency, the focus is on formulating emission reduction strategies, improving the energy structure. Thermal energy is one of the most promising clean and renewable energy sources, and it is freely obtained from daily industrial exhaust gas and solar radiation [1-3]. In addition, thermal energy can be storage by three main methods: latent heat storage, sensible heat storage, and chemical heat storage [4]. Latent heat storage (LHS) method also is called phase change heat storage due to that it can draw upon phase change materials (PCMs) to absorb and release heat energy during the melting process [5-7]. PCMs can contribute to their high latent heat storage density and steady phase change temperature. However, traditional PCMs have longstanding bottlenecks during the melting process such as liquid phase leakage, solid phase rigidity, phase separation, and volume change [8-9]. There is a facile method that encapsulates PCMs into organic or inorganic materials to prepare shape-stable PCMs, which can not only resist phase change and volume change but also improve its thermal stability and thermal conductivity [10].

The microencapsulated phase change materials (MEPCMs) technique can sufficiently isolate the PCM from the outside environment to avoid leakage of melted PCMs and control the volume change during the phase change process [11]. MEPCMs are widely used in the realm of intelligent temperature control fibbers and textiles [12], slurries [13], building energy conservation [14]. The extensively used organic shells possess stable shapes and a larger heat transfer area and excellent sealing properties, which are prepared by interfacial polymerization and in-situ polymerization methods [15]. Due to the limitations of the shell material and structure, unmodified MEPCMs thermal conductivity has decreased. It has actually limited their application range. In order to improve the thermal conductivity of MEPCMs, it is an effective way to add high thermal conductivity modified materials to the core or shell material so as to modify the core and shell material of MEPCMs [16], such as Al_2O_3 [17],graphene oxide(GO) [18], expand graphite [19], carbon nanotube(CNTs) [20] et al. Li et al. [21] synthesized MEPCMs using multi-walled carbon nanotubes grafted with stearyl alcohol (CNTs-SA) as the core material and urea-formaldehyde resin (UF) as the shell material. Compared with the unmodified MEPCMs, the thermal conductivity of the MEPCMs with 4% CNTs increased from 0.08 W/(m·K) to 0.14 W/(m·K), an increase of 79.2%. Wei et al. [22] prepared MEPCMs using Al_2O_3 nanoparticle-modified MF shells with different mass fractions. The results showed that the added Al_2O_3 nanoparticles were uniformly distributed in the shell, which made the inner and outer layers of the MEPCMs form a connected thermal conductivity network. This structure effectively enhanced the thermal conductivity of the modified MEPCMs. As the mass fraction of nano-Al_2O_3 is 8 wt%, the thermal conductivity of the MEPCMs was highest, reaching 0.5977 W/(m·K). Wang et al. [32] developed a multifunctional magnetic microcapsule phase change material composed of SiO_2@Solar Salt microcapsule and Fe_3O_4-functionalized carbon nanotubes (CNTs-Fe_3O_4). The microcapsule not only has a good latent heat-storage capability with satisfactory phase-change enthalpies of over 88.6 J/g under an encapsulation efficiency of over 61.6 %, but also possesses high temperature stability and cycling stability. Recent research shows that combining phase change microcapsules with high thermal conductivity materials creates multifunctional phase change microcapsules with superior thermal conductivity, high energy storage density, and satisfactory thermal stability.

As a precursor of graphene, graphene oxide (GO) has high thermal conductivity and a typical amphiphilic structure [23]. GO has preferable wettability. This feature not only makes the graphene oxide particles stay more in water than in oil, but also tends to stabilize in oil-water emulsions. Due to the advantages of large surface area and small dimensions, GO can help them settle on the oil-water interface and effectively encapsulate oil droplets [24]. Ji et al. [33] used TiO_2 shell modified by GO nanosheets and paraffin as the core material to prepare the microcapsules via interfacial condensation polymerization in a sol-gel system. The latent heat of microcapsules is more than 160.75 J/g, and the thermal conductivity enhanced from 0.195 to 0.297 W/(m·K) thanks to the highly thermally conductive of GO nanosheets. In addition, the thermal conductivity is almost doubled compared to that of paraffin and the microcapsules preserve a high phase change enthalpy. Chen et al. [25] prepared regular-shaped MEPCMs by a new type of octadecyl amine grafted graphene oxide (GO-ODA) as the core material and Melamine formaldehyde resin (MF) as the shell material. Their results showed that the thermal conductivity of the modified MEPCMs with 0.5 wt% GO-ODA increased to 0.26 W/(m·K), 36.84% higher than the unmodified MEPCMs (0.19 W/(m·K)). Wang et al. [26] used decanoic acid as the core material, urea-formaldehyde resin (UF) along with GO as additives to the shell for the preparation of modified MEPCMs based on in-situ polymerization method. At a consistent temperature, the thermal conductivity of MEPCMs significantly increased with the addition of GO. Compared with the unmodified MEPCMs, the thermal conductivity of MEPCMs - 0.9 wt% GO at 20, 30 and 40°C was respectively enhanced by 75.1%, 64.2% and 73.6%. The maximum thermal conductivity of their modified MEPCMs reached around 0.125 W/(m·K). It is worth pointing out that GO can be stable and evenly embedded in the UF and form heat transfer channels on the surface and inside of the UF, to improve the thermal conductivity of MEPCMs.

The studies indicate that adding high thermal conductivity modified materials to the shell was conducive to expanding the application fields, such as energy efficiency in buildings [27], temperature-controlled textiles [28] and slurries [29]. It enriches the existing theories about heat storage of composite PCMs and contributes to the development of efficient and high-reliability thermal energy storage technologies. In the existing research to improve the thermal conductivity of traditional MEPCMs, the mainly studies the combination of GO with different core materials, and there are some reports about the combination of GO with different shells. However, there have been no studies combining GO with melamine urea-aldehyde shells. In this paper, the controllable microfluidic strategy was applied to first fabricated melamine urea-aldehyde@n-hexadecane MEPCMs with high latent heat. In addition, individual GO was added to melamine urea-aldehyde@n-hexadecane MEPCMs. The specific effects of GO on the thermal conductivity and heat storage capacity of modified MEPCMs were systematically investigated.

2. EXPERIMENT
2.1. Materials

n-hexadecane (98%), Graphene oxide (> 99%), Sodium lauryl sulfate (AR,92.5-100.5%) and ammonium chloride (AR,99.5%) were provided by Aladdin Chemical Reagents Co., Ltd. Melamine (CP), Urea (AR), Triethanolamine (AR), acetic acid (AR,36%) were obtained from Sinopharm Chemical Reagent Co., Ltd. Formaldehyde solution (37%) provided by Haibiao Technology Co., Ltd. Absolute ethanol (AR,99.7%) were provided by McLean Chemical Reagents Ltd.

2.2. Preparation of MEPCMs

The MEPCMs samples were prepared by n-hexadecane as the core material and melamine urea-formaldehyde (MUF) as the shell material based on in-situ polymerization. Then, the schematic illustration of the preparation principle about the thermally conductive enhanced modified MEPCMs is shown in Fig.1. The experimental procedure is mainly divided into the following three steps: in the first step, we prepared the melamine urea-formaldehyde precursor solution, melamine, meanwhile triethanolamine as a catalyst, urea and formaldehyde undergo a multi-step reaction process to co-condense to form a prepolymer solution. In the second step, GO is added to the melamine urea-formaldehyde prepolymer solution. Finally, N-hexadecane forms small droplets under the operation of high-speed shear forces, and under the catalysis of ammonium chloride and acetic acid, the GO-modified melamine urea-formaldehyde prepolymer solution is coated on the surface of the n-hexadecane droplets, so as to obtain thermally enhanced modified MEPCMs.

As the GO proportion is 0 wt%, 0.1 wt%, 0.2 wt%, 0.3 wt% and 0.4 wt%, the prepared modified MEPCMs were recorded as MEPCM-B1, MEPCM-B2, MEPCM-B3, MEPCM-B4 and MEPCM-B5, respectively, shown in Table1.

Table 1: Formulation of GO-modified MUF prepolymer solution.

Samples	GO proportion/wt%	GO/g	melamine/g	urea /g	formaldehyde /mL
MEPCM-B1	0	0	1	2	6
MEPCM-B2	0.1	0.008	1	2	6
MEPCM-B3	0.2	0.016	1	2	6
MEPCM-B4	0.3	0.024	1	2	6
MEPCM-B5	0.4	0.032	1	2	6
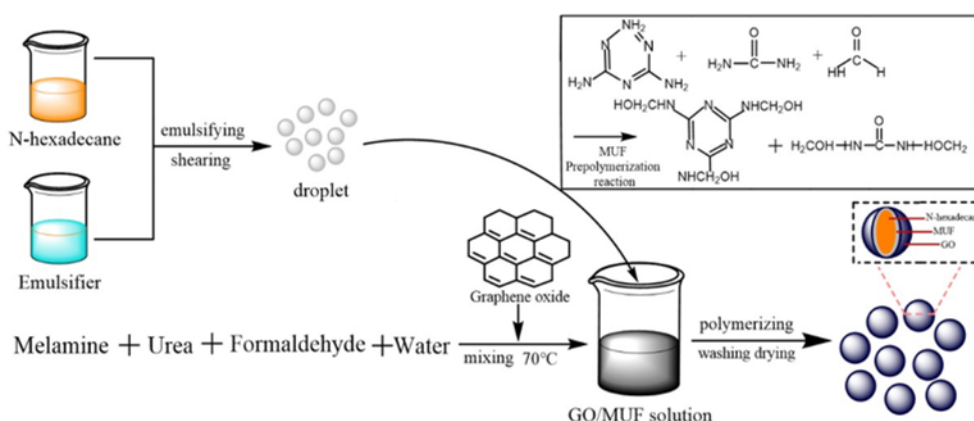
Figure 1: Scheme of the preparation process of GO/MUF@n-hexadecane MEPCMs

1.1. Characterization and measurement

MEPCMs prepared under different working conditions were softly coated on the uniform conductive adhesive of the metal carriers, fixed and then vacuum sprayed. The surface morphology and microstructure of the MEPCMs were captured by using a field emission electron microscopy (FE-SEM). MEPCM samples and potassium bromide were mixed polishing at a ratio of 1:100 and lightly pressed into pieces, and FT-IR spectra of the images were recorded from 500cm-1~4000 cm-1 using a FA2004N. The thermal properties of the MEPCM samples analysed using a differential calorimetry scanner (DSC, 3500 Sirius). Under nitrogen purge, the samples were heated from 0°C to 40°C and then cooled to 0°C at a constant rate of 5°C/min. Then the measured data was loaded into the Proteus Analysis application to calculate the values of the MEPCM samples, such as the phase change temperature and the latent heat of phase change. The thermal properties of MEPCM samples were evaluated by a thermogravimetric analyser (TGA/DSC2, 1600LF). Under nitrogen purge (20mL/min gas flow), the samples were heated from 25 to 800°C at a constant rate of 20°C/min. The Hot Disk thermal constant analyser (Hot Disk, tps 2500S) is based on the principle of the hot plate method. It was employed to measure the thermal conductivity of microcapsules at room temperature. The MEPCM samples were added into a cylindrical mold and compacted to obtain two flat surfaces, and the Type 7577 thermal probe was placed between the two round samples. And add the appropriate weight above the samples to ensure the accuracy of the measurement.

2. RESULTS AND DISCUSSION
2.1. Morphologies and microstructures

The SEM morphology of modified MEPCMs prepared with different amounts of GO are shown in Fig. 2. When the graphene oxide content is 0 wt%, MEPCM-B1 is a regular spherical structure with tight and adhesive surface. With the increase of GO content, modified MEPCMs have a slight difference in micromorphology as shown in Fig. 2 (a). As the GO proportion is 0.3 wt%, it can be seen that MEPCM-B4 shows a better spherical structure, and there is less adhesion, as shown in Fig. 2 (d). However, the particle size is obviously different. The surface becomes smooth along with the increasing of GO proportion. It is due to the fact that the ratio of GO is generally low. There are many oxygen-containing groups on the surface of GO, which can be better embedded in the

melamine urea formaldehyde shell. A very small fraction of the GO will agglomerate on the surface of the shell, while the surface of the modified MEPCMs become rough. Meanwhile, some exposed flaky structures on the surface are seen in Fig. 2 (b) and (e), which indicates that GO has been successfully exist in the microcapsules. In addition, as the melamine urea-formaldehyde shell material are coated with n-hexadecane droplets, a certain amount of GO may still be presented on the outside of the shell. Adding GO added in microcapsules does not destroy the overall structure, and potentially enhances the functional modification effect to a certain extent.

(a)MEPCM-B1   (b)MEPCM-B2   (c)MEPCM-B3
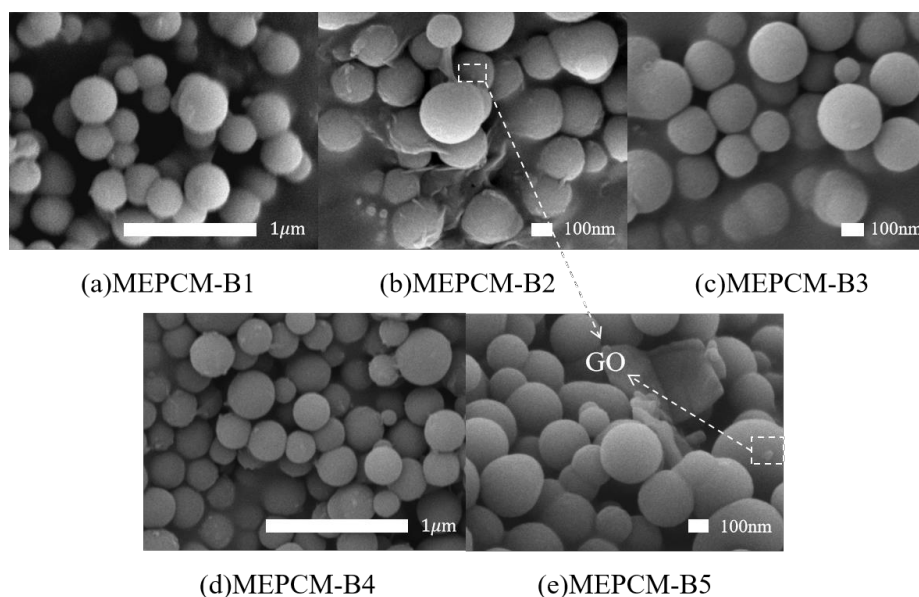
(d)MEPCM-B4   (e)MEPCM-B5

Figure 2: SEM images of GO/MUF@ n-hexadecane MEPCMs

2.2. Chemical composition of the microcapsules

The FT-IR spectra of melamine urea-formaldehyde, n-hexadecane, GO and MEPCM- B4 are shown in Fig. 3. In the n-hexadecane spectrum, the absorption peaks at 2922 and 2852 cm-1 are assigned to the asymmetric and symmetrical stretching vibrations bands of methylene-CH2 in alkanes, respectively. The absorption peaks at 1458 corresponds to the asymmetric deformation vibrations bands of methyl-CH3, and 1379 cm-1 corresponds to symmetrical deformation vibrations bands. The peaks at 719 cm-1 represents the out-of-plane bending vibrations bands of -CH. They are all characteristic absorption peaks of n-hexadecane. In the melamine urea-formaldehyde curve spectrum, there are strong and wide absorption peaks at around 3444 and 3348 cm-1 are the overlay of stretching vibration bands of N-H and O-H. The peak at 1641 cm-1 represents the in-plane bending bands of C=N on the triazine ring. The peak at 1026 cm-1 corresponds to the expansion and contraction bands of the ether bond C-O-C. The above peaks are characteristic absorption peaks of melamine urea-formaldehyde. Compared with the three curves of melamine urea-formaldehyde, n-hexadecane and MEPCM-B4, the curve spectra of MEPCM-B4 overlaps with the above absorption peaks, which indicate that the addition of GO has little influence on the chemical structure of MEPCM-B4. In the curve spectrum of GO, the broad peak at 3149 cm-1 corresponds to the -OH chemical bond, which shows that GO has contained bound water. The characteristic peaks at 1670 and 1062 cm-1 are assigned to the stretching vibration bands of C-C and C-O, which confirm the existence of GO. Generally, the FTIR spectra of the modified MEPCMs (MEPCM-B4) shows corresponding vibrational peaks. The results suggest that the GO/MUF@ n-hexadecane MEPCMs have been mainly composed of n-hexadecane, MUF and GO.
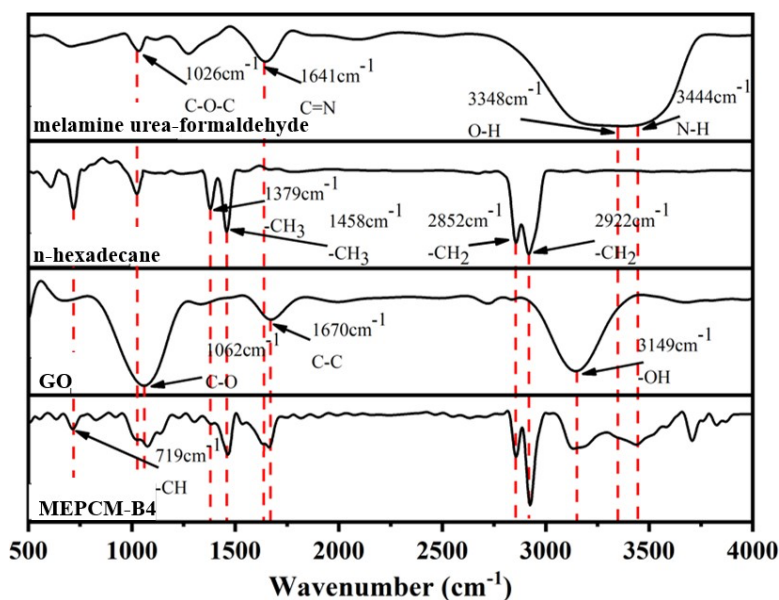
Figure 3: FTIR spectrums of the n-hexadecane and GO/MUF@ n-hexadecane MEPCMs

2.3. Phase change properties of the microcapsules

In the thermal energy storage application, thermal reliability and thermal stability are important characteristics of microcapsules. Figure 4 shows the DSC curve heat map of n-hexadecane and GO/MUF@ n-hexadecane MEPCMs. It can be seen from the graph that an endothermic peak and an exothermic peak are clearly visible during the phase changing process in all test samples. During the heating process, the latent heat of MEPCM-B1 without GO is 184.0 J/g, and with the combination of GO, the mean latent heat of microcapsules is increased to 212.4J/g. During the freezing process, the latent heat of MEPCM-B1 without GO is 178.7 J/g, and with the combination of GO, the mean latent heat of microcapsules is increased to 211.4 J/g. This is due to the addition of GO, which makes the structure of melamine urea-formaldehyde shell material more compact. The specific surface area on the outside of MEPCMs increased, so as to improve the latent heat of phase change. The addition of GO has a positive effect on the phase change enthalpy compared with unmodified MEPCMs. This is due to the interaction between the oxygen-containing polar groups on the GO sheet and the polar groups in the shell material prepolymer solution and emulsifier. As discusses in Fig.2, the morphology of microcapsules with GO is similar to that of the microcapsules without any filler, which had little effect on the coating process of n-hexadecane droplets. The less GO added, the smaller the effect on n-hexadecane. In a word, GO/MUF@ n-hexadecane MEPCMs still had fantastic heat storage properties.
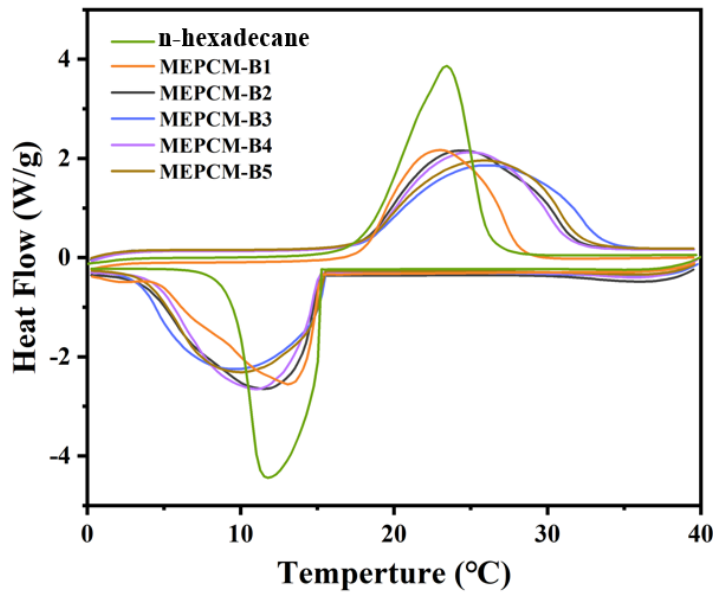
Figure 4: DSC curves of n-hexadecane and GO/MUF@ n-hexadecane MEPCMs

The encapsulation efficiency (ER) and latent heat-storage efficiency (ES) are two key parameters that judge the thermal performance and indicate the proportion of the fully encapsulated core material in the total core material in the MEPCMs. They can be deduced by equations (1)-(2) [30-31]:

$$ER = \left(\frac{\Delta H_{m,MEPCM}}{\Delta H_{m,PCM}} \right) \times 100\% \tag{1}$$

$$ES = \left(\frac{\left(\Delta H_{c,MEPCM} + \Delta H_{m,MEPCM} \right)}{\left(\Delta H_{c,PVM} + \Delta H_{m,PCM} \right)} \right) \times 100\% \tag{2}$$

Where:

- $\Delta H_{m,MEPCM}$ = the average fusion enthalpies of microcapsules(J/g)
- $\Delta H_{m,PCM}$= the average fusion enthalpies of the core(J/g)
- $\Delta H_{c,MEPCM}$ = the average solidification latent heat of the microcapsules(J/g)
- $\Delta H_{c,PVM}$ = the average solidification latent heat of the core (J/g)

The thermal property features obtained from the above equations are listed in Table 2. As can be seen Table 2, the encapsulation efficiency of GO-modified MEPCMs decreases appropriately with the increase of GO addition. As GO proportion is 0.1 wt%, the encapsulation efficiency is 96% and the latent heat-storage efficiency is 95%. In this case, the mean latent heat of GO-modified MEPCMs is also the highest, reaching 218.1 J/g, indicating that GO is well dispersed in the melamine urea-formaldehyde prepolymer solution. The oxygen-containing functional groups on the surface of GO formed a polar interaction with the urea-formaldehyde resin with polymerization. With the gradual increase of the mass ratio of GO, there would be different degrees of agglomeration in melamine urea-formaldehyde prepolymer solution. The larger the size of the agglomerated GO is, the more polar surface oxygen-containing functional group is. GO can adsorb hydrogen ions and cause precipitation of shell material. Therefore, part of the n-hexadecane core material is not encapsulated by melamine urea formaldehyde shell material, which reduces the

encapsulation efficiency and latent heat-storage efficiency of GO-modified MEPCMs.

Table 2: Phase change properties of n-hexadecane and modified MEPCMs

Sample	Tm (℃)	ΔHm(J/g)	Tc (℃)	ΔHc(J/g)	ER(%)	ES (%)
n-hexadecane	23.4	226.9	11.7	226.6	——	——
MEPCM-B1	23.1	184.0	13.1	178.7	81	80
MEPCM-B2	24.4	218.1	11.5	216.3	96	95
MEPCM-B3	26	215.8	9.5	213.3	95	94
MEPCM-B4	25	210.5	11	208.0	93	92
MEPCM-B5	25.8	210.0	10	207.9	93	92

2.4. Thermal stability of the microcapsules

Figure 5 shows the TGA curves of n-hexadecane and GO/MUF@ n-hexadecane MEPCMs. The weight loss curve of n- hexadecane shows a one-step weight loss process, starting at 101 °C and ending at 229 °C. These indicate that the -hexadecane has been almost completely evaporated. In contrast, the modified MEPCMs have a two-step weight loss, the specific test results are shown in Table 3. The thermogravimetric curves of MEPCM-B2~MEPCM-B5 are observed, the first stage is related to that MEPCMs have been heated to around 130°C. Under the circumstances, the shell material is broken, n-hexadecane leaks and begins to volatilize. The mass decay stops at about 300°C, and the mass fraction lost is basically about 85%. The second stage is due to the degradation of the melamine urea formaldehyde shell. Its weight loss percentage is basically about 8% until 800°C. MEPCM-B1 without GO has the fastest mass decay during the temperature range of 144°C~400°C, and the weight loss rate is 77.62%. The first-stage weight loss rates of MEPCM-B1, MEPCM-B2, MEPCM-B3, MEPCM-B4 and MEPCM-B5 are 77.62%, 86.16%, 86.68%, 87.77% and 84.70%, respectively. In general, the TGA curves of MEPCMs with GO are close to that the TGA curves of MEPCMs without GO, because the lower GO addition has less influence on the thermal stability of MEPCMs. In addition, the initial decomposition temperature of the MEPCMs increases along with the GO addition gradually. GO can improve the mechanical strength and heat resistance of melamine urea-formaldehyde shell material due to its special two-dimensional structure and strong thermal stability. It effectively delays the decomposition of the shell at high temperature. This functional modification enables MEPCMs to maintain stable performance in a high-temperature stage, which provides strong support for their popularization and use in practical applications.

Table 3: TGA test data for n-hexadecane and GO/MUF@ n-hexadecane MEPCMs

| Sample	Temperature range (℃)	Mass decay (%)	Sample	Temperature range (℃)	Mass decay (%)
n-hexadecane	25~101(1. step)	1.00	MEPCM-B3	25~129(1. step)	3.40
	101~229(2. step)	97.2		129~294(2. step)	87.68
	229~800(3. step)	1.40		294~800(3. step)	8.00
MEPCM-B1	25~111(1. step)	2.64	MEPCM-B4	25~128(1. step)	3.25
	111~292(2. step)	77.62		128~292(2. step)	87.77
	292~800(3. step)	18.93		292~800(3. step)	7.72
MEPCM-B2	25~127(1. step)	3.12	MEPCM-B5	25~127(1. step)	3.12
	127~299(2. step)	86.16		127~376(2. step)	84.70
	299~800(3. step)	9.46		376~800(3. step)	9.43
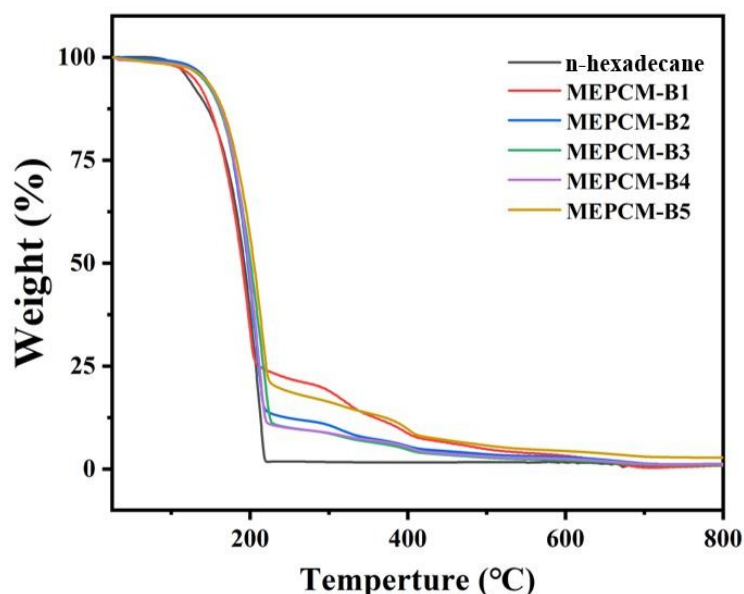
Figure 5: TGA curves of n-hexadecane and GO/MUF@ n-hexadecane MEPCMs

2.5. Thermal conductivity of the microcapsules

It is expected that GO modified MUF@ n-hexadecane composite can enhance the thermal conductivity of the composite phase change materials. Figure 6 shows the thermal conductivity of modified MEPCMs with different GO ratios. When the GO proportion adds from 0 wt% to 0.2 wt%, the thermal conductivity improves from 0.0822 W/(m·K) to 0.1535 W/(m·K), an increasement of 86.74%. When the GO proportion adds from 0.2 wt% to 0.3 wt%, the thermal conductivity of the GO-modified MEPCMs improves by only 1.24%. Compared with the outcome of previous study [35], the thermal conductivity of our microcapsule is 0.1535 W/(m·K), 66.8% higher than that of GO/ MUF@ n-octadecane microcapsule, 0.092 W/(m·K).   In addition, as the GO proportion is 0.3wt%, the thermal conductivity of MEPCMs is the highest, which is 0.1554 W/(m·K). the constructed thermal conductivity network structure trends to be saturated, and the rise rate of thermal conductivity decreases to 0.1191W/(m·K). And when the GO mass score increases to 4%, the network structure trends to be saturated and the thermal conductivity increase slows down. This phenomenon suggests that when the GO ratios are small, the oxygen-containing functional groups on the surface of GO can be well dispersed in the melamine urea-formaldehyde prepolymer. The thermal conductivity network structure constructed by GO and melamine urea-formaldehyde shell material tends to be complete, creating an excellent thermal conduction path in MEPCMs shell. According to the favourable heat conduction path, heat can be quickly transferred through the GO heat path inside the MEPCMs. As the heat transfer rate gradually increases, the thermal conductivity of the MEPCMs has significantly improved. In particular, the thermal conductivity of the MEPCMs increased to the least with the addition of 0.4 wt%. This is because when the GO proportion is small, the oxygen-containing functional groups on the GO surface have excellent dispersion in the MF prepolymer. Due to the heat transfer anisotropy of the GO, excessive GO easily accumulates. The network structure constructed by the GO tends to be complete, which improves the heat transfer rate. This cannot effectively increase the thermal conductivity [34]. Therefore, appropriate GO is needed to obtain modified microcapsules with a more balanced heat transfer performance. In summary, it indicated that heat could be transferred through the thermal path made by the addition of GO, which could significantly improve the thermal conductivity of MEPCMs.
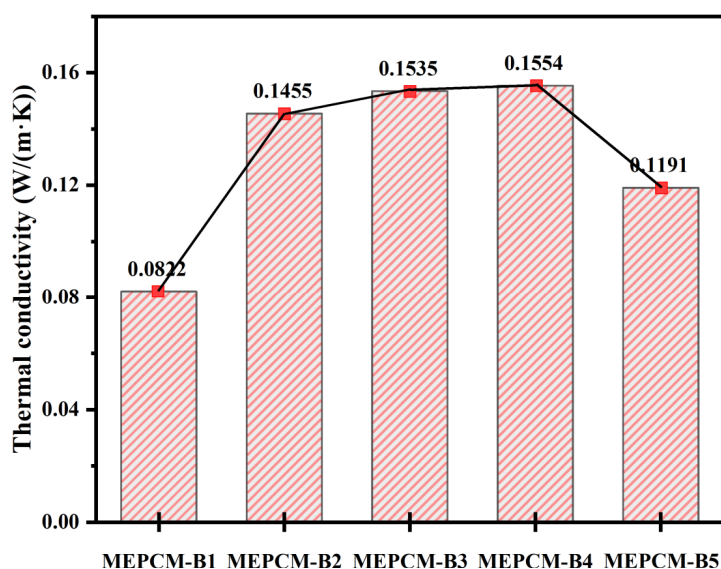
Figure 6: Thermal conductivity of GO/MUF@ n-hexadecane MEPCMs

3.   CONCLUSION

In this paper, microcapsules with n-hexadecane as the core and melamine urea-formaldehyde (MUF) as the shell modified by graphene oxide (GO) were prepared by in-situ polymerization. The GO/MUF@ hexadecane MEPCMs had favourable heat storage performance, and the latent heat of phase change increased. The addition of GO had little influence on the micromorphology and chemical structure of MEPCMs. As the GO proportion was 0.1 wt%, the average latent heat value of MEPCMs was the highest, reaching 217.2 J/g, the encapsulation efficiency was also the highest, reaching 95%. As GO proportion is 0.3 wt%, thermal conductivity coefficient of MEPCMs is 0.1554W/(m·K), 89.05% higher than unmodified MEPCMs. The prepared microcapsules had good thermal reliability and thermal stability. The thermally conductively enhanced MEPCMs prepared with different GO additions were mainly a two-step degradation process. It indicated that the GO-modified melamine urea formaldehyde shell played a certain role in blocking the thermal decomposition of the core. With the increasement of GO content, the thermal conductivity of GO-modified MEPCMs was significantly improved. When the GO content added from 0 wt% to 0.3 wt%, the thermal conductivity of GO-modified MEPCMs increased from 0.0822 W/(m·K) to 0.1554 W/(m·K), 89.05% higher than the unmodified. However, the thermal conductivity of modified MEPCM largely depends on the materials with high thermal conductivity, so in the future, we need research on how to discover and utilize more and better materials with high thermal conductivity. It is necessary to explore the large- scale and low-cost preparation process of the MEPCM, achieving multi-faceted applications in more fields. Meanwhile, new strategies of modified MEPCM can be explored to achieve an effective balance between superior thermal conductivity, high energy storage density, and low leakage rate.

4.   REFERENCES

[1] Abhat A., 1983. Low temperature latent heat thermal energy storage: heat storage materials. Solar Energy,30(4):313-32.

[2] Hasnain S. M., 1998. Review on sustainable thermal energy storage technologies, Part I: heat storage materials and techniques. Energy Convers Manage,39(11):1127-1138.

[3] Kenisarin M. M., 2012. Form-stable phase change materials for thermal energy storage. Renew Sustain Energy Rev,16(4):1999-2040.

[4] Singh P., Sharma R. K., Ansu A. K., et al., 2020. Study on thermal properties of organic phase change materials for energy storage. Materials Today: Proceedings,28(Pt 4):1-5.

[5] Liu C. H., Zhang J. H., Liu J., et al., 2021. Highly Efficient Thermal Energy Storage Using a Hybrid Hypercrosslinked Polymer. Angewandte Chemie International Edition,60(25):13978-13987.

[6] Velasco, J.A.C., Tawarmalani, M., and Agrawal R., 2021. Systematic analysis reveals thermal separations are not necessarily most energy intensive, Joule,5:330–343.

[7] Alva G., Lin Y. X., Liu L. K., et al., 2017. Synthesis, characterization and applications of microencapsulated phase change materials in thermal energy storage. Energy & Buildings,144:276-294.

[8] Zhang Y., Jia Z. Y., Moqeet H. A., et al., 2022. Shape-stabilization micromechanisms of form-stable phase change materials-A review. Composites Part A,160:107047.

[9] Cai Z. D., Liu J., Zhou Y. X., et al., 2021. Flexible phase change materials with enhanced tensile strength, thermal conductivity and photo-thermal performance. Solar Energy Materials and Solar Cells, 219:110728.

[10] Peng H., Zhang D., Ling X., et al., 2018. N-alkanes phase change materials and their microencapsulation for thermal energy storage: a critical review, Energy Fuel,32:7262–7293.

[11] Huang D. W., Wang H. M., 2012. Phase change materials of microcapsules containing paraffin. Advanced Materials Research, 1674(482-484):1596-1599.

[12] He F. G., 2013. Study on manufacturing technology of phase change materials and smart thermo-regulated textiles. Advanced Materials Research,2735(821-822):130-138.

[13] Qiu Z. Z., Ma X. L., Li P., et al., 2017. Micro-encapsulated phase change material (MPCM) slurries: Characterization and building applications. Renewable and Sustainable Energy Reviews, 77:246-262.

[14] Khadiran T., Hussein M. Z., Zainal Z., et al., 2016. Advanced energy storage materials for building applications and their thermal performance characterization: A review. Renewable and Sustainable Energy Reviews, 57:916-928.

[15] Başyiğit B., Sağlam H., Kandemir Ş., et al., 2021. Microencapsulation of sour cherry oil by spray drying: evaluation of physical morphology, thermal properties, storage stability, and antimicrobial activity. Powder Technol. 364 (2020) 654–663.

[16] Cheng P., Chen X., Gao H. Y., et al., 2021. Different dimensional nanoadditives for thermal conductivity enhancement of phase change materials: Fundamentals and applications. Nano Energy, 85:105948.

[17] Jiang X., Luo R. L., Peng F. F., et al., 2015. Synthesis, characterization and thermal properties of paraffin microcapsules modified with nano-Al2O3. Applied Energy, 137:731–737.

[18] Liu J., Chen L. L., Fang X. M., et al., 2017. Preparation of graphite nanoparticles-modified phase change microcapsules and their dispersed slurry for direct absorption solar collectors. Solar Energy Materials and Solar Cells, 159:159-166.

[19] Wang T. Y., Wang S. F., Geng L. X., et al., 2016. Enhancement on thermal properties of paraffin/calcium carbonate phase change microcapsules with carbon network. Applied Energy, 179:601-608.

[20] Han Z. D., Fina A., 2011. Thermal conductivity of carbon nanotubes and their polymer nanocomposites: A review. Progress in Polymer Science, 36(7):914-944.

[21] Li M., Chen M. R., Wu Z. S., 2014. Enhancement in thermal property and mechanical property of phase change microcapsule with modified carbon nanotube. Applied Energy, 27:166-171.

[22] Wei W., Duan Z. J., Xia Y. P., et al., 2019. Preparation and thermal performances of microencapsulated phase change materials with a nano-Al2O3-doped shell. Journal of Thermal Analysis and Calorimetry, 138(1):233-241.

[23] Zhen Q., Jian M., 2017. Enhanced thermal properties with graphene oxide in the urea-formaldehyde microcapsules containing paraffin PCMs. Journal of Microencapsulation, 34(1):1-9.

[24] Balandin A. A., 2011. Thermal properties of graphene and nanostructured carbon materials. Nature Materials, 10:569-581.

[25] Chen D. Z., Qin S. Y., Tsui G. C., et al., 2018. Fabrication, morphology and thermal properties of octadecylamine-grafted

graphene oxide-modified phase-change microcapsules for thermal energy storage. Composites Part B, 157:239-247.

[26] Wang X. G., Chen Z. F., Xu W., et al., 2019. Capric acid phase change microcapsules modified with graphene oxide for energy storage. Journal of Materials Science, 54(24):14834-14844.

[27] Liu L. Z., Xiang M. Y., Lyu D., et al., 2019. Encapsulation of polar phase change materials via multiemulsification and crosslinking method and its application in building. Journal of Applied Polymer Science, 136(32):47837.

[28] Sarier N., Onder E., 2006. The manufacture of microencapsulated phase change materials suitable for the design of thermally enhanced fabrics. Thermochimica Acta, 452(2):149-160.

[29] Xu B., Chen C. H., Zhou J., et al., 2019. Preparation of novel microencapsulated phase change material with Cu-Cu2O/CNTs as the shell and their dispersed slurry for direct absorption solar collectors. Solar Energy Materials and Solar Cells, 200(C):109980.

[30] Niu J. F., Liu H., Wang X. D., et al., 2019. Molecularly Imprinted Phase-Change Microcapsule System for Bifunctional Applications in Waste Heat Recovery and Targeted Pollutant Removal. Ace Applied Materials & Interfaces,11:37644-37664.

[31] Jiang B. B., Wang X. D., Wu D. Z., 2017. Fabrication of microencapsulated phase change materials with TiO2/Fe3O4 hybrid shell as thermoregulatory enzyme carriers: a novel design of applied energy microsystem for bioapplications. Applied Energy, 201:20–33.

[32] Wang L.Y., Huang Y.G., Li L.F., et al., 2023. Binary nitrate molten salt magnetic microcapsules modified with Fe3O4-functionalized carbon nanotubes for accelerating thermal energy storage. Journal of Energy Storage, 74(B), 109394.

[33] Ji W., Cheng X., Chen S., et al., 2021. Self-assembly fabrication of GO/TiO2@ paraffin microcapsules for enhancement of thermal energy storage. Powder Technology, 385:546–556.

[34] Lin Y.X., Zhu C.Q., Fang G.Y., 2019. Synthesis and properties of microencapsulated stearic acid/silica composites with graphene oxide for improving thermal conductivity as novel solar thermal storage materials. Solar Energy Materials and Solar Cells, 189:197–205.

[35] Wu B.Y., Zheng G., Sun Y., et al., 2016. Preparation and thermal properties of graphene/n-octadecane microcapsules. Journal of Polymer Science, 2:242-249.

#220: Assessment of bio-hydrogenated diesel and its blends with biodiesel as alternative fuels: a study onengine emissions and particle characteristics

Niti KLINKAEW[1], Anupap PUMPUANG[2], Atthaphon MANEEDAENG[3], Ekarong SUKJIT[1]

[1] School of Mechanical Engineering, Suranaree University of Technology, Nakhon Ratchasima 30000, Thailand
[2] Institute of Research and Development, Suranaree University of Technology, Nakhon Ratchasima 30000, Thailand
[3] School of Chemical Engineering, Suranaree University of Technology, Nakhon Ratchasima, 30000 Thailand
ekarong@sut.ac.th

Abstract: This study examines the influence of diesel, bio-hydrogenated diesel (BHD), and biodiesel fuels on engine performance, combustion characteristics, and emissions across various engine loads. Fuel properties were evaluated according to American Society for Testing and Materials (ASTM) standards, with blends of BHD and biodiesel at different ratios analysed. Engine performance parameters, combustion characteristics, and emissions were measured using specialized instruments, including pressure sensors and gas analysers, across engine loads from 25% to 90%. Results demonstrate that BHD generally outperforms diesel and biodiesel in terms of brake specific fuel consumption (BSFC) and brake thermal efficiency (BTE), particularly at higher engine loads. Combustion characteristics such as the rate of heat release (RoHR) and in-cylinder pressure (ICP) varied with fuel type and load, indicating the importance of combustion stability and fuel-air mixing. Emissions analysis reveals trends in NOx, HC, CO, and smoke emissions, with BHD showing lower emissions compared to diesel and biodiesel under certain conditions. Additionally, exhaust particle distributions, analysed using an Engine Exhaust Particulate Sizer Spectrometer (EEPS), provided insights into particulate matter (PM) characteristics. Thermogravimetric analysis (TGA) reveals that soot from BHD and biodiesel is more readily oxidized and undergoes decomposition at lower temperatures compared to diesel fuel, contributing to our understanding of fuel effects on engine performance and emissions for future fuel formulation and combustion optimization strategies.

Keywords: Bio-Hydrogenated Diesel, Green Diesel, PM Distribution, Biofuels, Diesel Particulate Matter

1. INTRODUCTION

From the awareness of the decreasing problem of fossil fuel, the world has been looking for alternative fuels with properties similar to conventional fossil fuels. For diesel fuel, there have been efforts to introduce various types of alternative fuels, such as biodiesel and bio-hydrogenated diesel (BHD).

BHD is a substitute fuel for diesel engines derived from vegetable oils through the hydrogenation process to convert the fatty acids in vegetable oils into alkanes, which are the sole components of diesel fuel (Hilbers et al., 2015, p.3, Boonrod et al., 2017, p.5). This results in reduced viscosity of vegetable oils, increased fuel heating value, and higher cetane index (Bhikuning et al., 2020, p.3). When used in engines, this leads to improved engine performance and helps reduce the emission of certain pollutants. However, a significant drawback of BHD is its poor lubricity compared to diesel fuel (Fathurrahman et al., 2021, p.15). Biodiesel is another popular alternative fuel for diesel engines. It is derived from animal fats or vegetable oils through a chemical process, typically Transesterification, to change the functional group of chemical compounds. The advantage of this type of fuel is the presence of oxygen in the components, which helps reduce pollutants such as carbon monoxide and hydrocarbons (Mofijur et al., 2016, p.275, Kim et al., 2018, p.6, He, 2016, p.575). Another advantage of biodiesel is its excellent lubricity, which comes from the ester groups in its composition (Hazrat et al., 2015). As a result, biodiesel is often blended with traditional diesel fuel to compensate for the lubricity properties lost during the desulfurization process. However, a major drawback of biodiesel is its relatively high viscosity, leading to poor atomization and increased smoke emission when used in real engines (Suh and Lee, 2016, p.1617). Another advantage in the realm of alternative fuels is the blend of BHD with biodiesel. This blend combines the benefits of both fuels, offering improved lubricity from biodiesel's ester groups and the reduced viscosity and enhanced performance of BHD (Prokopowicz et al., 2015, p.7474, Lapuerta et al., 2011, p.2409). The blend addresses the drawbacks of each fuel individually, providing a balanced solution for diesel engines.

Furthermore, comprehending the emission characteristics of alternative fuels used in diesel engines, as opposed to conventional fossil diesel fuel, holds significant importance. Nitrogen oxides (NOx) emissions demonstrated significant reductions with BHD compared to diesel, whereas the BHD-biodiesel blends exhibited notable increases in NOx emissions (McCaffery et al., 2022, p.2). Utilization of bio-hydrogenated diesel in the passenger car can reduce almost of regulated emissions significantly (except NOx which is not clear reduction) due to BHD's higher cetane number, lower viscosity and shorter ignition delay behaviour which promote the better combustion process and fuel atomization (Dimitriadis et al., 2018, p.12). Moreover, understanding the distinct particulate matter (PM) distribution characteristics of biodiesel and BHD fuels compared to conventional diesel is crucial. BHD typically yields higher PM concentrations in both nucleation and accumulation modes due to its shorter ignition delay and potential catalytic effects on PM formation (Karavalakis et al., 2016, p.185). Conversely, biodiesel often results in lower PM concentrations due to its oxygen content, which enhances soot oxidation and reduces volatile organic compounds (Wang et al., 2016, p.574). Blending biodiesel with BHD may alter PM distribution, potentially increasing total PM concentrations compared to neat BHD, possibly due to synergistic effects influencing PM formation. This understanding is essential for evaluating the environmental impact of alternative fuels on PM emissions.

This study aims to evaluate the performance, combustion characteristics, and emissions of a KAWAMA KWM 155 diesel engine fueled by bio-hydrogenated diesel (BHD) and BHD blended with biodiesel, using conventional diesel as a benchmark. Engine operation includes four loads (25%, 50%, 75%, and 90% of maximum torque) with constant speed (1,500 rpm). Fuel consumption, nitrogen oxides (NOx), hydrocarbons (HC), carbon monoxide (CO), particulate matter (PM), and smoke emissions are measured, and combustion characteristics are analyzed across 100 cycles. PM size and concentration in exhaust are assessed using an Engine Exhaust Particulate Sizer Spectrometer (EEPS 3090), with PM decomposition analyzed via Thermogravimetric analysis (TGA).

2. METHODOLOGY
2.1. Test fuels

The test fuels in this study include diesel, BHD and biodiesel. The diesel is the Thailand's commercial diesel which is the blended fuel of diesel fuel and 7% of biodiesel supplied by standard gas station of Petroleum Authority of Thailand, PTT Public Company Limited. BHD is sponsored from Veerasuwan Company limited, Thailand. Biodiesel is supplied by Bio-Synergy Company limited. GC/MS was employed to identify the fuel chemical composition, the detected composition of diesel fuel, BHD and biodiesel were reported in our previous work (Sriprathum et al., 2023, p.31461). The main composition of BHD is hexadecane (C16), pentadecane (C15), and tetradecane (C14). While biodiesel's main composition includes palmitic acid (C16:0), oleic acid (C18:1) and linoleic acid (C18:2).

The biodiesel is mixed with BHD in volume ratios of 10%, 20%, and 30% (yielding BHD90, BHD80, and BHD70 respectively), and their respective fuel properties are evaluated as outlined in Table 1. All properties are assessed following ASTM standards, with criteria determined by the Department of Energy Business, Thailand. Notably, pure BHD oil failed to meet the specific gravity and wear scar diameter (lubricity) standards. However, while BHD90 and BHD80 showed specific gravity values exceeding the standard, their wear scar diameter remained within the specified testing parameters. Conversely, BHD70 exhibited specific gravity and were wearing scar diameter values falling within the prescribed testing range for both properties.

Table 1 : Fuel properties

Fuel Properties	Test Method	Limit	Diesel	BHD	Biodiesel	BHD90	BHD80	BHD70
Kinemetric Viscosity at 40 ℃ (cSt)	ASTM D445	1.8-4.1	3.12	2.58	5.16	2.65	2.80	2.84
Specific Gravity at 15 ℃	ASTM D1298	0.81-0.87	0.830	0.770	0.875	0.788	0.801	0.815
API Gravity at 15 ℃	ASTM D1298	-	39	52	30	48	45	42
Density at 15 ℃ (kg/m^3)	ASTM D1298	-	829	769	874	787	800	814
Cetane Index	ASTM D976	>50	56	78	48	70	65	60
Gross Calorific Value (MJ/kg)	ASTM D240	-	43.48	47.02	39.62	46.26	45.21	44.54
Flash Point (℃)	ASTM D93	>52	78	87	169	86	86	90
Wear Scar Diameter (μm)	ASTM D6079	460	220	570	180	180	180	180
Distillation Temperature	ASTM D86							
50% Recovered (℃)			280	258	356	262	266	270

2.2. Engine test

In this section a KAWAMA KWM 155 diesel engine was employed, its specification detail is shown in Table 2. The study aimed to evaluate the performance parameters, combustion characteristics, and emissions of an engine fueled by BHD and BHD blended with biodiesel, using conventional diesel fuel as the benchmark. Engine speed was maintained at 1,500 rpm while applying four different engine loads (25%, 50%, 75%, and 90% of maximum torque), facilitated by a dynamometer. Fuel consumption rates were meticulously monitored using a fuel consumption rate meter. NOx emissions were quantified using a Testo 350 instrument, while HC and CO were quantified using a Horiba Mexa-441 ME gas analyzer, and smoke emissions were assessed using a Horiba MEXA-600s. Detailed specifications of the measurement equipment are outlined in Table 3 and Table 4. Fuel consumption and emissions were measured three times, with resulting average values calculated. Combustion characteristics were evaluated using pressure sensors (Kistler 6052C) and angular displacement sensors (Kistler 2614C11) positioned on the flywheel, with signals converted using Encoder Electronic 2614C21. The data underwent analysis across 100 cycles, with average values determined using Kibox Cockpit software. A schematic diagram of the test engine is provided in Figure 1.

Table 2: Test engine specification.

Engine	Specification
Engine Model	KWM 155
Engine type	4 stroke, single cylinder, water cooled
Bore x Stroke	100x98 mm
Cylinder volume	769 cc
Compression ratio	18:01
Maximum horse power	13.5 hp @ 2400 rpm
Maximum torque	5.3 kg-m @ 1600 rpm

Table 3: Exhaust gas analysers specification.

Analyzer Model	Measurement Parameter	Measuring Techniques	Measurement Rang	Accuracy
TESTO350	NO	Chemiluminescence	0-4000 ppm	± 5 ppm (0-99 ppm)
				± 5 ppm of reading 100-1,999 ppm
				± 10 ppm of reading (rest of range)
	NO$_2$	Chemiluminescence	0-500 ppm	± 5 ppm (0-99 ppm)
				± 5 ppm of reading (rest of range)
Horiba MEXA-600S	Smoke	Opacity	Opacity: 0.0 to 99.9%	± 0.15 m^{-1} (for ND filter of 1.7 m^{-1} ± 0.05 m^{-1}
			Light absorption coefficient: 0.000 to 9.999 m^{-1}	
Horiba MEXA-441 ME	CO	non-dispersive infrared absorption	0.00% vol to 10.00 % vol	± 0.03 % vol or ± 3% of reading(whichever is greater)
	CO$_2$		0.00% vol to 20.00 % vol	±10 ppm vol or ±4% of reading(whichever is greater)
	HC		0 ppm vol to 20000 ppm vol	±0.4 % vol or ±4% of reading (whichever is greater)
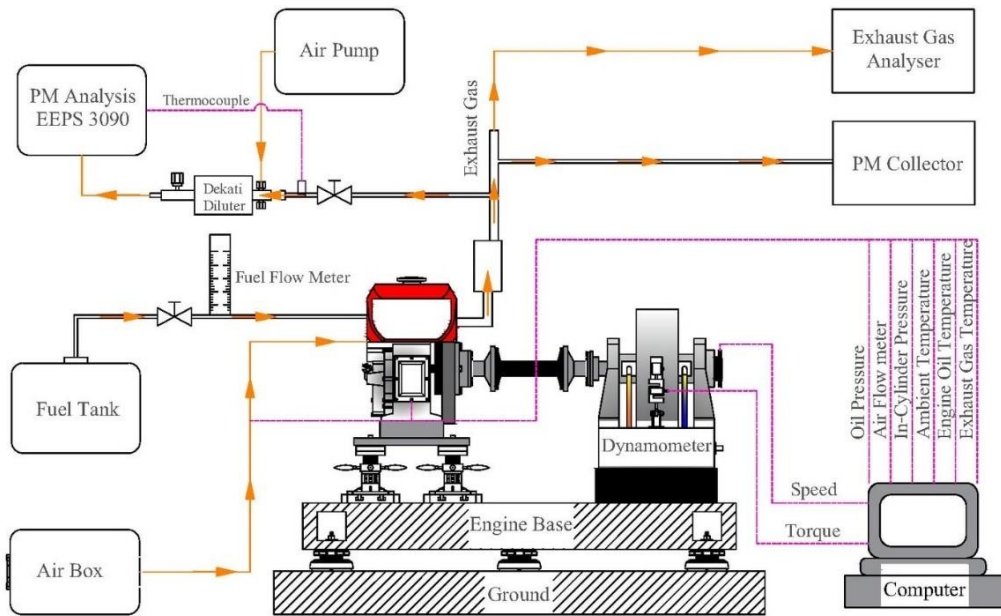
Figure 1: Schematic diagram of the test engine

2.3. Particulate matter analysis

In the assessment of particulate matter (PM) characteristics within engine exhaust, the engine operates at 90% engine load with constant engine speed of 1,500 rpm, a portion of the exhaust gas undergoes dilution with pure air at a temperature of 400°C and a pressure of 4 bars to prevent gas condensation. The dilution ratio is standardized at 64:1. Subsequently, the diluted exhaust gas is directed into the Engine Exhaust Particulate Sizer Spectrometer 3090 (EEPS 3090) manufactured by TSI, facilitating analysis of PM size and concentration. Table 5 shows the specification of EEPS 3090. Meanwhile, the remaining exhaust gas is discharged into the environment through the primary exhaust duct, featuring stainless-steel grids designed to capture PM for subsequent decomposition analysis. The stainless-steel grid filter was tapped to dislodge the particulate matter (PM) onto a stainless-steel tray. Thermogravimetric analysis (TGA) was conducted using the METTLER TOLEDO model TGA/dsc1. Approximately 10 mg of PM was collected, placed in a ceramic crucible, and heated from room temperature to 700°C at a rate of 10°C/min. Analytical-grade oxygen (99.999% purity) was used as the oxidizer, flowing at a rate of 50 ml/min.

Table 4: Specification of EEPS 3090

Particle size range	5.6 to 560 nanometers
Particle size resolution	16 channels per decade (32 total)
Electrometer channels	24 total, 22 active
Charger mode of operation	Dual unipolar diffusion chargers
Inlet cyclone 50% cutpoint	1 μm
Maximum data rate	10 size distributions per second
Aerosol inlet	10 L/min
Sheath air	40 L/min
Inlet aerosol temperature	10 to 52 ℃
Storage temperature	-20 to 50 ℃
Atmospheric pressure correction range	700 to 1034 mbar

3. RESULTS AND DISCUSSION

3.1. Engine performance

The engine's brake specific fuel consumption (BSFC) and brake thermal efficiency (BTE) with various fuels are illustrated in Figure 2. At engine loads up to 75%, BSFC decreases and BTE increases as load rises due to improved energy conversion from higher combustion temperatures (An et al., 2012, p.366). However, at 90% load, excessive fuel injection leads to incomplete combustion, raising fuel consumption and lowering thermal efficiency. BHD's higher heating value and cetane index result in lower BSFC and higher BTE than diesel (Dimitriadis et al., 2020, p.13). Conversely, biodiesel's higher viscosity and lower heating value elevate BSFC and decrease BTE compared to diesel. Increasing biodiesel content lowers BSFC compared to neat biodiesel but remains higher than BHD. The BTE of the blended fuel is lower than BHD at engine loads below 50%, but it becomes higher than BHD's BTE at loads above 50%.
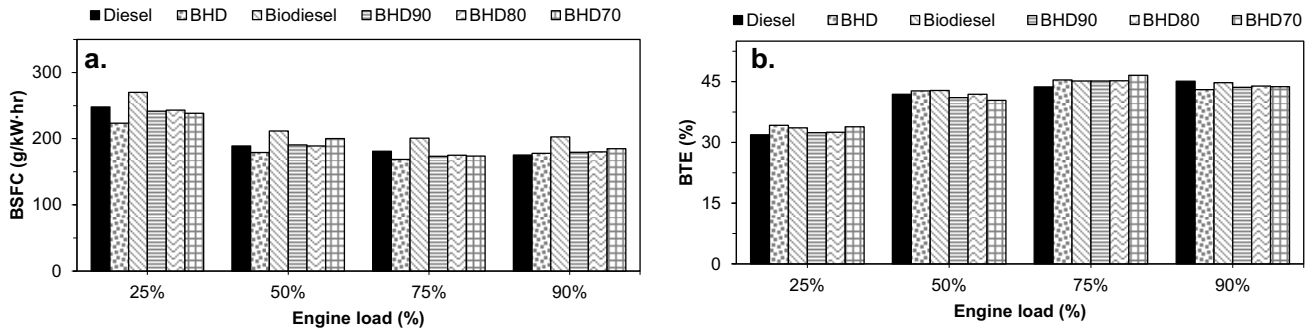
Figure 2: Engine performance at various engine loads.; a. BSFC, b. BTE

3.2. Combustion characteristics

The rate of heat release (RoHR) and in-cylinder pressure (ICP) produced from the engine when operated with different load are shown in Figure 3. It can be observed that the RoHR tends to decrease while ICP tends to increase when engine load increased due to enhanced combustion stability and increased diffusion combustion which is the influence of higher amount of fuel used during combustion process (Liew et al., 2010, p.11362). The start of combustion tends to be shorter as engine load increased due to higher temperature inside the combustion chamber. BHD and biodiesel exhibit shorter ignition delays compared to diesel fuel. This is due to BHD's higher cetane index, which facilitates better fuel-air mixing. Additionally, the higher bulk modulus of biodiesel, influenced by its higher fuel density, results in earlier fuel injection into the combustion chamber, allowing more time for the fuel to absorb heat and combust. Biodiesel provides slightly higher ICP and similar RoHR than diesel fuel due to its higher density which refers to higher fuel mass contributes to increased heat release and pressure buildup during combustion. BHD and its blend provide lower RoHR and ICP may be due to 1) BHD's chemical composition leads to differences in combustion chemistry compared to diesel fuel and 2) BHD's lower density which refer to lower energy concentration (Parravicini et al., 2021, p.6).
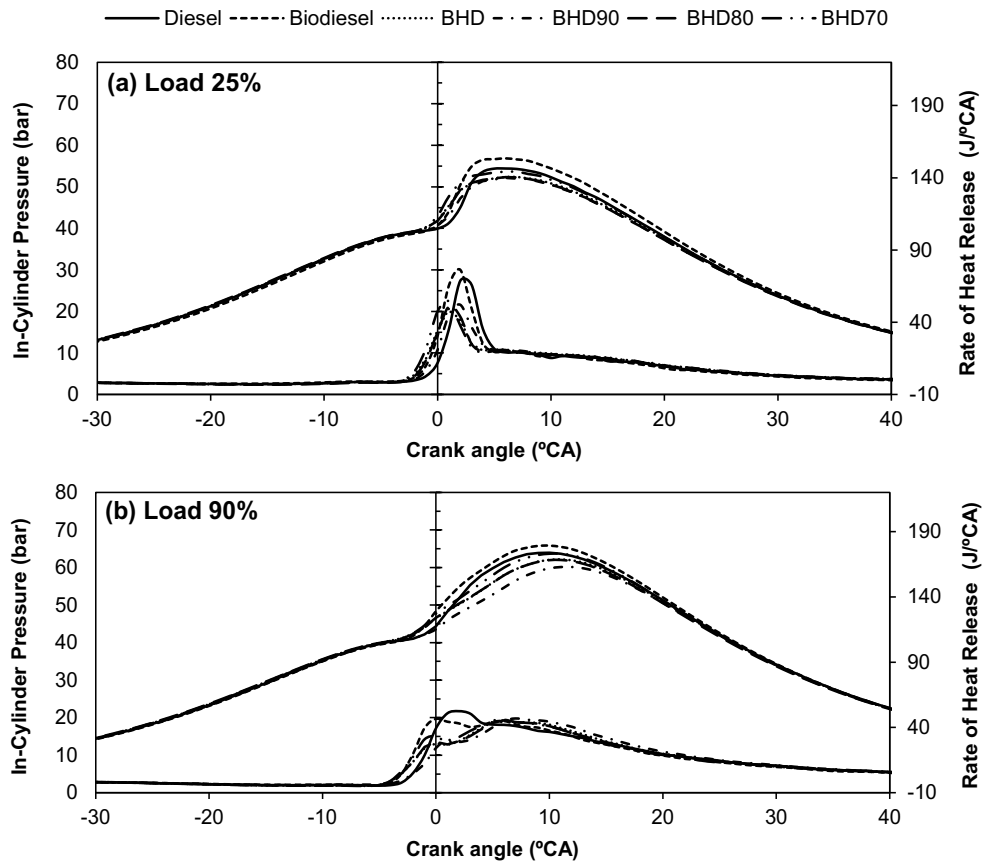
Figure 3: In-cylinder pressure and rate of heat release over crank angle at various engine loads

3.3. Emissions

The emissions from the engine when operating with different engine loads are shown in Figure 4. It was found that as the load increased, NOx emissions increased to the highest point at 50% load for diesel fuel, BHD, and BHD80, and at 75% load for the remaining fuels. This may be due to the appropriate air-to-fuel ratio at these loads, resulting in reduced NOx formation. It can be observed that each fuel has a different optimal air-to-fuel ratio at different loads. BHD fuel releases less NOx than diesel fuel at all loads due to its shorter ignition delay leading to longer periods of controlled combustion and reduced NOx emissions (Parravicini et al., 2021, p.13, Karavalakis et al., 2016, p.181, Singer et al., 2015, p.600). Biodiesel and BHD-biodiesel blends release higher levels of NOx than diesel fuel and BHD significantly due to lower turbulence within the combustion chamber which influenced by higher kinematic viscosity property result in localized regions of rich or lean fuel-air mixtures, promoting uneven combustion and NOx formation (Som and Longman, 2011, p.1383, Saqr et al., 2010, p.612). Unburnt hydrocarbon (HC) emission from diesel fuel and biodiesel tend to decrease as engine load increased while there is no clear trend from BHD and its blended fuel. Carbon monoxide (CO) emission tends to decrease when engine load rises from 25% to 50% and then CO emission tends to increase when engine load increases to 75% and 90% may be due to at 50% engine load closer to its design conditions, resulting in more efficient combustion while at higher engine loads, there is a greater demand for power, leading to increased fuel injection. However, under these conditions, the combustion process may not be as efficient, resulting in incomplete combustion of the fuel-air mixture. BHD provides lower CO emission than diesel fuel and biodiesel due to BHD's lower kinematic viscosity and shorter ignition delay behavior result in better fuel atomization and longer combustion duration (Wu et al., 2017, p.901). Biodiesel and BHD-biodiesel blends provide higherCO emission than BHD due to its higher kinematic viscosity refer to worse fuel atomization. Smoke emission tends to increase as engine load increased due to more engine power required for maintaining engine operating speed which contributes to higher amount of fuel being injected to combustion chamber. At 25% engine load, biodiesel provides higher smoke emission than the other fuels due to its higher kinematic viscosity which refers to worse fuel atomization behavior. At 50% load, there is a minimal disparity in smoke emissions across all fuels, likely attributable to these conditions being optimal for engine operation. While at 75% and 90% engine load, BHD provides slightly lower smoke emission than that diesel fuel due to shorter ignition delay and long combustion duration behavior. Biodiesel provides lower smoke emission than BHD due to oxygen content in biodiesel composition which can promote the soot oxidation (Song et al., 2006, p.603). At 25% and 50% engine loads, the smoke emissions from BHD-biodiesel blend fuels are not significantly different from those of pure BHD, likely due to optimized fuel injection quantities. However, at 75% and 90% engine loads, smoke emissions from blend fuels tend to be higher than those from BHD. This is due to the higher kinematic viscosity of biodiesel, which affects the blend fuels' kinematic viscosity, resulting in poorer fuel atomization and reduced soot oxidation.
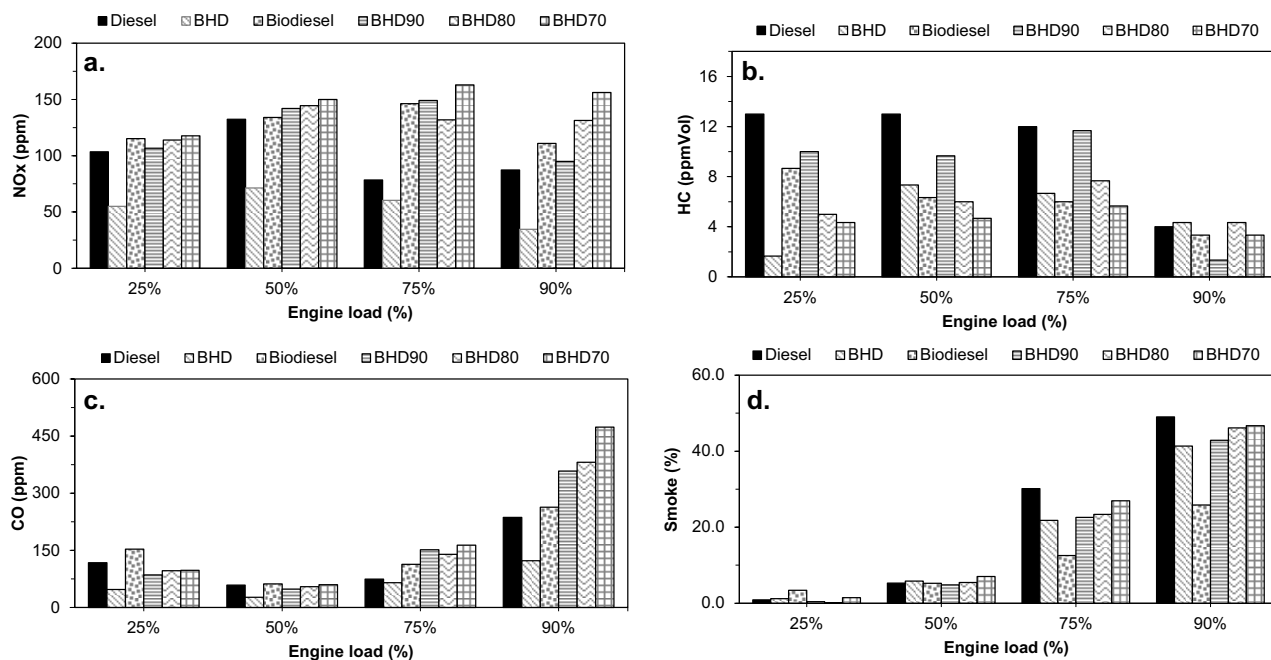
. Figure 4: Exhaust emission from the engine when operated with different engine load; a. NOx, b. HC, c. CO and d. smoke

3.4. Particulate matter

The particle number versus size distributions from the engine, fuelled with various fuels, are depicted in Figure 5. It is evident that the particle numbers in BHD exhaust exceed those in diesel fuel for both the nucleation (ultrafine particles formed through nucleation and condensation during combustion) and accumulation modes (larger particles formed through coagulation and surface growth). This due to BHD's shorter ignition delay behaviour accelerates combustion, leading to heightened temperatures and more reactive species in the combustion chamber. This environment can foster accumulation mode PM formation through processes such as coagulation and surface growth (Xu et al., 2013, p.7581). As a result, biodiesel yields lower particle numbers in both nucleation and accumulation modes compared to BHD and diesel fuel, attributable to its lower aromatic hydrocarbon content than diesel fuel and higher oxygen content than BHD which can promote the soot oxidation. The presence of biodiesel in blend fuels tends to further reduce particle numbers in both modes due to biodiesel's oxygen content, which promotes soot oxidation. Figure 6 illustrates the total concentration of particulate matter across various engine loads, revealing that BHD yields a higher total PM concentration than diesel fuel, while biodiesel yields lower concentrations than both BHD and diesel fuel. This suggests that the oxygen content in the fuel reduces the total PM concentration by promoting soot oxidation, resulting in lower PM concentrations (Su et al., 2013, p.4). The utilization of BHD-biodiesel blend fuels might result in higher total PM concentrations than neat BHD fuel, despite the potential

decrease attributed to biodiesel's oxygen content. This could be due to the interaction between biodiesel and BHD, potentially altering the fuel composition and generating additional PM precursors during combustion. However, as the biodiesel content increases in the blend fuel, there is a tendency for PM emissions to decrease.

To gain deeper insights into the impact of biodiesel on PM decomposition, thermogravimetric analysis was conducted, and the results were presented in Figure 7 and the derivative of weight loss was shown in Figure 8. The decomposition temperature of PM from BHD was observed to be 4.71 ℃ lower than that of diesel fuel, possibly due to the influence of BHD or its combustion by-products, which aid in the thermal degradation of PM at lower temperatures compared to diesel fuel. Additionally, biodiesel exhibited a decomposition temperature 10.22 ℃ lower than diesel fuel, attributed to the oxygen functionalities present in biodiesel enhancing the reactivity of PM, resulting in earlier decomposition at lower temperatures compared to PM derived from diesel fuel. Moreover, the inclusion of biodiesel in blend fuel formulations tended to reduce the decomposition temperature of PM slightly, attributable to the biodiesel's chemical composition promoting the PM oxidation.
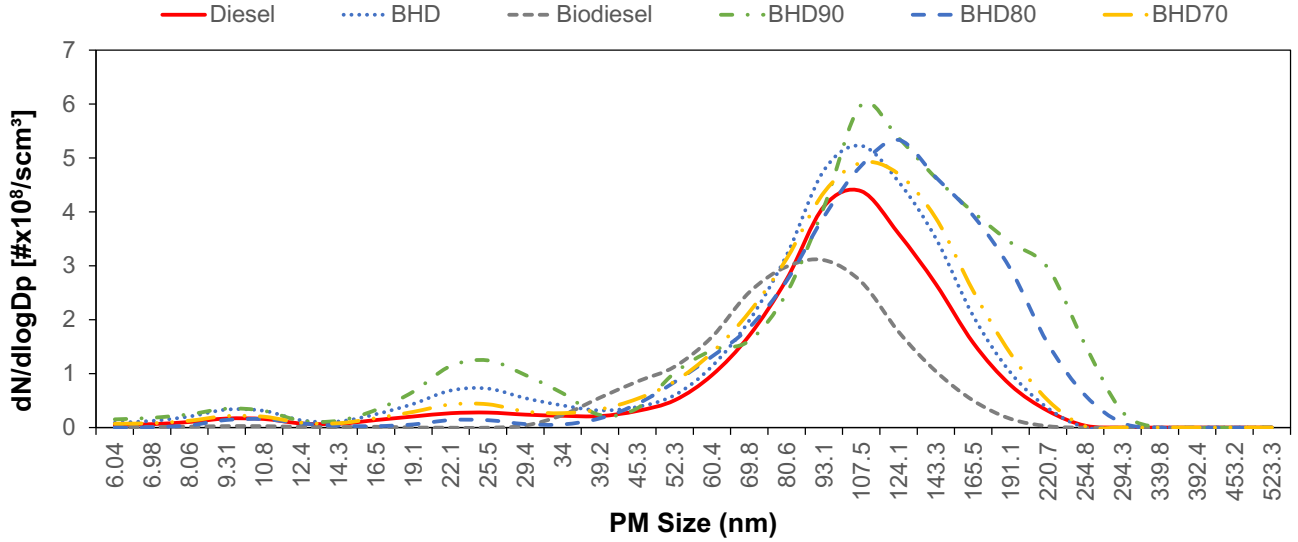
Figure 5: Particulate matter size distribution from different fuel at 90% engine load
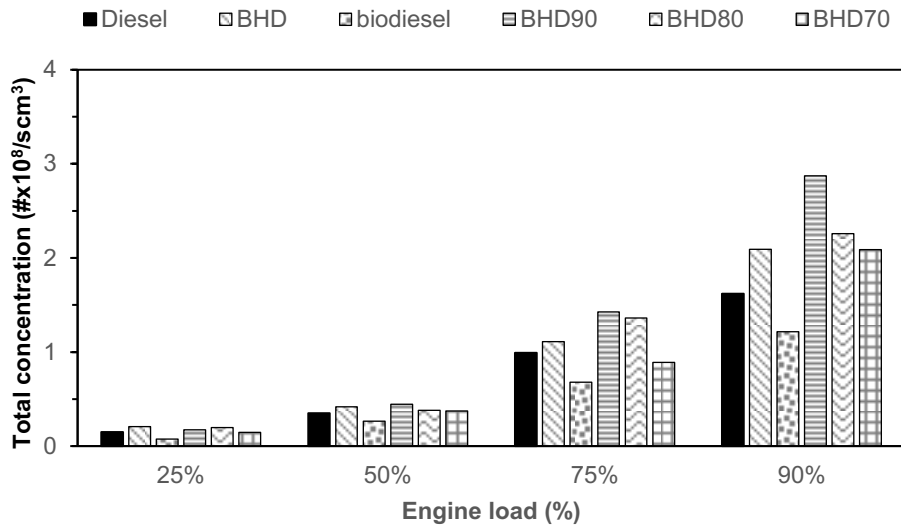
Figure 6: Total PM concentration from different engine load
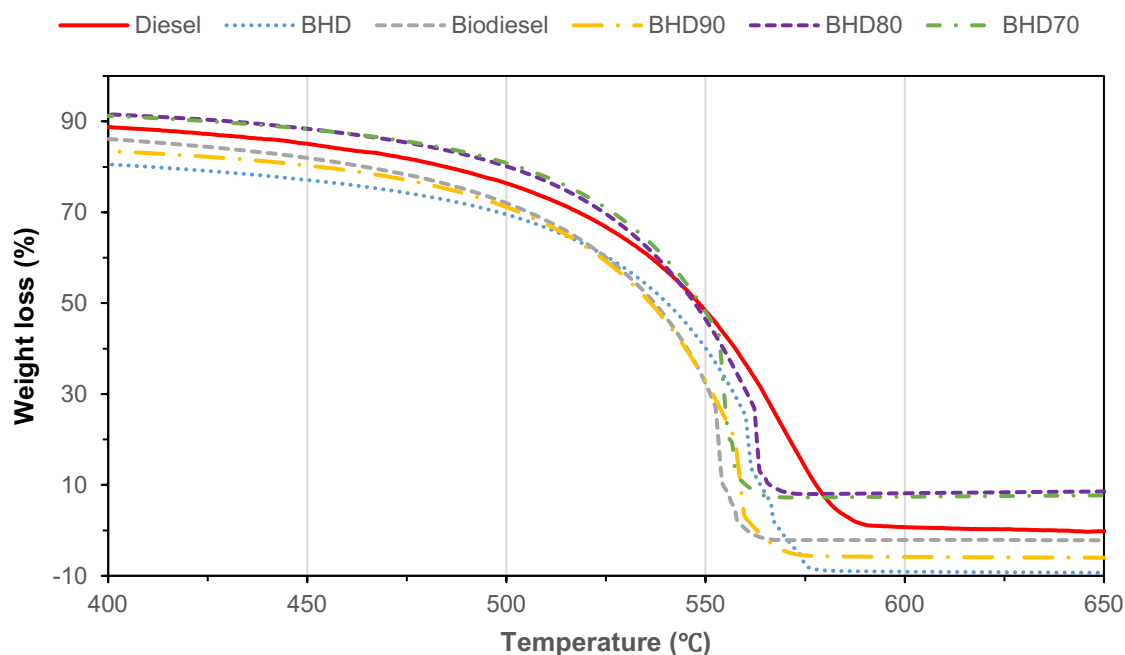
Figure 7: Thermogravimetric analysis curve of PM from different fuel
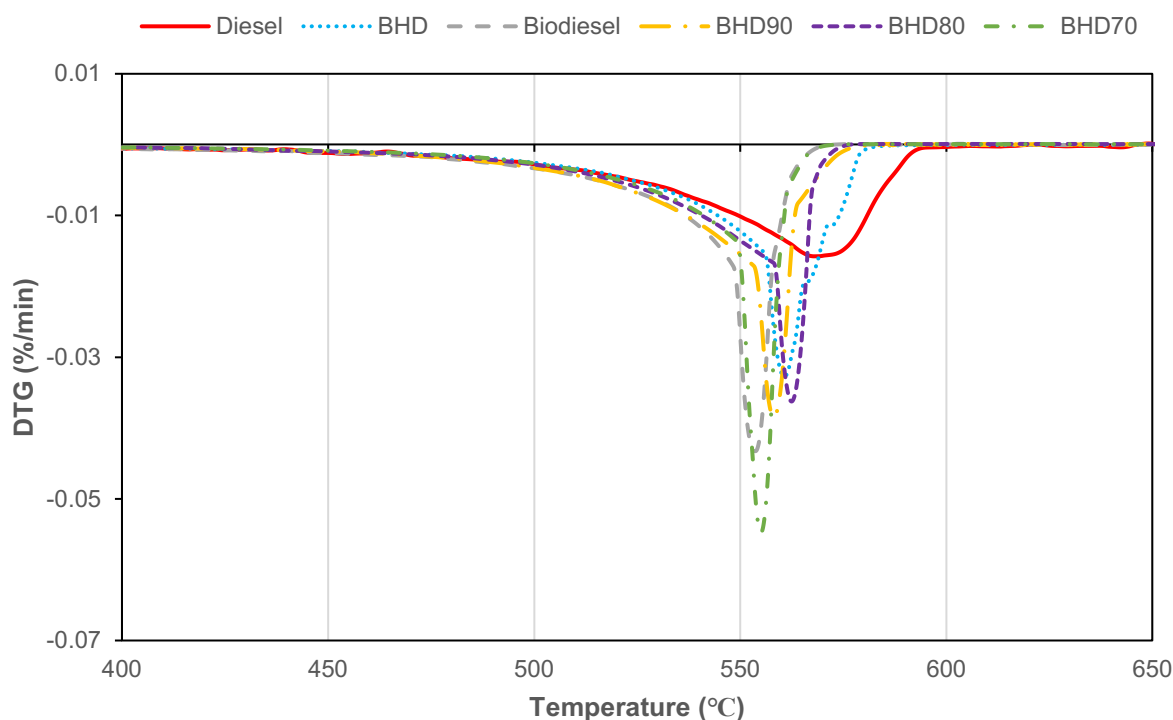
Figure 8: Derivative of weight loss over temperature from different fuel

4. CONCLUSION

- Engine performance varies with fuel types and loads. BHD generally outperformed diesel and biodiesel in efficiency, except at higher loads. Higher loads improved combustion stability, increased pressure, and decreased heat release. BHD and biodiesel had shorter ignition delays than diesel.
- Emissions varied with fuel and load. NOx emissions increased with load up to certain points. BHD produced less NOx than diesel, while biodiesel produced more. HC and CO emissions showed mixed trends. Smoke emissions increased with load, but biodiesel produced less smoke due to its oxygen content. BHD-biodiesel blends had higher smoke emissions than pure BHD.
- BHD produced more exhaust particles than diesel, while biodiesel reduced particle numbers. Total PM concentration was higher with BHD than diesel, but lower with biodiesel. BHD-biodiesel blends produced more PM than pure BHD.
- Thermogravimetric analysis showed that PM from BHD and biodiesel decomposed at lower temperatures than diesel PM, indicating enhanced oxidation potential. Adding biodiesel to BHD further lowered PM decomposition temperature.

5. REFERENCES

AN, H., YANG, W., CHOU, S. & CHUA, K. 2012. Combustion and emissions characteristics of diesel engine fueled by biodiesel at partial load conditions. Applied energy, 99**,** 363-371.

BHIKUNING, A., SUGAWARA, R., MATSUMURA, E. & SENDA, J. 2020. Investigation of spray characteristics from waste cooking oil, bio-hydro fined diesel oil (BHD) and n-tridecane in a constant volume chamber. Case Studies in Thermal Engineering, 21**,** 100661.

BOONROD, B., PRAPAINAINAR, C., NARATARUKSA, P., KANTAMA, A., SAIBAUTRONG, W., SUDSAKORN, K., MUNGCHAROEN, T. & PRAPAINAINAR, P. 2017. Evaluating the environmental impacts of bio-hydrogenated diesel production from palm oil and fatty acid methyl ester through life cycle assessment. Journal of Cleaner Production, 142**,** 1210-1221.

DIMITRIADIS, A., NATSIOS, I., DIMARATOS, A., KATSAOUNIS, D., SAMARAS, Z., BEZERGIANNI, S. & LEHTO, K. 2018. Evaluation of a hydrotreated vegetable oil (HVO) and effects on emissions of a passenger car diesel engine. Frontiers in Mechanical Engineering, 4**,** 7.

DIMITRIADIS, A., SELJAK, T., BAŠKOVIČ, U. Ž., DIMARATOS, A., BEZERGIANNI, S., SAMARAS, Z. & KATRAŠNIK, T. J. F. 2020. Improving PM-NOx trade-off with paraffinic fuels: A study towards diesel engine optimization with HVO. Fuel, 265**,** 116921.

FATHURRAHMAN, N. A., AUZANI, A. S., ZAELANI, R., ANGGARANI, R., AISYAH, L., MAYMUCHAR, M. & WIBOWO, C. S. 2021. Lubricating Properties of Diesel Fuel and Hydrogenated Vegetable Oil with Palm Oil Biodiesel Blends Using HFRR Method. Available at SSRN 3978729.

HAZRAT, M., RASUL, M. & KHAN, M. 2015. Lubricity improvement of the ultra-low sulfur diesel fuel with the biodiesel. Energy Procedia, 75**,** 111-117.

HE, B.-Q. 2016. Advances in emission characteristics of diesel engines using different biodiesel fuels. Renewable Sustainable Energy Reviews, 60**,** 570-586.

HILBERS, T. J., SPRAKEL, L. M., VAN DEN ENK, L. B., ZAALBERG, B., VAN DEN BERG, H., VAN DER HAM, L. G. & TECHNOLOGY 2015. Green diesel from hydrotreated vegetable oil process design study. Chemical Engineering, 38**,** 651-657.

KARAVALAKIS, G., JIANG, Y., YANG, J., DURBIN, T., NUOTTIMäKI, J. & LEHTO, K. 2016. Emissions and fuel economy evaluation from two current technology heavy-duty trucks operated on HVO and FAME blends. SAE International Journal of Fuels Lubricants, 9**,** 177-190.

KIM, D. S., HANIFZADEH, M. & KUMAR, A. 2018. Trend of biodiesel feedstock and its impact on biodiesel emission characteristics. Environmental Progress Sustainable Energy, 37**,** 7-19.

LAPUERTA, M., VILLAJOS, M., AGUDELO, J. R. & BOEHMAN, A. L. 2011. Key properties and blending strategies of hydrotreated vegetable oil as biofuel for diesel engines. Fuel processing technology, 92**,** 2406-2411.

LIEW, C., LI, H., NUSZKOWSKI, J., LIU, S., GATTS, T., ATKINSON, R. & CLARK, N. 2010. An experimental investigation of the combustion process of a heavy-duty diesel engine enriched with H2. International Journal of Hydrogen Energy, 35**,** 11357-11365.

MCCAFFERY, C., ZHU, H., AHMED, C. S., CANCHOLA, A., CHEN, J. Y., LI, C., JOHNSON, K. C., DURBIN, T. D., LIN, Y.-H. & KARAVALAKIS, G. 2022. Effects of hydrogenated vegetable oil (HVO) and HVO/biodiesel blends on the physicochemical and toxicological properties of emissions from an off-road heavy-duty diesel engine. Fuel, 323**,** 124283.

MOFIJUR, M., RASUL, M., HYDE, J., AZAD, A., MAMAT, R., BHUIYA, M. J. R. & REVIEWS, S. E. 2016. Role of biofuel and their binary (diesel–biodiesel) and ternary (ethanol–biodiesel–diesel) blends on internal combustion engines emission reduction. Renewable Sustainable Energy Reviews, 53**,** 265-278.

PARRAVICINI, M., BARRO, C. & BOULOUCHOS, K. 2021. Experimental characterization of GTL, HVO, and OME based alternative fuels for diesel engines. Fuel, 292**,** 120177.

PROKOPOWICZ, A., ZACIERA, M., SOBCZAK, A., BIELACZYC, P. & WOODBURN, J. 2015. The effects of neat biodiesel and biodiesel and HVO blends in diesel fuel on exhaust emissions from a light duty vehicle with a diesel engine. Environmentalscience technology, 49**,** 7473-7482.

SAQR, K. M., ALY, H. S., SIES, M. M. & WAHID, M. A. 2010. Effect of free stream turbulence on NOx and soot formation in turbulent diffusion CH4-air flames. International Communications in Heat Mass Transfer, 37**,** 611-617.

SINGER, A., SCHRöDER, O., PABST, C., MUNACK, A., BüNGER, J., RUCK, W. & KRAHL, J. 2015. Aging studies of biodiesel and

HVO and their testing as neat fuel and blends for exhaust emissions in heavy-duty engines and passenger cars. Fuel, 153,595-603.

SOM, S. & LONGMAN, D. 2011. Numerical study comparing the combustion and emission characteristics of biodiesel to petrodiesel. Energy Fuels, 25, 1373-1386.

SONG, J., ALAM, M., BOEHMAN, A. L., KIM, U. & FLAME 2006. Examination of the oxidation behavior of biodiesel soot. Combustion flame, 146, 589-604.

SRIPRATHUM, S., MANEEDAENG, A., KLINKAEW, N. & SUKJIT, E. 2023. Comprehensive analysis of properties of green diesel enhanced by fatty acid methyl esters. RSC advances, 13, 31460-31469.

SU, J., ZHU, H. & BOHAC, S. V. 2013. Particulate matter emission comparison from conventional and premixed low temperature combustion with diesel, biodiesel and biodiesel–ethanol fuels. Fuel, 113, 221-227.

SUH, H. K. & LEE, C. S. 2016. A review on atomization and exhaust emissions of a biodiesel-fueled compression ignition engine. Renewable Sustainable Energy Reviews, 58, 1601-1620.

WANG, Y., LIU, H. & LEE, C.-F. F. 2016. Particulate matter emission characteristics of diesel engines with biodiesel or biodiesel blending: A review. Renewable Sustainable Energy Reviews, 64, 569-581.

WU, Y., FERNS, J., LI, H. & ANDREWS, G. 2017. Investigation of combustion and emission performance of hydrogenated vegetable oil (HVO) diesel. SAE International Journal of Fuels Lubricants, 10, 895-903.

XU, Z., LI, X., GUAN, C. & HUANG, Z. 2013. Characteristics of exhaust diesel particles from different oxygenated fuels. Energy fuels, 27, 7579-7586.

#221: Building integrated total-salt solution-system

Heinz-axel Guo[1], Zhao-chuan Hou[2]

[1] Sino-German College Applied Sciences Tongji University, Shanghai, China, Haixinguo@Hotmail.Com
[2] yuan-Neng (Suzhou) Environment Technology Co., Ltd., Suzhou, China, 13520478743@139.Com

Abstract: As an advantageous technology with energy density much higher than that of water and phase change materials in various energy storage technologies, although the application of salt-solution energy storage has been fully studied, there is still a lack of further expansion in the substitution of cold and heat sources in buildings. Most of the research results are limited to the use of absorption heat pumps for cold and heat conversion, and there is a lack of further use of salt solutions as a "the fourth medium" to replace refrigerants or water or air to drive the indoor ends, further, to complete the 10 tasks of creating a suitable hot and humid indoor environment. Since the salt-solution has both heat exchange as a liquid through the temperature difference between it and the environment, and as a humidifier through the difference between its surface vapor pressure and the ambient water vapor partial pressure to cause moisture migration, a salt-solution as a medium of heat and moisture exchange end is conceivable and achievable. The energy density and efficiency of the system will be much higher than that of the traditional system if the salt-solution-only heat and moisture exchange end is 15 fully applied and the salt-solution-only transmission and distribution system is set up in the building. At the same time, due to the high density and durability of salt-solution energy storage, as well as the better adaptability between salt-solution regeneration and renewable energy, the all-salt-solution integrated thermal and humid environment construction system should have much higher performance than the traditional system in improving system efficiency, applying renewable energy, and storing energy across seasons, until the realization of zero-carbon buildings.

1. INTRODUCTION

Since the introduction of radiant heat transfer technology in Europe, it has been flourishing in China for more than 20 years, gradually forming a complete industrial chain with manufacturers, engineering integrators, and 25 R&D departments, providing comfortable indoor thermal and humidity environments for many industrial and civilian customers. However, it cannot be denied that there are many technical barriers in the process of localization and the implementation of engineering practices. The biggest challenge is adaptability to climate. We know that the technology originated in Western and Central Europe, where the latitude is high, the summer temperature is low, and the humidity is not high, which is very different from the monsoon climate 30 in China, especially in the southern region where high temperature and high humidity are the norm in summer, and there are even more severe natural conditions such as the rainy season and the phenomenon of "return 2 / 10 of the south." in order to make radiant heat transfer technology take root, a lot of effort has been put into indoor humidity control technology in China, and many new air dehumidification equipment have been developed to adapt to various climate zones from north to south, and great achievements have been made. However, there is still ongoing exploration in improving energy efficiency utilization, and there are indeed not many excellent 5 energy-saving case studies among the engineering projects that have been implemented in China. Currently, professionals in this field are also doing a lot of work in technical research, hoping to achieve a qualitative breakthrough in control systems, product energy optimization, and integration of wind and water systems. The innovation of this article lies in the attempt to find a suitable medium, terminal device, or a completely new system for simultaneous heat and moisture exchange in indoor environments, which can have good 10 adaptability to high temperature and high humidity climate and create a more suitable indoor thermal and humidity environment.

2. "THE FOURTH MEDIUM" - SALT SOLUTION

The task of maintaining the thermal and humid environment of buildings can be carried out using more than just water, air, and refrigerants as the medium. Solutions can serve the same purpose as these three media. 15 Moreover, water and refrigerants can only transport heat, but cannot deliver air with the desired indoor air quality directly to the people in the room, so they have got to rely on terminal equipment to further process the air in the room through circulation, which requires a certain amount of heat energy reserve for the preparation and transportation of the medium, thus limiting the overall system's efficiency. However, solutions should have the ability to carry chemical energy, and by adjusting the concentration of the solution, they can form chemical 20 potential energy, also known as "solution potential energy," which provides much greater energy carrying capacity than air, water, and refrigerants in cases where high humidity control is required. As a solution with chemical potential energy, it can not only provide the chemical energy needed for dehumidification, but also the chemical energy needed for absorption refrigeration. In principle, the concentrated solutions required by the two devices can be the same medium. Therefore, it is possible to regard the solution as the "fourth medium" 25 suitable for high temperature and high humidity climate conditions.

3. KEY COMPONENTS OF A SALTWATER SOLUTION SYSTEM

3.1. The Separate Absorption Heat Pump （As shown in Figure 1）

The Separate Absorption Heat Pump employs the absorption refrigeration/heat pump principle but is not 30 a complete absorption refrigeration/heat pump machine. In the system, there is only a combined absorber A and evaporator B, which absorb the steam in the sealed cavity through the absorber and release heat, while creating a vacuum; then, the heat in the phase change and dilution process of the solution in the absorber's heat exchanger is extracted by the evaporator's heat exchanger, and the heat of the medium in the evaporator's heat exchanger is provided to the water vaporization to provide cold to the surrounding area. The 35 entire device maintains a certain degree of vacuum, which depends on the water temperature required by the system (pressure-phase change point relationship). The partition is an insulating material, and the semiconductor cooling element is distributed on it. When additional cold is needed, it can be further enhanced by applying electricity to transfer heat from the evaporator side to the absorber side. The medium in the heat exchanger is also a solution, which circulates and is heated or cooled depending on the required operating 3 / 10 conditions, switching between the flow of heated and cooling the solution in the winter and summer operation, and pure dehumidification operation.
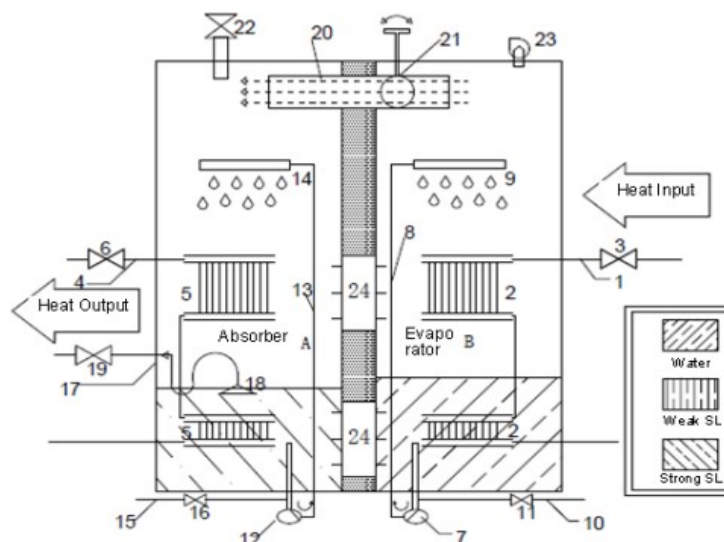

Figure 1: Principle of separate-type absorption refrigeration cycle

1. Cold medium circulation; 2. Cold medium heat 5 exchanger; 3. Cold medium control valve; 4. Hot medium circulation; 5. Hot medium heat exchanger 6. Hot medium control valve; 7. Cold water circulation pump; 8. Cold water inner circulation pipe; 9. Cold water distributor; 10. Cold water make-up pipe; 11. 10 Cold water make-up control valve ;12. Solution circulation pump; 13. Solution inner circulation pipe; 14. Solution distributor; 15. Concentrated solution make-up pipe; 16. Concentrated solution controlvalve; 17. Dilute solution discharge pipe ;18. Dilute solution suction port; 15 19. Dilute solution control valve; 20. Steam channel; 21. Steam control valve; 22. Negative pressure control valve; 23. Vacuum pump24. Semiconductor refrigeration element

3.2. Energy Storage and Damping Integrated Solution Tank (As shown in Figure 2)

Principle Description

In the indoor temperature and humidity regulation process, a concentrated solution is supplied to the system, and a dilute solution is collected. The buffer solution tank can maintain the system's ability to operate without the need for continuous supply of concentrated solutions from the regeneration end and continuous discharge of dilute solution for a certain time;

The siphon tube 5 between the concentrated solution and diluted solution can maintain a continuous balance of the solution levels on both sides during operation, so that the solution circulation remains continuous.

The addition of cold and heat to the system will be carried out by a separating absorption heat pump, and the thermal energy will be transferred between the concentrated solution and dilute solution by the heat dissipation ability of the buffer tank's shell and the embedded semiconductor cooling plate. The temperature of one of the 30 solutions will be adjusted deliberately to improve the system's thermal efficiency, and the other solution will be used as a storage medium to simplify the system.

At the bottom (or lower side) of the equipment, multiple outlet ports (9, 10) are provided separately on the side of the concentrated solution side (1-SS) and diluted solution side (2-DS), which are used as distributors for connecting to the end devices (absorption heat pump, integrated panel, fresh air treatment device, etc.). Depending on the complexity of the system, multiple outlets can be provided, or additional distributors can be added outside the outlets. Each outlet is equipped with a corrosion-resistant control valve. The negative Figure 1: Principle of Separate-Type Absorption Refrigeration Cycle 4 / 10 pressure required for discharge is generated by the system drive pump (peristaltic pump) connected to each discharge port;

At the top (or upper side) of the equipment, multiple inlet ports (7, 8) are provided separately on the side of the concentrated solution side (1-SS) and diluted solution side (2-DS) as collectors for recovering the solutions 5 after each circulation is completed. Depending on the complexity of the system, multiple inlets can be provided, or additional collectors can be added outside the inlets. Each inlet is equipped with a corrosion-resistant control valve, and a peristaltic pump is installed at the inlet to serve as the circulation drive for the corresponding solution loop;

The peristaltic pump will generate negative pressure in the corresponding circulation loop, overcoming system 10 resistance and completing the solution circulation. At this point, the single system will start from the corresponding suction port (9, 10) and consist of pipes, fittings, end devices (absorption heat pumps, integrated panels, air treatment devices, etc.), peristaltic pumps, and injection ports (7, 8), with the zero-pressure point being the accumulator tank. The entire system is under a negative pressure state, thereby reducin g the potential loss of indoor decoration and furniture caused by system leaks;
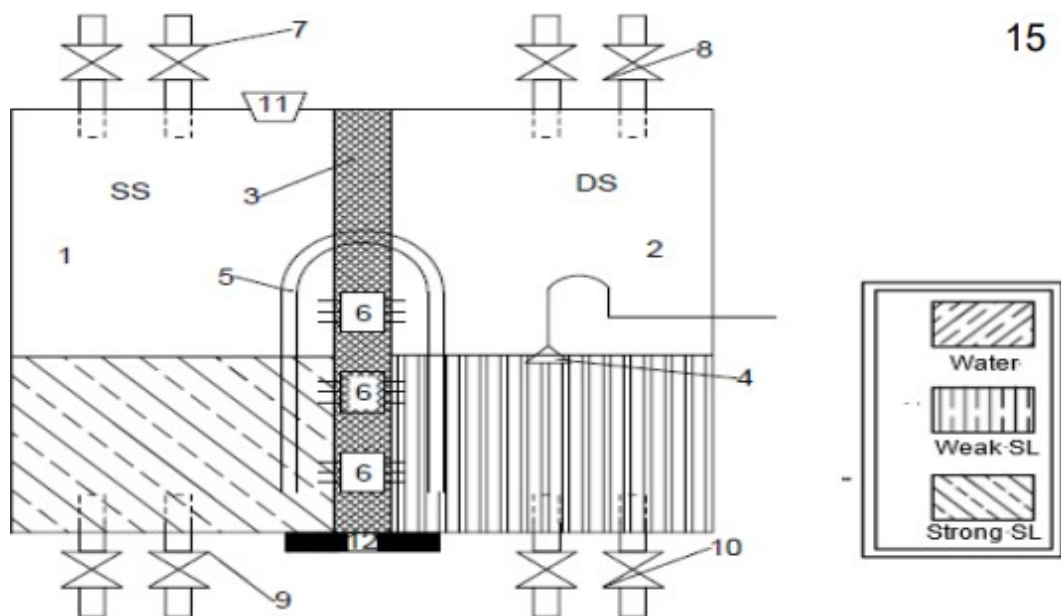
Figure 2: A schematic diagram of an integrated energy storage and buffer solution tank

1. Concentrated Solution Storage Tank; 2. Diluted Solution Storage Tank; 3. Separation Plate; 4. Diluted Solution High-Elevation Suction Outlet; 5. Siphon Tube; 6. Semiconductor Thermoelectric Cooling Sheet; 7. Concentrated Solution Return Liquid Inlet; 8. Diluted 20 Solution Return Liquid Inlet; 9. Concentrated Solution Suction Outlet; 10. Diluted Solution Suction Outlet; 11. Powder/Concentrated Paste Inlet; 12. Ultrasonic Oscillator

3.3. Diatom mud absorbent panel + integrated panel with hollow Fiber membrane (As shown in Figure 3)

The Challenges Faced by Radiant Panels in High Temperature and High Humidity Regions

We know that the wet environment in buildings is a key factor affecting human thermal comfort, human health, building structural durability, and building energy consumption. The indoor wet environment is not only the relative humidity of the air, but also the humidity of the walls. The process of absorbing and releasing moisture by the building envelope affects both the dynamic moisture balance of the indoor air and the thermal balance process of the indoor air. The condensation and dew on the building surfaces and interior will make the thermal performance of the building envelope worse, increase the building heating and air conditioning energy consumption, and make the durability of the building envelope worse. Excessively high indoor relative humidity will inevitably cause the materials in the building to absorb moisture, especially the wall surfaces will experience moist migration under the combined action of water vapor in the air and the moisture content of the wall materials. Excessively high wall material moisture content will cause mold growth and trigger variety. Figure 2 shows a schematic diagram of an integrated energy storage and buffer solution tank 5 / 10 of human diseases. Therefore, humidity control is the top priority in the high temperature and high humidity areas of the south.

In high temperature and high humidity regions, the outdoor air moisture content is too high, which causes the air system to have excessively high preparation energy consumption throughout the year, further limiting the ability of the fresh air system to alleviate the moisture load. This problem will further affect the contribution of the air system in controlling indoor moisture migration, with the hidden danger being uncontrolled moisture migration between indoor air and the inner wall surface. The radiant panel air conditioning system with gypsum board/calcium silicate board as the surface material needs to be combined with fresh air dehumidification but can only solve the control of indoor air relative humidity and cannot solve the problem of moisture migration within the wall.

Currently, there are two solutions to this problem in China: passive use of moisture-regulating materials and active wiring-type electromigration dehumidification. For high-temperature and high-humidity areas, due to the need to remove a large amount of moisture load indoors, the moisture-regulating performance of the material will decrease after a certain period of use. How to let the nearly saturated moisture-regulating material release 15 moisture without affecting the indoor relative humidity control is also a key issue to be considered in passive moisture-regulating technology. Wiring-type electromigration dehumidification mainly solves the problem of water seepage from the soil side into the structural wall of the underground room, causing the wall to become damp and moldy. However, the wall is a porous medium material, and it is inevitable that water vapor will migrate within the wall under the long-term erosion of outdoor rain and snow and other harsh weather 20 conditions. Therefore, the ideal solution is to find a medium or air-conditioning end product that can simultaneously solve the problems of temperature and humidity control.

As an "upgraded" version of radiant cooling systems, the structure of enthalpy-panel is more likely to that of radiant panels, but their heat and moisture exchange capabilities are entirely different. By changing the physical properties of the materials used to construct the enthalpy-panel body and channels, it is possible to 25 enable water migration within the panel, thereby allowing for simultaneous control of indoor temperature and humidity.
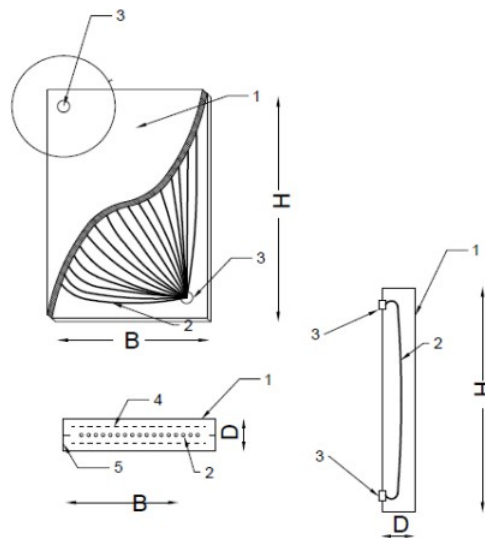
Figure 3: Enthalpy-panel embedded in porous material with hollow Fiber

1. *Diatom mud and additives (such as plant Fibers) 2. Hollow Fiber membrane 3. Bundle joint 4. Nylon Fiber mesh 5. Edge trimComparison of the structure and function of radiation panels*

Table1: Comparison of radiant panels and integrated radiant panels in structure and function

	Radiant Panels	Integrated Radiant Panels
Sheet materials	Metal sheets/gypsum boards/ calcium silicate boards	Diatom mud composite boards
Pipe materials	Copper pipes/plastic pipes	Hollow Fiber membrane filaments
Medium	Water/steam	Desiccant solution
Functions	Thermal exchange (cold/hot radiation)	Heat and mass transfer (cold/hot radiation + absorption and regeneration)

In the enthalpy-, hollow fiber membrane strands are embedded, and the solution (calcium chloride, lithium chloride, lithium bromide) circulates within the strands. The concentration of the solution is adjusted according to the needs. When the indoor air humidity is high, the moisture in the indoor humid air is adsorbed by the wall moisture regulation material. When the moisture content of the moisture regulation material is higher than the relative surface vapor pressure of the solution in the hollow fiber membrane strands, the moisture will further migrate from the moisture regulation material through the hollow fiber membrane wall to the solution in the tube, so that the moisture content of the moisture regulation material decreases again and has its ability to further absorb moisture from the indoor air. Under the premise of the continuous circulation of the solution to maintain the concentration of the solution in the hollow fiber, the moisture regulation wall's adsorption dehumidification process can continue, in fact forming a dehumidification process for the indoor air. If the solution concentration is low, i.e., the solution surface 15 vapor pressure is high, and the indoor air humidity is low, the moisture in the moisture regulation material will evaporate and migrate to the air, while when the moisture content of the moisture regulation material is lower than the relative surface vapor pressure of the solution, the moisture in the solution 20 will migrate from the hollow fiber membrane wall to the moisture regulation material to increase its moisture content, thus making the moisture regulation material's evaporation from the indoor air continue, in fact forming a humidification process for the indoor air. As shown in Figure 4.
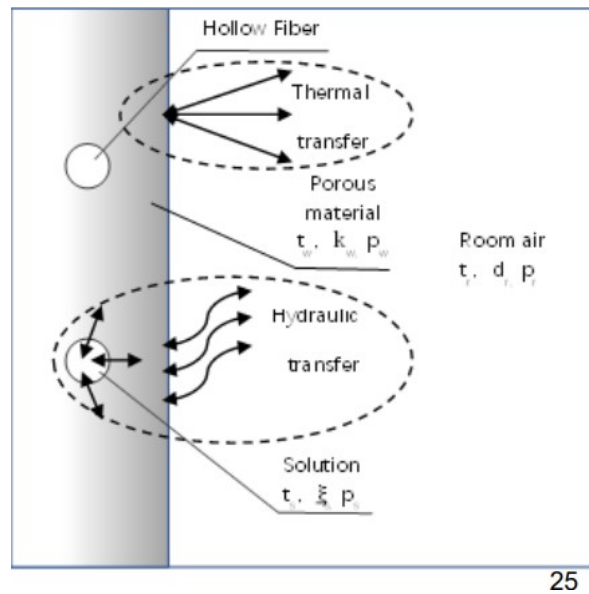
Figure 4: Water migration of diatom mud composite board

Example of calculating indoor dehumidification capacity for a 60m2 office with 10 workstations, assuming an adult male evaporation rate of 102g/h, the indoor moisture load is 1020g/h. The hygrothermal panel is installed on the ceiling with an effective area of 60%, i.e. 36m². The moisture load that needs to be handled by each square meter of the panel is 1020/36 = 28.3g/h. Each square 7 / 10 meter of the panel covers an area of 5 square meters of the expanded surface area of the hollow fiber membrane, so the moisture load that needs to be handled by each square meter of the expanded surface area of the hollow fiber membrane is 28.3/5 = 5.66g/h, which will cause a change of about 1% in the solution concentration.

3.4. Hollow Fiber membrane thermal and moisture exchange module

Because hollow Fiber itself can pass water vapor bidirectionally under the condition of different water vapor partial pressures on both sides of the membrane, it can be imagined that when one end of a membrane filament has a higher/lower water vapor partial pressure than the water vapor partial 10 pressure in the filament, the solution flowing through the filament can transmit water vapor from one end to the other, likely to the "heat pipe" effect of a "wet pipe". As shown in Figure 5.
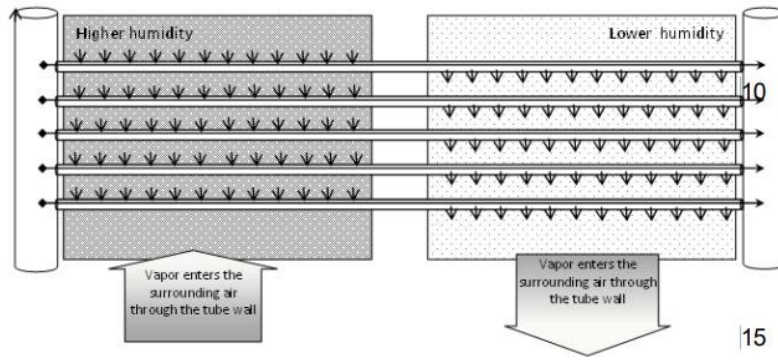
Figure 5: The "wet tube" function of hollow fibers

For practical purposes, unless the "wet tube" can be controlled to absorb moisture and obtain sensible and latent heat, as well as water vapor, while its temperature rise is lower than that of high humidity end air and higher than that of the low humidity end air, the full heat recovery process can be achieved. Furthermore, there is absolutely no 20 need to place the high humidity end and low humidity end together and use a direct connected "wet tube" for heat recovery. In the case where the dilute solution tank and the heat from the dehumidifier are collected, the heat in the exhaust air can be recovered completely by exchanging through a hollow fiber heat exchanger and exhaust air, and the exhaust air can also remove moisture.

For practical purposes, unless the "wet tube" can be controlled to absorb moisture and obtain sensible and latent heat, as well as water vapor, while its temperature rise is lower than that of high humidity end air and higher than that of the low humidity end air, the full heat recovery process can be achieved. Furthermore, there is absolutely no 20 need to place the high humidity end and low humidity end together and use a direct-connected "wet tube" for heat recovery. In the case where the dilute solution tank and the heat from the dehumidifier are collected, the heat in the exhaust air can be recovered completely by exchanging through a hollow fiber heat exchanger and exhaust air, and the exhaust air can also remove moisture.

Rectangular Module Function Sections

The design concept of the rectangular box unit is to maintain the manufacturing process of traditional rectangular air handling units and add an enthalpy exchanger in the middle to replace the conventional dehumidification function section of the unit and make dehumidification 30 the main function. As shown in Figure 6.
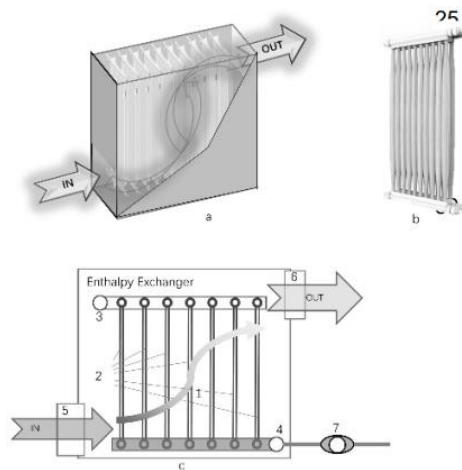
Figure 6: Rectangular hollow fiber membrane enthalpy exchanger

1. Equipment casing 2. Hollow fiber curtain membrane 3. Concentrated solution inlet 4. Diluted solution outlet 5. Fresh air inlet 6. Exhaust air outlet 7. Peristaltic pump

Circular module functional section

1. Cylindrical shell 2. Hollow fiber curtain membrane 3. Air valve 4. Solution separating and collecting pipe 5. Cone-shaped inner 5 cylinder 6. Baffle When considering a circular box for a hollow fiber air handling unit, it is based on the fact that hollow fiber heat exchangers have greater 10 flexibility than traditional metal heat exchangers and can adapt to cylindrical or conical shapes. At the same time, with the widespread use of inlet diffuser fans, it is no longer a problem for the fan to adapt to a circular box. Furthermore, circular valves such as butterfly valves and ring valves have already been widely used. As shown in Figure 7.
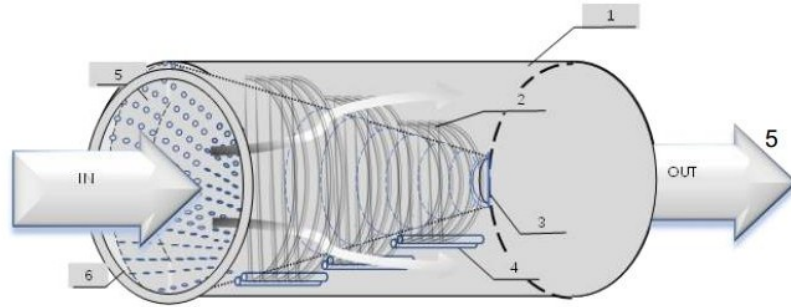
Figure 7: Round hollow fiber membrane enthalpy exchanger

4. SALTWATER SOLUTION SYSTEM

4.1. A schematic diagram of the principle （As shown in Figure 8）

If you use the predefined styles (Home> Styles), all the texts will be automatically adapted. If you are in doubt, you can use the 'Format Painter' tool to match the properties of 2 texts. It looks like this:
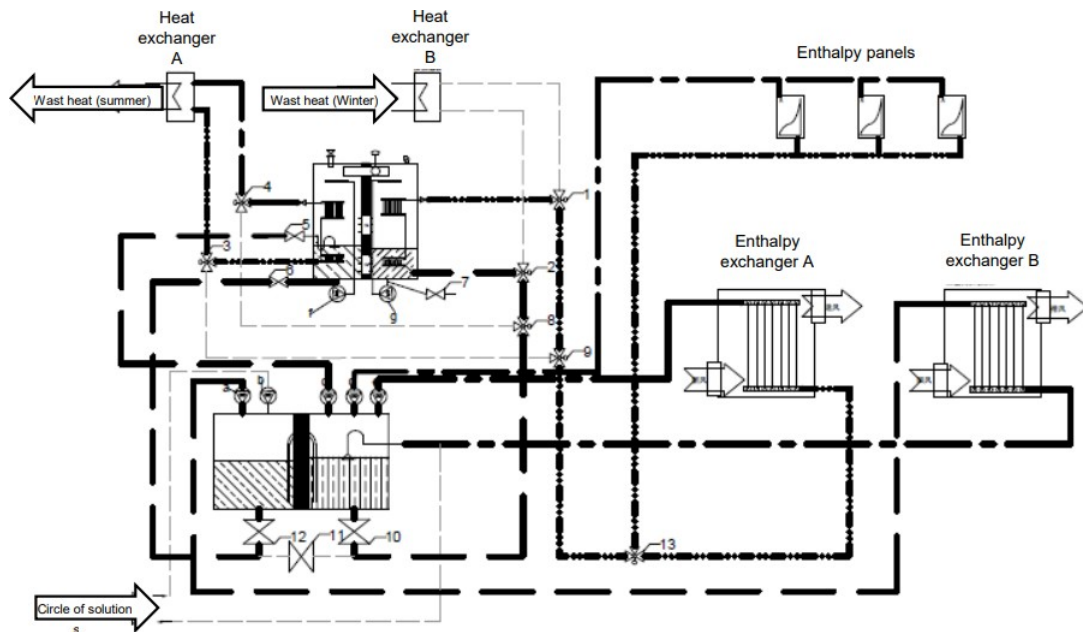
Figure 8: Integrated system for saltwater solution

Cold and heat source system: Separate absorption heat pump (including absorber A, evaporator B, heat exchanger A/B, solution 20 circulation pump f, circulating water pump g), directional valve 1-9 Solution distribution system: Energy buffer and integrated solution tank, solution pump a-e, directional valve 10-12, diverting valve 13 Air treatment system: Hollow Fiber membrane heat and moisture exchange module A/B Control area: Diatom mud moisture-absorbing board + Integrated hollow Fiber membrane board embedded in the middle.

4.2. A systematic energy storage solution

Although phase change energy storage can provide several times or even more than ten times the thermal energy storage capacity, the heat stored will continuously be lost through heat transfer to the environment, and therefore it is not suitable for long-term storage and long-distance transportation. However, absorption 5 energy storage and chemical energy storage can provide much higher heat storage density than phase change energy storage, as well as the ability to store heat for a long time without losing the stored heat energy. Utilize solar and geothermal energy for cross-seasonal energy storage Unlike traditional absorption refrigeration/heat pump systems, absorption systems with energy storage feature a set of sufficient capacity energy storage tanks, and the number of energy storage tanks varies according to 10 the design principle. Since the energy storage tank essentially serves as a buffer, it decouples the absorption/desorption process in the absorption system. The feature of the integrated system is that the energy storage device is still installed together with other components in the same device, with no significant distance between them, so the decoupling ability mainly manifests in decoupling the absorption/desorption process in time, making it possible for the regeneration and use of the working fluid to no longer need to be synchronized. 15 The capacity of the energy storage tank determines the degree of decoupling, and a sufficient capacity can achieve long-term energy storage, i.e., across seasons. As shown in Figure 9.
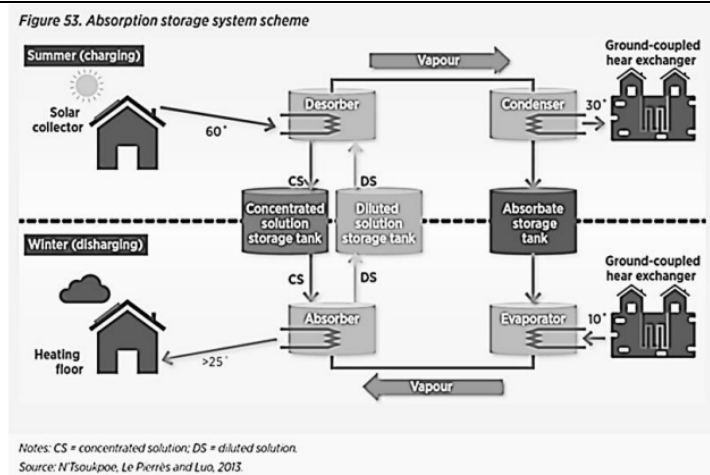
Figure 4: Cross-Seasonal Energy Storage

Despite the huge amount of industrial waste heat, its utilization rate has been 20 very limited so far. This may be due to technical and economic difficulties in applying conventional heat recovery methods, as well as the temporal or spatial mismatch between the released 25 energy and its thermal demand. The principle of a decentralized system is to totally separate the absorption and desorption processes by using a storage tank as a boundary, thus achieving 30 spatial decoupling as well. Spatial decoupling allows the application and regeneration of the working fluid to be designed and operated optimally based on their respective needs, and the use of energy storage devices can be used to balance the demand between the two. Using a mobile energy storage vehicle can effectively solve the problem of temporal and spatial mismatch.

5. TECHNOLOGICAL PROSPECTS

With the basic reference process flow diagram of the integrated salt solution system shown in Figure 8 as a reference, it is possible to expand in the following areas (not limited to):

(1) Combining solution dehumidification technology with evaporative cooling technology;

(2) Maximizing the use of solar energy, industrial waste heat and low-grade heat from other sources as the driving heat for absorption heat pumps;

(3) Using embedded hollow Fiber membrane filaments + solution circulation dehumidification materials in the 5 inner and outer walls of the building (combined with the building structure);

(4) Using suspended heat and moisture activization curtains on the walls (independent of the building structure);

(5) Using hollow Fiber membrane as the regenerator;

(6) Using cylinder-cylinder or cylinder-cone hollow Fiber dehumidification modules;

(7) Combining phase change energy storage, solution energy storage technology with absorption heat pumps.

6. REFERENCES

[1] Liu L, Li L, Zhang Z, 2014. Solution Dehumidification. Beijing: China Architecture & Building Press.

[2] Jiang J, Xie X, Liu L, 2011. Thermodynamic Principles of Heat and Moisture Conversion in Humid Air. HV&AC, Vol. 41, 15 No. 3, 51-64.

[3] Li L, Zhang Z, 2012. Flow and Heat Transfer Performance of Air Crossing Hollow Fiber Membrane Bundle. Chemical Journal of Chinese Universities (Science Edition), Vol. 63, No. S1, 23-27.

[4] Wang W, Feng F, Li L, Gu G, 2009. Experimental and Theoretical Study on Heat and Mass Transfer Characteristics of Hollow Fiber Membrane Heat Exchanger. Journal of Xi'an Jiaotong University, Vol. 43, No. 5, 40-45. 20

[5] Quinnell J A, Davidson J H,2014. Heat and Mass Transfer during Heating of a Hybrid Absorption/Sensible Storage Tank. Solar Energy, Vol.104, P19-28.

[6] Yao Y, Yu Y, Zhu Z,2016. Experimental investigations on surface vapor pressure models for LiCl-CaCl2 desiccant solutions. Solar Energy, Vol.126, P1-13.

[7] Dai D,2001. Absorption Refrigeration Technology and Application. Beijing: Mechanical Industry Press. 25

[8] Kong K, 2011. Preparation and performance study of silica gel-based humidity regulating materials. Beijing University of Technology. [9] Huang H, Jin J, 2002. Feasibility analysis of humidity regulating building materials for indoor humidity regulation. HV&AC, Vol. 32, No. 1, 105-106.CONCLUSION

#222: A novel curved CIGS and Polycrystalline silicon photovoltaic-thermal-catalysis roof for energy generation and air purification: experimental and numerical analysis

Lei CHE[1], Bendong YU[2]

[1] College of Urban Construction, Nanjing Tech University, chelei15660952079@163.com
[2] College of Urban Construction, Nanjing Tech University, bendongyu@njtech.edu.cn

Abstract: The application of building integrated photovoltaic/thermal technology (BIPV/T) in roofs is popular because of enough solar receiving area. Meanwhile, after the post-COVID-19 era, indoor air quality has become the focus. The curved characteristics of traditional Chinese building roofs incorporated the aesthetic characteristics bring new challenges for the application of BIPV/T. Thus, a novel curved CIGS+Si hybrid photovoltaic-thermal-catalysis (PV-TC) roof for electrical, thermal energy and air purification was proposed. Analysis of the proposed novel roof based on experimental and numerical modelling. Main results were: (1) According to the experimental analysis, the average thermal efficiency of the system applied in Nanjing for two days was 16.32% and 22.16%, respectively, and the average electrical efficiency was 8.7% and 8.2%, respectively. The amount of clean air generated by the removal of formaldehyde were 266.54 m^3/m^2 and 239.4 m^3/m^2, respectively. (3) The experimental data were verified by modelling, and the RMSD of the average thermal efficiency, electrical efficiency, and clean air volume generated by formaldehyde removal were 9.83%, 13.20%, 5.92%, and 4.12%, respectively. (4) Based on the model with a small error, the seasonal performance analysis of the system was conducted using this model. The average electric power in summer, winter and transition seasons was 8.7%, 10.6%, 8.9%, the average thermal efficiency was 28%, 43.6%, 29.9%, and the clean air volume was 236.9, 228.6, 220 m^3/m^2.

Keywords: PV Roof; PV/T; Air Purification; Thermal Catalysis; Multifunctional

1. INTRODUCTION

With China's rapid development, the demand for energy continues to increase, and the scale of renewable energy applications is further expanding. Combining renewable energy with buildings is an effective way to reduce building energy consumption and address energy crises. Solar energy has become a promising option. In order to better serve buildings and increase the conversion efficiency of photovoltaic cells, photovoltaic/thermal (PV/T) technology was developed, which utilizes both electrical and thermal energy. BIPV/T technology is now widely used in buildings. Mainly including building walls, windows and roofs. Moreover, researchers adopted some methods, such as setting up heat transfer channels (Jie, Hua, Gang, Bin, & Wei, 2007), reducing photovoltaic coverage, and coating low-radiation layers, to mitigate the impact of temperature rise on the system's electrical performance. The combination of BIPV/T and walls is mostly represented by Trombe. Ji et al. (Jie, et al., 2007) proposed a PV-Trombe system, where PV cells were installed on one side close to the glass in a traditional Trombe wall. The results showed that the air temperature in the room increased by 14.42°C compared to rooms without the Trombe system. Meanwhile, research on PV-Trombe has been limited to the sole use of thermal energy for heating and ventilation. In addition, some systems are prone to overheating in indoor environments during the summer. To address this issue, Luo et al. (Luo et al., 2017) combined louvers with PV-Trombe wall systems, which not only had satisfactory summer insulation and lighting effects but also generated electricity. Regarding the combination of BIPV/T systems and windows, considering that directly integrating guan PV cells with single-layer glass would lead to a high U-value (Zhang, Lu, & Chen, 2017). In addition, PV cells can only utilize 10%~20% of solar energy, with more than 70% of the absorbed energy being ineffective and unfavourable heat, resulting in thermal discomfort near PV windows. Therefore, many researchers have begun to consider multi-layer PV components (Wang et al., 2017). Peng et al. (Peng et al., 2019; Peng, Curcija, Thanachareonkit, Lee, & Selkowitz, 2021) studied the overall performance of PV insulated glass units (PV-IGU) and integrated research on PV-IGU window systems with different types of solar cells and energy-saving glass. Han et al. (Han, Lu, & Yang, 2010) numerically studied the performance of low-emissivity coating PV-IGU systems.

Figure 1: Integration of curved elements of traditional Chinese roofs

In addition, the energy consumption of traditional buildings cannot be ignored, and the curved elements of traditional building roofs bring new challenges to the application of PV/T. As shown in Figure 1, the unique curved elements of traditional building roofs can provide researchers with more ideas to improve the performance of photovoltaic cells. For the integration of BIPV/T on building roofs, research has mainly focused on flat and curved panel systems. Flat roofs are further divided into PV/air roofs and PV/water roofs. The main advantage of PV/air roofs is that airflow can cool the surface of the PV panels, thereby improving the electrical efficiency of the PV cells. Anurag et al. (Shrivastava et al., 2022) reposed a forced-air-cooled crystalline silicon flat-panel system. This research resulted in a relative improvement in energy efficiency of 5.00%-7.00%. For PV/water roofs, water not only reduces temperature but can also be recycled by the building when heated. For curved-panel roof systems, Wang et al. (J. Wang et al., 2022) proposed a curved CIGS thin-film PV panel, which fully utilizes the excellent ductility of thin-film panels for better application in traditional building roofs. Furthermore, in light of the mounting concerns surrounding indoor environmental quality, the utilization of Trombe in winter leads to the closure of outdoor ventilation, thereby impeding the prompt expulsion of indoor pollutants. At present, the pred ominant techniques employed in the purification of indoor air are adsorption and filtration. However, this may result in the generation of secondary pollutants. Photocatalysis (PC) and thermal catalysis (TC) represent more advanced air purification technologies with considerable potential for application in solar energy. Yu et al. (B. D. Yu, Liu, Li, Liu, & Ji, 2020) combined photocatalysis, thermal catalysis, and Trombe wall purification systems, proposing photocatalytic Trombe walls, thermal catalytic Trombe walls, and thermal catalytic PV-Trombe walls. In addition, the research group conducted detailed experimental and numerical studies on the system performance of these purified Trombe walls, including thermal performance and formaldehyde degradation performance (Che et al., 2024; B. D. Yu et al., 2018; B. D. Yu, Li, Xie, & Ji, 2021). Among them, thermal catalytic Trombe walls exhibit excellent air heating performance and formaldehyde degradation performance due to their high solar absorption rate and catalytic activity (B. Yu, He, Li, Yang, & Ji, 2016).

In conclusion, while the curved photovoltaic tile roof reflected the curved elements of the traditional building roof, it nevertheless exhibited a notable deficiency in terms of power generation efficiency. Given the high-power generation efficiency and excellent electrical performance of polycrystalline silicon cells, a combination of these two elements has the potential to enhance the overall power generation efficiency of a roof system while simultaneously preserving the aesthetic integrity of traditional architectural structures. Furthermore, the effect of heat on the electrical performance of photovoltaic cells under a curved photovoltaic roof must be considered. Based on the above research, a methodology was devised to attenuate the impact of heat on electrical performance by leveraging photo-thermal catalysts. This approach was devised in response to the current demand for enhanced indoor air quality.

To this end, this paper presents a hybrid configuration comprising CIGS thin-film cells and polycrystalline silicon flat-plate cells. The installation of air ducts beneath the photovoltaic (PV) panels serves to enhance the electrical power generation of the PV cells. Meanwhile, thermal catalytic materials for formaldehyde purification are positioned beneath the curved tiles of the system. This method of formaldehyde purification offers several advantages, including environmental friendliness, low cost, high efficienc y, and straightforward integration with solar energy. Furthermore, the purified indoor air can be regarded as a certain quantity of fresh air, which can effectively reduce the fresh air load of the indoor air conditioning system during the design phase. This results in a reduction in the energy consumption of the air conditioning system, achieved by decreasing the amount of fresh air introduced and conserving energy. Based on this, the present study combined PV/T with thermal catalysis technology and proposed a novel curved CIGS+Si hybrid PV-thermal-catalysis (PV-TC) roof for the generation of electrical energy, recovery of thermal energy and purification of air. The main study contents included: (1) The outdoor experimental testing platform for CIGS+Si hybrid PV-TC roof was built and the electrical, thermal and air purification performances were tested by two days experiments; (2) A electrical, thermal, and mass transfer model was established, the experiments were verified (3) Based on the model, the seasonal performance of CIGS+Si curved hybrid roofs is simulated.

2. SYSTEM DESCRIPTION

This section describes the composition of each component, the operating mode of the proposed novel curved CIGS+Si hybrid PV-thermal-catalysis (PV-TC) roof system, and the setup process of the experimental platform.

2.1. Basic description of CIGS+Si PV-thermal-catalysis roof

Fig. 2 illustrates the schematic diagram of the CIGS+Si photovoltaic-thermal (PV-TC) roof system. The main body was subdivided into two sections: the hybrid CIGS+Si photovoltaic power generation component and the air purification component. The hybrid CIGS+Si device power generation section is primarily constituted of CIGS thin-film cells and polycrystalline silicon cells, arranged in an alternating sequence. An aluminium plate is positioned beneath the PV cells to provide support. The purification part comprises an air flow channel comprising a MnO_2-coated film on the inner surface and the lower part of the thin film cells.
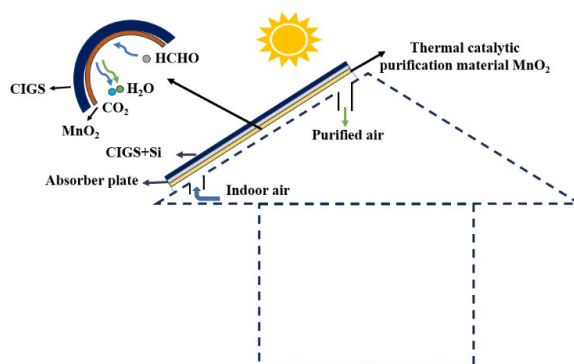
Figure 2: The schematic diagram of CIGS+Si PV-TC roof

When the system is irradiated by solar radiation, the CIGS thin-film cells and crystalline silicon cells on the surface of the system absorb light and operate, converting the absorbed light energy into electrical energy and thermal energy. Furthermore, the intrinsic characteristics of the photovoltaic (PV) cells result in an increase in the surface temperature of the PV cells. The PV cell with a higher temperature transfers heat to the purification material situated below it and to the air within the air flow channel. This is achieved through the processes of heat conduction and convective heat transfer, facilitated by the heat conduction properties of the curved tile. With regard to the air within the air flow channel, the inlet and outlet temperatures of the internal air are disparate, thereby exerting thermal pressure upon the air within the flow channel as a consequence of the temperature differential. The air flowing in the air flow channel can reduce the temperature of the environment when the PV cell is working by convective heat transfer, thereby improving the electrical efficiency of the PV cell. For the purification material MnO_2, it absorbs the heat conduction on the inner surface of the curved PV cell, drives its own purification effect, decomposes formaldehyde into H_2O and CO_2. Moreover, the flow of air in the flow channel will discharge the purified product in time, so as to improve the purification efficiency of MnO_2. The PV component can be combined with the roof as shown in the schematic diagram, taking into account the advantages of the beautiful and generous appearance of traditional curved buildings, and also meeting the functions of power generation and air purification.

2.2. The design and construction of curved CIGS+Si PV-TC component

This section introduces the connection between curved CIGS thin-film solar cells and crystalline silicon solar cells, as well as the preparation process of the thermal catalytic purification material MnO_2. As illustrated in Fig. 3, tin wires were employed for the interconnection between the crystalline silicon cells and between the CIGS cells. The interconnected CIGS thin-film cells should be attached to the polycrystalline silicon with heat-conducting silicone, and then pasted separately onto the curved tile and the upper surface of the flat plate. Preparation of thermal catalytic material was shown in Fig.3(Li, Yu, & Li, 2023). Apply thermal catalytic material to the back of curved photovoltaics. The test bench was constructed with an aluminium frame, measuring 1300×800×2 mm (length, width, and height).
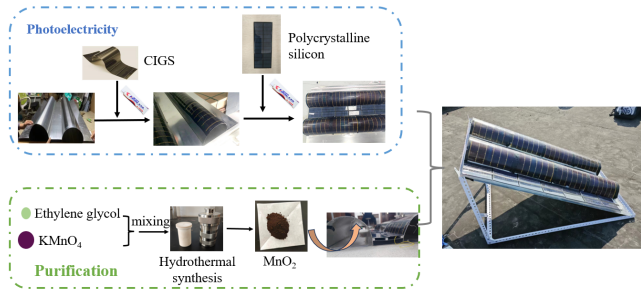
Figure 3: The design and construction of curved CIGS+Si PV-TC component

3. EXPERIMENTAL AND MODEL

This section presented the basic conditions and contents of the experiment. It explained the functions and parameters of the measurement instruments used in the experiment. Moreover, it introduced the principle of the system and established a system model.

3.1. Basic description of CIGS+Si PV-thermal-catalysis roof

The experimental testing platform was carried on the roof of the Tiangong Building of Nanjing Tech University, Jiangsu Province (N32°04′, E118°38′), and was used to evaluate the thermal performance, electrical performance and formaldehyde purification performance of the system. The actual photograph of the experimental device was shown in Fig.4 and in the two-day test results, the experimental platform was placed facing due south, and the tilt angle of the experimental device was 30° for both days. The device was performed in clear weather and the surroundings were open and unscreened climatic conditions. The experiment includes the following contents: environmental conditions, PV/T performance, formaldehyde purification performance, and temperature distribution (including thermal performance). Environmental conditions include solar radiation, ambient temperature, and wind speed. Electrical performance is evaluated by the PV output power and the photoelectric conversion efficiency. The formaldehyde purification performance is evaluated by the single-pass conversion of formaldehyde and CADR. The temperature distribution covers the temperature of thin film cells and plate cells, the inlet and outlet temperature of air flow channel, the inner surface temperature of curved tile and the inner surface temperature of experimental plate.

Figure 4: The PV-TC roof system: (a) Physical diagram (b) Schematic diagram

During the experiment, the temperature was measured by the K-type thermocouple. Solar radiation is detected by a sun intensity meter placed parallel to the skirting line at the same angle of incident and transfers the output signal to an Agilent instrument to output by voltage. Data recordings were recorded at 10s intervals. The ambient wind speed is measured by a thermal anemometer. The thin film cells and crystalline silicon cells are connected to the I-V tester, and the output power is captured every 10 minutes through Solar Module Analyzer 12 A. The six temperature measurement points of the thin film cells and crystal silicon flat cells are equally distributed on their surface. The thermocouple in the air flow channel is located in the upper, middle and lower part s of the channel. The thermocouple measuring the inlet and outlet air temperature is located in two vertical sections. The fluid flow velocity in the air channel is obtained according to the heat difference action formula. The formaldehyde detector is placed at the inlet and outlet of the air duct respectively to measure the formaldehyde concentration.

According to the above test device, the meteorological parameters such as solar irradiance, wind speed, and ambient temperature were measured. Fig.5 showed the variations of global tilted radiation (I_r), wind speed (u_{wind}) and ambient temperature (T_{am}) on October 15 and October 29, respectively. On October 15, the average radiation was 510 W/m², the average temperature was 27.5 °C, and

the average wind speed was 0.79 m/s. On October 29, the average solar radiation was 583.03 W/m², the average temperature was 29 °C, and the average wind speed was 0.77 m/s. At the same time, we can observe the unstable change of outdoor temperature on October 15, which may be due to the wind speed.
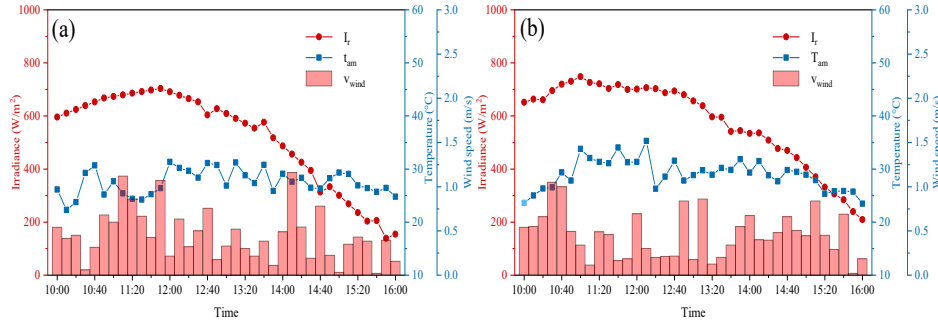
Figure 5: The meteorological parameters of Nanjing include solar radiation, outdoor temperature and outdoor wind speed: (a) October 15,2023, (b) October 29,2023

3.2. System model

The dynamic model is a transient model, including electrical and heat transfer in the PV components and mass transfer in the airflow channel. The electrical model includes CIGS thin film cells and polysilicon cells. The thermal model of the system includes heat exchange between the aluminium plate with PV cells and the environment, ground, sky, and airflow, denoted by subscripts amb, gnd, sky, and air, respectively. The mass model of the system involves the degradation of gaseous formaldehyde on the catalyst surface. Fig.7 illustrates the basic scheme of electrical, heat and mass transfer for each component of the system. Based on these components, energy and mass transfer equations were established. Some assumptions were as follows: (1) All the thermal physical parameters used in the system model are assumed to be constant (Jun Wang et al., 2022). (2) Treat the PV cells, aluminium sheet, and underlying catalytic material as a unit, and the model of the system was regarded as a one-dimensional heat transfer model. (3) The heat development of airflow in the air duct, convective heat, and mass are uniformly distributed inside the cavity. (4) Due to the very low concentration of formaldehyde, the heat from formaldehyde reactions is neglected (B. Yu et al., 2017).
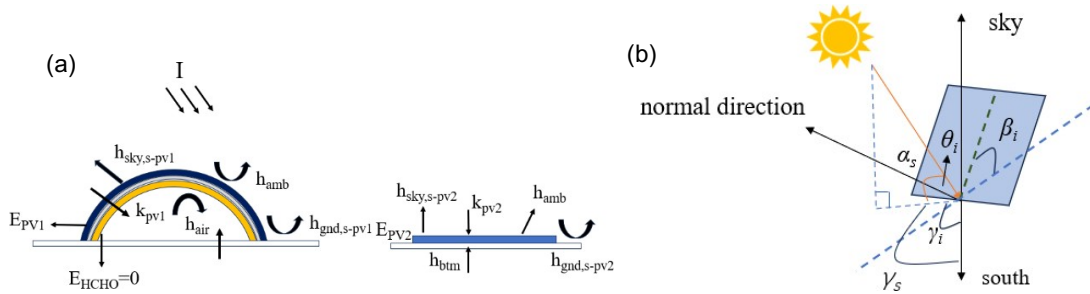
Figure 6: Modelling of the system (a) Electrical, heat and mass transfer schematic diagram. (b) The structure chart of micro facet

The curved surface structure is easy to block each other. In order to reduce this error, the radiation distribution of curved surface PV and plane PV under different solar altitude angles should be calculated. As shown in Fig. 6, for a system located at latitude Φ, there is an elemental unit i with an inclination angle β_i and an azimuth angle γ_i (where the azimuth angle is defined as the angle between the normal direction of the surface and the projection onto the horizontal plane, with a value of 0 indicating the surface facing true south, positive values indicating the surface facing southwest, and negative values indicating the surface facing southeast).

Calculate the solar irradiance at a specific moment (the moment is the n day of the Julian day at time tsolar, and the specific method for determining the Julian day and solar true time can be referred to in the literature (Duffie & Beckman, 2013)). The total solar radiation includes direct solar radiation, diffuse sky radiation and diffuse sky radiation. The formulae are as follows:

Equation 3: The total solar radiation received on surface i of the device	$G_{total,i} = G_{bm,i} + G_{gnd,i} + G_{diff,i}$
Equation 2: The solar direct radiation received by this elemental unit	$G_{bm,i} = G_{bm,h} r_{bm,i}$
Equation 3: The ground-reflected radiation received by surface i of the device	$G_{r,i} = \rho_{gnd} G_{total,hor} (\sin(\beta_i/2))^2$
Equation 4: The sky diffuse radiation on inclined surface i of the device	$G_{diff,i} = G_{diff,hor}[(\cos\frac{\beta_i}{2})(1 - F_1) + F_1(\frac{f_1}{f_2}) + F_2 \sin\beta_i]$

Where:

- $r_{bm, I}$ = direct radiation intensity on the horizontal plane (W/m²)
- ρ_{gnd} = ground reflectance (0.2)
- $G_{diff,hor}$ = sky diffuse radiation received on the horizontal plane (W/m²)
- F_1, F_2, f_1, f_2 = constant, available in the literature(Perez, Ineichen, Seals, Michalsky, & Stewart, 1990)

The basic energy balance equation of the system is divided into two parts: CIGS thin film cells and polycrystalline silicon cells. For

CIGS thin film solar cells and Polycrystalline silicon cells, the heat transfer was regarded as a one-dimensional heat conduction model. The formulae are as follows:

Equation 5: The heat transfer of CIGS thin film solar cells

$$(\rho c d)_{CIGS,PV} \frac{\partial T_{pv1}}{\partial t} =$$

$$k_{pv1} d_{pv1} \frac{\partial^2 T_{pv1}}{\partial y^2} + h_{amb}(T_{amb} - T_{pv1}) + h_{sky,s-pv1}(T_s - T_{pv1})$$

$$+ h_{gnd,s-pv1}(T_{gnd} - T_{pv2}) + h_{btm}(T_{btm} - T_{pv1})$$

$$+ h_{air}(T_{air} - T_{pv1}) + \alpha_{pv1} G_{total1} - \frac{A_{pv1}}{A_{c1}} E_{CIGS,pv}$$

Equation 6: The heat transfer of Polycrystalline silicon cells

$$(\rho c d)_{Si,PV} \frac{\partial T_{pv2}}{\partial t} =$$

$$k_{pv2} d_{pv2} \frac{\partial^2 T_{pv2}}{\partial y^2} + h'_{atm}(T_{atm} - T_{pv2}) + h'_{sky,s-pv2}(T_s - T_{pv2})$$

$$+ h'_{gnd,s-pv2}(T_{gnd} - T_{pv2}) + h'_{btm}(T_{btm} - T_{pv2})$$

$$+ h'_{air}(T_{air} - T_{pv2}) + \alpha_{pv2} G_{total2} - \frac{A_{pv2}}{A_{c2}} E_{Si,pv}$$

Where:

- T_{pv1} = PV temperature (°C)
- T_{amb} = ambience temperature (°C)
- T_s = sky temperature (°C)
- T_{gnd} = ground temperature (°C)
- T_{btm} = baseboard temperature (°C)
- T_{air} = air flow paths temperature (°C)
- E_{CIGS} = electricity generation per unit area of CIGS thin-film solar cell (kW·h)
- $E_{SI, pv}$ = electricity generation per unit area of PV solar cell (kW·h)
- α_{pv1} = absorptance of the curved heat-absorbing plate
- α_{pv2} = absorptance of the curved heat-absorbing plate
- A_{pv1} = area of CIGS (m²)
- A_{pv2} = area of PV (m²)
- A_{c1} = area of curved heat-absorbing plate (m²)
- A_{c2} = area of PV plate (m²)
- h_{amb} = heat transfer coefficient of the absorption plate and the environment (W·m⁻²·K⁻¹)
- $h_{sky,s-pv1}$ = heat transfer coefficient of the sky and the PV cells (W·m⁻²·K⁻¹)
- $h_{gnd,s-pv1}$ = heat transfer coefficient of the ground and the PV cells (W·m⁻²·K⁻¹)
- h_{air} = heat transfer coefficient of the flow paths (W·m⁻²·K⁻¹)

For the air inside the duct, its temperature can be determined by the following equation:

Equation 7: The heat transfer of air inside the duct

$$\dot{m}_{air} c_a \frac{\partial T_a}{\partial t} = \dot{m}_{air} c_a (T_{in} - T_{out}) + h_{air} A_{pv1}(T_{pv1} - T_a) + h_{air} A_b(T_b - T_a)$$

Where:

- m_{air} = air mass flow rate (kg/s)
- T_{in} = Inlet air temperature (°C)
- T_{out} = outlet air temperature (°C)

The mass transfer model considers the degradation of gaseous formaldehyde on the surface of the catalytic coating. For the thermal catalytic oxidation process, there is the following steady-state mass conservation equation at the interface between air and catalyst:

Equation 8: The mass transfer of degradation of gaseous formaldehyde on the surface

$$W l_a \frac{\partial C(z)}{\partial t} \delta z = -Q \frac{\partial C(z)}{\partial z} \delta z - m(z) W \delta z$$

Where:

- Q = volume flow rate in the air channel (m^3/s)
- W = width of the reaction surface perpendicular to the direction of air flow
- C = mainstream formaldehyde concentration in the air channel (ppb)
- m = mass transfer rate at the surface of catalysts (ppb·m/s)

The system integrates power generation, formaldehyde purification and other functions. In order to comprehensively evaluate the performance of the system, power generation, air thermal efficiency, electrical efficiency, and single-pass conversion of formaldehyde were studied. The thermal efficiency(ηth) and electrical efficiency(ηe), respectively, are ratio of thermal gain of air and electrical gain in the total received solar radiation by the collector aperture at a given time. Considering the presence of the curved structure in the system, and that the curved part receives non-uniform solar energy, which is difficult to measure directly with instruments, the formula for electrical efficiency was redefined, including a redefined A.

Equation 9: The electrical power output of PV cells
$$E_{pv} = G\tau_g\zeta\eta_{ref}[1 - B_r(T_{pv} - T_{ref})]$$

Equation 10: The thermal efficiency of device
$$\eta_{th} = \frac{mc\Delta T}{GA}$$

Equation 11: The average thermal efficiency of device
$$\overline{\eta_{th}} = \frac{\int_0^\tau m_{air}c\Delta T}{\int_0^\tau GA}$$

Equation 12: The electrical efficiency of device
$$\eta_e = \frac{E_e}{GA}$$

Equation 13: The average electrical efficiency of device
$$\overline{\eta_e} = \frac{\int_0^\tau E_{pv}}{\int_0^\tau GA}$$

Equation 14: The formaldehyde purification performance of device
$$CADR = Q\varepsilon$$

Equation 15: The total formaldehyde purification performance of device
$$V_{total} = \int_0^\tau CADRdt$$

Where:

- ξ = reference temperature (°C)
- η_{ref} = standard PV efficiency under the reference temperature
- B_r = temperature coefficient
- T_{PV} = PV temperature (°C)
- m = mass flow rate of water or air (kg/s)
- A = projected area of the system's photovoltaic cells onto the inclined surface (m^2)
- ΔT = temperature difference of the air inside the duct before and after being heated
- τ = experimental time (s)
- ε = single-pass conversion of formaldehyde

4. RESULTS AND DISCUSSIONS

An analysis and discussion were made of the thermal performance, electrical performance, and formaldehyde purification performance used to evaluate the system's functionality. The effectiveness of the experimental data was validated through model verification. Moreover, a simulation analysis was conducted to compare the performance of three different rooftop systems, namely CIGS+Si, CIGS thin-film solar cells, and multi-crystalline silicon flat-plate solar cells, thereby highlighting the superiority of the system model proposed in this paper.

4.1. Experimental analysis

In this section, the thermal performance, electrical performance, and formaldehyde purification performance of the experimental system were analysed separately. Thermal performance was evaluated using thermal efficiency, electrical performance included the electrical power and electrical efficiency of the experimental apparatus, while formaldehyde purification performance encompassed the single-pass conversion of formaldehyde, CADR, and the total amount of clean air. Fig. 9 described the inlet temperature (T_{in}), outlet temperature (T_{out}) and thermal efficiency (η_{th}) of the air flow channel under the curved tile of CIGS thin film cells on October 15 and October 29, respectively. It can be seen from Fig. 7 that the inlet and outlet temperatures of the air flow channel over the two-day period showed a trend of first rising and then gradually decreasing, and the difference between the inlet temperature and the outlet temperature of the air flow channel gradually decreases with the progress of the experiment. The inlet temperature of theair flow channel was significantly affected by the environment, and its changing trend was similar to that of the ambient temperature. The outlet temperature of the air flow channel, on the other hand, was related to its heat exchange ability with the surrounding environment over a certain period of time. As time passed, the solar radiation absorbed by the photovoltaic components decreased, and the heat absorbed by the curved heat absorption plate also decreased, resulting in a weakened convective heat exchange effect between the plate and the air inside the channel. Since the amount of air that could be heated was limited, the rising trend of the airtemperature inside the channel gradually weakened, and the temperature difference gradually decreased.
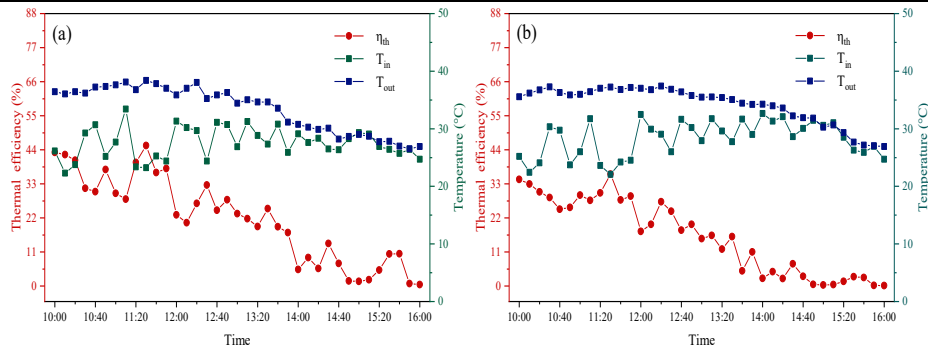
Figure 7: The inlet temperature, outlet temperature and thermal efficiency in the air flow channel: (a) October 15,2023, (b) October 29,2023

During the whole experiment, on October 15, the air temperature in the flow channel increased by an average of 6.07 °C, the highest rise was 13.7 °C, the average thermal efficiency was 16.32%, and the highest thermal efficiency was 36.1%. On October 29, the air in the flow channel increased by an average of 7.01 °C, the highest rise was 15.1 °C, the average thermal efficiency was 22.16%, and the highest thermal efficiency was 38.5%.
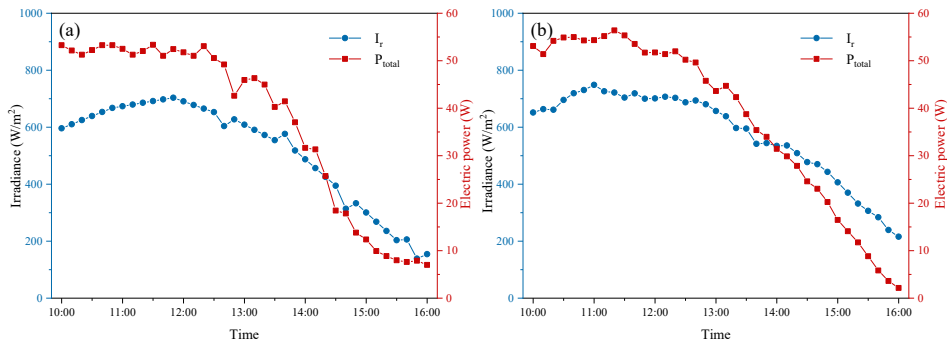
Figure 8: The solar radiation and electrical power of the system: (a) October 15, 2023, (b) October 29, 2023

Fig.8 showed the variation of solar radiation and electrical power over time over the entire experimental platform on October 15 and October 29. We can observe that the electric power of the system is similar to the trend of solar radiation, On October 15, the electric power of all day was 240 W, and the maximum instantaneous electric power was 55 W; on October 29, the electric power of all day was 230 W, and the maximum instantaneous electric power was 52 W. The system showed good electrical performance.
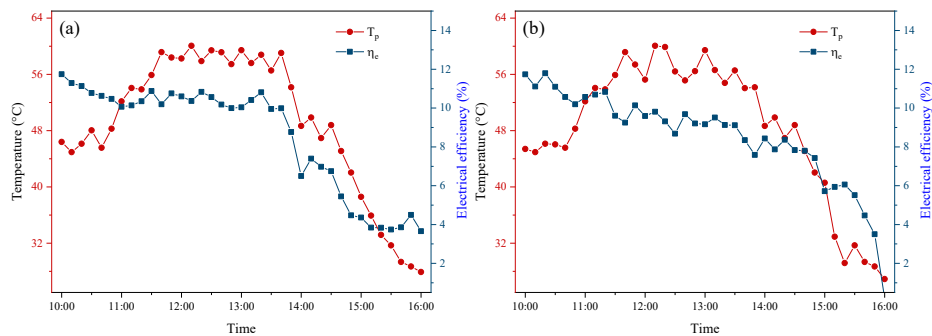
Figure 9: The electrical efficiency and PV cell temperature change:(a) October 15, 2023, (b) October 29, 2023

In the experiment, formaldehyde gas was prepared by bubbling method, which was introduced into the lower part of the air flow channel. After passing through the air flow channel, it was purified by the thermal catalyst on the back of the PV panel and discharged from the upper part of the flow channel. The above analysis discussed the variation in power generation. In a typical evaluation, another important performance metric is electrical efficiency. Fig.9 shows the variation of electric power and PV surface temperature with time. Because the temperature on the surface of the photovoltaic cells was measured by thermistors during the experiment, the presence of wind speed in the environment easily altered the temperature field around the measurement points, significantly changing the convective heat transfer effect between the measurement points and their surroundings, resulting in more pronouncedtemperature variations. The efficiency of PV cells decreases with increasing temperature. As the temperature increases, the voltage of the PV cells decreases, leading to a reduction in current and thus lowering the electrical power output. Additionally, high temperatures can increase the rate of recombination of electrons and holes within the PV cells, which can decrease the conversionefficiency of PV cells. Electrical efficiency on October 15 reached its maximum value of 11.7% at 10:00 am, and on October 29, it reached its maximum value of 11.8% at 10:30 am. The average electrical efficiency of the two days was 8.7% and 8.2%, respectively.
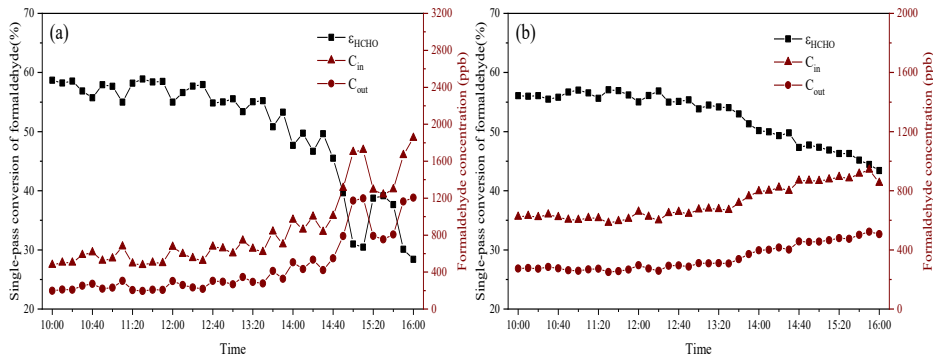
Figure 10: The import and export concentration and single-pass conversion of formaldehyde change: (a) October 15, 2023, (b) October 29, 2023

As shown in Fig.10, the import and export concentration and the single-pass conversion of formaldehyde change over time in a day. On October 15, the average concentration of formaldehyde at the entrance was 808 ppb, the average concentration of formaldehyde at the outlet was 426 ppb, the single-pass conversion of formaldehyde was 51%, and the highest single-pass conversion of formaldehyde was 58.67%. On October 29, the average concentration of formaldehyde at the entrance was 713 ppb, the average concentration of formaldehyde at the outlet was 341 ppb, the single-pass conversion of formaldehyde was 52.8%, and the highest single-pass conversion of formaldehyde was 56.07%. It can be seen from Fig.11 that it has a good purification effect on formaldehyde, but the single-pass conversion of formaldehyde gradually decreases, which is due to the gradual decrease of temperature and the reduction of energy provided for the catalyst. Fig.11 described the Clean Air Delivery Rate (CADR) on October 15 and October 29 for the experimental system's purification performance. The total amount of clean air for the two days of experiments was 266.54 m^3/m^2 and 239.4 m^3/m^2, respectively.
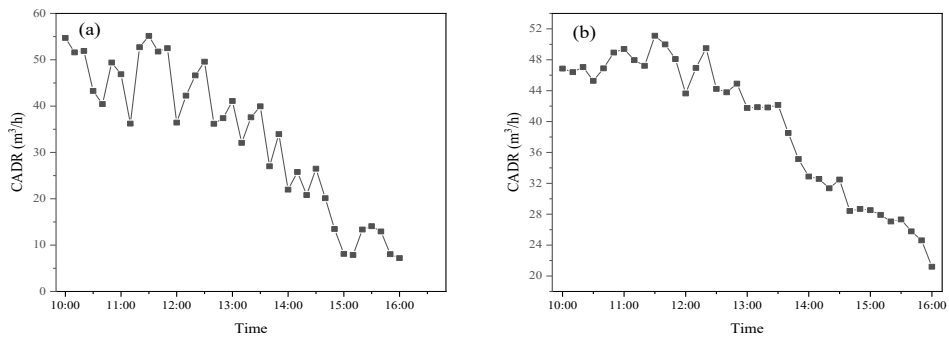
Figure 11: The amount of clean air generated by the system: (a) October 15, 2023, (b) October 29, 2023

4.2. Seasonal Analysis of the System

Table 1: RMSD comparison of each parameter of the system

Parameter	Thermal efficiency	Electrical efficiency	Single-pass
RMSD	6.83%	7.20%	5.92%

In this section, we first compared the proposed model with experimental data. The RMSD was then used to evaluate the magnitude of the error in the proposed model. The RMSD values for each parameter are shown in Table 1, with the maximum RMSD being less than 8%, indicating that the error in the model proposed in this paper was relatively small. Then, the model was used to analyse the thermal performance, electrical performance, and formaldehyde purification performance of the system in different seasons. The simulated system had an average thermal efficiency of 16.32%, with a peak thermal efficiency of 41.9% at 11:30 am; an average electrical efficiency of 8.7%, with a peak electrical efficiency of 13.5% at 10:00 am; and an average single-pass conversion rate of formaldehyde of 51%, with a peak single-pass conversion rate of 58.88% at 11:30 am. And the maximum RMSD is within 8%. Considering comprehensively, the established theoretical model can better describe and predict the thermal performance, electrical performance and formaldehyde purification performance of the system.

To evaluate the application potential of the system throughout the year, we selected summer, transitional season, and winter in Nanjing as research objects and conducted simulation analyses of the system's performance. The location of the simulation was also built on the roof of the Nanjing Tech University, Jiangsu Province (N32°04′, E118°38′), with the experimental platform facing directly south and an inclination angle of 30°. The selected dates were July 2nd, 9th, 16th, 23rd, and 30th for summer; September 2nd, 9th, 16th, 23rd, and 30th for the transitional season; and December 2nd, 9th, 16th, 23rd, and 30th for winter. In summer, July 2nd and 16th were cloudy days, while the others were sunny days; in the transitional season, September 23rd and 30th were cloudy days, while the others were sunny days; and in winter, all selected days were sunny days.
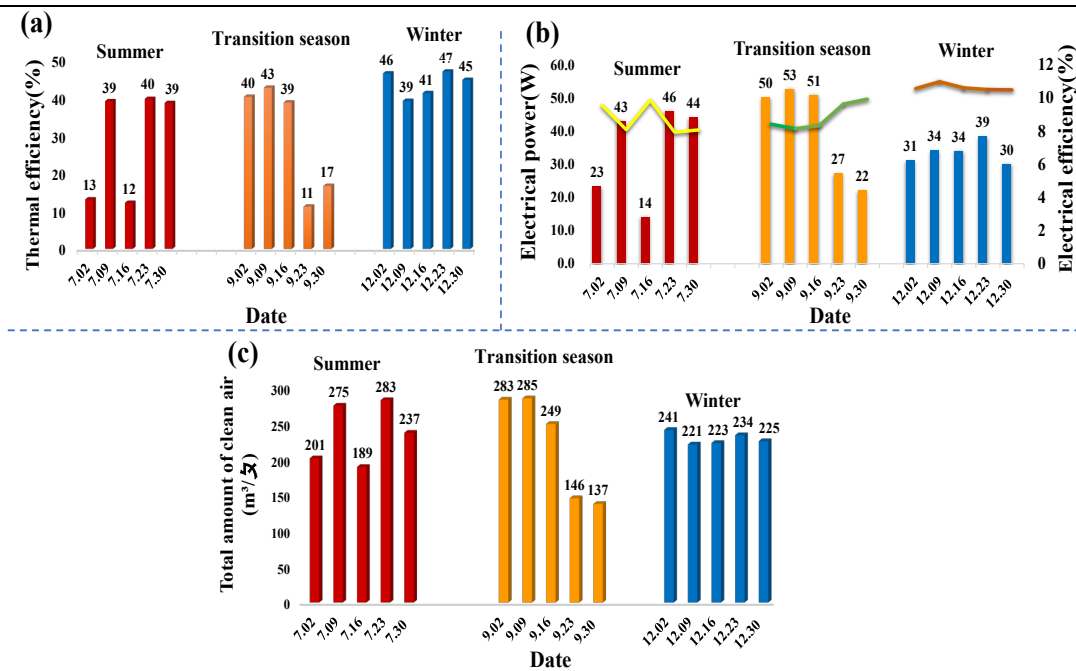
Figure 12: Performance in different seasons (a) Electrical performance (b)Thermal performance (c) Formaldehyde purification performance

As could be seen from Fig.12, for the system's electrical performance, the average power output in the transitional season on sunny days was 51.32 W, with an average efficiency of 8.3%; on cloudy days, the average power output was 24.7 W, with an average efficiency of 9.78%. In summer, the average power output on sunny days was 44.5 W, with an average efficiency of 8.03%; on cloudy days, the average power output was 18.75 W, with an average efficiency of 9.71%. In winter, the average power output on sunny days was 33.6 W, with an average efficiency of 10.6%. The size of the system's power output was directly related to the solar irradiance intensity, and the solar irradiance intensity was stronger in summer than in the transitional season and winter, resulting in higher power output. However, for efficiency, the working temperature of the photovoltaic cells was an important influencing factor. In winter, although the solar irradiance was weaker, the low environmental temperature could effectively eliminate the decrease in electrical performance of the photovoltaic cells due to temperature rise during operation, whereas in summer, it was the opposite. Regarding the system's thermal performance, the average thermal efficiency on sunny days in summer was 39.1%, and on cloudy days, it was 12.65%. In the transitional seasons, the average thermal efficiency on sunny days was 40.5%, and on cloudy days, it was 13.9%. In winter, the average thermal efficiency on sunny days was 43.7%. The thermal efficiency was mainly affectedby the combined influence of solar irradiance intensity and airflow rate within the air duct. In summer, due to the high ambient temperature, the air temperature inside the duct increased, which led to a slower airflow rate caused by the temperature difference,resulting in a lower thermal efficiency compared to winter and transitional seasons. Regarding the total amount of clean air used to evaluate the system's formaldehyde purification performance, the total amount of clean air on sunny days in summer was 264.7 m^3/m^2, and on cloudy days, it was 195.21 m^3/m^2. In the transitional seasons, the total amount of clean air on sunny days was 272.4 m^3/m^2, and on cloudy days, it was 141.5 m^3/m^2. In winter, the total amount of clean air on sunny days was 228.6 m^3/m^2. The system's total amount of clean air is related to its thermal performance, and good thermal performance can provide energy for the thermal catalytic material MnO_2 used for formaldehyde purification, and also facilitate the removal of catalysed products through airflow within the air duct, thereby improving the formaldehyde decomposition efficiency.

5. CONCLUSION

This paper proposed a novel curved-surface roof that integrated CIGS thin-film PV cells with polycrystalline silicon flat-plate PV cells. Airflow channels were set under the PV cells, and a purification material with a thermal catalytic effect was innovatively integrated with the curved-surface roof, which enabled the system to improve air quality while generating electricity. A numerical model of the system was also established. The model was used to conduct a seasonal performance analysis of the system. The thermal, electrical, and formaldehyde purification performances of the system were discussed, and the comprehensive performances of the flat-cell roof, curved-cell roof, and curved-flat combined roof systems were compared.

The conclusions are as follows: (1) The system incorporated the aesthetic characteristics of traditional Chinese architectural roofs. It endowed the roof with power generation and air purification functions while meeting the basic requirements of the roof. (2) According to the experimental analysis, the average thermal efficiency of the system applied in Nanjing for two days was 16.32% and 22.16%, respectively, and the average electrical efficiency was 8.7% and 8.2%, respectively. The amount of clean air generated by the removal of formaldehyde were 266.54 m^3/m^2 and 239.4 m^3/m^2, respectively. This indicates that the system has good power generation and air purification performance. (3) The experimental data were verified by modelling, and the RMSD of the average thermal efficiency, electrical efficiency, and clean air volume generated by formaldehyde removal were 9.83%, 13.20%, 5.92%, and 4.12%, respectively. This indicates that the error between the model and the experiment was within a reasonable range. (4) Based on the model with a small error, the seasonal performance analysis of the system was conducted using this model. The average electric power in summer, winter and transition seasons was 8.7%, 10.6%, 8.9%, the average thermal efficiency was 28%, 43.6%, 29.9%, and the clean air volume was 236.9, 228.6, 220 m^3/m^2.

This paper established a curved-surface PV roof experiment bench and analysed its electrical, thermal, and purification performances.

However, the deep integration of the indoor environment with this component remains to be explored. In the future, our research group will consider the comprehensive performance of this component under the influence of indoor environmental factors.

6. REFERENCES

Che, L., Li, N. S., Fan, M. M., Zhang, G. J., Zhang, G. Y., & Yu, B. D. (2024). A novel catalytic/sterilization PV-Trombe wall system: Analysis on PV electrical and air purification performance in winter. Building and Environment, 255.

Duffie, J. A., & Beckman, W. A. (2013). Solar Engineering of Thermal Processes (Duffie/Solar Engineering 4e) || D: Meteorological Data. 10.1002/9781118671603, 863-869.

Han, J., Lu, L., & Yang, H. (2010). Numerical evaluation of the mixed convective heat transfer in a double-pane window integrated with see-through a-Si PV cells with low-e coatings. Applied Energy, 87(11), 3431-3437.

Jie, J., Hua, Y., Gang, P., Bin, J., & Wei, H. (2007). Study of PV-Trombe wall assisted with DC fan. Pergamon(10).

Li, Y., Yu, B., & Li, N. (2023). The performance analysis of a novel manganese oxide solar low-temperature thermal-catalyst in building multifunctional applications. Energy and Buildings, 297, 113477.

Luo, Y., Zhang, L., Wang, X., Xie, L., Liu, Z., Wu, J., et al. (2017). A comparative study on thermal performance evaluation of a new double skin faade system integrated with photovoltaic blinds. Applied Energy, 199(AUG.1), 281-293.

Peng, J., Curcija, D. C., Thanachareonkit, A., Lee, E. S., Goudey, H., & Selkowitz, S. E. (2019). Study on the overall energy performance of a novel c-Si based semitransparent solar photovoltaic window. Applied Energy, 242(PT.1-1284), 854-872.

Peng, J., Curcija, D. C., Thanachareonkit, A., Lee, E. S., & Selkowitz, S. E. (2021). Comparative study on the overall energy performance between photovoltaic and Low-E insulated glass units. Solar Energy, 214, 443-456.

Perez, R., Ineichen, P., Seals, R., Michalsky, J., & Stewart, R. (1990). Modeling daylight availability and irradiance components from direct and global irradiance. Solar Energy, 44(5), 271-289.

Shrivastava, A., Jose, J. P. A., Borole, Y. D., Saravanakumar, R., Sharifpur, M., Harasi, H., et al. (2022). A study on the effects of forced air-cooling enhancements on a 150 W solar photovoltaic thermal collector for green cities. Sustainable Energy Technologies and Assessments, 49.

Wang, J., Tian, X., Ji, J., Zhang, C., Ke, W., & Yuan, S. (2022). Field experimental investigation of a multifunctional curved CIGS photovoltaic/thermal (PV/T) roof system for traditional Chinese buildings. Energy conversion & management.

Wang, J., Tian, X. Y., Ji, J., Zhang, C. Y., Ke, W., & Yuan, S. (2022). Field experimental investigation of a multifunctional curved CIGS photovoltaic/thermal (PV/T) roof system for traditional Chinese buildings. Energy Conversion and Management, 271.

Wang, M., Peng, J., Li, N., Yang, H., Wang, C., Li, X., et al. (2017). Comparison of energy performance between PV double skin facades and PV insulating glass units. Applied Energy, 194, 148-160.

Yu, B., He, W., Li, N., Wang, L., Cai, J., Chen, H., et al. (2017). Experimental and numerical performance analysis of a TC-Trombe wall. Applied Energy, 206(nov.15), 70-82.

Yu, B., He, W., Li, N., Yang, F., & Ji, J. (2016). Thermal catalytic oxidation performance study of SWTCO system for the degradation of indoor formaldehyde: Kinetics and feasibility analysis. Building and Environment, 108(nov.), 183-193.

Yu, B. D., Hou, J. X., He, W., Liu, S. S., Hu, Z. T., Ji, J., et al. (2018). Study on a high-performance photocatalytic-Trombe wall system for space heating and air purification. Applied Energy, 226, 365-380.

Yu, B. D., Li, N. A. S., Xie, H., & Ji, J. (2021). The performance analysis on a novel purification-cleaning trombe wall based on solar thermal sterilization and thermal catalytic principles. Energy, 225.

Yu, B. D., Liu, X. Y., Li, N. S., Liu, S. S., & Ji, J. (2020). The performance analysis of a purified PV/T-Trombe wall based on thermal catalytic oxidation process in winter. Energy Conversion and Management, 203.

Zhang, W., Lu, L., & Chen, X. (2017). Performance Evaluation of Vacuum Photovoltaic Insulated Glass Unit ☆. Energy Procedia, 105, 322-326.

#224: A scalable solar-based thermal catalytic purification battery for day and night heating and HCHO removal

Yulin LI[1], Huabo WU[1], Bendong YU[1] *, Niansi LI[1, 2]

[1] College of Urban Construction, Nanjing Tech University, Nanjing 210009, Jiangsu, China
[2] Department of Thermal Science and Energy Engineering, University of Science and Technology of China, Hefei 230026, China

Abstract: The excessive reliance on air conditioning for comfortable indoor environment, due to over 80% of individuals' time being spent indoors, with nighttime occupancy reaching 100%, leads to considerable energy consumption and sick building syndrome. A promising solution to simultaneously tackle these challenges involves harnessing solar thermal energy during the day to facilitate the all-day heating and removal of indoor pollutants. Here, a proof-of-concept solar-based Trombe-wall thermal catalytic purification battery (TCPB), integrating multi-layer-design phase changing materials (PCM) and room-temperature thermal catalysts (RTTC), is reported for the first time. The density functional theory simulation shows that RTTC stoichiometric surface (100) occurs abundant active sites, and reduced surface (100) facilitates adsorption/activation of oxygen in atmosphere, thereby enhancing room-temperature formaldehyde oxidation activity. Based on the designed prototype, two adoptable operation modes can be flexible on residential and office buildings, maintaining charging and/or discharging in daytime and discharging in nighttime to realize all-day heating and purification. With calculation of verified mathematical model, the combination of RTTC and PCM technology exhibited excellent heating and purification performance. The amount of clean air stored during the day was 7.12 m3 and the amount of clean air at night could be 39.39 m3. The heat absorption efficiency of TCPB prototype could reach 40.85 %, and the heat release efficiency was 58.08 %.

1. INTRODUCTION

Research indicated that individuals spent approximately 80% of their day indoors, with increasing demands for quality living environments accompanying improvements in thermal comfort and indoor air quality (J.F. Nicol, 2002, Santamouris, 2014). Presently, the energy consumed to enhance occupants' comfort comprises roughly 15–20% of global energy consumption, a figure anticipated to surge exponentially in the forthcoming decades (Rode et al., 2021). Specifically, excessive dependence on air conditioning to attain comfortable indoor temperatures lead to considerable energy consumption and contributes to sick building syndrome (SBS) (Kılıç Depren et al., 2022, Zhou et al., 2019).

With society's pursuit of sustainable remedies to address these challenges, passive solar building systems (Li and Zeng, 2024, Santamouris, 2014, de Gracia and Cabeza, 2015, He et al., 2021) emerged as a promising approach to curbing energy consumption while enhancing indoor air quality concurrently. Among them, low-temperature thermal catalytic technology is a method of catalytic reaction conducted in the temperature range from room temperature to moderate temperatures (Kumar et al., 2023, Ye et al., 2020). Compared to traditional high-temperature catalysis, room-temperature thermal catalytic technology driven byheat consumes less energy and exhibits higher catalytic efficiency.

Considering the characteristics of the attenuation and fluctuation of the heat source required for indoor catalytic technology, along with human circadian rhythms, meeting the indoor air quality needs during both daytime and night-time has become a research focus. In urban residential buildings, the demand for purification decreases during daytime on workdays, increases after returning home at night, and requires purification throughout the day on weekends. Therefore, the development of multi-mode systems with adjustable modes to achieve primary purification during the day, primary purification at night, and overall purification will be beneficial for ensuring residents' health and reducing energy consumption for health needs. The key issue lies in the capture, storage, and release of solar energy. Solar energy (Tabah et al., 2017), as a renewable and eco-friendly energy source, can be harnessed by the extensive surfaces of buildings' facades and rooftops. In such scenarios, solar-thermal energy storage technology (STES) utilizing phase change materials (PCM) emerged as a necessary solution to align and regulate heat generation and consumption (Hu et al., 2022). The PCM energy storage system, with its high energy storage density, effectively addressed thedisparity between energy supply and load demands, thereby providing significant energy savings for space heating and cooling(Hu et al., 2024, Amidu et al., 2023). The PCM could be integrated into building envelopes, with the PCM floor, PCM ceiling, PCM wall, and PCM window being extensively proposed and investigated (Khadiran et al., 2016, Bland et al., 2017). For the space cooling purpose of the PCM roof and PCM wall, Sajith and Tabares Velasco (Wijesuriya and Tabares-Velasco, 2021, Wijesuriya and Tabares-Velasco, 2020) conducted testing and simulation of the surface temperature of macro-encapsulated PCM walls for space cooling applications in the PCM roof and PCM wall. Typically, PCM floors and PCM ceilings were primarily suitable for spaceheating and cooling, respectively, due to their thermal comfort properties (Al-Ahmed et al., 2020, Zhang et al., 2023). PCM roofs and PCM walls were particularly emphasized because they constitute the largest areas of buildings and exert the most significant influence on space heating and cooling loads. Consequently, encapsulated PCM modules can be designed and employed as thermal energy storage batteries in various sections of the building envelope, thereby enhancing practicality in real-world applications.

Studies in this domain demonstrated that passive solar design principles utilized sunlight and thermal energy to minimize dependence on conventional heating and cooling systems, thereby reducing energy consumption and mitigating greenhouse gas emissions while enhancing indoor environmental sustainability (Jyotirmoy Mandal1, 2018, Cao et al., 2016, Luo et al., 2019). The Trombe wall (T-wall), as a promising integral structural feature of passive solar building systems, found extensive application in areas such as space heating (Zeng et al., 2024), photovoltaic power generation (Aftab et al., 2021), air purification (Yu et al., 2017), and virus inactivation (Yu et al., 2022), holding critical importance for human health, particularly amid escalating environmental pollution and the rising prevalence of volatile organic compounds (VOCs) (Zeng et al., 2024). The T-wall utilized its thermal mass tocapture and retain solar energy, thus facilitating building ventilation, passive heating, and other benefits without reliance on mechanical power or conventional energy consumption.

Usually, solar-to-thermal conversion and thermal transport process were involved in STES technology. Additionally, the utilization of solar low-temperature driven photo-thermal conversion/catalytic processes for room-temperature purification functions not only expanded the application potential but also complement STES technology, especially when integrated with PCM modules operating at lower temperatures. Recognizing the need for the thermal catalytic process to reach an optimal reaction temperature, we proposed a scalable solar-based thermal catalytic purification battery (TCPB), as illustrated in Fig. 1a). PCM, as a material providing latent heat through phase change at a constant temperature, can sustain the operating temperature for room- temperature thermal catalysis (RTTC). Moreover, integrating room-temperature thermal catalytic purification technology enhanced the functionality of passive solar buildings. Utilizing catalytic reactions to degrade harmful indoor pollutants like formaldehyde (Zheng et al., 2023) and volatile organic compounds (VOCs) (Salthammer, 2023), thermal catalytic purification systems can greatlyenhance indoor air quality, thereby promoting occupants' health and well-being. This synergistic approach not only addressed energy efficiency objectives but also contributed to creating healthier and more sustainable built environments.

Inspired by the idea of passive solar heating, a novel concept combining a T-wall with RTTC technology and PCM technology has been introduced. This concept merges a solar-based thermal catalytic purification battery with T-wall architectural design, as presented in Fig. 1b). This paper aims to investigate the potential synergies among the T-wall, PCM technology, and room-temperature thermal catalytic purification systems in the framework of passive solar building design.
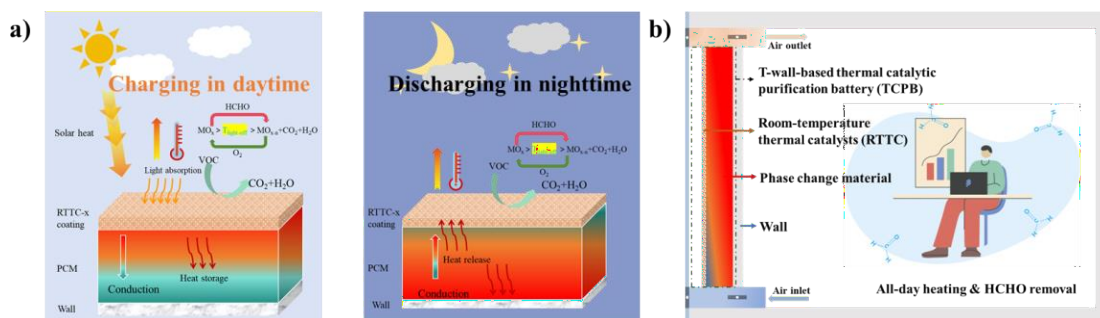
Figure 1: The design, synthesis and characterization of the structure solar-based thermal catalytic purification battery (TCPB) modules. a) A schematic illustration of the scalable solar-based thermal catalytic purification battery module. b) The T-wall with solar-based TCPB for low carbon buildings inthe application of day and night heating and HCHO removal

2. RESULTS

2.1 Characterizations and physicochemical properties of RTTC-X
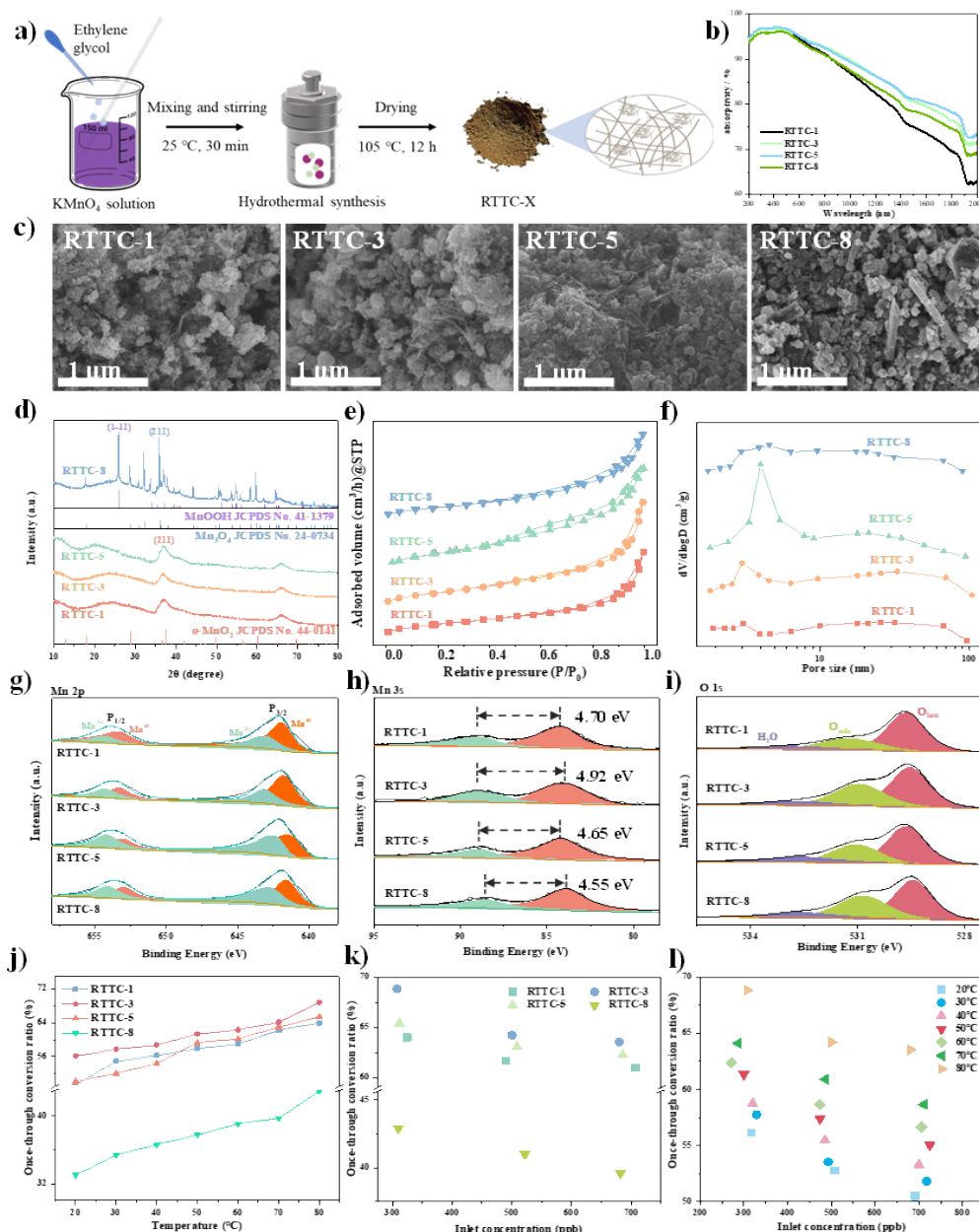
Figure 2: a) The synthesis route of RTTC-X. b) Full spectrum absorption characteristics of RTTC-X. c) SEM images of RTTC-X in the sectional view. d)XRD patterns of different as-synthesized RTTC-X. e-f) N2 adsorption-desorption isotherms and pore size distribution curves of RTTC-X. g-i) XPS spectra of Mn 2p, Mn 3s, O 1s for as-synthesized RTTC-X. j) The once-through ratio of thermal catalysts under different hydrothermal time and catalytic temperature. k) Once-through formaldehyde rate at initial concentration range of 300 ppb, 500 ppb, 700 ppb at 80℃ with RTTC-1, RTTC-3, RTTC-5, RTTC-8. l) Once-through conversion radio at concentration range of 300±21 ppb, 500±33 ppb, 700±35 ppb at different temperature with TC-3

Fig. 2b) illustrated that the as-synthesized catalysts exhibited strong absorption across the entire solar spectrum range from 200 nm to 2000 nm. The average absorptivity values for RTTC-1, RTTC-3, RTTC-5, and RTTC-8 were 83.55%, 86.98%, 87.38%, and 85.19%, respectively. Despite RTTC-3 exhibiting a slightly lower average absorptivity than RTTC-5, it surpassed RTTC-5 in the 600-1200 nm spectrum range. The outstanding full spectrum absorptivity contributed to enhancing catalytic activity.

Fig. 2e-f) depicts the nitrogen adsorption-desorption isotherms and pore size distribution of the synthesized RTTC-X samples. All samples exhibited type IV isotherms with type H3 hysteresis loops, indicating the presence of irregular slit-like mesopores. In the case of samples RTTC-3 and RTTC-5, the hysteresis loop of the adsorption curve occurred between relative pressures of approximately 0.45 and 0.95. This broad hysteresis loop indicated a wide pore size distribution and confirmed the mesoporous characteristics of the samples. RTTC-1 exhibited a specific surface area of 218.03 m2/g, while RTTC-3 and RTTC-5 possessed higher specific surface areas of 234.68 m2/g and 310.08 m2/g, respectively, attributed to their interwoven net structures of ultrafine nanowires observed in the SEM images in Fig. 1c). The presence of larger nanorods in RTTC-8 led to a decrease in specific surface area to 185.66 m2/g, limiting the available surface area for catalytic reactions. The substantial specific surface area of the catalyst provided ample adsorption sites, increasing the likelihood of interaction between the catalyst and formaldehyde even at room temperature. However, it is noteworthy that although RTTC-5 possesses the highest specific surface area (310.08 m2/g), it does not necessarily exhibit the highest catalytic activity.

Fig. 2g-i) depict the XPS analysis of surface elemental composition and chemical states. The average oxidation state (AOS) of Mn was determined using the empirical formula: $AOS = 8.956 - 1.126 \times \Delta E$, where ΔE denotes the disparity in binding energy between the Mn 3s doublet peaks (Galakhov et al., 2002). The Mn AOS values for the samples were found to be 3.66, 3.42, 3.72, and 3.83, respectively, as indicated in Table 1. The decrease in Mn AOS could be attributed to the additional reduction of Mn^{4+} to Mn^{3+} during the hydrothermal process. The highest proportion of Mn^{3+} in the α-MnO_2 structure was observed in the RTTC-3 sample, leading to the creation of numerous oxygen vacancies to preserve charge neutrality. The elevated proportion of Mn^{3+} in RTTC-8 was consistent with the formation of larger nanorods of γ-MnOOH. The peaks detected at binding energies of 643.28 and 654.28 eV correspond to Mn 2p3/2 and Mn 2p1/2 of Mn^{4+}, whereas those at 641.74 eV and 653.05 eV were attributed to Mn^{3+}. The ratios of Mn^{4+}/Mn^{3+} listed in Table 1 were consistent with the Mn AOS results derived from the Mn3s spectra.

The O1s spectra were resolved into three peaks, representing lattice oxygen (Olatt), surface-adsorbed oxygen species (Oads), and surface-adsorbed water, respectively. The ratios of Oads/Olatt were calculated and presented in Table 1. Among the samples, RTTC-3 showed the highest Oads content, suggesting a higher prevalence of surface oxygen vacancies, consistent with the observations from the Mn3s spectra. It is widely acknowledged that Oads exhibit higher reactivity than lattice oxygen at low temperatures and also aids in the regeneration of surface lattice oxygen during catalytic reactions (Setvin et al., 2013).

2.2 Comparative study of adsorption and oxidation mechanism
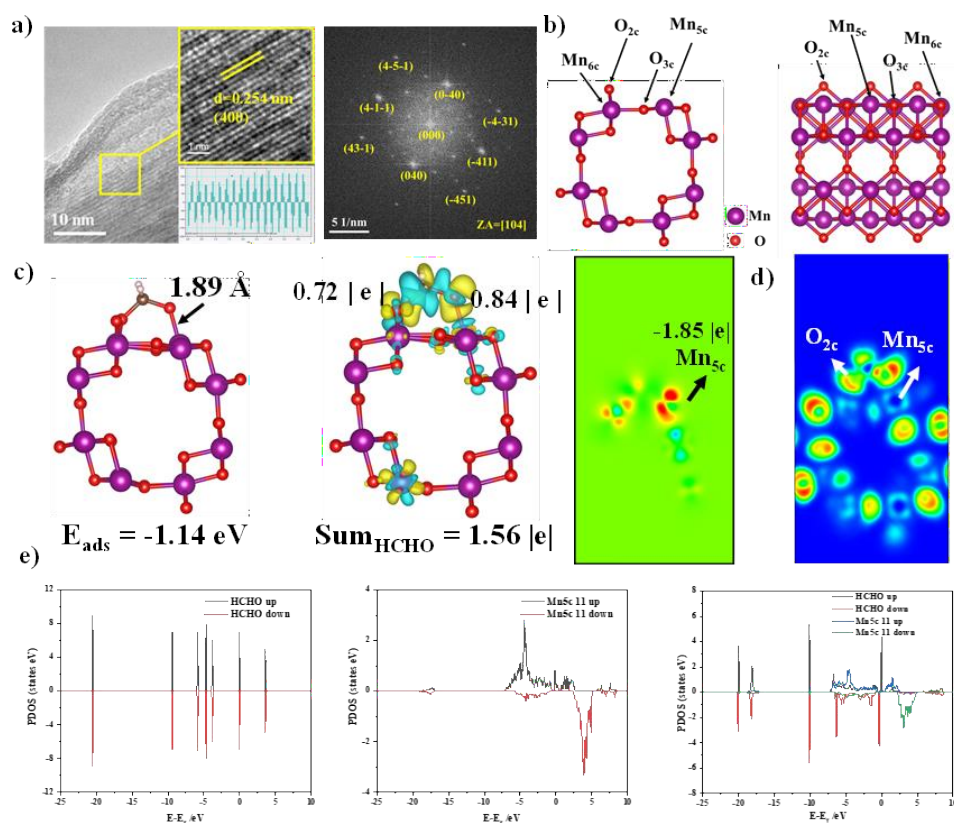
Figure 3: a) TEM image of RTTC-3 and the corresponding FFT image. b) Optimized geometry structure of RTTC-3 (100) surface: front view and side view. c) Adsorption of HCHO on the Mn5c atom of RTTC-3 (100) surface. 2D isosurface map of charge density difference of formaldehyde on the stoichiometric surface and corresponding d) ELF. e) TDOS of HCHO molecule and Mn5c atom of RTTC-3

The adsorption and oxidation mechanisms of formaldehyde were investigated through density functional theory (DFT) calculations using the Vienna Ab-initio Simulation Package (VASP) in this study. From the TEM image Fig. 3a), a lattice spacing of 0.254 nm corresponding to the (400) planes of RTTC are observed. It is noteworthy that the α-MnO2 (100) surface exhibits a typical high-energy state with the least surface energy. As shown in Fig. 3b), α-MnO2 (100) is terminated by two-coordination O (O2c) and five-coordination Mn (Mn5c) atoms. The two kinds of configuration are unsaturated, indicating high bonding ability of the surface. Carbonyl group in HCHO is electrophilic, which tends to adsorb on unsaturated atom on surface and form stable adsorption. DFT calculations of formaldehyde molecules adsorbed on the stoichiometric surface were performed, considering two possible positions (Mn5c and O2c) for the adsorption of gas molecules. The adsorption energies of formaldehyde at these positions on the stoichiometric (100) surface were − 1.14 eV (Mn5c) and + 0.79 eV (O2c). A positive adsorption of energy indicates an endothermic process, which cannot occur spontaneously. A negative adsorption energy indicates an exothermic process, which can occur spontaneously, and the larger the absolute value indicates a more stable adsorption configuration. As shown in Fig. 3c), the oxygen atoms of the gas molecules fall down to form Mn−O bonds with the Mn atoms on the surface of MnO2. The bond length is also related to the adsorption energy binding the adsorbed molecule to the surface: stronger binding typically results in shorter bonds. The calculation showed that the formaldehyde molecules bind with the Mn5c atom to form Mn−O bonds with lengths of 1.89 Å and 2.13 Å, respectively. This indicated that the interaction between the formaldehyde molecule and the surface was stronger than those other configurations. Additionally, the carbonyl bond (C = O) of the formaldehyde molecule was only minimally stretched (Wu et al., 2024), thereby eliminating the possibility of catalytic cracking of formaldehyde. The adsorbed formaldehyde formed a surface dioxymethylene species by bridging the Oads and Mn5c sites, consistent with observations in Fig. 4).

Charge transfer analysis is crucial for elucidating the adsorption mechanism. Bader charge analysis was conducted to quantitatively determine the electronic properties by calculating the amount of charge transferred between the molecules and the surfaces during adsorption. Fig. 3c) shows the charge density difference diagrams for formaldehyde adsorbed on the stoichiometric (100) surface. Blue represents electron depletion, while yellow represents electron gain. The isosurface level was set to 0.03 e/Å3. Fig. 3c) also shows that the charge density is mostly localized on the oxygen atoms. Charge transfer to the gas molecules formaldehyde occurs via a double-fold interaction mechanism transfer mode between Mn5c-Ogas and C4c-O2c (oxygenin gas molecules and MnO2). The net amount of charge transferred to formaldehyde was 1.56 |e|, and active adsorption point Mn5c loss 1.65 |e|. Furthermore, the synergistic interaction between the Mn5c atom and formaldehyde molecule was investigated by examining the HCHO and Mn5c total density of states (TDOS), revealing that the overlapping peaks of formaldehyde and RTTCare split, as depicted in Fig. 3d). Both the electron localization function (ELF) and TDOS confirm the stable adsorption configurationbetween formaldehyde and RTTC-3.

2.3 Design and optimization of solar-based thermal catalytic purification battery
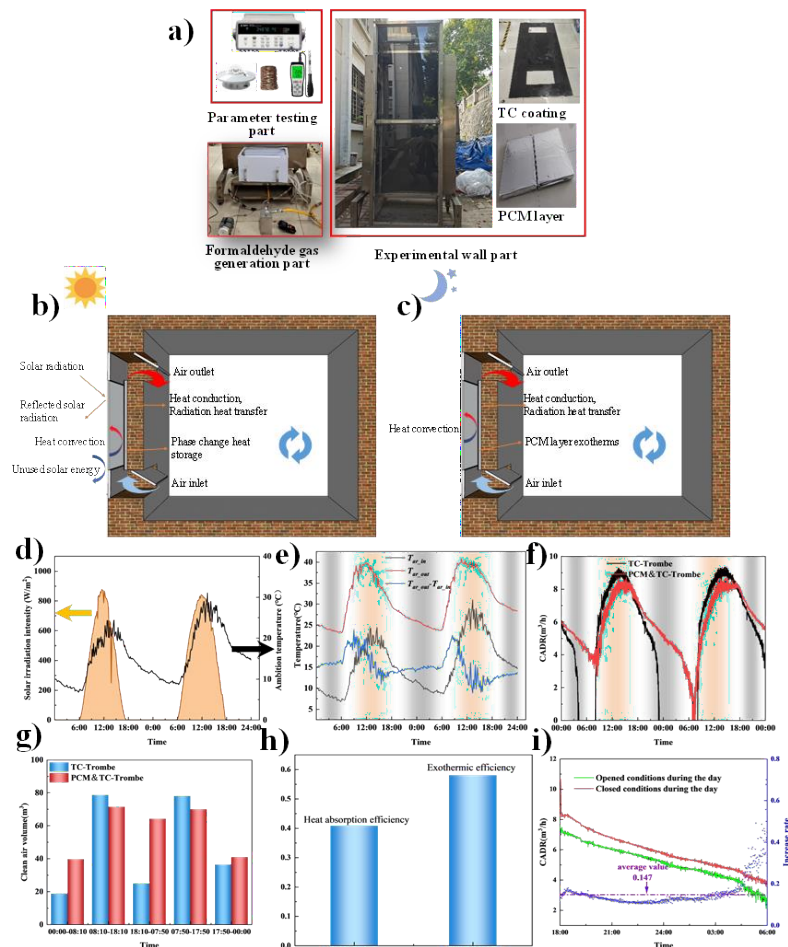
Figure 4: Realization and field test of concept prototype a) Photo of the T-wall TCPB prototype and meteorological equipment for collecting local climatic conditions. b) Daytime operation principle diagram for thermal charging stage. c) Night operation principle diagram for discharge stage. d) Local meteorological data for two consecutive days. e) Inlet and outlet temperature and temperature difference. f) Compared with the ordinary TC-Twall, the CADR generated by the T-wall with TCPB prototype is compared. g) Compared with the ordinary

TC-T wall, the CADR generated by the T- wall with TCPB prototype in each time period is compared. h) Heat absorption efficiency of the TCPB module during the day and exothermic efficiency at night. i) The amount of CADR that can be boosted when closed during the day compared to daytime open conditions

Based on the above proposed RTTC catalyst and PCM technology, a TCPB prototype based on the concept of Trombe wall was constructed and tested on site. As shown in Fig. 4a), TCPB module included two block TCPB thermal unit, each TCPB unit size was 1000 mm * 300 mm * 25 mm and the cost of the material, and the construction of the test bench was within the acceptable range. This experiment took the industrial solar T-wall as the experimental object and continuously measured the thermal performance and purification performance of the TCPB module for two days. The main parameters of TCPB-T-Wall during the experiment can be seen in Table S4. The daytime operation mode was depicted in Fig. 4b). The phase change of the phase change material could effectively absorb the heat of the daytime solar radiation. The nighttime operation mode was depicted in Fig. 4c). The condensation heat release of the phase change material provides power for the chimney effect. In this study, the industrial solar T-wall products with the same shape and size were used as the control group. The maximum heat storage density of the TCPB prototype was 142.2 kwh/m3. Considering that the volume of the PCM layer was 0.06 m3, its heat storage capacity was 8.532 kw*h. The phase transition temperature of PCM (paraffin wax) was 38-43 °C.

The experiment was based on two consecutive days of sunny winter days, presented in Fig. 4d). On November 4 and 5, 2022, the sunrise and sunset times were 6: 23, 17: 12 and 6: 24, 17: 12, respectively. The measuring instrument and its measuring range and accuracy can be seen in Table S5. The average wind speed was 1.9 m/s, the maximum solar radiation intensity was 905.4 W/m2, the average solar radiation intensity was 463.9 W/m2, 523.7 W/m2, and the maximum and minimum ambient temperatures were 21.1 °C and 6.76 °C, respectively. The output air temperature of the TCPB prototype reached 39.87 °C and 40.85 °C respectively due to solar heating, and the temperature difference between the inlet and outlet was 14.94 ~ 23.80 °C, which could achieve the same solar heating performance as the solar T-wall. The average temperature of the TCPB prototype was 38.7 °C during the day and 32.9 °C at night. After 6 o'clock in the daytime, the PCM began to absorb heat under the heating of solar energy and began to phase change and store heat at 12: 10. With the decrease of solar radiation intensity, the PCM layer began to absorb heat and began to condense and release heat at 19: 30. The sensible heat of PCM-T-wall and T-wall could be released into the air flow channel to provide power for the solar chimney effect. The T-wall without PCM layer could not continue to work after sunset at night due to lack of heat storage capacity. At 19:30 at night, when the ambient temperature was reduced to below 14.5 °C, the PCM began to condense and release heat. The ambient temperature was 14.5 ~ 9 °C during the heat release process of about 11 hours at night. The highest temperature in the air flow channel rose to 19.01 °C, and the average temperature rise could reach 14.95 °C. In Fig. 4f-g), based on the ordinary TC-T wall, it could be seen in the two-day test that the PCM-TC-T wall and the TC-T wall could produce almost the same amount of clean air during the daytime, and at night due to the thermal storage of the TCPB prototype and the low temperature catalytic advantage could produce more clean air. Thanks to its excellent low-temperature catalytic performance and heat storage capacity, the TCPB prototype could store clean air during the day and use it at night. In Fig. 4g), the amount of clean air stored during the day was 7.12 m3 and the amount of clean air at night could be 39.39 m3, showing a geometric increase.
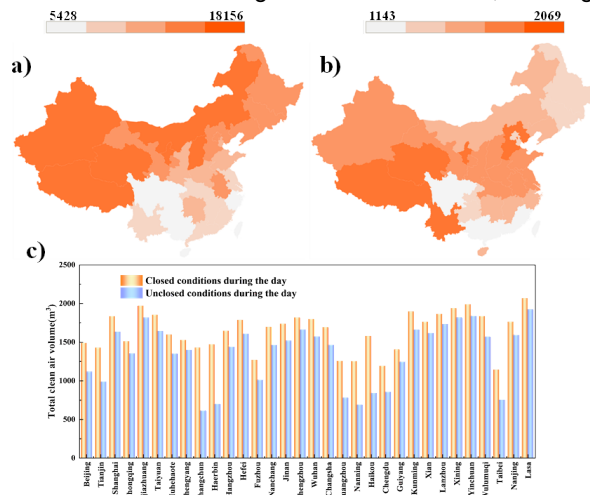
Figure 5: Usage of TCPB prototypes in various cities a) The amount of clean air that can be produced throughout the day by the TCPB prototype ineach city. b) Total clean air volume that the TCPB prototype can produce at night in each city under daytime closed conditions. c) Comparison of total nighttime clean air volumes that can be generated in different cities under closed versus open conditions during the day for the TCPB prototype.

Fig. 4h) shows the heat absorption efficiency of TCPB prototype during the day and the heat release efficiency at night. In the calculation of heat absorption efficiency, only solar energy was used as energy input. The heat absorption efficiency of TCPB prototype could reach 40.85 %, and the heat release efficiency was 58.08 %. The specific calculation method can be seen in Supporting Information Section S3. In order to compare the amount of CADR generated by TCPB at night under different operating modes, as shows in Fig. 4i), the TCPB prototype could produce more clean air at night under closed conditions during the day. The average CADR generated at night under closed conditions was 5.90 m3. The average CADR generated under open conditions was 5.14 m3, and the average CADR throughout the night increased to 14.70 %.

With mathematical simulation of the various cities in the country, the model used could be seen in Supporting Information Section S4. In order to fully evaluate the availability of TCPB prototypes, we chose to simulate the performance of TCPB prototypes in various cities across the country. Considering the heating season in different regions and the all-day opening, the purification capacity of the TCPB prototype shown a trend of strong in the north and weak in the south and strong in the west and weak in the east, as shown in Fig. 5a). The specific data could be seen in Table S6. The reason for this situation was that the instability of solar radiation in the eastern and southern regions and the relatively high ambient temperature compared with the northwest region led to less heat

absorption in the daytime of the TCPB prototype and the weakening of the chimney effect, resulting in reduced power. In order to solve this phenomenon, the flow channel was closed during the daytime when there was no one in the room to enhance the heat storage of the TCPB prototype. Fig. 5b) shows the total amount of clean air that the nighttime TCPB prototype could produce at night under closed conditions during the day. Although TCPB still shows the trend of strong in the north and weak in the south and strong in the west and weak in the east, the difference was reduced. The total clean air volume of all cities in the daytime closed operation mode and the daytime non-closed mode in January can be seen in Table S7. In addition, the total amount of clean air that could be generated at night could be significantly improved compared with the daytime opening conditions, as shown in Fig. 5c). Especially in the case of bad weather, for example, the overall weather in Changchun in January was not very ideal, so it could produce 772.81 m3 more clean air after adopting the closed operation mode during the day. In addition, considering the overall building energy management, especially in terms of renewable energy, more daytime heat can be stored in the TCPB prototype and provided according to the needs of users in the absence of indoor personnel during the day. Using the daytime closed operation mode as the TCPB prototype based on the t-wall may be a reliable option, especially in weather with unstable or insufficient solar energy.

The concept verification prototype of this TCPB space heating system based on TC-T wall was implemented and developed for the first time, showing impressive energy storage, heat redistribution indicators and all-day purification capabilities. The TCPB system based on TC-T wall had the characteristics of high heat storage capacity, low cost, energy saving and purification. It could realize continuous heating and purification day and night, and had shown market potential, making it closer to marketization and industrialization.

3. DISCUSSION

From the perspectives of materials, advanced structural design, and operational modes, a comprehensive design and development of a T-wall-based TCPB prototype was undertaken to enable efficient all-day heating. By controlling the hydrothermal time, specific surface area, pore size distribution, and average surface oxidation state, the material exhibited impressive low-temperature degradation performance at a hydrothermal time of 3 hours. It demonstrated good cyclic stability in continuous adsorption- desorption experiments. RTTC-3 exhibited excellent photothermal performance, with a solar spectrum absorption capacity exceeding 87% in the ultraviolet-visible-near-infrared range, contributing to enhanced photothermal conversion efficiency. Due to its large specific surface area, favorable pore size distribution, average oxidation state, and abundant surface oxygen vacancies, RTTC-3 provided adsorption and catalytic sites for the adsorption and catalytic degradation of gaseous pollutants, thereby enhancing its low-temperature catalytic degradation performance. First-principles calculations indicated that surface oxygen vacancies enhanced the adsorption of pollutants, oxygen, and water, improving surface charge transfer capability, which was favorable for the catalytic degradation of gaseous pollutants.

At the same time, PCM exhibited a robust heat storage capacity, with a heat storage density reaching 8.532 kWh. This exceptional heat storage capability effectively absorbed the heat transferred by RTTC-3. A TCPB prototype, incorporating both RTTC-3 and PCM, was meticulously designed and optimized through a combination of experimental and simulation approaches. This module demonstrated excellent heat storage capacity, photothermal performance, and purification characteristics. To verify the feasibility of the T-wall-based TCPB prototype within a building, a concept verification prototype was constructed and tested on-site. The T-wall-based TCPB prototype employed an all-day operation mode to maximize indoor heating and air purification. It also utilized a closed heat storage mode during the day to ensure maximum retention of stored heat when solar intensity was insufficient, thereby maintaining heat output, cyclic power requirements at night, and indoor air purification in low-temperature nighttime environments. The TCPB prototype leveraged solar energy to achieve 24-hour room purification and heating. Over two consecutive days of outdoor experiments, the output temperature increased by 14.94 °C to 23.80 °C, with a heat absorption efficiency of 40.85 % and a heat release efficiency of 58.08%. In a simulation study of the heating season across various cities in the country, it was concluded that the TCPB prototype's effectiveness was lower in the eastern and southern regions, where solar radiation is unstable, compared to the western and northern regions. Nonetheless, even in areas with insufficient solar radiation, such as Changsha, the TCPB-T-wall could still produce at least 1669.123 m³ of clean air. Additionally, considering the building's overall energy consumption, the entire airflow channel was closed when no one was in the room during the day. This allowed more heat to be stored when solar radiation was weak, facilitating use at night. Moreover, excess electricity generated within the building could provide additional heat for the TCPB prototype, serving as an alternative heat storage method during adverse weather conditions. Experimental results indicated that closed heat storage during the day could increase the CADR by an average of 14.70 % at night compared to the all-day open mode. In simulation studies conducted during the heating season across various cities, the TCPB prototype exhibited significant application potential. The daytime closed mode further enhanced the TCPB prototype's application potential in poor weather conditions, increasing the CADR by at least 6.6 %.

The concept-verified TCPB prototype successfully achieved efficient solar energy absorption, continuous indoor heating, and air circulation purification. It also reduced energy loss during heat storage and release, enabling low-temperature catalytic degradation of indoor pollutants without the need for external power sources. This innovative material and system design approach offers significant potential for indoor air purification and building energy consumption reduction.

4. CONCLUSION

A novel all-day purified Trombe wall combined PCM with thermal catalytic technology was proposed and designed. The experimental and modelling works on the proposed TCPB in two continuous days were conducted. Then, the application of TCPB prototype in the whole country was analysed, and the TCPB prototype was optimized by using the daytime closed operation mode. The main results were as follows:

RTTC-3 demonstrated significant potential for real-world application in the TCPB prototype with its excellent room temperature catalytic performance and advantages in large-scale preparation.

The TCPB prototype had an output temperature rise of 14.94 ℃~23.80 ℃ in two consecutive days of experiments and can achieve a heat absorption efficiency of 40.85 % and a heat release efficiency of 58.08 %.

In the simulation study of the national heating season, the TCPB prototype had a good application. It could produce at least 1669.12 m3 of clean air and could effectively increase the clean air volume at night by at least 6.6 % under the closed operation mode during the day.

5. ACKNOWLEDGEMENT

6. REFERENCES

AFTAB, W., USMAN, A., SHI, J., YUAN, K., QIN, M. & ZOU, R. 2021. Phase change material-integrated latent heat storage systems for sustainable energy solutions. Energy & Environmental Science, 14, 4268- 4291.

AL-AHMED, A., SARı, A., MAZUMDER, M. A. J., HEKIMOĞLU, G., AL-SULAIMAN, F. A. & INAMUDDIN 2020. Thermal energy storage and thermal conductivity properties of Octadecanol-MWCNT composite PCMs as promising organic heat storage materials. Scientific Reports, 10.

AMIDU, M. A., ALI, M., ALKAABI, A. K. & ADDAD, Y. 2023. A critical assessment of nanoparticles enhanced phase change materials (NePCMs) for latent heat energy storage applications. Scientific Reports, 13. BLAND, A., KHZOUZ, M., STATHEROS, T. & GKANAS, E. 2017. PCMs for Residential Building Applications: A Short Review Focused on Disadvantages and Proposals for Future Development. Buildings, 7.

CAO, X., DAI, X. & LIU, J. 2016. Building energy-consumption status worldwide and the state-of-the-art technologies for zero-energy buildings during the past decade. Energy and Buildings, 128, 198- 213.

DE GRACIA, A. & CABEZA, L. F. 2015. Phase change materials and thermal energy storage for buildings. Energy and Buildings, 103, 414-419.

GALAKHOV, V. R., DEMETER, M., BARTKOWSKI, S., NEUMANN, M., OVECHKINA, N. A., KURMAEV, E. Z., LOBACHEVSKAYA, N. I., MUKOVSKII, Y. M., MITCHELL, J. & EDERER, D. L. 2002. Mn3sexchange splitting in mixed-valence manganites. Physical Review B, 65.

HE, F., WEON, S., JEON, W., CHUNG, M. W. & CHOI, W. 2021. Self-wetting triphase photocatalysis for effective and selective removal of hydrophilic volatile organic compounds in air. Nature Communications, 12.

HU, W., LIN, S., CAO, Y., FENG, X. & PAN, Q. 2022. Preparation and characterization of attapulgite- supported phase change energy storage materials. RSC Advances, 12, 15180-15189.

HU, Z., LI, W., YANG, C., HUANG, H., GUO, Y., GE, F. & ZHANG, Y. 2024. Thermal performance of an active casing pipe macro-encapsulated PCM wall for space cooling and heating of residential building in hot summer and cold winter region in China. Construction and Building Materials, 422.

J.F. NICOL, M. A. H. 2002. Adaptive thermal comfort and sustainable thermal standards for buildings. Energy and Buildings, 34, 563-572.

JYOTIRMOY MANDAL1, Y. F., ADAM C. OVERVIG1, MINGXIN JIA2, KERUI SUN1,NORMAN N. SHI1, HUA ZHOU3,4, XIANGHUI XIAO3,4, NANFANG YU1*, YUAN YANG1* 2018. Hierarchically porous, polymercoatings for highly efficient passivedaytime radiative cooling. Science, 362, 315-319.

KHADIRAN, T., HUSSEIN, M. Z., ZAINAL, Z. & RUSLI, R. 2016. Advanced energy storage materials for building applications and their thermal performance characterization: A review. Renewable and Sustainable Energy Reviews, 57, 916-928.

KıLıç DEPREN, S., KARTAL, M. T., ÇOBAN ÇELIKDEMIR, N. & DEPREN, Ö. 2022. Energy consumption and environmental degradation nexus: A systematic review and meta-analysis of fossil fuel and renewable energy consumption. Ecological Informatics, 70.

KUMAR, P., ANTAL, P., WANG, X., WANG, J., TRIVEDI, D., FELLNER, O. F., WU, Y. A., NEMEC, I., SANTANA, V. T., KOPP, J., NEUGEBAUER, P., HU, J., KIBRIA, M. G. & KUMAR, S. 2023. Partial Thermal Condensation

Mediated Synthesis of High- Density Nickel Single Atom Sites on Carbon Nitride for Selective Photooxidation of Methane into Methanol. Small, 20.

LI, B. & ZENG, S. 2024. Bilateral passive thermal management for dynamical temperature regulation. Scientific Reports, 14.

LUO, H., LI, Q., DU, K., XU, Z., ZHU, H., LIU, D., CAI, L., GHOSH, P. & QIU, M. 2019. An ultra-thin colored textile with simultaneous solar and passive heating abilities. Nano Energy, 65.

RODE, A., CARLETON, T., DELGADO, M., GREENSTONE, M., HOUSER, T., HSIANG, S., HULTGREN, A., JINA, A., KOPP, R. E., MCCUSKER, K. E., NATH, I., RISING, J. & YUAN, J. 2021. Estimating a social cost of carbon for global energy consumption. Nature, 598, 308-314.

SALTHAMMER, T. 2023. Acetaldehyde in the indoor environment. Environmental Science: Atmospheres, 3, 474-493.

SANTAMOURIS, M. 2014. Cooling the cities – A review of reflective and green roof mitigation technologies to fight heat island and improve comfort in urban environments. Solar Energy, 103, 682-703.

SETVIN, M., ASCHAUER, U., SCHEIBER, P., LI, Y. F., HOU, W., SCHMID, M., SELLONI, A. & DIEBOLD, U. 2013. Reaction of O_2 with subsurface oxygen vacancies on TiO_2 anatase (101). Science, 341, 988-91.

TABAH, B., PULIDINDI, I. N., CHITTURI, V. R., REDDY ARAVA, L. M., VARVAK, A., FORAN, E. & GEDANKEN, A. 2017. Solar-energy-driven conversion of biomass to bioethanol: a sustainable approach. Journal of Materials Chemistry A, 5, 15486-15506.

WIJESURIYA, S. & TABARES-VELASCO, P. C. 2020. Experimental apparatus and methodology to test and quantify thermal performance of micro and macro-encapsulated phase change materials in building envelope applications. Journal of Energy Storage, 32.

WIJESURIYA, S. & TABARES-VELASCO, P. C. 2021. Empirical validation and comparison of methodologies to simulate micro and macro-encapsulated PCMs in the building envelope. Applied Thermal Engineering, 188.

WU, L., WANG, Z., LIU, J., LIU, C., LI, X., ZHANG, Y., WANG, W., MA, J. & SUN, Z. 2024. Selective ozone catalyzation modulated by surface and bulk oxygen vacancies over MnO_2 for superior water purification. Applied Catalysis B: Environmental, 343.

YE, J., YU, Y., FAN, J., CHENG, B., YU, J. & HO, W. 2020. Room-temperature formaldehyde catalytic decomposition. Environmental Science: Nano, 7, 3655-3709.

YU, B., HE, W., LI, N., WANG, L., CAI, J., CHEN, H., JI, J. & XU, G. 2017. Experimental and numerical performance analysis of a TC-Trombe wall. Applied Energy, 206, 70-82.

YU, B., LI, N., YAN, C., LIU, X., LIU, H., JI, J. & XU, X. 2022. The comprehensive performance analysis on a novel high-performance air-purification-sterilization type PV-Trombe wall. Renewable Energy, 182, 1201-1218.

ZENG, Z., YANG, X., ZHAO, B., CHEN, Z., CHUA, K. J. E. & WANG, R. 2024. A scalable solar-based adsorption thermal battery for day and night heating in a low-carbon scenario. Energy & Environmental Science, 17, 800-812.

ZHANG, Y. F., TANG, J. B., CHEN, J. L., ZHANG, Y. H., CHEN, X. X., DING, M., ZHOU, W. J., XU, X. J., LIU, H. &

XUE, G. B. 2023. Accelerating the solar-thermal energy storage via inner-light supplying with optical waveguide. Nature Communications, 14, 3456.

ZHENG, J. Y., ZHANG, H., HE, J. D., TIAN, B. H., HAN, C. B., CUI, Z. & YAN, H. 2023. Bimetallic oxide

$Cu_2O@MnO_2$ with exposed phase interfaces for dual-effect purification of indoor formaldehyde and pathogenic bacteria. Nanoscale Advances, 5, 2027-2037.

ZHOU, L., SONG, H., LIANG, J., SINGER, M., ZHOU, M., STEGENBURGS, E., ZHANG, N., XU, C., NG, T., YU, Z., OOI, B. & GAN, Q. 2019. A polydimethylsiloxane-coated metal structure for all-day radiative cooling. Nature Sustainability, 2, 718-724.

#226: Study on energy consumption characteristics and optimization scheduling of dormitories in southwest China universities based on student energy consumption behavior

Kun YANG[1,2], Wei ZHANG[1,2*], Xiding ZENG[1,2], Zhangyu LI[1,2], Jiahong GUO[1,2], Ruiwen ZOU[1,2]

[1] College of Architecture and Environment, Sichuan University, 610065, Chengdu, China
[2] Yibin Industrial Research Institute, Sichuan University, 644000, Yibin, China
*Corresponding Author: A/Prof. Wei Zhang, Email: zhangwei821@scu.edu.cn

Abstract: Buildings contribute to over one-third of global energy-related carbon emissions. Among these, university buildings, especially dormitories, have high energy consumption and density, making them a key focus for energy conservation and emission reduction. Considering that individual energy use behavior significantly impacts building energy consumption, it is crucial to effectively manage and regulate dormitory energy loads based on students' usage habits to reduce energy consumption. This study targets universities in southwestern China and proposes a two-stage energy optimization scheduling strategy based on data mining and flexible load control, tailored to students' energy use behavior. A survey was conducted to collect data on dormitory energy use behavior among university students. Typical energy use characteristics were extracted, and key influencing factors were identified. Subsequently, a two-step clustering analysis method was employed to categorize student dormitories into four major types, analyzing their main features. The type with the highest energy-saving potential was selected to establish a typical energy use model for student dormitories, producing typical energy load curves for summer and winter seasons. Regulatory demands were identified, and flexible load control was utilized for optimization. The research results indicate that employing demand-side management methods, with the scheduling of flexible loads, can smooth dormitory energy usage curves while significantly reducing energy consumption. Additionally, energy-saving potential can be further explored through building design optimization and the incorporation of renewable energy sources.

Keywords: University Dormitory; Energy Consumption; Student Energy Behaviors; Questionnaire Survey; Demand Side Management

1. INTRODUCTION

As global energy resources become increasingly scarce and environmental pollution intensifies, energy conservation and emission reduction have become focal points for governments and academia worldwide. To address these challenges, various climate and energy targets, such as the Paris Agreement and the 2030 Climate and Energy Framework, have been proposed to enhance energy efficiency, reduce carbon emissions, and promote sustainable development [1]. China's 14th Five-Year Plan for Building Energy Efficiency and Green Building Development sets a goal for 70% of new buildings to be green by 2025 [2]. Buildings are one of the primary energy-consuming sectors, accounting for over one-third of global final energy consumption, with carbon emissions in many countries representing 30% to 40% of total emissions [3]. With the global population growing and urbanization accelerating, the demand for building energy continues to rise. The energy-saving potential in buildings is significant, offering substantial economic and social benefits, and is a key focus in global efforts for energy conservation and emission reduction.

Among all types of buildings, research on energy management in campus buildings, particularly student dormitories, is relatively limited. The 2022 China Building Energy Efficiency Annual Report indicates that while university students represent 3% of the national population, their energy consumption accounts for 8% of the total energy use in the country. Dormitories, in particular, constitute a substantial part of this energy use. As the primary living spaces for students, dormitories are occupied for most of the year, with near-constant energy consumption, especially during academic terms [4]. Students' schedules are relatively consistent, leading to a pronounced concentration of energy use during specific times, resulting in clear peaks and troughs in energy demand [5]. Additionally, dormitories are centrally managed by the university, facilitating the implementation of energy-saving measures and management strategies. In summary, student dormitories, due to their unique energy consumption patterns and usage characteristics, present significant potential for optimization in building energy efficiency. By conducting in-depth studies and effective management of dormitory energy use, not only can substantial energy savings be achieved, but a model for energy conservation can also be established, fostering awareness and habits among students that could lead to broader energy-saving effects in the future. University dormitories present unique challenges in building energy efficiency. Many dormitory buildings are older, with outdated designs and equipment, leading to low energy efficiency. Additionally, the general lack of energy awareness among students makes energy consumption data difficult to collect and energy management challenging, often resulting in energy wastage. Scholars have addressed these issues and proposed various solutions for improving building energy efficiency. For instance, Yingzi Zhang [6] used NETLOGO to construct an agent-based dormitory energy consumption model, proposing optimization measures for ventilation and lighting. These optimizations reduced energy consumption by 14.24% in summer and 17.85% in winter compared to existing dormitories. Optimizing dormitory design is an effective way to achieve energy savings, and the integration of renewable energy can significantly reduce carbon emissions. Ceylin Sirin [7] applied Building-Integrated Photovoltaics (BIPV) systems to building facades, which met a significant portion of the building's thermal and electrical loads while reducing carbon emissions by 32%. Martin Thebault [8] analyzed optimal PV configurations for a building in France, demonstrating that photovoltaic systems not only reduce reliance on conventional energy sources but also lower energy costs. Ying Yu [9] proposed a dual-layer optimization design for campus buildings, reducing electricity purchase costs by 4.6% and increasing photovoltaic self-consumption by 15.4%. Rajavelu Dharani [10] used demand-side management to reduce energy consumption in an Indian university campus, lowering annual electricity costs by approximately 10%. In a study of Seoul National University's teaching buildings, Song et al. found that optimizing class schedules could save 4% of energy during air-conditioning seasons (summer and winter). Yaxian Zhou [11] conducted a case study on three typical dormitory types at a Chinese university—undergraduate, master's, and doctoral dormitories—providing insights into the electricity usage of different dormitory types. Xu Ying [12] combined digital gene mapping with a multi-objective genetic algorithm to optimize the performance of university dormitories, adaptable to various climate conditions. These studies highlight the significant potential for energy savings in university buildings, particularly dormitories. However, current research on energy consumption behavior in student dormitories and its optimization is limited, with a lack of targeted strategies based on students' energy usage habits.

The literature review indicates that both domestic and international scholars have extensively studied building energy efficiency, focusing on aspects such as building structure and load management, while emphasizing the importance of student dormitories in campus energy conservation research. However, dormitory energy consumption is closely related to student energy usage behaviors [13]. Previous research on energy saving in university dormitories often centered on the buildings themselves, overlooking the impact of student behavior on dormitory load. Additionally, the energy consumption characteristics of dormitories vary depending on the type of students and dormitories. While earlier studies have analyzed the influence of user behavior on energy efficiency in university dormitories, they have not specifically addressed how to improve energy efficiency based on student energy usage patterns. Furthermore, significant regional and seasonal variations in climate lead to distinct differences in energy demand across different areas, necessitating targeted studies to accurately understand dormitory energy consumption characteristics under varying climatic conditions [14]. Consequently, this study focuses on universities in Southwest China, exploring the impact of the region's unique climatic and geographic conditions on student dormitory energy use. By combining survey questionnaires with actual monitoring data, the study collects comprehensive information on student energy usage habits and employs cluster analysis to categorize this data, identifying key factors that influence energy consumption. Based on these findings, the study optimizes energy use in university dormitories by balancing flexible load control with student willingness to adjust energy usage, and finally provides recommendations for dormitory energy consumption optimization from multiple perspectives.

This paper is divided into four sections. The second section provides a detailed overview of the research methodology, including the selection of the university, data collection methods, the design of student surveys, and data processing and analysis techniques. It also discusses the optimization pathways for energy efficiency in university dormitories, laying the groundwork for subsequent analysis. The third section presents an in-depth case study, analyzing energy consumption patterns and typical daily load curves based on data from a university in western China. The methodology proposed in the second section is then applied to optimize the dormitory energy load, demonstrating its feasibility and effectiveness. The fourth section discusses the results of the dormitory energy optimization, offering recommendations from various perspectives on improving energy use in university dormitories. Finally, the fifth section provides a summary of the paper, outlining the main findings, presenting optimization strategies and results, and suggesting directions for future research and potential improvements to enhance university energy management practices.

2. METHODOLOGY

The research methodology is illustrated in Figure 1 and comprises four main steps.

Step 1: Questionnaire Design and Data Collection

Student characteristics and basic dormitory energy usage behaviors were gathered through a questionnaire survey. Additionally, smart plugs were used to collect energy consumption data from student dormitories.

Step 2: Dormitory Energy Data Processing and Analysis

The data collected in the first step were processed using cluster analysis to identify energy consumption characteristics and typical usage patterns in student dormitories.

Step 3: Development of a Typical Dormitory Energy Consumption Model

Based on the identified usage patterns, an energy system model for student dormitories was developed. A simulation was conducted to generate typical daily load curves, which reflect the energy consumption of various appliances at different times, helping to identify peak load periods and major energy-consuming devices.

Step 4: Optimization of Dormitory Flexible Load Scheduling

Energy-consuming devices in dormitories were categorized into base load and flexible load (including shiftable and reducible loads) [15]. Flexible load management was applied to optimize the typical daily load of dormitories, aiming to smooth load curves and reduce overall energy consumption.
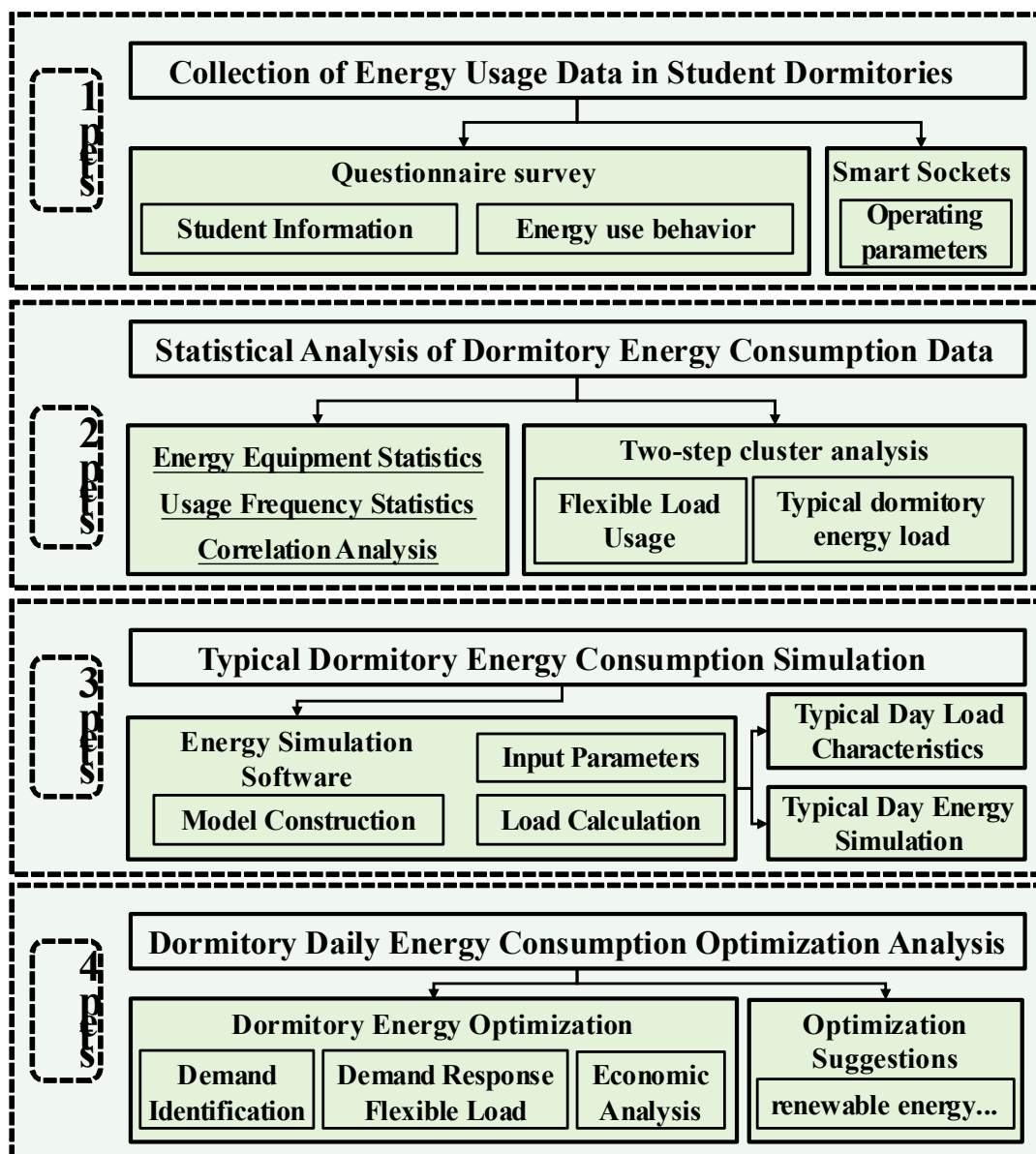
Figure 1: Methodology for optimizing energy efficiency in university dormitory

2.1. Energy use data collection for university dormitories

This study aims to optimize energy scheduling in university dormitories. Dormitory energy consumption is closely related to students' energy use habits. In this research, we focus on a university in western China. A questionnaire survey will be conducted to collect data on students' energy usage and behavior in the dormitories. This method provides a comprehensive and accurate understanding of how various energy-consuming devices are used by students, while being cost-effective, efficient, and conducive to statistical

analysis. The insights gained will reveal patterns in students' energy usage behavior and provide foundational data to support the development of effective energy management strategies.

The field survey was conducted by one graduate student and two undergraduates. To gain insight into the energy use habits of graduate student dormitories, a detailed questionnaire was designed. The questionnaire consists of two parts. The first part collects personal information, including gender, grade, major, and consumption level. The second part gathers data on dormitory energy use, focusing on the types of energy-consuming devices, their power ratings, and usage times throughout the day. Special attention was given to ensuring anonymity to protect respondents' privacy and enhance the authenticity and completeness of responses. Furthermore, to ensure the accuracy of the collected data, ten student dormitories were randomly selected for simultaneous monitoring. Smart sockets were used to track the operational data of energy-consuming devices in these dormitories, as illustrated in Figure 2. Data collected through Zigbee protocol were transmitted to a gateway device and subsequently uploaded to a cloud-based data storage platform for centralized analysis and processing.

Figure 2: Collection of dormitory energy consumption data

2.2. Energy optimization pathways for university dormitories

Due to variations in student energy usage habits, significant fluctuations in dormitory energy consumption may occur. To investigate the typical energy use characteristics of student dormitories and identify key influencing factors, this study employs a clustering analysis approach [16]. Initially, a two-step clustering analysis is conducted to identify various typical energy behavior patterns in dormitories and explore the critical factors influencing these patterns. Dormitory energy behaviors are categorized based on similarity, taking into account factors such as students' academic backgrounds, personal lifestyles, and ownership of electric vehicles, thereby revealing the typical energy use characteristics of different groups.

Based on the typical dormitory energy consumption features obtained from the clustering analysis, a simulation model for dormitories is developed. Energy consumption simulation software is used to generate typical daily load curves for dormitories. The study identifies the control needs for typical daily loads and proposes energy-saving strategies from the perspectives of demand side, supply side, and user side, offering optimization recommendations for dormitory energy consumption.

3. CASE STUDY OF SICHUAN UNIVERSITY DORMITORIES

3.1. Analysis of survey subjects' characteristics

This study conducted a random sampling questionnaire survey in 2023 at a university in southwestern China. The survey collected basic information about students and data on their energy usage behavior in dormitories. A total of 217 questionnaires were distributed, with 200 valid responses received, resulting in a response rate of 92%. The collected data were initially subjected to descriptive statistical analysis, with key characteristics of dormitory energy use summarized through charts and graphs. Table 1 presents the basic characteristics of the surveyed students, including gender, grade, major, consumption level, residence campus, and housing type. The gender distribution was nearly equal, with males and females comprising 53.50% and 46.50%, respectively. Undergraduates made up the majority at 75.00%. Engineering students represented the largest group among majors, at 69.00%, followed by those in liberal arts, medicine, and sciences. In terms of consumption levels, 70% of students fell to the 1,000-2,000 RMB/month range. The most common housing type was four-person rooms, at 80.00%. Analyzing these basic characteristics provides a clearer understanding of the overall profile of the students surveyed.

Table 1: Statistical table of basic characteristics of students surveyed

Characteristics	Classification	Quantity	Percentage	Characteristics	Classification	Quantity	Percentage
Gender	male	52	53.50%		< 1K	10	5.00%
	female	48	46.50%		1K-1.5K	70	35.00%
grade	Freshman	6	6.00%	Consumption	1.5K-2K	68	34.00%
	Sophomore	16	15.50%		2K-3K	43	21.50%
	Junior	21	21.50%		> 3K	9	4.50%
	Senior	32	32.00%	Dorm	two-person	9	4.50%

			Type			
Graduate	18	17.50%		three-person	31	15.50%
PhD	7	7.50%		four-person	160	80.00%

3.2. Dormitory flexible load usage patterns

This study also analyzed the usage frequency and duration of energy-consuming devices in dormitories. Certain devices and appliances, such as washing machines and electric scooters, exhibit flexible usage patterns that allow adjustments to their operation times [17]. Additionally, the settings of air conditioning units, including temperature and power, can be modified. These devices represent flexible loads within the energy consumption profile of student dormitories, as they can be adjusted based on students' needs. Consequently, the study further examined the usage times and frequencies of these devices and investigated the reasons behind their impacts. Figure 3-4 illustrate the probability distributions of the usage times for electric scooters and washing machines.
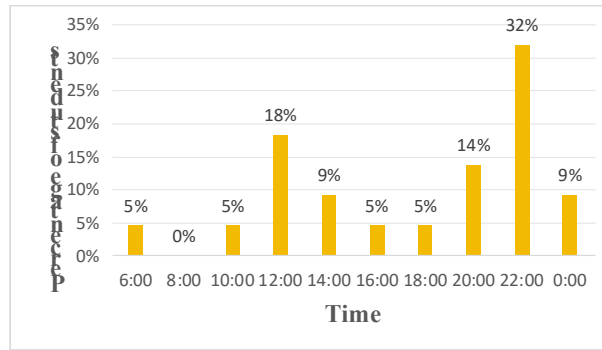
Figure 3: Probability distribution of electric vehicle charging time
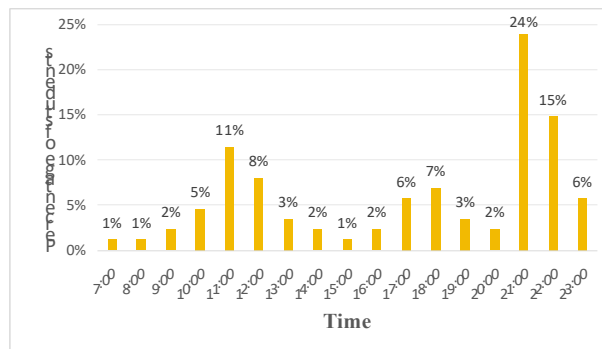
Figure 4: Probability distribution of washing machine charging time

This study also examined the relationship between student gender and the temperature settings of air conditioning units during winter and summer, as shown in Table 2. Seasonal temperature variations significantly influence air conditioning temperature settings and usage frequency. Users can adjust the power of the air conditioning units by modifying the temperature settings, thereby regulating the daily load in dormitories.

Table 2: Air conditioning set temperatures in university dormitories during typical seasons

Weather	Gender	Setting Temperature（℃）					
		18-20	20-22	22-24	24-26	26-28	28-30
Summer	male	7	5	12	26	2	0
	female	7	6	17	17	1	0
Winter	male	0	4	5	16	17	10
	female	0	2	7	5	21	13

3.3. Clustering analysis of typical energy usage dormitory types

Understanding the configuration and usage of dormitory equipment is crucial for improving management practices and optimizing resource allocation. Correlation analysis, as a statistical method, can reveal relationships between different variables, helping to identify key factors influencing student dormitory life [18]. This study aims to use correlation analysis to uncover the relationships between equipment usage in student dormitories and basic student information, with correlation heatmaps generated using ChiPlot (https://www.chiplot.online/).
Figure 5 illustrates the results of the correlation analysis between multiple variables, with the heatmap displaying the strength of these correlations. Overall, most variables show low correlation coefficients, indicating a high degree of independence between them. Similarities in student energy usage are observed, with minimal differences across various majors and academic years. The usage of dormitory equipment is primarily influenced by the duration students spend in their dormitories, with longer residence times

leading to increased energy consumption.
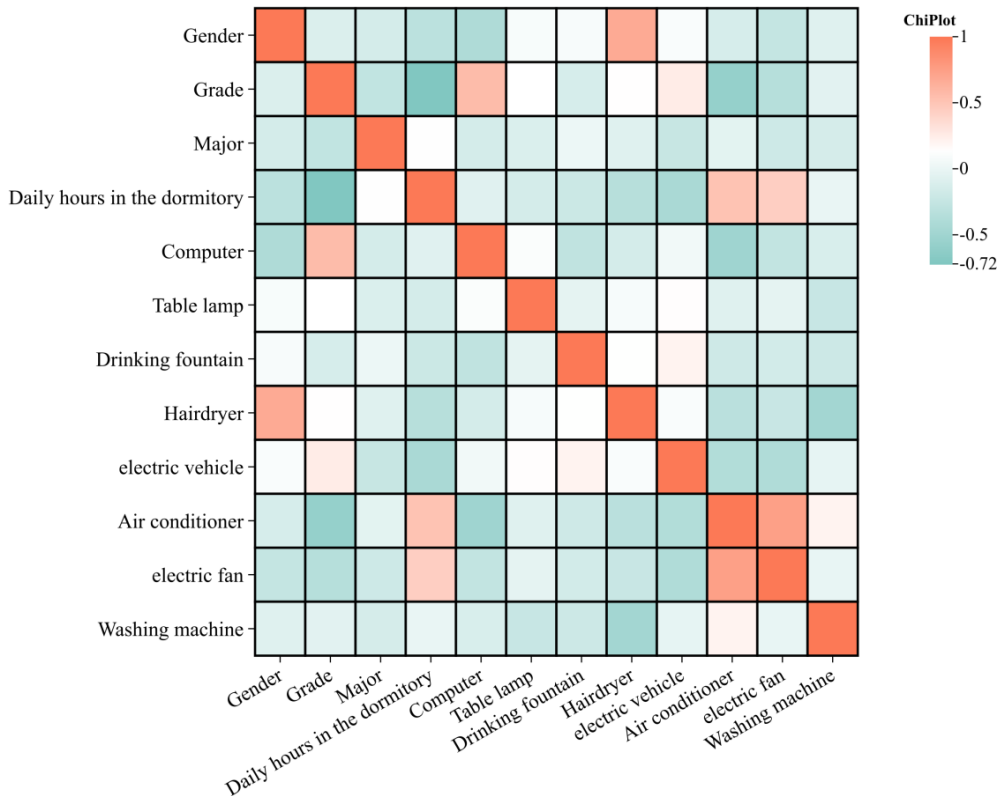
Figure 5: Heatmap of correlation analysis for dormitory energy use equipment

To further investigate the energy usage characteristics of university dormitories, a two-stage cluster analysis was conducted to extract typical student energy consumption patterns for subsequent analysis. After 13 iterations, the data were categorized into four types: low-energy, moderate-energy, high-energy, and luxury. The high-energy dormitories account for the largest proportion. In summer, air conditioning runs for nearly 12 hours, while in winter, it operates for around 10 hours. Energy consumption in these dormitories is 54.3% higher in summer and 58.5% higher in winter compared to low-energy dormitories. Their average daily energy consumption is also high, at 33.57 kW/day in summer and 31.96 kW/day in winter. This makes them the dormitory type with the greatest potential for energy savings.

4. RESULTS AND DISCUSSION

4.1. Development of typical dormitory energy consumption models

Based on the results of the two-stage clustering analysis, the study selected the high energy consumption category for energy use analysis. The base electrical load was calculated using the load factor method, while the heating and cooling loads were determined using building energy simulation software [19]. Following the establishment of the model and parameter settings, simulations were conducted for two typical days, one in summer and one in winter, resulting in detailed energy consumption curves for high-energy type dormitories. As shown in Figure 6, these curves illustrate the variations in power load within a 24-hour period for the dormitories. Figure 6(a) presents the energy consumption curve for a typical summer day. The peak load during this period is 2.70 kW, with an average daily load of 1.40 kW. The summer curve exhibits two main peaks: the first peak occurs from 12:00 to 14:00, when air conditioning is in operation, and some students begin using computers for work or gaming. Major energy-consuming devices include air conditioners, computers, and dormitory lighting. The second peak occurs from 20:00 to 23:00, primarily involving devices such as electric vehicles, hairdryers, and washing machines. Various flexible loads within the peak range in summer have potential for load adjustment. Figure 6(b) displays the energy consumption curve for a typical winter day, with a peak load of 2.64 kW and an average daily load of 1.33 kW. The winter curve also shows two peaks. The first peak is observed from 08:00 to 10:00, with primary energy-consuming devices being computers, heaters, and dormitory lighting. The second peak, occurring from 19:00 to 23:00, is similar to the summer peak, as students return to their dormitories after dinner. Major devices during this period include electric vehicles, hairdryers, computers, and dormitory lighting. Multiple flexible loads within the peak range in winter also exhibit potential for load regulation.
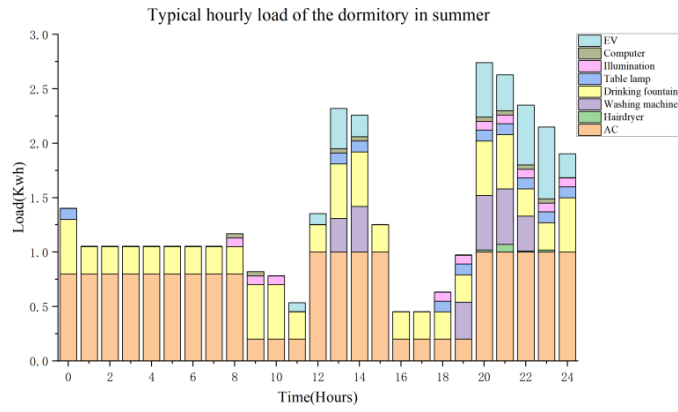
(a) Typical hourly load in summer
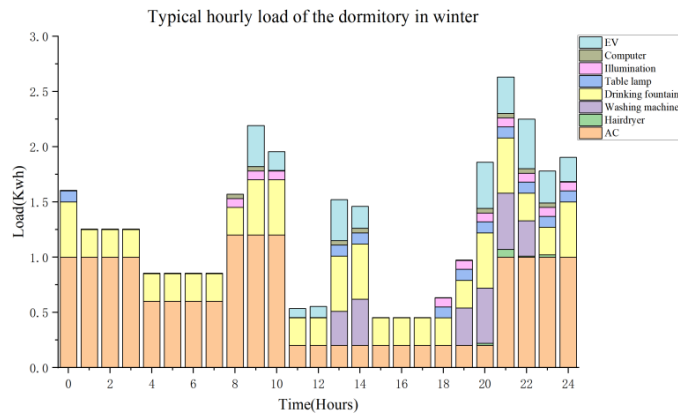
(b) Typical hourly load in winter

Figure 6: Typical seasonal load profile for High-Energy dormitories

4.2. Optimization of dormitory energy use with flexible load

In this case study, the energy load of student dormitories is categorized into three types: base load, shiftable load, and reducible load [20]. The shiftable load includes electric vehicles, washing machines, and hair dryers, while the reducible load pertains to air conditioning. Based on research on dormitory energy consumption, this study applies two demand management strategies—load reduction and load shifting—to optimize the energy load of high-consumption dormitories. The load reduction method targets air conditioning loads during peak periods to decrease peak energy consumption. The load shifting method focuses on shiftable loads, such as electric vehicles, washing machines, and hair dryers, allowing students to use these devices during off-peak times to reduce peak loads and smooth the load curve.

This study optimizes the scheduling of typical daily loads in summer and winter for high-energy dormitories. Figure 7 shows the load curves for student dormitories after optimization. The optimized summer load curve indicates a peak load of 2.02 kW, representing a 25.18% reduction compared to pre-optimization levels, and a daily average load reduction of 10.71%. For winter, the peak load is 1.99 kW, a 24.62% decrease, and the daily average load is 1.20 kW, reduced by 9.77%. The study applied load reduction and shifting strategies for high-consumption dormitories. Flexible loads such as electric vehicles, washing machines, and hairdryers were adjusted to low-demand periods based on student acceptance, thus lowering peak loads and smoothing daily load curves. Additionally, since air conditioning constitutes a significant portion of dormitory energy use, adjusting air conditioner temperature settings helped reduce daily loads. Consequently, peak loads were reduced, and energy costs decreased by nearly 10% following the optimization of load scheduling.

(a) Comparison of summer daily load optimization

(b) Comparison of winter daily load optimization
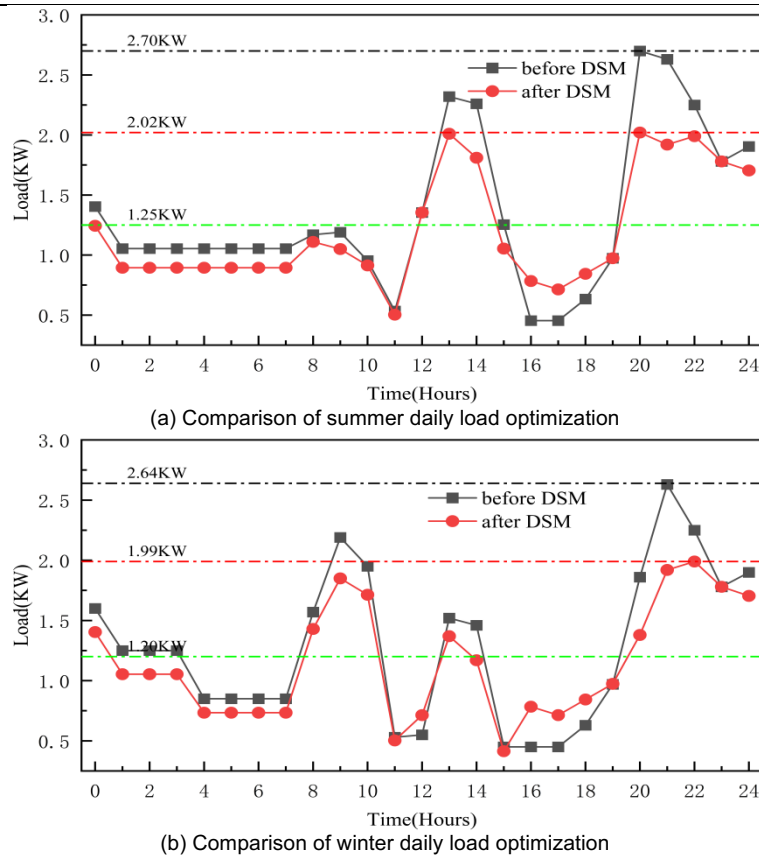
Figure 7: Comparison of DSM approaches in daily load profile curve

Optimizing dormitory energy use through flexible load adjustments can yield favorable results. However, due to a lack of energy conservation awareness among students and its impact on their habits, the potential of flexible load regulation is often overlooked. To effectively optimize load scheduling in university dormitories, a comprehensive energy data collection system should first be established to identify dormitory load regulation needs. Subsequently, targeted adjustments using flexible loads should be implemented. Given the diversity in student energy use behaviors, a user energy profile should be developed to optimize within acceptable limits for students. Therefore, energy optimization in dormitories requires consideration from both the supply and demand sides, as well as an understanding of students' energy use habits. Systematic energy conservation education is essential to enhance students' awareness of energy utilization and its environmental impacts, emphasizing the importance and necessity of flexible load adjustments. Furthermore, factors such as dormitory orientation, lighting, and ventilation significantly affect building energy consumption. These factors should be carefully considered in dormitory design, with efforts made to integrate local renewable energy sources. By implementing these measures, significant reductions in dormitory energy consumption can be achieved, advancing campus energy management optimization.

5. CONCLUSION AND OUTLOOK

This study optimized the load scheduling of university student dormitories. Based on the energy usage characteristics of the dormitories, an energy consumption model was developed, yielding typical daily consumption curves. By optimizing energy usage behavior and employing demand response strategies, the study significantly reduced peak loads on typical summer and winter days, smoothed the daily load curves, and effectively lowered energy costs.

This study classified student dormitory energy use behaviors and established an energy profile. This study focuses on Sichuan University in Western China, classifying dormitory energy consumption based on student behavior into four categories: low, moderate, high, and luxury consumption types. High-consumption dormitories account for the largest proportion, with energy usage in summer and winter exceeding low-consumption dormitories by 54.3% and 58.5%, respectively, making them the dormitories with the greatest potential for energy savings.

Demand-side management was used to effectively smooth the system load curve through load regulation. This study employed DSM strategies to reduce peak loads in high-energy-consuming dormitories by nearly 25%. Additionally, it minimized the load variation between peak and off-peak periods during summer and winter, leading to a smoother load curve. The optimization results also indicate that this method reduced energy costs by approximately 10% compared to the pre-regulation scenario.

Combining dormitory load optimization scheduling with dormitory structure optimization can better realize energy-saving potential. Based on the typical dormitory model established in this study, it was found that modifying ventilation, orientation, and lighting can significantly impact energy consumption. Future research should integrate load energy scheduling with building structure optimization and conduct studies in different regions to maximize the energy-saving potential of university dormitories.

6. REFERENCES

[1] Gomez-Echeverri, Luis. "Climate and development: enhancing impact through stronger linkages in the implementation of the Paris Agreement and the Sustainable Development Goals (SDGs)." Philosophical Transactions of the Royal Society A:

Mathematical, Physical and Engineering Sciences 376.2119 (2018): 20160444.

[2] Yang, Yiqun, and Kevin Lo. "China's renewable energy and energy efficiency policies toward carbon neutrality: A systematic cross-sectoral review." Energy & Environment 35.1 (2024): 491-509.

[3] Nejat, Payam, et al. "A global review of energy consumption, CO2 emissions and policy in the residential sector (with an overview of the top ten CO2 emitting countries)." Renewable and sustainable energy reviews 43 (2015): 843-862.

[4] Spitler, Jeffrey D., and Signhild Gehlin. "Measured performance of a mixed-use commercial-building ground source heat pump system in Sweden." Energies 12.10 (2019): 2020.

[5] Smil, Vaclav. Energy in nature and society: general energetics of complex systems. MIT press, 2007.

[6] Zhang, Yingzi, Bo Zhang, and **gwen Hou. "Simulation Study on Student Residential Energy Use Behaviors: A Case Study of University Dormitories in Sichuan, China." Buildings 14.5 (2024): 1484.

[7] Şirin, Ceylin, Jamie Goggins, and Magdalena Hajdukiewicz. "A review on building-integrated photovoltaic/thermal systems for green buildings." Applied Thermal Engineering 229 (2023): 120607.

[8] Thebault, Martin, and Leon Gaillard. "Optimization of the integration of photovoltaic systems on buildings for self-consumption–Case study in France." City and Environment Interactions 10 (2021): 100057.

[9] Yu, Ying, et al. "Dual-layer optimization design method for collaborative benefits of renewable energy systems in building clusters: Case study of campus buildings." Energy and Buildings 303 (2024): 113802.

[10] Dharani, Rajavelu, et al. "Load shifting and peak clipping for reducing energy consumption in an Indian university campus." Energies 14.3 (2021): 558.

[11] Zhou, Yaxian, et al. "Clustering and statistical analyses of electricity consumption for university dormitories: A case study from China." Energy and Buildings 245 (2021): 110862.

[12] Xu, Ying. "Building performance optimization for university dormitory through integration of digital gene map into multi-objective genetic algorithm." Applied Energy 307 (2022): 118211.

[13] Liu, Xiaodan, et al. "Research on the factors influencing college students' energy-use behavior in dormitories: group-level factors and time factors." International Journal of Low-Carbon Technologies 18 (2023): 836-849.

[14] Dirks, James A., et al. "Impacts of climate change on energy consumption and peak demand in buildings: A detailed regional approach." Energy 79 (2015): 20-32.

[15] Hou, Lei, et al. "Low-carbon demand response strategy of buildings considering load rebound." Energy Reports 10 (2023): 3599-3607.

[16] Yu, Zhun, et al. "A systematic procedure to study the influence of occupant behavior on building energy consumption." Energy and buildings 43.6 (2011): 1409-1417.

[17] Paetz, Alexandra-Gwyn, et al. "Demand response with smart homes and electric scooters: an experimental study on user acceptance." ACEEE Summer Study. 2012.

[18] Zhou, Jiangping. "Sustainable commute in a car-dominant city: Factors affecting alternative mode choices among university students." Transportation research part A: policy and practice 46.7 (2012): 1013-1029.

[19] Khan, Muhammad Hilal, et al. "Modeling and optimization of smart building energy management system considering both electrical and thermal load." Energies 15.2 (2022): 574.

[20] Cai, Zhi, et al. "Multi-area Joint Scheduling Model in Consideration of Flexible Loads." 2020 IEEE 3rd Student Conference on Electrical Machines and Systems (SCEMS). IEEE, 2020.

#229: Standard thermal impedance-based approach for dynamic response analysis of the solid oxide fuel cell system

Tong HAO[1], Junhong HAO[2*], Xingce WANG[3], HONGKUN LV[4], Hongyin CHEN[5], Jiaying CHEN[6], Zhenlan DOU[7], Xiaoze DU[8]

[1] North China Electric Power University, Changping District, Beijing 102206, China, htht0506@163.com
[2] North China Electric Power University, Changping District, Beijing 102206, China, hjh@ncepu.edu.cn
[3] North China Electric Power University, Changping District, Beijing 102206, China, qq904477136@163.com
[4] State Grid Zhejiang Electric Power Research Institute，Zhejiang 310014，China, hongkunlv@126.com
[5] China Electric Power Research Institute, Haidian District, Beijing 100192, China, ccagchenhongyin@126.com
[6] State Grid Zhejiang Electric Power Research Institute，Zhejiang 310014，China, jiayingchen@zju.edu.cn
[7] State Grid Shanghai Power Supply Company, Shanghai 200023, China, douzhl@126.com
[8] North China Electric Power University, Changping District, Beijing 102206, China, duxz@ncepu.edu.cn

Abstract: Accurately predicting and analyzing the dynamic coupling between the internal multi-physical processes and the external multi-heat transfer devices of solid oxide fuel cells (SOFCs) is the key to the high-performance operation of fuel cell systems and integration in distributed energy systems. Neither complex multidimensional simulation models nor simplified external characteristic models can achieve fast and accurate dynamic performance analysis of the SOFC system. This paper constructed a new cross-scale dynamic model of SOFC systems by using the standard thermal resistance method to analyze the external heat transfer subsystem and the equivalent circuit method to analyze the internal heat and mass transfer and electrochemical multi-physics coupling processes. The model realizes the overall cross-scale dynamic modeling of the SOFC system from the internal heat and mass transfer and electrochemical processes to the external heat exchange processes by using the characteristic parameters. The cross-scale dynamic model could be used for the holistic modeling of distributed energy systems including other energy conversion devices.

Keywords: Solid Oxide Fuel Cell; Dynamic Modelling; Standard Thermal Impedance; Characteristic Analysis

1. INTRODUCTION

Solid oxide fuel cell (SOFC) is an energy exchange device which can directly convert the chemical energy of fuel and oxidant into electrical energy through an electrochemical reaction. Therefore, accurate and reliable SOFC modelling is essential for the simulation, analysis and optimal control of SOFC systems. SOFC system is a multivariable, nonlinear and strongly coupled system, where electrical, thermal, and gas dynamics are tightly interwoven. Heat sources are predominantly located in the preheater, stack, and burning chamber, while electric sources are located in the SOFC stack. This spatial and functional separation emphasizes the strong interdependence of heat and electrical power within the system, which pose significant challenges for controlling and analysing the steady and dynamic characteristics of the system.

Recently, advanced dynamic modelling techniques have dynamically developed. Yang et al. (2024) proposed this method to build a thermo- electric response model that can accurately predict the comprehensive dynamic characteristics of PEMFCs under various operating conditions, verifying the model against experimental data. This approach not only reflected the coupling between thermal and electrical energy but also laid the foundation for cross-scale dynamic modeling in fuel cell systems. Hao et al. (2023) provided a comprehensive framework for cross-scale modeling of SOFC cogeneration systems using the heat current method. This approach simplified the analysis of external heat exchangers, which are essential for managing the heat and mass transfer processes, without introducing unnecessary intermediate variables. Hao et al. (2024) proposed an optimal scheduling framework that takes into account the spatial-temporal characteristics of heat and power sources and loads. Their work addresses the need for a comprehensive model that optimizes the active distribution network by minimizing system operation costs while considering the complex interactions between various energy sources, including photovoltaic cells, fuel cells, and electric heat pumps. He et al. (2023) examined the role of heat storage in district heating systems, which is crucial for accommodating fluctuating renewable energy sources such as wind power. Their research emphasized the integration of power and thermal systems, showing that the proper evaluation and utilization of heat storage could significantly improve system flexibility. Xin et al. (2022) presented a heat current method-based real-time coordination framework for the power and heat generation of multi-CHP units. Their approach addressed the need for flexibility retrofits to enhance energy utilization efficiency under off-design conditions, demonstrating improvements in the overall efficiency of multi-CHP units. By leveraging the heat current method for precise energy conversion processes, the study underscored the importance of real-time coordination and optimization for improving system performance. Wang et al. (2024) proposed a novel integrated SOFC and photovoltaic-thermal (PVT) energy supply system that leverages the heat current method for system optimization. Their model integrates the benefits of SOFCs' high-temperature exhaust for cogeneration with the variability of solar energy, improving the overall energy efficiency of the system. The system includes a heat pump to store excess electricity and optimize performance during periods of high solar radiation. Hao et al. (2021) introduced a correction factor-based general thermal resistance formula, providing a standardized approach for heat exchanger design and performance analysis across various flow arrangements. Their method integrates the correction factor, heat transfer coefficient, and surface area into a unified thermal resistance formula, making it applicable to different types of heat exchangers, such as parallel-flow, cross-flow, and shell-and-tube exchangers. The new formula enables accurate performance analysis without requiring complex iterations, proving valuable for integrated energy system modeling using the heat current method. He et al. (2019) introduced a transient heat current model to capture the dynamic characteristics of heat exchangers, especially during unsteady-state operations. This model provides a framework to optimize heat transfer systems by constructing transient heat current models that represent series, parallel, and multi-loop heat exchangers. The integrated approach ensures better performance by addressing cross-correlations among different heat exchangers in a system. Through optimal control, significant energy savings can be achieved, as demonstrated in a four-loop heat transfer system that reduced total pumping power by 25.7%.

This paper proposed and constructed a new cross-scale dynamic model of SOFC systems by applying the standard thermal resistance method to analyze the external heat transfer subsystem and the equivalent circuit method to analyze the internal heat and mass transfer and electrochemical multi-physics coupling processes. And the effect of the air flow rate, the initial temperature, the inlet temperature of the air and the fuel inlet temperature on the output characteristics of SOFC was analyzed.

2. CROSS-SCALE DYNAMIC MODEL OF SOFC SYSTEM

The cross-scale dynamic model of SOFC systems is a powerful tool for understanding and improving the performance of SOFC systems, which can predict the dynamic behaviour of SOFC systems under different operating conditions, such as temperature, pressure, and fuel flow rate. This chapter presents a new cross-scale dynamic model of SOFC systems based on its electrochemical and thermodynamic properties and the mass and energy conservation laws by applying the standard thermal resistance method and the equivalent circuit method.

2.1. Electrochemical impedance modeling for SOFC stack

The equations representing the anode and cathode reactions and the overall reaction of SOFCs are as follows.

Equation 1: anode reaction	$H_2 + O^{2-} \Rightarrow H_2O + 2e^-$
Equation 2: cathode reaction	$\frac{1}{2}O_2 + 2e^- \Rightarrow O^{2-}$
Equation 3: overall reaction	$H_2 + \frac{1}{2}O_2 \Rightarrow H_2O$

The Nernst potential represents the electromotive force (Ecell) between the cathode and anode (Xingguo 2023). When current flows through the SOFC, the potential difference between the cathode and anode creates a resistance to the flowing current, such as

Ract, Rconc, and Rohm, which are the internal electrochemical impedances of the SOFC. The Nernst equation used to calculate the reversible potential can be calculated by Leonide et al. (2009)

$$Equation\ 4 \qquad E_{\text{cell}} = E_0 + \frac{RT_{\text{cell}}}{4F}\ln[\frac{(p_{H_2}^{\text{ch}})^2 \cdot p_{O_2}^{\text{ch}}}{(p_{H_2O}^{\text{ch}})^2}]$$

E0 consists of a constant term and a temperature-dependent term as follows Lan and Strunz (2020)

$$Equation\ 5 \qquad E_0 = E_0^{\text{o}} - k_{\text{E}}(T_{\text{cell}} - 298)$$

Where

E_0 = Standard reference potential at the standard state, 298 K, and 1 atm pressure.

k_{E} = Constant term.

In the electrochemical reaction process, activation polarization, concentration polarization, and ohmic polarization represent different factors that can contribute to the overall resistance of the SOFC. Therefore, the actual output voltage of the fuel cell is lower than the open-circuit voltage of the cell, and the SOFC output voltage can be written as:

$$Equation\ 6 \qquad V_{\text{cell}} = E_{\text{cell}} - V_{\text{act}} - V_{\text{ohm}} - V_{\text{conc}}$$

The output voltage of the individual cells connected in series can be lumped together to obtain the output voltage of an SOFC stack as follows:

$$Equation\ 7 \qquad V_{\text{out}} = N_{\text{cell}}V_{\text{cell}}$$

Therefore, the SOFC stack output voltage can be calculated by deducing the voltage drops or internal electrochemical impedances.

The activation voltage drop can be expressed as:

$$Equation\ 8 \qquad V_{\text{act}} = \frac{2RT_{\text{cell}}}{zF}\sinh^{-1}(\frac{I}{2I_0})$$

where I0 is the apparent exchange current (A), and z is the number of participating electrons .The apparent exchange current is a function of temperature and can be expressed as an exponential function as follows

$$Equation\ 9 \qquad I_0 = k_{\text{a1}}T\exp(-\frac{k_{\text{a2}}}{T_{\text{cell}}})$$

The equivalent activation electrochemical impedance can then be defined as

$$Equation\ 10 \qquad R_{\text{act}} = \frac{V_{\text{act}}}{I} = \frac{2RT_{\text{cell}}}{zFI}\sinh^{-1}(\frac{I}{2I_0})$$

The ohmic electrochemical impedance of SOFC consists mainly of the resistance of the electrodes, electrolyte, and the interconnection between cells. The overall ohmic voltage drop inside SOFC can be expressed as

$$Equation\ 11 \qquad V_{\text{ohm}} = V_{\text{electrodes}} + V_{\text{ohm,elecyt}} + V_{\text{ohm,interc}} = IR_{\text{ohm}}$$

In general, the resistance of electrodes is negligible compared to that of electrolytes and interconnects. Hence, only ohmic losses of electrolytes and interconnects are included in calculating the ohmic voltage drop. The ohmic electrochemical impedance of electrolyte and interconnects decreases exponentially with temperature, and Rohm can be written as follows:

$$R_{\text{ohm}} = \frac{a_{\text{elecyt}}\exp(b_{\text{elecyt}}/T_{\text{cell}})}{A_{\text{cell}}}\delta_{\text{elecyt}} + \frac{a_{\text{interc}}\exp(b_{\text{interc}}/T_{\text{cell}})}{A_{\text{interc}}}\delta_{\text{interc}}$$

$$Equation\ 12$$

Where

a = Constant (Ωm).

b = Constant (K).

δ = Thickness (m).

A = Effective cross-sectional area (m^2).

Concentration voltage drop refers to loss caused by the concentration gradient of the reactants at the cathode and anode. This type of electrochemical impedance is due to the difference in the concentration of the reactants between the cathode and anode. The difference is called concentration voltage drop or concentration overpotential. The concentration voltage drop in the fuel cell can be obtained as (Chan et al. 2002)

Equation 13
$$V_{\text{conc}} = \frac{RT_{\text{cell}}}{4F} \{\ln[\frac{(p_{\text{H}_2}^{\text{ch}})^2 p_{\text{O}_2}^{\text{ch}}}{(p_{\text{H}_2\text{O}}^{\text{ch}})^2}] - \ln[\frac{(p_{\text{H}_2}^*)^2 p_{\text{O}_2}^*}{(p_{\text{H}_2\text{O}}^*)^2}]\} = V_{\text{conc,a}} + V_{\text{conc,c}}$$

Equation 14
$$V_{\text{conc,a}} = \frac{RT_{\text{cell}}}{2F} \ln[\frac{1 + (RT_{\text{cell}} l_a I_{\text{den}}) / (2FD_{\text{H}_2\text{O,H}_2} p_{\text{H}_2\text{O}}^{\text{ch}})}{1 - (RT_{\text{cell}} l_a I_{\text{den}}) / (2FD_{\text{H}_2\text{O,H}_2} p_{\text{H}_2}^{\text{ch}})}]$$

Equation 15
$$V_{\text{conc,c}} = -\frac{RT}{4F} \ln\{\frac{1}{p_{\text{O}_2}^{\text{ch}}}[p_{\text{c}}^{\text{ch}} - (p_{\text{c}}^{\text{ch}} - p_{\text{O}_2}^{\text{ch}}) \exp(\frac{RTI_{\text{den}} l_{\text{c}}}{4Fp_{\text{c}}^{\text{ch}} D_{\text{O}_2,\text{N}_2}})]\}$$

Where

$p_{\text{H}_2}^{\text{ch}}$ = Partial pressures of H$_2$ (Pa).

$p_{\text{H}_2\text{O}}^{\text{ch}}$ = Partial pressures of H$_2$O (Pa).

$p_{\text{O}_2}^{ch}$ = Partial pressures of O$_2$ (Pa).

$p_{\text{H}_2}^{\cdot}$, $p_{\text{O}_2}^{\cdot}$, and $p_{\text{H}_2\text{O}}^{\cdot}$ = Effective partial pressures (Pa).

The equivalent impedance for the concentration voltage drop can be determined by dividing the concentration voltage drop by the SOFC current.

Equation 16
$$R_{\text{conc}} = \frac{V_{\text{conc}}}{I}$$

In an SOFC, the electrolyte separates the two electrodes, and two boundary layers are formed: the anode-electrolyte layer and the electrolyte-cathode layer. Due to the polarization effect, these layers, known as the electrochemical double-layer charge effect, can store electrical energy and behave like a super-capacitor.

According to the equivalent circuit (Figure 1), Cdl is the equivalent capacitance of the double-layer charge effect, Ract, Rohm, and Rconc are equivalent resistances of activation, ohmic, and concentration voltage drops. The voltage across Cdl can be written as:

Equation 17
$$V_{\text{C}} = (I - I_{\text{C}})(R_{\text{act}} + R_{\text{conc}}) = (I - C\frac{dV_{\text{C}}}{dt})(R_{\text{act}} + R_{\text{conc}})$$

According to the above, Figure 1 introduces the internal equivalent circuit model of the SOFC for representing the internal electrochemical processes (Nehrir and Wang 2009). R_{act}、R_{conc} and R_{ohm} are the equivalent resistances of activation polarization, concentration polarization, and ohmic polarization, respectively.
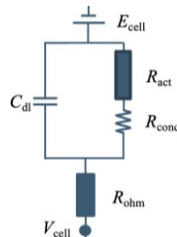

Figure 1: The internal equivalent electrical circuit of the SOFC

2.2. Thermal impedance modeling for SOFC system

Figure 2 shows the heat transfer processes of the SOFC stack. The air is fed through a central air supply tube (AST) and forced to flow back past the interior of the cell (cathode surface) to the open end (Roushenas et al. 2021). The fuel (hydrogen and water vapor mixture) flows past the exterior of the cell (anode surface) while the air flows through the interior of the cell (cathode surface). The major thermal and electrochemical phenomena of interest occur within the cells, and the impact of minor temperature variations between cells on overall stack performance is often marginal, in this study, the assumption of heat transfer or temperature difference between neighboring cells is simplified and the heat transport inside each fuel cell occurs mainly using radiation, convection, and mass flow. In this system, air flows into the AST at temperature T_{air2} (air outlet temperature at preheater 2) through the AST at a temperature of $T_{air,AST}$ flows and undergoes convective heat transfer with the AST at a temperature of T_{AST}, with the heat exchange being represented by $Q_{conv, AST, inner}$. After entering the cell, the air temperature becomes $T_{air, cell}$. Within the cell, the air undergoes convective heat transfer with both the AST and the cell tube, with the heat exchanges being represented by $Q_{conv, AST, outer}$, and $Q_{conv, air}$, respectively. In the meantime, the fuel enters the cell at temperature T_{fuel2} (fuel outlet temperature at preheater 2) and undergoes convective heat transfer with the cell at temperature $T_{fuel,cell}$ with the heat exchange represented by $Q_{conv, fuel}$. Additionally, there is radiation heat transfer between the cell tube and the AST, represented by Q_{rad}. In addition, $Q_{flow, air, cell}$, $Q_{flow, air, AST}$, and $Q_{flow, fuel}$ are defined as heat exchanges due to different mass flows and the temperature different caused by the mass flows is represented by the additive thermomotive forces.

The heat generation rate by the chemical reaction inside SOFC can be written as

Equation 18
$$Q_{gen} = Q_{chem} - Q_{elec}$$

Equation 19
$$Q_{chem} = n\Delta H$$

Equation 20
$$Q_{elec} = I \cdot V_{out}$$

Equation 21
$$Q_{rad} = \varepsilon_{AST}\sigma A_{AST,outer}(T_{cell}^4 - T_{AST}^4)$$

Where

- Q_{chem} = Available power (kJ).
- Q_{elec} = Fuel cell electrical output power(kJ).
- Q_{rad} = Radiation heat transfer between the cell and the AST (kJ).
- ΔH = Change in enthalpy of the chemical reaction (kJ).

In the SOFC stack, the four heat currents, $Q_{conv, AST, inner}$, $Q_{conv, AST, outer}$, $Q_{conv, air}$ and $Q_{conv, fuel}$ flow through four thermal impedances, $R_{conv,AST,inner}$, $R_{conv,AST,outer}$, $R_{conv,air}$ and $R_{conv,fuel}$, driven by four linear temperature differences, $T_{AST} - T_{air,AST}$, $T_{air, cell} - T_{AST}$, $T_{cell} - T_{air, cell}$ and $T_{cell} - T_{fuel}$, respectively. In the equivalent thermal circuit, the temperature difference of each fluid before and after entering the cell and the AST, such as $T_{fuel,cell} - T_{fuel2}$, $T_{air, cell} — T_{air, AST}$ and $T_{air,AST} - T_{air2}$ could be analogized as additive thermomotive forces (like the electromotive forces) (Xingguo 2023). The limited fluid flow rate causes a temperature difference in the working fluid. The elevated thermal potential is the ratio of the absorbing power to the heat capacity flow rates of the corresponding fluid. The four thermal impedances are defined as

Equation 22
$$R_{conv,AST,inner} = \frac{T_{AST} - T_{air, AST}}{Q_{conv,AST,inner}} = \frac{1}{G_{air, AST}(1 - e^{-a_{air, AST}})}$$

Equation 23
$$R_{conv,AST,outer} = \frac{T_{air, cell} - T_{AST}}{Q_{conv,AST,outer}} = \frac{1}{G_{air, cell}(1 - e^{-a_{air,cell}})}$$

Equation 24
$$R_{conv,air} = \frac{T_{cell} - T_{air, cell}}{Q_{conv,air}} = \frac{1}{G_{air, cell}(1 - e^{-a_{air, cell}})}$$

Equation 25
$$R_{conv,fuel} = \frac{T_{cell} - T_{fuel, cell}}{Q_{conv, fuel}} = \frac{1}{G_{fuel, cell}(1 - e^{-a_{fuel, cell}})}$$

Where
- $a_{air, AST} = (KA)_{air, AST}/G_{air, AST}$
- $a_{air, cell} = (KA)_{air, cell}/G_{air, cell}$
- $a_{air3} = (KA)_{air, cell}/G_{air, cell}$
- $a_{fuel, cell} = (KA)_4/G_{fuel, cell}$
- K = Heat transfer coefficient (W/m²K).
- A = Heat transfer area (m^2).
- G = Heat capacity rate (Product of mass flow rate and specific heat capacity).

In the preheater1 and 2, the high-temperature burned gas produced by the burner enters the preheaters and preheat the air and hydrogen before entering the fuel cell stack. Cold fluids (air and fuel) flow counter to the hot fluid (high-temperature burned gas). Heat exchange between the cold and hot fluids occurs through the metal pipe walls. Specifically, burned gas at temperature $T_{bur1\,(2)}$ enters the preheater. It then undergoes convective heat exchange with the air tube at $T_{air,\,tube1\,(2)}$ and the fuel tube at $T_{fuel1\,(2)},\,tube$, and the heat exchange quantities are $Q_{conv,\,bur,\,airtube1\,(2)}$ and $Q_{conv,\,bur,\,fueltube1\,(2)}$. Concurrently, air and hydrogen enter their respective channels. They subsequently exchange convective heat with the air and fuel tubes, respectively. The heat exchange quantities for these processes are $Q_{conv,\,air,\,tube1\,(2)}$, $Q_{conv,\,fuel,\,tube1\,(2)}$, respectively. In addition, $Q_{flow,\,air,\,pre1\,(2)}$, $Q_{flow,\,air,\,pre1\,(2)}$, and $Q_{flow,\,bur,\,pre1\,(2)}$ are defined as heat exchanges due to different mass flows of air, fuel and burned gas through the two preheaters, and the temperature difference caused by the mass flows is represented by the additive thermomotive forces.
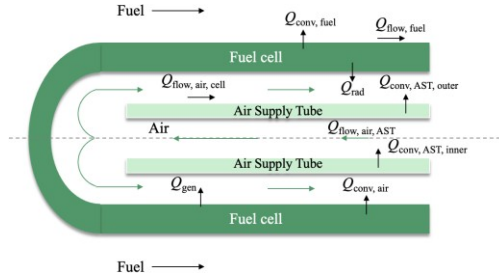
Figure 2: Schematic of SOFC stack.

According to Kirchhoff's law and the equation of conservation of energy for the AST and the cell, the differential energy conservation equations are

Equation 26
$$C_{AST}\frac{dT_{AST}}{dt} = Q_{rad} + \frac{(T_{aircell,o} - T_{AST})}{R_{conv,AST,outer}} - \frac{(T_{AST} - T_{air,i})}{R_{conv,AST,inner}} - G_{air}(T_{air,i} - T_{air,o})$$

Equation 27
$$C_{cell}\frac{dT_{cell}}{dt} = Q_{chem} - Q_{elec} - Q_{rad} - \frac{(T_{cell} - T_{aircell,i})}{R_{conv,air}} - \frac{(T_{cell} - T_{fuel,i})}{R_{conv,fuel}}$$
$$- G_{aircell}(T_{aircell,i} - T_{aircell,o}) - G_{fuel}(T_{fuel,i} - T_{fuel,o})$$

Equation 28
$$(mc)_{air}\frac{dT_{air}}{dt} = Q_{conv,AST,inner}$$

Equation 29
$$(mc)_{aircell}\frac{dT_{aircell}}{dt} = Q_{conv,air}$$

Equation 30
$$(mc)_{fuel}\frac{dT_{fuel}}{dt} = Q_{conv,fuel}$$

Where

- C = Heat capacities (J/(Kg-K).
- $(mc)_{air}$, $(mc)_{aircell}$, $(mc)_{fuel}$ = The product of heat capacity and mass of different fluids

Figure 3 provides the standard electrochemical-thermal impedance model of the SOFC system by integrating the thermal and electrochemical dynamic models. The electric and thermal capacities and these thermal impedances reflect the dynamic performance of the SOFC system.
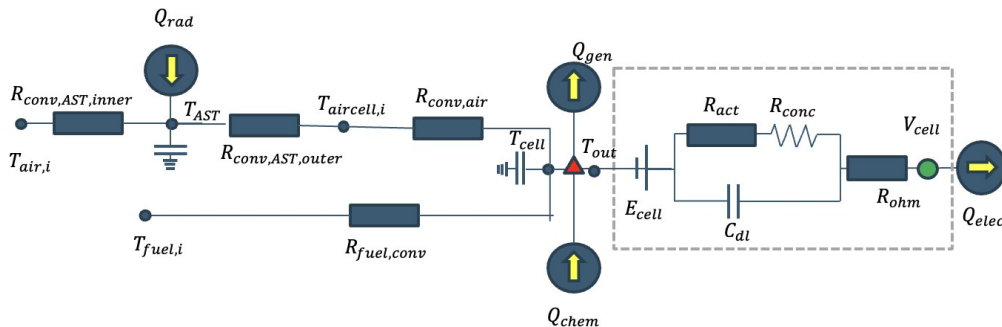
Figure 4: The standard electrochemical-thermal impedance model of the SOFC system

3. DYNAMIC RESPONSE OF THE SOFC SYSTEM

The model implemented the previously discussed model equations in MATLAB to gain a comprehensive understanding of the dynamic characteristics of a 5kW SOFC system. The approach incorporated meticulous heat transfer, mass transfer, and electrochemical modelling within the SOFC stack accounting for the air, fuel and cell temperature. Embracing the principles of thermal conduction, convective heat transfer, and energy balance established a robust framework for the simulation. Following the parameterization detailed in Table 1 for the SOFC system (Minh and Takahashi 1995)—constituting 96 serially connected cells, the model achieved a granular level of detail in predicting the voltage output of the SOFC.

External factors such as fuel composition, fuel flow rate, and operating temperature can affect the output voltage of a SOFC over time. Changes in these factors can alter the rate at which the SOFC consumes fuel and generates electricity, which can impact the output voltage of the SOFC. The output voltage of a SOFC can be affected by the air flow rate, especially. Under fixed catalyst conditions, the higher the temperature difference between the cathode and anode (also known as the source/drain temperature difference), the higher the output voltage of the SOFC. Therefore, controlling the air flow rate is one way to adjust the output voltage of the SOFC.

Table 1: Parameters of the SOFC system

Item	Unit	Value
Cell Length	m	0.001
Cell Mass	kg	0.738
Anode Channel Volume	m³	62×10^{-6}
Cathode Channel Volume	m³	99×10^{-6}
Air Supply Tube Mass	kg	0.023

3.1. Dynamic response under sudden current change

In Figure5, as the air flow rate increases, the output voltage of the SOFC decreases from 107 V. The effect of air flow rate on the output voltage of SOFC reaches its maximum between 10000 s-12000 s. Within this range, the output voltage decreases by around 0.8 V as the air flow velocity increases by 3e-3. Over time, this effect gradually decreases to 0. This is because increasing the air flow rate increases the cooling effect, reducing the source/drain temperature difference and reducing the output voltage of the SOFC. However, the decrease of the air flow rate can also affect the output voltage of the SOFC. If the air flow rate is too low, the temperature of the SOFC may increase, causing the catalyst to become hot, which will lower the output voltage of the SOFC. Therefore, in practical applications, it is necessary to adjust the air flow rate to obtain the optimal output voltage of the SOFC, taking into account the source/drain temperature difference and avoiding the negative effects of excessively high or low air flow rates on the output voltage.
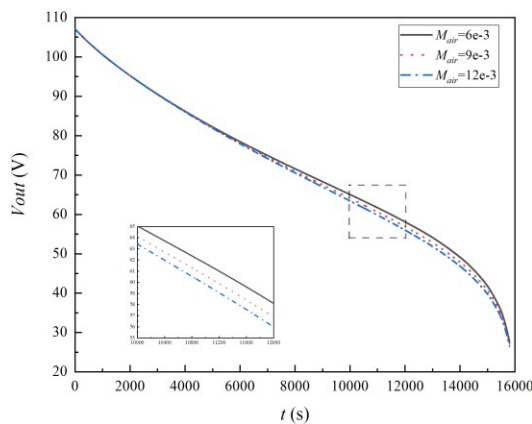
Figure 5: The output voltage of a SOFC at different air flow rates

Figure 6 shows the trend of the cell output temperature under three different conditions, the temperature of the cell starts to change from 973 K, 1073 K, and 1173 K, respectively. Due to the difference in the initial temperature of the cell, there is a large temperature gap at the beginning. Until around 5000 s, the initial temperature of the cell no longer impacts the temperature of the cell and is approximately 1192 K at this point. Until 15800 s, the cell temperature rises to 1373 K, which changes from the initial temperature are 400 K, 300 K, and 200 K. Generally, the higher the initial temperature of the SOFC, the higher the output temperature of the cell. This is because the initial temperature can affect the rate at which the SOFC consumes fuel and generates electricity, which can impact the cell's output temperature. However, it's also important to consider that excessively high temperatures can lead to thermal degradation of the cell components and reduced durability. Therefore, proper temperature management is crucial for maintaining the performance and longevity of SOFCs.
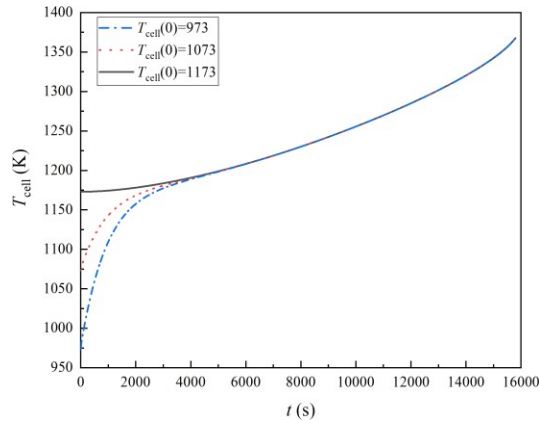
Figure 6: The output temperature of the cell at different initial temperatures

In SOFC, the energy generated by chemical reactions is outputted in two ways: electrical and thermal energy. Electrical power is generated by the flow of electrons through the external circuit, while thermal energy is generated as a byproduct of the chemical reactions occurring within the cell. The output power of a SOFC is closely related to the energy produced by the reaction within the cell, which are depicted in the relationship in Figure 7. The chemical reactions between the fuel and the oxygen produce energy in the form of electricity and heat. The output power is also a measure of the rate at which the electricity is being produced. As the SOFC generates more energy, the output power of the cell first gradually increases to a peak and then gradually decreases. The output power is also closely related to the inlet temperature of the air. In Figure 7, the higher the inlet temperature of the air, the greater the power output. When the energy generated by the electrochemical reaction of the cell reaches around 15800 W, the output power is the highest. When the inlet temperature of the air is 973 K, the maximum output power of the SOFC is approximately 5350 W. When the inlet temperature of the air is 1073 K, the maximum output power is 6175 W; When the inlet temperature of the air is 1173 K, the maximum output power is 6745 W. It is easy to see that the air inlet temperature rises from 973 K to 1073 K, and the output power increases by 825 W, the air inlet temperature rises from 1073 K to 1173 K, and the output power rises by approximately 570 W.
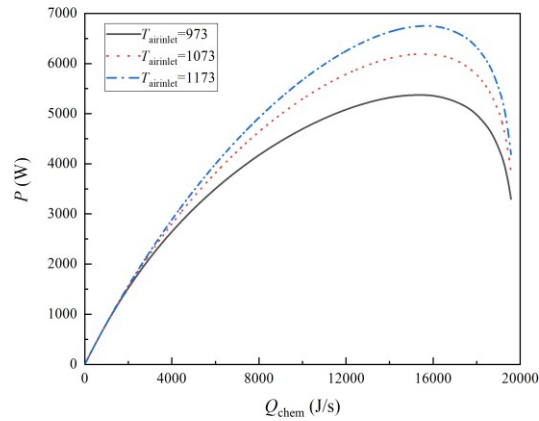
Figure 7: The output power at different initial temperatures of the air

The output power is also influenced by external factors such as the fuel inlet temperature. In Figure 8, the output power increases continuously as the reaction progresses, reaching a peak at about 13000 s, then decreasing gradually. The peak output power difference is around 37 W for every 100K interval in the fuel inlet temperature. The reaction rate increases with temperature, leading to an initial increase in output power. However, as the reaction continues, the temperature may rise too quickly, causing the reaction to become unstable and decreasing output power. Another reason is that the fuel concentration decreases over time, leading to a slower reaction rate. Finally, the electrode material becomes depleted as the reaction proceeds, resulting in a decrease in output power.

The fuel inlet temperature also significantly affects the output power of SOFC. As seen in Figure 8, as the fuel inlet temperature increases, the cell's output power increases. In SOFC, the fuel is heated before entering the cell, which undergoes an oxidation reaction to produce electricity. As the fuel inlet temperature increases, the heat energy of the fuel also increases, which can increase the rate of the reaction and, thus the output power. However, suppose the fuel inlet temperature becomes too high. In that case, it can damage the cell's island structure (the solid material in the fuel cell used to transport the fuel and oxygen), reducing the cell's performance and lifespan. Therefore, it is essential to control the fuel inlet temperature appropriately in the design and operation of SOFC to ensure optimal performance.
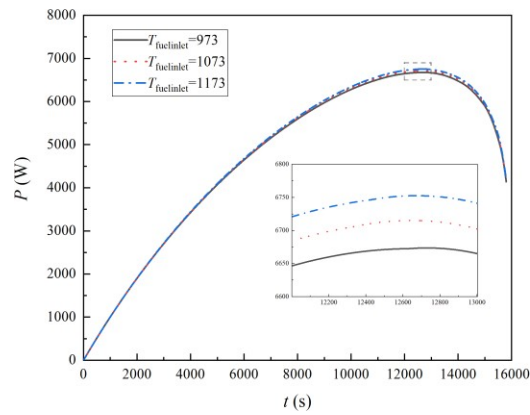
Figure 8: The output power at different initial temperatures of the fuel

4. CONCLUSION

The solid oxide fuel cell cogeneration system will be one of the most promising future energy technologies because of their excellent energy efficiency and fuel flexibility. Based on the combination of the equivalent electrical circuit and standard thermal resistance, this contribution provided a novel cross-scale dynamic modeling method for the SOFC unit. The dynamic model can achieve the internal heat and mass transfer and electrochemical multi-physics coupling processes of SOFC accurately. The influence of inlet temperatures and mass flow rates of the air and fuel on the power generation dynamic variation are analyzed by the proposed model. The higher inlet temperature and suitable mass flow can achieve better fuel cell performance. Meanwhile, the synergy consideration of fluid flow, heat transfer and electrochemical reaction is necessary for improving the fuel cell performance. Finally, the cross-scale dynamic model provides a reliable basis for the holistic modeling of the distributed energy systems in the future.

5. ACKNOWLEDGEMENT

6. REFERENCES

Stambouli, A.B., Traversa, E., 2002. Solid oxide fuel cells (SOFCs): a review of an environmentally clean and efficient source of energy. Renewable and Sustainable Energy Reviews, 6(5), 433-455.

Yang, Y., Hao, J., Ju, C., Hao, T., Wang, X., Li, Y., Du, X., 2024. Dynamic cross-scale modeling and thermo-electric response characteristics of PEMFC based on standardized thermal resistance. Energy Conversion and Management, 302, 118133.

Hao, J., Hao, T., Lu, Z., Hong, F., Du, X., Ge, Z., 2023. Cross-scale modeling and optimization analysis of the solid oxide fuel cell cogeneration system based on the heat current method. Energy Conversion and Management, 280, 116828.

Hao, J., Feng, X., Chen, X., Jin, X., Wang, X., Hao, T., Hong, F., Du, X., 2024. Optimal scheduling of active distribution network considering symmetric heat and power source-load spatial-temporal characteristics. Applied Energy, 373, 123974.

He, K.-L., Zhao, T., Ma, H., Chen, Q., 2023. Optimal operation of integrated power and thermal systems for flexibility improvement based on evaluation and utilization of heat storage in district heating systems. Energy, 274, 127421.

Xin, Y.-L., Zhao, T., Chen, X., He, K.-L., Ma, H., Chen, Q., 2022. Heat current method-based real-time coordination of power and heat generation of multi-CHP units with flexibility retrofits. Energy, 252, 124018.

Wang, X., Hao, J., Feng, X., Hao, T., Sun, J., Du, X., Liu, K., Jin, L., 2024. Modeling and performance analysis of a new integrated solid oxide fuel cell and photovoltaic-thermal energy supply system by heat current method. Energy Science & Engineering, 12(9), 3823-3839.

Hao, J., Chen, Q., Li, X., Zhao, T., 2021. A correction factor-based general thermal resistance formula for heat exchanger design and performance analysis. Journal of Thermal Science, 30(3), 892-901.

He, K.-L., Chen, Q., Liu, Y.-T., Hao, J.-H., Wang, Y.-F., Yuan, Y., 2019. A transient heat current model for dynamic performance analysis and optimal control of heat transfer system. International Journal of Heat and Mass Transfer, 145, 118767.

Xingguo, L., 2023. Hydrogen fuel gas turbine and large-scale hydrogen power generation. Chinese Journal of Nature, 45(2), 113-118.

Leonide, A., Apel, Y., Ivers-Tiffee, E., 2009. SOFC Modeling and Parameter Identification by Means of Impedance Spectroscopy. ECS Transactions, 19(20), 81.

Lan, T., Strunz, K., 2020. Modeling of multi-physics transients in PEM fuel cells using equivalent circuits for consistent representation of electric, pneumatic, and thermal quantities. International Journal of Electrical Power & Energy Systems, 119, 105803.

Chan, S.H., Low, C.F., Ding, O.L., 2002. Energy and exergy analysis of simple solid-oxide fuel-cell power systems. Journal of Power Sources, 103(2), 188-200.

Minh, N.Q., Takahashi, T., 1995. Preface, in: Minh, N.Q., Takahashi, T. (Eds.), Science and Technology of Ceramic Fuel Cells, Elsevier Science Ltd, Oxford, pp. vii-viii.

Nehrir, M.H., Wang, C., 2009. Modeling and Control of Fuel Cells: Distributed Generation Applications. Wiley.

Darowicki, K., Janicka, E., Mielniczek, M., Zielinski, A., Gawel, L., Mitzel, J., Hunger, J., 2019. The influence of dynamic load changes on temporary impedance in hydrogen fuel cells, selection and validation of the electrical equivalent circuit. Applied Energy, 251.

Roushenas, R., Zarei, E., Torabi, M., 2021. A novel trigeneration system based on solid oxide fuel cell-gas turbine integrated with compressed air and thermal energy storage concepts: Energy, exergy, and life cycle approaches. Sustainable Cities and Society, 66, 102667.

Campanari, S., 2001. Thermodynamic model and parametric analysis of a tubular SOFC module. Journal of Power Sources, 92(1), 26-34.

Chen, Q., Fu, R.-H., Xu, Y.-C., 2015. Electrical circuit analogy for heat transfer analysis and optimization in heat exchanger networks. Applied Energy, 139, 81-92.

#230: Streamlining thermal analysis: chart-lookup technique enabled by machine learning for chip thermal management systems with sodium acetate trihydrate

Yuhao LAN[1,2], Ziye LING[1,2,*], Zhengguo ZHANG[1,2], Xiaoming FANG[1,2]

[1] Key Laboratory of Enhanced Heat Transfer and Energy Conservation, The Ministry of Education, School of Chemistry and Chemical Engineering, South China University of Technology, Guangzhou 510640, China
[2] Guangdong Engineering Technology Research Center of Efficient Heat Storage and Application, South China University of Technology, Guangzhou 510640, China
[*] Corresponding author, e-mail: zyling@scut.edu.cn

Abstract: Sodium acetate trihydrate (SAT), due to its high enthalpy value during exothermic decomposition reactions, has emerged as a potential candidate for chemical energy storage materials. However, there remains a lack of convenient and accurate prediction methods for calculating temperature and energy storage progress of SAT. This study aims to develop a fast chart-lookup strategy for chip thermal management systems with SAT using machine learning, which utilizes existing complex reaction kinetics models. Specifically, we extensively collected training data corresponding to variousoperating conditions such as material thermal properties, heat source power, and time from model calculations. And dimensionalityreduction techniques were used to consolidate numerous variables that affect heat transfer rates into a single variable: characteristic time, which helps to extract principal components for visualizing machine learning results. Then we utilized back propagation (BP) neural networks to identify the relationship between characteristic time, energy storage progress, and temperature from the trainingdataset, which is plotted on the chart. The R-values for the training outcomes all exceeded 0.999, ensuring reliability across most thermal management scenarios. With the chart-lookup strategy generated by machine learning, engineers can now use a pocket calculator and charts to estimate the working temperature and progress of SAT within minutes, as well as predict system parameters and appropriate material properties based on temperature requirements, rather than relying on hours of simulation calculations.

1. INTRODUCTION

Thermal energy storage materials are generally categorized into three main types: sensible heat storage, latent heat storage, and thermochemical heat storage. Currently, the utilization of sensible heat and latent heat has been gradually perfected, and comprehensive solutions have been developed for their thermal management applications (Ghosh *et al.*, 2022). However, the thermal management of high-power electronic devices, such as large-capacity batteries and radar components, demands higher energy storage density from materials (Mei *et al.*, 2023). Consequently, researchers have shifted their focus to thermochemical heat storage. Among the various materials studied, sodium acetate trihydrate (SAT) has emerged as a promising candidate for thermochemical heat storage, attracting academic attention. SAT offers a substantial energy storage density, with a phase change enthalpy of 247 J/g and a decomposition reaction enthalpy of 693 J/g, amounting to nearly 1000 J/g (Lin *et al.*, 2023). Furthermore, SAT exhibits low corrosiveness and low toxicity, possesses safe combustion properties, and is environmentally benign (Informationabout sodium acetate trihydrate in the CAS database, 2024).

Researchers have explored numerous thermal management applications and solutions based on SAT as a thermal energy storage material. For example, Mei *et al.* (2023) directly filled SAT around a single cylindrical lithium-ion battery, achieving a 75% delay in the onset of thermal runaway. Similarly, Lin *et al.* (2023) prepared SAT-urea/expanded graphite composites and filled them in the gaps between battery cells, effectively suppressing the chain propagation of thermal runaway within the battery pack.

SAT has shown promising results at the laboratory stage, indicating the need to develop predictive methods for SAT thermal management conditions to further guide its design for industrial applications. Currently, finite element methods are the most common approach. These methods aim to couple the kinetics model of SAT thermal decomposition and phase change with the heat conduction model, thereby incorporating the material's endothermic effects into the heat conduction process. For instance, Cao *et al.* (2022) developed a model in which they conducted detailed reaction kinetics measurements and fitting for SAT's thermal decomposition reactions, obtaining kinetic equations. They then divided the heat into sensible heat, latent heat, and reaction heat, and incorporated these segments into the heat conduction equations to form the governing equations—a complex system of partial differential equations with multivariable and piecewise expressions. Finally, they implemented the simulation of battery thermal runaway using ANSYS Fluent's custom function capabilities, achieving an error margin of less than 5%. This approach, relying on well-established finite element software and comprehensive theoretical equations, demonstrated excellent accuracy. However, it also has notable drawbacks: high learning costs, substantial workload, and time-consuming processes.

Machine learning methods, particularly neural networks, offer the potential to overcome the aforementioned limitations. With their strong generalization and nonlinear mapping capabilities (Gómez *et al.*, 2020), neural networks can maintain low error margins when trained on data generated by finite element methods. To further achieve visualization, we have additionally introduced dimensionality reduction techniques to compress numerous independent variables while retaining as much information as possible, ultimately expressing the results in graphical form. Specifically, we extensively collected training data from model calculations corresponding to various operating conditions, such as the thermal properties of materials, heat source power, and time. Dimensionality reduction techniques were applied to merge the numerous variables affecting the heat transfer rate into a single variable: characteristic time. This aids in extracting the principal components for visualizing the machine learning results. We then employed a backpropagation (BP) neural network to identify the relationship between characteristic time, the energy storage process, and temperature from the training dataset. The results were plotted to create a quick lookup method. Using our invented lookup method, one can quickly estimate the energy storage progress and temperature of SAT material during operation through simple numerical calculations, requiring only a few minutes. This significantly enhances the design efficiency of chip thermal management applications using SAT compared to the several hours needed for finite element simulations. Additionally, it provides guidance for the thermal property regulation of composite SAT thermal storage materials and can serve as a reference for thermal management applications of other thermochemical storage materials.

2. METHODS
2.1. Finite element model

This study employs the results from finite element model calculations to train the neural network, ensuring that the final lookup strategy retains the high accuracy characteristic. Cao et al. (2022) comprehensively measured the kinetic process of SAT phase change and thermal decomposition reactions and validated their model. Therefore, we utilized their reaction kinetic equations to construct the governing equations of our finite element model. These calculations were then performed to generate the training data for our neural network.

Equation 1: Heat conduction equation with heat source

$$c\frac{\partial T}{\partial t} = \nabla(\lambda \nabla T) + \dot{\Phi}_{pc} + \dot{\Phi}_r$$

Where:

- c = Specific heat capacity [$J \cdot m^{-3} \cdot K^{-1}$]
- T = Temperature [℃] or [K]
- t = Time [s]
- λ = Thermal conductivity [$W \cdot m^{-1} \cdot K^{-1}$]
- Φ = Internal heat source [$W \cdot m^{-3}$]

Equation 1 is the heat conduction equation for solid materials, with two additional heat source terms included to account for the endothermic effects of SAT. $\dot{\Phi}_{pc}$ represents the heat absorption due to phase change, and $\dot{\Phi}_r$ represents the heat absorption due to thermal decomposition. These terms are expanded as follows.

Equation 2: Expanded form of $\dot{\Phi}_{pc}$	$\dot{\Phi}_{pc} = -\Delta H_{pc} \cdot \dfrac{\partial \beta}{\partial t}$
Equation 3: Expanded form of $\dot{\Phi}_r$	$\dot{\Phi}_r = -\Delta H_r \cdot \dfrac{\partial \alpha}{\partial t}$
Equation 4: Definition of β	$\beta = \begin{cases} 0 \\ \dfrac{T - T_s}{T_l - T_s} \\ 1 \end{cases}$
Equation 5: Definition of α	$\dfrac{\partial \alpha}{\partial t} = A \cdot \exp\left(\dfrac{-E_a}{RT}\right)(1 - \alpha)^{0.75}$

Where:

- ΔH = Enthalpy [J·m^{-3}]
- α = Thermal decomposition reaction process [%]
- β = Phase change process [%]
- T_s, T_l = Solidus temperature and Liquidus Temperature
- A = The pre exponential factor of the Arrhenius equation
- E_a = Apparent activation energy

Equation 4 represents the commonly used melting-solidification model for describing the solid-liquid phase transition process, which is widely employed in the simulation of phase change materials (Irwan et al., 2020). Equation 5 is the differential equation describing the decomposition reaction process, the form of which is determined by SAT reaction kinetics measurements. During the thermal storage process of SAT, there exists a sensible heat storage stage where the phase change is completed but the thermal decomposition reaction has not yet begun. The progress of this stage is defined by time (Equation 6).

Equation 6: Definition of γ, process of sensible heat storage stage	$\gamma = \dfrac{t - t_{e,pc}}{t_{b,r} - t_{e,pc}}$

Where:
- γ = process of sensible heat storage stage [%]
- $t_{e,pc}$ = The moment when the phase change ends
- $t_{b,r}$ = The moment when the thermal decomposition reaction begins

It is also important to note that during computation, the one-dimensional x-axis is given in units, ranging from 0 to L. However, when processing the computed results, the position x with units is converted to dimensionless form, representing a percentage within the range. We utilize the aforementioned equations to compute the temperature and energy storage progress of SAT material for chip thermal management. So, the computational domain can be simplified to a one-dimensional case with a single-sided heat source (see *Figure 1*). Additionally, as the material operates within a closed space, the heat exchange between the thermal storage system and the environment is minimal, allowing for adiabatic boundary conditions. The initial conditions are set such that the global initial temperature is 298.15 K (25°C), and both progress variables, **α** and **β**, are initialized to 0. Finite element calculations are performed using SIMULINK, MATLAB R2020a (The MathWorks, Inc.).
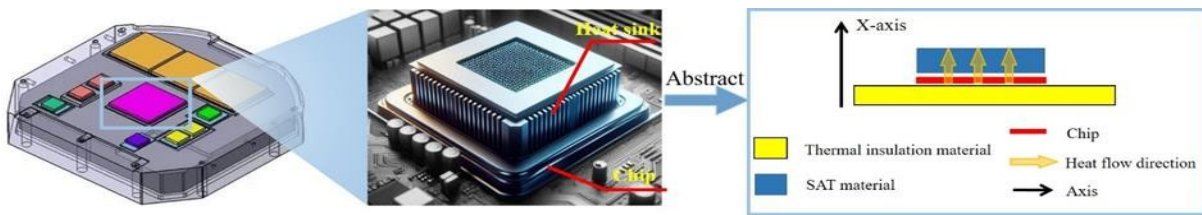
Figure 1: Calculation simplification for SAT material used in chip thermal management

2.2. Dimensionality reduction method

Using the finite element model, we can deduce the thermal storage progress (i.e., **α** and **β**) and the temperature **T** of the SAT material at a specific time and position, given the known material properties, material quantity, and heat source power. Therefore, the temperature is related to time, position, external heat source, and material properties, as detailed in *Equation 7*.

Equation 7: Variables that affect temperature T	$(x, t, \lambda, c, \dot{q}, L, H)$

Where:

- x = position in one dimension
- $\dot{q}$ = heat flux density of heat source
- L = the thickness of SAT material
- H = The total enthalpy of the material (sum of phase transition enthalpy and thermal decomposition enthalpy)

Due to the excessive number of variables, the results cannot be displayed in a simple 2D graph. Therefore, it is necessary to introduce dimensionality reduction methods to combine the numerous variables into one while retaining as much original information as possible. Notably, most variables (e.g., λ, $\boldsymbol{c}$, $\dot{\boldsymbol{q}}$, etc.) mainly influence the heat transfer process by accelerating or delaying the evolution of temperature over time. Hence, it is appropriate to use a power function product form to combine the variables, as described below.

For a relationship determined by a bivariate function $T = f(X_1, X_2)$, we aim to describe it using a univariate function $T = g(X_1 \cdot X_2^n)$. This way, the two independent variables are combined into one, in the form of a power function product of the original two variables. We expect the univariate function to accurately describe the original bivariate relationship as much as possible, meaning that for any given X_1 and X_2, there exists an n such that $f(X_1, X_2) = g(X_1 \cdot X_2^n)$.

Next, we collected numerous sets of X_1 and X_2 from finite element calculations that result in the function value T, denoted as: $T = f(_1^T X_1, {}_1^T X_2) = \cdots = f(_i^T X_1, {}_i^T X_2)$, where i denotes the i-th set.

Therefore, after combining into a univariate function, it should have: $T = g(_1^T X_1 \cdot {}_1^T X_2^n) = \cdots = g(_i^T X_1 \cdot {}_i^T X_2^n)$.

In this thermal management calculation, the temperature T is monotonically increasing. Therefore, in the univariate function, each dependent variable can only map to a single independent variable. Consequently, the independent variables in the equations should all be equal. Thus, we have: $_1^T X_1 \cdot {}_1^T X_2^n = \cdots = {}_i^T X_1 \cdot {}_i^T X_2^n$. Due to the loss of information, equality in this equation is not achievable. However, we can continually adjust n to find the optimal value that makes them as equal as possible. The degree of this equality is described by the objective function in Equation 8.

$$Goal(n) = \frac{1}{m}\sum_T^m \left\{ \frac{1}{s}\sum_{i=1}^s Abs\left[{}_i^T X_1 \cdot {}_i^T X_2^n - \frac{1}{s}\sum_{i=1}^s {}_i^T X_1 \cdot {}_i^T X_2^n \right] \right\}$$

Equation 8: Objective function

When $Goal(n)$ reaches its minimum value, the corresponding $\boldsymbol{n}$ results in the least information loss during the merging process. Moreover, the value of the objective function represents the average relative error after describing the data with the univariate function. In our study, we used this method to sequentially merge $t, \lambda, c, \dot{q}, L$ and H into a single variable: characteristic time $\boldsymbol{t_{ch}}$.

2.3. Neural networks

The training data for the neural network is generated by the finite element model. We used the Monte Carlo method, randomly selecting model parameters to perform finite element calculations 100 times (the random value ranges for each parameter are shown in *Table 1*). Each calculation covers a time range of 0-3000 seconds, and the results are then compiled and analysed.

Table 1: The random value ranges for each parameter

Parameter	Unit	Value range
c	[J·m⁻³·K⁻¹]	$1.2\text{-}2.0 \diamond 10^6$
λ	[W·m⁻¹·K⁻¹]	4-20
$\dot{q}$	[W·m⁻²]	$2\text{-}8 \diamond 10^4$
L	[m]	0.02-0.08
H	[J·m⁻³]	$4\text{-}10 \diamond 10^8$

Each data point in the calculation results includes information on temperature, position, progress variables, material thermal properties, heat source, etc. (i.e., *T, t, x, α, β, γ ,c, λ,q̇, L, H*). Subsequently, we calculate the characteristic time $\boldsymbol{t_{ch}}$ for each data point and split the data into six datasets representing the mapping relationships: (t_{ch}, α), (t_{ch}, γ), (t_{ch}, β), (α, T), (γ, T), and (β, T). A BP neural network is used to identify these mapping relationships, and the results will be arranged in graphical form as shown in *Figure 2*, creating a lookup method.
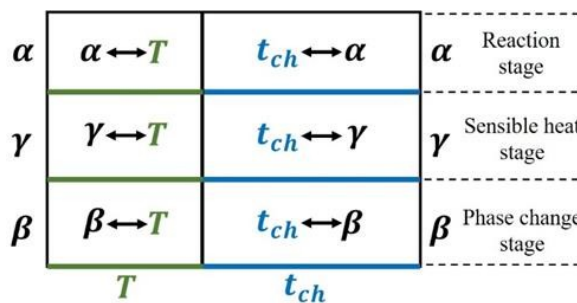
Figure 2: Mapping relationships displayed by the lookup strategy

BP neural network is a type of multilayer feedforward neural network trained using the error backpropagation algorithm. It consists of an input layer, hidden layers, and an output layer (Karimi *et al.*, 2022). In simple terms, data is processed in each layer, with the result of one layer being passed to the next for further processing, until the output layer produces the prediction result. Specifically,

in this study, the hidden layers use the Tan-Sig transfer function, and the output layer uses the Purelin transfer function.

Essentially, the BP algorithm minimizes the error between the training data results and the predicted results by continuously adjusting the computational parameters within each layer to reduce the error as much as possible. The objective function used to measure this error is the mean squared error (MSE), as shown in Equation 9. The Levenberg-Marquardt training algorithm is employed to adjust the computational parameters within the layers, ensuring the MSE converges quickly to its minimum value. The final fitting effectiveness is evaluated using the R value, as defined in Equation 10.

Equation 9: Mean squared error (MSE)

$$MSE = \frac{1}{N} \sum_{i=1}^{N} \left(X_{exp(i)} - X_{pred(i)} \right)^2$$

Equation 10: R value

$$R = \sqrt{1 - \frac{\sum_{i=1}^{N} \left(X_{exp(i)} - X_{pred(i)} \right)^2}{\sum_{i=1}^{N} \left(X_{exp(i)} \right)^2}}$$

Where:

- $X_{exp(i)}$ = the results of training data
- $X_{pred(i)}$ = the results of neural network prediction
- N = number of data points

3. RESULTS AND DISCUSSION
3.1. The expression of characteristic time

In order to merge numerous variables together using power function products, we varied the variables of interest while keeping the other variables fixed during finite element calculations, obtaining sufficient data to determine the optimal ***n*** value for the variables of interest. From *Figure 3*, we can observe the variation of ***Goal*** with ***n*** for different variables. We select the ***n*** value corresponding to the minimum Goal as the exponent when merging this variable, as listed in *Table 2*.

*Table 2: Tthe **n** values obtained for each variable along with the relative error.*

Independent variables	Heat capacity **c**	Thermal conductivity **λ**	Heat flux density **q̇**	Material length **L**	Total enthalpy of material **H**
Exponent: **n**	-0.4	0.3	1.0	-1.0	-0.6
Unit	[J·m^{-3}·K^{-1}]	[W·m^{-1}·K^{-1}]	[W·m^{-2}]	[m]	[J·m^{-3}]
Average relative error	0.0255	0.145	0.143	0.124	0.0179
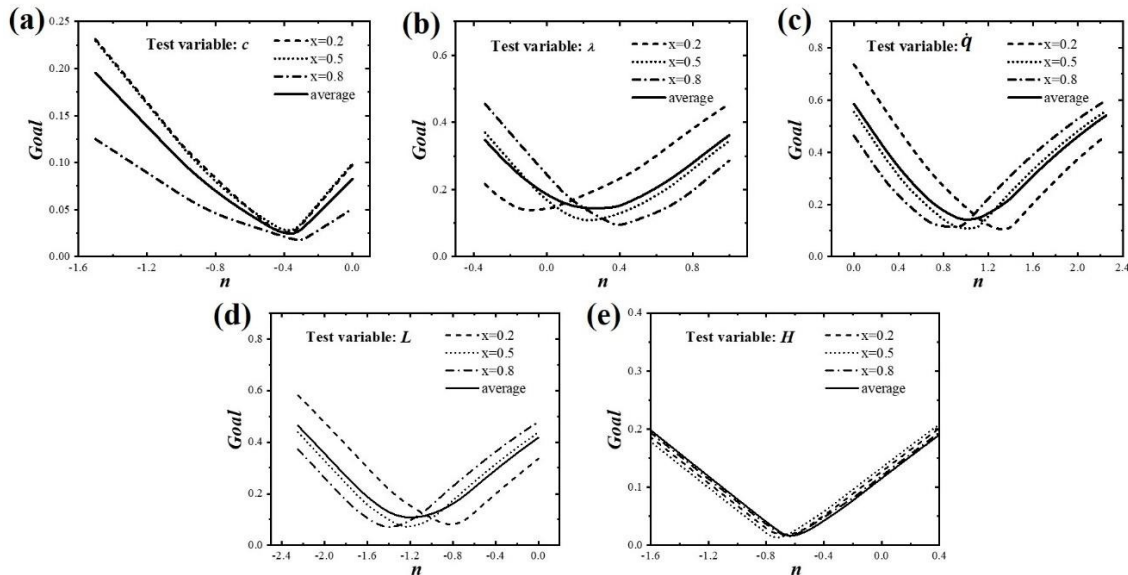
*Figure 3: Illustrates the variation of Goal with **n** when examining different variables. The variables under examination are: (a) specific heat capacity **c**; (b) thermal conductivity **λ**; (c) heat source heat flux density **q̇** ; (d) material length **L**; (e) total enthalpy of the material **H***

We have obtained the ***n*** values that maximize the preservation of information when merging various variables into a power function product form. Therefore, the result of the merging is expressed as *Equation 11*. It is important to note that calculations must be performed using the units provided in *Table 2*. This dimensionality reduction effectively eliminates the influence of differences in specific heat capacity, thermal conductivity, heat source power, and material volume on the rate of heat transfer, allowing different

material properties to be compared on the same scale. Hence, the merged variable is referred to as the characteristic time t_{ch}, and it is dimensionless by definition.

Equation 11: The expression of characteristic time

$$t_{ch} = c^{-0.4} \lambda^{0.3} \dot{q} L^{-1} H^{-0.6}$$

3.2. Neural network training

The developed lookup strategy needs to display six mapping relationships. During a single calculation process, the parameters included in the characteristic time remain constant. Combined with *Equation 6*, it is evident that the (t_{ch}, γ) relationship is a linear mapping. Therefore, the (t_{ch}, γ) mapping does not require neural network training and can be represented by connecting the initial and final state values with a straight-line during plotting. Additionally, the (β, T) mapping is described by *Equation 4*, which also does not require neural network training.

BP neural networks were used to train the (t_{ch}, α) and (t_{ch}, β) mapping relationships. The training results are shown in *Figure 4*. The **R** values for these mappings are 0.99988 and 0.99955, respectively, indicating that excellent training results were achieved.
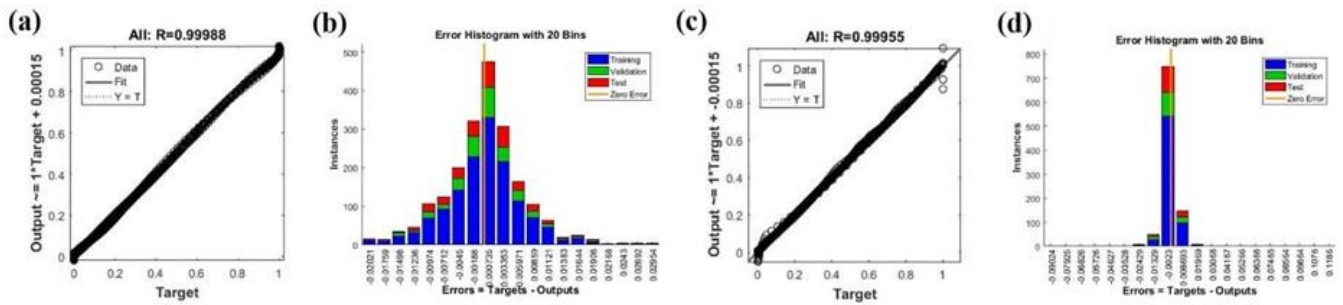
Figure 4: Regression diagram (a) and deviation distribution diagram (b) of neural network training (t_{ch}, α); Regression plot (c) and bias distribution plot (d) of neural network training (t_{ch}, β)

Due to the fact that the mappings (α, T) and (γ, T) did not involve dimensionality reduction, we conducted Sobol sensitivity analysis prior to neural network training to assess the influence of other parameters on these mapping relationships (see *Figure 5*). The results indicate that when training the (α, T) mapping, the influence of $\dot{q}$ needs to be considered, and when training the (γ, T) mapping, the influence of x needs to be considered. Therefore, we effectively trained the relationships $(\alpha, T, \dot{q})$ and (γ, T, x) using BP neural networks. The training results are shown in *Figure 6*, with **R** values of 0.99983 and 0.99956 obtained for the two mappings, respectively.
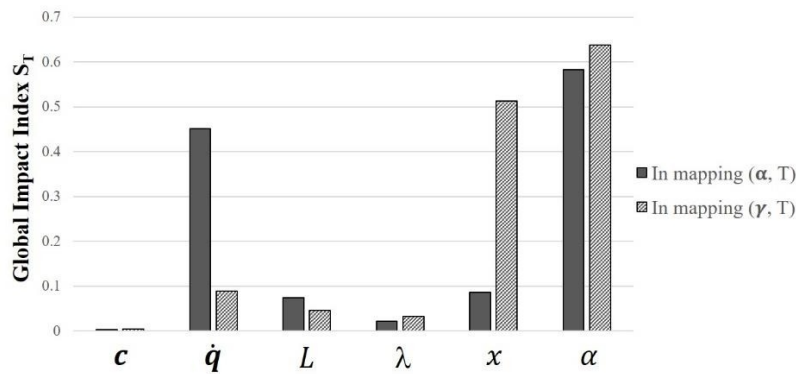
Figure 5: Influence of other parameters on mapping relationships
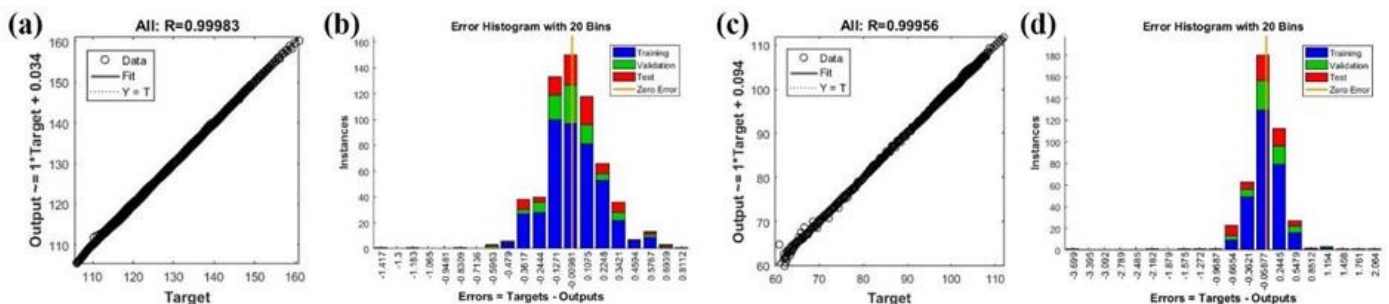
Figure 6: Regression diagram (a) and deviation distribution diagram (b) of neural network training (α, T); Regression plot (c) and bias distribution plot (d) of neural network training (γ, T)

335

3.3. Chart-lookup strategy

Based on the layout shown in *Figure 2*, we utilized the training results of the neural networks to plot the operational query chart for the SAT-based chip thermal management system, as depicted in *Figure 7*. The right half of the figure represents the progress variable plot, allowing users to determine which heat storage stage the material is in and the percentage of completion. The left half of the figure represents the temperature plot, enabling the correspondence of the percentage progress variable to temperature.

We would introduce its usage method. If we know the material properties and heat source power, and we need to find the temperature and energy storage progress of the SAT material at the central position (*x*=0.5) at time *t*, the steps are as follows:

STEP 1: Calculate the characteristic time t_{ch}.

STEP 2: In the right half of Figure 7, find the corresponding ordinate to determine the stage and progress of the material (refer to the curve at *x*=0.5).

STEP 3: Correspond with the progress variable to the left half, and find the corresponding abscissa on the graph to obtain the temperature of the SAT.

These steps can be reversed. When the temperature requirement is known, the corresponding characteristic time can be found in reverse, thereby estimating the combination of SAT material properties that meet the requirements, guiding the material preparation. Therefore, this is a very simple prediction method, which is more timesaving and less difficult to use than finite element methods, which is extremely beneficial for quickly estimating scenarios based on SAT chip thermal management. In addition, the process of constructing the query chart in this paper can also serve as a reference for the thermal management systems of other materials.
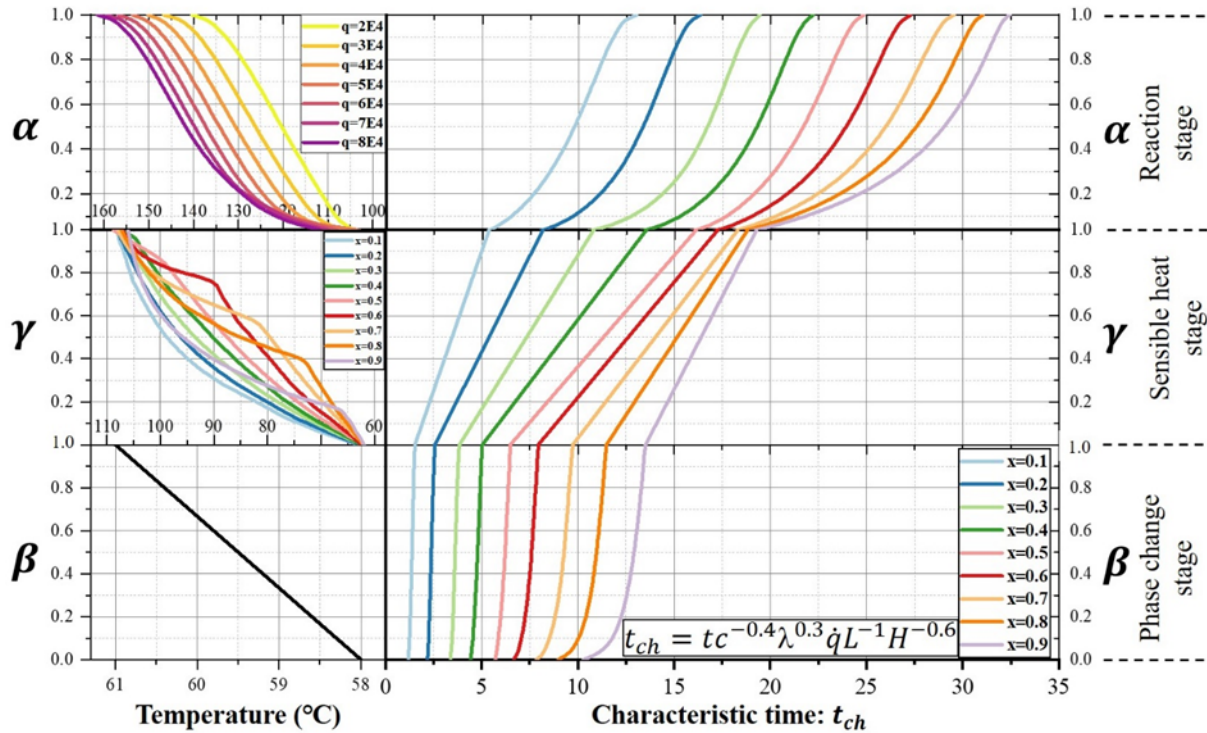
Figure 7: Operational query chart for SAT-based chip thermal management system formed by neural network

4. CONCLUSION

This work presents a rapid chart-lookup strategy developed for chip thermal management systems utilizing SAT, leveraging machine learning techniques. We generated a comprehensive dataset, widely recognized for its accuracy, through finite element simulations, encompassing temperature, position, progress variables, material thermal properties, heat sources, and more. Subsequently, we employed a power function product to merge variables to achieve dimensionality reduction. This reduction effectively mitigates the influence of differences in heat capacity, thermal conductivity, heat source power, and material volume on the heat transfer process, resulting in the formation of a combined variable known as characteristic time. Finally, we utilized BP neural networks to fit the mapping relationships within these datasets, thus forming a rapid lookup table strategy. This innovation enhances the design efficiency of chip thermal management applications using SAT, reducing prediction time from hours to minutes. Moreover, this method can be extended to thermal management of other thermochemical materials, providing valuable reference for the development of operational prediction methods for other materials.

5. ACKNOWLEDGEMENT

6. DECLARATION OF INTEREST STATEMENT

The authors declare that they have no known competing financial interests or personal relationships that could have appeared to influence the work reported in this paper.

7. REFERENCES

CAS (Chemical Abstracts Service). (2024) Sodium acetate trihydrate (6131-90-4). Available at: https://commonchemistry.cas.org (Accessed: 22 May 2024)

Cao, J. et al. (2022) 'Thermochemical heat storage system for preventing battery thermal runaway propagation using sodium acetate trihydrate/expanded graphite', Chemical Engineering Journal, 433(2), 133536.

Ghosh, D. et al. (2022) 'Strategies for phase change material application in latent heat thermal energy storage enhancement: Status and prospect', Journal of Energy Storage, 53, 105179.

Gómez, I. et al. (2020) 'Improving learning and generalization capabilities of the C-Mantec constructive neural network algorithm', Neural Computing and Applications, 32, pp. 8955-8963.

Irwan, M.A.M. et al. (2020) 'Review on numerical simulations for nano-enhanced phase change material (NEPCM) phase change process', Journal of Thermal Analysis and Calorimetry, 141, pp. 669-684.

Karimi, M. et al. (2022) 'Intelligent modeling for considering the effect of bio-source type and appearance shape on the biomass heat capacity', Measurement, 189, 110529.

Lin, S. et al. (2023) 'Mitigation of lithium-ion battery thermal runaway and inhibition of thermal runaway propagation using inorganic salt hydrate with integrated latent heat and thermochemical storage', Energy, 266, 126481.

Mei, J. et al. (2023) 'Experimental study on the effect of passive retardation method for thermal runaway mitigation of lithium-ion battery', 230(B), 120861.

Wang, Y. et al. (2022) 'Review on Coupled Thermo-Hydraulic Performance of Nanofluids and Microchannels', Nanomaterials, 12(22), 3979.

#234: Design and optimization of carbon capture processes

Haiyan SHEN[1], Fangqin LI[2], Jianxing REN[3], Jiang WU[4], Zhenzhen GUAN[5], Weiguo PAN[6], Binlin DOU[7]

[1] College of Energy and Mechanical Engineering, Shanghai University of Electric Power, Shanghai 1825504173@qq.com
[2] College of Energy and Mechanical Engineering, Shanghai University of Electric Power, Shanghai Shanghai Non-Carbon Energy Conversion and Utilization Institute, Shanghai, lifangqin@shiep.edu.cn
[3] College of Energy and Mechanical Engineering, Shanghai University of Electric Power, Shanghai, ren608@163.com
[4] College of Energy and Mechanical Engineering, Shanghai University of Electric Power, Shanghai, wjcfd2002@163.com
[5] College of Energy and Mechanical Engineering, Shanghai University of Electric Power, Shanghai, guanzzhen@163.com
[6] College of Energy and Mechanical Engineering, Shanghai University of Electric Power, Shanghai Shanghai Non-Carbon Energy Conversion and Utilization Institute, Shanghai, pweiguo@163.com
[7] School of Energy and Power Engineering, Shanghai Key Laboratory of Multiphase Flow and Heat Transfer in Power Engineering, University of Shanghai for Science and Technology, Shanghai bldou@usst.edu.cn

Abstract: One of the best carbon capture methods is alcohol amine solution. This article uses Aspen Plus software to simulate the capture of CO_2 in flue gas by MDEA solution absorbent. Investigations were conducted into the impacts of operating factors on the rate of absorption and regenerated use of energy, including flue gas inlet temperature, desorption tower pressure, reflux ratio, lean CO_2 load, rich feed position, and temperature. and optimal process parameters were obtained. The simulation results show that various operating parameters have an impact on the rate of absorption and the energy used for regeneration. The absorption tower's typical forthcoming flue gas temperature is 40 °C, the lean liquid CO_2 load is 0.18 mol/mol, the reflux ratio is 0.8, The rich fluid intake location is a second plate down from the top of the desorption tower, with a temperature for inlet of 95 °C and a pressure of 2.2 bar. Compared with before optimization, the CO_2 absorption rate of the system increases from 84.1% to 94.4%, the regeneration energy consumption increases from 3.29 GJ/t CO_2 to 3.56 GJ/t CO_2, and the regeneration energy consumption only increases by 0.27 GJ/t CO_2.

Keywords: Carbon Capture, Mdea, Simulation, Optimization

1. INTRODUCTION

Carbon capture, utilization, and storage technology is one of the important solutions to alleviate CO_2 emissions[1]. This technology captures CO_2 from gas mixtures produced by fossil fuel combustion, stores or reuses it, and prevents a large amount of CO_2 from being released into the atmosphere[2]. The massive amount of CO_2 emissions has led to the greenhouse effect, which is now a global issue. Therefore, capturing CO_2 is of great significance for controlling CO_2 emissions, and power plant flue gas is an important centralized emission source of CO_2[3-5]. Therefore, researching appropriate CO_2 capture processes to capture power plant flue gas is extremely important for reducing the greenhouse gas emissions[6]. Among the existing carbon capture technologies, alcohol amine solution absorbent is the most mature technology[7], which has the advantages of large absorption capacity and fast absorption rate[8], but there is a problem of high energy consumption for regeneration[9-11].

These instructions apply for all papers. Considering how caustic MDEA solution is[12-14], it is not advisable to choose a concentration that is too high when selecting the absorbent for MDEA solution[15]. This article uses 30 wt% MDEA solution as the absorbent for simulation. By controlling the mass flow rate of the inlet flue gas to remain unchanged, the absorption rate of CO_2 absorbed by the absorbent reaches 90%. In addition, regeneration energy consumption is also an important parameter for evaluating carbon capture performance. This chapter conducts sensitivity analysis on various parameters and simulates under different parameters, The capture situation of MDEA solution absorbent is determined to obtain the optimal operating parameters.

2. Process flow description
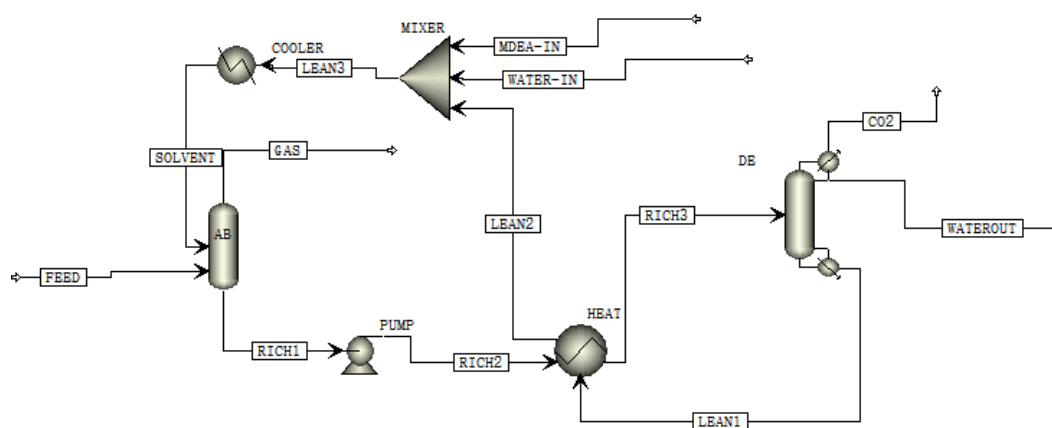
Figure 2-1: Process flow diagram of MDEA solution CO_2 capture system

After desulfurization and denitrification, the flue gas FEED is cooled and enters the absorption tower from the bottom, as seen in Figure 2-1. When it gets into touch with the absorbent SOLVENT that has been sprayed atop the absorption tower, it reacts with the CO_2 present in the flue gas. The cleaned GAS flue gas is released from the tower above the absorption. Rich liquid RICH1, which emerges from the absorption tower's bottom, is created when the absorbent combines with CO_2 in the flue gas. Rich liquid RICH1 enters the lean rich liquid exchanger HEAT as a result of the rich liquid pump's activity. The rich liquid in the lean rich liquid exchanger is heated by the lean liquid LEAN1 that emerges from the bottom of the desorption tower. The rich liquid enters the desorption tower after gaining heat. The steam produced by the reboiler at the bottom of the desorption tower exchanges heat with the rich liquid sprayed at the top of the tower. The rich liquid is desorbed as a result of pressure and temperature. After being separated, the lean liquid LEAN1 flows into the lean rich liquid exchanger to cool down. It then passes through the cooler COOLERto cool down even more before going to the top of the absorption tower for the subsequent cycle.

3. Simulation conditions and regulations

This article selects a domestic 600 MW unit as the research object, with a flue gas mass flow rate of 1995.2 t/h at thetail of the boiler. The mass fractions of each component are shown in Table 3 -1. The relevant parameters of the absorption tower and desorption tower are shown in Table 3-2.

Table 3-1: Smoke Composition

Smoke composition	Mass fraction （wt%)
N_2	0.72
CO_2	0.18
H_2O	0.05
O_2	0.05

Table 3-2: Initial Parameter Settings for Main Logistics and Modules

Logistics or modules	Main parameters
Absorption tower	Number of trays：10
	Pressure：1 bar
	Absorption rate：90%
	Calculation type：Rate mode
	Heating/cooling equipment: None
Desorbing tower	Number of trays：10
	Pressure：2 bar
	Temperature：45 °C
	Reboiler type: Rate type
	Condenser: Partial condensation
	Reflux ratio：0.6
	CO_2 purity：90%
Pump	Outlet pressure：3 bar
Lean rich liquid heat Exchanger	Cold side outlet temperature：90 °C
Cooler	Temperature：40 °C
Mixer	Temperature：40 °C
FEED	Temperature：50 °C
	Pressure：1 bar

4. System optimization

4.1. Analysis of flue gas temperature at the inlet of the absorption tower

Figure 4-1: Relationship curve between inlet flue gas temperature of absorption tower and regeneration energy consumption and absorption rate

The absorption rate of CO_2 absorbed by the absorption tower actually increases as the flue gas's entrance temperature drops, as Figure 4-1 illustrates. This is due to the fact that a drop in the absorption tower's incoming flue gas temperature causes CO_2 to become more soluble in the MDEA solution. The rate of CO_2 absorption will increase, but the solution's reaction rate will drop. Therefore, an absorbent solution containing 30% MDEA does not catch CO_2 well at higher temperatures. In addition, the alkalinity of the MDEA solution absorbent is also influenced by the environmental conditions of the flue gas at the absorption tower's entrance. When the absorption tower's incoming flue gas temperature drops, the alkalinity of the 30 wt% MDEA solution absorbent becomes stronger. When the temperature rises, the alkalinity of the 30 wt% MDEA solution absorbent actually decreases. Therefore, the lower the inlet flue gas temperature of the absorption tower, the more favorable it is for the 30 wt% MDEA solution absorbent to capture CO_2. Furthermore, the equilibrium partial pressure of CO_2 gas in the absorbent will fall when the temperature of the flue gas entering the absorption tower decreases. The lower the partial pressure, the more favorable it is for the MDEA solution absorbent to capture CO_2. Therefore, the inlet flue gas temperature of the absorption tower should not be too high, as an increase in temperature will reduce the CO_2 absorption rate of the 30 wt% MDEA solution absorbent. Meanwhile, lowering the absorption tower's incoming fumes temperature can not only reduce regeneration energy consumption, but also improve the rate of CO_2 absorption captured bythe

system. Consequently, 40 ºC is the ideal temperature for the absorption tower's incoming flue gas.

4.2. Analysis of CO₂ load in lean solution
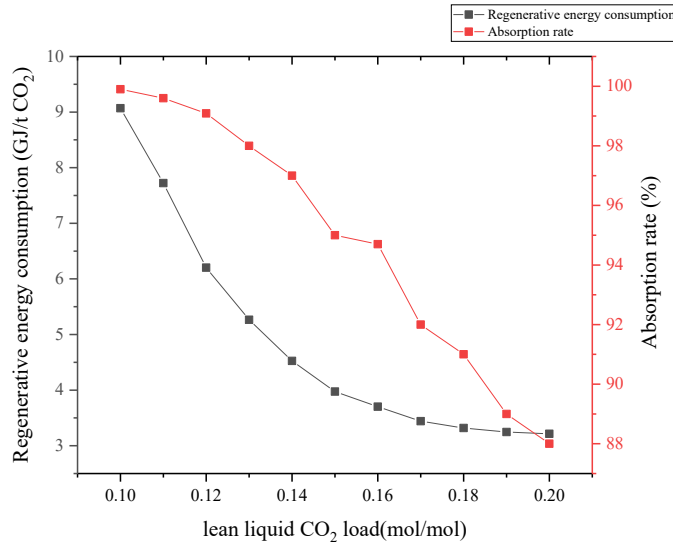
Figure 4-2: Relationship curve between lean liquid CO₂ load and regeneration energy consumption and absorption rate

As the load of lean liquid CO2 increases, the regeneration energy consumption first rapidly decreases, and then the decline rate gradually becomes gentle. Regenerative energy consumption is an important indicator for evaluating the performance of CO2 capture systems. The lower the CO2 load of the lean solution, the greater the difference between the rich solution load and the lean solution load, indicating a higher degree of desorption of the rich solution by the desorption tower. Therefore, the regeneration of the reboiler in the desorption tower is also higher. In addition, the lower the load of lean liquid CO2, the smaller the driving force at the bottom of the desorption tower. Therefore, additional energy needs to be provided to the desorption tower to maintain its driving force, which increases the regeneration of energy consumption of the reboiler. Regeneration energy use drastically decreases while the total amount of lean liquid CO2 grows, the distinction among the payload of lean liquids CO2 drops, and the motive power that drives the desorption tower develops. However, the amount of carbon that may interact with MDEA dropsand its incorporation rate diminishes as the volume of light remedy CO2 increases. Therefore, to ensure the absorption rate of CO2 captured by the 30 wt% MDEA solution absorbent, 0.18 mol/mol of lean solution CO2 load is selected.

4.3. Reflux ratio analysis
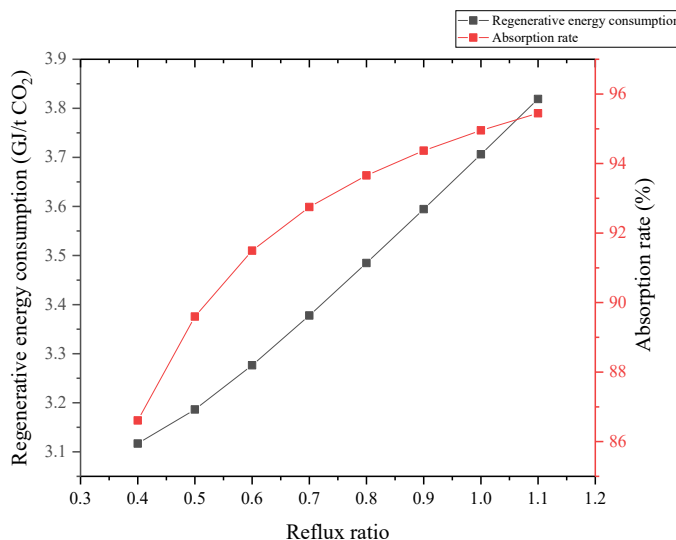
Figure 4-3: Relationship curve between reflux ratio and regeneration energy consumption and absorption rate

As shown in Figure 4-3, as the proportion of reflux comes up, so do the rates of regeneration use of energy and the rate of absorption. There's no avoiding boosting the removal tower's reflux proportion that will result in increasing the condenser's drainage liquid volume. Enhancing the CO₂ and water vapor for the summit of the desorption tower is essential for guaranteeing an adequateextraction volume at that point. Therefore, the system will desorb the rich liquid more fully, indirectly increasing the absorption of CO₂, thereby improving the absorption rate of CO₂ and increasing the load of the reboiler. In addition, the increase in CO₂ desorption leads to a reduction in the load of lean liquid CO₂ after desorption, resulting in higher requirements for desorption in the desorption tower. This also increases regeneration energy consumption. In addition, heating and condensing the reflux liquid will also increase the energy consumption of the desorption tower. In summary, when the reflux ratio of the desorption tower increases,the regeneration energy

consumption of the desorption tower increases significantly. Therefore, the reflux ratio of the desorption tower should not be too high. The reflux ratio of the 30 wt% MDEA solution absorbent CO_2 capture system should be selected as 0.8.
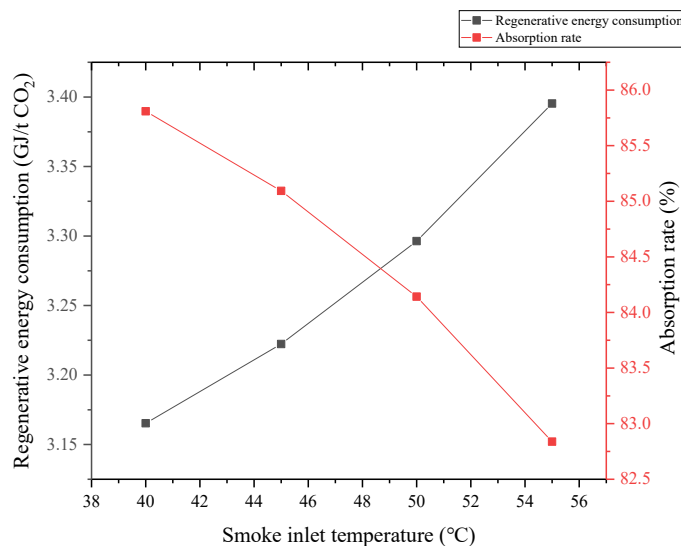
4.4. Analysis of inlet temperature of desorption tower
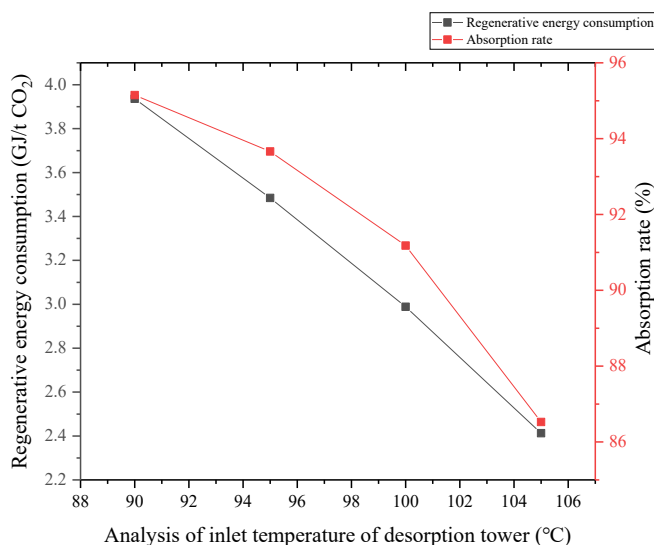
Figure 4-4: Relationship curve between inlet temperature of desorption tower and regeneration energy consumption and absorption rate

The liquid that enters the desorption tower after absorbing CO_2 by the absorbent is called low-temperature rich liquid, and lean liquid is the liquid that emerges towards the bottom underneath the desorption column afterwards desorption. At this time, the lean liquid's current temperature is a comparatively high 124 ℃. The high-temperature lean liquid within the lean rich liquid heat exchanger transmits heat to the freezing-rich liquid that comes from the bottom inside the absorption tower. As a result, the temperature of the abundant liquid that reaches the desorption tower improves, limiting the heat load on the reboiler and eventually decreasing the electrical load for the desorption tower. In addition, by raising the temperature of the rich liquid near the desorption tower's entrance, less cooling water will be required until the less rich liquid reaches the absorption tower. From Figure 4-4, it can be seen that the change in richer liquid temperature at the entrance of the desorption tower has a significant influence on the regeneration energy consumption for the system. Enhancing the heat transfer promotion of the poor rich liquid heat exchanger and lowering the energy consumption of regeneration can be achieved by increasing the temperature of the rich liquid at the desorption tower's input. Therefore, while ensuring the stable operation of the rich and poor liquid heat exchanger, seeking the optimal inlet rich liquid temperature of the desorption tower is of great significance in reducing the regeneration energy consumption of the 30 wt% MDEA solution absorbent CO_2 capture system and reducing the amount of supplementary cooling water. This article raises the rich liquid's temperature to 95 ℃ at the desorption tower's entrance.

4.5. Pressure analysis of desorption tower
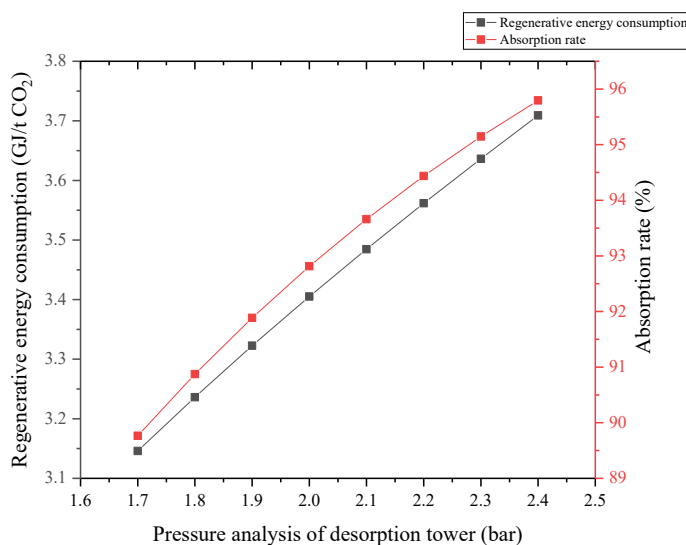
Figure 4-5: Relationship curve between desorption tower pressure, regeneration energy consumption, and absorption rate

The abundant liquid's temperature within the decontamination tower's outflow will rise due to an increase in pressure inside the tower, which will enhance the carbon dioxide desorption rate for transferring mass from the abundant liquid and the desorption tower's

driving force. However, if the degree of temperature of the desorbed lean solution is too high, there may be a problem of high-temperature thermal degradation of the lean solution, and it may cause corrosion to the equipment. Therefore, the temperature of the desorbed lean solution should not be too high. When the temperature of the rich liquid at the point of consumption continues constant, the variance in temperature of the absorbent found in the desorption tower occurs as the pressure that builds inside the tower rises. Therefore, the desorption tower needs to provide more heat to heat the lean liquid, leading to a gradual increas e in regeneration energy consumption and a more thorough desorption process, thereby improving the absorption rate of CO_2. Althoughincreasing the pressure of the desorption tower can effectively enhance the rate with which CO_2 is absorbed by the 30 wt% MDEA solution, the impact of pressure on the normal operation of the desorption tower should also be considered. Although boosting the desorption tower's pressure can speed up CO_2 absorption, doing so will unavoidably cause the tower to use more energy for regeneration, which will raise production costs. As a result, 2.2 bar is determined to be the ideal desorption tower pressure.

4.6. Analysis of Rich Liquid Feed Location
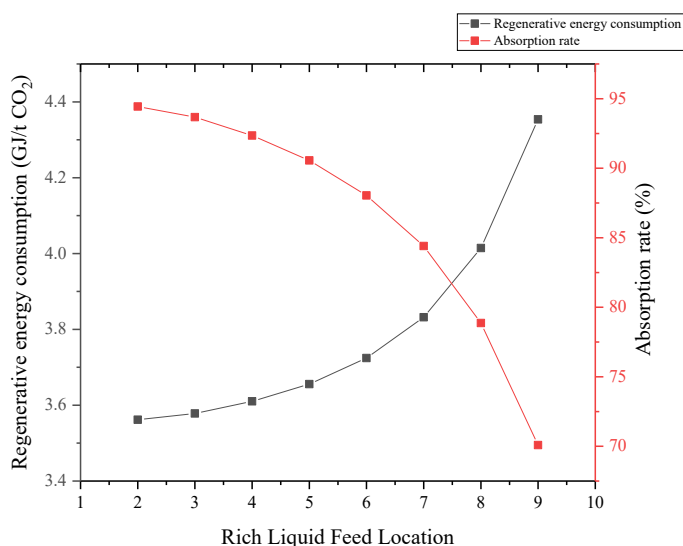
Figure 4-6: Relationship curve between feed tray and regeneration energy consumption and absorption rate

Rich liquid can enter the desorption tower from any tray between the 2nd and 9th trays located at the top of the tower. The condenser is located on the 1st tray of the desorption tower, and the reboiler is located on the 10th tray of the desorption tower at the bottom of the tower. The reboiler produces steam, which rises in the desorption tower and undergoes heat and mass transfe r reactions with the rich liquid in the desorption tower. As shown in Figures 4-6, when the feed tray is lowered from the 2nd stage tray to the 9th stage tray, and as the absorption rate falls, the process of regeneration use of energy rises. The rich liquid's position in the desorption tower continues to shift downhill, the rate of increase in regeneration energy consumption gradually accelerates, the rate of decrease in CO_2 absorption is also accelerating. This is due to the fact that the rich fluid comes down from the upper section of the desorption tower while the feed position is still in the higher section, giving it ample opportunity to exchange heat with the steam produced at the bottom of the tower. The speed of heat transfer and mass movement between the rich liquids and the steam it produces essentially does not change. Therefore, when the feed position is in the upper section of the desorption tower, the influence of the feed position on the desorption process of the desorption tower is relatively small, and the regeneration energy consumption and absorption rate change slowly; The rate of transfer of heat and mass between rising steam rapidly decreasing, and rich liquid results in a gradual shift in the feed position of the rich liquid to the middle and lower sections of the desorp tion tower, which accelerates changes in absorption rate and regeneration energy consumption. This lessens the rich liquid's desorption action in the absorption tower and significantly lowers CO_2 product. In order to guarantee the system's overall absorption of carbon dioxide rate, it is necessary to further increase regeneration energy consumption. Therefore, this article chooses to fill the desorption towerwith the rich liquid. at the second tray away from the top of the tower.

5. SYSTEM OPTIMIZATIONS

Table 5-1: System simulation results before and after optimization

	Before optimization	After optimization
Absorption rate（%）	84.1	94.4
Regenerative energy consumption （GJ/t CO_2）	3.29	3.56

According to Table 5-1, after sensitivity analysis and optimization, the absorption rate of the 30 wt% MDEA solution absorbent increased by 10.3%, while the regeneration energy consumption only increased by 0.27 GJ/t CO_2. It can be seen that the optimized system performance is better than the original system. Therefore, the optimization of the system in this chapter is successful. In addition, the following series of conclusions were obtained:

(1) The energy consumption of 30 wt% MDEA solution absorbent is greatly affected by the load of lean liquid CO_2 and the inlet temperature of the desorption tower, and the load of lean liquid, the reflux ratio, the inlet temperature of the desorption tower, the pressure of the desorption tower and the flooded feed tray have a great influence on the absorption rate of the absorbent of 30 wt% MDEA solution.

(2) The optimal operating parameters of the CO_2 capture system with 30 wt% MDEA solution absorbent were as follows: flue gas inlet temperature of 40 °C, lean liquid CO_2 load of 0.18 mol/mol, reflux ratio of 0.8, inlet of desorption tower rich liquid temperature of 95 °C, flooded feed position of the second tray from the top of the desorption tower, and desorption tower pressure of 2.2 bar.

6. REFERENCES

[1] JIANG C, GAO G, JIANG W F, et al. Energy Consumption Assessment and Reaction Kinetics Analysis of Catalytic Amine-based Carbon Capture Techology[J]. Journal of Chinese Society of Power Engineering, 2024, 44(06): 956-963.

[2] ZHANG Z E. Energy and environment issues in carbon capture, utilization and storage[J]. Energy Sources Part A, 2020: 1770899.

[3] S. M A,Omid M,Yue W, et al. Catalytic Solvent Regeneration for Energy-Efficient CO_2 Capture[J]. ACS SUSTAINABLE CHEMISTRY & ENGINEERING, 2020, 8(51): 18755-18788.

[4] LIN Z H, WU D W, FAN Y C, et al. DEvelopment progress of liquid-liquid biphasic solvents for carbon dioxide chemical absorption capture from flue gas of coal-fired power plants[J]. Clean Coal Technology, 2023,29(04): 21-30.

[5] NGUYEN N N, LA V T, HUYNH C D, et al. Technical and economic perspectives of hydrate-based carbon dioxide capture[J]. Applied Energy, 2022,307(0): 118237.

[6] BAI Y X, ZHENG R F, WEI L X, et al. Performance comparison between phase change absorbent and ethanolamine absorbent for CO_2 capture[J]. Chemical Engineering of Oil & Gas, 2024.

[7] ZHANG J W, GU W B, ZHANG F L.Research progress of carbon dioxide capture technology based on chemical absorption method[J]. Low-Carbon Chemistry and Chemical Engineering, 2023, 48(04): 96-106.

[8] Wanlin G, Shuyu L, Rujie W, et al. Industrial carbon dioxide capture and utilization: state of the art and future challenges[J]. Chemical Society reviews, 2020, 49(23): 8584-8686.

[9] LIU D L, WANG C, LIU X W, et al, Research advances in chemical absorbents for carbon dioxide capture[J]. Low-Carbon Chemistry and Chemical Engineering, 2024, 49(01): 94-104+112.

[10] ZHAO R L, MA W T, XU X, et al. Research progress of chemical absorbents for carbon dioxide capture[J]. Fine Chemicals 2023, 40(01): 1-9.

[11] Wu Y, Xu J, Mumford K, et al.Recent advances in carbon dioxide capture and utilization with amines and ionic liquids[J]. Green Chemical Engineering, 2020, 1(01): 16-32.

[12] Aida R, Mert A, Ramazan K. Corrosion Behavior of Carbon Steel in CO_2 Saturated Amine and Imidazolium-, Ammonium-,and Phosphonium-Based Ionic Liquid Solutions[J]. Industrial & Engineering Chemistry Research, 2016, 55(2): 446-454.

[13] Karnwiboon K, Saiwan C, Idem R, et al. Solvent Extraction of Degradation Products in Amine Absorption Solution for CO_2 Capture in Flue Gases from Coal Combustion: Effect of Amines[J]. Energy Procedia, 2017, 1141980-1985.

[14] HONG Z P, YE C M, WU H, et al. Research progress in CO_2 removal technology of nutural gas[J]. CIESC Journal, 2021, 72(12): 6030-6048.

[15] LIN H Z, LUO H Z, PEI A G, et al. Simulation and analysis of carbon dioxide capture process using MDEA/PZ blendsolution in a coal-fired power plant[J]. Chemical Industry and Engineering Progress, 2019, 38(04): 2046-2055.

#235: Thermal performance analysis of phase change material in ship cabin: an experimental study under mooring and sailing conditions

Hui Hu[1]; Lijie Xu[*1]; Wenzhu Huang[2], Jie Ji[2]; Shangkun Zhong[1]; Jingyong Cai[**3]; Leyang Dai[1]; Chen Cheng[1];

*Corresponding author, Email: * lijiexu@jmu.edu.cn,** caijingyong@shiep.edu.cn
[1] Provincial Key Laboratory of Naval Architecture & Ocean Engineering, Jimei University, Xiamen,361021, China.
[2] Shanghai Micro Electronics Equipment (Group) CO., LTD
[3] Department of Thermal Science and Energy Engineering, University of Science and Technology of China, Hefei, 361021, China.
[4] College of Energy and Mechanical Engineering, Shanghai University of Electric Power, Shanghai, 200090, China.

Abstract: Cooling load is an important component of ship energy consumption. The ship's envelope constructed from aluminium alloy possesses a very low thermal storage capacity. This results in the temperature of ship cabin being significantly influenced by changeable solar energy reception angles and dynamic thermal transfer boundary conditions, necessitating a higher cooling load to maintain a comfortable cabin temperature. At present, research on reducing cooling load primarily focuses on active energy-saving technologies, exemplified by enhancements in air conditioning system performance. However, there is limited research on reducing cooling load through passive energy-saving methods. Therefore, a dynamic energy-saving strategy that incorporates phase change materials (PCMs) into the ship's hull is firstly proposed. In this study, the dynamic energy-saving strategies utilizing PCM panels are investigated through both mooring and sailing experiments. The PCM melting time, dimensionless temperature rise (DTR), thermal insulation performance (TIP), heat exchange rate (HER), comfort temperature rate (CTR) and air conditioning load (ACL) have been analyzed to evaluate the thermal performance of the ship cabin. It can be observed that ships equipped with PCMs have increased thermal storage capacity, increased temperature comfort zones and decreased air conditioning loads, especially under complex sailing conditions. The experimental results indicate: (1) The total energy storage is 43.72kW•h per hour, with a heat exchange with the cabin environment of 14.76kW•h; (2) PCM panels installed at the bottom of the ship offer longer insulation duration; (3) Under sailing conditions, the DTR is 15.19%, the TIP is 12.27%, and the HER is 60.45%. Compared to mooring conditions, these indicators have increased by 36.23%, 24.29%, and 71.32%, respectively, suggesting that PCM panels have shown superior performance during sailing.

Keywords: Pcms, Cabin Thermal Environment, Energy Storage; Mooring and Sailing Experiment, Heat Flux Analysis

1. INTRODUCTION

The ocean transportation industry plays a vital role in the global economy, accounting for more than 80% of the total volume of global trade across the ocean (Dere et al., 2024). With the development of the shipping industry, fossil energy consumption and carbon dioxide emissions from ships have received more attention (Xing et al., 2020). In order to achieve sustainable development of the shipping industry, the European Union's carbon emission trading system aims for an 86~88% reduction in emissions from the shipping sector by 2050(Mao et al., 2024). The International Maritime Organization (IMO) is dedicated to developing and refining policies and technical strategies aimed at reducing emissions (Koričan et al., 2023). However, the regulation of the thermal environment in the ship's cabin is mainly dependent on the ship's air-conditioning system (Hu et al., 2022), which has led to higher energy consumption and CO_2 emissions, posing challenges to the goal of reducing energy use and emissions on ships (Feng et al., 2024).

To maintain comfortable temperatures in the ship cabin while reducing the cooling demand of the air conditioner, research is primarily focused on several key areas: Optimizing air conditioning systems: Wang et al. proposed a novel ship refrigeration system that employs eco-friendly refrigerants and enables temperature and humidity control within ship compartments. The findings indicate that a 5°C reduction in EJE cooling results in a 10.47%~13.04% decrease in optimal pressure and a 21.16%~29.10% improvement in the refrigeration performance coefficient (Wang et al., 2024). Kosmadakis et al. suggested a creative use of high-temperature heat pump (HTHP) integration on ships, achieving a net emissions reduction that constitutes 60% of the savings from the auxiliary boiler's emissions (Kosmadakis et al., 2024). Reviews by Fisher et al. in 2024 outlined the cooling and refrigeration systems for fishing boats. The results indicated that heat recovery in most systems was not expected to exceed 40% (Fisher et al., 2024). Utilizing renewable energy: Xuet al. introduced a semi-transparent CdTe PV(Photovoltaic) window for ships to achieve active (electricity generation) and passive (cooling load reduction) energy conservation, the average and maximum cabin air temperatures are decreased by 6.5 °C and 11.0 °C (Xu et al., 2023). Braekken et al. evaluated the effectiveness of various energy-saving solutions on an existing cruise ship. Heating setbacks in port and at night can achieve energy-use reductions of 5.3% (Brækken et al., 2023a). Zhang et al. suggested using wind energyto support a ship's air conditioning system, improving performance by 6.5% at the optimal model (Zhang et al., 2023). Using heat storage strategies: Acanfora et al. introduced an energy storage system (ESS) for the leveling action to the period of the sea waves. The finding corresponds to a variation of energy that can be made available by the ultracapacitor equal to 1.81 kWh (Acanfora et al., 2023). Brækken et al. introduced a 200 m3 water tank system for thermal energy saving in the cabin, the energy storage capacity was 6.97 MWh with a uniform temperature varying between 50 and 80 °C and the annual energy savings were 1233 MWh (Brækken et al., 2023b).

The energy-saving methods for ship cabins are effective but have limitations. (1) Spatial constraints. Large energy-saving equipment like hot water tanks requires significant space, challenging for ships with limited room and potentially adding operational load. (2) Insufficient stability. Solar and wind systems' energy-saving effects are limited by insufficient solar radiation or limited wind speed. (3) Complex operation. Energy-saving systems often need to be started, stopped, or adjusted according to actual needs, which requires trained crew members, increasing the complexity of the operation. (4) Limitations of active energy saving. The energy consumption of the cooling system is not only influenced by the air conditioning system's efficiency but is significantly affected by the thermal environment of ship cabin. Due to the low thermal storage capacity of metal ship hulls, fluctuations in the cooling load within the ship's cabin are complex. Especially under sailing conditions, changes in the solar irradiation reception angle and the convective heat transfer rate on the surface of the ship envelope become even more intricate than in mooring conditions. At present, research on improving the thermal performance of ship cabins by enhancing the heat storage capacity of cabin hull is still rare, and the relationship between cooling load and the dynamic external environment under sailing conditions has not been researched before.

Phase change materials (PCMs) are extensively utilized to enhance indoor thermal performance. They are highly efficient energy storage materials that harness the phase change process in response to ambient temperature (Ghamari et al., 2024; Reddy et al., 2024). One of the most important applications of PCMs is integrating them with stationery building envelopes. The research proved that PCMs canenhance the thermal storage capacity of building's envelopes, improving static building energy efficiency at specific temperatures, and creating more comfortable, energy-efficient, and sustainable buildings (Wei and Calautit, 2024). Unlike the brick envelope of traditional buildings, ship hulls are generally constructed with metal materials with lower specific heat capacity and lighter weight, causing significant cabin temperature fluctuations (Jonnala et al., 2024; S. Xu et al., 2024). Moreover, the solar radiation received and the convective heat transfer rate on the ship's surface is influenced by dynamic environments, especially under sailing conditions. The alterations in theship's posture further amplify these effects, leading to dynamic cooling loads. Thus, integrating PCM panels into ships' internal envelopes is proposed for thermal regulation and reducing reliance on marine air conditioning systems. The energy-saving effects are assessed for 12 PCM panels in three different locations under mooring and sailing conditions through experimental research. The experimental platform is detailed in Section 2. Thermal model and performance indicators are proposed in Section 3. A quantitative assessment of the thermal energy saving is provided in Section 4.

2. EXPERIMENT DESIGNS

2.1 Experimental platform

Phase Change Materials (PCMs) are composed of organic or inorganic substances that possess specific thermophysical properties, allowing them to absorb or release latent heat through phase changes. This enables them to function effectively in energy storage and temperature regulation. RT27 PCM panels were selected for this study, using solid-liquid phase change to store and release thermal energy at nearly constant temperatures of 25°C~28°C, the PCM panels and their thermal energy storage capacity are shown in Figure 1. The minimum phase change temperature of the PCM panels was set close to the human comfort temperature range (22°C~26°C). Three different installation locations for PCM panels within a ship's interior were studied: top left side (M1), top right side (M2), and bottom side (M3). The thermal property parameters are shown in Table 1. A macro-encapsulated design was adopted for easy installation, attaching them to the ship's inner envelope using an adhesive method.
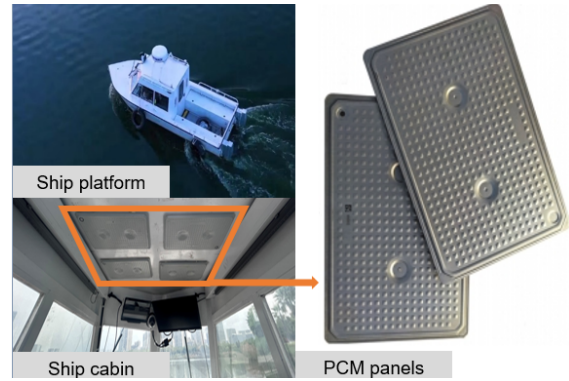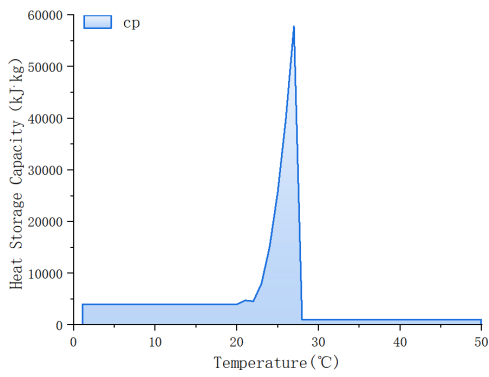
Figure 5: (a)Specific Heat Capacity of PCM panels   (b) Ship platform and PCM panels

Table 1: Main characteristics of PCM panels

RT filling (kg)	Melting area (℃)	Heat conductivity (W/(m·K))	Heat storage capacity (kJ/kg)	Solid density (kg/l) 15℃）	liquid density (kg/l) （40℃）
0.5	25-28	0.2	179	0.88	0.76

A small-scale ship with dimensions of 2.5 meters in length, 1.5 meters in width, and 1.6 meters in height, with an internal space of approximately six cubic meters, was constructed from glass and aluminium alloy in Xiamen, China (24°28′47" N, 118°05′20" E). The insights into the interior space and exterior appearance of the platform are depicted in Figure 1(b). The ship was moored on the water surface with a northwest orientation in an open environment, and its port side was adjacent to the dock. The experiment was conducted under non-ventilated conditions, with a door and all windows of the ship kept closed throughout the experiment.

On May 10th, the testing schedule consisted of morning from 9:00 AM to 4:00 PM and sailing from 4:00 PM to 6:00 PM. The ambient temperature and radiation received during this period are documented in 错误!未找到引用源。. Throughout the experimental process, the external environment fluctuated in real-time. The air temperature outside the cabin was significantly affected by factors such as solar radiation, wind speed, and air humidity. The temperatures were recorded between 22°C and 36°C.

2.2 Preparation of measurment instrument

Temperature measurements in this work were taken using Type-T thermocouples with a 0.5mm wire diameter and a measurement range of -200°C to +300°C, accurate to 0.5°C. Five temperature measurement points are set up with a 1 min time step: three for the PCMs (T_{M1}, T_{M2}, T_{M3}), one for the internal cabin air (Tair), and one for the external ambient temperature (Tamb). The measurement points are shown in Figure. 2.
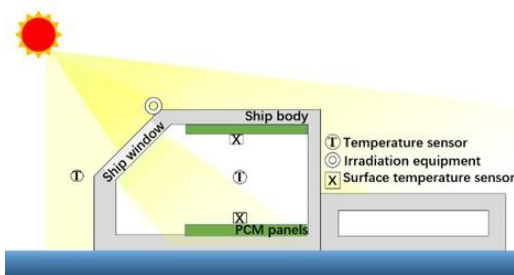
Figure 2: Measurement points of test work
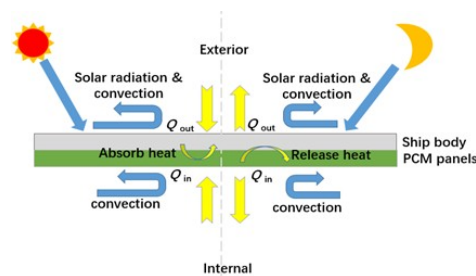
Figure 3: Heat transfer model for the PCMs system

3. MATHEMATICAL MODEL

A heat flux analysis model was conducted to evaluate the thermal performance of the ship system with PCM panels. To simplify the calculations, all external influences on the system such as received solar radiation and wind speed were compiled into Q_{out}, the impact of the ship's cabin on the system was denoted as Qin, and based on these influences, the internal state of the PCM panels changed. The net heat transfer in the system can be expressed as Q_s. The heat flux model of the integrated PCM panels on the ship hull is shown in Figure 3.

In this theoretical model, PCM in the phase change layer was assumed to be uniform and isotropic, and heat transfer was one-dimensional, occurring only in the thickness direction. The effective heat capacity method was used to calculate the heat transfer in

this work. Q_{in} can be calculated using Equation 1 and Equation 2, which indicate the total heat transfer from an initial time t_0 to a final time t_{end} between the PCM panels and the air temperature inside the ship cabin.

Equation 1: Convective heat transfer coefficient.
$$h = 2.03 \times (T_i - T_{ini})^{1/3}$$

Equation 2: Heat transfer between ship cabin and PCM panels.
$$Q_{ini} = hA(T_i - T_{ini})$$
$$Q_{in} = \int_{t_0}^{t_{end}} Q_{ini}dt$$

Where h is the convective heat transfer rate between the surface of the PCM panels and the air inside the cabin (L. Xu et al., 2024), i represent the time node of the test, and A is the contact area between the PCM panel and the air. The thermal storage of the PCM panels is calculated using Equation 3.

$$Q_{s(i+1)} = mC_p(T_{i+1} - T_i)$$

Equation 3: Heat storage of PCM panels.
$$Q_s = \int_{t_0}^{t_{end}} Q_{si}dt$$

Where m represents the charged mass of the PCM, Cp is the specific heat capacity of the PCM. Q_{out} is the heat exchange between the PCM panel and the external air, which is calculated using Equation 4

Equation 4: Heat transfer between PCM panels and external environment.
$$Q_{outi} = Q_{ini} - Q_{si}$$
$$Q_{out} = \int_{t_0}^{t_{end}} Q_{outi}dt$$

Dimensionless temperature rise (DTR) represents the performance of PCM panels in regulating cabin temperature. It is calculated by Equation 5. A smaller value of DTR indicates a slower rate of cabin temperature change, suggesting that the PCM superior regulatory performance of the PCM panels.

Equation 5: Dimensionless temperature rise.
$$DTR = \frac{T_i - T_{ave}}{T_{max} - T_{min}}$$

Thermal storage performance (TIP) is a quantitative measure defined by Equation 6, which assesses the differential heat storage capacity between the phase change zone and the non-phase change zone. This metric was calculated as the absolute difference in heat storage between these two zones, normalized by the total heat storage, all evaluated over a standard unit of time.

Equation 6: Thermal storage performance.
$$TIP = \frac{Q_{s(pc)} - Q_{s(npc)}}{Q_{s(pc)} + Q_{s(npc)}}$$

The heat exchange rate (HER) represents the rate of heat transfer between the PCM panels and the surrounding environment. It is calculated by Equation 7. This metric was crucial for assessing the effectiveness of the PCM panels in managing thermal energy exchange with its external context.

Equation 7: Heat exchange rate.
$$HER = \frac{Q_{out(pc)} - Q_{out(npc)}}{Q_{out(pc)} + Q_{out(npc)}}$$

Comfort temperature rate (CTR) is the proportion of time during the experiment that the temperature of the PCM panels remains within the range of human thermal comfort. It is calculated by Equation 8. This metric is essential for evaluating the effectiveness of PCM panels in maintaining indoor environments at temperatures conducive to human comfort, thereby directly impacting the occupants' well-being and satisfaction with their living or working spaces.

Equation 8: Comfort temperature rate.
$$CTR = \frac{t_{(22\div\ \sim\ 26\div)}}{t_{all}}$$

To maintain a comfortable thermal environment in the cabin, when the temperature inside exceeds 26℃，the air conditioning system starts to work. Air conditioning load (ACL) was calculated based on the cooling load of the refrigeration unit and its coefficient of performance (COP). COP represents the amount of cooling provided per unit of power consumed; a higher COP indicates better refrigeration performance. A conventional air conditioner has a COP ranging from 2.5 to 3.0, and in this study, the COP was set at 2.5. It is calculated by Equation 9.

Equation 9: Air conditioning load
$$ACL = \frac{hA(T_{PCM} - 26)}{COP}$$

4. RESULTS AND DISCUSSIONS

4.1 Temperature regulation performance

The temperature changes of the indoor air and PCM panels are clearly illustrated in Figure 5. It can be seen that the temperature was higher than the external environment while moored, but the reverse was true under sailing conditions from 错误!未找到引用源。. This was because the ability to dissipate heat effectively was limited in a static, enclosed space. The phase change time for the PCM panels installed at the top was from 9:00 AM to 11:00 AM, lasting approximately two hours, while the phase change time for the PCM panels at the bottom was from 10:00 AM to 2:00 PM, lasting approximately four hours. It can be observed that different installations of PCM panels can significantly affect their regulatory performance. During the experimental period, solar irradiance was a significant heat source contributing to the temperature rise within the ship cabin. The solar irradiance can be directly received by the ship roof, causing the temperature of M1 and M2 to increase rapidly and quickly reach the phase change threshold. Compared with the ship roof, the bottom of the ship cabin received less solar irradiance, resulting in a slower temperature increase for M3 and a prolonged phase change duration.

Under sailing conditions, the DTR values for M1, M2, and M3 were found to be 24.00%, 23.90%, and 23.56%, respectively. In contrast, during sailing, the DTR values were 17.30%, 13.82%, and 15.19% respectively. It can be observed that the status of the ship body also can influence the thermal performance of PCM panels. This was due to the changeable situations of the ship's orientation and relative wind speed, which not only affected the convective heat transfer boundary conditions of the hull, reducing some of the internal heat accumulation but also made a wider range of temperatures fall within the phase change interval of the PCM panels, significantly enhancing the thermal insulation and heat storage capabilities of the PCM panels.

4.2 Thermal energy storage potential

Throughout the experiment, the cumulative heat stored by PCM panels M1, M2, and M3 amounted to 4.19kW•h, 2.76kW•h, and 3.98kW•h respectively, culminating in total storage of 43.72kW•h with 12 PCM panels as shown in Figure 8. During the phase transition period, the latent heat capacity of these materials significantly increases, allowing them to absorb a substantial amount of thermal energy through the solid-liquid transition. This process is crucial for mitigating the effects of external temperature fluctuations on the cabin's internal thermal environment. During phase change intervals, the latent heat capacity of the PCM panels substantially increases, allowing them to absorb a significant amount of thermal energy through the solid-liquid transition. This process was crucial in mitigating the impact of external temperature fluctuations on the ship cabin's interior thermal performance.

The TIP values for mooring conditions were 10.15%, 9.82%, and 7.90% for M1, M2, and M3, respectively, with an overall energy- saving potential of 9.29%. Under sailing conditions, these values increased to 12.16%, 10.96%, and 13.69%, respectively, with the overall energy-saving potential rising to 12.27%. Under mooring conditions, the confined space resulted in the actual temperature range of the PCMs seldom overlapping with their phase change temperature interval. However, under sailing conditions, factors such as changes in ship orientation and relative wind speed meant the temperature range of the PCMs more frequently fell within the phase change interval. This rise not only significantly enhanced the TIP values but also improved the thermal storage performance of the PCMs, thus more thermal energy conservation through this thermal storage process when sailing inside the cabin.
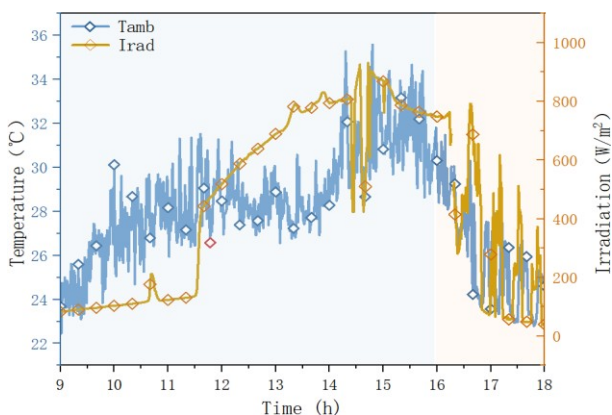
Figure 4: The test environment
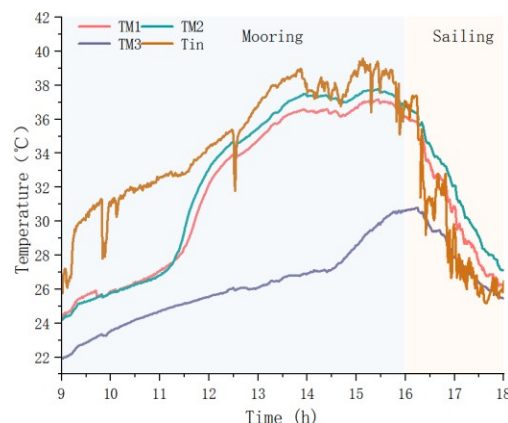
Figure 5: Temperature of PCM panels and cabin air

The cumulative heat exchange per hour by PCM panels M1, M2, and M3 amounted to 0.63kW•h, 0.62kW•h, and 2.44kW•h respectively, culminating in total heat exchange of 14.76kW•h with 12 PCM panels which is shown in Figure 6. Compared with Figure 7, most of the external heat exchange is absorbed by the PCM panels during the phase change stage of the PCMs, with only a small portion of heat entering the cabin. This demonstrated that PCMs can effectively reduce the impact of the external environment on the internal temperature of the cabin through phase change. The phase change process of PCMs occurs within a relatively constant temperature range (25-28°C), which helps to maintain a stable indoor environment，   thereby reducing the demand for cooling systems such as air conditioning within the ship cabin.

The HER values during morning showed an overall energy-saving potential of 17.29%, while this potential increased to 60.45% under sailing conditions. The higher heat exchange capacity of PCMs can be achieved during sailing. This is attributed to fluid dynamic impacts. The continuous flushing of water around the ship's hull while sailing causes part of the heat to be absorbed by the water. This effect diminishes when the ship is moored. Moreover, the contact area of the hull with the external environment can be expanded under sailing conditions, potentially exposing different areas to varying water temperatures and thus enhancing heat exchange efficiency.
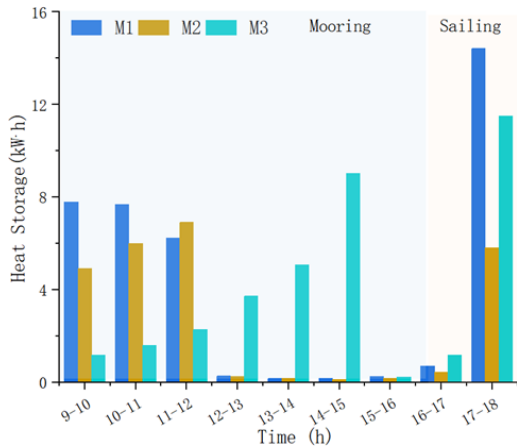
Figure 6:   Heat storage of PCM panels
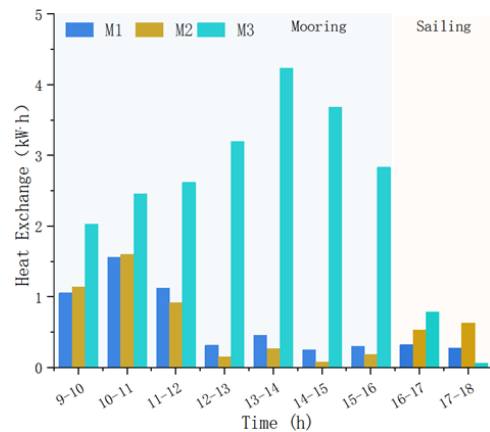
Figure 7:   Heat exchange of PCM panels

4.3 Energy efficiency and comfort analysis

The CTR of M1, M2, and M3 were 11.41%, 12.21%, and 38.46% respectively. Before 10 AM, the PCM panels of M1 and M2 underwent a solid-liquid phase change process, which was crucial for maintaining comfortable cabin temperatures. The PCM panels of M3 could extend this temperature regulation effect until around 1:00 PM. As the relative wind speed increased, the conditions for convective heat exchange on the ship's body altered under sailing conditions, leading to an expansion of the comfortable temperature range within the cabin.

During the experiment, the total energy load for the air conditioner was 9.51kW•h, as shown in Figure 10. There was a gradual increase in energy usage from 9:00 to 12:00, followed by a sharp rise in energy consumption, peaking at 14:00. This was because the PCM panels in the phase change zone can regulate the temperature inside the cabin, so even if the external temperature rises significantly, the cabin temperature can remain stable under the action of the PCM panels, thereby reducing part of the air conditioning load.
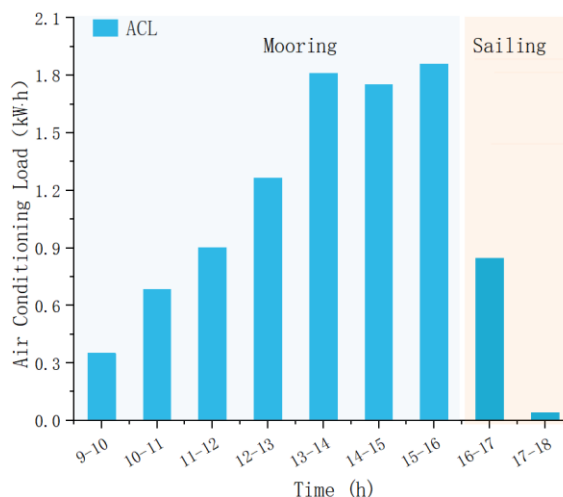
Figure 8: Air conditioning load of ship cabin

5. CONCLUSION

This study investigated the thermal performances within the cabin for PCM panels integration into the ship's envelope under mooring and sailing conditions. An actual ship with 12 PCM panels installed at three different sites was examined. The research proves that the solar radiation received angle and the relative wind speed between the ship's hull and the environment have significant effects on the thermal performance of the system with PCM panels. Other key findings are summarized in the following.

1)   PCM panels integrated ships have demonstrated excellent temperature regulation capabilities and energy-saving potential, with a total energy storage of 43.72kW•h and a heat exchange with the cabin environment of 14.76kW•h.
2)   Compared to the mooring conditions, PCM panels have shown superior performance during sailing. Under sailing conditions, the temperature rise was 15.19%, heat storage was 12.27%, and the heat exchange rate was 60.45%, which is higher at 36.23%, 24.29%, and 71.32% than mornring, respectively.
3)   The CTR of PCM panels installed at the top left side of the ship, top right side of the ship, and bottom side of the ship are 11.41%,12.21%, and 38.46%, respectively. The PCM installed at the bottom of the cabin was able to maintain a longer thermal insulation time.

6. REFERENCES

Abass, P.J., Muthulingam, S., 2024. Thermal energy storage performance of biaxial voided RCC roof slab integrated with macroencapsulated PCM for passive cooling of buildings. J. Energy Storage 88, 111478. https://doi.org/10.1016/j.est.2024.111478

Acanfora, M., Balsamo, F., Fantauzzi, M., Lauria, D., Proto, D., 2023. Design of an electrical energy storage system for hybrid diesel electric ship propulsion aimed at load levelling in irregular wave conditions. Appl. Energy 350, 121728. https://doi.org/10.1016/j.apenergy.2023.121728

Bagley, F., Atlar, M., Charles, A., Anderson, C., 2015. The use of copper-based antifoulings on aluminium ship hulls. Ocean Eng. 109, 595–602. https://doi.org/10.1016/j.oceaneng.2015.09.044

Brækken, A., Gabrielii, C., Nord, N., 2023a. Energy use and energy efficiency in cruise ship hotel systems in a Nordic climate. Energy Convers. Manag. 288, 117121. https://doi.org/10.1016/j.enconman.2023.117121

Brækken, A., Gabrielii, C., Nord, N., 2023b. Energy use and energy efficiency in cruise ship hotel systems in a Nordic climate. Energy Convers. Manag. 288, 117121. https://doi.org/10.1016/j.enconman.2023.117121

Dere, C., Inal, O.B., Zincir, B., 2024. Utilization of waste heat for onboard hydrogen production in ships. Int. J. Hydrog. Energy 75, 271–283. https://doi.org/10.1016/j.ijhydene.2024.01.246

Feng, Y., Qu, J., Wu, Y., Zhu, Y., Jing, H., 2024. Utilizing waste heat from natural gas engine and LNG cold energy to meet heat-electric-cold demands of carbon capture and storage for ship decarbonization: Design, optimization and 4E analysis. J. Clean. Prod. 446, 141359. https://doi.org/10.1016/j.jclepro.2024.141359

Fisher, R., Ciappi, L., Niknam, P., Braimakis, K., Karellas, S., Frazzica, A., Sciacovelli, A., 2024. Innovative waste heat valorisation technologies for zero-carbon ships − A review. Appl. Therm. Eng. 253, 123740. https://doi.org/10.1016/j.applthermaleng.2024.123740

Ghamari, M., See, C.H., Hughes, D., Mallick, T., Reddy, K.S., Patchigolla, K., Sundaram, S., 2024. Advancing sustainable building through passive cooling with phase change materials, a comprehensive literature review. Energy Build. 312, 114164. https://doi.org/10.1016/j.enbuild.2024.114164

Hu, B., Guo, J., Yang, Y., Shao, Y., 2022. Performance analysis and working fluid selection of organic Rankine steam compression air conditioning driven by ship waste heat. Energy Rep. 8, 194–202. https://doi.org/10.1016/j.egyr.2022.01.094

Hu, Z., Li, W., Yang, C., Huang, H., Guo, Y., Ge, F., Zhang, Y., 2024. Thermal performance of an active casing pipe macro-encapsulated PCM wall for space cooling and heating of residential building in hot summer and cold winter region in China. Constr. Build. Mater. 422, 135831. https://doi.org/10.1016/j.conbuildmat.2024.135831

Jonnala, S.N., Gogoi, D., Devi, S., Kumar, M., Kumar, C., 2024. A comprehensive study of building materials and bricks for residential construction. Constr. Build. Mater. 425, 135931. https://doi.org/10.1016/j.conbuildmat.2024.135931

Khayyaminejad, A., Fartaj, A., 2024. Unveiling the synergy of passive cooling, efficient ventilation, and indoor air quality through optimal PCM location in building envelopes. J. Energy Storage 89, 111633. https://doi.org/10.1016/j.est.2024.111633

Koričan, M., Frković, L., Vladimir, N., 2023. Electrification of fishing vessels and their integration into isolated energy systems with a high share of renewables. J. Clean. Prod. 425, 138997. https://doi.org/10.1016/j.jclepro.2023.138997

Kosmadakis, G., Meramveliotakis, G., Bakalis, P., Neofytou, P., 2024. Waste heat upgrading with high-temperature heat pumps for assisting steam generation in ships: Performance, cost and emissions benefits. Appl. Therm. Eng. 236, 121890. https://doi.org/10.1016/j.applthermaleng.2023.121890

Kulumkanov, N., Memon, S.A., Khawaja, S.A., 2024. Evaluating future building energy efficiency and environmental sustainability with PCM integration in building envelope. J. Build. Eng. 93, 109413. https://doi.org/10.1016/j.jobe.2024.109413

Mao, Z., Ma, A., Zhang, Z., 2024. Towards carbon neutrality in shipping: Impact of European Union's emissions trading system for shipping and China's response. Ocean Coast. Manag. 249, 107006. https://doi.org/10.1016/j.ocecoaman.2023.107006

Reddy, V.J., Ghazali, M.F., Kumarasamy, S., 2024. Advancements in phase change materials for energy-efficient building construction: A comprehensive review. J. Energy Storage 81, 110494. https://doi.org/10.1016/j.est.2024.110494

Wang, Z., Cao, M., Tang, H., Dong, B., Ji, Y., Han, F., 2024. Marine temperature and humidity regulation combined system: performance analysis and multi-objective optimization. Case Stud. Therm. Eng. 56, 104215. https://doi.org/10.1016/j.csite.2024.104215

Wei, Z., Calautit, J.K., 2024. Field experiment testing of a low-cost model predictive controller (MPC) for building heating systems and analysis of phase change material (PCM) integration. Appl. Energy 360, 122750. https://doi.org/10.1016/j.apenergy.2024.122750

Xing, H., Spence, S., Chen, H., 2020. A comprehensive review on countermeasures for CO_2 emissions from ships. Renew. Sustain. Energy Rev. 134, 110222. https://doi.org/10.1016/j.rser.2020.110222

Xu, L., Hu, H., Ji, J., Cai, J., Dai, L., 2024. Hybrid energy saving performance of translucent CdTe photovoltaic window on small ship under sailing condition. Energy 295, 131070. https://doi.org/10.1016/j.energy.2024.131070

Xu, L., Ji, J., Yuan, C., Cai, J., Dai, L., 2023. Electrical and thermal performance of multidimensional semi-transparent CdTe PV window on offshore passenger ships in moored and sailing condition. Appl. Energy 349, 121672. https://doi.org/10.1016/j.apenergy.2023.121672

Xu, S., Ma, J., Lv, Y., Shen, W., Wu, Y., Li, M., 2024. Fatigue strength of welded joints of marine aluminum alloy extrusion stiffened plate considering welding effects. Ocean Eng. 310, 118755. https://doi.org/10.1016/j.oceaneng.2024.118755

Zhang, R., Huang, L., Peng, G., Ma, R., Wang, K., Tian, F., Song, Q., 2023. A novel method of desynchronized operation of sails for ship wind-assisted propulsion system. Ocean Eng. 288, 115964. https://doi.org/10.1016/j.oceaneng.2023.115964

#238: Thermal property optimization and energy-saving potential of building integrated heat pipes and phase change materials

Fangcheng KOU, Xin WANG

Department of Building Science, Tsinghua University, Beijing, 100084, China
E-mail address: wangxinlj@tsinghua.edu.cn

Abstract: The novel solar building integrated heat pipes and phase change materials (BIHPPCM) can greatly improve the indoor thermal environment in winter and reduce heating energy consumption by using the variable thermal conductivity of flat gravity heat pipes and the variable specific heat of phase change materials. The heating energy consumption of BIHPPCM is closely related to the thermal properties of the interior envelope. In this paper, the thermal properties of the interior envelope of BIHPPCM are optimized and the optimal heating effect is obtained at 61 locations in severe cold and cold regions of China. The relationship between the ratio of solar radiation to temperature difference during the local heating season $RRTD_{HS}$ and the energy-saving potential of BIHPPCM is analyzed. The results show that: (1) The optimal phase change materials of the interior wall are of high thermal conductivity and maximum phase change enthalpy, and the phase change temperature is higher than the lower limit of the thermal comfort zone by 1-2°C; (2) The energy-saving ratios of BIHPPCM at the studied locations are between 20%-100% and canreach more than 30% at most locations; (3) A linear correlation between the $RRTD_{HS}$ and the energy-saving ratio is obtained, and the energy-saving ratio increases by 14.8% for every 1 W/(m^2·K) increase of the $RRTD_{HS}$. This study is of great significance for theapplication of BIHPPCM in severe cold and cold regions of China to reach zero-carbon heating.

Keywords: Solar House; Phase Change Material; Energy Storage; Thermal Diode; Building Envelope

1. INTRODUCTION

China has committed to peak carbon emissions before 2030 and strive to achieve carbon neutrality before 2060, and promoting building energy efficiency is an important measure to achieve the dual carbon target. In China, heating energy consumption accounts for 27.0% and 41.5% of building operation energy consumption in urban areas and rural areas, respectively (Ding et al., 2022). Solar energy resources are abundant in China (Li and Huang, 2020), and solar thermal energy is the most accessible and plentiful source of renewable energy (Chen and Yang, 2022). The solar house utilizes solar radiation resources for indoor heating to effectively decrease heating energy consumption and create a comfortable indoor thermal environment, thereby reducing the dependence on fossil fuels.

A novel solar house integrated L-shaped flat gravity heat pipes was recently put forward (Gong et al., 2022), as shown in Figure 1. This novel building integrated heat pipes (BIHP) makes use of the thermal diode characteristic and ultrahigh equivalent thermal conductivity of the L-shaped flat gravity heat pipe (Kou et al., 2023b), and the interior wall (constructed with conventional building materials or phase change materials) functions as a heat storage body and large-area heating terminal. During the daytime, the heat pipe transfers the solar radiation heat collected on the outer surface of the exterior envelope to the interior envelope, and then the heat is stored and released indoors. During the nighttime, the heat pipe operates in reverse heat transfer mode and is of large thermal resistance to avoid massive heat dissipation to the outdoor space, while the interior envelope releases stored heat to the indoor environment to maintain thermal comfort. The novel BIHP improves the utilization of solar energy by building envelopes for indoor heating to reduce heating energy consumption. A numerical model has been developed to simulate the heat transfer processes of the novel building in MATLAB and has been verified by an experimental study (Gong et al., 2022). The simulation results showed that the average indoor operative temperature of the BIHP reached 16.7°C during January in Beijing and was 6.8°C higher than that of a reference house. An experimental study on the application of a real-scale lightweight BIHP was conducted and the results showed that the actual proportion of solar energy used for indoor heating increased from 9% to 57% (Kou et al., 2022). However, the above studies mainly focus on passive solar houses without heating equipment, whose natural room temperature could be lower than the lower limit of the thermal comfort zone. Buildings are usually equipped with active heating equipment such as heat pumps to ensure the thermal comfort of indoor personnel in practical applications, and the BIHP equipped with active heating equipment is termed the active BIHP. There is a lack of research on the solar heating effect of the active BIHP at present.
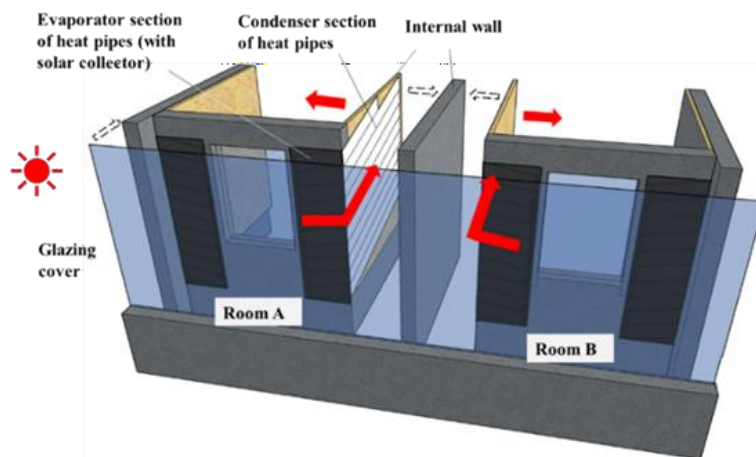
Figure 1: Schematic diagram of the structure of the BIHP (Kou et al., 2022)

The interior envelope greatly influences the effect of indoor heating as a heat storage and release media, therefore, the thermophysical design of the interior envelope has an important impact on the actual utilization of BIHP. Through the careful design of the thermophysical properties of the interior wall, the indoor thermal environment could be further improved. An efficient algorithm improved from particle swarm optimization to optimize the thermophysical properties of the BIHP interior envelope was put forward (Kou et al., 2023a), and the optimal thermophysical parameters of conventional building materials (including the thermal conductivity and the thermal capacity of the material, and the installing position of the heat pipe condenser) of building envelopes of BIHP at 61 locations in severe cold and cold regions of China were explored (Kou et al., 2024). The research showed that compared with the evaluation indexes of climate resources such as heating degree-day *HDD18* and average solar radiation intensity, the ratio of solar radiation to temperature difference better reflected the application potential of BIHP. However, the abovestudies only focus on BIHP with conventional building materials, and the research on the energy-saving potential of building integrated heat pipes and phase change materials (BIHPPCM) is still lacking. Phase change materials (PCM) have a large heat storage capacity within a narrow temperature range (Xu et al., 2020) and can better store solar radiation heat compared with conventional building materials, which are expected to significantly reduce heating energy consumption.

In this paper, parameter optimizations of the thermophysical properties of the BIHPPCM interior envelope at 61 locations in severe cold and cold regions of China are simulated. The relationship between the local climate resource indicator and the energy-saving potential of the BIHPPCM is obtained. This study is of important significance for the widespread promotion of BIHPPCM to effectively and efficiently use solar energy.

2. METHODOLOGY
2.1. Optimization and evaluation of BIHPPCM

Thermal conductivity λ, volumetric phase change enthalpy ρH and phase change temperature T_m are three independent thermophysical parameters to be optimized in this study. Particle swarm optimization makes use of the information sharing of each individual inside the group to make the whole population move orderly and finally reach the optimal solution in the parameter space. The three variables constitute a three-dimensional solution domain. A coordinate inside the space represents a combination of thermophysical parameters of the interior wall. Every particle has a searching speed in three dimensions respectively. In each iteration, the global minimum value and personal minimum value of each particle are recorded as target positions, and the velocity of every particle is updated based on its target positions, which would guide all particles to move to the optimal solution step by step. For time and convergence considerations, the particle population and the maximum iteration number are set to be 20 and 30 in this study, respectively.

The heating equipment of BIHPPCM works to maintain the indoor temperature not lower than the lower limit of the thermal comfort zone, which is 18°C. The heating energy consumption to achieve this purpose is different with different thermal properties of the interior envelope. The total heating energy consumption of the heating season Q is an indicator to evaluate the thermal performance of the building, which is defined as Equation 1.

Equation 1: Total heating energy consumption of the heating season.
$$Q = \int_{heating\ season} q(\tau)d\tau$$

Where:

- $q(\tau)$ = heating load of the room (W)

The Q values of BIHPPCM at different locations are difficult to compare directly because the local climate resources and heating seasons are very different. The energy-saving ratio ESR is used to describe the energy-saving effect of the BIHPPCM compared with the reference building without heat pipes and PCMs at the same location, as defined by Equation 2. The ESR of BIHPPCM is between 0% and 100%, with the ESR of 100% indicating that Q_{HP} is 0 and zero-carbon heating is realized. The smaller the Q_{HP} is, the higher the ESR is, which is the goal of BIHPPCM.

Equation 2: Energy-saving ratio of BIHPPCM.
$$ESR = \frac{Q_{RB} - Q_{HP}}{Q_{RB}} \times 100\%$$

Where:

- Q_{RB} = total heating energy consumption of reference building (J)
- Q_{HP} = total heating energy consumption of BIHPPCM (J)

The ratio of solar radiation to temperature difference is the ratio of the local solar radiation intensity to the temperature difference between indoor and outdoor air temperatures (Liu et al., 2022) and describes the most contribution the solar resources could make for creating a certain temperature difference between indoor and outdoor environments at the local temperature level. Considering that the heating demand periods of different locations are various, the local heating season is taken as the calculation period in this study. For a south-facing building, the ratio of southern solar radiation and temperature difference during the local heating season RRTDHS is obtained by Equation 3. T_{set} is set as 18°C.

Equation 3: The ratio of southern solar radiation and temperature difference during the local heating season.
$$RRTD_{HS} = \frac{Q_{sol,ave}}{T_{set} - T_{out,ave}}$$

Where:

- $Q_{sol,ave}$ = average southern solar radiation intensity during the heating season (W/m^2)
- $T_{out,ave}$ = average outdoor air temperature during the heating season (°C)
- T_{set} = the setting temperature for indoor heating (°C)

2.2. Simulation settings

Location selection

According to the building climate zoning of China in GB 50176, 61 locations in the severe cold region and the cold region are selected for simulation, as shown in Figure 2. The selection principles are: (1) provincial capital cities and big cities with largepopulations are preferred; (2) evenly geographically distributed; (3) no more than five locations in a province (except Xinjiang and Inner Mongolia). The climate data is obtained from DeST, a simulation software for building energy.
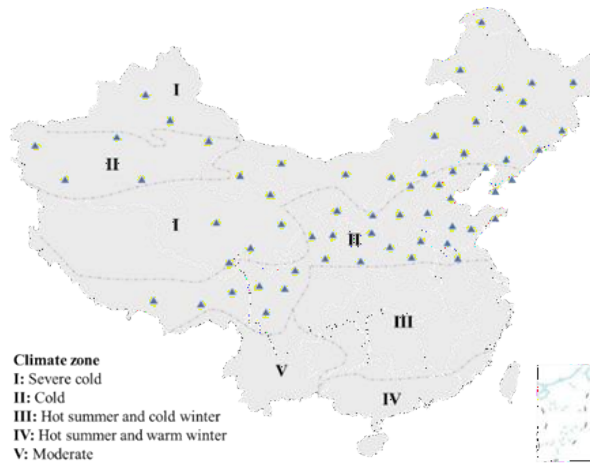
Figure 2: Selected locations in the present study

Building information

In the present study, a southward room of a multi-story BIHPPCM is simulated. The dimensions of the room are 4 m long, 3 m wide, and 3 m high. The window-wall ratio of the south wall is set to be 0.3. All envelopes are interior envelopes except the south wall, and the neighbor heat transfer between the studied room and adjacent rooms is not taken into consideration. The evaporator section of the heat pipe is attached to the outside surface of the south wall, and the east and west walls are embedded with the condenser section of the heat pipe. The east and west walls are constructed with conventional building materials or phase change materials. The exterior building envelope meets the thermal performance regulations of the corresponding building climate zone according to GB 55015, as shown in Table 1. The solar absorption rate of the heat-absorbing surface is 0.9. The solar radiation transmittance of the window is 0.75. When the operative temperature is under and above 26°C, the air change per hour of the room is 0.5 and 5.0, respectively. Based on the thermophysical properties of PCMs commonly used in buildings and reported in theliterature, λ, ρH, and T_m are in the range of 0-10 W/(m·K), 0-420 MJ/m^3 and 10-30°C, respectively. As a comparison of the optimized BIHPPCM (BIHP$_{PCM,OPT}$), the reference building (RB) does not have heat pipes and PCMs, and the east and west walls are constructed with concrete hollow blocks. The interior wall material of the initial non-optimized BIHPPCM (BIHP$_{PCM,INI}$) is potassium fluoride tetrahydrate, and λ, ρH, and T_m are 0.5 W/(m·K), 333.5 MJ/m^3 and 19°C, respectively.

Table 1: Heat transfer coefficient of the exterior building envelope

Building climate zone	K_{wall} (W/(m^2·K))	K_{win} (W/(m^2·K))
Severe Cold A	0.35	1.6
Severe Cold B	0.35	1.8
Severe Cold C	0.40	2.0
Cold A	0.45	2.2
Cold B	0.45	2.2

3. RESULTS AND DISCUSSION

The optimization shows that zero-carbon heating can be achieved by BIHPPCM at 22 locations and cannot be achieved at 39 locations. This paper concentrates on the optimal thermal properties and energy-saving potential of BIHPPCM at non-zero-carbon heating locations. Taking Tianjin as an example, the optimal results are 6.8 W/(m·K) for λ, 420 MJ/m^3 for ρH, and 19.5°C for T_m, and the minimum Q with this thermal design is 68 MJ, which is the best utilization effect achieved by BIHPPCM in Tianjin. Figure 3(a) shows the indoor operative temperature curves of the initial non-optimized BIHPPCM (subscript PCM,INI), the optimized BIHPPCM (subscript PCM,OPT), and the reference building (subscript RB) during the whole local heating season in Tianjin, and Figure 3(b) is the box plot. In periods of weak solar radiation, such as late November and mid-January, the heating equipment of the reference building and the non-optimized BIHPPCM need to work for a long time to maintain the operative temperature not lower than the lower limit of the thermal comfort temperature zone 18°C. However, because the PCM releases a lot of heat near the phase change temperature, the natural room temperature of the optimized BIHPPCM meets the requirements of thermal comfort most of the time, and the heating equipment needs to work only for a few days around Jan. 14.
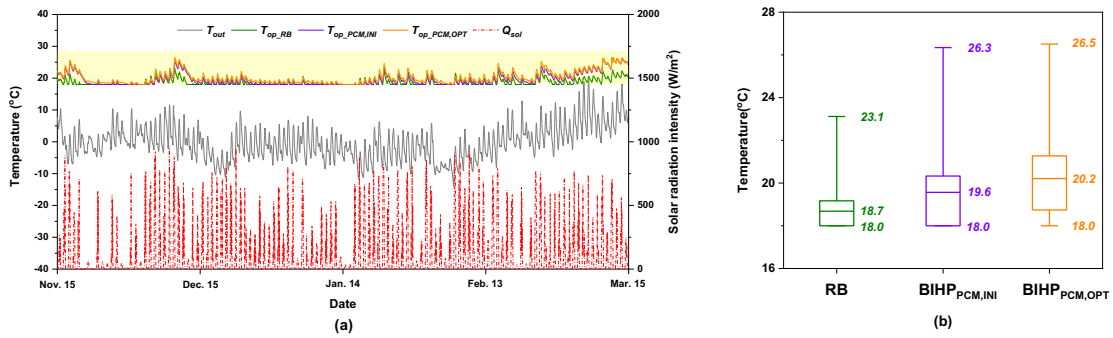
Figure 3: Room operative temperature in the heating season (Tianjin): (a) curve graph and (b) box plot

Figure 4(a) shows the heating load curves of the three houses. Figure 4(b) shows the total heating energy consumption Q, operation time of heating equipment τ_{on}, and average heating load q'_a. Q is the product of τ_{on} and q'_a. Q of the reference building is 1220 MJ, and Q of the non-optimized BIHPPCM and the optimized BIHPPCM are 341 MJ and 68 MJ, respectively, and ESR are 72.1% and 94.4%, respectively. The τ_{on} of the reference building, the non-optimized BIHPPCM, and the optimized BIHPPCM are 1475 h, 735 h, and 131 h, respectively, and the q'_a are 19.2 W/m^2, 10.7 W/m^2, and 12.1 W/m^2, respectively. It shows that the significant reduction of Q is due to the large decrease of both τ_{on} and q'_a. As for τ_{on}, the natural room temperature of BIHPPCM maintains above 18°C much longer compared with the reference building, so the heating equipment needs to work for less time. Asfor q'_a, when the room temperature reaches 18°C and the heating equipment is in operation, the temperature of the PCM with a T_m of 19.5°C is not lower than the lower limit of the phase change temperature zone, which is 18.5°C. Therefore, PCM is still releasing latent heat into the room, which leads to a significant reduction in q'_a.
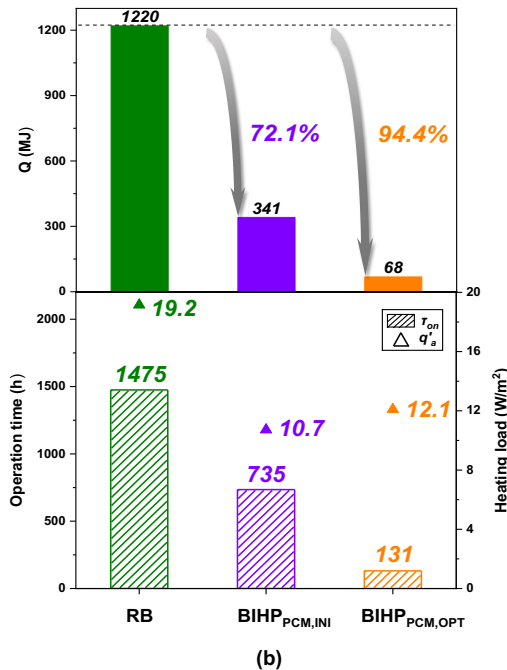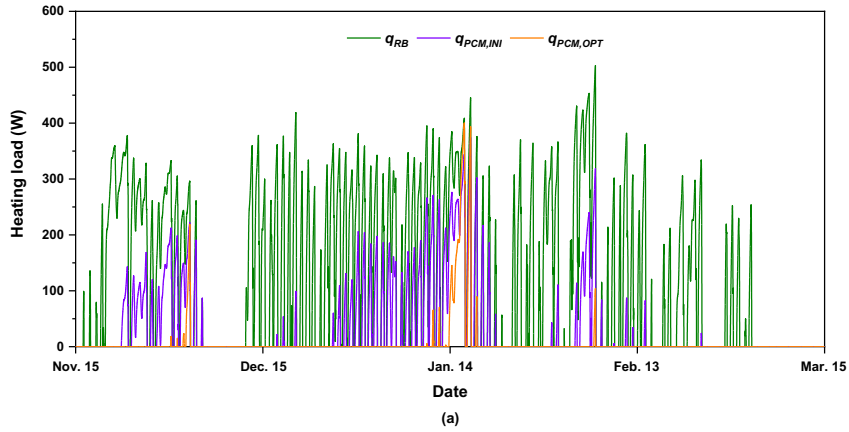
Figure 4: Heating load (Tianjin): (a) Curve graph; (b) Heating energy consumption, operation time of heating equipment, and average heating load

To further explain the role of the optimized phase change interior wall in improving the indoor thermal environment, Nov. 17 - 22 is

investigated as an example. Solar radiation is abundant on Nov. 17 - 19 and weak on Nov. 20 - 22. Climate resources of the studied period are shown in Figure 5, including outdoor air temperature Tout and solar radiation Qsol. The wall surface temperature, releasing heat flux, available internal energy, and melting fraction of PCM with different λ, ρH, and Tm are simulated. The available internal energy Eint and the melting fraction f are defined as Equation 4 and Equation 5, respectively. T_{base} is set as 12°C.

<div style="text-align:center">

Equation 4: Available internal energy of PCM.

$$E_{int} = \int_{T_{base}}^{T_{PCM}} mc_p(T)\mathrm{d}T$$

</div>

Where:

- m = total amount of PCM (kg)
- $c_p(T)$ = equivalent specific heat capacity of PCM (J/(kg·K))
- T_{PCM} = average temperature of PCM (°C)
- T_{base} = base temperature for energy calculation (°C)

<div style="text-align:center">

Equation 5: Melting fraction of PCM.

$$f = \frac{\int_{T_1}^{T_{PCM}} c_p(T)\mathrm{d}T}{\int_{T_1}^{T_2} c_p(T)\mathrm{d}T}$$

</div>

Where:

- T_1 = lower limit of phase change temperature zone of PCM (°C)
- T_2 = upper limit of phase change temperature zone of PCM (°C)
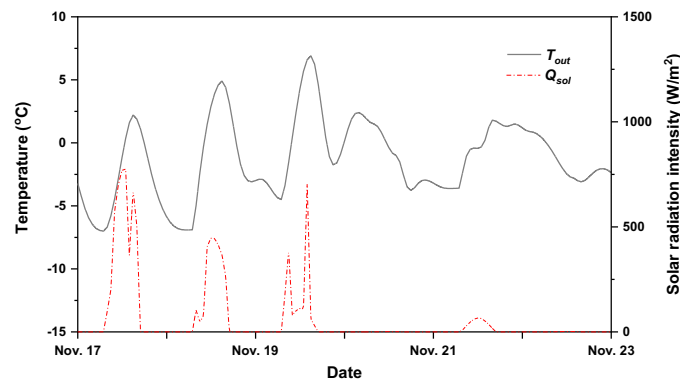
Figure 5: Climate resources of the studied period (Nov. 17 - 22)

Figure 6(a) shows the thermal performance of the interior wall with different λ. The wall with λ of 0.5 W/(m·K) (green line in the figure) shows the lowest surface temperature and heat flux. In the first three days, the PCM temperature is always higher than its phase change temperature zone and remains in the liquid state, so the surface temperature fluctuation is obvious as the PCM usessensible heat for heat storage. In the last three days, the PCM temperature decreases to the phase change temperature zone as solar radiation is very weak, so latent heat is released indoors with the phase change process of PCM, and E_{int} decreases rapidly, and f decreases from 1. However, the thermal performance with different λ is close, especially for PCM with a large λ (blue line andred line). Figure 6(b) shows the thermal performance with different ρH. For the PCM with the smallest ρH (100 MJ/m^3, green line), the surface temperature and the heat flux decrease significantly on Nov. 22, as the PCM has already released all the latent heat and f drops to 0. On the contrary, the f with ρH of 200 MJ/m^3 (blue line) and 420 MJ/m^3 (red line) at the last moment of the studied period are 0.27 and 0.62, respectively, meaning the latent heat still has not been completely released. Figure 6(c) shows the thermal performance with different T_m. The PCM with T_m of 22.0°C (red line) starts to release latent heat on Nov. 19 and the surface temperature is stable at around 22.0°C, however, this heat release time is too early since the room operating temperature is still several degrees higher than 18°C. The phase change temperature zone of the PCM with T_m of 17.0°C (green line) is all lower than the thermal comfort zone and f remains as 1 all the time, except the wall temperature drops to the phase change temperature zone on the last day due to radiative heat transfer with the inner surface of the exterior wall, and only about 1.1% of the latent heat is released. The moment of the phase change process with T_m of 19.5°C (blue line) is between the other two, and a large amount of latent heat is released to maintain indoor thermal comfort when the room temperature is close to 18°C, which is the most suitable choice of T_m.
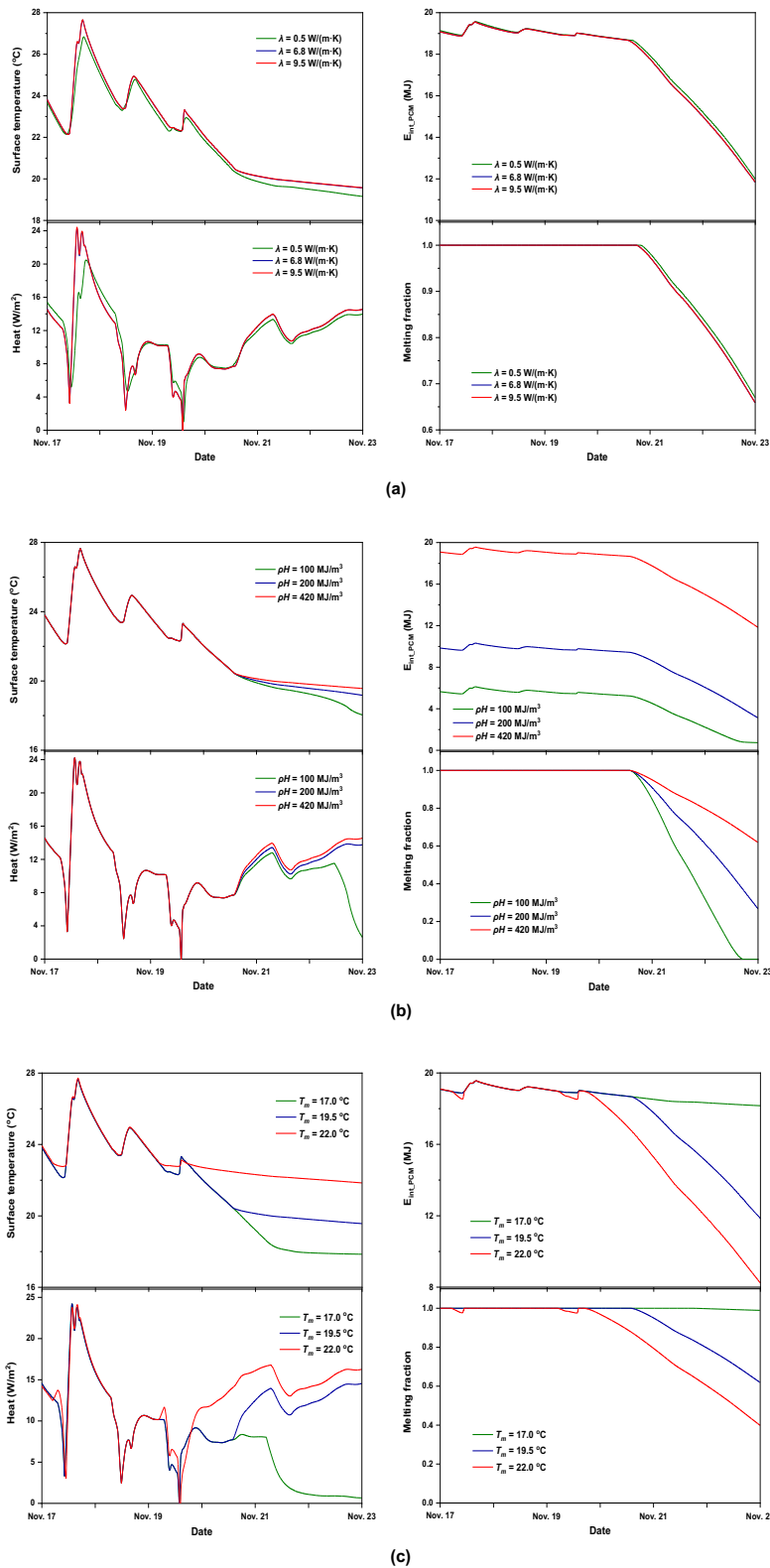
Figure 6: Thermal performance of the interior wall with different thermal properties: (a) λ; (b) ρH; (c) Tₘ

From the above analysis, it can be seen that the reasonable selection of ρH and T_m of the phase change interior wall is crucial to the indoor heating effect. Taking λ as 0.5 W/(m·K), the effects of ρH and T_m on Q and ESR of the whole heating season are shown in Figure 7. With ρH and T_m of 50 MJ/m³ and 22°C respectively, Q is 581 MJ and ESR is 52.4%. With ρH and T_m of 420 MJ/m³ and 20°C respectively, Q is 266 MJ and ESR is 78.2%. The Q decreases with the increase of ρH and decreases with T_m approaching 20°C, and Q is unchanged with different T_m lower than 17°C. On the one hand, if T_m is too high, the PCM releases latent heat too early when the room operative temperature is still significantly higher than 18°C, resulting in heating energy consumption as the room temperature continues to decrease later. On the other hand, if T_m is too low so that the phase change temperature zone is completely below the thermal comfort zone, the PCM remains in the liquid state during the whole heating season and its advantageof massive heat storage and release during the process of phase change is completely unexploited.
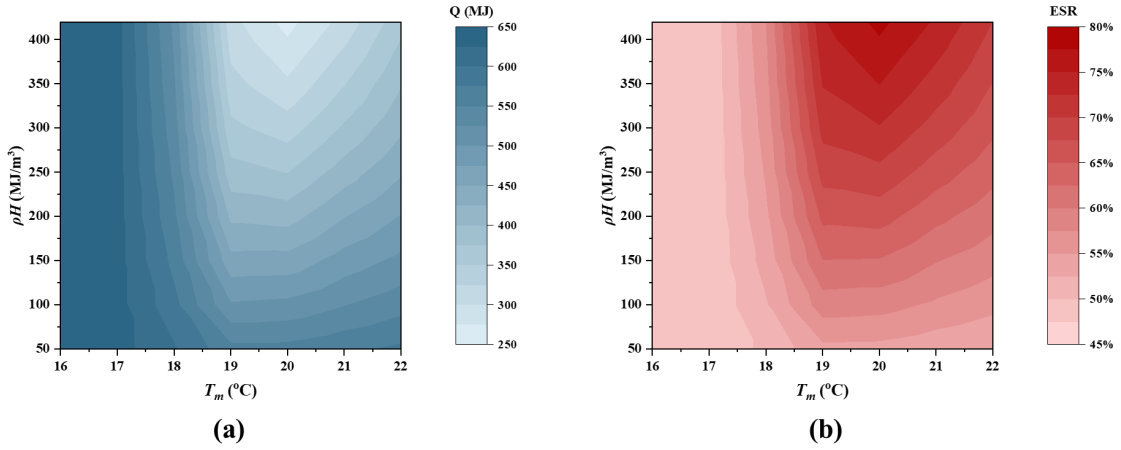
Figure 7: Influence of ρH and T_m on heating effect: (a) Total heating energy consumption; (b) Energy-saving ratio

The optimal results of all the non-zero-carbon heating locations show that the optimal ρH are all the maximum value, which is 420 MJ/m³, and the optimal λ range from 3.5 to 9.0 W/(m·K), as shown in Figure 8(a). It indicates that to achieve the goal of improving the indoor thermal environment, the interior envelope should be of high thermal conductivity and the largest heat storage capacity. As shown in Figure 8(b), the optimal T_m are various but in the range of 19.0 to 20.5°C, slightly higher than 18°C. It should be noted that the optimal T_m corresponds to the optimal λ, and λ of the current PCM is much lower, so the T_m under the current λ would be higher than this optimal T_m.
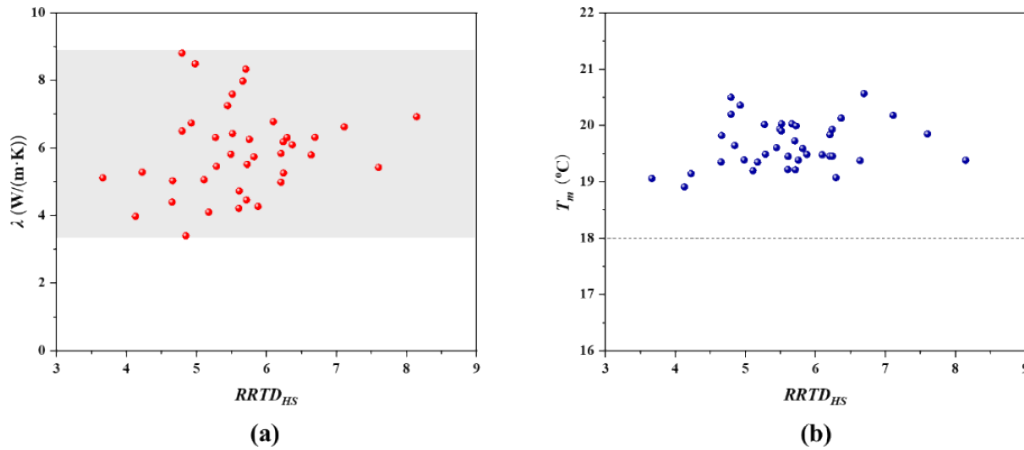
Figure 8: Optimal thermal properties at non-zero-carbon heating locations: (a) λ; (b) T_m

The fitting results of ESR and local $RRTD_{HS}$ of all non-zero-carbon heating locations are shown in Figure 9. $ESR_{PCM,INI}$ and $ESR_{PCM,OPT}$ show a highly linear positive correlation with $RRTD_{HS}$ respectively, and the fitting degrees are good with R^2 no less than 0.98. The fitting formulas are shown as Equation 6 and Equation 7. The coefficients of $ESR_{PCM,INI}$ and $ESR_{PCM,OPT}$ to $RRTD_{HS}$ are 0.105 and 0.148, respectively, that is, for every 1 W/(m²·K) increase of the local $RRTD_{HS}$, the ESR can be increased by 10.4% and 14.8% with the initial BIHPPCM and the optimized BIHPPCM, respectively. For locations not selected in this study, the formulas are helpful for estimating the energy-saving potential of local BIHPPCM. For instance, for location A with the $RRTD_{HS}$ of 5 W/(m²·K), it could be predicted that the maximum ESR by BIHPPCM is up to 74.0%. This conclusion provides an important reference for the pre-evaluation of the utilization effect and economic analysis of the BIHPPCM.

Equation 6: Linear fitting of ESR_{PCM,INI} and RRTD_{HS}.	$ESR_{PCM,INI} = 0.105 \cdot RRTD_{HS}$
Equation 7: Linear fitting of ESR_{PCM,OPT} and RRTD_{HS}.	$ESR_{PCM,OPT} = 0.148 \cdot RRTD_{HS}$
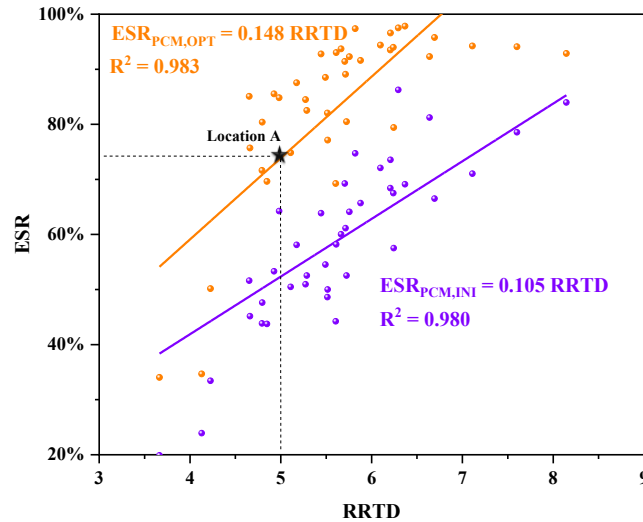
Figure 9: Linear fitting of ESR and $RRTD_{HS}$

According to the simulation results of all the selected locations, the spatial distribution maps of heating degree days during the local heating season $HDD18$, average solar radiation intensity during the local heating season $Q_{sol,ave}$, and $RRTD_{HS}$ as evaluation indexes of local climate resources, and $ESR_{PCM,INI}$ and $ESR_{PCM,OPT}$ are illustrated by ArcGIS using the inverse distance weight method, as shown in Figure 10. It can be seen that the distribution trend of ESR is more consistent to that of $RRTD_{HS}$ than $HDD18$ and $Q_{sol,ave}$. The Qinghai-Tibet Plateau of western China is the region with the best utilization potential of BIHPPCM, where zero- carbon heating can be achieved. The northwest Gansu and the western Inner Mongolia also are regions with good energy-saving effects, where ESR is higher than 70%. In contrast, the ESR of BIHPPCM is less than 40% and the lowest is 20% in northeast China and northern Xinjiang, where the outdoor air temperature is low and the solar radiation resources are poor. In general, the ESR of BIHPPCM at most locations in severe cold and cold regions of China can reach more than 30%, which shows a great energy-saving effect.
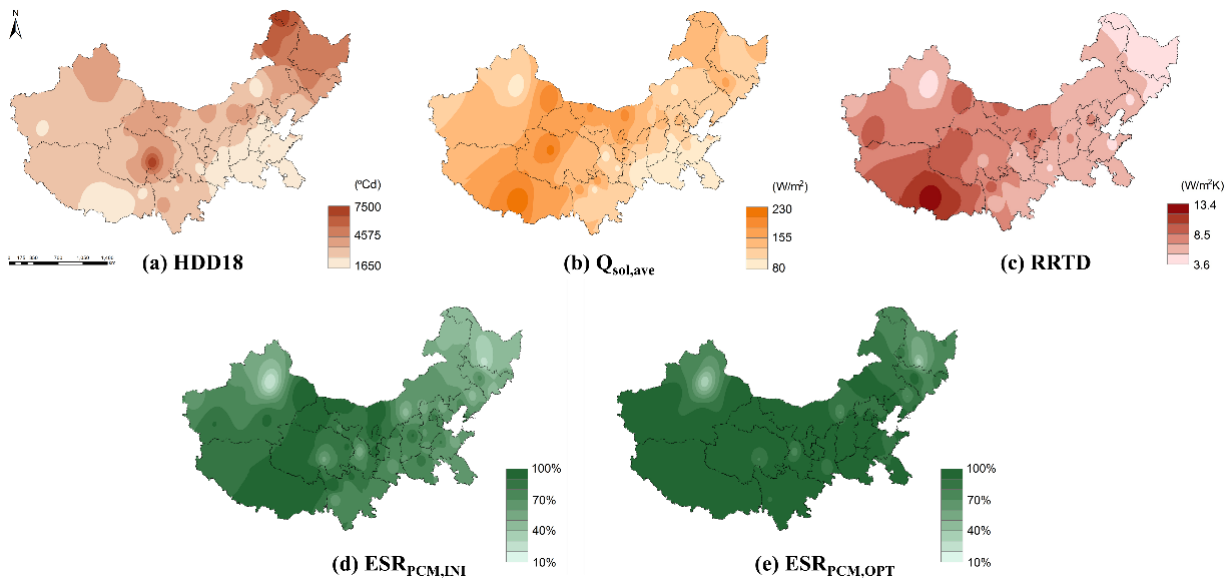
Figure 10: Spatial distribution of the evaluation indexes of climate resources and indicators of the energy-saving potential of BIHPPCM

4. CONCLUSION

In this paper, the thermal property parameters of the phase change interior envelope of BIHPPCM at 61 locations in severe cold and cold regions of China are optimized and the optimal heating effect is obtained. The relationship between $RRTD_{HS}$ and ESR of BIHPPCM is analyzed. The results show that: (1) The optimal PCMs of the interior wall are of high λ and maximum ρH, and the T_m is higher than the lower limit of the thermal comfort zone by 1-2°C; (2) The ESR at the selected locations are between 20%-100% and can reach more than 30% at most locations; (3) A linear correlation between the $RRTD_{HS}$ and ESR is obtained, and the ESR increases by 14.8% for every 1 W/(m²·K) increase of the $RRTD_{HS}$. This study shows that the BIHPPCM has a significant energy-saving potential and is of great significance for the application of BIHPPCM to reach zero-carbon heating.

361

5. ACKNOWLEDGEMENT

6. REFERENCES

CHEN, X. M. & YANG, X. D. 2022. Heat transfer enhancement for U-pipe evacuated tube solar absorber by high-emissivity coating on metal fin. JOURNAL OF BUILDING ENGINEERING, 50.

DING, X. L., MA, R. J., SHAN, M., WANG, X. L. & YANG, X. D. 2022. Occupants' on-demand control of individual heating devices in rural residential buildings: An experimental scheme and on-site study. ENERGY AND BUILDINGS, 259.

GONG, Q. P., KOU, F. C., SUN, X. Y., ZOU, Y., MO, J. H. & WANG, X. 2022. Towards zero energy buildings: A novel passive solar house integrated with flat gravity-assisted heat pipes. APPLIED ENERGY, 306.

KOU, F. C., GONG, Q. P., ZOU, Y., MO, J. H. & WANG, X. 2023a. Solar application potential and thermal property optimization of a novel zero-carbon heating building. ENERGY AND BUILDINGS, 279.

KOU, F. C., SHI, S. H., ZHU, N., SONG, Y. A., ZOU, Y., MO, J. H. & WANG, X. 2022. Improving the indoor thermal environment in lightweight buildings in winter by passive solar heating: An experimental study. INDOOR AND BUILT ENVIRONMENT, 31, 2257-2273.

KOU, F. C., WANG, X., ZOU, Y. & MO, J. H. 2023b. Heat transfer performance of the L-shaped flat gravity heat pipe used for zero-carbon heating houses. JOURNAL OF BUILDING ENGINEERING, 76.

KOU, F. C., XU, T. X., WANG, X., ZOU, Y. & MO, J. H. 2024. Towards zero-carbon solar heating in severe cold and cold regions of China by building integrated heat pipes. BUILDING AND ENVIRONMENT, 255.

LI, J. L. & HUANG, J. S. 2020. The expansion of China's solar energy: Challenges and policy options. RENEWABLE & SUSTAINABLE ENERGY REVIEWS, 132.

LIU, Y. F., YU, Z. X., SONG, C. & WANG, D. J. 2022. Heating load reduction characteristics of passive solar buildings in Tibet, China. BUILDING SIMULATION, 15, 975-994.

XU, L., DAI, L. C., YIN, L. Z., SUN, X. Y., XU, W., YANG, R., WANG, X. & ZHANG, Y. P. 2020. Research on the climate response of variable thermo-physical property building envelopes: A literature review. ENERGY AND BUILDINGS, 226.

#239: Application of gradient boosting modeling method in building energy consumption prediction: a case study of a secondary school

Xingyu Pei[1], Wenjie Ji[2,*], Shuli Liu[3], Yingxin Zhu[4]

[1] Beijing Institute of Technology, Beijing, China, 3120230463@bit.edu.cn
[2] Beijing Institute of Technology, Beijing, China, jiwenjie@bit.edu.cn
[3] Beijing Institute of Technology, Beijing, China, shuli79@126.com
[4] Tsinghua University, Beijing, China, zhuyx@tsinghua.edu.cn

Abstract: In recent years, the energy issue has gained increasing attention from the world, with buildings contributing significantly to global energy consumption and carbon emissions. The issue of energy conservation and carbon reduction in middle school campuses had received little attention, as most schools' energy-saving potential remained untapped. Energy management was oftenrough, and there was a lack of awareness about energy conservation. This study aims to address the high energy consumption in middle school buildings by proposing an improved bottom-up energy consumption model. Traditional models used in the area expansion method may not accurately reflect actual conditions. The improved method integrated the real energy consumption data and refined predictions using a gradient boosting algorithm. The modeling process included zone classification, data extraction andpreprocessing, physical model establishment, and bottom-up analysis. Applied to a secondary school in Beijing, the improved model demonstrated significantly higher accuracy, particularly during high-consumption winter months, with monthly errors kept below 10%. This accuracy is influenced by the sample size and iteration counts, ensuring optimal results. Given the issues of poor energy management and high carbon emissions in middle school campuses, this model excelled in capturing energy use patterns and suggesting potential energy-saving strategies. This innovative modeling technique provided a robust tool for policymakers and stakeholders to evaluate and implement energy conservation measures effectively, which could promote the development of green,sustainable campuses. The method was broadly applicable to all buildings with energy monitoring systems and could contribute to broader energy conservation efforts by enhancing energy efficiency and sustainability.

Keywords: Energy Consumption Prediction, School Buildings, Monitoring Data, Gradient Boosting, Building Energy Conservation

1. INTRODUCTION

In recent years, the energy issue has gained increasing attention from the international community. According to data from the World Watch Institute, among the three major sectors - construction, industry and transportation - the construction sector accounted for 40% of the world's annual energy consumption and contributed to 36% of global carbon emissions (Wang et al., 2019, Jain et al., 2014). In China, the energy consumption of buildings accounted for 27.8% of the overall energy consumption (He, Cheng and Chen, 2016). Given these issues, numerous experts and scholars have conducted extensive research on energy conservation and emission reduction in the context of building design and operation. As a result, many new buildings increasingly met the criteria for green buildings and achieved the standards for ultralow or near-zero energy consumption (Ma and Wang, 2011). However, in most developing countries like China, the number of existing buildings was substantial and significantly surpasses the number of planned new constructions. Due to time and technical constraints, these buildings exhibited high energy consumption and poor comfort levels, necessitating urgent retrofitting.

Especially, based on the 2023 census data, China had approximately 84,200 middle schools with around 49.7 million students enrolled. According to reference (Xu et al., 2021), the energy consumption of school buildings in China currently accounted for 7 % of the total energy consumption of all public buildings. In middle school campuses, where population density was high, activity patterns were complex, and energy consumption management was lacking, the potential for building energy conservation and carbon reduction was urgently needed to be tapped, making the construction of green campuses even more imperative. In addition to the obvious benefits of energy conservation and carbon reduction, the improved lighting and thermal comfort environments through energy consumption management can also enhance students' learning efficiency (Xu et al., 2021). Hence, the retrofitting of school buildings must consider the requirements of daylighting, thermal comfort, and energy.

For regional buildings which are similar to campus constructions, creating a bottom-up energy consumption model is an effective method to analyze energy usage patterns and assess energy conservation plans. Unlike the top-down model, its primary advantage is the ability to evaluate the energy-saving potential of new technologies and alternative energy sources. In recent times, scholars had conducted extensive and in-depth research on the energy consumption models of regional buildings, achieving notable results (Swan and Ugursal, 2009, Christoph and Carlos, 2016, Lim and Zhai, 2017). During the modeling process, researchers frequently employed the area expansion method to forecast zone energy consumption. This technique calculates energy use based on the energy density of prototype buildings and the total area of these building types (Zhao et al., 2021). Hu's group collected data on urban residential cooling in China, developed a bottom-up model of cooling energy consumption, and found that total consumption reached 85 billion kWh in 2015. They analyzed variations in cooling behavior and energy intensity, identified single-split ACs as the most common, and provided technology outlook and policy recommendations based on their findings (Hu, Yan and Qian, 2019). Turki's team developed a baseline energy profile for Kuwait's residential sector until 2040 using a bottom-up approach. They forecasted the quantity of residential energy-consuming equipment and calculated the unit energy consumption for each type. Results indicated that air conditioning loads accounted for 67% of residential electrical consumption and 72% of peak demand, with an annual growth rate of 2.9%. In addition, refrigerators and freezers were also significant energy consumers (Turki and Patrick, 2020). Diao's team proposed identifying and classifying occupant behavior in residential buildings using direct energy consumption outcomes and energy time use data through unsupervised clustering. Integrating k-modes clustering and demographic-based probability neural networks, they identified 10 distinctive behavior patterns from the American Time Use Survey (ATUS). Their bottom-up engineering model offered more accurate and reliable predictions of energy consumption than the ASHRAE standard schedule, demonstrating its capability to estimate energy consumption on larger geographic scales with sufficient time use data (Diao et al., 2017).

In the studies mentioned above, most of the data used was historical, survey-based, or basic building information. Researchers used these data to create prototype building models and simulate energy consumption for similar buildings. However, using a single prototype to represent all buildings of a type of can lead to inaccuracies due to variations among buildings. This mismatch can cause significant errors between simulated results and actual results (Kavgic et al., 2009). To overcome the limitations of traditional bottom-up models, many scholars have proposed innovative and improved modeling methods. Xu and his group estimated the monthly and annual average electricity consumption of large public buildings in Shanghai for 2015 using Bayesian statistical methods. They compiled and analyzed data from 711 buildings, applied a Bayesian framework to predict consumption distributions, and used MC sampling to obtain estimates. They proposed a new multi-layer Bayesian model for more accurate annual electricity consumption estimates (Xu et al., 2017). Brogger and his teammates developed a hybrid bottom-up building stock energy model to address the limitations of traditional building-physics-based models, which often rely on normative assumptions due to data deficiencies. They calibrated individual building-physics models against energy use data from over 100,000 residential buildings using multiple linear regression, creating a more accurate model. The hybrid model provided significantly better energy use estimates and allowed for the assessment of energy-saving measures, offering a reliable approach for informing policy makers and stakeholders about building stock energy efficiency (Brogger, Batcher and Wittchen, 2019).

This paper proposed an improved method to establish an energy consumption prediction model based on measured data and machine learning algorithm. This method innovatively adjusted the energy usage intensity of a prototype zone in the building using actual energy consumption monitoring data. Unlike traditional bottom-up models that rely on simulated prototype data and extrapolate it to predict whole zone energy consumption, this approach enhanced the accuracy by incorporating real-monitoring data to refine the energy estimates of the prototype zone before applying them to broader predictions. Gradient boosting, a well-performing algorithm in machine learning, was used in the correction process. Monitoring data from prototype zones was treated as the target variable for optimization, while initial simulation data was used as input features. This algorithm iterated to make the simulation results align more closely with actual conditions. It effectively combined actual and simulated energy use intensity data, leveraging the energy monitoring platform's capabilities. Here a new-built middle school in Beijing was taken as a case to exert this study, withthe main contents as flollows:

- A monitoring data-based modeling method of building energy consumption was proposed, and the specific modeling steps were defined.
- The energy consumption prediction model of the case middle school was established by the improved method, and the model accuracy was compared with a traditional model.

2. METHOD

The modeling process in this paper consists of four main steps, which is illustrated in Figure 1. Initially, zones in the building were categorized, similar to traditional methods. The second step involved data extraction and preprocessing, which can ensure the purity of the data. In the third step, real energy consumption data was combined with the simulated energy usage intensity (EUI) of the prototype buildings to obtain adjusted EUI values. The final step was a bottom-up prediction. The detailed analysis process is described in the following sections.
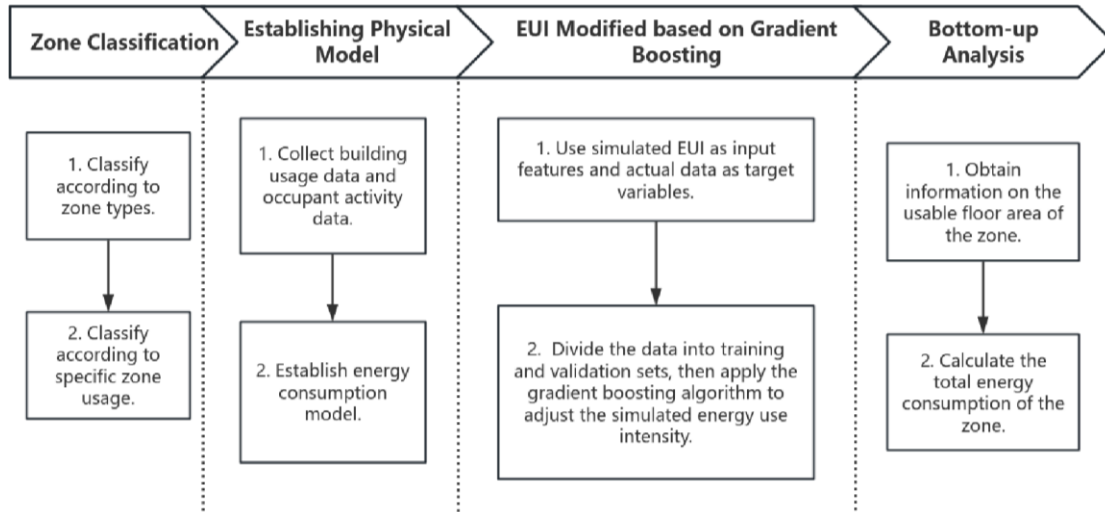
Figure 1: Modeling method of improved bottom-up campus building energy consumption prediction model

2.1. Zone classification

The first step in modeling was to classify school indoor zones based on energy use characteristics. Initially, school indoor zones should be categorized by zone type. In common, school buildings can be classified into various types such as classroom, activity room, dinning room, office room and other types. Secondly, in most middle schools, zones of the same type often serve multiple functions, depending on specific teaching tasks. For example, a classroom can be used both as a regular teaching space and as an activity room for large events. Therefore, it was necessary to perform a secondary classification based on the specific usage of each area within the building. Finally, according to the classification results, the prototype zones were selected to represent each type of zone. When selecting prototype zones, priority should be given to areas where occupant activity patterns and energy use behavior closely align with the school's schedule. This ensured the representativeness of the zone.

2.2. Establishing Physical Model

Next step was to establish a physical model for the prototype zones. Currently, widely used building energy simulation software includes DesT, Energy Plus, DOE-2, among others. eQUEST, based on DOE-2, is one of the most outstanding. Its key feature and advantage are the ability to individually and thoroughly set and simulate air conditioning and control systems. Additionally, it can set different energy-saving scenarios to determine the energy-saving potential of various equipment, helping to identify the optimal energy-saving strategy. It is noteworthy that the scholars mentioned above who used eQUEST for their research also achieved excellent simulation results. Overall, eQUEST modeling not only met the requirements for accurate building energy consumption predictions but also aided in building energy-saving analysis. Therefore, this paper chose eQUEST as the energy simulation software. By inputting information about the building envelope, indoor occupant activities, electrical equipment, air conditioning systems and other parameters, physical modeling was performed. After modeling, the model needed to be evaluated and calibrated based on relevant standards. Several main model error evaluation criteria are listed in Table 1. The verification indexes of the model include monthly error, annual error, and coefficient of variation of the root mean square error (CVRSME). The smaller the index value, the more accurate the model. This study chose international performance measurement and verification protocol (IPMVP) as the standard.

Table 1: Acceptable error range of energy consumption model

Standards	Monthly error	Annually error	CVRSME
JGJ176-2009 Code for energy saving renovation of public buildings	± 15%	-	±10%
ASHRAE 14–2014	± 5%	± 5%	±15%
International Performance Measurement and Verification Protocol (IPMVP)	± 20%	± 10%	±5%

2.3. EUI modified based on Gradient Boosting

The third step was to modify the simulation results of the physical model. In the correction process, gradient boosting algorithm needed to be used. This required training data, validation data, and a predefined loss function. The algorithm iteratively built decision trees, each one correcting error from the previous tree, to improve model accuracy and minimize prediction errors. In this paper, we used the simulated data as input features and actual data as target variables. The basic ideas and steps are as follows:

First of all, the model was initialized as Equation 1. The entire process started by generating a simple model, such as one that outputs only the mean value, which is the most commonly used.

Equation 4: Predicted values of the initial model
$$F_0(x) = arg \min_c \sum_{i=1}^n L(y_i, c)$$

where:

- $F_0(x)$ = the prediction of the initial model, which is a constant value at this initialization stage;
- c = constant;
- L = the loss function;
- y_i = the actual value.

Then, iteratively updated the model by Equation 2, 3 and 4. Specifically, this process started by calculating the difference between the predictions of the simple model and the actual values, known as "residuals." A new decision tree was then trained to predict these residuals, aiming to minimize them and improve the accuracy of the predictions. The new tree was added to the existing model to enhance its predictive power. This process was repeated iteratively to continually improve the model until the desired accuracy is achieved.

Equation 2: Pseudo-Residuals calculation
$$r_{im} = -\left[\frac{\partial L(y_i, F(x_i))}{\partial F(x_i)}\right]_{F(x)=F_{m-1}(x)}$$

where:

- r_{im} = pseudo-residuals;
- $F(x_i)$ = the current model's predicted value for the i-th data point;
- m = number of iterations.

Equation 3: Weak learner fitting
$$h(x) = arg \min \sum_{i=1}^n (r_{im} - h(x_i))^2 h$$

where:

- $h_m(x)$ = the weak learner fitted in the m-th iteration
- $h(x_i)$ = the prediction made by the weak learner h for the i-th data point

Equation 4: Model updating
$$F(x) = F_{m-1}(x) + \eta \cdot h_m(x)$$

where:

- η = learning rate

The initial model $F_0(x)$ served as the baseline for subsequent iterations, where each step will iteratively improve the model by fitting to the pseudo-residuals (errors), so we can acquire the updated model $F_m(x)$. Through these steps, the simulated data and the actual measured data were employed in each step of the gradient boosting algorithm to produce a model that can more accurately predict energy consumption. It should be noted that the energy consumption data referred to here is all EUI data.

2.4. Bottom-up analysis

After obtaining the corrected EUI data, we can calculate the building's final total energy consumption using the following formula:

Equation 5: Final total energy consumption

$$Q = \sum_{i=1}^{k} EUI_i S_i$$

where:

- Q = final total energy consumption (kJ)
- EUI_i = prediction value of energy using intensity (kJ/m^2)
- S_i = usable floor area of the building (m^2)

And this result can be used to compare and evaluate the effectiveness of the two modeling approaches.

3. RESULTS AND DISCUSSIONS

In this paper, both traditional and improved modeling methods were employed to create an energy consumption model for a middle school zone in Beijing, China. In China, many newly built middle schools were equipped with energy monitoring devices, however, technical and cost constraints limited a comprehensive monitoring across all campus areas. A typical zone was used to represent a larger area. This study focused on a middle school built in 2021 in Beijing, where all campus buildings were interconnected, essentially forming a single structure. In this middle school, there are five main buildings and an energy consumption monitoring system has been deployed during construction period. The interface of the energy consumption monitoring platform is shown in Figure 2.
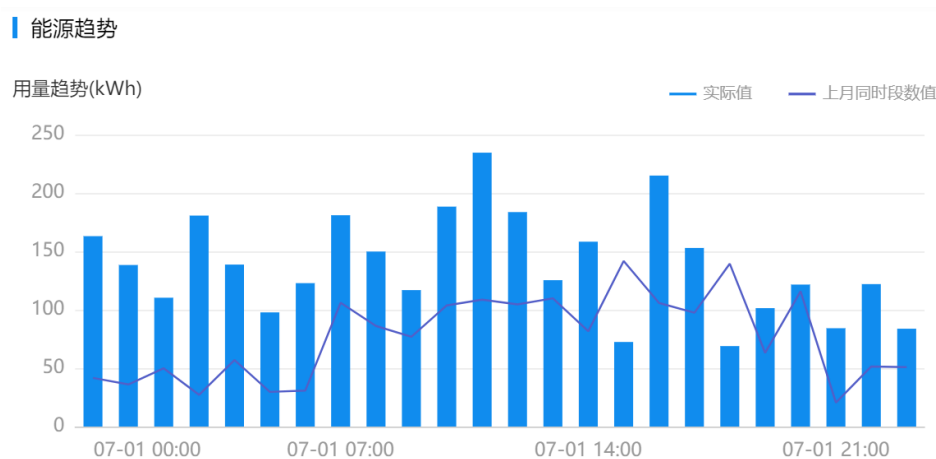
Figure 2: Data display of energy monitoring platform

3.1. Zone classification results

Based on zone types, all zones in the middle school building were categorized into six types: classrooms, office rooms, restrooms, dinning rooms, theater and library. Considering that this middle school in Beijing was renowned for its personalized student development and diverse offerings, classrooms were divided into regular classrooms, laboratory classrooms, and activity classrooms. Besides, theater and library were lacking monitoring equipment, so they were not taken into consideration in the simulation process. The final zone classification results and some basic information are listed in Table 2.

Table 2: Zone classification results

Zone category		Number of zone	Floor area (m^2)
	Regular classroom	62	6233
Classroom	Laboratory classroom	8	789
	Activity classroom	8	856
Office room		21	1511
Restroom		18	577
Dinning room		1	738
Theater		1	1200
Library		1	2638

3.2. Model simulation results

The eQUEST was used as the simulation tool to establish physical models. The modeling results and errors of different zones are listed in Table 3. It should be noted that both the simulated and measured data represent hourly energy consumption over 8760 hours in a year. The bar chart in the third column of the table displays monthly simulated and actual energy consumption for the year, with blank bars representing actual consumption and striped bars indicating simulated consumption, and the x-axis and y-axis represent the months and energy consumption, respectively. Additionally, due to missing or abnormal values in the monitoring platform's data, preprocessing was performed when calculating monthly errors. Based on relevant literature (Kim et al., 2023), the average value imputation method, which has minimal impact on the data, was chosen to complete the missing data.

Due to article length constraints, a prototype regular classroom was selected as an example to demonstrate the detailed simulation results from the software in Table 4. This includes measured energy consumption, simulated energy consumption, and monthlyerrors for each month from January to December. As shown in Tables 3 and 4, the model errors remain within ±20%, meeting the requirements of the IPMVP. After the simulation, the EUI can be calculated with total energy consumption and floor area, which is shown in the fourth column of Table 4.

Table 3: Modeling results of prototype zone

Zone category	The prototype zone	Simulation results of prototype zone (Y axis: energy consumption, kWh)	Error range
Regular classroom	Y404		-18%~17%
Laboratory classroom	Z402		-19%~19%
Activity classroom	S201		-18%~17%
Office room	X404		-10%~17%

| Restroom | S406 | | -15%~19% |

| Dinning room | Y101 | | -15%~19% |
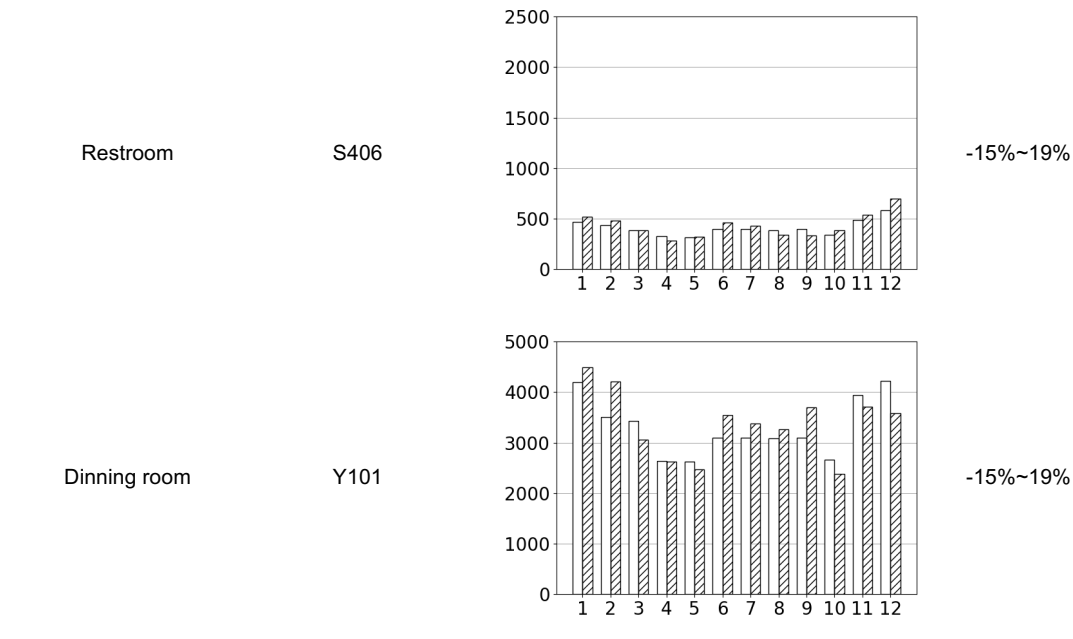
Table 4: Y404 simulation results before and after optimization

Month	Measured data (kWh)	Simulated data (kWh)	Monthly error	Measured EUI (kWh/m^2)	Simulated EUI before optimization (kWh/m^2)	Simulated EUI after optimization (kWh/m^2)
1	2007.13	1755.64	-12.53%	22.94	20.06	22.73
2	1015.76	858.22	-15.51%	11.61	9.81	11.32
3	803.62	710.80	-11.55%	9.18	8.12	9.94
4	549.89	648.16	17.87%	6.28	7.41	6.77
5	505.06	418.80	-17.08%	5.77	4.79	5.6
6	851.27	750.22	-11.87%	9.73	8.57	9.05
7	854.07	961	12.52%	9.76	10.98	9.1
8	802.47	651.12	-18.86%	9.17	7.44	9.87
9	846.55	944.67	11.59%	9.67	10.8	9.04
10	613.59	542.05	-11.66%	7.01	6.19	7.72
11	1231.94	1376.45	11.73%	14.08	15.73	14.66
12	2070.07	2393	15.6%	23.66	27.35	23.99

3.3. Modified EUI results

In this part, we take regular classroom as an example to demonstrate how the gradient boosting algorithm improves simulation accuracy. First, to ensure sufficient sample size, we selected the daily average EUI of 62 classrooms as the optimization target. This way, the measured values and simulated values each can obtain approximately 20,000 sample data points after feature selection. While monthly EUI could also be chosen, it would require extended monitoring to meet the sample size requirements. Then we randomly split the data into training and validation sets and initialize the model $F_0(x)$. Here, the model can be initialized to the average value of the measured data to simplify subsequent iterations. Similarly, the loss function is set to mean squared error (MSE). Minimizing this loss function during iterations aims to reduce the discrepancy between the measured and simulated values as much as possible.

In addition, setting hyperparameters such as the number of iterations and the learning rate is crucial for the algorithm's optimization effectiveness. These settings require multiple attempts based on the sample data and specific needs, which will not be detailed here. In general, different values can be set initially to observe the outcomes, and adjustments can be made based on the differences before and after. Once the optimized daily average EUI is obtained, daily energy consumption can be calculated by multiplying it by the area of each zone. These daily values are then summed up to obtain the monthly energy consumption, as the error comparison is based on monthly data. The optimization method for other zone types is similar, but due to insufficient sample sizes in this study, comparisons are not made. The optimized EUI results for regular classrooms, as well as the error values for total energy consumption under both modeling methods, are shown in Table 5. The gradient boosting algorithm in this study is implemented using the XGBOOST module in Python 3.12.

Table 5: Energy consumption prediction of regular classrooms

Month	Measured data (kWh)	Energy consumption prediction of traditional model (kWh)	Energy consumption prediction of improved model (kWh)	Monthly error of traditional model	Monthly error of improved model
1	145338.26	123786.34	141416.31	-14.83%	-2.7%
2	74447.82	76183.99	73069.36	+2.33%	-1.85%
3	45388.74	35796.15	46813.95	-21.13%	+3.14%
4	20744.24	16431.65	20274.15	-20.79%	-2.27%
5	33816.54	27699.65	31887.56	-18.09%	-5.7%
6	57732.42	51859.65	51289.77	-10.17%	-11.19%
7	49289	39399.85	48542.79	-20.06%	-1.51%
8	46717.4	47739.27	42087.79	+2.19%	-9.76%
9	34802.32	29215.89	32879.58	-16.05%	-5.52%
10	21258.56	21572.66	22333.28	+1.48%	+4.74%
11	52503.5	60594.73	53923.79	+15.41%	+2.71%
12	172468.64	195683.08	171485.43	+13.46%	-0.57%

3.4. Further discussions

Based on the results of energy simulation and error in Table 5, we can analyze the two modeling methods. For regular classrooms, the improved modeling method achieved an average monthly error of less than 5% in simulating total monthly energy consumption, compared to less than 15% for the traditional method, which is significantly higher. Although a 15% average error is not very high, some months still show errors above 20%. Compared to the traditional model, the improved model's average error rate decreased by more than 60%. The main cause of error in the traditional method is the selection of typical zones, which is influenced by zone diversity. Other factors, such as the imprecision in building parameter settings and the inability to fully capture changes in human activities, also contribute to the error rate. The gradient boosting method better captures zone energy usage characteristics, resulting in lower errors for the 62 different classrooms in this experiment.

From Tables 4 and 5, it is evident that the winter energy consumption in regular classrooms is higher than in the summer and transition seasons. This indicates potential issues such as over-heating, low COP of air conditioning units during winter, or poor building insulation. Further analysis can be conducted by examining HVAC operation and indoor environment monitoring. During the heating months of November, December, January, and February, the new model's error remains within 3%, while the old model's error is around 15%. This demonstrates the improved model's higher accuracy during winter months, compared to both the traditional model and summer months. From an energy-saving and environmental perspective, there is substantial potential for energy conservation within the campus, particularly in winter. The monthly EUI for regular classrooms can exceed 20 kWh/m². These findings suggest that addressing issues related to excessive heating, improving the efficiency of winter air conditioning units, and enhancing building insulation could significantly reduce energy consumption. This would not only improve the accuracy of energy consumption predictions but also contribute to the development of greener and more sustainable campuses. The improved modeling method thus proves to be more effective in identifying and addressing energy inefficiencies, providing a robust tool for energy management in educational institutions. This enhanced accuracy is crucial for planning and implementing energy-saving measures, ensuring that resources are used more efficiently, and environmental goals are met.

4. CONCLUSION

This study introduced a simulation modeling method for building energy consumption based on monitoring data, utilizing a gradient boosting algorithm to enhance the traditional models. Through a middle school buildings case study, it was found that the improved method provided higher accuracy in energy consumption simulations, particularly during high-energy-use winter months. Specifically, the improved method refined the results of physical modeling by capturing energy consumption data characteristics, thereby keeping monthly errors below 10%. This accuracy was influenced by the sample size and iteration count. The method required energy monitoring data from buildings and effectively utilized the collected data. To ensure optimal correction results, a sufficient number of samples was necessary. Given the issues in middle school campuses such as rough energy management, lack of student awareness about energy conservation, and significant potential for energy savings and carbon reduction, the proposed modeling method excelled in capturing campus energy use patterns. It also suggests potential energy-saving strategies to build green, sustainable campuses. Notably, this method can be extended to apply in other types of building which have an energy monitoring system, provided there is sufficient monitoring duration to expand the sample size. This broad applicability made it a valuable tool for enhancing energy efficiency and sustainability in various contexts.

5. ACKNOWLEDGEMENT

6. REFERENCES

Wang, W., et al. (2019) 'Forecasting district-scale energy dynamics through integrating building network and long short-term memory learning algorithm' , Applied Energy, 248(C), pp. 217-230.

Jain, R.K., et al. (2014) 'Forecasting energy consumption of multi-family residential buildings using support vector regression: Investigating the impact of temporal and spatial monitoring granularity on performance accuracy', Applied Energy, 123(0), pp. 168-178.

He, N., Cheng, M.Y. and Chen, S. (2016) 'Construction and application of energy-saving campus energy-saving supervision platform', Building Energy Efficiency, 44(7), pp. 76-78, 87. Available at: https://doi.org/10.3969/j.issn.1673-7237.2016.07.020.

Ma, Z.J. and Wang, S.W. (2011) 'Enhancing the performance of large primary-secondary chilled water systems by using bypass check valve', Energy, 36(1), pp. 268-276.

Xu, Y.Z., et al. (2021) 'A Novel optimization method for conventional primary and secondary school classrooms in southern china considering energy demand, Thermal Comfort and Daylighting', Sustainability, 13(23), pp. 13119.

Xu Y.Z., et al. (2021) 'A two-stage multi-objective optimization method for envelope and energy generation systems of primary and secondary school teaching buildings in China', Building and Environment, 204(0), pp. 108142.

Swan, L.G. and Ugursal, V.I. (2009) 'Modeling of end-use energy consumption in the residential sector: A review of modeling techniques', Renewable and Sustainable Energy Reviews, 13(0), pp. 1819-1835.

Christoph, F.R. and Carlos, C.D. (2016) 'Urban building energy modeling – a review of a nascent field', Building and Environment, 97(0), pp. 196-202.

Lim, H.W. and Zhai, Z.Q. (2017) 'Review on stochastic modeling methods for building stock energy prediction', Building Simulation, 10(5), pp. 607-624.

Zhao, T.Y., et al. (2021) 'A monitoring data based bottom-up modeling method and its application for energy consumption prediction of campus building', Journal of Building Engineering, 35, pp. 101962.

Hu, S., Yan, D. and Qian, M.Y. (2019) 'Using bottom-up model to analyze cooling energy consumption in China's urban residential building', Energy and Buildings, 202(0), pp. 109352.

Turki, A. and Patrick, P. (2020) 'Modeling and Forecasting End-Use Energy Consumption for Residential Buildings in Kuwait Using a Bottom-Up Approach', Energies, 13(8), pp. 1981.

Diao, L.Q. et al. (2017) 'Modeling energy consumption in residential buildings: a bottom-up analysis based on occupant behavior pattern clustering and stochastic simulation', Energy and Buildings, 147(1), pp. 47-66.

Kavgic, M. et al. (2010) 'A review of bottom-up building stock models for energy consumption in the residential sector', Building and Environment, 45(7), pp. 1683-1697.

Xu, P.T. et al. (2017) 'Bayesian Statistical Analysis of energy consumption of large public buildings in Shanghai', Journal of Shanghai Normal University(Natural Sciences), 46(2), pp. 169-177.

Brogger, M., Bacher, P. and Wittchen, K.B. (2019) 'A hybrid modelling method for improving estimates of the average energy-saving potential of a building stock', Energy and Building, 199(0), pp. 287-296.

Kim, J.W. et al. (2023) 'Imputation of missing values in residential building monitored data: Energy consumption, behavior, and environment information', Building and Environment, 245(Suppl C), pp. 110919.

#240: Performance study of MAPA/DEEA composite organic amine absorber for CO2 capture

Di WANG[1], Fang-qin LI[1],Wei-guo PAN[1], Qun-zhi ZHU[1], Jiang WU[1], Zhen-zhen GUAN[1]

[1] Di WANG, College of Energy and Mechanical Engineering, Shanghai University of Electric Power, No.1851, Hucheng Huan Road, Pudong New Area, Shanghai, China, 962875082@qq.com
[1] Fang-qin LI, College of Energy and Mechanical Engineering, Shanghai University of Electric Power, No.1851, Hucheng Huan Road, Pudong New Area, Shanghai, China, lifangqin@shiep.edu.cn
[1] Wei-guo PAN, College of Energy and Mechanical Engineering, Shanghai University of Electric Power, No.1851, Hucheng Huan Road, Pudong New Area, Shanghai, China, pweiguo@163.com
[1] Qun-zhi ZHU, College of Energy and Mechanical Engineering, Shanghai University of Electric Power, No.1851, Hucheng Huan Road, Pudong New Area, Shanghai, China, zhuqunzhi@shiep.edu.cn
[1]Jiang WU, College of Energy and Mechanical Engineering, Shanghai University of Electric Power, No.1851, Hucheng Huan Road, Pudong New Area, Shanghai, China, wjcfd2002@163.com
[1] Zhen-zhen GUAN, College of Energy and Mechanical Engineering, Shanghai University of Electric Power, No.1851, Hucheng Huan Road, Pudong New Area, Shanghai, China, guanzzhen@163.com

Abstract: In this paper, 3-methylaminopropylamine (MAPA) and diethylaminoethanol (DEEA) were mixed in certain ratios, and a novel 3-methylaminopropylamine (MAPA)/diethylaminoethanol (DEEA) composite organic amine sorbent was investigated for CO2 absorption and desorption. By controlling different solvent ratios and experimental temperatures, the absorption and desorption experiments were carried out under different concentration ratios and temperatures, and the optimal CO2 capture performance of the new composite organic amine absorbent was investigated under different conditions. The experimental results showed that when the solvent ratio of the new composite organic amine absorber was MAPA:DEEA=10 wt%:20 wt%, and the absorption temperature was kept at 308.15 K, the CO2 absorption of the new composite organic amine absorber was as high as 0.97 mol CO2/mol amine, and the CO2 desorption of the new composite organic amine absorber was investigated next. Next, the CO2 desorption effect of this new composite organic amine absorber was investigated. It was found that when the desorption temperature was 90℃, the desorption rate of the absorbent rich liquid was as high as 77.74%, at this time, the absorbent did not reach the boiling point, so as to avoid the loss of absorbent due to the evaporation of the absorbent by thermal boiling. The MAPA/DEEA absorption system was analyzed by NMR spectroscopy, and the reaction principle of the absorbent and CO2 was deduced: MAPA first reacted with CO2 to generate an amphoteric intermediate product. Then DEEA deprotonates the product to form carbamate, and MAPA can promote the reaction rate of the composite absorber with CO2, while DEEA can act as a proton acceptor to enhance the CO2 absorption capacity of MAPA.

Keywords: CO2 Capture, Chemical Absorption, Composite Organic Amine Absorbent

1. INTRODUCTION

Energy is the basis for ensuring the steady progress of human society [1]. Excessive use of coal leads to excessive emissions of greenhouse gases such as CO_2, methane, and NO_2. The Global Climate Status Report 2022 published by the World Meteorological Organization shows that in 2021, the concentrations of three major greenhouse gases (CO_2, methane, and NO_2) reached record highs [2].

Researchers have found that primary amines as well as secondary amines absorb CO_2 at a fast rate, but their CO_2 uptake is low, and the products of the reaction with CO_2 are relatively stable in nature and require higher temperatures for their desorption. Tertiary amines and spatially hindered amines can capture large amounts of CO_2, but their rate of CO_2 uptake is too slow [3]. In order to synthesize their advantages, researchers added tertiary amines to primary or secondary amines to obtain composite organic amine absorbers [4].

When Luo et al. [5] looked at how the mixing ratio of DEEA and MEA affected CO_2 uptake, they discovered that the cycling capacity of the mixed system with a molar ratio of 2.5:2.5 was 38.2% higher than that of the system with 30 weight percent MEA.According to SEMA et al. [6], the combined MEA/MDEA solution outperformed the MEA solution in terms of mass transfer and reaction kinetics during CO_2 uptake. CHEN et al [7] used N-methyldiethanolamine solution (MDEA) as the main body and found that when MDEA solution and diethanolamine (DEA) solution were mixed in a ratio of 2:1, the CO_2 desorption performance of the MDEA/DEAsolution was improved as compared to MDEA solution alone. When Hairul et al. [8] combined piperazine (PZ) solution with 2-amino-2-methyl -1propanol (AMP) in various ratios, they discovered that the rate at which the absorbent absorbed CO_2 rose in proportion to the PZ solution's content. Sutar et al. [9] created a CO_2 mixture using 2,50 mol/L diethylaminoethanol (DEEA) solution and 1,6-hexanediamine (HMDA) solution at concentrations between 0.1 and 0.5 mol/L. The new absorbent's rate of CO_2 absorption is equal to the total of the rates at which the HMDA and DEEA solutions react with CO_2 on their own.

The tertiary amine group found in diethylaminoethanol (DEEA) is a type of tertiary amine that has CO_2 trapping potential. MAPA provides a number of benefits, including a quick rate of interaction with CO_2, a high water solubility, non-toxicity, and a high rate of environmental biodegradation. In order to create a CO_2 absorption system that would outperform the conventional ethanolamine in terms of absorption load, desorption rate, and energy consumption, MAPA and DEEA were combined in this work.

2. EXPERIMENTAL PART

2.1 Experimental reagents

The reagents used in the experiments were 3-methylaminopropylamine (mass fraction ≥98%, Adamas), diethylaminoethanol (mass fraction ≥98%, Adamas), carbon dioxide, and nitrogen, and gases were purchased from Shanghai Jiangnan Gas Co.

2.2 Absorption experiments

The absorption device is shown in Figure 2-1. Turn on the thermostatic magnetic stirrer and set the appropriate heating temperature to make the water temperature reach the target temperature of the CO_2 absorption experiment and keep the temperature stable. To guarantee that the CO_2 gas intake flow rate is 150 mL/min, regulate the CO_2 inlet flow rate via the rotameter. Heat the prepared fresh CO_2 absorbing solution in the water bath to the target temperature and pour it into the three- necked round-bottomed flask after the absorbing solution temperature reaches the set temperature of the thermostatic water bath. Turn on the stopwatch, attach the CO_2 conduit to the flask with three necks, and use the soap film flow meter at the outlet to gaugethe CO_2 flow rate. The experiment is over when the absorbent has fully reacted with CO_2 and the difference between the soap film flow meter's outlet gas flow rate and the inlet gas flow rate is less than 5%.

2.3 Desorption experiments

The desorption setup is shown in Figure 2-1. Thermostatic magnetic stirrer water was heated to the desired temperature needed for the rich liquid to desorb. The rich liquid that had absorbed CO_2 was transferred to a flask with three necks. The flask was then placed on a thermostatic magnetic stirrer, and nitrogen gas was added to the flask at a rate of 150 mL per minute to act as a purgegas, removing any desorbed CO_2. A condenser tube is used to condense the gas generated from the heat vaporization in the three-necked flask to prevent volatilization loss of the absorbent due to high temperature vaporization of the absorbent.
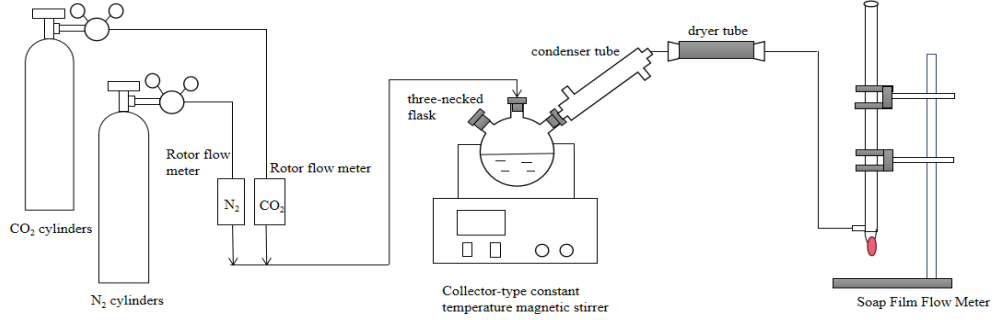
Figure 2-1: CO2 absorption and desorption device

2.4 Testing and calculation of experimental parameters

The CO2 absorption rate is the amount of CO2 absorbed by the absorber from inlet to outlet per unit time. The specific calculation formula is as follows:

$$r_{ab} = \frac{Q_{in} - Q_{out}}{22.4 \times 1000} \left(\frac{P_{act} T_0}{T_{act} P_0} \right) \tag{2-1}$$

Style:

r_{ab}--CO2 absorption rate, mol/min;
Q_{in}--CO2 gas flow rate at the inlet of the absorption device, mL/min; Q_{out}--CO2 gas flow rate at the outlet of the absorption device, mL/min; P_{act}--Actual atmospheric pressure, kPa;
P_0--standard atmospheric pressure, kPa; T_{act}--actual temperature, K;
T_o--standard temperature, K;

The CO2 capacity in the absorbent is tested using a titration method. The calculation formula is as follows:

$$R_{rich} (\text{or } R_{lean}) = \frac{n_{CO_2}}{V_{rich}} (\text{or } \frac{n_{CO_2}}{V_{lean}}) \tag{2-2}$$

Style:

R_{rich}--CO2 absorption capacity of rich liquid phase, mol /L;
R_{lean}--Capacity of CO2 absorption in the lean liquid phase, mol /L; n_{co2}--Molar amount of CO2 absorbed by the lean or rich liquid, mol; V_{rich}--Absorbent rich liquid volume, L;

The CO2 absorption load is calculated as follows:
V_{lean}--absorbent-poor liquid volume, L; $\alpha = \frac{n_{CO_2}}{n_{amine}}$ (2-3)

Style:

α--absorption load, mol CO2/mol amine;
n_{co2}--Total molar amount of CO2 absorbed by the absorbent, mol; n_{amine}--Total molar amount of amine in the absorbent, mol;

The rate of CO2 desorption was calculated as follows:

$$r_{de} = \frac{\Delta Q}{V_{rich\ phase} \times 22.4 \times 1000} \left(\frac{P_{act} T_0}{P_0 T_{act}} \right) \tag{2-4}$$

Style:

r_{de}--Desorption rate of CO2 desorption by the absorbent, mol/(L-min);

ΔQ--Desorption flow rate of absorber desorption of CO2, ml/min; V_{rich}--volume of rich liquid phase, L;

P_{act}--Actual atmospheric pressure, kPa; P_0--Standard atmospheric pressure, kPa; T_0--Temperature at standard state, K;

T_{act}--Temperature in the actual state, K;

2.5 Characterization methods

Characterization and analysis work was carried out on the samples tested using a Nuclear Magnetic Resonance Spectrometer (Bruker Avance NEO 600 MHZ) to determine the reaction products after absorption of CO_2 by the absorbent.

3. EXPERIMENTAL RESULTS AND DISCUSSION

3.1 Effect of ratio and concentration of MAPA/DEEA system on CO_2 absorption by solution

As shown in Figure 3-1, At the same total amine concentration, the rate of CO_2 absorption by the absorption system increases as the concentration of MAPA solvent increases. As can be seen, MAPA, a primary amine, primarily determines the absorption rate of the MAPA/DEEA absorption system. The reaction rate with CO_2 is also very fast. It has been suggested in the literature [10] that adding primary amine can increase the absorption rate of CO_2 in the absorption system, which is consistent with the findings of the current set of experiments. Table 3-1 illustrates how, for the same total amine concentration, the absorption system's CO_2 absorption load rose as the concentration of MAPA solvent increased. Additionally, comparing Tables 3-1 and 3-2, it was discovered that the absorber with a total amine concentration of 40 wt% had a lower CO_2 loading than the absorber with a concentration of 30 wt%. This was explained by the fact that the absorber's concentration causes the absorption system's viscosity to increase. It has been suggested in the literature [11] that too much viscosity of the absorption system viscosity is detrimental to the CO_2 capture effect of the absorber.

In summary, it was concluded that the MAPA/DEEA composite organic amine absorption system has the best absorption effect when $W_{MAPA}:W_{DEEA}=10:20$ and the total amine concentration is 30 wt%.
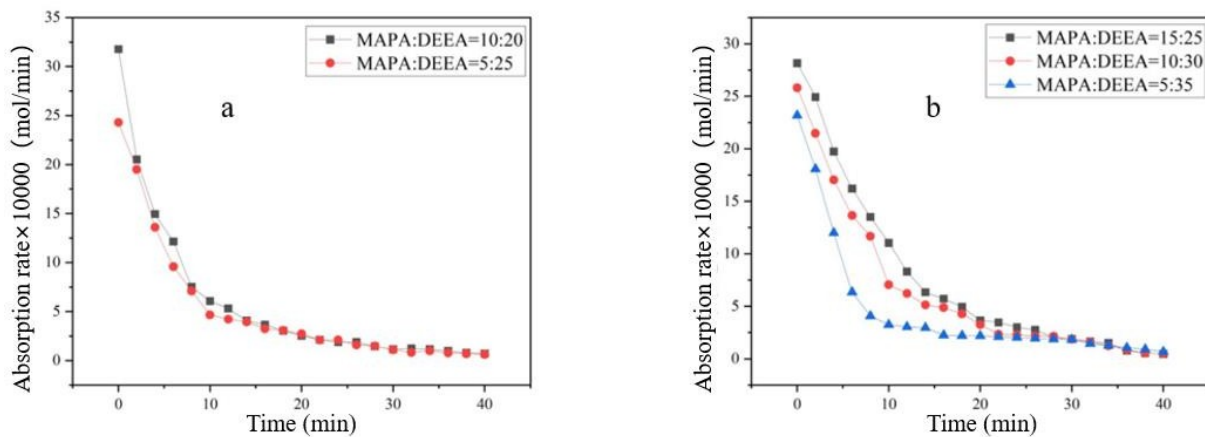
Figure 3-:1 Comparison of CO_2 absorption rates by MAPA/DEEA absorbers with total amine concentrations of 30 wt% (a) and 40 wt% (b)

Table 3-1: CO_2 Absorption Load in Complex Organic Amines Solutions of MAPA/DEEA at 30 wt% Total Amines Concentration

Total amine concentration(wt%)	W_{MAPA}：W_{DEEA}	Absorbed load(mol CO_2/mol amine)
30	5:25	0.824
30	10:20	0.895

Table 3-2: CO2 uptake loads in MAPA/DEEA complex organic amine solutions with total amine concentration of 40 wt%

Total amine concentration(wt%)	W_{MAPA}：W_{DEEA}	Absorbed load(mol CO_2/mol amine)
40	5:35	0.726
40	10:30	0.731
40	15:25	0.757

3.2 Effect of temperature on CO_2 absorption by MAPA/DEEA system

From Figure 3-2 and Table 3-3, it can be seen that the absorption rate and absorption load of CO_2 by the absorber system gradually increased when the absorption temperature increased from 298.15 K to 308.15 K with a certain ratio and concentration of the absorber system. The absorption rate and absorption load of CO_2 by the absorbent, however, decreased when the absorbent's absorption experimental temperature was raised from 308.15 K to 313.15 K. This could be because raising the experimental temperature lowers CO_2's solubility in the absorbent, which in turn reduces the drive for mass transfer between the liquid and gas phases [12]. In conclusion, the absorbent's best CO_2 absorption performance was attained when the experimental temperature of CO_2 absorption was maintained at 308.15 K. The absorbent's absorption of CO_2 was also minimized when the total amine

concentration was 30 wt% and W_{MAPA}: W_{DEEA} = 10:20.
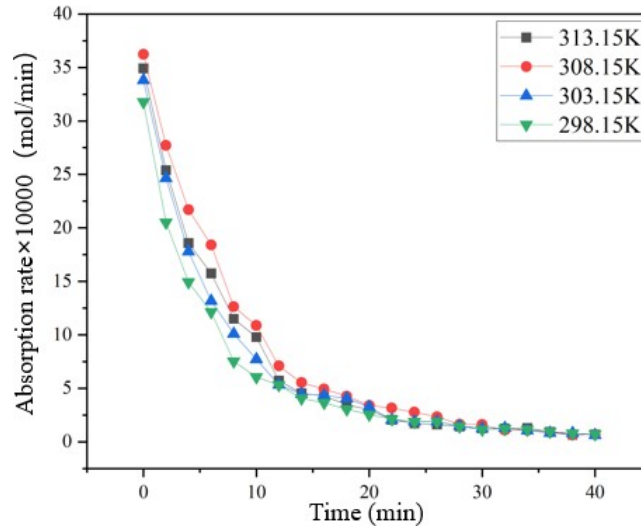
Figure 3-2: Effect of temperature on CO_2 uptake by MAPA/DEEA (30 wt%, 10:20) absorption system

Table 3-3: Effect of temperature on the CO_2 uptake load of the MAPA/DEEA (30 wt%, 10:20) absorption system

absorption system	temp（K）	Absorbed load（mol CO_2/mol amine）
	298.15	0.895
MAPA/DEEA（30wt%，10:20）	303.15	0.934
	308.15	0.970
	313.15	0.942

3.3 Effect of temperature on the desorption of CO2 from MAPA/DEEA system

As can be seen from Figure 3-3, the resolution rate increases gradually with the increase of desorption temperature. However, when the desorption temperature of the absorbent is increased from 90 ℃ to 95 ℃, the resolving rate of the absorbent is only increased by 1.52%, which is not a substantial increase. Considering that the higher the desorption temperature, the more energy is consumed, and it will cause the absorbent to reach the boiling point, resulting in vaporization and loss of the absorbent. At 90 ℃, the absorber already has a good desorption effect, and the desorption rate of the rich liquid of the absorber at this time is as high as 77.74%. And the absorbent did not reach the boiling point at 90 ℃, avoiding the loss of absorbent caused by the vaporization of the absorbent by boiling heat. Therefore, it is considered that the desorption efficiency of the absorbent at 90 ℃ is the best.
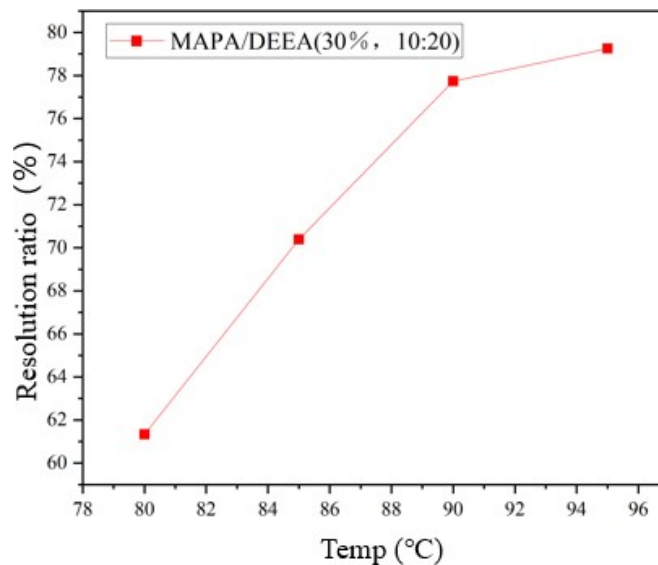
Figure 3-3: Effect of temperature on CO_2 desorption by MAPA/DEEA (30 wt%, 10:20) absorption system

3.4 13C NMR Characterization of MAPA/DEEA Absorbents

The The species of substances contained in the absorbent were analyzed by using a nuclear magnetic resonance spectroscopy analyzer (13C NMR) to characterize the solutions before, after, and after desorption of CO_2, respectively. Figures 3-4 show some of the substance species that may be present in the absorbent. The results of the characterization analysis are shown in Figure 3-5.
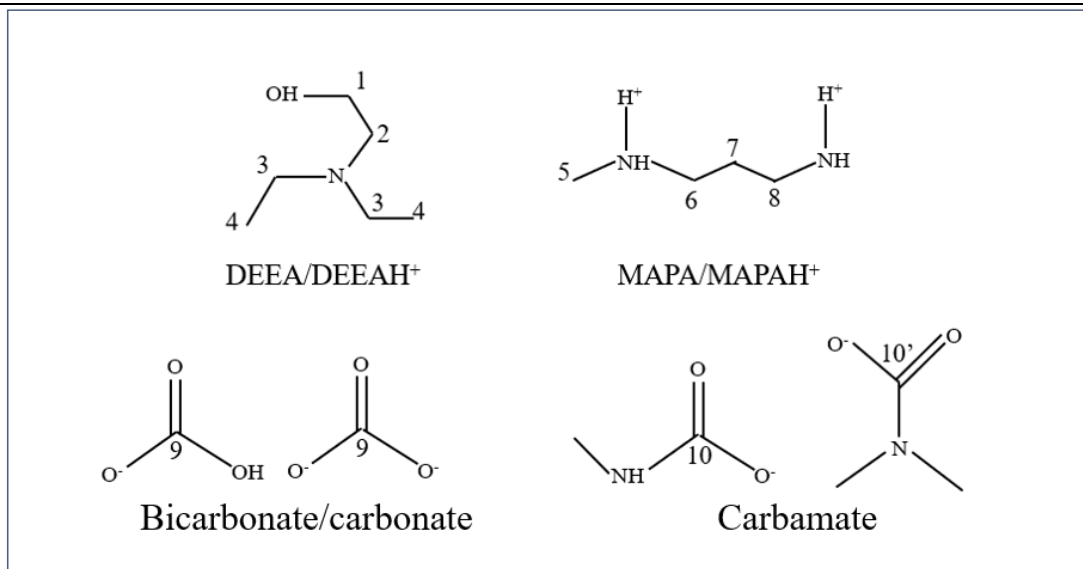
Figure: 3-4 Molecular structure of the main substances contained in MAPA/DEEA absorbents

NMR analysis of the fresh solvent before CO_2 absorption by the MAPA/DEEA absorber in Figures 3-5 (Spectrum 1) revealed four carbon signals at 58.77 ppm, 53.17 ppm, 48.47 ppm, and 10.13 ppm in the 13C NMR spectra, which corresponded to C1, C2, C3, and C4 in the molecular structure of DEEA, respectively. Four carbon signals at 34.59 ppm, 46.77 ppm, 31.80 ppm, and 38.58 ppm, which correspond to C5, C6, C7, and C8 in the structure of the MAPA molecule, were also observed.

After the absorption of CO_2 by the absorber, three new signal peaks were found in the spectrum (2) in Figs. 3-5 at 164.68 ppm, 164.32 ppm, and 161.18 ppm, which represent C10 and C10' in the structure of carbamate and C9 in the structure of carbonate/bicarbonate, respectively. Analyzing the amphiphilic ion mechanism[13], it can be inferred that when the MAPA/DEEA absorber absorbs CO_2, MAPA will react with CO_2 first, and the reaction product is carbamate, and then DEEA will react with CO_2 to produce bicarbonate. This phenomena can be explained by the fact that MAPA is a primary amine and that, in contrast to DEEA, which is a tertiary amine, MAPA reacts with CO_2 first.

Plot (3) in Figure 3-5 shows the solution characterization results after the rich solution was resolved at a temperature of 90 °C. As can be seen from the figure, after the absorber was desorbed at high temperature, the signal peaks of bicarbonate as well as almost all disappeared, but the signal peaks of carbamate still existed. According to this phenomenon, it can be inferred that in the desorption process of the absorbent, the bicarbonate was hydrolyzed first by heat, and then the carbamate started to hydrolyze. As a result, the absorption and desorption processes are diametrically opposed, with the desorption process being the response that the absorption process reverses.
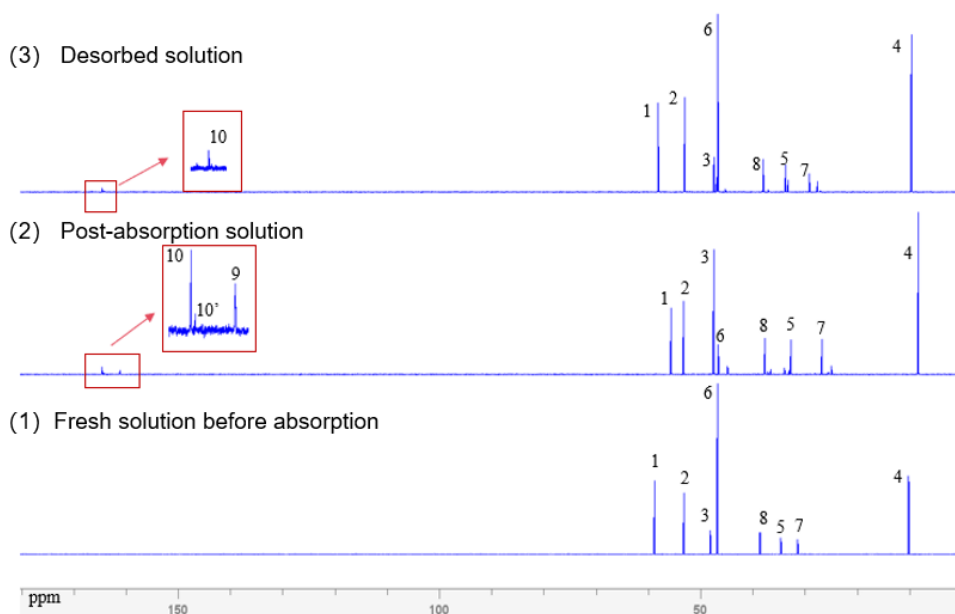
Figure 3-5: NMR carbon spectra of fresh, post-absorption and desorbed solutions before CO_2 absorption by MAPA/DEEA absorbent (30 wt%, 10:20)

3.5 Mechanism of CO_2 Capture by MAPA/DEEA System

Figure 3-6 shows the mechanism of CO_2 capture by the MAPA/DEEA system.
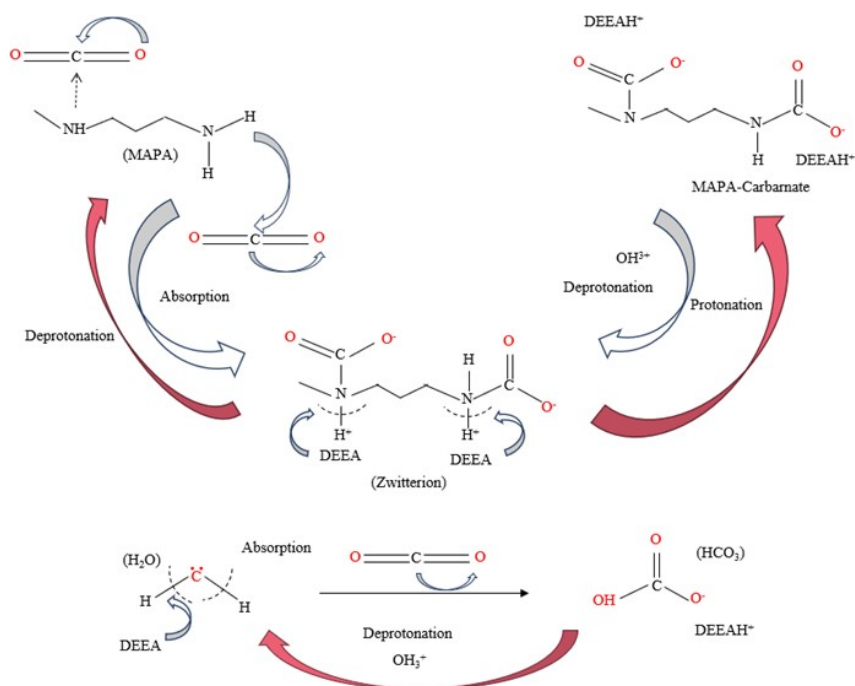
Figure 3-6: Mechanism of CO_2 capture by MAPA/DEEA system

MAPA first reacts with CO_2 at a high rate, a process that generates amphoteric intermediates, and DEEA converts the amphoteric intermediates generated by MAPA into carbamates. During the whole absorption process, DEEA's ability to absorb CO_2 is weaker than that of MAPA, but DEEA can promote the dissolution of CO_2 in water to carbonate or bicarbonate. It can also react with the protonated amine MAPAH+ to generate MAPA again, and the generated MAPA can continue to react with CO_2. Therefore, in the MAPA/DEEA absorption system, MAPA can not only promote the reaction rate of the composite absorber to CO_2, but also greatly improve the loading capacity of the composite absorber to CO_2. And DEEA can act as a proton receptor to improve the CO_2 absorption capacity of MAPA.

3.6 Summary of the chapter

The MAPA/DEEA composite organic amine CO_2 collection system was examined in this chapter, and the following findings were made:

- The absorber had the best CO_2 absorption performance with an absorption load of 0.97 mol CO_2/mol amine when the MAPA/DEEA absorption system was controlled with a total amine concentration of 30 wt%, a concentration ratio of 10 wt%:20 wt%for MAPA and DEEA, and an absorption temperature of 308.15 K.

- At 90 ℃, the saturated absorbent after absorbing CO_2 has a good desorption effect, at this time, the absorbent has not reached the boiling point, to avoid the loss of the absorbent caused by the absorption of the absorbent by thermal boiling and evaporation. Combined with the desorption effect and energy consumption of desorption, it was determined that the combined desorption effect of the absorbent at 90 ℃was the best.

- The MAPA/DEEA absorption system was analyzed by NMR spectroscopy and the reaction principle between the absorber and CO_2 was deduced: MAPA reacted with CO_2 firstly to generate the amphoteric intermediate product. Then DEEA deprotonates the product to produce carbamate, MAPA can promote the reaction rate of the compound absorbent to CO_2, and DEEA can act as a proton acceptor to enhance the CO_2 absorption ability of MAPA.

4. REFERENCES

[1]   Hou Meifang. Current Status, Challenges, and Countermeasures of China's Energy Transition and Energy Security Under the Goal of Carbon Neutrality [J]. Journal of Southwest Petroleum University (Natural Science Edition), 2023, 45(2): 1-10.

[2]   World Meteorological Organization: Released the "State of the Global Climate 2022" Report [J]. Energy Conservation and Environmental Protection, 2023(05): 8.

[3]   Liu Y, Fan W, Wang K, et al. Studies of CO2 absorption/regeneration performances of novel aqueous monothanolamine (MEA)-based solutions [J]. Journal of Cleaner Production, 2016, 112: 4012-4021.

[4]   Du J, Yang W, Xu L, et al. Review on post-combustion CO2 capture by amine blended solvents and aqueous ammonia, Chemical Engineering Journal, 2024, 488: 1385-8947.

[5]   X. Luo, S. Liu, H. Gao, et al. Tontiwachwuthikul, Z. Liang, An improved fast screening method for single and blended amine-based solvents for post-combustion CO2 capture, Separation and Purification Technology, 2016, 169: 279–288.

[6]   T. Sema, A. Naami, K. Fu, et al. Comprehensive mass transfer and reaction kinetics studies of CO2 absorption into aqueous solutions of blended MDEA–MEA, Chemical Engineering Journal, 2012, 209: 501–512.

[7]   Chen Jie, Guo Qing, Hua Yihua, et al. Experimental Study on Decarbonization Performance of MDEA+MEA/DEA Mixed Amine Solution [J]. Natural Gas Industry, 2014, 34(5): 137-143.

[8]   Hairul N A H, Shariff A M, Bustam M A. Mass transfer performance of 2-amino-2-methyl-1-propanol and piperazine promoted 2-amino-2-methyl-1-propanol blended solvent in high pressure CO2 absorption [J]. International Journal of Greenhouse Gas Control, 2016, 49: 121-127.

[9]   SUTAR P N, VAIDYA P D, KENIG E Y. Activated DEEA solutions for CO2 capture-A study of equilibrium and kinetic characteristics [J]. Chemical Engineering Science, 2013, 100: 234-241.

[10]   Ji L, Yu H, Li K, et al. Integrated absorption-mineralisation for low-energy CO2 capture and sequestration [J]. Applied Energy, 2018, 225: 356-366.

[11]   Li Y, Liu C, Parnas R, et al. The CO2 absorption and desorption performance of the triethylenetetramine + N, N-diethylethanolamine + H2O system [J]. Chinese Journal of Chemical Engineering, 2018, 26(11): 2351-2360.

[12]   Diamond L W, Akinfiev N N. Solubility of CO2 in water from -1.5 to 100 °C and from 0.1 to 100 MPa: evaluation of literature data and thermodynamic modelling [J]. Fluid Phase Equilibria, 2003, 208(1): 265-290.

[13]   P. V. Danckwerts. The reaction of CO2 with ethanolamines [J]. Chemical Engineering Science, 1979, 34(4): 443-446.

#243: Assessment of pedestrian health risk under the coupling effect of urban street canyon pollutants and heat waves

Xu Li[1], Jizhou Liu[2], Xiangyuan Zhu[3], Jiying Liu[4]

[1] School of Thermal Engineering, Shandong Jianzhu University, Jinan, China, lixu8333@163.com
[2] School of Thermal Engineering, Shandong Jianzhu University, Jinan, China, liujizhou20@sdjzu.edu.cn
[3] School of Thermal Engineering, Shandong Jianzhu University, Jinan, China, xyzhu0117@foxmail.com
[4] School of Thermal Engineering, Shandong Jianzhu University, Jinan, China, JXL83@sdjzu.edu.cn

Abstract: In urban environments, pedestrian health is affected by both temperature and pollutants during commuting, and the shape of urban structures and afforestation can mitigate these health risks. Computational fluid dynamics (CFD) was used to establish a method considering different aspect ratios (building height/street width, AR = H/W =1, 1.25; W = 20 m) and leaf area density (LAD) were used to obtain the distribution of pollutant concentration and temperature in the street valley. Meanwhile, Environmental Quality index (EQI) was introduced to better evaluate the health risk to pedestrians under the coupling of the two. The results show that high LAD can improve the thermal environment of urban street valley and can reduce the pedestrian activity area by up to 2 ℃, but it also leads to the accumulation of pollutants. Trees can reduce the air flow in the street canyon, and the vortex effect leads to the accumulation of pollutants mainly on the leeward side, and the concentration of leeward side is significantly higher than that on windward side. In the deep street valley, vegetation has great influence on the area above the tree canopy but has limited influence on the area below the tree canopy. In the deep street valley, EQI is significantly lower than that in the shallow street valley. At the pedestrian level, EQI almost does not change with the change of trees. Finally, we found that the deep street valley is more suitable for taller trees and the shallow street valley is more suitable for pedestrians.

Keywords: Computational Fluid Dynamics; Tree Planting; Air Quality; Environmental Quality Index; Pedestrian Health

1. INTRODUCTION

In recent decades, with the acceleration of urbanization, the urban heat wave has also been intensifying (Pu and Yang, 2014, Juan et al., 2017), which poses a great risk to the health of pedestrians in urban blocks (Lu et al., 2023, Chen et al., 2023a). Therefore, outdoor thermal comfort has become an increasingly concerned health issue. At the same time, traffic pollution, as the largest outdoor source of urban pollution, has also increased sharply, resulting in the continuous deterioration of urban air quality (Hang et al., 2012, Cui et al., 2023), and air quality has also become a key factor affecting pedestrian health. In order to effectively improve the air quality and thermal environment, it is necessary to make reasonable planning for the block shape parameters.

Urban tree planting can effectively reduce the temperature of urban blocks, and research on the decrease of surface and air temperature caused by urban tree planting has been widely carried out (Sharmin et al., 2023, Chen et al., 2023b). The main purpose of urban planting is to enhance urban beauty (Barron et al., 2021) and improve urban microclimate. The tree canopy can effectively intercept short-wave radiation from the sun and reduce ambient temperature through evaporation and heat dissipation (Simon et al., 2018). Planting tall trees with high porosity in urban built-up areas has a positive impact on reducing street valley temperature (Morakinyo et al., 2017), and the transpiration of street trees can reduce the temperature at 1.5 m by 0.43℃ (Gromke et al., 2015). Although urban tree planting can improve the thermal environment comfort of urban blocks, due to the obstructive effect of vegetation on air flow, it will lead to insufficient diffusion of pollutants, which will have a negative impact on air quality (Zhu et al., 2022, Yang et al., 2020). Planting trees in double rows will increase the pollutant concentration in the street valley (Cui et al., 2023), and with the increase of Leaf Area Index (LAI), the decrease of pollutant concentration in the street valley will be more unfavorable (Yang et al., 2020). Block shape parameters also play an important role in pollutant concentration and temperature (Guo et al., 2022, Zheng et al., 2022). In urban blocks with low building density, the diffusion rate of pollutants is higher (Hang et al., 2012). With the increase of block buildings, the thermal comfort of pedestrians will be effectively improved (Li et al., 2020).

At present, studies on urban street and valley environment mainly focus on a single thermal environment or air quality level (Gromke et al., 2015, Yang et al., 2020), but there are few studies on the impact of the coupling of thermal environment and air pollutants on pedestrian health, and there are also few studies on the change of vegetation transpiration on street and valley microenvironment. Therefore, the paper adopted numerical simulation technology to obtain the distribution of pollutant concentration and temperature in the street valley by setting the shape parameters of different blocks and the leaf area density (*LAD*) of plants and obtained the weight of temperature and pollutant concentration through sensitivity analysis (Li et al., 2023). The two were coupled into an Environmental Quality Index (*EQI*) to assess pedestrian health risks under the dual impact.

2. STREET VALLEY MODEL AND NUMERICAL SIMULATION
2.1. Street valley model

Figure 1 shows the urban street valley model when the aspect ratio (*AR*) is equal to 1. In the figure, the building height, road width and tree crown length are *H*, the tree crown height and width are 0.2 *H*, the two pollution sources are 0.05 *H* wide, are 0.2 *H* apart and located in the middle of the road, and the flow field is 3 *H* high and *H* wide, where *H* = 20 m. Road pollution is mainly automobile exhaust emission (Cui et al., 2023), CO is selected as a pollution source, and the mass flow rate is 0.000365 kg/s (Cui et al., 2023). The density of the building envelope is 2000 kg/m³, the specific heat capacity is 900 J/(kg K), the thermal conductivity is 0.8 W/(m K), the ground density is 1600 kg/m³, the specific heat capacity is 300 J/(kg K), and the thermal conductivity is 1.5 W/(m K). During the simulation of solar radiation, DO radiation model was selected to change the solar incidence Angle by adjusting the vector value, and direct solar radiation and diffuse solar radiation were set to 750 W/m² and 200 W/m² (Gromke et al., 2015). Set plants as porous media, the measurement of canopy porosity of vegetation refers to the method of kenney et al. (Kenney, 1987), and the transpiration of vegetation is reflected by changing the leaf area density (*LAD*) of plants (Li et al., 2022). The setting of the mathematical model of vegetation is introduced later.

Figure 1: AR=1 time street valley numerical simulation calculation model

2.2. Organisation of the paper

Leaf area index (LAI) is the projected area per unit of land, usually expressed by the leaf area density, expressed by equation 1. Plants increase the flow resistance of the surrounding environment, and the momentum source term of plants has been established (Buccolieri et al., 2019), which is expressed by equation 2. Moreover, the gaps between the leaves of the tree crown led to sharp changes in fluid pressure, changes in turbulent kinetic energy and turbulent diffusion rate, and plants convert uniform flow into wake turbulence. However, compared with turbulence generated by shear, the inner size of the tree crown is smaller, resulting in faster dissipation. Therefore, the researchers parameterized the energy source terms of turbulent kinetic energy k and turbulent dissipation rate ε. It is represented by equations 3 and 4.

Equation 1: Relation between LAD and LAI.

$$LAI = \int_0^{H_{tree}} LAD(z)\, dz$$

Where:

H_{tree} = Crown height (m)

LAD = leaf area density (m²/m³)

Equation 2: Quantity of momentum term in canopy.

$$S_{ui} = -\rho_{air} LAD C_d |u| u_i$$

Where:

ρ_{air} = air density (kg/m³)

C_d = drag coefficient (C_d = 0.2)

u = wind speed (m/s)

ui = vector wind speed (m/s)

Equation 3: Turbulent kinetic energy source term in canopy.

$$S_k = -\rho_{air} LAD C_d (\beta_p |u|^3 - \beta_d |u| k)$$

Equation 4: Turbulent dissipation rate source term in canopy.

$$S_\varepsilon = -\rho_{air} LAD C_d (C_{\varepsilon 4} \beta_p \frac{\varepsilon}{k} |u|^3 - C_{\varepsilon 5} \beta_d |u| \varepsilon)$$

Where:

β_p = the fraction of turbulent kinetic energy (β_p = 0 ~ 1)

β_d = dimensionless coefficient of turbulent cascade in short circuit

k = turbulent kinetic energy (m²/s²)

ε = turbulent dissipation rate (m³/s²)

$C_{\varepsilon 4}, C_{\varepsilon 5}$ = model constants (Obtained by consulting the references) (Hefny Salim et al., 2015, Amorim et al., 2013)

Due to the temperature difference between the tree crown leaves and the surrounding air, complex mass and heat exchange will be generated, and energy exchange mainly includes radiation flux and sensible heat flux. Tree canopy can cool its surrounding environment through transpiration, and the leaf surface energy balance model of transpiration effect is shown in Equation 5:

Equation 5: The energy balance of transpiration on leaves.

$$R_n - C - \lambda E = M + S$$

Where:

R_n = net radiation flux (W/m²)

C = net sensible heat flux (W/m²)

λ = latent heat of water evaporation (KJ/kg) (λ = 2450 KJ/kg) (Pattnaik et al., 2024)

λE = net latent heat flux (W/m^2)

M = the energy stored by photosynthesis and respiration in trees (W/m^2)

S = the energy stored in the tree's internal form (W/m^2)

Many studies believe that the energy stored by trees themselves can be ignored (Manickathan et al., 2018), so the equation 6 can be simplified as:

Equation 6: The energy balance after simplification.
$$R_{\mathrm{n}} = C + \lambda E$$

The net sensible heat flux and net latent heat flux of the blade can be calculated by equations 7 and 8.(Tian et al., 2017)

Equation 7: The net sensible heat flux on leaves.
$$C = \frac{2}{r_{\mathrm{a}}} \rho_{\mathrm{air}} C_{\mathrm{p,air}} (T_{\mathrm{l}} - T)$$

Where:

r_{a} = resistance to sensible heat exchange between blade and air (s/m)

$C_{\mathrm{p,air}}$ = specific heat capacity of air at constant pressure (J/(kg·K))

T_{l} = blade surface temperature (℃)

T = ambient temperature (℃)

Equation 8: The net latent heat flux on leaves.
$$\lambda E = \frac{2}{r_{\mathrm{a}} + r_{\mathrm{s}}} \frac{\rho_{\mathrm{air}} R_{\mathrm{a}} L_{\mathrm{v}}}{P_0 R_{\mathrm{v}}} (\varepsilon_{\mathrm{vl}} - \varepsilon_{\mathrm{v}})$$

Where:

r_{a} = resistance to sensible heat exchange between blade and air (s/m) (Equation 9)

r_{s} = diffusion resistance of stomata (s/m) (200 ~ 400 s/m) (Leuzinger et al., 2010)

R_{a} = dry air gas constant (J/(kg·K)) (287.042 J/(kg·K))

L_{v} = latent heat of water evaporation (J/kg)

P_0 = local atmosphere (pa) (101.325 kPa)

R_{v} = wet air gas constant (J/(kg·K)) (461.524 J/(kg·K))

$\varepsilon_{\mathrm{vl}}$ - ε_{v} = pressure difference between blade surface and surrounding air (Pa)

Equation 9: Resistance to sensible heat exchange between blade and air.
$$r_{\mathrm{a}} = A \left(\frac{u}{d}\right)^{-0.5}$$

Where:

A = empirical coefficient of resistance (s$^{0.5}$/m) (87 s$^{0.5}$/m)

d = characteristic blade diameter (m)

2.3. Health risk comprehensive assessment indicators

In order to better assess the dual effects of air pollutants and temperature on pedestrian health, we introduce a new parameter, the Environmental Health Index (*EQI*), to represent the degree of impact on pedestrian health. Since pollutant concentration and

temperature are two parameters that are not highly correlated, they are converted into the corresponding pollutant score *S(P)* and temperature score *S(T)* and coupled into *EQI* by setting weights for the two parameters. The calculation of *EQI* is shown in Equation 10.

Equation 10: EQI calculation formula.

$$EQI = \alpha S(P) + \beta S(T)$$

Where:

- *α, β* = weighted value (*α + β = 1*)
- *S(P), S(T)* = scores of pollutants and temperatures (Equation 11 and Equation 12)

Here, we used back propagation (BP) neural network to predict the data of the impact of temperature and pollutant coupling on human health (Zhou et al., 2023), and then calculated the weight corresponding to temperature and pollutant through Sobol sensitivity analysis after the predicted data and obtained α = 0.67 and β = 0.33 after analysis. For the calculation of S(P) and S(T), the logistic function is introduced for pre-processing calculation. The logistic function is shown in Equation 11.

Equation 11: EQI calculation formula.

$$EQI = \alpha S(P) + \beta S(T)$$

Where:

α, β = weighted value (*α + β = 1*)

S(P), S(T) = scores of pollutants and temperatures (Equation 11 and Equation 12)

Here, we used back propagation (BP) neural network to predict the data of the impact of temperature and pollutant coupling on human health (Zhou et al., 2023), and then calculated the weight corresponding to temperature and pollutant through Sobol sensitivity analysis after the predicted data, and obtained α = 0.67 and β = 0.33 after analysis. For the calculation of S(P) and S(T), the logistic function is introduced for pre-processing calculation. The logistic function is shown in equation 11.

Equation 11: Logistic function.

$$f(x) = \frac{L}{1 + e^{-b(x-x_0)}}$$

Where:

L = curve maximum

b = curve steepness

x_0 = the midpoint of the curve

Select the pollutant concentration range from 40 to 120 μg/m3 and the temperature from 28 to 42 ° C, so $f(p) = \frac{120}{1+e^{-0.05(P-120)}}$, $f(T) = \frac{24}{1+e^{-0.3(T-42)}}$ (Li et al., 2022)

Equation 12: Pollutant scoring function.

$$S(P) = \frac{f(P)_{\text{predicted}} - f(P)_{\text{upper}}}{f(P)_{\text{lower}} - f(P)_{\text{upper}}}$$

Equation 13: Temperature scoring function.

$$S(T) = \frac{f(T)_{\text{predicted}} - f(T)_{\text{upper}}}{f(T)_{\text{lower}} - f(T)_{\text{upper}}}$$

In the formula, subscripts are predicted, upper and lower are divided into simulated data, maximum data and minimum data. In the range of temperature and pollutants, the lower the impact on human health, so the higher the score, the better the environment.

2.4. Grid independence test and experimental verification

The numerical simulation usually requires a grid independence test, which selects 1.44 million coarse grids, 2.21 million medium grids, and 2.8 million fine grids. Figure 2 shows the simulated values of air temperature and wind speed pollutant concentration of the three grids at different z/H. For the simulation results at the temperature of z/H = 0, the coarse grid data has a large gap with the results of the other two grids, and the results of the coarse grid of air pollutants have a large deviation from the other two grids. Through the grid independence test, 2.21 million grids are finally selected.
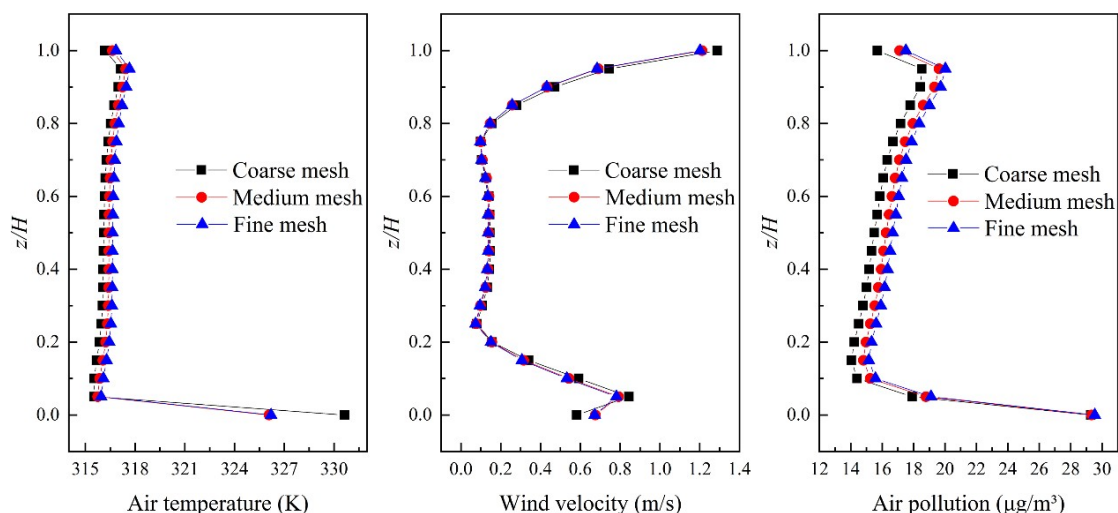
Figure 2: Grid independence test

After the grid independence test, the simulation needs to be verified experimentally. We used the k-e model to simulate the influence of vegetation on the flow field in the street valley, so the wind tunnel experiment data of the CODASC project (Concentration Data of Street Canyons, http://www.codasc. de) was used for experimental verification. At the leeward side of Wall A, y/*H* = 0, y/*H* = 1.68, y/*H* = 3.38, 11 points in each z direction 0 to 1 *H* were evenly selected for monitoring concentration values. The comparison between the simulation results and the experimental results is shown in Figure 3. The CFD simulation value is much smaller than the experimental value, so the lowest position is not taken into account. Figure 3 shows that the maximum numerical error between CFD simulation and experimental simulation is 6.2%. By comparing with the wind tunnel experimental data of CODASC project, it is found that the simulation has a good agreement, so the model is sufficient for further study.
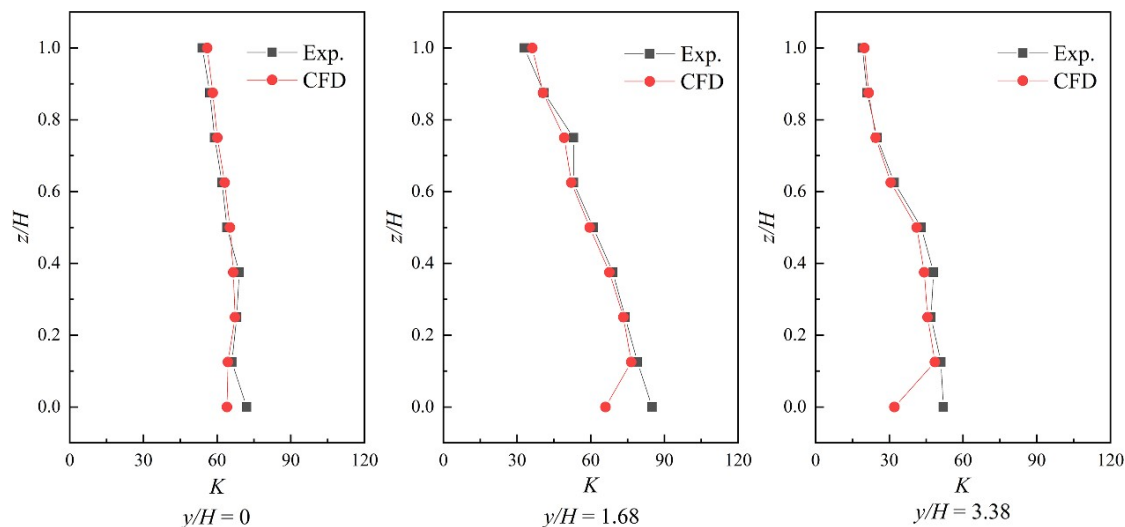

Figure 3: Comparison of wind tunnel experiment and simulation results

3. RESULTS

In order to study the effects of plant transpiration and obstruction on street valley temperature and pollutant concentration under different aspect ratios, street valley aspect ratios of 1 and 1.25 were selected in the research model. The larger the *LAD*, the higher the crown density, the greater the transpiration effect, and the greater the airflow resistance. The *LAD* selected 2.0, 2.5, and 3.0 m^2/m^3 respectively to simulate the street valley environment with different crown densities. The intensity of solar radiation is unchanged, and the direction of solar irradiation is downwind irradiation and downwind irradiation.

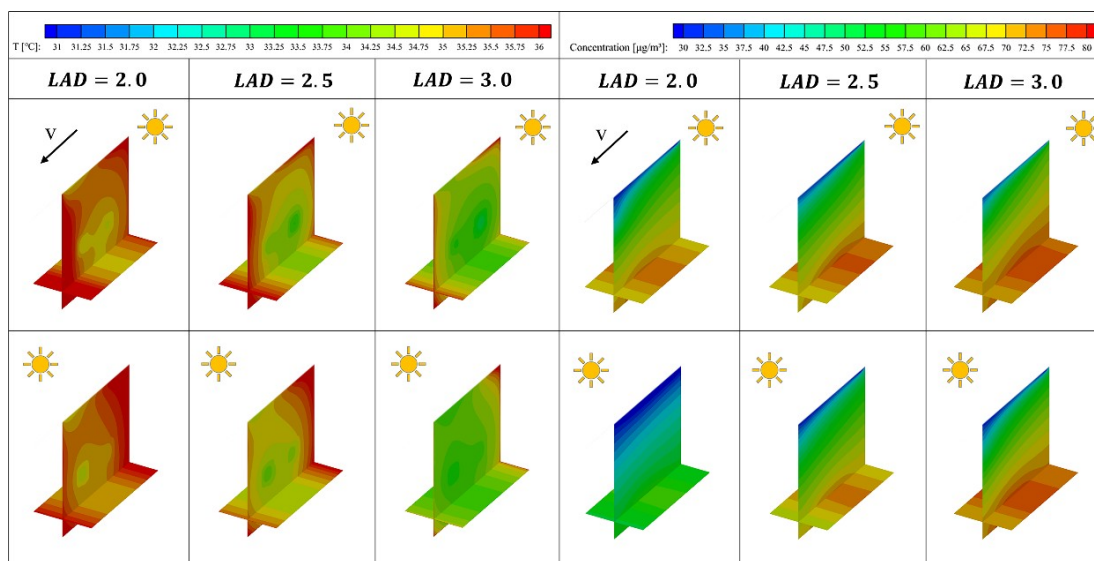### 3.1. Numerical simulation results in shallow street Valley

Figure 4(a) shows the temperature distribution of the street valley under different solar incidence angles and *LAD*. With the increase of *LAD*, the transpiration of plant crown leaves is intensified, which increases the internal latent heat transfer and lowers the tree crown temperature. Then, the sensible heat transfer between the tree crown and the surrounding air reduces the ambient air temperature. Every 0.5 m^2/m^3 increase in *LAD*, the temperature around the vegetation irradiated by the downwind side and the leeward side will decrease by about 0.5℃. Due to the physical properties of the building envelopes and ground materials, the building and ground walls will absorb a large amount of solar heat, thus forming a high-temperature environment around them. When *LAD* =

2.0 m^2/m^3, the building and ground temperature is about 2℃ higher than the temperature around the tree canopy, and the high-temperature area is large. When LAD = 3.0 m^2/m^3, the temperature of the building and ground is about 2℃ higher than that around the tree canopy. The temperature difference between the building and the ground temperature and the temperature around the tree canopy becomes larger, up to 3℃, but due to the stronger transpiration of plants, the high temperature area is significantly smaller than the former. Under different LAD, the ambient temperature under downwind irradiation is higher than that under leeward irradiation, which may be due to the increase in the temperature of the downwind as the sun continues to irradiate the downwind, and the heat is transferred to the street valley environment through wind flow, thus aggravating the street valley thermal environment.

When studying the thermal environment of street valley, it is necessary to pay attention to the temperature distribution at pedestrian level. We chose a plane temperature distribution with a height of 1.5 m as the temperature perceived by pedestrians. Figure 4 shows that with the increase of LAD, the thermal comfort of the pedestrian level is improved to some extent. When LAD is increased by 1 m^{-2}/m^{-3}, the temperature decreases by about 1.2℃, and the temperature decreases by up to 2℃ near the building wall. Therefore, planting larger LAD trees in shallow street valley can effectively improve the thermal environment of the street valley.

Figure 4(b) shows the distribution of pollutants in the street valley under different solar incidence angles and LAD. The increase of LAD increases the resistance of the tree crown to the air flow, impedes the gas flow, reduces the gas diffusion rate, and leads to the deposition of pollutants, and increases the pollutant concentration in the street and valley. For every 0.5 m^2/m^3 increase in LAD, the pollutant concentration increases by 5 to 10 µg/m^3. Due to the obstruction effect of the tree crown and the gravity effect of pollutants, the concentration of pollutants is small in the high place and large in the low place, and the concentration of pollutants around the tree crown is obviously greater than that in the surrounding environment. Similar to the temperature distribution, the concentration of pollutants under downwind irradiation is higher than that under leeward irradiation.

Due to the shear effect of buildings and vegetation on the gas, the airflow forms a vortex in the street valley, and the pollutants are carried by the airflow to the leeward side and gather in the leeward area, so that the concentration of pollutants on the leeward side is higher than that on the windward side. Figure 4(b) shows that the concentration of pollutants gradually increases in the direction of the upwind at the same height plane. The concentration of pollutants near the leeward side of the pedestrian level was higher, and the concentration of pollutants under the vegetation was higher, and the concentration under the vegetation of the pedestrian level was 5-15 µg/m^3 higher than that at other locations. Near the leeward side of the pedestrian level, the accumulation of pollutants and the increase in temperature, especially in the case of upwind exposure, will inevitably make the area unsuitable for pedestrian activities and increase the pedestrian health risk.

(a) Temperature distribution in shallow street valleys   (b) Air pollution distribution in shallow street valleys
Figure 4: Temperature and pollutant distribution map of shallow street valley

3.2. Numerical simulation results in deep street valley

In the deep street valley, the gas flow efficiency is reduced, and only part of the building walls on the windward or leeward side are directly exposed to the sun, resulting in uneven temperature distribution in the deep street Valley. It can be observed from Figure 5(a) that the temperature above the vegetation is significantly higher than that below the vegetation. This is because the density of cold air is higher than that of hot air, resulting in the settlement of cold air. Through the observation of the opposite side, with the increase of LAD, the thermal environment in the upper part of the street valley has a significant improvement, and the temperature above the vegetation can be reduced by 3℃.

However, due to the lack of sun irradiation at the bottom of the building and the ground, and the low temperature under the vegetation, the temperature difference between the leaves at the lower part of the tree crown and the surrounding environment is small, which reduces the transpiration of the leaves at the bottom. Therefore, in the deep street valley, the thermal environment under the vegetation does not improve significantly with the increase of LAD. When LAD = 2.0 m^2/m^3, the temperature distribution at the pedestrian level under downwind irradiation and leeward irradiation is relatively average, about 33.4℃, and with the increase of LAD,

the improvement effect of thermal environment is less obvious than that at the pedestrian level in shallow valley.

As mentioned above, due to the joint action of the deep street valley and the tree crown, air vortex is formed above the tree crown, and the gas diffusion effect is poor, especially the air flow effect below the tree crown is weak. It can be seen from Figure 5(b) that pollutants are mainly distributed below the tree crown. Unlike the shallow street valley, the concentration of pollutants above the canopy gradually decreases as the *LAD* increases, due to higher temperatures above the canopy and more intense gas diffusion, which intensifies the flow of the gas. In the vicinity of the tree crown, due to its obstructing effect on air flow, pollutants are deposited in this area to form a high-pollutant area, which increases with the increase of *LAD*.

As in the shallow street valley, the concentration of pollutants is higher on the lee side due to airflow, especially above the tree canopy. Similarly, at the pedestrian level, the concentration of pollutants below the tree canopy is higher than in other areas, mainly accumulating in the side near the lee side. Since the temperature under the tree canopy is significantly higher than that in the area above the tree canopy, and with the increase of *LAD*, the thermal environment under the tree canopy in deep street valley has a low improvement effect, and the concentration of pollutants also increases. Therefore, plants with higher height or smaller *LAD* can be planted in deep Street valley area.
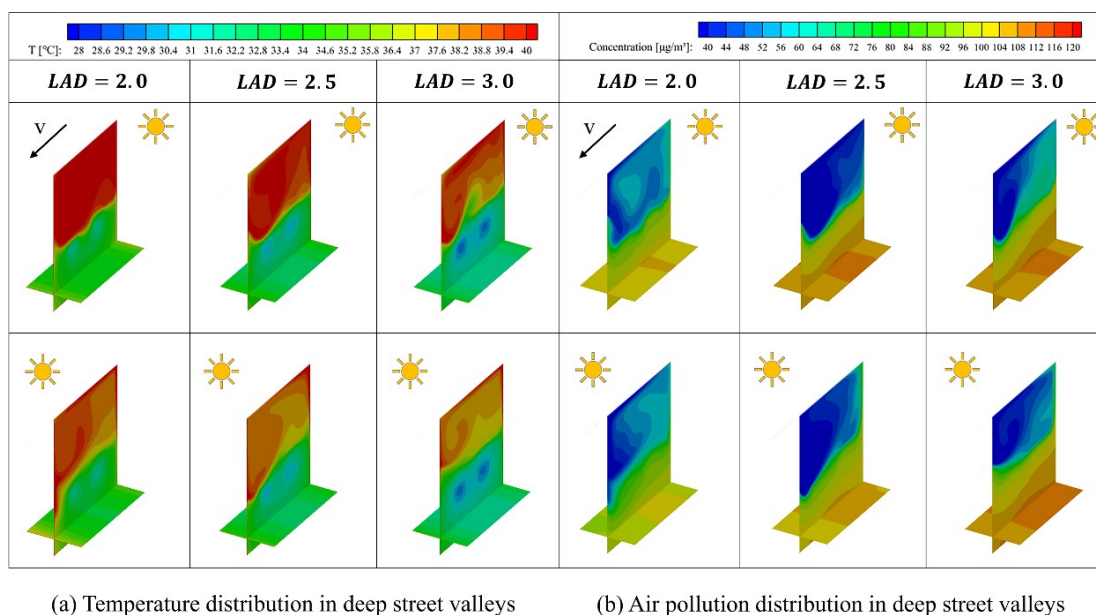

(a) Temperature distribution in deep street valleys (b) Air pollution distribution in deep street valleys

Figure 5: Temperature and pollutant distribution map of shallow street valley

3.3. Calculation and distribution of *EQI* in street valley

Chapter 2.3 introduces the purpose of introducing *EQI* and the calculation methods of pollutant score *S(P)* and temperature score *S(T)*. A higher *EQI* value means there is less risk to pedestrians and the area is more suitable for pedestrian activity.

Figure 6(a) shows the distribution of *EQI* values in the urban shallow street valley. In shallow street valley, due to the vortex effect of air flow, pollutants are mainly concentrated in the lee side. Meanwhile, under the sunlight irradiation of two different positions, the temperature of the lee side is higher than that of the central area of the street valley. Therefore, the *EQI* of the lee side of the shallow street valley is lower than that of other areas of the street valley. In Figure 4(a), it can be seen that under the irradiation of the windward side, the street temperature is generally higher than that under the irradiation of the leeward side. At the same time, there is little difference in pollutant concentration between the two cases, and the weight value of pollutant score is smaller than that of temperature, forming an area with a larger *EQI* value under the irradiation of the leeward side. At the pedestrian level, when the windward side is illuminated, there is a wider range of higher temperature areas near the windward side at the pedestrian level, and the *EQI* near the windward side is lower. At the same time, when the leeward side is illuminated, there is a wider range of higher temperature areas near the leeward side at the pedestrian level, and the *EQI* near the leeward side is lower.

Figure 6(b) shows the distribution of *EQI* values in the urban deep street valley. There is a high temperature area above the tree canopy in deep street valley, which is at the peak of the temperature range in the selected temperature score *S(T)*, so the *EQI* above the tree canopy is low. In the main activity area of pedestrians below the tree canopy, in the deep street valley, due to the weakening of air flow and the blocking of sun irradiation, the increase of tree *LAD* has little influence on temperature, but the overall trend of temperature also increases. Although the overall pollutant concentration also increases slightly, the weight of pollutant concentration score is small. Therefore, the overall *EQI* value of the area below the tree canopy of deep canyon increases with the increase of *LAD* value. At the pedestrian level, under different lighting conditions, the temperature distribution in the deep street valley is uniform and the pollutant concentration near the windward side is lower, so the *EQI* near the windward side is higher.

Through the analysis of *EQI* in shallow street valley and deep street valley, it is found that *EQI* in shallow street valley is generally higher than that in deep street valley, so shallow street valley has less risk to pedestrian health and is more suitable for pedestrian activities.
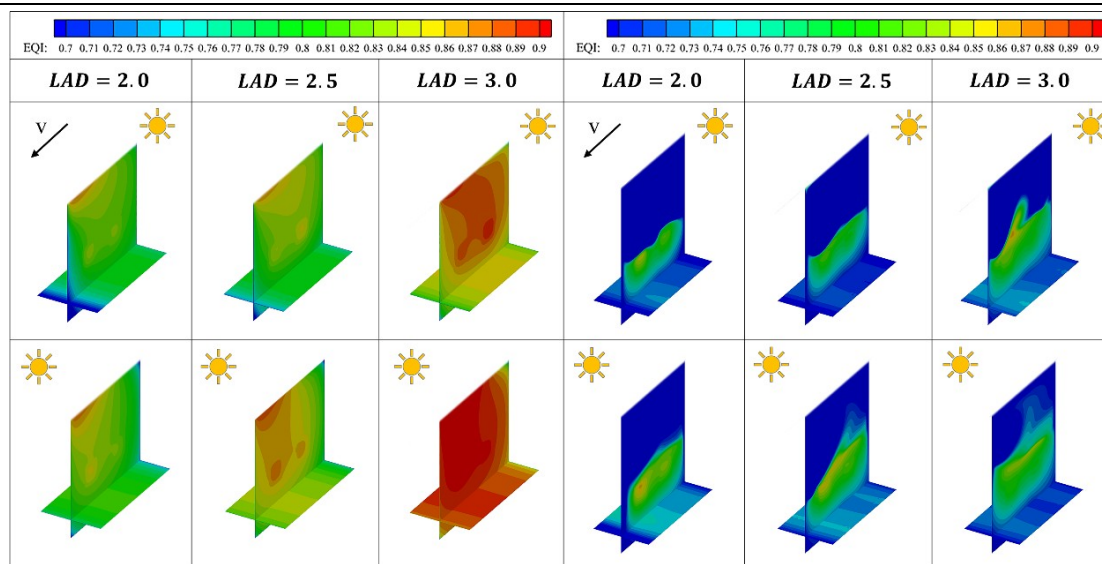
(a) EQI distribution in shallow street valleys   (b) EQI distribution in deep street valleys

Figure 6: EQI distribution of shallow street valley and deep street valley

4. CONCLUSION

A three-dimensional urban street valley model was established, and the distribution of pollutant concentration and temperature in street valley was obtained through numerical simulation technology, and *EQI* was introduced to evaluate the impact of pollutant and temperature coupling on pedestrian health. The following main conclusions were obtained through a series of work

(1) The *EQI* value of deep street valley is generally lower than that of shallow street valley, and pedestrians are more suitable for activities in shallow street valley.

(2) The concentration of pollutants in the street valley mostly accumulates on the leeward side, and the air temperature is higher than that on the leeward side.

(3) In the shallow street valley, the increase of green plant *LAD* can effectively improve the thermal environment in the street valley, and the maximum temperature drop can reach $2°C$, but it will also increase the concentration distribution of pollutants inside the valley. In the deep street valley, changing *LAD* has a greater effect on the area above the tree crown, but a limited effect on the area below the tree crown.

In this paper, only air temperature is considered as a single parameter in the thermal environment, and more temperature parameters will be considered in future studies. In the future, other building form parameters, tree planting density and tree porosity will be further considered, and the street environment of a larger area will be studied, which will be combined with the experiment to obtain more practical conclusions.

5. REFERENCES

AMORIM, J. H., RODRIGUES, V., TAVARES, R., VALENTE, J. & BORREGO, C. 2013. CFD modelling of the aerodynamic effect of trees on urban air pollution dispersion. Science of The Total Environment, 461-462, 541-551.

BARRON, S., SHEPPARD, S., KOZAK, R., DUNSTER, K., DAVE, K., SUN, D. & RAYNER, J. 2021. What do they like about trees? Adding local voices to urban forest design and planning. Trees, Forests and People, 5, 100116.

BUCCOLIERI, R., SANTIAGO, J.-L., RIVAS, E. & SáANCHEZ, B. 2019. Reprint of: Review on urban tree modelling in CFD simulations: Aerodynamic, deposition and thermal effects. Urban Forestry & Urban Greening, 37, 56-64.

CHEN, L., WANG, H., WANG, Z. & DONG, Z. 2023a. Estimating the mortality attributable to indoor exposure to particulate matter of outdoor origin in mainland China. Science of The Total Environment, 872, 162286.

CHEN, T., MEILI, N., FATICHI, S., HANG, J., TAN, P. Y. & YUAN, C. 2023b. Effects of tree plantings with varying street aspect ratios on the thermal environment using a mechanistic urban canopy model. Building and Environment, 246, 111006.

CUI, P.-Y., JI, R., HE, L., ZHANG, Z., LUO, Y., YANG, Y. & HUANG, Y.-D. 2023. Influence of GI configurations and wall thermal effects on flow structure and pollutant dispersion within urban street canyons. Building and Environment, 243, 110646.

GROMKE, C., BLOCKEN, B., JANSSEN, W., MEREMA, B., VAN HOOFF, T. & TIMMERMANS, H. 2015. CFD analysis of transpirational cooling by vegetation: Case study for specific meteorological conditions during a heat wave in Arnhem, Netherlands. Building and Environment, 83, 11-26.

GUO, G. Z., YU, Y., KWOK, K. C. S. & ZHANG, Y. 2022. Air pollutant dispersion around high-rise buildings due to roof emissions. Building and Environment, 219, 109215.

HANG, J., LI, Y., SANDBERG, M., BUCCOLIERI, R. & DI SABATINO, S. 2012. The influence of building height variability on pollutant dispersion and pedestrian ventilation in idealized high-rise urban areas. Building and Environment, 56, 346-360.

HEFNY SALIM, M., HEINKE SCHLüNZEN, K. & GRAWE, D. 2015. Including trees in the numerical simulations of the wind flow in urban areas: Should we care? Journal of Wind Engineering and Industrial Aerodynamics, 144, 84-95.

JUAN, Y.-H., YANG, A.-S., WEN, C.-Y., LEE, Y.-T. & WANG, P.-C. 2017. Optimization procedures for enhancement of city breathability using arcade design in a realistic high-rise urban area. Building and Environment, 121, 247-261.

KENNEY, W. A. 1987. A method for estimating windbreak porosity using digitized photographic silhouettes. Agricultural and Forest Meteorology, 39, 91-94.

LEUZINGER, S., VOGT, R. & KöRNER, C. 2010. Tree surface temperature in an urban environment. Agricultural and Forest Meteorology, 150, 56-62.

LI, Z., ZHANG, H., JUAN, Y.-H., LEE, Y.-T., WEN, C.-Y. & YANG, A.-S. 2023. Effects of urban tree planting on thermal comfort and air quality in the street canyon in a subtropical climate. Sustainable Cities and Society, 91, 104334.

LI, Z., ZHANG, H., JUAN, Y.-H., WEN, C.-Y. & YANG, A.-S. 2022. Effects of building setback on thermal comfort and air quality in the street canyon. Building and Environment, 208, 108627.

LI, Z., ZHANG, H., WEN, C.-Y., YANG, A.-S. & JUAN, Y.-H. 2020. Effects of frontal area density on outdoor thermal comfort and air quality. Building and Environment, 180, 107028.

LU, C., LIU, Z., YANG, W., LIAO, H., LIU, Q., LI, Q. & DENG, Q. 2023. Early life exposure to outdoor air pollution and indoor environmental factors on the development of childhood allergy from early symptoms to diseases. Environmental Research, 216, 114538.

MANICKATHAN, L., DEFRAEYE, T., ALLEGRINI, J., DEROME, D. & CARMELIET, J. 2018. Parametric study of the influence of environmental factors and tree properties on the transpirative cooling effect of trees. Agricultural and Forest Meteorology, 248, 259-274.

MORAKINYO, T. E., KONG, L., LAU, K. K.-L., YUAN, C. & NG, E. 2017. A study on the impact of shadow-cast and tree species on in-canyon and neighborhood's thermal comfort. Building and Environment, 115, 1-17.

PATTNAIK, N., HONOLD, M., FRANCESCHI, E., MOSER-REISCHL, A., RöTZER, T., PRETZSCH, H., PAULEIT, S. & RAHMAN, M. A. 2024. Growth and cooling potential of urban trees across different levels of imperviousness. Journal of Environmental Management, 361, 121242.

PU, Y. & YANG, C. 2014. Estimating urban roadside emissions with an atmospheric dispersion model based on in-field measurements. Environmental Pollution, 192, 300-307.

SHARMIN, M., TJOELKER, M. G., PFAUTSCH, S., ESPERON-RODRIGUEZ, M., RYMER, P. D. & POWER, S. A. 2023. Tree crown traits and planting context contribute to reducing urban heat. Urban Forestry & Urban Greening, 83, 127913.

SIMON, H., LINDéN, J., HOFFMANN, D., BRAUN, P., BRUSE, M. & ESPER, J. 2018. Modeling transpiration and leaf temperature of urban trees – A case study evaluating the microclimate model ENVI-met against measurement data. Landscape and Urban Planning, 174, 33-40.

TIAN, Y., BAI, X., QI, B. & SUN, L. 2017. Study on heat fluxes of green roofs based on an improved heat and mass transfer model. Energy and Buildings, 152, 175-184.

YANG, H., CHEN, T., LIN, Y., BUCCOLIERI, R., MATTSSON, M., ZHANG, M., HANG, J. & WANG, Q. 2020. Integrated impacts of tree planting and street aspect ratios on CO dispersion and personal exposure in full-scale street canyons. Building and Environment, 169, 106529.

ZHENG, X., MONTAZERI, H. & BLOCKEN, B. 2022. Impact of building façade geometrical details on pollutant dispersion in street canyons. Building and Environment, 212, 108746.

ZHOU, W., WANG, Q., LI, R., ZHANG, Z., WANG, W., ZHOU, F. & LING, L. 2023. The effects of heatwave on cognitive impairment among older adults: Exploring the combined effects of air pollution and green space. Science of The Total Environment, 904**,** 166534.

ZHU, X., WANG, X., LEI, L. & ZHAO, Y. 2022. The influence of roadside green belts and street canyon aspect ratios on air pollution dispersion and personal exposure. Urban Climate, 44**,** 101236.

#244: Evaluation of thermal comfort in transportation micro-environments under different vegetation configurations

Xue Zhou [1], Wenhan An [2], Yubin Qiu [3], Jiying Liu [4]

[1] School of Thermal Engineering, Shandong Jianzhu University, Jinan, China, zx7snowy@163.com
[2] School of Thermal Engineering, Shandong Jianzhu University, Jinan, China, awh1633@163.com
[3] School of Thermal Engineering, Shandong Jianzhu University, Jinan, China, qyb200008@163.com
[4] School of Thermal Engineering, Shandong Jianzhu University, Jinan, China, JXL83@sdjzu.edu.cn

Abstract: As an important part of road system, green plants play a significant role in improving road thermal comfort. Different vegetation configurations can effectively promote road air circulation, thus significantly improving the comfort of transportation micro-environments. In this paper, ENVI-met simulation software was used to establish a numerical model of the transportation micro-environments in Jinan City, and the general Thermal climate index (UTCI) under different canopy ratio (CR) and leaf area density (LAD) under the southeast wind direction was calculated. Combined with the spatial distribution of temperature and relative humidity, the thermal comfort of the transportation micro-environments under different vegetation configurations was evaluated. The results showed that the street trees with H = 5 m and CR = 0.4 had the best cooling effect at 12:00 noon, and the temperature drop was 0.80ºC. The higher the tree height, the larger the tree crown, the worse the humidification effect, H = 5m, CR = 0.4 the best humidification effect, the moisture increment can reach 0.76%. Street trees with H = 5 m and CR = 0.6 showed the best performance in improving thermal comfort, reducing UTCI by 2.01ºC. When LAD increased by 0.5, the temperature increased by 23.75% to 24.90%, and the cooling and humidification effects of street trees with LAD = 0.5 were the most significant. Under LAD = 0.5, LAD = 1, LAD = 1.5 and LAD = 2, the UTCI of street trees was increased, and the average UTCI value ranged from 38.28°C to 39.13°C. The research results can provide references for the planning and design of road green plants, thermal comfort improvement, microclimate regulation and ecological benefit enhancement in the sustainable development of cities.

Keywords: Vegetation Configuration; transportation micro-environments; ENVI-met; UTCI; Thermal Comfort

1. INTRODUCTION

The acceleration of urbanization and population growth are increasingly impacting the urban transportation micro-environment. As a key component of the urban thermal environment, the transportation micro-environment not only plays a decisive role in improving public health and quality of life but also is essential for achieving environmental sustainability (Banerjee et al., 2024). With environmental sustainability becoming a global focus, vegetation, as a fundamental element of the urban ecosystem, has received significant attention for its ability to regulate the urban micro-climate and optimize the thermal environment (Altunkasa et al.,2020, Liu et al., 2020). Outdoor thermal comfort is influenced by climate variables such as temperature, relative humidity, mean radiant temperature, and wind speed (Meili et al., 2021), and different vegetation configurations can significantly affect the thermal comfort of the transportation micro-environment by modulating these climate variables (Xiao et al., 2024). Therefore, in-depth research into the role of different vegetation configurations on the thermal comfort of the transportation micro-environment has profound significance for enhancing the thermal comfort experience of urban residents and promoting the progress of green transportation.

Samain et al. (Sabrin et al., 2021) combined the human energy balance model to measure the direct impact of temperature changes on pedestrian comfort and quantitatively analyzed the cooling benefits of urban canopies, obtaining the effectiveness of summer plant cooling in different urban canopy geometric scenarios. Hyunjung et al. (Lee et al., 2020) used the ENVI-met software to model street canyons and adjacent sidewalks with Platanus trees, simulating the impact of tree canopy spacing on reducing human thermal stress during the day, finding that the alleviation of human thermal stress significantly enhanced as the canopy spacing decreased. Marincic et al. (Marincic et al., 2021) analyzed the impact of green vegetation on micro-climate temperature and outdoor thermal comfort in three different architectural spaces, clearly indicating that in sub-climate outdoor spaces, appropriate vegetation configurations can improve outdoor environmental thermal comfort. Loibl et al. (Loibl et al., 2021) conducted a comparative study of the greening situation in typical sample areas in Vienna through micro-climate analysis, exploring the impact of greening measures on local energy demand and indoor temperature, obtaining that green facades have a significant effect on increasing regional mean radiant temperature during the day, while green roofs have a relatively smaller effect. Jamil et al. used the ENVI-met software to simulate different types of vegetation and their spacing, assessing the impact of various vegetation configurations on the level of thermal stress in school outdoor spaces, and proposed a series of solutions to improve the thermal comfort of school outdoor spaces.

Many studies have explored in depth the specific mechanism of regional thermal comfort affected by building structure and vegetation type (Haeri et al., 2023, Salehi et al., 2024), and many studies have systematically analyzed the effects of different vegetation types on enhancing outdoor thermal comfort through detailed simulation of realistic scenarios (Lee et al.,2020, Loibl et al., 2021). However, for the same plant type inside, In other words, the research on the influence of different tree forms and density on the thermal comfort of t transportation micro-environments is still insufficient. The lack of such evaluation studies limits our in-depth understanding and optimization of transportation micro-environments regulation strategies. Therefore, this paper establishes a numerical model of a transportation micro-environments in Jinan City using the ENVI-met simulation software, calculating the Universal Thermal Climate Index (UTCI) under different canopy ratios (CR) and leaf area density (LAD) with the southeast wind direction, combined with the spatial distribution of temperature, relative humidity, and wind speed, to assess the thermal comfort of the transportation micro-environment under different vegetation configurations.

2. METHODS
2.1 Study area

Figure 1 shows the research area of the paper. Jinan City of Shandong Province (36º01´ - 36 º40´N, 116º45´ - 117 º32´E) is located in the middle and west of Shandong Province in eastern China. It has a temperate monsoon climate with distinct four seasons, sufficient sunlight, concentrated precipitation and obvious dry and wet seasons. The hottest period of the year in Jinan is June, July and August, during which the temperature can reach more than 30ºC and the highest can exceed 35ºC, and the high temperature is accompanied by high humidity and thunderstorms, making the precipitation the highest throughout the year. In 2019-2023 years, the climate characteristics of Jinan City in 2023 are characterized by the occurrence and intensity of extreme weather and climate events. The average temperature for the whole year was an unusually high 1.3°C, reaching 15.4°C, the highest since meteorological records began in 1951. The average temperature in summer (June-August) was 27.6°C, also the highest since 1951. In addition, a total of 35 high temperature days appeared in Jinan in 2023, indicating that the summer temperature of the year was unusually hot. According to the definition in the Design Standards for the Thermal Environment of Urban Residential Areas, 2023 was selected as a typical meteorological year, and June 9, 2023, was selected as a typical meteorological day.
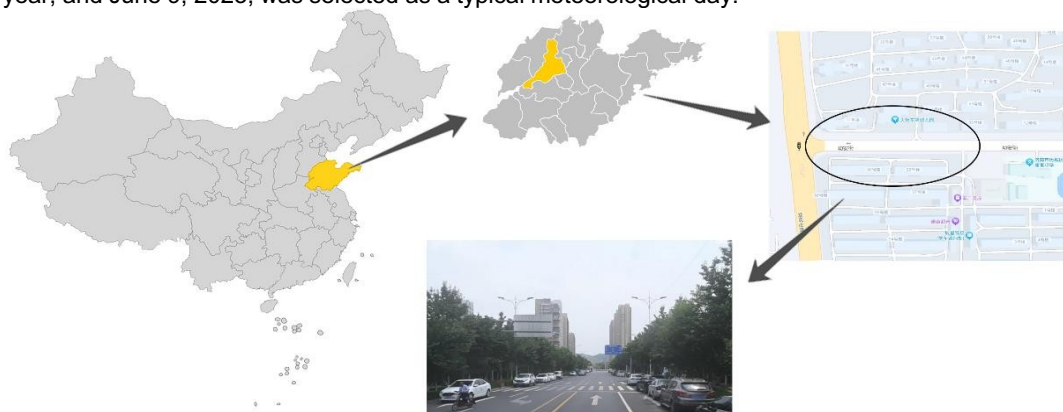

Figure 1: Study area

2.2 Data collection

The information collected includes building information, road information, green plant information and meteorological data information. According to the building information Jinan Architectural Design Guidelines, the height of residential buildings generally does not exceed 80 m, and the height of buildings on both sides of the road is set at 20 m. The road is four lanes in both directions,with a width of 4 m. According to some specific provisions in road greening in the Notice of the General Office of Jinan Municipal People's Government on Issuing the Implementation Rules of Jinan Urban Greening Regulations, the width of the simulated green belt is set at 2 m. The historical meteorological data from the weather network on June 9, 2023, are selected for meteorological data. The temperature (T) and relative humidity (rH) collected are shown in Figure 2.
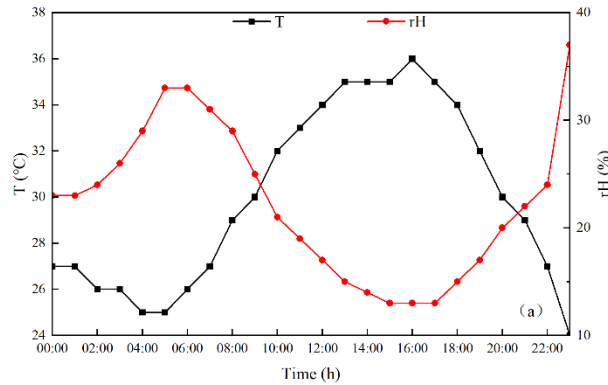

Figure 2: Meteorological data input to the model
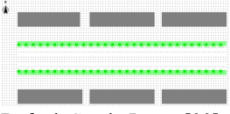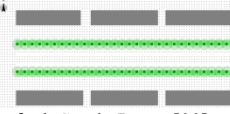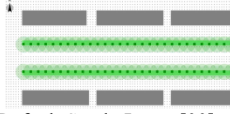
2.3 Model setup

The ENVI-met software is selected for numerical simulation in the article. ENVI-met is an advanced Computational fluid dynamics (CFD) software that is capable of detailed simulation of energy, moisture, and gas exchange processes in urban ecosystems based on computational fluid dynamics principles. The article utilizes the Albero tool that comes with the ENVI-met software to manually draw green plants with different CR and LAD, and then plants them in the modeling area using the Spaces tool to achieve different vegetation configurations. Three scenarios with CR values of 0.4, 0.6, and 0.8 are explored, corresponding to tree heights of H = 5 m, H = 10 m, and H = 15 m, respectively. For the case of H = 10 m, tree models with LAD values of 0.5, 1.0, 1.5, and 2.0 are constructed. Specific plant models with different CR values and LAD = 1 are presented in Table 1.

Table 1: Plant model diagram with different crown ratios at LAD = 1

	CR = 0.4	CR = 0.6	CR = 0.8
H = 5			
H = 10			
H = 15			

The ENVI-met model created in the article is divided into a grid of 100 × 50 × 50, with a grid resolution of 2 m × 2 m × 4 m, including buffer grids of 20 m in the horizontal direction at the model's boundaries and 30 m in the vertical direction. The specific details of the model constructed by ENVI-met are presented in Table 2.

Table 2: Model details built by ENVI-met

	H = 5	H = 10	H = 15
Location		36º40′N, 117º00′E	
Climatic type		Temperate monsoon climate	
Simulation days		2024.05.05	
Simulation duration		11 h	
Start time		6:00	
Graphic model (LAD = 1, CR = 0.8)			
Soil	Default Sandy Loam [00] Brick road (yellow stones) [KG] Asphalt Road [ST] Loamy Soil [LO]	Default Sandy Loam [00] Brick road (yellow stones) [KG] Asphalt Road [ST] Loamy Soil [LO]	Default Sandy Loam [00] Brick road (yellow stones) [KG] Asphalt Road [ST] Loamy Soil [LO]
Trees	Deciduous Trees (sparse canopy)	Deciduous Trees (sparse canopy)	Deciduous Trees (sparse canopy)
Wind direction	South wind (160º)	South wind (160º)	South wind (160º)
Wind speed	3 m/s	3 m/s	3 m/s

The ENVI-met software utilizes its built-in Bio-met component for human body setup and thermal comfort calculation. Figure 3 shows the human thermal comfort model set up in the Bio-met component.
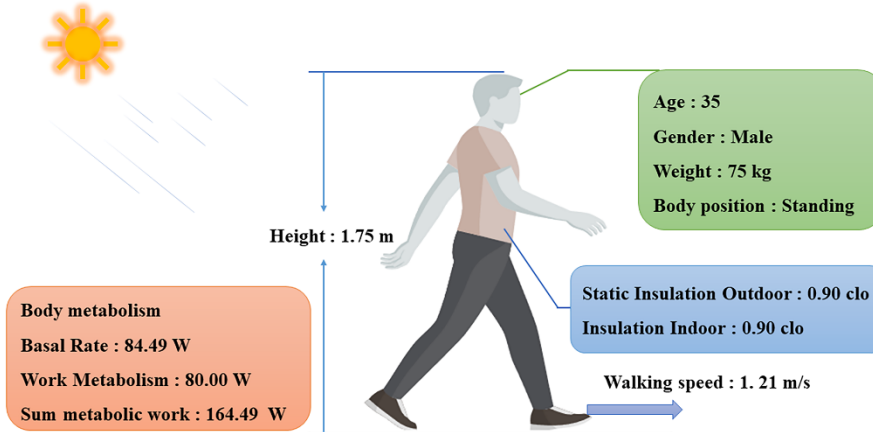

Figure 3: Human thermal comfort model setting

2.4 Universal thermal climate index

Outdoor thermal comfort can be assessed using various indices, and the article uses UTCI to quantify thermal comfort at 1.5 m above ground level. The calculation formula for UTCI is as follows (Bröde et al., 2012):

UTCI calculation formula

$$UTC(T, Tr, va, pa) = T + Offset(T, Tr, va, pa)$$

Where:

- T = the air temperature (ºC)
- Tr = the average radiation temperature (ºC)
- va = the wind speed, (m/s)
- pa = the water vapor pressure (Pa)

Compared to other thermal comfort indices, UTCI takes into account a more comprehensive range of factors. Many studies have confirmed that UTCI demonstrates exceptional performance in assessing the thermal comfort of outdoor spaces (Matzarakis et al., 2014, Binarti et al., 2020). Table 3 presents the thermal stress ranges corresponding to UTCI values (Mahdavinejad et al., 2024), which is used to objectively reflect the human body's response to various UTCI values.

Table 3: UTCI corresponds to the range of heat stress

Heat tension	UTCI (ºC)
Very cold (Extreme cold stress)	< −40
Very strong cold stress	27- to 40-
Cold (Strong cold stress)	13- to 27-
Cool (Moderate cold stress)	0 to 13-
Slightly cool (Slight cold stress)	9+ to 0
Comfortable (No thermal stress)	26+ to 9+
Warm (Moderate heat stress)	32+ to 26+
Hot (Strong heat stress)	38+ to 32+
Very hot (Extreme heat stress)	+46 to 38+
Sweltering (Extereme danger)	> + 46

3. RESULTS

3.1 Effects of different crown ratios

Figure 4 shows the comparison of temperatures at a height of 1.5 m in the transportation micro-environments under different crown ratios. The results indicate that as the height of the street trees increases, the cooling effect of the street trees shows a decreasing trend. With a fixed tree height, an increase in CR leads to a reduction in the cooling effect of the street trees, but this trend is not validated for all tree heights. As seen in Figure 4, when the height of the street trees is 15 m, there is little difference in the cooling effect with CR values of 0.4, 0.6, and 0.8; however, the cooling effect at CR = 0.8 is actually better than that at CR = 0.6. Street trees play a significant role in mitigating the temperature of the transportation micro-environments, with a cooling range of 0.00ºC to 0.80ºC. When H = 5 m and CR = 0.4, the cooling effect reaches its peak at 12:00 noon, with a temperature reduction of 0.80ºC.
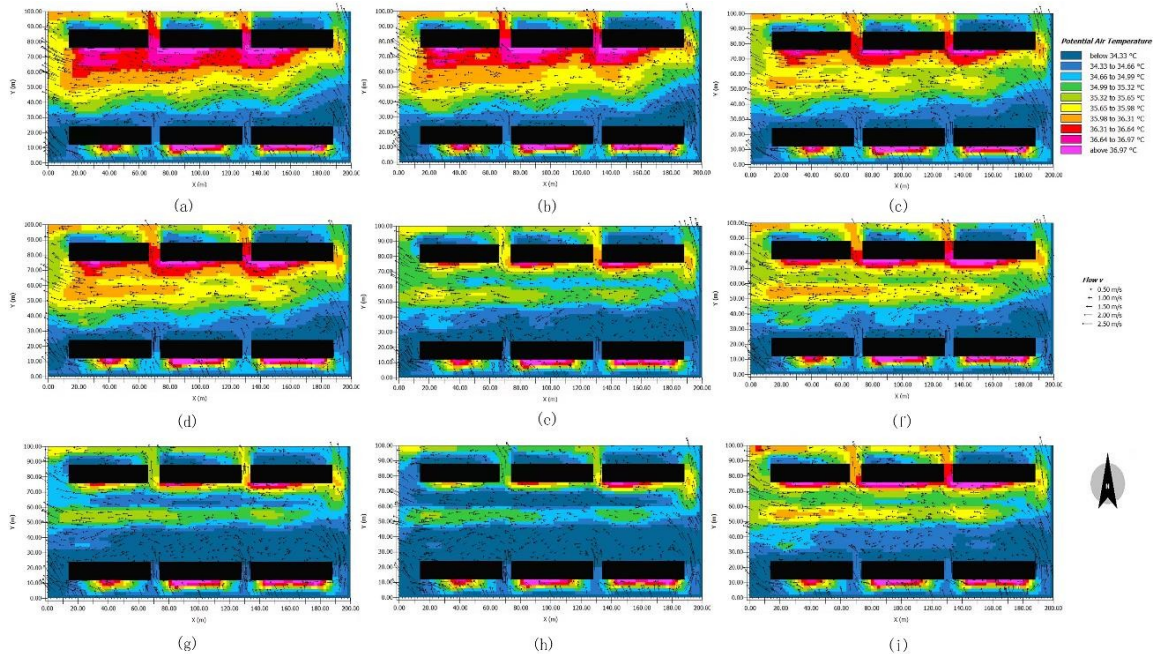

Figure 4: Temperature comparison of street microenvironment at 12：00 at the height of 1.5m under different canopy ratios. (a) H = 5, W = 2, LAD = 1; (b) H = 5, W = 3, LAD = 1; (c) H = 5, W = 4, LAD = 1; (d) H = 10, W = 4, LAD = 1; (e) H = 10, W = 6, LAD = 1; (f) H = 10, W = 8, LAD = 1; (g) H = 15, W = 6, LAD = 1; (h) H = 15, W = 9, LAD = 1; (i) H = 15, W = 12, LAD = 1

Figure 5 compares the relative humidity at a height of 1.5 m in the transportation micro-environments under different crown ratios. In the morning, the humidifying effect of street trees with different crown ratios shows little difference. As time progresses, the humidifying effect of shorter street trees (5 m) generally increases first and then decreases, reaching a maximum around 12:00. The humidifying effect of taller street trees (10 m, 15 m) generally exhibits a trend of decreasing first, then increasing, and finally decreasing again. The higher the street trees and the larger their crowns, the worse the humidifying effect. The results indicate that, overall, street trees have a significant humidifying effect on the transportation of micro-environments. Under different crown ratios, thehumidity increases in the transportation micro-environments ranges from -0.04% to 0.76%. The best humidifying effect is observed when H = 5 m and CR = 0.4, with a humidity increase of up to 0.76%. The pattern of humidification by street trees is highly consistent with their cooling pattern, which indirectly confirms that street trees in the transportation micro-environments can increase air humidity through transpiration and simultaneously reduce the temperature of the surrounding environment through shading and evaporation. This indicates that street trees play an important role in regulating the temperature and humidity of the transportation micro-
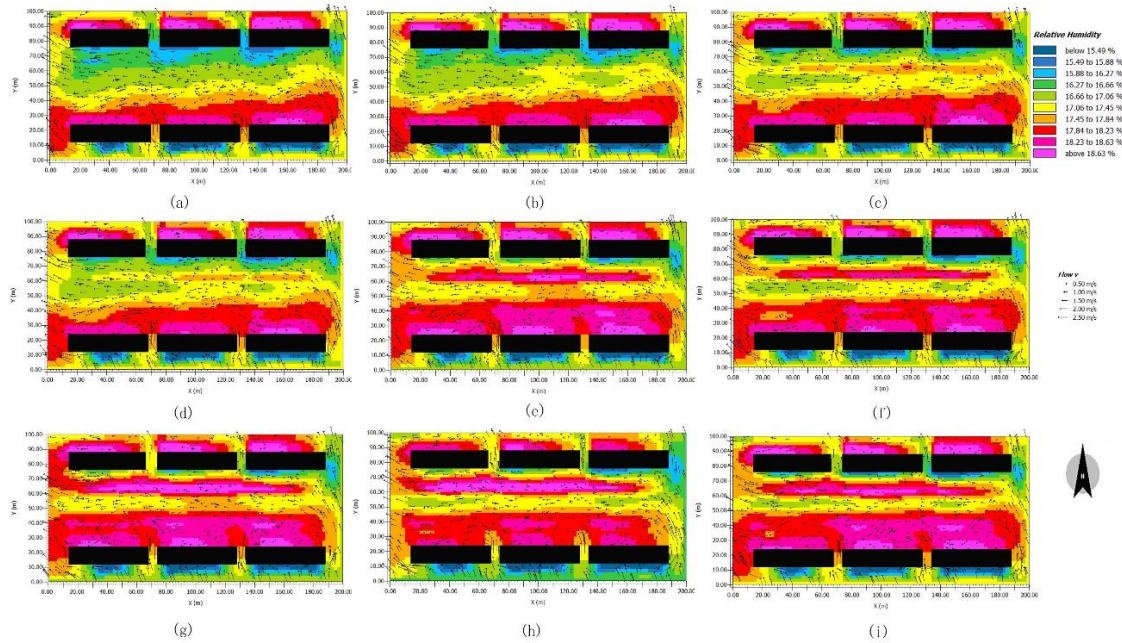
environments.

Figure 5: Comparison of relative humidity at 12:00 at the height of 1.5m below the canopy ratio of different trees, (a) H = 5, W = 2, LAD = 1; (b) H = 5, W = 3, LAD = 1; (c) H = 5, W = 4, LAD = 1; (d) H = 10, W = 4, LAD = 1; (e) H = 10, W = 6, LAD = 1; (f) H = 10, W = 8, LAD = 1; (g) H = 15, W = 6, LAD = 1; (h) H = 15, W = 9, LAD = 1; (i) H = 15, W = 12, LAD = 1

Figure 6 shows the UTCI values and UTCI differences after isolation by street trees with different crown ratios. Figure 6 (a) shows that in the morning, the UTCI values are relatively low, around 32°C, under all crown ratios, with people feeling warm but not experiencing significant heat stress. As time progresses, the UTCI values first rise sharply, then decline slowly, and after another sharp rise, they gradually stabilize, with no significant differences in this pattern of change under different crown ratios. Figure 6 (b) indicates that street trees with H = 5 m and CR = 0.6 are most effective in improving the thermal comfort of the transportation micro-environments, reducing the UTCI by 2.01ºC. However, when the height of the street trees increases to 15 m, they have the most significant effect on increasing the UTCI values, which can rise by up to 8.42°C, reaching 42.89°C, causing an uncomfortable feeling of stuffiness. This finding suggests that lower-height street trees (5 m) are more helpful in alleviating the thermal stress in the transportation micro-environments, while taller street trees (10 m, 15 m) may exacerbate this sense of thermal discomfort.
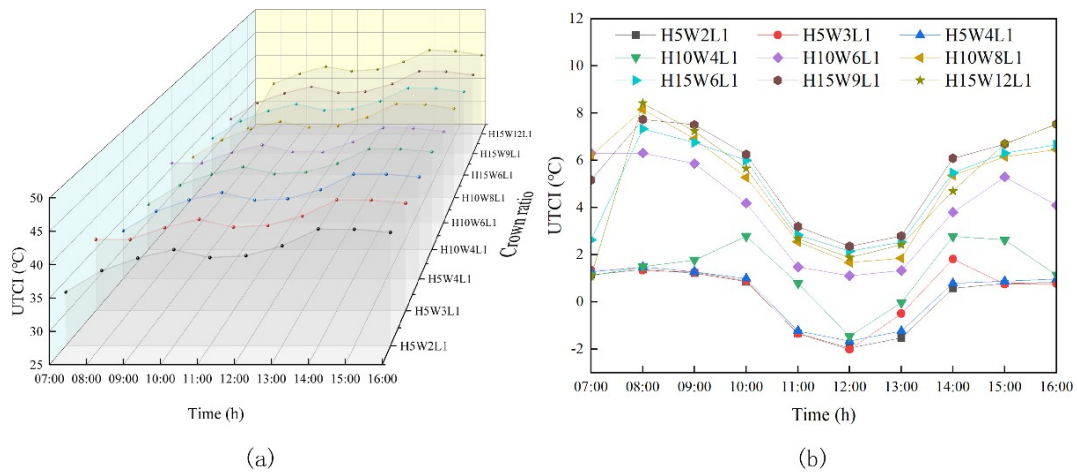

Figure 6: (a) UTCI value after isolation of trees under different crown ratios (b) Comparison of UTCI difference after isolation of trees under different crown ratios

Through the analysis of the effects of different crown ratios on temperature, relative humidity, and UTCI in the transportation micro-environments, it is found that the height of the street trees is inversely proportional to the cooling and humidifying effects of the street trees. Lower street trees are more helpful in alleviating thermal stress in the transportation micro-environments.

3.2 Effect of different leaf area density

Figure 7 reveals the impact of street trees with different LAD conditions on temperature reduction in the transportation micro-environments. At 7:00 am, street trees with different LADs show similar cooling effects, with an average temperature reduction of about 0.1°C. As time progresses, significant differences in temperature regulation capabilities are observed among street trees with different LADs, with LAD = 0.5 exhibiting the most significant cooling effect, recording a maximum temperature reduction of 0.53°C. The data shown in Figure 5 indicate that as LAD increases, the cooling effect of street trees gradually decreases. Specifically, for

every 0.5 increase in LAD, the temperature in the transportation micro-environments rises by 23.75% to 24.90%. This finding suggests that an increase in leaf area density does not always effectively reduce the temperature in the transportation micro-environments and may sometimes even exacerbate temperature increases.
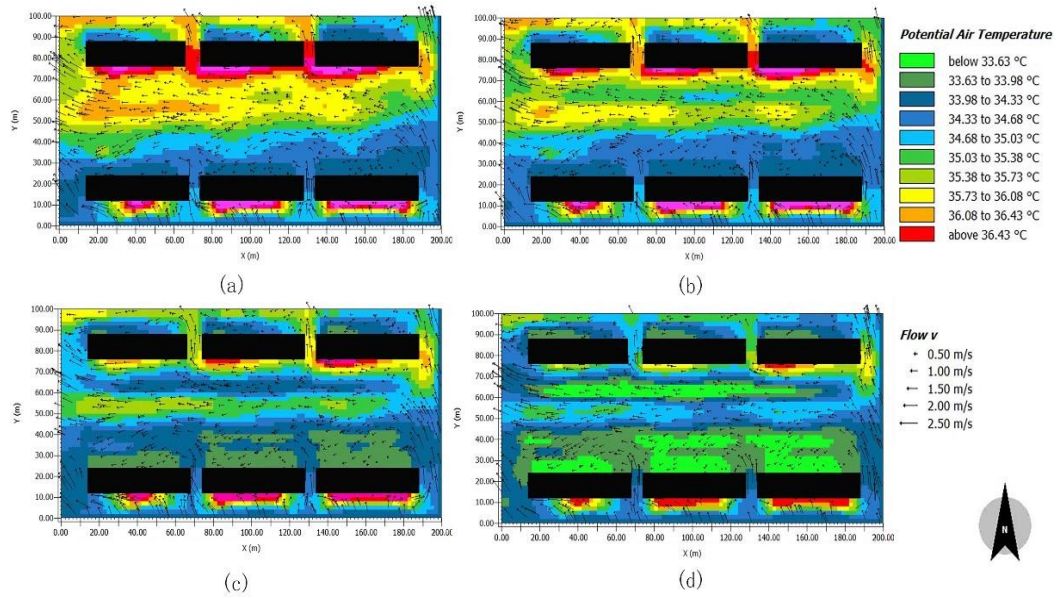

Figure 7: Comparison of temperature at a height of 1.5m under different LAD at 12:00

Figure 8 presents the increase in relative humidity in the transportation micro-environments under different LAD conditions. The results indicate that compared to LAD = 0.5, LAD = 1 increases the humidity in the transportation micro-environments by 26.60%; LAD = 1.5, when compared to LAD = 1, increases the humidity by 24.17%; and LAD = 2, when compared to LAD = 1.5, increases the humidity by 23.71%. Overall, the order of humidifying capacity from highest to lowest is LAD = 0.5, followed by LAD = 1, then LAD = 1.5, and finally LAD = 2.
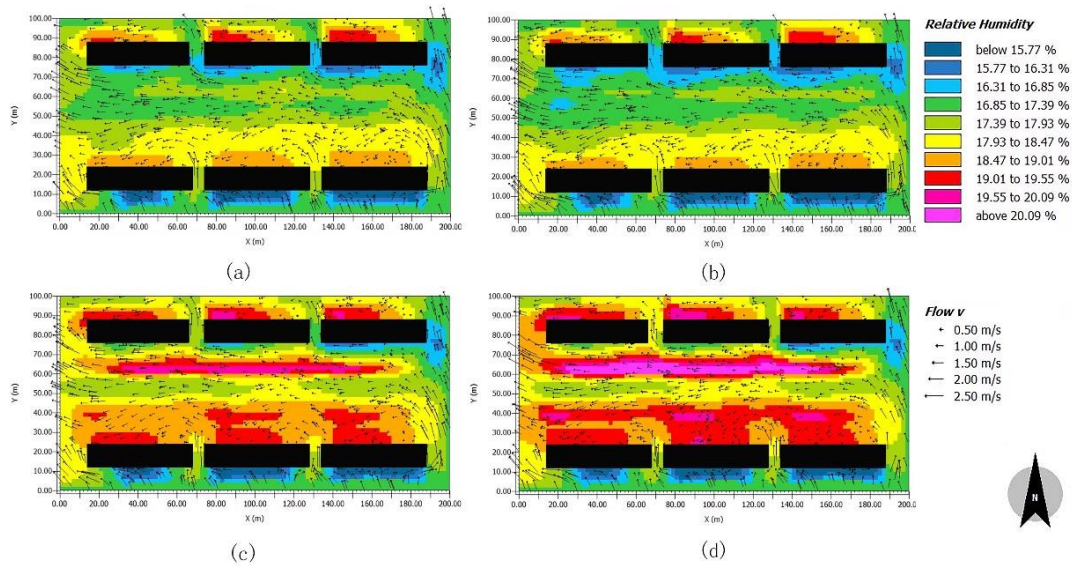
Figure 8: Comparison of relative humidity at a height of 1.5m under different LAD at 12:00

Figure 9 shows the differences in the impact of street trees with different LAD conditions on thermal comfort in the transportation micro-environments at a height of 1.5 m. Under all studied LAD conditions, the presence of street trees results in an increase in UTCI values behind them. As shown in Figure 9 (a), the average UTCI values range from 38.28°C to 39.13°C, reflecting a thermal stress level of "Hot" to "Very hot". Figure 9 (b) indicates that regardless of the LAD of the street trees, the improvement in thermal comfort in the transportation micro-environments exhibits a consistent trend: it first gradually strengthens, then rapidly weakens, strengthens again, and finally weakens gradually. This suggests that a higher leaf area density is not an effective means of enhancing thermal comfort in the transportation micro-environments.

Figure 9: (a) UTCI distribution in traffic microenvironment at 12:00 at 1.5m under different LAD conditions (b) Thermal comfort comparison of UTCI over time at 1.5m under different LAD conditions
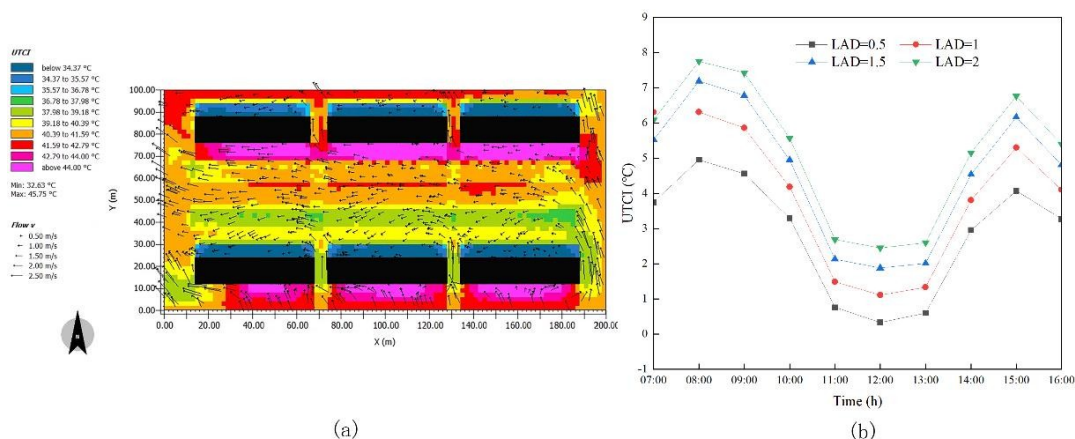
By analyzing the effects of different leaf area densities on temperature, relative humidity, and UTCI in the transportation micro-environments, it is found that as the LAD of street trees increases, both the cooling and humidifying effects of the street trees weaken. Larger leaf area densities are not an effective means of enhancing thermal comfort in the transportation micro-environments.

4. CONCLUSION

The transportation micro-environments of Jinan City was simulated using the ENVI-met model in the article. The impact of vegetation configuration on thermal comfort was analyzed, and the enhancement of comfort through the optimization of vegetation configuration was discussed by calculating the UTCI and analyzing the distribution of temperature and relative humidity. The main conclusions are as follows:

(1) The cooling effect of street trees decreases with increasing height, and the cooling effect decreases with increasing crown ratio. Street trees with H = 5 m and CR = 0.4 had the best cooling effect at 12:00 noon, with a temperature drop of 0.80ºC.

(2) For H = 5 m, the humidification effect of street trees first increased and then decreased, reaching a peak value at around 12:00; The humidification effect of street trees with 10 m and 15 m height decreased first, then increased and then decreased, and the humidification effect of street trees with higher trees and larger crowns was worse. With H = 5m and CR = 0.4, the humidification effect of street trees is the best, and the moisture increment can reach 0.76%.

(3) Lower height street trees are more conducive to reducing the thermal pressure of the transportation micro-environments, while higher height street trees may aggravate the thermal discomfort. Street trees with H = 5 m and CR = 0.6 performed best in terms of thermal comfort, reducing the UTCI by 2.01ºC, while street trees with 15 m height could cause the UTCI to rise by 8.42ºC to 42.89ºC, causing discomfort.

(4) In terms of temperature reduction, street trees with LAD=0.5 showed the most significant cooling effect, and the temperature increased by 23.75% ~ 24.90% for every 0.5 increase in LAD. In terms of relative humidity increase, street trees with LAD=0.5 had the most significant humidification effect. In terms of thermal comfort effects, street trees improved UTCI in all LAD conditions, reflecting a heat stress level of "Hot" or "Very hot", indicating that a larger LAD does not necessarily improve thermal comfort.

5. REFERENCES

Banerjee, S., Pek, R.X.Y., Yik, S.K., Ching, G.N., Ho, X.T., Dzyuban, Y., Crank, P.J., Acero, J.A. & Chow, W.T.L., 2024. Assessing impact of urban densification on outdoor microclimate and thermal comfort using ENVI-met simulations for Combined Spatial-Climatic Design (CSCD) approach. Sustainable Cities and Society, 105, 105302.

Altunkasa, C. & Uslu C., 2020. Use of outdoor microclimate simulation maps for a planting design to improve thermal comfort. Sustainable Cities and Society, 57, 102137.

Liu, Z.X., Brown, R.D., Zheng, S.L., Jiang, Y. & Zhao, L.H., 2020. An in-depth analysis of the effect of trees on human energyfluxes. Urban Forestry & Urban Greening, 50, 126646.

Meili, N., Acero, J.N., Peleg, N., Manoli, G., Burlando, P. & Fatichi, S., 2021. Vegetation cover and plant-trait effects on outdoor thermal comfort in a tropical city. Building and Environment, 195, 107733.

Xiao, Q.K., Fan, X., Guo, Y.Y., Li, S.T., He, W., Deng, Y.C., Xiao, Z.Y., Wang, P.C. & Wu, C.G., 2024. Tree form characteristics as criteria for tree species selection to improve pedestrian thermal comfort in street canyons: Case study of a humid subtropical city. Sustainable Cities and Society, 105, 105339.

Sabrin, S., Karimi, M., Nazari, R., Pratt, J. & Bryk, J., 2021. Effects of Different Urban-Vegetation Morphology on the Canopy-level Thermal Comfort and the Cooling Benefits of Shade Trees: Case-study in Philadelphia. Sustainable Cities and Society, 66, 102684.

Lee, H., Mayer, H. & Kuttler, W., 2020. Impact of the spacing between tree crowns on the mitigation of daytime heat stress for pedestrians inside E-W urban street canyons under Central European conditions. Urban Forestry & Urban Greening, 48, 126558.

Marincic, L. & Ochoa, J.M., 2021. Urban Microclimatic Conditions in Arid Climates, in Urban Microclimate Modelling for Comfortand Energy Studies. Cham: Springer International Publishing.

Loibl, W., Vuckovic, M., Etminan, G., Ratheiser, M., Tschannett, S. & Österreicher, D., 2021. Effects of Densification on Urban Microclimate—A Case Study for the City of Vienna. Atmosphere, 12 (4), 511.

Haeri, T., Hassan, N. & Ghaffarianhoseini, A., 2023. Evaluation of microclimate mitigation strategies in a heterogenous street canyon in Kuala Lumpur from outdoor thermal comfort perspective using Envi-met. Urban Climate, 52, 101719.

Salehi, A. & Nasrollahi, N., 2024. Assessing vegetation distribution based on geometrical and morphological characteristics of the urban fabric to provide thermal comfort for pedestrians: A case study in Sanandaj. Sustainable Cities and Society, 104, 105297.

Bröde, P., Fiala, D., Błażejczyk, K., Holmér, I., Jendritzky, Kampmann, G., Tinz, B. & Havenith, G., 2012. Deriving the operational procedure for the Universal Thermal Climate Index (UTCI). International Journal of Biometeorology, 56 (3), 481-494.

Matzarakis, A., Muthers, M.S. & Rutz, F., 2014. Application and comparison of UTCI and PET in temperate climate conditions. Finisterra, 48 (98), 21-31.

Binarti, F., Koerniawan, M.D., Triyadi, S., Utami, S.S. & Matzarakis, A., 2020. A review of outdoor thermal comfort indices and neutral ranges for hot-humid regions. Urban Climate, 31, 100531.

Mahdavinejad, M., Shaeri, J., Nezami, A. & Goharian, A., 2024. Comparing universal thermal climate index (UTCI) with selected thermal indices to evaluate outdoor thermal comfort in traditional courtyards with BWh climate. Urban Climate, 54, 101839.

#245: Sensitivity analysis of thermal design parameters for building integrated heat pipes

Nian ZHU, Fangcheng KOU, Xin WANG*

Department of Building Science, Tsinghua University, Beijing 100084, China

Abstract: Building integrated heat pipes (BIHP) utilizes flat gravity heat pipes (FGHP) with the thermal diode characteristic and ultra-high thermal conductivity, which can transfer a large amount of solar energy to the interior walls. The interior walls with phase change materials (PCM) can store the solar energy transferred by FGHP during the day and release it at night, greatly improving the indoor environment. However, current research mainly focuses on specific case studies, analyzing a single parameter with other given parameters. Thus, there is a lack of systematic research on the key design parameters of BIHP under different climates and building forms, and it cannot determine the key thermal design parameters in the entire process of energy collection, conduction, storage and release. This study proposes a Morris sensitivity method to analyze the thermal design parameters of BIHP in light and heavy buildings in Beijing, selecting 34 parameters such as window to wall ratio and thermal properties of interior and exterior enclosure. The selected parameters are ranked based on the impact of building energy consumption during the heating season. This study compares the analysis results of light and heavy buildings, identifying the similarities and differences in key design parameters between the two types of buildings. Analyzing the directionality of parameter influence, it is found that the ideal BIHP is a building form with high insulation for the external envelope and large heat capacity for the internal envelope embedded in heat pipes. Analyzing the nonlinearity and correlation of parameters to obtain parameters worth further analysis can help improve and perfect the thermal design of BIHP.

1. INTRODUCTION

China promises to peak carbon emissions by 2030 and achieve carbon neutrality by 2060 (Xi, 2020). In 2022, the operating energy consumption of buildings in China accounted for 21% of the total energy consumption, with heating energy consumption in northern urban areas reaching 217 million tce, accounting for 19% of the total building energy consumption in the country. The carbon emissions during the operation of buildings are 2.2 billion tCO2, accounting for 21% of energy related carbon emissions. Among them, the carbon emissions from heating in northern urban areas are 490 million tCO2 (Jiang et al., 2024).

Zero/low energy buildings that efficiently utilize solar energy are considered an effective means of achieving carbon neutrality. Heat pipe is an efficient heat transfer element that utilizes internal working fluid phase change for heat transfer. Building Integrated Heat Pipes (BIHP) are receiving increasing attention due to the ability of heat pipes to achieve variable thermal properties of envelope (kou et al., 2023). Robinson et al., (2013) tested the performance of a heat pipe integrated solar system during the heating season, and the results showed that the system achieved a daily average peak efficiency of 61.4% throughout the entire heating season. Gong et al., (2022) proposed a new type of passive solar room integrated with flat gravity heat pipes (FGHP). The solar energy on the outer surface of the south wall is absorbed and stored in the inner wall through FGHP to improve the indoor thermal environment. The results showed that the Indoor average operating temperature reached 16.7 ℃, which is 6.8 ℃ higher than the reference room. (Kou et al., 2023) optimized the thermal conductivity, heat capacity, and heat pipe insertion position of the internal wall of BIHP, and the results showed that compared to the initial BIHP, the indoor thermal discomfort of BIHP was improved by 6%, and the minimum operating temperature was increased by 3.3 ℃. Furthermore, the potential application of BIHP was partitioned in heating areas in China (Kou et al., 2024).

However, solar energy resources are of uncertainty and intermittency, and latent heat storage technology is an effective way to alleviate the supply-demand contradiction of building solar energy (Jiang, Wang and Zhang, 2011). Yu et al., (2023) proposed a ventilated roof integrated phase change materials (PCM) to improve the thermal performance of the roof. The results showed that when a 30 mm thick PCM was applied, the peak indoor air temperature and internal surface temperature were reduced by 2.9 ℃ and 5.5 ℃, respectively, and the cumulative cooling load of the building was reduced by 19.2%. Yu et al., (2024) further proposed a dynamic insulation roof integrated PCM, and the results showed that the sum of annual cooling and heating loads was reduced by 16.4% in Beijing.

Although there are currently many studies on BIHP, there is a lack of relevant research on the coordination and matching of energy collection, conduction, storage, and release during the whole thermal process of BIHP. Therefore, it is necessary to further understand the impacts of various parameters on the performance of BIHP through thermal analysis. In recent years, many searchers have made significant efforts in using global sensitivity analysis to determine key thermal design parameters. Global sensitivity analysis is a method used to quantify the impact of input parameter uncertainty on model output and evaluate the relative importance of each parameter to the output results. The Morris sensitivity analysis method was proposed by Morris (Morris, 1991) and later improved by Campolongo (Campolongo, Cariboni and Saltelli, 2007). This method is based on a single sampling experimental design and has good applicability for models with numerous analysis parameters and high computational load. It is a compromise betweenaccuracy and efficiency. Zhao, Li and Wang, (2022) used the Morris sensitivity analysis method to analyze high-rise and low-rise buildings in different climate zones and determined the key design parameters for different types of buildings in different regions.

This paper proposes a Morris sensitivity analysis method to analyze the thermal design parameters of BIHP in two types of building forms: light and heavy buildings in Beijing, respectively. Figure 1 shows the analysis process of this study. In this paper, firstly, to select the key design parameters based on their impacts on room energy consumption; secondly, to analyze the directionality of the impacts of various parameters on room energy consumption to explore the most ideal form of BIHP; finally, to filter out parameters with strong correlation and nonlinearity for subsequent analysis and optimization. The research results provide guide for the thermal design of BIHP.
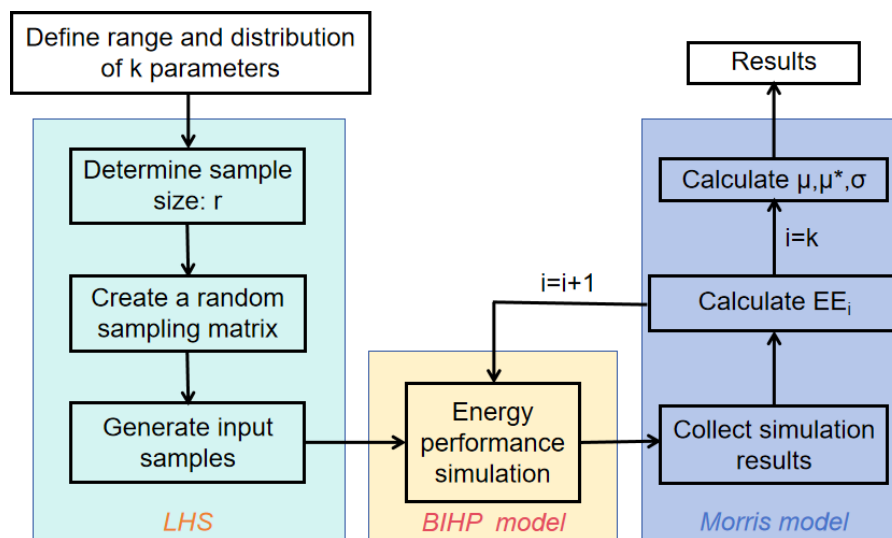

Figure 1: Sensitivity analysis process

2. METHODOLOGY
2.1. Building model

This study selected a south-facing middle top-floor room in a multi-layer BIHP, as shown in the Figure 2 (a). The south wall, roof, and north wall are external enclosures with external insulation, The east wall, west wall, and floor are internal enclosures, and the neighbor heat transfer can be ignored. The heat pipe is divided into two parts: the evaporation section and the condensation section, arranged at an inclination angle. The evaporation section is attached to the south exterior wall, and the condensation section is placed between the inner wall and PCM. There is a glass cover outside the south wall to reduce heat loss as shown in Figure 2 (b) (c). This study is based on the BIHP numerical model, which has been experimentally validated Gong et al., (2022).

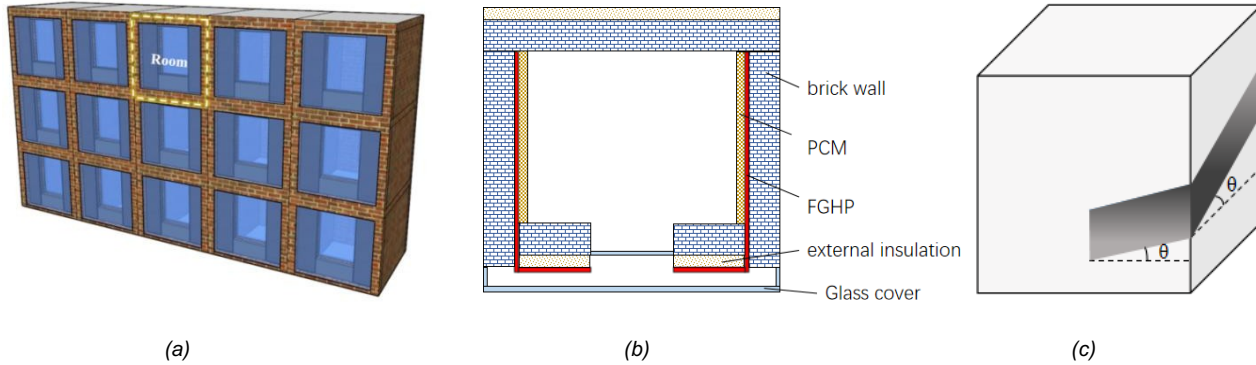|		
(a)	(b)	(c)

Figure 2: Building model (a) building model the south-facing middle top-floor room (b) plan view (c) stereogram

As the two main forms of buildings, light and heavy buildings each have unique advantages and limitations, and their applicability varies in different regions. This study conducts sensitivity analysis on light and heavy rooms in Beijing, comparing their differences in key thermal parameters. Table 1 lists two types of room information.

Table 6: BIHP information

	Parameters (heavy)	Parameters (light)
Geographical location	Beijing	
Geometry	3 m (east-west length) * 4 m (north-south length) * 3 m (height)	
Air change per hour	0.5 h⁻¹	
Lower limit temperature of thermal comfort zone	18 ℃	
Building exterior enclosure	Wall: 0.06m external insulation + 0.24m the main body of the wall Roof:0.06m external insulation + 0.20m the main body of the roof	Wall: 0.06m external insulation + 0.19m the main body of the wall Roof: 0.06m external insulation + 0.15m the main body of the roof
Building interior enclosure	Wall: 0.12m PCM: 0.06m Floor: 0.20m	Wall: 0.10m PCM: 0.06m Floor: 0.15m

2.2. Parameters selection

To understand the impacts of the thermal design parameters on energy consumption, 34 thermal parameters are selected including thermal conductivity, density, and specific heat of each wall, floor and roof, the solar radiation transmittance and heat transfer coefficient of transparent exterior envelope, the thermal conductivity coefficient, phase change latent heat, and phase change temperature of PCM. Table 2 lists the selected parameters, and the ranges of the parameters agree with the design specifications (Feng, 2007). The minimum and maximum values of all parameters are known, and the probability distribution is uniformly distributed (Mechri, Capozzoli and Corrado, 2010).

Table 2: Selection of analysis parameters

Category	Parameter	Abbreviation	Range (Heavy)	Range (Light)	Unit
South wall	Wall thermal conductivity	SWTC	0.42-1.74	0.14-0.31	W/(m·K)
	Wall specific heat	SWSH	920-1050		J/(kg·K)
	Wall density	SWD	1100-2500	500-800	kg/m³
	Insulation materials thermal conductivity	SITC	0.025-0.065		W/(m·K)
	Insulation materials specific heat	SISH	760-1380		J/(kg·K)
	Insulation materials density	SID	30-220		kg/m³
North Wall	Wall thermal conductivity	NWTC	0.42-1.74	0.14-0.31	W/(m·K)
	Wall specific heat	NWSH	920-1050		J/(kg·K)
	Wall density	NWD	1100-2500	500-800	kg/m³
	Insulation materials thermal conductivity	NITC	0.025-0.065		W/(m·K)
	Insulation materials specific heat	NISH	760-1380		J/(kg·K)
	Insulation materials density	NID	30-220		kg/m³
Roof	Solar energy absorption rate	RSAR	0.2-0.9		--
	Long wave emissivity	RLWE	0.1-0.9		--
	Roof thermal conductivity	RTC	0.42-1.74	0.14-0.31	W/(m·K)
	Roof specific heat	RSH	920-1050		J/(kg·K)
	Roof density	RD	1100-2500	500-800	kg/m³
	Insulation materials thermal conductivity	RITC	0.025-0.065		W/(m·K)
	Insulation materials specific heat	RISH	760-1380		J/(kg·K)
	Insulation materials density	RID	30-220		kg/m³
Interior wall	Wall thermal conductivity	IWTC	0.42-1.74	0.14-0.31	W/(m·K)
	Wall specific heat	IWSH	920-1050		J/(kg·K)
	Wall density	IWD	1100-2500	500-800	kg/m³
Floor	Floor thermal conductivity	FTC	0.42-1.74	0.14-0.31	W/(m·K)
	Floor specific heat	FSH	920-1050		J/(kg·K)
	Floor density	FD	1100-2500	500-800	kg/m³
PCM	Thermal conductivity	PTC	0.1-2.7		W/(m·K)
	Volumetric latent heat	PVLH	15-350		MJ/m³
	Phase transition temperature	PTT	15-25		℃
Window	Window to wall ratio	WWR	0.3-0.7		--
	Solar radiation transmittance	WSRT	0.7-0.9		--
	Heat transfer coefficient	WHTC	1.7-3.5		W/(m²·K)
Glass cover	Heat transfer coefficient	GHTC	5.62-6.80		W/(m²·K)
	Solar radiation transmittance	GSRT	0.7-0.9		--

2.3. Sensitivity analysis

Latin hypercube sampling (LHS) in stratified sampling is used, as its effective stratified characteristics can cover the entire input parameter space with relatively low computational costs (Helton et al., 2006). 30 sample points for each parameter are selected with a calculation cost of 1050 groups (the calculate cost is calculated by Equation 1).

Equation 1: The calculation cost $\qquad C=r(k+1)$

Where,

- − C is the calculation cost
- − r is the sample size
- − k is the number of variables

The elementary effects are calculated by Equation 2, which is taken as 5% of the parameter input range. The advantage of this formula compared to the traditional Morris method is that it does not need to map the parameter ranges to [0,1], and the proc ess is more concise.

Equation 2: Definition of elementary effects

$$EE_i = Y(x_1, x_2, \cdots, x_{i-1}, x_i + \Delta, \cdots, x_k) - Y(x_1, x_2, \cdots, x_{i-1}, x_i, \cdots, x_k)$$

Where,

- x_i represents input parameter
- EE_i is the elementary effect of input parameter x_i, MJ
- Δ is the step size of input parameter variation

Y is the model output parameter, which is the BIHP heating season energy consumption, MJ Sensitivity is measured through the following parameters:

Equation 35: The calculation formula for μ

$$\mu_i = \frac{1}{r} \sum_{j=1}^{r} EE_i^j$$

Equation 4: The calculation formula for μ*

$$\mu_i^* = \frac{1}{r} \sum_{j=1}^{r} \left| EE_i^j \right|$$

Equation 5: The calculation formula for σ

$$\sigma_i^2 = \frac{1}{r-1} \sum_{j=1}^{r} (EE_i^j - \mu_i)^2$$

Where,

- EE_i^j refers to the elementary effects generated by the j-th sample point of the i-th variable x_i, MJ
- r is the sample size

μ* reflects the strength of sensitivity of variable parameters to output parameters. The larger the value, the stronger the sensitivity of the variable parameter. The value of σ represents the strength of the correlation between parameters or the nonlinear effects of parameters.

3. RESULTS AND DISCUSSIONS
3.1. Sensitivity strength analysis of parameters

After taking 30 sample points within the parameter range for 34 design parameters, a simulation calculation was performed on the obtained 1050 groups. Figure 3 shows the calculation results of the input parameter sensitivity index μ*.
From Figure 3, it can be seen that:

1) For the transparent enclosure of the two types of rooms, glass cover solar radiation transmittance (GSRT) is highly sensitive. Because GSRT directly affects the solar radiation heat received by the evaporation section of the heat pipe and the solar radiation heat entering the room through the window, which directly affects the daytime heat gain and storage of BIHP, it has a significant impact on BIHP energy consumption and therefore has strong sensitivity. The sensitivities of window to wall ratio (WWR) and window heat transfer coefficient (WHTC) are also strong, indicating that the size and insulation of windows have significant impacts on BIHP energy consumption.
2) For the opaque exterior envelope of the two types of rooms, the thermal conductivity of the external insulation material is stronger than that of the wall/roof main body. The thermal conductivity of the exterior insulation of the north wall/roof is more sensitive than that of the south wall, because in winter in Beijing, the north wall does not receive solar radiation and has greater heat dissipation. Therefore, the thermal insulation of the north wall is important, making it more sensitive. In winter, the effective sky temperature is low, and the roof will dissipate a large amount of heat through thermal radiation with the sky, so roof insulation is also important and sensitive.
3) For the internal enclosure, the sensitivity strength queue of both types of rooms is PCM phase change temperature (PTT) > PCM volumetric latent heat (PVLH) > PCM thermal conductivity (PTC). When designing and select materials, priority should be given to relatively more sensitive parameters.
4) The differences between the analysis results of the two types of buildings are: light buildings have a higher sensitivity to PVLH, while heavy buildings have a higher sensitivity to the thermal conductivity of the external insulation materials, indicating that light buildings should pay attention to the thermal storage of the internal enclosure, while heavy buildings should pay attention to the thermal insulation of the external enclosure.
5) The sensitivity of the specific heat, thermal conductivity, or density of the main body of the interior/exterior wall, roof and floor on room energy consumption is weak, and no further analysis will be conducted.
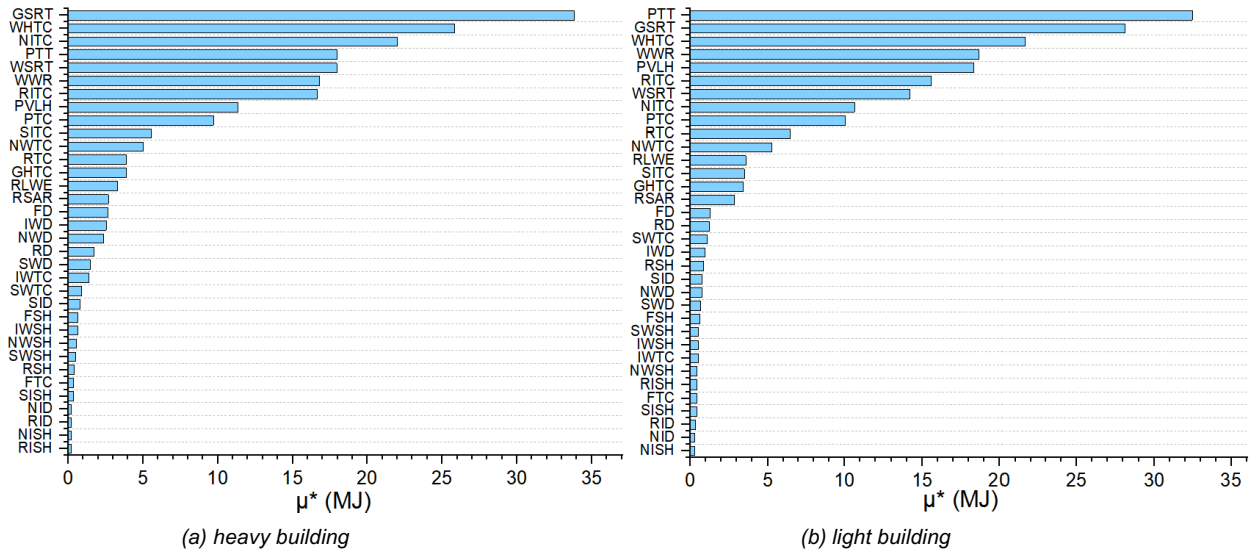
(a) heavy building   *(b) light building*

Figure 3: Parameter sensitivity strength sorting

3.2. Directional analysis of parameter influence

As the Equation 3*Equation 4*, Equation 5 defined, the comparison between μ and μ^* provides characterization information on the impact of input parameters on output. When the parameters μ and μ^* are equal, it indicates that the smaller the value of the parameter within the range, the lower the energy consumption of the BIHP. When the parameter μ is opposite to μ^*, it indicates that the larger the value of the parameter within the range, the lower the energy consumption of the BIHP. When the μ value of the parameter is between $[-\mu^*, \mu^*]$, it indicates that there may be an optimal value for the parameter within the range, and further analysis is needed. From Figure 4, we can see that:

1) The input parameters values vary in the same direction as the building energy consumption ($\mu = \mu^*$), including the thermal conductivity of each external enclosure, WWR, and longwave radiation emissivity of the outer surface of the roof (RLWE).
2) The input parameters vary inversely with the building energy consumption ($\mu = -\mu^*$), including the solar radiation transmittance of each transparent enclosure, PTC, PVLH, and solar absorption rate of the outer surface of the roof (RSAR).
3) The special parameter that needs further optimization is PTT. The selection of PTT has a significant impact on room energy consumption. Both too high and too low PTT cannot effectively utilize the latent heat of PCM for heat storage. Moreover, when PTT is selected too low, PCM will absorb indoor heat and increase energy consumption. Therefore, it is crucial to select an appropriate PTT based on indoor setting parameters, meteorological parameters, and building forms.

In one word, whether for heavy or light building, the ideal BIHP requires high insulation for the external envelope and large heat capacity for the internal envelope embedded in heat pipes, moderate PTC and appropriate PTT to release the stored heat in a timely manner.
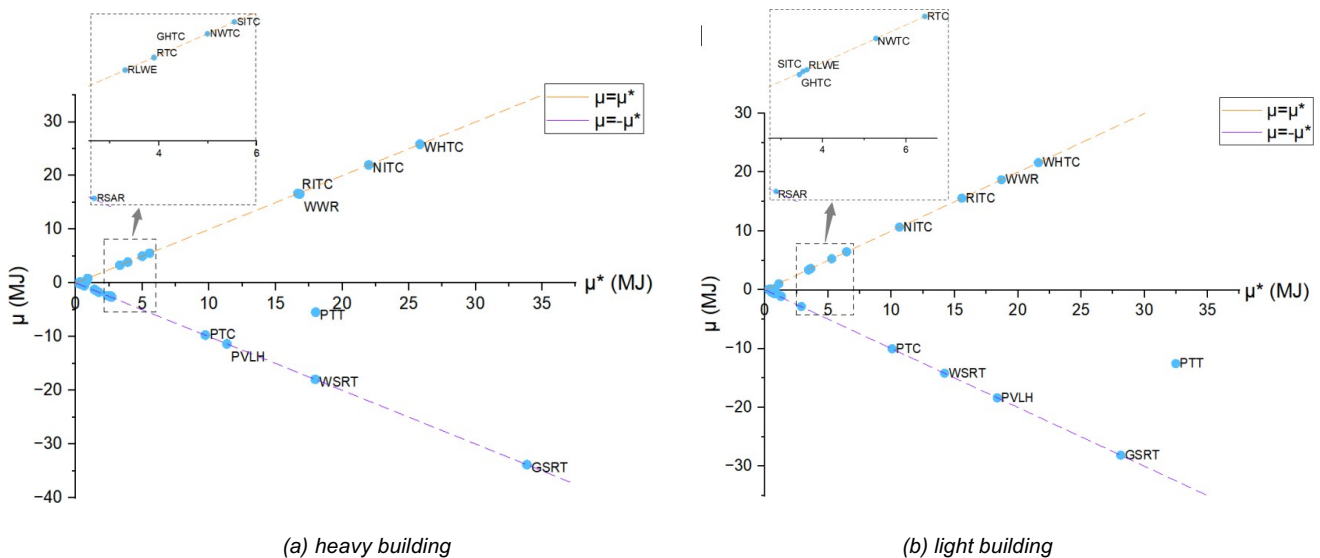

(a) heavy building   *(b) light building*

Figure 4: Directional analysis of parameter influence

3.3. Parameter Linearity and Correlation Analysis

In the Figure 5, if the parameter σ/μ*<0.1 (green area), it indicates that the influence of the parameter on the model is almost linear. If the parameter σ/μ*>1 (yellow area), it indicates that the parameter is non-linear or has strong correlation with other parameters (Sanchez et al., 2014). From Figure 5, we can see that:

1) Most parameters in both heavy and light buildings are between two straight lines, indicating that these parameters have both linear, nonlinear, and interactive effects on the model.
2) There are no parameters in the green area, so there are no parameters in the selected parameters that have a linear impact on the energy consumption of BIHP.
3) In the two types of buildings, the PTT, PTC and PVLH fall in the yellow area, indicating that these parameters are strongly nonlinear or have strong correlation with other parameters is worth further investigation.
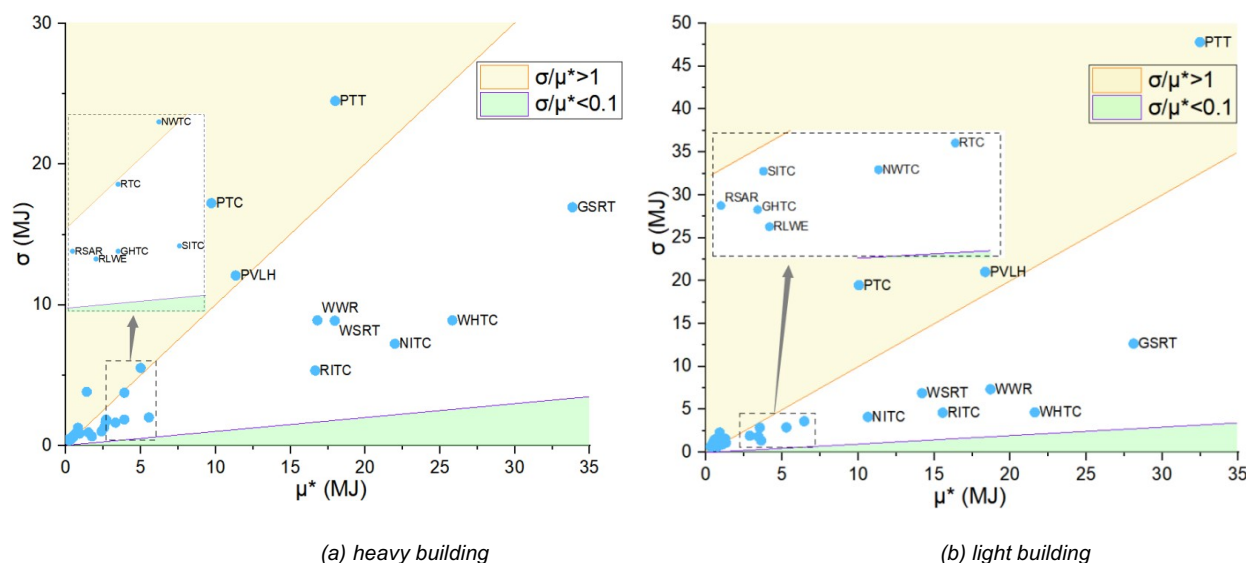

(a) heavy building   *(b) light building*

Figure 5: Parameter linearity and correlation analysis

4. CONCLUSION

This study proposes a Morris sensitivity method to analyze the thermal design parameters of BIHP in light and heavy buildings in Beijing. We found that: 1) The WWR, WHTC, GSRT, thermal conductivity of external insulation materials, and PCM parameters are all highly sensitive parameters in the two types of buildings. More attention should be paid to these parameters during design. 2) Light buildings should pay more attention to the heat capacity of the internal envelope embedded in heat pipes, while heavy buildings should pay more attention to the insulation of the external enclosure. 3) The ideal BIHP requires high insulation for the external envelope and large heat capacity for the internal envelope embedded in heat pipes, moderate PTC and appropriate PTT to release the stored heat in a timely manner. 4) In the two types of buildings, the PTT, PTC and PVLH are strongly nonlinear or have strong correlation with other parameters. There are no parameters in the selected parameters that have a linear impact on the energy consumption of BIHP.

This article analyzes the sensitivity intensity, directional influence, correlation, and nonlinear influence of BIHP thermal design parameters, deepening our understanding of BIHP and helping us further explore the coordination and matching of energy collection, conduction, storage, and release processes in BIHP.

5. ACKNOWLEDGEMENT

6. REFERENCES

Campolongo, F. Cariboni, J. and Saltelli, A. (2007) 'An effective screening design for sensitivity analysis of large models', EnvironmentalModelling & Software22 (2007) 1509-1518. Available at: https://www.sciencedirect.com/science/article/pii/S1364815206002805. .

Robinson, B.S. Chmielewski, N.E. Andrea, K-K. Brehob, E.G. Sharp, M.K. (2013) 'Heating season performance of a full-scale heat pipe assisted solar wall', Solar Energy 87 (2013) 76-83. Available at: https://www.sciencedirect.com/science/article/pii/S0038092X12003623.

Feng, Y. (2007) 'Building thermal engineering and energy conservation', in Lu,Y.Q. (ed) Practical Heating and Air Conditioning Design Manual (Second Edition). Beijing, pp. 231-244.

Gong, Q. Kou, F. Sun, X. Zou, Y. Mo, J. Wang, X. (2022) 'Towards zero energy buildings: A novel passive solar house integrated with flat gravity-assisted heat pipes', Applied Energy 306 (2022) 117981. Available at: https://www.sciencedirect.com/science/article/pii/S0306261921012848.

Helton, J.C. Johnson, J.D. Sallaberry, C.J. Storlie, C.B. (2006) 'Survey of sampling-based methods for uncertainty and sensitivity analysis', Reliability Engineering and System Safety 91 (2006) 1175–1209. Available at: https://www.sciencedirect.com/science/article/pii/S0951832005002292.

Jiang, Y. et al. (2024) 'China's building energy consumption and greenhouse gas emissions', in China Urban Science Research Association (ed.) 2024 Annual Report on China Building Energy Efficiency. Beijing, pp. 1-30.

Jiang, F. Wang, X. and Zhang, Y. (2011) 'A new method to estimate optimal phase change material characteristics', Energy Conversion and Management 52 (2011) 2437–2441. Available at: https://www.sciencedirect.com/science/article/pii/S0196890411000549.

kou, F. Wang, X. Zou, Y. Mo, J. (2023) 'Heat transfer performance of the L-shaped flat gravity heat pipe', Journal of Building Engineering 76 (2023) 107389. Available at: https://www.sciencedirect.com/science/article/pii/S2352710223015693.

Kou, F. Gong, Q. Zou, Y. Mo, J. Wang, X. (2023) 'Solar application potential and thermal property optimization of a novel zero-carbon heating building',Energy & Buildings 279 (2023) 112688. Available at: https://www.sciencedirect.com/science/article/pii/S0378778822008593.

Kou, F. Xu, T. Wang, X. Zou, Y. Mo, J. (2024) 'Towards zero-carbon solar heating in severe cold and cold regions of China by building integrated heat pipes ', Building and Environment 255 (2024) 111430. Available at: https://www.sciencedirect.com/science/article/pii/S0360132324002725.

Mechri, H.E. Capozzoli, A. and Corrado, V. (2010) 'USE of the ANOVA approach for sensitive building energy design', Applied Energy 87 (2010) 3073–3083. Available at: https://www.sciencedirect.com/science/article/pii/S030626191000108X.

Morris, M.D. (1991) 'Factorial sampling plans for preliminary computational experiments',TECHNOMETRICS 33 (1991) 161-174. Available at: https://www.tandfonline.com/doi/abs/10.1080/00401706.1991.10484804.

Sanchez, D.G. Lacarrière, B. Musy, M. Bourges, B. (2014) 'Application of sensitivity analysis in building energy simulations: Combining first- and second-order elementary effects methods', Energy and Buildings 68 (2014) 741–750. Available at: https://www.sciencedirect.com/science/article/pii/S0378778812004768.

State Council Communique. (2020) Statement at the General Debate of the 75th Session of the United Nations General Assembly — President of the People's Republic of China, Xi Jinping. Available at:https://www.gov.cn/gongbao/content/2020/content_5549875.htm (Accessed: 27 June 2024).

Yu, J. Qian, C. Yang, Q. Xu, T. Zhao, J. Xu, X. (2023) 'The energy saving potential of a new ventilation roof with stabilized phase change material in hot summer region', Renewable Energy 212 (2023) 111–127. Available at: https://www.sciencedirect.com/science/article/pii/S0960148123006262.

Yu, J. Yang, H. Zhao, J. Zhang, C. Qian, C. Chen, Y. Tang, X. (2024) 'Study on thermal performance of dynamic insulation roof integrated with phase change material', Energy & Buildings 303 (2024) 113832. Available at: https://www.sciencedirect.com/science/article/pii/S0378778823010629.

Zhao, Z. Li, H. Wang, S. (2022) 'Identification of the key design parameters of Zero/low energy buildings and the impacts of climate and building morphology', Applied Energy 328 (2022) 120185. Available at: https://www.sciencedirect.com/science/article/pii/S0306261922014428.

#246: Comprehensive evaluation of a multi-energy complementary system

Xiaolong LI[1], Hailong YU[1*], Shuntang ZHU[1], Lanhua DAI[2]

[1] Changzhou university, China, *yhl@cczu.edu.cn
[2] Changzhou institute of technology, China

Abstract: The multi-energy complementary system has the advantages of being clean, low-carbon, safe, and efficient. However, the standardized evaluation system has not yet been formed, and it is easy to have the problem of unclear construction goals. Therefore, a new comprehensive evaluation system that includes economic benefits, energy efficiency, environmental benefits, technical benefits, and social benefits was proposed. In the evaluation process, the analytic hierarchy process was used to determine the weight of each indicator, and the fuzzy comprehensive evaluation method was utilized to evaluate and analyze the indicators. In addition, the multi-energy complementary system of the Nanjing building complex was taken as an example for model verification. The results showed that compared with the primary system, the optimized system had great advantages in terms of economy, energy efficiency, and social impact. The fuzzy evaluation results of the primary system and the optimized system were 0.69 and 0.75, respectively. The comprehensive evaluation of the optimized system was better.

Keywords: Multi-Energy Complementary System; Analytic Hierarchy; Fuzzy Comprehensive Evaluation; Comprehensive Evaluation

1. INTRODUCTION

With the proposal of China's carbon peak and carbon neutrality goals, people are aware of the importance of clean energy in national production and the necessity of energy conservation and emission reduction, and the multi-energy complementary system has received more attention (Liu et al. 2023). A multi-energy complementary system integrates various energy sources to meet the needs of multiple loads. Through the use of advanced information control and energy dispatching technology, the coupling of different energy sources and the cascade utilization of energy can be realized (Liu et al. 2022).

As shown in Figure 1, a multi-energy complementary system was designed according to the various load changes and resource distribution in Nanjing. The system consists of the ground source heat pump (GSHP), the surface water source heat pump(WSHP), the solar photovoltaic solar thermal integrated system, the storage battery, the wind turbine, and the combined cooling, heating and power system(CCHP). It can provide users with cooling, heating, and electrical energy, and can also store excess energy to release when needed. The multi-energy complementary system consists of energy input, production, conversion, storage and utilization. However, the complexity of the system makes it difficult to evaluate.
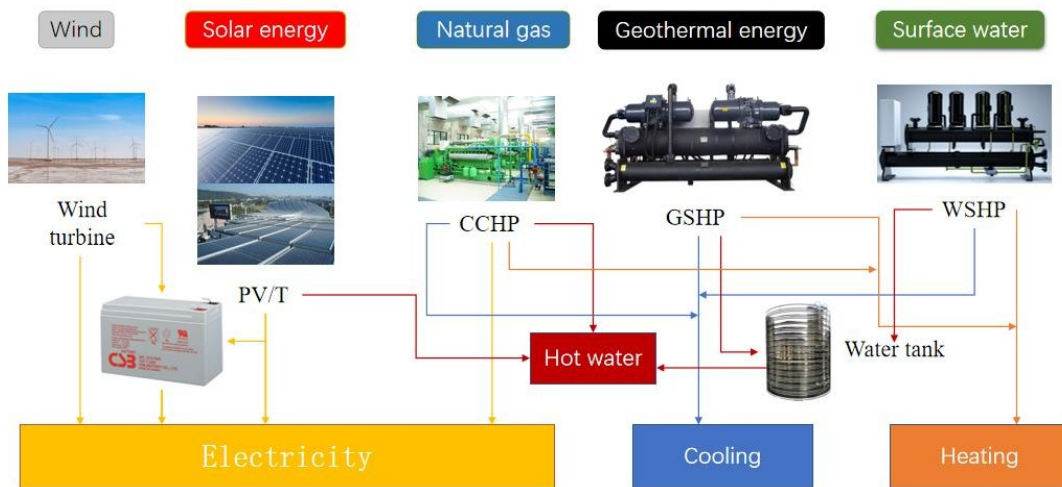

Figure 1: Multi-energy complementary system structure

In terms of multi-energy complementary system evaluation, different scholars often have different opinions. To study the sustainability of the system, Liu et al. (2024) employed a life cycle assessment approach encompassing energy, economic, environmental, and social dimensions. The optimal combination of the system achieved a sustainability index of 0.999. Wu et al. (2023) evaluated the multi-energy complementary system with different capacity configurations from three aspects: sustainability, efficiency, and reliability. Yin et al. (2021) and Geng et al.(2022) optimized the system based on the evaluation criteria of economy, reliability, and environmental protection. Currently, the evaluation of multi-energy complementary systems often has different objectives. Few studies have studied its full and comprehensive evaluation criteria. Huang et al. (2024) constructed a 5D comprehensive evaluation standard system including environment, economy, technology, safety, and systematicness. However, the evaluation system is only suitable for small and medium-sized enterprises, and there is a lack of research on public buildings.

Therefore, based on the requirements of a multi-energy complementary system, a new comprehensive evaluation system was constructed. The system has five first-level evaluation indicators, including economic benefits, energy efficiency, environmental benefits, technical benefits, and social benefits. There are also 19 secondary indicators under the primary indicators. The weights of each evaluation index were determined by the analytic hierarchy process. The comprehensive benefit evaluation was realized by the fuzzy comprehensive evaluation method. Finally, the multi-energy complementary system in Nanjing was taken as an example to verify the evaluation system.

2. COMPREHENSIVE EVALUATION SYSTEM

For multi-energy complementary systems, if the factors selected are different, the indicators used will also be different, which will lead to differences in the evaluation results. Therefore, a certain factor should not be selected unilaterally, and the weight of each factor should be comprehensively considered from the aspects of economy, energy efficiency, and environment, to ensure the scientificity and accuracy of the evaluation results. The evaluation index hierarchy used in this paper is described in Figure 2.
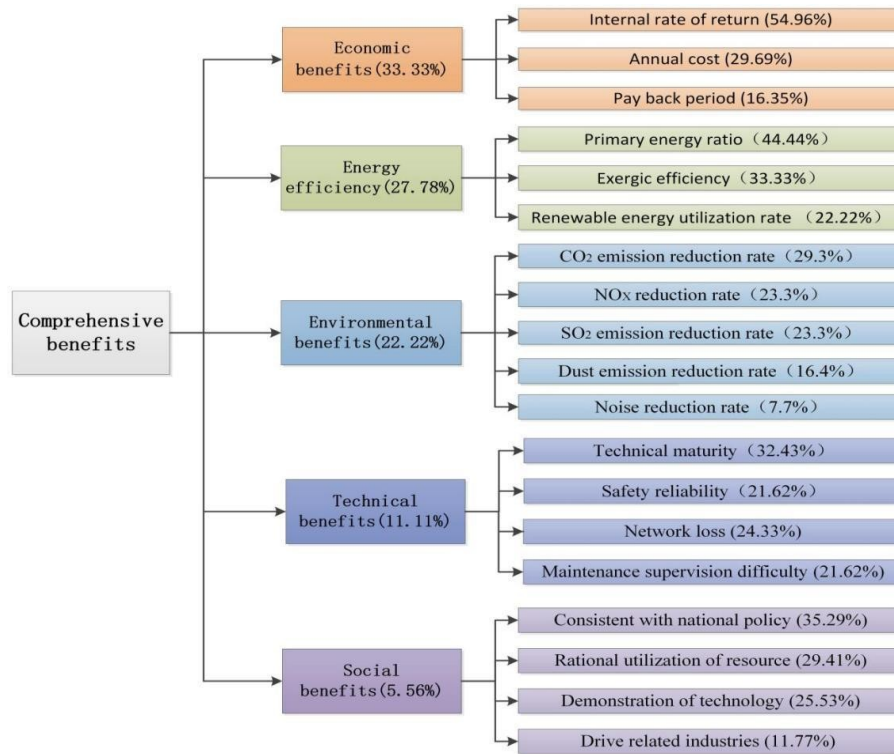
Figure 2: Comprehensive evaluation system

2.1. Economic benefit evaluation indicators

Compared with the static evaluation method, the dynamic evaluation method considers the value-added of funds in the process of circulation, which can fully reflect the profitability of the project life cycle. The evaluation indicators of economic benefits include annual cost, internal rate of return, and payback period. Each indicator can be calculated using the following equations.

Equation 1: Annual cost

$$AC = \frac{i \times (1+i)^n}{(1+i)^n - 1} \times CL + CY + CW$$

Where:

AC = Annual cost of the system (Yuan)

i = Interest rate (%)

n = Service life of the system (Yuan)

CL= Initial investment of the system (Yuan)CY= Perating cost of the system (Yuan)

CW= Maintenance cost of the equipment (Yuan)

Equation 2: Internal rate of return

$$\sum_{i=1}^{n} \left(C_i - C_o \right)_t \left(1 + IRR \right)^{-t} = 0$$

Where:

C_{it} = cash inflow in year t (Yuan) C_{ot} = cash outflow in year t (yuan)

Equation 3: Payback period.

$$\sum_{t=0}^{P_t}(C_i - C_o)_t(1+i_c)^{-t} = 0$$

Where:

P_t = Dynamic payback period (Years)

I_c = Refer to the industry standard rate of return (%)

2.2. Energy efficiency evaluation indicators

The primary energy ratio refers to the ratio of the total output energy of the system to the total primary energy input, and the expression is as follows.

Equation 4: Primary energy ratio.

$$PER_{SP} = \frac{E + Q_H + Q_C}{F_{gh}}$$

Where:

Q_C = The cooling capacity (kJ)

Q_H = The heat supply required by the user (kJ)

E = The amount of electricity required by the system (kJ)

F_{gh} = Energy consumed by natural gas (kJ)

Exergic efficiency is based on the second law of thermodynamics and is commonly used to characterize consumption, conversion, and loss during the energy cycle, and the expression is shown below.

Equation 5: Exergic efficiency.

$$\eta_{ex} = \frac{3600\sum P_0 + \sum A_h Q_H + \sum A_c Q_C}{VQ_L A + 3600\sum P_i}$$

Where:

η_{ex} = Exergy efficiency

P_0 = Power generation (kW)

V = Gas consumption (m3)

Q_L = Low calorific value of natural gas

P_i = Input power (kW)

A_h = Thermal mass coefficient

A_C = Mass coefficient of cold energy

A = Natural gas mass factor

Renewable energy utilization rate refers to the ratio of the amount of renewable energy consumed by the system to the total energy consumed by the system, which can be calculated using the following equation.

Equation 6: Renewable energy utilization rate.

$$\eta_q = \frac{Q_R}{Q_S}$$

Where:

η_q = Renewable energy utilization rate of the system

Q_R = Renewable energy utilization of the system (kJ)

Q_S = total energy consumption of the system (kJ)

2.3. Environment benefit evaluation indicators

The multi-energy complementary system mainly uses renewable energy, which is more low-carbon and environmentally friendly than the traditional energy system. As a result, the system's pollutant emissions are also significantly reduced. The amount of pollutant emissions can be calculated using the following equation.

Equation 7: Pollutant emissions.
$$P_{xi} = E_{grid}\lambda_x + F_g\mu_x$$

Where:

λ_x = Emission factors of coal-fired power generation polluted areas

μ_x = Pollutant emission factors after combustion of natural gas

x = Types of contaminated areas, including CO_2, NOX, SO2 and soot

For noise pollution, the severity of noise pollution should be determined by a comprehensive review by residents and experts.

2.4. Technical benefit evaluation indicators

The indicators of technical benefits include safety and reliability, average failure rate, network loss, and operation and maintenance difficulty, which are qualitative indicators and are generally reviewed by experts in the field of multi-energy complementarity based on existing project experience.

2.5. Social benefit evaluation indicators

In order to comprehensively evaluate the social impact of the multi-energy complementary system, it should be considered to the satisfaction of the government, system equipment suppliers, and users, and the expressions that define the social impact indicators are as follows.

Equation 8: Social Impact Indicators.
$$N = \frac{\sum_{k=1}^{P} N_K}{P}$$

Where:

N = Social impact index

P = The number of relevant parties in the system, including the government, system equipment suppliers, users

N_K = Satisfaction with the various parties concerned, generally based on questionnaire.

3. COMPREHENSIVE EVALUATION OF MATHEMATICAL MODELS

3.1. A mathematical model for evaluating the weights of indicators

In this paper, the analytic hierarchy process was used to determine the weight of each evaluation indicator, and the specific steps are as follows:

Step 1: Build a hierarchical model

Step 2: Construct a judgment matrix for pairwise comparison

The evaluation indicators were compared in pairs, and the following judgment matrix was constructed according to the values corresponding to the relative importance. a_{ij} denotes the result of the i-th factor compared to the j-th factor for the judgment matrix A. The scaling method is shown in Figure 3.

$$A = \begin{pmatrix} a_{11} & \cdots & a_{1n} \\ \vdots & \ddots & \vdots \\ a_{m1} & \cdots & a_{mn} \end{pmatrix}$$
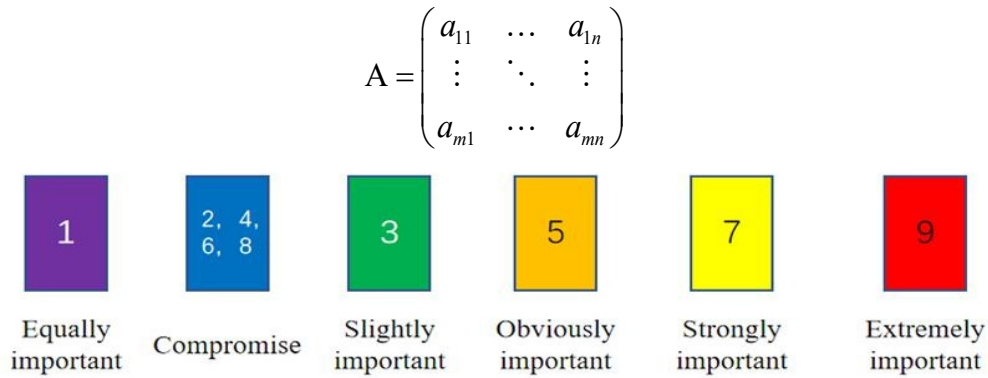

Figure 3: The scale and definition Judgment matrix

Step 3: Determine the weight of each evaluation indicator

MATLAB was used to find and normalize the eigenvectors corresponding to the maximum eigenvalues of the judgment matrix, and then the weights of each evaluation index were mapped to 0-1 according to the corresponding proportions.

The weights of each indicator are shown in Figure 2. Among all the first-level indicators, economic benefits accounted for the largest weight of 33.33%. The social benefits account for at least 5.56%. The weight of energy efficiency was 27.78%, the weight of technical benefits was 11.11%, and the weight of environmental benefits was 22.22%.

3.2. Comprehensive evaluation methodology

In this paper, the fuzzy comprehensive evaluation method was proposed to comprehensively evaluate the multi-energy complementary system. The steps of the fuzzy comprehensive evaluation method are as follows:

Step 1: Establish a set of factors for five types of first-level evaluation indicators

According to the hierarchical system of evaluation indicators, the five first-level indicators that affect the comprehensive evaluation of the multi-energy complementary energy system were combined into a collection U = {u_1, u_2, u_3, u_4, u_5} . Each of these factors can be divided into several subsets representing secondary indicators, such as u_{ij} for U = {u_{11}, u_{12}, u_{13}}.

Step 2: Establish a collection of comments for comprehensive evaluation

The set of all results made by evaluator consisted of the evaluation object $V\{v_1, v_2 \cdots v_{n-1}, v_n\}$, and v_i is the evaluation level.

Step 3: Establish the evaluation matrix of each secondary index
According to the degree of membership of each element u_{ij} of subset u_i to the comment set V, the fuzzy comprehensive evaluation matrix R_i is obtained:

$$R_i = \begin{pmatrix} r_{11} & r_{12} & \cdots & r_{1m} \\ r_{21} & r_{22} & \cdots & r_{2m} \\ \vdots & \vdots & \vdots & \vdots \\ r_{n1} & \cdots & \cdots & r_{nm} \end{pmatrix}$$

Suppose that the vector formed by the weights of each secondary indicator of U_i in the subset was $\zeta_i = (\varphi_1, \varphi_2, \varphi_3 \cdots \varphi_n)$

$$B_i = \zeta_i \cdot R_i, \quad i = 1, 2, 3, 4, 5$$

In general, membership values are usually constructed based on expert reviews, case project experience, industry standard data or existing literature.

Step 4: Comprehensive evaluation

Assuming that the weight vector of indicators u_1, u_2, u_3 u_4, and u_5 at each level was $\psi = \left(\lambda_1, \lambda_2, \lambda_3, \lambda_4, \lambda_5 \right)$, the comprehensive evaluation results were obtained:

$$F = \left(\lambda_1, \lambda_2, \lambda_3, \lambda_4, \lambda_5 \right) \begin{bmatrix} B_1 \\ B_2 \\ B_3 \\ B_4 \\ B_5 \end{bmatrix}$$

4. RESULTS AND DISCUSSION

In this paper, the Nanjing architectural complex was selected as the research object. The complex includes hotels, office buildings, and residential villas. In order to explore the evaluation effect under different schemes, the multi-energy complementary system was designed into two energy supply methods. The primary scheme is the energy supply method that is dispatched through the overall load change. According to the actual load demand, the energy supply mode of the unit with frequency conversion technology was the optimized scheme.

4.1. First-level indicator benefit evaluation

As can be seen from Table 1, the optimized scheme reduced the annual cost by about 30% compared to the primary scheme. The internal rate of return has increased by 2% and the payback period has been shortened by almost two years. The membership function was constructed based on the case project data, the calculation results of economic benefit indicators, and the existing literature (Fu 2011, Xu 2011). The membership value derived from the membership function constitutes the evaluation matrix R1. The economic benefit was assessed as follows.

Table 1: Comparative analysis of economic benefit indicators of two schemes

Items	Primary scheme	Optimized scheme
Annual operation cost/Yuan	4912100	2653600
Annual maintenance cost/Yuan	984800	916100
Annual cost/Yuan	13724500	9799500
Internal rate of return	14.86%	16.24%
Payback period/Year	6.28	4.37

$$R_1 = \begin{pmatrix} 0.42 & 0.68 \\ 0.66 & 0.75 \\ 0.85 & 0.95 \end{pmatrix} \qquad B_1 = \zeta_1 \cdot R_1 = \left(0.63, 0.77 \right)$$
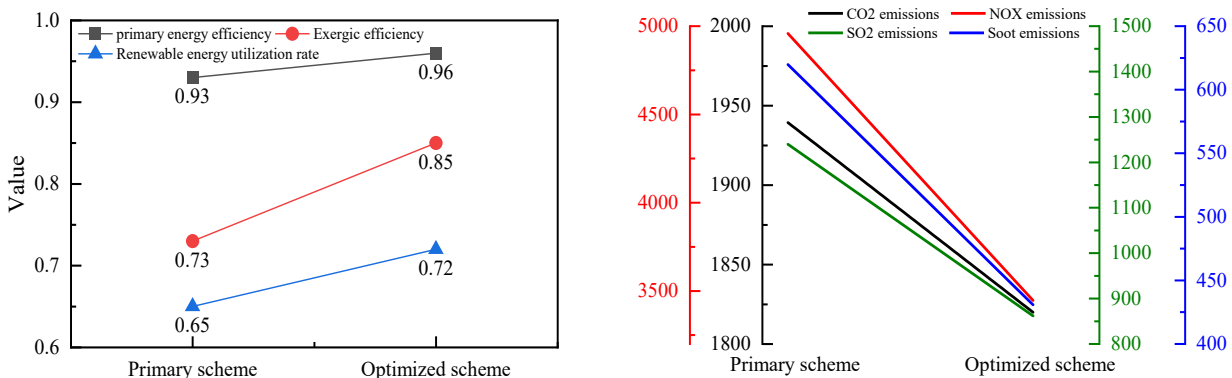

Figure 4: Comparative analysis of energy efficiency and environmental benefit indicators of two schemes

414

The energy efficiency and environmental benefits of the primary and optimized schemes are shown in Figure 4. In terms of energy efficiency, the primary energy ratio, the exergic efficiency, and the renewable energy utilization rate of the designed system had increased by 3%, 12%, and 9% respectively. In terms of environmental benefits, both schemes can reduce a large number of pollutant emissions. Due to the large selection of equipment in the primary scheme, the pollutant emission reduction was also 6% more than that of the optimized scheme. The membership function was constructed based on the case project data, the calculation results of economic benefit indicators, and the existing literature (Li 2019). The evaluation matrices composed of energy efficiency and environmental benefits are R2 and R3. The energy efficiency and environmental benefits were assessed as follows.

$$R_2 = \begin{pmatrix} 0.93 & 0.96 \\ 0.73 & 0.85 \\ 0.63 & 0.72 \end{pmatrix} \qquad B_2 = \zeta_2 \cdot R_2 = (0.68, 0.73)$$

$$R_3 = \begin{pmatrix} 0.94 & 1 \\ 0.69 & 1 \\ 0.69 & 1 \\ 0.69 & 1 \\ 0.7 & 0.5 \end{pmatrix} \qquad B_3 = \zeta_3 \cdot R_3 = (0.76, 0.96)$$

Since most of the indicators of technical and social benefits are qualitative parameters, the specific values can only be obtained through references (Ling 2012, Song 2019) and expert review. By establishing membership functions, the evaluation matrix can be obtained as R4 and R5. The assessment of the technical and social benefits is shown below.

$$R_4 = \begin{pmatrix} 0.7 & 0.5 \\ 0.8 & 0.6 \\ 0.75 & 0.83 \\ 0.6 & 0.4 \end{pmatrix} \quad B_4 = \zeta_4 \cdot R_4 = (0.71, 0.58)$$

$$R_5 = \begin{pmatrix} 1 & 1 \\ 0.7 & 1 \\ 0.9 & 0.7 \\ 0.7 & 0.75 \end{pmatrix} \qquad B_5 = \zeta_5 \cdot R_5 = (0.85, 0.89)$$

4.2. Comprehensive benefit evaluation

The comprehensive evaluation matrix of the five types of first-level indicators of the reference system and the design system was listed below.

$$R = \begin{pmatrix} 0.63 & 0.77 \\ 0.68 & 0.73 \\ 0.76 & 0.96 \\ 0.71 & 0.58 \\ 0.85 & 0.89 \end{pmatrix}$$

The weight of the five types of first-level evaluation indicators was $\psi = (0.33, 0.28, 0.11, 0.22, 0.06)$, and the fuzzy comprehensive benefit evaluation of the multi-energy complementary system was as follows.

$$F = \psi \cdot R = (0.69, 0.75)$$

From the results of the comprehensive benefit evaluation, it is clear that the optimized scheme is superior to the primary scheme.

5. CONCLUSION

In this paper, a comprehensive evaluation system of multi-energy complementary system was established. The analytic hierarchy process was used to calculate the weights of each of the five first-level indicators and the nineteen second-level indicators. The fuzzy comprehensive evaluation method was utilized to establish a corresponding mathematical model to evaluate the two energy supply schemes of the proposed multi-energy complementary system. The main conclusions of this paper are as follows:

(1) In the comprehensive assessment system, economic benefits, energy efficiency, and environmental benefits accounted for 33.33%, 27.78%, and 22.22%, respectively. These three indicators have a great influence on the design of multi-energy complementary systems.

(2) The comprehensive evaluation results of the primary scheme and the optimized scheme were 0.69 and 0.75. Although the primary scheme was better than the optimized scheme in terms of environmental and technical benefits, the overall optimized scheme was more advantageous.

6. REFERENCES

Liu T.H., T J, Zhu H.Y., Goh H H, Liu H, Wu T, Zhang D.D., 2023. Key technologies and developments of multi-energy system: Three-layer framework, modelling and optimisation. Energy, 277, 127697.

Liu C.R., Wang H.Q., Wang Z.Y., Liu Z.Q., Tang Y.F., Yang S, 2022. Research on life cycle low carbon optimization method of multi-energy complementary distributed energy system: A review. Journal of Cleaner Production, 336, 130380.

Liu L.T., Zhai R.G., Xu Y, Hu Y.D., Liu S.Y., Yang L.Z., 2024. Comprehensive sustainability assessment and multi-objective optimization of a novel renewable energy driven multi-energy supply system. Applied Thermal Engineering, 236, 121461.

Wu, Y.J., Chen J, Zhang X.Y., He K.W., J L, 2023. Research on optimal configuration of park-level multi-energy complementary system with multiple evaluation indexes. Frontiers in Energy Research, 11, 1281772.

Yin B.X., Li Y.W., Miao S.H., Lin Y.J., Zhao H.P., 2021. An economy and reliability co-optimization planning method of adiabatic compressed air energy storage for urban integrated energy system. Journal of Energy Storage, 40, 102691.

Geng J, Z T, C J, Y Y.F., J Y.L., F J.Z., 2022. Research on multi-objective operation optimization of multi energy integrated service stations based on autonomous collaborative control. Energy Reports, 8, 278-284.

Huang S.Y., Zou X.T., Liang H.G. C J, 2024.Comprehensive evaluation of multi-energy complementary ecosystem based on improved multicriteria decision-making method. Clean Energy, 8, 226-236.

Fu X.W., 2011. Research and application of fuzzy comprehensive evaluation based on analytic hierarchy process. Harbin Institute of Technology.

Xu X.Y., 2011. Research and application of fuzzy comprehensive evaluation model. Southwest Petroleum University.

Li G.P., 2019. Construction of energy system in a community and comprehensive evaluation and analysis of multiple indicators. North China Electric Power University.

Ling P.F., 2012. Research on energy-saving renovation of the pipe network of a central heating system. Chongqing University.

Song J.C., Li Y.T., Chen Z.W., 2019. Research on comprehensive evaluation indexes of multi-energy complementary distributed energy system. Comprehensive utilization of China's resources(in chinese), 37, 39-42.

#247: Proposed hybrid ARIMA-ETS model for mid-term heat load prediction

Asim SHAKEEL[1], Daotong CHONG[1]*, Muhammad SALMAN[2], nimra JAVED[2], Junjie YAN[1]

[1] Xi'an Jiaotong University, State Key Laboratory of Multiphase Flow in Power Engineering, Xi'an, Shaanxi 710049, PR China
[2] MOE Key Laboratory of Thermo-Fluid Science and Engineering, Xi'an Jiaotong University, Xi'an, Shaanxi 710049, PR China
*Corresponding author's Tel: +86-29-82665359, E–mail: dtchong@mail.xjtu.edu.cn

Abstract: Mid-term load forecasting is essential for scheduling operational tasks, optimizing energy consumption, and boosting system output. It requires capturing complex patterns as it spans from several weeks to months; therefore, the model must be able to capture short-term as well as long-term patterns in the dataset. Handling the dataset's temporal variation while maintaining the model's adaptability to evolving trends over a longer time horizon is a challenge. To overcome this challenge, a hybrid solution has been proposed to accurately determine 1-month and 3-months of hourly heat load prediction. The proposed hybrid model is intended to take advantage of the two forecasting models, namely ARIMA and ETS. The optimal values of the ARIMA model's autoregressive, moving average, and integrated components are evaluated, which allows the model to capture longer linear time horizons in the dataset accurately. Concurrently, the ETS model focuses on simulating errors, trend, and seasonal components in the dataset, and these components are also tuned to train an accurate hybrid model. A forward feature selection approach is employed to select the optimum number of features. The performance of another ten machine learning algorithms is compared to the accuracy of the proposed hybrid model. The proposed hybrid model showed accurate results for 1-month prediction with MAE = 3.54, MSE = 41.74, and RMSE = 6.45 and accurate 3-months of prediction results with MAE = 12.38, MSE = 216.52, and RMSE = 14.66; therefore, it could serve a productive guiding role in DHN energy distribution.

Keywords: Hybrid Forecasting Model; ARIMA Model; ETS Model; District Heating Network; Machine Learning

1. INTRODUCTION

A district heating network (DHN) is a system that generates heat at one or more heat units and delivers it through an extensive system of insulated pipes to heat exchangers or substations that are located within individual buildings. Schematic diagram is shown in Figure 1. Building energy use has increased significantly over the past few decades. Based on the data (Juan et al.,2009) developed countries, including Europe as well as China, contribute approximately 20–40% of their total energy consumption to DHNs. Accurate mid-term load forecasting (MTLF) for DHN is critical for effective allocation of heat resources, operation optimization, and cost control. Compared to short-term heat load forecasting, there is limited literature on multi-term load forecasting (MTLF) (Liu et al., 2020).
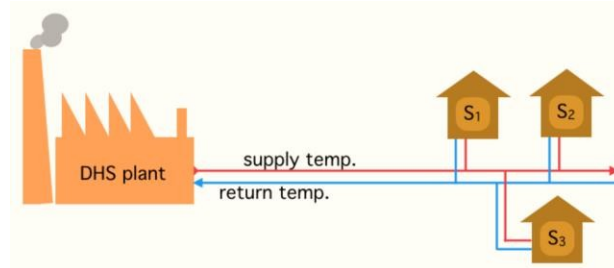

Figure 1: Simple diagram of DHN (Eriksson, 2012)

Developing an accurately estimated MTLF model for DHN usage is a difficult task, and obtaining weather estimates of this nature from weather bureaus for extended periods is also usually difficult. That's why some of the researchers trained the models in different MTLF studies without incorporating any weather dataset features into their models (Rallapall et al., 2012; Niu et al., 2021; Peng et al., 2022). Some researchers choose to circumvent the issue by incorporating future weather datasets into their prediction models (Wu et al., 2021; Gao et al., 2022; Nop et al., 2021). These models' predictive capabilities are inauthentic and inaccurate because they fail to account for the influence of real meteorological characteristics on load forecasting. Some authors incorporate weather forecasts into their MTLF models. The researchers employed linear regression and support vector machine (SVM) algorithms to predict the monthly load consumption in Italy (De et al., 2013; De et al., 2015).

Artificial neural networks (ANN) have been used for the assessment of the MTLF models. In general, ANN methodologies are more appropriate for predicting short-term load patterns (Baek et al., 2019). ANN networks, specifically recurrent neural networks (RNNs), are designed to effectively process sequential data, making them well-suited for anticipating short-term heat load trends. However, multiple studies have utilized ANN models (Pan et al., 2012; Zhang e al., 2010) to train the MTLF models. In order to address the problem, hybrid models are employed for MTLF. Specifically, the hybrid ARIMA and CNN-Bi-LSTM models are implemented to generate MTLF predictions. The hyperparameters of ARIMA and neural network models are adjusted to increase their accuracy [Gul et al., 2021]. CNN-BiLSTM models are susceptible to overfitting due to their ability to learn intricate patterns. A different approach to hybrid algorithms has been developed involving a convolutional neural network (CNN) and bi-directional long short-term memory (Bi-LSTM). This combination of algorithms surpasses the current state-of-the art models in forecasting load utilization across various timespans (Le et al., 2019). The model is trained to obtain predictions for MTLF and long-term load forecasting. The precise challenges and restrictions of MTLF, such as the difficulty in capturing long-term dependencies, seasonal variations, and the impact of external factors like weather, have not been adequately discussed in the literature.

This study proposes a hybrid ARIMA-ETS model to tackle the challenges of mid-term load forecasting (MTLF) over extended hourly periods. The model effectively captures hourly changing trends across longer time horizons by integrating real weather data with actual district heating network (DHN) data. Combining ARIMA and ETS, the hybrid model effectively adjusts to changes in both linear and non-linear trends. The combination leverages the advantages of both models (after hyperparameter adjustment of ARIMA and ETS models) to provide accurate and consistent predictions for medium-term timeframes

2. METHODOLOGY
2.1. Basic ARIMA model methodology

Box et al. proposed the ARIMA model (Box et al., 1967). The three common ARIMA parameters, p, d, and q, simply describe the processing of the ARIMA model. The three parameters p, d, and q represent the auto-regressive (AR), integrated (I), and moving average (MA) components. The auto-regressive parameter indicates the number of prior observations incorporated into the model. It illustrates the relationship between the current observation and the ones that came before it. "P" also denotes the AR parameter as described in Equation 1. The integrated parameter indicates the extent to which the time series data has undergone differencing to satisfy the stationarity requirement. To get rid of patterns or seasonality, differencing entails subtracting the current data from an earlier observation made at a particular time interval, the term "I" describes the d parameter. The moving average indicates the number of lag errors in the prediction model. It illustrates the relationship between the differences in the forecast and the current observation. The parameter "q" can also represent by MA as described in Equation 2. In actuality, the stationary condition of the data set must be satisfied by the time series data in order for the ARIMA model to work, which is nearly impossible. Therefore, differencing Equation is used to eliminate the non-stationarity of the time series data. Equation 3 described the formula for differentiating.

Equation 1: Equation for AR	$y_t = c + \phi_1 y_{t-1} + \phi_2 y_{t-2} + \cdots + \phi_p y_{t-p} + \varepsilon_t$
Equation 2: Equation for MA	$y_t = c + \theta_1 \varepsilon_{t-1} + \theta_2 \varepsilon_{t-2} + \cdots + \theta_q \varepsilon_{t-q} + \varepsilon_t$

Equation 3: Differencing equation

$$y_t^{(d)} = c + \varepsilon_t + \phi_1 y_{t-1}^{(d)} + \phi_2 y_{t-2}^{(d)} + \cdots + \phi_p y_{t-p}^{(d)} + \theta_1 \varepsilon_{t-1} + \theta_2 \varepsilon_{t-2} + \cdots + \theta_p \varepsilon_{t-q}$$

Where:

- c = represents a constant or drift
- y_t = It represents the variable of interest's present value (t), value one timestep prior (t-1), and value two timesteps prior (t-2).
- , θ = coefficients calculated by fitting the training data.
- p and q= total number of coefficient
- ε_t = error term
- $y_t^{(d)}$ = Integrated value

2.2. Basic ETS model Methodology

The ETS models belong to a group of time-series models. It is named ETS because the abbreviation E is used for error, T is used for trend component, and S is used for seasonality. All these three components are used to explain the ETS model. The ETS model relies on the principle of exponential smoothing. Exponential smoothing uses a weighted average of previous observations. The weight of previous findings diminishes dramatically. A smoothing parameter α ranging from zero to one sets the rate of decay. Equation 4 describes the Exponential Smoothing Equation.

Equation 4: Exponential Smoothing Equation

$$y_t = \alpha \cdot y_{t-1} + \alpha \cdot (1 - \alpha) y_{t-2} + \alpha \cdot (1 - \alpha)^2 y_{t-3} + \cdots$$

Where:

- y_t = Current value of the time series at time *t*,
- α = Smoothing parameter
- y_{t-1} = Value of the time series at the previous time step *(t−1)*
- $1 - \alpha$ = Smoothing parameter and it represents the weight.

The above equation can alternatively be simplified as the forecast equation stated in Equation 5.

Equation 5: Equation for prediction

$$f_t = \alpha \cdot y_{t-1} + (1 - \alpha) f_{t-1}$$

Where:

- yt−1 = Predicted value from the previous time step (t-1)
- f_t = Represents the exponential smoothing value at a given time *t*.
- f_{t-1} = Exponential smoothing value at the preceding time step *(t−1)*.
- α = Represents smoothing constant

2.3. Hybrid model construction

The first step of the forecasting methodology incorporates the automated estimation of the model's parameters, namely E, T, and S for the ETS model and p, d, and q for the ARIMA model. Following the automatic estimation, a significant optimization procedure adjusts the model parameters to evaluate the optimal component values. To fine-tune the ARIMA model's hyperparameters, different combinations of the p, d, and q components are tested over and over again until the best combination is found that makes accurate predictions. An ARIMA model is generated using various combinations of p (33–38), d (0–1), and q (20–23) component values. The model is then trained using all the provided variables. The 48 ARIMA models are trained, and a grid search strategy is applied to determine the optimal values of ARIMA model components. Before integrating the ARIMA model with the ETS model, optimal component values (p, q, and d) of the ARIMA models are used to adjust the error (E), trend (T), and seasonality (S) components of the ETS model. Initially, the various combinations of E, T, and S components are systematically assessed by iterating through the hyperparameter values within specified ranges. The model's performance is then evaluated for each combination. After training models using different combinations of hyperparameters, the results are displayed in a 3D scatter plot. The x, y, and z axes reflect the values of distinct components (p, d, and q), and a grid search technique is employed to tune the values of the E, T, and S components in ETS models.

The ultimate goal is to develop a hybrid model that overcomes MTLF challenges while benefiting from the advantages of both models. After hyperparameter tuning, the optimized ARIMA model is combined with the tuned ETS model. Figure 2 displays a comprehensive schematic representation. After the hyperparameter tuning of ARIMA and ETS models, they are integrated as represented in Equation 6.

Equation 6: Hybrid Model Equation

$$X_t = I_1 \widehat{X_t^1} + I_2 \widehat{X_t^2}$$

Where:

X_t = Proposed hybrid model

$\widehat{X_t^1}$ = ARIMA model estimation

X_t^2 = ETS model estimation

I_1, I_2 = weight factors of ARIMA and ETS model
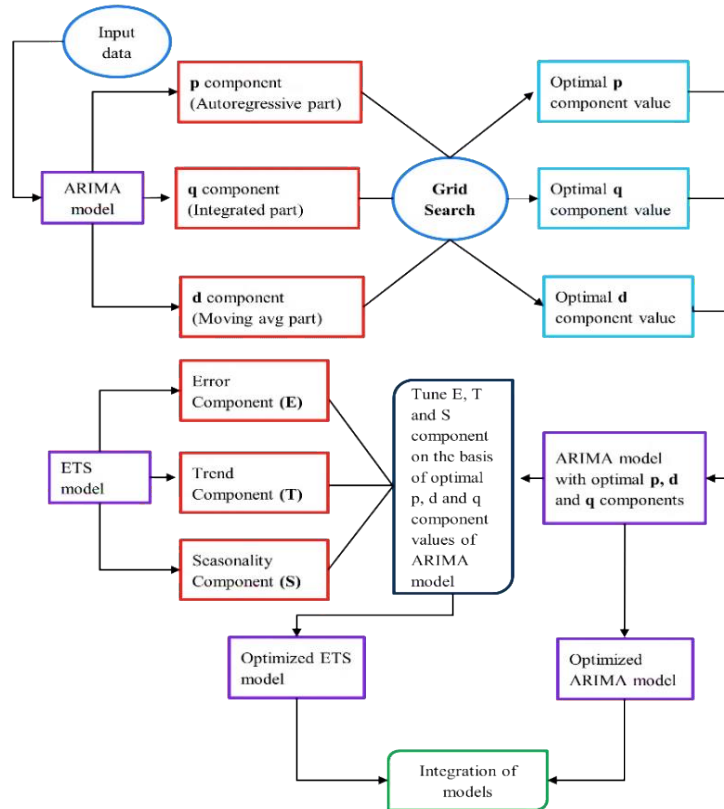

Figure 2: Proposed Hybrid ARIMA-ETS methodology

3. DATA HANDLING AND EXPLORATORY ANALYSIS

In order to train the proposed hybrid model, a historical dataset has been obtained from the years 2014 to 2016, measured in megawatts (MW). This data relates to a district heating system located in Flensburg, Germany. In addition, a historical weather dataset is gathered from the closest meteorological station, which includes a range of different parameters:

- Outdoor temperature (degree centigrade, oC)
- wind speed (Kilometer/hour, Km/h)
- Humidity (percentage, %)
- Pressure (millibar, mbar)
- Visibility (Kilometer, Km)
- wind direction (degrees, O)
- Clouds cover (sunny, cloudy, overcast)

In order to guarantee that the model is not impacted by extreme values, handling outliers and missing values in a time series dataset for forecasting is crucial. To fill in the missing values, the interpolation method is applied. By following a methodical process, the interquartile range (IQR) approach is used to identify outliers in the datasets, including meteorological variables and historical data from DHN. The first quartile (Q1) is determined, followed by the third quartile (Q3). Next, the difference between Q3 and Q1 is calculated to get the IQR (IQR = Q3 - Q1). After this, the equation Q1 + 1.5 * IQR is used to define the lower bound, and Q3 + 1.5 * IQR is used to define the upper bound of the usual data range. Any data point that deviates from this range is regarded as an outlier as shown in Table 1 and is not included in the study.

Table 1: Data outliers in historical dataset

Parameter	Number of missing values	Number of Outliers detected
District heating data	586	1197
Outdoor temperature	387	589
Clouds cover	401	658
Wind speed	259	369
Wind direction	658	1025
Humidity	578	486
Pressure	552	687
Visibility	741	987

Figure 3 illustrates the computation of the Pearson correlation for each gathered meteorological feature, based on the predicted parameter of heat load consumption. The correlation factors show the links between environmental variables and DHN usage. The outdoor temperature has a strong negative correlation of -0.76, indicating that the need for heat increases with decreasing temperatures. Cloud cover exhibits a significant negative correlation of -0.69, suggesting that elevated cloudiness corresponds with elevated heat demand. The somewhat negative correlation between wind speed and heat demand, which is -0.62, indicates that heat demand tends to decrease as wind speed increases. There is not much of a relationship between wind direction and heat demand, as seen by the wind direction's small positive correlation of 0.11. Humidity and heat demand have a positive correlation of 0.41, suggesting a link between higher humidity levels and increased heat demand. Pressure and visibility, with weak positive correlations of 0.10 and 0.08, respectively, indicate a slight correlation with heat demand.
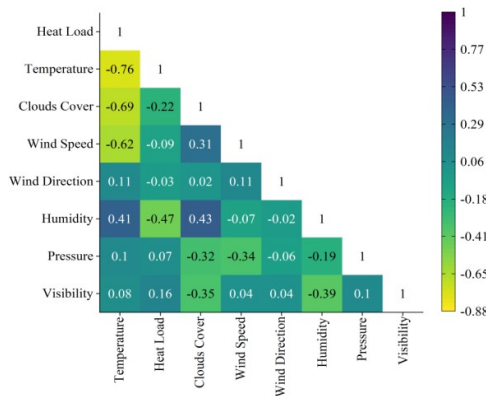

Figure 3: Visual representations of all the correlation values
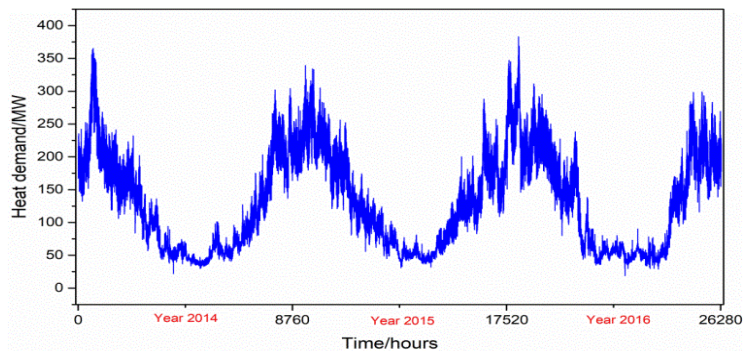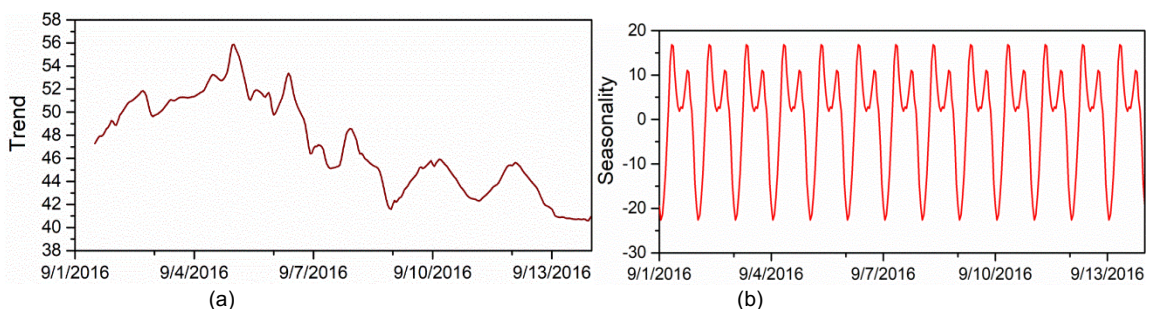

Figure 4: Heat demand of Helsinki district heating system

Figure 5 breaks down the time series data, as shown in Figure 4, into different systematic components for selecting forecasting methods and more detailed dataset analysis. Three components comprise a systematic breakdown into 'error', 'trend', and 'seasonality'.
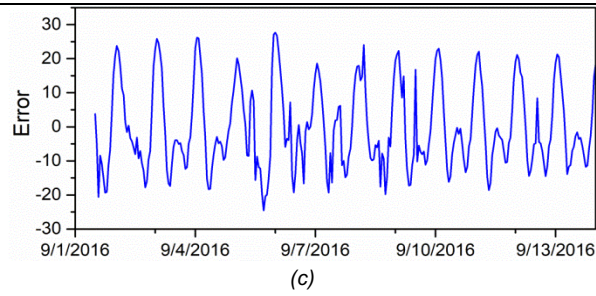

(a)   (b)

(c)

Figure 5: Decomposition of dataset into different components

As demonstrated in Figure 5(a), a dataset with a trend component that shows both upward and downward movements indicates a complicated or dynamic pattern in the underlying data. Because ARIMA-ETS models can adjust to cyclical patterns, they are suitable for datasets with alternating growth and decline phases. The model can adapt to the cyclical nature of the mixed trend and generate predictions that match the complex patterns exhibited by the combination of ARIMA and ETS components. As seen in Figure 5(b), a dataset with a seasonality component that exhibits a continuous trend repeating after a predetermined period refers to a distinct and consistent pattern in the data. The seasonality component's repeated and constant characteristics fit in nicely with the ARIMA-ETS model's capabilities. ARIMA-ETS models specifically engineered to manage this type of regular and cyclical activity make them an appropriate choice for forecasting results in datasets exhibiting consistent seasonal patterns. Figure (c) displays the values of the dataset's error component, which aligns well with the actual values. In summary, it shows that the accuracy and precision of the ARIMA-ETS model are working admirably. Alignment achieves model validation, demonstrating the ARIMA-ETS model's good fit for your dataset. The model confirms its capture of the key dynamics and patterns present in the data.

4. RESULTS AND DISCUSSIONS
4.1. Initial Processing to construct the hybrid model

To train the ARIMA model, the dataset must maintain consistency over time. If it exhibits non-stationary behavior, the ARIMA model cannot manage the dataset to produce reliable prediction output. A popular unit root test, the Augmented Dickey-Fuller test, determines the stationarity of a time series as explained in Equation 7:

Equation 7: Augmented Dickey-Fuller test
$$y_t = c + \beta t + \alpha y_{t-1} + \phi_1 \Delta Y_{t-1} + \phi_2 \Delta Y_{t-2} \cdots + \phi_p \Delta Y_{t-p} + e_t$$

Where:

- y_t = Value of the time series data
- c = Constant term
- βt = Deterministic time trend component.
- $\Delta Y_{t-1} + Y_{t-2} + \cdots + \Delta Y_{t-p}$ = Lagged differences of the time series data
- α = Co-efficient of lagged term
- $\phi_1 + \phi_2 \cdots + \phi_p$ = coefficients of the lagged difference terms

Table 2 displays the test's outcomes. These findings support the notion that the data is stationary as the p-value exceeds the significance level and the ADF statistics are more negative than the crucial values.

Table 2: Stationarity test results performed on ARIMA model

Parameter	Value
ADF statistics	-16.33
P-Value	3.013
Critical value	1% value = 3.46, 5% values = -2.87, 10% values = -2.57

4.2. Effect of number of features on accuracy

The heat load forecasting model's findings with various numbers of features provide useful insights into the model's predictive ability on the hybrid ARIMA-ETS model. The forward feature selection method is used to determine the number of features for the proposed hybrid model. Starting with the most correlated variable, the number of features is increased to assess the ARIMA-ETS model's performance. Figure 3 shows the findings of the Pearson correlation analysis. The forward feature selection analysis reveals that adding all the features does not improve model performance. However, careful evaluation reveals that utilizing four features (outdoor temperature, cloud's cover, wind speed, and wind direction) boosts the efficiency of the model. These features display the least error deviation of MSE error metrics, demonstrating that the model can produce reliable results when employing these features as shown in Table 3. The model may overfit the projected outcomes by including more features. So, the prediction analysis for one and three months is carried out, utilizing four features to train the proposed hybrid model.

Table 3: Forward Feature selection results

Number of features	MSE value deviation (1-months)	MSE value deviation (3-months)
Outdoor Temperature	6.22	9.14
Outdoor temperature + Clouds cover	5.44	8.04
Outdoor temperature + clouds cover + wind speed	3.66	7.11
Outdoor temperature + clouds cover + wind speed + wind direction	2.44	5.96
Outdoor temperature + clouds cover + wind speed + wind direction + Humidity	6.67	11.33

4.3. Evaluation of optimal prediction length

The optimal length of the training dataset may differ depending on the dataset's specific properties and the forecasting task. The incremental dataset expansion approach is used to determine the appropriate prediction length. The results are displayed in Figure 6. These metrics provide data on the model's accuracy and predictability. The model's performance fluctuates as the size of the training dataset grows. Overall, these results imply that increasing the size of the training dataset improves hybrid model performance, as evidenced by lower MAE, MSE, and RMSE values. This suggests that the model's predictions become increasingly accurate and precise as the training data set grows in size and diversity. In addition, the model showed the lowest error ratio values at 2190 training dataset values and 5840 dataset values in the 1-month and 3-month prediction periods. As the number of dataset values increased, the model's performance deteriorated due to unknown phenomena.
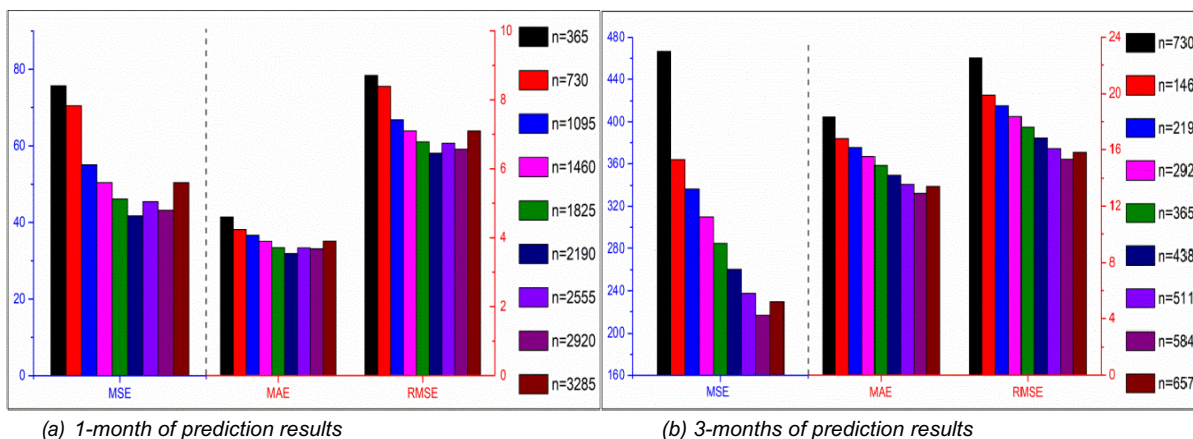

(a) 1-month of prediction results   (b) 3-months of prediction results

Figure 6: perdition results under different training dataset values

4.4. Hybrid model prediction results

We train the proposed hybrid model, ARIMA-ETS, to produce prediction results for 1 and 3 months. Figure 7 illustrates how the comprehensive view includes the training and testing datasets. The training data captures historical patterns and trends, which serve as the foundation for the model's historical understanding. The testing dataset indicates predicted data and allows for an assessment of the hybrid ARIMA-ETS model's predictive capabilities. The graph illustrates how the model's predictions and the historical values as they occurred interact. The goal of putting the training and testing datasets side by side is to compare and contrast them, and it also involves arranging elements close together to draw attention to any differences, similarities, or connections between them. It is also beneficial to gain an understanding of how well the model matches the patterns observed during the training phase and extends its accuracy to unseen data during the testing phase. Any differences or similarities betweenthe actual and predicted values offer a detailed insight into how well the model performs across various data sets.
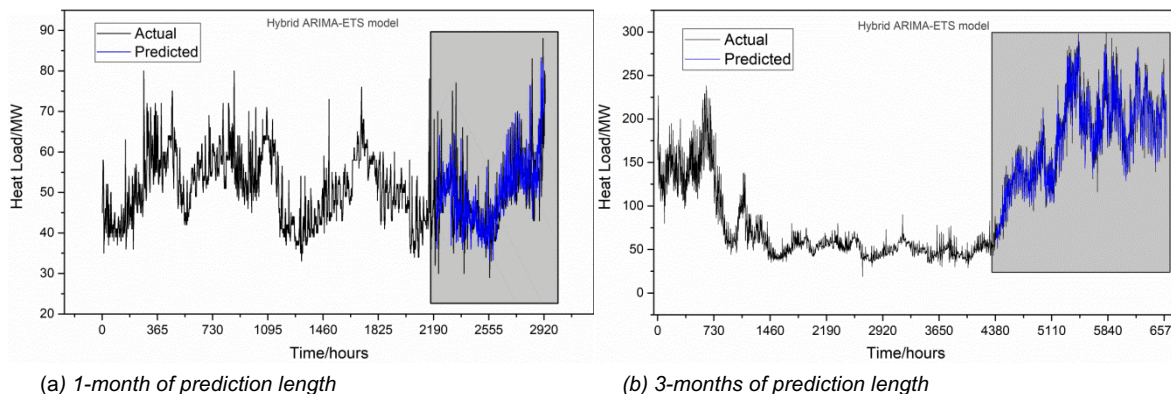

(a) 1-month of prediction length   (b) 3-months of prediction length

Figure 7: Proposed ARIMA-ETS model prediction results

5. COMPARISON STUDY

After obtaining the predictions from the ARIMA-ETS model, we conduct an analysis of the 1 and 3-month prediction length results to assess the model's performance. The evaluation analysis includes training an additional set of ten machine learning models to fully assess the forecasting performance. Some of these models include FB-Prophet, Imp-FB-Prophet, LSTM, XGBoost, MLP, RNN, SVR, FB-Prophet/MLP, and DeepVAR. The goal is to benchmark the hybrid ARIMA-ETS model against various modern machine learning algorithms. We selected the models for this comparison based on their industry popularity and relevance. We use three distinct metrics MAE, MSE, and RMSE through a thorough evaluation process to assess each trained model's performance. The 1-month and 3-month comparison studies thoroughly evaluated a variety of machine learning models using a common dataset. Table 4 displays the results. ARIMA and ETS, two of the more established time series forecasting models, performed competitively; however, ARIMA-ETS stood out as the best model, displaying the lowest errors in all three metrics. This hybrid model seamlessly combines the strengths of ARIMA and ETS components, showcasing its robustness in identifying underlying patterns in the dataset, achieving the lowest values of MAE, MSE, and RMSE in both the 1-month and 3-month prediction cases.

Table 4: Comparison analysis results for 1 and 3 months of prediction length

Model	MAE (1-months)	MSE (1-months)	RMSE (1-months)	MAE (3-months)	MSE (3-months)	RMSE (3-months)
FB-Prophet	7.40	83.53	9.14	15.78	450.14	21.23
Imp-FB-Prophet	6.20	64.32	8.04	14.02	390.14	19.75
DeepVAR	8.20	117.31	10.82	20.16	801.74	28.32
LSTM	8.41	140.89	11.87	18.70	658.74	25.66
XGBoost	8.17	131.56	11.47	18.78	704.14	26.54
MLP	9.26	143.52	11.98	16.20	501.74	22.41
RNN	9.54	146.41	12.10	15.28	441.54	21.01
SVR	12.10	248.44	15.78	17.02	610.52	24.70
ARIMA	11.40	218.03	14.76	25.20	455.01	21.43
ETS	7.12	131.25	11.45	16.12	356.55	18.18
XGBoost/MLP	5.10	58.83	7.67	13.41	310.31	17.67
FB-Prophet/MLP	4.98	51.35	7.16	13.45	267.21	16.36
ARIMA-ETS	3.54	41.74	6.45	12.38	216.52	14.66

6. CONCLUSION

This paper focuses on the importance of MTLP for energy system reliability and economic efficiency. When it comes to planning maintenance tasks, maximizing energy use, and increasing system output, MTLF is essential. Optimizing transmission and improving distribution networks depend heavily on MTLF accuracy. The proposed hybrid ARIMA-ETS model is trained to predict hourly time series data over longer time horizons by leveraging the strengths of both traditional time series forecasting models.

The ARIMA component successfully captures linear trends by modeling autoregressive and moving average features. Simultaneously, the ETS component highlights seasonality patterns, trends, and modelling error, all of which are recognized for their ability to adjust to different data behaviors. Through this integration, the hybrid model overcomes the limitations of the individual ARIMA and ETS models to learn from historical data in an efficient manner.

The proposed hybrid model, known as the hybrid ARIMA-ETS model, is subjected to hyperparameter tuning for the machine learning components. To do this, optimal values for the ARIMA model's autoregressive (p), moving average (q), and trend (d) components are evaluated. The error (E), trend (T), and seasonal (S) parts are also be tuned in order to get better results.

The ARIMA-ETS model performed well for a 1-month of prediction results, with MAE of 3.54, MSE of 41.74, and RMSE of 6.45. Similarly, ARIMA-ETS displayed the values of MAE = 12.38, MSE = 216.52, and RMSE = 14.66 for the 3-monthsprediction results. These metrics show how well the ARIMA-ETS model can forecast district heating consumption.

7. REFERENCES

Baek, S.M., 2019. Mid-term load pattern forecasting with recurrent artificial neural network. Ieee Access, 7, pp.172830-172838.

Box, G.E., Jenkins, G.M. and Bacon, D.W., 1967. Models for forecasting seasonal and non-seasonal time series (p. 0043). University of Wisconsin--Madison, Department of Statistics.

De Felice, M., Alessandri, A. and Catalano, F., 2015. Seasonal climate forecasts for medium-term electricity demandforecasting. Applied Energy, 137, pp.435-444.

De Felice, M., Alessandri, A. and Ruti, P.M., 2013. Electricity demand forecasting over Italy: Potential benefits using numerical weather prediction models. Electric Power Systems Research, 104, pp.71-79.

Eriksson, N., 2012. Predicting demand in district heating systems: A neural network approach

Gao, T., Niu, D., Ji, Z. and Sun, L., 2022. Mid-term electricity demand forecasting using improved variational mode decomposition and extreme learning machine optimized by sparrow search algorithm. Energy, 261, p.125328.

Gul, M.J., Urfa, G.M., Paul, A., Moon, J., Rho, S. and Hwang, E., 2021. Mid-term electricity load prediction using CNN and Bi- LSTM. The Journal of Supercomputing, 77, pp.10942-10958.

Juan, Y.K., Gao, P. and Wang, J., 2010. A hybrid decision support system for sustainable office building renovation and energy performance improvement. Energy and buildings, 42(3), pp.290-297.

Le, T., Vo, M.T., Vo, B., Hwang, E., Rho, S. and Baik, S.W., 2019. Improving electric energy consumption prediction using CNN and Bi-LSTM. Applied Sciences, 9(20), p.4237.

Liu, Y., Zhao, J., Liu, J., Chen, Y. and Ouyang, H., 2020. Regional midterm electricity demand forecasting based on economic, weather, holiday, and events factors. IEEJ Transactions on Electrical and Electronic Engineering, 15(2), pp.225-234.

Niu, D., Ji, Z., Li, W., Xu, X. and Liu, D., 2021. Research and application of a hybrid model for mid-term power demand forecasting based on secondary decomposition and interval optimization. Energy, 234, p.121145.

Nop, P. and Qin, Z., 2021, March. Cambodia mid-term transmission system load forecasting with the combination of seasonal ARIMA and Gaussian process regression. In 2021 3rd Asia Energy and Electrical Engineering Symposium (AEEES) (pp. 700-707).IEEE.

Pan, X. and Lee, B., 2012, March. A comparison of support vector machines and artificial neural networks for mid-term load forecasting. In 2012 IEEE International conference on industrial technology (pp. 95-101). IEEE.

Peng, L., Wang, L., Xia, D. and Gao, Q., 2022. Effective energy consumption forecasting using empirical wavelet transform and long short-term memory. energy, 238, p.121756.

Rallapalli, S.R. and Ghosh, S., 2012. Forecasting monthly peak demand of electricity in India—A critique. Energy policy, 45, pp.516-520.

Wu, X., Dou, C. and Yue, D., 2021. Electricity load forecast considering search engine indices. Electric Power SystemsResearch, 199, p.107398.

Zhang, Q. and Liu, T., 2010, March. Research on mid-long term load forecasting base on wavelet neural network. In 2010 Second International Conference on Computer Engineering and Applications (Vol. 2, pp. 217-220). IEEE.

#248: Combining PV double-skin ventilated window with thermal-catalytic air-type PV/T collector system in series: energy performance evaluation and comparison during the heating season

Chengyan ZHANG [1], Jie JI[2], Yayun TANG[3]

[1] Department of Thermal Science and Energy Engineering, University of Science and Technology of China, Hefei, Anhui, China, zcy19013@mail.ustc.edu.cn
[2] Department of Thermal Science and Energy Engineering, University of Science and Technology of China, Hefei, Anhui, China, jijie@.ustc.edu.cn
[3] Department of Thermal Science and Energy Engineering, University of Science and Technology of China, Hefei, Anhui, China, tangyayun@mail.ustc.edu.cn

Abstract: Removing indoor formaldehyde through solar thermal-catalytic technology has been deemed a reliable and promising solution. In recent years, solar thermal catalytic technology, combining solar thermal utilization with thermal catalysis for formaldehyde degradation, has received attention and deep research. In this paper, a PV double-skin façade integrated with a thermal-catalytic air-type PV/T collector (PV-DSF-TCPV/T) is proposed. The combined system is proposed to obtain a higher catalytic temperature and enhance formaldehyde degradation. Besides, because of the simultaneous heat recovery of both PV-DSF and TCPV/T, the combined system offers a higher indoor heat gain and a reduction of heating load in winter. The simulation work mainly focuses on the comprehensive energy performance as well as the formaldehyde degradation performance of the PV-DSF-TCPV/T applied in four Chinese cities, including Beijing, Changchun, Shanghai, and Kunming, which all have energy demand for space heating in heating seasons. The Main conclusions of the study are: (1) Compared to the conventional system, the electricity of the proposed system was increased by 36.17%, 34%, 36.7%, and 38.62%, respectively. (2) The air-conditioning energy consumption of the aforementioned cities had a 1.33%, 0.7%, 2.36%, and 2.27% reduction in comparison with the results of the conventional system. (3) The proposed system surpassed the conventional system with aspect to the formaldehyde degradation, and the provision of the clean air volume was increased by 61%, 211.13%, 16.86%, and 75.66%, respectively.

Keywords: PV-DSF, Air-Type PV/T, Thermal Catalytic Oxidation, Formaldehyde Degradation

1. INTRODUCTION

Enhancing the energy performance of glazed areas of buildings is essential to the building energy saving since the heat loss through glazed areas account for more than 60% in the total heat loss through the building fabrics [1]. In many former research, ventilated double-skin ventilated façade (DSF) has been proven to be one of the most promising façades that is beneficial for the sustainability of buildings. It contains outer and inner glass layers, an intermediate air gap and several openings for the ventilation of DSFs. As shown in Fig. 1, there are totally five working modes of DSFs, which are classified according to the direction of air inflow and outflow [2]. With the aforementioned working modes, DSFs can realize different functions in different seasons, such as reducing indoor heat gain in summer or providing space heating in winter.
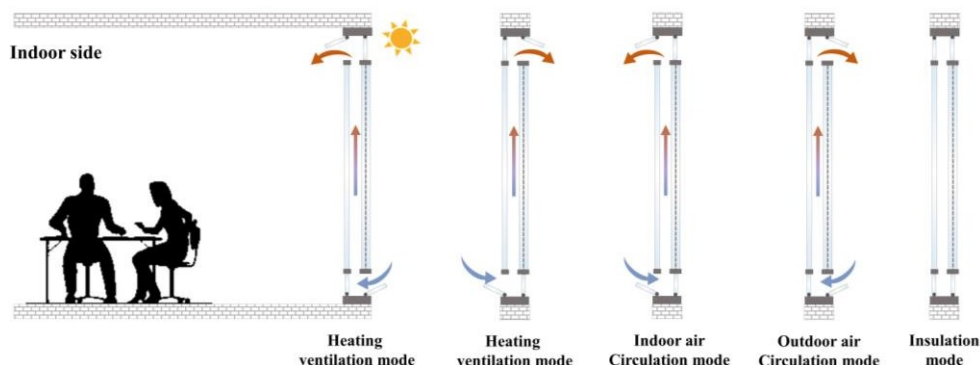

Figure 1: Working modes of a typical PV-DSF

Based on the structure of traditional DSFs, the photovoltaic double-skin ventilated façade (PV-DSF) substitute semi-transparent PV glazings for common transparent glazings, thus conferring DSFs with the function of power generation. In past two decades, PV-DSFs have been proven to possess several benefits, including lowering building energy consumption [3], enhancing indoor thermal comfort [4], reducing indoor glare [5], etc. Besides, PV-DSFs can preheat the air that enters indoor rooms in heating seasons under indoor air circulation. However, the indoor air has no exchange with the outdoor air under this mode, thus existing air quality deterioration with the existence of indoor air pollution sources.

As one of the most common indoor air pollutants, formaldehyde has received continuous attention because it poses a threat to human health with its existence in some home decoration materials and it may be ignored particularly due to its features of colourless and unnoticeable under low concentration. Removing formaldehyde through thermal catalytic oxidation (TCO) technology is a kind of reliable approach and has drawn widespread attention. In the thermal catalytic reaction, when the gaseous formaldehyde contacts with the thermal catalyst, of which the temperature reaches the star-off temperature, the formaldehyde will be degraded and meantime, producing H_2O and CO_2 [6]. A better degradation efficiency can be achieved with a higher reaction temperature. Considering that the thermal catalytic reaction requires heat as the driving force of the catalytic reaction, the solar thermal catalytic oxidation for formaldehyde removal has received a lot of attention and has been proven to be a reliable and effective approach [7].

Considering the poor indoor air quality with PV-DSFs working under the indoor air circulation mode, the contradiction between the opaque characteristic of thermal catalytic materials and the demand of daylighting of PV-DSFs, and a low air purification performance of the current PV-DSF, a composite system that combines a PV-DSF with a thermal-catalytic air-type PV/T collector (PV-DSF-TCPV/T) is proposed, which both realizes the increase in the temperature of the air that sent indoors and decrease indoor formaldehyde concentration.

The objective of this study is to investigate the seasonal energy consumption of the PV-DSF-TCPV/T in heating seasons of different Chinese cities (Changchun, Shanghai, Xian, and Kunming), which are located in different thermal climatic zones of China. The seasonal energy consumption of the proposed system, including seasonal electrical output and the air-conditioning energy consumption, as well as the formaldehyde degradation performance, were evaluated and then compared with a conventional system, in which the PV-DSF and the TCPV/T were both independent.

2. SYSTEM DESCRIPTION AND WORKING PRINCIPLE

In this section, the structure and composition of the proposed system were introduced, with detailed information of the geometric and thermo-physical parameters of the system being provided. Besides, the working principle of the proposed system was in detailed explanation.

2.1. System description

In the entire system, which was shown in Fig. 2, there are two main components: one is the CdTe-based semi-transparent PV-DSF and the other one is the poly-Si-based air-type thermal-catalytic PV/T collector (TCPV/T). The PV-DSV serves as the south façade of a room while the TCPV/T is placed on the roof and faces in the south direction. The PV-DSF contains four parts: the outer semi-transparent CdTe PV glazing, the inner single-layer clear glass, the intermediate air channel (Channel-1), and serval single-glazed vents set at both the top and bottom sides of the PV-DSF. From the outside to the inside of the TCPV/T, it mainly contains seven

parts: the outer clear glass cover, the seal air gap, the poly-Si cell layer that was laminated on the absorber plate, the thermal catalyst coating, the air channel (Channel-2), and the insulation backboard. The material used as the thermal catalyst is MnO_x-CeO_2. The proposed system combines the PV-DSF with the TCPV/T by connecting both channels of the two main components in series. The airflow inside two channels is driven by a fan, which is used to provide a stable airflow.

2.2. Working principle

The proposed system operates under the condition of sunny days of heating seasons. As illustrated in Fig. 3. During the daytime, with the driving force provided by the fan and the inside bottom vents all being opened, the indoor air with a certain formaldehyde concentration will first enter Channel-1 through the opened vents. Part of the waste heat of the semi-transparent PV glazing will be taken away by the air and the air temperature will increase consequently. Then the air will enter Channel-2, with the waste heat produced by the solar cell layer of the TCPV/T, which will be delivered by the air, causing the air temperature to increase again. In Channel-2, the formaldehyde of the air will be degraded when the formaldehyde molecules contact with the surface of the thermal catalyst under the star-off temperature of the thermal catalytic reaction. After the dual-stage heating and air purification, the warm clean air will finally be sent indoors. When the outdoor solar radiation is weak during daytime or non-existent at night, all vents of the PV-DSF should be closed, the proposed system operates under the insulation mode, in which the PV-DSF serves as an air buffer to reduce heat loss itself.
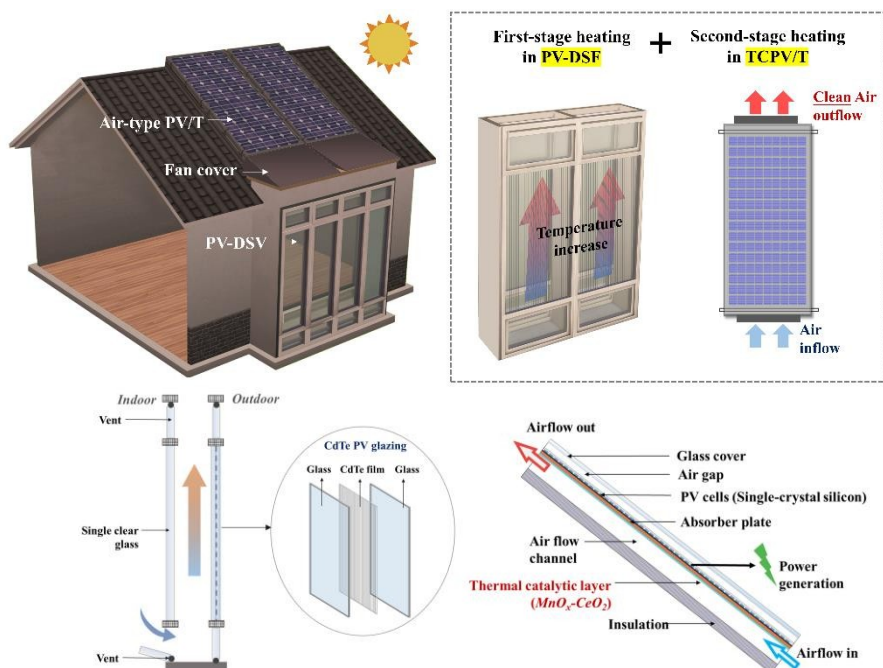

Figure 2: Construction and components of the combined system
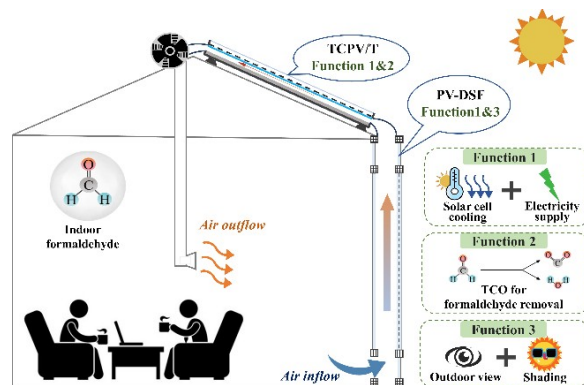

Figure 3: Working principle of the proposed system

3.   INTRODUCTION OF EVALUATION INDICATORS AND CASE INTRODUCTION

To evaluate comprehensive energy performance and formaldehyde degradation performance, serval evaluation indicators are used. In the energy performance evaluation, three evaluation indicators are introduced, including electricity output (E_{elec}), average electrical efficiency (η_{elec}), and air-conditioning energy consumption (AEC). In the formaldehyde degradation performance evaluation, two evaluation indicators, including clean air volume and formaldehyde conversion efficiency, are employed. A detailed explanation of the calculation of these indicators is offered in this section. Besides, the introduction of the case study of the simulation work is provided.

3.1. Evaluation indicators

The electricity of PV modules is calculated by:

Equation 1: Electricity (E_{elec})

$$\mathrm{E}_{elec} = \int_0^\tau P_{elec} dt$$

Where:

- P_{elec}= instantaneous power output (W)
- r = Power generation duration (s)

The electrical efficiency is calculated by:

Equation 2: Electrical efficiency (η_{ele})

$$\eta_{elec} = \eta_0[1 - (Br(T_c - 298.15))]$$

Where:

- η_0= standard electrical efficiency of solar cells
- Br = Temperature coefficient (K^{-1})
- T_c = Temperature of solar cells (K)

The air-conditioning energy consumption is calculated by:

Equation 3: air-conditioning energy consumption (AEC)

$$AEC = \frac{\int_0^\tau Q_{ac} dt}{COP}$$

Equation 4: indoor air-conditioning load (Q_{ac})

$$Q_{ac} = m_a c_a (T_r - T_{set})$$

Where:

- *COP* = Coefficient of performance
- m_a = Indoor air mass (kg)
- c_a = Heat capacity of the indoor air (J/kg•K)
- T_r = Indoor air temperature (K)
- T_{set} = Design temperature of the air-conditioning system (K)

The clean air volume is calculated by:

Equation 5: Clean air volume.(m^3)

$$V_{clean} = \int_0^\tau CADR\, dt$$

Equation 6: Clean air delivery rate.(m^3/s)

$$CADR = \varepsilon_{HCHO} \frac{\dot{m}_{in}}{\rho_a}$$

Where:

- ρ_a = Indoor air density (kg/m^3)
- ε_{HCHO} = Formaldehyde conversion ratio
- m_{in} = Mass flow rate of the inlet air of the air channel (kg/m^3)

3.2. Case introduction

In the studied case, the PV-DSF of the proposed system was installed on the south façade while the TCPV/T was placed on the roof at an inclination angle of 31 degrees. The depth of the PV-DSF and the TCPV/T were 0.07m and 0.02m, respectively. The room model as well as the layout of the PV-DSF is given in Fig. 4. There were totally four pieces of semi-transparent CdTe PV glazing and single-layer clear glass, serving as the outer and inner windows, respectively. Besides, only the south facade was exposed to the outdoor environment while ceilings, floor, and other walls of the room were all arranged inside the building. The proposed system operated under the indoor air circulation mode on sunny days from 9 am to 5 pm while the insulation mode was adopted at other times. To investigate the energy-saving potential of the PV-DSF-TCPV/T, its seasonal energy consumption was compared with that of a separate system, in which the PV-DSF and TCPV/T were independent. The conventional system had the same operating time as the PV-DSF-TCPV/T, and the PV-DSF was naturally ventilated while the TCPV/T was in mechanical ventilation. The mass flow

rates of the fans of the two systems were both 110m³/h.

The indoor air temperature was controlled by an air-conditioning system, which also operated between 9:00 and 17:00. In the design case, the indoor design temperature was set at 18 and the coefficient of performance (COP) of the air-conditioning system was set to 4.5 in heating seasons. Besides, the weather data of four cities (Beijing, Changchun, Kunming, and Shanghai) that were used in the simulation was obtained from the file of the typical meteorological year (TMY) by importing the TMY file into Energyplus software and then exporting the hourly weather data. The exported results of the annual weather data and division of seasons are shown in Fig. 5. Beijing, Changchun, Kunming, and Shanghai are located in different thermal climatic zones, and they belong to regions with cold winter, severe cold winter, mild climate, hot summer and cold winter. The average outdoor temperature during daytime in Beijing, Changchun, Kunming, and Shanghai was -4.28, 1.48,9.84, 7.03 respectively.
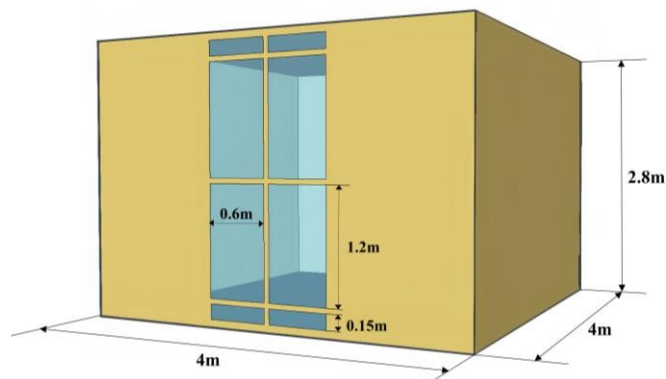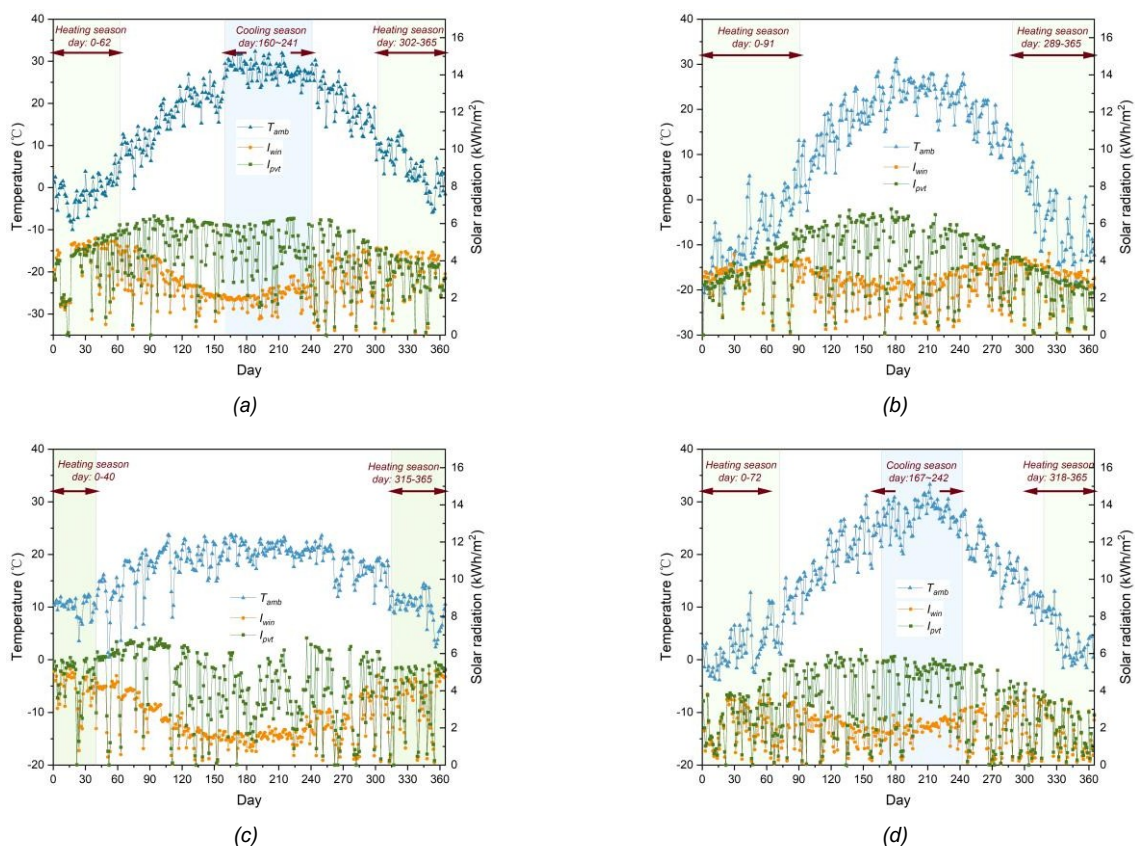

Figure 4: Room model and the layout of the PV-DSF

Figure 5: Annual weather data and seasonal division (a) Beijing; (b) Changchun; (c) Kunming; (d) Shanghai

4. RESULTS AND DISCUSSIONS

In this section, on the basis of the comprehensive energy consumption and formaldehyde degradation performance, the seasonal energy performance of the combined system was evaluated and then compared with that of an conventional system.

4.1. Electrical performance

Results of the seasonal electricity of the proposed system applied in four cities were illustrated in Fig. 6. The seasonal electricity included two parts: the electricity of the PV-DSF and TCPV/T. The proposed series system could produce 645.55kWh, 588.58 kWh, 526.71kWh, and 501.75kWh of electricity in Beijing, Changchun, Kunming, and Shanghai, respectively. In the four different cities, the difference in electricity was in close relevant with the outdoor incident solar radiation and the duration of heating seasons. In the conventional system, the results of seasonal electricity of the aforementioned four cities were 452.03 kWh, 439.26 kWh, 385.31 kWh, and 361.96 kWh, respectively. Compared to the electrical performance of the two systems, it could be found that the two systems shared similar electrical efficiency while the proposed system outputs more electricity. The result could be explained in two aspects: on one hand, in the system operation mode setting, only when the outlet air temperature was higher than that of the indoor room could the fan be opened; thus, the fan of the proposed system had a longer working time than that of the conventional system. Therefore, the proposed system had a higher electrical output due to the reduction of the working temperature of the PV modules. On the other hand, the poly-crystalline cell was more sensitive to the working temperature due to a higher temperature coefficient. The difference in electrical output of the two systems was mainly caused by the difference in the electricity of TCPV/T.
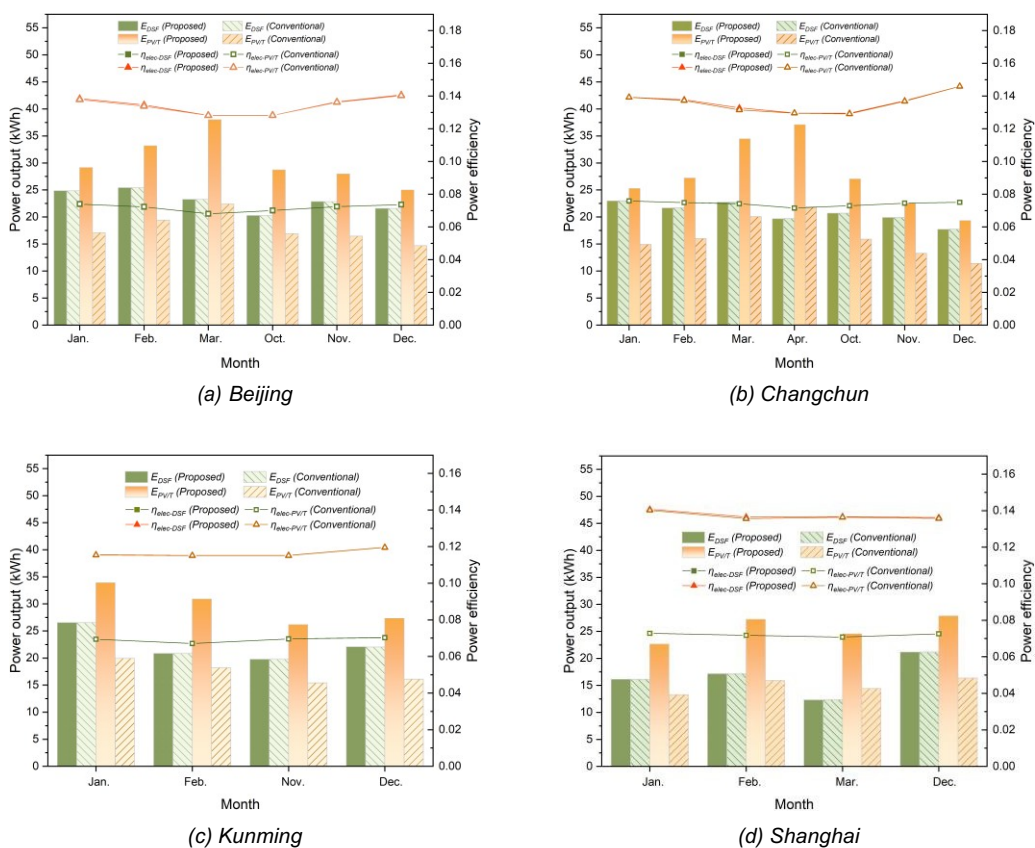

(a) Beijing

(b) Changchun

(c) Kunming

(d) Shanghai

Figure 6: Seasonal electricity output of two systems in comparison

4.2. Air-conditioning energy consumption

Results of the air-conditioning energy consumption of four cities were shown in Figure 7. In Beijing, Changchun, Kunming, and Shanghai, the seasonal AECs were 698.36 kWh, 1360.13 kWh, 182.65 kWh, and 383.78 kWh, respectively. For Beijing, Changchun, and Shanghai, the highest monthly AEC all emerged in January while in Kunming, the highest AEC was in December. The seasonal AEC was mainly influenced by the outdoor air temperature and the duration of the heating season. Among the four cities, Changchun had the highest latitude and longest space heating duration, leading to the highest seasonal AEC. Kunming was featured in a short and mild winter; hence its seasonal AEC was the lowest. Compared with the conventional system, the proposed system gave rise to 1.33%, 0.7%, 2.36%, and 2.27% reduction of the seasonal AEC in Beijing, Changchun, Kunming, and Shanghai, respectively. The results indicated that the proposed system was in favour of the air-conditioning energy saving. Moreover, the AEC reduction effect was not significant enough in Changchun, and this could be explained by the low outdoor temperature and the short operating duration of the indoor air circulation mode of the proposed system.
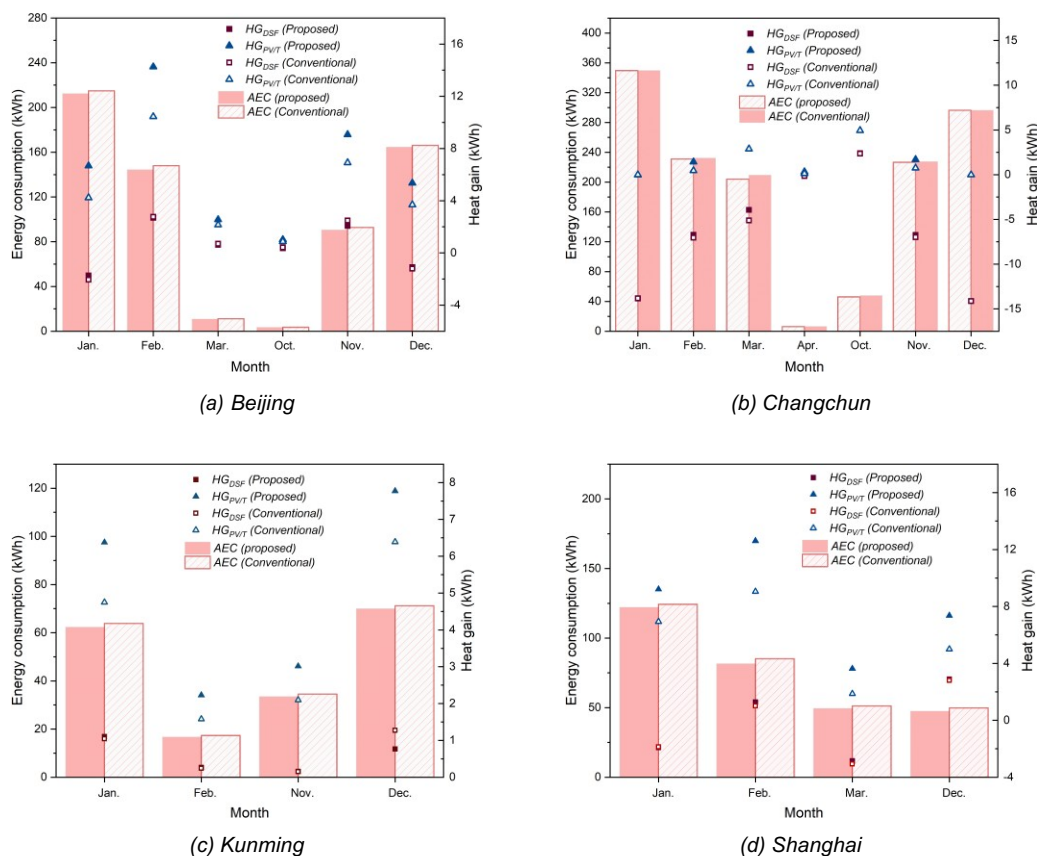
(a) Beijing

(b) Changchun

(c) Kunming

(d) Shanghai

Figure 7: Seasonal air-conditioning energy consumption of two systems in comparison

4.3. Formaldehyde degradation performance

The results of the monthly total clean air volume and average formaldehyde conversion ratio were depicted in Fig. 8. The evaluation results indicated that the monthly clean air volumes of Beijing, Changchun, Kunming, and Shanghai were 13180.47 m^3, 11633.34 m^3, 22946.33 m^3, 16596.32 m^3, respectively. The average formaldehyde conversion ratios were 19.13%, 12.88%, 21.98%, and 18.9%, respectively. Among four cities, the proposed system had a better formaldehyde degradation performance in Kunming while the performance was relatively poor in Changchun. This result was similar to that of the seasonal AECs of different cities and was bear on the temperature of thermal catalytic temperature. Although the thermal catalytic temperature increased with the use of the proposed system, the severe cold winter of Changchun impaired the formaldehyde degradation performance. Moreover, when comparing the results of the total clean air volume of the two systems, it could be found that the proposed system brought 61%, 211.13%, 16.86%, 75.66% increase in Beijing, Changchun, Kunming, and Shanghai, respectively. The result reflected an obvious improvement in the formaldehyde degradation performance with the application of the proposed system.
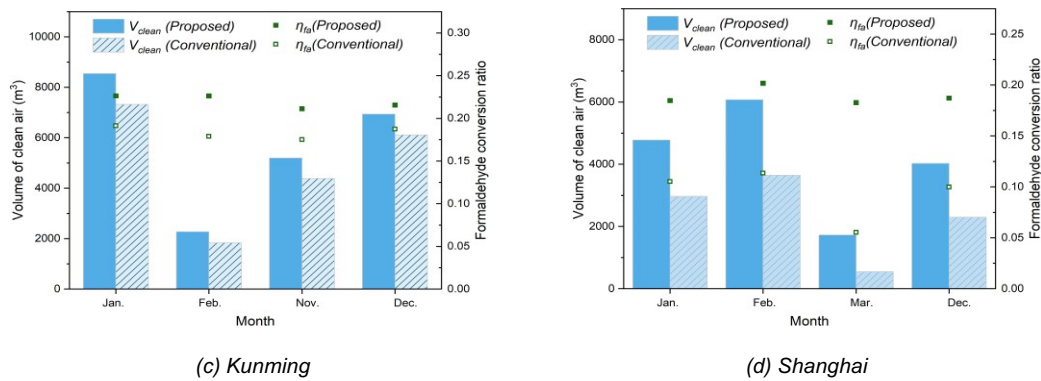

(a) Beijing

(b) Changchun

(c) Kunming *(d) Shanghai*
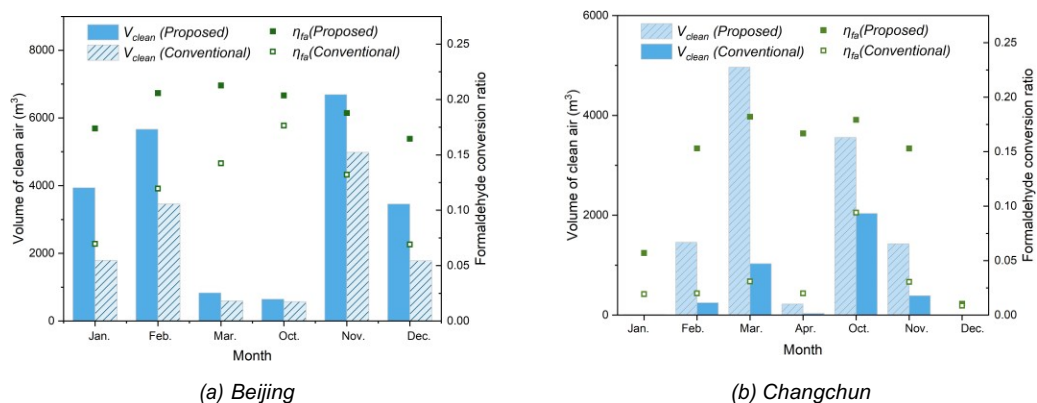
Figure 8: The clean air volume and average formaldehyde conversion ratio of two systems in comparison

5. CONCLUSION

To improve the indoor air quality of the PV-DSF working under the indoor air circulation mode and enhance the utilization efficiency of the waste of the PV-DSF, this paper proposed a series system, which combined the PV-DSF with a thermal-catalytic air-type PV/T collector to reach a higher catalytic temperature and increase the indoor heat gain. The energy consumption evaluation of the proposed system was made under weather conditions of four different Chinese cities: Beijing, Changchun, Kunming, and Shanghai, which are located in different thermal climatic zones. The seasonal energy consumption was then compared with a conventional system. The main conclusions of the study were as follows:

- With regard to the seasonal electricity, the proposed system could produce more electricity than that of the conventional system. The seasonal electricity of the proposed system in Beijing, Changchun, Kunming, and Shanghai was 645.55kWh, 588.58 kWh, 526.71kWh, and 501.75kWh, respectively. Compared with the conventional system, the electricity of the proposed system in the aforementioned four cities increased by 36.17%, 34%, 36.7%, and 38.62%, respectively.
- The proposed system led to the reduction of air-conditioning energy consumption. The air-conditioning energy consumption for space heating in Beijing, Changchun, Kunming, and Shanghai was 698.36 kWh, 1360.13 kWh, 182.65 kWh, 383.78 kWh, respectively. Compared with the conventional system, the proposed system brought 1.33%, 0.7%, 2.36%, and 2.27% reduction of the seasonal AEC in Beijing, Changchun, Kunming, and Shanghai, respectively. The reduction was close relative to the outdoor air temperature. Changchun was the coldest city among the four cities, and the energy-saving performance in Changchun was the poorest.
- With regard to the formaldehyde degradation performance, the proposed system also led to performance enhancement in formaldehyde removal. The seasonal clean air volume of the proposed system in Beijing, Changchun, Kunming, and Shanghai was 13180.47 m^3, 11633.34 m^3, 22946.33 m^3, and 16596.32 m^3, respectively, and the clean air volume increased by 61%, 211.13%, 16.86%, and 75.66%, respectively.

6. REFERENCES

[1] Cuce, E., & Riffat, S. B. (2015). A state-of-the-art review on innovative glazing technologies. Renewable and Sustainable Energy Reviews, 41, 695–714.

[2] Wang, E., Wang, H., Deng, M., Wang, K., & Wang, Y. (2017). 10th International Symposium on Heating, Ventilation and Air Conditioning, Ishvac2017/Simulation of the ventilation and energy performance of a PV-integrated breathing window.1. Amsterdam: Elsevier Science Bv.

[3] Peng, J., Curcija, D. C., Lu, L., Selkowitz, S. E., Yang, H., & Zhang, W. (2016). Numerical investigation of the energy saving potential of a semi-transparent photovoltaic double-skin facade in a cool-summer Mediterranean climate. Applied Energy, 165, 345–356.

[4] Wang, C., Ji, J., Uddin, M. M., Yu, B., & Song, Z. (2021). The study of a double-skin ventilated window integrated with CdTe cells in a rural building. Energy, 215, 119043.

[5] Wang, C., Ji, J., Yu, B., Zhang, C., Ke, W., & Wang, J. (2022). Comprehensive investigation on the luminous and energy-saving performance of the double-skin ventilated window integrated with CdTe cells. Energy, 238, 121757.

[6] Tang X, Li Y, Huang X, Xu Y, Zhu H, Wang J, et al. MnOx–CeO2 mixed oxide catalysts for complete oxidation of formaldehyde: Effect of preparation method and calcination temperature. Applied Catalysis B: Environmental 2006;62:265–73.

[7] Yu, B., Jiang, Q., He, W., Hu, Z., Chen, H., Ji, J., & Xu, G. (2018). The performance analysis of a novel TC-Trombe wall system in heating seasons. Energy Conversion and Management, 164, 242–261.

[8] Yu, B., Liu, X., Li, N., Liu, S., & Ji, J. (2020). The performance analysis of a purified PV/T-Trombe wall based on thermal catalytic oxidation process in winter. Energy Conversion and Management, 203, 112262.

[9] Yu, B., Li, N., Ji, J., & Wang, C. (2021). Thermal, electrical and purification performance of a novel thermal-catalytic CdTe double-layer breathing window in winter. Renewable Energy, 167, 313–332.

#250: Correlations for the transport characteristics of Radiative Rayleigh-Bénard convection in optically thick media

Jia-jun SONG[1], Pan-xin LI[2], Lu CHEN[3], Yu-hang ZHAO[1], Feng-shi TIAN[1], Ben-wen LI[1,*]

[1] Key Laboratory of Ocean Energy Utilization and Energy Conservation of Ministry of Education, School of Energy & Power Engineering, Dalian University of Technology, Dalian, 116024, China, email: songjjdut@163.com, 1136970615@qq.com, 13134342044@163.com, heatli@dlut.edu.cn
[2] Institute of Thermodynamics and Fluid Mechanics, Technische Universität Ilmenau, P.O. Box 100565, Ilmenau, 98684, Germany, email: panxin.li@tu-ilmenau.de
[3] MCC Jingcheng Engineering Technology Co., Ltd., Beijing, 100176, China, email: 1044690294@qq.com

Abstract: Due to stable chemical properties and large latent heat of phase change, molten salt has been widely used as energy storage material, especially in the technology of solar power. For example, the salt is heated to the molten state by the sunlight in concentrated solar power and the natural convection plays an important role in this process. Accounting to the high working temperature, it is obvious that thermal radiation shows extraordinary effects on the molten salt flow and heat transport. In this paper, we focus on the influence of thermal radiation on the classical Rayleigh-Bénard (RB) convection, a paradigmatic representation of thermal convection in which the fluid is heated from below and cooled from above. The theoretical derivation has been conducted by modifying the Grossmann-Lohse theory. Because of the particularity of thermal radiation transfer in the form of electromagnetic waves, the optically thick limit approximation, i.e., Rosseland diffusion approximation has been used. Based on the turbulent dissipation theory and the relative contribution of bulk and boundary layers to dissipation, four main regimes can be obtained and one of them has been investigated in this paper. One can easily find that, although thermal radiation stabilizes flow, it can significantly enhance the heat transfer efficiency. Besides, by comparing the results between DNS and theoretical analysis, the summarized scaling law can effectively predict the Nu of radiative Rayleigh-Bénard convection, and the deviation is about 9%.

Keywords: Energy Storage and Conversion; Renewable Energy Technologies; Radiative Rayleigh-BÉnard Convection; Scaling Law; Conjudge Heat Transfer

1. INTRODUCTION

Buoyancy driven convection widely exists not only in astrophysics or geophysical, but also in lots of industrial applications, like energy conversion and storage technology. One of the most paradigmatic representations of buoyancy driven convection is the classical Rayleigh-Bénard (RB) convection, in which the fluid is heated from below and cooled from above.

In the past few decades, RB convection has been extensively studied, but it is still an idealized model to study the coupling of flow and heat transfer, as well as nonlinear dynamics, especially for the flow under the influence of complicating factors (Song, 2023). Ravichandran et al. (Ravichandran, 2021) simulated the melting process driven by rotating RB convection. Sharma et al. (Sharma, 2022) focused on the effect of horizontal aspect ratio on RB convection in liquid metals in the presence of an external horizontal magnetic field. Li et al. (Li, 2024) investigated the effects of external vertical magnetic field on transport characteristics of RB convection in a closed cavity filled with molten salt.

With the continuous development of new energy technologies, molten salt or nanofluid flow have attracted a lot of attention in many fields, such as nuclear reactor cooling, concentrated solar power generation, and photothermal energy storage. It is easy to understand that the most significant difference between molten salt or nanofluid thermal convection and classical RB convection is that thermal radiation shows extraordinary effects in the latter. There are many literatures on the radiative RB convection (Amber, 2017; Balakin, 2019; Chang, 2023). Song et al. (Song, 2023) have provided a comprehensive review introducing the effect of both surface and media radiation on natural convection. Nevertheless, one can easily see that the conclusions in the literatures on whether thermal radiation has an inhibitory or enhancing effect on RB convective transport characteristics are not yet unified.

In addition to numbers of qualitative research, many scaling models have been proposed. Since Rayleigh established the mathematical model of convection driven by thermal buoyancy on the basics of Navier-Stokes equations, many models have been developed, including the marginal stability theory (Malkus, 1954), Chicago mixing zone model (Heslot, 1987; Castaing, 1989; Sano, 1989), Shraiman-Siggia model (Shraiman, 1990; Siggia, 1994), Grossmann-Lohse theory (Grossmann, 2000; Grossmann, 2001; Grossmann, 2002; Grossmann, 2004), and so on. What is more, there are also some related studies on the constitutive law of RB convective transport characteristics under the influence of additional factors. Chakraborty (Chakraborty, 2008) suggested that, by introducing the concept of magnetic energy dissipation, the arguments and assumptions in Grossmann-Lohse theory can be extended to the case of turbulent magnetohydrodynamic (MHD) RB convection influenced by vertical magnetic field. Based on this idea, Zürner et al. (Zürner, 2016; Zürner, 2020) have given a set of implicit scaling equations between Nu, Re and Ra, Pr, Ha in a restricted parameter range ($Pr \leq 0.03, Pm = \mu\sigma_b u \leq 10^{-5}$). Moreover, the scaling behaviors of heat and momentum transport in MHD-RB convection is analyzed by Yan et al. (Yan, 2021), on the basis of the ratio of magnetic energy to kinetic energy and the contribution of viscous and ohmic dissipation. As for the radiative RB convection, Soucasse et al. (Soucasse, 2020; Soucasse, 2021) derived both observed and predicted POD-based low-order models in the range of $Ra \in [10^6, 10^8]$. Both of them can capture the dynamic and energy transport features of the natural convection coupled with radiation. However, as the models were developed at a certain Pr=0.7, its applicability to a wider Pr range remains to be verified.

It should be noted that the difficulty in studying radiative RB convection lies in the fact that radiative energy propagates as an electromagnetic wave, which means the heat transfer happens between all the elements. Besides, the spectral and directional nature of radiation increases the dimensionality of the problem, making the determination of radiative heat flux complex. Therefore, many simplified models have been proposed. For the melt or nanofluid flow, the optically thick limit approximation, i.e., Rosseland diffusion approximation is usually used (Alnaqi, 2019; Sheikholeslami, 2017; Timofeev, 2015). In this paper, we focus on the transport characteristic in radiative Rayleigh-Bénard convection of optically thick media ($r \gg 1$). The relevant scaling laws will be given by modifying the Grossmann-Lohse theory and verified by the results obtained from direct numerical simulation.

2. THE MODEL

Considering an incompressible fluid layer differentially heated by two rigid plates, the following governing equations under the Boussinesq approximation can be obtained:

Equation 1: Mass conservation equation.
$$\nabla \cdot \boldsymbol{u} = 0$$

Equation 2: Momentum conservation equation.
$$\partial_t \boldsymbol{u} + (\boldsymbol{u} \cdot \nabla)\boldsymbol{u} = -\nabla p + \upsilon\nabla^2\boldsymbol{u} + g\beta(T - T_{\text{ref}})\boldsymbol{e}_z$$

Equation 3: Energy conservation equation.
$$\partial_t T + \boldsymbol{u} \cdot \nabla T = \kappa\nabla^2 T - \nabla q^R$$

The radiative heat flux by employing Rosseland approximation is defined as:

Equation 4: Radiative heat flux.
$$q^R = -\frac{4}{3}\frac{\sigma}{\beta_\lambda}\nabla T^4$$

When neglecting the high-order terms from the Taylor series of T4 about Tref, the radiative heat source in Equation 3 can be gotten as:

Equation 5: Radiative heat source in Equation 3.
$$\nabla q^R = -\frac{16}{3}\frac{\sigma T_{\text{ref}}^3}{\beta_\lambda}\nabla^2 T$$

Here the three important criterion numbers, viz. the Rayleigh number Ra, Prandtl number Pr and radiation parameter $\mathbb{R}$, as well as two response criterion numbers, Nusselt number Nu and Reynold number Re, to characterize the RB convection are defined as:

Equation 6: Important criterion numbers.

$$Ra = \frac{g\beta\Delta h^3}{\upsilon\kappa}, Pr = \frac{\upsilon}{\kappa}, \mathbb{R} = 1 + \frac{4}{3}\frac{1}{\tau_\lambda Pl}$$

$$Nu = \frac{\langle u_z T\rangle_A - \kappa\partial_z\langle T\rangle_A}{\kappa\Delta h^{-1}}, Re = \frac{\overline{U}h}{\upsilon}$$

Where:

- $\mathbf{e}_z$ = the unit vector in the z direction (-)
- $\boldsymbol{u} = \{\boldsymbol{u_x}, \boldsymbol{u_y}, \boldsymbol{u_z}\}$ = velocity vector (m/s)
- t = time (s)
- p = pressure (kg·m^{-1}·s^{-2})
- υ = kinematic viscosity (m^2/s)
- T = temperature (K)
- $\Delta = T_h - T_c$ = temperature difference between the two plates (K)
- g = gravitational acceleration (m/s^2)
- β = thermal expansion coefficient (1/K)
- κ = thermal diffusivity (m^2/s)
- λ = thermal conductivity (W·m^{-1}·K^{-1})
- h = distance between the two plates (m)
- $\overline{U}$ = the mean large-scale velocity (m/s)
- β_λ = spectral extinction coefficient (1/m)
- σ = Stefan-Boltzmann constant ($\sigma = 5.67 \times 10^{-8}$W · m^{-2} · K^{-4})
- τ_λ = the optical thickness, $\tau_\lambda = \beta_\lambda h$ (-)
- Pl = the Planck number $Pl = \frac{\lambda/h}{4\sigma T_{ref}^3}$
- T_{ref} = the reference temperature $T_{ref} = \frac{T_c + T_h}{2}$ (K)
- $\langle\cdot\rangle_A$ = the average over any horizonal plane (z-plane).

3. SCALING LAW

In correspondence with classical RB convection, one can derive the following rigorous relations for the global averaged kinetic and thermal dissipation rates, ε_u and ε_T, according to the theory of Shraiman and Siggia (Shraiman, 1990; Siggia, 1994):

Equation 7: The global averaged kinetic dissipation rates.

$$\varepsilon_u = \langle\varepsilon_u(x,t)\rangle_V = \frac{\upsilon^3}{h^4}(Nu-1)RaPr^{-2}$$

Equation 8: The global averaged thermal dissipation rates.

$$\varepsilon_T = \langle\varepsilon_T(x,t)\rangle_V = \kappa\frac{\Delta^2}{h^2}Nu$$

Where:

- $\langle\cdot\rangle_V$ denotes the volume average.

The main idea of Grossmann-Lohse theory is that the global averaged energy dissipation can be decomposed into the bulk and boundary layer (BL) contributions, which is to say:

Equation 9: Decomposition of dissipation rate.

$$\varepsilon = \varepsilon_{bulk} + \varepsilon_{BL}$$

By means of dimensional analysis, the different contribution can be estimated as:

Equation 10: The kinetic dissipation rates in bulk.

$$\varepsilon_{u-bulk} \sim \frac{\overline{U}^3}{h} = \frac{\upsilon^3}{h}Re^3$$

Equation 11: The thermal dissipation rates in bulk for $Pr \sim \frac{\delta_u}{\delta_T} < 1$.

$$\varepsilon_{T-bulk} \sim \frac{\overline{U}\Delta^2}{h} = \kappa\frac{\Delta^2}{h^2}PrRe$$

Equation 12: The thermal dissipation rates in bulk for $Pr \sim \frac{\delta_u}{\delta_T} > 1$.

$$\varepsilon_{T-bulk} \sim \overline{U}\frac{\delta_u}{\delta_T}\frac{\Delta^2}{h} = \kappa\frac{\Delta^2}{h^2}\mathbb{R}PrRe^{3/2}Nu^{-1}$$

Equation 13: The kinetic dissipation rates in BL.

$$\varepsilon_{u-BL} \sim \upsilon\frac{\overline{U}^2}{\delta_u^2}\frac{\delta_u}{h} \sim \frac{\upsilon^3}{h^4}Re^{5/2}$$

$$\varepsilon_{T-\mathrm{BL}} \sim \kappa \frac{\Delta^2}{\delta_T^2} \frac{\delta_T}{h} \sim \kappa \frac{\Delta^2}{h^2} \mathbb{R}^{1/2} Pr^{1/2} Re^{1/2}$$

Equation 14: The thermal dissipation rates in BL for $Pr \sim \frac{\delta_u}{\delta_T} < 1$.

Equation 15: The thermal dissipation rates in BL for $Pr \sim \frac{\delta_u}{\delta_T} > 1$..

$$\varepsilon_{T-\mathrm{BL}} \sim \kappa \frac{\Delta^2}{\delta_T^2} \frac{\delta_T}{h} \sim \kappa \frac{\Delta^2}{h^2} \mathbb{R}^{2/3} Pr^{1/3} Re^{1/2}$$

Where:

- $\delta_u \sim h Re^{-1/2}$ = the thickness of the kinetic BL
- $\delta_T \sim \mathbb{R} h Nu^{-1}$ = the thickness of the thermal BL

It should be emphasized that the kinetic BL is assumed to be of Prandtl-Blasius type in Grossmann-Lohse theory.

Armed with the above relations, four main regimes can be easily obtained, depending on whether the bulk or BL is the chief contributor to dissipation:

Regime Ⅰ: $\varepsilon_u \sim \varepsilon_{u-\mathrm{BL}}, \varepsilon_T \sim \varepsilon_{T-\mathrm{BL}}$

Regime Ⅱ: $\varepsilon_u \sim \varepsilon_{u-\mathrm{bulk}}, \varepsilon_T \sim \varepsilon_{T-\mathrm{BL}}$

Regime Ⅲ: $\varepsilon_u \sim \varepsilon_{u-\mathrm{BL}}, \varepsilon_T \sim \varepsilon_{T-\mathrm{bulk}}$

Regime Ⅳ: $\varepsilon_u \sim \varepsilon_{u-\mathrm{bulk}}, \varepsilon_T \sim \varepsilon_{T-\mathrm{bulk}}$

In addition, based on the relative thickness of the kinetic and thermal BL, each regime can be divided into two sub-regions, i.e., (a) $\frac{\delta_u}{\delta_T} < 1$ and (b) $\frac{\delta_u}{\delta_T} > 1$.

Table 1: The physical properties of molten salt at 523K (Li, 2024)

Density	Specific heat	Thermal conductivity	Thermal diffusivity	Kinematic viscosity
1600	1529	0.425	1.737×10^{-6}	1.216×10^{-5}
$kg \cdot m^{-3}$	$J \cdot kg^{-1} \cdot K^{-1}$	$W \cdot m^{-1} \cdot K^{-1}$	$m^2 \cdot s^{-1}$	$m^2 \cdot s^{-1}$

For most application scenarios of molten salt, the flow intensity of natural convection is not very strong (about $Ra \sim 10^8$), and the Pr of molten salt is generally around 10 (in this paper the Pr was fixed at 7 and the physical properties of molten salt at 523K is shown in Table 1). Therefore, according to the applicable scope of the Grossmann-Lohse theory, we focus on the Regime I-a and I-b, i.e.,**Regime Ⅰ-a**: $\varepsilon_u \sim \varepsilon_{u-\mathrm{BL}}, \varepsilon_T \sim \varepsilon_{T-\mathrm{BL}}, \frac{\delta_u}{\delta_T} < 1$ (small Pr)

Substituting Eq. (7) and (8) into Eq. (13) and (14), respectively, one can get:

Equation 16: The scaling of Re in Regime Ⅰ-a. $\qquad Re = \mathbb{R}^{1/4} Ra^{1/2} Pr^{-3/4}$

Equation 17: The scaling of Nu in Regime Ⅰ-a. $\qquad Nu = \mathbb{R}^{5/8} Ra^{1/4} Pr^{1/8}$

Regime Ⅰ-b: $\varepsilon_u \sim \varepsilon_{u-\mathrm{BL}}, \varepsilon_T \sim \varepsilon_{T-\mathrm{BL}}, \frac{\delta_u}{\delta_T} > 1$ (large Pr)

Substituting Eq. (7) and (8) into Eq. (13) and (15), respectively, one can get:

Equation 18: The scaling of Re in Regime Ⅰ-b. $\qquad Re = \mathbb{R}^{1/3} Ra^{1/2} Pr^{-5/6}$

Equation 19: The scaling of Nu in Regime Ⅰ-b. $\qquad Nu = \mathbb{R}^{5/6} Ra^{1/4} Pr^{-1/12}$

4. DIRECT NUMERICAL SIMULATIONS
4.1. Description of numerical model

In order to verify the above scaling law derived from theorical analysis, direct numerical simulation (DNS) has been conducted. The convection cell adopted in this paper was a 2D square cavity with length h and aspect ratio $\Gamma = 1$, as shown in Figure 1. The temperature of top and bottom wall was fixed at Tc and Th. The sidewall was taken to be perfectly adiabatic. No-slip velocity boundary conditions

were considered for all the walls. By setting the length h, free-fall velocity $uf = (g\beta\Delta h)/2$ and temperature difference Δ to one, the dimensionless governing equations can be conventionally got (refer to Equation 1~3) and the dimensionless boundary conditions can be found in Figure 1.

Equation 20: Dimensionless mass conservation equation.

$$\nabla \cdot \boldsymbol{U} = 0$$

Equation 21: Dimensionless Momentum conservation equation.

$$\partial_\tau \boldsymbol{U} + (\boldsymbol{U} \cdot \nabla)\boldsymbol{U} = -\nabla P + \sqrt{\frac{Pr}{Ra}}\nabla^2\boldsymbol{U} + \Theta\boldsymbol{e}_z$$

Equation 22: Dimensionless energy conservation equation.

$$\partial_\tau \Theta + \boldsymbol{U} \cdot \nabla\Theta = \sqrt{\frac{1}{RaPr}}\nabla^2 T - \nabla\widetilde{q^R}$$

Where:

$\boldsymbol{U} = \{\boldsymbol{U_x}, \boldsymbol{U_y}, \boldsymbol{U_z}\}$ = dimensionless velocity vector $\boldsymbol{U} = \dfrac{\boldsymbol{u}}{(g\beta\Delta h)^{1/2}}$

τ = dimensionless time $\tau = \dfrac{h}{U}$

P = dimensionless pressure $P = \rho\boldsymbol{u} \cdot \boldsymbol{u}$

Θ = dimensionless temperature $\Theta = \dfrac{T - T_{\text{ref}}}{\Delta}$
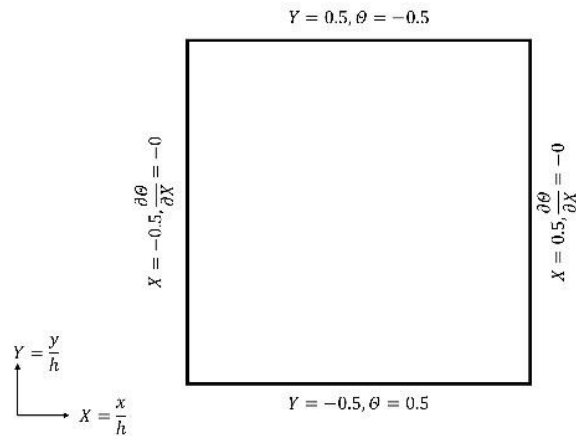

Figure 1: The convection cell and dimensionless boundary conditions

4.2. Numerical method and validation

The governing equations were discretized by adopting the finite volume method. The pressure-velocity coupling was handled by the PISO algorithm. The CrankNicolson discretisation scheme was used for the transient terms and the second order upwind scheme was applied to treat the convective terms.

The grid independence test was carried out for $Ra = 4.12 \times 10^8, Pr = 7$. As shown in Figure 2, the grid size of 256×256 was chosen, since the deviation was less than 0.5%.
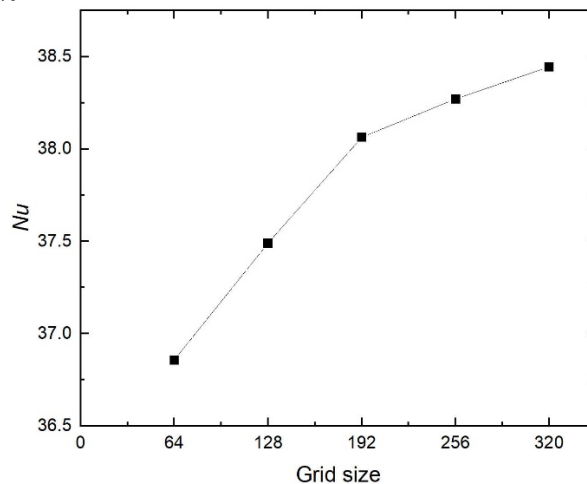

Figure 2: The grid independence test for $Ra = 4.12 \times 10^8, Pr = 7$

In order to validate the present code, the results for $Ra = 1.00 \times 10^8, Pr = 4.3$ were compared with those in References (Huang, 2022; Yang, 2021), as shown in Table 2. It can be easily seen that the maximum relative errors for Nu is less than 3.5%. Therefore,the correctness of present numerical method code is verified.

Table 2: Comparisons of public results from References

	Present	Huang et al.	Yang et al.
Nu	24.90	25.38	25.80
%Error		1.89%	3.49%

4.3. Comparison of results with and without considering thermal radiation effects

Effect of radiation on flow structure

Figure 3 shows the time-evolution of isotherm contours (background) and streamlines (blue lines) for $Ra = 4.12 \times 10^8, Pr = 7$. It can be easily seen that, regardless of whether thermal radiation is considered or not, the large-scale circulation (LSC) has been formed. The shape of LSC is approximately elliptical, which follows the diagonal of the cavity as the major axis and accompanied by two small rolls in the short axis direction. The two small rolls may expand, causing the large-scale circulation to gradually collapse and change its tilt direction. Interestingly, with the increasing of $\mathcal{R}$, the collapse and redirection frequencies of LSC decrease. It can be inferred to be related to the weakening of the development of small rolls, due to the increase in temperature uniformity.
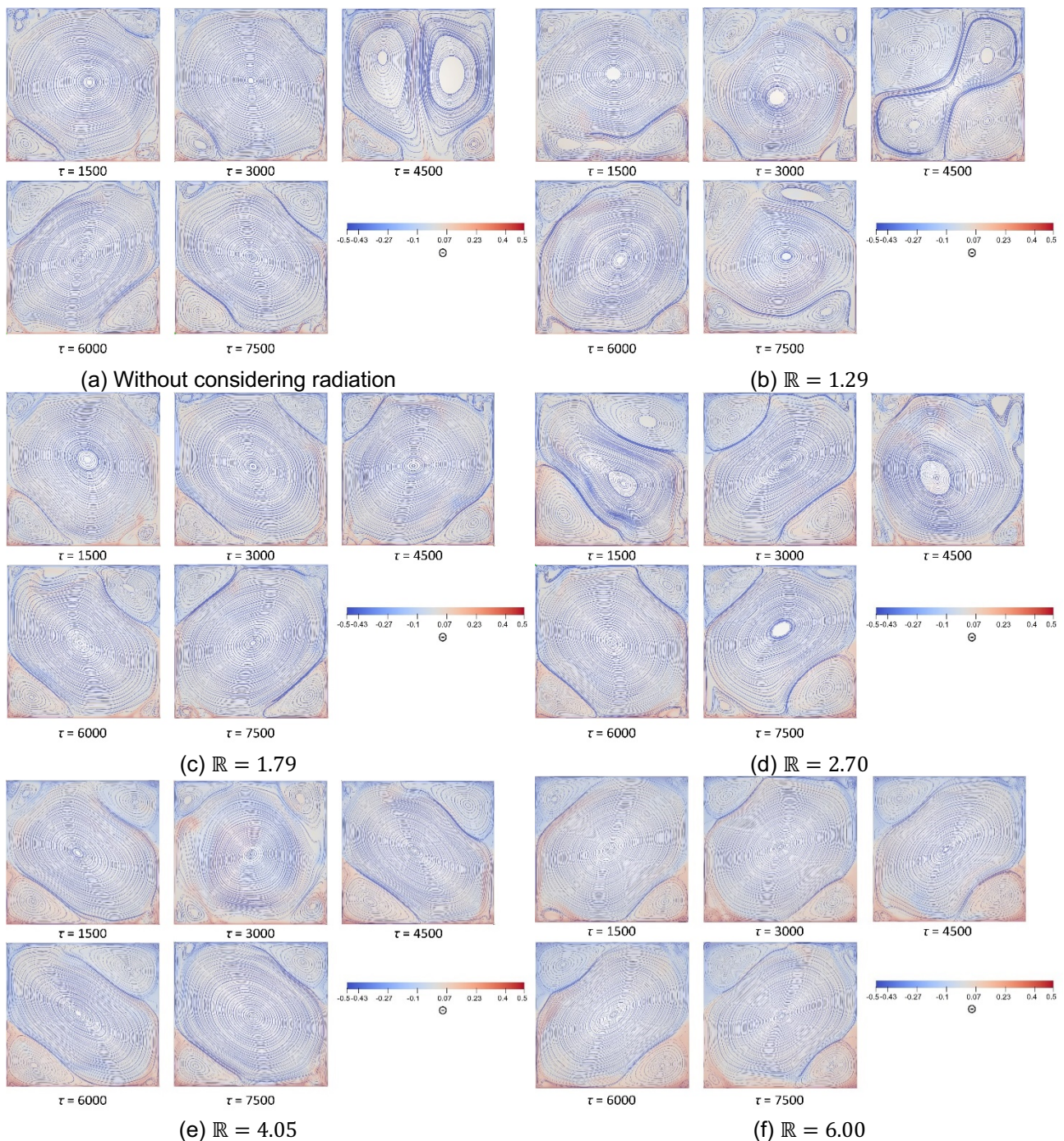

Figure 3: The time-evolution of isotherm contours (background) and streamlines (blue lines) for $Ra = 4.12 \times 10^8, Pr = 7$ at different $\mathcal{R}$.
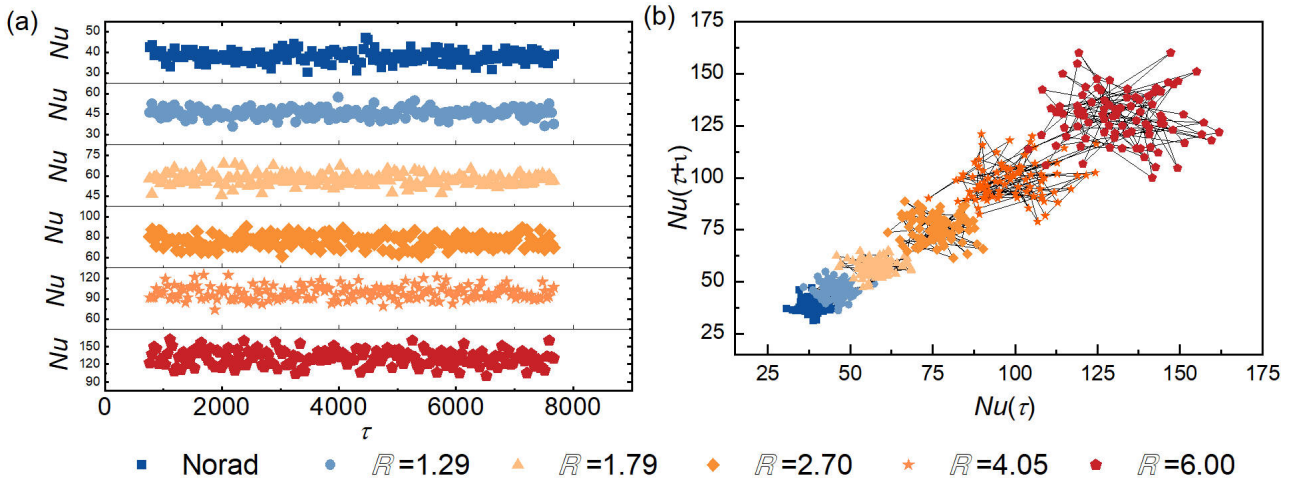
The global heat transfer efficiency

Figure 4: The transient Nu for $Ra = 4.12 \times 10^8, Pr = 7$ at different $\mathbb{R}$. (a) The time-evolution of Nu; (b) The 2D phase trajectory (where $\iota = 3450$)

The transient *Nu* for $Ra = 4.12 \times 10^8, Pr = 7$ at different $\mathbb{R}$ has been depicted in Figure 4. It can be seen that the flow for all the cases has fully developed into turbulent state. When considering thermal radiation, the heat transfer has been significantly enhanced, which is consistent with the conclusion obtained from the previous theoretical analysis, i.e., Equation 17 and 19.

In order to quantitatively verify the correctness of the prediction model, the comparison of the exponent of $\mathbb{R}$ between DNS results and the theoretical analysis has been done, as shown in Figure 5. It should be noticed that the temporal average was performed over a duration of more than 5000 dimensionless time units after the convective flow has been fully developed. According to the original GL model, the parameter range of $Ra = 4.12 \times 10^8, Pr = 7$ should be located in Regime I-b. Interestingly, the exponent of $\mathbb{R}$ obtained from DNS is closer to the predicted results of Regime I-a, rather than that of Regime I-b. This may be related to the suppression of convection by radiation. The deviation of the exponents of $\mathbb{R}$ obtained from DNS and theoretical analysis is about 8.8%. What is more, the results for $Ra = 3.0 \times 10^8, Pr = 1$ (it is usually the *Pr* of gas) are also shown in Figure 5, and the deviation between DNS and prediction model is about 9.4%. It indicates that the derived scaling law can effectively predict the *Nu* of radiative Rayleigh-Bénard convection by applying Rosseland approximation.
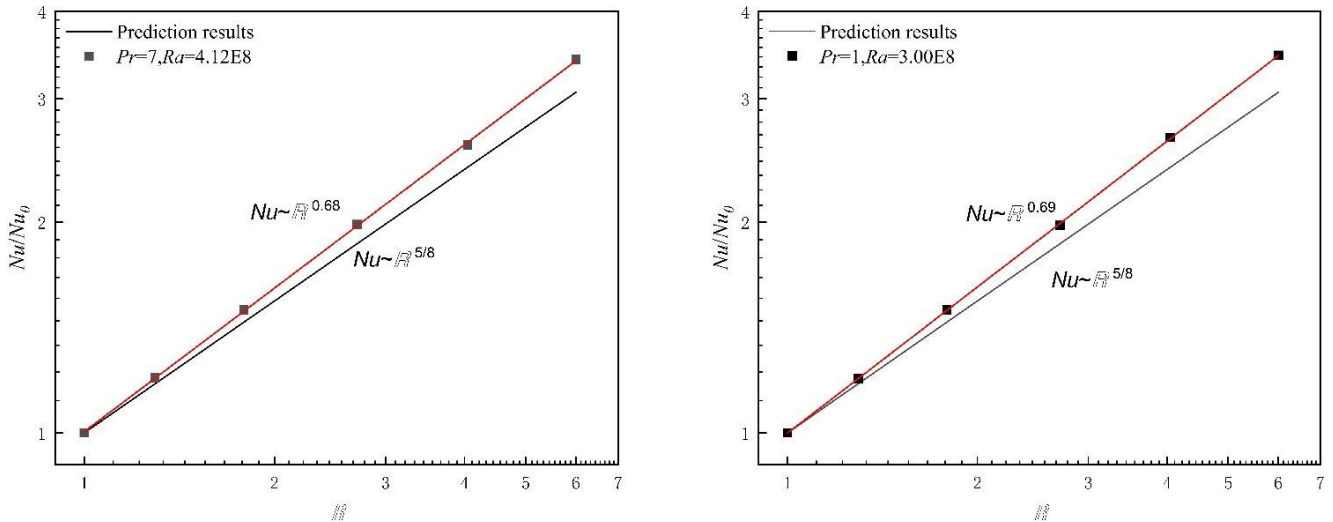

Figure 5: The comparison between DNS and theoretical analysis results: the exponent of $\mathbb{R}$.

5. CONCLUSION

In summary, the transport characteristic of radiative Rayleigh-Bénard convection in optically thick media has been investigated by theorical analysis and DNS. Main conclusions can be summarized as follows:

– Based on the turbulent dissipation theory and Rosseland approximation, the scaling law has been summarized as the form of $Re = \mathbb{R}^{1/4} Ra^{1/2} Pr^{-3/4}, Nu = \mathbb{R}^{5/8} Ra^{1/4} Pr^{1/8}$.

- When $Ra = 4.12 \times 10^8$, $Pr = 7$, the LSC has been formed regardless of whether thermal radiation is considered or not. The effect of radiation can stabilize flow, specifically manifested by a decrease in the collapse and redirection frequencies of

  LSC as $\mathcal{R}$ increases. However, heat transfer is significantly enhanced when considering thermal radiation.
- According to the comparison in the exponent of $\mathcal{R}$ between DNS and theoretical analysis, the summarized scaling law can effectively predict the Nu of radiative Rayleigh-Bénard convection and the deviation is about 9%.

6. ACKNOWLEDGEMENT

7. REFERENCES

Alnaqi, A.A., Aghakhani, S., Pordanjani, A.H., Bakhtiari, R., Asadi, A., Tran, M.D., 2019, Effects of magnetic field on the convective heat transfer rate and entropy generation of a nanofluid in an inclined square cavity equipped with a conductor fin: Considering the radiation effect. International Journal of Heat and Mass Transfer, 133, 256–267.

Amber, I., O'Donovan, T.S., 2017, Heat transfer in a molten salt filled enclosure absorbing concentrated solar radiation. International Journal of Heat and Mass Transfer, 113, 444–455.

Balakin, B.V., Zhdaneev, O.V., Kosinska, A., Kutsenko, K.V., 2019, Direct absorption solar collector with magnetic nanofluid: CFD model and parametric analysis. Renewable Energy, 136, 23-32.

Castaing, B., Gunaratne, G., Heslot, F., Kadanoff, L., Libchaber, A., Thomae, S., Wu, X. Z., Zaleski, S., Zanetti, G., 1989, Scaling of hard thermal turbulence in Rayleigh- Bénard convection. Journal of Fluid Mechanics, 204, 1-30.

Chakraborty, S., 2008, On scaling laws in turbulent magnetohydrodynamic Rayleigh–Bénard convection. Physica D, 237, 3233-3236
Chang, Y., Scotti, A., 2023, Characteristic scales during the onset of radiatively driven convection: linear analysis and simulations. Journal of Fluid Mechanics, 973, A14.

Grossmann, S., Lohse, D., 2000, Scaling in thermal convection: a unifying theory. Journal of Fluid Mechanics, 407, 27-56.

Grossmann, S., Lohse, D., 2001, Thermal convection for large Prandtl numbers. Physical Review Letters, 86, 3316-3319.

Grossmann. S., Lohse, D., 2002, Prandtl and Rayleigh number dependence of the Reynolds number in turbulent thermal convection. Physical Review E, 66, 016305.

Grossmann, S., Lohse, D., 2004, Fluctuations in turbulent Rayleigh-Benard convection: The role of plumes. Physics of Fluids, 16, 4462-4472.

Heslot, F., Castaing, B., Libchaber, A., 1987, Transitions to turbulence in helium gas. Physical Review A, 36, 5870-5873.

Huang, M.J., Wang, Y., Bao, Y., He, X.Z., 2022, Heat transport and temperature boundary-layer profiles in closed turbulent Rayleigh–Bénard convection with slippery conducting surfaces. Journal of Fluid Mechanics, 943, A2.

Malkus, W.V.R., 1954, The Heat Transport and Spectrum of Thermal Turbulence. Proceedings of the Royal Society of London Series a-Mathematical and Physical Sciences, 225, 196-212.

Li, P.X., Luo, X.H., Chen, L., Song, J.J., Li, B.W., Karcher, C., 2024, Numerical research for the effect of magnetic field on convective transport process of molten salt in Rayleigh- Bénard system. International Journal of Thermal Sciences, 195, 108605.

Ravichandran, S., Wettlaufer, J. S., 2021. Melting driven by rotating Rayleigh- Bénard convection. Journal of Fluid Mechanics, 916, A28.

Sano, M., Wu, X. Z., 1989, Turbulence in helium-gas free-convection. Physical Review A, 40, 6421-6430.

Sharma, L., Ghosh, M., Pal, P., 2022. Effect of horizontal aspect ratio on magnetoconvective instabilities in liquid metals. Physical Review Fluids, 7, 023502.

Sheikholeslami, M., Shehzad, S.A., 2017, Thermal radiation of ferrofluid in existence of Lorentz forces considering variable viscosity. International Journal of Heat and Mass Transfer, 109, 82–92.

Shraiman, B. I., Siggia, E. D., 1990, Heat-transport in high-Rayleigh-number convection. Physical Review A, 42, 3650-3653.Siggia, E. D., 1994, High Rayleigh number convection. Annual Review of Fluid Mechanics, 26, 137-168.

Song, J.J., Li, P.X., Chen, L., Li, C.H., Li, B.W., Huang, L.Y., 2023. A review on Rayleigh-Bénard convection influenced by the complicating factors. International Communications in Heat and Mass Transfer, 144, 106784.

Soucasse, L., Podvin, B., Rivière, P., Souflani, A., 2020, Reduced-order modelling of radiative transfer effects on Rayleigh-Bénard convection in a cubic cell. Journal of Fluid Mechanics, 898, A2.

Soucasse, L., Podvin, B., Rivière, P., Souflani, A., 2021, Low-order models for predicting radiative transfer effects on Rayleigh–Bénard convection in a cubic cell at different Rayleigh numbers. Journal of Fluid Mechanics, 917, A5.

Timofeev, V.V., Kalaev, V.V., Ivanov, V.G., 2015, 3D melt convection in sapphire crystal growth: Evaluation of physical properties. International Journal of Heat and Mass Transfer, 87, 42–48.

Yan, M., Tobias, S.M., Calkins, M.A., 2021, Scaling behaviour of small-scale dynamos driven by Rayleigh–Bénard convection. Journal of Fluid Mechanics, 915, A15.

Yang, J.L., Zhang, Y.Z., Jin, T.C., Dong, Y.H., Wang, B.F., Zhou, Q., 2021, The Pr-dependence of the critical roughness height in two-dimensional turbulent Rayleigh–Bénard convection. Journal of Fluid Mechanics, 911, A52.

Zürner, T., Liu, W.J., Krasnov, D., Schumacher, J., 2016, Heat and momentum transfer for magnetoconvection in a vertical external magnetic field. Physical Review E, 94, 043108.

Zürner, T., 2020, Refined mean field model of heat and momentum transfer in magnetoconvection. Physical of Fluids, 32, 107101.

#255: Research on ultra-short-term power prediction for photovoltaic modules based on improved generative adversarial networks

Peng YAN, Xiaofeng ZHU, Mengxin FANG, Daolei WANG[*]

Shanghai University of Electric Power, No. 1851, Hucheng Ring Road, Nanhui New Town, Pudong New Area, Shanghai, China, fancy782181@mail.shiep.edu.cn, fmx1218@163.com, 2197500083@qq.com,Alfredwdl@shiep.edu.cn

Abstract: Aiming at the problem of inaccurate power generation efficiency prediction due to the strong randomness and volatility of photovoltaic power output, this paper proposes an improved autoregressive feedforward neural model based on Generative Adversarial Networks (GAN) to predict the ultra-short-term power of photovoltaic modules. Firstly, identifying the internal parameters of photovoltaic modules by the improved Coati Optimization Algorithm(COA) with Token-Ring integrated with Sequential Least Squares Programming(SLSQP), and selecting the internal and external factors that have tremendous impact on the output power based on Grey Relation Analysis(GRA); then, considering the global time correlation and long-term dependence of the data, a Generator Network with Self-Attention mechanism module as encoder and Long Short Term Memory(LSTM) module as decoder and a Discriminator Network are constructed for recursive multi-step training. At the same time, building a pre-trained SVM to construct Hinge loss, Discriminator loss and Generator loss to generate accurate PV power sequences. The results show that the proposed method can improve the prediction accuracy of output power of photovoltaic module and fault identification accuracy effectively and has certain engineering practicality.

Keywords: Photovoltaic Modules; Power Prediction; Coati Optimization Algorithm; Generative Adversarial Network.

1. INTRODUCTION

Affected by factors such as meteorological conditions and internal parameters, the prediction of photovoltaic power generation has problems such as strong randomness and volatility and inaccurate prediction accuracy. With the advancement of statistics and artificial intelligence technology, various methods of photovoltaic power prediction have been proposed, and they can be divided into medium and long-term forecast, short-term forecast and ultra-short-term forecast according to different time scales. Medium and long-term forecasts are mainly used to evaluate the annual power generation of photovoltaic power stations, as well as to formulate medium and long-term maintenance plans. A short-term forecast is used for dispatch so as to improve the quality of power supply. Ultra-short-term forecast is usually used for real-time schedule and controlling equipment. In order to ensure the safe and stable operation of the power system and make real-time scheduling decisions, it is necessary to make ultra-short-term accurate predictions of photovoltaic power generation.

At present, a lot of relevant research has been done on the ultra-short-term power prediction of photovoltaic power generation. Tian (2023) introduced dilated causal convolutions to extract features, stacked long-term and short-term networks are used to enhance the prediction accuracy of LSTM, and the accuracy and stability of the model are verified by comparing with mainstream prediction models such as LSTM, RNN, GRU, etc. Bai (2023) combined K-means++, optimal look-alike day method, and long short-term memory (LSTM) networks to predict PV power by means of historical power data and meteorological factors. Wang (2024) proposed an efficient shrinkage temporal convolutional network model, which is used to predict by combining temporal convolutional network and an improved deep residual shrinkage network. Hu (2024) proposed a prediction model that combines long short-term memory and self-attention mechanism, which captures time features through LSTM network and the correlation between multiple time series through self-attention mechanism, and the results show good performance. Dou (2024) proposed a spatiotemporal feature encoder-decoder model based on LSTM network and Space-Time Attention mechanism and designs an adaptive prediction framework based on pre-fusion and post-fusion to meet the comprehensive feature learning needs under different data input and further improves the prediction accuracy. Yang (2023) constructed an improved grey wolf optimizer based on improved adaptive factors and elite reverse learning strategies to optimize the prediction model of long short-term memory networks, and the PV power is predicted by constructing a combined IGWO-LSTM model, which has good convergence speed and solution efficiency. Liu and L (2023) proposes a PV power prediction model that uses the improved Aquila optimization algorithm to optimize the parameters of the LSTM neural network, and the results show that its overall performance is significantly improved compared with the AO-CNN model. Aiming at the missing value in historical data, Peter and Ujwal Ambadas Lanjewar (2023) introduced GAN to estimate. In order to reduce the threat of learning the long-term dependencies embedded in the time series, the LSTM is used to consider the changing model of time series data in each period, and the verification results show that the model has good performance in time series prediction. Xu (2019) proposed a GAN-LSTM model for satellite image prediction, which is better than the traditional LSTM by combining the generative ability of GAN (Labaca-Castro,2023) and the prediction ability of LSTM network.

In this paper, we propose an ultra-short-term power prediction method for photovoltaic power generation based on an improved autoregressive feedforward generative neural model network. The main contributions are as follows: 1. A photovoltaic power prediction method combining internal parameters and external environmental factors is proposed, which has a good improvement in the prediction accuracy of photovoltaic power data at the scale of 3-4h. 2. Speaking of internal parameter recognition, the improved coati optimization algorithm (Dehghani *et al.* ,2023) combined with the token ring and the Sequential Least Squares Programming (SLSQP) is used for hybrid optimization recognition. With respect to predict power, a Generator Network with self-attention mechanism module (Davies and Jones,1994) as encoder and the Long Short-Term Memory (LSTM)(Hochreiter and Schmidhuber,1997) module as decoder and a Discriminator Network trained by the improved raccoon optimization algorithm were built for recursive multi-step training, and the SVM(Cortes and Vapnik,1995) was used for pre-training to calculate the Hinge loss, and the reconstruction error and the adversarial loss were combined for optimization.

2. IDENTIFICATION OF INTERNAL PARAMETERS OF PHOTOVOLTAIC ARRAYS

2.1 Mathematical model of photovoltaic cells

In the photoelectric power station, what is actually measured is the output current and output voltage of the photovoltaic arrays, which are composed of photovoltaic modules through series-parallel, while the photovoltaic modules are composed of photovoltaic cells in series-parallel. A photovoltaic cell is essentially a PN junction that uses the photoelectric effect of semiconductors to convert light energy into electrical energy, and its mathematical model is also built based on the equivalent circuit of the photovoltaic cell. Common equivalent circuits include single-diode circuits (Ayodele, Ogunjuyigbe and Ekoh,2016), double-diode circuits (Sudhakar Babu et al. ,2016), etc. Considering the complexity of the algorithm, we think of the photovoltaic arrays as a large photovoltaic cell in this study to identify the internal parameters. The single-diode equivalent model is shown in Figure 1 with the following I-V characteristic equations (AlRashidi et al. ,2011) by Eqs. (1) to (2).

Equation 1: The output current of the single-diode module

$$I = I_{ph} - I_0(e^{\frac{V+IR_s}{nV_t}} - 1) - \frac{V + IR_s}{R_{sh}}$$

Equation 2: Thermal voltage of photovoltaic modules

$$V_t = \frac{kTN_s}{q}$$

Where:

- I_{ph} = photogenerated current

- I_o = saturation current of the diode
- Rs = series resistance
- R_{sh} = shunt resistance
- n = the ideal factor
- V = voltage of the load
- T = temperature of the photovoltaic cell
- q = electron charge(1.60217646 * 10^{-23}C)
- k = Boltzmann constant (1.3806503*10^{-23}J/K)
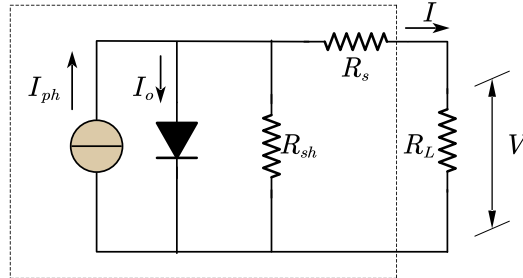- Ns = number of series cells

Figure 1: Equivalent circuit of the SDM

Based on the theoretical model of photovoltaic modules, we define the optimization objective function f(X) listed as Eq. (3) to obtain the internal parameters X, which are { Iph, Io, Rs, Rsh,n } to minimize the error between the actual value and the estimated value. The smaller the fitness value, the higher the accuracy of parameters identification.

Equation 3: Value of fitness function $\quad f(X) = \sqrt{\dfrac{1}{N}\sum_{k=1}^{N}(I_{cal} - I_{mea})^2}$

Where:

- N = number of samples of experimental data
- Ical = value calculated by Eq. (1)
- Imea = actual measured value

2.2 Coati Optimization Algorithm

The Coati Optimization Algorithm (COA) is a heuristic algorithm proposed by M Dehghani in January 2023 that simulates through the two behaviours of coatis in nature as they attack and hunt iguanas and flee from predators. The algorithm mainly includes the exploration and the exploitation phase. The mathematical model of the exploration phase is represented in Eqs. (4) to (6).

Equation 4: Position of the coat in the tree $\quad x_i^{t+1}(j) = x_i^t(j) + r \cdot (x_{best}^t(j) - I \cdot x_i^t(j)), i = 1,2,...,\dfrac{N}{2}$

Where:

- t = iteration
- r = a random number between [0,1]
- I = a random integer from the set of {1,2}
- N = population size

Equation 5: Position of the iguana $\quad Iguana_{ground}^t(j) = lb_j + r \cdot (ub_j - lb_j)$

Where:

- ubj = the upper bounds of the j-dimensional variable
- lbj = the lower bounds of the j-dimensional variable

Equation6: Position of the coati on the ground $\quad x_i^{t+1}(j) = \begin{cases} x_i^t(j) + r \cdot (Iguana_{ground}^t(j) - I \cdot x_i^t(j)), if\ fitness(Iguana_{ground}^t) < fitness(x_i^t) \\ x_i^t(j) + r \cdot (x_i^t(j) - Iguana_{ground}^t(j)), else \end{cases} \quad i = \frac{N}{2}+1, \frac{N}{2}+2,...,N$

Where:

- Iguanatground = new position of the iguana after it falls to the ground
- xti(j) = value of the j-dimensional variable of the ith individual under the current iteration.

The author believes that half of the coatis climb the tree and the other half wait for the iguana to fall to the ground. The two parts of the individual update the individual position through Eq. (4) and Eqs. (5) to (6), respectively, and then perform a greedy search through Eq. (7).

Equation7: Update location based on greedy search
$$x_i^{t+1} = \begin{cases} x_i^{t+1}, & \text{if } fitness(x_i^{t+1}) < fitness(x_i^t) \\ x_i^t, & else \end{cases}$$

During the exploitation phase, a strategy of evading predators was simulated by Eqs. (8) to (9) by generating a random location for each coati, followed by a greedy search using Eq. (7).

Equation8: Redefine the upper and lower bounds
$$lb_j^{local} = \frac{lb_j}{t}, ub_j^{local} = \frac{ub_j}{t}, t = 1, 2, ..., T$$

Equation9: Make a random position for every coati
$$x_i^{t+1}(j) = x_i^t(j) - (1-2r) \cdot (lb_j^{local} + r \cdot (ub_j^{local} - lb_j^{local}))$$
$$i = 1, 2, ..., N$$

2.3 Improvements

Due to the problems of slow convergence speed, insufficient global exploration ability, and easy to fall into local optimum in the internal parameter identification of photovoltaic modules, we propose some improvements, which include chaotic initialization of populations, update of token rings and SLSQP, and the overall framework of the improved algorithm is in Figure 2.
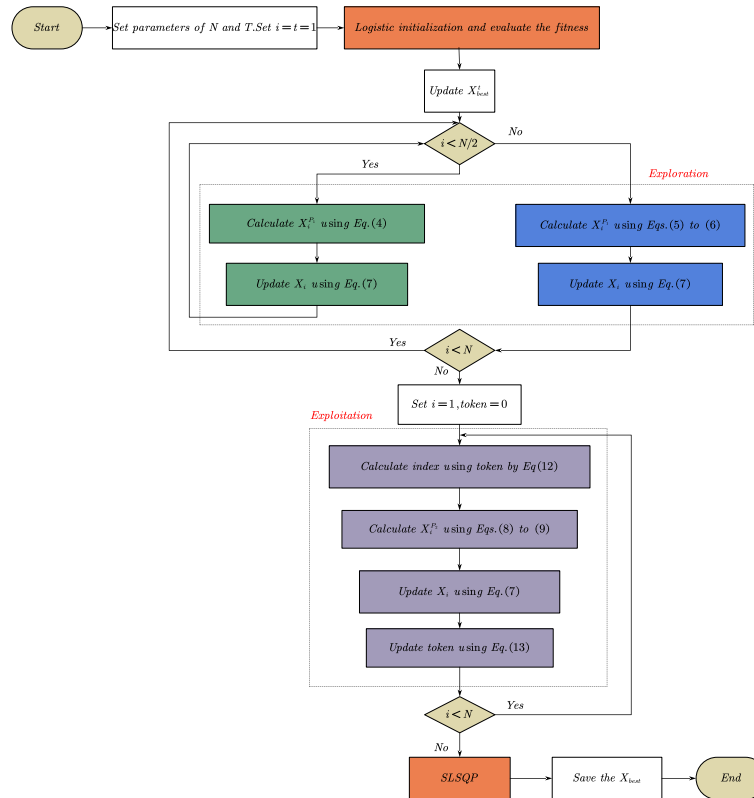

Figure 2: Flowchart of Improved COA

Chaos initialization

Considering the randomness and extensiveness of the distribution of coatis, the chaos technique is introduced to generate initial populations all over the search space to increase the probability of finding the optimal solution, listed as Eqs. (10) to (11).

Equation10: Make chaotic sequences
$$Z_{ij} = \mu Z_{ij}(1 - Z_{ij}) \ (j = 1, 2, ..., d)$$

Where:

- μ = control parameter
- Z_{ij} = component in d-dimensional vectors Z_i

Equation11: Map each component
$$X_{ij} = b_{lj} + (b_{uj} - b_{lj})Z_{ij} \ (i = 1, 2, ..., M; j = 1, 2, ..., d)$$

Where:

- b_{lj} = lower bound of mapping interval
- b_{uj} = upper bound of mapping interval

Update with the token ring

During the exploitation, the COA mainly searches around the current individual, and there is no guidance of population information, so it is not conducive for later convergence. Therefore, the token ring transmission is added to update the global optimal information. Eq. (12) is used to update the current index of the token and at the end of each iteration, the token position is adjusted by Eq. (13) so that the search starts from a different starting point in the next iteration.

$$Equation12: Update\ the\ index\ of\ solution \quad solution\_index = \begin{cases} i, if\ token = 0 \\ (i + token)\%SearchAgents\_no, else \end{cases}$$

Where:

- SearchAgents_no = number of the population
- token = a customized changing value

$$Equation13: Update\ the\ position\ of\ token \quad token = (token + 1)\%SearchAgents\_no$$

Sequential Least Squares Programming

SLSQP is a sequential quadratic programming algorithm that decomposes a large problem into small problems and solves small problems through a linear constraint. After each iterative update, the convergence property is used to update the parameters of all individuals to achieve the balance between local optimization and global search.

3. POWER FORECAST OF SELF-REGRESSIVE FEEDFORWARD GAN

Generative Adversarial Network is a deep learning model, which produces better output results through mutual game learning of generators and discriminators. Because traditional GANs are difficult to capture the time-varying dynamics in sequences, an improved self-regressive feedforward GAN is proposed, which combines the generative ability of GAN with the prediction ability of LSTM, introduces a self-attention mechanism to further improve the feature extraction and expression ability of the network, and builds a pre-trained SVM to construct Hinge loss, Discriminator loss and Generator loss to generate accurate PV power sequence, the structure of which is depicted in Figure3.
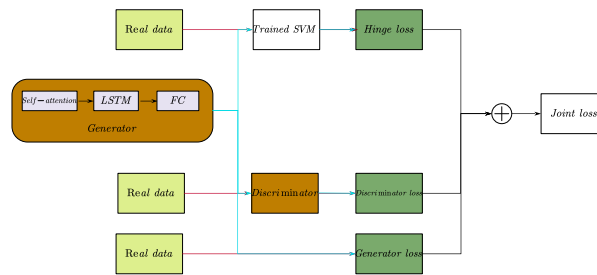
Figure3: Structure of improved GAN model

In the improved autoregressive feedforward GAN we construct the loss function consists of three parts: $\ell = \ell_h + \ell_D + \ell_G$. They are listed in Eqs. (14) to (16).

$$Equation14: Expression\ of\ Hinge\ loss \quad \ell_h = \max(0, 1 - y \cdot f(x))$$

Where:

- y = label of data
- f = confidence level

$$Equation15: Expression\ of\ Discriminator\ loss \quad \ell_D = -E_{x \sim P_r}[D(x)] + E_{z \sim p_z(z)}[D(G(z))]$$

Where:

- P_r = true distribution
- P_z = noise distribution

Equation16: Expression of Generator loss $\ell_G = -E_{z \sim p_z(z)}[D(G(z))]$

Where l_h is the hinge loss, which separates the real data and the data generated by the generator at the maximum interval; ID is the discriminator loss, the Wasserstein distance is used to measure the distance between the true distribution Pr and the resulting distribution; IG is the generator loss and z is the input noise complying with the distribution pz(z), which aims to generate samples that are as close to the true distribution as possible.

4. EXPERIMENTS

4.1 Data introduction

The experiment uses the PyTorch deep learning framework and conducts on a single NVIDIA GeForce RTX 3050 GPU. Experimental data come from the Connellan Airport in the Yulara solar system at the desert knowledge Australia solar center, and the specific parameters of this photovoltaic motor are shown in Table 1.

Table 1: Parameters of photovoltaic motors

Key parameters	Specification
Array Rating/KW	105.9
Number of Panels	326
Panel Type	SubPower SPR-327NE
Inverter Size/Type	SMA STP 25000TL-30 & 20000TL-30
Array Tilt/Azimuth	Tilt = 10, Azi = 40 (E of N)

4.2 Overall process

We study the original data from March 2023 to February 2024, and its sampling interval is 5 minutes. Aiming at the problem of missing data such as irradiance and temperature due to equipment failure, we fill in monthly to get 366 days of measured data. Considering the power output at night and dawn is almost zero, it is of little significance to the study of this paper, so only the power data from 07:00 to 19:00 are considered.

After identifying the inner parameters by improved COA, we use Grey Relation Analysis (GRA) to select factors that have a greater impact on the power output through Eq. (17).

Equation17: Expression of Grey Relation Analysis (GRA) $G^l = \dfrac{1}{n}\sum_{j=1}^{n} \dfrac{\min\limits_{l}\min\limits_{j}\left|y_j^0 - y_j^l\right| + \rho\max\limits_{l}\max\limits_{j}\left|y_j^0 - y_j^l\right|}{\left|y_j^0 - y_j^l\right| + \rho\max\limits_{l}\max\limits_{j}\left|y_j^0 - y_j^l\right|}$

Where:

- y_j^0 = the jth power output
- y_j^l = the jth data of the lth index
- ρ = the constant (0.5 is taken in this experiment)

And its correlation analysis is as Table 2 shows:

Table 2: Results of Grey Relational Analysis

Attribute	Correlation_Degree
Current_Phase_Average_Mean	0.978401
Pyranometer_1	0.840577
Global_Horizontal_Radiation	0.839809
Temperature_Probe_2	0.756926
Temperature_Probe_1	0.745684
I_{ph}	0.688477
n	0.688186
Max_Wind_Speed	0.680044
Weather_Temperature_Celsius	0.66505
I_o	0.658149
Wind_Speed	0.646592
Air_Pressure	0.644044
Active_Energy_Delivered_Received	0.637762
Wind_Direction	0.594031
R_{sh}	0.560728
R_s	0.556278
Weather_Daily_Rainfall	0.508151
Hail_Accumulation	0.508151

Considering the joint influence of internal and external parameters, the first seven parameters Current_Phase_Average_Mean, Pyranometer_1, Global_Horizontal_Radiation, Temperature_Probe_2, Temperature_Probe_1 and Iph were selected to predict the output power of photovoltaic power plants. Then the improved GAN is used according to the seasonal division data to predict and analyze the photovoltaic power in the next four hours.

4.3   The improved COA for identifying parameters of PV modules

The effectiveness of the improved COA in the identification of PV module model parameters was analysed by six compared algorithms, including GA (Juan David Bastidas-Rodriguez et al. ,2017), DE (Li et al. ,2019), ACO (Dorigo et al. ,2006), SA (El-Naggar et al. ,2012), GWO (Pan et al. ,2021), WOA (Oliva et al. ,2017), and the algorithm parameters are shown in Table 3.

Table 3: Parameters settings of algorithms

Algorithm	Parameters
GA	N_{pop}=30,P_m=0.05
DE	N_{pop}=30
ACO	N_{pop}=30
SA	N_{pop}=30,α=0.9
GWO	N_{pop}=30
WOA	N_{pop}=30
Improved COA	N_{pop}=30

Table 4: RMSE of Improved COA and comparative algorithms

Algorithm	RMSE			
	Minimum	Maximum	Mean	STD
GA	6.803192E-03	7.420462E-02	1.692071E-02	1.377045E-02
DE	4.358189E-04	2.289195E-01	3.423820E-02	4.885532E-02
ACO	5.560906E-02	4.560907E-01	7.672480E-02	3.996257E-02
SA	1.897732E-02	3.655055E-01	4.538058E-02	3.726068E-02
GWO	4.125941E-02	7.767134E-02	5.228975E-02	8.793388E-03
WOA	1.012943E-02	9.527047E-02	4.135420E-02	2.084744E-02
Improved COA	**4.116775E-04**	**4.152254E-04**	**4.119322E-04**	**5.638247E-07**

In order to illustrate the superiority of the algorithm proposed in this paper, the maximum, minimum, mean and standard deviation of RMSE obtained by running all algorithms independently for 30 times are compared, and the results are listed in Table 4, among which improved COA is better than other algorithms in RMSE, which proves the effectiveness of the proposed algorithm.

The iterative convergence curves of different algorithms are shown in Figure 4 for the parameter identification of PV module models, from which it can be seen that the proposed algorithm has the best performance in all indicators of RMSE and has faster convergence and better stability than other algorithms. Among them, the mean RMSE of the DE algorithm still has a downward trend when the number of iterations is 40, while the Improved COA basically converges to near the optimal value when the function is evaluated at 40 times. It shows that the algorithm can effectively avoid the algorithm falling into local optimum, and has strong local and global search capabilities.
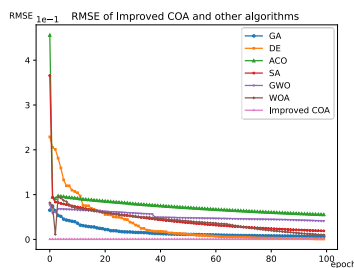

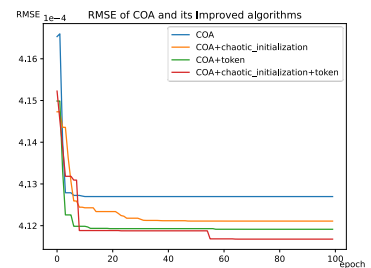*Figure 4: RMSE of improved COA and its compared algorithms*

Figure 5: RMSE of COA and its improved algorithms

In order to further verify the influence of each improved module on the performance of the algorithm, the maximum, minimum, mean and standard deviation of RMSE obtained by running the algorithm with different improved modules independently for 30 times, the results are as shown in Table5. It can be seen that the COA algorithm with additional chaos initialization and token ring improvement has the best comprehensive performance, with the smallest minimum and mean of RMSE, although

max and standard deviation of RMSE are not optimal, but it is considered that the population initialization distribution brought by chaos initialization is uneven, compared with the superimposed token ring search expands the search space of the algorithm so as to lead to weak algorithm stability.

Table 5: RMSE of COA with different modules

Algorithm	RMSE			
	Minimum	Maximum	Mean	STD
COA	4.126978E-04	4.165976E-04	4.127920E-04	5.548077E-07
COA+chaotic_initialization	4.121098E-04	**4.147294E-04**	4.122894E-04	5.040626E-07
COA+token	4.119137E-04	4.149869E-04	4.120112E-04	**4.506507E-07**
COA+chaotic_initialization+token	**4.116775E-04**	4.152254E-04	**4.119322E-04**	5.638247E-07

In order to reflect the optimization performance of the algorithm, the iterative convergence curve of each improved module of the PV module model is shown in Figure 5, from which it can be seen that although the COA algorithm with chaotic initialization and the token ring is less stable, it has better convergence and search ability and can avoid the local best.

4.4 The improved GAN for predicting power output

In order to verify the effectiveness and availability of the improved autoregressive feedforward neural model based on GAN in predicting output power, we divide the data of photovoltaic power plants from 2023.3 to 2024.2 into seasons, comparing it with the LSTM, using MSE, RMSE, MAE, and Goodness of Fit as indicators for analysis, as shown in Table 6. From the results, the Improved GAN gets the best performance in all four quarters of each metric. This is especially true for the first quarter, where the Goodness of Fit increases by 15.64%, and the MSE, RMSE and MAE decreased by 0.759%, 6.052%, and 6.31%, respectively. We argue that the reduction of loss and the improvement of fitting degree are mainly due to the effective use of the self-attention mechanism to understand the sequence context so as to enhance the key information in the global and local features, and the joint loss introduced by the pre-trained SVM network to make the model accurately predict the time series.

Table 6: Statistics of Improved GAN and LSTM in four seasons

		MSE	RMSE	MAE	r2_score
Spring	LSTM	0.008639879	0.09295095	0.086	0.821922496
	Improved GAN	**0.001051848**	**0.032432202**	**0.022905404**	**0.978320253**
Summer	LSTM	0.004371521	0.06611748	0.043711722	0.94362732
	Improved GAN	**0.001787604**	**0.04228007**	**0.0383**	**0.977466983**
Autumn	LSTM	0.000779291	0.027915777	0.023640119	0.986693516
	Improved GAN	**0.00059071**	**0.024304521**	**0.020258537**	**0.990978444**
Winter	LSTM	0.000576025	0.024000519	0.019668405	0.991202717
	Improved GAN	**0.000391134**	**0.019777111**	**0.016071772**	**0.994026443**

In order to clearly demonstrate the difference in performance between the LSTM and the improved GAN, we compare and analyse on the results on the test set, drawing the change curves of the power forecasts for the four quarters and the predicted output power curves for the next four hours, as shown in Figure 6-9.
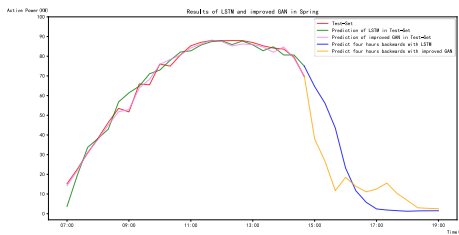

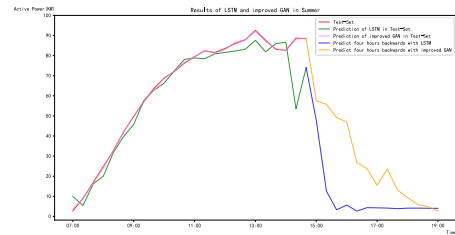*Figure 6: Results of LSTM and improved GAN in Spring*

Figure 7: Results of LSTM and improved GAN in Summer

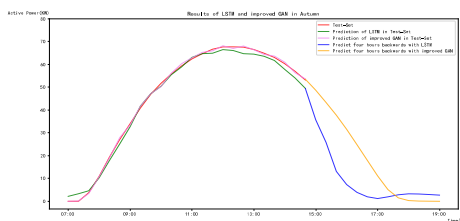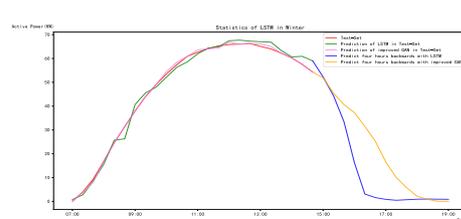*Figure 8: Results of LSTM and improved GAN in Autumn*

Figure 9: Results of LSTM and improved GAN in Winter

The polylines in the graph show that the Improved GAN has performed good performance in model testing, with a better fit than LSTM. At the same time, the results are also common sense in predicting the output power in the next 4 hours, decreasing with the delay of time, which have good applicability.

5. CONCLUSION

In this paper, we fully consider the internal parameters and external environment factors that affect the output power of photovoltaic stations and propose an ultra-short-term power prediction method for photovoltaic power generation based on improved autoregressive feedforward neural model based on GAN. We identify the internal parameters of PV modules by the improved COA, and select indicators with high correlation with power prediction by GRA, which provides a basic for accurate power prediction. We combine the self-attention mechanism and LSTM to improve the feature extraction and expression ability of the network, at the same time constructing SVM to make a joint loss function to generate more accurate photovoltaic power sequences. The paper uses LSTM and GAN as the basic modules, and the use of GRU, RNN and other modules can be discussed in the future. In this article, the power forecast is classified according to the season, and then it can be finely divided according to the weather again. Experimental verification shows that the proposed model has higher accuracy than LSTM, which further illustrates the feasibility and accuracy of improved GAN in ultra-short-term power prediction and can be used for real-time dispatch of power grid and control of photovoltaic power generation equipment to ensure the safe and stable operation of the power system.

6. REFERENCES

[1] Ayodele, T.R., Ogunjuyigbe, A.S.O. and Ekoh, E.E. (2016). Evaluation of numerical algorithms used in extracting the parameters of a single-diode photovoltaic model. Sustainable Energy Technologies and Assessments, 13, pp.51–59. doi:https://doi.org/10.1016/j.seta.2015.11.003.

[2] AlRashidi, M.R., AlHajri, M.F., El-Naggar, K.M. and Al-Othman, A.K. (2011). A new estimation approach for determining the I–V characteristics of solar cells. Solar Energy, 85(7), pp.1543–1550. doi:https://doi.org/10.1016/j.solener.2011.04.013.

[3] Ruxue Bai，Yuetao Shi，Meng Yue，Xiaonan Du.Hybrid model based on K-means++ algorithm, optimal similar day approach, and long short-term memory neural network for short-term photovoltaic power prediction[J].Global Energy Interconnection,2023,volumn 6(2): 184-196

[4] Cortes, C. and Vapnik, V. (1995) 'Support-vector networks,' Machine Learning, 20(3), pp. 273–297. https://doi.org/10.1007/bf00994018.

[5] Davies, H. and Jones, B. (1994). Attention All Surveyors: Our Schools Need You. Structural Survey, 12(5), pp.31–34. doi:https://doi.org/10.1108/02630809410074466.

[6] Dehghani, M. et al. (2023) 'Coati Optimization Algorithm: A new bio-inspired metaheuristic algorithm for solving optimization problems,' Knowledge-based Systems, 259, p. 110011. https://doi.org/10.1016/j.knosys.2022.110011.

[7] Dorigo, M., Birattari, M. and Stutzle, T. (2006). Ant colony optimization. IEEE Computational Intelligence Magazine, [online] 1(4), pp.28–39. doi:https://doi.org/10.1109/MCI.2006.329691.

[8] Dou, X., Deng, Y., Wang, S., Chu, T., Li, J. and Luo, H. (2024). Adaptive Encoder-Decoder Model Considering Spatio-Temporal Features for Short-Term Power Prediction of Distributed Photovoltaic Station. IEEE transactions on industry applications, pp.1–11. doi:https://doi.org/10.1109/tia.2024.3351613.

[9] El-Naggar, K.M., AlRashidi, M.R., AlHajri, M.F. and Al-Othman, A.K. (2012). Simulated Annealing algorithm for photovoltaic parameters identification. Solar Energy, 86(1), pp.266–274. doi:https://doi.org/10.1016/j.solener.2011.09.032.

[10] Hochreiter, S. and Schmidhuber, J. (1997). Long Short-Term Memory. Neural Computation, [online] 9(8), pp.1735–1780. doi:https://doi.org/10.1162/neco.1997.9.8.1735.

[11] Hu, Z., Gao, Y., Ji, S., Mae, M. and Imaizumi, T. (2024). Improved multistep ahead photovoltaic power prediction model based on LSTM and self-attention with weather forecast data. Applied Energy, [online] 359, p.122709. doi:https://doi.org/10.1016/j.apenergy.2024.122709.

[12] Juan David Bastidas-Rodriguez, Petrone, G., Carlos Andrés Ramos-Paja and Spagnuolo, G. (2017). A genetic algorithm for identifying the single diode model parameters of a photovoltaic panel. Mathematics and Computers in Simulation, 131, pp.38–54. doi:https://doi.org/10.1016/j.matcom.2015.10.008.

[13] Labaca-Castro, R. (2023) 'Generative adversarial Nets,' in Springer eBooks, pp. 73–76. https://doi.org/10.1007/978-3-658-40442-0_9.

[14] Li, S., Gong, W., Yan, X., Hu, C., Bai, D. and Wang, L. (2019). Parameter estimation of photovoltaic models with memetic adaptive differential evolution. Solar Energy, 190, pp.465–474. doi:https://doi.org/10.1016/j.solener.2019.08.022.

[15] Liu, L. and Li, Y. (2023). Research on a Photovoltaic Power Prediction Model Based on an IAO-LSTM Optimization Algorithm. Processes, 11(7), pp.1957–1957. doi:https://doi.org/10.3390/pr11071957.

[16] Oliva, D., Abd El Aziz, M. and Ella Hassanien, A. (2017). Parameter estimation of photovoltaic cells using an improved

chaotic whale optimization algorithm. Applied Energy, 200, pp.141–154. doi:https://doi.org/10.1016/j.apenergy.2017.05.029.

[17] Peter and Ujwal Ambadas Lanjewar (2023). Improving Air Quality Prediction with a Hybrid Bi-LSTM and GAN Model. ECTI Transactions on Computer and Information Technology, 17(3), pp.388–398. doi:https://doi.org/10.37936/ecti-cit.2023173.251670.

[18] Pan, J., Gao, Y., Qian, Q., Feng, Y., Fu, Y., sun, M. and Sardari, F. (2021). Parameters identification of photovoltaic cells using improved version of the chaotic grey wolf optimizer. Optik, 242, p.167150. doi:https://doi.org/10.1016/j.ijleo.2021.167150.

[19] Sudhakar Babu, T., Prasanth Ram, J., Sangeetha, K., Laudani, A. and Rajasekar, N. (2016). Parameter extraction of two diode solar PV model using Fireworks algorithm. Solar Energy, 140, pp.265–276. doi:https://doi.org/10.1016/j.solener.2016.10.044.

[20] Tian, C., Lin, L., Yan, Y., Wang, R., Wang, F. and Chi, Q. (2023). Photovoltaic power prediction based on dilated causal convolutional network and stacked LSTM. Mathematical biosciences and engineering, 21(1), pp.1167–1185. doi:https://doi.org/10.3934/mbe.2024049.

[21] Wang, M., Rao, C., Xiao, X., Hu, Z. and Goh, M. (2024). Efficient Shrinkage Temporal Convolutional Network Model for Photovoltaic Power Prediction. Energy, 297, pp.131295–131295. doi:https://doi.org/10.1016/j.energy.2024.131295.

[22] Xu, Z., Du, J., Wang, J., Jiang, C. and Ren, Y. (2019). Satellite Image Prediction Relying on GAN and LSTM Neural Networks. doi:https://doi.org/10.1109/icc.2019.8761462.

[23] Xue, Yang;Yan, Yucheng;Jia, Wei;Heng, Yuxi;Zhang, Shuxiang;Qin, Yao.PHOTOVOLTAIC POWER PREDICTION MODEL BASED ON IGWO-LSTM[J].Taiyangneng Xuebao/Acta Energiae Solaris Sinica,2023,Vol.44(7): 207-213

[24] Zheng, Z.W., Chen, Y.Y., Huo, M.M. and Zhao, B. (2011). An Overview: the Development of Prediction Technology of Wind and Photovoltaic Power Generation. Energy Procedia, 12, pp.601–608. doi:https://doi.org/10.1016/j.egypro.2011.10.081.

#258: Performance analysis of a disinfected PV-Trombe wall based on air filtration and thermal sterilization

Hao Xie[1], Jie Ji[2], Hengming Jia[3], Yu Qian[4], Hongju Meng[5]

[1] University of Science and Technology of China, China, xh1140@mail.ustc.edu.cn
[2] University of Science and Technology of China, China, jijie@ustc.edu.cn
[3] University of Science and Technology of China, China, jiahengmin2004@163.com
[4] University of Science and Technology of China, China, qian_yu@mail.ustc.edu.cn
[5] University of Science and Technology of China, China, hjmeng@mail.ustc.edu.cn

Abstract: Bioaerosols have received widespread attention since the outbreak of Coronavirus Disease 2019 owing to their harmful effect on public health. To deal with indoor bioaerosols, air filtration and sterilization PV-Trombe wall was proposed in this study. An experiment rig concerning thermal sterilization of aerosolized bacteria Escherichia coli (E. coli) and Staphylococcus aureus (S. aureus) was set up to test its feasibility and effectiveness at different exposure temperature and residence time. With the experimental data, an inactivation model was derived based on the first kinetic model and Arrhenius equation. Besides, a mathematical model concerning heat and mass transfer was established for simulating the system performance at different conditions. The results of experiment and simulation reveal that: (1) The survival ratio for E. coli and S. aureus was 0.935, 0.767, 0.582, 0.175, 0.033 and 1.000, 1.000, 0.96, 0.842, 0.738 at the wall temperature of 45°C, 60°C, 80°C, 100°C and 120°C and the residence time of 3 seconds, respectively. (2) the survival ratio predicted by the inactivation model corresponded well with the experimental results and the root mean square error was 0.0491 and 0.0467 for E. coli and S. aureus, respectively. (3) The electrical and thermal efficiencies were 0.142 and 0.226 while the clean air production was 177.7 m^3 and 143.4 m^3 for E. coli and S. aureus, respectively. (4) Due to the thermal sterilization effect, the bacterial quantity on the filter could be maintained at a low level during the operation of the system.

Keywords: Solar Energy; PV-Trombe Wall; Bioaerosol; Thermal Inactivation; Filtration

1. INTRODUCTION

PV-Trombe wall, which possesses the ability of generating electricity and lowering heating load by utilization of solar energy, has received attention from numerous researchers since its proposal, owing to its simple configuration, high efficiency and low running cost (Hu et al., 2017). However, the functions of PV-Trombe wall seem to include but are not limited to that. In order to enhance the indoor air quality (IAQ), Yu et al. (Yu et al., 2016) put forward the air purification Trombe wall with catalytic coatings in the duct, aiming to deal with indoor air pollution like volatile organic compounds (VOCs) through photocatalytic (PC) oxidation reaction (Yu etal., 2018) and thermal-catalytic (TC) oxidation reaction (Yu et al., 2017). Besides, a novel concentrating PC-TC-PV-Trombe wall system was investigated by Gao et al. (Gao et al., 2022), in which the photocatalyst was coated on the compound parabolic concentrator while the thermal catalyst was coated on the absorber. The results revealed that with a daily photoelectrical conversion efficiency of 6.68%, the thermal efficiency was 0.36 and 0.26 for the PC and TC channel while the single-pass formaldehyde degradation ratio was 0.25-0.56 and 0.18-0.38, respectively.

The proposal of air purification PV-Trombe opened up new horizons in this field, making human health apart from thermal comfort of built environment become the focus of research. In addition to VOCs, bioaerosols containing microbial pathogens which may spread diseases also pose a severe challenge to public health security (Song et al., 2022). Taking the recent outbreak of the Corona Virus Disease 2019 (COVID-19) for example, aerosol transmission of severe acute respiratory syndrome coronavirus 2 (SARS-CoV-2) has been shown to be an important pathway (Yao et al., 2020), especially in poor ventilated and/or crowded indoor settings (Lewis, 2022). Nevertheless, most viruses and bacteria cannot survive under high temperatures and their lifetimes decrease rapidly with the increase of exposure temperature (Yap et al., 2020, Mastwijk et al., 2017), which makes it possible to inactivate the bioaerosols by exposure to high temperature but short time conditions (Grinshpun et al., 2010) and thus can be integrated with solar heating systems. To this end, Yu et al. recently have explored the feasibility of thermal sterilization for five kinds of bacteria (Yu et al., 2021) and three kinds of viruses (Xie et al., 2021) in the heating process of Trombe wall.

For the systems mentioned above, due to the short residence time for the bioaerosols passing through the duct, a high temperature isindispensable in order to inactivate the viruses and bacteria. However, such a process will not last long during the operation of a PV-Trombe wall system. Then, it is of necessity to seek other measures such as the complement of thermal sterilization for ensuring the purification performance over the whole period of system operation. As a common method for airborne particles removal, air filtration technology is widely applied in HVAC systems due to low cost and convenient operation (Choi et al., 2015). But it should be noted that even though bioaerosols are captured by an air filter, microbes may still survive and be resuspended into the air stream under appropriate conditions, putting the filter at a risk of becoming a secondary source of pollutant (Choi et al., 2018). The combination of filtration and thermal sterilization provides a strategic direction to solve this problem (Wang et al., 2023b), considering that thermal sterilization has long been regarded as an effective way to cope with microorganisms which is featured by easy operation and no secondary pollution (Lee and Lee, 2006). Wang et al. (Wang et al., 2018) fabricated an iron oxide nanowires-based filter which demonstrated a log inactivation efficiency of > 7 within 10 seconds towards the bacteria *Staphylococcus epidermidis* with filter temperature reaching 70°C and emphasized the important role Joule heating played in inactivating the bacteria. Although these antimicrobial filters were demonstrated to be effective in preventing proliferation of filtered bacteria, the thermal sterilization process driven by Joule heating effect resulted in large energy consumption.

In this study, an air filtration and sterilization PV-Trombe wall system was proposed, which could realize power generation, air heating and purification through utilization of solar energy. The combination of filtration and solar-driven thermal sterilization in this study was intended to explore an effective and energy-saving method for dealing with indoor bioaerosols. It not only improved the purification performance for Trombe wall at low solar irradiance but also reduced the energy demand for disinfecting the filter. Besides, a predictive model for describing the thermal stability of aerosolized *Klebsiella pneumoniae* was established and validated, which also filled the research gap concerning thermal inactivation model for bacteria in the media of aerosol. This article mainly includes: (1) configuration and principle of the proposed system, (2) set up of the experimental system and derivation of the inactivation model, (3) establishment of the system model, (4) evaluation of the system performance. (5) parametric study on the impact of PV coverage ratio and air velocity.

2. MATERIALS AND METHODS
2.1. System description

The concept of the air filtration and thermal inactivation PV-Trombe wall is proposed here, which is able to realize power generation, air heating and purification through utilization of solar energy. As shown in the schematic diagram (Figure 1), the proposed system is mainly composed of a glass cover, an air cavity, an absorber plate with PV cells laminated on the front surface, an air duct, a back plate, an insulation layer, a massive wall, a medium efficiency fibrous filter, a circulation fan and several vents. Due to the pressure drop of air stream through the filter, a circulation fan is installed at the outlet of the duct to ensure the flow of air.
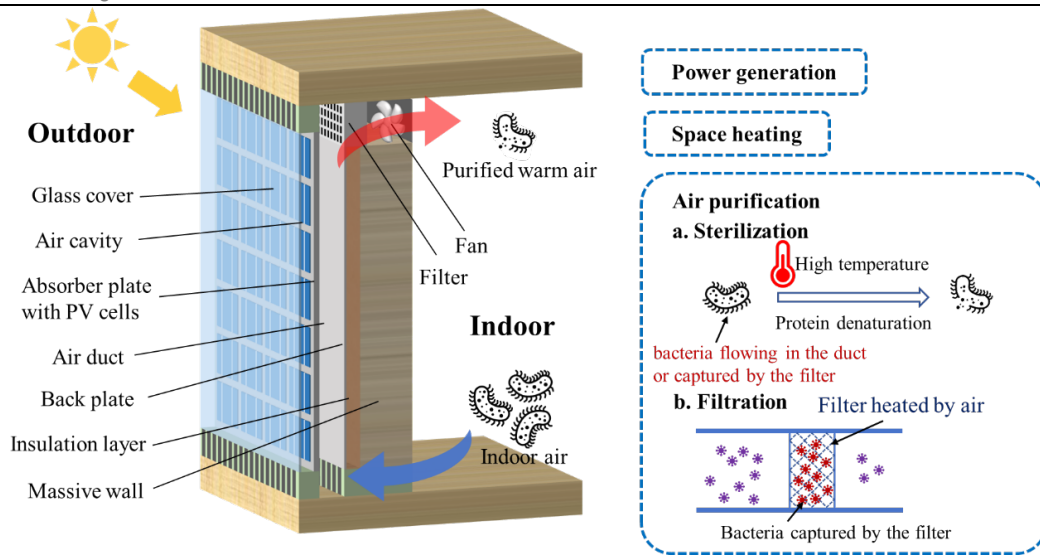
Figure 1: Concept of the novel disinfected PV-Trombe wall based on air filtration and thermal inactivation

Considering that an indoor environment with poor ventilation is usually formed in winter to reduce heating load, which increases the risk of aerosol transmission, the proposed system for air heating and purification is supposed to be of great use especially in the heating season. The operation principle is explained below. When hitting the system, the solar radiation transmits the glazing and is absorbed by the absorber plate with PV cells, of which a small amount is converted to electricity by the PV cells while a large amount is transformed to thermal energy. After that, heat is transferred from the absorber plate to the air in the duct through forced convection driven by the circulation fan. In this period, the indoor air containing bioaerosols flows into the duct, gets heated to a much higher temperature and passes through the filter before entering the room, making it possible to purify the air through thermal inactivation and filtration. When exposed to the high temperatures in the duct, a part of the bacteria is inactivated within a short time due to thermal inactivation. After that, a large portion of the surviving bacteria is captured by the filter installed at the outlet of the duct and then is rapidly inactivated by continuous exposure to the heated air, thus reducing the chance for the filter to become a potential pollution source. As a result, power generation, air heating and purification are achieved simultaneously. The detailed parameters for each component of the system are presented in *Table 1*.

Table 1: Detail parameters for the novel air filtration and sterilization PV-Trombe wall system

Component	Parameter	Value	Unit
Glass cover	Density	2200	kg/m^3
	specific heat capacity	750	$J/(kg·K)$
	Thickness	0.003	m
	thermal conductivity	1.4	$W/(m·K)$
	Absorptivity	0.1	-
	Emissivity	0.88	-
	Transmissivity	0.9	-
PV cells	reference efficiency	0.2	-
	temperature coefficient	0.0045	-/K
	coverage ratio	0.6	-
	Absorptivity	0.92	-
	Emissivity	0.75	-
Absorber plate	Density	2700	kg/m^3
	specific heat capacity	902	$J/(kg·K)$
	Thickness	0.001	m
	thermal conductivity	236	$W/(m·K)$
	Emissivity	0.12	-
	Absorptivity	0.95	-
Air duct	Height	2.6	m
	Width	1	m
	Thickness	0.04	m
Back plate	Density	2700	kg/m^3
	specific heat capacity	840	$J/(kg·K)$
	Thickness	0.001	m
	thermal conductivity	236	$W/(m·K)$
	Emissivity	0.4	-
Massive wall	Density	1800	kg/m^3
	specific heat capacity	840	$J/(kg·K)$
	Thickness	0.3	m
	thermal conductivity	0.814	$W/(m·K)$
Insulation layer	thermal conductivity	0.046	$W/(m·K)$
	Thickness	0.05	m
Pleated filter	Height	0.1	m
	Width	0.6	m
	Thickness	0.05	m

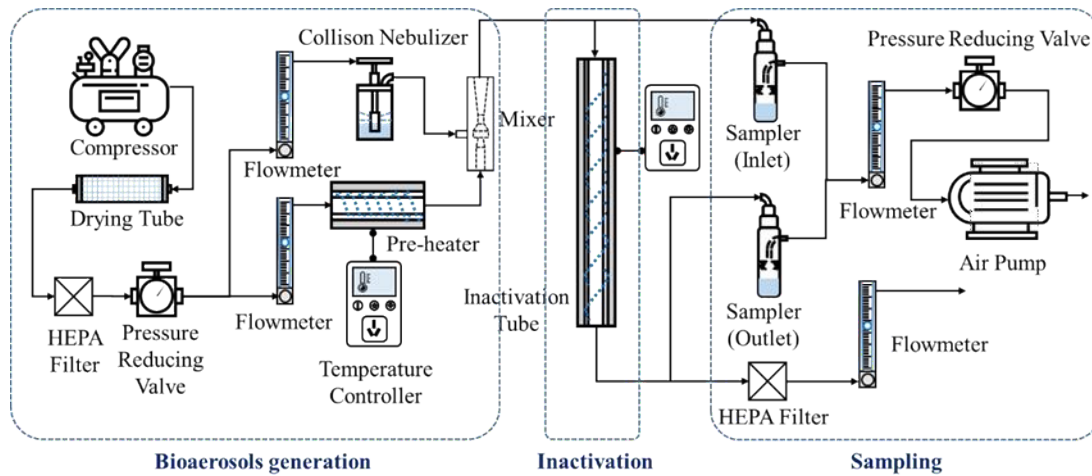| media thickness | 430 | µm |
| fiber diameter | 4.15 | µm |
| packing density | 0.00757 | - |

2.2. Experiment

Figure 2: Schematic diagrams of the experimental set up for determining the inactivation model

To explore the feasibility of inactivating indoor bioaerosols by exposure to high temperature environment, experiments concerning aerosolized bacteria, including *Escherichia coli* (*E. coli*) (ATCC 25922) and *Staphylococcus aureus* (*S. aureus*) (ATCC 29213) were designed and conducted. The experiments were carried out in a Biological Safety Level 2 laboratory at Department of Infection Control, the First Affiliated Hospital of USTC from September to November 2023. During the experiments, the indoor temperature and relative humidity were about 25°C and 50%, respectively. This study mainly focused on investigating the thermal inactivation effect at the medium temperature range of 45°C -120°C and the residence time of several seconds, which commonly occurred in solar air heating systems integrated with buildings like Trombe wall. The schematic diagram w*as* shown in *Figure 2*. As illustrated by the schematic, the experimental system included three major parts:

Generation of bioaerosols

In this study, the gram-negative bacteria *E. coli* as well as the gram-positive bacteria *S. aureus* were chosen to characterize the thermal sterilization performance. The bacterial suspension was prepared with bacterial turbidity meter (WGZ-XT, Hangzhou Qi Wei Instrument Co., Ltd., China) to reach the concentration of 1 MCF (McFarland), which was equal to 3×10^8 colony forming unit per millilitre (CFU/mL). After that, a 2 mL bacterial suspension was diluted with 0.85% NaCl solution to 40 mL and then was atomized to aerosols of 0.2-3 µm by a 6-Jet Collison Nebulizer (NSF-6A, Shanghai TOW Intelligent Technology Co., Ltd., China) at the flow rate of 5 L/min. Before entering the inactivation tube, the air flow carrying bacterial bioaerosols was mixed with a dry, filtered, preheated air flow to reach the temperature of 25°C and the relative humidity of 30%.

Thermal inactivation of bioaerosols

The electric heating system mainly consisted of quartz tubes (length: 1 m; thickness: 2mm; inner diameter: 3cm and 6 cm) winded with heating tapes and covered with insulation materials. In addition, a temperature controller was employed to ensure that the designed wall temperature of the quartz tube (which was set as 45°C, 60°C, 80°C, 100°C and 120°C in this study) was reached in the experiment. Besides, the impact of residence time on the inactivation process was investigated through changing tubes with different diameters or adjusting the flow rate of diluted air and then the residence time was estimated to be several seconds. The air temperature at the inlet and the outlet were measured with T-type thermocouples.

Sampling of bioaerosols and determination of survival ratio

Two liquid impinger type samplers (LL225-9595, Qingdao Loobo Environmental Protection Technology Co., Ltd., China) were employed to sample the bioaerosols before and after the thermal inactivation process for determining the survival ratio. The samplers each with 20 mL 0.85% NaCl solution were operated under the nominal flow rate of 12.5 L/min for 5 min with the assistance of a vacuum pump. After the sampling process, the aliquots of 0.1 mL of suspensions in the inlet and outlet samplers were respectively pipetted and spread on the Columbia Agar Medium and then were incubated at 37°C for 24 h to form colonies on the plate for further colony count. The survival ratio of bioaerosols was defined in Equation 1, which was calculated by dividing the colony count forming on the plate inoculated from the outlet sampler by that inoculated from the inlet sampler.

Equation 1: Determination of survival ratio.

$$S = \frac{C_{out}}{C_{in}}$$

Where:

- S = survival ratio of aerosolized bacteria after exposure to thermal energy
- C_{out} = outlet bacterial concentration (CFU/m^3)
- C_{in} = inlet bacteria concentration (CFU/m^3)

2.3. System model and criteria for performance evaluation

Due to lack of experimental conditions for field test of the whole system, simulation has been conducted to evaluate the system performance. The mathematical model mainly includes the heat transfer model and the mass balance model. Besides, the criteria for evaluating the system performance are given at the last of this section. Assumptions have been made for the purpose of simplifying the mathematical model, which are listed below: (1) thermophysical properties are regarded as constant; (2) the heat dissipation at edges are neglected then the boundary conditions are set to be adiabatic unless otherwise stated; (3) the temperature gradients of flowing air, back plate and massive wall are considered to be one dimensional; (4) the deposition loss at the passage of the duct and the activity loss of bacterial aerosols when being caught by the filter are negligible; (5) the bioaerosols existing in the air and captured by the filter share the same thermal sensitivity; (6) the temperature of the filter is identical to the air outlet temperature of the duct; (7) the impact of dust load on the pressure drop and filtration efficiency of filter is ignored here.

Heat transfer model

The heat transfer model includes the energy balance equations for the glass cover, the PV-absorber plate, the flowing air, the back plate and the massive wall. Since these equations have been described in many published literatures (Yu et al., 2022, Xie et al., 2021), they will not be reiterated here.

Mass transfer model

During the operation of the proposed system, the indoor air containing bioaerosols is first sucked into the duct, afterwards passes through the filter. Then, the mass balance model is accordingly split into two parts.

For the heat inactivation process happening in the air duct, if the first order inactivation model is applied, the mass balance equation is expressed as

Equation 2: Mass balance equation for bioaerosols in the duct.

$$\frac{\partial C}{\partial t} = -V_{air}\frac{\partial C}{\partial y} - kC$$

Where:

- C = bacterial concentration (CFU/m^3)
- V_{air} = air velocity in the duct (m/s)
- k = rate constant (1/s)

Considering that the Arrhenius equation is often employed to describe the thermal inactivation process of microbes (Yap et al., 2020), the temperature dependence of the rate constant is then expressed expressed as:

Equation 3: Arrhenius equation for determining the temperature dependence of rate constant.

$$k = A exp\left(-\frac{E_a}{RT}\right)$$

Where:

- A = pre-exponential factor
- E_a = activation energy for thermal sterilization (kJ·mol^{-1})
- R = universal gas constant (8.314 J·mol^{-1}K^{-1})
- T = air temperature (K)

Assuming that the temperature of the filter has the same value as that of the air outlet temperature, the mass balance equation for bacterial quantity at the filter is written as:

Equation 4: Mass balance equation for filtered bioaerosols.

$$\frac{\partial N}{\partial t} = QC_{out}\eta_{filt} - kN$$

Where:

- N = bacterial quantity on the filter (CFU)
- Q = volumetric flow rate of air (m^3/s)
- η_{filt} = filtration efficiency of the filter

Criteria for performance evaluation

Since power generation, air heating and purification are achieved at the same time in the proposed system, the criterions for performance evaluation should be selected with these three aspects taken into consideration accordingly.

The electrical efficiency is defined as the ratio of the net generated power to the solar radiation received by the solar cells:

Equation 5: Definition of electrical efficiency.
$$\eta_{ele} = \frac{E_{PV}}{GA_{PV}}$$

Where:

- η_{ele} = electrical efficiency
- E_{PV} = generated electrical power by PV cells (W)
- G = solar irradiance (W/m^2)
- A_{PV} = aera of PV cells (m^2)

The thermal efficiency is calculated by dividing the heat transferred to the flowing air by the solar radiation received by the collector, which is presented as:

Equation 6: Definition of the thermal efficiency.
$$\eta_{th} = \frac{\rho_{air} c_{air} Q \left(T_{air,out} - T_{air,in} \right)}{GA_c}$$

Where:

- η_{th} = thermal efficiency
- ρ_{air} = density of air (kg/m^3)
- c_{air} = specific heat capacity of air (kJ·kg^{-1}·K^{-1})
- A_c = aera of the collector (m^2)

As to the criteria for evaluating the air purification performance, the single-pass purification efficiency is the ratio of the bioaerosols purified during the passage through the duct and the filter while the total volume of clean air can be regarded as the volume of fresh air introduced into the room and can be calculated by:

Equation 7: Definition of the single-pass purification efficiency.
$$\eta_{pur} = \frac{C_{sys,in} - C_{sys,out}}{C_{sys,in}}$$

Where:

- η_{pur} = single-pass purification efficiency
- $C_{sys,in}$ = bacterial concentration at the inlet of the system (CFU/m^3)
- $C_{sys,out}$ = bacterial concentration at the outlet of the system (CFU/m^3)

Equation 8: Definition of the total volume of clean air production.
$$V_{clean} = \int Q\eta_{pur} dt$$

3. RESULTS AND DISCUSSION
3.1. Experimental results and inactivation model

The experiments concerning the thermal inactivation of aerosolized *E. coli* and *S. aureus* were carried out in a Biological Safety Level 2 laboratory at Department of Infection Control, the First Affiliated Hospital of USTC from February to April 2024. To investigate the thermal inactivation process under different temperatures, the wall temperature of the inactivation tube was set to 45°C, 60°C, 80°C, 100°C and 120°C. As to the effect of residence time, it was studied by adjusting the volume flow rate (Q = 21.5 L/min and Q = 9.5L/min) as well as replacing inactivation tubes with different diameters (d = 3 cm and d = 6 cm). The approximate residence time for the four cases was 1.5 s, 3 s, 6 s and 12 s, respectively. It should be noted that the volume flow rate here was corrected by the operation pressure so that it could be less than the nominal sampling flow rate (12.5 L/min). Besides, for determining the survival

ratio of bioaerosols at each operation condition, the bacterial recovery experiment was performed no less than three times.
The survival ratios of aerosolized *E. coli* and *S. aureus* after passing through the inactivation tube were plotted in Figure 3: The survival ratios of aerosolized (a) E. coli and (b) S. aureus after the thermal exposure. It was clear that both the elevated exposure temperature and prolonged residence time contributed to an obvious decrease in the survival ratio of bioaerosols. Besides, it could be inferred that the gram-negative bacteria (*E. coli*) tended to possess lower thermal resistance than gram-positive bacteria (*S. aureus*). Similar phenomena were also observed in the UV-induced decay reported by Wang et al. (Wang et al., 2023a). It was observed that gram-negative bacteria were more susceptible to UV treatment than gram-positive bacteria, which could be attributed to their differences in the cell envelope (Silhavy et al., 2010). The bacteria cell envelope is a complex multilayered structure that serves to protect these organisms from their unpredictable and often hostile environment. Gram-positive bacteria usually possess a thick cell wall (20-80 nm) as outer shell of the cell while gram-negative bacteria have a relatively thin layer of cell wall (<10 nm), thus resulting in their different responses to external stresses (Mai-Prochnow et al., 2016). For the gram-negative bacteria *E. coli*, 20% bacteria could be inactivated even at the wall temperature of 45°C. However, for the gram-positive bacteria *S. aureus*, there was no obvious decrease in the single-pass survival ratio until the wall temperature reached 80°C. Even under the wall temperature of 120°C, nearly 40% of *S. aureus* could survive the 12-second thermal exposure, under which case over 99% of *E. coli* were inactivated.
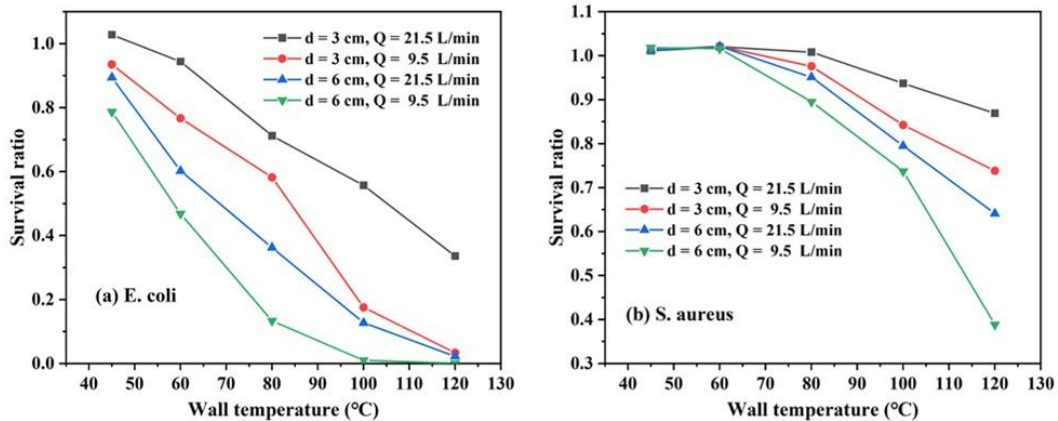

Figure 3: The survival ratios of aerosolized (a) E. coli and (b) S. aureus after the thermal exposure

With the experimental results, the inactivation model was derived on the basis of the first-order kinetic model and Arrhenius equation. The identified model parameters were presented in Table 2. The root mean square error (RMSE) for the two types of bacteria were 0.0491 and 0.0467, indicating that the survival ratio predicted by the model corresponded well with that observed in the experiment. Then, the inactivation model was used for the performance analysis in the following section.

Table 2: The identified model parameters *for* thermal inactivation based on the first-order kinetic model and Arrhenius equation

Bacteria type	ln(A) (1/s)	Ea/R (K)	Root mean square error
Escherichia coli	22.38	8182	0.0491
Staphylococcus aureus	22.25	9203	0.0467

3.2. Performance evaluation

To simulate the performance of the proposed system, weather data within heating season on February 20, 2023, in Hefei is employed, which was a sunny day with maximum irradiance on the south facade approximately 700 W/m^2. Besides, the average ambient temperature and the average global solar irradiance were 13.5°C and 529 W/m^2, respectively.

The electrical and thermal performance of the proposed system was shown in Figure 4. The left figure presented the variation trends of electrical efficiency and generated power. Similar to the variation trend of solar irradiance, the generated power increased at first and then dropped, with the maximum generated power reaching 140 W. By contrast, the variation of the electrical efficiency presented an opposite trend due to the adverse impact imposed by the increased cell temperature on the conversion efficiency. During the operation, the average electrical efficiency was 0.142 while the generated power was 117 W. As to the thermal performance, owing to the high solar irradiance and low mass flow rate in the duct, the air was able to be heated to about 70°C, which was advantageous for the thermal sterilization of bioaerosols but exerted an adverse impact on the thermal efficiency. Due tothe high operation temperature, the heat loss from the system to the ambient environment was considerable, leading to the average thermal efficiency being approximately 0.226.
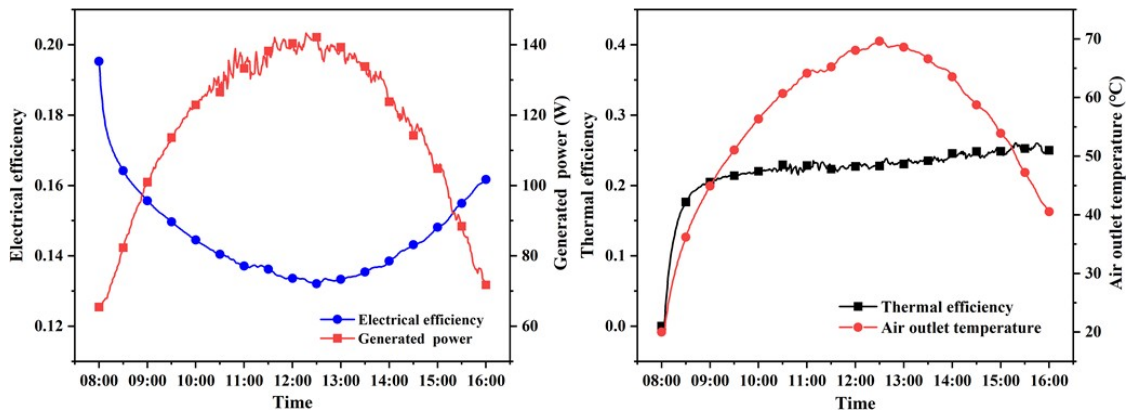
Figure 4: The electrical and thermal performance of the system

Assuming that the diameter of the bioaerosol was 1 μm and the air velocity in the duct was 0.2 m/s, the calculated single-pass purification efficiency for aerosolized bacteria E. coli and S. aureus was plotted in Figure 5. The red curves in the figure presented the purification performance purely depending on the thermal sterilization effect while the black curves represented the combined effect of thermal sterilization and air filtration. It was shown that at most 60% of *E. coli* could be inactivated in a single pass by exposure to thermal energy while the ratio for *S. aureus* was only about 4%, due to the difference of thermal resistance between gram-negative bacteria and gram-positive bacteria. Besides, when the filter was used, the single-pass purification ratio for *E. coli* and *S. aureus* could be lifted up to over 0.8 and 0.6, indicating that the employment of filter could improve the purification performance significantly especially at times with low solar irradiance and for bacteria with high thermal resistance. During the operation of the system, the total volume of clean air production was 177.7 m^3 and 143.4 m^3 for *E. coli* and *S. aureus*, respectively.
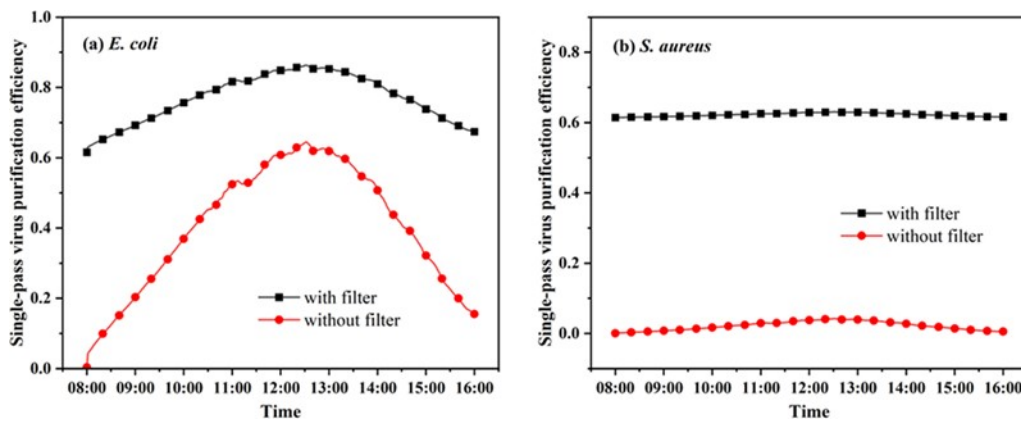

Figure 5: The variation of single-pass purification efficiency for (a) E. coli and (b) S. aureus

Even though filters were effective and were widely used in HVAC systems, indoor bioaerosols accumulating on them may be able to multiply under certain conditions, thus making themselves become a source of bioaerosols (Yoon et al., 2008). Therefore, safety disposals for filters should not be ignored. Considering thermal sterilization is an effective and safe method for disinfecting bioaerosols, the filter in the proposed system was placed at the outlet of the duct, so that the heated air traveling through could maintain the filter at a relatively high temperature, which provided the condition for the captured bacteria to be sterilized by heat. When the inlet bacterial concentration was set as 1000 CFU/m^3, the bacterial quantity on the filter was plotted in Figure 6. For the filter placed at the inlet, which was not heated by the air, the bacterial quantity on the filter rose rapidly to a high level. By contrast, when the filter was positioned at the outlet, as the air outlet temperature climbed up, the bacterial quantity on the filter started to decreasedue to the extended exposure time at high temperatures. Besides, the bacterial quantity of the filter was kept at a low level for mostof the time during the operation of the system, thus inhibiting the proliferation of the captured bioaerosols and reducing the possibility for the filter of becoming a secondary pollution source.
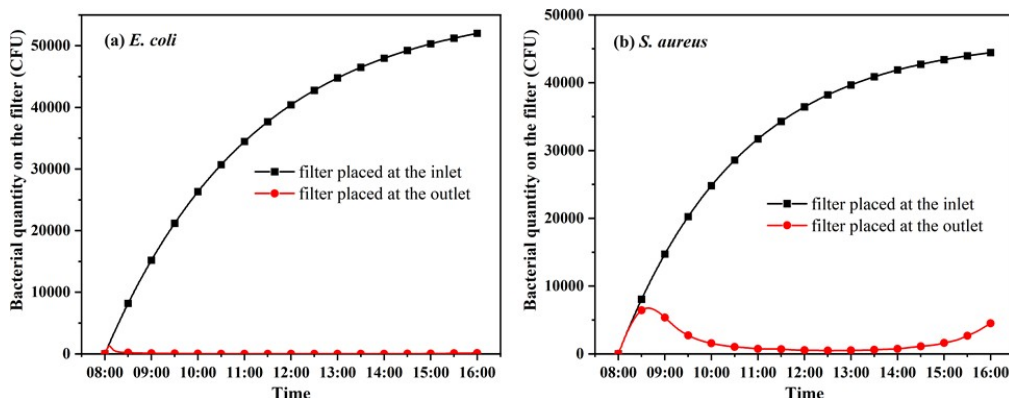

Figure 6: The variation of bacteria quantity on the filter for (a) E. coli and (b) S. aureus

4. CONCLUSION

A novel air filtration and sterilization PV-Trombe wall system for power generation, air heating and purification was proposed. A continuous flow experiment rig was established and tested to determine the inactivation model of gram-negative bacteria E. coli and gram-positive bacteria S. aureus in aerosol. Besides, the mathematical model of the system including heat and mass transfer was established, on the basis of which the performance analysis was carried out. To conclude, the main results are listed below:

- According to the experimental results, after the 3-second exposure to thermal energy with wall temperature of 45°C, 60°C, 80°C, 100°C and 120°C, the survival ratio for the gram-negative bacteria *E. coli* was 0.935, 0.767, 0.582, 0.175, 0.033 while the survival ratio for the gram-positive bacteria *S. aureus* was 1.000, 1.000, 0.96, 0.842, 0.738, indicating that gram-positive bacteria possessed higher thermal resistance than gram-negative bacteria.
- With the experimental data, the inactivation model was derived based on the first kinetic model and Arrhenius equation. The survival ratio predicted by the inactivation model corresponded well with the experimental results with the root mean square error being 0.0491 and 0.0467 for *E. coli* and *S. aureus*, respectively.
- In the simulation, when the average ambient temperature and the solar irradiance were 13.5°C and 529 W/m^2, the electrical and thermal efficiencies of the proposed system were 0.142 and 0.226 respectively. Besides, the maximum air outlet temperature was about 70°C, providing good condition for thermal sterilization of both airborne and filtered bacteria.
- The usage of filter could drastically enhance the purification performance with the single-pass purification efficiency increased from 0.6 and 0.04 to 0.8 and 0.6 for *E. coli* and *S. aureus*, respectively. Besides, the corresponding total volume of clean air production was 177.7 m^3 and 143.4 m^3 for the two kinds of bacteria.
- Due to the thermal sterilization effect, the bacterial quantity of the filter at the outlet was kept at a low level for most of the time during the operation of system, thus preventing the filter from becoming a potential secondary pollution source.

In the present work, air filtration and thermal sterilization were combined and integrated with the PV-Trombe wall system. Compared with self-sterilization filters depending on Joule heating effect, the utilization of solar energy made the system more energy-efficient and could be applied to most filters available at the market. Then, not only did the proposed system reduce the energy demand for HVAC in buildings, but also it improved the indoor environment with both air heating and purification taken into consideration, thus providing a new approach to the multiple utilization of solar energy. However, to achieve a deeper understanding of the thermal sterilization process that happened in the duct and at the filter, further experimental studies concerning the inactivation of different kinds of bioaerosols either in the air or at the filter need to be conducted. Besides, if condition permits, field test of the whole system should be conducted in the future work.

5. REFERENCES

CHOI, D. Y., HEO, K. J., KANG, J., AN, E. J., JUNG, S. H., LEE, B. U., LEE, H. M. & JUNG, J. H. 2018. Washable antimicrobial polyester/aluminum air filter with a high capture efficiency and low pressure drop. J Hazard Mater, 351, 29-37.

CHOI, J., YANG, B. J., BAE, G. N. & JUNG, J. H. 2015. Herbal Extract Incorporated Nanofiber Fabricated by an Electrospinning Technique and its Application to Antimicrobial Air Filtration. ACS Appl Mater Interfaces, 7, 25313-20.

GAO, R., HE, W., LIU, X., HU, Z., YU, H. & WANG, K. 2022. The performance analysis of a novel photocatalytic-thermal-catalytic-photovoltaic-Trombe wall system integrated with compound parabolic concentrator. Building and Environment, 221.

GRINSHPUN, S. A., ADHIKARI, A., LI, C., YERMAKOV, M., REPONEN, L., JOHANSSON, E. & TRUNOV, M. 2010. Inactivation of Aerosolized Viruses in Continuous Air Flow with Axial Heating. Aerosol Science and Technology, 44, 1042-1048.

HU, Z., HE, W., JI, J. & ZHANG, S. 2017. A review on the application of Trombe wall system in buildings. Renewable and Sustainable Energy Reviews, 70, 976-987.

LEE, Y. H. & LEE, B. U. 2006. Inactivation of Airborne E. coli and B. subtilis Bioaerosols Utilizing Thermal Energy. Journal of Microbiology and Biotechnology, 16, 1684-1689.

LEWIS, D. 2022. Why the WHO took two years to say COVID is airborne. Nature, 604.

MAI-PROCHNOW, A., CLAUSON, M., HONG, J. & MURPHY, A. B. 2016. Gram positive and Gram negative bacteria differ in their sensitivity to cold plasma. Scientific Reports, 6.

MASTWIJK, H. C., TIMMERMANS, R. A. H. & VAN BOEKEL, M. 2017. The Gauss-Eyring model: A new thermodynamic model for biochemical and microbial inactivation kinetics. Food Chem, 237, 331-341.

SILHAVY, T. J., KAHNE, D. & WALKER, S. 2010. The bacterial cell envelope. Cold Spring Harb Perspect Biol, 2, a000414.

SONG, L., ZHOU, J., WANG, C., MENG, G., LI, Y., JARIN, M., WU, Z. & XIE, X. 2022. Airborne pathogenic microorganisms and air cleaning technology development: A review. Journal of Hazardous Materials, 424.

WANG, D., ZHU, B., HE, X., ZHU, Z., HUTCHINS, G., XU, P. & WANG, W.-N. 2018. Iron oxide nanowire-based filter for inactivation

of airborne bacteria. Environmental Science: Nano, 5**,** 1096-1106.

WANG, M. H., ZHANG, H. H., CHAN, C. K., LEE, P. K. H. & LAI, A. C. K. 2023a. Experimental study of the disinfection performance of a 222-nm Far-UVC upper-room system on airborne microorganisms in a full-scale chamber. Building and Environment, 236.

WANG, W., ZHAO, S., TANG, X., CHEN, C. & YI, H. 2023b. Electrothermal catalysis for heterogeneous reaction: Mechanisms and design strategies. Chemical Engineering Journal, 455.

XIE, H., YU, B., WANG, J. & JI, J. 2021. A novel disinfected Trombe wall for space heating and virus inactivation: Concept and performance investigation. Applied Energy, 291.

YAO, M., ZHANG, L., MA, J. & ZHOU, L. 2020. On airborne transmission and control of SARS-Cov-2. Sci Total Environ, 731**,** 139178.

YAP, T. F., LIU, Z., SHVEDA, R. A. & PRESTON, D. J. 2020. A predictive model of the temperature-dependent inactivation of coronaviruses. Applied Physics Letters, 117.

YOON, K. Y., BYEON, J. H., PARK, C. W. & HWANG, J. 2008. Antimicrobial Effect of Silver Particles on Bacterial Contamination of Activated Carbon Fibers. Environmental Science & Technology, 42**,** 1251-1255.

YU, B., HE, W., LI, N., WANG, L., CAI, J., CHEN, H., JI, J. & XU, G. 2017. Experimental and numerical performance analysis of a TC-Trombe wall. Applied Energy, 206**,** 70-82.

YU, B., HE, W., LI, N., YANG, F. & JI, J. 2016. Thermal catalytic oxidation performance study of SWTCO system for the degradation of indoor formaldehyde: Kinetics and feasibility analysis. Building and Environment, 108**,** 183-193.

YU, B., HOU, J., HE, W., LIU, S., HU, Z., JI, J., CHEN, H. & XU, G. 2018. Study on a high-performance photocatalytic-Trombe wall system for space heating and air purification. Applied Energy, 226**,** 365-380.

YU, B., LI, N., XIE, H. & JI, J. 2021. The performance analysis on a novel purification-cleaning trombe wall based on solar thermal sterilization and thermal catalytic principles. Energy, 225.

YU, B., LI, N., YAN, C., LIU, X., LIU, H., JI, J. & XU, X. 2022. The comprehensive performance analysis on a novel high-performance air-purification-sterilization type PV-Trombe wall. Renewable Energy, 182**,** 1201-1218.